Reconciliation of local and long-range tilt correlations in underdoped $La_{2-x}Ba_xCuO_4$ $(0 \leqslant x \leqslant 0.155)$

Emil S. Bozin,[1,*] Ruidan Zhong,[1,2] Kevin R. Knox,[1] Genda Gu,[1] John P. Hill,[1] John M. Tranquada,[1] and Simon J. L. Billinge[1,3]

[1]*Department of Condensed Matter Physics and Materials Science, Brookhaven National Laboratory, Upton, New York 11973, USA*
[2]*Materials Science and Engineering Department, Stony Brook University, Stony Brook, New York 11790, USA*
[3]*Department of Applied Physics and Applied Mathematics, Columbia University, New York, New York 10027, USA*

A long-standing puzzle regarding the disparity of local and long-range CuO_6 octahedral tilt correlations in the underdoped regime of $La_{2-x}Ba_xCuO_4$ is addressed by utilizing complementary neutron powder diffraction and inelastic neutron scattering (INS) approaches. This system is of interest because of the strong depression of the bulk superconducting transition at $x = 1/8$ in association with charge and spin stripe order. The latter unidirectional order is tied to Cu-O bond-length anisotropy present in the so-called low-temperature tetragonal (LTT) phase. On warming, the lattice exhibits two sequential structural transitions, involving changes in the CuO_6 tilt pattern, first to the low-temperature orthorhombic (LTO) and then the high-temperature tetragonal (HTT) phase. Despite the changes in static order, inspection of the instantaneous local atomic structure suggests that the LTT-type tilts persist through the transitions. Analysis of the INS spectra for the $x = 1/8$ composition reveals the dynamic nature of the LTT-like tilt fluctuations within the LTO and HTT phases. Within the low-temperature phase, the Cu-O bond-length splitting inferred from lattice symmetry and fitted atomic position parameters reaches a maximum of 0.3% at $x = 1/8$, suggesting that electron-phonon coupling may contribute to optimizing the structure to stabilize stripe order. This splitting is much too small to be resolved in the pair distribution function, and in fact we do not resolve any enhancement of the instantaneous bond-length distribution in association with stripe order. This study exemplifies the importance of a systematic approach using complementary techniques when investigating systems exhibiting a large degree of complexity and subtle structural responses.

I. INTRODUCTION

Since the discovery of high-temperature superconductivity in $La_{2-x}Ba_xCuO_4$ [1], the connection between the lattice and electronic structures has been the subject of considerable attention [2,3]. The further discovery [4] of the "1/8 anomaly"—a dramatic dip in the superconducting transition temperature T_c at the dopant concentration of $x = 1/8$—motivated careful powder diffraction studies of the structural phase diagram [5–8]. The latter revealed a low-temperature transition (∼60 K) to a crystal structure with inequivalent Cu-O bonds in orthogonal directions within the CuO_2 planes. It is this structural anisotropy, associated with a particular pattern of tilts of the CuO_6 octahedra, that pins charge stripes [9,10]. While the charge stripes are compatible with superconducting correlations within the CuO_2 planes [11,12], the 90° rotation of the structural anisotropy from one layer to the next leads to frustration of the interlayer Josephson coupling and the depression of the onset of bulk superconducting order [13,14].

Given the strong response of the electronic properties to the crystal symmetry, it is of considerable interest to understand the nature of the structural transitions in $La_{2-x}Ba_xCuO_4$. Both powder [8,15] and single-crystal [16–18] diffraction studies clearly demonstrate that the transition to the low-temperature structure, involving a change in tilt direction of the CuO_6 octahedra, is of first order. A surprisingly different perspective is given by a pair-distribution-function (PDF) analysis of neutron scattering measurements [19]. In the latter analysis, the local structure appears to be unaffected by warming through

the transition, retaining the low-temperature tilt pattern to higher temperatures. That picture is supported by an x-ray absorption fine structure (XAFS) study [20]. Furthermore, the local tilts appear to remain in the high-temperature phase where the average tilts are zero [20–22]. The aim of the present paper is to resolve the apparent conflict between local and long-range measures of tilt correlations in $La_{2-x}Ba_xCuO_4$.

In terms of the symmetry of the average structure, the thermal sequence of structural transitions is well understood [23]. The high-temperature tetragonal (HTT) phase (space group $I4/mmm$) has the highest symmetry, with no octahedral tilts (see Table I and Fig. 1); here, the in-plane lattice parameters, $a_t = b_t$, correspond to the shortest Cu-Cu distance. On cooling, there is a second-order transition to the low-temperature orthorhombic (LTO) phase (space group $Bmab$), involving tilts of the CuO_6 octahedra about $[110]_t$ axes of the HTT phase; as nearest-neighbor octahedra must rotate in opposite directions, the unit cell volume increases by a factor of two, with $a_o \approx b_o \approx \sqrt{2}a_t$. (This is the structure of $La_{2-x}Sr_xCuO_4$ in the superconducting phase [24].) Further cooling leads to a second transition involving a change in the octahedral tilt axis towards the $[100]_t$ and $[010]_t$ directions. When the shift in the tilt axis is complete, the structure is the low-temperature tetragonal (LTT; space group $P4_2/ncm$), while a partial shift results in the low-temperature less-orthorhombic (LTLO; space group $Pccn$); in both cases, the unit cell size is the same as for LTO.

For charge ordering, the key distinction among these different phases is the degree of symmetry among the Cu-O bonds. The tilt pattern in the LTO phase leaves the Cu-O bonds in (approximately) orthogonal directions equivalent; we will

---

TABLE I. Wyckoff positions for atomic sites in each of the structural phases, which are identified by acronym and space group. We distinguish between cases where orthogonal Cu-O(1) bonds are equivalent (OE) or inequivalent (OI); note that all O(1) sites are equivalent in OE phases, but that there are two inequivalent O(1) sites in the OI phases. Relative to the HTT phase, the other structures have a doubled unit cell volume.

	HTT $I4/mmm$ OE	LTO $Bmab$ OE	LTLO $Pccn$ OI	LTT $P4_2/ncm$ OI
Cu	2(a): 0, 0, 0	4(a): 0, 0, 0	4(a): 0, 0, 0	4(d): 0, 0, 0
O(1)	4(c): 0, $\frac{1}{2}$, 0	8(e): $\frac{1}{4}$, $\frac{1}{4}$, z	4(c): $\frac{1}{4}$, $\frac{1}{4}$, z 4(c): $\frac{1}{4}$, $\frac{3}{4}$, z	4(e): $\frac{1}{4}$, $\frac{1}{4}$, z 4(e): $\frac{1}{4}$, $\frac{3}{4}$, 0
La, Ba, O(2)	4(e): 0, 0, z	8(f): 0, y, z	8(e): x, y, z	8(i): x, x, z

denote such a symmetry as "orthogonal equivalent" (OE). In contrast, the tilt of an octahedron about a $[100]_t$ axis, as in the LTT phase, leaves two in-plane oxygens within the CuO$_2$ plane but shifts the orthogonal pair above and below the plane; together with slight distortions of the octahedra to satisfy the tetragonal lattice symmetry, this results in inequivalent O(1) sites (see Table I) and two different Cu-O bond lengths. We will label this case as "orthogonal inequivalent" (OI), and note that the LTLO phase also has an OI symmetry. The phase diagram for the relevant range of doping in La$_{2-x}$Ba$_x$CuO$_4$ is shown in Fig. 2(a).

The structural transformations have been analyzed in terms of a Landau-Ginzburg model, in which the degenerate octahedral tilts about $[110]_t$ and $[1\bar{1}0]_t$ axes are taken as the order parameters [5,23]. When only one order parameter is finite, one obtains the LTO phase; when both are finite and equal, the structure is LTT. This model allows an elegant analysis of the phase diagram, and predicted the possible

occurrence of the LTLO phase as confirmed in a closely related system [25]. It has also motivated detailed studies of the octahedral tilts in La$_{2-x}$Sr$_x$CuO$_4$ [26–28], La$_{1.65}$Nd$_{0.35}$CuO$_4$ [29], and La$_{2-x}$Ba$_x$CuO$_4$ [30,31]; however, these studies have been done at points of reciprocal space that have a finite structure factor for both LTO- and LTT-like tilts. Hence, while these measurements have been interpreted in terms of LTO-like (OE) tilts, they could not uniquely distinguish the fluctuations from LTT-like (OI) tilts.

Helpful guidance is provided by a calculation of the potential-energy surface as a functional of octahedral tilts performed with density functional theory for a rough model of La$_{2-x}$Ba$_x$CuO$_4$ with $x = 0.10$ [32]. The calculation finds that the lowest energy is given by LTT tilts, with local minima corresponding to LTO tilts higher in energy by about 15 meV. It was proposed that the LTO phase might be stabilized with increasing temperature due to the entropy associated with low-energy octahedral tilt fluctuations [32]. This proposal gained support from a Monte Carlo study of the temperature dependence of a model including both the mean-field potential energy and interactions between neighboring octahedra [33]. The latter calculation yielded evidence for strong local LTT-like tilt amplitudes throughout the LTO phase.

In this paper, we present neutron total scattering measurements on polycrystalline samples of La$_{2-x}$Ba$_x$CuO$_4$ with $x = 0.095$, 0.125, and 0.155 obtained as a function of temperature. We analyze these data sets both by Rietveld refinement and
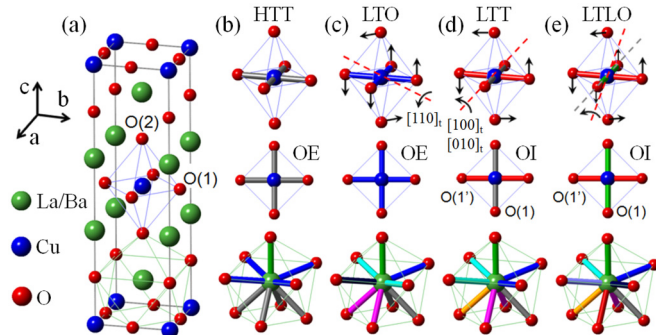

FIG. 1. (Color online) Structural details of La$_{2-x}$Ba$_x$CuO$_4$. La/Ba are shown as large green spheres, Cu as intermediate blue spheres, and O as small red spheres. (a) Basic structural motif is shown for $I4/mmm$ (HTT) phase, featuring CuO$_6$ octahedral unit and La/BaO$_9$ cage. O(1) and O(2) denote planar and apical oxygen, respectively. Panels (b)–(e) highlight various aspects of the average crystal structures as follows: CuO$_6$ octahedral tilt symmetry (top row), in-plane bond-length distribution within CuO$_4$ plaquette (middle row), and dispersion of La/Ba-O distances within the La/BaO$_9$ cage (bottom row). Equal interatomic distances are represented by the same color. HTT denotes high-temperature tetragonal ($I4/mmm$), LTO is low-temperature orthorhombic ($Bmab$), LTT is low-temperature tetragonal ($P4_2/ncm$), and LTLO is low-temperature less orthorhombic ($Pccn$). The underlying in-plane symmetry is OE in HTT and LTO models, and OI in LTT and LTLO models, as indicated.
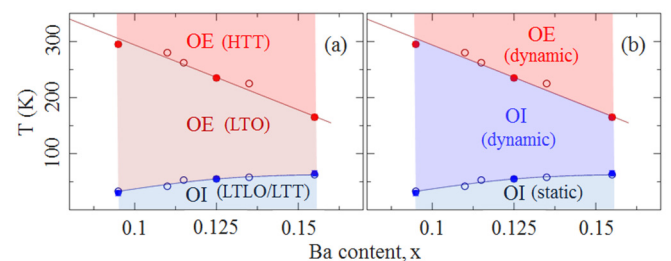

FIG. 2. (Color online) (a) Average structure (x, T) phase diagram of LBCO which has been replotted to highlight whether the structure is OE or OI. Open symbols and solid lines are from Hücker *et al.* [17], solid symbols are from the present study. Shaded are regions of interest for this study having average OE (HTT and LTO) and OI (LTLO/LTT) symmetries, as indicated. (b) Local structure phase diagram with phase designations based on the results presented in this study. Please see text for definitions of OE and OI.

by the pair distribution function analysis technique. The two approaches yield complementary evidence for dynamical LTT-like tilts within the LTO phase, as well as local tilt fluctuations in the HTT phase. We directly confirm the LTT-like tilt fluctuations in the LTO phase through inelastic neutron scattering measurements on a single crystal of $La_{2-x}Ba_xCuO_4$ with $x = 0.125$.

The rest of the paper is organized as follows: In Sec. II we describe the experimental and analysis methods, and the choice of reciprocal lattice used to index the reflections. In Sec. III we present three subsections dedicated to our results on average crystal structure, local structure, and octahedral tilt dynamics. In Sec. IV we discuss the various properties as a function of the nominal Ba content and temperature, compare our results with the literature, and in Sec. V finish with a short summary.

II. EXPERIMENTAL

Finely pulverized samples of $La_{2-x}Ba_xCuO_4$, with Ba content in the $0.095 \leqslant x \leqslant 0.155$ range, as well as an undoped La_2CuO_4 polycrystalline reference, were grown using standard solid state protocols; these were used for the total scattering atomic PDF experiments. Neutron time-of-flight measurements were carried out on the NPDF instrument at Los Alamos Neutron Scattering Center at Los Alamos National Laboratory. Powders (15 grams each) were loaded under helium atmosphere into standard extruded vanadium containers and sealed. Temperature-dependent measurements in the $15 \text{ K} \leqslant T \leqslant 550 \text{ K}$ range were performed using a closed-cycle cryofurnace sample environment for 2 hours at each temperature on each sample, yielding good statistics and a favorable signal to noise ratio at high momentum transfers. Raw data were normalized and various experimental corrections performed following standard protocols [34]. High-resolution experimental PDFs were obtained from the sine Fourier transform of the measured total scattering structure functions, $F(Q)$, over a broad range of momentum transfers, Q ($Q_{max} = 28 \text{ Å}^{-1}$). Data reduction to obtain the PDFs, $G(r)$, was carried out using the program PDFGETN [35]. The average structure was assessed through Rietveld refinements [36] to the raw diffraction data using GSAS [37] operated under EXPGUI [38], utilizing $I4/mmm$ (HTT), $Bmab$ (LTO), $P4_2/ncm$ (LTT), and $Pccn$ (LTLO) models from the literature [17]. Structural refinement of PDF data was carried out using PDFFIT2 operated under PDFGUI [39] using the same models.

The single crystal of $La_{2-x}Ba_xCuO_4$ with $x = 0.125$ was grown using the traveling-solvent floating zone method and has been characterized previously, as described elsewhere [17]. The crystal, of size $\phi \sim 8 \text{ mm} \times 20 \text{ mm}$, was studied by inelastic neutron scattering using the HYSPEC instrument (beam line 14B) at the Spallation Neutron Source, Oak Ridge National Laboratory [40]. For the experiment on HYSPEC, the crystal was mounted in a Displex closed-cycle cryostat. With the c axis vertical, scattering wave vectors $\mathbf{Q} = (H, K, 0)$ are in the horizontal scattering plane. A fixed incident energy of 27 meV and a chopper frequency of 300 Hz were used for all data shown here, and the graphite-crystal array in the incident beam was put in the flat mode (no vertical focusing) to improve the resolution along Q_z. For a typical measurement, the position-sensitive detector tank was placed at a particular

mean scattering angle, and then measurements were collected for a series of sample orientations, involving rotations about the vertical axis in steps of $0.2°$. From such a set of scans, a four-dimensional data set was created and analyzed with the MANTID [41] and DAVE [42] software packages. Slices of data corresponding to particular planes in energy and wave-vector space can then be plotted from the larger data set. Wave vectors will be expressed in units of $(2\pi/a, 2\pi/b, 2\pi/c)$ with $a = b = 5.355$ Å and $c = 13.2$ Å, corresponding to the LTT phase.

The measurements of the soft phonon that tilts along the Cu-O bonds were performed in the vicinity of the (330) position, which corresponds to a superlattice peak in the LTT but not the LTO phase. To sample the fluctuations associated with the tilts of the LTO phase, it was necessary to tilt the sample so as to put (032) in the scattering plane. We then looked at the behavior along $(H,3,2)$.

III. RESULTS

A. Average crystal structure

Typical Rietveld fits are shown in Fig. 3 for reference. The resulting temperature evolution of the in-plane lattice parameters is shown in Fig. 4, where the vertical dashed lines indicate the temperatures of the structural phase transitions.
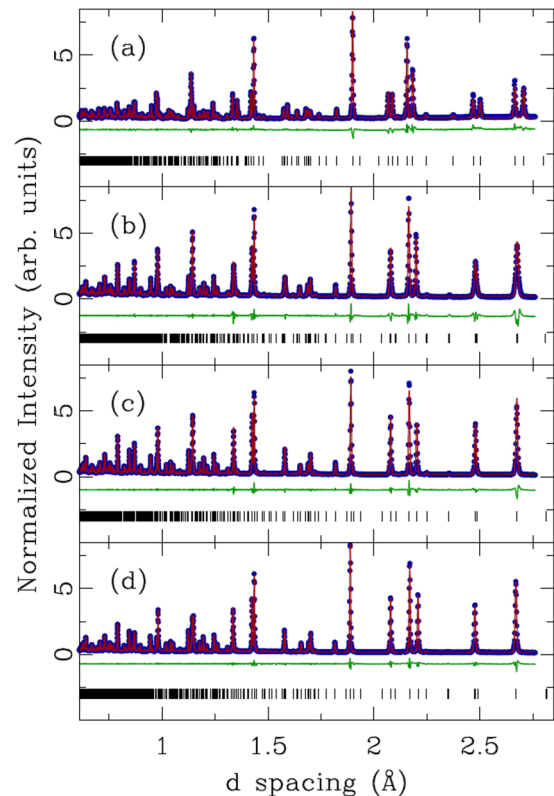

FIG. 3. (Color online) Rietveld fits of the average structure models to LBCO data at 15 K. Closed blue symbols represent the data, solid red lines are the models, and solid green lines are the differences (offset for clarity). Vertical ticks mark reflections. (a) $x = 0$ using $Bmab$ model, (b) $x = 0.095$ using $Pccn$ model, (c) $x = 0.125$ using $P4_2/ncm$ model, and (d) $x = 0.155$ using $Pccn$ model.
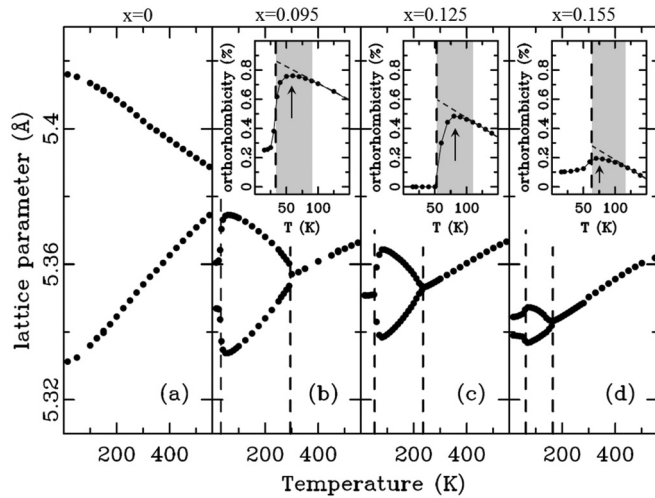
FIG. 4. Temperature evolution of in-plane lattice parameters of La$_{2-x}$Ba$_x$CuO$_4$ obtained from Rietveld refinements for $x = 0$ (a), $x = 0.095$ (b), $x = 0.125$ (c), and $x = 0.155$ (d). HTT parameters are given in $F4/mmm$ setting. Vertical dashed lines indicate crystallographic phase transitions as specified in the text. Insets to (b)–(d) display temperature evolution of the lattice orthorhombicity [$\eta = 2(a - b)/(a + b)$] for doped samples, with their maxima marked by vertical arrows. Vertical dashed lines indicate low-temperature structural phase transitions. Sloping dashed straight lines are guides to the eye emphasizing anomalous trends seen in highlighted regions and discussed in the main text.

These are in good agreement with published work [17], as indicated in the phase diagram shown in Fig. 2.

Figure 5 shows the evolution of the Rietveld refined average in-plane Cu-O distances. Undoped La$_2$CuO$_4$ is in the LTO phase down to the lowest temperature and has a single Cu-O planar-bond length (solid black circles in all panels of Fig. 5),
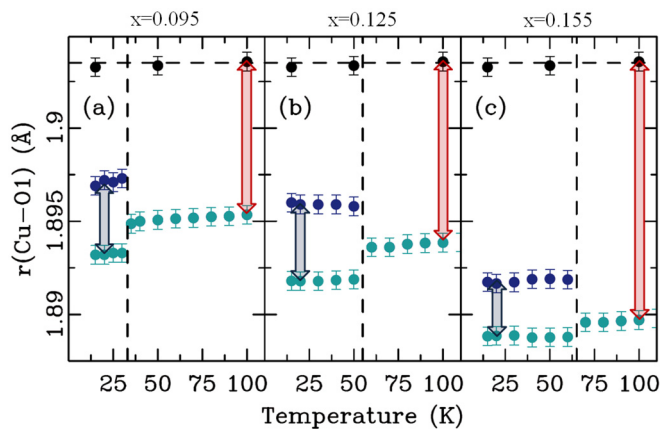

FIG. 5. (Color online) Temperature evolution of the average in-plane Cu-O bond lengths (solid blue circles) in La$_{2-x}$Ba$_x$CuO$_4$ obtained from Rietveld refinements: $x = 0.095$ (a), $x = 0.125$ (b), and $x = 0.155$ (c). In all three panels: solid black symbols show in-plane Cu-O bond for $x = 0$ sample as a reference. Horizontal dashed lines are guide to the eye, vertical dashed lines mark crystallographic phase transitions. Vertical double arrows highlight the magnitude of changes discussed in the main text.

highlighting the OE nature of the LTO tilts. The biggest effect on doping is a significant shortening of the average Cu-O bond length, highlighted by the red arrows in Fig. 5. This is due to the decrease in electronic charge in the Cu-O bonds, which are stabilized because charge is removed from antibonding states. At low temperature, where the doped samples enter the LTT/LTLO phase [17], Rietveld analysis reveals two distinct Cu-O bond lengths consistent with the OI tilts.

It is noteworthy that the difference in the in-plane Cu-O bond lengths of doped samples at base temperature is quite small—0.005(1) Å at most at 20 K, as indicated by the blue double arrows in Figs. 5(a)–5(c). This may be compared to the distortions of ∼0.25 Å observed in the ground state of LaMnO$_3$ due to the cooperative Jahn-Teller effect [43,44], which are nearly two orders of magnitude larger. Nonetheless, because they are long-range ordered and can be observed crystallographically, such a small difference in the average bond lengths can be reliably measured, giving us a direct indication of the broken symmetry between orthogonal Cu-O bonds. Notably, despite the average tilt angles decreasing monotonically with increasing doping we see that the bond length mismatch (the difference between the x and y bond lengths) increases from $x = 0.095$ to $x = 0.125$ before decreasing again at $x = 0.15$, suggesting a stronger electronic stabilization of the orthogonal inequivalency around 1/8 doping.

The first-order character of the low-temperature transition has a signature in the temperature dependence of the orthorhombic strain, shown in the insets to Figs. 4(b)–4(d). On cooling through the LTO phase, the strain grows with decreasing temperature. This growth slows as the low-temperature transition is approached so that at ∼30 K above the low-T transition the average orthorhombicity even decreases, followed by a sharp drop at the transition. The small decrease in strain on approaching the transition is consistent with the presence of a 2-phase coexistence region, as identified in past studies [8,17,18,45].

If the LTO-HTT transition were purely displacive, then we would expect the atomic displacements associated with the octahedral tilts of the LTO phase to decrease continuously to zero on approaching the transition from below. Figure 6 demonstrates that this is not the case: the longer La-O2 bonds (O2 = apical oxygen) are split into three distances in the LTO phase, and this splitting abruptly drops to zero at the transition to the HTT phase. The residual, disordered displacements in the HTT phase are apparent in the jump in the mean-squared atomic displacements, shown in Fig. 7. Nevertheless, given the clear evidence that the transition is second order [16,17], the apparent jump in the bond lengths must be an artifact of the Rietveld refinement. The La-O2 bond length is affected most strongly by displacements of the apical oxygens, associated with octahedral tilts, which are anisotropic. Note that in the fitting, we have assumed isotropic mean-squared atomic displacements, $U_j = \langle u_j^2 \rangle$, where u_j is the displacement of an atom at site j and the average is over all equivalent sites in the sample. If there are disordered tilts present in the LTO phase, then the fitting process may result in unrealistic O2 displacements to compensate for the associated impact on Bragg peak intensities. It follows that anisotropic local displacements of the apical oxygens, such as
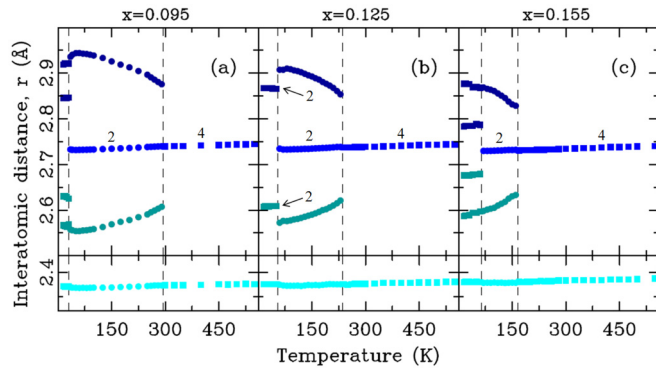
FIG. 6. (Color online) Temperature evolution of the average La-O(2) interatomic distances for (a) $x = 0.095$, (b) $x = 0.125$, and (c) $x = 0.155$ composition. Bond multiplicity is indicated by a number where applicable. Short La-O(2) bond that connects two LaO_2 planes is shown in separate panels. Vertical dashed lines indicate structural phase transitions.

occur in tilt fluctuations, might be modeled by finite average displacements, even when the true *average* static displacement is essentially zero (just below the transition).

If the disordered tilts change continuously across the transition, then we should expect to see an anomalous jump in U_{iso} for O2 on entering the HTT phase. Figure 7 shows that this, indeed, is the case. In fact, there is also a jump at the low-temperature transition, indicating that there are anisotropic fluctuations present in the LTO phase that cannot be compensated by adjusting the symmetry-allowed atomic displacements. The lower red curve corresponds to a Debye-
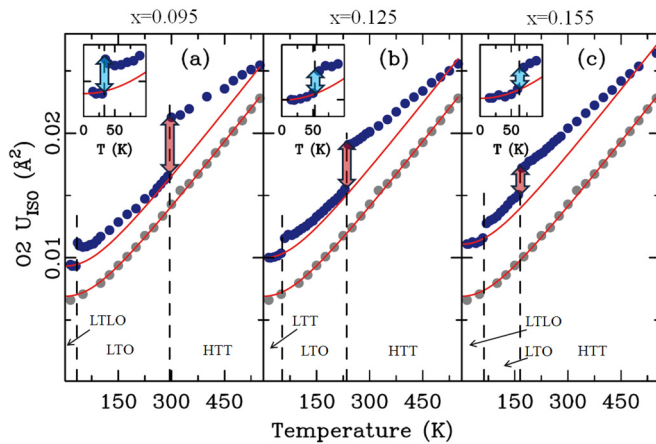

FIG. 7. (Color online) Temperature evolution of atomic displacement parameter (ADP) of apical oxygen (solid blue symbols) in $La_{2-x}Ba_xCuO_4$ for $x = 0.095$ (a), $x = 0.125$ (b), and $x = 0.155$ (c). Vertical dashed lines indicate transitions between crystallographic phases as labeled and specified in the text. In all panels ADP data for $x = 0$ sample are presented by solid gray symbols, with solid red line representing a fit of the Debye model, as discussed in the text. Debye model for ADPs of doped samples has the same Debye temperature as for $x = 0$, but different offset such as to provide a good fit to ADP in the low-temperature phases. Anomalous jumps in ADP discussed in the main text are indicated by double arrows. Insets focus on low-temperature transitions.

model fit [46] to the O2 U_{iso} of La_2CuO_4 (gray circles). This involves two parameters, the Debye temperature θ_D and an offset factor U_0 [47,48]; the behavior for La_2CuO_4 is well described by the parameter values θ_D of 500(2) K and U_0 of 0.0023(2) $Å^2$. In the other figure panels, in each case the upper red curve is obtained by adding a doping-dependent offset to match the experimental values at the lowest temperature, but keeping the Debye temperature the same as that obtained for the undoped end member. The offset grows with Ba concentration, which is consistent with the disorder in O2 positions induced by Ba substitution for La [20]. It appears to capture the underlying trend in each case, with the excess disorder associated with the jumps gradually becoming indistinguishable from the thermal effects with increasing temperature. This is in agreement with earlier observations in $La_{2-x}Ba_xCuO_4$ and $La_{2-x}Sr_xCuO_4$ of persisting local tilt fluctuations across these macroscopic phase transitions [19,21,49,50]. Similar anomalies have been seen in other systems, where they are typically ascribed either to the inadequacy of the structural model used, or sometimes more specifically to the presence of nanoscale structural features, such as broken-symmetry states, that do not propagate over long length scales [47,48,51,52].

B. Local structure

Using the same neutron scattering data, we have characterized the local structure of $La_{2-x}Ba_xCuO_4$ by the PDF approach. Figure 8 shows PDF fits over intermediate r ranges at 15 K using the average structure models, establishing the overall data quality and displaying that good fits can be obtained on this length scale. Here, we have taken account of the correlated motion of short interatomic bonds [53–55] by defining the mean-squared relative displacement σ_{ij}^2 of atoms at positions i and j, separated by distance r_{ij}, as

$$\sigma_{ij}^2 = (\langle u_i^2 \rangle + \langle u_j^2 \rangle)[1 - (r_0/r_{ij})], \quad (1)$$

where the parameter r_0 is fixed at 1.6 Å for all PDF calculations in this paper.

To explore the origin of enhanced mean-squared displacements in the Rietveld refinements shown in Fig. 7, we focus on the very local structure. We first evaluate the expected effects on the PDF of the symmetry change across the low-temperature transition in the case where the local and average structures agreed. Figures 9(b)–9(d) show a comparison of PDFs simulated using parameters from the Rietveld refinements at base temperature (blue profile, OI model) and at the temperature of maximum orthorhombic strain (red profile, OE model), bracketing the low-temperature transition in the doped samples. The changes expected in the PDF across the transition are clearly observable in the respective difference curves, with the strongest features just below 3 Å (marked by arrows), corresponding to La-O2 bonds.

The actual measured PDFs at the same temperatures are shown in Figs. 9(f)–9(h). The difference curves show nothing above the noise level, indicating the absence of change in the local structure across the transition, in contrast to the predictions from the average structure. In fact, the temperature difference is similar to that observed in pure La_2CuO_4,
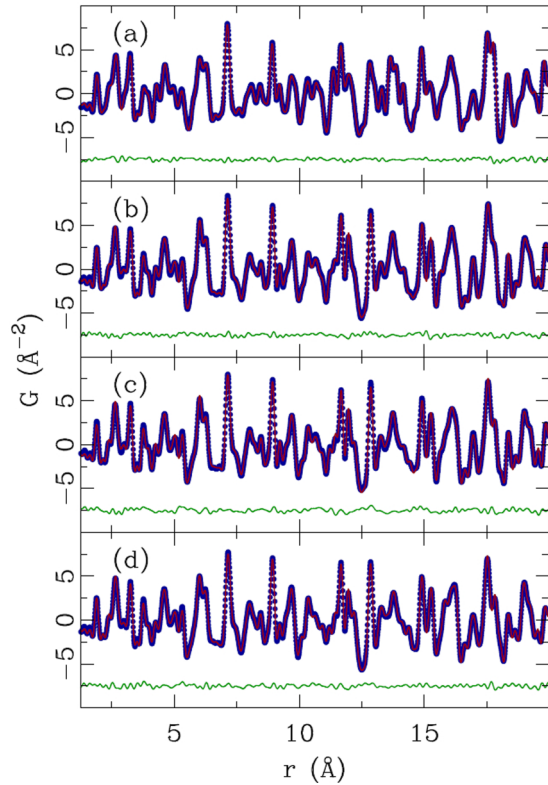
FIG. 8. (Color online) PDF fits of the average structure models to LBCO data at 15 K. Closed blue symbols represent the data, solid red lines are the models, and solid green lines are the differences (offset for clarity). (a) $x = 0$ using *Bmab* model, (b) $x = 0.095$ using *Pccn* model, (c) $x = 0.125$ using $P4_2/ncm$ model, and (d) $x = 0.155$ using *Pccn* model.

FIG. 9. (Color online) PDF comparison of the average and local structure behavior in $La_{2-x}Ba_xCuO_4$. Top row: simulated PDFs calculated using parameters from fully converged Rietveld refinements reflecting average structure behavior. Low-T profiles are shown in blue, higher-T profiles are shown in red. (a) 15 K vs 50 K LTO structure PDFs for $x = 0$; (b) 15 K LTLO vs 60 K LTO PDFs for $x = 0.095$; (c) 15 K LTT vs 80 K LTO PDFs for $x = 0.125$; (d) 15 K LTLO vs 70 K LTO PDFs for $x = 0.155$. Bottom row: comparison of the raw experimental PDF data for the same respective temperatures as considered in (a)–(d); lower temperature data shown in blue, higher temperature data shown in red. Difference curves (high-T minus low-T PDF) are offset for clarity. Shaded areas represent span of the difference curves observed for $x = 0$ composition. Changes observed in the average structure (marked by filled arrows) are not observed in the local structure (empty arrows), as experimental PDFs do not change across the OE/OI phase transitions in doped $La_{2-x}Ba_xCuO_4$ samples.

Fig. 9(e), where there is no change in the average structure. These results are consistent with earlier work [19].

Further confirmation of this comes from explicit short-range PDF modeling that was carried out using both OE-type and OI-type models fitted to the data at base temperature and at the maximum orthorhombicity temperature in the doped samples. These fits are shown in Fig. 10. While the OE-type model readily explains the La_2CuO_4 data at both base and intermediate temperature, Figs. 10(a) and 10(e), it gives an unsatisfactory fit to the region of the La-O2 bonds in the doped samples. Such a discrepancy at base temperature [Figs. 10(b)–10(d)] is expected, since the underlying atomic structure there is OI. At the temperature of maximum orthorhombic strain, the discrepancy with the OE fits remains, as shown in Figs. 10(f)–10(h), whereas OI fits do much better, as indicated in Figs. 10(i)–10(k).

We saw previously that $U_{iso}(O(2))$ provides a distinctive measure of the tilt disorder that cannot be simulated by the symmetry-allowed structural parameters in the Rietveld refinements. We now consider the behavior of $U_{iso}(O(2))$ obtained from fits to the PDF data (for the range $15 < r < 40$ Å), as shown in Figs. 11(a)–11(c). At each temperature, separate fits have been performed with the LTT (LTLO), LTO, and HTT models. At all temperatures, we find that the R factor, measuring the quality of fit, is always smallest for LTT (LTLO), followed by LTO, and then HTT. As one can see, $U_{iso}(O(2))$
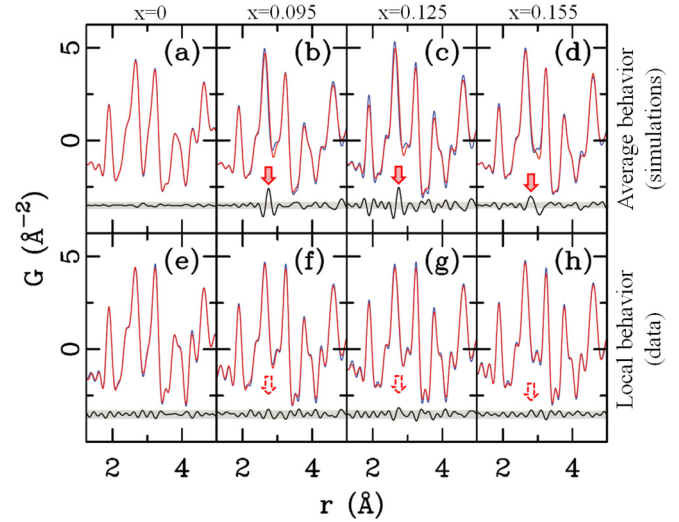
from the LTT (LTLO) fit shows a monotonic increase with temperature, with no anomalies at the transition temperatures. The LTO fit is consistent with LTT at high temperature, but is larger in the LTO and LTT phases. The results for HTT are considerably larger at all temperatures.

As a measure of the distinctly OI tilts, we define the parameter δ as

$$\delta = \Delta U_{iso}/\langle x_{O(2)}\rangle^2, \qquad (2)$$

where ΔU_{iso} is the difference in parameter values obtained from the LTO and LTT (LTLO) fits, normalized to the square of the average transverse displacement of the O(2) site in the LTT phase at low temperature, $\langle x_{O(2)}\rangle^2$. The temperature dependence of δ is plotted in Figs. 11(d)–11(f) for the doped samples. For $x = 0.125$, we find evidence for substantial OI tilts throughout the LTO phase, with a reduced magnitude for $x = 0.095$ and 0.155. On entering the HTT phase, we have already seen evidence that tilt disorder is present; however, the fact that $\delta \approx 0$ suggests that there is little preference between OI and OE tilts at high temperature. It is consistent with the idea that, in the HTT phase, the Cu-O(2) bond precesses rather smoothly around the z axis as discussed before [5,32,56].

We now address the length scale of the local OI tilts. This can be obtained qualitatively from a direct comparison of the
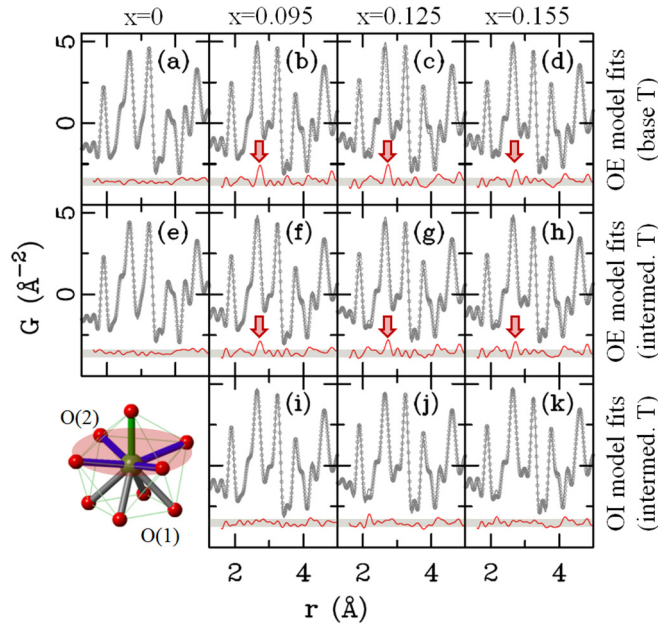
FIG. 10. (Color online) OE versus OI PDF models for the local structure (solid gray lines). Data are shown as open gray symbols, difference curves (solid red lines) are offset for clarity. (a)–(d) 15 K data vs LTO model (OE symmetry) explains $x = 0$ data well (as it should), fails for $x = 0.095$, 0.125, and 0.155 (as it should). The largest discrepancies are marked by arrows. (e) LTO for $x = 0$ sample at 50 K, (f)–(h) data at T of maximum orthorhombicity (60 K, 80 K, and 70 K for $x = 0.095$, 0.125, and 0.155, respectively) vs LTO model (fails at same places as at 15 K); (i)–(k) same as (f)–(h) but with LTLO/LTT models (OI symmetry)—underlying data correspond to OI symmetry. Inset: La/Ba-O(2) distances (shaded area) contribute principally to the misfits marked by arrows in (b)–(d) and (f)–(h).
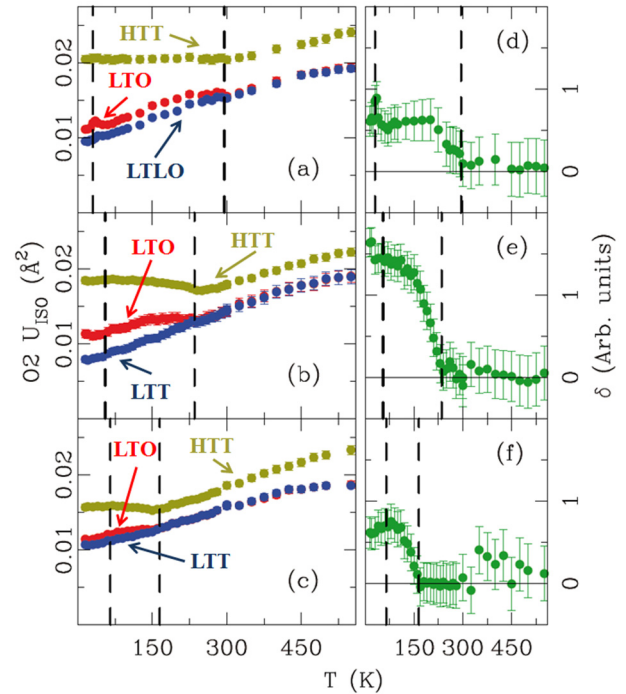

FIG. 11. (Color online) Semiquantitative exploration of the OI-ness of LBCO via assessment of T dependence of apical oxygen isotropic atomic displacement parameter (ADP) as obtained by fitting different structural models [as indicated by arrows in (a)–(c)] to the PDF data over 4 nm r range. (a) $x = 0.095$, (b) $x = 0.125$, and (c) $x = 0.155$. Difference between the observed ADPs using LTO and LTLO/LTT models from panels (a)–(c) are displayed in (d)–(f) for $x = 0.095$, $x = 0.125$, and $x = 0.155$, respectively, normalized by the square of the average transverse displacement of apical oxygen. See text for details.

experimental PDF data at 15 K and 100 K (well above the phase coexistence region) for all samples studied. This is shown in Figs. 12(a)–12(d). Panel (a) shows the result for La_2CuO_4; only small differences are seen in the PDFs beyond the expected uncertainties (e.g., indicated by the green arrow), and these provide a measure of the signal we should expect due to thermal effects within the same phase. From Figs. 12(b)–12(d), it is clear that in the doped samples there are additional signals in the difference curve, starting near a distance of 9 Å, that are reproducible from sample to sample and especially evident in the running average of the difference curve (red curve). This suggests that the OI tilt correlations within the LTO phase have a correlation length that is <9 Å.

The PDF analysis presented here is based on total scattering data that do not discriminate between the elastic and inelastic scattering channels, and hence the PDF does not distinguish whether the underlying short-range features are static or dynamic. This is in contrast to the Rietveld analysis, which is sensitive only to the time-averaged information in the Bragg peaks; the inelastic information is largely in the tails of the Bragg peaks. To test the static or dynamic character, we turn next to inelastic neutron scattering on a single crystal, focusing on $La_{2-x}Ba_xCuO_4$ with $x = 0.125$.

C. Octahedral tilt dynamics

The inelastic scattering about the (330) reciprocal point of our $La_{2-x}Ba_xCuO_4$ with $x = 0.125$ is shown in Fig. 13. The cuts in reciprocal space that were taken are shown schematically in Fig. 13(a). Figures 13(b) and 13(d) show the dispersion of excitations along the transverse and longitudinal directions, respectively, within the LTO phase at $T = 180$ K. In both cases, one can see a soft phonon with intensity that can be resolved between 2 and 10 meV. In the transverse direction, these excitations connect to the transverse acoustic modes dispersing from the neighboring (240) and (420) fundamental Bragg points. Another perspective is given by the constant-energy slices shown in Fig. 14 for several different energies, where we compare with results at 60 K, slightly above the low-temperature transition. For dispersion in the longitudinal direction, the intensity becomes quite weak as one moves away from the (330) point. Figure 13(c) shows that the excitations, integrated between 2 and 4 meV, have a finite width along Q_z, demonstrating that the LTT tilt fluctuations have 3D character.

The temperature dependence of the scattering near (330) is presented in Fig. 15. There is a clear superlattice reflection at (330) in the LTT phase at 50 K. Warming to 60 K, just across the transition to the LTO phase, very weak elastic
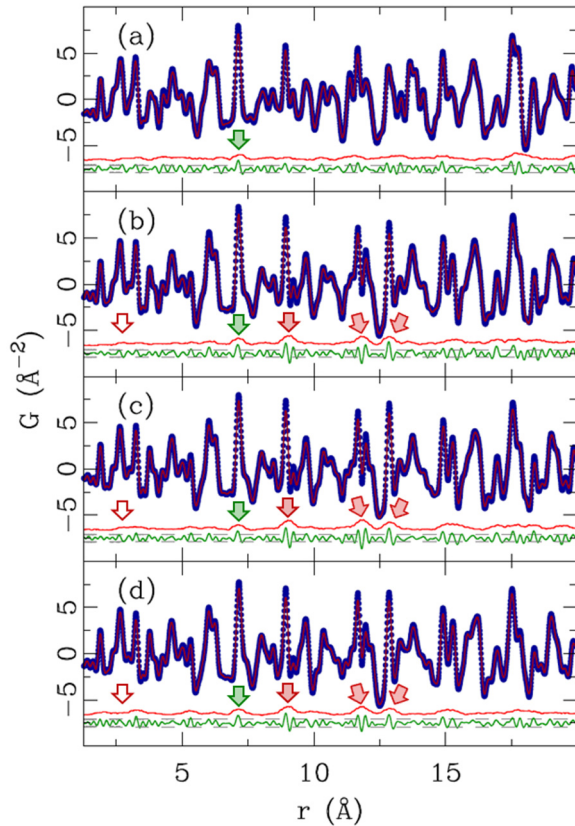
FIG. 12. (Color online) Comparison of LBCO PDF data at 15 K (closed blue symbols) and at 100 K (solid red line) with difference curve (solid green line) offset for clarity. Horizontal gray dashed lines mark experimental uncertainty on 2σ level. Light-red solid line represents a 0.5 Å running average of the absolute value of the difference curve, multiplied by 2 and offset for clarity. (a) $x = 0$, (b) $x = 0.095$, (c) $x = 0.125$, and (d) $x = 0.155$. Difference in data for $x = 0$ sample displays the change expected from canonical thermal evolution effects without symmetry changes. Differences in the data for all three doped samples display similar level of change as $x = 0$ sample up to ~9 Å with first substantial changes seen on longer length scale. Low r assessment: green arrows mark changes seen in the data for all the samples, while the red arrows mark significant changes seen only in the doped samples, presumably associated with the change in average symmetry. Empty arrows around 3 Å mark places where changes are expected from the average structure, but not observed locally, as shown in Fig. 9 and discussed in the text. Local structure across the global OI to OE phase transition is preserved on subnanometer length scale.

scattering is still detectable; however, this is completely gone at 120 K. In contrast, soft phonon fluctuations (integrated over 2 to 5 meV) centered at (330) are clearly seen in the LTO phase and even in the HTT, at 250 K. At 50 K, the intensity from the soft fluctuations has all condensed into the elastic superlattice peak. (There must be acoustic phonons dispersing out of the superlattice peak, but these are too weak for us to detect.) The temperature dependencies of both the elastic and inelastic signals are summarized in Fig. 15(a).

The correlation length for the LTT-like tilts within the LTO phase can be estimated from the Q width of the soft-phonon scattering. (Here, for simplicity, we ignore resolution
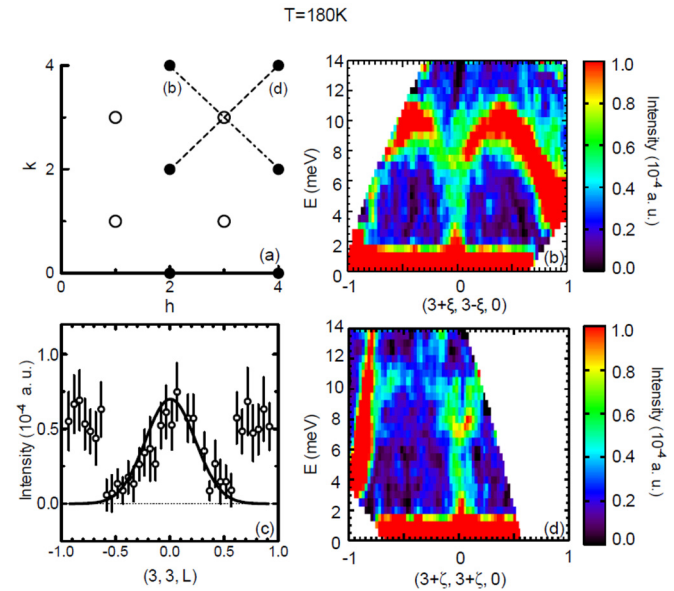

FIG. 13. (Color online) (a) Diagram of the $(H,K,0)$ plane of reciprocal space indicating fundamental Bragg peaks (filled circles) and LTT superlattice peaks (open circles), with dot-dashed (dashed) line indicating the orientation of the data slice in (b) [(d)]. (b) Map of scattering intensity for E vs $\mathbf{Q} = (3 + \xi, 3 - \xi, 0)$. (c) Intensity (integrated over $2 \leqslant E \leqslant 4$ meV) vs $\mathbf{Q} = (3,3,L)$. (d) Intensity map for E vs $\mathbf{Q} = (3 + \zeta, 3 + \zeta, 0)$. All measurements are at $T = 180$ K, in the LTO phase.
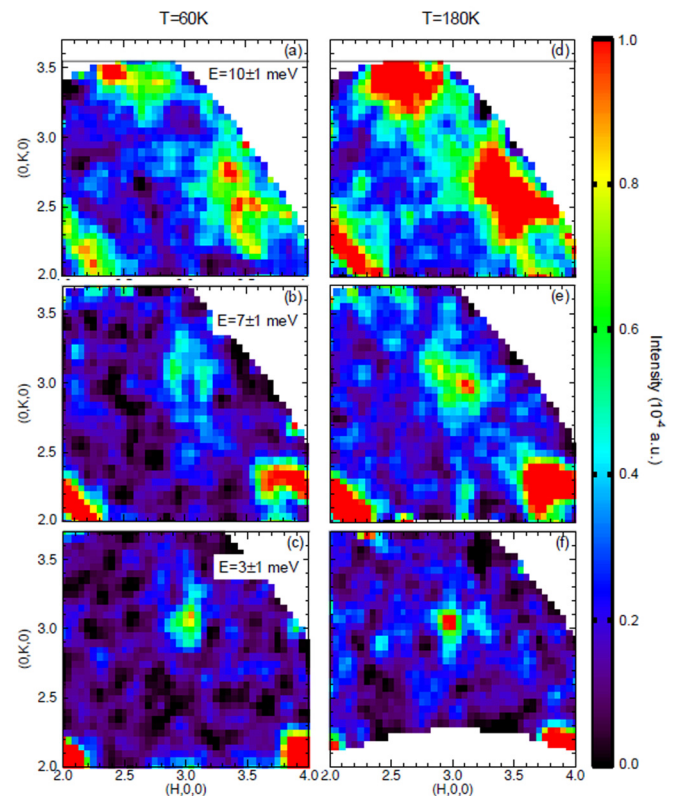

FIG. 14. (Color online) Constant-energy slices, with signal integrated over ± 1 meV, through the soft-phonon scattering around (330). (a), (d) $E = 10$ meV; (b), (e) $E = 7$ meV; (c), (f) $E = 3$ meV. Data obtained at $T = 60$ K for (a)–(c) and 180 K for (d)–(f).
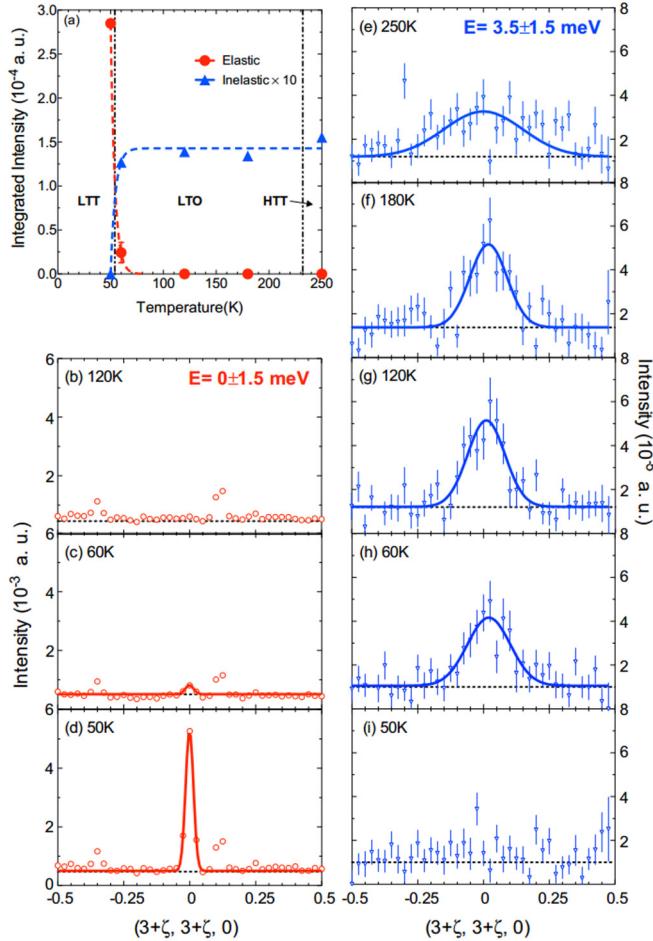
FIG. 15. (Color online) Single-crystal results at the (330) LTT superlattice position for $x = 0.125$. (a) Summary of the temperature dependence of the elastic (red circles) and inelastic (blue triangles) integrated intensities obtained from the following panels; vertical dashed lines denote phase boundaries, while dashed lines through data points are guides to the eye. (b)–(d) Elastic channel (integrated over ± 1.5 meV) measured along the longitudinal direction at 120, 60, and 50 K, respectively. Solid lines are Gaussian-peak fits, used to determine the integrated intensity; weak, T-independent peaks are diffraction from the aluminum sample holder. (e)–(i) Inelastic signal from the soft-phonon fluctuations (2–5 meV integration) measured at 250, 180, 120, 60, and 50 K, respectively. Lines are Gaussian-peak fits.

corrections.) Taking the inverse of the half width at half maximum for the fitted peaks in Figs. 15(e)–15(h), we find an effective correlation length of ~5 Å in the LTO phase, decreasing to about half of that in the HTT phase. This is consistent with estimate of <9 Å obtained from the PDF analysis.

For comparison, Figs. 16(a) and 16(b) show the dispersion of tilt fluctuations in the transverse direction about the (032) position (an LTO superlattice peak) in the LTO and HTT phases, respectively. The intensity is much stronger than at (330) because of a much larger structure factor. There is substantial intensity from soft tilt fluctuations, and even quasielastic scattering, at 250 K in the HTT phase, as seen previously [30]. In the LTO phase at 180 K, much of the
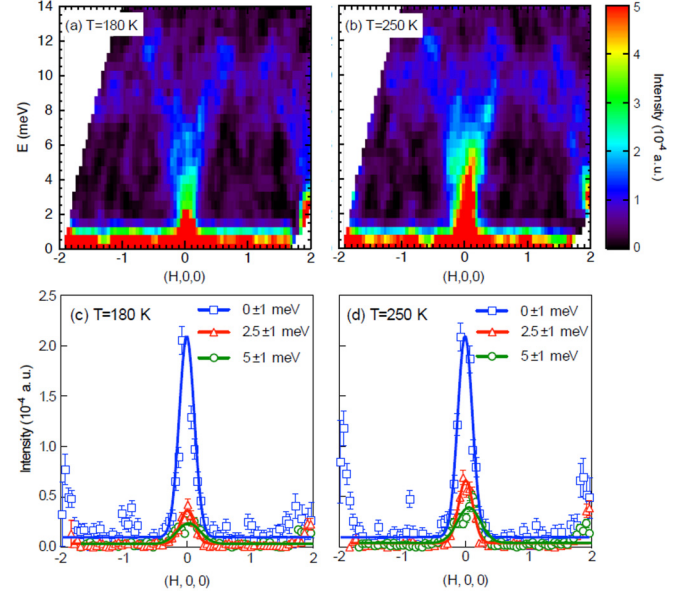

FIG. 16. (Color online) (a), (b) Intensity map as a function of energy vs $\mathbf{Q} = (H, 3, 2)$, showing the transverse dispersion of tilt modes about the (032) superlattice peak position of the LTO phase, obtained at $T = 180$ and 250 K, respectively. (c), (d) Intensity, integrated over a window of ± 1 meV along the transverse direction, for $E = 0$ (blue squares), 2.5 (red triangle), and 5 meV (green circles), at $T = 180$ and 250 K, respectively.

low-energy weight is due to the residual soft mode that condenses at the LTT transition. We note that scattering at (032) is allowed in both the LTO and LTT phases; it follows that one cannot uniquely distinguish between OE and OI soft tilt fluctuations at this $\vec{Q}$ point, in contrast to fluctuations at (330).

IV. DISCUSSION

The distribution of Cu-O(1) nearest-neighbor bond lengths has been the subject of some controversy over the years, and so deserves some discussion. Our Rietveld analysis finds a maximum bond length splitting of just 0.005 Å in the LTT phase of $La_{2-x}Ba_xCuO_4$ with $x = 0.125$, consistent with earlier diffraction work on $La_{2-x}Ba_xCuO_4$ [7]. To appreciate how small this splitting is, we compare various measures of the bond-length distribution in Fig. 17(a). The peak obtained from the PDF analysis is a simple Gaussian that shows a very slight broadening with doping. The width of the PDF peak is significantly smaller than that obtained from the Rietveld analysis, as the former is sensitive to the correlated motion of nearest neighbors, whereas diffraction intensities only have information on the independent fluctuations of the distinct atomic sites. The PDF peak also broadens slightly with increasing temperature as shown in Fig. 17(b). The mean-squared relative displacement, σ^2, obtained as a function of temperature for the $x = 0.125$ sample is shown in Fig. 17(c). The solid line corresponds to the Einstein model [57],

$$\sigma^2 = \frac{\hbar}{2\mu\omega_E} \coth\left(\frac{\hbar\omega_E}{2k_B T}\right), \quad (3)$$
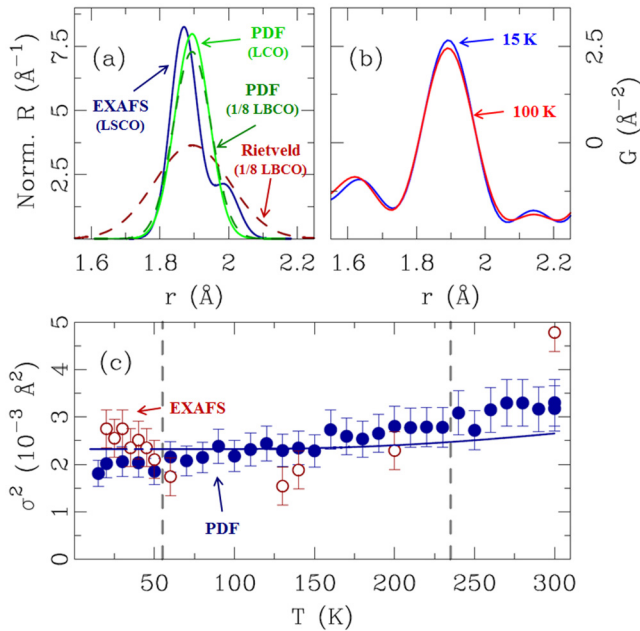
FIG. 17. (Color online) (a) Normalized radial distribution function $R(r)$ for Cu-O(1) bonds comparing results from different analyses. Green lines show the Gaussian peaks obtained from PDF analysis for $La_{2-x}Ba_xCuO_4$ with $x = 0$ (solid) and $x = 0.125$ (dashed). The effective profile for the latter sample from the Rietveld refinement (red dashed line) is not sensitive to correlated motion. The blue solid line indicates the model for $La_{2-x}Sr_xCuO_4$ with $x = 0.15$ and $T = 15$ K from the XAFS study by Bianconi *et al.* [59]. (b) Pair distribution function for $La_{2-x}Ba_xCuO_4$ with $x = 0.125$ at 15 K (blue) and 100 K (red). (c) Results for Cu-O(1) σ^2 for $x = 0.125$ from PDF (blue filled circles) and the EXAFS analysis (red open circles) of Lanzara *et al.* [60]. The solid line corresponds to an Einstein-model calculation, as described in the text.

where μ is the reduced mass, and we have set $\hbar\omega_E = 70$ meV, the zone-boundary energy of the Cu-O bond-stretching phonon [58]. The calculation indicates that the zero-point fluctuations of the Cu-O bond, corresponding to a bond-length spread of 0.05 Å, is an order of magnitude greater than the bond-length splitting in the LTT phase.

Besides the bond-length splitting, one might anticipate an enhanced bond-length disorder in association with the ordering of charge stripes. Such enhanced disorder has been detected in the case of nickelates, such as $La_{1.67}Sr_{0.33}NiO_4$ [61]. In the closely related $La_2NiO_{4.125}$, model fits to superlattice intensities indicated displacements of in-plane O atoms on the order of ± 0.02 Å [62]. In contrast, a similar analysis of displacements in the cuprate $La_{1.48}Nd_{0.4}Sr_{0.12}CuO_4$ indicates displacements of order ± 0.004 Å [63], which would be quite difficult to detect in the PDF analysis.

The Cu-O pair distribution can also be probed with the x-ray absorption fine structure (XAFS) technique. In a polarized Cu K-edge XAFS study, Bianconi and coworkers [59,64] have reported a splitting of the Cu-O bond distribution by 0.08 Å below 100 K in $La_{1.85}Sr_{0.15}CuO_4$. Their low-temperature distribution is reproduced in Fig. 17(a). The large splitting in this model appears to be inconsistent with our PDF data, which would detect a splitting of this magnitude. In a study of

$La_{1.875}Ba_{0.125}CuO_4$ [60], a corresponding anomalous increase of σ^2 by 0.001 Å^2 on cooling below 60 K was reported; those data are indicated by open circles in Fig. 17(c). The magnitudes of σ^2 from the EXAFS and PDF analyses are consistent within error bars; however, the PDF results do not indicate any significant anomalous enhancement in the LTT phase. While small atomic displacements associated with stripe order are certainly present, as indicated by single-crystal diffraction [10,63], the present work indicates that they are significantly smaller than the zero-point bond-length fluctuations.

Next, we turn to the doping dependence of the Cu-O bond anisotropy, where we have two competing trends. One of these involves the decrease in the average octahedral tilt with doping. The shortening of the in-plane Cu-O bond length reduces the mismatch with bond lengths in the La_2O_2 layer, resulting in one contribution to the reduction in average tilt. Another comes from the quenched disorder associated with substituting Ba^{2+} for La^{3+}. The Ba acts effectively as a negative defect, repelling the neighboring apical oxygens and disrupting the octahedral tilt pattern. These effects lead to the decrease in the average orthorhombic strain with x, as summarized in Fig. 18. The competing trend involves the onset temperature for the LTT (LTLO) transition, resulting in ordering of OI tilts. The empirical trend is that this should grow with Ba concentration
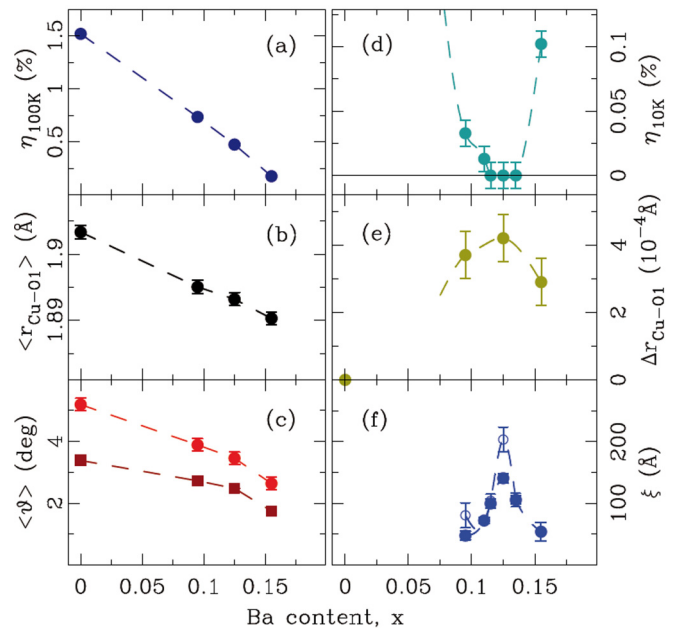

FIG. 18. (Color online) Doping dependence of various system parameters of $La_{2-x}Ba_xCuO_4$. (a) Orthorhombicity at 100 K (dark blue solid symbols) from Rietveld. (b) Average planar Cu-O bond distance (solid black symbols) at 100 K temperature. (c) Average CuO_6 tilt angle extracted from apical oxygen (light red solid circles) and planar oxygen (dark red solid squares) positions at maximum orthorhombicity. (d) Orthorhombicity at 10 K after Hücker *et al.* [17] (light blue solid symbols). (e) Planar Cu-O bond length anisotropy at 15 K (olive solid symbols). (f) In-plane correlation lengths ξ of charge ordering parallel (solid blue circles) and perpendicular (open blue circles) to the stripe direction at base temperature [17].
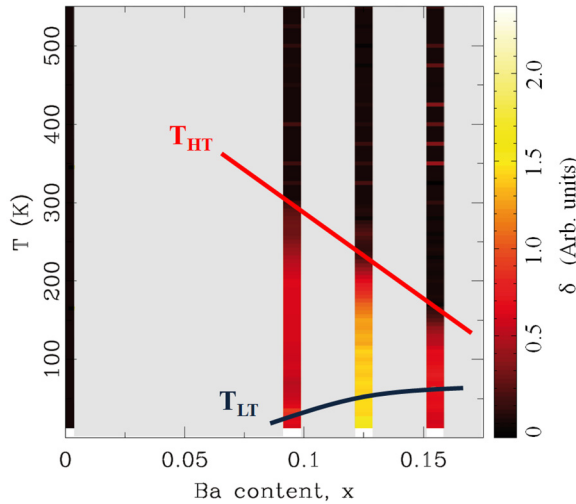
FIG. 19. (Color online) (x,T) evolution of δ shown in Figs. 11(d)–11(f). Solid lines mark structural transition temperature: T_{HT} (red) and T_{LT} (blue).

(as it depends on the average ionic radius of the 2+ ions relative to that of the 3+ ions [65]). These competing trends lead to the bond-length anisotropy reaching a maximum that appears to occur coincidentally near $x = 0.125$, where stripe order is strongest [17].

We get a somewhat different perspective from the temperature and doping dependence of parameter δ, defined in Eq. (2), which measures the LTT-like component of the octahedral tilts; a false-color representation is shown in Fig. 19. Here we see that the OI tilts appear in a significant way at the onset of LTO order. Furthermore, the relative magnitude is largest at $x = 0.125$ even before LTT order is achieved. This behavior is suggestive that the degree of Cu-O(1) bond-length splitting might be influenced by electron-phonon coupling and the particular stability of the stripe-ordered phase at $x = 0.125$. Regarding stability, it is interesting to note the results of recent optical pump-probe studies. Pumping the $x = 0.125$ phase in $La_{1.8-x}Eu_{0.2}Sr_xCuO_4$ with 80-meV photons with polarization *parallel* to the planes induces interlayer superconducting coherence for $T \lesssim 15$ K [66]; this also causes stripe melting in $La_{2-x}Ba_xCuO_4$ [67]. In contrast, pumping $La_{2-x}Ba_xCuO_4$ with polarization *perpendicular* to the planes enhances interlayer superconducting coherence for $x = 0.115$, but not for $x = 0.125$ [68].

It is also relevant to compare with observations of charge-density-wave (CDW) order in $YBa_2Cu_3O_{6+d}$ [69,70]. While there are differences in the doping dependence of the charge-ordering wave vectors and the connection to the spin correlations, the CDW order in $YBa_2Cu_3O_{6+d}$ is strongest for hole concentration near 0.12 [71,72], a remarkable similarity to $La_{2-x}Ba_xCuO_4$ [17] and $La_{1.6-x}Nd_{0.4}Sr_xCuO_4$ [73]. The CDW order in $YBa_2Cu_3O_{6+d}$ appears at temperatures as high as $\sim$150 K in a lattice with OI order present to above room temperature.

Finally, we note that charge-stripe order has recently been detected by x-ray diffraction in $La_{2-x}Sr_xCuO_4$ with $x \sim 0.12$ [74–77], confirming an earlier identification by nuclear magnetic resonance [78]. This result is somewhat

surprising, as the average structure of $La_{2-x}Sr_xCuO_4$ is LTO (although electron diffraction studies have indicated LTT-like regions at LTO twin boundaries for $x = 0.12$ [79] and LTLO order for $x = 0.115$ [80]). A key difference from $La_{2-x}Ba_xCuO_4$ is that the average orientation of the charge stripes is rotated away from the Cu-O bond direction by a small amount. Despite this difference, it seems relevant to ask whether dynamic or quasistatic OI tilts may be present in $La_{2-x}Sr_xCuO_4$. We hope to test this possibility in the future.

V. SUMMARY

Experimental evidence for the persistence, on a nanometer length scale, of CuO_6 LTT-like octahedral tilt correlations deep into the LTO crystallographic phase in $La_{2-x}Ba_xCuO_4$ with $0.095 \leqslant x \leqslant 0.155$ has been presented. Despite the average structure becoming orthorhombic above T_{LT} as evidenced by Rietveld refinements of neutron scattering data, PDF analysis of the same data shows that the local structure retains its base temperature signatures consistent with orthogonal inequivalent state up to at least T_{HT}, where LTO transforms to HTT. The analysis also suggests that there is little preference between OI and OE tilts at high temperature, consistent with the idea that, in the HTT phase, the Cu-O(2) bond precesses rather smoothly around the c axis. The bond-length modulation that pins stripe order is found to be remarkably subtle, with no anomalous bond length disorder at low temperature, placing an upper limit on in-plane Cu-O bond-length anisotropy of 0.005 Å. Complementary inelastic neutron scattering measurements on an $x = 1/8$ single-crystal sample reveal that upon heating across T_{LT} the tilt correlations become extremely short-range and dynamic. The finite width of excitations around $\mathbf{Q} = (3,3,L)$ along Q_z further indicates that the LTT tilt fluctuations have 3D character. The relative magnitude of the effect is maximum at $x = 1/8$ doping where bulk superconductivity is most strongly suppressed, suggesting that the splitting of Cu-O(1) bond lengths might be influenced by electron-phonon coupling and the particular stability of the stripe-ordered phase at this composition.

[1] J. Bednorz and K. Müller, Z. Phys. B **64**, 189 (1986).

[2] J. D. Jorgensen, H. B. Schüttler, D. G. Hinks, D. W. Capone II, K. Zhang, M. B. Brodsky, and D. J. Scalapino, Phys. Rev. Lett. **58**, 1024 (1987).

[3] D. M. Paul, G. Balakrishnan, N. R. Bernhoeft, W. I. F. David, and W. T. A. Harrison, Phys. Rev. Lett. **58**, 1976 (1987).

[4] A. R. Moodenbaugh, Y. Xu, M. Suenaga, T. J. Folkerts, and R. N. Shelton, Phys. Rev. B **38**, 4596 (1988).

[5] J. D. Axe, A. H. Moudden, D. Hohlwein, D. E. Cox, K. M. Mohanty, A. R. Moodenbaugh, and Y. Xu, Phys. Rev. Lett. **62**, 2751 (1989).

[6] T. Suzuki and T. Fujita, J. Phys. Soc. Jpn. **58**, 1883 (1989).

[7] D. E. Cox, P. Zolliker, J. D. Axe, A. H. Moudden, A. R. Moodenbaugh, and Y. Xu, Mat. Res. Symp. Proc. **156**, 141 (1989).

[8] S. J. L. Billinge, G. H. Kwei, A. C. Lawson, J. D. Thompson, and H. Takagi, Phys. Rev. Lett. **71**, 1903 (1993).

[9] J. M. Tranquada, B. J. Sternlieb, J. D. Axe, Y. Nakamura, and S. Uchida, Nature (London) **375**, 561 (1995).

[10] M. Fujita, H. Goka, K. Yamada, J. M. Tranquada, and L. P. Regnault, Phys. Rev. B **70**, 104517 (2004).

[11] Q. Li, M. Hücker, G. D. Gu, A. M. Tsvelik, and J. M. Tranquada, Phys. Rev. Lett. **99**, 067001 (2007).

[12] J. M. Tranquada, G. D. Gu, M. Hücker, Q. Jie, H.-J. Kang, R. Klingeler, Q. Li, N. Tristan, J. S. Wen, G. Y. Xu, Z. J. Xu, J. Zhou, and M. v. Zimmermann, Phys. Rev. B **78**, 174529 (2008).

[13] E. Berg, E. Fradkin, S. A. Kivelson, and J. M. Tranquada, New J. Phys. **11**, 115004 (2009).

[14] A. Himeda, T. Kato, and M. Ogata, Phys. Rev. Lett. **88**, 117001 (2002).

[15] T. Suzuki and T. Fujita, Physica C **159**, 111 (1989).

[16] Y. Zhao, B. D. Gaulin, J. P. Castellan, J. P. C. Ruff, S. R. Dunsiger, G. D. Gu, and H. A. Dabkowska, Phys. Rev. B **76**, 184121 (2007).

[17] M. Hücker, M. v. Zimmermann, G. D. Gu, Z. J. Xu, J. S. Wen, G. Xu, H. J. Kang, A. Zheludev, and J. M. Tranquada, Phys. Rev. B **83**, 104506 (2011).

[18] J. Wen, Z. Xu, G. Xu, Q. Jie, M. Hücker, A. Zheludev, W. Tian, B. L. Winn, J. L. Zarestky, D. K. Singh, T. Hong, Q. Li, G. Gu, and J. M. Tranquada, Phys. Rev. B **85**, 134512 (2012).

[19] S. J. L. Billinge, G. H. Kwei, and H. Takagi, Phys. Rev. Lett. **72**, 2282 (1994).

[20] D. Haskel, E. A. Stern, F. Dogan, and A. R. Moodenbaugh, Phys. Rev. B **61**, 7055 (2000).

[21] E. Božin, S. Billinge, and G. Kwei, Physica B **241–243**, 795 (1997).

[22] G. Fabbris, M. Hücker, G. D. Gu, J. M. Tranquada, and D. Haskel, Phys. Rev. B **88**, 060507 (2013).

[23] J. D. Axe and M. K. Crawford, J. Low Temp. Phys. **95**, 271 (1994).

[24] P. G. Radaelli, D. G. Hinks, A. W. Mitchell, B. A. Hunter, J. L. Wagner, B. Dabrowski, K. G. Vandervoort, H. K. Viswanathan, and J. D. Jorgensen, Phys. Rev. B **49**, 4163 (1994).

[25] M. K. Crawford, R. L. Harlow, E. M. McCarron, W. E. Farneth, J. D. Axe, H. Chou, and Q. Huang, Phys. Rev. B **44**, 7749 (1991).

[26] R. J. Birgeneau, C. Y. Chen, D. R. Gabbe, H. P. Jenssen, M. A. Kastner, C. J. Peters, P. J. Picone, T. Thio, T. R. Thurston, H. L. Tuller, J. D. Axe, P. Böni, and G. Shirane, Phys. Rev. Lett. **59**, 1329 (1987).

[27] T. R. Thurston, R. J. Birgeneau, D. R. Gabbe, H. P. Jenssen, M. A. Kastner, P. J. Picone, N. W. Preyer, J. D. Axe, P. Böni, G. Shirane, M. Sato, K. Fukuda, and S. Shamoto, Phys. Rev. B **39**, 4327 (1989).

[28] H. Kimura, K. Hirota, C.-H. Lee, K. Yamada, and G. Shirane, J. Phys. Soc. Jpn. **69**, 851 (2000).

[29] B. Keimer, R. J. Birgeneau, A. Cassanho, Y. Endoh, M. Greven, M. A. Kastner, and G. Shirane, Z. Phys. B **91**, 373 (1993).

[30] H. Kimura, Y. Noda, H. Goka, M. Fujita, K. Yamada, and G. Shirane, J. Phys. Soc. Jpn. **74**, 445 (2005).

[31] S. Wakimoto, H. Kimura, M. Fujita, K. Yamada, Y. Noda, G. Shirane, G. Gu, H. Kim, and R. J. Birgeneau, J. Phys. Soc. Jpn. **75**, 074714 (2006).

[32] W. E. Pickett, R. E. Cohen, and H. Krakauer, Phys. Rev. Lett. **67**, 228 (1991).

[33] Z.-X. Cai and D. O. Welch, Physica C **231**, 383 (1994).

[34] T. Egami and S. J. L. Billinge, *Underneath the Bragg Peaks: Structural Analysis of Complex Materials*, 2nd ed. (Elsevier, Amsterdam, 2012).

[35] P. F. Peterson, M. Gutmann, T. Proffen, and S. J. L. Billinge, J. Appl. Crystallogr. **33**, 1192 (2000).

[36] H. M. Rietveld, Acta Crystallogr. **22**, 151 (1967).

[37] A. C. Larson and R. B. Von Dreele, General Structure Analysis System, Los Alamos National Laboratory Report No. LAUR-86-748 (1987).

[38] B. H. Toby, J. Appl. Crystallogr. **34**, 201 (2001).

[39] C. L. Farrow, P. Juhás, J. Liu, D. Bryndin, E. S. Božin, J. Bloch, T. Proffen, and S. J. L. Billinge, J. Phys: Condens. Matter **19**, 335219 (2007).

[40] B. Winn, U. Filges, V. O. Garlea, M. Graves-Brook, M. Hagen, C. Jiang, M. Kenzelmann, L. Passell, S. M. Shapiro, X. Tong, and I. Zaliznyak, EPJ Web Conf. **83**, 03017 (2015).

[41] O. Arnold, J. Bilheux, J. Borreguero, A. Buts, S. Campbell, L. Chapon, M. Doucet, N. Draper, R. F. Leal, M. Gigg, V. Lynch, A. Markvardsen, D. Mikkelson, R. Mikkelson, R. Miller, K. Palmen, P. Parker, G. Passos, T. Perring, P. Peterson, S. Ren, M. Reuter, A. Savici, J. Taylor, R. Taylor, R. Tolchenov, W. Zhou, and J. Zikovsky, Nucl. Instrum. Methods Phys. Res., Sect. A **764**, 156 (2014).

[42] R. T. Azuah, L. R. Kneller, Y. Qiu, P. L. W. Tregenna-Piggott, C. M. Brown, J. R. D. Copley, and R. M. Dimeo, J. Res. Natl. Inst. Stan. Technol. **114**, 341 (2009).

[43] X. Qiu, T. Proffen, J. F. Mitchell, and S. J. L. Billinge, Phys. Rev. Lett. **94**, 177203 (2005).

[44] E. S. Božin, A. Sartbaeva, H. Zheng, S. A. Wells, J. F. Mitchell, T. Proffen, M. F. Thorpe, and S. J. L. Billinge, J. Phys. Chem. Solids **69**, 2146 (2008).

[45] S. J. L. Billinge, G. H. Kwei, and H. Takagi, Physica B **199–200**, 244 (1994).

[46] P. Debye, Ann. Phys. (Leipzig) **39**, 789 (1912).

[47] K. R. Knox, A. M. M. Abeykoon, H. Zheng, W.-G. Yin, A. M. Tsvelik, J. F. Mitchell, S. J. L. Billinge, and E. S. Bozin, Phys. Rev. B **88**, 174114 (2013).

[48] E. S. Božin, K. R. Knox, P. Juhás, Y. S. Hor, J. F. Mitchell, and S. J. L. Billinge, Sci. Rep. **4**, 4081 (2014).

[49] E. S. Božin and S. J. L. Billinge, Solid State Phenomena **61–62**, 271 (1998).

[50] E. S. Božin, S. J. L. Billinge, G. H. Kwei, and H. Takagi, Phys. Rev. B **59**, 4445 (1999).

[51] E. S. Božin, C. D. Malliakas, P. Souvatzis, T. Proffen, N. A. Spaldin, M. G. Kanatzidis, and S. J. L. Billinge, Science **330**, 1660 (2010).

[52] K. R. Knox, E. S. Bozin, C. D. Malliakas, M. G. Kanatzidis, and S. J. L. Billinge, Phys. Rev. B **89**, 014102 (2014).

[53] I. K. Jeong, T. Proffen, F. Mohiuddin-Jacobs, and S. J. L. Billinge, J. Phys. Chem. A **103**, 921 (1999).

[54] T. Proffen and S. J. L. Billinge, J. Appl. Crystallogr. **32**, 572 (1999).

[55] I. K. Jeong, R. H. Heffner, M. J. Graf, and S. J. L. Billinge, Phys. Rev. B **67**, 104301 (2003).

[56] E. D. Isaacs, G. Aeppli, P. Zschack, S.-W. Cheong, H. Williams, and D. J. Buttrey, Phys. Rev. Lett. **72**, 3421 (1994).

[57] E. Sevillano, H. Meuth, and J. J. Rehr, Phys. Rev. B **20**, 4908 (1979).

[58] D. Reznik, L. Pintschovius, M. Ito, S. Iikubo, M. Sato, H. Goka, M. Fujita, K. Yamada, G. D. Gu, and J. M. Tranquada, Nature (London) **440**, 1170 (2006).

[59] A. Bianconi, N. L. Saini, A. Lanzara, M. Missori, T. Rossetti, H. Oyanagi, H. Yamaguchi, K. Oka, and T. Ito, Phys. Rev. Lett. **76**, 3412 (1996).

[60] A. Lanzara, N. L. Saini, T. Rossetti, A. Bianconi, H. Oyanagi, H. Yamaguchi, and Y. Maeno, Solid State Commun. **97**, 93 (1996).

[61] A. M. M. Abeykoon, E. S. Božin, W.-G. Yin, G. Gu, J. P. Hill, J. M. Tranquada, and S. J. L. Billinge, Phys. Rev. Lett. **111**, 096404 (2013).

[62] J. M. Tranquada, J. E. Lorenzo, D. J. Buttrey, and V. Sachan, Phys. Rev. B **52**, 3581 (1995).

[63] J. M. Tranquada, J. D. Axe, N. Ichikawa, Y. Nakamura, S. Uchida, and B. Nachumi, Phys. Rev. B **54**, 7489 (1996).

[64] N. L. Saini, A. Lanzara, H. Oyanagi, H. Yamaguchi, K. Oka, T. Ito, and A. Bianconi, Phys. Rev. B **55**, 12759 (1997).

[65] T. Suzuki, M. Sera, T. Hanaguri, and T. Fukase, Phys. Rev. B **49**, 12392 (1994).

[66] D. Fausti, R. I. Tobey, N. Dean, S. Kaiser, A. Dienst, M. C. Hoffmann, S. Pyon, T. Takayama, H. Takagi, and A. Cavalleri, Science **331**, 189 (2011).

[67] M. Först, R. I. Tobey, H. Bromberger, S. B. Wilkins, V. Khanna, A. D. Caviglia, Y.-D. Chuang, W. S. Lee, W. F. Schlotter, J. J. Turner, M. P. Minitti, O. Krupin, Z. J. Xu, J. S. Wen, G. D. Gu, S. S. Dhesi, A. Cavalleri, and J. P. Hill, Phys. Rev. Lett. **112**, 157002 (2014).

[68] D. Nicoletti, E. Casandruc, Y. Laplace, V. Khanna, C. R. Hunt, S. Kaiser, S. S. Dhesi, G. D. Gu, J. P. Hill, and A. Cavalleri, Phys. Rev. B **90**, 100503 (2014).

[69] G. Ghiringhelli, M. Le Tacon, M. Minola, S. Blanco-Canosa, C. Mazzoli, N. B. Brookes, G. M. De Luca, A. Frano, D. G. Hawthorn, F. He, T. Loew, M. M. Sala, D. C. Peets, M. Salluzzo, E. Schierle, R. Sutarto, G. A. Sawatzky, E. Weschke, B. Keimer, and L. Braicovich, Science **337**, 821 (2012).

[70] J. Chang, E. Blackburn, A. T. Holmes, N. B. Christensen, J. Larsen, J. Mesot, R. Liang, D. A. Bonn, W. N. Hardy, A. Watenphul, M. v. Zimmermann, E. M. Forgan, and S. M. Hayden, Nat. Phys. **8**, 871 (2012).

[71] M. Hücker, N. B. Christensen, A. T. Holmes, E. Blackburn, E. M. Forgan, R. Liang, D. A. Bonn, W. N. Hardy, O. Gutowski, M. v. Zimmermann, S. M. Hayden, and J. Chang, Phys. Rev. B **90**, 054514 (2014).

[72] S. Blanco-Canosa, A. Frano, E. Schierle, J. Porras, T. Loew, M. Minola, M. Bluschke, E. Weschke, B. Keimer, and M. Le Tacon, Phys. Rev. B **90**, 054513 (2014).

[73] N. Ichikawa, S. Uchida, J. M. Tranquada, T. Niemöller, P. M. Gehring, S.-H. Lee, and J. R. Schneider, Phys. Rev. Lett. **85**, 1738 (2000).

[74] H. H. Wu, M. Buchholz, C. Trabant, C. F. Chang, A. C. Komarek, F. Heigl, M. v. Zimmermann, M. Cwik, F. Nakamura, M. Braden, and C. Schüßler-Langeheine, Nat. Commun. **3**, 1023 (2012).

[75] N. B. Christensen, J. Chang, J. Larsen, M. Fujita, M. Oda, M. Ido, N. Momono, E. M. Forgan, A. T. Holmes, J. Mesot, M. Hücker, and M. v. Zimmermann, arXiv:1404.3192.

[76] T. P. Croft, C. Lester, M. S. Senn, A. Bombardi, and S. M. Hayden, Phys. Rev. B **89**, 224513 (2014).

[77] V. Thampy, M. P. M. Dean, N. B. Christensen, L. Steinke, Z. Islam, M. Oda, M. Ido, N. Momono, S. B. Wilkins, and J. P. Hill, Phys. Rev. B **90**, 100510 (2014).

[78] A. W. Hunt, P. M. Singer, K. R. Thurber, and T. Imai, Phys. Rev. Lett. **82**, 4300 (1999).

[79] Y. Horibe, Y. Inoue, and Y. Koyama, Physica C **282–287**, 1071 (1997).

[80] Y. Koyama, Y. Wakabayashi, K. Ito, and Y. Inoue, Phys. Rev. B **51**, 9045 (1995).

Insulating and metallic spin glass in Ni-doped K$_x$Fe$_{2-y}$Se$_2$ single crystals

Hyejin Ryu (류혜진),[1,2,*] Milinda Abeykoon,[1] Kefeng Wang (王克锋),[1,†] Hechang Lei (雷和畅),[1,‡] N. Lazarevic,[3]
J. B. Warren,[4] E. S. Bozin,[1] Z. V. Popovic,[3] and C. Petrovic[1,2]

[1]*Condensed Matter Physics and Materials Science Department, Brookhaven National Laboratory, Upton, New York 11973, USA*
[2]*Department of Physics and Astronomy, Stony Brook University, Stony Brook, New York 11794-3800, USA*
[3]*Center for Solid State Physics and New Materials, Institute of Physics Belgrade, University of Belgrade,
Pregrevica 118, 11080 Belgrade, Serbia*
[4]*Instrument Division, Brookhaven National Laboratory, Upton, New York 11973, USA*

We report electron doping effects by Ni in K$_x$Fe$_{2-\delta-y}$Ni$_y$Se$_2$ ($0.06 \leqslant y \leqslant 1.44$) single-crystal alloys. A rich ground-state phase diagram is observed. A small amount of Ni ($\sim$4%) suppressed superconductivity below 1.8 K, inducing insulating spin-glass magnetic ground state for higher Ni content. With further Ni substitution, metallic resistivity is restored. For high Ni concentration in the lattice the unit cell symmetry is high symmetry $I4/mmm$ with no phase separation whereas both $I4/m + I4/mmm$ space groups were detected in the phase separated crystals when concentration of Ni < Fe. The absence of superconductivity coincides with the absence of crystalline Fe vacancy order.

I. INTRODUCTION

The discovery of LaFeAsO$_{1-x}$F$_x$ has generated considerable attention due to unexpectedly high T_c's of up to 52 K in isostructural Fe-based materials [1–5]. Since then, several other types of iron-based superconductors have been discovered to include 122 structure (AFe$_2$As$_2$, A=Ca, Sr, Ba, and Eu) [6,7], 111 structure (AFeAs, A=Li and Na) [8,9], and 11 structure (α-PbO type FeSe) [10]. Recently, a new family of iron-based superconductors A$_x$Fe$_{2-y}$Se$_2$ (A = K, Rb, Cs, and Tl) with maximum $T_c \sim 33$ K [11–14] added not only to the materials' variety but also to the complexity of the Fe-based superconductivity problem due to the intrinsic nanoscale phase separation and proximity to an insulating magnetic state with long-range order [15–23].

Perturbation of the ground state in Fe-based superconductors by chemical substitutions is rather instructive. Ba substitution on KFe$_2$As$_2$ increases T_c to 38 K [6], whereas S doping in KFe$_2$Se$_2$ suppresses superconductivity [24]. Equally interesting is substitution of transition metal with unpaired 3d electrons and with similar ionic radius on Fe site. For instance, superconductivity is induced by Co and/or Ni doping in LaFeAsO, CaFeAsF, SrFe$_2$As$_2$, and BaFe$_2$As$_2$ [25–29]. On the other hand, Co or Ni substitutions on Fe atomic positions in FeSe significantly suppresses superconductivity [30].

In this work, we have investigated structure, transport, magnetic, and optical properties of the Ni-substituted K$_x$Fe$_{2-\delta}$Se$_2$ single-crystal series, where δ is Fe vacancy. Superconductivity is suppressed with a much faster rate when compared to crystallographic phase separation. We observe a rich ground-

state phase diagram where insulating magnetic spin glass gives way to metallic with further Ni concentration.

II. EXPERIMENT

Single crystals of K$_x$Fe$_{2-\delta-y}$Ni$_y$Se$_2$ used in this study were grown as described previously [24,31]. The platelike crystals with typical size $5 \times 5 \times 2$ mm^3 were grown. High-energy synchrotron x-ray experiment at 300 K was conducted on the X7B beamline of the National Synchrotron Light Source (NSLS) at Brookhaven National Laboratory (BNL). The setup utilized an x-ray beam 0.5 mm $\times$ 0.5 mm in size with a wavelength of 0.3196 Å ($E = 38.7936$ keV) configured with a focusing double crystal bent Laue monochomator, and Perkin-Elmer amorphous silicon image plate detector mounted perpendicular to the primary beam path. Finely pulverized samples were packed in cylindrical polyimide capillaries 1 mm in diameter and placed 377.81 mm away from the detector. Multiple scans were performed to a total exposure time of 240 s. The two-dimensional (2D) diffraction data were integrated and converted to intensity versus 2θ using the software FIT2D [32]. Structural refinements were carried out using the GSAS modeling program [33] operated by the EXPGUI platform [34]. The average stoichiometry was determined by energy-dispersive x-ray spectroscopy (EDX) in a JEOL JSM-6500 scanning electron microscope. Magnetization measurements, electric and thermal transport, and heat capacity were performed in a Quantum Design MPMS-XL5 and PPMS-9. Raman scattering measurements were performed on freshly cleaved samples using a JY T64000 Raman system in the backscattering micro-Raman configuration. The 514.5-nm line of a mixed Ar$^+$/Kr$^+$ gas laser was used as an excitation source. The corresponding excitation power density was less than 0.2 kW/cm^2. Low-temperature Raman measurements were performed using KONTI CryoVac continuous flow cryostat with a 0.5-mm thick window.

The in-plane resistivity $\rho_{ab}(T)$ was measured using a four-probe configuration on cleaved rectangularly shaped single crystals with current flowing in the ab plane of the

---

*Present address: Advanced Light Source, E. O. Lawrence Berkeley National Laboratory, Berkeley, California 94720, USA.

†Present address: CNAM, Department of Physics, University of Maryland, College Park, Maryland 20742, USA.

‡Present address: Department of Physics, Renmin University of China, Beijing, 100872, China.

tetragonal structure. Thin Pt wires were attached to electrical contacts made of silver paste. Thermal transport properties were measured in Quantum Design PPMS-9 from 2 to 350 K using a one-heater two-thermometer method. The relative error was $\frac{\Delta\kappa}{\kappa} \sim 5\%$ and $\frac{\Delta S}{S} \sim 5\%$ based on the Ni standard measured under identical conditions.

III. RESULTS AND DISCUSSION

Obtained high-energy synchrotron XRD results of the $K_x Fe_{2-\delta-y} Ni_y Se_2$ series can be fitted very well with $I4/m$ and $I4/mmm$ space groups when $y \leqslant 0.73(0)$, while they are fitted by the $I4/mmm$ space group only when $y \geqslant 1.13(1)$ [Fig. 1(a)]. This implies $I4/m$ and $I4/mmm$ phases coexist when $y \leqslant 0.73(0)$. There is small amount of SeO_2 due to the oxidization. To make a quantitative comparison of the average structure in the alloy series [Fig. 1(b)] only the $I4/m$ space group is used for the refinements when $y \leqslant 0.73(0)$, since this results in the same goodness-of-fit when compared to the refinements using both $I4/m$ and $I4/mmm$ space groups. For $y \geqslant 1.13(1)$, the $I4/mmm$ space group is used to determine the lattice parameters which are then converted into comparable numbers for the $I4/m$ space group using the formula $I4/m = \sqrt{5} \, I4/mmm$ for a-axis lattice parameters. Notice that there are considerable changes in lattice parameter a around $y = 0.73(0)$ and $y = 1.44(1)$. On the other hand, the lattice parameter c starts to decrease when $y = 0.73(0)$ as the Fe/Ni sites are filled with Ni. Nonmonotonic evolution of lattice parameters highlights the complex crystal structure
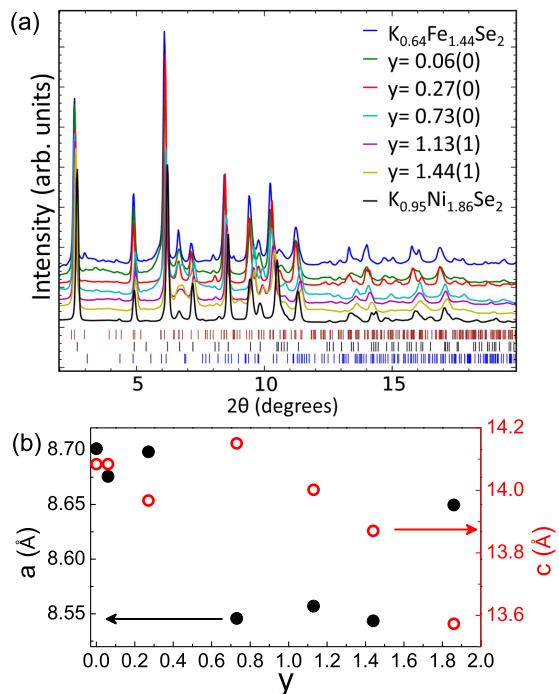
TABLE I. Summary of measured stoichiometry of $K_x Fe_{2-\delta-y} Ni_y Se_2$ samples. The first column shows nominal values used in the synthesis process.

K:Fe:Ni:Se	K	Fe	Ni	Se
1:1.8:0.2:2	0.73(0)	1.37(1)	0.06(0)	2
1:1.4:0.6:2	0.87(2)	1.15(1)	0.27(0)	2
1:1:1:2	0.84(0)	0.85(0)	0.73(0)	2
1:0.6:1.4:2	0.83(0)	0.56(0)	1.13(1)	2
1:0.2:1.8:2	0.82(0)	0.26(1)	1.44(1)	2

and bonding in $K_x Fe_{2-y} Ni_y Se_2$. The average atomic ratio of K, Fe, Ni, and Se in crystals is shown in Table I. Defects and deficiency of Fe(Ni) stoichiometry is commonly found in AFeCh-122 compounds [11,35,36]. As the Ni ratio increases, deficiency of K and the sum of Fe and Ni decreases, consistent with results on KNi_2Se_2 single crystals [31].

$K_{0.8}Fe_2Se_2$ shows superconductivity below 30 K and the metal-to-semiconductor transition at higher temperatures [11]. As shown in Fig. 2(a), 4.2% of Ni doping on the $K_{0.8}Fe_2Se_2$ single crystal suppresses not only superconductivity but also conductivity and results in an insulating $\rho(T)$. However, as Ni substitutes for Fe further, conductivity increases up to the

FIG. 1. (Color online) (a) High-energy synchrotron x-ray diffraction data of the $K_x Fe_{2-\delta-y} Ni_y Se_2$ series. Upper, middle, and lower vertical tick marks are for the $I4/m$ phase, the $I4/mmm$ phase, and SeO_2 reflections, respectively. (b) Lattice parameters as a function of Ni content y in $K_x Fe_{2-\delta-y} Ni_y Se_2$. Solid circles are for lattice parameter a and open circles are for lattice parameter c.

FIG. 2. (Color online) (a) Temperature dependence of the in-plane resistivity on the $K_x Fe_{2-\delta-y} Ni_y Se_2$ series at zero and 9-T field. (b) The relation between C/T and T^2 for the $K_x Fe_{2-\delta-y} Ni_y Se_2$ series at low temperature. The solid lines represent fits by the equation $C/T = \gamma + \beta_3 T^2 + \beta_5 T^4$. (c) Temperature dependence of thermoelectric power $S(T)$ for the $K_x Fe_{2-\delta-y} Ni_y Se_2$ series. The inset shows the thermoelectric power at $T = 150$ K for different Ni concentrations with added results for $y = 0$ and $y = 1.86(2)$ from Refs. [38,31].

TABLE II. Summary of γ values and Debye temperatures in $K_xFe_{2-\delta-y}Ni_ySe_2$.

y	γ (mJ mol^{-1} K^{-2})	Θ_D(K)
0.06(0)	0.6(4)	210(3)
0.27(0)	0.3(2)	230(6)
0.73(0)	0.2(1)	232(2)
1.13(1)	45(7)	218(3)
1.44(1)	72(9)	208(5)

highest Ni concentration in $K_{0.95}Ni_{1.86}Se_2$, consistent with previous study [31].

The relation between C/T and T^2 also shows insulator-to-metal transition as Ni concentration increases, as shown in Fig. 2(b). The electronic specific heat and Debye temperature are obtained by the fitting on $C/T - T^2$ curves from the 5- to 10-K region using the formula $C/T = \gamma + \beta_3 T^2 + \beta_5 T^4$. The Debye temperatures are estimated by the formula $\Theta_D = (12\pi^4 NR/5\beta)^{1/3}$, where N is the atomic number in the chemical formula and R is the gas constant. The obtained γ values and Debye temperatures Θ_D for different Ni concentrations are listed in Table II. All samples in the $K_xFe_{2-\delta-y}Ni_ySe_2$ series have similar Θ_D values which reflects no significant changes in atomic weight, structure, and bonding. In addition, γ values are negligible for $y \leqslant 0.73(0)$ suggesting minute density of states at the Fermi level as expected for an insulator. Larger γ values for the $y > 0.73(0)$ region reflect rapid pileup of the density of states $N(E_F)$ in the metallic region and possible heavy fermionlike behavior [31,37].

Temperature dependence of thermoelectric power $S(T)$ for the $K_xFe_{2-\delta-y}Ni_ySe_2$ series is shown in the main part whereas $S(y)$ at 150 K is presented in the inset of Fig. 2(c). Large Fermi surface changes are evident around $y = 0.73(0)$; this coincides with the notable lattice parameter change in XRD results. The changes are related to the metal insulator transition. It is interesting that the dominant carriers for the end members of $K_xFe_{2-\delta-y}Ni_ySe_2$ [$y = 0$ and $y = 1.86(2)$] [31,38] are electrons at high temperature whereas they are holes for samples in the middle of the series.

Temperature-dependent anisotropic magnetization for the $K_xFe_{2-\delta-y}Ni_ySe_2$ series is shown in Figs. 3(a) and 3(b). A pronounced irreversible behavior between zero-field-cooling (ZFC) and field-cooling (FC) curves below 50 K is observed. The irreversibility implies a magnetic spin glass where the spins are locked or frozen into random orientations below a characteristic temperature T_f. Similar behavior has been reported in $TlFe_{2-x}Se_2$, $KFeCuS_2$, and $K_xFe_{2-\delta}S_2$ [35,39,40]. M-H loops in the insets of Figs. 3(a) and 3(b) also support the glassy nature of the transition by presenting nearly linear field dependence with no hysteresis at 300 K or s-shape loop at 1.8 K [39]. Figure 3(c) shows the frequency-dependent peak of the real part in ac susceptibility $\chi'(T)$. As the frequency increases, the peak position moves to the higher temperature while magnitude decreases, another hallmark of the typical spin-glass behavior [41]. Relation between T_f and frequency can be fitted by $K = \Delta T_f/(T_f \Delta \log f)$, and the obtained K value is 0.0050(2). Similarly, the K value for $y = 0.73$ is 0.030(3) and for $y = 1.44$ is 0.020(2) [Figs. 3(e)–3(h)]. This
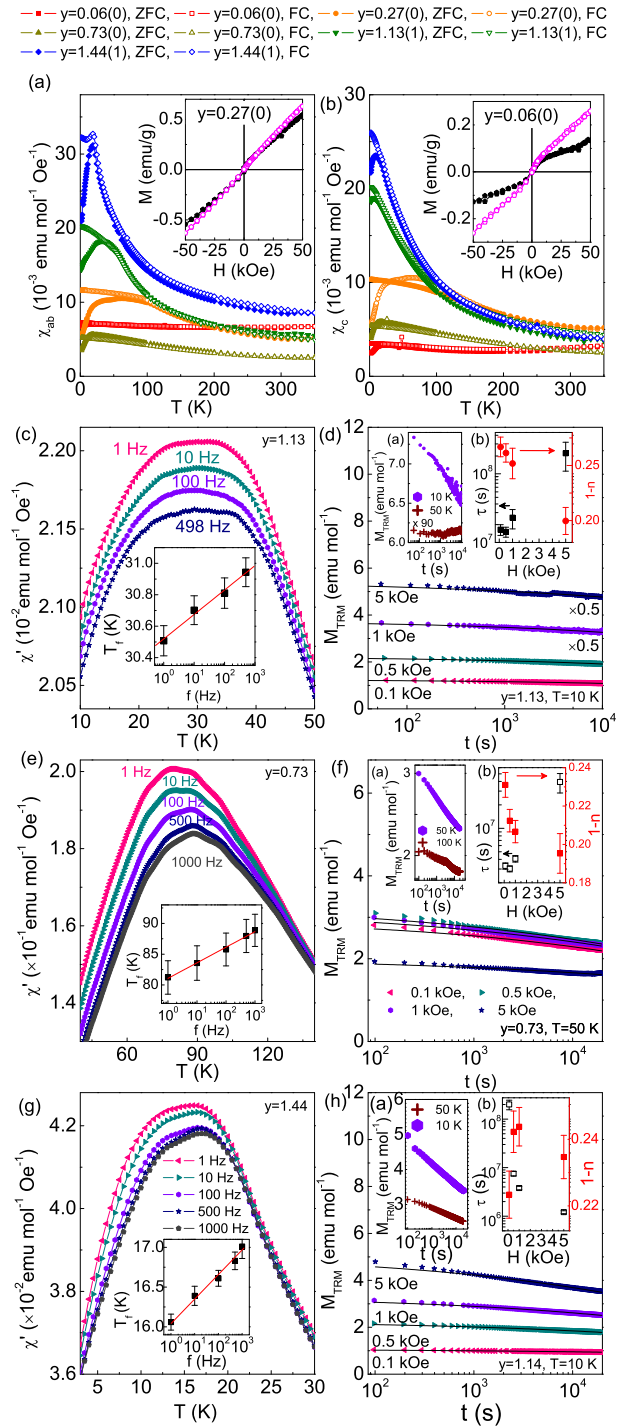

FIG. 3. (Color online) Temperature dependence dc magnetic susceptibilities for the $K_xFe_{2-\delta-y}Ni_ySe_2$ series for (a) $H \perp c$ and for (b) $H \parallel c$ at $H = 1$ kOe in ZFC and FC. Inset figures of (a) and (b) are M-H loops for $H \perp c$ and $H \parallel c$, respectively, at 1.8 K (solid pentagon) and 300 K (open pentagon). (c) Temperature dependence of $\chi'(T)$ measured at several fixed frequencies for $y = 1.13(1)$ of $K_xFe_{2-\delta-y}Ni_ySe_2$. Inset is the frequency dependence of T_f with the linear fitting (solid line). (d) TRM versus time for $y = 1.13(1)$ of $K_xFe_{2-\delta-y}Ni_ySe_2$ at 10 K and $t_w = 100$ s with different dc field with fitting (solid lines). Inset (a) is M_{TRM} vs t at 10 K and 50 K at $H = 1$ kOe and $t_w = 100$ s. Inset (b) is H-field dependence $\tau(s)$ (solid square) and 1-n (solid circle). (e)–(h) Similar data for $y = 0.73$ and 1.44.

is in agreement with the values ($0.0045 \leqslant K \leqslant 0.08$) for a canonical spin glass [41]. Thermoremanent magnetization (TRM) is shown in Fig. 3(d). The sample was cooled down from 100 K (above T_f) to 10 K (below T_f) in different magnetic fields, and kept there for $t_w = 100$ s. Then, magnetic field was switched off and magnetization decay $M_{\text{TRM}}(t)$ was measured. At $t = 10$ K, $M_{\text{TRM}}(t)$ shows slow decay, so $M_{\text{TRM}}(t)$ has nonzero values even after several hours. The slow decay of $M_{\text{TRM}}(t)$ is another typical property of the magnetic spin glass [41]. On the other hand, at $t = 50$ K (above T_f), $M_{\text{TRM}}(t)$ decays rapidly in a short time and stays nearly constant, when compared to the data at $t = 10$ K as shown in Fig. 3(d), inset (a). $M_{\text{TRM}}(t)$ decay in the spin-glass system is commonly explained by stretched exponential function, $M_{\text{TRM}}(t) = M_0 \exp[-(t/\tau)^{1-n}]$, where M_0, τ, and $1-n$ are the glassy component, the relaxation characteristic time, and the critical exponent, respectively. We observe that τ is significantly increased while $1-n$ is slightly decreased in magnetic field [Fig. 3(d), inset (b)]. The value of $1-n$ is close to $1/3$, as expected for a magnetic spin glass [42,43].

According to symmetry considerations one can expect four Raman-active phonons for the $I4/mmm$ phase (A_{1g}, B_{1g}, and $2E_g$) [44]. However, ordering of the vacancies, as reported for $K_x Fe_{2-\delta} Se_2$ [45], locally reduces the symmetry to $I4/m$. This leads to a substantial increase in the number of Raman modes. Symmetry analysis predicts a total of 27 Raman modes ($9A_g$, $9B_g$, and $9E_g$) originating from the vibrations within the $I4/m$ phase. When Raman spectra are measured from the ab plane of the sample, only two Raman modes can be seen for the $I4/mmm$ phase ($A_{1g} + B_{1g}$) and 18 for the $I4/m$ phase ($9A_g + 9B_g$).

Figure 4(a) shows Raman scattering spectra measured at 100 K from the ab plane of the $K_x Fe_{2-\delta-y} Ni_y Se_2$ single-crystal series. For the high concentration of Ni [$y = 1.44(1)$] only two modes can be observed. These modes were previously assigned as A_{1g} (185 cm^{-1}) and B_{1g} (141 cm^{-1}) modes. We notice traces of an additional structure around 248 cm^{-1} for the $y = 1.13(1)$ crystal. The structure is present for all investigated samples $y \leqslant 1.13(1)$ but it is highly pronounced for the $y = 0.73(0)$ and $y = 0.27(0)$ samples. The origin of this structure is most likely related to crystalline disorder. Disorder breaks the conservation of the momentum during the Raman scattering process enabling contributions of finite wave-vector phonons to Raman spectra. Another possibility is the appearance of a new high-symmetry phase. However this finding is not supported by XRD measurements. For the low concentrations of Ni the structure at around 248 cm^{-1} vanishes and the large number of vibrations of the $I4/m$ phase are observed, suggesting vibrations from vacancy ordered domains in the crystal. The A_{1g} mode [marked by an arrow in Fig. 4(a)], which represent the vibration of selenium ions in the $I4/mmm$ phase, persist for all Ni concentrations. This shows the presence of the $I4/mmm$ phase in all samples.

Our main results are summarized in the Fig. 4(b) phase diagram. As shown in the lower left corner of the phase diagram, superconducting (SC) phase disappears rapidly by $y = 0.06(1)$. The $I4/mmm$ space group is found for all $K_x Fe_{2-\delta-y} Ni_y Se_2$ series whereas the crystalline disordered $I4/m$ space group persists up to $y = 0.73$. Hence, Fe-based high-temperature

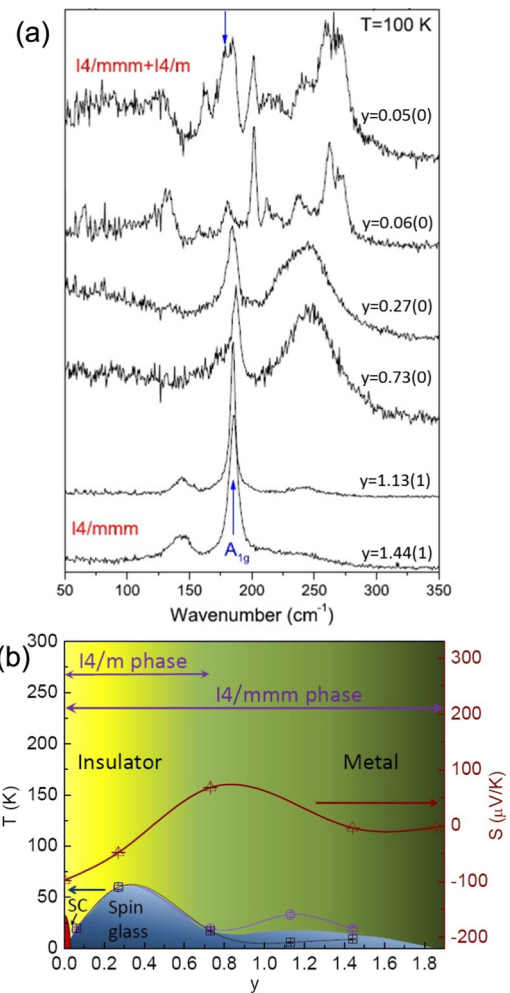FIG. 4. (Color online) (a) Raman scattering spectra of $K_x Fe_{2-\delta-y} Ni_y Se_2$ single-crystal series measured from the ab plane at 100 K. (b) Magnetic, transport, and structural phase diagram. The purple circles are $H \perp c$ and the black squares are for $H \parallel c$, respectively.

superconductivity in $K_x Fe_{2-\delta-y} Ni_y Se_2$ does vanish before the crystalline superstructure of Fe vacancies (crystalline ordered $I4/m$ phase) disappears when y is increased from 0. We note that in high-pressure studies superconductivity vanishes simultaneously with the $I4/m$ superstructure peak [46]. A high degree of crystalline disorder in the $I4/mmm$ and $I4/m$ phases results in an insulating or bad metal magnetic glass state that borders the superconducting region, similar to copper oxides [47,48]. In the insulating region of $K_x Fe_{2-\delta-y} Ni_y Se_2$ single-crystal alloys ground-state phase diagram [Fig. 4(b)], freezing temperatures T_f of the magnetic spin glass are higher (~ 60 K) when compared to metallic regions (~ 20 K) [$y > 1.13(1)$].

The mechanism of the nonmetallic states in proximity to $K_x Fe_{2-\delta} Se_2$ is of great importance for the understanding of superconductivity [49,50]. An intimate nanoscale mix of superconducting and insulating magnetic regions may also add states at interfaces [51,52]. This makes interpretation of many, and in particular bulk measurements difficult. In $K_x Fe_{2-\delta} Se_2$ nanoscale phase separation is found below $T_s = 560$ K [15],

hence the majority of conductivity changes at temperature below T_s should come from the metallic regions. This is supported by recent angle-resolved photoemission results where orbital-selective Mott transition in $K_x Fe_{2-\delta} Se_2$ was observed above 150 K [53]. This temperature corresponds to metal-insulator crossover in bulk measurements, suggesting that conductivity changes in bulk measurements may not be simply due to the ratio of metallic and insulating regions in the crystal [11,54]. Although only metallic nanoscale regions contribute to thermopower and metallic heat capacity [Figs. 2(b) and 2(c)], the absolute values of resistivity and magnetization reflect the contribution of both ($I4/mmm$) and insulating parts of the crystal ($I4/m$). Assuming that Ni substitutes Fe in both space groups, small Ni substitution therefore is likely to have a strong effect on states associated with itinerant d_{xz}/d_{yz} orbitals, perhaps via the localization effect in an orbital-selective Mott localization scenario [55,56]. Further Ni substitution and disorder might enhance conductivity by raising chemical potential and enlarging electron pockets [57–59]. This is in agreement with our phase diagram.

IV. CONCLUSION

We have investigated transport, magnetic, and structure changes in the $K_x Fe_{2-\delta-y} Ni_y Se_2$ single-crystal series. A small amount of Ni doping $y = 0.06$ suppressed Fe-based high-temperature superconductivity. The suppression of superconductivity is more sensitive to Ni substitution than crystalline superstructure of Fe vacancies. Further Ni substitution results in insulating and bad metal magnetic spin-glass ground state. However, when the Ni concentration in the lattice is higher than Fe, the metallic ground state with relatively large density of states at the Fermi level emerges. Similar to copper oxides, insulating/bad metal spin glass is found in proximity to the superconducting state. In Ni substituted in $K_x Fe_{2-\delta} Se_2$ the spin-glass state covers nearly all y values, from superconductivity up to the paramagnetic metal $K_x Ni_{2-\delta} Se_2$.

[1] Y. Kamihara, T. Watanabe, M. Hirano, and H. Hosono, J. Am. Chem. Soc. **130**, 3296 (2008).

[2] X. H. Chen, T. Wu, G. Wu, R. H. Liu, H. Chen, and D. F. Fang, Nature (London) **453**, 761 (2008).

[3] G. F. Chen, Z. Li, D. Wu, G. Li, W. Z. Hu, J. Dong, P. Zheng, J. L. Luo, and N. L. Wang, Phys. Rev. Lett. **100**, 247002 (2008).

[4] Z. A. Ren, J. Yang, W. Lu, Y. Wei, X. L. Shen, Z. C. Li, G. C. Che, X. L. Dong, L. L. Sun, F. Zhou, and Z. X. Zhao, Europhys. Lett. **82**, 57002 (2008).

[5] H.-H. Wen, G. Mu, L. Fang, H. Yang, and X. Y. Zhu, Europhys. Lett. **82**, 17009 (2008).

[6] M. Rotter, M. Tegel, and D. Johrendt, Phys. Rev. Lett. **101**, 107006 (2008).

[7] G. F. Chen, Z. Li, G. Li, W. Z. Hu, J. Dong, X. D. Zhang, P. Zheng, N. L. Wang, and J. L. Luo, Chin. Phys. Lett. **25**, 3403 (2008).

[8] X. C. Wang, Q. Q. Liu, Y. X. Lv, W. B. Gao, L. X. Yang, R. C. Yu, F. Y. Li, and C. Q. Jin, Solid State Commun. **148**, 538 (2008).

[9] J. H. Tapp, Z. Tang, B. Lv, K. Sasmal, B. Lorenz, P. C. W. Chu, and A. M. Guloy, Phys. Rev. B **78**, 060505 (2008).

[10] F. C. Hsu, J. Y. Luo, K. W. Yeh, T. K. Chen, T. W. Huang, P. M. Wu, Y. C. Lee, Y. L. Huang, Y. Y. Chu, D. C. Yan, and M. K. Wu, Proc. Nat. Acad. Sci. **105**, 14262 (2008).

[11] J. Guo, S. Jin, G. Wang, S. Wang, K. Zhu, T. Zhou, M. He, and X. Chen, Phys. Rev. B **82**, 180520(R) (2010).

[12] A. F. Wang, J. J. Ying, Y. J. Yan, R. H. Liu, X. G. Luo, Z. Y. Li, X. F. Wang, M. Zhang, G. J. Ye, P. Cheng, Z. J. Xiang, and X. H. Chen, Phys. Rev. B **83**, 060512 (2011).

[13] A. Krzton-Maziopa, Z. Shermadini, E. Pomjakushina, V. Pomjakushin, M. Bendele, A. Amato, and R. Khasanov, J. Phys. Condens. Matter **23**, 052203 (2011).

[14] H. D. Wang, C. H. Dong, Z. J. Li, Q. H. Mao, S. S. Zhu, C. M. Feng, H. Q. Yuan, and M. H. Fang, Europhys. Lett. **93**, 47004 (2011).

[15] W. Bao, Q. Z. Huang, G. F. Chen, M. A. Green, D. M. Wang, J. B. He, and Y. M. Qiu, Chin. Phys. Lett. **28**, 086104 (2011).

[16] D. H. Ryan, W. N. Rowan-Weetaluktuk, J. M. Cadogan, R. Hu, W. E. Straszheim, S. L. Budko, and P. C. Canfield, Phys. Rev. B **83**, 104526 (2011).

[17] Z. Wang, Y. J. Song, H. L. Shi, Z. W. Wang, Z. Chen, H. F. Tian, G. F. Chen, J. G. Guo, H. X. Yang, and J. Q. Li, Phys. Rev. B **83**, 140505 (2011).

[18] Y. Liu, Q. Xing, K. W. Dennis, R. W. McCallum, and T. A. Lograsso, Phys. Rev. B **86**, 144507 (2012).

[19] F. Chen, M. Xu, Q. Q. Ge, Y. Zhang, Z. R. Ye, L. X. Yang, Juan Jiang, B. P. Xie, R. C. Che, M. Zhang, A. F. Wang, X. H. Chen, D. W. Shen, J. P. Hu, and D. L. Feng, Phys. Rev. X **1**, 021020 (2011).

[20] A. Ricci, N. Poccia, B. Josesph, G. Arrighetti, L. Barba, J. Plaiser, G. Campi, Y. Mizuguchi, H. Takeya, Y. Takano, N. L. Saini, and A. Bianconi, Supercond. Sci. Technol. **24**, 082002 (2011).

[21] W. Li, H. Ding, P. Deng, K. Chang, C. Song, K. He, L. Wang, X. Ma, J.-P. Hu, X. Chen, and Q.-K. Xue, Nat. Phys. **8**, 126 (2011).

[22] R. H. Yuan, T. Dong, Y. J. Song, P. Zheng, G. F. Chen, J. P. Hu, J. Q. Li, and N. L. Wang, Sci. Rep. **2**, 221 (2012).

[23] D. Louca, K. Park, B. Li, J. Neufeind, and J. Yan, Sci. Rep. **3**, 2047 (2013).

[24] H. Lei, M. Abeykoon, E. S. Bozin, K. Wang, J. B. Warren, and C. Petrovic, Phys. Rev. Lett. **107**, 137002 (2011).

[25] A. Leithe-Jasper, W. Schnelle, C. Geibel, and H. Rosner, Phys. Rev. Lett. **101**, 207004 (2008).

[26] A. S. Sefat, A. Huq, M. A. McGuire, R. Jin, B. C. Sales, D. Mandrus, L. M. D. Cranswick, P. W. Stephens, and K. H. Stone, Phys. Rev. B **78**, 104505 (2008).

[27] S. Matsuishi, Y. Inoue, T. Nomura, H. Yanagi, M. Hirano, and H. Hosono, J. Am. Chem. Soc. **130**, 14429 (2008).

[28] A. S. Sefat, R. Jin, M. A. McGuire, B. C. Sales, D. J. Singh, and D. Mandrus, Phys. Rev. Lett. **101**, 117004 (2008).

[29] L. J. Li, Q. B. Wang, Y. K. Luo, H. Chen, Q. Tao, Y. K. Li, X. Lin, M. He, Z. W. Zhu, G. H. Cao, and Z. A. Xu, New J. Phys. **11**, 025008 (2009).

[30] Y. Mizuguchi, F. Tomioka, S. Tsuda, T. Yamaguchi, and Y. Takano, J. Phys. Soc. Jpn. **78**, 074712 (2009).

[31] H. Lei, M. Abeykoon, K. Wang, E. S. Bozin, H. Ryu, D. Graf, J. B. Warren, and C. Petrovic, J. Phys. Condens. Matter **26**, 015701 (2014).

[32] A. P. Hammersley, S. O. Svenson, M. Hanfland, and D. Hauserman, High Press. Res. **14**, 235 (1996).

[33] A. C. Larson and R. B. Von Dreele, Los Alamos National Laboratory Report No. LAUR 86-748 (Los Alamos National Laboratory, Los Alamos, 1994).

[34] B. H. Toby, J. Appl. Crystallogr. **34**, 210 (2001).

[35] H. C. Lei, M. Abeykoon, E. S. Bozin, and C. Petrovic, Phys. Rev. B **83**, 180503(R) (2011).

[36] D. M. Wang, J. B. He, T.-L. Xia, and G. F. Chen, Phys. Rev. B **83**, 132502 (2011).

[37] J. R. Neilson, A. Llobet, A. V. Stier, L. Wu, J. Wen, J. Tao, Y. Zhu, Z. B. Tesanovic, N. P. Armitage, and T. M. McQueen, Phys. Rev. B **86**, 054512 (2012).

[38] K. Wang, H. Lei, and C. Petrovic, Phys. Rev. B **83**, 174503 (2011).

[39] J. J. Ying, A. F. Wang, Z. J. Xiang, X. G. Luo, R. H. Liu, X. F. Wang, Y. J. Yan, M. Zhang, G. J. Ye, P. Cheng, and X. H. Chen, arXiv:1012.2929.

[40] M. Oledzka, K. V. Ramanujachary, and M. Greenblatt, Mater. Res. Bull. **31**, 1491 (1996).

[41] J. A. Mydosh, *Spin Glasses: An Experimental Introduction* (Taylor & Francis, London, 1993).

[42] I. A. Campbell, Phys. Rev. B **37**, 9800 (1988).

[43] D. Chu, G. G. Kenning, and R. Orbach, Phys. Rev. Lett. **72**, 3270 (1994).

[44] N. Lazarevic, M. Radonjic, M. Scepanovic, H. Lei, D. Tanaskovic, C. Petrovic, and Z. V. Popovic, Phys. Rev. B **87**, 144305 (2013).

[45] N. Lazarevic, M. Abeykoon, P. W. Stephens, H. Lei, E. S. Bozin, C. Petrovic, and Z. V. Popovic, Phys. Rev. B **86**, 054503 (2012).

[46] J. Guo, X. J. Chen, J. Dai, C. Zhang, J. Guo, X. Chen, Q. Wu, D. Gu, P. Gao, L. Yang, K. Yang, X. Dai, H. K. Mao, L. Sun, and Z. Zhao, Phys. Rev. Lett. **108**, 197001 (2012).

[47] I. Raicevic, J. Jaroszynski, D. Popovic, C. Panagopoulos, and T. Sasagawa, Phys. Rev. Lett. **101**, 177004 (2008).

[48] X. Shi, G. Logvenov, A. T. Bollinger, I. Božović, C. Panagopoulos, and D. Popović, Nat. Mater. **12**, 47 (2013).

[49] Z. P. Yin, K. Haule, and G. Kotliar, Nat. Mater. **10**, 933 (2011).

[50] P. Dai, J. Hu, and E. Dagotto, Nat. Phys. **8**, 709 (2012).

[51] Y. J. Yan, M. Zhang, A. F. Wang, J. J. Ying, Z. Y. Li, W. Qin, X. G. Luo, J. Q. Li, J. Hu, and X. H. Chen, Sci. Rep. **2**, 212 (2012).

[52] S. Mukherjee, M. N. Gastiasoro, P. J. Hirschfeld, and B. M. Andersen, Phys. Rev. B **88**, 014519 (2013).

[53] M. Yi, D. H. Lu, R. Yu, S. C. Riggs, J.-H. Chu, B. Lv, Z. K. Liu, M. Lu, Y.-T. Cui, M. Hashimoto, S.-K. Mo, Z. Hussain, C. W. Chu, I. R. Fisher, Q. Si, and Z.-X. Shen, Phys. Rev. Lett. **110**, 067003 (2013).

[54] D. P. Shoemaker, D. Y. Chung, H. Claus, M. C. Francisco, S. Avci, A. Llobet, and M. G. Kanatzidis, Phys. Rev. B **86**, 184511 (2012).

[55] R. Yu and Q. Si, Phys. Rev. Lett. **110**, 146402 (2013).

[56] R. Yu, J.-X. Zhu, and Q. Si, Phys. Rev. Lett. **106**, 186401 (2011).

[57] T. Berlijn, P. J. Hirschfeld, and W. Ku, Phys. Rev. Lett. **109**, 147003 (2012).

[58] L. Craco, M. S. Laad, and S. Leoni, Phys. Rev. B **84**, 224520 (2011).

[59] F. Lu, J. Z. Zhao and W. H. Wang, J. Phys. Condens. Matter **24**, 495501 (2012).

Sustained phase separation and spin glass in Co-doped $K_xFe_{2-y}Se_2$ single crystals

Hyejin Ryu (류혜진),[1,2,*] Kefeng Wang (王克锋),[1,†] M. Opacic,[3] N. Lazarevic,[3] J. B. Warren,[4]
Z. V. Popovic,[3] Emil S. Bozin,[1] and C. Petrovic[1,2]

[1]*Condensed Matter Physics and Materials Science Department, Brookhaven National Laboratory, Upton, New York 11973, USA*
[2]*Department of Physics and Astronomy, Stony Brook University, Stony Brook, New York 11794-3800, USA*
[3]*Center for Solid State Physics and New Materials, Institute of Physics Belgrade, University of Belgrade,*
Pregrevica 118, 11080 Belgrade, Serbia
[4]*Instrument Division, Brookhaven National Laboratory, Upton, New York 11973, USA*

We present Co substitution effects in $K_xFe_{2-y-z}Co_zSe_2$ ($0.06 \leqslant z \leqslant 1.73$) single-crystal alloys. By 3.5% of Co doping superconductivity is suppressed, whereas phase separation of semiconducting $K_2Fe_4Se_5$ and superconducting/metallic $K_xFe_2Se_2$ is still present. We show that the arrangement and distribution of the superconducting phase (stripe phase) are connected with the arrangement of K, Fe, and Co atoms. Semiconducting spin glass is found in proximity to the superconducting state, persisting for large Co concentrations. At high Co concentrations a ferromagnetic metallic state emerges above the spin glass. This is coincident with changes of the unit cell and arrangement and connectivity of the stripe conducting phase.

I. INTRODUCTION

Since the discovery of high-temperature Fe-based superconductivity [1], many types of Fe-based superconductors have been reported, including $K_xFe_{2-y}Se_2$ [2,3]. Various novel phenomena were observed by chemical substitution on the Fe site. For example, Co and Ni doping in FeAs tetrahedra of $LaFeAsO$ and $BaFe_2As_2$-based pnictides gives rise to superconductivity [4–7], whereas Co doping in FeSe suppresses superconductivity [8,9]. In particular, $A_xFe_{2-y}Se_2$ ($A =$ K, Cs, Rb, Tl) materials are strongly sensitive to chemical substitutions [10–12].

Among several different types of Fe-based superconductors, $A_xFe_{2-y}Se_2$ ($A =$ K, Cs, Rb, Tl) materials generate significant attention due to unique characteristics such as the absence of the pocket in the Brillouin zone center and phase separation with the Fe-vacancy order where the crystal separates into (super)conducting stripes (block) and magnetic semiconducting matrix regions on the 0.01–100-μm scale [13–18]. The mechanism of the conducting and nonconducting states in proximity to $K_xFe_{2-y}Se_2$ is of great importance for understanding superconductivity [19,20]. Consequently, the details of phase separation, phase stoichiometry, compositions, and their magnetic and electric ground states are currently being debated and are of high interest.

In this study we have investigated $K_xFe_{2-y-z}Co_zSe_2$ ($0.06 \leqslant z \leqslant 1.73$) single-crystal alloys, where y is a Fe/Co vacancy. A rich phase diagram is discovered, where a phase-separated superconducting state of $K_xFe_{2-y}Se_2$ turns into a spin glass and then into a $KCo_{1.73}Se_2$ ferromagnetic metal with no phase separation. We show that the microstructure arrangement and connectivity are rather important for ground-state changes, in addition to changes induced by Co substitution for Fe.

II. EXPERIMENT

Single crystals of $K_xFe_{2-y-z}Co_zSe_2$ ($0.06 \leqslant z \leqslant 1.73$) were synthesized as described previously [21]. Platelike crystals with size up to $10 \times 10 \times 3$ mm^3 were obtained. A high-energy medium-resolution synchrotron x-ray experiment at 300 K was conducted on the X7B beamline of the National Synchrotron Light Source at Brookhaven National Laboratory. The setup utilized an x-ray beam 0.5×0.5 mm in size with a wavelength of 0.3196 Å ($E = 38.7936$ keV) configured with a focusing double-crystal bent Laue monochromator and a Perkin-Elmer amorphous silicon image plate detector mounted perpendicular to the primary beam path. Finely pulverized samples were packed in cylindrical polyimide capillaries 1 mm in diameter and placed 377.81 mm away from the detector. Multiple scans were performed to a total exposure time of 240 s. The two-dimensional (2D) diffraction data were integrated and converted to intensity versus 2θ using the software FIT2D [22]. Structural refinements were carried out using the GSAS modeling program [23] operated by the EXPGUI platform [24]. The backscattered images and energy dispersive x-ray spectroscopy (EDX) mappings were performed in a JEOL-6500 scanning electron microscope (SEM). Electrical transport, thermal transport, heat capacity, and magnetization measurements were carried out in Quantum Design PPMS-9 and MPMS-XL5. Raman scattering measurements were performed on freshly cleaved (001)-oriented samples using TriVista 557 and Jobin Yvon T64000 Raman systems in backscattering micro-Raman configuration. The 514.5-nm laser line of a mixed Ar$^+$/Kr$^+$ gas laser was used as an excitation source. All measurements were carried out at room temperature in the vacuum.

III. RESULTS AND DISCUSSION

The obtained high-energy synchrotron x-ray-diffraction data of the $K_xFe_{2-y-z}Co_zSe_2$ series [Fig. 1(a)] can be fitted very well with $I4/m$ and $I4/mmm$ space groups for $z \leqslant 0.92(4)$, while they are fitted by the $I4/mmm$ space group only for $z > 0.92(4)$. This implies coexistence of

---

*Present address: Advanced Light Source, E. O. Lawrence Berkeley National Laboratory, Berkeley, California 94720, USA.
†Present address: CNAM, Department of Physics, University of Maryland, College Park, Maryland 20742, USA.
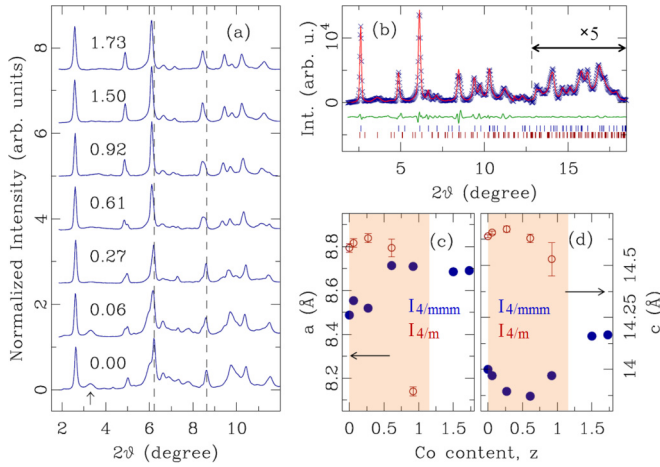
FIG. 1. (Color online) (a) High-energy synchrotron x-ray diffraction data of the $K_x Fe_{2-y-z} Co_z Se_2$ series, normalized by the intensity of (002) reflection for comparison. Data are offset for clarity and labeled by respective Co content as measured by EDX. Vertical dashed lines are provided as a visual reference. Vertical arrow indicates (110) reflection, which is a hallmark of the $I4/m$ phase. Coexistence of the $I4/m$ and $I4/mmm$ phases can be visually tracked up to $z = 0.92(4)$ cobalt content in the samples studied. (b) Modeling of powder diffraction data for a sample with $z = 0.92(4)$. Crosses represent data, red solid line is the model, and green solid line is the difference, which is offset for clarity. Vertical ticks mark the reflections in the $I4/mmm$ (top row) and $I4/m$ (bottom row) phases. (c) and (d) Evolution with EDX-established Co content of refined lattice parameters for $I4/mmm$ (solid blue circles) and $I4/m$ (open red circles). All parameters are expressed in the $I4/m$ metrics (see text). The shaded region is where the signatures of the phase coexistence could be reliably established from the diffraction data.

$I4/m$ and $I4/mmm$ phases when $z \leqslant 0.92(4)$. The typical fit for a phase-separated sample with $z = 0.92(4)$ is shown in Fig. 1(b). Notably, for $0.27 \leqslant z \leqslant 0.92$ intensities of reflections characteristic of the $I4/m$ phase become appreciably weaker and rather broad, indicative of disorder and loss of structural coherence of this structural component, as well as its presumably diminishing contribution. However, quantitative phase analysis was not feasible due to the limited resolution of the measurement and due to the diffuse nature of the signal with broad and overlapping reflections. The evolution of extracted lattice parameters with Co content is shown in Figs. 1(c) and 1(d). Lattice parameters for the a axis of the $I4/mmm$ space group are converted into comparable numbers for the $I4/m$ space group using the formula $I4/m = \sqrt{5}\, I4/mmm$. Nonmonotonic evolution of the lattice parameters highlights the complex crystal structure and bonding in $K_x Fe_{2-y-z} Co_z Se_2$.

The surface morphologies (Fig. 2) show that the Co-doped crystals separate into two regions, a stripe- (domain-) like brighter area that is 1–2 μm thick and a darker matrix area, similar to pure $K_x Fe_{2-y} Se_2$ [17], implying that the phase separation is preserved with Co doping. Distributions of the elements of $K_x Fe_{2-y-z} Co_z Se_2$ in the samples investigated by EDX mapping are shown in Figs. 2(a)–2(c). The bright colored area is the area covered by each element. Se is uniformly distributed for all three samples, while K, Fe, and Co display
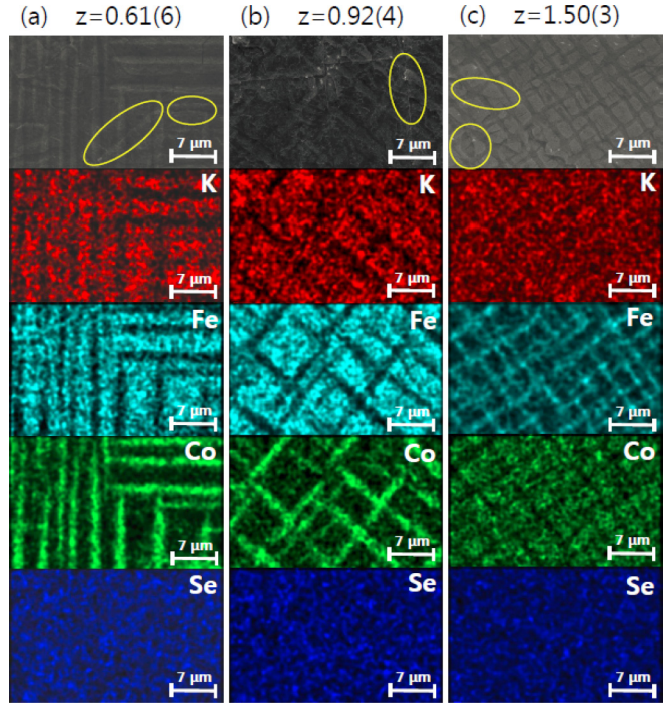

FIG. 2. (Color online) Backscattered electron images of SEM measurement and EDX mappings of $K_x Fe_{2-y-z} Co_z Se_2$ when (a) $z = 0.61(6)$, (b) $z = 0.92(4)$, and (c) $z = 1.50(3)$.

a pattern similar to the backscattered electron image. This suggests that only K, Fe, and Co elements are responsible for phase separation. It is clear that the K and Fe concentrations are lower in the stripes (domains) than in the matrix, while Co concentration is higher in the stripes than in the matrix. Hence, Co atoms prefer to enter into the stripe (domain) phase, which is consistent with the report that Co substitution strongly suppresses superconductivity [12]. The stripe- (domain-) like brighter area maintain its shape across the terraces created by the cleaving, as shown by the marked ellipses in Fig. 2. This may suggest that the stripe- (domain-) like brighter areas form a three-dimensional spider-web-like network [17].

The average stoichiometry was measured by EDX for several single crystals in the same batch with multiple measuring points. The results indicate that the crystals are homogeneous within the scale of around $1 \times 1 \times 0.5$ mm^3. The determined stoichiometries when fixing Se stoichiometry to 2 are shown in Table I. Defects and vacancies of Fe and Co

TABLE I. Summary of measured compositions of $K_x Fe_{2-y-z} Co_z Se_2$ samples.

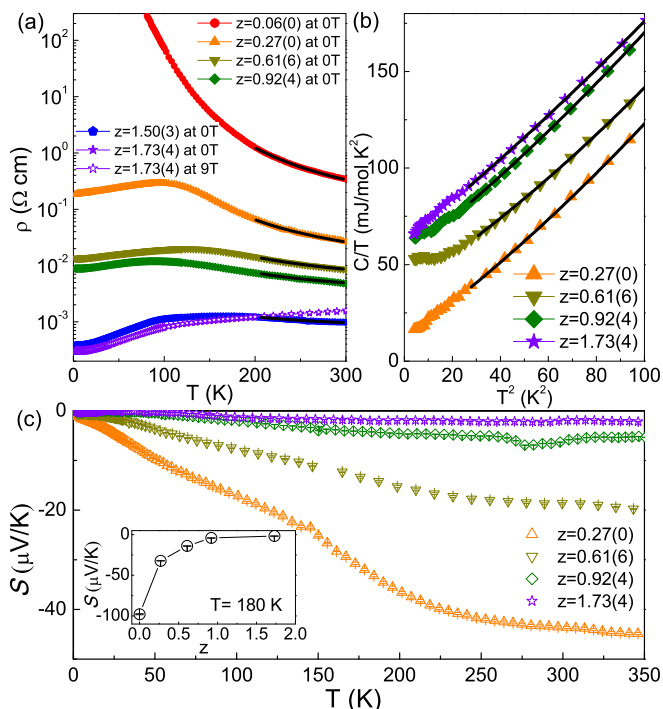| Nominal composition	Measured composition			
K:Fe:Co:Se	K	Fe	Co	Se
1:1.8:0.2:2	0.79(5)	1.37(3)	0.06(0)	2
1:1.4:0.6:2	0.76(1)	1.12(1)	0.27(0)	2
1:1:1:2	0.77(2)	0.92(4)	0.61(6)	2
1:0.6:1.4:2	0.81(2)	0.60(3)	0.92(4)	2
1:0.2:1.8:2	0.78(2)	0.19(1)	1.50(3)	2
1:0:2:2	0.60(6)	0	1.73(4)	2

FIG. 3. (Color online) (a) Temperature dependence of the in-plane resistivity $\rho(T)$ of $K_x Fe_{2-y-z}Co_z Se_2$ series at zero (solid symbols) and 9 T field (open symbols). The black solid lines are the fitted result using the thermal activation model. (b) The relation between C/T and T^2 for $K_x Fe_{2-y-z}Co_z Se_2$ series at low temperature. The solid lines represent fits by the equation $C/T = \gamma + \beta_3 T^2 + \beta_5 T^4$. (c) Temperature dependence of thermoelectric power $S(T)$ for $K_x Fe_{2-y-z}Co_z Se_2$ series. The inset shows the thermoelectric power at $T = 180$ K for different Co concentrations.

are observed for all investigated crystals, which is common in $A_x Fe_{2-y}Se_2$ ($A = K$, Cs, Rb, Tl) compounds [3,25,26]. As the ratio of Co increases, the sum of Fe and the Co ratio slightly increases, while the K ratio remains almost constant, similar to Ni-doped $K_x Fe_{2-y}Se_2$ series [27].

As shown in Fig. 3(a), 3.5% of Co doping in $K_x Fe_{2-y}Se_2$ completely suppresses the superconductivity and results in a semiconducting $\rho(T)$, consistent with previous research [12]. As Co composition increases, there is a crossover from a semiconductor to metallic state. Besides $K_x Co_{1.73(4)}Se_2$, all other crystals are metallic below a resistivity maximum ρ_{max} and semiconducting above ρ_{max}, similar to $K_x Fe_{2-y}Se_{2-z}S_z$ [21]. The high-temperature part (above 200 K) of $\rho(T)$ can be fitted by the thermal activation model $\rho = \rho_0 \exp(E_a/k_B T)$, where ρ_0 is a prefactor, E_a is an activation energy, and k_B is Boltzmann's constant [Fig. 3(a)]. The obtained ρ_0 and E_a are listed in Table II and are mostly smaller than values for $K_x Fe_{2-y}S_2$ and $KFe_{0.85}Ag_{1.15}Te_2$ [25,28].

The heat capacity of the $K_x Fe_{2-y-z}Co_z Se_2$ series also exhibits the crossover from semiconductor to metal as Co increases, consistent with resistivity [Fig. 3(b)]. $C/T - T^2$ relations between 5 and 10 K can be fitted by the formula $C/T = \gamma + \beta_3 T^2 + \beta_5 T^4$. The Debye temperatures are obtained from $\Theta_D = (12\pi^4 N R/5\beta)^{1/3}$, where N is the atomic number in the chemical formula and R is the gas constant. The obtained γ values and Debye temperatures Θ_D for different

TABLE II. Summary of ρ_0 values and activation energy E_a in $K_x Fe_{2-y-z}Co_z Se_2$.

z	ρ_0 (mΩ cm)	E_a (meV)
0.06(0)	24.3(4)	67.7(4)
0.27(0)	4.20(9)	47.1(5)
0.61(6)	3.07(1)	26.6(1)
0.92(4)	2.15(3)	21.4(3)
1.50(3)	0.597(7)	12.4(2)

Co ratios are listed in Table III. The Debye temperature for the $K_x Fe_{2-y-z}Co_z Se_2$ series are similar, suggesting that there are no considerable changes in atomic weight, structure, and bonding. A small γ value for $z = 0.27(0)$ implies a low density of states at the Fermi level, similar to typical semiconductors, while large γ values for $z \geqslant 0.92(4)$ suggest accumulation of the density of states, as expected in metals.

Thermoelectric power $S(T)$ of the $K_x Fe_{2-y-z}Co_z Se_2$ series shows negative values for all different Co concentrations, which reveals that dominant carriers are electrons [Fig. 3(c)]. The magnitude of $S(z)$ decreases as the Co ratio increases to around 50% [$z = 0.92(4)$] and saturates [inset in Fig. 3(c)]. There are no obvious peaks in the thermoelectric power for the $K_x Fe_{2-y-z}Co_z Se_2$ series between 2 and 350 K, suggesting that there are no dramatic Fermi surface changes.

The temperature-dependent dc magnetic susceptibilities of the $K_x Fe_{2-y-z}Co_z Se_2$ series show irreversible behaviors between zero-field cooling (ZFC) and field cooling (FC) at low temperature [Fig. 4(a)]. This is a typical behavior of a spin glass in magnetic field caused by the frozen magnetic spins in random directions below the characteristic temperature T_f. Insets in Figs. 4(a) and 4(b) also suggest a spin glass due to the linear field dependence of the magnetic susceptibility with no hysteresis above T_f (measured at 300 K) and an S-shaped loop of the $M-H$ curve below T_f (measured at 1.8 K). Hence, 3.5% Co doping ($z = 0.06$) not only suppresses superconductivity but also may result in a spin glass. Ferromagnetic behavior appears when $z \geqslant 1.50(3)$ [29]. High-temperature regions ($T \geqslant 150$ K) of the $K_x Fe_{2-y-z}Co_z Se_2$ series follow the Curie-Weiss law $\chi(T) = \chi_0 + C/(T - \theta)$, where χ_0 includes core diamagnetism and van Vleck and Pauli paramagnetism, C is the Curie constant, and θ is the Curie-Weiss temperature [Figs. 4(a) and 4(b)]. The obtained parameters are summarized in Table IV. Negative θ values are observed even for crystals that order ferromagnetically, suggesting prevalent antiferromagnetic interactions probably come from the localized moment of the block (stripe) domain due to the phase separation.

TABLE III. Summary of γ values and Debye temperatures of $K_x Fe_{2-y-z}Co_z Se_2$.

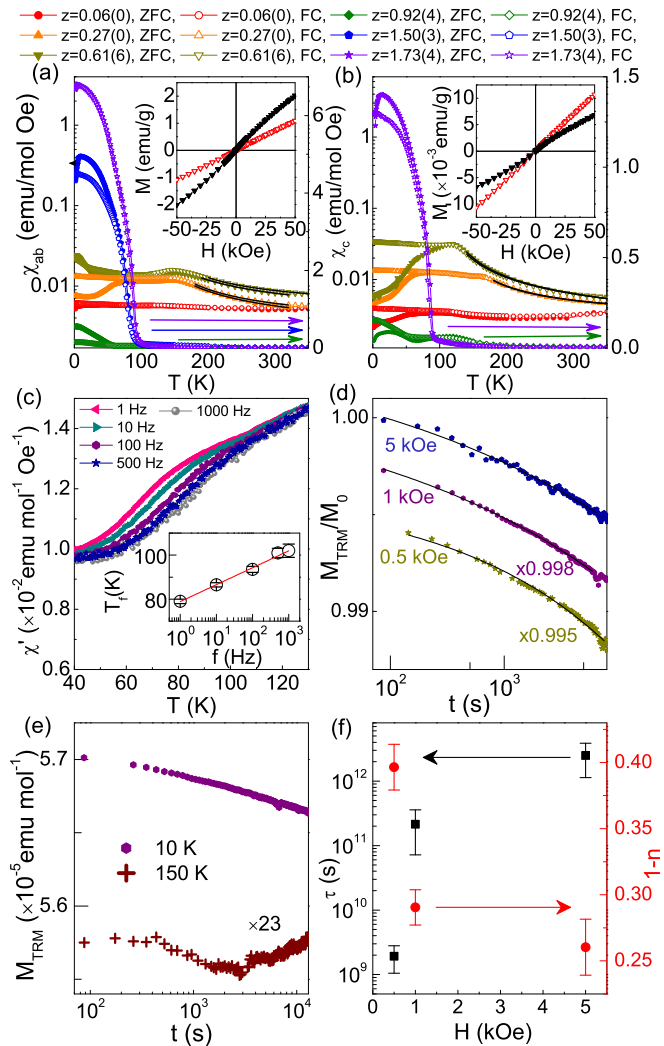| z	γ (mJ mol^{-1} K^{-2})	Θ_D (K)
0.27(0)	11(1)	220(4)
0.61(6)	38(1)	227(3)
0.92(4)	54(1)	215(3)
1.73(4)	63(1)	213(2)

FIG. 4. (Color online) Temperature dependence of dc magnetic susceptibilities of $K_xFe_{2-y-z}Co_zSe_2$ series for (a) $H \perp c$ and (b) $H \parallel c$ at $H = 1$ kOe in ZFC and FC below 350 K. Insets in (a) and (b) are $M-H$ curves of $K_xFe_{2-y-z}Co_zSe_2$ with $z = 0.61(6)$ for $H \perp c$ and $H \parallel c$, respectively, at 1.8 K (black solid inverse triangle) and 300 K (red open inverse triangle). (c) Temperature dependence of ac susceptibility $\chi'(T)$ measured at five different frequencies for $z = 0.27(0)$ of $K_xFe_{2-y-z}Co_zSe_2$. The inset shows the frequency dependence of T_f with the linear fitting (solid line). (d) TRM vs time for $z = 0.27(0)$ of $K_xFe_{2-y-z}Co_zSe_2$ at 10 K and $t_w = 100$ s with different dc fields with fittings using stretched exponential function (solid lines). (e) M_{TRM} vs t at 10 and 150 K with $H = 1$ kOe and $t_w = 100$ s. (f) H-field dependence $\tau(s)$ (black solid square) and $1 - n$ (red solid circle).

Confirmation of the spin glass comes from the frequency dependence of the real part of ac susceptibility and thermoremanent magnetization. The frequency-dependent susceptibility $\chi'(T)$ is shown in Fig. 4(c). As frequency increases, the characteristic temperature T_f peak position increases, whereas its magnitude decreases [30]. The frequency dependence of the peak shift is fitted by $K = \Delta T_f/(T_f \Delta \log f)$ (Fig. 4), and the obtained K value is 0.036(1), in agreement with the canonical spin-glass values $(0.0045 \leqslant K \leqslant 0.08)$ [30]. Thermoremanent magnetization (TRM) is shown in Fig. 4(d).

TABLE IV. Summary of χ_0, effective moment μ_{eff}, and θ values from Curie-Weiss fitting of $K_xFe_{2-y-z}Co_zSe_2$.

z		χ_0 (emu mol^{-1}Oe^{-1})	μ_{eff} (μ_B/Fe)	θ (K)
0.27(0)	$H \perp c$	$2.4(2) \times 10^{-3}$	2.33(8)	$-91(5)$
	$H \parallel c$	$2.7(1) \times 10^{-3}$	1.88(6)	$-118(3)$
0.61(0)	$H \perp c$	$1.6(1) \times 10^{-3}$	2.76(3)	$-98(1)$
	$H \parallel c$	$3.7(4) \times 10^{-3}$	2.79(9)	$-81(9)$
0.92(4)	$H \perp c$	$3.6(4) \times 10^{-3}$	2.7(2)	$-120(9)$
	$H \parallel c$	$2.8(1) \times 10^{-3}$	2.38(2)	$-146(1)$
1.50(3)	$H \perp c$	$9.9(1) \times 10^{-3}$	1.42(4)	$-218(2)$
	$H \parallel c$	$8.2(2) \times 10^{-3}$	0.65(9)	$-257(6)$
1.73(4)	$H \perp c$	$7.9(9) \times 10^{-4}$	3.2(4)	$-86(9)$
	$H \parallel c$	$2.9(8) \times 10^{-3}$	1.8(6)	$-138(9)$

The sample was cooled down from 200 K (above T_f) to 10 K (below T_f) in four different magnetic fields, then kept at 10 K for $t_w = 100$ s. After that, the magnetic field was removed, and $M_{TRM}(t)$ was measured. As observed in Fig. 4(d), $M_{TRM}(t)$ decays very slowly for all three different magnetic fields towards its nonzero equilibrium value [30]. On the other hand, $M_{TRM}(t)$ measured at 150 K (above T_f) relaxes quickly in a short time [less than $\sim$100 s; Fig. 4(e)]. Slow relaxation behavior is fitted well by the stretched exponential function, $M_{TRM}(t) \sim M_0 \exp[-(t/\tau)^{1-n}]$, where M_0, τ, and $1 - n$ are the glassy component, the relaxation characteristic time, and the critical exponent, respectively. As shown in Fig. 4(f), the obtained τ increases as the H field increases, while $1 - n$ stays close to 1/3, consistent with theoretical and experimental results for a spin-glass system [31,32].

Figure 5(a) shows polarized Raman scattering spectra of a $K_{0.6}Co_{1.73}Se_2$ single crystal measured from the (001) plane for the two sample orientations at 100 K using the Jobin Yvon T64000 Raman system. According to selection rules for the $I4/mmm$ space group, peaks at about 174 and 184 cm^{-1} (at 100 K) are assigned as B_{1g} and A_{1g} Raman modes, respectively [33,34].

Unpolarized Raman scattering spectra of $K_xFe_{2-y-z}Co_zSe_2$ single crystals are presented in Fig. 5(b). For $z = 1.73(4)$ samples, only two peaks, which were assigned as A_{1g} ($\sim$180 cm^{-1}) and B_{1g} ($\sim$169 cm^{-1}) modes, can be observed in the Raman spectrum. These modes are also observed for $z = 1.50(3)$ and $z = 0.92(4)$ samples. In fact, the A_{1g} mode can be observed in Raman spectra for all concentrations of cobalt, suggesting that superconducting/metallic $K_xFe_2Se_2$ phase is present in all investigated samples. The energy of this mode does not change significantly by varying concentrations of Co or for different transition-metal ions [33,34]. For the intermediate concentration $[0.61(6) \leqslant z \leqslant 1.50(3)]$ a broad structure around 250 cm^{-1} has been observed, which probably originates from the crystalline disorder in the semiconducting $K_2Fe_4Se_5$ phase. In general, high disorder may cause relaxation of the selection rules, resulting in the appearance of broad asymmetric structures. With further decreasing the Co concentration $[z \leqslant 0.27(0)]$, a large number of Raman modes can be clearly observed in the spectra in addition to the A_{1g} mode of the superconducting/metallic $K_xFe_2Se_2$ phase. These
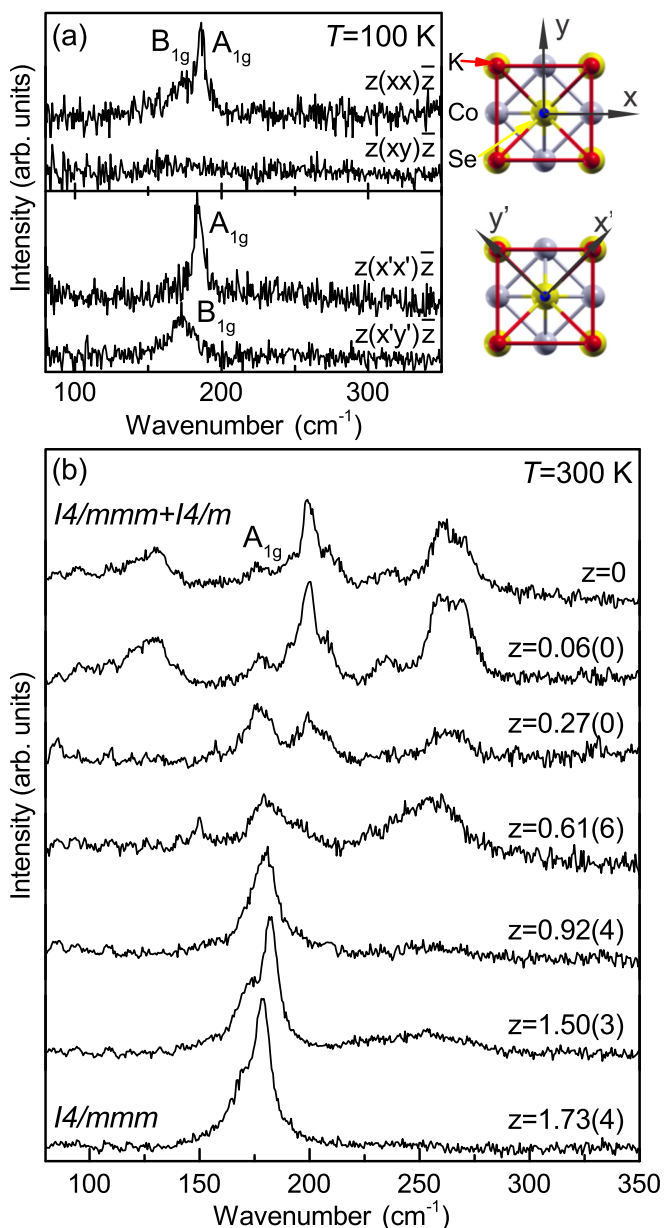
FIG. 5. (Color online) (a) Raman scattering spectra of $K_{0.6}Co_{1.73}Se_2$ single crystals in various scattering configurations ($\mathbf{x} = [100], \mathbf{y} = [010], \mathbf{x}' = 1/\sqrt{2}[110], \mathbf{y}' = 1/\sqrt{2}[1\bar{1}0]$). (b) Raman scattering spectra of $K_xFe_{2-y-z}Co_zSe_2$, $[0 \leqslant z \leqslant 1.73(4)]$ single crystals measured at room temperature from the (001) plane of the samples.

modes originate from the lattice vibrations within the ordered low-symmetry semiconducting $K_2Fe_4Se_5$ phase [33,35].

The magnetic and transport phase diagram of $K_xFe_{2-y-z}Co_zSe_2$ series is presented in Fig. 6. When $z \sim 0$ there is superconductivity below $T_c \sim 30$ K and metallic resistivity below and semiconducting above about 125 K [3]. By 3.5% Co doping, not only is superconductivity completely suppressed, but so is conductivity with emerging spin-glass magnetic order below $T_f \sim 70$ K in 1 kOe. A semiconducting/bad-metal spin glass is found in proximity to the superconducting state, similar to copper oxides. As Co
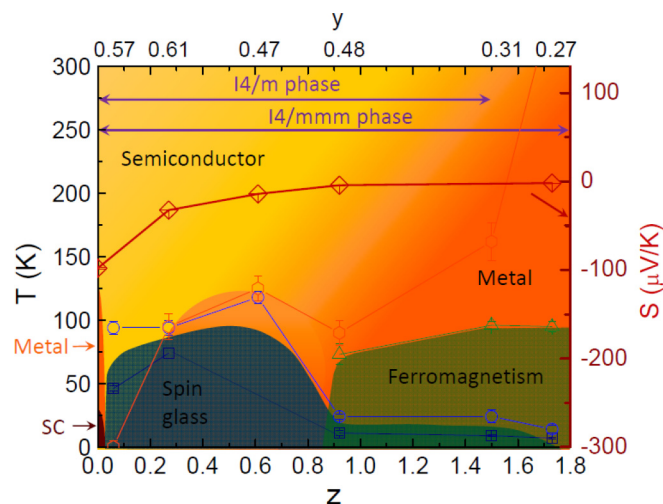

FIG. 6. (Color online) Magnetic and transport phase diagram. Open squares and open circles are spin-glass characteristic temperature T_f for the $H \perp c$ and $H \parallel c$ directions, respectively. Open triangles are the ferromagnetic transition temperature, and open diamonds are the thermoelectric power S_T at 180 K. Open hexagons are resistivity maximums ρ_{max}, which show the semiconductor (brighter yellow region) to metal (darker orange region) crossover. The lines at the top denote the regions of the ordered $I4/m$ and $I4/mmm$ space groups.

concentration increases, the spin-glass state is maintained, while the semiconductor to metal crossover is present at low temperatures up to $z \sim 0.6$. After that, the spin glass and metallicity decrease up to $z \sim 0.9$. With a further increase in Co concentration, metallic conductivity spreads to higher temperatures, while the spin glass is suppressed to the lower-temperature region (below ~ 20 K), and the ferromagnetic ground state emerges above the spin glass. $K_xCo_zSe_2$ with $z = 1.73(4)$ is a metal, consistent with previous reports [29]. We also note that ground-state changes (Fig. 6) are concurrent with lattice parameter variations. Lattice parameters a and c for $I4/m$ show a general drop as z is increased, in contrast to lattice parameters of $I4/mmm$. When the ferromagnetism emerges, lattice parameter c in $I4/mmm$ rapidly increases and is saturated, similar to the temperature dependence of the Curie temperature.

It should be noted that both metallic conductivity and the total area of brighter stripe (block) regions increase with z. This could imply that the brighter stripe (block) area is metallic, whereas the matrix is semiconducting, both with and without Co doping [36,37]. The $z = 0.06(0)$ crystal shows semiconducting behavior through the entire temperature region we measured (1.8 K $\leqslant T \leqslant$ 300 K), even though the metallic brighter stripe (block) areas are present (Fig. 2). This is most likely because the connectivity of the three-dimensional metallic stripe (block) area is insufficient to create metallic percolation in the crystal.

The composite nature of our crystals and nano- to mesoscale mix of (super)conducting and semiconducting magnetic regions may also create states at interfaces [38,39]. This somewhat complicates the physical interpretation of bulk measurements. However, since in $K_xFe_{2-\delta}Se_2$ nanoscale phase

separation exists below $T_s = 560$ K [18], most of the conductivity changes below T_s should come from the metallic regions. This is supported by recent angle-resolved photoemission results where an orbital-selective Mott transition in $K_x Fe_{2-\delta} Se_2$ was observed above the crossover temperature [40]. Therefore, the absolute values of resistivity and magnetization reflect the contribution of both the semiconducting $K_2 Fe_4 Se_5$ and superconducting/metallic $K_x Fe_2 Se_2$ parts of the crystal. Obtained thermoelectric power and heat capacity are contributed by the metallic phase and the semiconducting phase, weighted by their conductivity. The estimated conductivity ratio between two phases is around $\sim 10^3$ at 180 K, which implies the contribution of the metallic region is 1000 times larger than that of the semiconducting region. Co substitution in the superconducting/metallic $K_x Fe_2 Se_2$ unit cell is likely to have a stronger effect on states associated with itinerant d_{xz}/d_{yz} orbitals, for example, via the localization effect in an orbital-selective Mott localization scenario [41,42]. Further Co substitution and disorder might enhance conductivity by raising the chemical potential and enlarging electron pockets, in agreement with our phase diagram [43–45].

IV. CONCLUSION

We have demonstrated how the structure, phase separation, transport, and magnetic property evolve with Co doping concentration in $K_x Fe_{2-y-z} Co_z Se_2$ single crystals. A rich ground-state phase diagram was discovered. By 3.5% Co doping superconductivity is suppressed, while phase separation is still present, which asserts the significance of the arrangement and connectivity of phases for superconductivity. A semiconducting spin glass was discovered in close proximity to the superconducting state in the phase diagram, similar to copper oxides. A ferromagnetic metal state emerged above $\sim 50\%$ Co concentration, in agreement with the structural changes. The metallicity becomes dominant as the area of stripe (block) phases increases; however, the connectivity of stripe phases may also be important for metallic conductivity.

[1] Y. Kamihara, T. Watanabe, M. Hirano, and H. Hosono, J. Am. Chem. Soc. **130**, 3296 (2008).

[2] S. Fujitsu, S. Matsuishi, and H. Hosono, Int. Mater. Rev. **57**, 311 (2012).

[3] J. Guo, S. Jin, G. Wang, S. Wang, K. Zhu, T. Zhou, M. He, and X. Chen, Phys. Rev. B **82**, 180520(R) (2010).

[4] A. S. Sefat, A. Huq, M. A. McGuire, R. Jin, B. C. Sales, D. Mandrus, L. M. D. Cranswick, P. W. Stephens, and K. H. Stone, Phys. Rev. B **78**, 104505 (2008).

[5] S. Matsuishi, Y. Inoue, T. Nomura, H. Yanagi, M. Hirano, and H. Hosono, J. Am. Chem. Soc. **130**, 14428 (2008).

[6] A. Leithe-Jasper, W. Schnelle, C. Geibel, and H. Rosner, Phys. Rev. Lett. **101**, 207004 (2008).

[7] S. R. Saha, N. P. Butch, K. Kirshenbaum, and J. Paglione, Phys. Rev. B **79**, 224519 (2009).

[8] Y. Mizuguchi, F. Tomioka, S. Tsuda, T. Yamaguchi, and Y. Takano, J. Phys. Soc. Jpn. **78**, 074712 (2009).

[9] H. Kotegawa, Y. Hara, S. Masaki, H. Tou, Y. Mizuguchi, and Y. Takano, Phys. C (Amsterdam, Neth.) **470**, S426 (2010).

[10] Y. Yu, C. J. Zhang, W. Tong, L. Zhang, D. Tan, L. Pi, Z. R. Yang, M. L. Tian, S. Tan, and Y. H. Zhang, New J. Phys. **14**, 023032 (2012).

[11] M. T. Li, Z. J. Feng, H. L. Yu, D. M. Deng, B. J. Kang, S. X. Cao, and J. C. Zhang, J. Magn. Magn. Mater. **324**, 3058 (2012).

[12] D. Tan, C. Zhang, C. Xi, L. Ling, L. Zhang, W. Tong, Y. Yu, G. Feng, H. Yu, L. Pi, Z. Yang, S. Tan, and Y. Zhang, Phys. Rev. B **84**, 014502 (2011).

[13] T. Qian, X.-P. Wang, W.-C. Jin, P. Zhang, P. Richard, G. Xu, X. Dai, Z. Fang, J.-G. Guo, X.-L. Chen, and H. Ding, Phys. Rev. Lett. **106**, 187001 (2011).

[14] Z. Wang, Y. J. Song, H. L. Shi, Z. W. Wang, Z. Chen, H. F. Tian, G. F. Chen, J. G. Guo, H. X. Yang, and J. Q. Li, Phys. Rev. B **83**, 140505(R) (2011).

[15] Y. Zhang, L. X. Yang, M. Xu, Z. R. Ye, F. Chen, C. He, H. C. Xu, J. Jiang, B. P. Xie, J. J. Ying, X. F. Wang, X. H. Chen, J. P. Hu, M. Matsunami, S. Kimura, and D. L. Feng, Nat. Mater. **10**, 273 (2011).

[16] W. Li, H. Ding, P. Deng, K. Chang, C. Song, K. He, L. Wang, X. Ma, J.-P. Hu, X. Chen, and Q.-K. Xue, Nat. Phys. **8**, 126 (2012).

[17] X. Ding, D.g Fang, Z. Wang, H. Yang, J. Liu, Q. Deng, G. Ma, C. Meng, Y. Hu, and H.-H. Wen, Nat. Commun. **4**, 1897 (2013).

[18] W. Bao, Q. Z. Huang, G. F. Chen, M. A. Green, D. M. Wang, J. B. He, and Y. M. Qiu, Chin. Phys. Lett. **28**, 086104 (2011).

[19] Z. P. Yin, K. Haule, and G. Kotliar, Nat. Mater. **10**, 932 (2011).

[20] P. Dai, J. Hu, and E. Dagotto, Nat. Phys. **8**, 709 (2012).

[21] H. Lei, M. Abeykoon, E. S. Bozin, K. Wang, J. B. Warren, and C. Petrovic, Phys. Rev. Lett. **107**, 137002 (2011).

[22] A. P. Hammersley, S. O. Svenson, M. Hanfland, and D. Hauserman, High Pressure Res. **14**, 235 (1996).

[23] A. C. Larson and R. B. Von Dreele, Los Alamos National Laboratory, Report No. LAUR 86-748, 1994 (unpublished).

[24] B. H. Toby, J. Appl. Crystallogr. **34**, 210 (2001).

[25] H. Lei, M. Abeykoon, E. S. Bozin, and C. Petrovic, Phys. Rev. B **83**, 180503(R) (2011).

[26] D. M. Wang, J. B. He, T.-L. Xia, and G. F. Chen, Phys. Rev. B **83**, 132502 (2011).

[27] H. Ryu, M. Abeykoon, K. Wang, H. Lei, N. Lazarevic, J. B. Warren, E. S. Bozin, Z. V. Popovic, and C. Petrovic, Phys. Rev. B **91**, 184503 (2015).

[28] H. Lei, E. S. Bozin, K. Wang, and C. Petrovic, Phys. Rev. B **84**, 060506(R) (2011).

[29] G. Huan and M. Greenblatt, J. Less Common Met. **156**, 247 (1989).

[30] J. A. Mydosh, *Spin Glasses: An Experimental Introduction* (Taylor and Francis, London, 1993).

[31] I. A. Campbell, Phys. Rev. B **37**, 9800 (1988).

[32] D. Chu, G. G. Kenning, and R. Orbach, Phys. Rev. Lett. **72**, 3270 (1994).

[33] N. Lazarevic, M. Abeykoon, P. W. Stephens, H. Lei, E. S. Bozin, C. Petrovic, and Z. V. Popovic, Phys. Rev. B **86**, 054503 (2012).

[34] N. Lazarević, M. Radonjić, M. Šćepanović, H. Lei, D. Tanasković, C. Petrovic, and Z. V. Popović, Phys. Rev. B **87**, 144305 (2013).

[35] N. Lazarević, H. Lei, C. Petrovic, and Z. V. Popović, Phys. Rev. B **84**, 214305 (2011).

[36] Y. Texier, J. Deisenhofer, V. Tsurkan, A. Loidl, D. S. Inosov, G. Friemel, and J. Bobroff, Phys. Rev. Lett. **108**, 237002 (2012).

[37] A. Charnukha, A. Cvitkovic, T. Prokscha, D. Pröpper, N. Ocelic, A. Suter, Z. Salman, E. Morenzoni, J. Deisenhofer, V. Tsurkan, A. Loidl, B. Keimer, and A. V. Boris, Phys. Rev. Lett. **109**, 017003 (2012).

[38] Y. J. Yan, M. Zhang, A. F. Wang, J. J. Ying, Z. Y. Li, W. Qin, X. G. Luo, J. Q. Li, J. Hu, and X. H. Chen, Sci. Rep. **2**, 212 (2012).

[39] S. Mukherjee, M. N. Gastiasoro, P. J. Hirschfeld, and B. M. Andersen, Phys. Rev. B **88**, 014519 (2013).

[40] M. Yi, D. H. Lu, R. Yu, S. C. Riggs, J.-H. Chu, B. Lv, Z. K. Liu, M. Lu, Y.-T. Cui, M. Hashimoto, S.-K. Mo, Z. Hussain, C. W. Chu, I. R. Fisher, Q. Si, and Z.-X. Shen, Phys. Rev. Lett. **110**, 067003 (2013).

[41] R. Yu and Q. Si, Phys. Rev. Lett. **110**, 146402 (2013).

[42] R. Yu, J.-X. Zhu, and Q. Si, Phys. Rev. Lett. **106**, 186401 (2011).

[43] T. Berlijn, P. J. Hirschfeld, and W. Ku, Phys. Rev. Lett. **109**, 147003 (2012).

[44] L. Craco, M. S. Laad, and S. Leoni, Phys. Rev. B **84**, 224520 (2011).

[45] F. Lu, J. Z. Zhao, and W. H. Wang, J. Phys. Condens. Matter **24**, 495501 (2012).

PAPER

Multiband electronic transport in α-Yb$_{1-x}$Sr$_x$AlB$_4$ [x = 0, 0.19(3)] single crystals

View the article online for updates and enhancements.

Multiband electronic transport in α-Yb$_{1-x}$Sr$_x$AlB$_4$ [$x = 0$, 0.19(3)] single crystals

Hyejin Ryu[1,2,4]**, Milinda Abeykoon**[1]**, Emil Bozin**[1]**, Yosuke Matsumoto**[3]**,
S Nakatsuji**[3] **and C Petrovic**[1,2,3]

[1] Condensed Matter Physics and Materials Science Department, Brookhaven National Laboratory, Upton, NY 11973, USA
[2] Department of Physics and Astronomy, Stony Brook University, Stony Brook, NY 11794-3800, USA
[3] Institute for Solid State Physics, University of Tokyo, Kashiwa, Chiba 277-8581, Japan

E-mail: petrovic@bnl.gov

CrossMark

Abstract

We report on the evidence for the multiband electronic transport in α-YbAlB$_4$ and α-Yb$_{0.81(2)}$Sr$_{0.19(3)}$AlB$_4$. Multiband transport reveals itself below 10 K in both compounds via Hall effect measurements, whereas anisotropic magnetic ground state sets in below 3 K in α-Yb$_{0.81(2)}$Sr$_{0.19(3)}$AlB$_4$. Our results show that Sr^{2+} substitution enhances conductivity, but does not change the quasiparticle mass of bands induced by heavy fermion hybridization.

Keywords: superconductivity, electronic transport, magnetism

(Some figures may appear in colour only in the online journal)

1. Introduction

Heavy-fermion systems have attracted much attention due to the large magnetic enhancement of quasiparticle mass, non-Fermi-liquid (NFL) behavior and unconventional superconductivity that is believed to arise without the mediating role of phonons [1]. The breakdown of Landau Fermi liquid framework at the magnetic boundary is often intimately connected with quantum critical point (QCP) [2–4]. Therefore spin-fluctuation mediated pairing may be relevant not only to heavy fermion superconductors (HFSC) but also to a wide class of materials of current interest [5]. Furthermore, the charge (valence) fluctuations were also suggested to play a role in superconductivity of some HFSC at ambient or high pressures such as CeCu$_2$(Si$_{1-x}$Ge$_x$)$_2$ and CeRhIn$_5$ [6–9].

Quantum valence criticality was proposed be the explanation of the unconventional critical phenomena observed in β-YbAlB$_4$ [6]. The β-YbAlB$_4$ crystallizes in the orthorhombic structure, space group *Cmmm* [10], and is a first Yb based analog of Ce HFSC that shows NFL behavior associated

with QCP in the normal state ($\rho \sim T^{1.5}$ and $C/T \sim \ln T$ as $T \to 0$) [11]. At nearly all ranges of thermodynamic parameters it coexists with α-YbAlB$_4$ which crystallizes in the ortho-rhombic structure, space group *Pbam*, and is a well defined Fermi liquid ($\rho \sim T^2$ and $C/T \sim$ const. as $T \to 0$) [12, 13]. Both crystal structures contain Yb and Al atoms sandwiched between boron layers, with somewhat different motifs for α and β phase. Despite the similarities in their crystal structure, the ground states of the two polymorphs of YbAlB$_4$ are rather different. Quantum valence criticallity in β-YbAlB$_4$ [6] is at odds with experimental observation that both polymorphs exhibit similar magnetic ground state and strong valence fluctuations with Yb valence estimated to be 2.73 and 2.75 for α and β polymorphs respectively [14, 15]. Hence, it is of interest to investigate charge transport in α-YbAlB$_4$ and its similarities or differences with β-YbAlB$_4$.

Here, we report on the multiband electronic transport in α-YbAlB$_4$ and α-Yb$_{0.81(2)}$Sr$_{0.19(3)}$AlB$_4$. Upon 19(3)% Sr substitution on α-YbAlB$_4$, antiferromagnetic state is induced at $T_N = 3$ K. As expected for a Yb-based compound [16, 17], contraction of the unit cell promotes the magnetic state in $4f^{13}$ by creating Kondo-hole and increasing the carrier density.

[4] Present address: Advanced Light Source, E. O. Lawrence Berkeley National Laboratory, Berkeley, CA 94720, USA

2. Experiment

Single crystals of α-YbAlB$_4$ and α-Yb$_{0.81(2)}$Sr$_{0.19(3)}$AlB$_4$ were prepared by self-flux method. Yb$_{1-x}$Sr$_x$, B and Al were mixed in 1 : 1 : 100 stoichiometric ratio, heated in alumina crucibles under an Ar atmosphere up to 1673 K, cooled down to 1073 K at 3.33 K h^{-1} and then cooled naturally in the furnace to the room temperature. Excess Al flux was removed by subsequent centrifugation at 1073 K and by etching in NaOH solution. Plate-like crystals up to $1 \times 1 \times 0.5$ mm^3 were found. Finely pulverized samples were filled into 1 mm diameter Kapton capillaries for x-ray diffraction (XRD) measurements using cyllindrical transmission geometry at X7B beamline of the national synchrotron light source (NSLS) at the Brookhaven National Laboratory. Data for both samples were collected at room temperature utilizing a 0.5 mm^2 monochromatic beam with energy of 38 keV (0.3196 Å) and Perkin Elmer two-dimensional (2D) image plate detector mounted orthogonal to the beam path 376.4 mm away from the sample. High quality data were collected up to $Q = 4\pi\sin(\theta)/\lambda = 17$ Å^{-1}. Chemical compositions of crystals were obtained by energy-dispersive x-ray spectroscopy (EDX) in an JEOL JSM-6500 scanning electron microscope. The average stoichiometry was determined by EDX with multiple points examination on the crystals and the measured compositions are YbAlB$_4$ and Yb$_{0.81(2)}$Sr$_{0.19(3)}$AlB$_4$. Magnetization and electrical measurements were performed in quantum design MPMS-5XL and PPMS-9. Electric transport measurement results were obtained by a four-probe method using epoxy contacts. Sample dimensions were measured by an optical microscope Nikon SMZ-800 with 10 μm resolution. The geometries of the epoxy contacts for α-YbAlB$_4$ and α-Yb$_{0.81(2)}$Sr$_{0.19(3)}$AlB$_4$ are around 0.2 mm $\times$ 0.8 mm $\times$ 0.4 mm and 0.3 mm $\times$ 0.8 mm $\times$ 0.4 mm, respectively. The uncertainty length is approximately 0.02 mm based on the contact shape in our optical microscope measurement. Therefore the relative error in geometry factor is at most 17.5% for pure material and 14.5% for Sr-doped crystal.

3. Results and discussion

The 2D XRD images were integrated into conventional 1D patterns with help of Fit2d computer program [18]. Successful Rietveld analysis was carried out on both α-YbAlB$_4$ and α-Yb$_{0.81(2)}$Sr$_{0.19(3)}$AlB$_4$, using a single phase *Pbam* structural model. Figure 1 shows model fits to the data. No impurity peaks were observed. Rietveld refinements produced excellent fits to the data up to a very high value of momentum transfer $Q(\sim17$Å$^{-1})$. This indicates the high purity of our samples and high quality of the XRD data. The Rietveld refinement was performed on XRD data using the general structure analysis system (GSAS/EXPGUI) [19, 20] computer package. A pseudo-Voigt function and a shifted Chebyshev polynomial were used to refine the peak profile and the background respectively. Gaussian and Lorentzian parameters [21] of the profile were refined after refining the zero-shift, lattice parameters, and the background. Then the atomic coordinates, occupation numbers, and the isotropic thermal
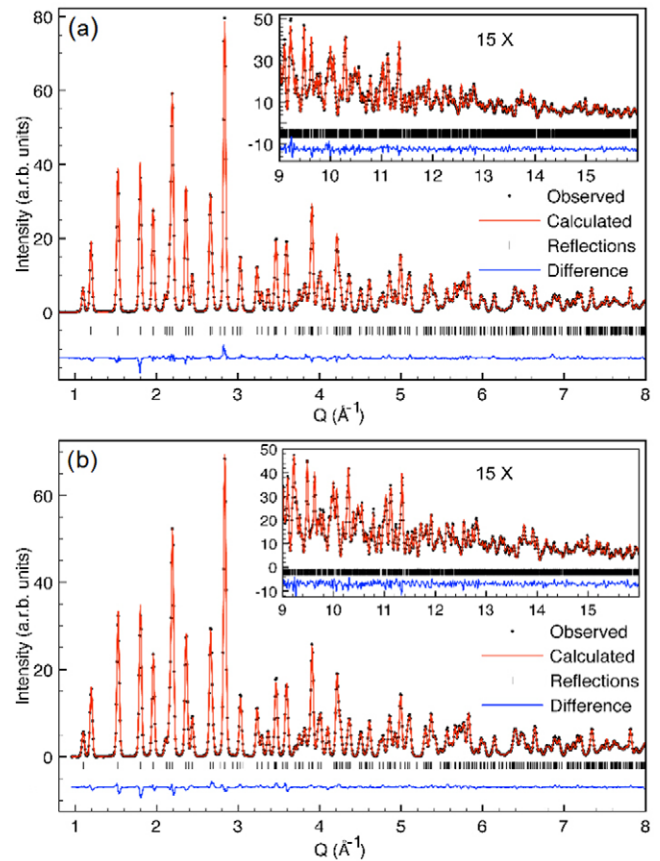
Figure 1. Rietveld refinements of the background subtracted synchrotron powder diffraction data of α-YbAlB$_4$ (a) and α-Yb$_{0.81(2)}$Sr$_{0.19(3)}$AlB$_4$ (b). Plots show the observed ($\bullet$) and calculated (solid red line) powder patterns with the difference curves (shown underneath each diffractogram) up to $Q \sim 16$ Å^{-1}. Vertical tick marks represent Bragg reflections in the α-YbAlB$_4$ and α-Yb$_{0.81(2)}$Sr$_{0.19(3)}$AlB$_4$ phases (space group Pbam). Fit residua, R(F**2), quantifying goodness of fit were 4% for α-YbAlB$_4$ and 3% for α-Yb$_{0.81(2)}$Sr$_{0.19(3)}$AlB$_4$.

displacement parameters (U_{iso}) were refined. At the last stage of the refinement, all profile and structural parameters were refined simultaneously to optimize the quality of fits and structural models. Atomic coordinates and U_{iso}'s agree well with published values for α-YbAlB$_4$ [10]. Refined lattice parameters are $a = 5.918\,21(12)$ Å, $b = 11.462\,39(22)$ Å, and $c = 3.491\,42(6)$ Å for α-Yb$_{0.81(2)}$Sr$_{0.19(3)}$AlB$_4$ and $a = 5.918\,78(12)$ Å, $b = 11.464\,91(23)$ Å, and $c = 3.492\,05(6)$ Å for α-YbAlB$_4$. The unit cell volume of α-Yb$_{0.81(2)}$Sr$_{0.19(3)}$AlB$_4$ $\left(V = 236.847(8)Å^3\right)$ is 1.00(1)% smaller than in pure material. Yb(Sr) atomic positions in α-YbAlB$_4$ have very high coordination number ($CN = 14$) [10]. Sr^{2+} has larger radius (1.26 Å) than Yb^{3+} (0.98 Å) and Yb^{2+} (1.14 Å) even at high $CN = 8$ where the data are available for comparison which suggests that small reduction in the lattice parameters could be attributed to the increase of metallic character of Sr-B bonds [22].

Temperature-dependent magnetic susceptibility $\chi = M/H$ taken in $\mu_0 H = 0.1$ T shows Ising anisotropy where χ_c is strongly temperature dependent in contrast to $\chi_{a,b}$. This is consistent with previous reports (figure 2(a)) [10, 13]. Moreover,
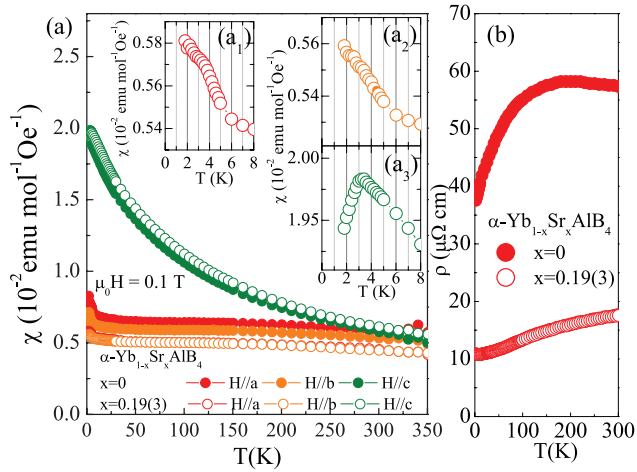
Figure 2. Magnetic susceptibility (a) and resistivity in the *ab* plane ρ_{ab} (b) of α-YbAlB$_4$ and α-Yb$_{0.81(2)}$Sr$_{0.19(3)}$AlB$_4$. Insets in (a) present anisotropy in low temperature magnetic susceptibility of α-Yb$_{0.81(2)}$Sr$_{0.19(3)}$AlB$_4$ around the magnetic transition.

figure 2(a) shows small anisotropy in the *ab*-plane of α-YbAlB$_4$. Similar to pure material, the *c*-axis magnetic susceptibility is also Curie–Weiss-like in α-Yb$_{0.81(2)}$Sr$_{0.19(3)}$AlB$_4$, with no significant differences at high temperatures. As temperature decreases, *M/H* for α-Yb$_{0.81(2)}$Sr$_{0.19(3)}$AlB$_4$ $H\|b$-axis show weak anomalies at around 6 K ($H\|a, b$-axes) and 3 K ($H\|c$-axes). This implies complex and rather anisotropic magnetic ground state as $T \to 0$. The easy axis of the antiferromagnetism is along the *c*-axis. Magnetic state and its anisotropy in α-Yb$_{0.81(2)}$Sr$_{0.19(3)}$AlB$_4$ are probably different from the canted antiferromagnetic state in Fe doped α, β-YbAlB$_4$ [23]. We note that magnetic ground state with small ordered moment ($\sim$0.6 μ_B/Yb) was predicted in α-YbAlB$_4$ by the local density approximation with on-site Coulomb repulsion correction (LDA+U) calculations, a testament to strong underlying magnetic correlations [24]. Due to the symmetry of Ce and Yb compounds that arises from the different electron configuration, $4f^{13}$ orbitals of Yb ('Kondo-hole') can be considered as analog of $4f^1$ orbitals of Ce ('Kondo-electron'). Application of pressure favors smaller ionic radii. In contrast to Ce-based compounds where pressure delocalizes electrons on $4f$ orbitals and promotes $4f^1(J = 5/2, Ce^{3+}) \to 4f^0(J = 0, Ce^{4+})$ nonmagnetic ground state, in Yb-based compounds magnetism is induced with pressure since $4f^{14}(J = 0, Yb^{2+}) \to 4f^{13}(J = 7/2, Yb^{3+})$. This has been observed in various Yb compounds [25, 26].

Effective moment was obtained from the high temperature part of the *c*-axis Curie–Weiss ($\chi = \chi_0 + C/(T - \theta)$) fits. The χ_0 is a temperature independent parameter that includes the contribution of core diamagnetism, Pauli paramagnetism, and Landau diamagnetism. Curie constant $C = N_A I_z^2/k_B$, where N_A is Avogadro number. This gives effective Ising moments $I_z = 2.88(3)\mu_B$/Yb for the α-YbAlB$_4$ and $I_z = 2.70(2)\mu_B$/Yb for the α-Yb$_{0.81(2)}$Sr$_{0.19(3)}$ AlB$_4$ which is consistent with the previous reports for pure compound [10, 13] and implies no significant change with Sr substitution. The Curie–Weiss temperatures are $-150(4)$ K and $-152(6)$ K for α-YbAlB$_4$ and α-Yb$_{0.81(2)}$Sr$_{0.19(3)}$AlB$_4$, respectively. We note that
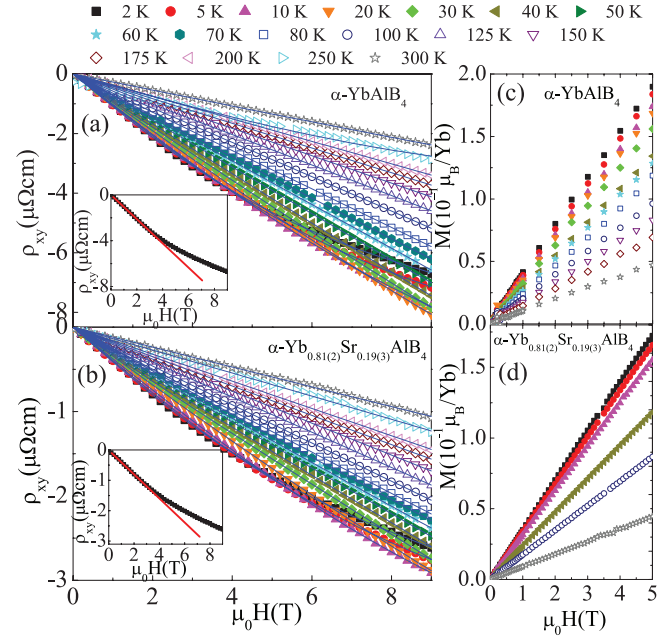

Figure 3. Hall resistivity ρ_{xy} ((a) and (b)) and corresponding magnetization for $\mu_0H\|c$-axis ((c) and (d)) of α-YbAlB$_4$ and α-Yb$_{0.81(2)}$Sr$_{0.19(3)}$AlB$_4$. Solid lines ((a) and (b)) represent fit results (see text). Inset shows ρ_{xy} at 2 K for clarity.

Curie–Weiss temperatures in literature vary from $-110(5)$ K to $-190(9)$ K [10, 23]. The discrepancies could be due to the fitting range, presence of surface impurities but also to disorder as we discuss below.

Temperature dependent resistivity $\rho_{xx}(T)$ of α-YbAlB$_4$ (figure 2(b)) is consistent with previous result [10, 13], however the residual resistivity value is larger when compared to crystals used in previous studies [13]. We note that in our samples of α-YbAlB$_4$ resistivity values varied by the factor of 3 at room temperature, much larger than the uncertainty in sample geometry. This attests to considerable contribution of the crystalline disorder scattering (the sample with lowest ρ_0 is shown in figure 2(b)). The approximate residual resisitivity of α-YbAlB$_4$ and α-Yb$_{0.81(2)}$Sr$_{0.19(3)}$AlB$_4$ is 36 $\mu\Omega$cm and 11 $\mu\Omega$cm, at 2 K respectively. Strontium substitution lowers the residual resistivity, however both crystals show metallic behavior. A broad peak in $\rho(T)$ of our disordered α-YbAlB$_4$ crystals at about 200 K corresponds to $\sim$250 K $\rho(T)$ peak of crystals used in [13]. This suggests that disorder in α-YbAlB$_4$ is intimately connected with magnetic disorder, i.e. with Yb^{3+} ions since the coherence peak in our crystals is observable without subtraction of ρ of nonmagnetic analog α-LuAlB$_4$.

Magnetic field dependence of Hall resistivity (ρ_{xy}) for several different temperatures from (2–300) K are shown in figures 3(a) and (b) for α-YbAlB$_4$ and α-Yb$_{0.81(2)}$Sr$_{0.19(3)}$AlB$_4$, respectively. The same sample was used for both $\rho_{xx}(T)$ and $\rho_{xy}(H)$ measurements. The $\rho_{xy}(H)$ is linear in the magnetic field at high temperatures, suggesting an ordinary Hall effect [$\rho_{xy}/B = R_H = -1/ne$] and conduction in a single band model with a carrier concentration n. However, when $T \lesssim 10$ K $\rho_{xy}(H)$ is curved (insets in figures 3(a) and (b)), similar to β-YbAlB$_4$ [27]. This is reminiscent of the anomalous Hall effect [28]:
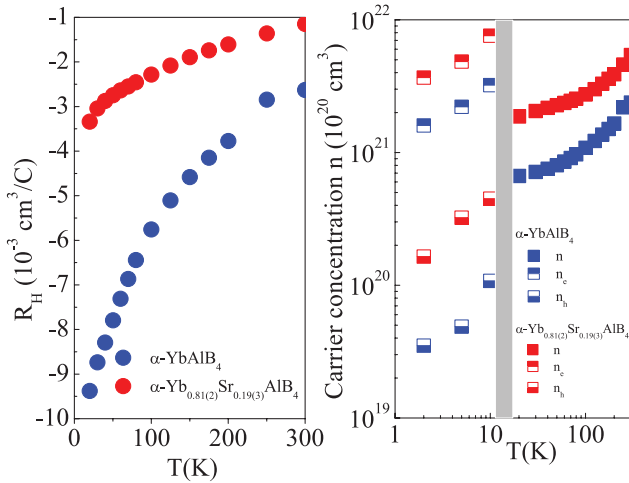
Figure 4. Hall constant $\rho_{xy}/B = R_H = -1/ne$ (a) and carrier concentrations for α-YbAlB$_4$ and α-Yb$_{0.81(2)}$Sr$_{0.19(3)}$AlB$_4$. Shaded area marks the crossover from single band ($T \leqslant 10$ K) to two band conduction ($T \geqslant 20$ K).

Table 1. Summary of mobility values for α-YbAlB$_4$ in multiband regime for $T \leqslant 10$ K.

α-YbAlB$_4$	μ_e (m^2 Vs^{-1})	μ_h (m^2 Vs^{-1})
2 K	0.12(1)	0.07(1)
5 K	0.09(1)	0.04(1)
10 K	0.06(1)	0.02(0)

Table 2. Summary of mobility values for α-Yb$_{0.81(2)}$Sr$_{0.19(3)}$AlB$_4$ in multiband regime for $T \leqslant 10$ K.

α-Yb$_{0.81(2)}$Sr$_{0.19(3)}$AlB$_4$	μ_e (m^2 Vs^{-1})	μ_h (m^2 Vs^{-1})
2 K	0.13(0)	0.08(1)
5 K	0.10(1)	0.05(1)
10 K	0.06(2)	0.03(1)

$\rho_{xy}(H) = R_0 H + R_s M(H)$, where R_0 and R_s are the normal and spontaneous Hall constants, and M is sample magnetization. Attempts to fit $\rho_{xy}(H)$ (figures 3(a) and (b)) using $M(H)$ obtained at the same temperature (figures 3(c) and (d)) were unsuccessful. Hence, the anomalous Hall effect is unlikely cause of the $\rho_{xy}(H)$ nonlinearity. We now proceed with the two-band analysis of electronic transport for $\rho_{xy}(H)$ for $T \leqslant 10$ K. Hall resistivity in the two band model is:

$$\rho_{xy} / \mu_0 H = R_H$$
$$= \frac{1}{e} \frac{(\mu_H^2 n_h - \mu_e^2 n_e) + (\mu_H \mu_e)^2 (\mu_0 H)^2 (n_h - n_e)}{(\mu_e n_h + \mu_h n_e)^2 + (\mu_H \mu_e)^2 (\mu_0 H)^2 (n_h - n_e)^2} \quad (1)$$

where n_e, n_h, μ_e, and μ_H are carrier density and mobility of electron and hall bands, respectively [29]. Fits to the single band model (high temperatures) and two band model ($T \leqslant 10$ K) are excellent. Interestingly, the multiband transport becomes important for $T \leqslant 10$ K, which is close to T^* temperature scale that marks the onset of a heavy fermion Fermi liquid [13].

As opposed to β-YbAlB$_4$ [27], we do not observe a peak of R_H at 40 K (figure 4(a)). The peak might appear at a similar temperature in the case of α-YbAlB$_4$ at its clean limit. The difference might come from the elastic scattering that generates the residual resistivity, which seems to substantially change the temperature dependence of the longitudinal resistivity. R_H (figure 4(a)) is negative over the measured temperature range and its magnitude decreases in α-Yb$_{0.81(2)}$Sr$_{0.19(3)}$AlB$_4$ whereas the carrier concentration n increases (figure 4(b), consistent with the resistivity result (figure 1(b)) since Sr substitution promotes metallic character of bonds. Since both α-YbAlB$_4$ and β-YbAlB$_4$ are metallic and since structural studies have confirmed nanoscale phase separation in both polymorphs (*Cmmm* and *Pbam* space group coexistence in both crystals) [30], Hall constant might be affected by sample differences.

Mobility values extracted from (1) for $T \leqslant 10$ K where the multiband transport is dominant are shown in tables 1 and 2. It can be observed that formation of heavy fermion Fermi liquids probably involve both electron and hole bands whereas hole bands have somewhat larger Kondo coupling. Moreover, Sr^{2+} substitution on Yb atomic sites does not induce significant change in mobility values. We note that electron and hole Fermi surface parts were also found in β-YbAlB$_4$ [31].

4. Conclusion

In summary, we showed that 19(3)% of Sr substitution on Yb site in α-YbAlB$_4$ induces magnetic ground state below 3 K. Both α-YbAlB$_4$ and α-Yb$_{0.81(2)}$Sr$_{0.19(3)}$AlB$_4$ show signature of multiband electronic transport for $T \leqslant 10$ K. Increased conductivity of α-Yb$_{0.81(2)}$Sr$_{0.19(3)}$AlB$_4$ could be attributed to slight lattice contraction with Sr doping that promotes Yb^{3+} state, i.e. enhancement of electron density by hybridization of $4f$ orbital and conduction electron bands. This promotes magnetic ground state via the RKKY mechanism since $T_{RKKY} \sim k_F r$ where k_F is the Fermi wavevector and r is the Yb^{3+} distance. The formation of heavy fermion Fermi liquid takes place in both electron and hole bands whereas the quasiparticle mass of heavy fermion bands is unchanged in Sr substituted crystals. Further band structure and experimental studies are needed to fully explain why α-YbAlB$_4$ and β-YbAlB$_4$ have profoundly different ground states despite similar crystal structure and multiband electronic transport.

Acknowledgments

References

[1] Monthoux P, Pines D and Lonzarich G G 2007 *Nature* **450** 1177
[2] Stewart G 2001 *Rev. Mod. Phys.* **73** 797
[3] Basov D N and Timusk T 2005 *Rev. Mod. Phys.* **77** 721
[4] Si Q and Steglich F 2010 *Science* **329** 1161
[5] Scalapino D J 2012 *Rev. Mod. Phys.* **84** 1383
[6] Watanabe S and Miyake K 2010 *Phys. Rev. Lett.* **105** 186403
[7] Yuan H Q, Grosche F M, Deppe M, Geibel C, Sparn G and Steglich F 2003 *Science* **301** 2104
[8] Yuan H Q, Grosche F M, Deppe M, Geibel C, Sparn G and Steglich F 2006 *Phys. Rev. Lett.* **96** 047008
[9] Watanabe S and Miyake K 2010 *J. Phys. Soc. Japan* **79** 033707
[10] Macaluso R T, Nakatsuji S, Kuga K, Thomas E L, Machida Y, Maeno Y, Fisk Z and Chan J Y 2007 *Chem. Mater.* **19** 1918
[11] Nakatsuji S *et al* 2008 *Nat. Phys.* **4** 603
[12] Fisk Z, Yang K N, Maple M B and Ott H R 1981 *Valence Fluctuations in Solids* ed L M Falicov *et al* (New York: North-Holland) pp 345–7
[13] Matsumoto Y, Kuga K, Tomita T, Karaki Y and Nakatsuji S 2011 *Phys. Rev. B* **84** 125126
[14] Okawa M *et al* 2010 *Phys. Rev. Lett.* **104** 247201
[15] Terashima T T *et al* 2015 *J. Phys. Soc. Japan* **84** 114715
[16] Thompson J D and Lawrence J L 1994 *Handbook on the Physics and Chemistry of Rare Earths* vol 19, ed K A Gschneidner Jr *et al* (Amsterdam: North-Holland) p 383
[17] Winkelmann H, Abd-Elmeguid M M, Micklitz H, Sanchez J P, Geibel C and Steglich F 1998 *Phys. Rev. Lett.* **81** 4947
[18] Hammersley A P, Svenson S O, Hanfland M and Hauserman D 1996 *High Press. Res.* **14** 235
[19] Larson A C and Dreele R B V 2000 GSAS (general structure analysis system) *Los Alamos National Laboratory Report* No. LAUR 86-748
[20] Toby B H 2001 *J. Appl. Crystallogr.* **34** 210
[21] Young R A 1995 *The Rietveld Method* (Oxford: Oxford University Press)
[22] Shannon R D 1976 *Acta Crystallogr.* A **32** 751
[23] Kuga K, Morrison G, Treadwell L, Chan J Y and Nakatsuji S 2012 *Phys. Rev. B* **86** 224413
[24] Nevidomskyy A H and Coleman P 2009 *Phys. Rev. Lett.* **102** 077202
[25] Winkelmann H, Abd-Elmeguid M M, Micklitz H, Sanchez J P, Vulliet P, Alami-Yadri K and Jaccard D 1999 *Phys. Rev. B* **60** 3324
[26] Bauer E *et al* 1994 *Phys. Rev. B* **50** 9300
[27] O'Farrel E C T, Matsumoto Y and Nakatsuji S 2012 *Phys. Rev. Lett.* **109** 176405
[28] O'Handley R C 1980 *The Hall Effect and Its Application* ed C L Chien and C R Westgate (New York: Plenum) P 417
[29] Smith R A 1978 *Semiconductors* (Cambridge: Cambridge University Press)
[30] Yubuta K, Mori T, Okada S, Prots Y, Borrmann H, Grin Y and Shishido T 2013 *Phil. Mag.* **93** 1054
[31] Ramires A, Coleman P, Nevidomskyy A H and Tsvelik A M 2012 *Phys. Rev. Lett.* **109** 176404

Charge-screening role of c-axis atomic displacements in YBa$_2$Cu$_3$O$_{6+x}$ and related superconductors

E. S. Božin,[1] A. Huq,[2] Bing Shen,[3] H. Claus,[3] W. K. Kwok,[3] and J. M. Tranquada[1]

[1]*Condensed Matter Physics & Materials Science Department, Brookhaven National Laboratory, Upton, New York 11973-5000, USA*

[2]*Chemical and Engineering Materials Division, Oak Ridge National Laboratory, Oak Ridge, Tennessee 37831, USA*

[3]*Materials Science Division, Argonne National Laboratory, Argonne, Illinois 60439, USA*

The importance of charge reservoir layers for supplying holes to the CuO$_2$ planes of cuprate superconductors has long been recognized. Less attention has been paid to the screening of the charge transfer by the intervening ionic layers. We address this issue in the case of YBa$_2$Cu$_3$O$_{6+x}$, where CuO chains supply the holes for the planes. We present a simple dielectric-screening model that gives a linear correlation between the relative displacements of ions along the c axis, determined by neutron powder diffraction, and the hole density of the planes. Applying this model to the temperature-dependent shifts of ions along the c axis, we infer a charge transfer of 5–10% of the hole density from the planes to the chains on warming from the superconducting transition to room temperature. Given the significant coupling of c-axis displacements to the average charge density, we point out the relevance of local displacements for screening charge modulations and note recent evidence for dynamic screening of in-plane quasiparticles. This line of argument leads us to a simple model for atomic displacements and charge modulation that is consistent with images from scanning-tunneling microscopy for underdoped Bi$_2$Sr$_2$CaCu$_2$O$_{8+\delta}$.

I. INTRODUCTION

The interactions key to electron pairing and superconductivity in the cuprates occur within the CuO$_2$ planes, and it follows that most research has focused on the characterization and analysis of in-plane behaviors [1–7]. There has been some consideration of the impact of out-of-plane disorder on the scattering rate of in-plane quasiparticles [8] and on the superconducting transition temperature T_c [9,10]. In a more positive sense, there has been recognition that screening of long-range Coulomb interactions within the planes can benefit from responses outside of the planes [11,12]. In particular, the beneficial impact of charge reservoir layers on the screening of long-range Coulomb interactions in the CuO$_2$ planes has recently been emphasized [12]. The purpose of the present paper is to investigate the role of the intervening ions in the screening process.

In the case of YBa$_2$Cu$_3$O$_{6+x}$ (YBCO), the role of the charge reservoir layers is played by the "chain" layers [13,14]. As demonstrated by x-ray spectroscopic studies [15–17], adding oxygen to the chain layers converts Cu^{1+} ions to Cu^{2+} plus a hole. A fraction of that hole is transferred to the neighboring planes, with dielectric screening provided by adjustments to the spacing between the intervening Ba^{2+} and O$^{2−}$ layers [18]. While the systematic trends of the atomic shifts with doping are clear from the early neutron-diffraction studies of structure with doping [13,14], we are not aware of any quantitative analysis of those results.

In this paper, we present a model that connects the hole density p per planar Cu to the atomic shifts of ions along the c axis relative to their positions in YBa$_2$Cu$_3$O$_6$. Applying this model to structural parameters from neutron powder diffraction, good agreement is obtained with the p vs x data of Liang *et al.* [19] with a single multiplicative scaling factor of order one. From new neutron powder diffraction data, we find that atomic positions along the c axis shift with temperature, from which we infer a decrease in p of 0.01 (10% of p for $x = 0.56$) on warming from T_c to 300 K.

Besides our observation of thermal shifts in average dielectric screening, there is also evidence from electron-energy-loss spectroscopy (EELS) studies of Bi$_2$Sr$_2$CaCu$_2$O$_{8+\delta}$ for dynamic coupling of in-plane electrons to c-axis optical phonons [20–22], especially those involving apical and in-plane oxygens [23]. We discuss the relevance of such modes to the short-range charge-density-wave (CDW) order detected in YBa$_2$Cu$_3$O$_{6+x}$ and related cuprates [24–26], where a recent analysis of superlattice intensities indicates significant atomic displacements along the c axis [27]. In high magnetic fields and temperatures below T_c, a new CDW, modulated only along the b axis, develops [28–30] that is compatible with the anisotropic soft bond-bending phonon observed by inelastic neutron scattering [31]. Assuming the latter displacement pattern is also relevant in Bi$_2$Sr$_2$CaCu$_2$O$_{8+\delta}$, we obtain a model for the hole distribution in good agreement with images from scanning tunneling microscopy (STM) studies [32].

The rest of the paper is organized as follows. In the following section, we briefly describe our sample preparation and neutron powder diffraction measurements. In Sec. III, we present sample characterizations, describe the charge-transfer screening model, and use it to analyze the changes with doping and temperature. We also note an anomalous enhancement of the orthorhombic strain due to differing lattice stiffnesses along the a and b axes. In Sec. IV, we discuss the role of c-axis atomic displacements and their relevance to recent studies of CDW order in several cuprates. The paper concludes with a summary in Sec. V.

II. EXPERIMENTAL METHODS

The synthesis of YBa$_2$Cu$_3$O$_{6+x}$ powders followed the procedures established in [13,33]. Specifically, the samples were prepared from powders of Y$_2$O$_3$ (99.999% Sigma-Aldrich), BaCO$_3$ (99.999% Sigma-Aldrich), and CuO (99.999% Sigma-Aldrich). These powders were mixed stoichiometrically and ground in an agate mortar for one hour. Subsequently, the
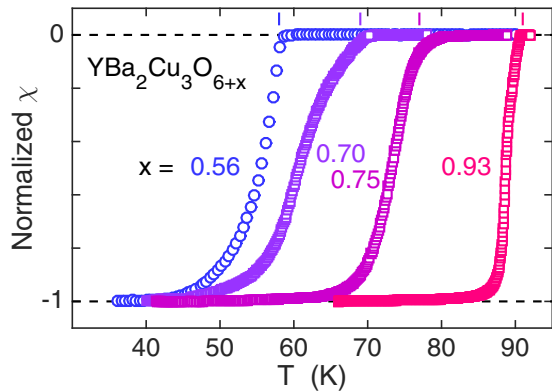
FIG. 1. Normalized bulk susceptibility measured on warming in a 1 Oe field after zero-field cooling. Vertical bars at the top indicate the superconducting transitions.

FIG. 2. Typical Rietveld refinement of the *Pmmm* structural model (line) to the $x = 0.56$, $T_c = 58$ K sample data (circles) at 10 K. Vertical bars indicate calculated peak positions; the line at the bottom indicates the difference between data and model. Goodness of fit parameters are $\chi^2 = 3.59$, $R_{wp} = 4.99\%$, and Bragg factor $R = 6.86\%$.

mixtures were placed in a $BaZrO_3$ crucible, heated to 960 °C, and sintered for 24 h in flowing O_2 (99.99%). Following that, the mixture was cooled and reground for 1 h, and then pressed into pellets with a diameter and thickness of 2 cm and 2.5 mm, respectively. The pellets were reheated to 960 °C in flowing O_2 (99.99%) for 24 h, followed by quenching in liquid nitrogen.

The oxygen content of the polycrystalline samples was adjusted by annealing in an appropriate partial pressure of O_2, followed by quenching in liquid nitrogen. The superconducting transition temperature T_c was determined from the zero-field-cooled susceptibility data shown in Fig. 1. To define T_c, we drew a line tangent to $\chi(T) = -0.15$ and found its intersection with $\chi = 0$. The oxygen content x was determined from the analysis of the neutron powder diffraction data, as described below. The samples and annealing conditions are listed in Table I.

Neutron powder diffraction measurements were performed on the POWGEN instrument, BL-11A at the Spallation Neutron Source, Oak Ridge National Laboratory. The samples were cooled in a closed-cycle refrigerator with *in situ* sample changer. The average structure was assessed through Rietveld refinements [34] to the raw diffraction data using GSAS [35] operated under EXPGUI [36], utilizing orthorhombic space group *Pmmm*. No diffraction peaks from impurity phases were observed, from which we estimate that the volume fraction of impurities is <1%. A typical refinement is presented in Fig. 2. Isotropic mean-square displacements from the fits exhibit a smooth and conventional increase with temperature, with no obvious anomalies. Relative position coordinates z along the c axis are consistent with those of Cava *et al.* [14], generally to better than 0.001.

III. RESULTS

A. Sample characterization

To compare the present samples of $YBa_2Cu_3O_{6+x}$ with previous work, we plot T_c vs x in Fig. 3. We find good agreement with both the early powder study of Cava *et al.* [14] and the single-crystal results of Liang *et al.* [19]. The doping dependence of the low-temperature lattice parameters is plotted in Fig. 4. Again, we see good agreement with Cava *et al.* [14] for a and b; however, our c lattice parameters are systematically smaller, which might be a consequence of different annealing conditions as these are known to impact the degree of Cu-O chain ordering.

B. Charge transfer from chains to planes

The superconducting properties of $YBa_2Cu_3O_{6+x}$ are dominated by the planes; however, the carrier concentration is controlled by the density of oxygen ions in the chain layers. A fraction of the holes created in the chain layers is transferred to the planes, and dielectric screening of this charge transfer occurs through displacements of ions along the c axis. A

TABLE I. Annealing conditions used for each sample of $YBa_2Cu_3O_{6+x}$ as characterized by its measured values of x and T_c.

x	T_c (K)	Gas mixture	T_{anneal} (°C)	Time (days)
0.56	58	0.1% O_2 + 99.9% Ar	450	14
0.70	69	1% O_2 + 99% Ar	430	10
0.75	77	1% O_2 + 99% Ar	400	14
0.93	91	100% O_2	440	10

FIG. 3. Superconducting transition temperature vs oxygen content in $YBa_2Cu_3O_{6+x}$: data from Liang *et al.* [19] (crosses), Cava *et al.* [14] (squares), and present work (circles).

FIG. 4. Lattice parameters in $YBa_2Cu_3O_{6+x}$: (a) c and (b) a and b. Data from Cava *et al.* [14] at $T = 5$ K (squares) and present work at 10 K (circles).

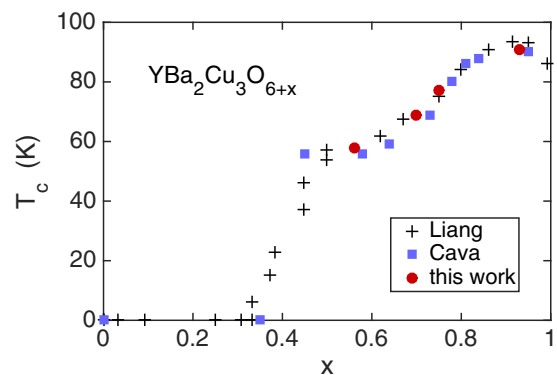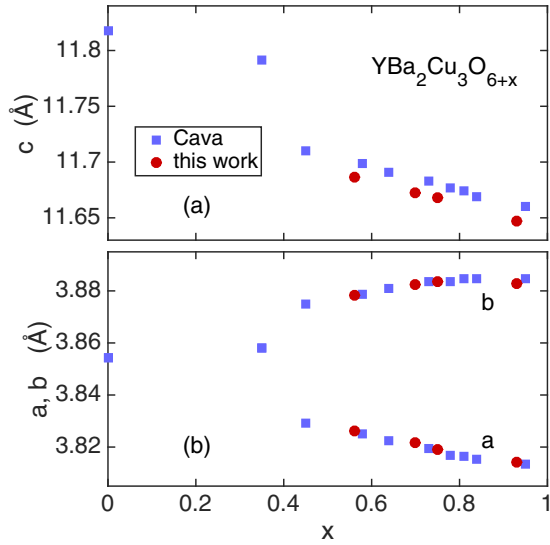FIG. 5. (a) Diagram of the orthorhombic unit cell of $YBa_2Cu_3O_{6+x}$, with the distinct sites labeled. Note that there are mirror planes at the Y and the chain layers. We choose to place the origin of z, the relative coordinate along c, at the chain layer. (b) Schematic of the unit cell projected along [100], labeled by nominal ionic valences. Long arrows indicate the transfer of doped holes from the Cu-O chains to the CuO_2 planes; short arrows indicate the compensating atomic displacements. The dashed line outlines the unit cell.

consequence is that there is a close connection between planar carrier concentration and relative coordinates along the c axis.

To analyze the hole creation, transfer, and screening, we start with some commonly accepted results. The doped holes have a predominant O $2p_\sigma$ character, as determined by measurements at O K and Cu L_3 absorption edges [37–39]. The CuO_2 planes have a net negative charge, so that adding holes (removing electrons) tends to cause a decrease in the in-plane Cu-O bond length, as observed in diffraction studies of single-layer cuprates [40]. $YBa_2Cu_3O_{6+x}$, whose crystal structure is indicated in Fig. 5(a), is somewhat unique in that the doping involves inserting O atoms into the O_{ch} lattice sites that are completely empty when $x = 0$, at which point the twofold coordinated Cu_{ch} sites have a valence of $+1$ and the CuO_2 planes are undoped (i.e., hole concentration p per Cu_{pl} is zero). Initially, inserting a neutral O between a pair of Cu_{ch} sites (making them threefold coordinated) pulls an electron from each, resulting in a pair of Cu^{2+} ions and O^{2-}, while maintaining $p = 0$. With further O addition, chain segments will form, leading to a transformation from tetragonal to orthorhombic symmetry, with the chains oriented along the b axis. For an infinite chain of fourfold coordinated Cu_{ch} sites, each added O creates one hole, in addition to a Cu^{2+} [15–17]. To obtain superconductivity, some of these holes need to be transferred from the O_{ch} sites in the chains to the O_{pl} sites in the planes. In between these positions, we have the Ba^{2+}-O_{ap}^{2-} layer, with the Ba and O_{ap} atoms having slightly different relative heights z along the c axis, and the Cu_{pl} sites that have a different z from the O_{pl} sites. We then expect that the charge transfer from the chains to the planes is screened by displacements of O_{ap} relative to Ba, and Cu_{pl} relative to O_{pl}, as indicated schematically in Fig. 5(b). In fact, a large jump in the Ba-O_{ap} spacing occurs at the tetragonal to orthorhombic transition [14], where there is a concomitant jump in p from negligible to finite [19]. Note that the insertion of the O atoms into the chains causes the b lattice parameter to expand,

competing with the tendency for hole doping to reduce the Cu_{pl}-O_{pl} bond length.

To describe this behavior, we will consider a rigid ion model, assuming integer valences of the ions. (This is not entirely accurate, as there is experimental evidence for a small hole concentration on the O_{ap} sites [39]; however, we will ignore such effects for the sake of simplicity.) We take the $x = 0$ composition as the reference configuration, and consider a two-step process in which we first introduce neutral O atoms into the chains and then transfer a density of holes p from the chain layer to each neighboring CuO_2 plane. This creates a potential difference V_1, given by

$$V_1 = p(z_{O_{pl}} - z_{O_{ch}})c/\epsilon_0, \qquad (1)$$

where $z_j c$ is the average distance from the chain layer along the c axis for atoms at site j, evaluated for the corresponding value of oxygen content x, and ϵ_0 is the vacuum permittivity. (Note that $z_{O_{ch}} = 0$.) This potential difference will be countered by displacements of the intervening ions $[O_{ap}^{2-}, Ba^{2+}, Cu_{pl}^{2+}$, as indicated in Fig. 5(b)], resulting in V_2, given by

$$V_2 = 2[d(x) - d(0)]/\epsilon_0, \qquad (2)$$

where

$$d(x) = (z_{Ba} - z_{O_{ap}} + z_{Cu_{pl}} - z_{O_{pl}})c, \qquad (3)$$

and we take $z_{O_{pl}}$ to be the average of the z parameters for the $O_{pl}(1)$ and $O_{pl}(2)$ sites. Assuming that $V_1 + V_2 = 0$, we get

$$p = -2\alpha \frac{d(x) - d(0)}{(z_{O_{pl}} - z_{O_{ch}})c}, \qquad (4)$$

where α is a doping-independent correction factor of order 1 that we include to account for corrections to our simple model.

FIG. 6. Plot of p vs x in $YBa_2Cu_3O_{6+x}$ from Liang *et al.* [19] (crosses) and calculated, as discussed in the text, from structural parameters determined by Cava *et al.* [14] (squares) and in the present work (circles).

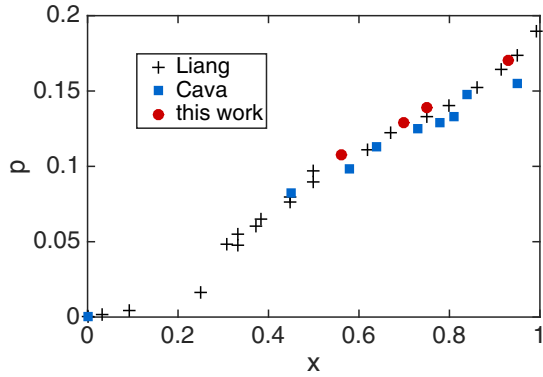In order to test this model, we need data for p vs x. It has been challenging to directly determine p in $YBa_2Cu_3O_{6+x}$. Perhaps the best analysis of the hole concentration is that by Liang *et al.* [19]; their results for p vs x are plotted in Fig. 6. We have also calculated p from the low-temperature structural parameters determined by Rietveld refinement in the present work and by Cava *et al.* [14] using Eqs. (3) and (4). (Note that we must reference our own results to Cava's $x = 0.0$ sample.) Fixing $\alpha = 1.4$, we obtain the results shown in Fig. 6. The differences between p values at similar x values between our results and those of Cava *et al.* [14] are consistent with the differences in the c lattice parameters in Fig. 4 and the relationship between p and c determined by Liang *et al.* [19].

C. Temperature dependence of the charge transfer

Our neutron powder diffraction measurements were performed in small temperature steps from 10 to 300 K. From the Rietveld refinements of these data, we obtain the temperature dependence of the structural parameters. In Fig. 7(a), we have plotted the temperature dependences of the z parameters relative to 10 K values. The biggest thermal changes occur for the Cu_{pl} and O_{ap} sites. Given that these ions provide screening of the charge transfer from the chains to the planes, the shifts in relative positions imply a change in the average hole concentration p of the CuO_2 planes. Using Eqs. (3) and (4), we have calculated the temperature dependence of p for each of our samples. To emphasize the similarities, Fig. 7(b) shows the change in p relative to its value at 10 K. Each sample shows a decrease in p of ~ 0.01 on warming to 300 K. For the $T_c = 58$ K sample, this corresponds to 10% of p.

It would be useful to compare our inferred T-dependent change in p with other measurements of $p(T)$; however, this proves to be a challenge. One might hope to get p from measurements of the Hall coefficient, but the Hall coefficient is temperature dependent due to correlation effects, and hence is not a precise measure of p [41,42]. Nevertheless, we note that a recent x-ray spectroscopy study of $YBa_2Cu_3O_{6.9}$ [43] is suggestive of a small decrease in p when the temperature is raised, in qualitative agreement with our analysis.
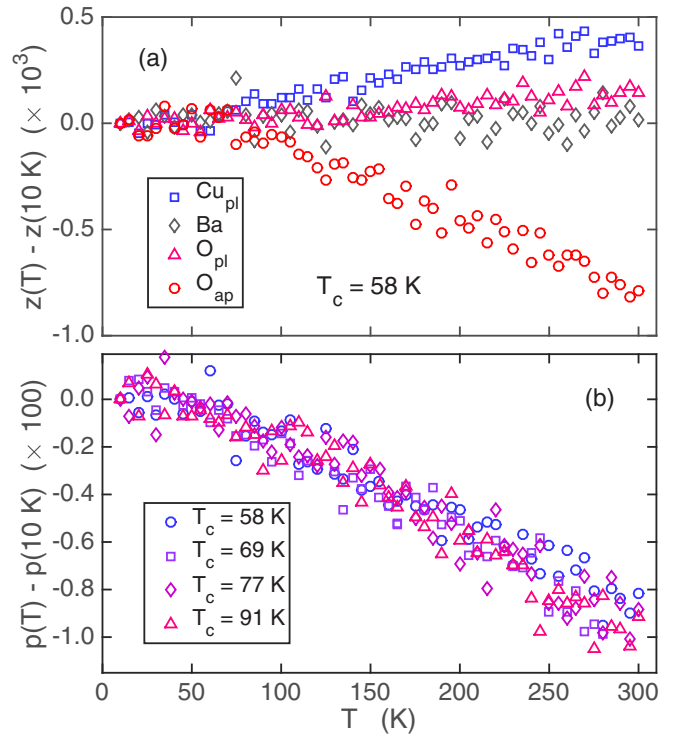
FIG. 7. Relative temperature dependence of the z parameters for the Cu_{pl} (squares), Ba (diamonds), O_{pl} (triangles), and O_{ap} (circles) sites determined by Rietveld refinement for the $x = 0.56$ sample. Uncertainties are comparable to the fluctuations.

D. Temperature dependence of lattice parameters and orthorhombic strain

The temperature dependence of lattice parameters can be sensitive to electronic transitions, as, for example, demonstrated in the case of charge-stripe ordering in $La_{1.67}Sr_{0.33}NiO_4$ [44]. Given the variety of unusual transitions reported for YBCO, it is worthwhile to briefly examine the data.

Figure 8 shows the temperature dependence of $\Delta d(T)/d_0$ for the $x = 0.56$ sample, where $d_0 = d(10$ K$)$, $\Delta d(T) = d(T) - d_0$, and $d = a, b, c$. We note that the temperature
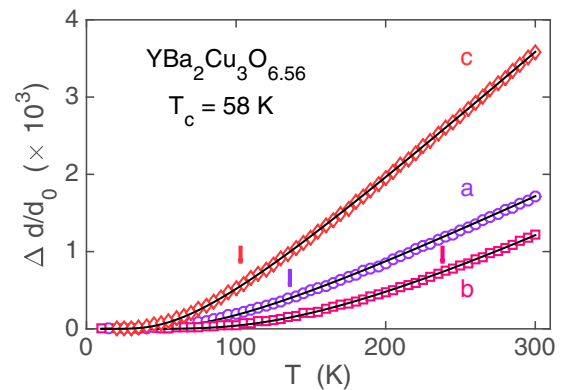
FIG. 8. Temperature dependence of the normalized change in the lattice parameters a, b, and c. Lines through the data points are fits with Eqs. (5) and (6), where the respective values of the parameter T_0 are indicated by the vertical bars.

dependence of each lattice parameter is similar in form to that of the mean-square relative displacement (MSRD) of a nearest-neighbor bond, which is often parametrized well by the Einstein model, $A \coth(T_0/T)$, with T_0 proportional to the Einstein frequency for the nearest-neighbor bond [45]. While thermal expansion is due to anharmonicity and the MSRD formula is for harmonic behavior, the anharmonic effects will grow as the MSRD increases. This has motivated the use of a one-parameter empirical model corresponding to

$$\frac{\Delta d(T)}{d_0} = \frac{\Delta d(300\ \text{K})}{d_0} \frac{f(T)}{f(300\ \text{K})}, \quad (5)$$

where

$$f(T) = \coth(T_0/T) - 1. \quad (6)$$

The lines through the data points are fits to this model with a different T_0 for each axis. For example, T_0 is 136(6), 238(12), and 103(4) K for a, b, and c, respectively, for the $x = 0.56$ sample. For $x = 0.93$, there are increases of T_0 by 5%, 1%, and 12% for a, b, and c, respectively.

One observation is that there are no obvious anomalies in the temperature dependences of the lattice parameters. There is a similar smooth evolution of each lattice parameter, becoming approximately linear in temperature above T_0. The magnitudes of T_0 appear to reflect the relative lattice stiffnesses along the corresponding directions. The bonding along the c axis is relatively ionic, resulting in weak interatomic forces and the smallest T_0. The largest T_0 occurs for the b axis, which is stiffer than a because of the Cu_{ch}-O_{ch} bonds.

The orthorhombic strain, $\eta = 2(b - a)/(b + a)$, is of interest because electronic nematicity should couple to it [46,47]. In Fig. 9(a), we plot the strain obtained experimentally for the $x = 0.56$ sample. There appears to be an anomalous enhancement of the magnitude of the temperature derivative of the strain on cooling below 200 K, which is the range where nematic effects appear in measurements of the Nernst effect [46]. Could this enhanced rate of growth of the strain be due to coupling to conduction electrons? While we cannot rule out such a coupling, a more mundane effect provides an adequate explanation of the observations. The "anomaly" in the strain growth appears to be a simple consequence of the different values of T_0 for $a(T)$ and $b(T)$, as the effect is well reproduced [solid line in Fig. 9(a)] by calculating the temperature dependence of the strain from the phenomenological fits to $a(T)$ and $b(T)$ (solid lines in Fig. 8). While $\eta(T)$ does not appear to require any significant contribution from the low-energy carriers, the temperature dependence of the strain might feed back on the electrons and contribute to the observed nematic response.

To compare the behavior of the thermal variation of the strain for our samples, we have plotted the change in strain, $\eta(T) - \eta(10\ \text{K})$, in Fig. 9(b). As one can see, there is remarkably similar behavior for the three underdoped samples. The $x = 0.93$ sample shows the largest change in strain, but with less upward curvature on cooling. The change between $x = 0.93$ and 0.75 is known from thermal expansion studies [48], but the lack of change in the underdoped region is intriguing.
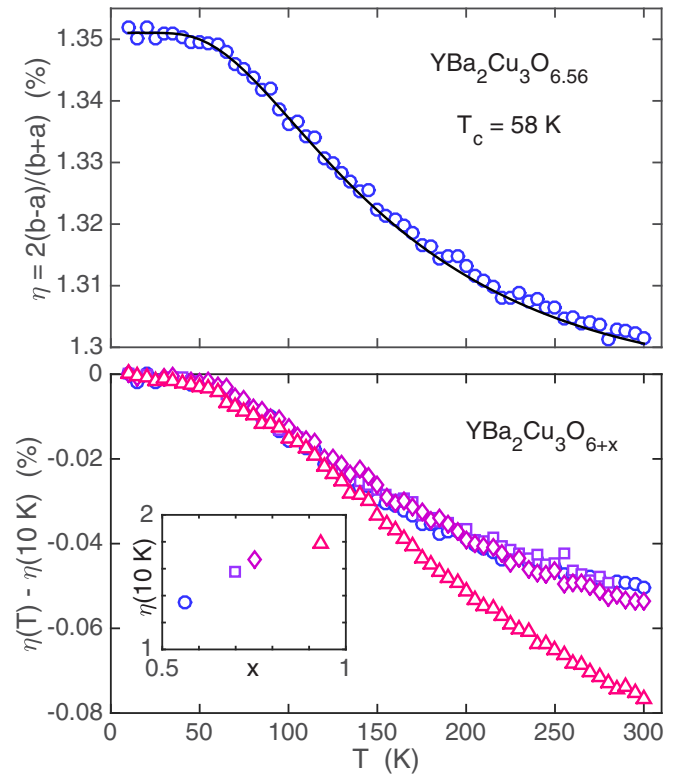
FIG. 9. (a) Orthorhombic strain vs temperature for the $x = 0.56$, $T_c = 58$ K sample. The line is calculated from the fits to $a(T)$ and $b(T)$, shown in Fig. 8. (b) Temperature dependence of the strain relative to the strain at 10 K for all four samples. The inset shows the low-temperature strain values as a function of x, providing an implicit symbol legend.

IV. DISCUSSION

We have seen that the charge transfer from the chains to the planes in $YBa_2Cu_3O_{6+x}$ is screened by c-axis displacements of intervening ions. Relaxation of these displacements with temperature implies a return of a fraction of the holes from the planes to the chains on warming. The point here is that electronic behavior in the planes has a substantial coupling to c-axis displacements of atoms in and out of the planes.

Of course, we have only considered the average structure. It is well known that for underdoped orthorhombic YBCO crystals, the O_{ch} atoms order in filled and empty Cu-O chains, with the periodicity of filled chains varying with the oxygen content [49,50]. Though the chain ordering is never long range, the periodicity is nevertheless indicated by diffuse superlattice peaks. Analyses of the **Q**-dependent superlattice intensities indicate that there are noticeable displacements of most atoms in the structure in response to the partial chain filling [51–54]. In particular, detailed studies of the structure in small crystals with $x = 0.50$ found significant displacements of the Y and Ba ions along the a axis, transverse to the chains, and of the Cu_{pl} and O_{ap} atoms along the c axis [51,52].

So far, we have only considered static variations of the average structure. One may expect that there should also be significant dynamic coupling, and, indeed, there is good evidence for this. For example, high-resolution EELS studies of $Bi_2Sr_2CaCu_2O_{8+\delta}$ indicate that the bosonic excitations to

which electrons couple correspond to c-axis polarized optical phonons [20–22]. Prominent peaks near 45 and 80 meV correspond to modes involving in-plane oxygens (bond-bending motion) and apical oxygens, respectively [23,55,56]. The importance of dynamic screening by c-axis phonons has also been demonstrated in an optical-pump–electron-probe study of a $La_2CuO_{4+\delta}$ film [57,58]. In $YBa_2Cu_3O_{6+x}$, the infrared-active modes of the apical oxygens vibrating along the c axis are coupled to the electronic conductivity [59]. In fact, Kaiser *et al.* [60] found that driving the apical oxygens with a midinfrared pulse dynamically increases the coherent c-axis conductivity. At least part of this response should be a consequence of driving charge transfer between the planes and chains.

Given the substantial static and dynamic responses, one might expect significant local displacements in response to disorder. In this context, it is interesting to consider the analysis of atomic displacements associated with the zero-field CDW in underdoped YBCO by Forgan *et al.* [27]. The biggest displacements are along the c axis, involving Ba, Cu_{pl}, and, especially, O_{pl} sites. The displacements have reflection symmetry about the chain layer, and the L dependence of the scattering requires correlations only within one unit cell above and below a chain. An important observation is that the O_{pl} displacements have a quadrupolar pattern, with sites along the a and b axes displaced in opposite directions along the c axis [27]. Since the average structure of each CuO_2 plane is dimpled, this modulation decreases half of the Cu_{pl}-O_{pl} bond lengths and increases the other half. One would expect the holes to prefer the short bonds, and hence this pattern reproduces the d density form factor proposed by several theorists [61–64] and confirmed by experimentalists [65,66].

The symmetry about the chain layer and the short correlation lengths suggest that the modulation is driven by local charge transfer between a chain segment and neighboring bilayers. That the chains might drive a modulation is plausible, as there is evidence from scanning-tunneling microscopy (STM) measurements on $YBa_2Cu_3O_{6+x}$ for CDW modulations with wave vector of $\sim 0.3b^*$ along the chains and a correlation length of a few lattice spacings in the transverse direction [67,68]. Nuclear magnetic resonance (NMR) studies of Cu_{ch} sites in filled chains indicate the development of an increased linewidth that has been interpreted as evidence of CDW order [69] or Friedel oscillations [70,71] in CuO chains. [We note that an angle-resolved photoemission spectroscopy (ARPES) study by Zabolotnyy *et al.* [72] reported an absence of a gap in the chains of underdoped YBCO. Of course, the ARPES measurements were performed in zero magnetic field, while the NMR studies used fields of 0 to 8 T.]

A new CDW order develops above a threshold magnetic field of 10 T applied along the c axis for $T < T_c$ [28,73]. X-ray diffraction measurements at high field find that in addition to the low-field CDW signal, new peaks appear that are incommensurate only along the b direction and that are commensurate along c, with a significantly enhanced correlation length [29,30]. The observation that the new peak intensities for $(0,k,l)$ reflections are strong for $l = 1$ but negligible for $l = 0$ is consistent with a displacement pattern that is reflection symmetric about the midplane of a bilayer, rather than about a chain layer.
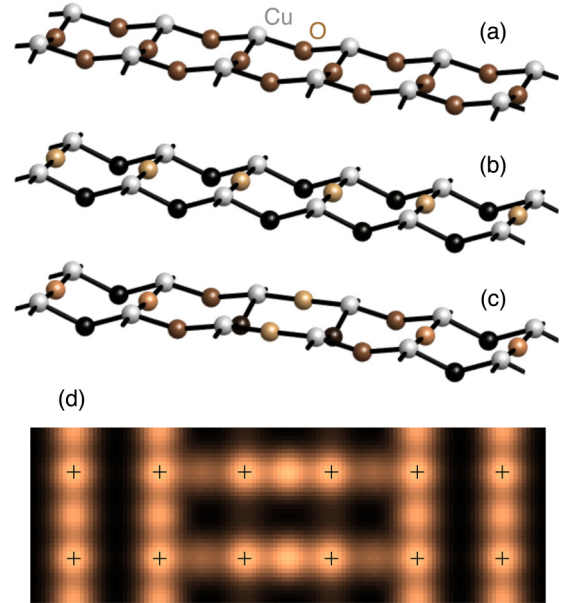
FIG. 10. (a) Upper CuO_2 plane of a bilayer in $Bi_2Sr_2CaCu_2O_{8+\delta}$, with O sites (brown) dimpled towards the Ca layer below, and Cu atoms (gray) above. (b) Same layer after application of B_{1g} symmetry displacements of the O sites, with O atoms shaded according to height along the c axis, with dark being furthest from the Cu layer. (c) Modulation of the B_{1g} displacements at $\mathbf{Q} = (0.25,0)$. (d) Resulting pattern if we associate hole density with the O sites with the shortest bond lengths in (c). Here, Cu sites (+) are also set to the same color as the hole-rich O sites, for comparison with STM images in [32].

The low-field CDW is associated with an anomaly found in low-frequency phonon branches [74,75]. For the high-field CDW, it may be relevant to consider the phonon anomaly that has been seen at $\mathbf{q} = (0,0.3)$ in the bond-bending branch of the CuO_2 planes in $YBa_2Cu_3O_7$ at low temperature [31]. This branch connects to the B_{1g} Raman-active mode at $\mathbf{q} = 0$, which exhibits a softening below T_c for samples near optimum doing [76,77]. An important experimental feature is that the anomaly at finite $\mathbf{q}$ occurs only along b^*, and not along a^* [31]; an anomaly at the same wave vector, with the same anisotropy, also occurs in the Cu-O bond-stretching mode [78].

The CDW modulation in $Bi_2Sr_2CaCu_2O_{8+\delta}$ as detected by STM [32,79] shares the d-wave form factor [65,80] detected in YBCO [66]; however, it appears to be locally unidirectional in $Bi_2Sr_2CaCu_2O_{8+\delta}$ [80], similar to the high-field CDW in YBCO. There are no CuO chains in $Bi_2Sr_2CaCu_2O_{8+\delta}$, but there is plenty of disorder, and one may anticipate significant c-axis atomic displacements in response to that disorder. Let us consider the impact of bond-bending displacements on the CuO_2 layers in $Bi_2Sr_2CaCu_2O_{8+\delta}$. In Fig. 10, applying the B_{1g} displacement pattern to the unperturbed, dimpled CuO_2 structure of Fig. 10(a) leads to the anisotropic structure shown in Fig. 10(b). Modulating these distortions at the CDW wave vector of $\mathbf{q} \sim (0.25,0)$, one obtains the pattern shown in Fig. 10(c). Associating hole density with the O sites along shortened bonds, one obtains the pattern displayed in Fig. 10(d); this looks quite similar to the images obtained in STM studies [32].

It is interesting to compare with $La_{2-x}Ba_xCuO_4$ (LBCO) and $La_{2-x}Sr_xCuO_4$ (LSCO). As pointed out by Raghu *et al.* [12], these compounds lack a charge reservoir layer. As a consequence, the screening of Coulomb interactions is different. The main instability of the planes is the tilting of the CuO_6 octahedra, which can result in low-temperature phases having long and short Cu-O bonds [81–83], as in the B_{1g} modulations discussed above for $YBa_2Cu_3O_{6+x}$ and $Bi_2Sr_2CaCu_2O_{8+\delta}$. The bond-length anisotropy pins both charge and spin stripes [84]. The stripe order is compatible with pairing and superconductivity [85], but it appears that the superconducting wave function forms a pair density wave (PDW) [7,86,87], which can frustrate interlayer Josephson coupling.

Given that the optimum doping concentration for charge order is $p \sim 0.12$ in all of the cuprate families studied [26,84,88–91], it is reasonable to look for common features among these systems. While the families other than LBCO and LSCO generally have significant spin gaps in the relevant doping range, there is evidence for electron nematic behavior [46,92] that couples to the local CDW order [93,94]. There is also photoemission evidence for some degree of pairing correlations in antinodal states at $T > T_c$ [95–98] defining the Fermi arcs [99] or pockets [96]. If c-axis atomic displacements are present due to out-of-plane disorder, it may be reasonable for them to be modulated at a wave vector that couples the ends of the Fermi arcs, creating a gap between the less-correlated arc states and the pairing correlations in the antinodal region; indeed, a theoretical analysis has indicated that the bond-bending mode should couple to states with increasing strength as one moves from the nodal to the antinodal region [100]. The result might be a bosonic CDW. (Think of a CDW along a charge stripe, formed from pairs, similar to the state described in [101].) Such a state would tend to compete somewhat with superconductivity, as the coherent pairing forms along the Fermi arcs [102,103]. We note that this picture differs from the PDW perspective of Lee [87], but is consistent with the concept that the CDWs in YBCO are not fundamental instabilities of the planes [104,105] but may be a consequence of incidental features [80,104].

V. SUMMARY

We have considered how charge transfer from chains to planes in $YBa_2Cu_3O_{6+x}$ is screened by atomic displacements of oppositely charged ions. Neutron powder diffraction measurements show that such displacements are temperature dependent, implying a change in the charge transfer. These results provide context for considering the CDW orders recently discovered in several cuprate families. Displacements of in-plane O atoms along the c axis, with patterns consistent with experimentally observed phonon anomalies, are compatible with reported images of electronic modulations in $Bi_2Sr_2CaCu_2O_{8+\delta}$.

[1] M. A. Kastner, R. J. Birgeneau, G. Shirane, and Y. Endoh, Magnetic, transport, and optical properties of monolayer copper oxides, Rev. Mod. Phys. **70**, 897 (1998).

[2] A. Damascelli, Z.-X. Shen, and Z. Hussain, Angle-resolved photoemission studies of the cuprate superconductors, Rev. Mod. Phys. **75**, 473 (2003).

[3] D. N. Basov and T. Timusk, Electrodynamics of high-T_c superconductors, Rev. Mod. Phys. **77**, 721 (2005).

[4] M. R. Norman, D. Pines, and C. Kallin, The pseudogap: Friend or foe of high T_c? Adv. Phys. **54**, 715 (2005).

[5] Patrick A. Lee, Naoto Nagaosa, and Xiao-Gang Wen, Doping a Mott insulator: Physics of high-temperature superconductivity, Rev. Mod. Phys. **78**, 17 (2006).

[6] D. J. Scalapino, A common thread: The pairing interaction for unconventional superconductors, Rev. Mod. Phys. **84**, 1383 (2012).

[7] Eduardo Fradkin, Steven A. Kivelson, and John M. Tranquada, Colloquium: Theory of intertwined orders in high temperature superconductors, Rev. Mod. Phys. **87**, 457 (2015).

[8] C. M. Varma and Elihu Abrahams, Effective Lorentz Force Due to Small-Angle Impurity Scattering: Magnetotransport in High-T_c Superconductors, Phys. Rev. Lett. **86**, 4652 (2001).

[9] H. Eisaki, N. Kaneko, D. L. Feng, A. Damascelli, P. K. Mang, K. M. Shen, Z.-X. Shen, and M. Greven, Effect of chemical inhomogeneity in bismuth-based copper oxide superconductors, Phys. Rev. B **69**, 064512 (2004).

[10] H. Hobou, S. Ishida, K. Fujita, M. Ishikado, K. M. Kojima, H. Eisaki, and S. Uchida, Enhancement of the superconducting critical temperature in $Bi_2Sr_2CaCu_2O_{8+\delta}$ by controlling disorder outside CuO_2 planes, Phys. Rev. B **79**, 064507 (2009).

[11] S. A. Kivelson, Making high T_c higher: A theoretical proposal, Physica B **318**, 61 (2002).

[12] S. Raghu, R. Thomale, and T. H. Geballe, Optimal T_c of cuprates: The role of screening and reservoir layers, Phys. Rev. B **86**, 094506 (2012).

[13] J. D. Jorgensen, B. W. Veal, A. P. Paulikas, L. J. Nowicki, G. W. Crabtree, H. Claus, and W. K. Kwok, Structural properties of oxygen-deficient $YBa_2Cu_3O_{7-\delta}$, Phys. Rev. B **41**, 1863 (1990).

[14] R. J. Cava, A. W. Hewat, E. A. Hewat, B. Batlogg, M. Marezio, K. M. Rabe, J. J. Krajewski, W. F. Peck Jr., and L. W. Rupp Jr., Structural anomalies, oxygen ordering and superconductivity in oxygen deficient $Ba_2YCu_3O_x$, Physica C **165**, 419 (1990).

[15] J. M. Tranquada, S. M. Heald, A. R. Moodenbaugh, and Youwen Xu, Mixed valency, hole concentration, and T_c in $YBa_2Cu_3O_{6+x}$, Phys. Rev. B **38**, 8893 (1988).

[16] H. Tolentino, F. Baudelet, A. Fontaine, T. Gourieux, G. Krill, J. Y. Henry, and J. Rossat-Mignod, Sequence and symmetry of hole injection in $YBa_2Cu_3O_{6+x}$ in situ and ex situ experiments on powders and single crystals using x-ray absorption spectroscopy, Physica C **192**, 115 (1992).

[17] G. Uimin and J. Rossat-Mignod, Role of Cu-O chains in the charge transfer mechanism in $YBa_2Cu_3O_{6+x}$, Physica C **199**, 251 (1992).

[18] J. M. Tranquada, Magnetic and Electronic Correlations in $YBa_2Cu_3O_{6+x}$, in *Earlier and Recent Aspects of Superconductivity*, edited by J. G. Bednorz and K. A. Müller (Springer, New York, 1990), p. 422.

[19] Ruixing Liang, D. A. Bonn, and W. N. Hardy, Evaluation of CuO_2 plane hole doping in $YBa_2Cu_3O_{6+x}$ single crystals, Phys. Rev. B **73**, 180505 (2006).

[20] Huajun Qin, Junren Shi, Yanwei Cao, Kehui Wu, Jiandi Zhang, E. W. Plummer, J. Wen, Z. J. Xu, G. D. Gu, and Jiandong Guo, Direct Determination of the Electron-Phonon Coupling Matrix Element in a Correlated System, Phys. Rev. Lett. **105**, 256402 (2010).

[21] Sean Vig, Anshul Kogar, Vivek Mishra, Luc Venema, Melinda S. Rak, Ali A. Husain, Genda D. Gu, Eduardo Fradkin, Michael R. Norman, and Peter Abbamonte, Low-energy bosonic modes in a high-temperature superconductor with incipient charge order, arXiv:1509.04230.

[22] R. B. Phelps, P. Akavoor, L. L. Kesmodel, J. E. Demuth, and D. B. Mitzi, Surface phonons on $Bi_2Sr_2CaCu_2O_{8+\delta}$, Phys. Rev. B **48**, 12936 (1993).

[23] N. N. Kovaleva, A. V. Boris, T. Holden, C. Ulrich, B. Liang, C. T. Lin, B. Keimer, C. Bernhard, J. L. Tallon, D. Munzar, and A. M. Stoneham, c-axis lattice dynamics in Bi-based cuprate superconductors, Phys. Rev. B **69**, 054511 (2004).

[24] G. Ghiringhelli, M. Le Tacon, M. Minola, S. Blanco-Canosa, C. Mazzoli, N. B. Brookes, G. M. De Luca, A. Frano, D. G. Hawthorn, F. He, T. Loew, M. Moretti Sala, D. C. Peets, M. Salluzzo, E. Schierle, R. Sutarto, G. A. Sawatzky, E. Weschke, B. Keimer, and L. Braicovich, Long-range incommensurate charge fluctuations in (Y,Nd)$Ba_2Cu_3O_{6+x}$, Science **337**, 821 (2012).

[25] J. Chang, E. Blackburn, A. T. Holmes, N. B. Christensen, J. Larsen, J. Mesot, Ruixing Liang, D. A. Bonn, W. N. Hardy, A. Watenphul, M. v. Zimmermann, E. M. Forgan, and S. M. Hayden, Direct observation of competition between superconductivity and charge density wave order in $YBa_2Cu_3O_{6.67}$, Nat. Phys. **8**, 871 (2012).

[26] R. Comin and A. Damascelli, Resonant x-ray scattering studies of charge order in cuprates, Annu. Rev. Condens. Matter Phys. **7** (2016).

[27] E. M. Forgan, E. Blackburn, A. T. Holmes, A. K. R. Briffa, J. Chang, L. Bouchenoire, S. D. Brown, Ruixing Liang, D. Bonn, W. N. Hardy, N. B. Christensen, M. V. Zimmermann, M. Hucker, and S. M. Hayden, The microscopic structure of charge density waves in underdoped $YBa_2Cu_3O_{6.54}$ revealed by x-ray diffraction, Nat. Commun. **6**, 10064 (2015).

[28] Tao Wu, Hadrien Mayaffre, Steffen Kramer, Mladen Horvatic, Claude Berthier, W. N. Hardy, Ruixing Liang, D. A. Bonn, and Marc-Henri Julien, Magnetic-field-induced charge-stripe order in the high-temperature superconductor $YBa_2Cu_3O_y$, Nature (London) **477**, 191 (2011).

[29] S. Gerber, H. Jang, H. Nojiri, S. Matsuzawa, H. Yasumura, D. A. Bonn, R. Liang, W. N. Hardy, Z. Islam, A. Mehta, S. Song, M. Sikorski, D. Stefanescu, Y. Feng, S. A. Kivelson, T. P. Devereaux, Z.-X. Shen, C.-C. Kao, W.-S. Lee, D. Zhu, and J.-S. Lee, Three-dimensional charge density wave order in $YBa_2Cu_3O_{6.67}$ at high magnetic fields, Science **350**, 949 (2015).

[30] J. Chang, E. Blackburn, O. Ivashko, A. T. Holmes, N. B. Christensen, M. Hücker, Ruixing Liang, D. A. Bonn, W. N. Hardy, U. Rütt, M. v. Zimmermann, E. M. Forgan, and S. M. Hayden, Magnetic field controlled charge density wave coupling in underdoped $YBa_2Cu_3O_{6+x}$, arXiv:1511.06092.

[31] M. Raichle, D. Reznik, D. Lamago, R. Heid, Y. Li, M. Bakr, C. Ulrich, V. Hinkov, K. Hradil, C. T. Lin, and B. Keimer, Highly Anisotropic Anomaly in the Dispersion of the Copper-Oxygen Bond-Bending Phonon in Superconducting $YBa_2Cu_3O_7$ from Inelastic Neutron Scattering, Phys. Rev. Lett. **107**, 177004 (2011).

[32] Y. Kohsaka, C. Taylor, K. Fujita, A. Schmidt, C. Lupien, T. Hanaguri, M. Azuma, M. Takano, H. Eisaki, H. Takagi, S. Uchida, and J. C. Davis, An intrinsic bond-centered electronic glass with unidirectional domains in underdoped cuprates, Science **315**, 1380 (2007).

[33] B. W. Veal, A. P. Paulikas, Hoydoo You, Hao Shi, Y. Fang, and J. W. Downey, Observation of temperature-dependent site disorder in $YBa_2Cu_3O_{7-\delta}$ below 150 °C, Phys. Rev. B **42**, 6305 (1990).

[34] H. M. Rietveld, Line profiles of neutron powder-diffraction peaks for structure refinement, Acta Crystallogr. **22**, 151 (1967).

[35] A. C. Larson and R. B. Von Dreele, *General Structure Analysis System (GSAS)*, Report LAUR 86-748 (Los Alamos National Laboratory, Los Alamos, NM, 2000).

[36] Brian H. Toby, *EXPGUI*, a graphical user interface for *GSAS*, J. Appl. Crystallogr. **34**, 210 (2001).

[37] H. Romberg, M. Alexander, N. Nücker, P. Adelmann, and J. Fink, Electronic structure of the system $La_{2-x}Sr_xCuO_{4+\delta}$, Phys. Rev. B **42**, 8768(R) (1990).

[38] C. T. Chen, F. Sette, Y. Ma, M. S. Hybertsen, E. B. Stechel, W. M. C. Foulkes, M. Schluter, S-W. Cheong, A. S. Cooper, L. W. Rupp, B. Batlogg, Y. L. Soo, Z. H. Ming, A. Krol, and Y. H. Kao, Electronic States in $La_{2-x}Sr_xCuO_{4+\delta}$ Probed by Soft-x-Ray Absorption, Phys. Rev. Lett. **66**, 104 (1991).

[39] N. Nücker, E. Pellegrin, P. Schweiss, J. Fink, S. L. Molodtsov, C. T. Simmons, G. Kaindl, W. Frentrup, A. Erb, and G. Müller-Vogt, Site-specific and doping-dependent electronic structure of $YBa_2Cu_3O_x$ probed by O 1s and Cu 2p x-ray-absorption spectroscopy, Phys. Rev. B **51**, 8529 (1995).

[40] P. G. Radaelli, D. G. Hinks, A. W. Mitchell, B. A. Hunter, J. L. Wagner, B. Dabrowski, K. G. Vandervoort, H. K. Viswanathan, and J. D. Jorgensen, Structural and superconducting properties of $La_{2-x}Sr_xCuO_4$ as a function of Sr content, Phys. Rev. B **49**, 4163 (1994).

[41] Yoichi Ando, Y. Kurita, Seiki Komiya, S. Ono, and Kouji Segawa, Evolution of the Hall Coefficient and the Peculiar Electronic Structure of the Cuprate Superconductors, Phys. Rev. Lett. **92**, 197001 (2004).

[42] Lev P. Gor'kov and Gregory B. Teitel'baum, Interplay of Externally Doped and Thermally Activated Holes in $La_{2-x}Sr_xCuO_4$

and Their Impact on the Pseudogap Crossover, Phys. Rev. Lett. **97**, 247003 (2006).

[43] M. Magnuson, T. Schmitt, V. N. Strocov, J. Schlappa, A. S. Kalabukhov, and L. C. Duda, Self-doping processes between planes and chains in the metal-to-superconductor transition of YBa$_2$Cu$_3$O$_{6.9}$, Sci. Rep. **4**, 7017 (2014).

[44] A. M. Milinda Abeykoon, Emil S. Božin, Wei-Guo Yin, Genda Gu, John P. Hill, John M. Tranquada, and Simon J. L. Billinge, Evidence for Short-Range-Ordered Charge Stripes Far Above the Charge-Ordering Transition in La$_{1.67}$Sr$_{0.33}$NiO$_4$, Phys. Rev. Lett. **111**, 096404 (2013).

[45] G. S. Knapp, H. K. Pan, and John M. Tranquada, Extended x-ray-absorption fine-structure Einstein frequency and moments of the phonon spectrum: An experimental and theoretical study, Phys. Rev. B **32**, 2006 (1985).

[46] R. Daou, J. Chang, David LeBoeuf, Olivier Cyr-Choiniere, Francis Laliberte, Nicolas Doiron-Leyraud, B. J. Ramshaw, Ruixing Liang, D. A. Bonn, W. N. Hardy, and Louis Taillefer, Broken rotational symmetry in the pseudogap phase of a high-T_c superconductor, Nature (London) **463**, 519 (2010).

[47] Laimei Nie, Gilles Tarjus, and Steven Allan Kivelson, Quenched disorder and vestigial nematicity in the pseudogap regime of the cuprates, Proc. Natl. Acad. Sci. USA **111**, 7980 (2014).

[48] C. Meingast, V. Pasler, P. Nagel, A. Rykov, S. Tajima, and P. Olsson, Phase Fluctuations and the Pseudogap in YBa$_2$Cu$_3$O$_x$, Phys. Rev. Lett. **86**, 1606 (2001).

[49] R. Beyers, B. T. Ahn, G. Gorman, V. Y. Lee, S. S. P. Parkin, M. L. Ramirez, K. P. Roche, J. E. Vazquez, T. M. Gur, and R. A. Huggins, Oxygen ordering, phase separation and the 60-K and 90-K plateaus in YBa$_2$Cu$_3$O$_x$, Nature (London) **340**, 619 (1989).

[50] M. v. Zimmermann, J. R. Schneider, T. Frello, N. H. Andersen, J. Madsen, M. Käll, H. F. Poulsen, R. Liang, P. Dosanjh, and W. N. Hardy, Oxygen-ordering superstructures in underdoped YBa$_2$Cu$_3$O$_{6+x}$ studied by hard x-ray diffraction, Phys. Rev. B **68**, 104515 (2003).

[51] A Simon, K. Trübenbach, and H. Borrmann, Single crystal x-ray structure analysis of YBa$_2$Cu$_3$O$_{6.5}$, J. Solid State Chem. **106**, 128 (1993).

[52] J. Grybos, D. Hohlwein, Th. Zeiske, R. Sonntag, F. Kubanek, K. Eichhorn, and Th. Wolf, Atomic displacements in the ortho-II phase of YBa$_2$Cu$_3$O$_{6.50}$ by synchrotron X-ray diffraction, Physica C **220**, 138 (1994).

[53] Zahirul Islam, S. K. Sinha, D. Haskel, J. C. Lang, G. Srajer, B. W. Veal, D. R. Haeffner, and H. A. Mook, X-ray diffraction study of lattice modulations in an underdoped YBa$_2$Cu$_3$O$_{6+x}$ superconductor, Phys. Rev. B **66**, 092501 (2002).

[54] Zahirul Islam, X. Liu, S. K. Sinha, J. C. Lang, S. C. Moss, D. Haskel, G. Srajer, P. Wochner, D. R. Lee, D. R. Haeffner, and U. Welp, Four-Unit-Cell Superstructure in the Optimally Doped YBa$_2$Cu$_3$O$_{6.92}$ Superconductor, Phys. Rev. Lett. **93**, 157008 (2004).

[55] Masato Kakihana, Minoru Osada, Mikael Käll, Lars Börjesson, Hiromasa Mazaki, Hiroshi Yasuoka, Masatomo Yashima, and Masahiro Yoshimura, Raman-active phonons in Bi$_2$Sr$_2$Ca$_{1-x}$Y$_x$Cu$_2$O$_{8+d}$ ($x = 0 - 1$): Effects of hole filling and internal pressure induced by Y doping for Ca, and implications for phonon assignments, Phys. Rev. B **53**, 11796 (1996).

[56] J. J. Tu, C. C. Homes, G. D. Gu, and M. Strongin, A systematic optical study of phonon properties in optimally doped Bi$_2$Sr$_2$CaCu$_2$O$_{8+\delta}$ single crystals, Physica B (Amsterdam) **316-317**, 324 (2002).

[57] Nuh Gedik, Ding-Shyue Yang, Gennady Logvenov, Ivan Bozovic, and Ahmed H. Zewail, Nonequilibrium phase transitions in cuprates observed by ultrafast electron crystallography, Science **316**, 425 (2007).

[58] Z. Radović, N. Božović, and I. Božović, Photoinduced expansion of cuprate superconductors: Evidence of strong electron-lattice coupling, Phys. Rev. B **77**, 092508 (2008).

[59] C. C. Homes, T. Timusk, D. A. Bonn, R. Liang, and W. N. Hardy, Optical phonons polarized along the *c* axis of YBa$_2$Cu$_3$O$_{6+x}$, for $x = 0.5 \rightarrow 0.95$, Can. J. Phys. **73**, 663 (1995).

[60] S. Kaiser, C. R. Hunt, D. Nicoletti, W. Hu, I. Gierz, H. Y. Liu, M. Le Tacon, T. Loew, D. Haug, B. Keimer, and A. Cavalleri, Optically induced coherent transport far above T_c in underdoped YBa$_2$Cu$_3$O$_{6+\delta}$, Phys. Rev. B **89**, 184516 (2014).

[61] Max A. Metlitski and Subir Sachdev, Quantum phase transitions of metals in two spatial dimensions. II. Spin density wave order, Phys. Rev. B **82**, 075128 (2010).

[62] Subir Sachdev and Rolando La Placa, Bond Order in Two-Dimensional Metals with Antiferromagnetic Exchange Interactions, Phys. Rev. Lett. **111**, 027202 (2013).

[63] K. B. Efetov, H. Meier, and C. Pepin, Pseudogap state near a quantum critical point, Nat. Phys. **9**, 442 (2013).

[64] J. C. Séamus Davis and Dung-Hai Lee, Concepts relating magnetic interactions, intertwined electronic orders, and strongly correlated superconductivity, Proc. Natl. Acad. Sci. USA **110**, 17623 (2013).

[65] Kazuhiro Fujita, Mohammad H. Hamidian, Stephen D. Edkins, Chung Koo Kim, Yuhki Kohsaka, Masaki Azuma, Mikio Takano, Hidenori Takagi, Hiroshi Eisaki, Shin-ichi Uchida, Andrea Allais, Michael J. Lawler, Eun-Ah Kim, Subir Sachdev, and J. C. Séamus Davis, Direct phase-sensitive identification of a *d*-form factor density wave in underdoped cuprates, Proc. Natl. Acad. Sci. USA **111**, E3026 (2014).

[66] R. Comin, R. Sutarto, F. He, E. H. da Silva Neto, L. Chauviere, A. Frano, R. Liang, W. N. Hardy, D. A. Bonn, Y. Yoshida, H. Eisaki, A. J. Achkar, D. G. Hawthorn, B. Keimer, G. A. Sawatzky, and A. Damascelli, Symmetry of charge order in cuprates, Nat. Mater. **14**, 796 (2015).

[67] D. J. Derro, E. W. Hudson, K. M. Lang, S. H. Pan, J. C. Davis, J. T. Markert, and A. L. de Lozanne, Nanoscale One-Dimensional Scattering Resonances in the CuO Chains of YBa$_2$Cu$_3$O$_{6+x}$, Phys. Rev. Lett. **88**, 097002 (2002).

[68] Makoto Maki, Terukazu Nishizaki, Kenji Shibata, and Norio Kobayashi, Layered charge-density waves with nanoscale coherence in YBa$_2$Cu$_3$O$_{7-\delta}$, Phys. Rev. B **72**, 024536 (2005).

[69] B. Grévin, Y. Berthier, and G. Collin, In-Plane Charge Modulation Below T_c and Charge-Density-Wave Correlations in the Chain Layer in YBa$_2$Cu$_3$O$_7$, Phys. Rev. Lett. **85**, 1310 (2000).

[70] Z. Yamani, B. W. Statt, W. A. MacFarlane, Ruixing Liang, D. A. Bonn, and W. N. Hardy, NMR evidence for Friedel-like oscillations in the CuO chains of ortho-II YBa$_2$Cu$_3$O$_{6.5}$, Phys. Rev. B **73**, 212506 (2006).

[71] M. Mori, T. Tohyama, S. Maekawa, and J. A. Riera, Friedel oscillations in a two-band Hubbard model for CuO chains, Phys. Rev. B **69**, 014513 (2004).

[72] V. B. Zabolotnyy, A. A. Kordyuk, D. Evtushinsky, V. N. Strocov, L. Patthey, T. Schmitt, D. Haug, C. T. Lin, V. Hinkov, B. Keimer, B. Büchner, and S. V. Borisenko, Pseudogap in the chain states of $YBa_2Cu_3O_{6.6}$, Phys. Rev. B **85**, 064507 (2012).

[73] Tao Wu, Hadrien Mayaffre, Steffen Krämer, Mladen Horvatić, Claude Berthier, Philip L. Kuhns, Arneil P. Reyes, Ruixing Liang, W. N. Hardy, D. A. Bonn, and Marc-Henri Julien, Emergence of charge order from the vortex state of a high-temperature superconductor, Nat. Commun. **4**, 2113 (2013).

[74] E. Blackburn, J. Chang, A. H. Said, B. M. Leu, Ruixing Liang, D. A. Bonn, W. N. Hardy, E. M. Forgan, and S. M. Hayden, Inelastic x-ray study of phonon broadening and charge-density wave formation in ortho-II-ordered $YBa_2Cu_3O_{6.54}$, Phys. Rev. B **88**, 054506 (2013).

[75] M. Le Tacon, A. Bosak, S. M. Souliou, G. Dellea, T. Loew, R. Heid, K-P. Bohnen, G. Ghiringhelli, M. Krisch, and B. Keimer, Inelastic X-ray scattering in $YBa_2Cu_3O_{6.6}$ reveals giant phonon anomalies and elastic central peak due to charge-density-wave formation, Nat. Phys. **10**, 52 (2014).

[76] E. Altendorf, J. C. Irwin, R. Liang, and W. N. Hardy, Raman investigation of the superconducting gap of $YBa_2Cu_3O_x$ for $6.85 < x < 7.0$, Phys. Rev. B **45**, 7551 (1992).

[77] D. Reznik, B. Keimer, F. Dogan, and I. A. Aksay, q Dependence of Self-Energy Effects of the Plane Oxygen Vibration in $YBa_2Cu_3O_7$, Phys. Rev. Lett. **75**, 2396 (1995).

[78] L. Pintschovius, Electron-phonon coupling effects explored by inelastic neutron scattering, Phys. Status Solidi B **242**, 30 (2005).

[79] Eduardo H. da Silva Neto, Pegor Aynajian, Alex Frano, Riccardo Comin, Enrico Schierle, Eugen Weschke, András Gyenis, Jinsheng Wen, John Schneeloch, Zhijun Xu, Shimpei Ono, Genda Gu, Mathieu Le Tacon, and Ali Yazdani, Ubiquitous interplay between charge ordering and high-temperature superconductivity in cuprates, Science **343**, 393 (2014).

[80] M. H. Hamidian, S. D. Edkins, Chung Koo Kim, J. C. Davis, A. P. Mackenzie, H. Eisaki, S. Uchida, M. J. Lawler, E. A. Kim, S. Sachdev, and K. Fujita, Atomic-scale electronic structure of the cuprate d-symmetry form factor density wave state, Nat. Phys. **12**, 150 (2016).

[81] J. D. Axe, A. H. Moudden, D. Hohlwein, D. E. Cox, K. M. Mohanty, A. R. Moodenbaugh, and Y. Xu, Structural Phase Transformations and Superconductivity in $La_{2-x}Ba_xCuO_4$, Phys. Rev. Lett. **62**, 2751 (1989).

[82] Emil S. Bozin, Ruidan Zhong, Kevin R. Knox, Genda Gu, John P. Hill, John M. Tranquada, and Simon J. L. Billinge, Reconciliation of local and long-range tilt correlations in underdoped $La_{2-x}Ba_xCuO_4(0 \leqslant x \leqslant 0.155)$, Phys. Rev. B **91**, 054521 (2015).

[83] H. Jacobsen, I. A. Zaliznyak, A. T. Savici, B. L. Winn, S. Chang, M. Hücker, G. D. Gu, and J. M. Tranquada, Neutron scattering study of spin ordering and stripe pinning in superconducting $La_{1.93}Sr_{0.07}CuO_4$, Phys. Rev. B **92**, 174525 (2015).

[84] M. Hücker, M. v. Zimmermann, G. D. Gu, Z. J. Xu, J. S. Wen, Guangyong Xu, H. J. Kang, A. Zheludev, and J. M. Tranquada, Stripe order in superconducting $La_{2-x}Ba_xCuO_4$ $(0.095 \leqslant x \leqslant 0.155)$, Phys. Rev. B **83**, 104506 (2011).

[85] Q. Li, M. Hücker, G. D. Gu, A. M. Tsvelik, and J. M. Tranquada, Two-Dimensional Superconducting Fluctuations in Stripe-Ordered $La_{1.875}Ba_{0.125}CuO_4$, Phys. Rev. Lett. **99**, 067001 (2007).

[86] E. Berg, E. Fradkin, S. A. Kivelson, and J. M. Tranquada, Striped superconductors: How the cuprates intertwine spin, charge and superconducting orders, New J. Phys. **11**, 115004 (2009).

[87] Patrick A. Lee, Amperean Pairing and the Pseudogap Phase of Cuprate Superconductors, Phys. Rev. X **4**, 031017 (2014).

[88] Colin V. Parker, Pegor Aynajian, Eduardo H. da Silva Neto, Aakash Pushp, Shimpei Ono, Jinsheng Wen, Zhijun Xu, Genda Gu, and Ali Yazdani, Fluctuating stripes at the onset of the pseudogap in the high-T_c superconductor $Bi_2Sr_2CaCu_2O_{8+x}$, Nature (London) **468**, 677 (2010).

[89] S. Blanco-Canosa, A. Frano, E. Schierle, J. Porras, T. Loew, M. Minola, M. Bluschke, E. Weschke, B. Keimer, and M. Le Tacon, Resonant x-ray scattering study of charge-density wave correlations in $YBa_2Cu_3O_{6+x}$, Phys. Rev. B **90**, 054513 (2014).

[90] M. Hücker, N. B. Christensen, A. T. Holmes, E. Blackburn, E. M. Forgan, Ruixing Liang, D. A. Bonn, W. N. Hardy, O. Gutowski, M. v. Zimmermann, S. M. Hayden, and J. Chang, Competing charge, spin, and superconducting orders in underdoped $YBa_2Cu_3O_y$, Phys. Rev. B **90**, 054514 (2014).

[91] W. Tabis, Y. Li, M. Le Tacon, L. Braicovich, A. Kreyssig, M. Minola, G. Dellea, E. Weschke, M. J. Veit, M. Ramazanoglu, A. I. Goldman, T. Schmitt, G. Ghiringhelli, N. Barišić, M. K. Chan, C. J. Dorow, G. Yu, X. Zhao, B. Keimer, and M. Greven, Charge order and its connection with Fermi-liquid charge transport in a pristine high-T_c cuprate, Nat. Commun. **5**, 5875 (2014).

[92] M. J. Lawler, K. Fujita, Jhinhwan Lee, A. R. Schmidt, Y. Kohsaka, Chung Koo Kim, H. Eisaki, S. Uchida, J. C. Davis, J. P. Sethna, and Eun-Ah Kim, Intra-unit-cell electronic nematicity of the high-T_c copper-oxide pseudogap states, Nature (London) **466**, 347 (2010).

[93] A. Mesaros, K. Fujita, H. Eisaki, S. Uchida, J. C. Davis, S. Sachdev, J. Zaanen, M. J. Lawler, and Eun-Ah Kim, Topological defects coupling smectic modulations to intra–unit-cell nematicity in cuprates, Science **333**, 426 (2011).

[94] M. H. Hamidian, S. D. Edkins, K. Fujita, A. Kostin, A. P. Mackenzie, H. Eisaki, S. Uchida, M. J. Lawler, E.-A. Kim, Subir Sachdev, and J. C. Séamus Davis, Magnetic-field induced interconversion of cooper pairs and density wave states within cuprate composite order, arXiv:1508.00620.

[95] H. B. Yang, J. D. Rameau, P. D. Johnson, T. Valla, A. Tsvelik, and G. D. Gu, Emergence of preformed Cooper pairs from the doped Mott insulating state in $Bi_2Sr_2CaCu_2O_{8+\delta}$, Nature (London) **456**, 77 (2008).

[96] H.-B. Yang, J. D. Rameau, Z.-H. Pan, G. D. Gu, P. D. Johnson, H. Claus, D. G. Hinks, and T. E. Kidd, Reconstructed Fermi Surface of Underdoped $Bi_2Sr_2CaCu_2O_{8+\delta}$ Cuprate Superconductors, Phys. Rev. Lett. **107**, 047003 (2011).

[97] T. J. Reber, N. C. Plumb, Z. Sun, Y. Cao, Q. Wang, K. McElroy, H. Iwasawa, M. Arita, J. S. Wen, Z. J. Xu, G. Gu, Y. Yoshida, H. Eisaki, Y. Aiura, and D. S. Dessau, The origin and non-quasiparticle nature of Fermi arcs in $Bi_2Sr_2CaCu_2O_{8+\delta}$, Nat. Phys. **8**, 606 (2012).

[98] Takeshi Kondo, Ari D. Palczewski, Yoichiro Hamaya, Tsunehiro Takeuchi, J. S. Wen, Z. J. Xu, Genda Gu, and Adam

Kaminski, Formation of Gapless Fermi Arcs and Fingerprints of Order in the Pseudogap State of Cuprate Superconductors, Phys. Rev. Lett. **111**, 157003 (2013).

[99] M. R. Norman, H. Ding, M. Randeria, J. C. Campuzano, T. Yokoya, T. Takeuchi, T. Takahashi, T. Mochiku, K. Kadowaki, P. Guptasarma, and D. G. Hinks, Destruction of the Fermi surface in underdoped high-T_c superconductors, Nature (London) **392**, 157 (1998).

[100] T. P. Devereaux, T. Cuk, Z.-X. Shen, and N. Nagaosa, Anisotropic Electron-Phonon Interaction in the Cuprates, Phys. Rev. Lett. **93**, 117004 (2004).

[101] Han-Dong Chen, Oskar Vafek, Ali Yazdani, and Shou-Cheng Zhang, Pair Density Wave in the Pseudogap State of High Temperature Superconductors, Phys. Rev. Lett. **93**, 187002 (2004).

[102] W. S. Lee, I. M. Vishik, K. Tanaka, D. H. Lu, T. Sasagawa, N. Nagaosa, T. P. Devereaux, Z. Hussain, and Z. X. Shen, Abrupt onset of a second energy gap at the superconducting transition of underdoped Bi2212, Nature (London) **450**, 81 (2007).

[103] I. M. Vishik, M. Hashimoto, Rui-Hua He, Wei-Sheng Lee, Felix Schmitt, Donghui Lu, R. G. Moore, C. Zhang, W. Meevasana, T. Sasagawa, S. Uchida, Kazuhiro Fujita, S. Ishida, M. Ishikado, Yoshiyuki Yoshida, Hiroshi Eisaki, Zahid Hussain, Thomas P. Devereaux, and Zhi-Xun Shen, Phase competition in trisected superconducting dome, Proc. Natl. Acad. Sci. USA **109**, 18332 (2012).

[104] Vivek Mishra and M. R. Norman, Strong coupling critique of spin fluctuation driven charge order in underdoped cuprates, Phys. Rev. B **92**, 060507(R) (2015).

[105] Xuetao Zhu, Yanwei Cao, Jiandi Zhang, E. W. Plummer, and Jiandong Guo, Classification of charge density waves based on their nature, Proc. Natl. Acad. Sci. USA **112**, 2367 (2015).

Thermal evolution of antiferromagnetic correlations and tetrahedral bond angles in superconducting FeTe$_{1-x}$Se$_x$

Zhijun Xu,[1,2] J. A. Schneeloch,[3,4] Jinsheng Wen,[5] E. S. Božin,[3] G. E. Granroth,[6] B. L. Winn,[7] M. Feygenson,[8]
R. J. Birgeneau,[1,2] Genda Gu,[3] I. A. Zaliznyak,[3] J. M. Tranquada,[3] and Guangyong Xu[3,*]

[1]*Physics Department, University of California, Berkeley, California 94720, USA*
[2]*Materials Science Division, Lawrence Berkeley National Laboratory, Berkeley, California 94720, USA*
[3]*Condensed Matter Physics and Materials Science Department, Brookhaven National Laboratory, Upton, New York 11973, USA*
[4]*Department of Physics and Astronomy, Stony Brook University, Stony Brook, New York 11794, USA*
[5]*Center for Superconducting Physics and Materials, National Laboratory of Solid State Microstructures
and Department of Physics, Nanjing University, Nanjing 210093, China*
[6]*Neutron Data Analysis and Visualization Division, Oak Ridge National Laboratory, Oak Ridge, Tennessee 37831, USA*
[7]*Quantum Condensed Matter Division, Oak Ridge National Laboratory, Oak Ridge, Tennessee 37831, USA*
[8]*Chemical and Engineering Materials Division, Oak Ridge National Laboratory, Oak Ridge, Tennessee 37831, USA*

It has recently been demonstrated that dynamical magnetic correlations measured by neutron scattering in iron chalcogenides can be described with models of short-range correlations characterized by particular choices of four-spin plaquettes, where the appropriate choice changes as the parent material is doped towards superconductivity. Here we apply such models to describe measured maps of magnetic scattering as a function of two-dimensional wave vectors obtained for optimally superconducting crystals of FeTe$_{1-x}$Se$_x$. We show that the characteristic antiferromagnetic wave vector evolves from that of the bicollinear structure found in underdoped chalcogenides (at high temperature) to that associated with the stripe structure of antiferromagnetic iron arsenides (at low temperature); these can both be described with the same local plaquette, but with different interplaquette correlations. While the magnitude of the low-energy magnetic spectral weight is substantial at all temperatures, it actually weakens somewhat at low temperature, where the charge carriers become more itinerant. The observed change in spin correlations is correlated with the dramatic drop in the electronic scattering rate and the growth of the bulk nematic response upon cooling. Finally, we also present powder neutron diffraction results for lattice parameters in FeTe$_{1-x}$Se$_x$ indicating that the tetrahedral bond angle tends to increase towards the ideal value upon cooling, in agreement with the increased screening of the crystal field by more itinerant electrons and the correspondingly smaller splitting of the Fe 3d orbitals.

I. INTRODUCTION

The roles of magnetic fluctuations and orbital ordering are at the center of a continuing debate in the field of iron-based superconductors (FeBS). While their contributions to the superconducting mechanism are of particular interest [1–3], another forum concerns the nature of the nematic electronic response [4]. In an attempt to look for minimal models, the discussion is often focused on an exclusive choice: either magnetic correlations [5–7] or orbital fluctuations [8,9] are the dominant factor.

Experimental evidence for nematic response was first obtained in the BaFe$_2$As$_2$ system [10–15], where a structural transition that lowers the rotational symmetry from C_4 to C_2 is closely followed by antiferromagnetic ordering [16–18], with modulation wave vector $(\pi,0)$ [19]. New interest has been generated by the recent observations of nematicity in FeSe [20], a superconducting compound that exhibits a symmetry-lowering structural transition but no magnetic order [21,22]. Of particular interest is the observation of a temperature-dependent splitting of d_{xz} and d_{yz} orbitals through angle-resolved photoemission spectroscopic (ARPES) studies [23–25].

While several analyses have shown that it is possible to have a nematic response due to dynamic magnetic correlations

alone [26–28], driving a transition to an orthorhombic phase [21] with fluctuations alone is another matter. In any case, one might wonder to what extent the distinction between magnetic and orbital correlations is artificial. Experimentally, there is no question that there are substantial instantaneous magnetic moments on Fe sites in the FeBS compounds, both from x-ray emission spectroscopy [29,30] and from neutron scattering [31,32], and that these moments are generally antiferromagnetically correlated [31,32], regardless of whether static order is observed. In particular, low-energy magnetic excitations about the $(\pi,0)$ wave vector have been observed in FeSe by neutron scattering [33,34]. These observations are supported by theoretical calculations using dynamical mean field theory (DMFT) [35]. At the same time, a number of analyses have found that models consistent with the magnetic order also exhibit partial orbital ordering [8,9,36–38], involving broken degeneracy of the d_{xz} and d_{yz} orbitals. Indeed, an energy splitting between bands of dominant d_{xz} and d_{yz} character has been observed [11] over the same range of temperatures as anisotropies of the intensity of spin excitations [15].

While FeSe has garnered a lot of attention, FeTe$_{1-x}$Se$_x$ in the regime of optimal superconducting transition temperature (T_c) is also rather interesting. Although the average crystal structure remains tetragonal, elastoresistance measurements demonstrate a strong nematic response in the B_{2g} symmetry channel that appears to diverge at low temperature, similar
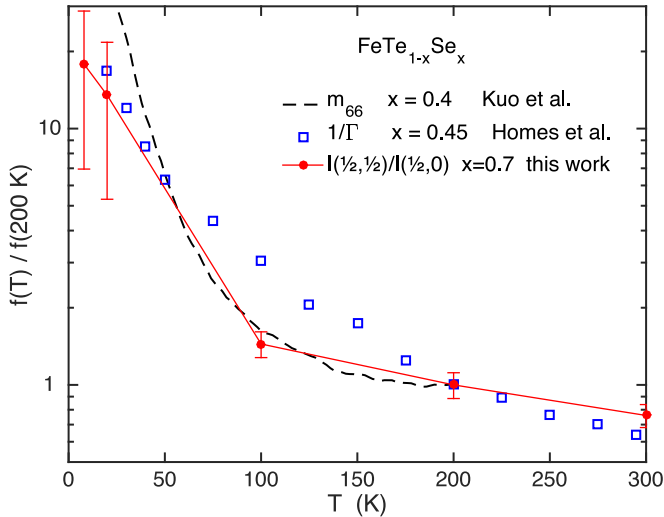

104517-1

FIG. 1. Comparison of the elastoresistance coefficient m_{66} for $x = 0.4$ (dashed line) [39], inverse scattering rate of the narrow Drude component from optical conductivity measurements of $x = 0.45$ (open squares) [42], and the ratio of 7-meV magnetic spectral weight integrated about the spin-stripe wave vector $(\frac{1}{2},\frac{1}{2})$ and the double-stripe wave vector $(\frac{1}{2},0)$ (filled circles connected by solid line), taken from Fig. 6, with error bars reflecting counting statistics. All quantities have been normalized at 200 K.

to other optimally doped Fe-pnictide superconductors [39], as reproduced in Fig. 1. Furthermore, there is evidence of the local C_4 symmetry breaking down to C_2 in the pattern of short-range dynamical magnetic correlations measured by neutron scattering in parent material FeTe with S, or Se doping, and also on cooling in a composition that is superconducting [40], while ARPES measurements at 25 K indicate a splitting of the xz and yz bands at zone center [41]. The coherence of the charge carriers also shows a strong temperature dependence: optical conductivity measurements find a component that becomes coherent only at low temperature, with the inverse of the energy width growing upon cooling [42].

An important aspect of the orbital nature of the electronic band structure involves splitting between bands with xy and xz/yz character, which is sensitive to deviations from the ideal tetrahedral bond angle of 109.5° [35]. In FeTe$_{1-x}$Se$_x$, the bond angles are essentially controlled by the height of the chalcogenide ions above and below the Fe layers, with the bond angle dropping from 104° in FeSe to ∼94° in Fe$_{1+y}$Te [43,44]. It was argued [45] that the change in height of the chalcogenide ions modifies the relative magnitudes of superexchange couplings (although the concept of superexchange is not well defined for multiorbital FeBS with a high degree of itinerancy [46]), resulting in a change of the characteristic antiferromagnetic wave vector from that describing the double-stripe $(\pi/2,\pi/2)$ order known to occur in Fe$_{1+y}$Te [47–49], to that of the dynamical single-stripe $(\pi,0)$ correlations in superconducting FeTe$_{1-x}$Se$_x$ [50–53]. (See Table I for a clear definition of the wave-vector notation used in this paper.)

In this paper, we study the temperature-dependent change of the antiferromagnetic correlations in FeTe$_{1-x}$Se$_x$ by inelastic neutron scattering. We [54,55] and others [56] have previously shown that the low-energy excitations centered at $(\pi,0)$ in the superconducting state shift in reciprocal space upon

TABLE I. Definitions of stripe antiferromagnetic (SAF) and double stripe antiferromagnetic (DSAF) wave vectors for two choices of unit cell. For the 1-Fe (2-Fe) unit cell, the units are $1/a_0$ $(2\pi/a)$, where a_0 and a are the corresponding lattice parameters.

	1-Fe unit cell	2-Fe unit cell
Q_{SAF}	$(\pi,0)$	$(\frac{1}{2},\frac{1}{2})$
Q_{DSAF}	$(\frac{\pi}{2},\frac{\pi}{2})$	$(\frac{1}{2},0)$

warming to 100 K and above; one-dimensional cuts through the $(\pi,0)$ "resonance" position reveal a change from a broad commensurate peak at $(\pi,0)$ to incommensurate correlations peaked near $(0.25\pi,0.75\pi)$ and $(0.75\pi,0.25\pi)$. Here we present measurements covering two-dimensional slices of reciprocal space, finding that the main locus of the low-energy spectral weight in fact shifts from $(\pi,0)$ to $(\pi/2,\pi/2)$ upon warming. Moreover, in a sample that is nonsuperconducting due to excess Fe, we show that the magnetic correlations remain pinned at $(\pi/2,\pi/2)$.

The pattern observed here at high temperature and in the nonsuperconducting sample is quite similar to that recently reported by one of us (I.Z.) [40] in a S-doped FeTe sample with filamentary superconductivity. There the pattern emerged upon cooling, replacing the high-temperature pattern characteristic of the parent Fe$_{1+y}$Te [57], indicating a transition between two different spin-liquid states. The measured spin-spin correlations were described by a model in which a long-range spin pattern is broken into four-spin plaquettes, with exponential decay of correlations between plaquettes with distance from the central plaquette. The change in symmetry of the model plaquettes needed to simulate the measured inelastic diffuse scattering suggested local breaking of the C_4 symmetry down to C_2 upon cooling, prior to reaching the superconducting state. In the present case, we find that the spin correlations at both high and low temperatures can be modeled with the same choice of plaquette (having only C_2 symmetry), but with the interplaquette correlations changing from the double-stripe to the single-stripe wave vector upon cooling.

Besides the change in characteristic wave vector, we also observe a decrease in low-energy magnetic weight upon cooling, which parallels the increased itinerancy of charge carriers. Such behavior is qualitatively consistent with recent theoretical work [58] and previous experimental results [40,57].

To gain further insight into this curious thermal evolution, we have used neutron powder diffraction to measure the temperature dependence of the lattice parameters for a series of FeTe$_{1-x}$Se$_x$ with $0 \leqslant x \leqslant 1$. For x away from the limiting values, we find an anomalous rise in the a/c ratio upon cooling, corresponding to an increase in the tetrahedral bond angles. We infer an associated change in both the crystal-field splitting and the hybridization of the t_{2g} states. This, together with the evidence for nematic correlations [39] and xz/yz splitting at low temperature [41], indicates that the change in magnetic correlations with temperature can be associated with changing exchange couplings.

The rest of the paper is organized as follows. The experimental methods are described in the next section. The results and analysis are presented in Sec. III. The results are summarized and discussed in Sec. IV.

II. EXPERIMENTAL METHODS

The single crystals of $FeTe_{1-x}Se_x$ studied here were grown by unidirectional solidification [59]. Here we study superconducting samples with $x = 0.50$ (SC50) and $x = 0.70$ (SC70), each with $T_c \gtrsim 14$ K, and a nonsuperconducting sample with $x = 0.45$ (NSC45) and excess Fe. Previous characterizations of these crystals have been reported in [51,55,60–62]. From here on, we will specify momentum transfer $\mathbf{Q} = (h,k,l)$ in units of $(2\pi/a, 2\pi/a, 2\pi/c)$, where we assume a tetragonal unit cell with 2 Fe atoms per unit cell, as illustrated in Fig. 2(a). (Room temperature lattice parameters are presented in Fig. 7.)

The inelastic neutron scattering experiments were performed on time-of-flight instruments at the Spallation Neutron Source (SNS), Oak Ridge National Laboratory (ORNL). The SC50 sample was measured on SEQUOIA (BL-17) [63], with an incident energy $E_i = 40$ meV, using Fermi chopper number 1 at 360 Hz, and the [001] direction of the crystal aligned with the incident beam direction. As the measurements were done with a fixed orientation of the crystal, we obtained data as a function of excitation energy $\hbar\omega$ and $\mathbf{Q} = (h,k,l_0)$, where l_0 is determined by E_i and $\hbar\omega$.

The SC70 and NSC45 samples were measured on HYSPEC (BL-14B) [64] with $E_i = 20$ meV and a chopper frequency of 180 Hz. With the [001] direction of the sample vertical (perpendicular to the scattering plane), the in-plane orientation was stepped by increments of $2°$ over a range of $180°$. The detectors were positioned to cover neutrons with scattering angles from $5°$ to $65°$. From the combined data, it is possible to extract slices at constant $\hbar\omega$ for the $(h,k,0)$ plane. The data

have been symmetrized to enforce the 4-fold symmetry for better presentations.

The neutron powder diffraction measurements were performed at the intermediate-resolution diffractometer NOMAD (BL-1B) at the SNS [65]. The samples were prepared by grinding pieces of single crystals. The compositions correspond to $x = 0, 0.1, 0.2, 0.3, 0.45, 0.5, 0.7, 1$, where the $x = 0$ sample has 10% excess of Fe, while the Fe excess in the other samples has been kept close to zero; superconducting transition temperatures for all samples except for $x = 1$ were reported in [66]. Note that the $x = 0.50$ and 0.70 powder samples are very similar to SC50 and SC70 samples; the $x = 0.45$ powder sample does not have excess Fe (unlike NSC45) and is superconducting. Each sample of ~8 g was loaded into a vanadium can under a helium atmosphere, and then cooled in an "orange" (liquid helium) cryostat. Temperature-dependent measurements were performed while warming from 10 K to 300 K, with a counting time of 1 h per temperature.

To extract lattice parameters from the data, Le Bail refinements [67] were performed using GSAS [68] operating under the ExpGui platform [69]; in general, only data from the highest-resolution backscattering detector bank were used. All data for all samples were fitted with a tetragonal model based on the $P4/nmm$ space group. In addition, the $Fe_{1+y}Te$ data were modeled with the $P21/m$ model below the phase transition temperature of ~65 K. For the FeSe sample, no phase transition was resolved.

III. RESULTS AND ANALYSIS

A. Magnetic excitations

1. Data

To make contact with previous work, we begin with the measurements on the SC50 sample at SEQUOIA. The magnetic excitation spectra about the stripe antiferromagnetic wave vector, $\mathbf{Q}_{SAF} = (0.5,0.5)$, along the $[1,-1,0]$ direction is plotted for several temperatures in Fig. 2. The spin gap of ~5 meV is clearly visible in the 6 K data. The intensity near the bottom of the dispersion is clearly enhanced in the superconducting phase and the magnetic excitations disperse outwards forming a U shape above this spin resonance energy [51,62,70,71]. In the normal state at $T = 20$ K, the spin resonance fades away and broadens in energy and Q, so that intensity moves into the spin gap; nevertheless, the overall shape of the magnetic excitation spectrum does not appear to change significantly.

In contrast, significant changes are observed for excitations near the bottom of the dispersion when the sample is warmed to 80 K, far above T_c. In Fig. 2(e), one can see that the scattered signal has broadened considerably in Q below 10 meV, and the bottom of the U-shaped dispersion appears to have split. This is consistent with the nominally incommensurate correlations previously observed in linear scans. Only for $\hbar\omega > 15$ meV does the spectrum remain relatively unchanged with temperature.

In order to understand the temperature-dependent changes in the low-energy scattering, however, we need to look at what is happening throughout the $(H,K,0)$ plane. For this, we turn to the measurements on the SC70 sample obtained at HYSPEC.
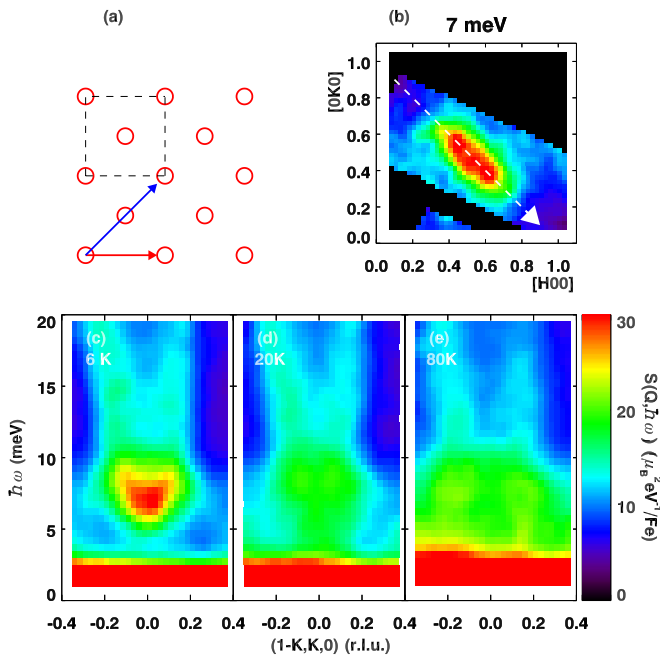
FIG. 2. (a) The two-Fe unit cell used in the paper. The circles denote Fe atom positions. The red and blue arrows respectively denote the [1,0] and [1,1] directions in real space. (b) $Q_{AF} = (0.5,0.5)$, location of the spin resonance in the $(H,K,0)$ plane. The dashed arrow denotes the transverse direction, along which we plot the inelastic magnetic neutron scattering for temperatures of (c) 6 K, (d) 20 K, and (e) 80 K, measured from the SC50 sample on SEQUOIA.
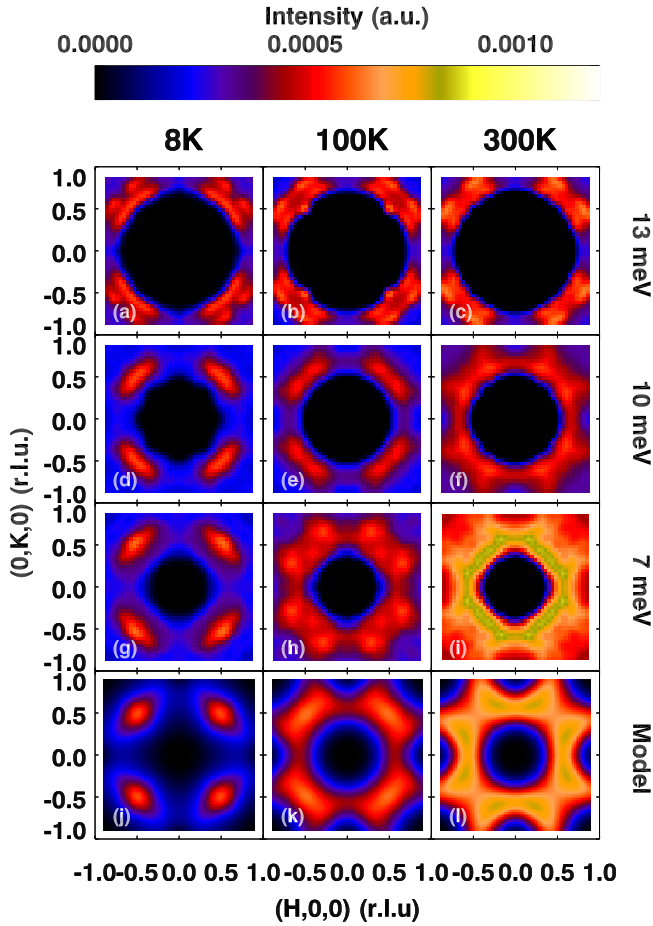
FIG. 3. Inelastic magnetic neutron scattering from the SC70 sample measured on HYSPEC at energy transfers $\hbar\omega = 13$ meV (a), (b), (c); 10 meV (d), (e), (f); and 7 meV (g), (h), (i). The sample temperatures are 8 K (a), (d), (g); 100 K (b), (e), (h); and 300 K (c), (f), (i). All slices were taken with an energy width of 2 meV. Measurements, covering approximately two quadrants, have been symmetrized to be 4-fold symmetric, consistent with sample symmetry. Intensity scale is the same in all panels, but 13-meV data have been multiplied by 1.5 to improve visibility. Black regions at the center of each panel are outside of the detector range. Panels (j), (k), (l) are model calculations simulating the 7-meV data, as described in the text, based on weakly correlated slanted UDUD spin plaquettes [see Figs. 5(a) and 5(b)]. The wave vectors for the AFM interplaquette correlations used in the calculation are (j) 100% Q_{SAF}, (k) 50% Q_{SAF} and 50% Q_{DSAF}, and (l) 100% Q_{DSAF}.

Such constant-energy slices are plotted in Fig. 3 for energy transfers of 7, 10, and 13 meV, and temperatures of 8, 100, and 300 K. In the superconducting phase ($T = 8$ K), the low-energy ($\hbar\omega = 7$ meV) magnetic excitations have ellipsoidal shapes centered on Q_{SAF} positions, with the long axis oriented in the transverse direction [Fig. 3(g)]. The excitations at higher energies spread out along the transverse directions away from Q_{SAF} [Figs. 3(d), 3(a)], consistent with the dispersion shown in Fig. 2. Upon warming to 100 K, the low-energy intensity maxima [Fig. 3(g)] move away from Q_{SAF}, again consistent with Fig. 2.

At 300 K, the redistribution of low-energy signal in reciprocal space and an intensity enhancement are more
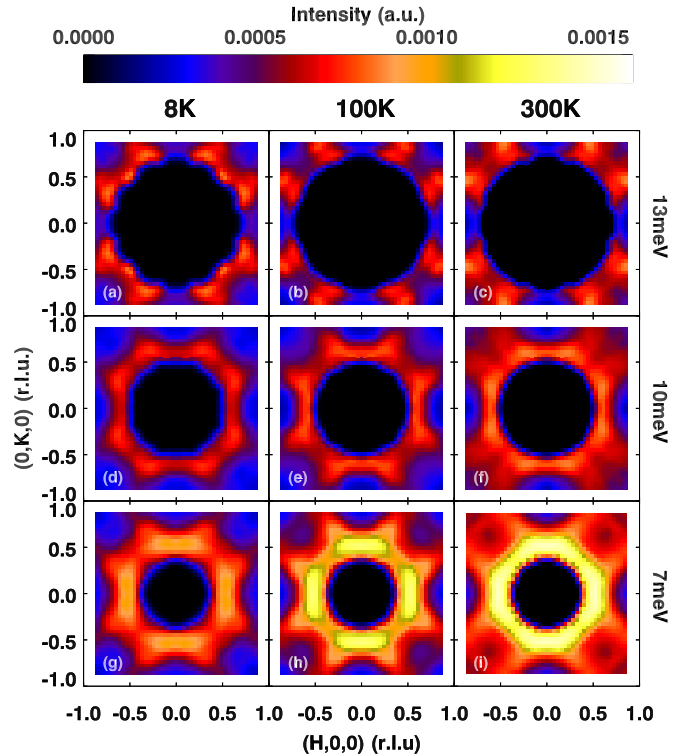
FIG. 4. Inelastic magnetic neutron scattering measured at energy transfers $\hbar\omega = 13$ meV (top row), 10 meV (second row from the top), and 7 meV (third row from the top) on HYSPEC. All slices were taken with an energy width of 2 meV. The sample used is the NSC45 sample. The temperatures for the measurements are 8 K, 100 K, 300 K, from left to right, respectively.

pronounced. The intensities appear to form a continuous, though structured, "squared" ring about $\mathbf{Q} = (0,0)$. Corners of a "squared" ring going through the four (0.5,0) positions are reminiscent of the pattern observed in $FeTe_{1-x}S_x$ [40]. In contrast, the temperature-induced changes in the intensity distribution are much less pronounced at 10 meV and are hardly noticeable at 13 meV, although the overall intensity increase is noticeable, similar to the trend observed in previous studies of FeTe and $FeTe_{1-x}S_x$ [40,57].

Similar measurements were performed on the NSC45 sample, and the results are shown in Fig. 4. The data at 300 K are rather similar to the high-temperature data for SC70. In contrast to SC70, however, cooling results in relatively little change to the scattering pattern at low energy, other than a reduction in intensity. In fact, low-temperature measurements on triple-axis spectrometers have shown that broad elastic scattering centered at (0.5,0,0.5) is present at low temperature for NSC45 but is absent for SC70 [72].

To put these results in perspective, the data for the SC50 and SC70 samples are consistent with one another and with our previous results on good bulk superconducting samples [54,55,62], though the latter results covered a more restricted part of $\mathbf{Q}$-ω space. Similarly, the data for the NSC45 sample are compatible with our previous measurements [55] on nonsuperconducting, Se-doped samples, where excess Fe induces short-range antiferromagnetic order at low temperature.
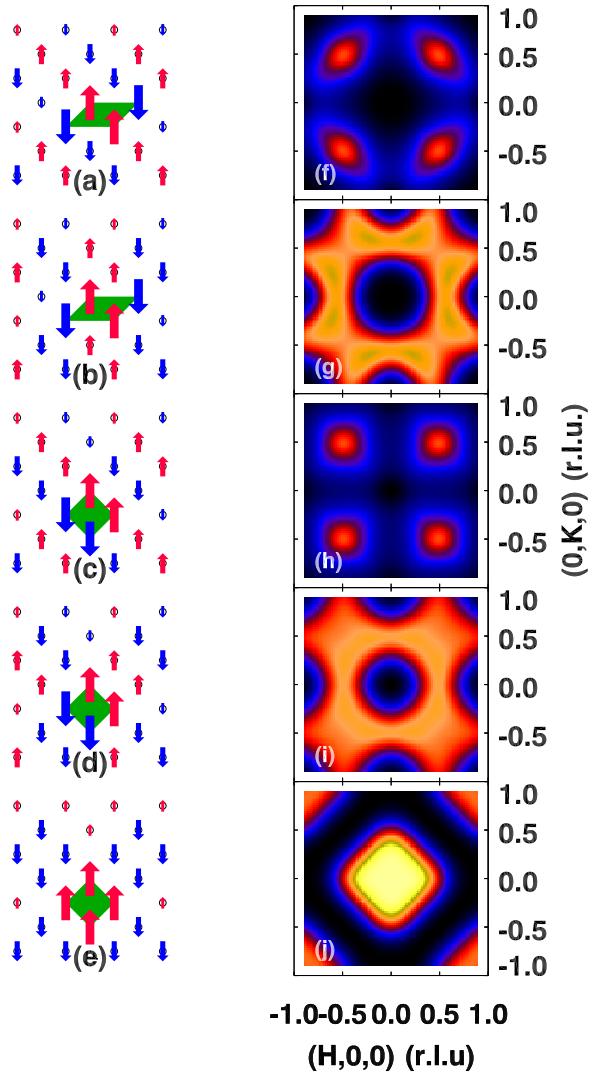
FIG. 5. Schematics of the spin plaquettes in the weakly correlated spin-liquid model described in the text. (a) A canted UDUD plaquette with modulation wave vector $\mathbf{Q}_{SAF}$. (b) Canted UDUD plaquette with $\mathbf{Q}_{DSAF}$. (c) Square UDUD plaquette with $\mathbf{Q}_{SAF}$. (d) Square UDUD plaquette with block antiferromagnetic correlations. (e) Square UUUU plaquette with block antiferromagnetic correlations. The frames (f) to (j) are model simulations described in the text, based on the liquid-like spin plaquette models in (a) to (e), respectively.

2. Modeling

Several studies have suggested that the exchange couplings governing magnetic correlations in the iron chalcogenides are strongly frustrated, resulting in a variety of spin configurations having very similar free energies [28,73–76]. This frustration inhibits long-range magnetic order, and is qualitatively consistent with our observations of dynamical magnetic correlations with short correlation lengths. Nevertheless, while the magnetic moments are clearly disordered, we find that they carry signatures of specific local spin configurations.

Following Zaliznyak *et al.* [40], we consider models of static, short-range spin correlations that may represent a snapshot of the behavior for low-energy spin excitations—specifically, for our $\hbar\omega = 7$ meV data. Figure 5 shows a variety

of models and their 4-fold symmetrized Fourier transforms. In each case, we start with a particular 4-spin plaquette; averaging over equivalent choices leads to the structure factor for the correlations. We then choose a particular antiferromagnetic wave vector to describe interplaquette phasing, with an exponential decay of the correlations with distance between plaquettes. For example, Figs. 5(a) and 5(b) use the same choice of plaquette (labeled up-down-up-down, or UDUD), but with longer-range correlations defined by $\mathbf{Q}_{SAF}$ and $\mathbf{Q}_{DSAF}$, respectively. This results in dramatically different scattering patterns, as indicated by Figs. 5(f) and 5(g). Figure 5 also shows several other choices of plaquette and modulation wave vector.

Looking back at the 7-meV results for the SC70 sample in Fig. 3, we find that the data are quite similar to the calculations for the UDUD plaquette, but with the modulation wave vector changing with temperature, from $\mathbf{Q}_{SAF}$ in the superconducting state to $\mathbf{Q}_{DSAF}$ at room temperature. At 100 K, a 50 : 50 mix of these models seems to apply. The corresponding simulations are plotted in Figs. 3(j)–3(l), for comparison with the data in Figs. 3(g)–3(i). The effective correlation length was chosen to be $\sim 0.5a$ in these cases, suggesting a highly disordered nature of the spin configuration that is consistent with a liquid phase. For the NSC45 sample, as already mentioned, there appears to be no change in characteristic wave vector, $\mathbf{Q}_{DSAF}$. Our data thus provide a direct probe of the spin-correlation wave vector, in addition to the type of the local order. In particular, we note that models with square plaquettes, such as Figs. 5(c) to 5(e), fail to reproduce important details of the data.

An alternative approach for analyzing the changing magnetic correlations is to simply compare the magnetic weight at the characteristic wave vectors $\mathbf{Q}_{SAF}$ and $\mathbf{Q}_{DSAF}$. The raw and background (BG) subtracted intensities for these regions at $\hbar\omega = 7$ meV are plotted in Figs. 6(a) and 6(b). Here, the magnetic scattering intensity (BG subtracted) at $\mathbf{Q}_{SAF} = (0.5, 0.5)$ positions decreases with warming while that at $\mathbf{Q}_{DSAF} = (0.5, 0)$ increases. For comparison, the solid line in Fig. 6(b) shows the detailed-balance factor $1/(1 - e^{-\hbar\omega/k_B T})$, which would characterize the thermal evolution of collective excitations whose dynamical susceptibility does not depend on temperature for the range of temperature studied, as one might expect in the case of a magnetically ordered state. The signal at $(0.5, 0)$ clearly grows even faster than predicted by the detailed balance factor, which means that the dynamical magnetic susceptibility increases. The ratio of the signal at $\mathbf{Q}_{SAF}$ to that at $\mathbf{Q}_{DSAF}$ is plotted in Fig. 1, where one can see that it evolves much like the nematicity from electroresistance measurements [39] and the inverse scattering rate of mobile charge carriers [42].

We also plot the background-corrected intensity integrated over the entire Brillouin zone for $\hbar\omega = 7$ meV in Fig. 6(c). Due to kinematics, there is a region around $\mathbf{Q} = (0, 0)$ that we cannot measure, so that we might miss some signal as the scattering spreads out with increasing temperature. Nevertheless, from 10 K to 300 K, the Q-integrated low-energy spectral weight has increased by at least a factor of two. At higher energy transfers, the Q range of our measurements becomes more limited and such integration over the entire Brillouin zone becomes unrealistic. Qualitatively, however, it is evident (see Fig. 3) that the increase of spectral weight with temperature also becomes much less pronounced at higher energy transfers.
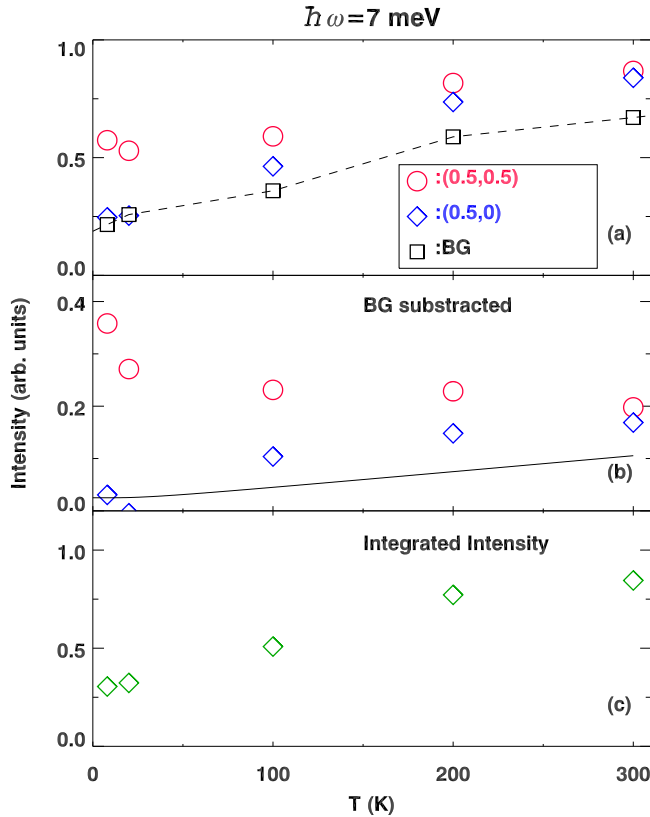
FIG. 6. Inelastic neutron scattering intensity measured at $\hbar\omega = 7$ meV with energy width $\delta E = 1$ meV from the SC70 sample on HYSPEC. (a) Raw intensity measured at $\mathbf{Q}_{\mathrm{DSAF}} = (0.5,0)$ (blue diamonds) and $\mathbf{Q}_{\mathrm{SAF}} = (0.5,0.5)$ (red circles). The numbers shown in the plot are averaged intensities taken within a square region with $\delta H = 0.1$ and $\delta K = 0.1$ (r.l.u.) centered at the measurement wave vectors. The background is measured by averaging intensities around $(1,0)$ and $(1,1)$, shown as black squares. (b) Background-subtracted intensities at $\mathbf{Q}_{\mathrm{DSAF}}$ (blue diamonds) and $\mathbf{Q}_{\mathrm{SAF}}$ (red circles). The solid line is the calculated detailed-balance factor. (c) Integrated intensity over the full Brillouin zone centered at $(0,0)$.

B. Temperature dependence of lattice tetragonality

The observed thermal evolution of the magnetic correlations is inconsistent with a model in which orbital hybridization and magnetic exchange couplings are independent of temperature. Given the changes, one might expect to see some sort of response in the lattice. As already mentioned, symmetry-lowering structural transitions are common to $\mathrm{Fe}_{1+y}\mathrm{Te}$ and FeSe. For mixed compositions, the situation is complicated by the very different Fe-Te and Fe-Se bond lengths. Scattering studies indicate that these bond lengths vary rather little [44,77]; as a consequence, scanning transmission electron microscopy [78] and scanning tunneling microscopy [79] studies provide evidence of segregation into Te-rich and Se-rich regions. Such disorder may frustrate long-range ordering of distortions away from tetragonal symmetry; nevertheless, other behavior may survive. Indeed, in our initial report of anomalous temperature-dependent changes of the magnetic correlations in $\mathrm{FeTe}_{0.5}\mathrm{Se}_{0.5}$ doped with Ni, we found an upturn in the a lattice parameter at low temperature [54]. Similar lattice behavior was reported earlier for $\mathrm{FeTe}_{1-x}\mathrm{Se}_x$
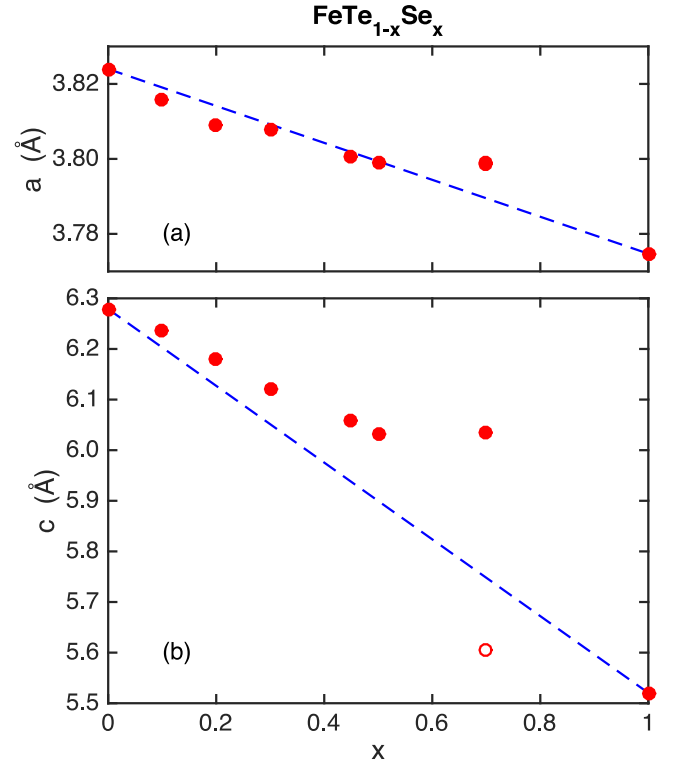
FIG. 7. Lattice parameters a (a), and c (b), for $\mathrm{FeTe}_{1-x}\mathrm{Se}_x$ as a function of x, measured by neutron powder diffraction at 300 K on NOMAD. Statistical uncertainties for a and c are smaller than the symbol size. The dashed lines simply connect the points at $x = 0$ and 1.

with $x = 0.1$ and 0.2 by Martinelli *et al.* [80]. As a result, we decided to take a more systematic look at the system with neutron powder diffraction measurements.

Figure 7 shows the room temperature values of the a and c lattice parameters as a function of x; here all samples have the tetragonal structure, with space group $P4/nmm$. Note that the c lattice parameter changes by 0.78 Å (13%) across this series, while a changes by only 0.046 Å (1.3%). This reflects the very different heights of the Te and Se ions relative to the Fe layer. The $x = 0.7$ sample is on the lower edge of the miscibility gap found by Fang *et al.* [81]. We found evidence for two tetragonal phases, with the lattice parameters of the less dominant phase ($\sim$30% by volume) indicated by open circles (a values are virtually identical). Note that the second phase, with reduced c, is expected to be similar to FeSe, which is superconducting and lacks magnetic order. The spin dynamics should be similar to that of the Te-doped superconducting phase, and no distinctive features were detected in the single-crystal inelastic measurements.

A representative example of the temperature dependence of the a and c lattice parameters for $x = 0.5$ is plotted in Fig. 8(a). As one can see, there is a distinct upturn in a below $\sim$150 K, while the c lattice parameter, if anything, appears to decrease a bit more rapidly in the same temperature range. We observe very similar behavior for all samples in the range $0.1 \leqslant x \leqslant 0.7$. To characterize this behavior, we have plotted the relative change in the a/c ratio in Fig. 8(b). To be specific, if $r = a/c$, then we plot $[r(T) - r(300\,\mathrm{K})]/r(300\,\mathrm{K})$. In the
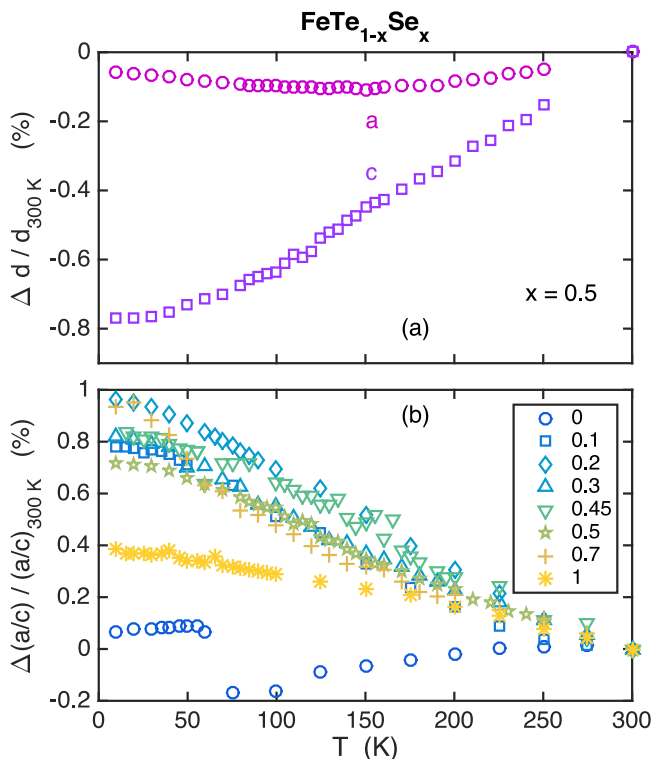
FIG. 8. (a) Change in a and c lattice parameters, normalized to 300 K, as a function of temperature for the $x = 0.50$ sample. Statistical uncertainties are comparable to the symbol size. (b) Change in a/c, normalized to 300 K, as a function temperature for FeTe$_{1-x}$Se$_x$; the values of x are noted in the symbol legend. The average of in-plane lattice parameters was used for a in the low-temperature phase of $x = 0$.

case of $x = 0$, we use the average in-plane lattice parameter in the low temperature phase; note that we did not resolve an orthorhombic phase in our $x = 1$ sample.

To interpret this behavior, we note that the tetrahedral bond angle can be expressed as $\theta = \tan^{-1}(a/2zc)$, where z is the relative coordinate of the chalcogenide ions. Given the evidence for phase segregation in FeTe$_{1-x}$Se$_x$ [78,79], it should be reasonable to think about local Te-Fe-Te and Se-Fe-Se bond angles. Regardless of the local z, the bond angle will move towards the ideal tetrahedral angle as a/c increases. The temperature dependence of a/c shown in Fig. 8(b) indicates that bond angle increases toward the ideal upon cooling, which implies a reduction of the crystal-field splitting [35], and a change in hybridization. The relative change of the bond angle in each sample upon cooling is relatively small; however, we believe it reflects a substantially larger change in orbital content and occupancy of the electronic band structure. We note that a recent ARPES study of FeTe$_{1-x}$Se$_x$ with $x = 0.44$ has found a significant growth upon cooling for spectral weight of the d_{xy} band near the Fermi level [82].

IV. SUMMARY AND DISCUSSION

By mapping the magnetic scattering over the entire $(H, K, 0)$ plane of reciprocal space, we have shown that the characteristic wave vector of the low-energy spin correlations

shifts from $\mathbf{Q}_{DSAF}$ to $\mathbf{Q}_{SAF}$ upon cooling in superconducting FeTe$_{1-x}$Se$_x$. The ratio of the magnetic signal at the latter point to the former grows at low temperature much like the nematic response of elastoresistance measurements [39] and the inverse scattering rate of the mobile carriers [42], as shown in Fig. 1. In a sample rendered nonsuperconducting by inclusion of excess Fe, the magnetic wave vector is $\mathbf{Q}_{DSAF}$ and shows no thermal shift. In all samples studied, local correlations are consistent with antiferromagnetic UDUD plaquettes having C_2 local symmetry indicative of nematicity, in agreement with the study of Ref. [40], where such correlations were found to develop with doping towards superconductivity. We thus conclude that the change in the wave vector which describes propagation of magnetic correlations from $\mathbf{Q}_{DSAF}$ to $\mathbf{Q}_{SAF}$ is a further necessary condition for superconductivity in 11 iron chalcogenides.

In our superconducting samples, the modeling of $\mathbf{Q}$ dependence of the low-energy magnetic scattering suggests local rotational symmetry breaking at all temperatures. However, it is the temperature-dependent change in characteristic magnetic wave vector that seems to qualitatively correlate with the growth in the nematic response of the elastoresistance measurements [39], as indicated in Fig. 1. The variation in antiferromagnetic wave vector implies a relative change among the exchange couplings over various Fe-Fe neighbor distances. A likely cause of this change is a temperature-dependent variation of the orbital overlaps, the corresponding hybridization, as well as the variation in the occupancies of Fe d levels. The ARPES evidence for local splitting of xz and yz bands [41], together with the temperature-dependent nematic response [39], supports this sort of variation. Our evidence for the thermal variation of the tetrahedral bond angle indicates a modification of the splitting, and hence the orbital content and the occupancy of the xy and xz/yz based bands that cross the Fermi level. Regarding the question of what drives the nematic response, we can conclude that it is *not* an approach to magnetic order; local orbital order is a more likely suspect. Nevertheless, it is clear that the magnetic, orbital, and lattice degrees of freedom are strongly entangled.

We have also observed a reduction of low-energy magnetic spectral weight upon cooling. This is consistent with nuclear magnetic resonance results for an $x = 0.5$ sample in which the quantity $1/T_1T$, where $1/T_1$ is the spin-lattice relaxation rate measured at the Te site, decreases as the temperature is reduced [83]. This loss of magnetic susceptibility is correlated with a growth in electronic conductivity [42,84] and a crossover from incoherence to coherence. This correlation parallels the more extreme changes observed in Fe$_{1+y}$Te [57,85]. Theoretically, a competition between antiferromagnetic correlations and conductivity is expected [58,86]. The same electrons must contribute to the magnetic moments, influenced by Coulomb and Hund's interactions, and to electronic conductivity, minimizing kinetic energy. This balance adjusts upon cooling, with changing hybridization, and this competition likely plays an important role in determining the superconducting state.

Altogether, there is evidence for temperature-correlated changes in characteristic magnetic wave vector, nematicity, electronic coherence, magnetic spectral weight, and tetrahedral bond angle. It would be surprising if there were not an

underlying connection that all of these happen together, and the temperature-dependent orbital hybridization and the orbital-selective electronic coherence provide a plausible connection. These relationships certainly deserve further study.

ACKNOWLEDGMENTS

[1] I. I. Mazin, D. J. Singh, M. D. Johannes, and M. H. Du, Phys. Rev. Lett. **101**, 057003 (2008).

[2] K. Kuroki, S. Onari, R. Arita, H. Usui, Y. Tanaka, H. Kontani, and H. Aoki, Phys. Rev. Lett. **101**, 087004 (2008).

[3] H. Kontani and S. Onari, Phys. Rev. Lett. **104**, 157001 (2010).

[4] R. M. Fernandes, A. V. Chubukov, and J. Schmalian, Nat. Phys. **10**, 97 (2014).

[5] C. Fang, H. Yao, W. F. Tsai, J. P. Hu, and S. A. Kivelson, Phys. Rev. B **77**, 224509 (2008).

[6] C. Xu, M. Müller, and S. Sachdev, Phys. Rev. B **78**, 020501 (2008).

[7] I. I. Mazin and M. D. Johannes, Nat. Phys. **5**, 141 (2009).

[8] W. Lv, J. Wu, and P. Phillips, Phys. Rev. B **80**, 224506 (2009).

[9] F. Krüger, S. Kumar, J. Zaanen, and J. van den Brink, Phys. Rev. B **79**, 054504 (2009).

[10] J.-H. Chu, J. G. Analytis, K. De Greve, P. L. McMahon, Z. Islam, Y. Yamamoto, and I. R. Fisher, Science **329**, 824 (2010).

[11] M. Yi, D. Lu, J.-H. Chu, J. G. Analytis, A. P. Sorini, A. F. Kemper, B. Moritz, S.-K. Mo, R. G. Moore, M. Hashimoto, W.-S. Lee, Z. Hussain, T. P. Devereaux, I. R. Fisher, and Z.-X. Shen, Proc. Natl. Acad. Sci. USA **108**, 6878 (2011).

[12] J.-H. Chu, H.-H. Kuo, J. G. Analytis, and I. R. Fisher, Science **337**, 710 (2012).

[13] H.-H. Kuo, M. C. Shapiro, S. C. Riggs, and I. R. Fisher, Phys. Rev. B **88**, 085113 (2013).

[14] M. C. Shapiro, P. Hlobil, A. T. Hristov, A. V. Maharaj, and I. R. Fisher, Phys. Rev. B **92**, 235147 (2015).

[15] X. Lu, J. T. Park, R. Zhang, H. Luo, A. H. Nevidomskyy, Q. Si, and P. Dai, Science **345**, 657 (2014).

[16] Q. Huang, Y. Qiu, W. Bao, M. A. Green, J. W. Lynn, Y. C. Gasparovic, T. Wu, G. Wu, and X. H. Chen, Phys. Rev. Lett. **101**, 257003 (2008).

[17] J.-H. Chu, J. G. Analytis, C. Kucharczyk, and I. R. Fisher, Phys. Rev. B **79**, 014506 (2009).

[18] D. K. Pratt, W. Tian, A. Kreyssig, J. L. Zarestky, S. Nandi, N. Ni, S. L. Bud'ko, P. C. Canfield, A. I. Goldman, and R. J. McQueeney, Phys. Rev. Lett. **103**, 087001 (2009).

[19] Here we have used the notation commonly used by theorists, which assumes a single Fe per unit cell and units of $1/a_0$. When discussing experimental data, we will refer to a unit cell containing two Fe atoms, in units of $2\pi/a$.

[20] S.-H. Baek, D. V. Efremov, J. M. Ok, J. S. Kim, J. van den Brink, and B. Büchner, Nat. Mater. **14**, 210 (2015).

[21] A. E. Böhmer, T. Arai, F. Hardy, T. Hattori, T. Iye, T. Wolf, H. v. Löhneysen, K. Ishida, and C. Meingast, Phys. Rev. Lett. **114**, 027001 (2015).

[22] T. Imai, K. Ahilan, F. L. Ning, T. M. McQueen, and R. J. Cava, Phys. Rev. Lett. **102**, 177005 (2009).

[23] T. Shimojima, Y. Suzuki, T. Sonobe, A. Nakamura, M. Sakano, J. Omachi, K. Yoshioka, M. Kuwata-Gonokami, K. Ono, H. Kumigashira, A. E. Bohmer, F. Hardy, T. Wolf, C. Meingast, H. V. Lohneysen, H. Ikeda, and K. Ishizaka, Phys. Rev. B **90**, 121111 (2014).

[24] K. Nakayama, Y. Miyata, G. N. Phan, T. Sato, Y. Tanabe, T. Urata, K. Tanigaki, and T. Takahashi, Phys. Rev. Lett. **113**, 237001 (2014).

[25] P. Zhang, T. Qian, P. Richard, X. P. Wang, H. Miao, B. Q. Lv, B. B. Fu, T. Wolf, C. Meingast, X. X. Wu, Z. Q. Wang, J. P. Hu, and H. Ding, Phys. Rev. B **91**, 214503 (2015).

[26] F. Wang, S. A. Kivelson, and D.-H. Lee, Nat. Phys. **11**, 959 (2015).

[27] R. Yu and Q. Si, Phys. Rev. Lett. **115**, 116401 (2015).

[28] J. K. Glasbrenner, I. I. Mazin, H. O. Jeschke, P. J. Hirschfeld, R. M. Fernandes, and R. Valenti, Nat. Phys. **11**, 953 (2015).

[29] H. Gretarsson, A. Lupascu, J. Kim, D. Casa, T. Gog, W. Wu, S. R. Julian, Z. J. Xu, J. S. Wen, G. D. Gu, R. H. Yuan, Z. G. Chen, N.-L. Wang, S. Khim, K. H. Kim, M. Ishikado, I. Jarrige, S. Shamoto, J.-H. Chu, I. R. Fisher, and Y.-J. Kim, Phys. Rev. B **84**, 100509 (2011).

[30] N. Mannella, J. Phys.: Condens. Matter **26**, 473202 (2014).

[31] P. Dai, Rev. Mod. Phys. **87**, 855 (2015).

[32] J. M. Tranquada, G. Xu, and I. A. Zaliznyak, J. Magn. Magn. Mater. **350**, 148 (2014).

[33] M. C. Rahn, R. A. Ewings, S. J. Sedlmaier, S. J. Clarke, and A. T. Boothroyd, Phys. Rev. B **91**, 180501 (2015).

[34] Q. Wang, Y. Shen, B. Pan, Y. Hao, M. Ma, F. Zhou, P. Steffens, K. Schmalzl, T. R. Forrest, M. Abdel-Hafiez, X. Chen, D. A. Chareev, A. N. Vasiliev, P. Bourges, Y. Sidis, H. Cao, and J. Zhao, Nat. Mater. **15**, 159 (2016).

[35] Z. P. Yin, K. Haule, and G. Kotliar, Nat. Mater. **10**, 932 (2011).

[36] C.-C. Lee, W.-G. Yin, and W. Ku, Phys. Rev. Lett. **103**, 267001 (2009).

[37] P. Dai, J. Hu, and E. Dagotto, Nat. Phys. **8**, 709 (2012).

[38] E. Bascones, M. J. Calderón, and B. Valenzuela, Phys. Rev. Lett. **104**, 227201 (2010).

[39] H.-H. Kuo, J.-H. Chu, S. A. Kivelson, and I. R. Fisher, arXiv:1503.00402.

[40] I. Zaliznyak, A. T. Savici, M. Lumsden, A. Tsvelik, R. Hu, and C. Petrovic, Proc. Natl. Acad. Sci. USA **112**, 10316 (2015).

[41] P. D. Johnson, H.-B. Yang, J. D. Rameau, G. D. Gu, Z.-H. Pan, T. Valla, M. Weinert, and A. V. Fedorov, Phys. Rev. Lett. **114**, 167001 (2015).

[42] C. C. Homes, Y. M. Dai, J. S. Wen, Z. J. Xu, and G. D. Gu, Phys. Rev. B **91**, 144503 (2015).

[43] T. M. McQueen, A. J. Williams, P. W. Stephens, J. Tao, Y. Zhu, V. Ksenofontov, F. Casper, C. Felser, and R. J. Cava, Phys. Rev. Lett. **103**, 057002 (2009).

[44] D. Louca, K. Horigane, A. Llobet, R. Arita, S. Ji, N. Katayama, S. Konbu, K. Nakamura, T.-Y. Koo, P. Tong, and K. Yamada, Phys. Rev. B **81**, 134524 (2010).

[45] C.-Y. Moon and H. J. Choi, Phys. Rev. Lett. **104**, 057003 (2010).

[46] I. I. Mazin, Nature (London) **464**, 183 (2010).

[47] W. Bao, Y. Qiu, Q. Huang, M. A. Green, P. Zajdel, M. R. Fitzsimmons, M. Zhernenkov, S. Chang, M. Fang, B. Qian, E. K. Vehstedt, J. Yang, H. M. Pham, L. Spinu, and Z. Q. Mao, Phys. Rev. Lett. **102**, 247001 (2009).

[48] S. Li, C. de la Cruz, Q. Huang, Y. Chen, J. W. Lynn, J. Hu, Y.-L. Huang, F.-C. Hsu, K.-W. Yeh, M.-K. Wu, and P. Dai, Phys. Rev. B **79**, 054503 (2009).

[49] J. Wen, G. Xu, Z. Xu, Z. W. Lin, Q. Li, W. Ratcliff, G. Gu, and J. M. Tranquada, Phys. Rev. B **80**, 104506 (2009).

[50] Y. Qiu, W. Bao, Y. Zhao, C. Broholm, V. Stanev, Z. Tesanovic, Y. C. Gasparovic, S. Chang, J. Hu, B. Qian, M. Fang, and Z. Mao, Phys. Rev. Lett. **103**, 067008 (2009).

[51] S. H. Lee, G. Xu, W. Ku, J. S. Wen, C. C. Lee, N. Katayama, Z. J. Xu, S. Ji, Z. W. Lin, G. D. Gu, H. B. Yang, P. D. Johnson, Z. H. Pan, T. Valla, M. Fujita, T. J. Sato, S. Chang, K. Yamada, and J. M. Tranquada, Phys. Rev. B **81**, 220502 (2010).

[52] M. D. Lumsden, A. D. Christianson, E. A. Goremychkin, S. E. Nagler, H. A. Mook, M. B. Stone, D. L. Abernathy, T. Guidi, G. J. MacDougall, C. de la Cruz, A. S. Sefat, M. A. McGuire, B. C. Sales, and D. Mandrus, Nat. Phys. **6**, 182 (2010).

[53] T. J. Liu, J. Hu, B. Qian, D. Fobes, Z. Q. Mao, W. Bao, M. Reehuis, S. A. J. Kimber, K. Prokeš, S. Matas, D. N. Argyriou, A. Hiess, A. Rotaru, H. Pham, L. Spinu, Y. Qiu, V. Thampy, A. T. Savici, J. A. Rodriguez, and C. Broholm, Nat. Mater. **9**, 718 (2010).

[54] Z. Xu, J. Wen, Y. Zhao, M. Matsuda, W. Ku, X. Liu, G. Gu, D.-H. Lee, R. J. Birgeneau, J. M. Tranquada, and G. Xu, Phys. Rev. Lett. **109**, 227002 (2012).

[55] Z. Xu, J. Wen, J. Schneeloch, A. D. Christianson, R. J. Birgeneau, G. Gu, J. M. Tranquada, and G. Xu, Phys. Rev. B **89**, 174517 (2014).

[56] N. Tsyrulin, R. Viennois, E. Giannini, M. Boehm, M. Jimenez-Ruiz, A. A. Omrani, B. D. Piazza, and H. M. Rønnow, New J. Phys. **14**, 073025 (2012).

[57] I. A. Zaliznyak, Z. Xu, J. M. Tranquada, G. Gu, A. M. Tsvelik, and M. B. Stone, Phys. Rev. Lett. **107**, 216403 (2011).

[58] Y.-T. Tam, D.-X. Yao, and W. Ku, Phys. Rev. Lett. **115**, 117001 (2015).

[59] J. Wen, G. Xu, G. Gu, J. M. Tranquada, and R. J. Birgeneau, Rep. Prog. Phys. **74**, 124503 (2011).

[60] J. Wen, G. Xu, Z. Xu, Z. W. Lin, Q. Li, Y. Chen, S. Chi, G. Gu, and J. M. Tranquada, Phys. Rev. B **81**, 100513(R) (2010).

[61] Z. Xu, J. Wen, G. Xu, Q. Jie, Z. Lin, Q. Li, S. Chi, D. K. Singh, G. Gu, and J. M. Tranquada, Phys. Rev. B **82**, 104525 (2010).

[62] Z. J. Xu, J. S. Wen, G. Y. Xu, S. X. Chi, W. Ku, G. D. Gu, and J. M. Tranquada, Phys. Rev. B **84**, 052506 (2011).

[63] G. E. Granroth, A. I. Kolesnikov, T. E. Sherline, J. P. Clancy, K. A. Ross, J. P. C. Ruff, B. D. Gaulin, and S. E. Nagler, J. Phys.: Conf. Ser. **251**, 012058 (2010).

[64] B. Winn, U. Filges, V. O. Garlea, M. Graves-Brook, M. Hagen, C. Jiang, M. Kenzelmann, L. Passell, S. M. Shapiro, X. Tong, and I. Zaliznyak, EPJ Web Conf. **83**, 03017 (2015).

[65] J. Neuefeind, M. Feygenson, J. Carruth, R. Hoffmann, and K. K. Chipley, Nucl. Instrum. Methods Phys. Res., Sect. B **287**, 68 (2012).

[66] N. Katayama, S. Ji, D. Louca, S.-H. Lee, M. Fujita, T. J. Sato, J. S. Wen, Z. J. Xu, G. D. Gu, G. Xu, Z. W. Lin, M. Enoki, S. Chang, K. Yamada, and J. M. Tranquada, J. Phys. Soc. Jpn. **79**, 113702 (2010).

[67] A. Le Bail, Powder Diffr. **20**, 316 (2005).

[68] A. C. Larson and R. B. Von Dreele, General Structure Analysis System (GSAS), Report LAUR 86-748 (Los Alamos National Laboratory, 2000).

[69] B. H. Toby, J. Appl. Cryst. **34**, 210 (2001).

[70] D. N. Argyriou, A. Hiess, A. Akbari, I. Eremin, M. M. Korshunov, J. Hu, B. Qian, Z. Mao, Y. Qiu, C. Broholm, and W. Bao, Phys. Rev. B **81**, 220503 (2010).

[71] S. Li, C. Zhang, M. Wang, H.-q. Luo, X. Lu, E. Faulhaber, A. Schneidewind, P. Link, J. Hu, T. Xiang, and P. Dai, Phys. Rev. Lett. **105**, 157002 (2010).

[72] Zhijun Xu, Jinsheng Wen, and Guangyong Xu (unpublished).

[73] W.-G. Yin, C.-C. Lee, and W. Ku, Phys. Rev. Lett. **105**, 107004 (2010).

[74] C. Fang, B. A. Bernevig, and J. Hu, Europhys. Lett. **86**, 67005 (2009).

[75] W. G. Yin, C. H. Lin, and W. Ku, Phys. Rev. B **86**, 081106 (2012).

[76] Q. Luo and E. Dagotto, Phys. Rev. B **89**, 045115 (2014).

[77] M. Tegel, C. Löhnert, and D. Johrendt, Solid State Commun. **150**, 383 (2010).

[78] H. Hu, J.-M. Zuo, J. Wen, Z. Xu, Z. Lin, Q. Li, G. Gu, W. K. Park, and L. H. Greene, New J. Phys. **13**, 053031 (2011).

[79] X. He, G. Li, J. Zhang, A. B. Karki, R. Jin, B. C. Sales, A. S. Sefat, M. A. McGuire, D. Mandrus, and E. W. Plummer, Phys. Rev. B **83**, 220502 (2011).

[80] A. Martinelli, A. Palenzona, M. Tropeano, C. Ferdeghini, M. Putti, M. R. Cimberle, T. D. Nguyen, M. Affronte, and C. Ritter, Phys. Rev. B **81**, 094115 (2010).

[81] M. H. Fang, H. M. Pham, B. Qian, T. J. Liu, E. K. Vehstedt, Y. Liu, L. Spinu, and Z. Q. Mao, Phys. Rev. B **78**, 224503 (2008).

[82] M. Yi, Z.-K. Liu, Y. Zhang, R. Yu, J. X. Zhu, J. J. Lee, R. G. Moore, F. T. Schmitt, W. Li, S. C. Riggs, J. H. Chu, B. Lv, J. Hu, M. Hashimoto, S. K. Mo, Z. Hussain, Z. Q. Mao, C. W. Chu, I. R. Fisher, Q. Si, Z. X. Shen, and D. H. Lu, Nat. Commun. **6**, 7777 (2015).

[83] Y. Shimizu, T. Yamada, T. Takami, S. Niitaka, H. Takagi, and M. Itoh, J. Phys. Soc. Jpn. **78**, 123709 (2009).

[84] Y. Sun, T. Taen, T. Yamada, Y. Tsuchiya, S. Pyon, and T. Tamegai, Supercond. Sci. Technol. **28**, 044002 (2015).

[85] D. Fobes, I. A. Zaliznyak, Z. J. Xu, R. D. Zhong, G. D. Gu, J. M. Tranquada, L. Harriger, D. Singh, V. O. Garlea, M. Lumsden, and B. Winn, Phys. Rev. Lett. **112**, 187202 (2014).

[86] K. Haule and G. Kotliar, New J. Phys. **11**, 025021 (2009).

Nonpercolative nature of the metal-insulator transition and persistence of local Jahn-Teller distortions in the rhombohedral regime of La$_{1-x}$Ca$_x$MnO$_3$

Mouath Shatnawi

Department of Physics, The Hashemite University, Zarqa 13115, Jordan

Emil S. Bozin[*]

Department of Condensed Matter Physics and Materials Science, Brookhaven National Laboratory, Upton, New York 11973, USA

J. F. Mitchell

Materials Science Division, Argonne National Laboratory, Argonne, Illinois 60439, USA

Simon J. L. Billinge

Department of Condensed Matter Physics and Materials Science, Brookhaven National Laboratory, Upton, New York 11973, USA
and Department of Applied Physics and Applied Mathematics, Columbia University, New York, New York 10027, USA

Evolution of the average and local crystal structure of Ca-doped LaMnO$_3$ has been studied across the metal to insulator (MI) and the orthorhombic to rhombohedral (OR) structural phase transitions over a broad temperature range for two Ca concentrations ($x = 0.18,0.22$). Combined Rietveld and high real space resolution atomic pair distribution function (PDF) analysis of neutron total scattering data was carried out with aims of exploring the possibility of nanoscale phase separation (PS) in relation to MI transition, and charting the evolution of local Jahn-Teller (JT) distortion of MnO$_6$ octahedra across the OR transition at $T_S \sim 720$ K. The study utilized explicit two-phase PDF structural modeling, revealing that away from $T_{\rm MI}$ there is no evidence for nanoscale phase coexistence. The local JT distortions disappear abruptly upon crossing into the metallic regime both with doping and temperature, with only a small temperature-independent signature of quenched disorder being observable at low temperature as compared to CaMnO$_3$. The results hence do not support the percolative scenario for the MI transition in La$_{1-x}$Ca$_x$MnO$_3$ based on PS, and question its ubiquity in the manganites. In contrast to LaMnO$_3$ that exhibits long-range orbital correlations and sizable octahedral distortions at low temperature, the doped samples with compositions straddling the MI boundary exhibit correlations (in the insulating regime) limited to only $\sim$1 nm with observably smaller distortions. In the $x = 0.22$ sample local JT distortions are found to persist across the OR transition and deep into the R phase (up to $\sim$1050 K), where they are crystallographically prohibited. Their magnitude and subnanometer spatial extent remain unchanged.

I. INTRODUCTION

Manganites, such as the perovskite structured calcium doped lanthanum manganite La$_{1-x}$Ca$_x$MnO$_3$ (LCMO), are considered as a model system for studying the response of materials to the presence of competing interactions [1–5], yet despite extensive study the emergent properties, such as the colossal magnetoresistance (CMR) and the metal-insulator (MI) transition, in these materials are far from well understood.

Much recent work has focused on an inhomogeneous, or what is called phase separation (PS), picture [6–13] where metallic domains are assumed to form in an insulating background and the MI transition proceeds via a percolative mechanism where the metallic cluster size increases as the MI transition is approached resulting in a conducting path extending from one side of the sample to the other. Although the PS picture has been supported by many experimental studies such as scanning tunneling spectroscopy [14], small angle neutron scattering [15], atomic pair distribution function (PDF) [16], and nuclear magnetic resonance [17], there are some experimental results that are better explained based on the homogeneous picture [18–21] and the issue needs a more careful assessment.

Through the strong electron-lattice interaction, the presence or absence of a JT distortion has been shown to be a sensitive indicator of the electronic state of the material, insulating or metallic [22]. It manifests itself in the MnO bond length ($r_{\rm Mn\text{-}O}$) distribution in the MnO$_6$ octahedron, irrespective of whether the distortions are long-range ordered or not [23,24]. When the JT distortion is present, the distribution of near neighbor $r_{\rm Mn\text{-}O}$ distances constituting the MnO$_6$ octahedron will consist of two long ($\sim$2.16 Å in LaMnO$_3$ endmember), two intermediate, and two short (<2 Å) Mn-O bonds [Fig. 1(a)]. When the JT distortion is absent there are six equal $r_{\rm Mn\text{-}O}$ distances on the octahedron [Fig. 1(b)]. Observation of the JT distortion in probes of local structure are associated with the insulating phase [22,25,26], whereas deep in the metallic regime at base temperature no appreciable signature of the JT distortions have been observed on any length scale [26].

Here we apply the PDF method to study structural changes in La$_{1-x}$Ca$_x$MnO$_3$ as a function of temperature for two carefully chosen concentrations: $x = 0.18$ and $x = 0.22$. These two concentrations straddle the doping-induced MI
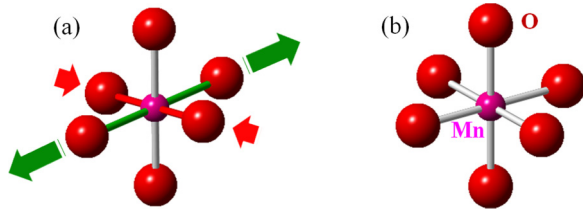
*Corresponding author: bozin@bnl.gov

FIG. 1. MnO_6 octahedra—basic building block of the $La_{1-x}Ca_xMnO_3$ structure: (a) JT distorted, with pairs of long (green), intermediate (gray), and short (red) Mn-O distances; (b) undistorted, with all Mn-O distances equal (gray).

transition, enabling us to cross the MI transition both as a function of doping and temperature. For $x = 0.18$ the system exhibits insulating behavior at all temperatures. For $x = 0.22$, at low temperatures the system is ferromagnetic metallic (FM). By heating to temperatures above $\sim$180 K it becomes a paramagnetic insulator (PI). The key result is that local JT distortions disappear abruptly at the MI transition both as a function of doping at fixed temperature, and by temperature at fixed doping. Explicit two-phase modeling reveals no evidence of phase coexistence away from T_{MI}. This is incompatible with a percolative picture of the phase transition.

Additionally, we have studied the transition to the high temperature rhombohedral phase on heating in the $x = 0.22$ material. Local JT distortions persist at high temperature, although they are crystallographically prohibited in the $R\bar{3}c$ phase, similar to the earlier observation in the $LaMnO_3$ endmember [23,27]. Transition to the rhombohedral regime appears rather continuous from the local structure perspective, with no observable change in the size and spatial extent of the local distortions.

II. EXPERIMENT AND MODELING

Finely pulverized samples of $La_{1-x}Ca_xMnO_3$ with two compositions, $x = 0.18$ and $x = 0.22$, were prepared using standard solid state synthesis methods [23], annealed to ensure oxygen stoichiometry [28], and characterized thoroughly [26]. Neutron powder diffraction measurements were carried out at the NPDF diffractometer at Los Alamos Neutron Scattering Center at Los Alamos National Laboratory. The samples, approximately 6 g each, were loaded into extruded vanadium containers and sealed under He atmosphere. The data were collected on warming for both samples at various temperatures between 10 and 550 K using a closed cycle cryo-furnace. In addition, in order to explore the atomic structure at various length scales within the high temperature rhombohedral phase, data on the $x = 0.22$ sample were also collected on warming in the ILL furnace up to a temperature of 1050 K. Transformation to rhombohedral phase for this composition occurs at $\sim$720 K [29]. Control furnace measurement at 550 K was conducted on cooling to ensure the sample integrity. Data were collected for 4 h at each temperature on each sample, providing good statistics and a favorable signal to noise ratio at high momentum transfers. Raw data were normalized and various experimental corrections performed following standard reduction protocols [30]. High resolution experimental PDFs were obtained from the sine Fourier transform of the measured total scattering

structure functions $F(Q)$ over a broad range of momentum transfers up to $Q_{max} = 35\,\mathring{A}^{-1}$. Data reduction to obtain the PDFs, $G(r)$, was carried out using the program PDFGETN [31].

The average structure was assessed through the Rietveld refinements [32] to the raw diffraction data using GSAS [33] operated under EXPGUI [34]. Structural refinements of the PDF data were carried out over $1.7 < r < 3.5\,\mathring{A}$ range using PDFFIT2 operated under PDFGUI [35]. In addition, for PDF data at selected temperatures refinements were also carried out using a variable r_{max} protocol [23]. In this, the low-r refinement bound was kept fixed at 1.7 Å, while the upper-r bound was systematically changed from 3.5 to 20 Å to provide an estimate of the correlation length of the locally ordered distortions.

The average structure refinements were carried out by the known structural models appropriate for the temperature and concentration ranges used. The O' structural model ($Pnma$) was used for temperatures up to 650 K [36] and the R structural model ($R\bar{3}c$) was used for the 750–1050 K range [37,38]. The local and intermediate structure refinements of PDF data for all temperatures were carried out with O' structural model. All refinements were carried out with isotropic atomic displacement parameters (ADP). Two-phase refinements were carried out to explore the phase separation scenario: both phases were described within the O' structure, with structural parameters fixed to values obtained deep in the metallic and insulating regimes, and only parameters allowed to vary were the phase fraction and the atomic ADPs. The later were constrained to be the same for related atomic sites across the two phases.

III. RESULTS AND DISCUSSION

A. Structural evolution across the MI transition from single phase modeling

1. Average and local structure

First, we briefly review the behavior of Mn-O bond lengths and isotropic ADPs of oxygen when modeled using a single phase model that was previously described and reported in earlier work [26].

Figure 2 summarizes the situation from the average structure perspective (Rietveld refinement). At these compositions in the 10–300 K temperature range the samples show a very small, or negligible [25,29,39–41], JT distortion with all six Mn-O bonds in the octahedra having a similar length in the range around 1.975 Å. For reference, the Mn-O bonds in the undoped endmember, where the JT distorted octahedra are long-range ordered, are 2.16, 1.96, and 1.93 Å, as shown in the figure as the dashed lines. On the other hand, an enlarged ADP of oxygen on the octahedra indicates that there is some disorder associated with the oxygen positions, consistent with the presence of disordered JT distorted octahedra (for comparison the isotropic ADP of the same oxygen site when no structural disorder is present, in the $CaMnO_3$ endmember [36], is shown as the dashed line) [42]. The value of the oxygen ADP rapidly decreases in the $x = 0.22$ sample as it enters the metallic phase at low temperature, approaching, but not reaching, the undistorted value [Fig. 2(d)]. The slightly enhanced value of this ADP at base temperature is presumably a signature of the quenched disorder component due to Ca/La
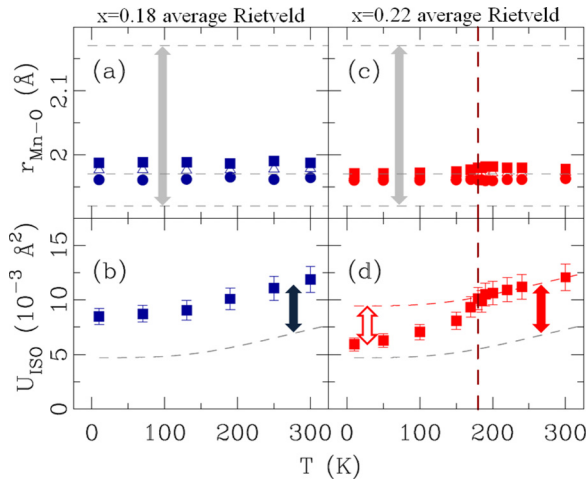
FIG. 2. Average structure behavior (Rietveld). Top row: Temperature evolution of the average Mn-O distances of MnO_6 octahedron for (a) $x = 0.18$ (blue symbols) and (c) $x = 0.22$ (red symbols). Horizontal dashed lines represent these distances in $LaMnO_3$ endmember with vertical gray double arrows indicating the distortion size. Bottom row: Temperature evolution of uncorrelated isotropic atomic displacement parameter (ADP) of 8d oxygen ($Pnma$ model) for (b) $x = 0.18$ (blue symbols) and (d) $x = 0.22$ (red symbols). Sloping dashed gray lines denote uncorrelated isotropic ADPs of the same oxygen site in $CaMnO_3$ endmember as a reference in the absence of disorder [36]. Sloping dashed red line in (d) represents the same, but with added constant offset to match the high temperature end of the ADP data. Double arrows indicate excess disorder in doped samples as compared to $CaMnO_3$. The vertical dashed red line marks T_{MI}.

substitution, which is a temperature independent quantity. Refinements of the PDF over a range $1.7 < r < 40$ Å (not shown) quantitatively agrees with the Rietveld results.

Examination of the measured PDFs in the low-r region of the data confirm that the enlarged ADPs seen in Rietveld are coming from the presence of non-long-range-ordered JT distorted octahedra. This is most effectively demonstrated by comparison between the experimental PDFs when the PDF profiles of the two concentrations are plotted on top of each other, as shown in Fig. 3. For temperatures lower than T_{MI} [Figs. 3(a)–3(c)] the PDFs for the two samples show different features. For higher temperatures [Figs. 3(d)–3(f)] the PDFs of $x = 0.18$ and $x = 0.22$ are very similar. For both samples and at all measured temperatures the PDF peak corresponding to the Mn-O bonds on the MnO_6 octahedra can be seen around 2 Å. This appears upside down, as a negative peak, due to the negative scattering length of Mn [30]. Furthermore, the compound peak at around 2.75 Å includes the O-O distances on the octahedron [36]. The first PDF peak for $x = 0.18$ and for all measured temperatures exhibits a shoulder on the high r side of the peak. Since at low temperatures the thermal broadening effect will be minor, the appearance of this shoulder indicates the existence of a longer Mn-O bond, and therefore the presence of a JT distortion. For $x = 0.22$ below 180 K (MI transition temperature) the Mn-O peak appears as a single, well defined, peak. Additionally, the compound peak describing O-O distances on the MnO_6 octahedron is
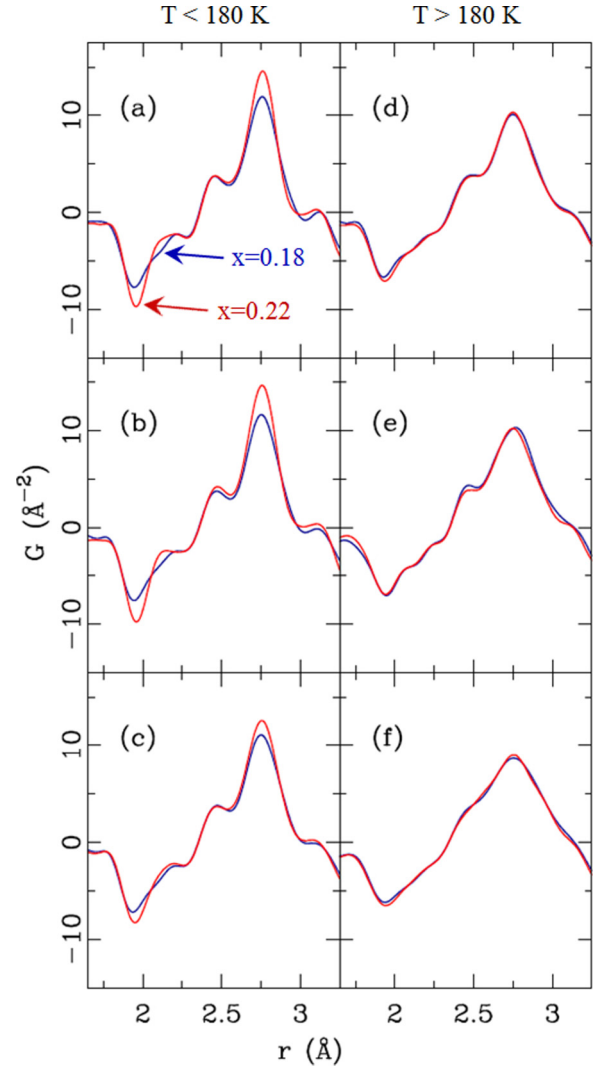
FIG. 3. Comparison of experimental PDFs over r range describing MnO_6 octahedron, for $x = 0.18$ (solid blue line) and $x = 0.22$ (solid red line) at various comparable temperatures: $T < T_{MI}$ (left column), and $T > T_{MI}$ (right column). (a) 10 K, (b) ∼50 K, (c) ∼150 K, (d) ∼250 K (e) 300 K, and (f) 550 K. Notable difference can be observed at low temperature where the $x = 0.18$ sample is insulating, whereas the $x = 0.22$ sample is metallic. At $T > T_{MI}$ visible difference vanishes.

sharp for $x = 0.22$ (undistorted MnO_6) and broad for $x = 0.18$ (distorted MnO_6). These structural features may be used to monitor changes in the JT content as the sample passes through the MI transition. As the measurement temperature of the $x = 0.22$ sample is increased above 180 K a shoulder starts to appear on the high-r side similar to the one seen in $x = 0.18$ sample coinciding with the MI transition observed in transport [26]. This was previously pointed out in the context of a temperature dependent study in $La_{1-x}Ca_xMnO_3$ [22] but we show that the effect is similarly seen when the MI transition is crossed as a function of doping at constant temperature.

Quantitative analysis from PDF refinements carried out over a narrow r range, reveal the distribution of bond lengths within the local JT distorted octahedra [Figs. 4(a) and 4(c)], with ADPs of 8d-O associated with these fits shown in
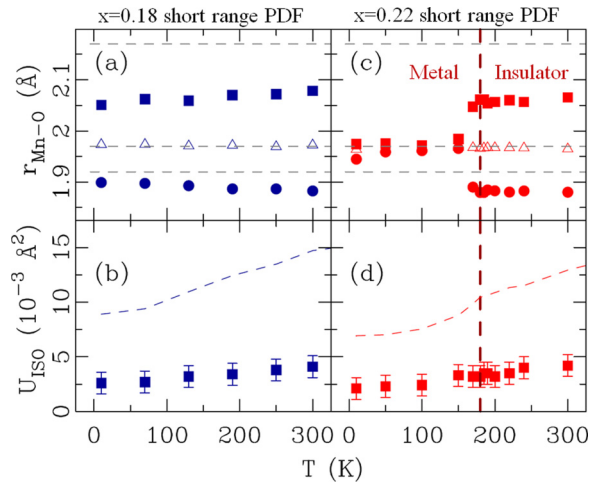
FIG. 4. Local structure behavior (PDF). Top row: Temperature evolution of the local Mn-O distances of MnO_6 octahedron for (a) $x = 0.18$ (blue symbols) and (c) $x = 0.22$ (red symbols). Horizontal dashed lines represent these distances in $LaMnO_3$ endmember. Bottom row: Temperature evolution of correlated isotropic ADPs of $8d$ oxygen ($Pnma$ model) for (b) $x = 0.18$ (blue symbols) and (d) $x = 0.22$ (red symbols). Dashed lines sketch the uncorrelated ADPs shown in Figs. 2(b) and 2(d) for reference. The vertical dashed red line marks T_{MI}.

Figs. 4(b) and 4(d). The latter show no anomalies at the MI transition temperature since all the information about the local distortions has been captured by the structure parameters rather than the ADPs [26].

These observations reinforce the well known result that the MI transition is accompanied by the formation of local JT distortions in the insulating phase, and, conversely, undistorted octahedra in the metallic regime. It also demonstrates that the local bond-length distribution in the insulating regime decreases in amplitude with increasing Ca content, as opposed to the assumption of the small polaron picture in which the local octahedral distortion is as large as in the $LaMnO_3$ endmember [16,43,44] associated with the charge localized Mn^{3+} sites, while Mn^{4+} sites are undistorted as in $CaMnO_3$.

2. Correlation length of local JT distortions

The PDF yields the structure on different length scales, revealing the locally JT distorted octahedra at low r and the average, undistorted, structure at high r. By studying how the PDF signal crosses over from the distorted to undistorted as a function of r we may extract a correlation length for any local ordering of the JT distorted octahedra. A variable range PDF refinement of the 300 K data was performed from $r_{min} = 1.7$ Å to r_{max}, where r_{max} was increased from 3.5 to 20 Å in steps of 0.5 Å. The r_{Mn-O} bond lengths extracted from these refinements are shown in Fig. 5. It can be seen that the amplitude of the measured octahedral distortion falls off gradually with increased fitting range until the r_{Mn-O} distances reach the values from the crystallographic analysis. The correlation length of the local JT distortions is $\sim$10.5 Å at $x = 0.18$, decreasing to $\sim$8 Å at $x = 0.22$. This is very similar to the observation above the JT transition in $LaMnO_3$ [23], albeit the length scale in the

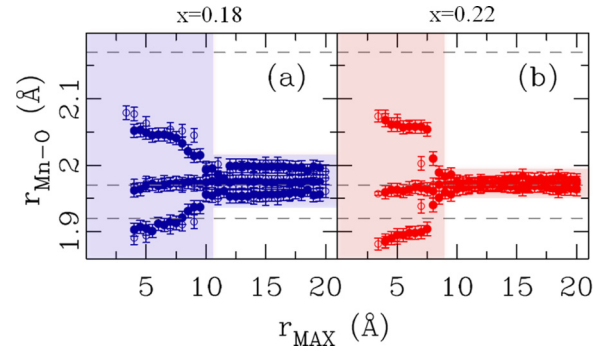
FIG. 5. Mn-O bond lengths from the refined structure model to PDF data as a function of upper refinement limit r_{max} for (a) $x = 0.18$ and (b) $x = 0.22$ compositions. Assessment for $x = 0.18$ was done at 10 K (solid symbols) and 300 K (open symbols), whereas for $x = 0.22$ at 300 K for PDF data obtained at Q_{max} values of 25 Å^{-1} (open symbols) and 35 Å^{-1} (solid symbols). Dashed lines indicate Mn-O bond lengths in $LaMnO_3$ at 300 K, where octahedral distortions are long-range ordered. See text for details.

present case appears to be smaller, suggesting the decrease of the local distortion correlation length with Ca doping.

We have tested whether the length scale of ordered local distortions changes with temperature for the $x = 0.18$ sample. Figure 5(a) shows results of the assessment at 10 and 300 K and we could not detect a temperature evolution of the characteristic length scale within the accuracy of the approach. We also tested whether the observations are dependent on the r resolution of the PDF for $x = 0.22$ by doing the analysis from PDFs obtained using Q_{max} values of 25 and 35 Å^{-1} [open and solid symbols, respectively, in Fig. 5(b)]. We find that slightly sharper and larger length scale (by $\sim$1 Å) is obtained with higher resolution data, giving us an estimate of the uncertainty on this value. While the absolute accuracy of the applied protocol could be somewhat challenging [45], it still provides very important insights about the average correlation length of the underlying ordered local distortions.

B. Phase separation

We now turn to the question of phase separation and what our data have to say on this topic. While phase separation with large length-scale domains is clearly dominating in systems with smaller A-site ions such as $La_{1-x}Pr_xMnO_3$ [46], for the systems that show robust CMR behavior such as Ca and Sr doped $LaMnO_3$, though the phase separation scenario has been invoked, our results suggest that phase coexistence is minimal in the vicinity of the MI transition at $x \sim 0.2$, at least for the Ca doped state. The rapid crossover from distorted to completely undistorted as the MI transition is crossed, both as a function of T at $x = 0.22$ and as a function of doping x at fixed temperature, would seem to rule out a percolation mechanism for that transition.

Observations of phase separation in these systems from other measurements may be a result of extrinsic effects such as doping or strain, or difficulties in data interpretation [6,14,16,44,47–50].

The situation may be different at higher doping, such as $La_{0.5}Ca_{0.5}MnO_3$ [51], and our results only explicitly address the low-doped region of the phase diagram.

Given the strong electron-phonon coupling and relatively large size of underlying structural distortions in the PI phase, it is sensible to utilize structural signatures of the charge localized and delocalized states to explore the existence and to quantify PS in $La_{1-x}Ca_xMnO_3$. In fact, there was one such attempt in the past from earlier $La_{1-x}Ca_xMnO_3$ PDF experiments [52]. In that study, a two-phase model based on the local structures of the FM and PI phases was used to refine the experimental PDFs quantitatively. The model involved $CaMnO_3$-like undistorted structural phase and $LaMnO_3$-like distorted structural phase with a distortion size associated with the PI component of the order of 0.23 Å (defined as difference between the long and short Mn-O bond) such as seen in the undoped La endmember. Based on the results, a claim was made of the observation of the coexistence of both phases over a wide temperature range. The fits resulted in approximately 10% of the localized JT phase (PI) being present even at the lowest temperature measured (20 K), whereas at room temperature nearly half of the sample remained in the delocalized (FM) phase. However, we note that in this approach to fitting data the quantification of the phase fraction is highly sensitive to the size of the distortion in the distorted PI phase. At the time of that work, the small polaron model was widely accepted for the insulating phase. In this model, the magnitude of the distortion associated with the charge localized Mn^{3+} sites is expected to be as large as that in the $LaMnO_3$ endmember [16,43,44]. However a later, higher resolution, neutron PDF study [26] of the insulating regime of $La_{1-x}Ca_xMnO_3$ revealed that the *local* JT-distortion amplitude in fact decreases dramatically with the increased Ca content, contrary to the small polaron model assumption. This observation calls for the early PDF report of temperature evolution of the phase fraction to be revisited and the phase fraction assignment to be re-examined by a model that uses a more realistic assignment of the underlying local structure of the metallic and insulating phases.

Here we carried out two-phase refinements in a fashion similar to the one described earlier [52] but with the JT distortions set to those observed in the local structure at 10 K for the $x = 0.18$ composition. The structure of the undistorted FM phase was set to that obtained by Rietveld at 10 K for $x = 0.22$ composition. This choice is not optimal as both the average and local structure change with changing the Ca content. However, the changes occurring between $x = 0.18$ and $x = 0.22$ are much smaller than those between $x = 0$ and the doped compositions used [26]. We believe that this assumption is therefore more realistic than the one used in the earlier work [52]. In the two-phase refinements all structural parameters were kept fixed. The only quantities that were allowed to vary were the phase fraction and isotropic correlated ADPs that were constrained to be the same for the two component phases. Typical fits at 10 K are shown in Figs. 6(b) and 6(c). Evolution of the observed undistorted fraction with temperature for the two compositions is presented in Fig. 6(a). No significant contribution of the undistorted phase could be detected in the $x = 0.18$ sample, whose undistorted fraction (and conversely distorted
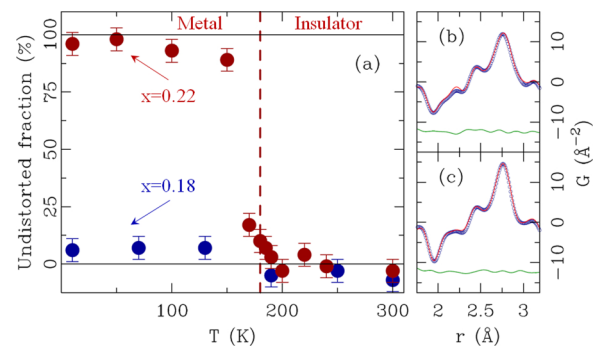
FIG. 6. (a) T evolution of undistorted fraction from two-phase short-range PDF modeling for $x = 0.18$ (solid blue symbols, no MIT), and for $x = 0.22$ (solid red symbols, MIT at $\sim$180 K indicated by a vertical dashed red line). Horizontal solid black lines are guides to the eye. Typical short-range refinements of the two-phase model are shown in (b) for $x = 0.18$ and in (c) for $x = 0.22$ data at 10 K. In both panels open blue symbols represent the data, solid red line is the model, and solid green line is the difference (offset for clarity).

fraction) display almost flat temperature dependence within the accuracy of the assessment. While our analysis cannot unambiguously rule out the existence of phase separation in this composition, it quite strongly suggests that there is virtually no temperature evolution of the local or long-range structure across the temperature range studied, and places an upper limit for undistorted fraction in the $x = 0.18$ sample to below 10%. Similarly, the $x = 0.22$ sample displays almost fully undistorted component in the metallic regime, and fully distorted component in the insulating regime, both displaying no temperature dependence, except in the immediate vicinity of the MI transition. Corresponding correlated ADPs obtained from two-phase fits are shown in Fig. 7(a) (solid symbols) and compared to the uncorrelated values obtained from single phase fits (open symbols). In addition to results for the
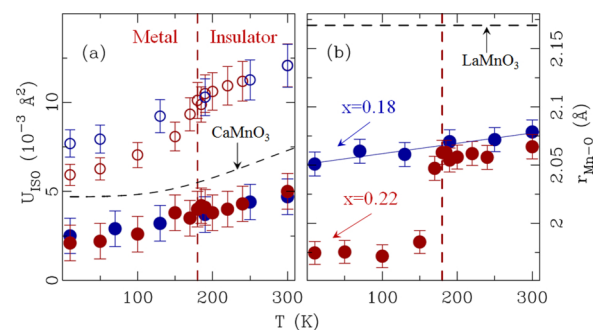
FIG. 7. (a) Comparison of T evolution of uncorrelated ADPs (Rietveld) for $x = 0.18$ (open blue symbols), $x = 0.22$ (open red symbols), and $x = 1.0$ (dashed black line, reference) compositions. Correlated ADPs obtained from two-phase refinements (PDF) are shown by solid symbols for $x = 0.18$ (blue) and $x = 0.22$ (red). (b) Evolution of long Mn-O bond with temperature from short-range PDF modeling. Solid blue symbols represent data for $x = 0.18$ (no MIT), solid red symbols represent data for $x = 0.22$ (MIT at $\sim$180 K, indicated by vertical dashed red line). Horizontal dashed black line marks long Mn-O bond for $x = 0$ (reference) composition. Solid blue line through $x = 0.18$ points is guide to the eye.
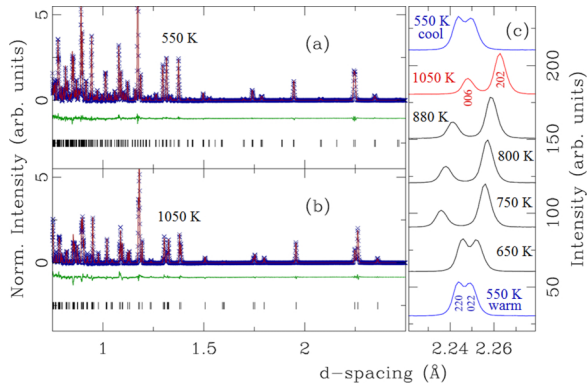
FIG. 8. Rietveld refinements of the average structure models to La$_{1-x}$Ca$_x$MnO$_3$ $x = 0.22$ data at (a) 550 K (*Pnma*) and (b) 1050 K ($R\bar{3}c$). Blue symbols represent the data, solid red lines are the model, and solid green lines are the differences (offset for clarity). Vertical ticks mark reflections. (c) Experimental diffraction patterns over a narrow range of d spacing sensitive to O-R average structural transition for temperature as indicated. Profiles have been offset for clarity. The bottom and top profiles correspond to the same 550 K temperature collected on warming and cooling, respectively. Oxygen content refined for these two data sets does not change within the experimental uncertainty, verifying that the sample integrity has been preserved through the heating cycle.

undistorted fraction from two-phase refinements that suggest an abrupt change with no appreciable doping and temperature dependence across the MI transition, changes in uncorrelated ADPs observed in Rietveld refinement, as well as the observed changes in the local long Mn-O bond [Fig. 7(b)], are also abrupt and localized to the immediate vicinity of the transition. The existence of some small amount of residual distorted phase deep in the metallic region, and conversely the existence of some small amount of residual undistorted phase in the insulating region, cannot be ruled out. What is observed here is a dramatic and rapid loss of the distorted Mn octahedra at the MI transition, and relative flatness of the phase fractions away from the transition. This is inconsistent with a picture of the MI transition being percolative in nature, a scenario where the physical properties change rapidly at the transition, but the phase composition evolves slowly through it.

C. High-*T* behavior: Rhombohedral phase

Finally, we explore the local structure in the high-temperature rhombohedral phase for the $x = 0.22$ sample. Figure 8 shows raw diffraction data and Rietveld refinement fits in this high-temperature region. Understanding nanoscale character of orbital correlations has always been a fundamental challenge in CMR systems in general, and in manganites in particular [53]. In La$_{1-x}$Ca$_x$MnO$_3$ a systematic study combining high energy x-ray scattering with elastic and inelastic neutron scattering has been employed recently to explore the character of the polaron order and dynamics [54]. It was found that, once established, the nanoscale polaron correlations are only weakly temperature dependent. These short-range correlations were found to have a static component seen in the elastic scattering channel, indicative of the presence of a glasslike state of the polarons, as well as

coexisting dynamic correlations with comparable correlation length, as observed by inelastic neutron scattering. It was further established that the elastic component disappears at some characteristic higher temperature T^*, above which the correlations are purely dynamic [54].

The character of nanoscale orbital correlations has been studied at temperatures comparable to the JT transition in LaMnO$_3$ endmember, and at temperatures below the characteristic temperature scale T^*, within what is known as the pseudocubic phase (still *Pnma* space group) [26,54]. Explorations of orbital correlations in the rhombohedral structural phase at temperatures much higher than both T_{JT} in LaMnO$_3$ and T^* in La$_{1-x}$Ca$_x$MnO$_3$ have been scarce. An atomic PDF study explored this temperature regime in the undoped LaMnO$_3$ endmember [23], and found that the local JT distortions persist deep into the rhombohedral phase. Since the PDF method relies indiscriminately on both elastic and inelastic scattering channels, it does not reveal whether the underlying nanoscale orbital correlations are static or dynamic, although it is reasonable to assume that at such high temperature they are probably purely dynamic. Studies of the rhombohedral regime for doped La$_{1-x}$Ca$_x$MnO$_3$ samples have been lacking to date. Recent high-resolution synchrotron x-ray powder diffraction measurement explored the existence and character of the rhombohedral phase for $x = 0.3$ composition [38]. A change of polaronic behavior at the pseudocubic (*Pnma*) to rhombohedral ($R\bar{3}c$) structural phase transition (at T_S) from nonadiabatic in the *Pnma* phase to adiabatic in the $R\bar{3}c$ phase was suggested from resistivity measurements. These results in conjunction with neutron and x-ray studies showing polaron correlations in the orthorhombic phase were interpreted as a scenario in which the structural transition triggers a crossover between distinct electronic states that may be classified as polaron liquid and polaron gas states, though the density of polarons does not change at this transition, so what this picture really means remains unclear.

In order to shed more light on this part of the phase diagram, we explored the evolution of the average and local atomic structure for $x = 0.22$ across the high temperature transition and deep in the $R\bar{3}c$ phase. At this composition T_S is ~720 K. We establish the average structural behavior through Rietveld refinements [Figs. 8(a) and 8(b)], and demonstrate that for the high temperature range studied the sample indeed exhibits the transition where expected. The structural phase transition is clear in the raw diffraction data shown in Fig. 8(c), and the respective Rietveld fits do confirm this [Figs. 8(a) and 8(b)], with data at and above 750 K being in the rhombohedral $R\bar{3}c$ space group. In this space group only a single Mn-O bond distance is allowed, and the temperature dependence of the refined value is shown in Fig. 9(a). It extends continuously from the value in the *Pnma* model at lower temperature. In that model three distinct distances are allowed; however they refine to almost the same, single value at higher temperatures indicating that on average the MnO$_6$ octahedra are already approximately regular even before entering the rhombohedral phase. However, close examination of the ADPs [Fig. 9(b)] show that in addition to an anomalous jump in 8*d*-O ADP temperature dependence at T_{MI}, indicative of the onset of local JT distortions in the insulating phase, there is also a hint of an additional jump, albeit smaller in size, at around T_S,
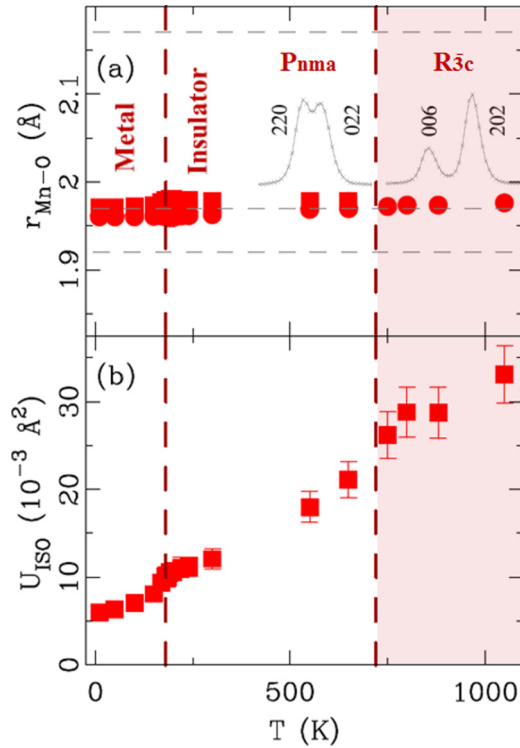
FIG. 9. (a) Temperature evolution of the average Mn-O distances of MnO_6 octahedron for the $x = 0.22$ sample, as obtained from Rietveld refinements across the entire T-range studied. Vertical dashed red lines at ∼180 and ∼720 K mark M-I and O-R transitions, respectively. Vertical dashed lines mark 300 K values for $x = 0$ reference. (b) T evolution of $8d$ oxygen ($Pnma$ model) ADP as obtained from Rietveld refinements. Inset to (a) sketches reflections in the diffraction data characteristic for O and R phases, as shown in Fig. 8(c).

similar to what was observed in $LaMnO_3$ [23]. As discussed earlier, the system below T_S already contains disordered local JT distortions, so this is quite suggestive that the local JT distortions are surviving all the way into the rhombohedral phase, and indeed all the way to our highest temperature data point at 1050 K. This is confirmed in the low-r region of the measured PDFs. Thermal motion of the atoms broaden the PDF peaks making it difficult to resolve clearly the peaks and shoulders directly, but low-r refinements of the PDF clearly prefer distorted MnO_6 octahedra extending to the highest temperatures, as shown in Fig. 10.

PDF analysis shows that JT distortions in $x = 0.22$ persist in the $R\bar{3}c$ phase pretty much in the same fashion as they do in $LaMnO_3$ endmember [23], irrespective of the fact that the JT distortion is crystallographically prohibited. Since the local distortions survive to the highest temperature measured, it is sensible to ask what does in fact change at T_S from the perspective of the local structural footprint of the electronic/orbital state. As was suggested earlier [54], at a characteristic temperature T^* which extends to T_{JT} for $x = 0$ composition ($LaMnO_3$) there is a change from presumably polaron glass (static polarons) below T^* to a polaron liquid (dynamic polarons) above T^*. Since clear JT-distortion signatures persist still above T_S, we suggest that
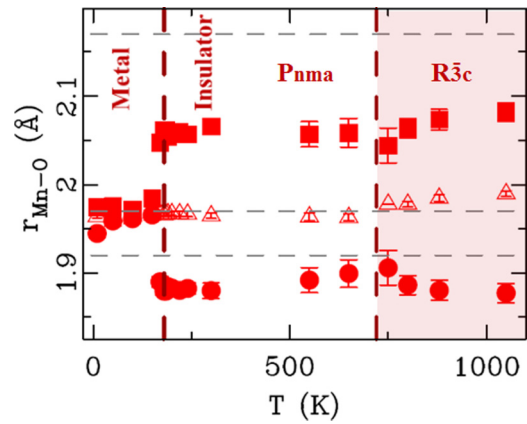
FIG. 10. Temperature evolution of the local Mn-O distances of MnO_6 octahedron for the $x = 0.22$ sample, as obtained from short-range PDF refinements. Local distortions that are onset upon entering the insulating state persist also in the rhombohedral phase, and are seen up to 1050 K—the highest temperature studied. Vertical dashed red lines mark T_{MI} and T_S.

at this point there could be a change in the correlations of the dynamic polarons. At such high temperatures, however, the r-dependent PDF fitting protocol is not so stable due to the thermal broadening of the PDF signal and resulting loss in information in the signal. Instead, we explored an alternative approach (Fig. 11). First, we compare experimental PDFs for $x = 0.22$ at the closest available temperatures bracing the T_S:
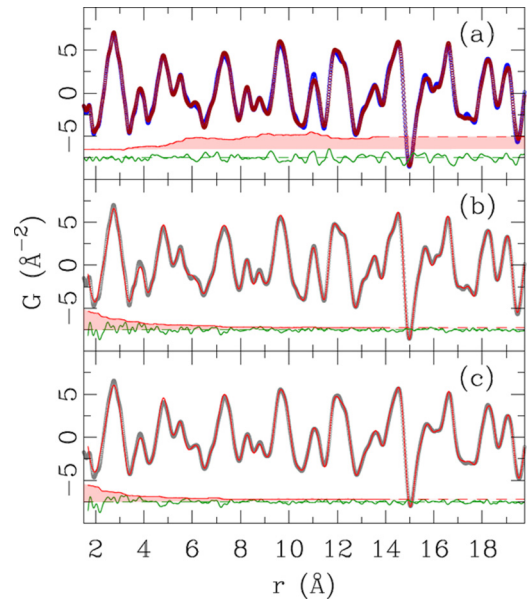
FIG. 11. (a) Comparison of experimental PDF data for $x = 0.22$ at 650 K ($Pnma$ phase, open blue symbols) and 750 K ($R\bar{3}c$ phase, open red symbols). (b) and (c) Comparison of the data (open gray symbols) and the $Pnma$ model based on intermediate range structure parameters (solid red line) for 650 and 850 K, respectively. In all panels the difference curve (solid green line) is offset for clarity. Light-red solid lines above the differences represent a 4 Å running average of the absolute value of the difference curve, multiplied by 10 and offset for clarity. Shaded areas emphasize the regions of disagreement of the compared PDFs.

650 K data correspond to *Pnma* phase, whereas 750 K data correspond to $R\bar{3}c$ phase, as can be verified from inspecting the respective diffraction patterns shown in Fig. 8(c). This comparison is shown in Fig. 11(a). The difference in the PDFs above and below the transition is captured in the difference curve that is plotted in green below the PDFs. This indicates that the local structure does not change over the length scale of ∼5–6 Å. Further insights can be gained from assessing how well the model that describes the intermediate range PDF data explains the data at low *r* [45]. To achieve this, a simple two-step procedure was used: in the first step, the PDF data were fit over $10 < r < 20$ Å range; in the second step the structure parameters obtained from the first step were adopted and kept fixed in a refinement of the PDF over $1.7 < r < 20$ Å range, with model parameters that describe correlated motion of nearest neighbors [30] being the only variables. The procedure was applied to 650 K data (below T_S) and 850 K data (above T_S). The resulting fits are shown in Figs. 11(b) and 11(c). The difference curves between the data and the model display behavior inverse of that seen in Fig. 11(a): agreement is good in the high-*r* region, but poorer at low *r*, with observable disagreement below ∼6 Å. This not only confirms the existence of local JT distortions in the high temperature regime, but also suggests that the range of correlations of the local JT distortions does not change appreciably on crossing T_S. These observations are in line with previous observations of correlated domain size smoothly changing across T_S in LaMnO$_3$ endmember [23], and also consistent with the change of octahedral rotational degrees of freedom. The PDF approach cannot address the origin or mechanism of the stability of the local distortions. However, it does show very clearly that these distortions do survive up to the highest temperatures, presumably because of Jahn-Teller stabilization energy being very high compared to thermal effects even at these temperatures.

The results of this study suggest that there does not appear to be a broad range of phase coexistence in this material through the MI transition as has been widely thought previously. In contrast, local JT distortions are rapidly suppressed in the metallic phase ($x = 0.22$ at low temperature) on entering both as a function of temperature at fixed doping, or as a function of doping at fixed temperature. These results suggest that the percolative picture for the phase transition is unlikely in our samples. The results are reconciled with earlier PDF studies that suggested otherwise. These studies [16,52] assumed a small-polaron model where the low-*r* region of the PDF could be rationalized as a mixture of fully JT distorted octahedra and undistorted octahedra. More recent data show that the amplitude of the local JT distortion actually decreases with doping [26] and a simple small polaron scenario is not correct. By taking this into account in the current analysis we obtain a rather different view of the evolution of the metallic and insulating phase fractions with temperature and doping in La$_{1-x}$Ca$_x$MnO$_3$. The behavior is different from cubic manganite systems with smaller *A*-site ions such as Pr$_{1-x}$Ca$_x$MnO$_3$ [55,56] where phase coexistence has been clearly established on a longer length scale. On the other hand, the behavior of La$_{1-x}$Ca$_x$MnO$_3$ and La$_{1-x}$Sr$_x$MnO$_3$ systems are likely to be similar to each other, despite the suggestion of a percolative transition in that system from early PDF data

[44]. The persistent feature that was attributed to the Mn-O long bond in that study may have been the feature that we attribute to a termination effect in the current work since it is longer in the doped compounds than the Mn-O long bond in undoped LaMnO$_3$ and not shorter as we now know to be the case.

If the mechanism is not percolative it is interesting to speculate on other mechanisms for the MI transition and CMR effect. A recent in-depth single crystal exploration of the insulating state in the underdoped regime of La$_{1-x}$Sr$_x$MnO$_3$ suggested dominant role of superexchange interactions in the ferromagnetic coupling [57]. In this picture orbital mixing alters the interatomic exchange interactions from type-*A* antiferromagnetic to ferromagnetic order, and can possibly also account for the decrease in the Jahn-Teller oxygen displacements with increasing *x*, providing a rationale for earlier PDF observations [26]. Such a band model of the σ-bonding 3*d* electrons with magnetic-polaron formation would also be consistent with the current results.

To understand these systems properly, it would be helpful to revisit the La$_{1-x}$Sr$_x$MnO$_3$ system using modern experimental and analysis protocols. The behavior of La$_{1-x}$Ca$_x$MnO$_3$ at higher dopings could also be understood better, where competition between the metallic and ordered-polaronic charge-ordered phases changes the energy balances and therefore phase coexistence behavior [50,51,58,59].

IV. CONCLUSION

In summary, we have revisited the metal-insulator transition in doped La$_{1-x}$Ca$_x$MnO$_3$ ($x = 0.18, 0.22$) with a careful neutron PDF study of the local structure. Distorted MnO$_6$ octahedra are clearly visible in the local structure wherever the samples are in the polaronic insulating phase. The local JT distortions disappear in the metallic phase. This is in contrast to the observations of the average crystal structure probed either by Rietveld refinement, or refinements of the PDFs carried out over intermediate ranges of *r* up to 40 Å. Both the correlation length of any ordered JT distortion, and also the phase fraction of metallic and insulating material, have been studied as a function of temperature and doping across the MI transition. We also establish that the local JT distortions persist into the high-temperature rhombohedral phase of the material. The results of the search for phase coexistence show that the undistorted fraction changes abruptly across the MI transition, and the phase fraction stays rather uniform at both sides of the phase line. These observations do not support the percolative scenario for the MI transition in La$_{1-x}$Ca$_x$MnO$_3$ and bring the ubiquity of phase separation in the broad class of manganites to question. On the other hand, local distortions of MnO$_6$ octahedra are found to persist across the pseudocubic to rhombohedral phase transition and deep into the rhombohedral phase where they are crystallographically prohibited.

ACKNOWLEDGMENTS

---

[1] A. J. Millis, Nature (London) **392**, 147 (1998).

[2] S. Yunoki, A. Moreo, and E. Dagotto, Phys. Rev. Lett. **81**, 5612 (1998).

[3] J.-S. Zhou and J. B. Goodenough, Phys. Rev. B **68**, 144406 (2003).

[4] E. Dagotto, Science **309**, 257 (2005).

[5] N. Bebenin, Phys. Met. Metallogr. **111**, 236 (2011).

[6] M. Uehara, S. Mori, C. H. Chen, and S.-W. Cheong, Nature (London) **399**, 560 (1999).

[7] E. Dagotto, J. Burgy, and A. Moreo, Solid State Commun. **126**, 9 (2003).

[8] J. Burgy, A. Moreo, and E. Dagotto, Phys. Rev. Lett. **92**, 097202 (2004).

[9] E. Dagotto, S. Yunoki, C. Sen, G. Alvarez, and A. Moreo, J. Phys.: Condens. Matter **20**, 434224 (2008).

[10] V. R. Singh, L. Zhang, A. K. Rajapitamahuni, N. Devries, and X. Hong, Phys. Status Solidi **9**, 109 (2012).

[11] D. G. Kuberkar, R. R. Doshi, P. S. Solanki, U. Khachar, M. Vagadia, A. Ravalia, and V. Ganesan, Appl. Surf. Sci. **258**, 9041 (2012).

[12] Z. H. Wu and H. Q. Xie, Physica B **407**, 2538 (2012).

[13] P. Phong, D. Manh, L. Bau, and I.-J. Lee, J. Electroceram. **31**, 364 (2013).

[14] M. Fath, S. Freisem, A. A. Menovsky, Y. Tomioka, J. Aarts, and J. A. Mydosh, Science **285**, 1540 (1999).

[15] J. M. de Teresa, M. R. Ibarra, P. A. Algarabel, C. Ritter, C. Marquina, J. Blasco, J. Garcia, A. del Moral, and Z. Arnold, Nature (London) **386**, 256 (1997).

[16] S. J. L. Billinge, T. Proffen, V. Petkov, J. L. Sarrao, and S. Kycia, Phys. Rev. B **62**, 1203 (2000).

[17] G. Allodi, R. De Renzi, G. Guidi, F. Licci, and M. W. Pieper, Phys. Rev. B **56**, 6036 (1997).

[18] P. A. Kumar, R. Mathieu, P. Nordblad, S. Ray, O. Karis, G. Andersson, and D. D. Sarma, Phys. Rev. X **4**, 011037 (2014).

[19] J. Mitra, M. Paranjape, A. K. Raychaudhuri, N. D. Mathur, and M. G. Blamire, Phys. Rev. B **71**, 094426 (2005).

[20] T. A. Tyson, J. Mustre de Leon, S. D. Conradson, A. R. Bishop, J. J. Neumeier, H. Röder, and J. Zang, Phys. Rev. B **53**, 13985 (1996).

[21] M. F. Hundley, M. Hawley, R. H. Heffner, Q. X. Jia, J. J. Neumeier, J. Tesmer, J. D. Thompson, and X. D. Wu, Appl. Phys. Lett. **67**, 860 (1995).

[22] S. J. L. Billinge, R. G. DiFrancesco, G. H. Kwei, J. J. Neumeier, and J. D. Thompson, Phys. Rev. Lett. **77**, 715 (1996).

[23] X. Qiu, T. Proffen, J. F. Mitchell, and S. J. L. Billinge, Phys. Rev. Lett. **94**, 177203 (2005).

[24] A. Sartbaeva, S. A. Wells, M. F. Thorpe, E. S. Božin, and S. J. L. Billinge, Phys. Rev. Lett. **99**, 155503 (2007).

[25] V. Kiryukhin, New J. Phys. **6**, 155 (2004).

[26] E. S. Božin, M. Schmidt, A. J. DeConinck, G. Paglia, J. F. Mitchell, T. Chatterji, P. G. Radaelli, T. Proffen, and S. J. L. Billinge, Phys. Rev. Lett. **98**, 137203 (2007).

[27] T. Chatterji, F. Fauth, B. Ouladdiaf, P. Mandal, and B. Ghosh, Phys. Rev. B **68**, 052406 (2003).

[28] B. Dabrowski, R. Dybzinski, Z. Bukowski, O. Chmaissem, and J. D. Jorgensen, J. Solid State Chem. **146**, 448 (1989).

[29] M. B. Salamon and M. Jaime, Rev. Mod. Phys. **73**, 583 (2001).

[30] T. Egami and S. J. L. Billinge, *Underneath the Bragg peaks: Structural Analysis of Complex Materials*, 2nd ed. (Elsevier, Amsterdam, 2012).

[31] P. F. Peterson, M. Gutmann, T. Proffen, and S. J. L. Billinge, J. Appl. Crystallogr. **33**, 1192 (2000).

[32] H. M. Rietveld, Acta Crystallogr. **22**, 151 (1967).

[33] A. C. Larson and R. B. Von Dreele, Report No. LAUR-86-748 (1987), Los Alamos National Laboratory, Los Alamos, NM 87545.

[34] B. H. Toby, J. Appl. Crystallogr. **34**, 210 (2001).

[35] C. L. Farrow, P. Juhás, J. Liu, D. Bryndin, E. S. Božin, J. Bloch, T. Proffen, and S. J. L. Billinge, J. Phys.: Condens. Matter **19**, 335219 (2007).

[36] E. S. Božin, A. Sartbaeva, H. Zheng, S. A. Wells, J. F. Mitchell, T. Proffen, M. F. Thorpe, and S. J. L. Billinge, J. Phys. Chem. Solids **69**, 2146 (2008).

[37] Q. Huang, A. Santoro, J. W. Lynn, R. W. Erwin, J. A. Borchers, J. L. Peng, and R. L. Greene, Phys. Rev. B **55**, 14987 (1997).

[38] J. A. Souza, H. Terashita, E. Granado, R. F. Jardim, N. F. Oliveira Jr., and R. Muccillo, Phys. Rev. B **78**, 054411 (2008).

[39] T. Chatterji, B. Ouladdiaf, P. Mandal, B. Bandyopadhyay, and B. Ghosh, Phys. Rev. B **66**, 054403 (2002).

[40] V. Kiryukhin, T. Y. Koo, H. Ishibashi, J. P. Hill, and S. W. Cheong, Phys. Rev. B **67**, 064421 (2003).

[41] V. Kiryukhin, A. Borissov, J. S. Ahn, Q. Huang, J. W. Lynn, and S. W. Cheong, Phys. Rev. B **70**, 214424 (2004).

[42] P. G. Radaelli, M. Marezio, H. Y. Hwang, S. W. Cheong, and B. Batlogg, Phys. Rev. B **54**, 8992 (1996).

[43] C. H. Booth, F. Bridges, G. H. Kwei, J. M. Lawrence, A. L. Cornelius, and J. J. Neumeier, Phys. Rev. Lett. **80**, 853 (1998).

[44] D. Louca, T. Egami, E. L. Brosha, H. Röder, and A. R. Bishop, Phys. Rev. B **56**, R8475(R) (1997).

[45] E. S. Božin, K. R. Knox, P. Juhás, Y. S. Hor, J. F. Mitchell, and S. J. L. Billinge, Sci. Rep. **4**, 4081 (2014).

[46] C. Martin, A. Maignan, M. Hervieu, and B. Raveau, Phys. Rev. B **60**, 12191 (1999).

[47] T. Becker, C. Streng, Y. Luo, V. Moshnyaga, B. Damaschke, N. Shannon, and K. Samwer, Phys. Rev. Lett. **89**, 237203 (2002).

[48] B. M. Ramesh, X. Han, W. Ning, Z.-h. Cheng, Y. Sun, and R. Jayavel, Mater. Lett. **63**, 1528 (2009).

[49] T. Z. Ward, Z. Gai, H. W. Guo, L. F. Yin, and J. Shen, Phys. Rev. B **83**, 125125 (2011).

[50] J. Tao, D. Niebieskikwiat, Q. Jie, M. A. Schofield, L. J. Wu, Q. Li, and Y. M. Zhu, Proc. Natl. Acad. Sci. USA **108**, 20941 (2011).

[51] J. C. Loudon, N. D. Mathur, and P. A. Midgley, Nature (London) **420**, 797 (2002).

[52] T. Proffen and S. J. L. Billinge, Appl. Phys. A **74**, 1770 (2002).

[53] N. Mathur, Nature (London) **390**, 229 (1997).

[54] J. W. Lynn, D. N. Argyriou, Y. Ren, Y. Chen, Y. M. Mukovskii, and D. A. Shulyatev, Phys. Rev. B **76**, 014437 (2007).

[55] Z. Jirák, S. Krupička, Z. Šimša, M. Dlouhá, and S. Vratislav, J. Magn. Magn. Mater. **53**, 153 (1985).

[56] T. Elovaara, H. Huhtinen, S. Majumdar, and P. Patur, J. Phys.: Condens. Matter **26**, 266005 (2014).

[57] J.-S. Zhou and J. B. Goodenough, Phys. Rev. B **91**, 064414 (2015).

[58] T. Wu, S. B. Ogale, J. E. Garrison, B. Nagaraj, A. Biswas, Z. Chen, R. L. Greene, R. Ramesh, T. Venkatesan, and A. J. Millis, Phys. Rev. Lett. **86**, 5998 (2001).

[59] J. Tao, D. Niebieskikwiat, M. B. Salamon, and J. M. Zuo, Phys. Rev. Lett. **94**, 147206 (2005).

Interlayer electronic transport in CaMnBi₂ antiferromagnet

Aifeng Wang (王爱峰),[1] D. Graf,[2] Lijun Wu,[1] Kefeng Wang (王克锋),[1,*] E. Bozin,[1] Yimei Zhu,[1] and C. Petrovic[1]

[1]*Condensed Matter Physics and Materials Science Department, Brookhaven National Laboratory, Upton, New York 11973, USA*

[2]*National High Magnetic Field Laboratory, Florida State University, Tallahassee, Florida 32306-4005, USA*

We report interlayer electronic transport in CaMnBi₂ single crystals. Quantum oscillations and angular magnetoresistance suggest coherent electronic conduction and valley polarized conduction of Dirac states. The small cyclotron mass, high mobility of carriers, and nontrivial Berry's phase are consistent with the presence of Dirac fermions on the side wall of the warped cylindrical Fermi surface. Similarly to SrMnBi₂, which features an anisotropic Dirac cone, our results suggest that magnetic-field-induced changes in interlayer conduction are also present in layered bismuth-based materials with a zero-energy line in momentum space created by the staggered alkaline earth atoms.

I. INTRODUCTION

Similar to graphene and topological insulators, ternary AMnBi₂ crystals (A = alkaline earth, such as Ca, Sr, or Ba) also host quasi-two-dimensional (2D) Dirac states [1–4]. The Dirac cone in SrMnBi₂ is strongly anisotropic due to spin-orbit coupling, which is an essential ingredient for the magnetic valley control and valley-polarized interlayer current [5–8]. There may be multiple degenerate "valleys" (conduction-band minima) for the carriers to occupy in the electronic structure of certain crystal lattices. Such a degeneracy can be lifted in a controllable way; i.e., magnetic valley control is a degeneracy controlled by the magnetic field. The valley degree of freedom can be used to develop electronic devices [7,9]. First-principle calculations and angle-resolved photoemission (ARPES) measurements indicate that the anisotropy of the Dirac cone is determined by the local arrangement of Sr/Ca surrounding the Bi square net [5,10]. The stacking configuration of the two alkaline earth atomic layers above and below the Bi square net is different for SrMnBi₂ and CaMnBi₂, creating an anisotropic Dirac cone (SrMnBi₂) or a zero-energy line in momentum space (CaMnBi₂) [5]. Therefore, it is of interest to probe interlayer conduction in CaMnBi₂.

Valley control in SrMnBi₂ is realized through field-dependent coherent interlayer conduction, sensitive to the curvature of the side wall of the quasi-2D Fermi surface (FS) [6]. This is similar to, for example, the quasi-2D organic superconductor magnetoresistance (MR) peak structure when the magnetic field is nearly parallel to the conducting plane. The MR is explained by the open orbits or small closed orbits formed on the side of the warped FS [11]. The warped FS is easily detected by Shubnikov de Haas (SdH) oscillations since the oscillation frequency is determined by the extremal orbit [12].

In-plane electronic transport reveals that CaMnBi₂ is a bad metal with antiferromagnetic transition at ∼250 K, showing giant magnetoresistance [3,13,14]. The MR and quantum oscillations results indicate the existence of quasi-2D Dirac fermions in CaMnBi₂ [3]. Negative thermopower suggests dominant electron-type carriers, whereas the magnetic field suppresses its absolute value, consistent with the presence of Dirac fermions [15].

Here we report the angular-dependent MR and SdH in CaMnBi₂ when the current runs along the c axis of the crystal. The fourfold symmetry of the azimuthal angle dependence of the out-of-plane resistivity (ρ_c) indicates a valley degeneracy contribution of Dirac fermions to the interlayer conductivity. Moreover, the contribution can be lifted and controlled by the in-plane magnetic field. Compared to SrMnBi₂, the out-of-plane resistivity and Hall resistance suggest a larger contribution of the three-dimensional (3D) FS to the conductivity. The peak of the MR when the field is in the ab plane and the narrow angle range of the SdH indicate the existence of small closed orbits on the side of the warped FS. The SdH along the c axis features three peaks, possibly due to several extremal orbits in the α band and consistent with the angle-dependent MR results. The temperature dependence of the SdH in the ab plane reveals a small cyclotron mass, large mobility, and nozero Berry's phase in the small closed pocket. This suggests that the zero-energy line of Dirac carriers in CaMnBi₂ contains small closed orbits [5,10].

II. EXPERIMENTAL DETAILS

CaMnBi₂ single crystals were grown from high-temperature bismuth flux [3]. Neutron time-of-flight powder diffraction measurement at 300 K was performed on the POWGEN instrument, BL-11A, at the Spallation Neutron Source, Oak Ridge National Laboratory. A vanadium can containing 0.5 g of finely pulverized sample was used with an *in situ* sample changer. Powder used in the neutron experiment was obtained by pulverizing single crystals from the same batch as the single crystal used in interlayer transport experiments. The average structure was assessed through Rietveld refinements to the raw diffraction data using the GSAS operated under EXPGUI, utilizing the tetragonal space group $P4/nmm$ [16–18]. A sample for transmission electron microscopy (TEM) was prepared by crushing the single-crystal sample and then dropping it onto a Lacey carbon grid. High-resolution TEM imaging was performed using a double aberration-corrected JEOL-ARM200CF microscope with a cold-field emission gun operated at 200 kV. Single crystals

---

*Present address: Department of Physics, University of Maryland, College Park, Maryland 20742-4111, USA.

free of bismuth flux for magnetotransport measurements were obtained by cleaving and cutting the six faces of the cuboid. Magnetotransport measurements up to 9 T were performed using the Quantum Design PPMS-9, and those up to 35 T at the National High Magnetic Field Laboratory in Tallahassee, Florida. For the out-of-plane resistance measurement, a thick single crystal was cut to produce a needlelike sample with the long side along the c axis with about 5° uncertainty in order to minimize the contribution of the in-plane resistivity component. This is in contrast to the method where voltage contacts are attached on the opposite [001] planes of rectangular crystal [3,19,20]. Electrical contacts used in resistivity measurements were made for the samples using silver paste to attach Pt wires in a standard four-probe configuration. The temperature dependences of the resistivity of three independently grown crystals from the same batch were reproducible and consistent with each other. Given the sample size, the error introduced by the geometry factor can be as high as 18%.

III. RESULTS AND DISCUSSION

The $P4/nmm$ structure of CaMnBi$_2$ was confirmed through neutron powder diffraction and TEM [Figs. 1(a)–1(c)]. Neutron diffraction lattice parameters [Fig. 1(a)] are in good agreement with the reported values [21]. In addition to the main phase, about 9%, by weight, elemental Bi phase was also observed due to the small amount of Bi metal flux droplets during pulverization of the single-crystal specimen. The TEM electron diffraction pattern of CaMnBi$_2$ is also consistent with the $P4/nmm$ space group [Figs. 1(b) and 1(c)] [3].

Figure 2(a) shows the temperature dependence of the interlayer resistivity (ρ_c) for CaMnBi$_2$ measured at 0 and 9 T in the Quantum Design PPMS. The overall behavior of ρ_c is similar to that of ρ_{ab} [3,14]. Neither the anomaly corre-
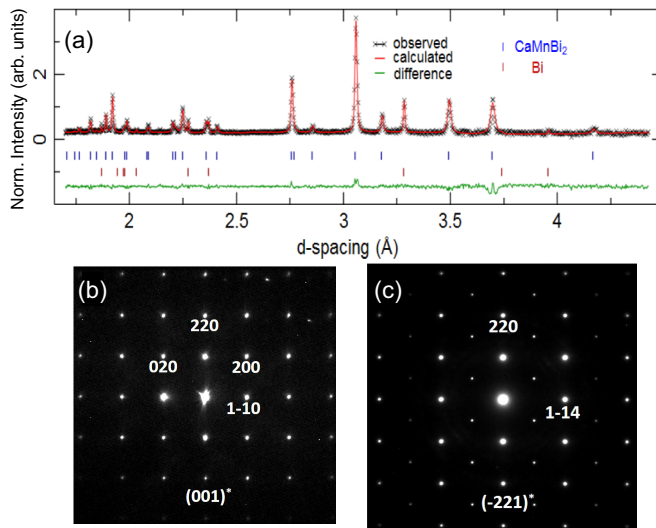

FIG. 1. (a) Structural refinement of neutron powder diffraction data on CaMnBi$_2$ at 300 K. Electron diffraction pattern of CaMnBi$_2$ viewed along the (b) [001] and (c) [−221] directions. Reflection conditions can be derived from (b) as $h + k = 2n$ (n is an integer) for $hk0$, consistent with the reflection condition of the $P4/nmm$ space group.
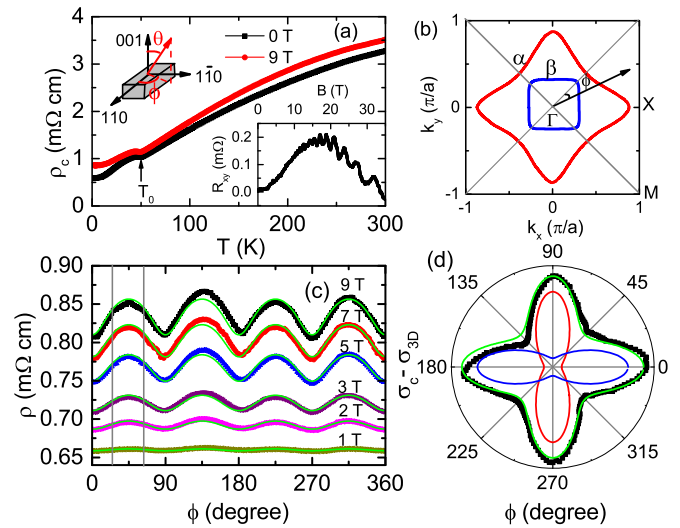

FIG. 2. (a) Temperature dependence of the out-of-plane resistivity of CaMnBi$_2$ in the $B = 0$ T and $B = 9$ T magnetic fields. The scheme shows how the polar (θ) and azimuthal (ϕ) are determined. Inset: MR of CaMnBi$_2$. (b) Fermi surface of CaMnBi$_2$ obtained by ARPES measurements [10]. The orientations of the Fermi pocket with respect to the crystal axes are also shown. (c) Azimuthal angle (ϕ) dependence of the out-of-plane resistivity at $T = 2$ K under different magnetic fields. Green lines represent fits using the three-parameter equation (see text). (d) Polar plot of $\sigma_c - \sigma_{3D}$ (black squares) and the three-parameter fit (green line); red and blue lines represent the contributions of valleys with odd and even indexes, respectively.

sponding to the antiferromagnetic transition at $T_N \cong 250$ K nor the broad maximum at about 170 K is observed [3,13,22]. The broad maximum in c-axis resistivity observed before [3] was probably introduced by the temperature gradient at the National High Magnetic Field Laboratory cryostat during the cooldown procedure. Due to antiferromagnetic order in CaMnBi$_2$, Mn-related bands are well spin polarized and separated away from the Fermi level; consequently, the electronic transport properties of CaMnBi$_2$ are dominated by the anisotropic Dirac cone formed by the Bi p band [5]. The origin of the resistivity anomaly at $T_0 = 50$ K has been attributed to weak ferromagnetic order or spin reorientation [3,14]. However, this anomaly does not stem from the change in the average crystal structure since there is a smooth evolution of lattice parameters of the $P4/nmm$ space group from 310 K to $T = 10$ K upon cooling [22]. Compared to the ρ_c of SrMnBi$_2$, the hump around 200 K is very weak [1], indicating that the FS is more 3D than that in SrMnBi$_2$. The magnetoresistance MR $= [\rho_c(B) - \rho_c(0)]/\rho_c(0)$ is about 10% above 50 K in a 9-T field but increases strongly below 50 K, to 44% at 2 K, similarly to the in-plane MR of CaMnBi$_2$. The slope of the Hall resistance $R_{xy}(B)$ changes from positive to negative at ∼16 T [Fig. 2(a), inset], suggesting the presence of multiple bands in the electronic transport. According to the classical expression for the Hall coefficient when both electron- and hole-type carriers are present [23],

$$\frac{\rho_{xy}}{\mu_0 H} = R_H$$

$$= \frac{1}{e} \frac{(\mu_h^2 n_h - \mu_e^2 n_e) + (\mu_h \mu_e)^2 (\mu_0 H)^2 (n_h - n_e)}{(\mu_e n_h + \mu_h n_e)^2 + (\mu_h \mu_e)^2 (\mu_0 H)^2 (n_h - n_e)^2}.$$

In the weak-field limit, the equation can be simplified as $R_H = e^{-1}(\mu_h^2 n_h - \mu_e^2 n_e)/(\mu_h n_h + \mu_e n_e)^2$, whereas $R_H = 1/(n_h - n_e)e$ in the high-field limit. If $\mu_h < \mu_e$, a change in the slope indicates that the dominant carriers in CaMnBi$_2$ are holes at low field and electrons at high field. This is different from SrMnBi$_2$, where the Hall resistance slope remains negative up to 60 T [1]. The interlayer resistivity and Hall resistance suggest that the transport of CaMnBi$_2$ is dominated by a 3D hole Fermi pocket at the Brillouin zone center and that the FS is more 3D when compared to that of SrMnBi$_2$.

The Fermi surfaces of CaMnBi$_2$ and SrMnBi$_2$ both have a holelike square-shaped part around the Γ point. Differently from the four small isolated FSs in the Γ-M direction in SrMnBi$_2$, there is a large diamondlike FS connecting four equivalent X points in the first Brillouin zone [10], as shown in Fig. 2(b). The similarity of CaMnBi$_2$ and SrMnBi$_2$ FSs indicates that valley-polarized interlayer conduction is possible in CaMnBi$_2$.

For a twofold anisotropic Fermi pocket and when the field is applied along the shorter axis, the electrons on the flat part of the FS experience nearly zero Lorentz force, whereas Lorentz force makes the electrons on the side wall move along the closed orbits. This leads to minima in ρ_c. Therefore, the magnetic field can be an effective tool to control the valley contribution to the out-of-plane resistivity [6,7]. The azimuthal angle (ϕ) dependence of ρ_c exhibits strong fourfold symmetry due to the different contribution of the valleys controlled by the in-plane field orientation. For a quasi-2D FS, $\rho_c(\phi)$ can be fitted with an empirical model; we assume that the holelike β FS has a negligible ϕ dependence, while the four α FSs are ellipsoid, with the long axis perpendicular to the Γ-M line. Therefore, $\sigma_c(\phi) \approx 1/\rho_c(\phi)$ can be described by the formula [6]

$$\sigma_c(\phi) = \sum_{n=1}^{4} \sigma_{\alpha,n}(\phi) + \sigma_\beta$$
$$= \frac{2\sigma_{2D}}{1 + r\cos^2\phi} + \frac{2\sigma_{2D}}{1 + r\cos^2(\phi + \pi/2)} + \sigma_{3D},$$

where σ_{2D} and σ_{3D} are the contributions of the α and β FSs, respectively. The parameter r is a measure of the anisotropy of magnetoconductivity. As shown in Fig. 2(c), all curves can be fitted with this empirical formula: $\sigma_{2D} = 0.06$ (mΩ cm)$^{-1}$, $\sigma_{3D} = 1.09$ (mΩ cm)$^{-1}$, and $r = 4.28$ can be obtained from the fitting of $\rho_c(\phi)$ at 9 T, and the contribution of the quasi-2D FS to $\sigma_{2D} - \sigma_{3D}$ is illustrated in Fig. 2(d). The ratio between the quasi-2D (four α bands) and the 3D (β band) conductivities $4\sigma_{2D}/\sigma_{3D} \sim 0.22$, indicating that $\rho_c(\phi)$ is dominated by the 3D holelike β FS. The quasi-2D electronlike α bands contribute only about $\sim$22% of the total out-of-plane conductivity, consistent with the small quasi-2D FSs observed by ARPES and quantum oscillations [3,10].

We note that the fourfold symmetry is broken at a high magnetic field [Fig. 2(c)] into twofold symmetry. The ρ_c value at $\pi/2$ and $3\pi/2$ is larger than those at $\pi/4$ and $3\pi/4$. A similar result has been observed for SrMnBi$_2$ and Bi, possibly due to the formation of nematic liquid of electrons [1,7,24].

Figure 3 shows the polar angle (θ) dependence of ρ_c at various azimuthal angles (ϕ). Magnetotransport of solids is governed by the extremal cross section S_F of the FS; as a result, $S_F(\theta) = S_0/|\cos(\theta)|$ is expected for a 2D FS. The $\rho_c(\theta)$ exhibits twofold symmetry at low temperatures and high fields
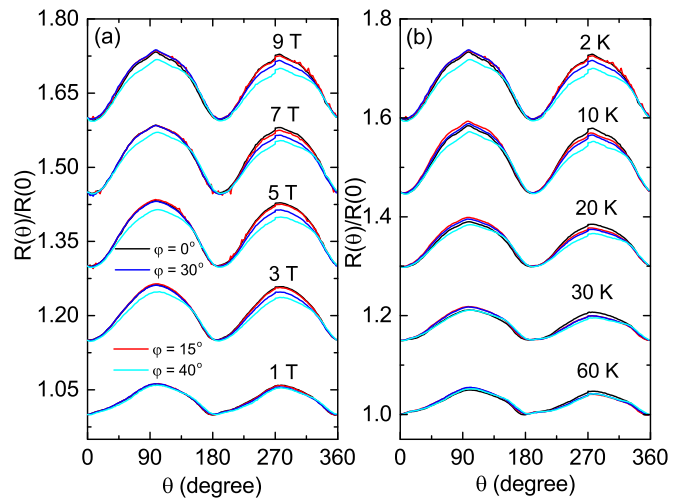

FIG. 3. (a) Normalized resistivity $\rho_c(\theta)/\rho_c(0)$ taken at 2 K for different azimuthal angles (ϕ) and in different fields. (b) Normalized resistivity $\rho_c(\theta)/\rho_c(0)$ taken at 9 T with varying ϕ and temperature. (a) and (b) have the same legend. Each subsequent data set is shifted upward by 0.15 for clarity.

and can be fitted by $|\cos(\theta)|$, consistent with the quasi-2D FS in CaMnBi$_2$. There are two shoulders around $\theta = 90^o$, where the field is parallel to the ab plane. The shoulder location (Yamaji) angles are magnetoresistance maxima where the carriers in the warped cylindrical FS behave as in a 2D electronic system [25].

The $\rho_c(\theta)$ measured in a high field is presented in Fig. 4(a). It shows a peak at around $90°$, which can be attributed to self-crossing orbits or closed orbits that appear on the side of the warped FS [6,11]. Moreover, the peak width is independent of the field strength, as shown in the inset in Fig. 4(a). In the case of self-crossing orbits, the angular width of the peak should be inversely proportional to the magnetic field. Thus, the peak at $\theta = 90°$ can be ascribed to closed orbits on the side of the cylindrical FS [11]. The series of peaks between $120°$ and $180°$ are due to Yamaji oscillations [11]. Our results indicate coherent interlayer conduction at low temperatures and the presence of the quasi-2D FS in CaMnBi$_2$, in agreement with the previous report [3].

Figure 4(b) shows the magnetic field dependence of ρ_c up to 35 T. No oscillation is observed below 10 T, indicating the absence of Bi flux in the MR signal since elemental bismuth shows quantum oscillations at very low magnetic fields [26]. The MR decreases with the increased angle. The slopes of the MRs decrease considerably at around 3 T. The resistance exhibits linear-in-field dependence at high magnetic fields. No transition corresponding to the magnetic order change is observed in the resistivity at high magnetic fields. Nonsaturating linear MR has been reported in several complex materials like Ag$_{2+\delta}$Se, SrMnBi$_2$, and BaFe$_2$As$_2$ [1,27,28]. Linear MR can be observed when Dirac electrons condense at the lowest Landau level (LL) [29,30]. This is easily realized in modest magnetic fields since the distance between the lowest LL and the first LLs of Dirac-like fermions in a magnetic field is large, in contrast to the conventional paraboliclike energy dispersion [28,29,31,32]. Whereas linear MR is also observed in simple metals, such as potassium [33], in-plane
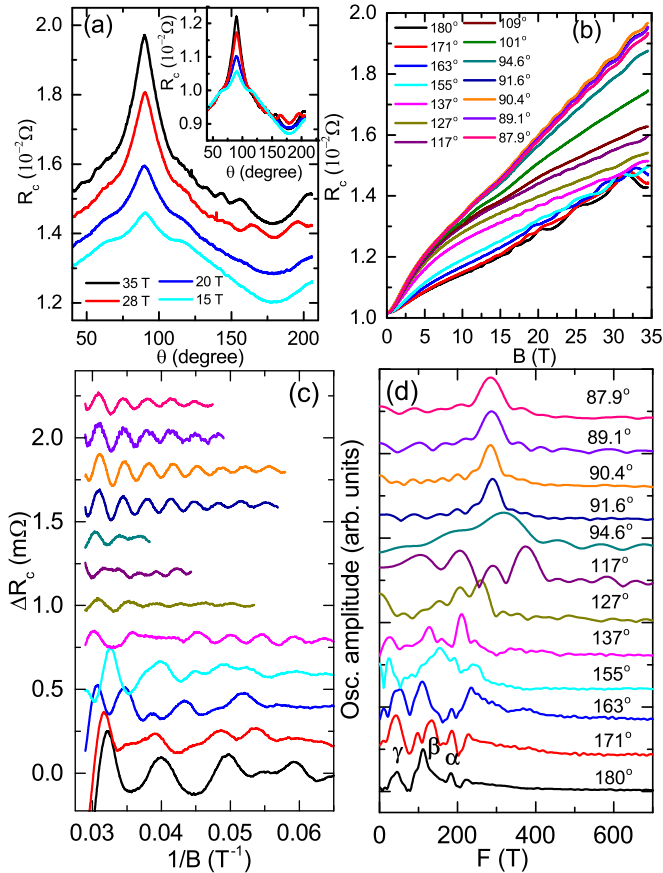
FIG. 4. (a) Angle dependence of the out-of-plane resistance $R_c(\theta)$ taken at 2 K in magnetic fields up to 35 T. Inset: $R_c(\theta)$ of CaMnBi$_2$ normalized to $R_c(114°)$. (b) Magnetic-field dependence of the out-of-plane resistance R_c up to 35 T for CaMnBi$_2$. (c) SdH oscillation component $\Delta R_c = R_c - \langle R_c \rangle$ vs $1/B$ for different angles measured up to 35 T at 0.7 K. (d) FFT spectra of the SdH oscillations corresponding to the oscillation component in (c). (c) and (d) have the same legend.

MR, quantum oscillations, thermal transport, ARPES studies, and first-principle calculations strongly suggest the presence of Dirac states in CaMnBi$_2$ [3,5,10,15].

Shubnikov–de Haas (SdH) oscillations are observed in the c-axis electronic transport [Figs. 4(b)–4(d)]. At first, the oscillation magnitude decreases very quickly with the angle increase, and the oscillation disappears at $\theta = 101°$. The oscillation appears again with further angle decrease. Hence, clear oscillation can be observed when the field is either along the c axis [3,14] or in the ab plane (this study). A 3D FS would produce oscillations for all directions of the magnetic field; therefore it is unlikely in CaMnBi$_2$ due to the absence of oscillation at 101°. Another possibility is that the oscillation is due to the Fermi-surface topological effect, where small closed orbits appear on the side of the warped cylindrical FS. This model can also interpret the absence of oscillations at 101° and the presence of the oscillations only in a narrow range around 90°, in agreement with $\rho_c(\theta)$. As shown in the calculated Fermi surfaces of CaMnBi$_2$ in Fig. 4 in Ref. [5], this closed orbit is very likely located on the convex part of the electron Fermi

pocket. A schematic of the closed orbits is given in Fig. 3(c) of Ref. [6].

In Fig. 4(c), we show the oscillatory component of ΔR_c versus $1/B$ for different angles after subtracting the smooth background. The oscillation component shows periodic behavior in $1/B$. We perform fast Fourier transform (FFT) on the oscillation component in Fig. 4(c); the results are presented in Fig. 4(d). There is only one frequency, $F = 286$ T, at which the field is parallel to the ab plane. When the field is applied along the c axis, three FFT peaks are observed. The peaks are located at 45.4, 111.8, and 184.0 T, and the corresponding FS cross sections are 0.43, 1.07, and 1.76 nm^{-2} according to the Onsager relation $F = (\Phi_0/2\pi^2)A_F$, where Φ_0 is the quantum flux and A_F is the cross-sectional area of the FS. All three Fermi pockets are very small, only about 0.2%, 0.5%, and 0.9% of the total area of the Brillouin zone. $F = 184$ T is very close to the dominant frequency observed before, therefore it can be assigned to an α band with a Dirac point [3,14]. Other frequencies could come from the α band, which is a warped cylindrical Fermi pocket with several extremal orbits. This is consistent with the closed orbits observed on the side wall of the cylindrical Fermi pocket. The oscillations show multiband behavior when the fields tilt from the c axis. In what follows we discuss the SdH when the field is applied parallel to ab plane [Figs. 5(a)–5(d)].

Temperature dependence of quantum oscillations is shown in Fig. 5(a) and Fig. 5(b). Semiclassically, the SdH oscillation can be described by

$$\Delta\rho \propto R_T R_D \cos\left[2\pi(F/B + \tfrac{1}{2} + \beta)\right],$$

where $R_T = \frac{\alpha m^* T}{B\sinh(\alpha m^* T/B)}$ is the thermal damping factor, and $R_D = \exp(-\alpha m^* T_D/B)$ is the Dingle damping factor, in which $\alpha = 14.69$ T/K. $2\pi\beta$ is Berry's phase. The thermal damping factor can be used to determine the cyclotron effective mass from the Lifshitz-Kosevich formula. As shown in Fig. 5(c), fitting of the amplitude gives the cyclotron mass $m^* \approx 0.53$, heavier compared to the values of 0.35 obtained from in-plane oscillation of CaMnBi$_2$ and 0.29 in SrMnBi$_2$ [1,3]. The Dingle temperature $T_D = 8.23$ K can be obtained from the Dingle plot in Fig. 5(c). Therefore, a scattering time of $\tau_q = 1.47 \times 10^{-13}$ s can be obtained by $T_D = \frac{\hbar}{2\pi k_B \tau_q}$. Then the mobility $\mu_q = e\tau_q/m_c$ is 488 cm^2 V^{-1} s^{-1}. The scattering time and mobility are even higher than in SrMnBi$_2$ and Cd$_3$As$_2$, typical Dirac materials, consistent with the presence of Dirac fermions in this Fermi pocket [1,34].

The Fourier transform spectrum of the oscillation at 0.7 K reveals a periodic behavior in $1/B$ with a frequency $F = 299$ T. The oscillation frequency determined by the slope of the linear fit of the Landau index is 299 T, in agreement with the FFT results. The FS cross section normal to the field is $A_F = 2.86$ nm^{-2}, and $k_F = 9.54 \times 10^8$ m^{-1} can be obtained. Therefore, the Fermi velocity $v_F = \hbar k_F/m^* = 2.08 \times 10^5$ m/s and the Fermi energy $E_F = 130$ meV. The mean free path is estimated to be by $l = v_F\tau = 30.6$ nm.

SdH oscillations in metals are related to successive emptying of the LL in the magnetic field whereas the LL index n is correlated with the cross section of the FS S_F as
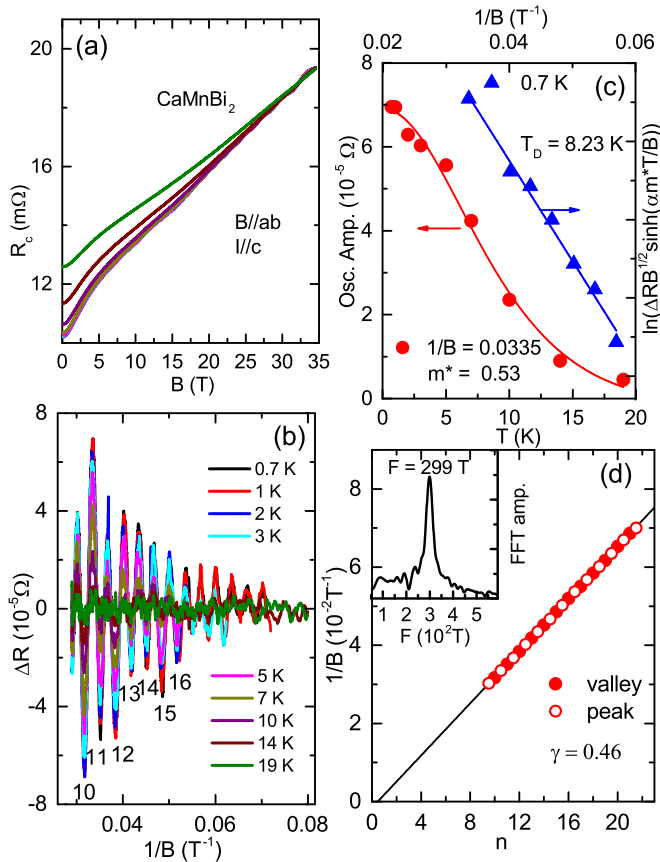
FIG. 5. (a) Magnetic-field dependence of the resistance of CaMnBi$_2$ measured at various temperatures up to 19 K. (b) The oscillatory component as a function of $1/B$. Integer indices of the Landau levels. (a) and (b) have the same legend. (c) Left: Temperature dependence of the oscillation amplitude at different fields. Solid lines are the fits by the Lifshitz-Kosevitch formula. Right: Dingle plot at 0.7 and 1 K. (d) Landau index plots n vs $1/B$ at 0.7 K. Inset: FFT spectra at 0.7 K.

$2\pi(n + \gamma) = S_F(\hbar/eB)$. In the Landau fan diagram [Fig. 5(d)] the peaks and valleys fall on a straight line. The linear fit gives $\gamma \cong 0.46$; γ should be 0 for conventional metals but is $\pm 1/2$ for Dirac fermions due to the nontrivial Berry's phase. The $\gamma \sim 1/2$ and high Fermi velocity confirm the existence of Dirac fermions at the orbits on the side of the warped cylindrical FS. The Dirac Fermion with large Fermi velocity on the side wall of the Fermi cylinder have important effect on the ρ_c which could explain why ρ_c does not show clear ϕ dependence.

IV. CONCLUSIONS

In conclusion, we studied the angle-dependent out-of-plane magnetotransport in CaMnBi$_2$. ρ_{xy} and out-of-plane ρ_{xx} indicate that the FS is more 3D when compared to SrMnBi$_2$. The interlayer conduction depends on the orientation of in-plane magnetic field. This suggests that the valley-polarized interlayer current through magnetic valley control can be realized in CaMnBi$_2$. The angular dependence of MR and the SdH show that the the closed orbits appear on the side of the warped cylindrical FS. Small FS, small cyclotron mass, large mobility, and nonzero Berry phase are consistent with the existence of Dirac fermions on the Fermi pocket on the side wall of the warped cylindrical FS.

[1] J. Park, G. Lee, F. Wolff-Fabris, Y. Y. Koh, M. J. Eom, Y. K. Kim, M. A. Farhan, Y. J. Jo, C. Kim, J. H. Shim, and J. S. Kim, Phys. Rev. Lett. **107**, 126402 (2011).

[2] K. Wang, D. Graf, H. Lei, S. W. Tozer, and C. Petrovic, Phys. Rev. B **84**, 220401(R) (2011).

[3] K. Wang, D. Graf, L. Wang, H. Lei, S. W. Tozer, and C. Petrovic, Phys. Rev. B **85**, 041101(R) (2012).

[4] L. Li, K. Wang, D. Graf, L. Wang, A. Wang, and C. Petrovic, Phys. Rev. B **93**, 115141 (2016).

[5] G. Lee, M. A. Farhan, J. S. Kim, and J. H. Shim, Phys. Rev. B **87**, 245104 (2013).

[6] Y. J. Jo, J. Park, G. Lee, M. J. Eom, E. S. Choi, J. H. Shim, W. Kang, and J. S. Kim, Phys. Rev. Lett. **113**, 156602 (2014).

[7] Z. Zhu, A. Collaudin, B. Fauqué, W. Kang, and K. Behnia, Nat. Phys. **8**, 89 (2012).

[8] R. Küchler, L. Steinke, R. Daou, M. Brando, K. Behnia, and F. Steglich, Nat. Mater. **13**, 461 (2014).

[9] D. Xiao, W. Yao, and Q. Niu, Phys. Rev. Lett. **99**, 236809 (2007).

[10] Y. Feng, Z. Wang, C. Chen, Y. Shi, Z. Xie, H. Yi, A. Liang, S. He, J. He, Y. Peng, X. Liu, Y. Liu, L. Zhao, G. Liu, X. Dong, J. Zhang, C. Chen, Z. Xu, X. Dai, Z. Fang, and X. J. Zhou, Sci. Rep. **4**, 5385 (2014).

[11] N. Hanasaki, S. Kagoshima, T. Hasegawa, T. Osada, and N. Miura, Phys. Rev. B **57**, 1336 (1998).

[12] D. Shoeneberg, *Magnetic Oscillation in Metals* (Cambridge University Press, Cambridge, UK, 1984).

[13] J. K. Wang, L. L. Zhao, Q. Yin, G. Kotliar, M. S. Kim, M. C. Aronson, and E. Morosan, Phys. Rev. B **84**, 064428 (2011).

[14] J. B. He, D. M. Wang, and G. F. Chen, Appl. Phys. Lett. **100**, 112405 (2012).

[15] K. Wang, L. Wang, and C. Petrovic, Appl. Phys. Lett. **100**, 112111 (2012).

[16] H. M. Rietveld, Acta Crystallogr. **22**, 151 (1967).

[17] A. C. Larson and R. B. von Dreele, Report No. LAUR-86-748, Los Alamos National Laboratory, Los Alamos, NM, 1987.

[18] B. H. Toby, J. Appl. Crystalogr. **34**, 210 (2001).

[19] X. F. Wang, T. Wu, G. Wu, H. Chen, Y. L. Xie, J. J. Ying, Y. J. Yan, R. H. Liu, and X. H. Chen, Phys. Rev. Lett. **102**, 117005 (2009).

[20] J. Edwards and R. F. Frindt, J. Phys. Chem. Solids **32**, 2217 (1971).

[21] E. Brochtel, G. Cordier, and H. Shäfer, Z. Naturforsch. b **35**, 1 (1980).

[22] Y. F. Guo, A. J. Princep, X. Zhang, P. Manuel, D. Khalyavin, I. I. Mazin, Y. G. Shi, and A. T. Boothroyd, Phys. Rev. B **90**, 075120 (2014).

[23] P. B. Allen, in *Handbook of Superconductivity*, edited by C. P. Poole, Jr. (Academic Press, New York, 1999), p. 478.

[24] E. Fradkin, S. A. Kivelson, M. J. Lawler, J. P. Eisenstein, and A. P. Mackenzie, Annu. Rev. Condens. Matter Phys. **1**, 153 (2010).

[25] E. Ohmichi, Y. Maeno, and T. Ishiguro, J. Phys. Soc. Jpn. **68**, 24 (1999).

[26] V. S. Edelman, Adv. Phys. **25**, 555 (1976).

[27] R. Xu, A. Husmann, T. F. Rosenbaum, M.-L. Saboungi, J. E. Enderby, and P. B. Littlewood, Nature **390**, 57 (1997).

[28] K. K. Huynh, Y. Tanabe, and K. Tanigaki, Phys. Rev. Lett. **106**, 217004 (2011).

[29] A. A. Abrikosov, *Fundamentals of the Theory of Metals* (North-Holland, Amsterdam, 1988).

[30] A. A. Abrikosov, Europhys. Lett. **49**, 789 (2000).

[31] Y. Zhang, Z. Jiang, Y.-W. Tan, H. L. Stormer, and P. Kim, Nature (London) **438**, 201 (2005).

[32] D. Miller, K. Kubista, G. Rutter, M. Ruan, W. de Heer, P. First, and J. Stroscio, Science **324**, 924 (2009).

[33] J. R. Reitz and A. W. Overhauser, Phys. Rev. **171**, 749 (1968).

[34] T. Liang, Q. Gibson, M. N. Ali, M. H. Liu, R. J. Cava, and N. P. Ong, Nat. Mater. **14**, 280 (2015).

Magnetotransport study of Dirac fermions in YbMnBi$_2$ antiferromagnet

Aifeng Wang (王爱峰),[1] I. Zaliznyak,[1] Weijun Ren (任卫军),[1,2] Lijun Wu,[1] D. Graf,[3] V. O. Garlea,[4]
J. B. Warren,[5] E. Bozin,[1] Yimei Zhu,[1] and C. Petrovic[1]

[1]*Condensed Matter Physics and Materials Science Department, Brookhaven National Laboratory, Upton, New York 11973, USA*
[2]*Shenyang National Laboratory for Materials Science, Institute of Metal Research, Chinese Academy of Sciences, Shenyang 110016, China*
[3]*National High Magnetic Field Laboratory, Florida State University, Tallahassee, Florida 32306-4005, USA*
[4]*Quantum Condensed Matter Division, Oak Ridge National Laboratory, Oak Ridge, Tennessee 37831, USA*
[5]*Instrument Division, Brookhaven National Laboratory, Upton, New York 11973, USA*
(Received 1 April 2016; revised manuscript received 27 July 2016; published 24 October 2016)

We report quantum transport and Dirac fermions in YbMnBi$_2$ single crystals. YbMnBi$_2$ is a layered material with anisotropic conductivity and magnetic order below 290 K. Magnetotransport properties, nonzero Berry phase, and small cyclotron mass indicate the presence of Dirac fermions. Angular-dependent magnetoresistance indicates a possible quasi-two-dimensional Fermi surface, whereas the deviation from the nontrivial Berry phase expected for Dirac states suggests the contribution of parabolic bands at the Fermi level or spin-orbit coupling.

I. INTRODUCTION

The energy dispersion of carriers in Dirac materials can be approximated by the relativistic Dirac equation [1]. By now it has been established that Dirac states can be found in a wide range of materials, such as iron-based or copper-oxide superconductors, graphene, and topological insulators [2–9]. In the quantum limit, all carriers are condensed to the lowest Landau level (LL) [10]. This is easily realized in laboratory magnetic fields for Dirac fermions since the distance between the lowest and first LL of Dirac fermions is large, in contrast to the conventional electron gas with parabolic energy dispersion. In such a case, the components of the resistivity tensor ρ_{xx} and ρ_{xy} are linear in the magnetic field [11]; the quantum Hall effect, nontrivial Berry phase, and large unsaturated linear magnetoresistance (MR) are observed [5,12–14].

Crystals with quasi-two-dimensional (quasi-2D) bismuth layers such as AMnBi$_2$ (A = alkaline earth) have also been shown to host quasi-2D Dirac states similar to graphene and topological insulators [15–20]. The local arrangement of alkaline-earth atoms and spin-orbit coupling is rather important for the characteristics of Dirac cone states. In SrMnBi$_2$, the degeneracy along the band-crossing line is lifted, except at the place of anisotropic Dirac cone. In contrast, the energy eigenvalue difference due to the perturbation potential created by staggered alkaline-earth atoms results in a zero-energy line in momentum space in CaMnBi$_2$.

In the presence of the time-reversal or space-inversion symmetry breaking, the doubly degenerate Dirac point can split into a pair of Weyl nodes with opposite chirality [21–23]. Weyl semimetal signatures due to the space-inversion symmetry breaking have been observed in, for example, TaAs, NbAs, TaP, and NbP [24–27]. YbMnBi$_2$ is a material isostructural to CaMnBi$_2$, featuring magnetic order at similar temperatures [16,28]. Therefore, the observation of Weyl points and the connecting arc of surface states in YbMnBi$_2$ might be experimental evidence of a Weyl semimetal due to time-reversal symmetry breaking [28]. It is of interest to study quantum transport in YbMnBi$_2$. In this paper, we perform magnetoresistance measurements up to 35 T. The nonzero Berry phase, small cyclotron mass, and large mobility

confirm the existence of Dirac fermions in Bi square nets. The quasi-2D in-plane magnetoresistance (MR) shows a crossover from parabolic-in-field semiclassical MR to high-field linear-in-field dependence. The temperature dependence of crossover field B^* is quadratic, as expected for Dirac fermions.

II. EXPERIMENTAL DETAILS

YbMnBi$_2$ single crystals were grown from excess Bi. Yb, Mn, and Bi were mixed together according to the ratio Yb:Mn:Bi = 1:1:10. Then, the mixture was placed into an alumina crucible, sealed in a quartz tube, heated slowly to 900 °C, kept at 900 °C for 2 h, and cooled to 400 °C, where the excess Bi flux was decanted. Shiny single crystals with typical size $3 \times 3 \times 1$ mm^3 can be obtained. The single crystals free of residual flux droplets can be obtained by cutting the six faces of the cuboid. The element analysis was performed using an energy-dispersive x-ray spectroscopy (EDX) in a JEOL LSM-6500 scanning electron microscope. Single-crystal neutron-diffraction measurements were performed using the HB3A four-circle diffractometer at the High Flux Isotope Reactor at Oak Ridge National Laboratory. A crystal specimen of approximately $2 \times 2 \times 1$ mm^3 was loaded in a closed-cycle refrigerator whose temperature was controlled in the range 4–350 K. For the measurements, we used a monochromatic beam with the wavelength 1.551 Å selected by a multilayer [110]-wafer silicon monochromator, and the scattered intensity was measured using an Anger-camera-type detector. The neutron-diffraction data were analyzed by using the FULLPROF SUITE package. A transmission-electron-microscopy (TEM) sample was prepared by crushing the single-crystal sample, and then dropping to a Lacey carbon grid. An x-ray powder-diffraction experiment was performed at the 28-ID-C beam line of NSLS-II at Brookhaven National Laboratory, and the data were collected on the pulverized sample in a cylindrical polyimide capillary by using a monochromatic beam with wavelength of 0.01858 nm and Perkin-Elmer image plate detector. Data integration to 2θ was carried out using FIT2D, while structural refinement of the $P4/nmm$ model used GSAS operated under the EXPGUI platform [29–31]. High-resolution TEM imaging and electron diffraction were performed using

the double aberration-corrected JEOL-ARM200CF microscope with a cold-field emission gun and operated at 200 kV. Magnetotransport measurements up to 9 T were conducted in a Quantum Design PPMS-9. Magnetotransport at high magnetic field up to 35 T was conducted at the National High Magnetic Field Laboratory (NHMFL) in Tallahassee. The transport measurements were performed on cleaved and polished single crystals. Polishing is necessary in order to remove residual bismuth droplets from the surface of as-grown single crystals. Electrical contacts used in resistivity measurements were put on the crystals using a standard four-probe configuration. Hall resistivity was measured by the four-terminal technique by switching the polarity of the magnetic field H//c to eliminate the contribution of ρ_{xx} due to the misalignment of the voltage contacts. The Hall resistivity is obtained by $\rho_{xy} = [V_{xy}(B) - V_{xy}(-B)] \times d/2I_{xx}$, where d is the thickness of the crystals, I_{xx} is the longitudinal current, $V_{xy}(B)$ is the transverse voltage of the positive field, and $V_{xy}(-B)$ is the negative field.

III. CRYSTAL AND MAGNETIC STRUCTURE

The crystal and magnetic structure of YbMnBi$_2$ determined by neutron diffraction and high-resolution TEM (HRTEM) is presented in Fig. 1. The nuclear lattice structure was determined from measurements at $T = 310$ K, where magnetic order is absent. The magnetic structure was determined at $T = 4$ K, and the refined saturated magnetic moment at this temperature is $4.3(1)\mu_B$/Mn. Refinements were carried out using data sets of 82 reflections; the resulting structural parameters are listed in Table I. R-factors ~5% were obtained for both temperatures. No indication of structural transformation between 300 and 4 K has been detected, and no orthorhombic or monoclinic distortions were observed within the HB3a wave-vector resolution. The data is fit equally well in both tetragonal and orthorhombic symmetry. The magnetic space group describing the antiferromagnetic (AFM) order at 4 K [Fig. 1(a)] can be refined in $P4'/n'm'm$: $(3/4,1/4,0|0,0,mz)(1/4,3/4,0|0,0,-mz)$. The scanning electron microscopy (SEM)-obtained atomic ratio of Yb:Mn:Bi is 26:26:48, consistent with the composition YbMnBi$_2$. Both HRTEM electron-diffraction pattern and fast Fourier transform can be well indexed as the (110)* zone of the YbMnBi$_2$ structure. Powder-diffraction data are well explained by the $P4/nmm$ model of YbMnBi$_2$ [$a = 4.488(2)$ Å, $c = 10.826(2)$ Å]; see Fig. 1(h). In addition to the main phase, about 10% by weight of the Bi$_2$O$_3$ phase was also observed due to secondary oxidation of unreacted Bi metal on a crystal surface during pulverization of the single-crystal specimen.

IV. RESULTS AND DISCUSSION

Figure 2(a) shows the temperature dependence of the in-plane (ρ_{ab}) and out-of-plane (ρ_c) resistivity at 0 and 9 T for a YbMnBi$_2$ single crystal. The in-plane resistivity becomes flat below 8 K, extrapolating to a residual resistivity $\rho_0(0$ T$) \approx 4.77$ $\mu\Omega$ cm. The residual resistivity ratio (RRR) $\rho(300$ K$)/\rho_0$ is about 20. The MR ratio, MR $= [\rho_{ab}(B) - \rho_{ab}(0)]$, is 234% at 2 K in a 9 T field. The MR is gradually suppressed with temperature increase. The resistivity is highly anisotropic. The hump below 300 K in $\rho_c(T)$ could indicate a crossover from high-T
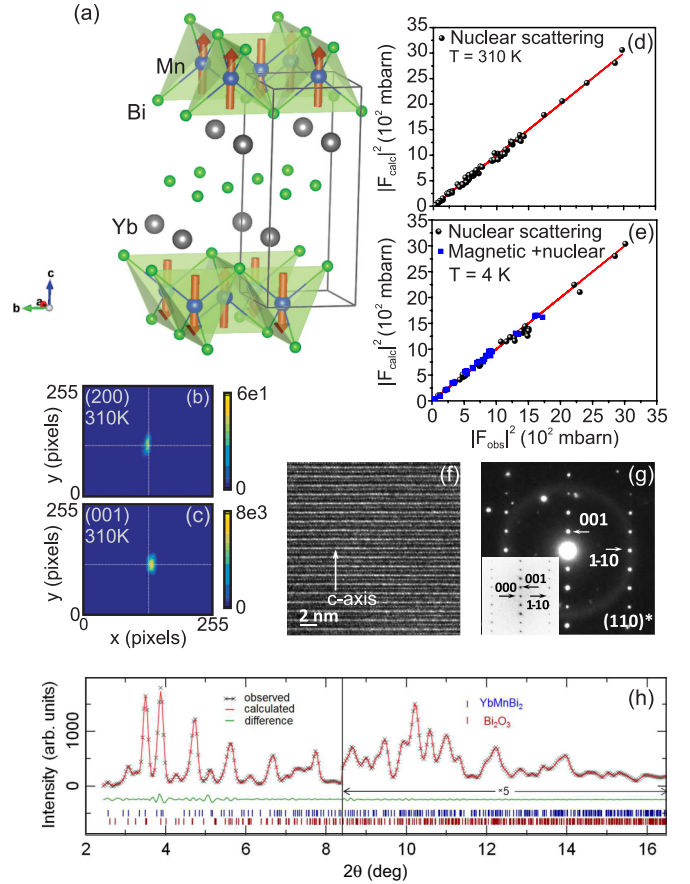
FIG. 1. (a) Crystal and magnetic structure of YbMnBi$_2$. Arrows show the ordered Mn magnetic moments, $\mu_{Mn} = 4.3(1)\mu_B$, refined at 4 K. The moments point along the c axis; the magnetic space group describing the AFM order is $P4'/n'm'm$: $(3/4,1/4,0|0,0,mz)(1/4,3/4,0|0,0,-mz)$. (b),(c) Neutron intensity patterns of (200) and (001) nuclear structural Bragg peaks, respectively, of a YbMnBi$_2$ single crystal on the two-dimensional position-sensitive detector on a HB3a diffractometer, indicating perfect crystalline structure. (d),(e) Summary of the structural refinement of YbMnBi$_2$ in the magnetically disordered phase at 310 K, and at 4 K where it is antiferromagnetically ordered. (f) High-resolution transmission electron microscopy (HRTEM) image and (g) corresponding electron diffraction pattern (EDP) viewed along the [110] direction. The inset in (g) is the FFT from the image shown in (f). (h) Structural refinement of powder-diffraction data. Ticks mark reflections, top row refers to the main phase, and bottom row refers to Bi$_2$O$_3$ due to sample preparation.

incoherent to low-T coherent conduction [32,33]. As shown in the inset in Fig. 2(a), ρ_{ab} is quadratic in temperature below about 5 K: $\rho(T) = \rho_0 + AT^2$ with $A = 5.74n$ Ω cm K^{-2}. The parameter A is inversely proportional to the Fermi temperature and is only one-third of that of SrMnBi$_2$ [17]. This indicates that the effective mass in YbMnBi$_2$ is rather small.

Specific-heat measurement on YbMnBi$_2$ is shown in Fig. 2(b). A peak is clearly observed at around 285 K, which could be attributed to the magnetic transition [34]. The fitting of the low-temperature data using $C_p = \gamma_n T + \beta T^3 + \eta T^5$ gives $\gamma_n = 2.16$ mJ mol^{-1} K^{-2}, $\beta = 2.36$ mJ mol^{-1} K^{-4}, and

TABLE I. The crystal and magnetic structure parameters of YbMnBi$_2$ determined by neutron diffraction. The refinement was carried out using 82 Bragg reflections measured on the HB3A diffractometer using a monochromatic neutron beam with wavelength $\lambda \approx 1.55$ Å. Each reflection was measured by performing the sample rotation (ω) scan to extract the integrated intensity.

T = 310 K					
Symmetry group: $P4/nmm$ Bragg R-factor: 5.25					
$a = b = 4.48(1)$, $c = 10.80(2)$ Magnetic moment $0\mu_B$/Mn.					
Atom	x	y	z	B_{iso}	Site multiplicity
Yb1	0.25	0.25	0.73174(19)	1.051(148)	2
Mn1	0.75	0.25	0.0	1.255(255)	2
Bi1	0.75	0.25	0.5	0.917(159)	2
Bi2	0.25	0.25	0.16700(29)	1.027(158)	2
T = 4 K					
Symmetry group: $P4/nmm$ Bragg R-factor: 4.83					
$a = b = 4.46(1)$, $c = 10.73(2)$ Magnetic moment $4.3(1)\mu_B$/Mn.					
Atom	x	y	z	B_{iso}	Site multiplicity
Yb1	0.25	0.25	0.73143(21)	0.379(173)	2
Mn1	0.75	0.25	0.0	0.707(272)	2
Bi1	0.75	0.25	0.5	0.188(194)	2
Bi2	0.25	0.25	0.16567(32)	0.256(187)	2

$\eta = 0.00695$ mJ mol^{-1} K^{-6}. Thus, a Debye temperature of 149 K can be obtained.

Clear oscillations in longitudinal ρ_{xx} and transverse ρ_{xy} resistivity are observed up to 35 Tesla [Figs. 3(a)–3(d)]. Whereas the oscillations ρ_{xx} are due to the Shubnikov–de Haas (SdH) effect, the changes of ρ_{xy} with magnetic field could also show a contribution from the quantum Hall effect similar to Bi$_2$Se$_3$ due to the layered crystal structure and quasi-2D electronic transport [35]. From the fast Fourier transform (FFT) background-subtracted oscillating component $\Delta\rho_{xx}$ features a single frequency $F = 130$ T at 2 K [Fig. 3(b)]. According to the classical expression for the Hall coefficient
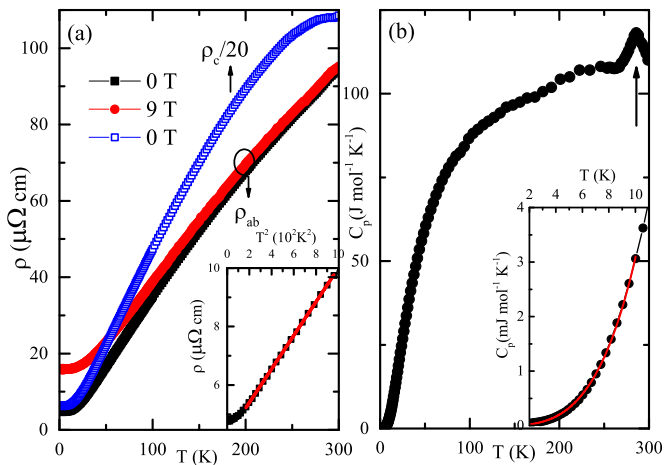

FIG. 3. (a)–(c) Longitudinal and transverse in-plane resistivity vs field at different temperatures. SdH oscillatory component $\Delta\rho_{xx}$. (b) is obtained after the background subtraction. (d) Field dependence of Hall conductivity σ_{xy} at 2 K. (e) Temperature dependence of the oscillating amplitude of longitudinal oscillations at $1/B = 0.33$ T^{-1}. The solid line is the fitting curve. Inset: Dingle plot for $\Delta\rho_{xx}$. (f) LL index plots $1/B_n$ vs n. Inset: The Fourier transform spectrum of $\Delta\rho_{xx}$.

when both electron- and hole-type carriers are present [36], we get

$$\frac{\rho_{xy}}{\mu_0 H} = R_H$$

$$= \frac{1}{e}\frac{(\mu_h^2 n_h - \mu_e^2 n_e) + (\mu_h\mu_e)^2(\mu_0 H)^2(n_h - n_e)}{(\mu_e n_h + \mu_h n_e)^2 + (\mu_h\mu_e)^2(\mu_0 H)^2(n_h - n_e)^2}.$$

In the weak-field limit, the equation can be simplified as $R_H = e^{-1}(\mu_h^2 n_h - \mu_e^2 n_e)/(\mu_h n_h + \mu_e n_e)^2$, while $R_H = 1/(n_h - n_e)e$ in the high-field limit. The positive slope of $\rho_{xy}(H)$ at high field gives $n_h > n_e$, and the negative slope of $\rho_{xy}(H)$ at weak field indicates $(\mu_h^2 n_h - \mu_e^2 n_e) < 0$. Therefore, $\mu_e > \mu_h$ at low field, and the nonlinear behavior is the result of the carrier density and mobility competition between hole- and electron-type carriers. Fitting $\rho_{xy}(2K)$ at high field using $R_H = 1/(n_h - n_e)e$ yields $n_h - n_e = 2.09 \times 10^{21}$ cm^{-3}, which is a large carrier concentration when compared to other Weyl semimetals, such as Cd$_3$As$_2$ and NbP [27,37].

Theoretical calculations reveal that the Fermi surface of YbMnBi$_2$ is constituted of holelike "lenses" and electronlike pockets near X points [28]. The main frequency of longitudinal

FIG. 2. (a) Temperature dependence of in-plane resistivity (ρ_{ab}) for YbMnBi$_2$ single crystals at 0 and 9 T, and out-of-plane resistivity (ρ_c) at 0 T. Inset shows the quadratic T dependence at low temperature of ρ_{ab} at 0 T. (b) Temperature dependence of the specific heat of YbMnBi$_2$. Inset shows the fitting of the low-temperature part.
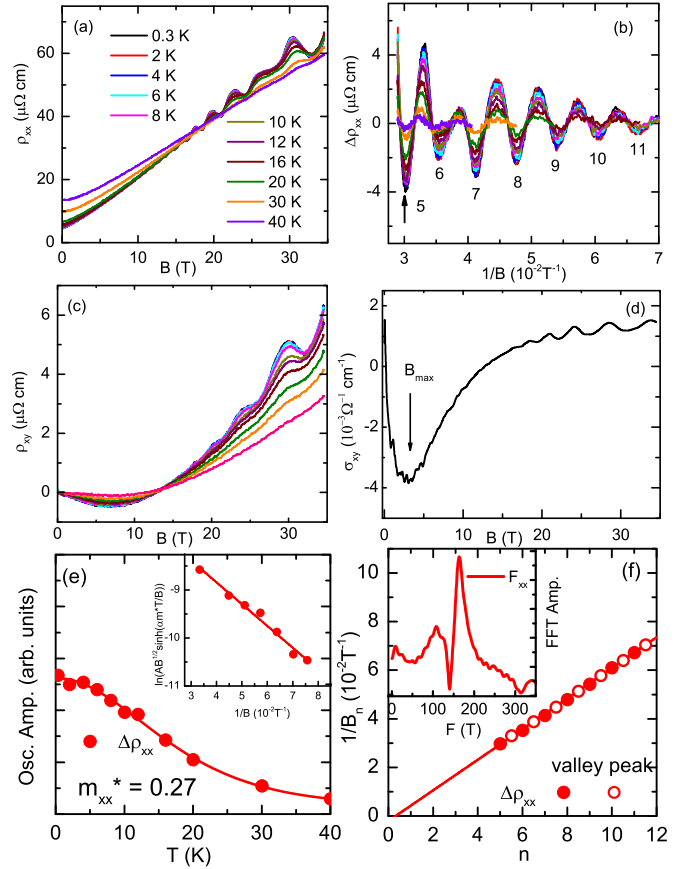
oscillation (130 T) is somewhat smaller than the frequencies of $SrMnBi_2$ (152 T) and $CaMnBi_2$ (185 T) [16,17]. From the Onsager relation, $F = (\Phi_0/2\pi^2)A_F$, where Φ_0 is the flux quantum and A_F is the orthogonal cross-sectional area of the Fermi surface, we estimate $A_F = 1.56$ nm^{-2}. This is rather small, similar to that in $SrMnBi_2$ (1.45 nm^{-2}), and is only a few % of the total area of the Brillouin zone in the (001) plane [16,17]. We can also approximate $k_F \approx 0.705$ nm^{-1}, assuming the circular cross section $A_F = \pi k_F^2$.

Weyl points and the Fermi arc connecting these points have been directly observed by angle-resolved photoemission spectroscopy (ARPES) in $YbMnBi_2$ [28]. It is reported that the Fermi arcs, which participate in unusual closed magnetic orbits by traversing the bulk of the sample to connect opposite surfaces, can be detected by quantum oscillation [38]. In our experiment, we do not observe the frequency associated with the Fermi arc, possibly due to macroscopic thickness of our sample that exceeds the mean-free path [38,39].

The cyclotron masses and quantum lifetime of carriers can be extracted from the temperature and field dependence of oscillation amplitude using the Lifshitz-Kosevich formula [40],

$$\frac{\Delta\rho_{xx}(T,B)}{\rho_{xx}(0)} = e^{-\alpha m^* T_D/B}\frac{\alpha m^* T/B}{\sinh(\alpha m^* T/B)},$$

where $\alpha = 2\pi^2 k_B/e\hbar \approx 14.69$ T/K, $m^* = m/m_e$ is the cyclotron mass ratio (m_e is the mass of the free electron), and $T_D = \frac{\hbar}{2\pi k_B\tau_q}$, with τ_q the quantum lifetime. By fitting the thermal damping of the oscillation peak indicated by the arrow in Fig. 3(b), we can extract the cyclotron mass $m^* \approx 0.27$, similar to that in $SrMnBi_2$ and $CaMnBi_2$ [15,17]. Then, a very large Fermi velocity $v_F = \hbar k_F/m^* = 3.01 \times 10^5$ m/s can be obtained. As shown in Fig. 3(e), $T_D = 11.4$ K can be obtained by fitting the field dependence of the oscillation amplitude, and T_D is larger than that in $SrMnBi_2$ and $BaMnBi_2$ [17,41]. As a result, $\tau_q = 1.05 \times 10^{-13}$ s. Within the standard Bloch-Boltzmann framework, the geometric mean of the mobility can be determined by the reciprocal value of the peak field, $1/B_{max}$. As shown in the inset of Fig. 3(c), the geometric-mean mobility $\mu_m = 3.48 \times 10^3$ cm^2 V^{-1} s^{-1} can be inferred from B_{max} in σ_{xy}. Hence, $\tau_m = 5.3 \times 10^{-13}$ s can be obtained using $\mu_m = e\tau_m/m^*$. This is five times larger than τ_q. This is because τ_m measures backscattering processes that relax the current, while τ_q is sensitive to all processes that broaden the Landau levels [42,43].

Using the effective mass obtained above, we can calculate the electronic specific heat in a quasi-two-dimensional approximation [44],

$$\gamma_N = \sum_i \frac{\pi N_A k_B^2 ab}{3\hbar^2}m^*,$$

where N_A is Avogadro's number, k_B is Boltzmann's constant, a and b are the in-plane lattice parameters, m^* is the quasiparticle mass, and $\hbar$ is Planck's constant. From the effective mass obtained by quantum oscillation, and four bands observed by ARPES [28], $\gamma_N = 2.16$ mJ mol^{-1} K^{-2} can be obtained, in excellent agreement with the γ_N derived from specific heat [Fig. 2(b)], consistent with ARPES measurement [28] and indicating that four bands detected by SdH alone contribute to the electronic specific heat.

One of the key pieces of evidence for the existence of Dirac fermions is the nontrivial Berry's phase [45]. Figure 3(f) presents the fan diagram of the Landau index. According to the Lifshitz-Onsager quantization rule, LL index n is related to the cross section of the Fermi surface (FS) S_F by $S_F(\hbar/eB) = 2\pi(n + \gamma)$. As shown in Fig. 3(f), the peak and valley positions of ρ_{xx} fall on a straight line; the fit gives $\gamma = 0.21$. γ should be zero for conventional metals, but ($\pm 1/2$) for Dirac fermions due to the nonzero Berry's phase associated with their cyclotron motion. Berry phase deviations from the exact π value have also been observed in NbP, Bi_2Se_3, and Bi_2Te_2Se [27]. One possible reason behind the deviation is the significant spin-orbit coupling since $\gamma = (1/2) + gm^*/4m$, where g is the g factor, m^* is the cyclotron mass, and m is the electron mass [46–48]. Another possibility is that parabolic bands at the Fermi surface contribute to quantum oscillations and to the high carrier concentration [28].

The Bi square nets in $SrMnBi_2$, and $CaMnBi_2$ host Dirac states with quasi-2D Fermi surface. We perform the field dependence of longitudinal resistance up to 35 T at different angles to study the topological structure of $YbMnBi_2$. The geometry of the measurement setup is shown in the inset of Fig. 4(a). Figure 4(a) presents an angle-dependent oscillation component after background subtraction. The oscillation peaks shift systematically with the angle increase. We perform FFT on the data in Fig. 4(a) and the results are shown in Fig. 4(b). Two peaks can be observed in the low-angle data; we only take the main peak into consideration. The positions of the main peak are summarized in Fig. 4(c); the frequency increases with the angle tilt from zero. The angle dependence of the FFT peaks can be roughly fitted assuming dominant contribution of quasi-2D conducting states [$F(0)/\cos\theta$] at the Fermi surface. However [Fig. 4(c)], the ellipsoid function $F(0)/(\varepsilon^2\sin^2\theta + \cos^2\theta)^{1/2}$ offers an alternative description. This makes it difficult to distinguish between the 2D cylinder Fermi surface and 3D ellipsoid Fermi surface, but nevertheless a quasi-2D Fermi surface can be inferred. In addition, a dip between $-23°$ to $-31°$ also confirms the nontrivial nature of the $YbMnBi_2$ Fermi surface.

The MR of solids only responds to the extremal cross section of the Fermi surface along the field direction. For a 2D Fermi surface, the MR will only respond to the perpendicular component of the magnetic field $B\cos(\theta)$. The angle-dependent MR of a $YbMnBi_2$ single crystal at $B = 9$ T and $T = 2$ K is shown in Fig. 4(d). The MR shows twofold symmetry; when the magnetic field parallels the c axis of the single crystal ($\theta = 0$), the MR is maximized and it gradually decreases with the field tilting away from the c axis. The MR is minimized when the field is applied in the ab plane. The curve can be fitted by a function of $|\cos(\theta)|$, indicating that the quasi-2D Fermi surface dominates magnetotransport in $YbMnBi_2$, consistent with the angle dependence of the quantum oscillation results.

Figure 5(a) presents the magnetic field dependence of MR at different temperatures. MR is also plotted in Fig. 5(b) on a log-log scale to emphasize the low-field behavior. From Fig. 5(b), we can observe that linear MR behavior is established above a crossover field B^*. With increasing temperature, MR gradually decreases and B^* increases. The normal MR of bands with parabolic dispersion either saturates
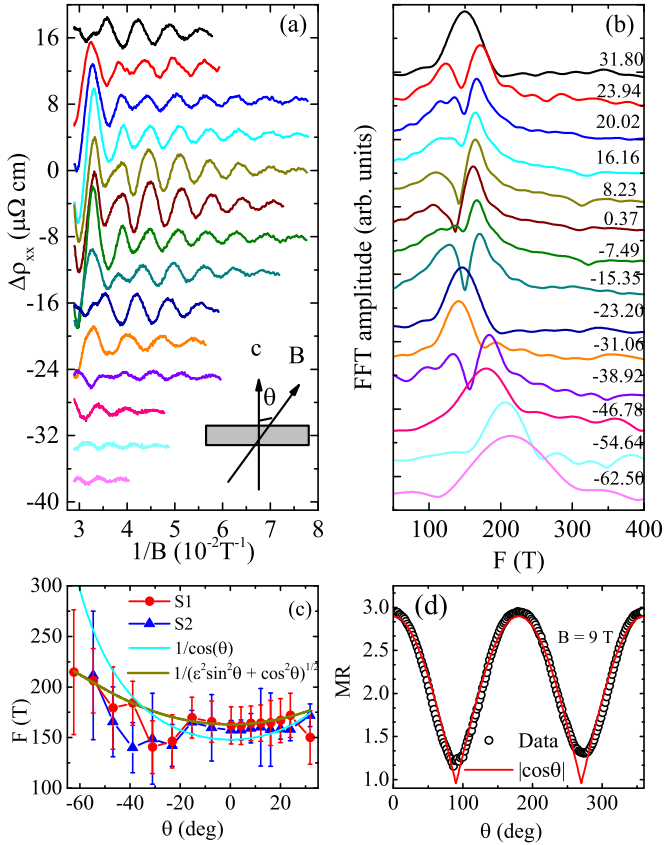
FIG. 4. (a) The SdH oscillatory component as a function of $1/B$ at various angles; the cartoon shows the geometry of the measurement setup. (b) FFT spectra of the SdH oscillations in (a). (a) and (b) use the same legend. (c) Angular dependence of the oscillation frequency. Sample 1 (S1) is the sample we used in this paper; sample 2 is the sample from the same batch and measured on the same probe. The cyan line is the fitting using the 2D model with $F(0)/\cos(\theta)$; the dark yellow line is the ellipse model $F(0)/(\varepsilon^2\sin^2\theta + \cos^2\theta)^{1/2}$ with an anisotropic factor $\varepsilon = -0.67$. The error bar is the peak width at half height of the FFT peaks. (d) Magnetoresistance as a function of the titled angle from the applied field. The red line is the fitting using the 2D model.

FIG. 5. (a) The magnetic field dependence of the in-plane MR at different temperatures. (b) Log-log plot of MR vs magnetic field. (c) A Kohler plot for YbMnBi$_2$. (d) Temperature dependence of the critical field B^* (black squares); the red solid line is the fitting results using $B^* = (1/2e\hbar v_F^2)(k_BT + E_F)^2$. The red circle corresponds to high-field MR linear coefficient A_1.

multiple bands, highly conducting (i.e., Dirac) states dominate the MR.

V. CONCLUSIONS

We have demonstrated quantum transport in antiferromagnetically ordered YbMnBi$_2$ single crystals. At 4 K, the saturated magnetic moment is $4.3(1)\mu_B$/Mn, whereas Mn magnetic moments are oriented along the c axis. High-magnetic-field magnetotransport is consistent with the presence of Dirac fermions and significant spin-orbit coupling of the Dirac-like carriers or with the presence of parabolic bands. It would be of interest to study in depth details of the magnetic structure, Berry phase in ultrathin samples, and putative ferromagnetic states in doped crystals.

ACKNOWLEDGMENTS

at high fields or increases as H^2. The unusual nonsaturating linear magnetoresistance has been reported in Ag$_{2-\delta}$(Te/Se), Bi$_2$Te$_3$,Cd$_3$As$_2$, BaFe$_2$As$_2$, and (Ca, Sr)MnBi$_2$ [15,16]. In the quantum limit where all of the carriers occupy only the lowest LL, the observed B^* corresponds to the quantum limit of $B^* = (1/2e\hbar v_F^2)(k_BT + E_F)^2$ [11]. As shown in Fig. 5(c), the B^* can be fitted quite well by the above equation, which confirms the the existence of Dirac states in YbMnBi$_2$. Furthermore, MR in YbMnBi$_2$ conforms to Kohler's rule, $\Delta\rho/\rho(0) = F[H/\rho(0)]$ [where $F(H)$ usually follows a power law] in high magnetic fields [Fig. 5(c)]. This indicates that there is a single salient scattering time in YbMnBi$_2$, i.e., that even though the Fermi surface contains a contribution from
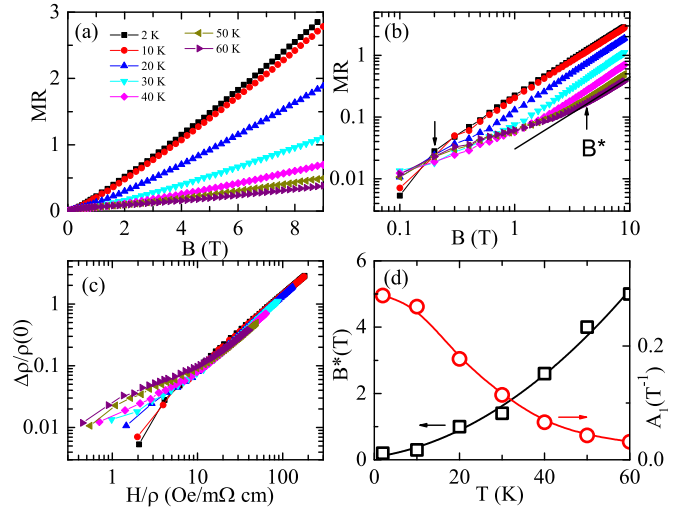
[1] T. O. Wehling, A. M. Black-Schaffer, and A. V. Balatsky, Adv. Phys. **63**, 1 (2014).

[2] O. Vafek and A. Vishwanath, Annu. Rev. Condens. Matter Phys. **5**, 83 (2014).

[3] P. Richard, K. Nakayama, T. Sato, M. Neupane, Y.-M. Xu, J. H. Bowen, G. F. Chen, J. L. Luo, N. L. Wang, X. Dai, Z. Fang, H. Ding, and T. Takahashi, Phys. Rev. Lett. **104**, 137001 (2010).

[4] J. Orenstein and A. J. Millis, Science **288**, 468 (2000).

[5] K. S. Novoselov, A. K. Geim, S. V. Morozov, D. Jiang, M. I. Katsnelson, I. V. Grigorieva, S. V. Dubonos, and A. A. Firsov, Nature (London) **438**, 197 (2005).

[6] A. K. Geim and K. S. Novoselov, Nat. Mater. **6**, 183 (2007).

[7] A. H. Castro Neto, F. Guinea, N. M. R. Reres, K. S. Novoselov, and A. K. Geim, Rev. Mod. Phys. **81**, 109 (2009).

[8] M. Z. Hasan and C. L. Kane, Rev. Mod. Phys. **82**, 3045 (2010).

[9] X. L. Qi and S. C. Zhang, Rev. Mod. Phys. **83**, 1057 (2011).

[10] A. A. Abrikosov, *Fundamentals of the Theory of Metals* (North-Holland, Amsterdam, 1988).

[11] A. A. Abrikosov, Phys. Rev. B **58**, 2788 (1998).

[12] Y. Zhang, Y.-W. Tan, H. L. Stormer, and P. Kim, Nature (London) **438**, 201 (2005).

[13] D. Miller, K. Kubista, G. Rutter, M. Ruan, W. de Heer, P. First, and J. Stroscio, Science **324**, 924 (2009).

[14] K. K. Huynh, Y. Tanabe, and K. Tanigaki, Phys. Rev. Lett. **106**, 217004 (2011).

[15] Kefeng Wang, D. Graf, Hechang Lei, S. W. Tozer, and C. Petrovic, Phys. Rev. B **84**, 220401(R) (2011).

[16] Kefeng Wang, D. Graf, Limin Wang, Hechang Lei, S. W. Tozer, and C. Petrovic, Phys. Rev. B **85**, 041101(R) (2012).

[17] J. Park, G. Lee, F. Wolff-Fabris, Y. Y. Koh, M. J. Eom, Y. K. Kim, M. A. Farhan, Y. J. Jo, C. Kim, J. H. Shim, and J. S. Kim, Phys. Rev. Lett. **107**, 126402 (2011).

[18] L.-L. Jia, Z.-H. Liu, Y.-P. Cai, T. Qian, X.-P. Wang, H. Miao, P. Richard, Y.-G. Zhao, Y. Li, D.-M. Wang, J.-B. He, M. Shi, G.-F. Chen, H. Ding, and S.-C. Wang, Phys. Rev. B **90**, 035133 (2014).

[19] G. Lee, M. A. Farhan, J. S. Kim, and J. H. Shim, Phys. Rev. B **87**, 245104 (2013).

[20] Y. Feng, Z. J. Wang, Ch. Y. Chen, Y. G. Shi, Z. J. Xie, H. M. Yi, A. J. Liang, S. L. He, J. F. He, Y. Y. Peng, X. Liu, Y. Liu, L. Zhao, G. D. Liu, X. L. Dong, J. Zhang, C. T. Chen, Z. Y. Xu, X. Dai, Z. Fang, and X. J. Zhou, Sci. Rep. **4**, 5385 (2014).

[21] Leon Balents, Physics **4**, 36 (2011).

[22] A. A. Burkov, M. D. Hook, and Leon Balents, Phys. Rev. B **84**, 235126 (2011).

[23] X. Wan, A. M. Turner, A. Vishwanath, and S. Y. Savrasov, Phys. Rev. B **83**, 205101 (2011).

[24] S. Y. Xu, C. Liu, S. K. Kushwaha, R. Sankar, J. W. Krizan, I. Belopolski, M. Neupane, G. Bian, N. Alidoust, T.-R. Chang, H.-T. Jeng, C.-Y. Huang, W.-F. Tsai, H. Lin, P. P. Shibayev, F.-C. Chou, R. J. Cava, and M. Z. Hasan, Science **347**, 294 (2015).

[25] S.-Y. Xu, I. Belopolski, D. S. Sanchez, C. Zhang, G. Chang, C. Guo, G. Bian, Z. Yuan, H. Lu, T.-R. Chang, P. P. Shibayev, M. L. Prokopovych, N. Alidoust, H. Zheng, C.-C. Lee, S.-M. Huang, R. Sankar, F. Chou, C.-H. Hsu, H.-T. Jeng, A. Bansil, T. Neupert, V. N. Strocov, H. Lin, S. Jia, and M. Z. Hasan, Sci. Adv. **1**, e1501092 (2015).

[26] S. Y. Xu, N. Alidoust, I. Belopolski, Z. J. Yuan, G. Bian, T.-R. Chang, H. Zheng, V. N. Strocov, D. S. Sanchez, G. Q. Chang, C. L. Zhang, D. X. Mou, Y. Wu, L. N. Huang, C.-C. Lee, S.-M. Huang, B. Wang, A. Bansil, H. Jeng, T. Neupert, A. Kaminski, H. Lin, S. Jia, and Z. Hasan, Nat. Phys. **11**, 748 (2015).

[27] C. Shekhar, A. K. Nayak, Y. Sun, M. Schmidt, M. Nicklas, I. Leermakers, U. Zeitler, Y. Skourski, J. Wosnitza, Z. K. Liu, Y. L. Chen, W. Schnelle, H. Borrmann, Y. Grin, C. Felser, and B. H. Yan, Nat. Phys. **11**, 645 (2015).

[28] S. Borisenko, D. Evtushinsky, Q. Gibson, A. Yaresko, T. Kim, M. N. Ali, B. Buechner, M. Hoesch, and R. J. Cava, arXiv:1507.04847.

[29] A. P. Hammersley, S. O. Swenson, M. Hanfland, and D. Hauseman, High Press. Res. **14**, 235 (1996).

[30] A. C. Larson and R. B. von Dreele, Report No. LAUR-86-748 (Los Alamos National Laboratory, New Mexico, 1987).

[31] B. H. Toby, J. Appl. Crystallogr. **34**, 210 (2001).

[32] D. B. Gutman and D. L. Maslov, Phys. Rev. Lett. **99**, 196602 (2007).

[33] D. B. Gutman and D. L. Maslov, Phys. Rev. B **77**, 035115 (2008).

[34] Y. F. Guo, A. J. Princep, X. Zhang, P. Manuel, D. Khalyavin, I. I. Mazin, Y. G. Shi, and A. T. Boothroyd, Phys. Rev. B **90**, 075120 (2014).

[35] H. Cao, Jifa Tian, I. Miotkowski, Tian Shen, Jiuning Hu, Shan Qiao and Yong P. Chen, Phys. Rev. Lett. **108**, 216803 (2012).

[36] R. A. Smith, *Semiconductors* (Cambridge University Press, Cambridge, 1978).

[37] L. P. He, X. C. Hong, J. K. Dong, J. Pan, Z. Zhang, J. Zhang, and S. Y. Li, Phys. Rev. Lett. **113**, 246402 (2014).

[38] A. C. Potter, I. Kimchi, and A. Vishwanath, Nat. Commun. **5**, 5161 (2014).

[39] P. J. W. Moll, N. L. Nair, T. Helm, A. C. Potter, I. Kimchi, A. Vishwanath, and J. G. Analytis, Nature (London) **535**, 266 (2016).

[40] D. Shoeneberg, *Magnetic Oscillation in Metals* (Cambridge University Press, Cambridge, 1984).

[41] L. J. Li, K. F. Wang, D. Graf, L. M. Wang, A. F. Wang, and C. Petrovic, Phys. Rev. B **93**, 115141 (2016).

[42] T. Liang, Q. Gibson, M. N. Ali, M. H. Liu, R. J. Cava, and N. P. Ong, Nat. Mater. **14**, 280 (2015).

[43] C. L. Zhang, Z. J. Yun, S. Y. Xu, Z. Q. Lin, B. B. Tong, M. Z. Hasan, J. F. Wang, C. Zhang, and S. Jia, arXiv:1502.00251.

[44] N. Kikugawa, A. W. Rost, C. W. Hicks, A. J. Schofield, and A. P. Mackenzie, J. Phys. Soc. Jpn. **79**, 024704 (2010).

[45] Yoichi Ando, J. Phys. Soc. Jpn. **82**, 102001 (2013).

[46] G. P. Mikitik and Yu. V. Sharlai, Phys. Rev. B **67**, 115114 (2003).

[47] G. P. Mikitik and Yu. V. Sharlai, Phys. Rev. B **85**, 033301 (2012).

[48] L. A. Falkovskii, J. Expt. Theor. Phys. **17**, 1302 (1963).

Complementary approaches for the evaluation of biocompatibility of ^{90}Y-labeled superparamagnetic citric acid $(Fe,Er)_3O_4$ coated nanoparticles

Bratislav Antic [a,*], Marko Boskovic [a], Jasmina Nikodinovic-Runic [b], Yue Ming [c,*], Hongguo Zhang [c], Emil S. Bozin [d], Drina Janković [a], Vojislav Spasojevic [a], Sanja Vranjes-Djuric [a]

[a] Vinča Institute of Nuclear Sciences, University of Belgrade, P. O. Box 522, 11001 Belgrade, Serbia
[b] Institute of Molecular Genetics and Genetic Engineering, University of Belgrade, Vojvode Stepe 444a, 11010 Belgrade, Serbia
[c] College of Materials Science and Engineering, Beijing University of Technology, Pingleyuan 100, Chaoyang District, Beijing 100124, PR China
[d] Condensed Matter Physics and Materials Science Department, Brookhaven National Laboratory, Upton, NY 11973, USA

ARTICLE INFO

ABSTRACT

Magnetic nanoparticles (MNPs) are of immense interest for diagnostic and therapeutic applications in medicine. Design and development of new iron oxide-based MNPs for such applications is of rather limited breadth without reliable and sensitive methods to determine their levels in body tissues. Commonly used methods, such as ICP, are quite problematic, due to the inability to decipher the origin of the detected iron, i.e. whether it originates from the MNPs or endogenous from tissues and bodily fluids. One of the approaches to overcome this problem and to increase reliability of tracing MNPs is to partially substitute iron ions in the MNPs with Er. Here, we report on the development of citric acid coated $(Fe,Er)_3O_4$ nanoparticles and characterization of their physico-chemical and biological properties by utilization of various complementary approaches. The synthesized MNPs had a narrow (6–7 nm) size distribution, as consistently seen in atomic pair distribution function, transmission electron microscopy, and DC magnetization measurements. The particles were found to be superparamagnetic, with a pronounced maximum in measured zero-field cooled magnetization at around 90 K. Reduction in saturation magnetization due to incorporation of 1.7% Er^{3+} into the Fe_3O_4 matrix was clearly observed. From the biological standpoint, citric acid coated $(Fe,Er)_3O_4$ NPs were found to induce low toxicity both in human cell fibroblasts and in zebrafish (*Danio rerio*) embryos. Biodistribution pattern of the MNPs after intravenous administration in healthy Wistar rats was followed by the radiotracer method, revealing that ^{90}Y-labeled MNPs were predominantly found in liver (75.33% ID), followed by lungs (16.70% ID) and spleen (2.83% ID). Quantitative agreement with these observations was obtained by ICP-MS elemental analysis using Er as the detected tracer. Based on the favorable physical, chemical and biological characteristics, citric acid coated $(Fe,Er)_3O_4$ MNPs could be further considered for the potential application as a diagnostic and/or therapeutic agent. This work also demonstrates that combined application of these techniques is a promising tool for studies of pharmacokinetics of the new MNPs in complex biological systems.

© 2017 Elsevier B.V. All rights reserved.

1. Introduction

Magnetic nanoparticles (MNPs) are currently being intensively investigated due to their wide range of possible applications in different branches of technology [1]. The field of medicine offers numerous opportunities for improvement of diagnostics and therapy using MNPs. The most promising medical applications of MNPs are in magnetic resonance imaging, drug delivery and as heating agents in magnetic hyperthermia [2–6]. In order to be used for medical applications, MNPs should be biocompatible, with suitable magnetic properties, narrow size distribution, as well as having chemical stability.

The only FDA approved magnetic material that can be used in human therapy so far is magnetite (Fe_3O_4) [7]. Nevertheless, applications of different methodologies for MNP detection *in vivo* [8] are scarce. One of the greatest challenges to that effect is reliably quantifying the biodistribution of exogenous iron oxide based nanoparticles in the presence of the background signal originating from very abundant endogenous iron ions. Usually, the distribution and accumulation of MNPs in different organs is evaluated using a combination of several techniques, including magnetic resonance imaging, X-ray fluorescence and X-ray absorption [9]. Elemental analysis based on inductively coupled plasma
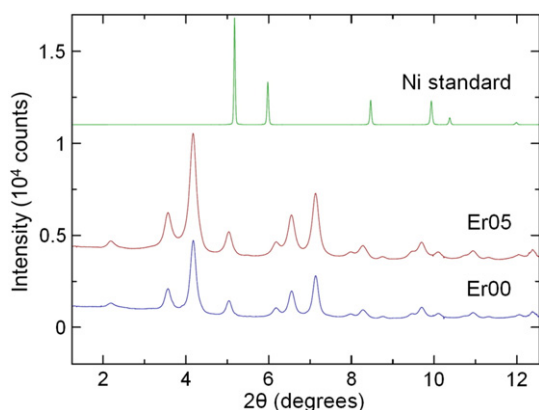
Fig. 1. Diffraction patterns obtained in far detector setup (medium-high resolution mode), at 300 K for Ni standard (top, green profile), Er05 (middle, red profile), and Er00 (bottom, blue profile). Sharp Bragg peaks are obtained for the standard, illustrating the measurement resolution. Dramatically broader profiles are observed for Er00 and Er05, indicating their nanoscale character.

optical emission (ICP-OES) and mass spectrometry (ICP-MS) is a frequently used method for studying both pharmacokinetics and biodistribution [10]. Although ICP-MS has a rather high sensitivity for detecting iron, it is not reliable as a MNP-specific tracer, since iron is found in abundance in all biological fluids and tissues in the forms of hemoglobin, ferritin, and myoglobin. The problem is potentiated in the case of detecting iron content in the liver, since this organ is not only the target organ for nanoparticles (>200 nm), but is also the storage organ for iron (the proteins, ferritin and hemosiderin). Ferritin is the major form of iron storage with a capacity of about 4500 iron (III) ions per protein molecule [11].

One possible way to overcome difficulties in studying the biodistribution of Fe_3O_4 nanoparticles is to partially substitute Fe cations with 4f elements, which are not typically found in living organisms [12]. This could circumvent the large systematic errors occurring due to the inability to distinguish the origin of Fe. From a structural point of view, magnetite crystallizes in the cubic spinel type structure, space group (S.G.) $Fd\overline{3}m$. In this structure, cations occupy two different non-equivalent crystallographic positions (8b and 24d). Partial Fe cation substitution with 4f rare earth (RE) elements in the spinel structure facilitates enhancement or alteration of the magnetic properties by changing the chemical composition of the compound. Due to appreciable ionic size mismatch between the host and dopant RE, associated structural distortions exert considerable crystallite strain [13]. Erbium has a large magnetic moment and high magnetic anisotropy, thereby potentially influencing the physical properties of the parent compound [13]. One of the concepts behind this study was to prepare magnetite nanoparticles, in which a proportion of the iron ions was substituted with erbium.

Information about the pharmacokinetics and biodistribution patterns of newly designed MPNs can be also obtained using a radiotracer technique [14,15]. Distribution of radiolabeled MNPs following intravenous administration is determined by measuring radioactivity in tissues and/or organs. Given the concerns pertaining to the radioactive character of the probe, limitations are prescribed to minimize animal exposure to radioactivity, while at the same time allowing a statistically sufficient number of counts to be collected from the studied specimens. Therefore, the radiation doses from the tracer, even when a beta emitting tracer such as ^{90}Y is used, neither produce any detectable radiation damage nor invoke detectable responses from the studied specimens that would alter the results. In addition, the amount of radioactive label, in the chemical form given to the animal under study, must not alter the physiological functions of the organism.

In order to examine the reliability of these methodologies for biodistribution studies, $(Fe,Er)_3O_4$ citric acid (CA) coated nanoparticles were firstly synthesized and characterized. The microstructural properties of the MNPs were studied and their magnetic properties were determined. Physicochemical characterization was followed by investigation of cytotoxicity as well as embryotoxicity of the MNPs. Through the radiolabeling of prepared samples, several important aspects were addressed: i) optimization of the radiolabeling protocol, ii) investigation of in vitro and in vivo stability of the radiolabeled MNPs and iii) determination of the biodistribution of the radiolabeled MNPs. Finally, for the precise determination of the MNP levels in tissues, a parallel approach was used: a combination of radiotracer and ICP methods.

2. Experimental

2.1. Sample preparation

Ferrofluids based on CA coated $Fe_{3-x}Er_xO_4$ nanoparticles, where x = 0 and 0.05 (further denoted by Er00 and Er05, respectively), were prepared via the modified Massart's method [16]. In a typical synthesis, 1.5 M NaOH was added dropwise to the initial solution with the stoichiometric ratio of $FeSO_4 \cdot 7H2O$, $FeCl_3 \cdot 6H_2O$, and $Er(NO_3)_3$. After reaching pH 10, the suspension was heated to 80 °C with vigorous stirring for 30 min. The co-precipitate was subjected to magnetic separation and rinsed repeatedly in deionized water to achieve neutral pH. CA-coated MNPs were obtained by initiating and conditioning the coating reaction until a stable suspension was established. Finally, the MNP suspension was centrifuged and washed several times with deionized water to rid it of any excess citric acid.

2.2. Physical characterization

TGA analyses were performed (30–700 °C range) on a SDT Q600 TGA/DSC instrument (TA Instruments, USA), by utilizing a 20 °C/min heating rate on <10 mg of sample. TGA was employed in order to determine the mass contribution of CA in dry MNPs. The CA content in Er00 and Er05 MNPs was found to be 18% and 11.5% of the mass, respectively.

Synchrotron experiments were conducted at 300 K on two samples of $Fe_{3-x}Er_xO_4$ with nominal compositions of x = 0 (Er00) and 0.05 (Er05). Experiments were carried out at the X17A beam line of the National Synchrotron Light Source (NSLS) at Brookhaven National
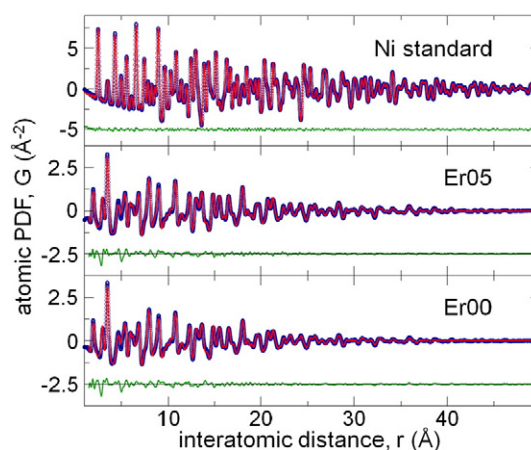
Fig. 2. Experimental atomic PDFs (open symbols) with converged structural models (solid red lines) and associate difference curves (green, offset for clarity) for Ni standard (top), Er05 (middle), and Er00 (bottom) materials. Data for MNPs were fitted using a spinel $Fd\overline{3}m$ model. PDF intensity is clearly observable in the of bulk Ni standard data at 50 Å, whereas the intensity is clearly washed out for the MNPs studied, indicating loss of structural coherence and the nanoscale character of Er00 and Er05.

Table 1

Structural parameters for the principal spinel ($Fd\overline{3}m$) phase of the MNPs: lattice parameter, a, Isotropic atomic displacement parameter, Uiso, for Fe in tetrahedral (Fe-t) and Fe in octahedral (Fe-o) positions, as well as oxygen. Fits, assuming spherical MNP shape also give particle diameter, d in nanometers. Finally, fit residuals r_{wp} give an indication of the goodness of fit.

MNP	a (Å)	Fe-t Uiso (Å²)	Fe-o Uiso (Å²)	O Uiso (Å²)	d (nm)	r_{wp}
Er00	8.355 (4)	0.007 (2)	0.018 (3)	0.022 (4)	6.5 (7)	0.16
Er05	8.364 (4)	0.008 (2)	0.020 (3)	0.025 (4)	5.3 (4)	0.18

Laboratory (Upton, NY, USA) using a monochromatic X-ray beam with wavelength of 0.1839 Å ($E = 67.42$ keV). Each sample was loaded into a polyimide capillary (1 mm in diameter) that was mounted 205.67 mm away from the Perkin Elmer amorphous silicon image plate detector positioned perpendicular to the beam path. Data was collected over multiple frames of 60 s each, which were further averaged for good statistics. Two-dimensional diffraction patterns were integrated, using *Fit2D* software, into their one-dimensional counterparts. These were corrected for various experimental effects, and the corresponding reduced total scattering functions, $F(Q)$, where Q is the momentum transfer, were then Sine Fourier transformed into the direct space to obtain the atomic pair distribution functions, PDF and $G(r)$. Data reduction was carried out using *PDFgetX3* software, with $Q_{MAX} = 24$ Å^{-1}, which was optimized for minimizing the signal to noise ratio and maximizing the r-space resolution.

Magnetic and TEM measurements were obtained using standard equipment and under standard conditions. Magnetic measurements of powder MNPs were performed on a *MPMS XL-5 SQUID* magnetometer. Magnetization *vs.* temperature, $M(T)$, was measured in the temperature range 2–300 K under zero-field-cooled (*ZFC*) and field-cooled (*FC*) regimes, in 100 Oe. Hysteresis loops were measured at 5 K and 300 K in a *ZFC* regime. Transmission electron micrographs and selected-area diffraction patterns were collected with a transmission electron microscope (JEM 2100 TEM, Jeol, USA) operating at 200 kV.

2.3. In vitro cell studies: antiproliferative activity assessed by MTT assay

Human lung fibroblast (*MRC5*) and melanoma (*A375*) cell lines were obtained from the ATCC culture collection and maintained and cultured as instructed by ATCC. In order to test cytotoxic effects, cells were maintained as monolayers (1×10^4 cells well^{-1}) and grown in a humidified atmosphere of 95% air and 5% CO_2 at 37 °C.

The viability of cells was evaluated using the 3-(4,5-dimethylthiazol-2-yl)-2,5-diphenyltetrazolium bromide (*MTT*) reduction assay [17]. This assay was carried out after 48 h of cell incubation in appropriate media containing test compounds (Er05 and Fe_3O_4 naked MNPs) at different concentrations and cell viability was measured as described [17]. Prepared 18 nm in size naked Fe_3O_4 MNPs

were used as a control for the coated MNPs in toxicity studies. Er05 and Fe_3O_4 solutions in deionized water were filter sterilized (0.2 μm, EMD Millipore, Billerica, USA) prior to usage in the cell culture experiments. The results were presented as percentage of viability of the control, untreated cells (arbitrarily set to 100%). IC_{50} values were calculated as concentrations at which 50% cell growth inhibition occurred. Experiments were conducted in hexaplicate in three independent determinations. Results are presented as means $\pm$ *SD*.

The morphological appearance of the treated cells was determined using a DM IL LED Inverted Microscope (Leica Microsystems, Wetzlar, Germany) under 20× magnification.

2.4. Embryotoxicity studies: zebrafish (Danio rerio) toxicity assay

The assessment of toxicity (lethality and teratogenicity) of Er05 MNPs on zebrafish embryos was performed following the general rules of the OECD Guidelines for the Testing of Chemicals [18]. Adult zebrafish (*Danio rerio*, wild type) were obtained from a commercial supplier (Pet Centar, Belgrade, Serbia) and maintained in fish medium (2 mM $CaCl_2$, 0.5 mM $MgSO_4$, 0.7 mM $NaHCO_3$, 0.07 mM KCl) at 27 $\pm$ 1 °C under a 14 h light/10 h dark cycle, and regularly fed twice daily with commercially dry flake food supplemented with *Artemia nauplii* (TetraMin™ flakes; Tetra Melle, Germany). Collected eggs at the 4- to 16-cellstages were individually treated with different concentrations of MNPs (5, 10 or 50 μg/ml) after being transferred into 96-well plates containing 200 μl of MNP test solution and one egg per well. The study was repeated two times using 32 embryos per MPN concentration. Er05 and Fe_3O_4 MNPs in deionized water were filter sterilized (0.2 μm, EMD Millipore, Billerica, USA) prior to usage in the zebrafish embryo experiments. Apical endpoints (Table S1) were examined and recorded 24, 48, 72, 96 and 114 h post fertilization (hpf) using an inverted microscope (CKX41; Olympus, Tokyo, Japan).

All studies involving zebrafish were performed in compliance with the European directive 86/609/*EEC* and the ethical guidelines given in the Guide for Care and Use of Laboratory Animals, Institute for Molecular Genetics and Genetic Engineering, University of Belgrade.
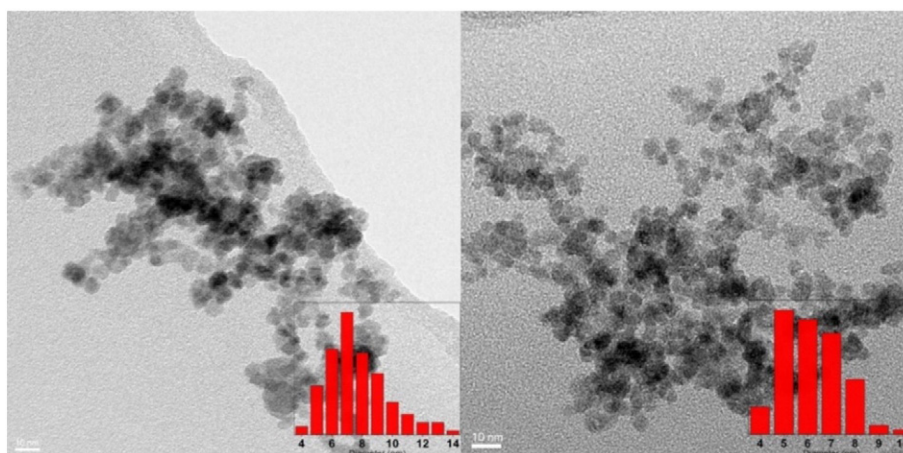
Fig. 3. TEM images of Er00 (left) and Er05 (right) MNPs. Inset: Particle counts. Scale bar is 10 nm in both pictures.

2.5. Radiolabeling of Er05 MNPs with ^{90}Y and in vitro stability studies

[90]YCl$_3$ was purchased from Polatom, Poland, in a no-carrier-added form (29.64 GBq/cm^3, in 0.05 M HCl, 18.5 TBq/mg Y, according to the product specification).

[90]Y labeling of Er05 MNPs was performed using the method previously applied for the radiolabeling of Fe$_3$O$_4$/PEG600 diacid MNPs [19]. Briefly, [90]YCl$_3$ solution (5 μl, containing approximately 370 MBq) was added to an aqueous suspension of 30 mg/ml Er05 MNPs at pH 6.5. The suspension was shaken for 1 h. Radiolabeled Er05 MNPs were then recovered by magnetic decantation, the supernatant was removed and the precipitate washed several times with deionized water to eliminate any unbound [90]Y^{3+}. The labeling yield was determined as the ratio of the measured MNP-associated activity obtained after magnetic separation and the known activity used for the radiolabeling. Formation of ^{90}Y-labeled Er05 MNPs and radiochemical purity were verified by instant thin layer chromatography performed on *SG* strips (*ITLC-SG*, glass microfiber chromatography paper impregnated with a silica gel) with saline as the mobile phase. With this system, ^{90}Y-labeled Er05 MNPs remained at the origin ($R_f = 0.0–0.1$), while unbound ^{90}Y migrated with the solvent front ($R_f = 0.9–1.0$).

The bremsstrahlung of ^{90}Y radioactivity was measured using a CRC-15 beta radioisotope dose calibrator (Capintec, USA) and a NaI (Tl) well-type gamma counter (Wizard 2480, Perkin Elmer, USA). All measurements were carried out under the same geometric conditions. The results are reported as the mean of at least three measurements ± standard deviation.

The stability of ^{90}Y-labeled Er05 MNPs during 72 h was determined after magnetic precipitation or *ITLC-SG* with saline as the mobile phase. Amounts (3 mg; 0.1 ml) of ^{90}Y-labeled Er05 MNPs were incubated with 1 ml of either saline or human serum at 37 °C. After 3 days of incubation, radiolabeled particles were precipitated with a permanent magnet and the activity was measured separately in a 0.1 ml aliquot of the supernatant and in the remaining sample (radiolabeled MNPs and 0.9 ml supernatant). The radioactivity bound to ^{90}Y-labeled Er05 MNPs was calculated as follows: the activity of the remainder – the activity of the 0.1 ml supernatant × 0.9.

2.6. Biodistribution of ^{90}Y-labeled Er05 MNPs

The biodistribution study was performed according to the guidelines of the European Council Directive (86/609/*EEC*) and the Serbian Laboratory Animal Science Association (SLASA). Three healthy male 4-week-old Wistar rats (100 ± 10 g body weight, Institute of Biology, Vinča Institute of Nuclear Sciences) received 0.1 ml of ^{90}Y-labeled Er05 MNPs (0.3 mg in saline, approx. 2.5 MBq) intravenously (i.v.) injected through the tail vein. The animals were sacrificed *via* spinal cord dislocation at
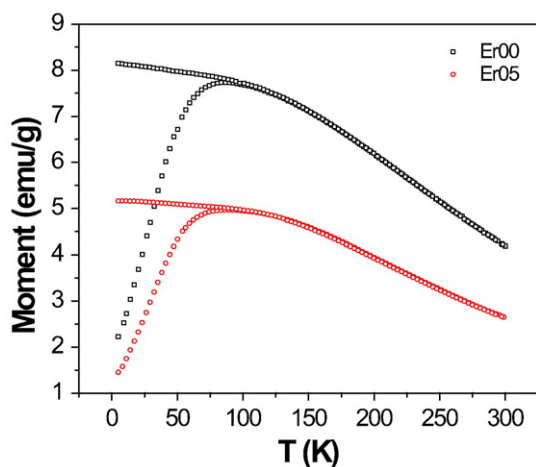

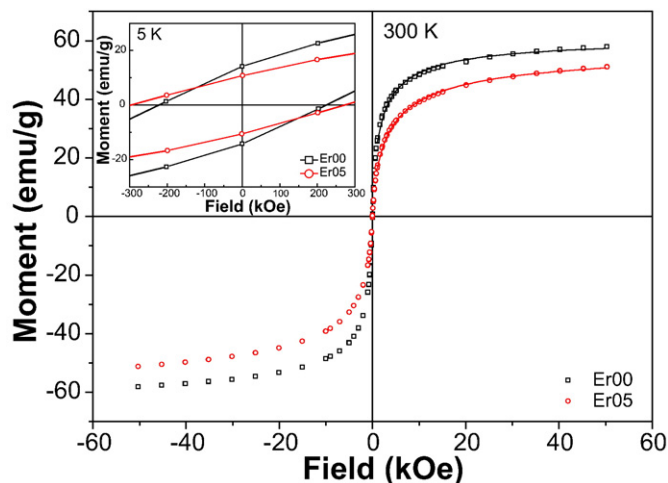**Fig. 4.** *ZFC-FC* curves for Er00 and Er05 MNPs, measured in 100 Oe.

Fig. 5. Hysteresis of Er00 and Er05 MNPs at 300 K. Lines represent weighted Langevin fits. Coercivity values at 5 K can be seen in the inset.

30 min after injection. Samples of blood and organs of interest were excised and weighed, then tissues were homogenized (Bio Spec Products, Inc., Bartlesville, USA) and diluted to a final volume of 5 ml with water to reach identical geometry and similar probe density. The percentage of injected dose (%ID/g) per gram of organ was calculated by comparing the activities with appropriate standards for injected dose (ID). The data are presented as average ± standard deviation from each group.

2.7. Elemental analysis by ICP-MS

Digestion of the samples for ICP measurements was performed on an Advanced Microwave Digestion System (ETHOS 1, Milestone, Italy) using a HPR-1000/10S high pressure segmented rotor. Pressure-resistant PTFE vessels (volume 100 ml) which were equipped with QS-50 Quartz inserts were used. This type of vessel permitted a maximum temperature of 240 °C and a maximum pressure of 100 bar to be applied. Sample digestion was performed as follow: whole organs of Wistar rats for biodistribution studies or zebrafish in case of ecotoxicity analysis were precisely weighed and mixed in quartz inserts with 5 ml HNO$_3$ (65%, Suprapure®, Merck, Germany) and then heated with microwave energy. The temperature was controlled with a predetermined power program. Digestion was conducted for 20 min at a constant temperature of 200 °C, with a prior warm-up linearly over 10 min to 200 °C. After total mineralisation and cooling to room temperature and without filtration, the solutions were diluted to a fixed volume in 10 ml volumetric flasks with ultra-pure water (Barnstead™ GenPure™ Pro, Thermo Scientific, Germany) with a conductivity of 0.055 μS/cm. The content of Er in digested sample solutions was determined by ICP-MS using an iCAP Qc ICP-MS (Thermo Scientific, Bremen, Germany) spectrometer with the operational software Qtegra. For Er determination, the spectrometer was adjusted for optimal performance in standard mode using the supplied auto tune protocols. The ICP-MS spectrometer was tuned using the solution TUNE B iCAPQ (1 μg/l of each: Ba, Bi, Ce, Co, In, Li, U), provided by the manufacturer (Thermo Scientific, Germany). Reference standard solutions for spectrometer calibration were prepared on the basis of the certified Semi quantitative Standard 1,

Table 2
Values of the M$_S$ and average diameter from weighted Langevin fit, TEM picture analysis and XRD refinement.

Sample	M_S^{room} (emu/g)	d_{Lang} (nm)	D_{TEM} (nm)	D_{XRD} (nm)
Er00	60.9 (2)	7 (4)	7 (2)	6.5 (7)
Er05	57.3 (2)	6 (3)	6 (1)	5.3 (4)

Table 3
Cytotoxic activity of naked Fe_3O_4 and Er05 MNPs on human lung fibroblasts and melanoma cell line expressed as IC_{50} values (μg/ml). IC_{50} values correspond to nanoparticle concentrations which inhibited 50% of cell growth during 48 h of treatment (mean ± SD).

MNP type	*MRC5* (lung fibroblasts)	*A375* (melanoma)
Naked Fe_3O_4	50 ± 4	20 ± 2
Er05	45 ± 6	150 ± 9

Table 4
Results of ICP-MS measurements: masses of MNPs in 1 g zebrafish and in 3 ml ISO water were shown.

Sample	Mass of MNPs calculated by measuring Er concentration (μg)
Er05 - zebrafish (50 μg/ml)	19.51
Er05 - ISO water (50 μg/ml)	76.20

Specpure® (Alfa Aesar GmbH & Co KG, Germany). Er determinations were done measuring two stable naturally occurring erbium isotopes, [166]Er and [167]Er, and the average values were used for further calculations. The limit of quantitation (LOQ) for erbium was determined to be 11 ng/l.

3. Results and discussion

3.1. Structure and microstructure analysis

Analysis of collected synchrotron XRD data showed that Er00 and Er05 crystallized in the *S.G. Fd$\overline{3}$m* and spinel structure type (Fig. 1). Structural modeling of the PDF data was carried out using the *PDFFIT2* program operated under the *PDFGui* platform using *S.G. Fd$\overline{3}$m* and spinel structure type. Er was assumed to occupy an octahedral 16d position within the spinel structure type. The Er content could not be independently verified for the Er-containing materials due to inter-parameter correlations within the modeling protocols used, so the Er content was considered to be the nominal Er-concentration and octahedral site occupancy. However, the presence of Er in the spinel structure was seen through small but observable changes in the lattice parameter of the spinel phase, which did not depend on the unit cell content. The lattice parameter of the spinel lattice depends on the complex interplay between the size of the ions and their distribution. Ionic radii for octahedral (VI) coordination are $Fe^{3+}(VI) = 0.645$ Å, while $Er^{3+}(VI) = 0.89$ Å [20]. Further verification of the presence of Er on the octahedral spinel sites originated from the increased isotropic displacement parameters of octahedral sites and oxygen sublattices, which were enlarged for the Er05 sample as compared to the Er00 sample. Final fits of PDF data are shown in Fig. 2. Small discrepancies between the model and the data in the low-*r* part of the PDF were consistently seen in both materials studied, and are likely attributable to surface effects as well as those of strain related to the finite particle size. Exploring these structural effects in greater detail is beyond the scope of this study.

Structural parameters resulting from the PDF refinements for the principal spinel phase, obtained over the 1.5 Å–50 Å fitting range, are summarized in Table 1.

The microstructure of the MNPs was further examined by TEM analysis. TEM images (Fig. 3) of both MNP types were analyzed using image processing software, Image J [21]. Results of the particle counts are given in the insets. Both histograms resemble log-normal size distributions. Average diameters deduced from the count data were 7(2) and 6(1) nm, for Er00 and Er05, respectively. In comparison with the X-ray analysis, crystallite size was close to the size of the particles. This indicated that the materials were indeed MNPs, were comprised of single crystallites, and were nearly spherical in shape according to the morphological analysis conducted.

3.2. Magnetic behavior

Fig. 4 shows *ZFC-FC* curves for both MNP types. Both Er00 and Er05 exhibited behavior typical for superparamagnetic samples, with maximum magnetization around 90 K and overlapping *ZFC* and *FC* curves at higher temperatures. The slight rise of the *FC* curves with temperature decreases below the maximum points to the presence of interparticle interactions, which is expected for powder samples [22].

Hysteresis curves for both MNP types at 5 K and 300 K are presented in Fig. 5. At 5 K, samples had a coercive field around 200 Oe, while it shrank to below 10 Oe at 300 K. Clearly, *SQUID* labels both MNP types as superparamagnetic at 300 K. A weighted Langevin fit was employed in order to deduce the magnetization saturation (M_S) at 300 K and average size of particles. A log-normal particle size distribution,

$$g_n(d, \sigma, D) = \frac{1}{\sqrt{2\pi}\sigma\frac{D}{d}} \exp\left[-\frac{\ln\left[\frac{D}{d}\right]^2}{2\sigma^2}\right], \quad (1)$$

was used. Here, *d* and *σ* represent coefficients of the log-normal distribution, and *D* is the diameter of the particle. The complete weighted
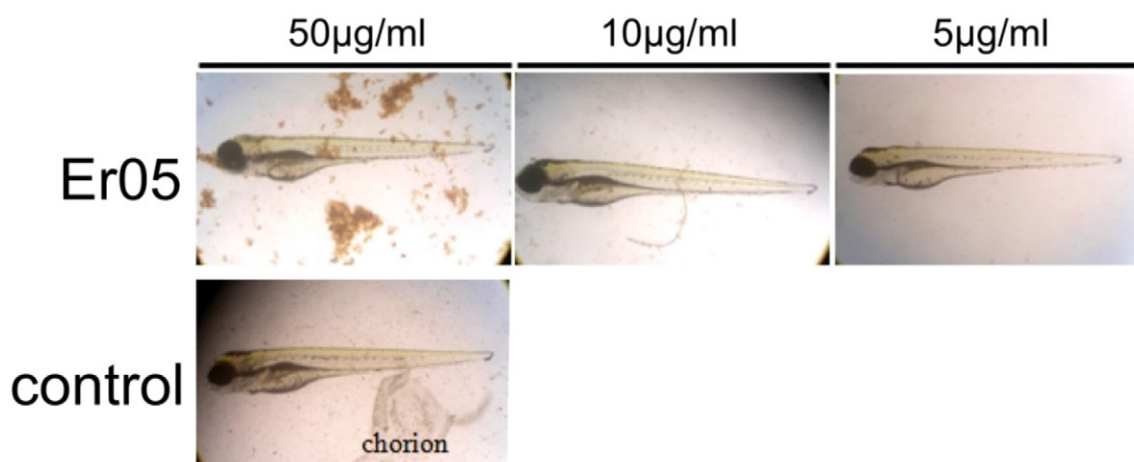

Fig. 6. Morphology of the zebrafish (*Danio rerio*) embryos 96 h after treatment with three concentrations ofEr05 MNPs.
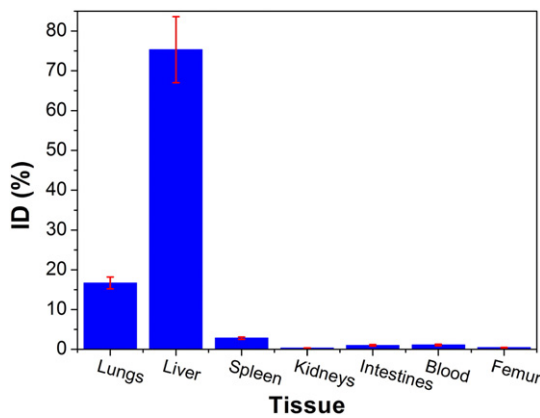
Fig. 7. Biodistribution of ^{90}Y-labeled Er05 MNPs in rats using the radiotracer technique.

Langevin function took the form:

$$M(B) = M_s \int g_n(d, \sigma, D) \left(coth\left(\frac{M_s \rho 1/6\pi D^3 B}{kT}\right) - \frac{kT}{M_s \rho 1/6\pi D^3 B} \right) dD. \quad (2)$$

Particles were approximated as spheres with volume $V = 1/6 \pi D^3 V = 1/6\pi D^3$. Density ρ was set to 5300 kg m^{-3}Řk gm^{-3}, which corresponds to the magnetite bulk value, kT represents thermal energy, and B is the magnetic flux density. Fitting parameters were d, σ and M_S. Expected MNP diameters d_{Lang} and standard deviations std were calculated using:

$$d_{Lang} = \int g_n(d, \sigma, D) D dD \text{ and } std$$
$$= \sqrt{\int g_n(d, \sigma, D) D^2 dD - (\int g_n(d, \sigma, D) D dD)^2}, \quad (3)$$

Final results are presented in Table 2. Derived average diameters showed excellent agreement with results of the TEM analysis and values acquired from XRD refinement.

Binary ferrites (MFe$_2$O$_4$; M= Zn, Mn, Fe, Ni, Cr) and magnetite have often been doped/substituted with RE in order to improve their physical properties due to the large anisotropy of RE^{3+} moments [23] or structural defects induced by RE ions in the parent compound [24]. However, the effects of RE substitution in magnetite and ferrites are still not well understood. Our observed M$_S$ value was slightly smaller in Er-substituted Fe$_3$O$_4$ MNPs (Er05) than in pure Fe$_3$O$_4$ MNPs (Er00) (Table 2). Consequently, from the magnetic
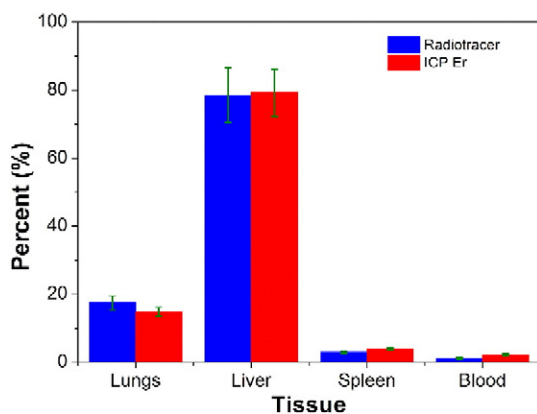

Fig. 8. Comparative biodistribution of ^{90}Y-labeled Er05 MNPs using the radiotracer technique and ICP-MS. Radiotracer technique results for four tissues were scaled to 100% in order to compare them with ICP-MS results.

point of view, the Er05 MNPs are deemed suitable for medical applications.

3.3. Cytotoxicity study

The cytotoxicity of Er05 MNPs was compared with that of naked Fe$_3$O$_4$ MNPs using two cell lines. Both MNP types exhibited cytotoxic effects on both cell lines when applied in high concentrations (500 µg/ml; data not shown). The IC$_{50}$ values for Fe$_3$O$_4$ and Er05 MNPs were comparable in the case of normal lung fibroblasts, but the selectivity towards the melanoma cell line was different (Table 3). Internalization and distribution of the Er05 MNPs was consistently good and even throughout the cell lawn (Fig. S1). Fe$_3$O$_4$ MPNs were 2.5 times more toxic towards the melanoma cell line, while Er05 MNPs were 3 times less toxic towards the same cell line. This could be due to the specific microenvironment (slight pH differences) that may be present in the cancer cell line.

3.4. Ecotoxicity study: embryotoxic influence of Er05 MNPs on zebrafish (Danio rerio)

Zebrafish embryos were used to test the potential toxic effects of Er05 MNPs. Zebrafish (Danio rerio) are an excellent in vivo model for physiologically relevant whole-organism and behavior-based screening, which cannot be achieved with conventional in vitro systems [25]. Zebrafish embryos were developed in suitable medium containing 5 µg/ml, 10 µg/ml or 50 µg/ml of MNPs, in 3 ml volumes.

MNP suspensions exerted no toxic effects on zebrafish embryos, even at the highest concentration examined (50 µg/ml). At this concentration, neither embryo mortality, nor any developmental defect, nor hatching delay was detected (Fig. 6). Furthermore, no signs of cardio- or neurotoxicity were observed (Fig. 6).

Nanoparticle aggregation was observed after 72 h incubation at 50 µg/ml (Fig. 6), and therefore, in order to rule out the possibility that the MPNs had aggregated and did not have the chance to exert harmful effect on zebrafish embryogenesis, ICP-MS analysis of treated and washed embryos was conducted. Special care was taken to avoid chorion material in the sample preparation for the ICP-MS analysis. Uptake of MNPs by zebrafish embryos was studied by both ICP-MS techniques. Results are presented in Table 4.

The mass of Er05 MPNs in zebrafish was calculated by measuring Er masses using ICP-MS. ICP-MS revealed that MNPs were internalized in the embryos treated with them. Consequently, it was concluded that the MPNs, which had displayed a slight antiproliferative effect on lung fibroblast and melanoma cell lines, were not toxic for zebrafish embryos indicating their biosafety and potential application.

3.5. Radiolabeling of Er05MNPs with ^{90}Y and in vitro stability studies

The radiotracer method, readily and efficiently used in the MNP biodistribution study, firstly required optimization of the radiolabeling itself, to ensure that modification of the MNPs did not occur, which would have let to misinterpretation of the biodistribution results.

The highest radiolabeling yield for ^{90}Y-labeled Er05 MNPs, achieved under the experimental conditions previously described, was 89%, as detected by ITLC-SG and 92% determined by magnetic precipitation. Even a small amount of free ^{90}Y^{3+} present in the suspension could rapidly accumulate in bone, thus giving false results, and therefore, the magnetite precipitate was intensely washed several times with deionizied water to remove excess, unbound ^{90}Y^{3+}.

After 72 h of incubation, ^{90}Y-labeled Er05 MNPs demonstrated very high stability in saline and human serum (94.1% and 92.7%, respectively), which can be attributed to the strong binding of ^{90}Y^{3+} by negatively charged carboxylate groups present on the surface of Er05 MNPs. At physiological pH, agglomeration of the

radiolabeled Er05 MNPs was not observed during 3 days. Carboxylic groups on the surface of ^{90}Y-labeled Er05 MNPs provided significant electrostatic repulsion between the nanoparticles, resulting in excellent solubility and stability of ^{90}Y-labeled Er05 MNPs in aqueous solution as well as in physiological saline, human serum and *in vivo*.

3.6. Comparative biodistribution study of ^{90}Y-labeled Er05 MNPs by radio-tracer technique and ICP-MS

The biodistribution of ^{90}Y-labeled Er05 MNPs was examined 30 minutes after intravenous injection in the animal model, healthy male Wistar rats, by two methods: radiotracer and ICP-MS. Using the radio-tracer method, accumulation of MNPs in organs was quantified by measuring the radioactivity of bound radionuclides, while for the ICP-MS method, Er in the nanoparticle cores was measured. Radioactivity measurements of dissected tissues showed accumulation of ^{90}Y-labeled Er05 MNPs mostly in the liver (75.33% ID), followed by lungs (16.70% ID) and spleen (2.83% ID), while the remaining ^{90}Y-labeled Er05 MNPs were spread across the rest of the body (Fig. 7). Such distribution is expected because nanoparticles of this size rapidly clear from the systemic circulation, predominantly by action of the liver and spleenic macrophages [26,27]. An insignificant amount of radioactivity (0.44% ID) was detected in femur, a target organ for free ^{90}Y, indicating that ^{90}Y was tightly attached to the MNPs. Lungs, liver, spleen and blood were selected for further ICP analysis. Measured concentrations of Er in prepared tissue samples were (in μg/organ): lung (49.32), spleen (13.13), liver (264.01) and blood (1.07 μg/ml). Results of the radiotracer technique and ICP-MS spectroscopy are presented in Fig. 8. In order to compare the results of these two methods, the percentages acquired by the radiotracer technique for four selected tissues were scaled so that their sum equaled 100%. *In vivo* stability of ^{90}Y-labeled Er05 MNPs was proved by *in vivo* retention of radioactivity in the liver, as well as by the constant amount of Er detected over time. This study demonstrates the unique advantages of the radiotracer technique: high sensitivity and simplicity. Although the ICP method enables detection of trace amount of elements in animal bodies, this measurement method suffers from low specificity due to inability to distinguish between endogenous elements and MNPs. The ICP-MS method using Er as a tracer proved to be a reliable method for quantifying accumulation of radiolabeled MNPs in blood and organs *in vivo*. Finally, our results show very good agreement between these methods and their combined application in our biodistribution study of ^{90}Y-labeled Er05 MNPs, providing additional credibility to these results.

4. Conclusion

The $Fe_{3-x}Er_xO_4$ (x = 0 and 0.05) citric acid coated nanoparticles synthesized using the modified Massart's method displayed high magnetic moments. Cytotoxicity analysis of Er05 citric acid coated and naked Fe_3O_4 MNPs indicated that the surface of the MNPs was non-toxic, while the toxicological test using zebrafish embryos pointed to the non-toxicity of the cores of the MNPs produced. In addition, ICP-MS showed that the MNPs entered the embryos and normal embryonal development ensued, so the particles are indeed non-toxic *in vivo*. The combination of the investigated toxicology test and the ICP-MS technique is an effective, fast, low cost and reliable method for *in vivo* toxicological studies.

MNPs labeled with radionuclide yttrium, ^{90}Y-Er05 MNPs, were obtained in a high radiolabeling yield and exhibit high *in vitro* and *in vivo* stability. Two complementary techniques, radiotracer and ICP-MS, supported each other, showing similar results of uptake in different *in vivo* rat tissues. Combined application of these methods should greatly enhance the reliability of studies into the biodistribution of MNPs in *in vivo* organs and tissues, and could be readily used for investigating organ and/or tissue distribution of MNPs potentially delivering a range

of therapeutics. Additionally, biocompatible Er05 MNPs labeled with ^{90}Y are promising candidates for combined radionuclide-hyperthermia therapy.

Appendix A. Supplementary data

Supplementary data to this article can be found online at http://dx.doi.org/10.1016/j.msec.2017.02.023.

References

[1] A.-H. Lu, E.L. Salabas, F. Schuth, Magnetic nanoparticles: synthesis, protection and application, Angew. Chem. Int. Ed. Eng. 46 (2007) 1222.
[2] L. Cao, Y. Liang, F. Zhao, X. Zhao, Z. Chen, Chelerythrine and Fe_3O_4 loaded multi-walled carbon nanotubes for targeted cancer therapy, J. Biomed. Nanotechnol. 12 (2016) 1312.
[3] M. Colombo, S. Carregal-Romero, M.F. Casula, L. Gutierrez, M.P. Morales, I.B. Bohm, J.T. Heverhagen, D. Prosperi, W.J. Parak, Biological applications of magnetic nanoparticles, Chem. Soc. Rev. 41 (2012) 4306.
[4] F. Liu, Y. Hou, S. Gao, Exchange-coupled nanocomposites: chemical synthesis, characterization and applications, Chem. Soc. Rev. 43 (2014) 8098.
[5] R. Hao, R. Xing, Z. Xu, Y. Hou, S. Gao, S. Sun, Synthesis, functionalization, and biomedical applications of multifunctional magnetic nanoparticles, Adv. Mater. 22 (2010) 2729.
[6] G.F. Goya, V. Grazu, M.R. Ibarra, Magnetic nanoparticles for cancer therapy, Curr. Nanosci. 4 (2008) 1.
[7] P. Tartaj, in: H.S. Nalwa (Ed.), Encyclopedia of Nanoscience and Nanotechnology, Vol. 6, American Scientific Publishers, USA 2004, pp. 822–831.
[8] A. Ruiz, Y. Hernandez, C. Cabal, E. Gonzalez, S. Veintemillas-Verdaguer, E. Martınez, M.P. Morales, Biodistribution and pharmacokinetics of uniform magnetite nanoparticles chemically modified with polyethylene glycol, Nanoscale 5 (2013) 11400.
[9] S. Smulders, A. Ketkar-Atre, K. Luyts, H. Vriens, S.D. Nobre, C. Rivard, K. Van Landuyt, S. Baken, E. Smolders, L. Golanski, M. Ghosh, J. Vanoirbeek, U. Himmelreich, P.H. Hoet, Body distribution of SiO_2-Fe_3O_4 core-shell nanoparticles after intravenous injection and intratracheal instillation, Nanotoxicology 10 (2016) 567.
[10] M. Varna, Ph. Ratajczak, I. Ferreira, C. Leboeuf, G. Bousquet, A. Janin, *In vivo* bistribution of inorganic nanoparticles in preclinical models, J. Biomater. Nanobiotechnol. 3 (2012) 269.
[11] H.W. Zhao, S.H. Wang, S.N. Nguyen, S.G. Elci, I.A. Kaltashov, Evaluation of nonferrous metals as potential *in vivo* tracers of transferrin-based therapeutics, J. Am. Soc. Mass Spectrom. 27 (2016) 211.
[12] S.H. Crayton, D.R. Elias, A.A. Zaki, Z. Cheng, A. Tsourkas, ICP-MS analysis of lanthanide-doped nanoparticles as a non-radiative, multiplex approach to quantify biodistribution and blood clearance, Biomaterials 33 (2012) 1509.
[13] M. Vucinic-Vasic, E.S. Bozin, A. Kremenovic, G. Stojanovic, U. Kozmidis-Luburic, M. Abeykoon, B. Jancar, A. Meden, L. Bessais, B. Antic, Thermal evolution of cation distribution/crystallite size and their correlation with magnetic state of Yb substituted Zn-ferrite nanoparticles, J. Phys. Chem. C 117 (2013) 12358.
[14] C. Tang, J. Edelstein, J.L. Mikitsh, E. Xiao, A.H. Hemphill II, R. Pagels, A.-M. Chackoand, R. Prud'homme, Biodistribution and fate of core-labeled (125) I polymeric nanocarriers prepared by flash nanoprecipitation (FNP), J. Mater. Chem. B 4 (2016) 2428.
[15] M. Radović, S. Vranješ-Đurić, N. Nikolić, D. Janković, G.F. Goya, T. Torres, P. Calatayud, I. Bruvera, R. Ibarra, V. Spasojević, B. Jančar, B. Antić, Development and evaluation of ^{90}Y-labeled albumin microspheres loaded with magnetite nanoparticles for possible applications in cancer therapy, J. Mater. Chem. 22 (2012) 24017.
[16] R. Massart, Preparation of aqueous magnetic liquids in alkaline and acidic media, IEEE Trans. Magn. 17 (1981) 1247.

[17] M.B. Hansen, S.E. Nielsen, K. Berg, Re-examination and further development of a precise and rapid dye method for measuring cell growth/cell kill, J. Immunol. Methods 119 (1989) 203.

[18] OECD, Test No. 236: Fish Embryo Acute Toxicity (FET) Test, OECD Publishing, Paris, 2013.

[19] M. Radovic, M.P. Calatayud, G.F. Goya, M.R. Ibarra, B. Antic, V. Spasojevic, N. Nikolic, D. Jankovic, M. Mirkovic, S. Vranjes-Duric, Preparation and in vivo evaluation of multifunctional ^{90}Y-labeled magnetic nanoparticles designed for cancer therapy, J. Biomed. Mater. Res. A103 (2015) 126.

[20] R.D. Shannon, C.T. Prewitt, Effective ionic radii in oxides and fluorides, Acta Crystallogr. B 25 (1969) 925.

[21] W.S. Rasband, ImageJ, U. S. National Institutes of Health, Bethesda, Maryland, USA, 1997–2014http://imagej.nih.gov/ij/.

[22] L.D. Tung, V. Kolesnichenko, G. Caruntu, D. Caruntu, Y. Remond, V.O. Golub, C.J. O'connor, L. Spinu, Annealing effects on the magnetic properties of nanocrystalline zinc ferrite, Physica B 319 (2002) 116.

[23] R.V. Upadhyay, A. Gupta, C. Sudakar, K.V. Rao, K. Parekh, R. Desai, R.V. Mehta, Effect of rare-earth Ho ion substitution on magnetic properties of Fe_3O_4 magnetic fluids, J. Appl. Phys. 99 (2006) 08M906 3pp.

[24] S.S. Laha, R. Regmi, G. Lawes, Structural origin for low-temperature relaxation features in magnetic nanoparticles, J. Phys. D. Appl. Phys. 46 (2013) 325004.

[25] Y. Peng, J. Li, Y. Sun, J.Y.-W. Chan, D. Sheng, K. Wang, P. Wei, P. Ouyang, D. Wang, S.M.Y. Lee, G.-C. Zhou, SAR studies of 3,14,19-derivatives of andrographolide on anti-proliferative activity to cancer cells and toxicity to zebrafish: an *in vitro* and *in vivo* study, RSC Adv. 5 (2015) 22510.

[26] S.M. Moghimi, A.C. Hunter, J.C. Murray, Nanomedicine: current status and future prospects, FASEB J. 19 (2005) 311.

[27] H. Arami, A. Khandhar, D. Liggitt, K.M. Krishnan, In vivo delivery, pharmacokinetics, biodistribution and toxicity of iron oxide nanoparticles, Chem. Soc. Rev. 44 (2015) 8576.

Pressure tuning of structure, superconductivity, and novel magnetic order in the Ce-underdoped electron-doped cuprate T′ -Pr$_{1.3-x}$La$_{0.7}$Ce$_x$CuO$_4$ ($x = 0.1$)

Z. Guguchia,[1,2,3,*] T. Adachi,[4] Z. Shermadini,[2] T. Ohgi,[5] J. Chang,[6] E. S. Bozin,[3] F. von Rohr,[6] A. M. dos Santos,[7]
J. J. Molaison,[7] R. Boehler,[7,8] Y. Koike,[5] A. R. Wieteska,[1] B. A. Frandsen,[9] E. Morenzoni,[2] A. Amato,[2] S. J. L. Billinge,[3,10]
Y. J. Uemura,[1] and R. Khasanov[2]

[1]*Department of Physics, Columbia University, New York, New York 10027, USA*
[2]*Laboratory for Muon Spin Spectroscopy, Paul Scherrer Institute, CH-5232 Villigen PSI, Switzerland*
[3]*Condensed Matter Physics and Materials Science Department, Brookhaven National Laboratory, Upton, New York 11973, USA*
[4]*Department of Engineering and Applied Sciences, Sophia University, 7-1 Kioi-cho, Chiyoda-ku, Tokyo 102-8554, Japan*
[5]*Department of Applied Physics, Tohoku University, 6-6-05 Aoba, Aramaki, Aoba-ku, Sendai 980-8579, Japan*
[6]*Physik-Institut der Universität Zürich, Winterthurerstrasse 190, CH-8057 Zürich, Switzerland*
[7]*Neutron Sciences Directorate, Oak Ridge National Laboratory, Oak Ridge, Tennessee 37831, USA*
[8]*Carnegie Institution of Washington, Washington, DC 20005, USA*
[9]*Materials Science Division, Lawrence Berkeley National Laboratory, Berkeley, California 94720, USA*
[10]*Department of Applied Physics and Applied Mathematics, Columbia University, New York, New York 10027, USA*

High-pressure neutron powder diffraction, muon-spin rotation, and magnetization studies of the structural, magnetic, and the superconducting properties of the Ce-underdoped superconducting (SC) electron-doped cuprate system with the Nd$_2$CuO$_4$ (the so-called T′) structure T′-Pr$_{1.3-x}$La$_{0.7}$Ce$_x$CuO$_4$ with $x = 0.1$ are reported. A strong reduction of the in-plane and out-of-plane lattice constants is observed under pressure. However, no indication of any pressure-induced phase transition from T′ to the K$_2$NiF$_4$ (the so-called T) structure is observed up to the maximum applied pressure of $p = 11$ GPa. Large and nonlinear increase of the short-range magnetic order temperature T_{so} in T′-Pr$_{1.3-x}$La$_{0.7}$Ce$_x$CuO$_4$ ($x = 0.1$) was observed under pressure. Simultaneous pressure causes a nonlinear decrease of the SC transition temperature T_c. All these experiments establish the short-range magnetic order as an intrinsic and competing phase in SC T′-Pr$_{1.3-x}$La$_{0.7}$Ce$_x$CuO$_4$ ($x = 0.1$). The observed pressure effects may be interpreted in terms of the improved nesting conditions through the reduction of the in-plane and out-of-plane lattice constants upon hydrostatic pressure.

I. INTRODUCTION

One of the most important unresolved problems in high-transition-temperature (high-T_c) superconductors [1] is the determination of the microscopic state when charge carriers, either holes [1] or electrons [2–7], are introduced to the CuO$_2$ planes of their insulating long-range antiferromagnetically ordered parent compounds [8]. One school of thought suggests that the doped charge carriers segregate into inhomogeneous patterns, such as stripes (spin and charge orders), to allow the antiferromagnetic (AFM) regions to survive [9]. In this picture, the observed quasi two-dimensional (2D) incommensurate spin density wave (SDW) in hole-doped high-T_c superconductors, such as La$_{2-x}$Sr$_x$CuO$_4$ [10–15] and La$_2$CuO$_{4+\delta}$ [16], is due to remnants of the AFM insulating phase that compete with superconductivity [17,18]. While the charge density wave (CDW) has emerged as a universal feature of hole-doped (*p*-type) cuprates [10,19–24], observation of charge ordering in the electron-doped (*n*-type) cuprate system Nd$_{2-x}$Ce$_x$CuO$_4$ (NCCO) with $x = 0.14 - 0.15$ was reported only very recently [25]. Note that in *n*-type cuprates there are only a limited number of comprehensive studies on SDW/CDW order and their interplay with superconductivity and structural properties [25–31], underscoring a need for further experimental studies of *n*-type cuprates.

Pr$_{1.3-x}$La$_{0.7}$Ce$_x$CuO$_4$ is an *n*-type cuprate system that has recently been the focus of increased experimental investigation. The representations of two possible crystal structures, T′ and T, for Pr$_{1.3-x}$La$_{0.7}$Ce$_x$CuO$_4$ are shown in Figs. 1(a) and 1(b), respectively. The T′ structure is $I4/mmm$, Nd$_2$CuO$_4$-type and the T structure is $I4/mmm$, K$_2$NiF$_4$ type. Cuprates with T′ crystal structure have no apical oxygen O$_{ap}$ above or below the copper ions of the CuO$_2$ plane [30], as shown in Fig. 1(a). The interesting characteristics of the electron-doped T′ cuprates is that as-grown samples contain excess oxygen at the apical site. The apical oxygen is believed to induce disorder of the electrostatic potential in the CuO$_2$ plane, leading to the destruction of Cooper pairs [32,33]. Therefore, completely removing the excess oxygen from as-grown samples is crucial to unveil intrinsic properties of the T′ cuprates. Interestingly, in T′-Nd$_{2-x}$Ce$_x$CuO$_4$ thin films, superconductivity is achieved at any doping x from 0.00 to 0.20 [34] by oxygen reduction annealing. This was claimed to be generic to T′ cuprates with no apical oxygen. The role of the reduction process in the superconductivity of electron-doped cuprates has been a long-standing unsolved problem. Although the reduction annealing process is widely believed to involve removal of the apical oxygen, Raman, infrared transmission, and ultrasound studies on NCCO and Pr$_{2-x}$Ce$_x$CuO$_4$ (PCCO) suggest that the reduction process removes the oxygen in the CuO$_2$ plane [35,36] at high Ce doping ($x > 0.1$) and the apical oxygen at low Ce doping. In this case, the in-plane oxygen defect created by the reduction is believed to be
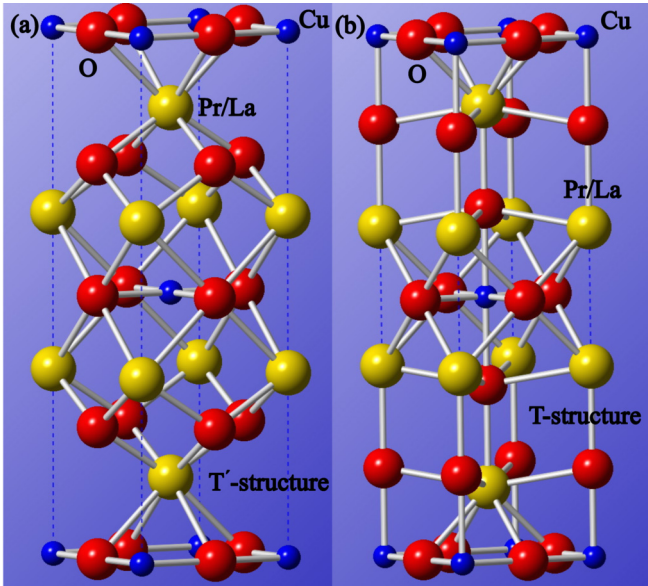
_____
[*]zg2268@columbia.edu

FIG. 1. Representations of both T′ (a) and T structures (b) of $Pr_{1.3-x}La_{0.7}Ce_xCuO_4$. T′ structure is $I4/mmm$, Nd_2CuO_4-type and T structure is $I4/mmm$, K_2NiF_4-type.

FIG. 2. The long-range AFM, the short-range magnetic, and the superconducting transition temperatures of T′-$Pr_{1.3-x}La_{0.7}Ce_xCuO_4$ ($x = 0.1$) as a function of the sample annealing temperature in vacuum. The arrow indicates the sample studied in the present work [26].

responsible for superconductivity by destroying the long-range antiferromagnetism and increasing the mobility of charge carriers. It was also shown [37] that the microscopic process of oxygen reduction repairs Cu deficiencies in the as-grown materials and creates oxygen vacancies in the stoichiometric CuO_2 planes, effectively reducing disorder and providing itinerant carriers for superconductivity. So far, there is no consensus as to which of the above-mentioned scenarios is relevant to explain the reduction annealing process.

Recent angle-resolved photoemission spectroscopy (ARPES) experiments [38] in superconducting (SC) single crystals of Ce-underdoped T′-$Pr_{1.3-x}La_{0.7}Ce_xCuO_4$ ($x = 0.1$) with the SC transition temperature $T_c = 27$ K, prepared through the improved reduction annealing [26,39], revealed the complete suppression of the AFM pseudogap at the "hot spots" [38], i.e., the intersecting points of the paramagnetic Fermi surface and the AFM Brillouin-zone boundary. This suggests that through improved annealing procedure, the long-range AFM phase is removed from the underdoped regime (see Fig. 2). The question arises as to whether the magnetic order is fully suppressed in improved annealed T′-$Pr_{1.3-x}La_{0.7}Ce_xCuO_4$ or it exhibits short-range magnetic order which cannot be seen by ARPES, since it cannot directly probe magnetism. In general, a fundamental question in electron-doped cuprates is whether SDW, CDW, or stripe phases [40] are emerging together with superconductivity as observed in the hole-doped cuprates. Interestingly, the presence of short-range magnetic order below ∼50 K in the SC T′-$Pr_{1.3-x}La_{0.7}Ce_xCuO_4$ ($x = 0.1$) was demonstrated using muon-spin rotation (μSR) experiments, implying that the reduction annealing gives rise to the change of the long-range AFM order to a short-range magnetic order [26]. This is schematically demonstrated in Fig. 2, where we show the dependence of the magnetic and SC transition temperatures as a function of the sample annealing temperature. Driving the long-range AFM state to short-range
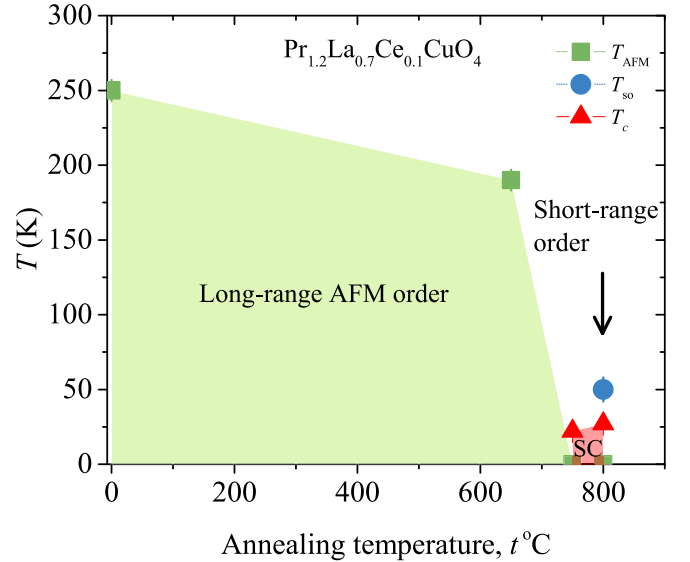
magnetic state by annealing was also previously reported for $Pr_{0.88}LaCe_{0.12}CuO_4$ [41]. Understanding the nature of this short-range magnetic order (i.e., whether it is intrinsic and related to the similar SDW, CDW, or stripelike order, as observed in hole-doped cuprates) and its relation to superconductivity is a main motivation of this work.

An important experimental parameter to tune the physical properties of the system is the hydrostatic pressure. In n-type cuprates, only a limited number of pressure effects studies exist [42–47]. To the best of our knowledge no pressure effect studies of the AFM order in n-type cuprates have been reported so far.

In this paper, we report on the results of high-pressure μSR [48,49], neutron powder diffraction, and ac and dc susceptibility experiments for polycrystalline samples of the improved reduction annealed T′-$Pr_{1.3-x}La_{0.7}Ce_xCuO_4$ ($x = 0.1$). Remarkably, substantial increase of the short-range magnetic order temperature T_{so} in T′-$Pr_{1.3-x}La_{0.7}Ce_xCuO_4$ ($x = 0.1$) was observed, providing an example of a giant pressure effect on magnetism in electron-doped cuprates. We also found that the pressure effects have opposite signs for T_{so} and T_c, providing direct evidence for the competition between superconductivity and short-range magnetic order in this system. The pressure experiments strongly suggest that the short range magnetic order is an intrinsic part of the phase diagram and is controlled by the Fermi surface properties of T′-$Pr_{1.3-x}La_{0.7}Ce_xCuO_4$ ($x = 0.1$). Thus, a competing phase to superconductivity in T′-$Pr_{1.3-x}La_{0.7}Ce_xCuO_4$ ($x = 0.1$) has been demonstrated.

II. EXPERIMENTAL DETAILS

A. Sample preparation and characterization

The details of the synthesis of the polycrystalline samples of T′-$Pr_{1.3-x}La_{0.7}Ce_xCuO_4$ were reported previously

[26,39]. μSR experiments under pressure were performed at the General Purpose Decay-Channel (GPD) Spectrometer (μE1 beamline) of the Paul Scherrer Institute (Villigen, Switzerland). The low background General Purpose Surface-Muon (GPS) (πM3 beamline) instrument was used to study the system T'-$Pr_{1.3-x}La_{0.7}Ce_xCuO_4$ ($x = 0.1$) at ambient pressure. The pressure effects on the structural properties of T'-$Pr_{1.3-x}La_{0.7}Ce_xCuO_4$ ($x = 0.1$) were studied using time-of-flight neutron powder diffraction at the high-pressure diffractometer SNAP (Spallation Neutrons and Pressure, Beamline-3) at the Spallation Neutron Source (SNS) of the Oak Ridge National Laboratory. All measurements reported here were performed on samples from the same batch.

B. Pressure cells for μSR, neutron powder diffraction, and magnetization experiments

Pressures up to 2.3 GPa were generated in a double-wall piston-cylinder type of cell made of MP35N material, especially designed to perform μSR experiments under pressure [48,49]. As a pressure-transmitting medium Daphne oil was used. The pressure was measured by tracking the SC transition of a very small indium plate by ac susceptibility. The amount of the sample in the pressure cell was optimized and the fraction of the muons in the sample was approximately 40%.

In neutron powder diffraction experiments, pressures up to 11 GPa were generated in a diamond anvil cell (DAC) using large synthetic diamonds and a new anvil design based on conical anvil support [50], a new generation of large cell developed at the SNAP beamline [51]. The SNAP DAC was pressurized using an integrated gas-driven membrane setup.

ac susceptibility measurements were performed by using a homemade ac magnetometer with a measuring field $\mu_0 H_{AC} \approx 0.1$ mT and frequency $\nu = 96$ Hz. In order to keep the position of the sample unchanged during the series of ac susceptibility under pressure measurements, the excitation and the two pickup coils were wound directly on the cell. Note that a single-phase lock-in amplifier is used, which allows measurement of either an in-phase component (the real part of susceptibility) or out-of-phase component (the imaginary part of susceptibility). For this particular sample, the imaginary part of ac susceptibility was measured.

The dc susceptibility was measured under pressures up to 2.5 GPa by a superconducting quantum interference device (SQUID) magnetometer (Quantum Design MPMS-XL). Pressures were generated using DAC [52] filled with Daphne oil which served as a pressure-transmitting medium. The pressure at low temperatures was determined by detecting the pressure dependence of the SC transition temperature of Pb.

III. RESULTS

A. High-pressure neutron powder diffraction experiments

A previous high-pressure x-ray study up to 0.6 GPa in undoped Nd_2CuO_4 and optimally doped $Nd_{1.835}Ce_{0.165}CuO_4$ [44] showed a decrease of the lattice parameters under pressure. Higher pressure experiments showed that in the parent compounds Nd_2CuO_4 [45] and Pr_2CuO_4 [46] a T'-to-T structural transition takes place at 21.5 GPa and 15.1 GPa,
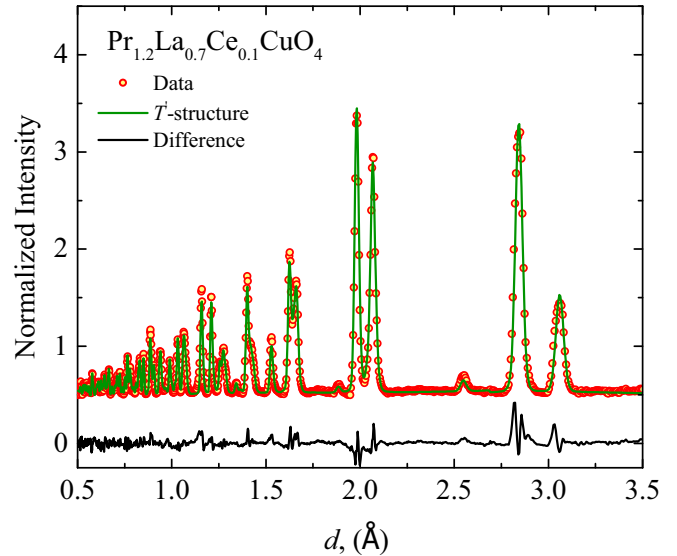
FIG. 3. Rietveld refinement of the neutron diffraction pattern for the T'-$Pr_{1.3-x}La_{0.7}Ce_xCuO_4$ ($x = 0.1$) at 300 K at ambient conditions. The observed, calculated, and difference plots are shown by solid circles, green solid line, and black solid line, respectively. Bragg reflections are compatible with space group $I4/mmm$, Nd_2CuO_4 type.

respectively. Recently, it was shown for $Nd_{1.835}Ce_{0.165}CuO_4$ [47] that the transformation of T' to T phase takes place at 2.7 GPa, i.e., at much lower pressure than for the parent compounds. This implies that the knowledge of the structural details of electron-doped cuprates under pressure are important in better understanding the pressure evolution of magnetic and superconducting properties. Below we show neutron diffraction data for the present Ce-underdoped electron-doped cuprate T'-$Pr_{1.2}La_{0.7}Ce_{0.1}CuO_4$ under pressure as high as $p = 11$ GPa.

The crystal structure of $Pr_{1.3-x}La_{0.7}Ce_xCuO_4$ ($x = 0.1$) at room temperature (RT) (see Fig. 3) was well refined through Rietveld refinements to the raw neutron diffraction data using the program GSAS-II [53], employing the tetragonal $I4/mmm$ space group (Nd_2CuO_4 type). An example of the refinement profile is shown in Fig. 3. The weighted fit residual is Rwp ≈ 2.8%, indicating a fairly good refinement. No obvious secondary phase, including the T-structural phase, can be detected, pointing to a pure T' phase in the studied $Pr_{1.3-x}La_{0.7}Ce_xCuO_4$ ($x = 0.1$) sample. Figure 4 shows the simulated Bragg peaks for the T and T' structures of $Pr_{1.3-x}La_{0.7}Ce_xCuO_4$ ($x = 0.1$). The crystal structure data for the simulations of T and T' structures are taken from the Refs. [46] and [54], respectively. The following lattice constants and the width parameters are used for the simulations: $a = b = 3.654(8)$Å, $c = 12.546(7)$Å, $u = 0.05$, $v = -0.06$, $w = 0.07$ for T structure, and $a = b = 3.9588(3)$Å, $c = 12.234(6)$Å, $u = 0.05$, $v = -0.06$, $w = 0.07$ for T' structure. There are obvious differences between the patterns, shown in Fig. 4, especially in the d-spacing range of 2.5–4 Å. In case of T structure, the high-intensity Bragg peaks (112), (110), and (101) as well as the much weaker (103) and (004) peaks are expected. These differences would make it possible to observe the transition between T' and T structures.
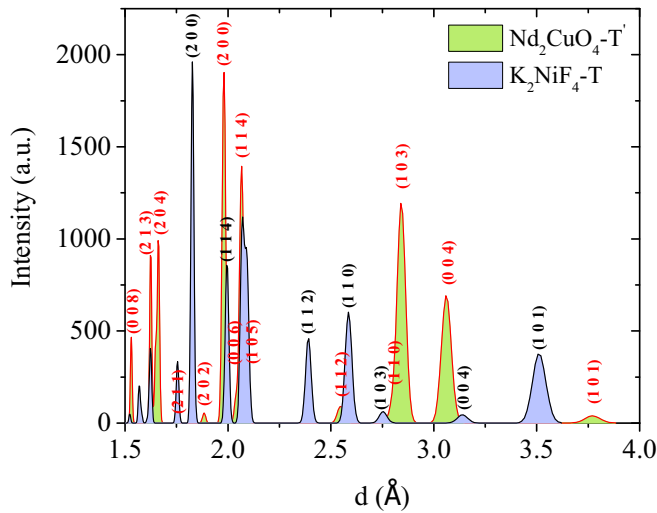
FIG. 4. Simulated Bragg peaks for the T and T$'$ structures, shown in the *d*-spacing range of 1.5–4 Å.

Figure 5(a) shows the evolution of the (112), (103), and (004) Bragg peaks from the T$'$ structure of

$Pr_{1.3-x}La_{0.7}Ce_xCuO_4$ ($x = 0.1$) measured at various pressures up to $p = 11$ GPa. We note that it is hard to achieve true ambient pressure conditions for the samples loaded to the DAC. The ambient pressure data shown in Fig. 3 is measured outside the cell. Then the sample was loaded and measured under pressures starting from 0.7 GPa and the data are shown in Fig. 5. A systematic shift of the peaks towards lower *d* spacing is observed under pressure, consistent with a monotonic reduction in the lattice constants. However, up to the maximum applied pressure of $p = 11$ GPa, there is no indication of the pressure-induced phase transition from T$'$ to T structure, as demonstrated by the simulated Bragg peaks from the T structure in Fig. 5(b). This points to the robustness of the T$'$ structure in $Pr_{1.3-x}La_{0.7}Ce_xCuO_4$ ($x = 0.1$) in the investigated pressure range. The (004) Bragg peaks are shown separately in Fig. 5(c). By fitting with a Gaussian function, drawn with the black solid lines through the data, the lattice constant *c* was estimated at various pressures. The pressure dependence of its relative shift $-\Delta c/c = (c(0)-c(p))/c(0)$ is shown in Fig. 5(d), showing the continuous decrease of the *c* axis under pressure. Using the value of *c* and the *d* spacing of the (103) Bragg peak, the lattice constant *a* was obtained. The pressure evolution of the relative change in the *a* axis $-\Delta a/a$ is shown in Fig. 5(d), revealing a similar linear pressure-induced reduction of the *a*

FIG. 5. (a) The (112), (103), and (004) Bragg peaks of T$'$-$Pr_{1.3-x}La_{0.7}Ce_xCuO_4$ ($x = 0.1$), recorded at various pressures up to $p = 11$ GPa. The data are corresponding to T$'$ structure. (b) Simulated Bragg peaks for the T structure of $Pr_{1.2}La_{0.7}Ce_{0.1}CuO_4$, shown in the same *d*-spacing range as in panel (a). (c) The (004) Bragg reflection, recorded at 300 K at various hydrostatic pressures, illustrating the continuous shift of the *c*-axis peak towards the lower *d* spacing with increasing the pressure. The solid lines represent the Gaussian fits to the data. (d) Pressure dependence of the relative pressure shifts $\Delta a/a$ and $\Delta c/c$ for the lattice parameters *a* and *c* of $Pr_{1.3-x}La_{0.7}Ce_xCuO_4$ ($x = 0.1$) at T = 300 K. The solid lines are linear fits of the data.

FIG. 6. ZF μSR (a) and WTF μSR (b) time spectra for T$'$-Pr$_{1.3-x}$La$_{0.7}$Ce$_x$CuO$_4$ ($x = 0.1$) recorded at various temperatures without the pressure cell. The solid lines represent fits to the data by means of Eqs. (2) and (3).

axis. These results point to a nearly isotropic compression of the lattice in T$'$-Pr$_{1.3-x}$La$_{0.7}$Ce$_x$CuO$_4$ ($x = 0.1$).

B. Zero-field (ZF) and weak-transverse-field (WTF) μSR experiments

Figure 6(a) shows representative ZF μSR time spectra for polycrystalline T$'$-Pr$_{1.3-x}$La$_{0.7}$Ce$_x$CuO$_4$ ($x = 0.1$), recorded at various temperatures. At high temperatures, only a very weak depolarization of the μSR signal is observed. This weak depolarization reflects the occurrence of a small Gaussian Kubo-Toyabe depolarization, originating from the interaction of the muon spin with randomly oriented nuclear magnetic moments. In addition, small Pr^{3+} moments, which are dense and randomly distributed, also contribute to this relaxation [55,56]. Upon lowering the temperature the relaxation rate of the μSR signal increases due to the development of the Cu-spin correlation. No muon-spin precession is observed even at the lowest temperature $T = 5$ K and only a rapidly depolarizing

μSR signal is observed. The fast depolarization of the μSR signal (with no trace of an oscillation) is due to a broad distribution of static fields. This is supported by the fact that ZF μSR signal observed at temperatures below 50 K shows the recovery of asymmetry at longer times [see Fig. 6(a)], which is typical for static magnetically ordered systems. Static short-range magnetic order in the single crystal of T$'$-Pr$_{1.3-x}$La$_{0.7}$Ce$_x$CuO$_4$ ($x = 0.1$) was previously established by ZF μSR and longitudinal field (LF) μSR experiments [26]. In the following, we present how the magnetic and the SC properties of T$'$-Pr$_{1.3-x}$La$_{0.7}$Ce$_x$CuO$_4$ ($x = 0.1$) evolve with hydrostatic pressure.

Figures 7(a) and 7(b) show the ambient and highest pressure ($p = 2.3$ GPa) ZF μSR spectra of T$'$-Pr$_{1.3-x}$La$_{0.7}$Ce$_x$CuO$_4$ ($x = 0.1$), recorded at 5 K and 40 K, respectively. It is clear that upon application of pressure magnetic response is enhanced both at 5 K and 40 K. To get the quantitative information about the pressure effects, the μSR data in the whole temperature range were analyzed by decomposing the signal into a contribution of the sample and a contribution of the pressure cell, since in the high-pressure μSR experiments, a substantial fraction of the μSR asymmetry originates from muons stopping in the MP35N pressure cell surrounding the sample:

$$A(t) = A_S(t) + A_{PC}(t), \tag{1}$$

where $A_S(t)$ and $A_{PC}(t)$ are the asymmetries, belonging to the sample and the pressure cell, respectively. The pressure cell signal was analyzed by a damped Kubo-Toyabe function [48,49]. The response of the sample [see Fig. 6(a)] is analyzed by the following function [57,58]:

$$A_S(t) = [A_\perp e^{-\lambda_T t} + A_\parallel e^{-\lambda_L t}]e^{-\sigma_N^2 t^2/2}. \tag{2}$$

λ_T and λ_L are the relaxation rates characterizing the damping of the transversal and the longitudinal components of the μSR signal, respectively. The transversal relaxation rate λ_T is a measure of the width of the static magnetic field distribution at the muon site and also reflects dynamical effects (spin fluctuations). The longitudinal relaxation rate λ_L is determined by dynamic magnetic fluctuations only [57,58]. σ_N is the Gaussian relaxation rate, caused by the nuclear spins and the small Pr^{3+} moments. $A_\perp$ and $A_\parallel$ are the fractions of the transversal and the longitudinal relaxing components of the asymmetry signal, respectively. The ratio $A_\perp/A_\parallel$ reveals the average degree to which the muon-spin polarization P_μ aligns with the local field. In a fully magnetic polycrystalline sample, with a static component to the local field, because the crystallites orient randomly with respect to P_μ, $A_\perp/A_{tot} = \frac{2}{3}$ ($A_{tot} = A_\perp + A_\parallel$), the isotropic average perpendicular component of the muon spin. The total initial asymmetry $A_{sum} = A_S(0) + A_{PC}(0) \simeq 0.28$ is a temperature-independent constant. A typical fraction of muons stopped in the sample was $A_S(0)/A_{sum} \simeq 0.40(3)$, which was assumed to be temperature independent in the analysis. The μSR time spectra were analyzed using the free software package MUSRFIT [59].

Figure 8 summarizes the results of the above analysis. Namely, in Figs. 8(a) and 8(b), we show the temperature dependences of the ratio $A_\perp/A_{tot}$ and the transverse relaxation rate
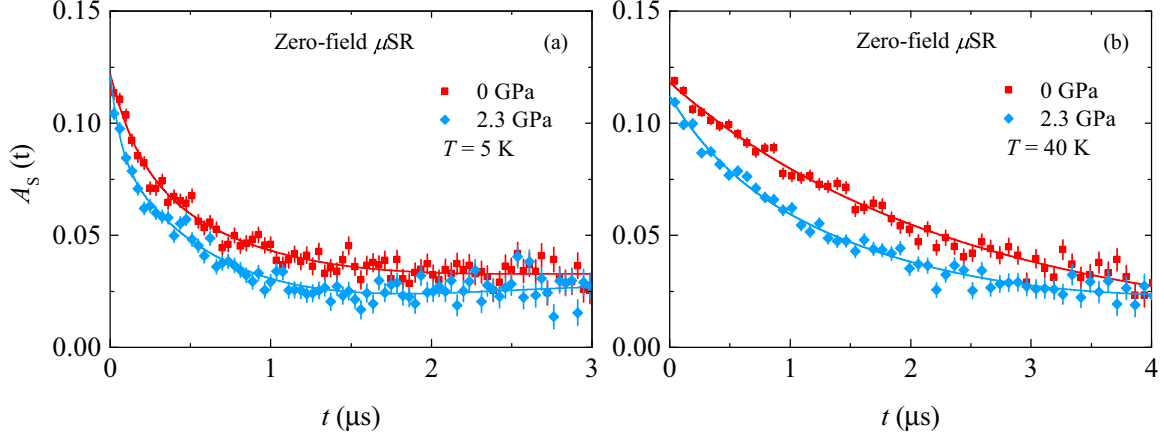
FIG. 7. ZF μSR time spectra A_S for T$'$-Pr$_{1.3-x}$La$_{0.7}$Ce$_x$CuO$_4$ ($x = 0.1$) recorded at $T = 5$ K (a) and 40 K (b) for ambient and maximum applied pressure of $p = 2.3$ GPa. The spectra are shown after substraction of the background signal from the pressure cell. The solid lines represent fits to the data by means of Eq. (2).

λ_T as well as the longitudinal relaxation rate λ_L, respectively, for T$'$-Pr$_{1.3-x}$La$_{0.7}$Ce$_x$CuO$_4$ ($x = 0.1$), measured at $p = 0$ GPa and 2.3 GPa. In the present case, $A_\perp/A_{tot}$ starts to increase below $T_{so} \simeq 45$ K and reaches the value of $V_m \simeq 0.8$ at the base temperature. Note that the obtained value $A_\perp/A_{tot} \simeq 0.8$ is higher than the value of $\frac{2}{3}$, expected for the polycrystalline

FIG. 8. The temperature dependence of the ratio $A_\perp/A_{tot}$ (a) and the relaxation rates λ_T, λ_L (b) of T$'$-Pr$_{1.3-x}$La$_{0.7}$Ce$_x$CuO$_4$ ($x = 0.1$), recorded at $p = 0$ GPa and $p = 2.3$ GPa. The arrows denote the static magnetic order temperature T_{so}. The solid lines are guides to the eye.

sample. This is may be related to some preferred orientation in our sample. Since T$'$-Pr$_{1.3-x}$La$_{0.7}$Ce$_x$CuO$_4$ ($x = 0.1$) has a two-dimensional structure (actually, the single crystal always grows in the direction parallel to the CuO$_2$ plane), even in powderized sintered pellets, there might be some preferred orientation. On the other hand, this could also be related to the existence of some fraction of fluctuating Cu spins, which was previously discussed [26]. The high value of $A_\perp/A_{tot}$ indicates that the short-range magnetic order occupies nearly the whole volume of this superconducting T$'$-Pr$_{1.3-x}$La$_{0.7}$Ce$_x$CuO$_4$ ($x = 0.1$). λ_T, characterizing the distribution of local fields, shows monotonous increase with decreasing the temperature below $T_{so} \simeq 45$ K. λ_L, characterizing the muon-spin relaxation due to fluctuating magnetic fields, also shows a clear peak at T_{so}, which is typical for the magnetic phase transition. Note that in the ordered state the values of λ_L are almost zero, consistent with the presence of dominant static magnetic order in T$'$-Pr$_{1.3-x}$La$_{0.7}$Ce$_x$CuO$_4$ ($x = 0.1$). It is evident from Fig. 8(a) that the magnetic fraction reaches 100% at low T for both pressures. In addition, the magnetic order temperature T_{so} in T$'$-Pr$_{1.3-x}$La$_{0.7}$Ce$_x$CuO$_4$ ($x = 0.1$) increases substantially, by $\sim$15 K, at the highest applied pressure of $p \simeq 2.3$ GPa. The pressure-induced enhancement of T_{so} can also be seen from the temperature dependences of λ_T and λ_L, shown in Fig. 8(b).

In order to gain more insight into the above short-range magnetic transition, TF-μSR experiments in weak-transverse field were carried out. Figure 6(b) shows a representative weak-transverse-field (WTF) μSR time spectra for polycrystalline T$'$-Pr$_{1.3-x}$La$_{0.7}$Ce$_x$CuO$_4$ ($x = 0.1$), recorded at various temperatures. This clearly shows the reduction of the amplitude of the μSR signal upon lowering the temperature below $\sim$50 K, indicating the appearance of the magnetic order. The WTF-μSR spectra, shown in Fig. 6(b) were fitted in the time domain with a slowly relaxing signal, with the precession frequency corresponding to the applied field of $\mu_0 H = 3$ mT:

$$A'(t) = A'_S(t) + A'_{PC}(t)$$
$$= (A'_S e^{-\lambda' t} + A'_{PC} e^{-\lambda'_{PC} t})\cos(\gamma_\mu B t + \varphi), \quad (3)$$
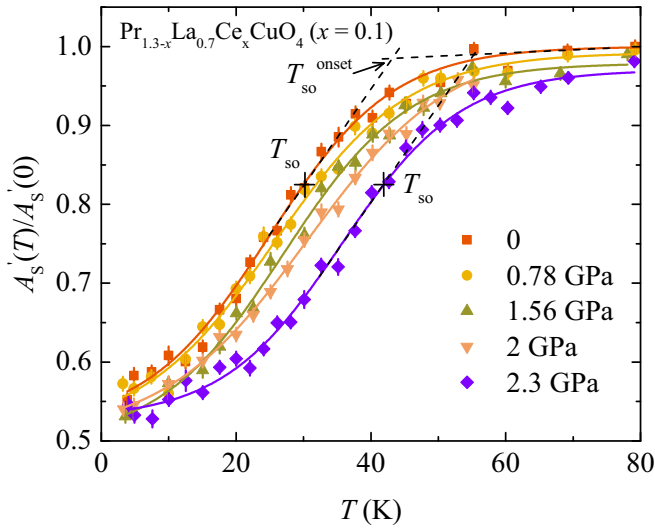
FIG. 9. The temperature dependence of the normalized WTF asymmetry $A'_S(T)/A'_S(0)$ for $Pr_{1.2}La_{0.7}Ce_{0.1}CuO_4$, recorded at various pressures up to $p = 2.3$ GPa. The crosses mark the magnetic order temperatures T_{so} for $p = 0$ and 2.3 GPa. The solid lines represent fits to the data by means of Eq. (1).

FIG. 10. Temperature dependence of the dc diamagnetic susceptibility χ_{ZFC} of T'-$Pr_{1.3-x}La_{0.7}Ce_xCuO_4$ ($x = 0.1$), measured at ambient and at various applied hydrostatic pressures. The arrows denote the superconducting transition temperature T_c. For clarity, the data for $p = 0$ and 0.3 GPa are shifted vertically down from the zero line.

where t is time after muon implantation, φ is the phase, $A'(t)$ is the time-dependent asymmetry, and $\gamma_\mu/(2\pi) \simeq 135.5$ MHz/T is the muon gyromagnetic ratio. $A'_S(t)$ is the amplitude of the oscillating component (related to the paramagnetic volume fraction of the sample). λ' is an exponential damping rate due to paramagnetic spin fluctuations and nuclear dipolar moments. B is the applied magnetic field, experienced by the muons stopped in the paramagnetic part of the sample. From these refinements, the paramagnetic volume fraction at each temperature T was estimated as $A'_S(T)/A'_S(0)$, where $A'_S(0)$ is the amplitude in the paramagnetic phase at high temperature. A'_{PC} and λ'_{PC} are the amplitude and the relaxation rate of the pressure cell signal. Pressure cell amplitude was estimated to be $A'_{PC} = 0.17$ and it was kept constant as a function of temperature in the analysis. Note that the data, shown in Figs. 6(a) and 6(b), are recorded without the pressure cell ($A'_{PC} = 0$).

Figure 9 shows the normalized WTF-μSR asymmetry $A'_s(T)/A'_s(0)$ for T'-$Pr_{1.3-x}La_{0.7}Ce_xCuO_4$ ($x = 0.1$) extracted from the μSR spectra, shown in Fig. 6(b) [following Eq. (3)], as a function of temperature for ambient and selected applied pressures in an applied field of $\mu_0H = 3$ mT. For $p = 0$ GPa and $T > 50$ K, $A'_s(T)/A'_s(0)$ saturates nearly at a maximum value, indicating that nearly the whole sample is in the paramagnetic state, and all the muon spins precess in the applied magnetic field. Below 50 K, $A'_s(T)/A'_s(0)$ continuously decreases with decreasing temperature. The reduction of $A'_s(T)/A'_s(0)$ signals the appearance of magnetic order, where the muon spins experience a local magnetic field larger than the applied magnetic field. As a result, the fraction of muons in the paramagnetic state decreases. The onset temperature T_{so}^{onset} is defined as the temperatures where the linearly extrapolated low- and high-temperature data points intersect. The midpoint of the transition (T_{so}) was determined

by using the phenomenological function [59,60]

$$A'_S(T)/A'_S(0) = k\left[1 - \frac{1}{\exp[(T - T_{so})/\Delta T_{so}] + 1}\right] + l,$$

$$(4)$$

where ΔT_{so} is the width of the transition, whereas k and l are empirical parameters. Analyzing the $p = 0$ GPa data in Fig. 9 with Eq. (4) yields $T_{so} = 30(1)$ K, which is indicated by the cross in Fig. 9. Remarkably, a strong and nonlinear increase of T_{so} in T'-$Pr_{1.3-x}La_{0.7}Ce_xCuO_4$ ($x = 0.1$) is observed under pressure.

C. High-pressure magnetic susceptibility data

Figure 10 shows the temperature dependence of dc magnetic susceptibility χ_{ZFC} for T'-$Pr_{1.3-x}La_{0.7}Ce_xCuO_4$ ($x = 0.1$) at ambient and at various applied pressures up to $p \simeq 2.1$ GPa after substraction of the background signal from the empty pressure cell. Note that zero-field-cooled (ZFC) dc susceptibility χ_{ZFC} was measured in a magnetic field of $\mu_0H = 0.5$ mT using the DAC, where only very tiny amount of sample is used.

At $p = 0$ GPa, the sample T'-$Pr_{1.3-x}La_{0.7}Ce_xCuO_4$ ($x = 0.1$) shows superconductivity with $T_c \simeq 27$ K. The magnitude of $\chi_{ZFC} = -0.49(3) \times 10^{-2}$ (emu/g) at $T = 10$ K, providing a lower limit of 49(3)% for the SC volume fraction. This implies the bulk character of superconductivity in the sample. The fact that we get 49% for the SC volume fraction and not 100% is due to the use of polycrystalline samples in which the Meissner diamagnetism is reduced by the magnetic penetration from the surface of the sample. For the same reason, the SC volume fraction estimated from the Meissner fraction using powder samples reaches only 30% in the optimally doped $La_{2-x}Sr_xCuO_4$ [61]. One more indirect but strong evidence for the bulk superconductivity

in T$'$-Pr$_{1.3-x}$La$_{0.7}$Ce$_x$CuO$_4$ ($x = 0.1$) is that the specific heat on single-crystalline samples, reduced in the same procedure as the present Pr$_{1.3-x}$La$_{0.7}$Ce$_x$CuO$_4$ powder, reveals the SC volume fraction of more than 60% [26]. Obviously, the surface area is larger in a powder than in a single crystal, so we naturally expect the powders reduced more than single crystals, resulting in the comparable or larger SC volume fraction in powder samples. T_c shows the modest decrease with increasing pressure, i.e., it decreases from $T_c \simeq 27$ K to $T_c \simeq 23$ K at $p \simeq 2.1$ GPa. On the other hand, application of pressure leads to the substantial decrease of the diamagnetic response, resulting in difficulties of observing the SC response above $p \simeq 2.1$ GPa. It is difficult to conclude whether superconductivity in T$'$-Pr$_{1.3-x}$La$_{0.7}$Ce$_x$CuO$_4$ ($x = 0.1$) is either fully suppressed above $p \simeq 2.1$ GPa or becomes filamentary.

IV. DISCUSSION AND CONCLUSION

In order to compare the influence of pressure on the superconductivity and short-range magnetic order in T$'$-Pr$_{1.3-x}$La$_{0.7}$Ce$_x$CuO$_4$ ($x = 0.1$), the pressure dependences of T_{so} (T_{so}^{onset}) and T_c are shown in Fig. 11(a). Moreover, the pressure dependences of χ'' and χ_{ZFC}, normalized to its ambient pressure value, are shown in Fig. 11(b). The most essential findings of the present work are the following: (1) The short-range magnetic order temperature T_{so} in T$'$-Pr$_{1.3-x}$La$_{0.7}$Ce$_x$CuO$_4$ ($x = 0.1$) exhibits the strong and nonlinear positive pressure effect. T_{so} is nearly constant in the pressure range between 0 and 0.8 GPa, increasing at higher pressure. For the highest applied pressure of $p \simeq 2.3$ GPa the T_{so} increases by $\sim$12 K. Note that the magnetic order remains short range even at $p \simeq 2.3$ GPa. (2) The SC transition temperature T_c in T$'$-Pr$_{1.3-x}$La$_{0.7}$Ce$_x$CuO$_4$ ($x = 0.1$) shows the nonlinear negative pressure effect. Likewise T_{so}, T_c is constant in the pressure range between 0 and 0.8 GPa. However, above $p \simeq 0.8$ GPa, T_c decreases instead of the observed increase for T_{so}. For the applied pressure of $p \simeq 2.1$ GPa, T_c decreases by $\sim$3–4 K. Moreover, the diamagnetic response decreases substantially and nonlinearly with increasing pressure, and above $p \simeq 2.1$ GPa, no diamagnetic signal is observed using bulk sensitive techniques. This means that the superconductivity in T$'$-Pr$_{1.3-x}$La$_{0.7}$Ce$_x$CuO$_4$ ($x = 0.1$) is either suppressed fully or becomes filamentary above $p \simeq 2.1$ GPa. Antagonistic pressure behavior between T_{so} and T_c gives direct evidence for the competition between superconductivity and the short-range magnetic order in T$'$-Pr$_{1.3-x}$La$_{0.7}$Ce$_x$CuO$_4$ ($x = 0.1$). It is interesting that the magnetic fraction is nearly pressure independent, while the SC fraction reduces substantially. This is different from hole-doped cuprates with the static spin and charge order in which μSR observes phase separation between magnetism and superconductivity [15,18]. In addition, the magnetic order in T$'$-Pr$_{1.3-x}$La$_{0.7}$Ce$_x$CuO$_4$ ($x = 0.1$) remains short range up to the highest applied pressure, which probably suggests that the superconductivity is not suppressed above $p \simeq 2.1$ GPa, but it becomes filamentary and still inhibits the long-range magnetic order in the system.

Additional results provide important clues of how pressure may induce the strong changes in magnetic and SC properties. In the closely related compounds Ln_{2-x}Ce$_x$CuO$_4$ ($Ln =$
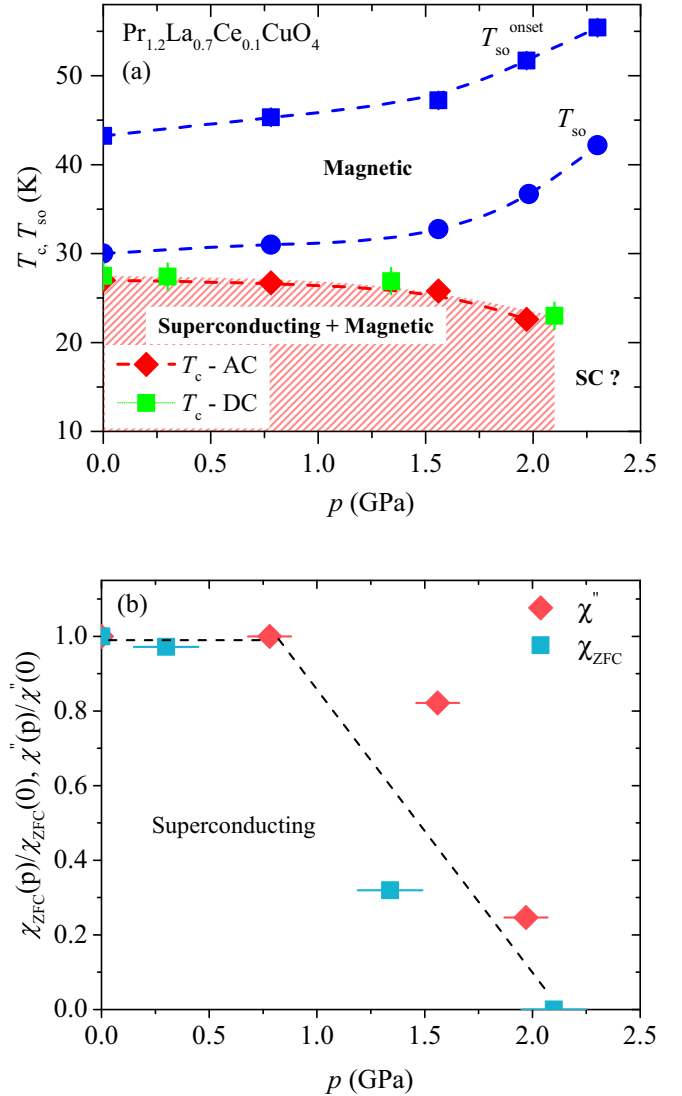
FIG. 11. (a) The superconducting transition temperature T_c and the short-range magnetic ordering temperatures T_{so} and T_{so}^{onset} of T$'$-Pr$_{1.3-x}$La$_{0.7}$Ce$_x$CuO$_4$ ($x = 0.1$), obtained from dc/ac susceptibilities and μSR experiments, are plotted as a function of pressure. (b) The pressure dependence of χ'' and χ_{ZFC}, normalized to ambient pressure value. The dashed lines are guides to the eye.

Nd, Sm, and Eu) (where isovalent substitution of Nd by Sm and Eu simulates a condition generally referred to as "chemical pressure," that is, both in-plane and out-of-plane lattice constants become small), ARPES and first-principles electronic-structure calculations revealed that the chemical pressure (the variation of the in-plane and out-of-plane lattice constants) has a great influence on the electronic structures and on the Fermi-surface shape [62]. Namely, reduction of the in-plane lattice constant causes the reduction of $-t'/t$, where t and t' denote transfer integrals between the nearest-neighbor and next-nearest-neighbor Cu sites and enhancement of AFM order. It was suggested that reduced $-t'/t$ enhances the AFM order through strengthened nesting, resulting in the increased gap in the nodal region. As we have shown through neutron powder diffraction experiments, hydrostatic pressure causes the continuous reduction of the in-plane and out-of-plane

lattice constants in T'-$Pr_{1.3-x}La_{0.7}Ce_xCuO_4$ ($x = 0.1$), which, according to the above discussion, might also improve nesting and enhance the AFM order, leading to the increase of T_{so} and decrease of T_c. Thus, we suggest that the short-range magnetic order and the strong increase of T_{so} is intrinsic and is controlled by the Fermi surface properties of T'-$Pr_{1.3-x}La_{0.7}Ce_xCuO_4$ ($x = 0.1$).

It is important to draw a parallel between the observation of short-range magnetic order at $T_{so} \simeq 45$ K in T'-$Pr_{1.3-x}La_{0.7}Ce_xCuO_4$ ($x = 0.1$) and the recent findings in the related SC n-type cuprate $Nd_{2-x}Ce_xCuO_4$ [25,63–66]. The existence of charge ordering with a short correlation length (15 to 27 Å) was reported for $Nd_{2-x}Ce_xCuO_4$ [25]. Time-resolved reflectivity studies in SC $Nd_{2-x}Ce_xCuO_4$ show the presence of a fluctuating order below $\sim$75 K, although they could not determine which electronic degrees of freedom (i.e., charge or spin) were responsible for such order [64]. In this SC $Nd_{2-x}Ce_xCuO_4$, resonant inelastic x-ray scattering measurements [65,66] have also recently shown the presence of an inelastic mode. All these observations suggest that some new phases are emerging together with superconductivity in electron-doped cuprates. The current results are in line with this suggestion. Additionally, we demonstrated the competing nature of the short-range magnetically ordered state to superconductivity in T'-$Pr_{1.3-x}La_{0.7}Ce_xCuO_4$ ($x = 0.1$). Our discovery of short-range magnetic order may contribute in understanding the complex electron-doped cuprate phase diagram.

In conclusion, hydrostatic pressure effects on short-range magnetic order and superconductivity in electron-doped cuprate T'-$Pr_{1.3-x}La_{0.7}Ce_xCuO_4$ ($x = 0.1$) were investigated by combining high-pressure μSR and ac as well as dc susceptibility experiments. At all applied pressures, nearly the whole sample volume exhibits the short-range magnetic order. The short-range magnetic order temperature T_{so} exhibits a large positive pressure effect which has never been observed before for electron-doped cuprates. Furthermore, the observed pressure-induced shifts of T_{so} and the superconducting transition temperature T_c have opposite signs. Moreover, the strong reduction of the in-plane and out-of-plane lattice constants is observed under pressure. However, no indication of the pressure-induced phase transition from T' to T structure is observed up to the maximum applied pressure of $p = 11$ GPa. These experiments establish the short-range magnetic order as an intrinsic part of the phase diagram and as a competing phase in electron-doped cuprate superconductor T'-$Pr_{1.3-x}La_{0.7}Ce_xCuO_4$ ($x = 0.1$). The observed pressure effects may be interpreted by assuming strong pressure-induced changes on the electronic structure and the Fermi surface through the variation of the lattice constants. Namely, the improved nesting upon pressure might be a possible explanation for the enhancement of T_{so} and suppression of T_c.

[1] J. G. Bednorz and K. A. Müller, Z. Phys. B: Condens. Matter **64**, 189 (1986).

[2] H. Takagi, S. Uchida, and Y. Tokura, Phys. Rev. Lett. **62**, 1197 (1989).

[3] Y. Tokura, H. Takagi, and S. Uchida, Nature (London) **337**, 345 (1989).

[4] M. B. Maple, MRS Bull. **15**, 60 (1990).

[5] Y. Dalichaouch, M. de Andrade, and M. Maple, Phys. C (Amsterdam, Neth.) **218**, 309 (1993).

[6] A. Shengelaya, R. Khasanov, D. G. Eshchenko, D. Di Castro, I. M. Savić, M. S. Park, K. H. Kim, S.-I. Lee, K. A. Müller, and H. Keller, Phys. Rev. Lett. **94**, 127001 (2005).

[7] A. Tsukada, Y. Krockenberger, M. Noda, H. Yamamoto, D. Manske, and L. Alff, and M. Naito, Solid State Commun. **133**, 427 (2005).

[8] M. A. Kastner, R. J. Birgeneau, G. Shirane, and Y. Endoh, Rev. Mod. Phys. **70**, 897 (1998).

[9] S. A. Kivelson, I. P. Bindloss, E. Fradkin, V. Oganesyan, J. M. Tranquada, A. Kapitulnik, and C. Howald, Rev. Mod. Phys. **75**, 1201 (2003).

[10] J. M. Tranquada, B. J. Sternlieb, J. D. Axe, Y. Nakamura, and S. Uchida, Nature (London) **375**, 561 (1995).

[11] H. Kimura, K. Hirota, H. Matsushita, K. Yamada, Y. Endoh, S.-H. Lee, C. F. Majkrzak, R. Erwin, G. Shirane, M. Greven, Y. S. Lee, M. A. Kastner, and R. J. Birgeneau, Phys. Rev. B **59**, 6517 (1999).

[12] M. Vojta, Adv. Phys. **58**, 699 (2009).

[13] B. Lake, H. M. Rønnow, N. B. Christensen, G. Aeppli, K. Lefmann, D. F. McMorrow, P. Vorderwisch, P. Smeibidl, N. Mangkorntong, T. Sasagawa, M. Nohara, H. Takagi, and T. E. Mason, Nature (London) **415**, 299 (2002).

[14] J. Chang, Ch. Niedermayer, R. Gilardi, N. B. Christensen, H. M. Rønnow, D. F. McMorrow, M. Ay, J. Stahn, O. Sobolev, A. Hiess, S. Pailhes, C. Baines, N. Momono, M. Oda, M. Ido, and J. Mesot, Phys. Rev. B **78**, 104525 (2008).

[15] Z. Guguchia, A. Maisuradze, G. Ghambashidze, R. Khasanov, A. Shengelaya, and H. Keller, New J. Phys. **15**, 093005 (2013).

[16] Y. S. Lee, R. J. Birgeneau, M. A. Kastner, Y. Endoh, S. Wakimoto, K. Yamada, R. W. Erwin, S.-H. Lee, and G. Shirane, Phys. Rev. B **60**, 3643 (1999).

[17] S. Katano, M. Sato, K. Yamada, T. Suzuki, and T. Fukase, Phys. Rev. B **62**, R14677(R) (2000).

[18] Z. Guguchia, R. Khasanov, A. Shengelaya, E. Pomjakushina, S. J. L. Billinge, A. Amato, E. Morenzoni, and H. Keller, Phys. Rev. B **94**, 214511 (2016).

[19] Y. Kohsaka, C. Taylor, K. Fujita, A. Schmidt, C. Lupien, T. Hanaguri, M. Azuma, M. Takano, H. Eisaki, H. Takagi, S. Uchida, and J. C. Davis, Science **315**, 1380 (2007).

[20] T. Valla, A. V. Fedorov, J. Lee, J. C. Davis, and G. D. Gu, Science **314**, 1914 (2006).

[21] M. Hücker, M. v. Zimmermann, G. D. Gu, Z. J. Xu, J. S. Wen, G. Xu, H. J. Kang, A. Zheludev, and J. M. Tranquada, Phys. Rev. B **83**, 104506 (2011).

[22] J. Chang, E. Blackburn, A. T. Holmes, N. B. Christensen, J. Larsen, J. Mesot, R. Liang, D. A. Bonn, W. N. Hardy, A. Watenphul, M. v. Zimmermann, E. M. Forgan and S. M. Hayden, Nat. Phys. **8**, 871 (2012).

[23] T. Wu, H. Mayaffre, S. Krämer, M. Horvatic, C. Berthier, W. N. Hardy, R. Liang, D. A. Bonn and M.-H. Julien, Nature (London) **477**, 191 (2011).

[24] G. Ghiringhelli, M. Le Tacon, M. Minola, S. Blanco-Canosa, C. Mazzoli, N. B. Brookes, G. M. De Luca, A. Frano, D. G. Hawthorn, F. He, T. Loew, M. Moretti Sala, D. C. Peets, M. Salluzzo, E. Schierle, R. Sutarto, G. A. Sawatzky, E. Weschke, B. Keimer, and L. Braicovich, Science **337**, 821 (2012).

[25] E. H. da Silva Neto, R. Comin, F. He, R. Sutarto, Y. Jiang, R. L. Greene, G. A. Sawatzky, and A. Damascelli, Science **347**, 282 (2015).

[26] T. Adachi, A. Takahashi, K. M. Suzuki, M. A. Baqiya, T. Konno, T. Takamatsu, M. Kato, I. Watanabe, A. Koda, M. Miyazaki, R. Kadono, and Y. Koike, J. Phys. Soc. Jpn. **85**, 114716 (2016).

[27] H. Saadaoui, Z. Salman, H. Luetkens, T. Prokscha, A. Suter, W. A. MacFarlane, Y. Jiang, K. Jin, R. L. Greene, E. Morenzoni, and R. F. Kiefl, Nat. Commun. **6**, 6041 (2015).

[28] H. J. Kang, P. Dai, J. W. Lynn, M. Matsuura, J. R. Thompson, S.-C. Zhang, D. N. Argyriou, Y. Onose, and Y. Tokura, Nature (London) **423**, 522 (2003).

[29] E. M. Motoyama, G. Yu, I. M. Vishik, O. P. Vajk, P. K. Mang, and M. Greven, Nature (London) **445**, 186 (2007).

[30] N. P. Armitage, P. Fournier, and R. L. Greene, Rev. Mod. Phys. **82**, 2421 (2010).

[31] G. Pascua, Ph.D. thesis, Universität Zürich, 2014.

[32] X. Q. Xu, S. N. Mao, W. Jiang, J. L. Peng, and R. L. Greene, Phys. Rev. B **53**, 871 (1996).

[33] T. Sekitani, M. Naito, and N. Miura, Phys. Rev. B **67**, 174503 (2003).

[34] O. Matsumoto, A. Utsuki, A. Tsukada, H. Yamamoto, T. Manabe, and M. Naito, Phys. C (Amsterdam, Neth.) **469**, 924 (2009).

[35] G. Riou, P. Richard, S. Jandl, M. Poirier, P. Fournier, V. Nekvasil, S. N. Barilo, and L. A. Kurnevich, Phys. Rev. B **69**, 024511 (2004).

[36] P. Richard, G. Riou, I. Hetel, S. Jandl, M. Poirier, and P. Fournier, Phys. Rev. B **70**, 064513 (2004).

[37] H. J. Kang, P. Dai, B. J. Campbell, P. J. Chupas, S. Rosenkranz, P. L. Lee, Q. Huang, S. Li, S. Komiya, and Y. Ando, Nat. Mater. **6**, 224 (2007).

[38] M. Horio, T. Adachi, Y. Mori, A. Takahashi, T. Yoshida, H. Suzuki, L. C. C. Ambolode II, K. Okazaki, K. Ono, H. Kumigashira, M. Anzai, M. Arita, H. Namatame, M. Taniguchi, D. Ootsuki, K. Sawada, M. Takahashi, T. Mizokawa, Y. Koike, and A. Fujimori, Nat. Commun. **7**, 10567 (2016).

[39] T. Adachi, Y. Mori, A. Takahashi, M. Kato, T. Nishizaki, T. Sasaki, N. Kobayashi, and Y. Koike, J. Phys. Soc. Jpn. **82**, 063713 (2013).

[40] X. F. Sun, Y. Kurita, T. Suzuki, S. Komiya, and Y. Ando, Phys. Rev. Lett. **92**, 047001 (2004).

[41] S. D. Wilson, S. Li, P. Dai, W. Bao, J.-H. Chung, H. J. Kang, S.-H. Lee, S. Komiya, Y. Ando, and Q. Si, Phys. Rev. B **74**, 144514 (2006).

[42] J. T. Markert, J. Beille, J. J. Neumeier, E. A. Early, C. L. Seaman, T. Moran, and M. B. Maple, Phys. Rev. Lett. **64**, 80 (1990).

[43] S. Ishiwata, D. Kotajima, N. Takeshita, C. Terakura, S. Seki, and Y. Tokura, J. Phys. Soc. Jpn. **82**, 063705 (2013).

[44] T. Kamiyama, F. Izumi, H. Takahashi, J. D. Jorgensen, B. Dabrowski, R. L. Hitterman, D. G. Hinks, H. Shaked, T. O. Mason, and M. Seabaugh, Phys. C (Amsterdam, Neth.) **229**, 377 (1994).

[45] H. Wilhelm, E. Cros, E. Reny, G. Demazeau, and M. Hanfland, J. Mater. Chem. **8**, 2729 (1998).

[46] H. Wilhelm, E. Cros, E. Reny, G. Demazeau, and H. Hanfland, J. Solid State Chem. **151**, 231 (2000).

[47] C. R. Rotundu, V. V. Struzhkin, M. S. Somayazulu, S. Sinogeikin, R. J. Hemley, and R. L. Greene, Phys. Rev. B **87**, 024506 (2013).

[48] R. Khasanov, Z. Guguchia, A. Maisuradze, D. Andreica, M. Elender, A. Raselli, Z. Shermadini, T. Goko, F. Knecht, E. Morenzoni, and A. Amato, High Pressure Res. **36**, 140 (2016).

[49] A. Maisuradze, B. Graneli, Z. Guguchia, A. Shengelaya, E. Pomjakushina, K. Conder, and H. Keller, Phys. Rev. B **87**, 054401 (2013).

[50] R. Boehler, M. Guthrie, J. J. Molaison, A. M. dos Santos, S. Sinogeikin, S. Machida, N. Pradhan, and C. A. Tulk, Diamond cells for neutron diffraction using multi-carat CVD anvils (unpublished).

[51] R. Boehler, J. J. Molaison, and B. Haberl, High Pressure Res. **33**, 546 (2013).

[52] G. Gaétan, W. Wang, J. P. Attfield, A. D. Huxley, and K. V. Kamenev, Rev. Sci. Instrum. **81**, 073905 (2010).

[53] B. H. Toby and R. B. Von Dreele, J. Appl. Crystallogr. **46**, 544 (2013).

[54] T. Uzumaki, N. Kamehara, and K. Niwa, Jpn. J. Appl. Phys. **30**, L981 (1991).

[55] R. Kadono, K. Ohishi, A. Koda, W. Higemoto, K. M. Kojima, S.-i. Kuroshima, M. Fujita, and K. Yamada, J. Phys. Soc. Jpn. **72**, 2955 (2003).

[56] Risdiana, T. Adachi, N. Oki, Y. Koike, T. Suzuki, and I. Watanabe, Phys. Rev. B **82**, 014506 (2010).

[57] Z. Guguchia *et al.*, J. Supercond. Novel Magn. **26**, 285 (2013).

[58] H. Maeter, H. Luetkens, Yu. G. Pashkevich, A. Kwadrin, R. Khasanov, A. Amato, A. A. Gusev, K. V. Lamonova, D. A. Chervinskii, R. Klingeler, C. Hess, G. Behr, B. Büchner, and H.-H. Klauss, Phys. Rev. B **80**, 094524 (2009).

[59] A. Suter and B. M. Wojek, Phys. Procedia **30**, 69 (2012).

[60] Z. Guguchia, R. Khasanov, M. Bendele, E. Pomjakushina, K. Conder, A. Shengelaya, and H. Keller, Phys. Rev. Lett. **113**, 057002 (2014).

[61] T. Adachi, N. Oki, Risdiana, S. Yairi, Y. Koike, and I. Watanabe, Phys. Rev. B **78**, 134515 (2008).

[62] M. Ikeda, T. Yoshida, A. Fujimori, M. Kubota, K. Ono, Hena Das, T. Saha-Dasgupta, K. Unozawa, Y. Kaga, T. Sasagawa, and H. Takagi, Phys. Rev. B **80**, 014510 (2009).

[63] M. d'Astuto, P. K. Mang, P. Giura, A. Shukla, P. Ghigna, A. Mirone, M. Braden, M. Greven, M. Krisch, and F. Sette, Phys. Rev. Lett. **88**, 167002 (2002).

[64] J. P. Hinton, J. D. Koralek, G. Yu, E. M. Motoyama, Y. M. Lu, A. Vishwanath, M. Greven, and J. Orenstein, Phys. Rev. Lett. **110**, 217002 (2013).

[65] W. S. Lee, J. J. Lee, E. A. Nowadnick, S. Gerber, W. Tabis, S. W. Huang, V. N. Strocov, E. M. Motoyama, G. Yu, B. Moritz, H. Y. Huang, R. P. Wang, Y. B. Huang, W. B. Wu, C. T. Chen, D. J. Huang, M. Greven, T. Schmitt, Z. X. Shen, and T. P. Devereaux, Nat. Phys. **10**, 883 (2014).

[66] K. Ishii, M. Fujita, T. Sasaki, M. Minola, G. Dellea, C. Mazzoli, K. Kummer, G. Ghiringhelli, L. Braicovich, T. Tohyama, K. Tsutsumi, K. Sato, R. Kajimoto, K. Ikeuchi, K. Yamada, M. Yoshida, M. Kurooka, and J. Mizuki, Nat. Commun. **5**, 3714 (2014).

ARTICLE   OPEN

Superconducting order from disorder in 2H-TaSe$_{2-x}$S$_x$

Lijun Li[1,2], Xiaoyu Deng[3], Zhen Wang[1], Yu Liu[1], Milinda Abeykoon[4], Eric Dooryhee[4], Aleksandra Tomic[5], Yanan Huang[1,8], John B. Warren[6], Emil S. Bozin[1], Simon J. L. Billinge[1,5], Yuping Sun[2,7], Yimei Zhu[1], Gabriel Kotliar[1,3] and Cedomir Petrovic[1]

We report on the emergence of robust superconducting order in single crystal alloys of TaSe$_{2-x}$S$_x$ ($0 \leq x \leq 2$). The critical temperature of the alloy is surprisingly higher than that of the two end compounds TaSe$_2$ and TaS$_2$. The evolution of superconducting critical temperature $T_c(x)$ correlates with the full width at half maximum of the Bragg peaks and with the linear term of the high-temperature resistivity. The conductivity of the crystals near the middle of the alloy series is higher or similar than that of either one of the end members 2H-TaSe$_2$ and/or 2H-TaS$_2$. It is known that in these materials superconductivity is in close competition with charge density wave order. We interpret our experimental findings in a picture where disorder tilts this balance in favor of superconductivity by destroying the charge density wave order.

INTRODUCTION

The interplay of disorder and interactions is a fruitful area of investigation. In the absence of electron–electron interactions, disorder can turn a metallic system into an Anderson insulator,[1] but can remain metallic when interactions are important. The additional complexity of competing orders such superconductivity with charge density wave (CDW) or magnetism makes this problem one of the most challenging frontiers in physics.[2–5] A large body of literature is devoted to this interplay in nearly magnetic materials.[6] The interplay of disorder and superconductivity in CDW materials have been less explored than its magnetic analog.

Superconductivity and CDW are traditionally viewed as weak-coupling Fermi surface instabilities due to electron–phonon coupling.[7] Arguments have been made both for their cooperation and competition.[8, 9] Hexagonal transition metal dichalcogenide 2H-TaSe$_2$ (*P63/mmc* space group) undergoes a second-order transition to an incommensurate CDW at 122 K followed by a first-order lock-in transition to a commensurate CDW (CCDW) phase at 90 K, eventually becoming superconducting below 0.14 K upon cooling.[10, 11] 2H-TaS$_2$ has $T_c = 0.8$ K below an in-plane CCDW at 78 K.[10, 12] The CDW mechanism in 2H-TaSe$_2$ involves an electron instability in the bands nested away from the Fermi surface, whereas 2H-TaS$_2$ features a polar charge and orbital order.[13, 14] CDW in 2H-TaSe$_2$ is dominated by hopping between next-nearest neighbors that creates three weakly coupled triangular sublattices.[15] It is of interest to note that the 2H-TaSe$_2$ is quasi-two-dimensional (2D) metal with pseudogap and with *c*-axis resistivity 25–50 times higher than the in-plane resistivity, i.e., $\rho_c(T) \gg \rho_{ab}(T)$.[10, 13, 16–18]

Here, we report that in the 2H-TaSe$_{2-x}$S$_x$ alloy series the CDW is suppressed and the superconductivity is maximized with

crystallographic disorder. The $T_c(x)$ evolution is correlated with the high-temperature linear resistivity $\rho(T) = aT + b$. The constant term b can be attributed to impurity-like carrier scattering of the local CDW fluctuations, and it also appears in dynamical mean field theory (DMFT) of bad metals at high temperature.[19–22] On very general grounds (Anderson theorem) *s*-wave superconductivity is immune to weak disorder,[23] on the other hand disorder is detrimental to CDW. We argue that the increase in superconducting T_c in the alloy is a direct result of disorder-induced suppression of CDW order. In a weak coupling picture, CDW suppression results in an increase in number of carriers available for superconductivity pairing at Fermi surface, thus enhancing T_c. The physical scenario that in systems where CDW competes with superconductivity disorder promotes the latter is very general and extends to a strongly coupled situation as long as disorder remains weak (see Supplementary Information).

RESULTS

Powder patterns for all samples have been successfully indexed within the *P63/mmc* space group. Representative refinement is shown in Fig. 1a and the unit cell is shown in Fig. 1b. Single crystal X-ray diffraction (XRD) patterns for a subset of single crystals used in this study (Fig. 1c) show (00l) reflections. Reflections shift to higher scattering angles with increasing S, indicating decrease of the unit cell volume. Evolution of unit cell parameters with S, obtained from fits to the powder patterns (Fig. 1d, e), is consistent with the single crystal data.

The resistivity of all single crystals (Fig. 2a) is metallic. The curves for $0 \leq x \leq 0.25$ show a change of slope in $\rho(T)/\rho(200 \text{ K})$ (Fig. 2b). As opposed to commonly observed increase in $\rho(T)$ at T_{CDW} the slope change is attributed to CDW transition that leaves the bands

[1]Condensed Matter Physics and Materials Science Department, Brookhaven National Laboratory, Upton, NY 11973, USA; [2]Key Laboratory of Materials Physics, Institute of Solid State Physics Chinese Academy of Sciences, Hefei 230031, China; [3]Department of Physics & Astronomy, Rutgers, The State University of New Jersey—Piscataway, Piscataway, NJ 08854, USA; [4]Photon Sciences Directorate, Brookhaven National Laboratory, Upton, NY 11973, USA; [5]Department of Applied Physics and Applied Mathematics, Columbia University, New York 10027, USA; [6]Instrumentation Division, Brookhaven National Laboratory, Upton, NY 11973, USA and [7]High Magnetic Field Laboratory, Chinese Academy of Sciences, Hefei 230031, China
Correspondence: Lijun Li (lilijun@issp.ac.cn) or Cedomir Petrovic (petrovic@bnl.gov)
[8]Present address: Key Laboratory of Materials Physics, Institute of Solid State Physics, Chinese Academy of Sciences, Hefei 230031, China
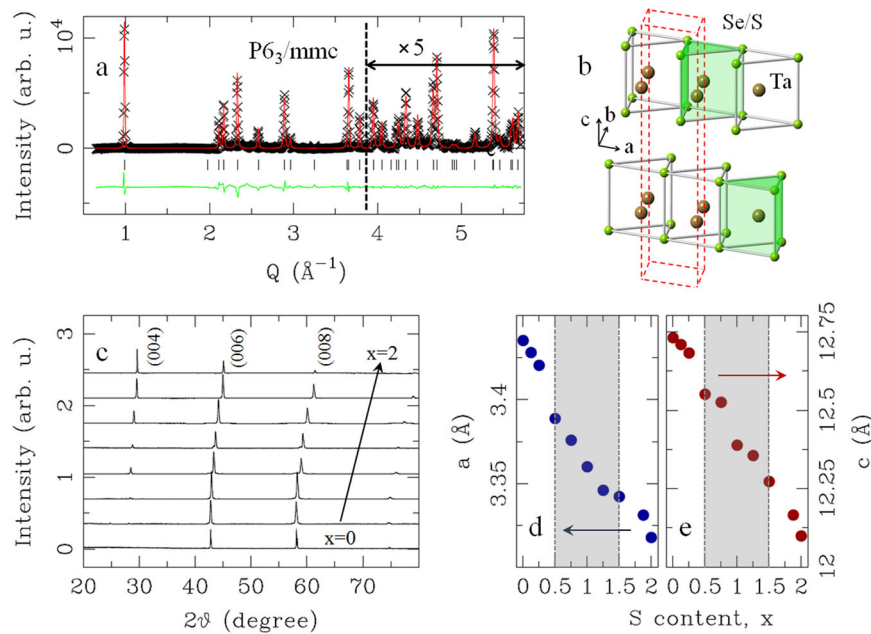
Fig. 1 Crystal structure aspects of 2H-TaSe$_{2-x}$S$_x$ ($0 \leq x \leq 2$) **a** Powder XRD pattern for 2H-TaSe$_2$ at 300 K, shown as scattering intensity vs. momentum transfer Q, indexed within P63/mmc space group. *Crosses* are data, *solid red line* is the model, *green solid line* is the difference (offset for clarity), and *vertical ticks mark* are the reflections. **b** Structural motif of the P63/mmc model. *Red dashed box* depicts the unit cell. **c** Single crystal XRD patterns at the room temperature. Patterns are offset for clarity. **d**, **e** Room temperature evolution of a and c lattice parameters, respectively, as obtained from powder diffraction data. *Shaded* is the range where CDW cannot be detected in resistivity
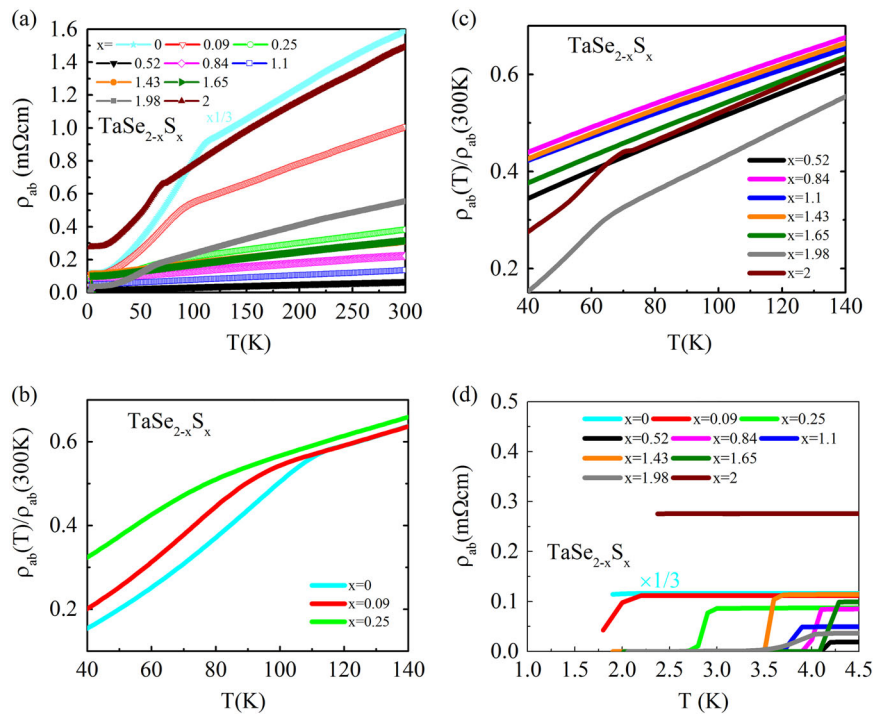
Fig. 2 Electrical resistivity of 2H-TaSe$_{2-x}$S$_x$ ($0 \leq x \leq 2$) **a** Temperature dependence of the resistivity for single crystals in the absence of magnetic field. **b**, **c** Temperature dependence of $\rho(T)/\rho$ (300 K) near CDW transitions. **d** $\rho(T)$ curves near superconducting transitions, indicating large enhancement of superconductivity

associated with the undistorted sublattice ungapped.[14–17] The hump shifts to lower temperature with S doping and vanishes for $x \geq 0.52$, but appears again for $x = 1.98$ at about 70 K, somewhat below the $T_{CDW} = 75$ K for pure 2H-TaS$_2$ (Fig. 2c). The

resistivity decreases to zero at lower temperatures, implying superconductivity (Fig. 2d). The magnetic susceptibility transitions and the large values of $-4\pi\chi$ at 1.9 K imply bulk superconductivity (Fig. 3a).
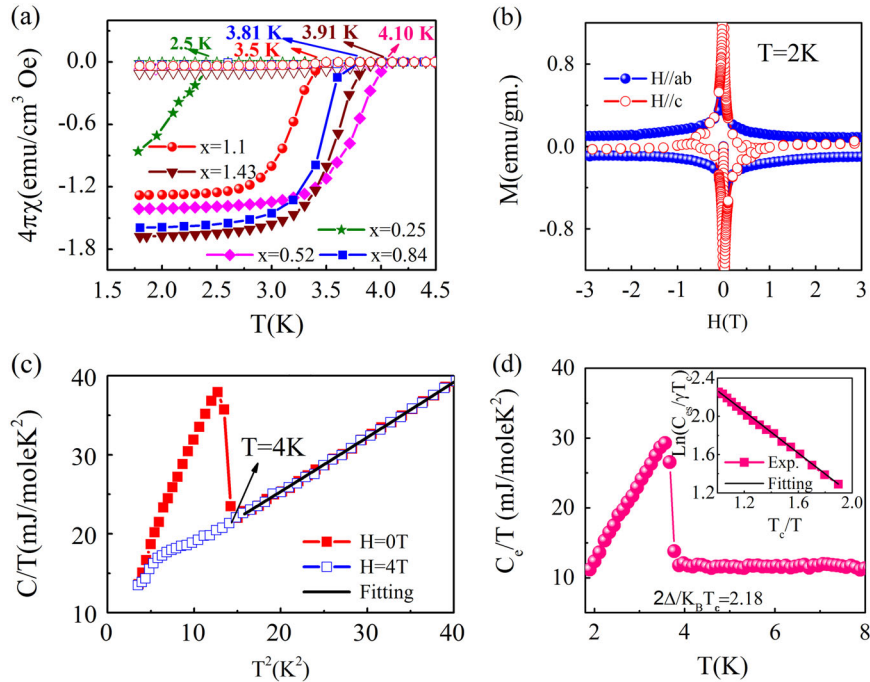
Fig. 3 Magnetic and thermodynamic properties of 2H-TaSe$_{2-x}$S$_x$ (0 ≤ x ≤ 2) **a** Magnetic susceptibility after zero-field-cooling (*filled*) and field-cooling (FC, *open symbols*). The smaller magnetization value for FC is likely due to the complex magnetic flux pinning effects. **b** Magnetization hysteresis loops M(H) of TaSe$_{1.48}$S$_{0.52}$ for H ∥ ab (*solid*) and H ∥ c (*open symbols*). **c** Low-temperature specific heat of TaSe$_{1.48}$S$_{0.52}$ measured at H = 0 (*solid*) and in 4 T (*open symbols*). **d** The electronic-specific heat in the superconducting state C_e for 2H-TaSe$_{1.48}$S$_{0.52}$ is obtained by subtracting the lattice contribution from the total specific heat: $C_e = C - C_{ph} = \gamma T$, where $C_{ph}(T) = \beta T^3 + \delta T^5$ and $\theta_D = [(n \cdot 1.944 \times 10^6)/\beta]^{1/3}$, where n is the number of elements per formula unit. *Inset*: below the superconducting transition temperature, electronic-specific heat temperature dependence follows an exponential decay, as $C_e \sim \exp[-\Delta(T)/k_BT]$. The *solid line* shows C_e/T calculated by assuming an isotropic s-wave BCS gap with $2\Delta = k_BT_c = 2.17$

Table 1. Superconducting parameters of 2H-TaSe$_2$, 2H-TaSe$_{1.48}$S$_{0.52}$, and 2H-TaS$_2$

Parameters	2H-TaSe$_2$	2H-TaSe$_{1.48}$S$_{0.52}$	2H-TaS$_2$
T_c(K)	0.14	4.20(1)	0.8
γ (mJ/mol K^2)	4.5	12.0(3)	7.5
β (mJ/mol K^4)	0.72	0.65(2)	0.44
δ (mJ/mol K^6)	–	6(1)·10^{-4}	–
λ_{e-ph}	0.397	0.73(1)	0.486
θ_D(K)	202	207(1)	236
$2\Delta/k_BT_c$	–	2.18(2)	–
Reported by	Ref 12	This work	Ref 12

Specifically, the anisotropic M(H) curves (Fig. 3b) confirm type-2 superconductivity for TaSe$_{1.48}$S$_{0.52}$ and imply anisotropic critical current density. The lambda anomaly in the specific heat jump around T = 4 K (Fig. 3c) is suppressed significantly in 4 T. A rough estimate of the average electron–phonon coupling $\lambda_{e-ph}\sim 0.73$[1] can be obtained from the McMillan equation, assuming the empirical value of the Coulomb pseudopotential $\mu^* = 0.15$ and taking the Debye frequency as the relevant phonon energy:[24]

$$\lambda = \frac{\mu^* \ln\left(\frac{1.45T_c}{\theta_D}\right) - 1.04}{1.04 + \ln\left(\frac{1.45T_c}{\theta_D}\right)(1 - 0.62\mu^*)}. \quad (1)$$

When compared with the parent 2H-TaSe$_2$ with electronic-specific heat coefficient $\gamma = 4.5$ mJ mol^{-1} K^{-2}, γ is larger for 50% S-doped sample (Fig. 3d, Table 1). The electron–phonon coupling $\lambda_{e-ph} = 0.73$ is somewhat larger than for 2H-TaSe$_2$ and 2H-TaS$_2$

(Table 1). The ratio of the gap at the critical temperature $2\Delta/k_BT_c$ = 2.17 can be obtained by linear fitting $\ln(C_e/\gamma T_c) - T_c/T$ data (Fig. 3d inset).

In a multiband electronic system with local CDW fluctuations[15–17, 20] above T_{CDW}, such as 2H-Ta(Se,S)$_2$, the carrier scattering mechanism arises from collective excitations below the CDW and from local CDW fluctuations above the CDW.[19] Above T_{CDW} $\rho(T) \sim aT + b$, immediately below T_{CDW} $\rho(T) \sim dT^2$ and at temperatures below about 15–20 K $\rho(T) \sim cT^5$. The T^5 is due to normal electron–phonon scattering, whereas the T^2 arises due to scattering of electrons by collective excitations of CDW; the rapid drop just below CDW is due to CDW phase ordering. The linear terms a, b above T_{CDW} arise due to electron–phonon scattering and phase disorder impurity-like scattering due to local CDW fluctuations. The fits of resistivity for the entire single crystal alloy series of 2H-TaSe$_{2-x}$S$_x$ (0 ≤ x ≤ 2) are satisfactory (Fig. 4a–c, Table 2). In all samples resistivity is linear at high temperatures. Just above the superconducting T_c interband scattering is negligible and individual s-band and d-band normal electron–phonon scattering dominates.[19] The constant term b for such crystals is much smaller than for CDW samples, because disorder suppresses the CDW therefore increases the number of carriers and thus the conductivity.

We present the evolution of superconducting T_c in 2H-TaSe$_2$ with S substitution x (normalized to T_c value for x = 0) in Fig. 4d. The T_c shows 30-fold increase and anticorrelation with the evolution of the high-temperature local charge fluctuation parameter b(x) (also normalized to b value for x = 0) (Fig. 4d). Note that weak decrease of T_c near x = 1 coincides with weak increase in normalized b(x) near the same S content. It appears that the considerable increase and evolution of $T_c(x)$ is related to an increase in available carrier concentration or mobility. These changes are matched (Fig. 4d) with the nearly identical evolution
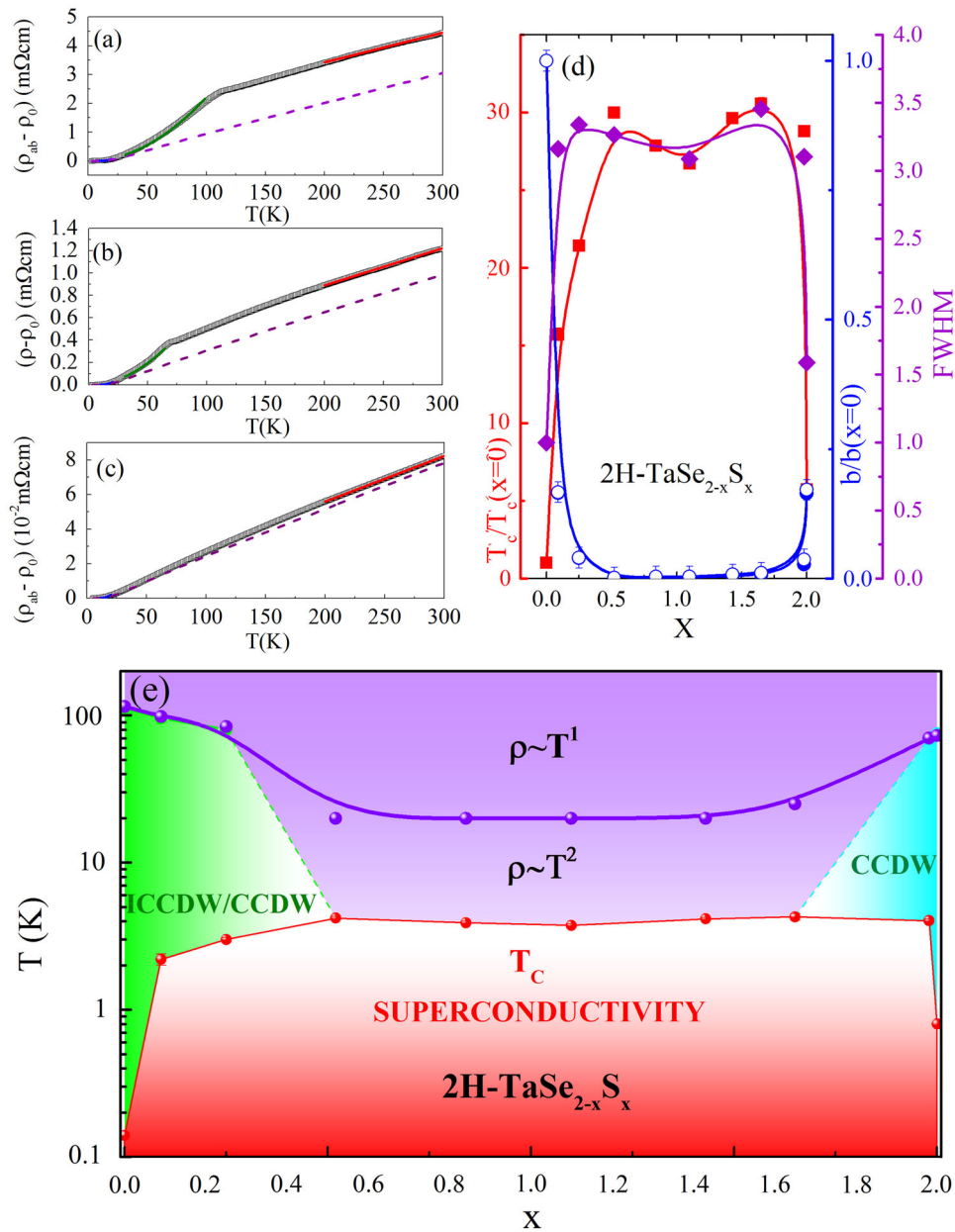
Fig. 4 Electronic phase diagram of 2H-TaSe$_{2-x}$S$_x$ ($0 \leq x \leq 2$) **a–c** Electronic scattering mechanism for **a** 2H-TaSe$_2$, **b** 2H-TaS$_2$, and **c** 2H-TaSe$_{0.9}$S$_{1.1}$. Low-temperature phonon scattering, scattering of collective excitations of CDW and high-temperature scattering of the local CDW fluctuations are shown by *blue*, *green*, and *red solid lines*, respectively. *Dashed violet line* shows the phonon resistivity approximated by the Bloch–Grüneisen formula (see text and Supplementary Information). **d** Note that the weak double dome evolution of superconducting $T_c(x)$ coincides with similar evolution of crystallographic disorder with sulfur content as revealed by FWHM of [006] Bragg peak in Fig. 1c. The intensity was normalized to 1 for each value of *x*. Moreover, $T_c(x)$ is in close correlation with disorder-induced changes in the high-temperature local charge fluctuations as seen by the changes in parameter *b*; all normalized to values of 2H-TaSe$_2$ ($x = 0$). The parameter *b* is shown from fits without (*open*) and with phonon subtraction from Bloch–Grüneisen formula (*full symbols*) (Supplementary Information). The error bars are about 0.01 for *x*, up to 0.04 for normalized T_c, and up to 0.01 for the normalized parameter *b* and FWHM (also see Table 1). **e** Phase diagram indicating the evolution of CDW (incommensurate ICCDW and commensurate CCDW) and superconductivity states with the change of *x*

of the crystallographic disorder as shown by the width of diffraction peaks taken on single crystals full width at half maximum (FWHM) normalized to width of $x = 0$ crystal. The linear resistivity $aT + b$ in the high-T_c crystals without CDW is rather close to the Bloch–Grüneisen phonon resistivity (Fig. 4c, Supplementary Information), suggesting that the strong suppression of parameter $b(x)$ in 2H-TaSe$_{2-x}$S$_x$ can be attributed to suppression of local CDW fluctuations for high-T_c crystals.

Figure 4e presents the electronic phase diagram. With the increase in *x*, the CDW transition of 2H-TaSe$_2$ is suppressed, whereas the superconducting transition temperature T_c increases up to 4.2 K for $x = 0.52$ where CDW disappears. Further sulfur increase shows weak but well resolved minimum in $T_c(x)$ for $x = 1.10$ up to the second maximal value of 4.28 K for $x = 1.65$ sulfur content in 2H-TaSe$_{1-x}$S$_x$. Signature of a CDW state, most probably CDW of the pure 2H-TaS$_2$, appears in $\rho(T)$ for higher S content up

Table 2. Superconducting T_c (defined as 90% of normal state resistivity; Fig. 2d), charge density wave T_{CDW} transition temperatures (defined as peak in resistivity; Fig. 2b, c), and fitting parameters of the CDW phase fluctuations scattering model for resistivity (see text)

x	T_c (K)	T_{CDW} (K)	c	c_{range} (K)	d	d_{range} (K)	a	b	L_{range} (K)	ρ_0
0	0.14	112(1)	2.12(7)	3–20	22.1(2)	30–100	102.8(1)	1.37(1)	200–300	3.4(5)
0.09(1)	2.2(1)	96(3)	0.52(2)	3–20	5.43(5)	34–86	22.4(3)	0.226(7)	200–300	1.1(2)
0.25(1)	3.0(5)	80(3)	0.27(2)	5–20	2.17(3)	34–65	8.08(1)	0.054(1)	200–300	0.9(1)
0.52(1)	4.2(1)	–	0.04(1)	5–20	–		1.6(1)	0.0004(1)	200–300	0.19(3)
0.84(1)	3.9(1)	–	0.10(1)	5–20	–		4.64(1)	0.0015(1)	200–300	0.8(1)
1.10(1)	3.7(2)	–	0.030(3)	5–20	–		2.64(1)	0.0031(1)	200–300	0.48(7)
1.43(1)	4.1(2)	–	0.20(1)	5–20	–		6.32(1)	0.0066(1)	200–300	1.1(1)
1.65(1)	4.3(1)	–	0.14(1)	5–20	–		6.82(1)	0.0099(3)	200–300	1.0(1)
1.98(1)	4.0 (1)	70(3)	0.20(1)	5–20	3.19(4)	30–60	16.8(1)	0.037(1)	200–300	0.36(5)
2.00(1)	0.8	75(1)	0.79(3)	3–20	7.78(3)	30–64	34.3(2)	0.225(1)	200–300	2.7(4)

Note: Considerable change in local CDW fluctuation scattering for crystals without CDW strives to increase conduction and is concomitant with the greatly enhanced superconducting T_c values. The units for c, d and a are in (10^{-8} mΩcm/K^5), (10^{-5} mΩcm/K^2), (10^{-4} mΩcm/K), respectively. The units for b and ρ_0 are in (mΩcm) and (10^{-1} mΩcm). For crystals near the middle of the alloy series where CDW cannot be detected in resistivity, the highest crystallographic disorder and consequently a substantial increase of ρ_0 (i.e., total $\rho(T)$ when $T{\to}0$) are expected. However, the impurity-like scattering due to local CDW fluctuations (phase disorder scattering) term b becomes small for that range of x, making the overall resistivity ρ_0 smaller or similar to $x=0$ and $x=2$ crystals (Table 2, Columns b and ρ_0). L_{range} denotes the temperature range of linear $aT+b$ fit

to $x=2$. The two T_c maxima in the double-dome appear at the critical doping, where CDW orders vanish similar to 1T-Se$_2$ and 2H-NbSe$_2$.[25, 26]

DISCUSSION

It should be noted that electron-irradiated 2H-TaSe$_2$ shows enhancement of superconducting T_c up to about 2.5 K.[27] Irradiation introduces defects, i.e., changes in stoichiometry similar to chemical substitutions. Cu-intercalated 2H-TaS$_2$ shows enhancement of T_c up to 4.7 K.[28] Copper behaves as *n*-type dopant and therefore its intercalation brings both disorder and charge transfer.[29] Similar doping and disorder interplay is expected with Na intercalation in 2H-TaS$_2$, where T_c was raised up to 4.4 K.[30] In contrast, isoelectronic substitution in 2H-TaSe$_{2-x}$S$_x$ single crystal alloy series allows for clear separation of disorder from doping-induced changes. The basic electronic structure of 2H-TaSe$_2$, 2H-TaSeS, and 2H-TaS$_2$ is quite similar as shown in the Local Density Approximation (LDA) calculations ([Supplementary Material]), leaving disorder as the origin of the increase in T_c. The intense variation of physical properties at low energy is a prime example of emergent phenomena.

Below the CDW transition temperature, a gap opens in 2H-TaSe$_2$ on two distorted sublattices in contrast to undistorted sublattice.[15] This makes for a small density of states at the Fermi level and consequently low superconducting T_c.[10] Sulfur substitution could introduce different Ta–S and Ta–Se bond lengths, disorder and puckering of metal plane. This would suppress CDW and increase density of electronic states, electron–phonon coupling, and superconducting T_c.[31] The lattice defect disorder increases superconducting T_c in CDW superconductor ZrTe$_3$ by factor of only 2–3.[32] Furthermore, $T_c(x)$ (Fig. 4e) cannot be explained by the *f*-wave model of CDW that predicts linear $T_c(x)$ in 2H-TaSe$_{2-x}$S$_x$ ($0 \leq x \leq 2$), whereas increased conductivity in high-T_c crystals argues against the change of the amplitude of ionic vibrations as in disordered films or amorphous lattices.[33, 34]

The normal state properties of this material are not well understood theoretically. Our experimental results indicate that the low-temperature specific heat coefficient of the alloy is very close to that computed in LDA (please see [Supplementary Material]), suggesting that the correlations due to Coulomb interactions are weak, while the electron–phonon coupling couples strongly to a few states not too close to the Fermi surface, which is consistent with the results of ref. 35. Alternatively, strong correlations are invoked in the exciton liquid model of 2H-TaSe$_2$. This model of CDW in 2H-TaSe$_2$ provides an explanation of some anomalous normal state properties such as linear resistivity above CDW transition, pseudogap, optical conductivity $\sigma(\omega,T)$, and incoherent metal features.[20, 36] Within that model and in contrast to ZrTe$_3$,[32] emergence of CDW reduces incoherent scattering, i.e., CDW-related bump in $\rho(T)$ is a coherence restoring transition that enables higher conductivity below T_{CDW}. The reduction in interband mixing dispersion that mixes the small number of d_{z2} electrons and p_z holes should remove the CDW, maximizing strong scattering of preformed incoherent excitons and enabling linear resistivity to progress to lower temperatures.[20] The observation of wide temperature range of linear resistivity in high-T_c crystals (Fig. 2a) suggests the rapid reduction in conduction and valence band mixing within that model. This calls for photoemission studies of newly synthesized alloy to test these theoretical models and to clarify the measure of the correlation strength.

Pressure should bring phonon hardening following the contraction of lattice parameters from 2H-TaSe$_2$ to 2H-TaS$_2$ (Fig. 1).[23, 37, 38] Assuming similar bulk modulus to WSe$_2$ (72 GPa),[39] the estimated chemical pressure differences of 2H-TaSeS ($T_c = 3.7$ K) when compared with 2H-TaSe$_2$ ($T_c = 0.14$ K) and 2H-TaS$_2$ ($T_c = 0.8$ K) are 6 GPa (positive pressure/contraction) and 2.8 GPa (negative pressure/expansion). Positive pressure increases considerably superconducting T_c in both 2H-TaS$_2$ and 2H-TaS$_2$; 6 GPa brings T_c in 2H-TaSe$_2$ up to about 3 K.[40] CDW is robust, surviving up to 20 GPa (2H-TaSe$_2$) and up to 16 GPa (2H-TaS$_2$). Clearly, chemical pressure may influence the rise of superconducting T_c in S-doped 2H-TaSe$_2$, but it cannot explain the absence of CDW in high-T_c samples in the phase diagram (Fig. 4e), the increase of superconducting T_c with lattice expansion in 2H-TaS$_2$ or the $T_c(x)$ evolution in 2H-TaSe$_{2-x}$S$_x$ ($0 \leq x \leq 2$) (Fig. 4e). The reduction in conduction and valence band mixing within DMFT framework facilitates not only the reduction of incoherence and stabilization of pseudogap characterized by linear $\rho(T)$, but also an increase in density of states at the Fermi level, thus highlighting

the effect of disorder, incoherent states, and the importance of local dynamical correlations.[20]

In summary, we show that disorder-induced superconducting states arise by isoelectronic substitution in 2H-TaSe$_2$. In contrast to all known CDW superconductors that have hitherto featured only a single dome of T_c with variation of any external parameter, the electronic phase diagram we present features a weak double dome in $T_c(x)$. The increase in superconducting T_c and changes in $T_c(x)$ are directly correlated with crystallographic disorder and disorder-induced scattering of the local CDW fluctuations. Our experimental findings can be understood on more general grounds without relying on a specific microscopic theory. For a given band structure, weak disorder does not affect the superconductivity of an s-wave superconductor (Anderson's theorem, Supplementary Information),[1, 23] but it is detrimental to the competing CDW order. The combination of these effects results in an enhanced superconducting critical temperature and a reduction of the CDW.

METHODS

Single crystals of 2H-TaSe$_{2-x}$S$_x$ ($0 \le x \le 2$) were grown via iodine vapor transport method. The source and growth zone were set at 900 °C for 3 days and then kept at 900 and 800 °C, respectively, for 10 days. Black plate-like single crystals with a typical size of $3 \cdot 3 \cdot 0.2$ mm^3 were obtained. The element analysis was performed using an energy-dispersive X-ray spectroscopy in a JEOL LSM-6500 scanning electron microscope. Electrical resistivity, specific heat, and magnetization measurements were performed in a Quantum Design PPMS-9 and MPMS XL-5. XRD patterns on single crystals were taken using a Rigaku Miniflex. Room temperature powder XRD measurements were carried out at the X-ray powder diffraction (28-ID-C) beam line at National Synchrotron Light Source II. The raw room temperature powder X-ray 2D data were integrated and converted to intensity vs. scattering angle using the software Fit2D.[41] The average structure was assessed from raw diffraction data using the General Structure Analysis System operated under EXPGUI utilizing $P63/mmc$ model from the literature.[42–44]

AUTHOR CONTRIBUTIONS

C.P. designed research. L.L. and Y.L. made crystals and carried out transport, magnetization, and thermal measurements. L.L. and Y.S. contributed single crystal X-ray diffraction data. Y.L., Y.H., and J.W. performed SEM measurements. Z.W. and Y.Z. performed TEM measurements. M.A., E.D., A.T., E.S.B., and S.J.L.B. carried out and analyzed powder X-ray diffraction data. C.P. supervised the project, analyzed the transport data with Y.L. and single crystal data with L. L. and wrote the paper with L.L. and with contributions from G.K. and Y.S. X.D. performed the LDA calculations and contributed to the theoretical interpretation of results. The manuscript reflects contribution and ideas of all authors.

COMPETING INTERESTS

The authors declare no competing interest.

REFERENCES

1. Anderson, P. Absence of diffusion in certain random lattices. *Phys. Rev.* **109**, 1492–1505 (1958).
2. Belitz, D. & Kirkpatrick, T. R. The Anderson-Mott transition. *Rev. Mod. Phys.* **66**, 261–380 (1994).
3. Zeljkovic, I. *et al.* Imaging the impact of single oxygen atoms on superconducting Bi$_{2+y}$Sr$_{2-y}$CaCu$_2$O$_{8+x}$. *Science* **337**, 320–323 (2012).
4. Seo, S. *et al.* Disorder in quantum critical superconductors. *Nat. Phys.* **10**, 120–125 (2014).
5. Mizykami, Y. *et al.* Disorder-induced topological change of the superconducting gap structure in iron pnictides. *Nat. Commun.* **5**, 5657 (2014).
6. Alloul, H. *et al.* Defects in correlated metals and superconductors. *Rev. Mod. Phys.* **81**, 45–108 (2009).
7. Grüner, G. The dynamics of charge-density waves. *Rev. Mod. Phys.* **60**, 1129–1181 (1988).
8. Kiss, T. *et al.* Charge-order-maximized momentum dependent superconductivity. *Nat. Phys.* **3**, 720–725 (2007).
9. Borisenko, S. V. *et al.* Two energy gaps and Fermi-surface "arcs" in NbSe$_2$. *Phys. Rev. Lett.* **102**, 166402 (2009).
10. Harper, J. M., Geballe, T. E. & Disalvo, F. J. Thermal properties of layered transition-metal dichalcogenides at charge-density-wave transitions. *Phys. Rev. B* **15**, 2943–2951 (1977).
11. Moncton, D. E., Axe, J. D. & DiSalvo, F. J. Study of superlattice formation in 2H-NbSe$_2$, and 2H-TaSe$_2$ by neutron scattering. *Phys. Rev. Lett.* **34**, 734–737 (1975).
12. Nishihara, H., Scholz, G. A., Naito, M., Frindt, R. F. & Tanaka, S. NMR of ^{181}Ta in 2H-TaS$_2$ and 2H-TaSe$_2$, observation of locally commensurate CDW. *J. Magn. Magn. Mater.* **31**, 717–718 (1983).
13. Laverock, J. *et al.* k-resolved susceptibility function of 2H-TaSe$_2$ from angle-resolved photoemission. *Phys. Rev. B* **88**, 035108 (2013).
14. Van Wezel, J. Polar charge and orbital order in 2H-TaS$_2$. *Phys. Rev. B* **85**, 035131 (2012).
15. Barnett, R. L., Polkovnikov, A., Demler, E., Yin, Wei-Guo & Ku, Wei Coexistence of gapless excitations and commensurate charge-density wave in the 2H transition metal dichalcogenides. *Phys. Rev. Lett.* **96**, 026406 (2006).
16. Vescoli, V., Degiorgi, L., Berger, H. & Forró, L. Dynamics of correlated two-dimensional materials: the 2H-TaSe$_2$ case. *Phys. Rev. Lett.* **81**, 453–456 (1998).
17. Ruzicka, B., Degiorgi, L., Berger, H., Gaál, R. & Forró, L. Charge dynamics of 2H-TaSe$_2$ along the less conducting c-axis. *Phys. Rev. Lett.* **86**, 4136–4139 (2001).
18. Yokota, K. I., Kurata, G., Matsui, T. & Fukuyama, H. Superconductivity in the quasi-two-dimensional conductor 2H-TaSe$_2$. *Phys. B* **284-288**, 551–552 (2000).
19. Naito, M. & Tanaka, S. Electrical transport properties in 2H-NbS$_2$, -NbSe$_2$, -TaS$_2$ and -TaSe$_2$. *J. Phys. Soc. Jpn.* **51**, 219–227 (1982).
20. Tarapder, A., Koley, S., Vidhyadhiraja, N. S. & Laad, M. S. Preformed excitonic liquid route to a charge density wave in 2H-TaSe$_2$. *Phys. Rev. Lett.* **106**, 236405 (2011).
21. Xu, W., Haule, K. & Kotliar, G. Hidden Fermi liquid, scattering rate saturation and Nernst effect: a dynamical mean field theory perspective. *Phys. Rev. Lett.* **111**, 036401 (2013).
22. Deng, X., Mravlje, J., Zitko, R., Ferrero, M., Kotliar, G. & Georges, A. How bad metals turn good: spectroscopic signatures of resilient quasiparticles. *Phys. Rev. Lett.* **110**, 086401 (2013).
23. Anderson, P. W. Theory of dirty superconductors. *J. Phys. Chem. Solids* **11**, 26–30 (1959).
24. McMillan, W. L. Transition temperature of strong-coupled superconductors. *Phys. Rev.* **167**, 331–344 (1968).
25. Kusmartseva, A. F., Sipos, B., Berger, H., Forró, L. & Tutiš, E. Pressure induced superconductivity in pristine 1T-TiSe$_2$. *Phys. Rev. Lett.* **103**, 236401 (2009).
26. Feng, Y. *et al.* Order parameter fluctuations at a buried quantum critical point. *Proc. Natl. Acad. Sci.* **109**, 7224–7229 (2012).
27. Mutka, H. Superconductivity in irradiated charge-density-wave compounds 2H-NbSe$_2$, 2H-TaS$_2$, and 2H-TaSe$_2$. *Phys. Rev. B* **28**, 2855–2858 (1983).
28. Wagner, K. E. *et al.* Tuning the charge density wave and superconductivity in Cu$_x$TaS$_2$. *Phys. Rev. B* **78**, 104520 (2008).
29. Zhao, J. F. *et al.* Evolution of the electronic structure of 1T-Cu$_x$TiSe$_2$. *Phys. Rev. B* **99**, 146401 (2007).
30. Fang, L. *et al.* Fabrication and superconductivity of Na$_x$TaS$_2$ crystals. *Phys. Rev. B* **72**, 014534 (2005).
31. Liu, Y. *et al.* Nature of charge-density-wave and superconductivity in 1T-TaSe$_{2-x}$Te$_x$. *Phys. Rev. B* **94**, 041531 (2016).
32. Zhu, X. *et al.* Disorder-induced bulk superconductivity in ZrTe$_3$ single crystals via growth control. *Phys. Rev. B* **87**, 024508 (2013).
33. Castro Neto, A. H. Charge density wave, superconductivity, and anomalous metallic behavior in 2D transition metal dichalcogenides. *Phys. Rev. Lett.* **86**, 4382–4385 (2001).
34. Garland, J. W., Bennemann, K. H. & Mueller, F. M. Effect of lattice disorder on the superconducting transition temperature. *Phys. Rev. Lett.* **21**, 1315–1319 (1968).
35. Varma, C. M. & Simons, A. L. Strong coupling theory of charge-density-wave transitions. *Phys. Rev. Lett.* **51**, 138–141 (1983).
36. Borisenko, S. V. *et al.* Pseudogap and charge density waves in two dimensions. *Phys. Rev. B* **100**, 196402 (2008).
37. Loa, I. & Syassen, K. Calculated elastic and electronic properties of MgB$_2$ at high pressures. *Solid State Comm.* **118**, 279–282 (2001).

38. Smith, T. F., Shelton, R. N. & Schwall, R. E. Superconductivity of TaSe$_{2-x}$Se$_x$ layer compounds at high pressure. *J. Phys. F: Metal. Phys.* **5**, 1713–1725 (1975).

39. Selvi, E., Aksoy, R., Knudson, R. & Ma, Y. High-pressure X-ray diffraction study of tungsten diselenide. *J. Phys. Chem. Solids* **69**, 2311–2314 (2008).

40. Freitas, D. C. *et al.* Strong enhancement of superconductivity at high pressures within the charge-density-wave states of 2H-TaS$_2$ and 2H-TaSe$_2$. *Phys. Rev. B* **93**, 184512 (2016).

41. Hammersley, A. P., Svensson, S. O., Hanfland, M., Fitch, A. N. & Hausermann, A. Two-dimensional detector software: from real detector to idealised image or two-theta scan. *High Pressure Res.* **14**, 235–248 (1996).

42. Larson, A.,C. and Von Dreele, R.,B. Report No. LAUR-86-748, Los Alamos National Laboratory, Los Alamos, NM 87545 (2004).

43. Toby, B. H. EXPGUI, a graphical user interface for GSAS. *J. Appl. Crystallogr.* **34**, 210–213 (2001).

44. Brixner, L. H. Preparation and properties of the single crystalline AB$_2$-type selenides and tellurides of niobium, tantalum, molybdenum and tungsten. *J. Inorg. Nucl. Chem.* **24**, 257–263 (1962).

On the Nanoscale Structure of $K_xFe_{2-y}Ch_2$ (Ch = S, Se): A Neutron Pair Distribution Function View

Panagiotis Mangelis [1],* [ID], Hechang Lei [2],†, Marshall T. McDonnell [3] [ID], Mikhail Feygenson [3],‡, Cedomir Petrovic [2], Emil S. Bozin [2] and Alexandros Lappas [1] [ID]

[1] Institute of Electronic Structure and Laser, Foundation for Research and Technology—Hellas, Vassilika Vouton, 711 10 Heraklion, Greece; lappas@iesl.forth.gr

[2] Condensed Matter Physics and Materials Science Department, Brookhaven National Laboratory, Upton, NY 11973, USA; hlei@ruc.edu.cn (H.L.); petrovic@bnl.gov (C.P.); bozin@bnl.gov (E.S.B.)

[3] Neutron Scattering Division, Oak Ridge National Laboratory, Oak Ridge, TN 37831, USA; mcdonnellmt@ornl.gov (M.T.M.); m.feygenson@fz-juelich.de (M.F.)

* Correspondence: mangelis@iesl.forth.gr

† Present Address: Department of Physics, Renmin University, Beijing 100872, China.

‡ Present Address: Forschungszentrum Jülich, JCNS, D-52425 Jülich, Germany.

Abstract: Comparative exploration of the nanometer-scale atomic structure of $K_xFe_{2-y}Ch_2$ (Ch = S, Se) was performed using neutron total scattering-based atomic pair distribution function (PDF) analysis of 5 K powder diffraction data in relation to physical properties. Whereas $K_xFe_{2-y}Se_2$ is a superconductor with a transition temperature of about 32 K, the isostructural sulphide analogue is not, which instead displays a spin glass semiconducting behavior at low temperatures. The PDF analysis explores phase separated and disordered structural models as candidate descriptors of the low temperature data. For both materials, the nanoscale structure is well described by the iron (Fe)-vacancy-disordered $K_2Fe_{5-y}Ch_5$ ($I4/m$) model containing excess Fe. An equally good description of the data is achieved by using a phase separated model comprised of $I4/m$ vacancy-ordered and $I4/mmm$ components. The $I4/mmm$ component appears as a minority phase in the structure of both $K_xFe_{2-y}Se_2$ and $K_xFe_{2-y}S_2$, and with similar contribution, implying that the phase ratio is not a decisive factor influencing the lack of superconductivity in the latter. Comparison of structural parameters of the Fe-vacancy-disordered model indicates that the replacement of selenium (Se) by sulphur (S) results in an appreciable reduction in the Fe-Ch interatomic distances and anion heights, while simultaneously increasing the irregularity of FeCh_4 tetrahedra, suggesting the more significant influence of these factors. Structural features are also compared to the non-intercalated FeSe and FeS parent phases, providing further information for the discussion about the influence of the lattice degrees of freedom on the observed properties in layered iron chalcogenides.

Keywords: neutron pair distribution function (PDF); intercalated iron superconductors; anion height; tetrahedron regularity

1. Introduction

Binary $Fe_{1+y}Se$ [1] has attracted considerable attention [2] due to its critical superconducting transition temperature (T_C) up to 8 K at ambient pressure. Externally applied pressure increases the T_C to 37 K at 7 GPa [3], whereas single FeSe layers grown on $SrTiO_3$ show strikingly higher T_Cs (ca. 65 K) [4,5] than many other Fe-based superconductors. Their crystal structure is quasi two-dimensional, composed of slabs of FeSe edge-sharing tetrahedra held together by van der Waals

interactions. Isovalent substitution with sulphur or tellurium for selenium does not change the carrier density [6,7], but substantially modifies the regularity of FeCh_4 (Ch = Se, S, Te) tetrahedron, which is believed to be a crucial factor governing electronic and magnetic properties, having particular influence on electron pairing. Consequently, the chemistry and physics of these simple iron-based materials result in complex relationships in the Fe$_{1+y}$Te$_{1-x}$Se$_x$ series [8].

The transition between itinerant antiferromagnetism and superconductivity can be controlled at elevated pressures, but also at ambient pressure by altering the crystal structure through substitutions either at the iron or chalcogen sites and favorably by intercalation of electron donating spacers (guests) between the FeCh sheets. Typically, alkali metals inserted between the FeCh layers expand the lattice and result in a ternary family of iron-superconductors, A_xFe$_2$Se$_2$ (A = K, Rb, Cs or Tl), with T_Cs in the order of 30 K. The first example of these so-called 122-iron selenides, the K$_{0.8}$Fe$_2$Se$_2$ derivative [9,10], was shown to adopt a ThCr$_2$Si$_2$-type structure. Much like the iron-pnicitides, with Fe tetrahedrally coordinated, superconductivity remains at the boundary with antiferromagnetism. However, whereas pnictides display superconductivity in the fully occupied, stoichiometric ThCr$_2$Si$_2$ structure, divalent Se^{2-} (instead of trivalent As^{3-}) leads to the presence of alkali and iron vacancies and issues of chemical instability that is promoted by the high-temperature solid-state synthesis of the K$_x$Fe$_{2-y}$Se$_2$ compounds. This entails microscale phase separation, with heterogeneity creating less than 20% of $I4/mmm$ K$_x$Fe$_2$Se$_2$, adopting the iron-pnictide ThCr$_2$Si$_2$ superconducting crystal structure, and the majority $I4/m$ K$_2$Fe$_4$Se$_5$ Fe-vacancy-ordered antiferromagnetic phase (Figure 1) [11,12]. The origin of superconductivity and the precise stoichiometry of iron and potassium content that leads to the superconducting phase are still under debate owing to the intrinsic phase separation and inhomogeneity in this type of chemically complex material [13,14]. Interestingly, the substitution of Se for S in the K$_x$Fe$_{2-y}$Se$_{2-z}$S$_z$ ($0 \leq z \leq 2$) series suppresses the superconducting state ($z = 1.6$) [15] and eventually the sulphide end-member, K$_x$Fe$_{2-y}$S$_2$, is not superconducting but exhibits a spin-glass behavior at temperatures below 32 K [16]. Therefore, experimental efforts to understand superconductivity in iron chalcogenides must not only tackle the sensitive stoichiometry required to observe a sizeable T_C, but also decipher the subtle differences in the atomic structure configuration that lead to such markedly different physical properties.
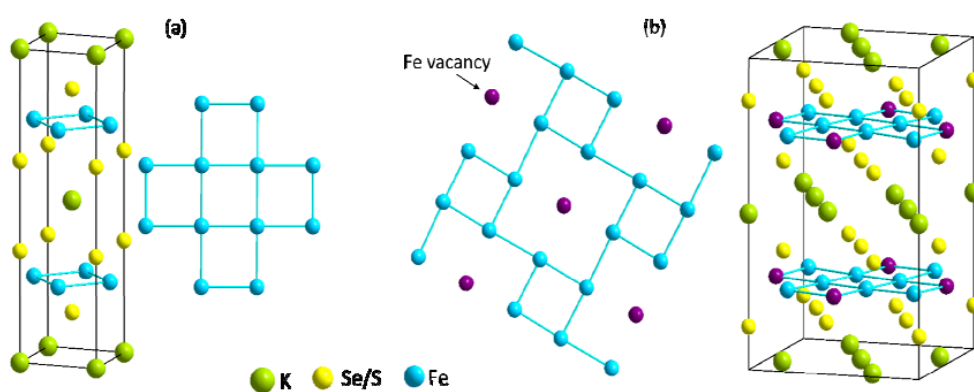
Figure 1. Atomic structure models for KFe$_2$$Ch_2$: (**a**) $I4/mmm$ featuring fully occupied Fe-layers and (**b**) $I4/m$, exhibiting Fe-vacancy order. Combinations of these models (not shown) were also used in the study.

Here, we use neutron total scattering experiments combined with atomic pair distribution function (PDF) analysis [17] to explore the nanometer scale aspects of phase separation and inhomogeneity for the two end-members of K$_x$Fe$_{2-y}$Se$_{2-z}$S$_z$ ($z = 0, 2$) series, at 5 K. We probe their structural evolution based on the regularity of the FeCh_4 tetrahedra and the Fe anion heights, which have been considered before as empirical parameters that mediate the evolution of the superconducting critical temperature in these intercalated materials.

2. Materials and Methods

Powdered samples of $K_xFe_{2-y}Se_2$ and $K_xFe_{2-y}S_2$ were prepared by pulverizing single crystals stored in a glove box. The single crystals were synthesized and characterized according to protocols reported previously [15]. Laboratory X-ray powder diffraction data of the samples used in this study were fully indexed within the $I4/m$ space group. Low temperature magnetic susceptibility and electrical resistivity measurements of the materials were previously reported [15]. The selenium-containing sample exhibited bulk superconductivity at T_C = 33 K, whereas the sulfur-containing sample was not superconducting and displayed magnetic semi-metallic behavior at low temperatures.

The neutron total scattering experiment was performed at the Nanoscale-Ordered Materials Diffractometer (NOMAD) [18] at the Spallation Neutron Source at Oak Ridge National Laboratory. Two pulverized samples, approximately 0.5 g each, were sealed in helium atmosphere in extruded cylindrical vanadium containers 6 mm in diameter, and mounted in the diffractometer equipped with an Orange cryostat sample environment. The instrument was calibrated using diamond standard. The data for each sample were collected at 5 K for 60 min. Data reduction was performed following standard protocols described elsewhere [19]. Pair distribution functions were obtained by Sine Fourier transformation of the measured reduced total scattering functions F(Q), where Q is the momentum transfer, over a range of Q_{MIN} = 0.5 $Å^{-1}$ to Q_{MAX} = 26 $Å^{-1}$. Refinement of the structural models against the experimental PDF data was completed over a 1 nm range via the small-box approach used within the PDFGUI software suite [20].

3. Results and Discussion

3.1. Qualitative Data Comparison

We began by observing and comparing the raw neutron powder diffraction data for $K_xFe_{2-y}Se_2$ and $K_xFe_{2-y}S_2$ shown in Figure 2, as seen by the forward scattering bank of detectors. Notably, this detector bank provided rather poor resolution featuring broad peaks and inherently lower statistics. This is a consequence of the construction of the NOMAD instrument, which is optimized for total scattering type measurements, where broad Q-range coverage and high resolution in backscattering banks are far more important, at the expense of the low angle banks. Nevertheless, for both, the data clearly identify the presence of, albeit weak, intensity associated with the (110) reflection that is a hallmark of $I4/m$ and is absent in $I4/mmm$ symmetry. This qualitative assessment revealed that both systems have, at least in part, $I4/m$ structural character, in agreement with previous reports [15,16].
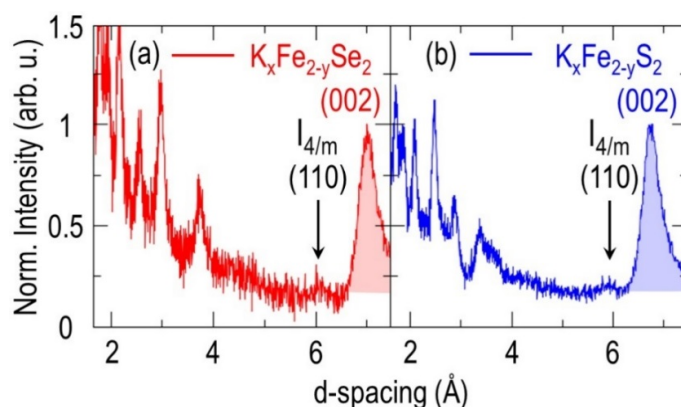
Figure 2. Neutron powder diffraction intensities for forward scattering 2θ = 15° NOMAD detector bank over selected d-spacing range. For easier comparison, the patterns were normalized to the intensities of (002) reflections (shaded): (**a**) $K_xFe_{2-y}Se_2$ and (**b**) $K_xFe_{2-y}S_2$. Arrows mark the (110) reflection that is allowed in the $I4/m$ but not in the $I4/mmm$ symmetry.

The neutron total scattering data collected over a broad range of momentum transfer Q were examined next. The findings are illustrated in Figure 3a,b for $K_xFe_{2-y}Se_2$ and $K_xFe_{2-y}S_2$, respectively, in the form of reduced total scattering structure function F(Q). Observable are appreciable arcs of diffuse scattering, particularly at higher momentum transfer values, indicative of appreciable disorder, as expected for this class of materials. Fourier transforms of F(Q) resulted in PDF and G(r), that are presented in Figure 3c,d, respectively. Some of the PDF peaks appear more intense in the $K_xFe_{2-y}Se_2$ pattern than in that of $K_xFe_{2-y}S_2$. In principle, this could be due to the differences in the underlying bond-length distributions reflecting the nanoscale structures and the complexity of underlying disorder. However, the coherent neutron scattering lengths, which scale the individual PDF contributions of any given pair of atoms in the structure, are nearly three times larger for selenium than for sulfur (b(Se) = 7.970 fm, whereas b(S) = 2.847 fm). The change in relative PDF peak intensity also originates from the renormalization due to different scattering properties of the samples.
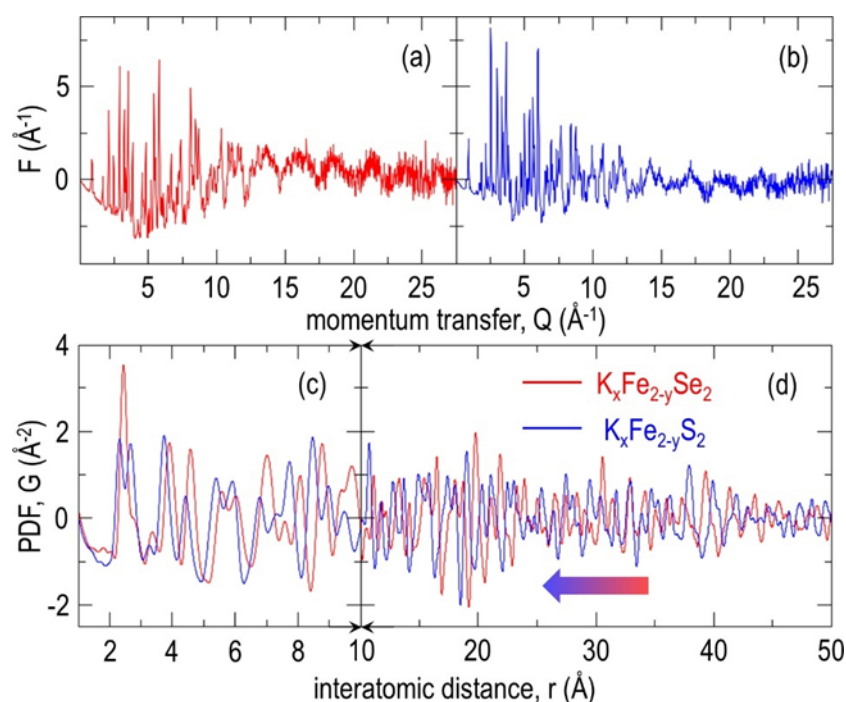
Figure 3. Neutron total scattering data for $K_xFe_{2-y}Ch_2$ (Ch = S, Se) at 5 K. Reduced neutron total scattering structure function, F(Q), for (**a**) $K_xFe_{2-y}Se_2$ (red) and (**b**) $K_xFe_{2-y}S_2$ (blue). Corresponding PDF data for $K_xFe_{2-y}Se_2$ (red) and $K_xFe_{2-y}S_2$ (blue) over a 5-nm PDF field of view are displayed below. (**c**) The low-r region is shown on an expanded scale, as compared to (**d**), which features intermediate distance range. The block arrow indicates the volume reduction trend from Ch = Se to S.

The PDFs of the two samples studied were directly compared in Figure 3. Notably, the PDF pattern of the sulphide is shifted considerably to lower interatomic distances, r, as indicated by the block arrow in Figure 3d, compared to the selenide counterpart. This lattice contraction occurred due to the lower ionic size of S^{2-} (ionic radius 1.84 Å) compared to that of Se^{2-} (ionic radius 1.98 Å) [21]. By examining the very local scale (Figure 3c), observably narrower bond-length distribution pertaining to the $FeCh_4$ tetrahedral environments was apparent in $K_xFe_{2-y}Se_2$ compared with $K_xFe_{2-y}S_2$. However, considering the appreciably different neutron scattering lengths of Se and S, as well as their effective radii, this assertion requires further confirmation from explicit structural modeling.

3.2. Model Dependent PDF Analysis

Structural information from experimental PDFs was extracted using the small box modeling approach based on small symmetrized unit cells (typically ~10 to 100 atoms) [17]. This approach provides a simple framework for crystal structure interpretation at the expense of being limited to the symmetry constraints of the underlying models. The approach was previously reported in detail [20].

Our modeling was based on the two phases described above and shown in Figure 1. The phase with $I4/mmm$ symmetry, often referred to as metallic, features stoichiometric slabs of FeCh_4 tetrahedra, whereas the phase with $I4/m$ symmetry, considered insulating and antiferromagnetic, contains two symmetrically distinct Fe crystallographic sites, one of which features Fe-vacancies and is completely empty in the case of full vacancy order. Here, we refer to the latter as the Fe-vacancy-ordered ($I4/m$ VO) model. In this model, the Fe and K occupancies at the low multiplicity sites, *4d* and *2b,* respectively, were fixed to zero under the assumption that all Fe and K atoms reside only at the high multiplicity sites, *16i* and *8h*, consistent with our room temperature Rietveld refinements reported earlier [22]. In addition, we considered a modified version of the $I4/m$ model, in which the occupancy of the Fe-vacancy *4d* site was allowed to vary, which we refer to as the vacancy-disordered ($I4/m$ VD) model. We used these atomic configurations both individually in single phase fits and combined in two-phase refinements. All fractional coordinates were constrained to follow the respective space group symmetries. All atomic displacement parameters (ADP) were set to be isotropic and identical for all atomic species of the same type. The occupancy and ADP constraints were introduced to minimize the number of refined parameters and to enable the sensible semiquantitative comparison of the two systems within the realm of these models. Although various model combinations were tested, the two that showed the best agreement with the data were (1) two-phase mixture composed of $I4/mmm$ and $I4/m$ VO ingredient phases, and (2) single phase $I4/m$ VD model. We limit our discussion to these two models.

The refinements of the structural models that result in the lowest fit residual (R_W) are summarized in Figure 4a for selenide and in Figure 4b for sulphide. The refinements results revealed that, at the nanoscale, the structures of both $K_xFe_{2-y}Se_2$ and $K_xFe_{2-y}S_2$ within the sensitivity of our data, were consistent with both a two-phase mixture (metallic $I4/mmm$ and insulating $I4/m$ VO) model and with a single phase disordered $I4/m$ VD model. Previous reports confirmed the coexistence of these two phases in both selenide [22] and sulphide analogue [23]. Notably, the single phase $I4/m$ VD model is effectively equivalent to a phase separated model, albeit disordered. In the explicit two-phase modeling of the selenide and sulphide data, the majority phase was found to be the $I4/m$ VO with a percentage of ca. 89(5)% and ca. 73(8)% by weight, respectively. Notably, according to this step in the analysis, the minority phase $I4/mmm$ in the case of $K_xFe_{2-y}S_2$ exhibited a higher percentage in the phase mixture than $K_xFe_{2-y}Se_2$. Whereas the exact phase percentage is difficult to acquire and is somewhat dependent on the type of constraints used, the robust observation in all our fits was that the metallic $I4/mmm$ phase contribution in non-superconducting $K_xFe_{2-y}S_2$ was at least comparable or probably slightly larger than in superconducting $K_xFe_{2-y}Se_2$. This implied that the presence or absence of this phase is not the sole factor that affects the superconductivity in this system. Furthermore, the phase separation picture on the nanoscale likely represents an oversimplification of the true complexity of the system, and may possibly reflect the limitations of the small box modeling approach.

We next explored the vacancy-disordered $K_2Fe_{5-y}Ch_5$ $I4/m$ VD model in which the Fe occupancy at the *4d* site is explicitly refined. The Fe occupancy at the high multiplicity *16i* site was fixed to one, as an attempt to explicitly refine the marginal deviations, in agreement with previous reports. Although attempts to refine K-content were made, this resulted in fit instabilities and the correlation of refined parameters was indicative of over-parametrization, so the occupancy of K sites was adjusted in all models to reflect nominal 0.8 potassium content. In $I4/m$-type models, the K *2b* site was empty. Importantly, the refinement results were qualitatively very similar to those of the phase mixture model. The refinements show finite and similar Fe occupancies at the *4d* site in both materials, which increase the overall Fe content to $K_2Fe_{4.27(1)}Se_5$ and $K_2Fe_{4.27(1)}S_5$, indicating no substantial difference across

the two systems in terms of phase-separation sensitive parameters and within the limitations of the applied modeling methodology. We interpreted this as an indicator that the phase separation aspect is not of fundamental importance for the lack of superconductivity in the sulphide, in the sense that non-superconducting sulphide does not account for a smaller fraction of the metallic phase.
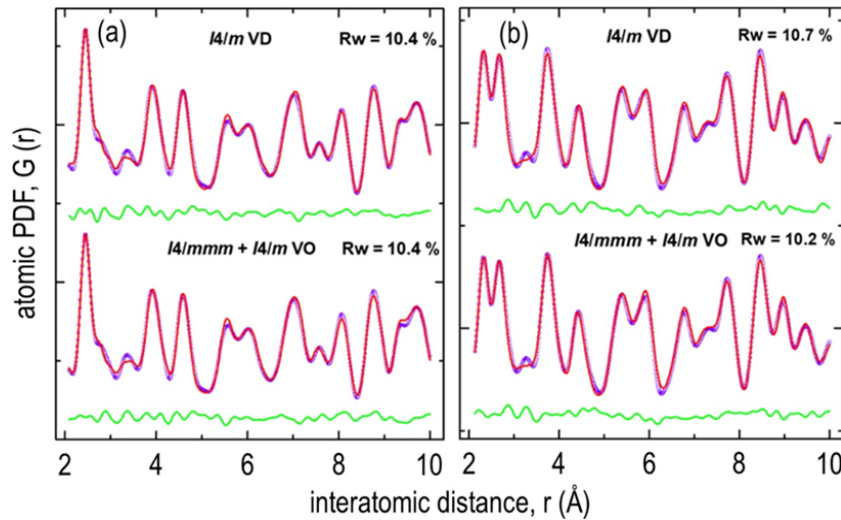
Figure 4. Refinements of neutron total scattering PDF data of (**a**) $K_xFe_{2-y}Se_2$ and (**b**) $K_xFe_{2-y}S_2$ at 5 K for the two structural models discussed in the text: (1) two-phase mixture of $I4/mmm$ KFe_2Ch_2 and $I4/m$ VO $K_2Fe_4Ch_5$ (bottom row), and (2) single phase $I4/m$ VD $K_2Fe_{5-y}Ch_5$ (top row). Observed (blue open symbols), calculated (red solid line), and difference (green solid line, offset for clarity) PDF profiles are illustrated. Fit residuals R_W are also shown.

In Tables 1 and 2, we quantitatively compare various structural parameters derived from the single-phase $I4/m$ VD model at 5 K, such as lattice parameters, interatomic Fe-Ch and Fe-Fe distances, anion heights, and ADP values. Most values are compared in reference to respective quantities obtained for non-intercalated FeSe [24] and FeS [25] parent materials. As expected, the lattice parameters and the interatomic distances (all Fe-Ch and the inter-cluster Fe-Fe lengths) are longer in the case of selenide, resulting in a large increase in the unit cell volume of ca. 11%. In the K-intercalated systems, two types of Fe-Fe distances are associated with the square Fe clusters: intracluster and intercluster, as defined within the $I4/m$ model. In the FeSe reference, there are two distinct Fe-Fe distances; however, these are along the two distinct crystallographic directions, as defined by the orthorhombic $Cmma$ model.

Table 1. Lattice parameters, interatomic Fe-Ch distances (d) and anion heights obtained from PDF refinements of $I4/m$ VD model to the $K_2Fe_{5-y}Ch_5$ 5 K data (Ch = Se, S). Neutron powder diffraction results for FeSe at 10 K [24] and x-ray powder diffraction results for FeS at 300 K [25] are also shown as a reference.

$I4/m$	a = b (Å)	c (Å)	d_1 (Å) [1]	d_2 (Å) [2]	d_3 (Å) [2]	d_4 (Å) [2]	h_{Ch} (Å)
$K_2Fe_{4.27(1)}Se_5$	8.683(1)	14.001(3)	2.337(8)	2.446(2)	2.451(3)	2.512(5)	1.396(9)
$K_2Fe_{4.27(1)}S_5$	8.395(2)	13.437(2)	2.283(5)	2.321(8)	2.332(5)	2.37(1)	1.282(8)
Cmma	**a (Å)**	**b (Å)**	**c (Å)**	**d (Å) × 4**	**-**	**-**	**h_{Ch} (Å)**
FeSe	5.3147(5)	5.3367(5)	5.4855(3)	2.383(1)	-	-	1.461(2)
P4/nmm	**a = b (Å)**	**c (Å)**	**d (Å) × 4**	**-**	**-**	**-**	**h_{Ch} (Å)**
FeS	3.6802(5)	5.0307(7)	2.235(1)	-	-	-	1.270(1)

[1] Fe-Ch(1) distance, where Ch(1) belongs to *4e* site; [2] Fe-Ch(2) distances, where Ch(2) belongs to *16i* site.

Table 2. Interatomic Fe-Fe distances and isotropic ADPs from the PDF refinements of $I4/m$ VD model to the $K_2Fe_{5-y}Ch_5$ data (Ch = Se, S) at 5 K and neutron powder diffraction refinement for FeSe at 10 K.

$I4/m$	Intra-Cluster Fe-Fe (Å)	Inter-Cluster Fe-Fe (Å)	K, Uiso (Å^2)	Fe, Uiso (Å^2)	Ch, Uiso (Å^2)
$K_2Fe_{4.27(1)}Se_5$	2.649(4)	2.897(5)	0.0231(7)	0.0087(1)	0.0067(1)
$K_2Fe_{4.27(1)}S_5$	2.672(1)	2.746(1)	0.0236(2)	0.0093(1)	0.0032(1)
Cmma	**Fe-Fe(1) (Å)**	**Fe-Fe(2) (Å)**			
FeSe	2.657(1)	2.667(1)	-	0.0043(7)	0.0033(9)

One prominent structural parameter known to be correlated with the superconducting transition temperature T_C in iron-based superconductors is the anion height, defined as the *c*-axis normal distance between the chalcogen/pnictogen and the Fe-sheet. According to this empirical observation, the critical temperature, T_C increases as the anion height approaches a value of ~1.38 Å, inferring the existence of an optimal bonding environment for maximizing the superconducting response [26]. The anion height values obtained for the samples studied here were generally consistent with the empirical rule established by Mizuguchi et al. [26]. For our superconducting $K_2Fe_{4.27(1)}Se_5$ sample, with $T_C \approx 32$ K, the anion height was indeed relatively close to this ideal value, whereas for the insulating $K_2Fe_{4.27(1)}S_5$ material, the anion height was appreciably further away from the optimal 1.38 Å. This is illustrated schematically in the inset of Figure 5. The replacement of Se by smaller S results in reduction of all interatomic cation-anion distances, which in turn gives rise to a decrease in the anion height to about ~1.28 Å. The anion height in the potassium-intercalated selenide can also be compared to the parent FeSe, which crystallizes in the *Cmma* structure at low temperatures. For the latter, the neutron powder diffraction data collected at 10 K on the same instrument were used [24]. Intercalation of K in between the FeSe layers induced an effective reduction in the anion height, shifting the value closer to the optimum, while simultaneously increasing the Fe-interlayer spacing from 5.316(1) Å to 7.001(1) Å, with a concomitant increase of T_C from about 8 K to about 32 K. In the sulphide analogue, the K intercalation also increased the Fe interlayer spacing from 5.031(1) Å to 6.747(4) Å, but the anion height increased only slightly, and at 1.28 Å, is still substantially far from the optimum value for superconductivity. Whereas FeS is a superconductor with a T_C ~5 K [25], the K-intercalated compound exhibited a spin-glass behavior.

Lastly, we considered the regularity of the FeCh_4 tetrahedron, which represents yet another structural aspect of relevance to superconductivity [12,15,27]. Indeed, the superconducting critical temperature T_C in some iron-based superconductors was maximized for structures featuring regular tetrahedral units, defined by the Ch-Fe-Ch angles all being equal to 109.47°, thus resulting in perfect tetrahedral geometry. Given this, the mean and standard deviation of the underlying bond angle distributions were estimated from the neutron scattering data analyzed for the systems of interest here. To facilitate the comparison, the data are schematically presented as Gaussian distributions in Figure 5, whose centroids reflect the average tetrahedral angle, whereas the widths represent the standard deviation of the angular distribution. For the samples studied, these values were obtained for the six tetrahedral angles of $K_2Fe_{5-y}Ch_5$ (Ch = Se, S) based on the $I4/m$ VD model for *16i* Fe site, and the three angles of FeSe (with multiplicity two) assuming an orthorhombic *Cmma* crystal type. In the case of FeS, the distribution was the narrowest (not shown), implying that the tetrahedral regularity is not a required condition for optimizing superconductivity. Nevertheless, PDF results evidenced a larger degree of tetrahedral irregularity in the case of $K_2Fe_{5-y}S_5$ as compared with $K_2Fe_{5-y}Se_5$. Replacement of Se by S substantially increased the irregularity of the FeCh_4 tetrahedron on average, which, together with the substantial departure of the anion height from the optimum value, coincide with the observed decrease in superconductivity and the appearance of the spin glass state in the sulphide. These modeling results confirm the narrower distribution of interatomic distances in the selenide, determined from the direct comparison of the experimental PDFs. Importantly,

the parent FeSe showed a slightly wider distribution compared with the K-intercalated counterpart, and consistently lower value of T_C. As the anion heights of the selenide and sulfide samples studied here were positioned on the opposite sides of the optimal value of 1.38 Å, where the observed T_C peaks in iron chalcogenides and pnictides, tracking this subtle structural parameter on the basis of the $K_xFe_{2-y}Se_{2-z}S_z$ solid-solution testing ground would be valuable. In particular, systematically and quantitatively characterizing the evolution of the disorder across the phase diagram of $K_xFe_{2-y}Se_{2-z}S_z$ at low temperatures would help correlate how the key building blocks relay the competition of magnetism with superconductivity (and vice versa), a concept of fundamental importance in Fe-based correlated electron systems.
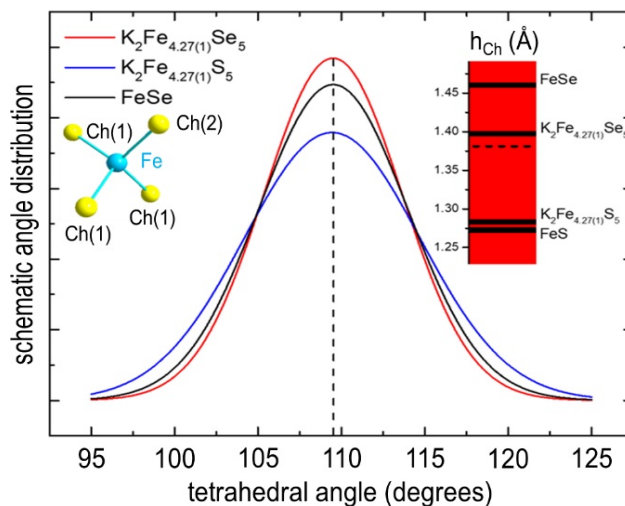
Figure 5. Schematic of the tetrahedral angle distribution (solid lines) extracted from the tetrahedral angles of the Fe *16i* site in $K_2Fe_{5-y}Ch_5$ $I4/m$ VD PDF model at 5 K and for FeSe in the *Cmma* symmetry at 10 K. The vertical dashed line marks the ideal tetrahedral angle of 109.47°. The inset (red bar) illustrates the placement of the average anion height h_{Ch} (black lines) for the material systems considered relative to the optimal value of ~1.38 Å (dashed line).

4. Conclusions

In summary, we performed a neutron PDF analysis to explore the nanoscale atomic structures of two $K_xFe_{2-y}Ch_2$ materials (*Ch* = S, Se) at 5 K. The study was motivated by the phase separation concept in these compositions, which enabled the comparison of their structural features to those observed in their non-intercalated counterparts. Interestingly, the diffraction patterns of both systems displayed the (110) reflection, a hallmark of $I4/m$ crystal symmetry. In the respective reduced total scattering structure functions F(Q), appreciable arcs of diffuse scattering, particularly at high momentum transfers Q, were indicative of the presence of substantial disorder in the system. The diffuse intensity appeared to be more pronounced for $K_xFe_{2-y}Se_2$ than for $K_xFe_{2-y}S_2$. The PDF analysis revealed that the data for both systems could be explained by either a mixture of majority $I4/m$ vacancy-ordered and minority $I4/mmm$ components, or by a single phase $I4/m$ vacancy-disordered model. Both descriptions are effectively consistent with the underlying phase separation and complex disorder on the nanoscale. Quantitatively, in the two-phase description, the $I4/mmm$ minority phase content did not decrease from $K_xFe_{2-y}Se_2$ to $K_xFe_{2-y}S_2$ as would be expected on the grounds that this phase is commonly associated with superconductivity. Similarly, the single-phase vacancy disordered model description resulted in comparable values of the occupancy of the Fe *4d* site for the two systems. This indicates that the potassium intercalated Fe*Ch* is more complex than outlined by the simplistic phase separation scenario, and implies that the phase separation does not play a key role in the collapse of superconductivity in the intercalated sulphide system. An explanation might be provided by the fine details of

disorder that are yet to be explored. Comparison of relevant structural parameters derived from the Fe-vacancy-disordered model demonstrated that replacement of larger Se by smaller S induced a dramatic reduction in the unit cell volume and interatomic Fe-*Ch* distances. Corresponding anion heights conformed to the empirical rule of Mizuguchi et al. [26]. Furthermore, the Fe*Ch*$_4$ tetrahedra were more irregular in the non-superconducting sulphide than in the superconducting selenide. The same parameters obtained for the non-intercalated parent materials appear to also follow the same empirical trend. Overall, this neutron total scattering study highlights that deciphering the subtle differences in the atomic structure configuration of the K-intercalated end-members and their markedly different physical properties is a complex physical crystallography problem. Seeking additional insights from K$_x$Fe$_{2-y}$Se$_{2-z}$S$_z$ solid-solutions may be crucial for uncovering the mediating role of key structural building blocks in this puzzle.

Author Contributions: Project conceived by E.S.B., A.L. and C.P.; Sample preparation and characterization, H.L. and C.P.; Data acquisition, E.S.B. and M.F.; Data reduction, M.F., E.S.B. and M.T.M.; Data modeling and interpretation, P.M., A.L. and E.S.B.; Writing-Original Draft Preparation, P.M., A.L. and E.S.B.; Writing-Review, all co-authors; Writing-Final Editing, P.M., C.P., A.L. and E.S.B.

Conflicts of Interest: The authors declare no conflict of interest.

References

1. Hsu, F.-C.; Luo, J.-Y.; Yeh, K.-W.; Chen, T.-K.; Huang, T.-W.; Wu, P.M.; Lee, Y.-C.; Huang, Y.-L.; Chu, Y.-Y.; Yan, D.-C.; et al. Superconductivity in the PbO-type structure α-FeSe. *Proc. Natl. Acad. Sci. USA* **2008**, *105*, 14262–14264. [CrossRef] [PubMed]

2. Malavasi, L.; Margadonna, S. Structure–properties correlations in Fe chalcogenide superconductors. *Chem. Soc. Rev.* **2012**, *41*, 3897–3911. [CrossRef] [PubMed]

3. Margadonna, S.; Takabayashi, Y.; Ohishi, Y.; Mizuguchi, Y.; Takano, Y.; Kagayama, T.; Nakagawa, T.; Takata, M.; Prassides, K. Pressure evolution of the low-temperature crystal structure and bonding of the superconductor FeSe (T_C = 37 K). *Phys. Rev. B* **2009**, *80*, 064506. [CrossRef]

4. Tan, S.; Zhang, Y.; Xia, M.; Ye, Z.; Chen, F.; Xie, X.; Peng, R.; Xu, D.; Fan, Q.; Xu, H.; et al. Interface-induced superconductivity and strain-dependent spin density waves in FeSe/SrTiO$_3$ thin films. *Nat. Mater.* **2013**, *12*, 634–640. [CrossRef] [PubMed]

5. Ge, J.-F.; Liu, Z.-L.; Liu, C.; Gao, C.-L.; Qian, D.; Xue, Q.-K.; Liu, Y.; Jia, J.-F. Superconductivity above 100 K in single-layer FeSe films on doped SrTiO₃. *Nat. Mater.* **2015**, *14*, 285–289. [CrossRef] [PubMed]

6. Fang, M.H.; Pham, H.M.; Qian, B.; Liu, T.J.; Vehstedt, E.K.; Liu, Y.; Spinu, L.; Mao, Z.Q. Superconductivity close to magnetic instability in Fe(Se$_{1-x}$Te$_x$)$_{0.82}$. *Phys. Rev. B* **2008**, *78*. [CrossRef]

7. Yeh, K.-W.; Huang, T.-W.; Huang, Y.; Chen, T.-K.; Hsu, F.-C.; Wu, P.M.; Lee, Y.-C.; Chu, Y.-Y.; Chen, C.-L.; Luo, J.-Y.; et al. Tellurium substitution effect on superconductivity of the α-phase iron selenide. *EPL Europhys. Lett.* **2008**, *84*, 37002. [CrossRef]

8. Katayama, N.; Ji, S.; Louca, D.; Lee, S.; Fujita, M.; Sato, T.J.; Wen, J.; Xu, Z.; Gu, G.; Xu, G.; et al. Investigation of the Spin-Glass Regime between the Antiferromagnetic and Superconducting Phases in Fe$_{1+y}$Se$_x$Te$_{1-x}$. *J. Phys. Soc. Jpn.* **2010**, *79*, 113702. [CrossRef]

9. Guo, J.; Jin, S.; Wang, G.; Wang, S.; Zhu, K.; Zhou, T.; He, M.; Chen, X. Superconductivity in the iron selenide K$_x$Fe$_2$Se$_2$ (0 ≤ *x* ≤ 1.0). *Phys. Rev. B* **2010**, *82*. [CrossRef]

10. Ye, F.; Chi, S.; Bao, W.; Wang, X.F.; Ying, J.J.; Chen, X.H.; Wang, H.D.; Dong, C.H.; Fang, M. Common Crystalline and Magnetic Structure of Superconducting A_2Fe$_4$Se$_5$ (*A* = K, Rb, Cs, Tl) Single Crystals Measured Using Neutron Diffraction. *Phys. Rev. Lett.* **2011**, *107*, 137003. [CrossRef] [PubMed]

11. Shoemaker, D.P.; Chung, D.Y.; Claus, H.; Francisco, M.C.; Avci, S.; Llobet, A.; Kanatzidis, M.G. Phase relations in $K_xFe_{2-y}Se_2$ and the structure of superconducting $K_xFe_2Se_2$ via high-resolution synchrotron diffraction. *Phys. Rev. B* **2012**, *86*. [CrossRef]

12. Vivanco, H.K.; Rodriguez, E.E. The intercalation chemistry of layered iron chalcogenide superconductors. *J. Solid State Chem.* **2016**, *242*, 3–21. [CrossRef]

13. Carr, S.V.; Louca, D.; Siewenie, J.; Huang, Q.; Wang, A.; Chen, X.; Dai, P. Structure and composition of the superconducting phase in alkali iron selenide $K_yFe_{1.6+x}Se_2$. *Phys. Rev. B* **2014**, *89*, 134509. [CrossRef]

14. Tanaka, M.; Yanagisawa, Y.; Denholme, S.J.; Fujioka, M.; Funahashi, S.; Matsushita, Y.; Ishizawa, N.; Yamaguchi, T.; Takeya, H.; Takano, Y. Origin of the Higher-T_c Phase in the $K_xFe_{2-y}Se_2$ System. *J. Phys. Soc. Jpn.* **2016**, *85*, 044710. [CrossRef]

15. Lei, H.; Abeykoon, M.; Bozin, E.S.; Wang, K.; Warren, J.B.; Petrovic, C. Phase Diagram of $K_xFe_{2-y}Se_{2-z}S_z$ and the Suppression of its Superconducting State by an Fe2-Se/S Tetrahedron Distortion. *Phys. Rev. Lett.* **2011**, *107*. [CrossRef] [PubMed]

16. Lei, H.; Abeykoon, M.; Bozin, E.S.; Petrovic, C. Spin-glass behavior of semiconducting $K_xFe_{2-y}S_2$. *Phys. Rev. B* **2011**, *83*. [CrossRef]

17. Billinge, S.J.L.; Egami, T. *Underneath the Bragg Peaks: Structural Analysis of Complex Materials*; Pergamon Materials Series; Elsevier: Oxford, UK, 2003; Volume 7.

18. Neuefeind, J.; Feygenson, M.; Carruth, J.; Hoffmann, R.; Chipley, K.K. The Nanoscale Ordered MAterials Diffractometer NOMAD at the Spallation Neutron Source SNS. *Nucl. Instrum. Methods Phys. Res. Sect. B* **2012**, *287*, 68–75. [CrossRef]

19. Peterson, P.F.; Gutmann, M.; Proffen, T.; Billinge, S.J.L. PDFgetN: A user-friendly program to extract the total scattering structure factor and the pair distribution function from neutron powder diffraction data. *J. Appl. Crystallogr.* **2000**, *33*, 1192. [CrossRef]

20. Farrow, C.L.; Juhas, P.; Liu, J.W.; Bryndin, D.; Božin, E.S.; Bloch, J.; Proffen, T.; Billinge, S.J.L. PDFfit2 and PDFgui: Computer programs for studying nanostructure in crystals. *J. Phys. Condens. Matter* **2007**, *19*, 335219. [CrossRef] [PubMed]

21. Shannon, R.D. Revised effective ionic radii and systematic studies of interatomic distances in halides and chalcogenides. *Acta Crystallogr. Sect. A* **1976**, *32*, 751–767. [CrossRef]

22. Lazarević, N.; Abeykoon, M.; Stephens, P.W.; Lei, H.; Bozin, E.S.; Petrovic, C.; Popović, Z.V. Vacancy-induced nanoscale phase separation in $K_xFe_{2-y}Se_2$ single crystals evidenced by Raman scattering and powder X-ray diffraction. *Phys. Rev. B* **2012**, *86*. [CrossRef]

23. Tsuchiya, Y.; Ikeda, S.; Zhang, X.-W.; Kishimoto, S.; Kikegawa, T.; Hirao, N.; Kawaguchi, S.I.; Ohishi, Y.; Kobayash, H. Pressure-Induced Phase Transition in $K_xFe_{2-y}S_2$. *J. Phys. Soc. Jpn.* **2017**, *86*. [CrossRef]

24. Xu, Z.; Schneeloch, J.A.; Wen, J.; Božin, E.S.; Granroth, G.E.; Winn, B.L.; Feygenson, M.; Birgeneau, R.J.; Gu, G.; Zaliznyak, I.A.; et al. Thermal evolution of antiferromagnetic correlations and tetrahedral bond angles in superconducting $FeTe_{1-x}Se_x$. *Phys. Rev. B* **2016**, *93*, 104517. [CrossRef]

25. Lai, X.; Zhang, H.; Wang, Y.; Wang, X.; Zhang, X.; Lin, J.; Huang, F. Observation of Superconductivity in Tetragonal FeS. *J. Am. Chem. Soc.* **2015**, *137*, 10148–10151. [CrossRef] [PubMed]

26. Mizuguchi, Y.; Hara, Y.; Deguchi, K.; Tsuda, S.; Yamaguchi, T.; Takeda, K.; Kotegawa, H.; Tou, H.; Takano, Y. Anion height dependence of T_c for the Fe-based superconductor. *Supercond. Sci. Technol.* **2010**, *23*, 054013. [CrossRef]

27. Lee, C.-H.; Iyo, A.; Eisaki, H.; Kito, H.; Fernandez-Diaz, M.T.; Ito, T.; Kihou, K.; Matsuhata, H.; Braden, M.; Yamada, K. Effect of Structural Parameters on Superconductivity in Fluorine-Free $LnFeAsO_{1-y}$ (Ln = La, Nd). *J. Phys. Soc. Jpn.* **2008**, *77*, 083704. [CrossRef]

Absence of local fluctuating dimers in superconducting Ir$_{1-x}$(Pt,Rh)$_x$Te$_2$

Runze Yu,[1,*] S. Banerjee,[2] H. C. Lei,[1,†] Ryan Sinclair,[3] M. Abeykoon,[4] H. D. Zhou,[3] C. Petrovic,[1]
Z. Guguchia,[1,5] and E. S. Bozin[1,‡]

[1]*Condensed Matter Physics and Materials Science Department, Brookhaven National Laboratory, Upton, New York 11973, USA*
[2]*Department of Applied Physics and Applied Mathematics, Columbia University, New York, New York 10027, USA*
[3]*Department of Physics and Astronomy, University of Tennessee, Knoxville, Tennessee 37996, USA*
[4]*Photon Sciences Division, Brookhaven National Laboratory, Upton, New York 11973, USA*
[5]*Department of Physics, Columbia University, New York, New York 10027, USA*

The compound IrTe$_2$ is known to exhibit a transition to a modulated state featuring Ir-Ir dimers, with large associated atomic displacements. Partial substitution of Pt or Rh for Ir destabilizes the modulated structure and induces superconductivity. It has been proposed that quantum critical dimer fluctuations might be associated with the superconductivity. Here we test for such local dimer correlations and demonstrate their absence. X-ray pair distribution function approach reveals that the local structure of Ir$_{0.95}$Pt$_{0.05}$Te$_2$ and Ir$_{0.8}$Rh$_{0.2}$Te$_2$ dichalcogenide superconductors with compositions just past the dimer/superconductor boundary is explained well by a dimer-free model down to 10 K, ruling out the possibility of there being nanoscale dimer fluctuations in this regime. This is inconsistent with the proposed quantum-critical-point-like interplay of the dimer state and superconductivity, and precludes scenarios for dimer fluctuations mediated superconducting pairing.

I. INTRODUCTION

Unconventional superconductivity (SC) often emerges in the proximity of symmetry-breaking electronic and magnetic orders upon their destabilization by chemical modifications, external pressure, and fields, as seen in a diverse variety of quantum systems [1–3]. The pairing mechanism remains elusive [4], in part because the role of fluctuations of adjacent ordered states and their ubiquity are not fully established and understood [5–7]. Studying such fluctuations is quite challenging [8], with one of the reasons being the lack of long-range coherence [9]. When broken-symmetry states, for example, electronic states involving $5d$ manifolds in CuIr$_2$S$_4$ [10,11] and IrTe$_2$ [12,13] where two Ir^{4+} $S = 1/2$ ions bind into spinless spatially ordered dimers, are coupled to the lattice, footprints of their fluctuations become evident in the local atomic structure and can be studied indirectly using a local structural probe [14,15] such as the atomic pair distribution function (PDF) analysis of powder diffraction data [16,17]. Here we use an x-ray PDF to probe the existence or absence of Ir^{4+}-Ir^{4+} dimer fluctuations in a doped IrTe$_2$ superconductor, which yields information essential for *bona fide* considerations of dimer/SC entanglement in this system.

Trigonal metallic iridium ditelluride, IrTe$_2$, has garnered significant attention over the past several years following the discovery of bulk superconductivity ($T_c \sim 3$ K) in its interca-

lated and substituted variants IrTe$_2$:Pd [18], Ir$_{1-x}$Pt$_x$Te$_2$ [19], Cu$_x$IrTe$_2$ [20], and Ir$_{1-x}$Rh$_x$Te$_2$ [21]. Interestingly, the appearance of SC also follows the suppression of a long-range ordered electronic state, in this case associated with charge-disproportionation-enabled Ir^{4+}-Ir^{4+} dimerization [12,13] established in IrTe$_2$ at its symmetry-lowering structural transition ($T_s \sim 250$ K) [22]. This results in familiar domelike phase diagrams, akin to those of high-temperature SCs and recently discovered Cu$_x$TiSe$_2$ [23], 1T-TaS$_2$ [24], 1T-TiSe$_2$ [25], T_d-MoTe$_2$ [26], ZrTe$_{3-x}$Se$_x$ [27], and 2H-TaSe$_{2-x}$S$_x$ [28] transition-metal dichalcogenide superconductors, where destabilization of the charge density wave (CDW) order leads to SC. Importantly, in Cu$_x$TiSe$_2$ quantum criticality associated with fluctuations of CDW order has been considered in relation to SC pairing [29,30]. A perceived analogy with these systems prompted a hypothesis of quantum critical point (QCP)-like interplay of SC and dimerization in IrTe$_2$ derivates [18] and speculations about dimer fluctuation-mediated superconductivity [19,31].

The importance of the IrTe$_2$ lattice in facilitating the long-range dimer order is well documented [32–34], with signatures of the dimer state found in a remarkable reduction of intradimer Ir-Ir (0.8 Å) and associated Te-Te (0.5 Å) distances [12], as illustrated in Figs. 1(a) and 1(b). Despite this and the importance of verifying the dimer fluctuation hypothesis, the utilization of experimental probes sensitive to the presence or absence of local distortions has been surprisingly scarce. Existing reports based on extended x-ray absorption fine-structure (EXAFS) spectroscopy focus on parent IrTe$_2$ under ambient [35] and high-pressure [36] conditions. The ambient study argues for persistence of *local* Ir dimers in the high-temperature regime where the structure is undistorted trigonal on average [35]. While this, if true, could hint at the presence of fluctuating

---

*Present address: Institute of Physics, Chinese Academy of Science, Beijing 100190, People's Republic of China.

†Present address: Department of Physics, Renmin University, Beijing 100872, People's Republic of China.

‡bozin@bnl.gov
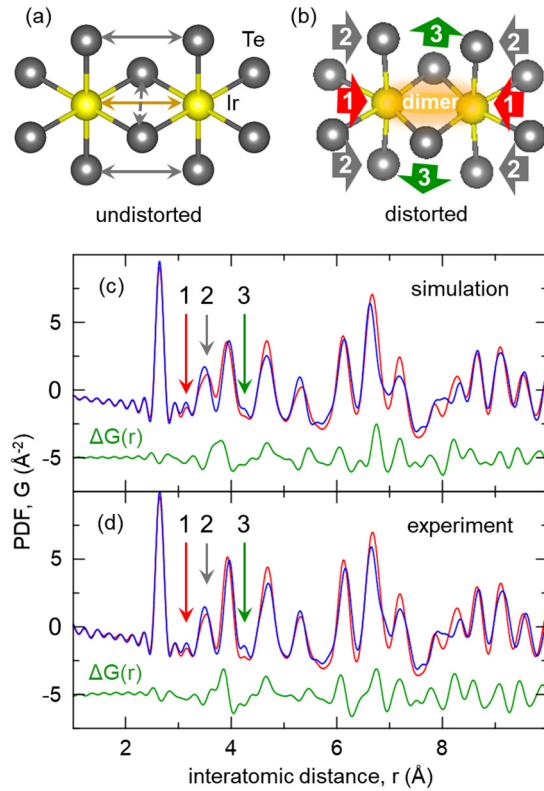
FIG. 1. Sketch of the local atomic environments in IrTe$_2$ for the (a) undistorted high-temperature structure (trigonal $P\bar{3}m1$) and (b) distorted low-temperature structure (triclinic $P\bar{1}$) featuring Ir-Ir and Te-Te dimers. Dimerization results in dramatic distortions of associated interatomic distances relative to the high-temperature structure, as indicated by block arrows and described in the text. Comparison of PDFs (c) calculated from trigonal (red line) and triclinic (blue line) models and (d) measured at 275 K (red line) and at 220 K (blue line). Numbered vertical arrows in (c) and (d) mark features associated with these distortions. $\Delta G(r)$ is the difference, offset for clarity.

dimers also in the superconducting compositions, experimental validation is still lacking.

Here we employ the PDF approach on superconducting compositions of two different Ir$_{1-x}$A$_x$Te$_2$ families just across the dimer/SC boundary to explore the existence of local dimer fluctuations. Since the PDF probes instantaneous atomic arrangements [17], when structural dimers are present, they should be observable in the local structure whether they are static or fluctuating. The PDF sensitivity to the presence of Ir-Ir dimers irrespective of the character of their ordering has been demonstrated in CuIr$_2$S$_4$ [10,37] and Cu(Ir$_{1-x}$Cr$_x$)$_2$S$_4$[38] spinels, where similar dimerization takes place on the Ir pyrochlore sublattice. When present, local dimers are clearly evident in the PDF of IrTe$_2$ due to the large change in the Ir-Ir and Te-Te interatomic distances associated with them. Here we provide conclusive evidence that the dimers are absent in Ir$_{0.95}$Pt$_{0.05}$Te$_2$ and Ir$_{0.8}$Rh$_{0.2}$Te$_2$ down to 10 K. This unambiguously rules out the popular hypothesis of quantum dimer fluctuations in this regime and that such fluctuations play a role in SC pairing. Moreover, the PDF finds no evidence for
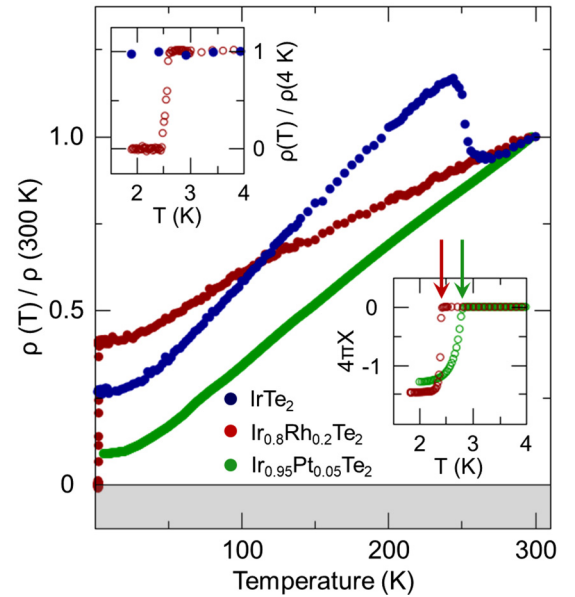
FIG. 2. Electrical resistivity of IrTe$_2$, Ir$_{0.95}$Pt$_{0.05}$Te$_2$, and Ir$_{0.8}$Rh$_{0.2}$Te$_2$ samples, normalized to their 300 K values. Insets: low-temperature resistivity (top left) and low-temperature susceptibility (bottom right) collected in the zero-field-cooling mode.

dimer fluctuations in IrTe$_2$ at $T > T_s$, in stark contrast to a previous EXAFS report [35].

II. EXPERIMENT

Polycrystalline samples of IrTe$_2$, Ir$_{0.95}$Pt$_{0.05}$Te$_2$, and Ir$_{0.8}$Rh$_{0.2}$Te$_2$ were synthesized using standard solid-state protocols and were found to be single phase based on x-ray powder diffraction [39,40]. Temperature-dependent electrical transport and magnetization measurements on these samples were carried out on warming in Quantum Design PPMS-9 and MPMS-XL5. These data are shown in Fig. 2. There is a clear anomaly seen in the parent IrTe$_2$ associated with a simultaneous structural and electronic phase transition where long-range dimer order is established. No such anomalies are seen in the data for Ir$_{0.95}$Pt$_{0.05}$Te$_2$ and Ir$_{0.8}$Rh$_{0.2}$Te$_2$ samples, implying the absence of a dimerization transition for these compositions. On the other hand, the low-temperature resistivity and susceptibility data shown in the insets in Fig. 2 clearly demonstrate the bulk superconductivity of these Pt- and Rh-substituted samples (vertical arrows indicate T_c).

Total-scattering PDF experiments were performed at the 28-ID-2 beamline at the National Synchrotron Light Source II at Brookhaven National Laboratory, with 67.7 keV x rays using the rapid acquisition mode with 60 s exposure for each data set [41]. The setup utilized a Perkin-Elmer area detector and a Cryoindustries of America cryostat for data collection between 10 and 300 K on warming. The raw two-dimensional (2D) diffraction data were integrated and converted to intensity versus Q using the software FIT2D [42], where Q is the magnitude of the scattering vector. Data reduction to measured total-scattering structure functions $F(Q)$ and their successive sine Fourier transform up to a momentum transfer of $Q_{\max} = 25$ Å^{-1} to obtain experimental PDFs $G(r)$ were carried out

using the PDFGETX3 [43] program. Models with $P\bar{3}m1$ and $P\bar{1}$ symmetry were used to describe nondimerized [Fig. 1(a)] and dimerized [Fig. 1(b)] structures, respectively, using the PDFGUI suite [44].

III. RESULTS

We begin by establishing qualitatively the sensitivity of our PDF data to the presence of dimers and concomitant structural distortions in $IrTe_2$. In the high-temperature phase above T_s all Ir atoms are in identical Te_6 octahedral environments displaying an edge-shared topology [Fig. 1(a)], constituting trigonal symmetry-average structure [45]. In the low-temperature phase just below T_s, where the dimer patterns with a stripe morphology corresponding to $\mathbf{q}_0 = 1/5(1,0,1)$ ordering are established [18,32], Ir atoms subject to dimerization sit in distorted Te_6 octahedral environments [Fig. 1(b)], and the average symmetry lowers to triclinic [12]. Pairs of dimerization-affected $IrTe_6$ octahedra exhibit dramatic structural rearrangements: Ir-Ir and Te-Te dimer distances decrease by 0.8 and 0.5 Å, respectively, while the lateral Te-Te distance (common edge) elongates by 0.3 Å [12]. The distortions are depicted by numbered block arrows in Fig. 1(b). Importantly, only ∼6% of all nearest-neighbor Ir-Ir distances on triangular Ir planes of $IrTe_2$ dimerize, in contrast to $CuIr_2S_4$, for which the fraction of dimerized Ir contacts is about 5 times larger [10].

We simulated PDF patterns for the average crystal structures for $T > T_s$ (trigonal) and $T < T_s$ (triclinic) using parameters from single-crystal x-ray diffraction [12]. These are shown in Fig. 1(c) as red and blue profiles, respectively, with their difference plotted underneath. Changes in the interatomic distance distribution arising from dimerization as seen by the PDF are marked by numbered vertical arrows. Examination of the high- and low-temperature profiles reveals a redistribution of intensity in PDF peaks centered around 3.5 Å (Te-Te) and 3.9 Å (lattice repeat distance), whereas new peaks appear at around 3.1 Å (Ir-Ir dimer), 3.4 Å (Te-Te dimer), and 4.2 Å (common Te-Te edge). It is evident that the Ir-Ir dimer signal at 3.1 Å is rather weak compared to that observed in $CuIr_2S_4$ spinel [37] and is barely visible above the parapet of termination ripples caused by the finite range of the Fourier transform. This comes about due to different dimer densities in the two materials. However, this analysis shows that, despite this relatively weaker signal, the PDF is still sensitive to the presence or absence of local dimers.

Experimental PDFs of $IrTe_2$ for temperatures straddling T_s are compared in Fig. 1(d), where the 275 K (red profile, $T > T_s$) and the 220 K (blue profile, $T < T_s$) data and their difference are displayed. A qualitative assessment readily demonstrates that all dimerization features described above and highlighted in the calculated PDFs, which contain the impact of the dimers, are well reproduced in the experimental PDF data. This clearly establishes the PDF sensitivity to dimer structural signatures and their detectability in our data. Comparisons in Figs. 1(c) and 1(d) also indicate that the dimers *disappear* in the local structure above T_s, which is further confirmed by explicit modeling that we discuss later. Notably, the proposed order-disorder scenario for the
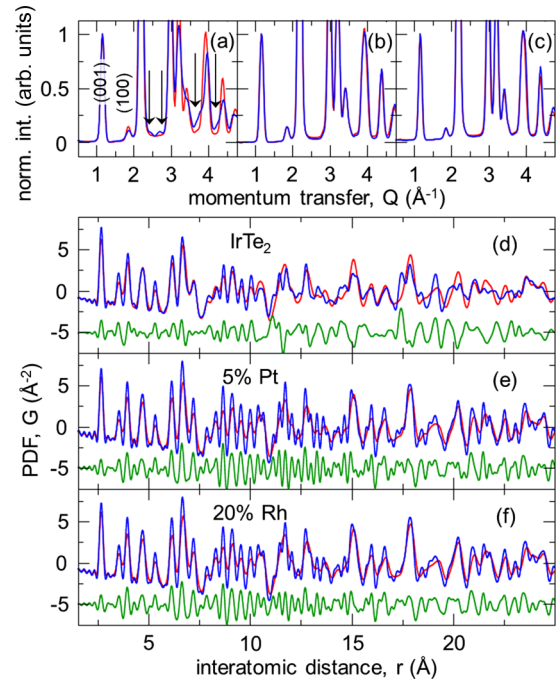
FIG. 3. Azimuthally integrated 2D diffraction patterns of $Ir_{1-x}(Pt,Rh)_x Te_2$ for 300 K (red line) and 10 K (blue line) over a narrow range of momentum transfer Q for (a) $x = 0$, (b) $x = 0.05$ Pt, and (c) $x = 0.2$ Rh. All patterns are normalized by the intensity of the (001) reflection ($P\bar{3}m1$ indexing). Vertical arrows in (a) indicate superlattice reflections observed in 10 K data. Corresponding PDFs are compared in (d), (e), and (f), respectively, with differences shown underneath and offset for clarity.

dimerization transition [35] is at odds with this observation. The first-order nature of the transition [22,32] also argues against the persistence of local fluctuating dimers above T_s.

Samples with SC compositions display qualitatively different behavior on all length scales accessible by our measurements. When the average $IrTe_2$ symmetry is lowered and the long-range dimer order is established, superlattice reflections appear in the integrated diffraction patterns, as seen in Fig. 3(a), where 10 and 300 K are compared. In contrast, no such features are observed in $Ir_{0.95}Pt_{0.05}Te_2$ [Fig. 3(b)] and $Ir_{0.8}Rh_{0.2}Te_2$ [Fig. 3(c)] data at any temperature, consistent with the average symmetry remaining trigonal down to 10 K and no long-range dimer order, as expected from the monotonic temperature variation of susceptibility and electrical resistivity [19,21]. Importantly, the dimers are also not observed at low temperature on intermediate and short length scales probed by the PDF. When symmetry lowering occurs, this causes redistribution of PDF intensities and overall broadening of the PDF patterns due to the appearance of new interatomic distances. Conversely, temperature lowering sharpens the PDF features as a consequence of decreasing the amplitudes of thermal vibrations [17]. Both effects are present in $IrTe_2$ PDFs [Fig. 3(d)], where the 300 K profile is observably sharper than that of 10 K at intermediate r, and their difference reveals a change corresponding to a superposition of these two opposite effects. Figures 3(e) and 3(f) show 300 and 10 K data for superconducting samples. Although there are also dramatic
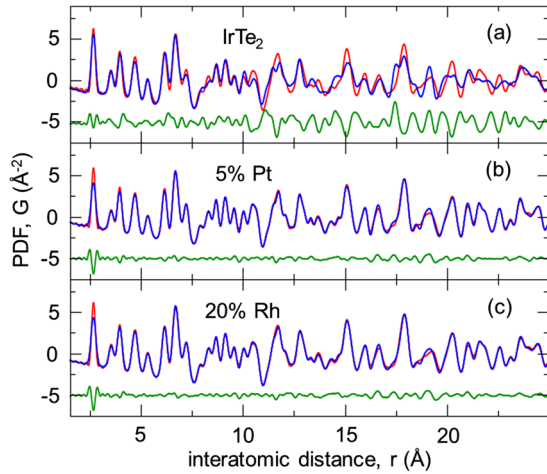
FIG. 4. A comparison of the 10 K (blue) and 300 K (red) PDF data for (a) $IrTe_2$, (b) $Ir_{0.95}Pt_{0.05}Te_2$, and (c) $Ir_{0.8}Rh_{0.2}Te_2$, where the 10 K data were adjusted in the simple optimization procedure described in the text. Differences are plotted underneath and offset for clarity.

changes evidenced in the respective difference curves, this is qualitatively different from what is seen in $IrTe_2$.

IV. DISCUSSION

It can be shown through a semiempirical scaling procedure that high- and low-temperature PDFs of doped samples can be successfully morphed into each other, whereas such a procedure fails in the case of $IrTe_2$. Figure 4 summarizes the comparisons of qualitative features of the 10 and 300 K PDF data for the three samples studied. For the comparisons, the low-temperature PDF profiles were subjected to a simple semiempirical protocol, dubbed morphing and described below. The morphing analysis indicates that, while symmetry breaking is required to explain the differences observed in the $IrTe_2$ data, the differences observed in the $Ir_{0.95}Pt_{0.05}Te_2$ and $Ir_{0.8}Rh_{0.2}Te_2$ data are likely due to only mundane thermal effects.

The morphing comparison procedure allows for an assessment of similarities of two sets of PDF data to be carried out without an assumption of any specific structure model. This allows, at least in principle, differentiation between symmetry-breaking effects and trivial lattice expansion effects as sources of the observed differences, such as those shown in Figs. 3(d)–3(f). In the morphing protocol one of the two experimental PDFs is selected as a reference and is not altered in any way (300 K data here). The other of the two profiles to be compared (10 K data in this case) is subjected to the morphing procedure. This is parametrized by three variables: horizontal and vertical linear scale factors, which stretch the r and G axes, respectively, and a smear parameter that convolutes the subjected PDF with a Gaussian of fixed width. A least-squares optimization protocol utilizing these three variables is then carried out until the best possible match between the morph and the reference PDFs is achieved. This is quantified by minimizing the weighted residual r_w of the PDF difference and by maximizing the Pearson correlation coefficient P. In the case of ideal morphing r_w would be zero, whereas P would take a value of 1, reflecting perfect agreement between the

morph and the reference PDF and a 100% positive correlation between the two profiles whose similarity is being evaluated. Formal mathematical treatment and more involved details of this protocol will be reported elsewhere. When the difference between the two measured PDFs originates from trivial lattice effects, such as thermal expansion, morphing results in a low value of r_w and a Pearson correlation coefficient close to 1. Conversely, when the difference originates from more complex effects, such as symmetry breaking, morphing results in suboptimal values of r_w and P.

To benchmark the comparison of our PDF data at 10 and 300 K when no morphing is applied [Figs. 3(d)–3(f)], we calculated (r_w, P) pairs for all three samples studied. This benchmarking yields (0.52, 0.86), (0.65, 0.89), and (0.56, 0.91) for $IrTe_2$, $Ir_{0.95}Pt_{0.05}Te_2$, and $Ir_{0.8}Rh_{0.2}Te_2$, respectively. On the other hand, the fully converged morphing yields (0.46, 0.89), (0.14, 0.99), and (0.15, 0.99) for $IrTe_2$, $Ir_{0.95}Pt_{0.05}Te_2$, and $Ir_{0.8}Rh_{0.2}Te_2$, respectively. Comparison of the observed r_w and P values with the benchmark references reveals that these parameters improve considerably by morphing in the case of $Ir_{0.95}Pt_{0.05}Te_2$ and $Ir_{0.8}Rh_{0.2}Te_2$ but do not improve much at all for the $IrTe_2$ parent. Corresponding difference curves shown in Fig. 4 reflect this as well. This analysis suggests that the difference in PDFs for SC samples is likely caused only by simple lattice effects without any symmetry breaking. This conclusion is further supported by the fact that the protocol successfully singles out symmetry breaking in $IrTe_2$, as expected when comparing the two data sets straddling the structural transition.

Although the morphing of the data for the SC samples is reasonably good, it is observably nonideal, which is evident from a careful inspection of the difference curves shown in Figs. 4(b) and 4(c). While the discrepancies could indicate underlying symmetry breaking, the more likely reason behind this lies in the oversimplifications upon which the morphing algorithm is based. The three parameters allowing for scaling, stretching, and smearing of the subjected PDF profile effectively mimic only spherically uniform and isotropic thermal effects, whereas in a real material thermal expansion and thermal vibrations have a more complex impact on the PDF profile. Notably, the largest discrepancies observed in Figs. 4(b) and 4(c) are confined to a narrow r range just underneath the first PDF peak around 2.5 Å. This region is known to be affected by the correlated motion of the nearest neighbors [17], an effect not accounted for in the morphing procedure. Despite these shortcomings the morphing analysis rather intuitively suggests that the changes in the SC samples are likely caused solely by thermal effects, without symmetry lowering, whereas the actual symmetry breaking is needed to explain the changes in the parent system.

To further search for the evidence that would indicate local dimerization in the SC samples we assess the temperature evolution of structural modeling parameters that are sensitive to the presence of disorder [38]. The undistorted trigonal $P\bar{3}m1$ model was refined in r space against the PDF data in the 10–300 K range for all three samples studied, and the obtained atomic displacement parameters (ADPs) were monitored (Fig. 5). While in $IrTe_2$ ADPs of both Ir and Te initially drop linearly with temperature [Fig. 5(a)], they exhibit an abrupt jump at the onset of the dimerization transition,
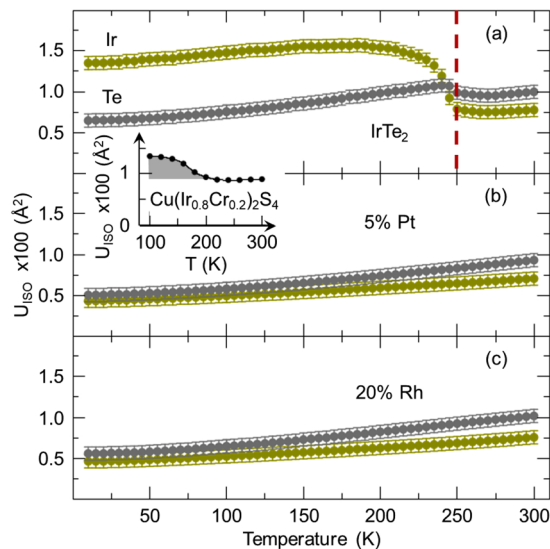
FIG. 5. Temperature dependence of the isotropic ADPs of Ir (olive symbols) and Te (gray symbols) in $Ir_{1-x}(Pt,Rh)_xTe_2$ obtained from $P\bar{3}m1$ model fits to (a) $x = 0$, (b) $x = 0.05$ Pt, and (c) $x = 0.2$ Rh sample data over the 10–300 K temperature range. Inset: detection of the onset of dimer fluctuations from temperature-dependent Ir-ADP in 20% Cr-doped $CuIr_2S_4$, where Ir-Ir dimerization sets in below 200 K on *only* a nanometer length scale, while the long-range dimer order is absent at all temperatures [38]. Such behavior is *not* observed in (b) and (c) for superconducting $Ir_{1-x}(Pt,Rh)_xTe_2$.

denoted by the vertical dashed red line in Fig. 5(a). This nominally implies "disorder" but actually reflects the inadequacy of the trigonal model to explain the symmetry breaking and underlying dimerization encoded in the data. In contrast, no such jumps are observed for $Ir_{0.95}Pt_{0.05}Te_2$ [Fig. 5(b)] and $Ir_{0.8}Rh_{0.2}Te_2$ [Fig. 5(c)] in the entire temperature range studied. It is important to realize that jumps in ADPs are observed not only across long-range symmetry-breaking transitions but also in cases when there is only a local structure change in the absence of any macroscopic transitions. The inset in Fig. 5 exemplifies such a situation seen in 20% Cr-doped $CuIr_2S_4$, where *local* Ir-Ir dimerization sets in just below 200 K, in the absence of long-range dimer order at any temperature in that system [38]. This demonstrates that there is neither average nor local symmetry lowering in $Ir_{0.95}Pt_{0.05}Te_2$ and $Ir_{0.8}Rh_{0.2}Te_2$ down to 10 K.

To quantitatively estimate the PDF sensitivity to the presence of dimers in $IrTe_2$ as seen through the ADP parameters, we carried out a test on a set of simulated data as follows. To mimic the dimer density variation between 0% and 6% [full dimer density observed in the ordered phase with $q_0 = 1/5(1,0,1)$], we used a two-phase model comprising the dimerized ($P\bar{1}$) and dimer-free ($P\bar{3}m1$) components. Corresponding PDFs were simulated for a range of mixing fractions [Fig. 6(a)]. These simulated PDF data were subsequently fit by the same dimer-free $P\bar{3}m1$ model as that used for the experimental data to obtain ADPs that are shown in Fig. 5. Values of Ir ADP obtained from fitting such synthetic data are then plotted against the fraction of dimerized Ir-Ir bonds (known from simulations), and the plot is overlaid with the uncertainty window centered around the ADP value corresponding to zero dimer density, as shown
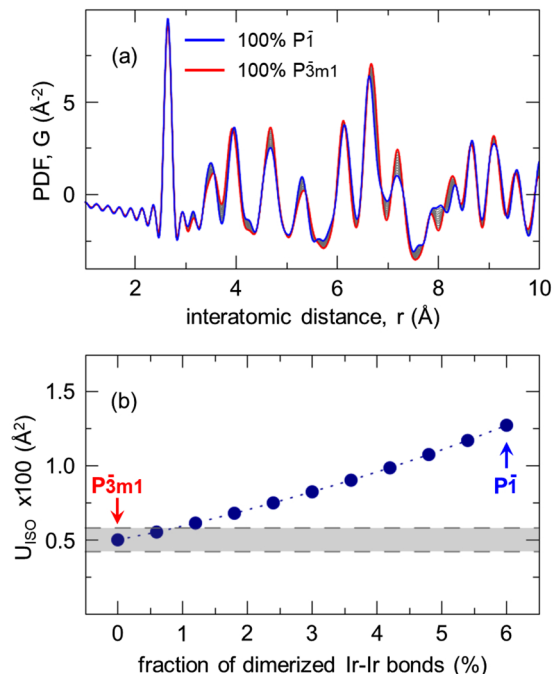
FIG. 6. Quantification of PDF sensitivity to the presence of dimers. (a) Simulated PDFs of $IrTe_2$ comprising mixtures of dimer ($P\bar{1}$) and nondimer ($P\bar{3}m1$) phases, with a mixing ratio increment of 0.1. The different solid profiles correspond to dimer fractions ranging from 6% of dimerized Ir-Ir nearest neighbors (as observed in the $P\bar{1}$ phase, blue) to no dimers (which is the case for $P\bar{3}m1$, red). PDFs for the intermediates are shown in gray. (b) Isotropic ADP of Ir obtained by fitting the dimer-free $P\bar{3}m1$ model to the simulated PDFs in (a) as a function of absolute fraction of dimerized Ir-Ir bonds. The gray shaded region represents typical uncertainty on the 2σ level in determining this parameter from the experimental PDFs using the same $P\bar{3}m1$ model.

in Fig. 6(b). The width of the uncertainty window (gray shaded area) corresponds to a typical estimated standard deviation on the 2σ level obtained from the fits to the experimental data (the error bars in Fig. 5). The sensitivity is defined as the value of the dimerized Ir-Ir fraction for which the ADP value of Ir sinks into the gray shaded region. The sensitivity floor is about 0.5% of dimerized Ir-Ir bonds (99.5% of Ir-Ir bonds are not dimerized). This corresponds to the dimer density that is an *order of magnitude* smaller than that observed in the $q_0 = 1/5(1,0,1)$ ordered phase. This establishes the dimer detectability floor from our measurements in $IrTe_2$ from Ir ADPs to be below $\sim 0.5\%$

It is noteworthy that the values of ADP parameters for both Ir and Te at 300 K obtained for $Ir_{0.95}Pt_{0.05}Te_2$ and $Ir_{0.8}Rh_{0.2}Te_2$ are comparable to those observed in $IrTe_2$ (Fig. 5). This indicates that any quenched disorder introduced by substituting Pt and Rh for Ir is immeasurably small, as one may also expect from their rather similar ionic radii [46]. Substantial disorder-induced strain is known to stabilize the local Ir dimer state in the related $Cu(Ir_{1-x}Cr_x)_2S_4$ dimer system and is, in fact, believed to be behind the appearance of local dimers at low temperature for Cr concentrations above 15% in the absence of the long-range dimer order (see inset in Fig. 5) [38]. On
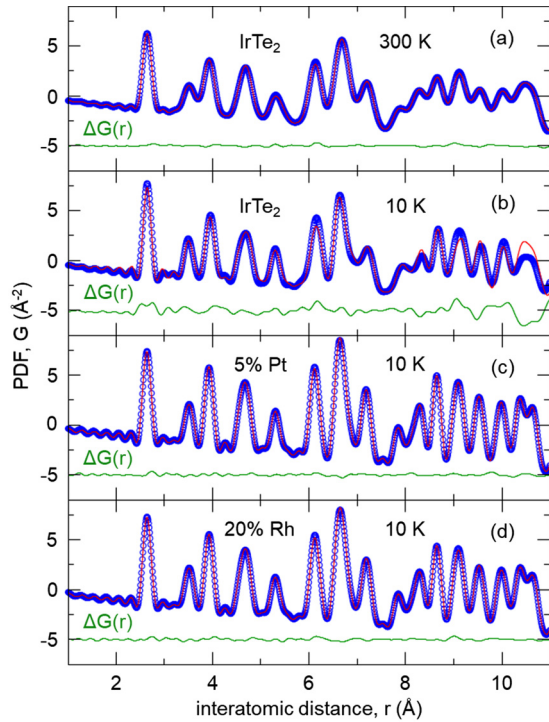
FIG. 7. Fits of the trigonal structure model (solid red lines) to experimental PDF data (open blue symbols) of the $IrTe_2$ sample at (a) 300 K and (b) 10 K and (c) 5% Pt-substituted sample at 10 K and (d) 20% Rh-substituted sample at 10 K. The difference between the data and the model $\Delta G(r)$, plotted below, is offset for clarity. See text for details.

the other hand, it has been established recently that external pressure stabilizes the dimer state in $Ir_{1-x}Pt_xTe_2$ [34]. It is therefore reasonable to expect that any substitution-related strains, if present, would likely enhance local dimerization in the $IrTe_2$ system, rather than suppress it. This implies that substitutional disorder is not responsible for the lack of observable signal that would indicate dimerization in SC compositions of $IrTe_2$.

Last, we consider the actual fits of the trigonal structure model to various PDF data over the 10-Å range, shown in Fig. 7 as solid red lines and open blue symbols, respectively. This undistorted dimer-free model explains the $IrTe_2$ 300 K data exceptionally well [Fig. 7(a)], which is evident from the flat difference curve and a low fit residual value of $r_w \sim 4\%$. The same model fails to explain the $IrTe_2$ data at 10 K ($r_w \sim 15\%$) in Fig. 7(b), as expected, given that at that temperature long-range dimer order is well established and that the attempted dimer-free model is strictly inadequate. Importantly, this failed fit charts substantial misfits in the difference curve that would reveal the presence of dimers in the data when they are confronted with a dimer-free model. Figures 7(c) and 7(d) show the results of such a fitting attempt carried out on 10 K $Ir_{0.95}Pt_{0.05}Te_2$ and $Ir_{0.8}Rh_{0.2}Te_2$ data, respectively. Not only do the corresponding difference curves not display the features observed in Fig. 7(b), but the fits of the trigonal model in fact agree rather well with the data ($r_w \sim 5\%$). The local structure at 10 K for these compositions is well explained by a dimer-free model. This quantitative analysis validates the
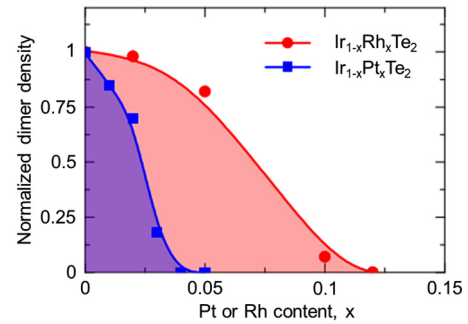
FIG. 8. Normalized dimer density as a function of Pt and Rh content in $IrTe_2$ estimated from published magnetic susceptibility measurements [19,21].

aforementioned qualitative conclusions about the absence of dimer fluctuations in the high-temperature phase of the parent system as well as at 10 K in superconducting compositions just past the dimer/SC boundary. The transition in $IrTe_2$ is argued to originate from a uniform lattice deformation combined with charge ordering and subsequent Ir dimerization [33], with the structural transition as a trigger [34]. Putative quantum critical fluctuations will thus inevitably appear in the structural channel.

Further, important insights can also be gained from the analysis of the diamagnetic response to dimerization in magnetic susceptibility in $Ir_{1-x}Pt_xTe_2$ and $Ir_{1-x}Rh_xTe_2$. Namely, dimerization transition in $IrTe_2$ is accompanied by anomalies in both resistivity (jump) and magnetic susceptibility (dip). Superconductivity is invoked upon suppression of the transition by chemical substitution in $Ir_{1-x}Pt_xTe_2$ [19] and $Ir_{1-x}Rh_xTe_2$ [21]. In both systems substitution causes the transition temperature to decrease with increasing substitute content. In addition, the dip in susceptibility, corresponding to the dimerization-related diamagnetic reduction of the total magnetic susceptibility, becomes smaller and eventually disappears in the superconducting range of compositions past the dimer/SC boundary [19,21].

It can be inferred from a combination of magnetic susceptibility, Ir $4f$ core-level photoemission spectroscopy (PES), and scanning tunneling microscopy (STM) measurements that this drop is proportional to the static dimer density [47]. The systematic study of Ko *et al.* [47] reveals two dimerization-related phase transitions on cooling in a high-quality single crystal of $IrTe_2$, one at $\sim$280 K associated with $\mathbf{q}_{1/5} = 1/5(1,0,1)$ order, followed by another one at $\sim$180 K associated with $\mathbf{q}_{1/8} = 1/8(1,0,1)$ order. The PES measurements reveal that the Ir^{4+}:Ir^{3+} ratio increases at the lower transition temperature. At the same time, according to the assessment of the STM images, the dimer density is found to increase on going from the $\mathbf{q}_{1/5}$ to $\mathbf{q}_{1/8}$ phase. Importantly, magnetic susceptibility dips twice, first at $\sim$280 K and then again at $\sim$180 K. Taken together, this implies that the size of the dip is proportional to the static dimer density.

Here we estimate the static dimer density for $Ir_{1-x}Pt_xTe_2$ and $Ir_{1-x}Rh_xTe_2$ as a function of Pt and Rh content from the size of the susceptibility dip taken from the reported data collected on warming [19,21]. This is shown in Fig. 8, where the density is further normalized to the value for $IrTe_2$. This

estimate clearly reveals that the static dimer density decreases gradually with chemical substitution and vanishes for SC compositions.

The PDF findings presented here rule out the presence of dimers, both static and *dynamic*, and impose the upper limit of 0.5% on the number of Ir pairs that could be dimerized in the SC range of compositions. Further systematic investigations utilizing techniques sensitive to fluctuations and local structure across the phase diagrams of $Ir_{1-x}Pt_xTe_2$ and $Ir_{1-x}Rh_xTe_2$ would be highly desirable to provide further insights on the interplay of these quantum orders, particularly in the vicinity of the dimer/SC boundary.

V. CONCLUSIONS

In summary, by using a state-of-the-art x-ray total-scattering-based PDF approach we established direct evidence of the absence of local dimer fluctuations in the phase diagrams of $Ir_{1-x}Pt_xTe_2$ and $Ir_{1-x}Rh_xTe_2$ beyond the dimer/superconductor phase boundary. The dimer fluctuations are also absent in the parent $IrTe_2$ in the temperature regime above the structural phase transition. These results imply that dimer fluctuations are not a relevant part of the phase diagram of $IrTe_2$-based systems, and thus their role in the superconducting pairing is implausible. The results provide important constraints for theoretical considerations of the complex interplay between superconductivity and other electronic orders in this class of materials.

[1] D. N. Basov and A. V. Chubukov, Nat. Phys. **7**, 272 (2011).

[2] G. Saito and Y. Yoshida, Chem. Rec. **11**, 124 (2011).

[3] L. Jiao, Y. Chen, Y. Kohama, D. Graf, E. Bauer, J. Singleton, J. Zhu, Z. Weng, G. Pang, T. Shang, J. Zhang, H. O. Lee, T. Park, M. Jaime, J. D. Thompson, F. Steglich, Q. Si, and H. Q. Yuan, Proc. Natl. Acad. Sci. USA **112**, 673 (2015).

[4] M. R. Norman, Science **332**, 196 (2011).

[5] P. A. Lee, N. Nagaosa, and X. Wen, Rev. Mod. Phys. **78**, 17 (2006).

[6] J. Chang, E. Blackburn, A. T. Holmes, N. B. Christensen, J. Larsen, J. Mesot, R. Liang, D. A. Bonn, W. N. Hardy, A. Watenphul, M. v. Zimmermann, E. M. Forgan, and S. M. Hayden, Nat. Phys. **8**, 871 (2010).

[7] R. Comin, A. Frano, M. Yee, Y. Yoshida, H. Eisaki, E. Schierle, E. Weschke, R. Sutarto, F. He, A. Soumyanarayanan, Y. He, M. Le Tacon, I. S. Elfimov, J. E. Hoffman, G. A. Sawatzky, B. Keimer, and A. Damascelli, Science **343**, 390 (2014).

[8] S. A. Kivelson, I. P. Bindloss, E. Fradkin, V. Oganesyan, J. M. Tranquada, A. Kapitulnik, and C. Howald, Rev. Mod. Phys. **75**, 1201 (2003).

[9] S. J. L. Billinge and I. Levin, Science **316**, 561 (2007).

[10] P. G. Radaelli, Y. Horibe, M. J. Gutmann, H. Ishibashi, C. H. Chen, R. M. Ibberson, Y. Koyama, Y. S. Hor, V. Kiryukhin, and S.-W. Cheong, Nature (London) **416**, 155 (2002).

[11] D. I. Khomskii and T. Mizokawa, Phys. Rev. Lett. **94**, 156402 (2005).

[12] G. L. Pascut, K. Haule, M. J. Gutmann, S. A. Barnett, A. Bombardi, S. Artyukhin, T. Birol, D. Vanderbilt, J. J. Yang, S.-W. Cheong, and V. Kiryukhin, Phys. Rev. Lett. **112**, 086402 (2014).

[13] T. Toriyama, M. Kobori, T. Konishi, Y. Ohta, K. Sugimoto, J. Kim, A. Fujiwara, S. Pyon, K. Kudo, and M. Nohara, J. Phys. Soc. Jpn. **83**, 033701 (2014).

[14] J. Lee, K. Fujita, K. McElroy, J. A. Slezak, M. Wang, Y. Aiura, H. Bando, M. Ishikado, T. Masui, J. X. Zhu, A. V. Balatsky, H. Eisaki, S. Uchida, and J. C. Davis, Nature (London) **442**, 546 (2006).

[15] E. S. Božin, M. Schmidt, A. J. DeConinck, G. Paglia, J. F. Mitchell, T. Chatterji, P. G. Radaelli, T. Proffen, and S. J. L. Billinge, Phys. Rev. Lett. **98**, 137203 (2007).

[16] S. J. L. Billinge, J. Solid State Chem. **181**, 1695 (2008).

[17] T. Egami and S. J. L. Billinge, *Underneath the Bragg Peaks: Structural Analysis of Complex Materials*, 2nd ed. (Elsevier, Amsterdam, 2012).

[18] J. J. Yang, Y. J. Choi, Y. S. Oh, A. Hogan, Y. Horibe, K. Kim, B. I. Min, and S.-W. Cheong, Phys. Rev. Lett. **108**, 116402 (2012).

[19] S. Pyon, K. Kudo, and M. Nohara, J. Phys. Soc. Jpn. **81**, 053701 (2012).

[20] M. Kamitani, M. S. Bahramy, R. Arita, S. Seki, T. Arima, Y. Tokura, and S. Ishiwata, Phys. Rev. B **87**, 180501 (2013).

[21] K. Kudo, M. Kobayashi, S. Pyon, and M. Nohara, J. Phys. Soc. Jpn. **82**, 085001 (2013).

[22] N. Matsumoto, K. Taniguchi, R. Endoh, H. Takano, and S. Nagata, J. Low Temp. Phys. **117**, 1129 (1999).

[23] E. Morosan, H. W. Zandbergen, B. S. Dennis, J. W. G. Bos, Y. Onose, T. Klimczuk, A. P. Ramirez, N. P. Ong, and R. J. Cava, Nat. Phys. **2**, 544 (2006).

[24] B. Sipos, A. F. Kusmartseva, A. Akrap, H. Berger, L. Forro, and E. Tutis, Nat. Mater. **7**, 960 (2008).

[25] A. F. Kusmartseva, B. Sipos, H. Berger, L. Forro, and E. Tutis, Phys. Rev. Lett. **103**, 236401 (2009).

[26] Z. Guguchia, F. von Rohr, Z. Shermadini, A. T. Lee, S. Banerjee, A. R. Wieteska, C. A. Marianetti, B. A. Frandsen, H. Luetkens, Z. Gong, S. C. Cheung, C. Baines, A. Shengelaya, G. Taniashvili, A. N. Pasupathy, E. Morenzoni, S. J. L. Billinge, A. Amato, R. J. Cava, R. Khasanov, and Y. J. Uemura, Nat. Commun. **8**, 1082 (2017).

[27] X. Zhu, W. Ning, L. Li, L. Ling, R. Zhang, J. Zhang, K. Wang, Y. Liu, L. Pi, Y. Ma, H. Du, M. Tian, Y. Sun, C. Petrovic, and Y. Zhang, Sci. Rep. **6**, 26974 (2016).

[28] L. Li, X. Deng, Z. Wang, Y. Liu, M. Abeykoon, E. Dooryhee, A. Tomic, Y. Huang, J. B. Warren, E. S. Bozin, S. J. L. Billinge, Y. Sun, Y. Zhu, G. Kotliar, and C. Petrovic, npj Quantum Mater. **2**, 11 (2017).

[29] H. Barath, M. Kim, J. F. Karpus, S. L. Cooper, P. Abbamonte, E. Fradkin, E. Morosan, and R. J. Cava, Phys. Rev. Lett. **100**, 106402 (2008).

[30] A. H. Castro Neto, Phys. Rev. Lett. **86**, 4382 (2001).

[31] J. Dai, K. Haule, J. J. Yang, Y. S. Oh, S.-W. Cheong, and W. Wu, Phys. Rev. B **90**, 235121 (2014).

[32] Y. S. Oh, J. J. Yang, Y. Horibe, and S.-W. Cheong, Phys. Rev. Lett. **110**, 127209 (2013).

[33] K. Kim, S. Kim, K.-T. Ko, H. Lee, J.-H. Park, J. J. Yang, S.-W. Cheong, and B. I. Min, Phys. Rev. Lett. **114**, 136401 (2015).

[34] O. Ivashko, L. Yang, D. Destraz, E. Martino, Y. Chen, C. Y. Guo, H. Q. Yuan, A. Pisoni, P. Matus, S. Pyon, K. Kudo, M. Nohara, L. Forró, H. M. Rønnow, M. Hücker, M. v. Zimmermann, and J. Chang, Sci. Rep. **7**, 17157 (2017).

[35] B. Joseph, M. Bendele, L. Simonelli, L. Maugeri, S. Pyon, K. Kudo, M. Nohara, T. Mizokawa, and N. L. Saini, Phys. Rev. B **88**, 224109 (2013).

[36] E. Paris, B. Joseph, A. Iadecola, C. Marini, H. Ishii, K. Kudo, S. Pascarelli, M. Nohara, T. Mizokawa, and N. L. Saini, Phys. Rev. B **93**, 134109 (2016).

[37] E. S. Božin, A. S. Masadeh, Y. S. Hor, J. F. Mitchell, and S. J. L. Billinge, Phys. Rev. Lett. **106**, 045501 (2011).

[38] E. S. Božin, K. R. Knox, P. Juhás, Y. S. Hor, J. F. Mitchell, and S. J. L. Billinge, Sci. Rep. **4**, 4081 (2014).

[39] H. Cao, B. C. Chakoumakos, X. Chen, J. Yan, M. A. McGuire, H. Yang, R. Custelcean, H. D. Zhou, D. J. Singh, and D. Mandrus, Phys. Rev. B **88**, 115122 (2013).

[40] N. Lazarevic, E. S. Bozin, M. Scepanovic, M. Opacic, H. Lei, C. Petrovic, and Z. V. Popovic, Phys. Rev. B **89**, 224301 (2014).

[41] P. J. Chupas, X. Qiu, J. C. Hanson, P. L. Lee, C. P. Grey, and S. J. L. Billinge, J. Appl. Crystallogr. **36**, 1342 (2003).

[42] A. P. Hammersley, S. O. Svenson, M. Hanfland, and D. Hauserman, High Press. Res. **14**, 235 (1996).

[43] P. Juhás, T. Davis, C. L. Farrow, and S. J. L. Billinge, J. Appl. Crystallogr. **46**, 560 (2013).

[44] C. L. Farrow, P. Juhás, J. Liu, D. Bryndin, E. S. Božin, J. Bloch, T. Proffen, and S. J. L. Billinge, J. Phys.: Condens. Matter **19**, 335219 (2007).

[45] E. F. Hockings and J. G. White, J. Phys. Chem. **64**, 1042 (1960).

[46] R. D. Shannon, Acta Crystallogr. A **32**, 751 (1976).

[47] K.-T. Ko, H.-H. Lee, D.-H. Kim, J.-J. Yang, S.-W. Cheong, M. J. Eom, J. S. Kim, R. Gammag, K.-S. Kim, H.-S. Kim, T.-H. Kim, H.-W. Yeom, T.-Y. Koo, H.-D. Kim, and J.-H. Park, Nat. Commun. **6**, 7342 (2015).

Thermoelectric studies of Ir$_{1-x}$Rh$_x$Te$_2$ ($0 \leqslant x \leqslant 0.3$)

Yu Liu (刘育),[1] Hechang Lei (雷和畅),[1,*] Kefeng Wang (王克锋),[1,†] Milinda Abeykoon,[2]
J. B. Warren,[3] Emil Bozin,[1] and C. Petrovic[1]

[1]*Condensed Matter Physics and Materials Science Department, Brookhaven National Laboratory, Upton, New York 11973, USA*
[2]*Photon Science Division, National Synchrotron Light Source II, Brookhaven National Laboratory, Upton, New York 11973, USA*
[3]*Instrumentation Division, Brookhaven National Laboratory, Upton, New York 11973, USA*

We report thermoelectric properties of Ir$_{1-x}$Rh$_x$Te$_2$ ($0 \leqslant x \leqslant 0.3$) alloy series where superconductivity at low temperatures emerges as the high-temperature structural transition (T_s) is suppressed. The isovalent ionic substitution of Rh into Ir has different effects on physical properties when compared to the anionic substitution of Se into Te, in which the structural transition is more stable with Se substitution. Rh substitution results in a slight reduction of lattice parameters and in an increase of number of carriers per unit cell. Weak-coupled BCS superconductivity in Ir$_{0.8}$Rh$_{0.2}$Te$_2$ that emerges at low temperature ($T_c^{\text{zero}} = 2.45$ K) is most likely driven by electron-phonon coupling rather than dimer fluctuations mediated pairing.

DOI: 10.1103/PhysRevB.98.094519

I. INTRODUCTION

The complex and unusual structural and physical properties of layered transition metal dichalcogenides (TMDCs) have been investigated for several decades, in part due to the competing orders such as charge density wave (CDW) order and superconductivity (SC) [1–5]. The interplay of competing orders is the fundamental question in these systems. The CDW state can be tuned into SC via intercalation, substitution, pressure, or electric-field effect [5–7]. Usually, there is a domelike phase diagram, i.e., the CDW transition temperature T_{CDW} decreases when the superconducting critical temperature T_c increases. This indicates that CDW and SC compete, however details of this competition are material dependent and not well understood [5–10].

The discovery of superconductivity in Pt, Pd, and/or Cu substituted/intercalated CdI$_2$-type IrTe$_2$ with its T_c up to ∼3 K has triggered a resurgence of interest in this field [11–13]. IrTe$_2$ is a TMDC that undergoes a structural transition at ∼270 K from trigonal $P\bar{3}m1$ symmetry to triclinic $P\bar{1}$ [14–16]. The transition is accompanied by partial Ir-Ir dimerization associated with substantial structural distortions [15,16]. Transmission electron microscope, photoemission, electron diffraction, and tight-binding electronic structure calculations all revealed a superstructure with $\mathbf{q} = (1/5, 0, -1/5)$ modulation vector associated with the low temperature phase and initially ascribed to an orbitally driven Peierls instability [12,17]. However, results from nuclear magnetic resonance (NMR), angle-resolved photoemission spectroscopy (ARPES), optical conductivity, and scanning tunneling microscopy/spectroscopy measurements brought to doubt the conventional CDW instability scenario and instead suggested that the transition is due to the reduction of the kinetic energy of Te p bands [18–21]. In addition, theoretical calculations suggest that the structural transition is mainly caused by the evolution of Te p bands rather than the instability of Ir d bands which results in a reduction of the kinetic energy of the electronic system [13,18]. On the other hand, with Pt, Pd, Cu substitution/intercalation, the structural transition is quickly suppressed and superconductivity appears at low temperature, indicating the competition between the two order parameters.

Isovalent substitution is an effective way to further inform the discussion about the origin of transition and induced superconductivity. It is similar to pressure because it changes the structural parameters, ionic size, and electronegativity of atoms in the unit cell without introducing extra carriers, thus affecting electronic structure and vibrational properties. Previous studies have shown that the structural transition at high temperature is enhanced while the superconducting transition is suppressed by either hydrostatic or chemical pressure [22–24]. The latter results are associated with stabilization of polymeric Te-Te bonds by replacing Te with the more electronegative Se. This is different from other TMDCs where pressure suppresses the CDW state and enhances the SC [6,7]. Isovalent Rh substitution in IrTe$_2$ also induces SC [25], however little is known about the nature of the superconducting state.

In this paper, we report the thermoelectric properties of Ir$_{1-x}$Rh$_x$Te$_2$ ($0 \leqslant x \leqslant 0.3$). Our results give a slight reduction of lattice parameters and an increase of number of carriers per unit cell. With suppression of the high-temperature structural transition, superconducting state that emerges at low temperature in Ir$_{0.8}$Rh$_{0.2}$Te$_2$ is weak-coupled BCS, suggesting conventional electron-phonon mechanism. This is consistent with recently reported absence of nanoscale dimer

fluctuations in Rh,Pt-substituted $IrTe_2$ and argues against the dimer fluctuations mediated exotic superconductivity with singlet-triplet pairing [26,27].

II. EXPERIMENT

Polycrystalline samples of $Ir_{1-x}Rh_xTe_2$ ($0 \leqslant x \leqslant 0.3$) were synthesized using solid-state reaction method as described previously [12]. The structure was characterized by powder x-ray diffraction (XRD) in transmission mode at the X7B beamline of the National Synchrotron Light Source (NSLS) at Brookhaven National Laboratory. Data were collected using a 0.5 mm^2 monochromatic beam of ~38 keV ($\lambda \sim 0.3916$ Å) at 300 K. A Perkin Elmer 2D detector was placed orthogonal to the beam path 376.4 mm away from the sample. The sample was loaded in a polyamide capillary 1 mm in diameter and mounted on a goniometer head. The data were collected up to $Q = 4\pi \sin\theta/\lambda = 12$ Å^{-1}. The average stoichiometry was determined by energy-dispersive x-ray spectroscopy (EDX) in a JEOL JSM-6500 scanning electron microscope (SEM). The specific heat was measured on warming procedure between 1.95 and 300 K by the heat pulse relaxation method using a QD physical property measurement system (PPMS) with sample mass of $20 \sim 30$ mg. The electrical resistivity (ρ), Seebeck coefficient (S), and thermal conductivity (κ) were measured on a QD PPMS using the thermal transport option (TTO) with standard four-probe technique. Continuous measuring mode was used. The maximum heat powder and period were set as 50 mW and 1430 s along with the maximum temperature rise of 3%. The drive current and frequency for resistivity is 1 mA and 17 Hz. The sample dimensions were measured by an optical microscope Nikon SMZ-800 with 10 μm resolution. The relative error in thermoelectric properties was less than 5% based on a Ni standard measured under identical condition. It should be noted that resistivity values of polycrystalline samples include grain boundary contribution.

III. RESULTS AND DISCUSSIONS

The EDX measurement confirmed $Ir_{1-x}Rh_xTe_2$ stoichiometry and nominal Ir/Rh ratio within up to 10% experimental error. Rietveld powder diffraction analysis was carried out on data sets obtained from the raw 2D diffraction data integrated and converted to intensity versus Q using the software Fit2d where Q is the magnitude of the scattering vector [28]. The refinement was performed using GSAS/EXPGUI modeling suite [29,30]. We used the room temperature CdI_2 prototype structure and trigonal symmetry ($P\bar{3}m1$, 1T phase) [31,32]. Figure 1(a) shows fits to the data with no impurity peaks present. Rietveld analysis produced excellent fits to the data up to a high Q, suggesting high purity of samples and high quality of the XRD data.

$Ir_{1-x}Rh_xTe_2$ crystalizes in a layered structure [inset in Fig. 1(b)]. There is a large number of compounds crystalizing in this structure, especially TMDCs such as MX_2 (M = Ti, Ta, or Nb, X = S, Se, or Te). In this structure, the edge-sharing Ir/Rh-Te octahedra form Ir/Rh-Te layers in the *ab* plane, resulting in the network of equilateral triangles populated by Ir ions. The sandwich-like Te-Ir/Rh-Te layers stack along
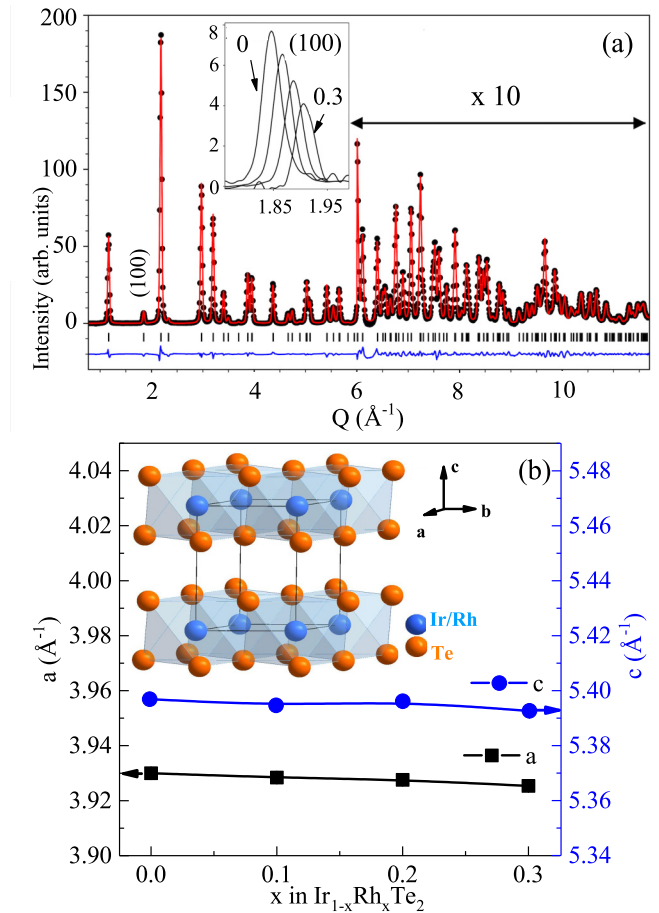
FIG. 1. (a) The Rietveld refinement of the background subtracted $IrTe_2$ synchrotron powder x-ray diffraction up to $Q \sim 12$ Å^{-1}. Plots show the observed (dots) and calculated (red solid line) powder patterns with a difference curve. The vertical tick marks represent Bragg reflections in the $P\bar{3}m1$ space group. Inset shows the evolution of the normalized intensity of (100) Bragg reflection with increasing x in $Ir_{1-x}Rh_xTe_2$. (b) Unit cell parameters as a function of Rh substitution up to $x = 0.3$. Inset shows crystal structure of $Ir_{1-x}Rh_xTe_2$ with Ir/Rh sites marked in blue and Te sites marked in orange.

the *c* axis with Te-Te bonds instead of weak van der Waals gap which has been often observed in TMDCs [12,33,34]. Although the interlayer interaction might be stronger than in typical TMDCs, there are still some ions that can be intercalated between Te-Ir/Rh-Te layers, such as Pd and Cu [12,13]. The intercalation usually results in the increase of the *c* axial lattice parameter [11,12]. On the other hand, for the Pt/Pd substitution, the *c* axial lattice parameter decreases with doping. The *a* and *c* axial lattice parameters of $Ir_{1-x}Rh_xTe_2$ ($0 \leqslant x \leqslant 0.3$) decrease only weakly with Rh substitution [Fig. 1(b)], which might be partially due to the similar ionic radii of Ir and Rh.

Temperature-dependent resistivity of pure $IrTe_2$ ($x = 0$) shows metallic behavior with a significant thermal hysteresis around ~250 K, as depicted in Fig. 2, which has been ascribed to a structural transition from the trigonal $P\bar{3}m1$ space group to triclinic symmetry $P\bar{1}$ [14–16]. However, the origin of this structural transition is still disputed. Electron diffraction
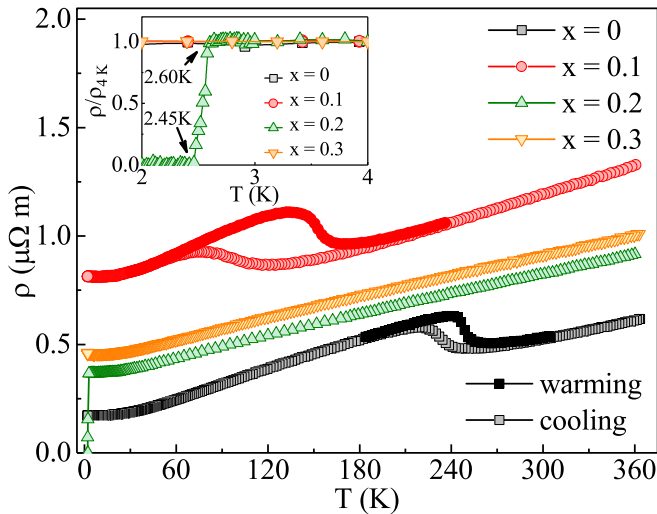
FIG. 2. Temperature dependence of electrical resistivity for Ir$_{1-x}$Rh$_x$Te$_2$ ($0 \leqslant x \leqslant 0.3$). Inset shows the enlarged low temperature part of $2 \sim 4$ K (normalized at 4 K).

FIG. 3. Temperature dependence of Seebeck coefficient for Ir$_{1-x}$Rh$_x$Te$_2$ ($0 \leqslant x \leqslant 0.3$). Inset shows the evolution of $S_{300 \, \text{K}}$ (balls) and S/T (circles) as a function of Rh content x.

suggests that the structural transition is driven by charge-orbital density wave with a wave vector of $q = \{1/5, 0, -1/5\}$ [12]. On the other hand, the NMR experiment does not provide the evidence for CDW and the optical spectroscopic as well as ARPES measurements do not observe the gap that would correspond to the CDW state near the Fermi level [18–20]. Additionally, the theoretical calculation suggests that the structural transition is mainly caused by the evolution of Te p bands rather than the instability of Ir d bands, which results in a reduction of the kinetic energy of the electronic system [13,18]. With Rh substitution, the hysteresis becomes broad and shifts to lower temperature. This anomaly disappears and the superconductivity (above 2 K) emerges in Ir$_{0.8}$Rh$_{0.2}$Te$_2$ with the transition temperatures $T_c^{\text{onset}} = 2.60$ K and $T_c^{\text{zero}} = 2.45$ K (inset in Fig. 2), comparable to those with other dopants or intercalating agents [11–13].

Figure 3 shows the temperature dependence of Seebeck coefficient $S(T)$ for Ir$_{1-x}$Rh$_x$Te$_2$ ($0 \leqslant x \leqslant 0.3$). The sign of $S(T)$ for all samples in the whole temperature range is positive, indicating the hole-type carriers. The $S(T)$ of pure IrTe$_2$ ($x = 0$) shows a reduction at (220–260) K, which reflects the reconstruction of the Fermi surface across the structural transition T_s; i.e., the dimer formation below the T_s is likely related to partial localization of some hole-type carriers at T_s [15,26]. With Rh substitution, the hysteresis becomes broad and shifts to lower temperature for $x = 0.1$ and disappears for $x = 0.2$ and 0.3. Rh doping suppresses not only structure transition but also the corresponding Fermi surface reconstruction, offering evidence that the structural and electronic transitions are closely coupled. The high-temperature transition is not present for the $x = 0.2$ sample, which is a much larger substitution content when compared to Pt, Pd, or Cu substitution/intercalation where only several percent (<5%) will suppress the T_s completely [11–13]. This possibly reflects the smaller atomic radii difference and isovalent character of substitution of Rh for Ir as compared to Pt substitution.

Thermopower gradually increases with decreasing temperature in all investigated samples. Below about (50–60) K the
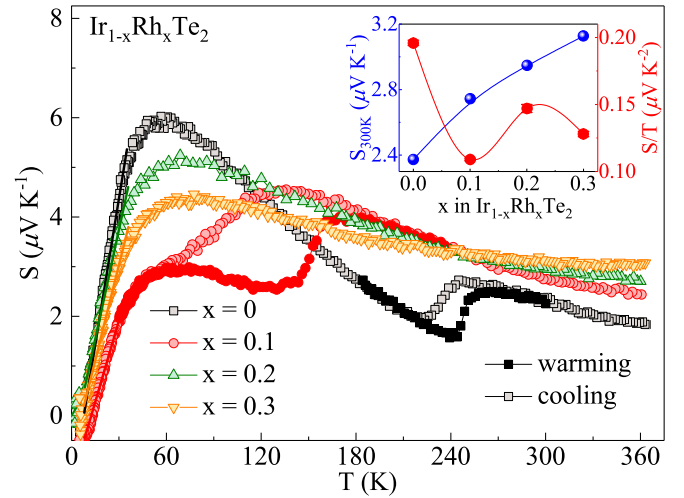
diffusive Seebeck response dominates. As we know, in a metal with dominant single-band transport, the Seebeck coefficient could be described by the Mott relationship, $S = \frac{\pi^2 k_B^2 T}{3e} \frac{N(\varepsilon_F)}{n}$, where $N(\varepsilon_F)$ is the density of states (DOS), ε_F is the Fermi energy, n is the carrier density, k_B is the Boltzmann constant, and e is the absolute value of electronic charge [35]. The room temperature value of $S_{300 \, \text{K}}$ increases with increasing x (inset in Fig. 3), implying the decrease in hole-type carriers with Rh substitution in Ir$_{1-x}$Rh$_x$Te$_2$ and the absence of their reduction due to transition in $x = 0.2$ and 0.3 samples. Interestingly, the S/T value determined by linear fitting below 35 K exhibit a nonmonotonic trend with x, with $x = 0.1$ composition close to dimer/SC boundary being affected by the suppressed structural/electronic transition close to the observed Seebeck peak. The S/T value is associated with the strength of electron correlations, calling for more theoretical study in-depth along with ARPES measurement. For the broad $S(T)$ peak around (50–60) K, generally, the phonon drag contribution to $S(T)$ gives $\sim T^3$ dependence for $T \ll \Theta_D$, $\sim 1/T$ for $T \gg \Theta_D$, and a peak feature for $T \sim \Theta_D/5$. The Debye temperature Θ_D of pure IrTe$_2$ ($x = 0$) is $\sim 215(1)$ K, decreasing to $\sim 198(1)$ K for $x = 0.3$ (as discussed below). Therefore, the peak position of $S(T)$ from phonon drag should be at $\sim 43.0(2)$ K for $x = 0$, decreasing to 38.8(2) for $x = 0.3$, which is lower than the experimentally observed values. This further suggests the dominance of electronic diffusion over the phonon drag effect in thermoelectricity of Ir$_{1-x}$Rh$_x$Te$_2$ ($0 \leqslant x \leqslant 0.3$).

Temperature-dependent total thermal conductivity κ for Ir$_{1-x}$Rh$_x$Te$_2$ ($0 \leqslant x \leqslant 0.3$) [Fig. 4(a)] shows that the $\kappa(T)$ drop that corresponds to the T_s is also clearly observed. Generally, $\kappa = \kappa_e + \kappa_L$ consists of the electronic part κ_e and the phonon term κ_L. The κ_L can be obtained by subtracting the κ_e part calculated from the Wiedemann-Franz law $\kappa_e/T = L_0/\rho$, where $L_0 = 2.45 \times 10^{-8}$ W Ω K^{-2} and ρ is the measured resistivity. The estimated κ_e and κ_L are depicted in Figs. 4(b) and 4(c). It shows that κ_e is larger and comparable to κ_L and confirms the substantial effect of crystal structure changes on heat-carrying phonons. Phonon-related thermal
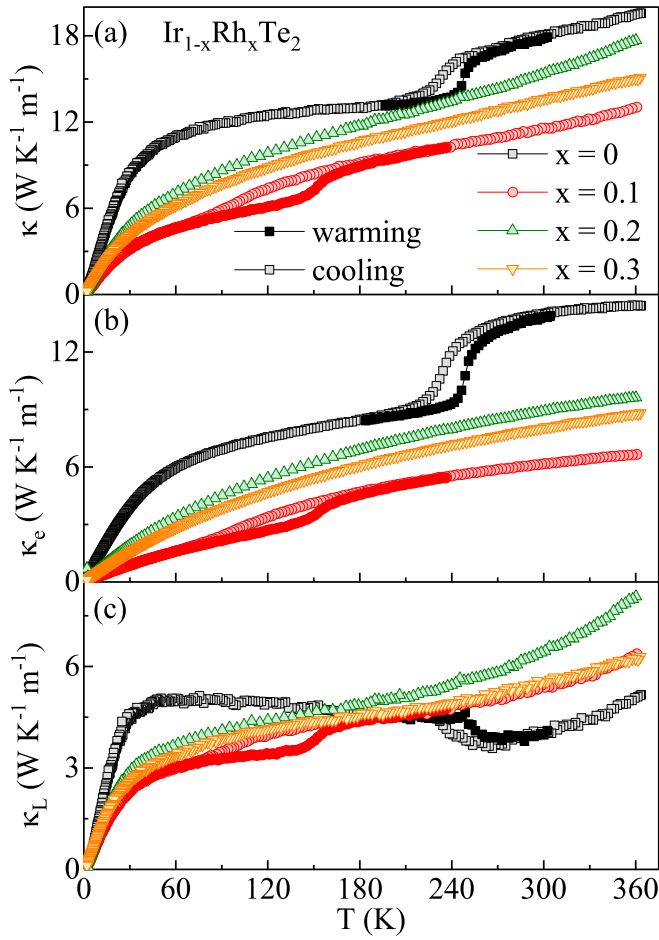
FIG. 4. Temperature dependence of (a) total thermal conductivity κ, (b) electronic part κ_e, and (c) phonon term κ_L for $Ir_{1-x}Rh_xTe_2$ ($0 \leqslant x \leqslant 0.3$).

FIG. 5. (a) Temperature dependence of specific heat C_p for $Ir_{1-x}Rh_xTe_2$ ($0 \leqslant x \leqslant 0.3$). (b) The low temperature specific heat divided by temperature C_p/T as a function of T^2 in zero field. The solid curve represents the fittings using $C_p/T = \gamma + \beta T^2$. Inset shows the evolution of Debye temperature Θ_D and electronic specific heat coefficient γ.

conductivity in pure $IrTe_2$ ($x = 0$) is slightly increased below the T_s whereas Rh substitution brings an increase in κ_L in the temperature range above the T_s. The κ_L of pure $IrTe_2$ ($x = 0$) features a broad maximum around (50–60) K, which is significantly suppressed with Rh doping at Ir sites. This is mostly contributed by the Rh/Ir doping disorder enhanced point defects scattering. It should be noted that the $x = 0.1$ sample shows the smallest value of $\kappa(T)$ as well as $S(T)$ at low temperature. The $\kappa(T)$ and $S(T)$ share the same tendency, suggesting increased possibility for phonon drag with Rh substitution x.

Figure 5(a) shows the specific heat of $Ir_{1-x}Rh_xTe_2$ ($0 \leqslant x \leqslant 0.3$) between 1.95 and 300 K. For pure $IrTe_2$ ($x = 0$), there is a peak at 251 K, corresponding to the anomaly in thermopower and thermal conductivity. The peak shape indicates that it is a first-order transition, consistent with the reported value in the literature [18]. With Rh doping, the peak shifts to 156 K for $x = 0.1$ and the intensity of peak also becomes weaker and less sharp than that in the pure one, indicating a possible change from the first- to the second-order transition near the T_s [25]. The specific heat $C_p(T)$ at low temperature above T_c can be well fitted by using $C_p/T = \gamma + \beta T^2$ [Fig. 5(b)]. The evolution of the obtained γ and derived Debye temperature Θ_D from β using the

relation $\Theta_D = (12\pi^4 N R/5\beta)^{1/3}$, where $N = 3$ is the number of atoms per formula unit and R is the gas constant, are plotted in the inset of Fig. 5(b). The electronic specific heat of $IrTe_2$ is $\gamma \sim 3.81$ mJ/mol-K^2, close to previously reported values [11,18]. With the increase of the Rh content, the value of γ reaches a maximum of 8.06 mJ/mol-K^2 for $x = 0.2$ and decreases to 6.82 mJ/mol-K^2 for $x = 0.3$. This is similar to the Pt doping where γ starts to decrease when $x \geqslant 0.04$, ascribed to the decrease of DOS of $IrTe_2$ above the Fermi level and the upward Fermi level shift due to the partial substitution of Pt for Ir [11].

The electronic specific heat $C_e = \frac{\pi^2}{3}k_B^2 T N(\varepsilon_F)$, where $N(\varepsilon_F)$ is the DOS, ε_F is the Fermi energy, and k_B is the Boltzmann constant. Taken into consideration the Mott relationship $S = \frac{\pi^2 k_B^2 T}{3e} \frac{N(\varepsilon_F)}{n}$, thermopower probes the specific heat per electron: $S = C_e/ne$, where the units are V K^{-1} for S, J K^{-1} m^{-3} for C_e, and m^{-3} for n, respectively. However, it is common to express $\gamma = C_e/T$ in J K^{-2} mol^{-1} units. In order to focus on the S/C_e ratio, let us define the dimensionless quantity, $q = \frac{S}{T} \frac{N_A e}{\gamma}$, where N_A the Avogadro number gives

the number of carriers in the unit cell (proportional to $1/n$) [36]. The constant $N_A e = 9.6 \times 10^5$ C mol^{-1} is also called the Faraday number. We observe reduction of q from 0.49(1) for pure IrTe$_2$, to 0.16(1) for $x = 0.1$, and 0.18(1) for $x = 0.2$ and 0.3. This implies an increase of carrier concentration as Rh enters the lattice.

Then we discuss the superconducting state observed in Ir$_{1-x}$Rh$_x$Te$_2$ ($x = 0.2$). According to the McMillan formula for electron-phonon mediated superconductivity [37], the electron-phonon coupling constant λ can be deduced by

$$T_c = \frac{\Theta_D}{1.45} \exp\left[-\frac{1.04(1+\lambda)}{\lambda - \mu^*(1 + 0.62\lambda)} \right],$$

where $\mu^* \approx 0.13$ is the common value for Coulomb pseudopotential. By using $T_c = 2.45(1)$ K and $\Theta_D = 201(1)$ K in Ir$_{0.8}$Rh$_{0.2}$Te$_2$, we obtain $\lambda \approx 0.59(2)$, a typical value of weak-coupled BCS superconductor. The specific heat jump at T_c, $\Delta C_{es}/\gamma T_c \approx 1.18$, is somewhat smaller than the weak coupling value 1.43 [37]. All these results indicate that Ir$_{0.8}$Rh$_{0.2}$Te$_2$ is a weak-coupled BCS superconductor, similar to Ir$_{0.95}$Pd$_{0.05}$Te$_2$ [38]. Recent x-ray pair distribution function approach reveals that the local structure of Ir$_{0.8}$Rh$_{0.2}$Te$_2$ could be well explained by a dimer-free model, as well as in Ir$_{0.95}$Rh$_{0.05}$Te$_2$, ruling out the possibility of there being nanoscale dimer fluctuations mediated superconducting pairing [26].

IV. CONCLUSION

In summary, we have investigated thermal transport properties of Ir$_{1-x}$Rh$_x$Te$_2$ ($0 \leqslant x \leqslant 0.3$). The decrease of thermopower in pure IrTe$_2$ at T_s implies that dimer formation is related to partial localization of hole-type carriers below the structural transition. The isovalent Rh substitution in Ir$_{1-x}$Rh$_x$Te$_2$ results in an increase of number of carriers per unit cell as Rh enters the lattice and weak-coupling BCS superconductivity. Further investigation of stripe phases existence in Ir$_{1-x}$Rh$_x$Te$_2$ using real-space resolving methods would be useful for addressing the microscopic connection of phonon-related Cooper pairing on the border of exotic structural transitions [39,40].

[1] J. A. Wilson and A. D. Yoffe, Adv. Phys. **18**, 193 (1969).

[2] J. A. Wilson, F. J. DiSalvo, and S. Mahajan, Adv. Phys. **24**, 117 (1975).

[3] A. H. Castro Neto, Phys. Rev. Lett. **86**, 4382 (2001).

[4] T. Valla, A. V. Fedorov, P. D. Johnson, J. Xue, K. E. Smith, and F. J. DiSalvo, Phys. Rev. Lett. **85**, 4759 (2000).

[5] L. J. Li, E. C. T. O'Farrel, K. P. Loh, G. Eda, B. Özylimaz, and A. H. Castro Neto, Nature (London) **529**, 185 (2016).

[6] Y. Liu, R. Ang, W. J. Lu, W. H. Song, L. J. Li, and Y. P. Sun, Appl. Phys. Lett. **102**, 192602 (2013).

[7] B. Sipos, A. F. Kusmartseva, A. Akrap, H. Berger, L. Forró, and E. Tutiš, Nat. Mater. **7**, 960 (2008).

[8] A. M. Gabovich, A. I. Voitenko, J. F. Annett, and M. Ausloos, Supercond. Sci. Technol. **14**, R1 (2001).

[9] Y. Liu, L. J. Li, W. J. Lu, R. Ang, X. Z. Liu, and Y. P. Sun, J. Appl. Phys. **115**, 043915 (2014).

[10] Y. Liu, W. J. Lu, L. J. Li, X. D. Zhu, W. H. Song, R. Ang, L. S. Ling, X. Z. Liu, and Y. P. Sun, J. Appl. Phys. **117**, 163912 (2015).

[11] S. Pyon, K. Kudo, and M. Nohara, J. Phys. Soc. Jpn. **81**, 053701 (2012).

[12] J. J. Yang, Y. J. Choi, Y. S. Oh, A. Hogan, Y. Horibe, K. Kim, B. I. Min, and S.-W. Cheong, Phys. Rev. Lett. **108**, 116402 (2012).

[13] M. Kamitani, M. S. Bahramy, R. Arita, S. Seki, T. Arima, Y. Tokura, and S. Ishiwata, Phys. Rev. B **87**, 180501(R) (2013).

[14] N. Matsumoto, K. Taniguchi, R. Endoh, H. Takano, and S. Nagata, J. Low Temp. Phys. **117**, 1129 (1999).

[15] G. L. Pascut, K. Haule, M. J. Gutmann, S. A. Barnett, A. Bombardi, S. Artyukhin, T. Birol, D. Vanderbilt, J. J. Yang, S.-W. Cheong, and V. Kiryukhin, Phys. Rev. Lett. **112**, 086402 (2014).

[16] T. Toriyama, M. Kobori, T. Konishi, Y. Ohta, K. Sugimoto, J. Kim, A. Fujiwara, S. Pyon, K. Kudo, and M. Nohara, J. Phys. Soc. Jpn. **83**, 033701 (2014).

[17] D. Ootsuki, Y. Wakisaka, S. Pyon, K. Kudo, M. Nohara, M. Arita, H. Anzai, H. Namatame, M. Taniguchi, N. L. Saini, and T. Mizokawa, Phys. Rev. B **86**, 014519 (2012).

[18] A. F. Fang, G. Xu, T. Dong, P. Zheng, and N. L. Wang, Sci. Rep. **3**, 1153 (2013).

[19] K. Mizuno, K.-i. Magishi, Y. Shinonome, T. Saito, K. Koyama, N. Matsumoto, and S. Nagata, Physica B **312–313**, 818 (2002).

[20] D. Ootsuki, S. Pyon, K. Kudo, M. Nohara, M. Horio, T. Yoshida, A. Fujimori, M. Arita, H. Anzai, H. Namatame, M. Taniguchi, N. L. Saini, and T. Mizokawa, J. Phys. Soc. Jpn. **82**, 093704 (2013).

[21] Q. Li, W. Lin, J. Yan, X. Chen, A. G. Gianfrancesco, D. J. Singh, D. Mandrus, S. Kalinin, and M. Pan, Nat. Commun. **5**, 5358 (2014).

[22] A. Kiswandhi, J. S. Brooks, H. B. Cao, J. Q. Yan, D. Mandrus, Z. Jiang, and H. D. Zhou, Phys. Rev. B **87**, 121107 (2013).

[23] Y. S. Oh, J. J. Yang, Y. Horibe, and S.-W. Cheong, Phys. Rev. Lett. **110**, 127209 (2013).

[24] O. Ivashko, L. Yang, D. Destraz, E. Martino, Y. Chen, C. Y. Guo, H. Q. Yuan, A. Pisoni, P. Matus, S. Pyon, K. Kudo, M. Nohara, L. Forró, H. M. Rønnow, M. Hücker, M. v. Zimmerman, and J. Chang, Sci. Rep. **7**, 17157 (2017).

[25] K. Kudo, M. Kobayashi, S. Pyon, and M. Nohara, J. Phys. Soc. Jpn. **82**, 085001 (2013).

[26] R. Yu, S. Banerjee, H. C. Lei, R. Sinclair, M. Abeykoon, H. D. Zhou, C. Petrovic, Z. Guguchia, and E. S. Bozin, Phys. Rev. B **97**, 174515 (2018).

[27] D. Ootsuki, T. Toriyama, M. Kobayashi, S. Pyon, K. Kudo, M. Nohara, T. Sugimoto, T. Yoshida, M. Horio, A. Fujimori, M. Arita, H. Anzai, H. Namatame, M. Taniguchi, N. L. Saini, T. Konishi, Y. Ohta, and T. Mizokawa, J. Phys. Soc. Jpn. **83**, 033704 (2014).

[28] A. P. Hammersley, S. O. Svenson, M. Hanfland, and D. Hauserman, High Pressure Res. **14**, 235 (1996).

[29] A. C. Larson and R. B. Von Dreele, General Structure Analysis System (GSAS), Los Alamos National Laboratory Report LAUR 86–748 (2004), https://11bm.xray.aps.anl.gov/documents/GSASManual.pdf.

[30] B. H. Toby, J. Appl. Crystallogr. **34**, 210 (2001).

[31] R. A. Young, *The Rietveld Method* (Oxford University Press, Oxford, 1995).

[32] E. F. Hockings and J. G. White, J. Phys. Chem. **64**, 1042 (1960).

[33] C. S. Lee and G. J. Miller, Inorg. Chem. **38**, 5139 (1999).

[34] C. Pettenkofer and W. Jaegermann, Phys. Rev. B **50**, 8816 (1994).

[35] R. D. Barnard, *Thermoelectricity in Metals and Alloys* (Taylor & Francis, London, 1972).

[36] K. Behnia, D. Jaccard, and J. Flouquet, J. Phys.: Condens. Matter. **16**, 5187 (2004).

[37] W. L. McMillan, Phys. Rev. **167**, 331 (1968).

[38] D. J. Yu, F. Yang, Lin Miao, C. Q. Han, M.-Y. Yao, F. Zhu, Y. R. Song, K. F. Zhang, J. F. Ge, X. Yao, Z. Q. Zou, Z. J. Li, B. F. Gao, Canhua Liu, D. D. Guan, C. L. Gao, D. Qian, and J.-f. Jia, Phys. Rev. B **89**, 100501 (2014).

[39] J. Dai, Kristjan Haule, J. J. Yang, Y. S. Oh, S.-W. Cheong, and W. Wu, Phys. Rev. B **90**, 235121 (2014).

[40] T. Mauerer, M. Vogt, P.-J. Hsu, G. L. Pascut, K. Haule, V. Kiryukhin, J. Yang, S.-W. Cheong, W. Wu, and M. Bode, Phys. Rev. B **94**, 014106 (2016).

Correction: Missing support information in the Acknowledgment section has been inserted.

Second Correction: Some statements in the Acknowledgment section have been updated.

Phase separation at the dimer-superconductor transition in Ir$_{1-x}$Rh$_x$Te$_2$

R. Yu,[1,*] S. Banerjee,[2] H. Lei,[1,†] M. Abeykoon,[3] C. Petrovic,[1] Z. Guguchia,[1,4] and E. S. Bozin[1,‡]

[1]*Condensed Matter Physics and Materials Science Department, Brookhaven National Laboratory, Upton, New York 11973, USA*
[2]*Department of Applied Physics and Applied Mathematics, Columbia University, New York, New York 10027, USA*
[3]*Photon Sciences Division, Brookhaven National Laboratory, Upton, New York 11973, USA*
[4]*Department of Physics, Columbia University, New York, New York 10027, USA*

The detailed evolution of the local atomic structure across the (x, T) phase diagram of transition metal dichalcogenide superconductor Ir$_{1-x}$Rh$_x$Te$_2$ ($0 \leqslant x \leqslant 0.3$, 10 K $\leqslant T \leqslant 300$ K) is obtained from high-quality x-ray diffraction data using the atomic pair distribution function (PDF) method. The observed hysteretic thermal structural phase transition from a trigonal ($P\bar{3}m1$) to a triclinic ($P\bar{1}$) dimer phase for low Rh content emphasizes the intimate connection between the lattice and electronic properties. For superconducting samples away from the dimer/superconductor phase boundary, structural transition is absent and the local structure remains trigonal down to 10 K. In the narrow range of compositions close to the boundary, PDF analysis reveals structural phase separation, suggestive of weak first-order character of the Rh-doping induced dimer-superconductor quantum phase transition. Samples from this narrow range show weak anomalies in electronic transport and magnetization, hallmarks of the dimer phase, as well as superconductivity albeit with incomplete diamagnetic screening. The results suggest that the dimer and superconducting orders exist in the mutually exclusive spatial regions.

I. INTRODUCTION

Appearance of superconductivity in the proximity and upon destabilization of other quantum states describes a number of complex electronic systems, as exemplified by the phase diagrams of unconventional superconductors [1,2]. Understanding how superconductivity emerges in these materials is among the central challenges in condensed matter physics. While long-range ordered phases are generally seen as detrimental for superconductivity, fluctuations of these phases are considered to have ties to superconducting pairing [3], but the details are intricate and still remain quite puzzling.

Layered transition metal dichalcogenides (TMD) as low dimensional solids provide an opportune platform to study various electronic instabilities, most notably the interplay between charge density wave (CDW) [4,5] and superconductivity (SC) [6,7]. Importantly, in some TMD classes, CDW can be readily tuned into SC by controlling system parameters such as the chemical composition and pressure [8–13] resulting in dome-shaped phase diagrams and linear dependence of T_c on the superfluid density [14], reminiscent of cuprates. The perceived similarity with cuprates that exhibit ubiquitous susceptibility to charge ordering [15–19] extends also to homologous pseudogaps [20–23]. Thus systematic explorations of TMDs are expected to provide further insights of relevance for the cuprate physics [17,24–26].

A polymorph of metallic iridium ditelluride, IrTe$_2$, displaying CdI$_2$-type structure [27], attracted considerable attention following the recent discovery of bulk superconductivity with $T_c \sim 3$ K in intercalated and/or Ir-site substituted derivates IrTe$_2$:Pd [28], Ir$_{1-x}$Pt$_x$Te$_2$ [29], Cu$_x$IrTe$_2$ [30], and Ir$_{1-x}$Rh$_x$Te$_2$ [31]. Given that superconductivity emerges upon suppression of a phase transition into an intriguing low-temperature CDW-like state associated with $\boldsymbol{q_0} = (1/5, 0, 1/5)$ instability [28,32], the discovery triggered a surge of research activity aimed at revealing the driving force behind this modulation and, ultimately, its relationship to superconductivity.

Below $T_s \sim 280$ K, IrTe$_2$ displays a first-order symmetry-lowering transition [33] from the high-temperature trigonal [$P\bar{3}m1$, Fig. 1(a)] [34] to a low-temperature triclinic [$P\bar{1}$, Fig. 1(b)] [35] phase. It is accompanied by sharp anomalies in electrical resistivity and magnetic susceptibility [33] akin to those seen in CDW bearing materials [36,37]. However, he mechanism turns out to be more complex than the Fermi surface nesting. This is evidenced by substantial electronic structure reconstruction [38], lack of discernible CDW gap features in spectroscopic measurements [38–41] and phonon softening instabilities in phonon dispersions [42], as well as observed pressure effects opposite to those expected for conventional CDW systems [43]. The low-temperature structure model obtained from single-crystal x-ray diffraction not only adequately accounts for the observed modulated state [28,32], but also reveals partial dimerization of Ir and Te sublattices and associated charge disproportionation [35,42,44] resulting in tremendous structural distortions [sketched in Fig. 1(c)]. Recent analysis based on first-principles total energy density functional theory calculations combined with angle-resolved photoemission spectroscopy indicates that, apart from a
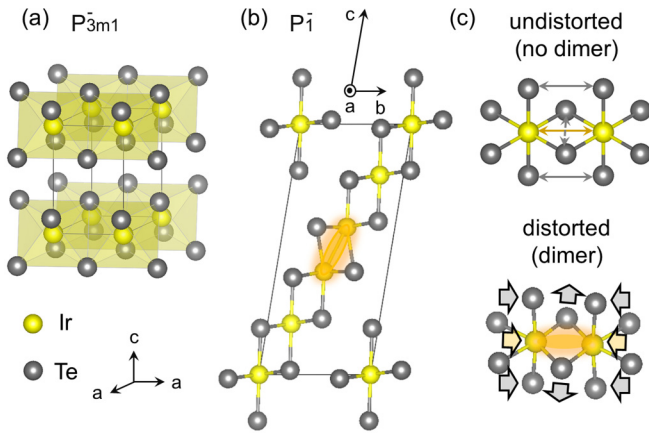
FIG. 1. Details of IrTe$_2$ structures. (a) Undistorted high-temperature trigonal model ($P\bar{3}m1$). (b) Distorted low-temperature triclinic model ($P\bar{1}$) featuring Ir dimers. (c) Sketch of local IrTe$_6$ octahedral environments expected in the absence/presence of Ir dimers (top/bottom). Dimerization results in dramatic distortions of associated interatomic distances relative to the high-temperature structure: Ir-Ir and Te-Te dimer distances reduce by 0.83 and 0.5 Å, respectively, while the lateral Te-Te distance elongates by 0.29 Å [35], as indicated by block arrows.

CDW-like instability, the uniform lattice deformation and the Ir dimerization play very important role [45].

It has been suggested that SC in chemically altered IrTe$_2$ variants competes with the low-T state in a quantum critical point (QCP) manner [28], and that fluctuations of this state possibly mediate superconductivity [29,46], tacitly implying similarity to unconventional SCs. Since most studies focus on the origin and mechanism of the phase transition [32,42,45–51], the question whether the suppression of the low-T phase with chemical doping proceeds in a first- or second-order (QCP-like) manner is still not resolved.

Strong coupling of the electronic state to the lattice enables utilization of local structure methods, such as the atomic pair distribution function (PDF) [52] and extended x-ray absorption fine structure (EXAFS) [53], to study the evolution of such a state across the doping-temperature, (x, T), phase diagrams of interest. Given the intimate involvement of the structure, the proposed fluctuations [28,29,46] should leave their footprint in the nanoscale atomic structure, which can be studied by the local probes sensitive to presence/absence of distortions irrespective of the length scale and character of their ordering. However, only a limited number of local structure studies of this system have been conducted to date. Two studies based on EXAFS are focused on undoped IrTe$_2$ under ambient [47] and high-pressure [54] conditions. The study of the transition under ambient conditions suggested that Ir dimers persist *locally* even in the high-temperature regime, despite the average structure being undistorted trigonal [47]. A recently reported PDF study of superconducting Ir$_{0.95}$Pt$_{0.05}$Te$_2$ and Ir$_{0.8}$Rh$_{0.2}$Te$_2$ did not find evidence of local fluctuating dimers in the superconducting regime, suggesting their absence [55]. This PDF study also did not find evidence of persisting dimer fluctuations in IrTe$_2$ at high temperature, in stark contrast to the EXAFS analysis based claims [47].

Here, we report results of detailed local structure characterization of Ir$_{1-x}$Rh$_x$Te$_2$ across the (x, T) phase diagram using an x-ray total scattering based PDF approach. The ability of the PDF method to reveal hidden nanometer scale structure aspects in a broad class of complex systems, including oxides and chalcogenides, which is important for more thorough understanding of their physical properties, is by now well established [56–62]. Ir$_{1-x}$Rh$_x$Te$_2$ displays an electronic phase diagram [31] very similar to that of other doped IrTe$_2$ variants, with superconductivity emerging close to $x = 0.1$, and involves substitution of Ir by isovalent Rh with nearly identical ionic radii, thereby providing the least involved stage to explore this matter. Our analysis directly maps out the suppression of *local* dimerization with Rh doping occurring in the same way on all length scales. The quantum phase transition from the long-range dimerized to the superconducting phase proceeds in a weakly first-order-like manner, as revealed by the observed intrinsic separation between nondimerized and dimerized phases in a narrow compositional range close to the dimer-superconductor phase boundary. In this range, the diamagnetic screening increases as the dimer fraction decreases, indicating that SC and dimers probably do not coexist within the same spatial regions. In addition, there is no evidence for local dimers persisting deep into the SC regime, in agreement with a previous report [55]. All these observations rule out the proposed QCP scenario.

II. EXPERIMENTAL

Polycrystalline samples of Ir$_{1-x}$Rh$_x$Te$_2$ ($0 \leqslant x \leqslant 0.3$) were synthesized via the standard solid-state route. Stoichiometric amounts of elemental Ir, Rh, and Te were thoroughly mixed, ground, and pelletized. The pellets were placed in alumina crucibles, sealed into quartz tubes under 0.2 atm argon gas, and sintered at 1000° C for 15 h, followed by cooling to room temperature. The process was repeated with intermediate grindings to ensure chemical homogeneity. The samples were found to be in a single phase based on laboratory x-ray powder diffraction and displayed almost no variation of lattice parameters with Rh content, in agreement with a previous report [31]. The final stoichiometries were confirmed by explicit refinement of the site occupancies in the structural modeling of the room-temperature PDF data.

The experimental PDFs were obtained from the collected two-dimensional (2D) diffraction data using standard protocols [52,63] based on synchrotron x-ray total scattering measurements carried out at 28-ID-2 x-ray powder diffraction (XPD) beamline of National Synchrotron Light Source II at Brookhaven National Laboratory. The setup utilized a 67.7 keV x-ray beam ($\lambda = 0.183$ Å), and was equipped with a flat panel image plate detector based on amorphous silicon technology (Perkin Elmer). This setup is optimized such as to provide a broad Q-space coverage, and in turn enhanced r-space resolution, at the expense of Q-space resolution, as is standard in rapid data acquisition xPDF setups [64]. The temperature-dependent measurements in the 10–300 K range (5-K steps) were done on warming using a closed cycle helium cryostat (Cryoindustries of America) featuring an evacuated chamber with a holder accommodating simultaneously three samples, and a set of thin mylar windows. In order to explore
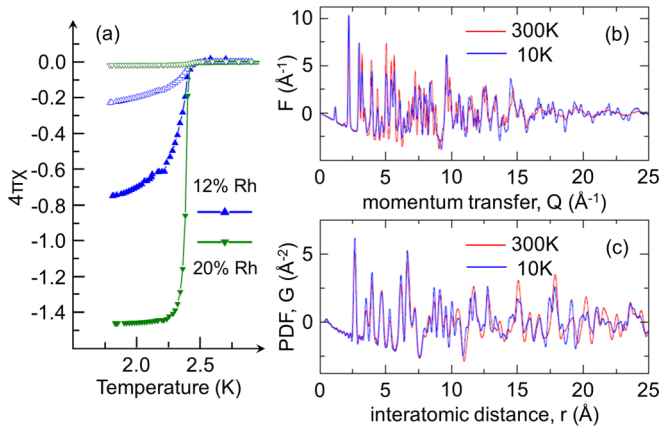
FIG. 2. Comparisons of magnetic susceptibility and total scattering data for selected $Ir_{1-x}Rh_xTe_2$ compositions: (a) dc susceptibility for $x = 0.12$ and 0.2 samples at H = 10 Oe in zero-field-cooling (solid symbols) and field-cooling (open symbols) modes at low-temperature. (b) Reduced total scattering functions, $F(Q)$, and (c) xPDFs, $G(r)$, for $x = 0$ sample at 300 (red) and 10 K (blue).

the system behavior on thermal cycling, additional measurements over the 80–300 K range were performed for all the samples on cooling and successive warming using a liquid nitrogen based cryostream (Oxford Cryosystems 700). The raw 2D diffraction data were integrated and converted to intensity versus Q using the software FIT2D [65], where Q is the magnitude of the scattering vector. Data reduction to measured total scattering structure functions, $F(Q)$ [Fig. 2(b)], and their successive sine Fourier transform up to a momentum transfer of $Q_{max} = 25$ Å^{-1} to obtain experimental PDFs, $G(r)$ [Fig. 2(c)], were carried out using the PDFGETX3 [63] program. PDF structure refinements using models based on $P\bar{3}m1$ and $P\bar{1}$ symmetries were carried out using the PDFGUI program suite [66].

III. RESULTS AND DISCUSSION

We begin by qualitatively comparing the data of parent $IrTe_2$ at endpoint temperatures (300 and 10 K) to assess the sensitivity of the total scattering approach to the symmetry lowering occurring across its structural phase transition [33,35,39,42]. Despite the rather poor Q-space resolution, the effects of symmetry lowering are apparent in the integrated data presented in the form of a derived reduced total scattering function, $F(Q)$ [Fig. 2(b)]. The peaks in, for example, 5–10 Å^{-1} range appear visibly sharper for 300 K (solid red line) than for 10 K (solid blue line), despite the opposite being expected due to the Debye-Waller effects at high-temperature. In the corresponding PDFs, one readily observes the appearance of new peaks in the 10-K $G(r)$ profile as compared to its 300 K counterpart, particularly apparent at, e.g., interatomic distances larger than 10 Å in Fig. 2(c). This establishes the sensitivity of both Q-space and r-space variants of our data to the symmetry lowering observed in $IrTe_2$.

A similar qualitative survey can then be extended to all the samples in the $Ir_{1-x}Rh_xTe_2$ series. Figure 3 provides a
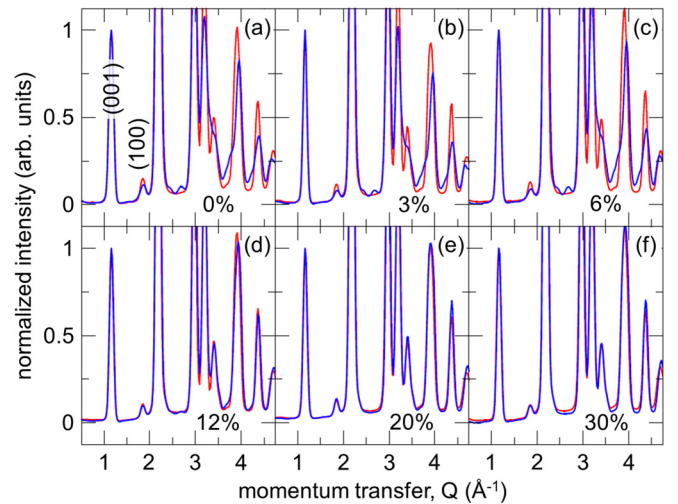
FIG. 3. Comparison of azimuthally integrated 2D diffraction patterns of $Ir_{1-x}Rh_xTe_2$ for 300 (solid red line) and 10 K (solid blue line) over a narrow range of momentum transfer Q for (a) $x = 0$, (b) 0.03, (c) 0.06, (d) 0.12, (e) 0.2, and (f) 0.3. All patterns are normalized by the intensity of (001) reflection ($P\bar{3}m1$ indexing).

comparison of diffraction patterns obtained by azimuthal integration of the raw 2D data. The patterns are further normalized by the intensity of (001) reflection ($P\bar{3}m1$ notation). Profiles in red correspond to 300 K, while profiles in blue represent 10 K. Samples with 0%, 3%, and 6% Rh display very similar behavior with the global symmetry lowered in the 10-K data as evident from additional, although poorly resolved, peaks emerging in the low-temperature patterns shown in Figs. 3(a)–3(c). The data for 300 K are also sharper than the data at 10 K, consistent with the lower symmetry at base temperature. On the other hand, no additional peaks appear at low-temperature for 20% and 30% Rh compositions, with 10 K profiles visibly sharper than those corresponding to 300 K [Figs. 3(e) and 3(f)], as expected from Debye-Waller effects in a system where global symmetry does not change [67], and opposite to what is observed for lower Rh concentrations. Given the limited Q-space resolution of our measurement, this observation does not immediately rule out the average symmetry lowering in these samples, but such conclusion would certainly be in line with the lack of observable anomalies in electrical resistivity and magnetic susceptibility for these Rh concentrations [31]. Samples with intermediate compositions close to the dimer/superconductor boundary [31] show an appreciably weaker response than those with low Rh-content, but still consistent with there being a structural change. This is shown for 12% composition in Fig. 3(d), with similar behavior also observed for the 10% Rh sample (not shown). This assessment indicates that the average structure changes up to and possibly including compositions close to the dimer/superconductor boundary, while it remains unchanged in the superconducting region of compositions.

Qualitative comparisons of as measured (without any scaling) PDFs, shown in Fig. 4 over the range of 10 Å, provide further noteworthy insights. At 300 K, all patterns are qualitatively very similar, with observable differences arising primarily in the PDF peak intensities, which is expected due to
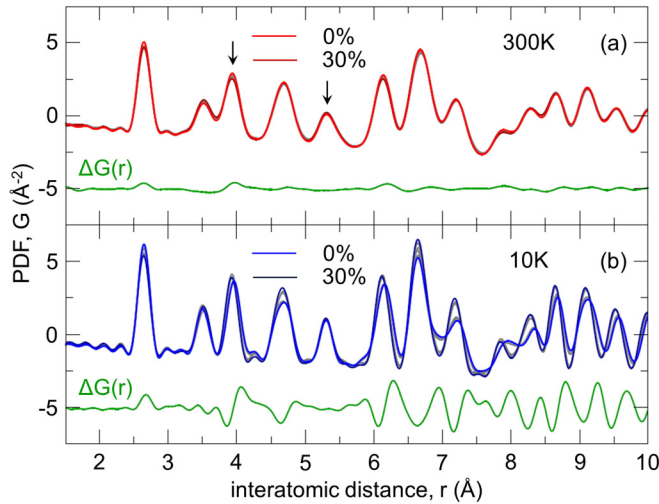
FIG. 4. Comparison of experimental xPDFs of $Ir_{1-x}Rh_xTe_2$ for $0 \leq x \leq 0.3$ over 10-Å range at (a) 300 and (b) 10 K. The data for the end members are shown as colored profiles, and for the intermediates as gray profiles. $\Delta G(r)$ in both panels represents the difference between $x = 0$ (light red/blue) and 0.3 (dark red/blue) xPDFs, shown as a solid green line and offset for clarity. At 300 K, all xPDF profiles look very similar. At 10 K, xPDF profiles apparently cluster into two groups, those resembling $x = 0$ (light blue), and those that are similar to $x = 0.3$ (dark blue). Arrows in (a) mark lattice repeat distance peaks in the trigonal phase.

the very different x-ray scattering form factors of Ir ($Z = 77$) and Rh ($Z = 45$) [52]. There is no observable variation with Rh content of the PDF peak positions, as can be seen by inspecting, e.g., the lattice repeat distance peaks centered around $a \approx 3.932$ Å and $c \approx 5.397$ Å marked by arrows in Fig. 4(a). This is consistent with the unchanged bond-length distribution and also consistent with the previously reported minute variability in lattice constants of $Ir_{1-x}Rh_xTe_2$ with Rh content at room temperature [31], in contrast to $Ir_{1-x}Pt_xTe_2$, where Pt doping alters the unit cell parameters appreciably [29]. This is exemplified by PDFs of 0% and 30% Rh data, shown in Fig. 4(a) as light red and dark red solid lines, respectively. Their difference, shown as green line underneath, displays signatures consistent with the PDF intensity variations. The profiles for all other compositions are superimposed as gray solid lines and gradually fill the small intensity gaps between the two PDFs corresponding to the end members and are virtually indistinguishable from already very similar end-member PDFs. Remarkably, the signal in the nonphysical region of r below 2.5 Å, and just before the nearest-neighbor peak, is exceptionally well matched across all data sets, with small ripples originating from the effects of the finite size of the Fourier transform window being well aligned for all Rh compositions. This reflects the exceptional reproducibility of PDF data across all seven studied samples with different Rh content, as well as the overall data quality [68].

On the other hand, the PDF data comparison at 10 K reveals quite different behavior. PDFs of 0% and 30% Rh data are shown in Fig. 4(b) as light blue and dark blue solid lines, respectively, with their difference (green line) reflecting additional positional mismatch characteristics of appreciable changes in the underlying bond-length distribution. This is
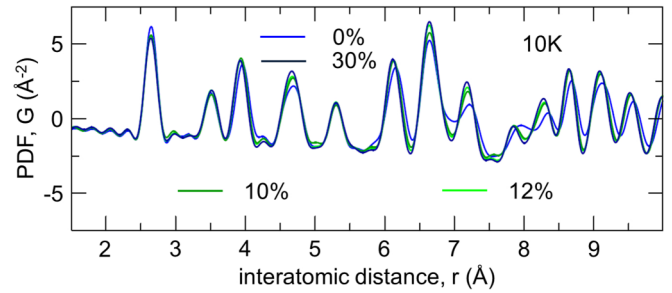
FIG. 5. Comparison of experimental xPDFs of $Ir_{1-x}Rh_xTe_2$ over 10-Å range at 10 K for $x = 0$ (solid light blue line), 0.1 (solid dark green line), 0.12 (solid light green line), and 0.3 (solid dark blue line). See text for details.

consistent with a change in symmetry on going from one composition to another at base temperature. For the samples with in-between compositions, the PDFs are again displayed as gray profiles. These PDFs appear to cluster together with either the 0% Rh PDF or the 30% Rh PDF in almost perfect binary registry of two states, with no visible gradual change. However, careful inspection reveals that 10% and 12% compositions deviate somewhat from this trend and show an intermediate behavior on a length scale of approximately 1 nm (Fig. 5), suggestive of possible phase separation. Details of this behavior will be explored quantitatively and addressed further below.

Next, we characterize the local structure evolution more quantitatively by explicitly fitting the structure models to the experimental PDF data using a full profile least squares approach, similar to that of the Rietveld method [69] in conventional powder diffraction as described in detail elsewhere [66]. Data at 300 K for all the samples are found to conform to trigonal $P\bar{3}m1$ model of $IrTe_2$ [33], and all obtained fits are of comparably good quality as shown in Fig. 6, consistent with all the samples being single phase. In order to map out the structural evolution with temperature and doping, and to observe the areas of the phase diagram where the local symmetry is broken, we utilize a high-temperature trigonal $P\bar{3}m1$ model for all the data of all the samples first. In this approach, a high-symmetry model is used to detect the locally broken symmetry by charting locations in an (x, T) phase diagram where such model fails to explain the PDF data. This is typically done by monitoring the evolution of the weighted fit residual, r_W, which quantifies the goodness of the fit of the used model [66]. Additionally, atomic displacement parameters (ADP), U, are also monitored, as these become anomalously enhanced when the underlying symmetry is lowered thus indicating inadequacy of the model to explain the established distortions [70,71]. This simple yet powerful approach has been very successful in detecting presence of low-temperature nanoscale Ir-dimer fluctuations in $Cu(Ir_{1-x}Cr_x)_2S_4$ thiospinel [62] for Cr concentrations for which long-range dimer order is not observed [72], as mentioned earlier, an information crucial for comprehensive understanding of observed anomalies in electronic transport in that system [62].

The results of this approach applied to $Ir_{1-x}Rh_xTe_2$ by utilizing the $P\bar{3}m1$ model over 50 Å range are summarized

FIG. 6. Structural refinements of $P\bar{3}m1$ model (solid red line) to $Ir_{1-x}Rh_xTe_2$ xPDF data at 300 K (open blue symbols) over 10-Å range. The difference between the data and the model is shown as a solid green line underneath and is offset for clarity. (a) $x = 0$ ($r_W = 3.9\%$), (b) $x = 0.03$ ($r_W = 3.8\%$), (c) $x = 0.06$ ($r_W = 4.1\%$), (d) $x = 0.12$ ($r_W = 4.2\%$), (e) $x = 0.2$ ($r_W = 4.1\%$), and (f) $x = 0.3$ ($r_W = 4.1\%$). Refinement of $x = 0.1$ data (not shown) results in a fit with residual of $r_W = 3.9\%$.

in Fig. 7. Both fit residual, Fig. 7(a), and Ir ADP, Fig. 7(b), are found to exhibit abrupt upturns for IrTe$_2$ at temperatures where anomalies in resistivity and susceptibility set in, evidencing (this time directly) the onset of structural transformation. Very similar anomalies are also seen in doped samples with Rh content up to and including 12%, with the transition temperature gradually decreasing and the transition generally becoming broader with increasing Rh content, in line with the temperature evolution of magnetic and transport properties [31] confirming coupling of the lattice degrees of freedom and the underlying physical properties [39]. For superconducting 20% and 30% Rh compositions away from the dimer/superconuctor phase boundary, anomalous upturns in the residual and Ir ADP fits are *not* observed down to the lowest accessible temperature (10 K), confirming that the average transition does not occur in these samples, and, more importantly, indicating absence of dimer fluctuations within the sensitivity of our data and the analysis protocol [55]. The weak gradual temperature dependence of r_W noticeable for 20% and 30% compositions in Fig. 7(a) is not an indication of underlying locally broken symmetry. This is rather a consequence of fits generally performing better at higher temperature due to thermal broadening masking any imperfections in experimental data that only become apparent at lower temperature. If these were related to local symmetry breaking, they would also be seen in the temperature dependent Ir ADPs in Fig. 7(b), but these exhibit canonical behavior [55,62,67,70].

Inspection of the fits of the $P\bar{3}m1$ model to 10-K PDF data over 10-Å range further corroborates this conclusion. Model clearly fails for 0%, 3%, 6%, and 10% data, Figs. 8(a)–8(d), with slightly better fits for 10% composition. The model does visibly better for 12%, but the discrepancies observed in the difference curve, Fig. 8(e), appear to correlate with similar discrepancies seen for lower doping and the fit residual is still larger than that for 300 K. On the other hand, the $P\bar{3}m1$
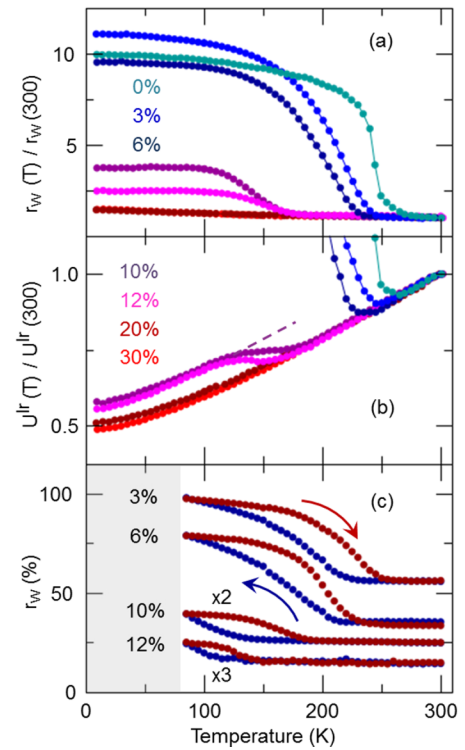
FIG. 7. Detection of structural transition in $Ir_{1-x}Rh_xTe_2$ by $P\bar{3}m1$ modeling of xPDF data. Rh content is indicated in the panels. (a) Fit residual, $r_W(T)$, normalized to 300 K value. (b) Isotropic atomic displacement parameter of Ir, $U(T)$, normalized to the 300-K value. (c) Fit residual, $r_W(T)$, for data collected on cooling (blue) and warming (red) for samples with selected Rh content. Hysteresis loops for 10% and 12% Rh samples are scaled for clarity, as indicated. Loops have been offset for clarity. Quantities shown in (a) and (b) are based on data acquired on warming using cryostat equipment; these shown in (c) are based on data collected on thermal cycling utilizing cryostream equipment. The shaded area in (c) denotes lack of data in the collection mode used.

model fits to 20% [Fig. 8(f)] and 30% data at 10 K are of comparable quality to those observed for the same model and samples at 300 K, indicating that this model provides a good description of the local structure for these compositions at low temperature and thus confirming that no observable dimer fluctuations are present [55].

In order to determine the character of the transition in Rh-substituted samples, the same approach is applied to the data obtained during thermal cycling. The transition is found to display observable hysteresis in the parameters sensitive to the transition for all the samples where it occurs, as shown in Fig. 7(c), indicating first-order behavior. Notably, the response becomes substantially weaker as Rh composition approaches the dimer/superconductor boundary, with the characteristic upturns in both the fit residual and Ir ADP measures nearly an order of magnitude smaller than for IrTe$_2$. This is consistent with there being a considerable reduction in the dimer density as the dimer/superconductor boundary is approached [55].

At this point, and before proceeding to low-temperature structure assessment, it is important to note that orderings other than 1/5 with higher dimer densities have also been observed in the IrTe$_2$ system. A second phase transition has
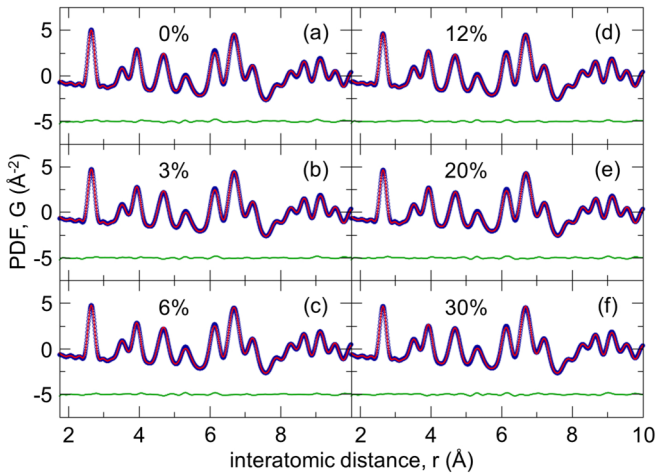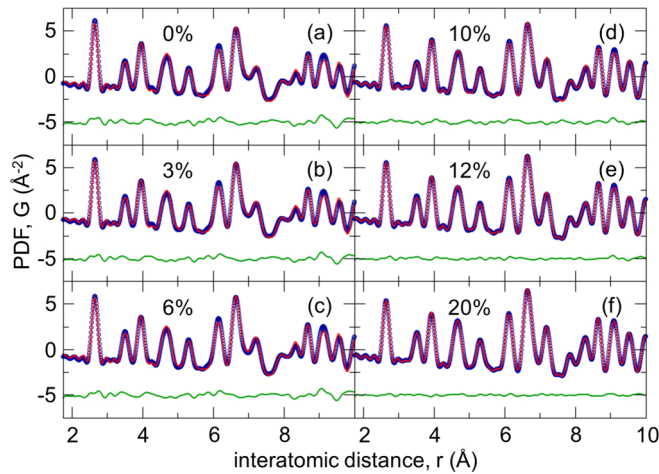
FIG. 8. Structural refinements of $P\bar{3}m1$ model (solid red line) to $Ir_{1-x}Rh_xTe_2$ xPDF data at 10 K (open blue symbols) over 10-Å range. Difference between the data and the model is shown as solid green line underneath (offset for clarity). (a) $x = 0$ ($r_W = 14.8\%$), (b) $x = 0.03$ ($r_W = 13.5\%$), (c) $x = 0.06$ ($r_W = 12.9\%$), (d) $x = 0.1$ ($r_W = 7.7\%$), (e) $x = 0.12$ ($r_W = 5.7\%$), and (f) $x = 0.2$ ($r_W = 3.9\%$). Refinement to $x = 0.3$ data (not shown) gives a similar quality fit to that for $x = 0.2$.

FIG. 9. Structural refinements at 10 K. Fits of $P\bar{1}$ model to the data of (a) $x = 0$ ($r_W = 2.0\%$), (b) $x = 0.03$ ($r_W = 2.1\%$), (c) $x = 0.06$ ($r_W = 2.3\%$), (d) $x = 0.1$ ($r_W = 6.3\%$), and (e) $x = 0.12$ ($r_W = 7.3\%$). (f) $P\bar{3}m1 + P\bar{1}$ two-phase model refinement to $x = 0.12$ data ($r_W = 2.7\%$). See text for details.

been reported to occur around $\sim$180 K from 1/5 to a higher dimer density 1/6 ordering state (presumed to be the ground state) [73], originally observed to occur as a function of Se doping in $IrTe_{2-x}Se_x$ [32], and confirmed in several followup studies [46,48–50,74,75]. However, one of the consequent studies revealed that the appearance of additional phases (beyond the 1/5 phase) is by no means ubiquitous, and that it very much depends on the sample synthesis protocols used [76]. The temperature-dependent assessments of our samples shown above do not exhibit any additional anomalies at lower temperature that could be attributed to presence of such higher dimer density phases in our samples. We therefore consider the local structure evolution at low-temperature within the framework of 1/5 ordering model.

For assessment of the local structure at low-temperature, the $P\bar{1}$ dimer model [Fig. 1(b)] with eight atoms in the asymmetric unit cell (three Ir and five Te atoms) is used to fit the PDF data at 10 K over a 10-Å range, utilizing lattice and fractional coordinate parameters as reported in the original single-crystal x-ray diffraction work of Pascut *et al.* [35]. Although this dimer model has considerably simpler unit cell than one previously reported in P1 setting by Cao *et al.* [42] (75 independent atoms: 25 Ir and 50 Te), it still has six lattice parameters and 21 independent fractional coordinates, a large number of variables as compared to three (two lattice parameters and one fractional coordinate) needed to describe the $P\bar{3}m1$ high-temperature structure. In order to avoid over-parametrization of the fits due to narrow PDF refinement range, we kept these parameters fixed to values reported for $IrTe_2$ [35], and refined only the overall scale factor and ADPs. The later were additionally constrained to be the same for the atoms of the same type. Even with this rather conservative approach, fits with exceptionally good agreement are achieved to the data for 0%, 3%, and 6% Rh compositions, as evident from Figs. 9(a)–9(c). Interestingly, this approach gave fits an
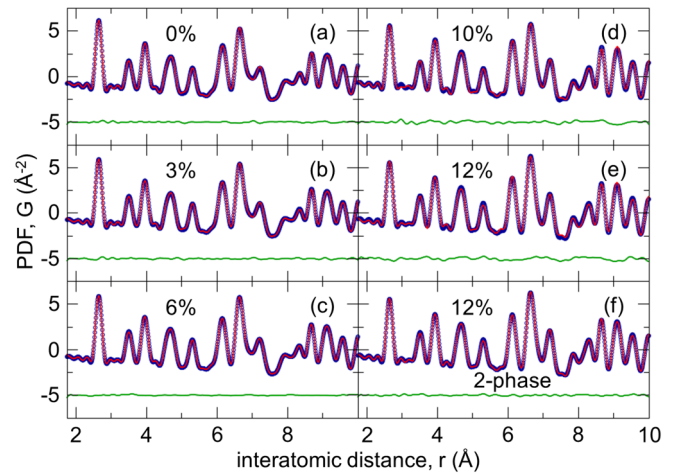
observably poorer quality for 10% and 12% Rh data, with the fit of the later being slightly worse than the fit of the former, as indicated by the values of the fit residual and also observable in the corresponding difference curves in Figs. 9(d) and 9(e). We recall here the qualitative comparison of 10-K PDF data (Fig. 5). There, one readily observes that data for 10% and 12% Rh samples display an intermediate behavior between that of low and high Rh content compositions, suggestive of a two-phase behavior. The increasing inability of the triclinic model to explain these data alone also points to a necessity to explore a two-phase mixture. Following this, these data were fit using an explicit two-phase modeling approach. The ingredient phases of this refinement were $P\bar{1}$ and $P\bar{3}m1$ using parameters for $IrTe_2$ at 10 and 300 K, respectively. These parameters were kept fixed, while refining one ADP for Ir and one for Te (shared across the phases), and one unique phase scale factor. This resulted in fits with significantly improved agreement as compared to cases when the two phases were refined independently within single phase refinements, as illustrated in Fig. 9(f) for 12% Rh data. The resulting phase fractions are 0.6(1) and 0.3(1) for 10% and 12% Rh samples at 10 K, respectively. We also estimated the dimer phase fraction from magnetic susceptibility measurements [77] and reported the Rh-content dependent size of the dip at the transition [31], normalized to its $x = 0$ value [55]. This shows good general agreement with the phase fraction estimated from the PDF analysis. Admittedly, in the PDF modeling of 10-K data of the undoped and low Rh-doped samples, the $P\bar{1}$ model results in fits of comparable quality to those of the two-phase model. This implies that the variation of the dimer density in this part of the phase diagram is relatively small and below the sensitivity of our approach [55], making the fraction of $P\bar{3}m1$ phase effectively inaccessible.

We summarize all observations resulting from the PDF analysis in a phase diagram shown in Fig. 10. The structure transition temperatures were determined as midpoint values obtained from the temperature dependence of parameters indicating failures of the $P\bar{3}m1$ model shown in Fig. 7. These
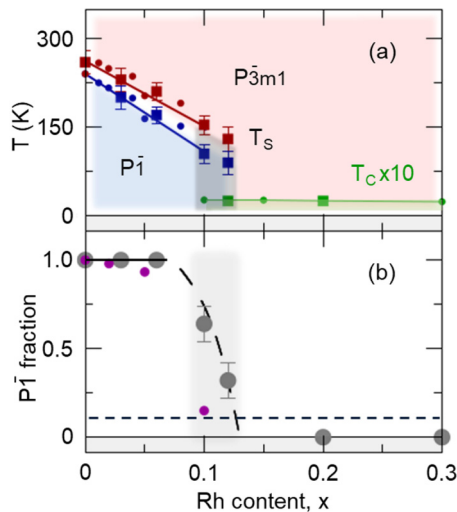
FIG. 10. (a) (x, T) phase diagram of $Ir_{1-x}Rh_xTe_2$. Solid blue and red circles represent magnetic phase transition temperature obtained from susceptibility measurements on cooling and warming, while the solid green circles denote superconducting transition temperature, after reference [31]. Solid blue and red squares mark the structural transition temperature in $Ir_{1-x}Rh_xTe_2$ from this study. Solid green squares denote superconducting transitions observed in samples used here. The values of superconducting T_c are multiplied by a factor of 10 for clarity. (b) $P\bar{1}$ phase fraction obtained from local structure refinements (solid gray symbols). The same phase fraction deduced from susceptibility measurements reported by Kudo *et al.* [31] (solid magenta circles). All lines are guides to the eye. Horizontal dashed line in (b) marks the estimated PDF sensitivity threshold to the presence of the local dimer phase [55].

are in generally good agreement with those reported from the measurements of the physical properties in $Ir_{1-x}Rh_xTe_2$ [31]. The superconducting temperatures for our samples were determined from dc susceptibility measurements. These are shown for two of our samples in Fig. 2(a). Although demagnetization corrections have not been done, these measurements suggest that the 12% Rh sample does not exhibit complete diamagnetic screening, whereas the 20% sample does. In addition, the 12% sample shows broader SC transition with weak pinning signatures as compared to the 20% sample. This clearly indicates that there is an enhancement of superconductivity with doping. On the other hand, the dimerized phase fraction [Fig. 10(b)] sharply decreases upon approaching the dimer/superconductor boundary on increasing Rh content, having the opposite trend to the superconducting fraction. This indicates that SC and dimerized phases likely do not coexist within the same spatial regions of the sample and that they are mutually exclusive.

The competitive nature of the interplay between SC and 1/5-dimer phase is also manifested in the following observations. Bulk superconductivity occurs without the presence of this phase in structural polymorphs of $IrTe_2$ other than trigonal, which have $IrTe_6$ connectivity different than edge sharing [78–81]. Apart from the character of the structural phase, significant depletion of the carrier density [82] accompanying the 1/5-ordering has been recently suggested as one of the contributing factors to the suppression of superconduc-

tivity. Recent STM studies also pointed to the incompatibility of the dimer phase and superconductivity, evidenced as nanoscale phase separation between these phases [82]. The adverse effect of dimerization is further seen in $AuTe_2$ [83] and $CuIr_2S_4$ [77] chalcogenides, where SC emerges as well only upon doping induced breaking of Te and Ir dimers, respectively. However, in $IrTe_2$, SC appears to be compatible with honeycomb-type charge order [82], suggesting that SC may couple only to a specific type of ordering [82,84].

IV. CONCLUSIONS

In summary, the nanometer scale structure of $Ir_{1-x}Rh_xTe_2$ has been studied across the (x, T) phase diagram by means of high-energy x-ray total scattering based atomic PDF analysis. The PDF data at 300 K for all samples ($0 \leqslant x \leqslant 0.3$) studied are equally well explained by the trigonal $P\bar{3}m1$ model, indicating their single-phase character within the sensitivity of our data. PDF analysis evidences a structural phase transition for all compositions up to $x = 0.12$, and no structural change for $x = 0.2$ and 0.3 down to the lowest accessible temperature (10 K). The structural phase transition temperature gradually decreases with increasing Rh content, and shows a thermal hysteresis consistent with previous transport and susceptibility measurements. For samples with compositions away from the dimer/superconductor phase boundary, the base temperature PDF data are well explained by single-phase models. However, samples with compositions close to to the boundary ($x = 0.1$ and 0.12) are found to display separation into nondimerized ($P\bar{3}m1$) and dimerized ($P\bar{1}$) phases as evidenced by explicit two-phase refinements of the PDF data. Qualitative measures of the transition become nearly order of magnitude weaker for the compositions close to the boundary, implying that the dimer density drops considerably as the superconducting regime is approached. Given the apparent reciprocal relationship between the doping evolution of the diamagnetic screening and the dimer fraction, the study suggests that below T_c, superconductivity emerges in the nondimerized region of the sample. This points to the macroscopic phase separation between dimer and superconducting phases, further reinforcing the idea of their competitiveness. Our results do not support the view of quantum critical behavior and further implicate that dimer fluctuations do not play significant role in the observed superconducting properties. The analysis carried out here does not rule out a possibility of ordering other than 1/5(1,0,1) in the regions of the phase diagram where dimerization is observed. However, absence of any additional anomalies in $P\bar{3}m1$ ADPs and fit residuals other than those associated with 1/5-order indicates that the cascade of phase transitions to states with different ordering vectors is not present in our samples.

[1] D. N. Basov and A. V. Chubukov, Nat. Phys. **7**, 272 (2011).

[2] L. Jiao, Y. Chen, Y. Kohama, D. Graf, E. Bauer, J. Singleton, J. Zhu, Z. Weng, G. Pang, T. Shang *et al.*, Proc. Natl. Acad. Sci. USA **112**, 673 (2015).

[3] J. C. Davis and D. Lee, Proc. Natl. Acad. Sci. USA **110**, 17623 (2013).

[4] K. Rossnagel, J. Phys.: Condens. Matter **23**, 213001 (2011).

[5] P. Monceau, Adv. Phys. **61**, 325 (2012).

[6] T. Valla, A. V. Fedorov, P. D. Johnson, J. Xue, K. E. Smith, and F. J. DiSalvo, Phys. Rev. Lett. **85**, 4759 (2000).

[7] A. H. Castro Neto, Phys. Rev. Lett. **86**, 4382 (2001).

[8] E. Morosan, H. W. Zandbergen, B. S. Dennis, J. W. G. Bos, Y. Onose, T. Klimczuk, A. P. Ramirez, N. P. Ong, and R. J. Cava, Nat. Phys. **2**, 544 (2006).

[9] B. Sipos, A. F. Kusmartseva, A. Akrap, H. Berger, L. Forro, and E. Tutis, Nat. Mater. **7**, 960 (2008).

[10] Y. Liu, R. Ang, W. J. Lu, W. H. Song, L. J. Li, and Y. P. Sun, Appl. Phys. Lett. **102**, 192602 (2013).

[11] P. Xu, J. O. Piatek, P.-H. Lin, B. Sipos, H. Berger, L. Forró, H. M. Rønnow, and M. Grioni, Phys. Rev. B **81**, 172503 (2010).

[12] R. Ang, Y. Miyata, E. Ieki, K. Nakayama, T. Sato, Y. Liu, W. J. Lu, Y. P. Sun, and T. Takahashi, Phys. Rev. B **88**, 115145 (2013).

[13] M. M. Ugeda, A. J. Bradley, Y. Zhang, S. Onishi, Y. Chen, W. Ruan, C. Ojeda-Aristizabal, H. Ryu, M. T. Edmonds, H. Tsai *et al.*, Nat. Phys. **12**, 92 (2016).

[14] Z. Guguchia, F. von Rohr, Z. Shermadini, A. T. Lee, S. Banerjee, A. R. Wieteska, C. A. Marianetti, B. A. Frandsen, H. Luetkens, Z. Gong *et al.*, Nat. Commun. **8**, 1082 (2017).

[15] J. M. Tranquada, B. J. Sternlieb, J. D. Axe, Y. Nakamura, and S. Uchida, Nature (London) **375**, 561 (1995).

[16] M. Hücker, M. v. Zimmermann, G. D. Gu, Z. J. Xu, J. S. Wen, G. Xu, H. J. Kang, A. Zheludev, and J. M. Tranquada, Phys. Rev. B **83**, 104506 (2011).

[17] E. H. da Silva Neto, P. Aynajian, A. Frano, R. Comin, E. Schierle, E. Weschke, A. Gyenis, J. Wen, J. Schneeloch, Z. Xu *et al.*, Science **343**, 393 (2014).

[18] R. Comin, A. Frano, M. Yee, Y. Yoshida, H. Eisaki, E. Schierle, E. Weschke, R. Sutarto, F. He, A. Soumyanarayanan *et al.*, Science **343**, 390 (2014).

[19] R. Comin, R. Sutarto, F. He, E. H. da Silva Neto, L. Chauviere, A. Frano, R. Liang, W. N. Hardy, D. A. Bonn, Y. Yoshida *et al.*, Nat. Mater. **14**, 796 (2015).

[20] S. V. Borisenko, A. A. Kordyuk, A. N. Yaresko, V. B. Zabolotnyy, D. S. Inosov, R. Schuster, B. Büchner, R. Weber, R. Follath, L. Patthey *et al.*, Phys. Rev. Lett. **100**, 196402 (2008).

[21] D. V. Evtushinsky, A. A. Kordyuk, V. B. Zabolotnyy, D. S. Inosov, B. Büchner, H. Berger, L. Patthey, R. Follath, and S. V. Borisenko, Phys. Rev. Lett. **100**, 236402 (2008).

[22] S. V. Borisenko, A. A. Kordyuk, V. B. Zabolotnyy, D. S. Inosov, D. Evtushinsky, B. Büchner, A. N. Yaresko, A. Varykhalov, R. Follath, W. Eberhardt *et al.*, Phys. Rev. Lett. **102**, 166402 (2009).

[23] A. A. Kordyuk, S. V. Borisenko, V. B. Zabolotnyy, R. Schuster, D. S. Inosov, D. V. Evtushinsky, A. I. Plyushchay, R. Follath, A. Varykhalov, L. Patthey *et al.*, Phys. Rev. B **79**, 020504 (2009).

[24] M. R. Norman, D. Pines, and C. Kallin, Adv. Phys. **54**, 715 (2005).

[25] J. Chang, E. Blackburn, A. T. Holmes, N. B. Christensen, J. Larsen, J. Mesot, R. Liang, D. A. Bonn, W. N. Hardy, A. Watenphul *et al.*, Nat. Phys. **8**, 871 (2010).

[26] V. Thampy, M. P. M. Dean, N. B. Christensen, L. Steinke, Z. Islam, M. Oda, M. Ido, N. Momono, S. B. Wilkins, and J. P. Hill, Phys. Rev. B **90**, 100510 (2014).

[27] E. F. Hockings and J. G. White, J. Phys. Chem. **64**, 1042 (1960).

[28] J. J. Yang, Y. J. Choi, Y. S. Oh, A. Hogan, Y. Horibe, K. Kim, B. I. Min, and S.-W. Cheong, Phys. Rev. Lett. **108**, 116402 (2012).

[29] S. Pyon, K. Kudo, and M. Nohara, J. Phys. Soc. Jpn. **81**, 053701 (2012).

[30] M. Kamitani, M. S. Bahramy, R. Arita, S. Seki, T. Arima, Y. Tokura, and S. Ishiwata, Phys. Rev. B **87**, 180501 (2013).

[31] K. Kudo, M. Kobayashi, S. Pyon, and M. Nohara, J. Phys. Soc. Jpn. **82**, 085001 (2013).

[32] Y. S. Oh, J. J. Yang, Y. Horibe, and S.-W. Cheong, Phys. Rev. Lett. **110**, 127209 (2013).

[33] N. Matsumoto, K. Taniguchi, R. Endoh, H. Takano, and S. Nagata, J. Low Temp. Phys. **117**, 1129 (1999).

[34] S. Jobic, P. Deniard, R. Brec, J. Rouxel, A. Jouanneaux, and A. N. Fitch, Z. Anorg. Allg. Chem. **598**, 199 (1991).

[35] G. L. Pascut, K. Haule, M. J. Gutmann, S. A. Barnett, A. Bombardi, S. Artyukhin, T. Birol, D. Vanderbilt, J. J. Yang, S. Cheong *et al.*, Phys. Rev. Lett. **112**, 086402 (2014).

[36] J. A. Wilson, F. J. Di Salvo, and S. Mahajan, Adv. Phys. **24**, 117 (1975).

[37] R. H. Friend and A. D. Yoffe, Adv. Phys. **36**, 1 (1987).

[38] A. F. Fang, G. Xu, T. Dong, P. Zheng, and N. L. Wang, Sci. Rep. **3**, 1153 (2013).

[39] K. Mizuno, K. Magishi, Y. Shinonome, T. Saito, K. Koyama, N. Matsumoto, and S. Nagata, Physica B **312-313**, 818 (2002).

[40] D. Ootsuki, Y. Wakisaka, S. Pyon, K. Kudo, M. Nohara, M. Arita, H. Anzai, H. Namatame, M. Taniguchi, N. L. Saini *et al.*, Phys. Rev. B **86**, 014519 (2012).

[41] D. Ootsuki, S. Pyon, K. Kudo, M. Nohara, M. Horio, T. Yoshida, A. Fujimori, M. Arita, H. Anzai, H. Namatame *et al.*, J. Phys. Soc. Jpn. **82**, 093704 (2013).

[42] H. Cao, B. C. Chakoumakos, X. Chen, J. Yan, M. A. McGuire, H. Yang, R. Custelcean, H. D. Zhou, D. J. Singh, and D. Mandrus, Phys. Rev. B **88**, 115122 (2013).

[43] A. Kiswandhi, J. S. Brooks, H. B. Cao, J. Q. Yan, D. Mandrus, Z. Jiang, and H. D. Zhou, Phys. Rev. B **87**, 121107 (2013).

[44] T. Toriyama, M. Kobori, T. Konishi, Y. Ohta, K. Sugimoto, J. Kim, A. Fujiwara, S. Pyon, K. Kudo, and M. Nohara, J. Phys. Soc. Jpn. **83**, 033701 (2014).

[45] K. Kim, S. Kim, K.-T. Ko, J.-H. Lee, J. Park, J. J. Yang, S.-W. Cheong, and B. I. Min, Phys. Rev. Lett. **114**, 136401 (2015).

[46] J. Dai, K. Haule, J. J. Yang, Y. S. Oh, S.-W. Cheong, and W. Wu, Phys. Rev. B **90**, 235121 (2014).

[47] B. Joseph, M. Bendele, L. Simonelli, L. Maugeri, S. Pyon, K. Kudo, M. Nohara, T. Mizokawa, and N. L. Saini, Phys. Rev. B **88**, 224109 (2013).

[48] K. Kim, S. Kim, and B. I. Min, Phys. Rev. B **90**, 195136 (2014).

[49] G. L. Pascut, T. Birol, M. J. Gutmann, J. J. Yang, S.-W. Cheong, K. Haule, and V. Kiryukhin, Phys. Rev. B **90**, 195122 (2014).

[50] K. Takubo, R. Comin, D. Ootsuki, T. Mizokawa, H. Wadati, Y. Takahashi, G. Shibata, A. Fujimori, R. Sutarto, F. He *et al.*, Phys. Rev. B **90**, 081104 (2014).

[51] T. Mizokawa, J. Electron. Spec. Related Phenomena **208**, 78 (2016).

[52] T. Egami and S. J. L. Billinge, *Underneath the Bragg Peaks: Structural Analysis of Complex Materials*, 2nd ed. (Elsevier, Amsterdam, 2012).

[53] B. K. Teo, *EXAFS: Basic Principles and Data Analysis* (Springer-Verlag, New York, 1986).

[54] E. Paris, B. Joseph, A. Iadecola, C. Marini, H. Ishii, K. Kudo, S. Pascarelli, M. Nohara, T. Mizokawa, and N. L. Saini, Phys. Rev. B **93**, 134109 (2016).

[55] R. Yu, S. Banerjee, H. C. Lei, R. Sinclair, M. Abeykoon, H. D. Zhou, C. Petrovic, Z. Guguchia, and E. S. Bozin, Phys. Rev. B **97**, 174515 (2018).

[56] X. Qiu, T. Proffen, J. F. Mitchell, and S. J. L. Billinge, Phys. Rev. Lett. **94**, 177203 (2005).

[57] E. S. Božin, M. Schmidt, A. J. DeConinck, G. Paglia, J. F. Mitchell, T. Chatterji, P. G. Radaelli, T. Proffen, and S. J. L. Billinge, Phys. Rev. Lett. **98**, 137203 (2007).

[58] E. S. Božin, A. S. Masadeh, Y. S. Hor, J. F. Mitchell, and S. J. L. Billinge, Phys. Rev. Lett. **106**, 045501 (2011).

[59] A. M. Abeykoon, E. S. Božin, W.-G. Yin, G. Gu, J. P. Hill, J. M. Tranquada, and S. J. L. Billinge, Phys. Rev. Lett. **111**, 096404 (2013).

[60] K. R. Knox, A. M. M. Abeykoon, H. Zheng, W.-G. Yin, A. M. Tsvelik, J. F. Mitchell, S. J. L. Billinge, and E. S. Bozin, Phys. Rev. B **88**, 174114 (2013).

[61] S. A. J. Kimber, I. I. Mazin, J. Shen, H. O. Jeschke, S. V. Streltsov, D. N. Argyriou, R. Valenti, and D. I. Khomskii, Phys. Rev. B **89**, 081408 (2014).

[62] E. S. Božin, K. R. Knox, P. Juhás, Y. S. Hor, J. F. Mitchell, and S. J. L. Billinge, Sci. Rep. **4**, 4081 (2014).

[63] P. Juhás, T. Davis, C. L. Farrow, and S. J. L. Billinge, J. Appl. Crystallogr. **46**, 560 (2013).

[64] P. J. Chupas, X. Qiu, J. C. Hanson, P. L. Lee, C. P. Grey, and S. J. L. Billinge, J. Appl. Crystallogr. **36**, 1342 (2003).

[65] A. P. Hammersley, S. O. Svenson, M. Hanfland, and D. Hauserman, High Pressure Res. **14**, 235 (1996).

[66] C. L. Farrow, P. Juhás, J. Liu, D. Bryndin, E. S. Božin, J. Bloch, T. Proffen, and S. J. L. Billinge, J. Phys.: Condens. Matter. **19**, 335219 (2007).

[67] P. Debye, Ann. Phys.-Berlin **344**, 789 (1912).

[68] P. F. Peterson, E. S. Božin, T. Proffen, and S. J. L. Billinge, J. Appl. Crystallogr. **36**, 53 (2003).

[69] H. M. Rietveld, Acta Crystallogr. **22**, 151 (1967).

[70] E. S. Bozin, R. Zhong, K. R. Knox, G. Gu, J. P. Hill, J. M. Tranquada, and S. J. L. Billinge, Phys. Rev. B **91**, 054521 (2015).

[71] M. Shatnawi, E. S. Bozin, J. F. Mitchell, and S. J. L. Billinge, Phys. Rev. B **93**, 165138 (2016).

[72] R. Endoh, J. Awaka, and S. Nagata, Phys. Rev. B **68**, 115106 (2003).

[73] P.-J. Hsu, T. Mauerer, M. Vogt, J. J. Yang, Y. S. Oh, S.-W. Cheong, M. Bode, and W. Wu, Phys. Rev. Lett. **111**, 266401 (2013).

[74] Q. Li, W. Lin, J. Yan, X. Chen, A. G. Gianfrancesco, D. J. Singh, D. Mandrus, S. V. Kalinin, and M. Pan, Nat. Commun. **5**, 5358 (2014).

[75] A. Glamazda, K. Choi, P. Lemmens, J. J. Yang, and S. Cheong, New J. Phys. **16**, 093061 (2014).

[76] M. J. Eom, K. Kim, Y. J. Jo, J. J. Yang, E. S. Choi, B. I. Min, J.-H. Park, S.-W. Cheong, and J. S. Kim, Phys. Rev. Lett. **113**, 266406 (2014).

[77] G. Cao, T. Furubayashi, H. Suzuki, H. Kitazawa, T. Matsumoto, and Y. Uwatoko, Phys. Rev. B **64**, 214514 (2001).

[78] Y. Qi, S. Matsuishi, J. Guo, H. Mizoguchi, and H. Hosono, Phys. Rev. Lett. **109**, 217002 (2012).

[79] L. Li, T. F. Qi, L. S. Lin, X. X. Wu, X. T. Zhang, K. Butrouna, V. S. Cao, Y. H. Zhang, J. Hu, S. J. Yuan *et al.*, Phys. Rev. B **87**, 174510 (2013).

[80] J. Guo, Y. Qi, and H. Hosono, Phys. Rev. B **87**, 224504 (2013).

[81] X. Li, J.-Q. Yan, D. J. Singh, J. B. Goodenough, and J.-S. Zhou, Phys. Rev. B **92**, 155118 (2015).

[82] G. Cao, W. Xie, W. A. Phelan, J. F. DiTusa, and R. Jin, Phys. Rev. B **95**, 035148 (2017).

[83] K. Kudo, H. Ishii, M. Takasuga, K. Iba, S. Nakano, J. Kim, A. Fujiwara, and M. Nohara, J. Phys. Soc. Jpn. **82**, 063704 (2013).

[84] H. S. Kim, S. Kim, K. Kim, B. I. Min, Y. Cho, L. Wang, S. Cheong, and H. W. Yeom, Nano Lett. **16**, 4260 (2016).

Emphanitic anharmonicity in PbSe at high temperature and anomalous electronic properties in the PbQ (Q = S, Se, Te) system

Runze Yu,[1] Emil S. Bozin,[1,*] Milinda Abeykoon,[2] Boris Sangiorgio,[3] Nicola A. Spaldin,[3] Christos D. Malliakas,[4] Mercouri G. Kanatzidis,[4,5] and Simon J. L. Billinge[1,6]

[1]*Condensed Matter Physics and Materials Science Department, Brookhaven National Laboratory, Upton, New York 11973, USA*
[2]*Photon Sciences Division, Brookhaven National Laboratory, Upton, New York 11973, USA*
[3]*Materials Theory, ETH Zurich, Wolfgang-Pauli-Strasse 27, CH-8093 Zürich, Switzerland*
[4]*Department of Chemistry, Northwestern University, Evanston, Illinois 60208, USA*
[5]*Materials Science Division, Argonne National Laboratory, Argonne, Illinois 60439, USA*
[6]*Department of Applied Physics and Applied Mathematics, Columbia University, New York, New York 10027, USA*

The temperature dependence of the local structure of PbSe has been investigated using pair distribution function (PDF) analysis of x-ray and neutron powder diffraction data and density functional theory (DFT) calculations. Observation of non-Gaussian PDF peaks at high temperature indicates the presence of significant anharmonicity, which can be modeled as Pb off-centering along [100] directions that grows on warming similar to the behavior seen in PbTe and PbS and sometimes called emphanisis. Interestingly, the emphanitic response is smaller in PbSe than in both PbS and PbTe indicating a nonmonotonic response with chalcogen atomic number in the PbQ (Q = S, Se, Te) series. The DFT calculations indicate a correlation between band gap and the amplitude of [100] dipolar distortion, suggesting that emphanisis may be behind the anomalous composition and temperature dependencies of the band gaps in this series.

I. INTRODUCTION

PbQ (Q = S, Se, Te) is an important thermoelectric system [1]. Also notable about this system is an anomalous temperature and composition dependence of the electronic band gap, i.e., the energy gap increases with increasing temperature for all three members of the PbQ series [2–4], and shows a nonmonotonicity with chalcogen atomic number [5–8], neither of which behaviors are observed in other binary compound semiconductors [9–11]. PbTe has also recently garnered research interest because of the observation of appreciable Pb anharmonicity at high temperatures, sometimes called emphanisis, that results in anomalously large excursions away from the high-symmetry average positions of the rock-salt structure [12–17]. While seen in other lone-pair materials [18,19] and therefore presumably related to the stereochemical activity of the Pb^{2+} lone pair, the precise nature and origins of this effect are believed to be strongly associated with the presence of the $6s^2$ lone pair in Pb^{2+}. Here we extend the study of the PbQ series to explore emphanisis in PbSe, and use the results to explore the relationship between the dynamic Pb off-centering and the band gap in the PbQ system.

There are increased amplitude atomic motions in all materials with increasing temperature, but what is remarkable in emphanitic systems is the large amplitude of the fluctuations, as large as 0.25 Å [12], and the extreme anharmonicity [20,21]. On average, the fluctuations do not break the long-range symmetry, as evident by the preservation of the average crystallographic cubic structure and the failure to see a net off-centering on average in EXAFS [22]. Inelastic neutron scattering (INS) measurements [20,21] showed that the atomic displacements are dynamic and that there is significant anharmonicity in the dynamics, consistent with the non-Gaussian atomic pair distribution function (PDF) peaks. For example, Delaire *et al.* [20] showed the appearance of an avoided crossing behavior in the phonon dispersions, as well as an anomalous lowering and damping of the longitudinal acoustic phonons and a "waterfall" effect at the zone center, consistent with strong anharmonicity, and Jensen *et al.* [21] identified the appearance on warming of a new dynamic mode at ∼6 meV that suggested a dynamic symmetry breaking. First-principles calculations [12,20,23] also indicate the presence of strong anharmonic effects in these materials, and, in combination with diffuse scattering measurements [13], have recently clarified the existence and nature of correlated local dipolar ordering in PbTe.

Emphanisis was originally reported in PbTe and PbS. Here we complete the investigation of the PbQ (Q = S, Se, Te) series by reporting results from the PbSe system, and comparing the behavior across the series. We carried out complementary x-ray and neutron pair distribution function analysis. We show that PbSe has a response very similar to PbS and PbTe and is also emphanitic. Interestingly, in PbSe the refined amplitude of the dynamic displacements at high temperature is smaller and the PDF remains harmonic to higher temperature than in either PbS or PbTe, indicating that the strength of the emphanisis across the series is nonmonotonic with the chalcogen atomic number being weaker in PbSe than in either PbS or

*bozin@bnl.gov

PbTe. This may explain the anomalous nonmonotonicity of the band gap in this series of materials [5–8], though the underlying origin of the nonmonotonicity of the emphanisis is not clear.

II. METHODS

The PbSe, PbS, and PbTe samples were prepared by methods previously reported [12]. The resulting polycrystalline samples were pulverized for total scattering experiments. The experiments were performed at the NPDF beamline at the Lujan Center at Los Alamos National Laboratory and the 28-ID-2 beamline of the National Synchrotron Light Source-II (NSLS-II) at Brookhaven National Laboratory (BNL). Data were collected over wide temperature ranges, $15 \leqslant T \leqslant 550$ K and $10 \leqslant T \leqslant 480$ K, for neutron and x-ray total scattering, respectively. The neutron and x-ray data reduction to obtain the PDFs was carried out using the PDFgetN [24] with $Q_{max} = 28$ Å and xPDFsuite software with $Q_{max} = 30$ Å, respectively [25,26], using standard methods [26,27]. The PDF approach treats both Bragg and diffuse scattering signals equally by utilizing a sine Fourier transform of the reduced total scattering function, $F(Q) = Q[S(Q) - 1]$, to obtain PDF, $G(r)$. PDF data in turn provide structural information on multiple length scales [26,28]. More details are provided in the Supplemental Material [29–37]. The data were modeled using PDFgui [38] with a cubic rock-salt structure model (space group $Fm\bar{3}m$). Our first-principles calculations were performed using the PAW [39,40] implementation of density functional theory (DFT) as in the VASP package [41]. For further calculation details consult the Supplemental Material [29,42–47].

III. RESULTS AND DISCUSSION

The emphanitic effects are substantial and it is possible to see the appearance of non-Gaussian PDF line shapes and anomalous temperature-dependent peak shifts by eye [12,18] as evident in the low-r region of PbSe PDF experimental data from x-ray and neutron measurements shown in Fig. 1. All the peaks significantly broaden with increasing temperature and become highly non-Gaussian at higher temperatures, similar to PbTe and PbS [12]. The nearest-neighbor peak becomes asymmetric and drops as rapidly in height as the higher-neighbor peaks, an effect that is unusual in PDFs since correlated motion effects tend to sharpen the nearest-neighbor correlations with respect to the others [48]. In addition, the third peak also shifts anomalously to higher r [Fig. 1(c)]. All these observations are characteristic of emphanisis.

To investigate this behavior more quantitatively the xPDF and nPDF data were fit with the rock-salt structure model, Fig. 2. At low temperature the cubic model explains the data well at all length scales [xPDF, Fig. 2(a) and nPDF Fig. 2(e)], confirming that there are no detectable distortions at this temperature. At high temperature the $Fm\bar{3}m$ model explains the average structure well, and is also consistent with the data on intermediate length scales. The model is less successful on short length scales, for example, visible below 6 Å as increased amplitude features in the green difference curve. Fits to the 450 K data are shown in Figs. 2(b) and 2(f).
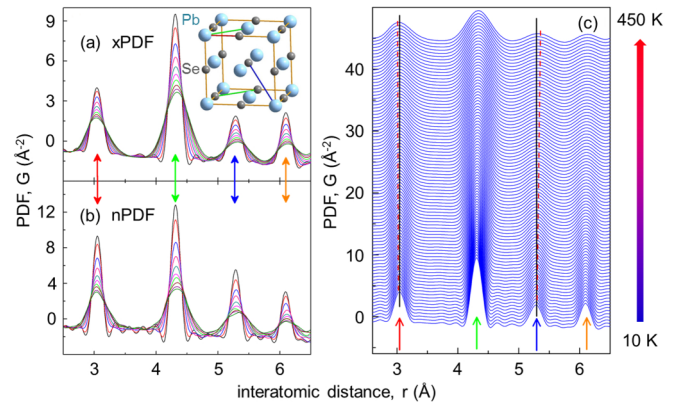
FIG. 1. Temperature evolution of PbSe PDF patterns over 10–450 K range in 50 K increments obtained by (a) x-ray (xPDF) and (b) neutron (nPDF) total scattering. Inset to (a) shows $Fm\bar{3}m$ structure of PbSe with interatomic distances color coded. (c) Waterfall representation of x-ray $G(r)$. Data are offset for clarity. Vertical solid black lines mark the PDF peak positions at base temperature. Sloping dashed red lines track the apparent PDF peak centroids with temperature.

They indicate the presence of significant local distortions on a length scale of a few unit cells, where we note that the PDF cannot, by itself, determine if these distortions are static or dynamic. Over the long range the locally distorted structure averages to the rock-salt structure. In Figs. 2(c), 2(d), 2(g), and 2(h) we show the Pb-Se nearest-neighbor PDF peaks on an expanded scale. At low temperature, Figs. 2(c) and 2(g), the peaks appear as sharp, well defined single-Gaussian functions
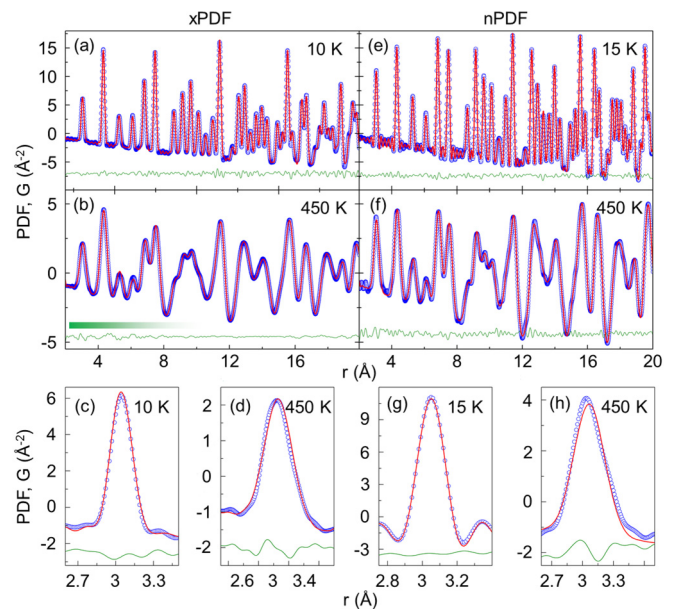
FIG. 2. Fits of $Fm\bar{3}m$ model (solid red line) to experimental PDFs (open blue symbols) obtained by (a)–(d) x-ray probe and (e)–(h) neutron probe. Top panels show broad r-range view, bottom panels focus on nearest-neighbor distributions. Solid green lines are the differences (offset for clarity). Temperature is as indicated. Shaded green rectangle in (b) sketches crossover from the local to average behavior.

with small termination ripples on each side originating from the finite Q range of the Fourier transform [26]. The red lines are calculated PDF profiles based on the rock-salt model having a pure Gaussian line shape, convoluted with a sinc function to account for the termination effects. This is characteristic of a single average bond length with harmonic motion taking place around that position, indicating that the ground state of PbSe at low temperature is the expected ideal rock-salt in both the local and average structures. However, at 450 K [Figs. 2(d) and 2(h)], the peaks are considerably broadened and qualitatively non-Gaussian, with intensity shifted to the high-r side of the peak. These observations unambiguously point to the appearance of significant anharmonic effects in PbSe with increasing temperature, and demonstrate that emphanitic behavior is universally seen in all three lead chalcogenides, PbS, PbSe, and PbTe.

Following the same approach as was taken in the initial study [12], and in order to quantify the underlying bond length distribution, the local structure was further explored by fitting experimental PDFs with several undistorted and distorted models, as described in the Supplemental Material [29]. The cubic model with Pb constrained to remain on its crystallographic positions (undistorted-000) and a model where the Pb is not allowed to displace off its high symmetry positions but the unit cell may take on a tetragonal distortion, as well as models where the Pb ion can display off its high symmetry position in different directions ([110] or [100] displacements) were all tested [12]. Just as observed in PbTe and PbS, we find that a model allowing displacements of Pb along [100] directions, similar to the PbO structure, is preferred at high temperature, consistent with the atomic probability distribution being highly non-Gaussian and appreciably elongated along the [100] direction [Fig. 3(a)], i.e., in the emphanitic state at high temperature the Pb ions spend significant amount of time away from the high-symmetry central position in the form of fluctuating dipoles.

We note that this type of modeling does not imply static displacements for Pb. The PDF yields the instantaneous structure and any offset may be static or dynamic, or have contributions from both. There is ample evidence in PbQ that these displacements are dynamic in nature. It also does not necessarily imply that the time average of the displacements is off-centered. In other words the *time or ensemble average* atomic probability distribution may be peaked at the center. It does imply that the Pb ions are making large excursions from the average position, and spending a significant amount of time away from the central position. Whether or not these excursions result in local dipoles depends on how the excursions are correlated between neighboring sites. If the excursions are correlated between neighboring sites, it implies the formation of local (and in general fluctuating) polar nanoregions. If the excursions are anticorrelated the material would be locally antiferrodistortive. Our one-dimensional (1D) PDF data are not sufficiently sensitive to detect the presence or nature of correlations between neighboring displacements with any certainty, but a recent three-dimensional (3D) Δ-PDF measurement does indeed detect that neighboring displacements tend to be correlated [13].

We extracted the amplitude of the local off-centering in the [100] direction that is needed to reproduce the data within this
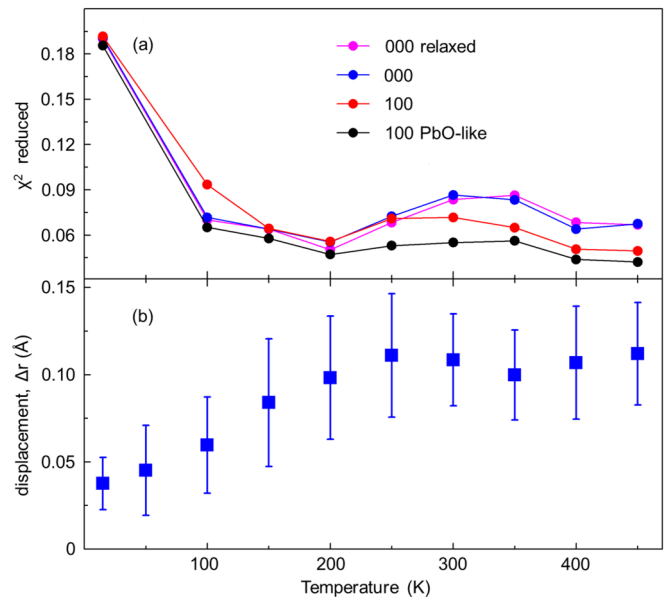
FIG. 3. (a) Assessment of different models (as indicated) for the local structure at various temperatures as seen by reduced χ^2 of the fits. (b) Temperature evolution of estimated Pb local off-centering amplitude obtained from a model with 100 PbO-like displacements. Fits were done to neutron PDF data and utilized the same protocols as those in the original report on PbTe and PbS [12], to allow direct comparison.

PbO-like model. Following the procedure carried out for PbTe and PbSe [12], we separate "normal" (harmonic) dynamics from the emphanitic dynamics by fitting a Debye curve [37] to the low temperature part of the atomic displacement parameter (ADP) data, below 200 K, and extrapolating it to high temperature. The Pb isotropic ADPs in the model are then fixed to the extrapolated Debye value, and any additional distortion that we may ascribe to the emphanisis is accounted for in the Pb [100] off-centering. This is justified as a way to include in a highly constrained small-box model the non-Gaussian anharmonic behavior superposed on top of any increased harmonic displacement amplitudes of the structure. Doing the modeling in this fashion also allows us to directly compare the results to earlier work on the PbTe and PbS which were analyzed this way. The refined Pb off-centering increases from zero at low temperature to a value of about 0.12 Å at high temperature [Fig. 3(b)]. This is a large amplitude distortion, but significantly, is the smallest distortion among the PbQ series of compounds (PbS = 0.25 Å, PbTe = 0.24 Å) [12]. This implies that there is a nonmonotonicity of the emphanisis with chalcogen atomic number on going from PbS, through PbSe to PbTe, with the PbSe being the least emphanitic of the three.

To further explore the nonmonotonicity of the emphanisis across the series PbS-PbSe-PbTe we consider other measures. The anharmonicity in the motions of the Pb atoms may be seen as an anomalous nonthermal increase in the ADP of Pb at high temperature. It was noticed [12] that this temperature dependence is consistent with the ADPs following a Debye model behavior at low temperature, and following the same Debye model at high temperature, but with the Debye curve offset
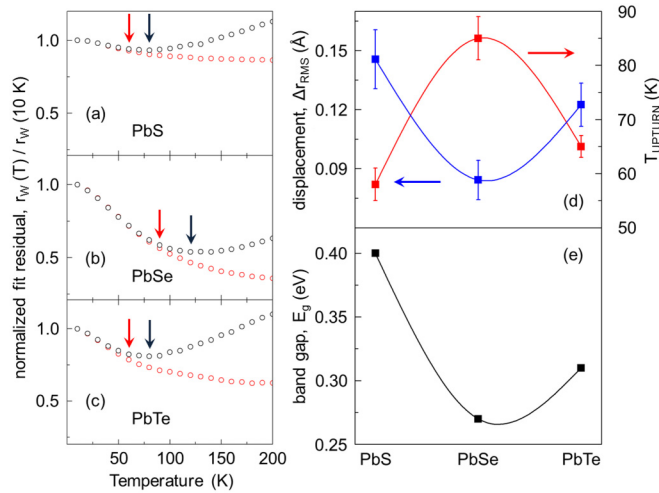
FIG. 4. (a)–(c) Normalized fit residual r_W of $Fm\bar{3}m$ model fit to xPDF data of PbS, PbSe, and PbTe (as indicated) over a range of temperatures. Open red symbols are obtained from fits carried over r range of PDF sensitive solely to average behavior (10–50 Å), excluding the short r range. Open black symbols originate from fits where short-range local structural information in PDF was included in the fitting. Vertical red arrows mark upturn temperature at which the two trends separate, and vertical black arrows mark temperature of the apparent minimum in the short-range sensitive trends. (d) Root mean square displacement in PbS, PbSe, and PbTe, estimated from the differential static offset of the Debye model as this is fit to the temperature dependence of the Pb isotropic atomic displacement parameter (left ordinate). Temperature of the apparent upturn in normalized fit residuals shown in (a)–(c) (right ordinate). See text for details. (e) Reported energy gaps of lead chalcogenides PbS, PbSe, and PbTe [7,49–52].

upwards to explain the high-T data. The offset parameter ΔU_{off} is taken as a measure of the additional "nonthermal" displacement amplitude coming from the anharmonicity. $\Delta r_{RMS} = \sqrt{\Delta U_{off}}$ from each of the three compounds is displayed in Fig. 4(d) [29]. Among the three chalcogen series, PbSe has the smallest ΔU_{off}, and therefore the smallest distortion, in agreement with the direct refinements of displacements in the PbO distorted models. Another way to quantify the strength of the emphanitic effects in each compound is by the temperature where the anharmonicity first becomes evident in the structure. One measure of this is the temperature at which fits to the PDF data of the undistorted cubic model first become inadequate as temperature increases, as measured by a goodness of fit parameter such as weighted fit residual R_w. As temperature increases from 10 K the R_w of the cubic model initially decreases. This decrease in R_w on warming is commonly observed in materials when the structural model correctly describes the structure. A good fit is obtained at all temperatures, but the R_w decreases somewhat on warming because the PDF peaks broaden and therefore become easier to fit. This R_w lowering effect normally continues to the highest temperature, as indeed is seen to be the case in our data for the $Fm\bar{3}m$ model fit over long length scale, but excluding the short-range data, shown in red in Figs. 4(a)–4(c). However, when fitting the low-r region, the R_w of the cubic model goes through a minimum and then starts to increase. This minimum

in R_w gives a characteristic temperature at which the harmonic cubic model is becoming inadequate to explain the local structure. The blue and red arrows in the figure indicate these points for each of the chalcogens, and it is clear that in PbSe the sample has to warm to a higher temperature than PbS and PbTe before significant anharmonicity is observed, suggesting that the anharmonic effects are less in that system. This crossover temperature T_{upturn} is shown in red in Fig. 4(d) vs chalcogen atomic number. The chalcogen dependence of the band gap for the series extracted from the literature [7,49–52] is shown in Fig. 4(e).

It is tempting to speculate on a possible relationship between the nonmonotonicity of the band gap and the strength of the emphanisis. To explore this we used density functional theory (DFT) to compute the dependence of the band gap on Pb [100]-displacement amplitude in the lead chalcogenides. Indeed, the calculations indicate that the computed band gap increases with increasing Pb off-centering [29]. We compared this evolution with the behavior of rock-salt structure NaCl, as well as a series of perovskite-structure materials (PbTiO$_3$, BaTiO$_3$, and LaAlO$_3$). For both structure types we observe a larger increase of the band gap in the systems possessing a lone pair. In the rock-salt materials, emphanitic displacements in PbQ have a larger effect than in NaCl and in the perovksites the band-gap effect is larger in PbTiO$_3$ than in BaTiO$_3$ (a ferroelectric without lone pair) and very small in LaAlO$_3$ which shows no tendency for a ferroelectric distortion. Thus, the stereochemical activity of the lone pair, be it static (PbTiO$_3$) or dynamic (PbQ), can be seen to correlate with the increase of the band gap.

IV. SUMMARY

We propose that this link between the emphanitic effects and the band gap could serve to explain both the poorly understood nonmonotonic chalcogen dependence of E_g in this series, but also the anomalous temperature dependence of the band gap. The emphanitic effects therefore have a significant effect on the electronic properties of the materials, as well as through increased scattering. The band gaps of all these materials increase with increasing temperature, which is the opposite of the behavior expected for semiconductors [53], but would be well explained by the increase in the emphanitic effects with increasing temperature and the positive correlation of band gap to those effects that is evident in the DFT calculations. A similar emphanitic effect associated with the $5s^2$ lone pair on Sn^{2+} in the perovskite halide CsSnBr$_3$ was reported recently and in this case too the widening of the energy gap E_g with rising temperature was linked to the increasing off-center displacement of the Sn^{2+} atom [19].

[1] Z. H. Dughaish, Physica B **322**, 205 (2002).

[2] Z. M. Gibbs, H. Kim, H. Wang, R. L. White, F. Drymiotis, M. Kaviany, and G. Jeffrey Snyder, Appl. Phys. Lett. **103**, 262109 (2013).

[3] M. Cardona and M. L. W. Thewalt, Rev. Mod. Phys. **77**, 1173 (2005).

[4] M. Baleva, T. Georgiev, and G. Lashkarev, J. Phys.: Condens. Matter **2**, 2935 (1990).

[5] R. N. Tauber, A. A. Machonis, and I. B. Cadoff, J. Appl. Phys. **37**, 4855 (1966).

[6] R. Dalven, Phys. Rev. B **3**, 3359 (1971).

[7] Y.-L. Pei and Y. Liu, J. Alloys Compd. **514**, 40 (2012).

[8] S. Nie, X. Y. Xu, G. Xu, and Z. Fang, Chinese Phys. B **25**, 037311 (2016).

[9] D. Long, *Energy Bands in Semiconductors* (Interscience, New York, 1968).

[10] Y. F. Tsay, S. S. Mitra, and J. F. Vetelino, J. Phys. Chem. Solids **34**, 2167 (1973).

[11] K. Baumann, Phys. Status Solidi B **63**, K71 (1974).

[12] E. S. Božin, C. D. Malliakas, P. Souvatzis, T. Proffen, N. A. Spaldin, M. G. Kanatzidis, and S. J. L. Billinge, Science **330**, 1660 (2010).

[13] B. Sangiorgio, E. S. Božin, C. Malliakas, M. Fechner, A. Simonov, M. G. Kanatzidis, S. J. L. Billinge, N. A. Spaldin, and T. Weber, Phys. Rev. Mater. **2**, 085402 (2018).

[14] C. Ghezzi, Phys. Status Solidi B **58**, 737 (1973).

[15] K. G. Subhadra and D. B. Sirdeshmukh, Pramana **10**, 357 (1978).

[16] A. I. Lebedev, I. A. Sluchinskaya, V. N. Demin, and I. Munro, Phys. Solid State **41**, 1275 (1999).

[17] Y. Zhang, X. Ke, P. R. C. Kent, J. Yang, and C. Chen, Phys. Rev. Lett. **107**, 175503 (2011).

[18] K. R. Knox, E. S. Bozin, C. D. Malliakas, M. G. Kanatzidis, and S. J. L. Billinge, Phys. Rev. B **89**, 014102 (2014).

[19] D. H. Fabini, G. Laurita, J. S. Bechtel, C. C. Stoumpos, H. A. Evans, A. G. Kontos, Y. S. Raptis, P. Falaras, A. V. der Ven, M. G. Kanatzidis *et al.*, J. Am. Chem. Soc. **138**, 11820 (2016).

[20] O. Delaire, J. Ma, K. Marty, A. F. May, M. A. McGuire, M.-H. Du, D. J. Singh, A. Podlesnyak, G. Ehlers, M. D. Lumsden *et al.*, Nat. Mater. **10**, 614 (2011).

[21] K. M. Ø. Jensen, E. S. Božin, C. D. Malliakas, M. B. Stone, M. D. Lumsden, M. G. Kanatzidis, S. M. Shapiro, and S. J. L. Billinge, Phys. Rev. B **86**, 085313 (2012), selected as PRB Editor's Suggestion paper.

[22] T. Keiber, F. Bridges, and B. C. Sales, Phys. Rev. Lett. **111**, 095504 (2013).

[23] T. Shiga, J. Shiomi, J. Ma, O. Delaire, T. Radzynski, A. Lusakowski, K. Esfarjani, and G. Chen, Phys. Rev. B **85**, 155203 (2012).

[24] P. F. Peterson, M. Gutmann, T. Proffen, and S. J. L. Billinge, J. Appl. Crystallogr. **33**, 1192 (2000).

[25] X. Yang, P. Juhás, C. Farrow, and S. J. L. Billinge, arXiv:1402.3163.

[26] T. Egami and S. J. L. Billinge, *Underneath the Bragg Peaks: Structural Analysis of Complex Materials*, 2nd ed. (Elsevier, Amsterdam, 2012).

[27] P. Juhás, T. Davis, C. L. Farrow, and S. J. L. Billinge, J. Appl. Crystallogr. **46**, 560 (2013).

[28] D. A. Keen and A. L. Goodwin, Nature (London) **521**, 303 (2015).

[29] See Supplemental Material at http://link.aps.org/supplemental/10.1103/PhysRevB.98.144108 for the details of the PDF method, modeling local Pb off-centering in PbSe, Debye model and determination of the U_{iso}, and details of first-principles computations.

[30] S. J. L. Billinge, J. Solid State Chem. **181**, 1695 (2008).

[31] S. J. L. Billinge and M. G. Kanatzidis, Chem. Commun. **7**, 749 (2004).

[32] C. L. Farrow and S. J. L. Billinge, Acta Crystallogr. Sect. A **65**, 232 (2009).

[33] S. J. L. Billinge, T. Dykhne, P. Juhás, E. Božin, R. Taylor, A. J. Florence, and K. Shankland, Cryst. Eng. Commun. **12**, 1366 (2010).

[34] T. Dykhne, R. Taylor, A. Florence, and S. J. L. Billinge, Pharmaceut. Res. **28**, 1041 (2011).

[35] P. Juhás, C. L. Farrow, X. Yang, K. R. Knox, and S. J. L. Billinge, Acta Crystallogr. Sect. A **71**, 562 (2015).

[36] P. Boher, P. Garnier, J. Gavarri, and A. Hewat, J. Solid State Chem. **57**, 343 (1985).

[37] P. Debye, Ann. Phys.-Berlin **344**, 789 (1912).

[38] C. L. Farrow, P. Juhás, J. Liu, D. Bryndin, E. S. Božin, J. Bloch, T. Proffen, and S. J. L. Billinge, J. Phys: Condens. Matter **19**, 335219 (2007).

[39] P. E. Blöchl, Phys. Rev. B **50**, 17953 (1994).

[40] G. Kresse and D. Joubert, Phys. Rev. B **59**, 1758 (1999).

[41] G. Kresse and J. Furthmüller, Phys. Rev. B **54**, 11169 (1996).

[42] J. P. Perdew, A. Ruzsinszky, G. I. Csonka, O. A. Vydrov, G. E. Scuseria, L. A. Constantin, X. Zhou, and K. Burke, Phys. Rev. Lett. **100**, 136406 (2008).

[43] J. P. Perdew and A. Zunger, Phys. Rev. B **23**, 5048 (1981).

[44] A. García and D. Vanderbilt, Phys. Rev. B **54**, 3817 (1996).

[45] Ph. Ghosez, First-Principles Study of the Dielectric and Dynamical Properties of Barium Titanate, Université Catholique de Louvain, Louvain-la-Neuve, 1997.

[46] A. Nakatsuka, O. Ohtaka, H. Arima, N. Nakayama, and T. Mizota, Acta Crystallogr. Sect. E **61**, i148 (2005).

[47] U. Waghmare, N. A. Spaldin, H. Kandpal, and R. Seshadri, Phys. Rev. B **67**, 125111 (2003).

[48] I. Jeong, T. Proffen, F. Mohiuddin-Jacobs, and S. J. L. Billinge, J. Phys. Chem. A **103**, 921 (1999).

[49] J. Androulakis, I. Todorov, J. He, D.-Y. Chung, V. Dravid, and M. Kanatzidis, J. Am. Chem. Soc. **133**, 10920 (2011).

[50] J. Androulakis, Y. Lee, I. Todorov, D.-Y. Chung, and M. Kanatzidis, Phys. Rev. B **83**, 195209 (2011).

[51] H. Wang, Y. Pei, A. D. LaLonde, and G. J. Snyder, Adv. Mater. **23**, 1366 (2011).

[52] S. Johnsen, J. He, J. Androulakis, V. P. Dravid, I. Todorov, D. Y. Chung, and M. G. Kanatzidis, J. Am. Chem. Soc. **133**, 3460 (2011).

[53] P. Dey, J. Paul, J. Bylsma, D. Karaiskaj, J. M. Luther, M. C. Beard, and A. H. Romero, Solid State Commun. **165**, 49 (2013).

Correlated local dipoles in PbTe

Boris Sangiorgio,[1] Emil S. Bozin,[2] Christos D. Malliakas,[3] Michael Fechner,[1] Arkadiy Simonov,[1] Mercouri G. Kanatzidis,[3] Simon J. L. Billinge,[4,2] Nicola A. Spaldin,[1] and Thomas Weber[1]

[1]*Department of Materials, ETH Zürich, Vladimir-Prelog-Weg 5, 8093 Zürich, Switzerland*
[2]*Condensed Matter Physics and Materials Science Department, Brookhaven National Laboratory, Upton, New York 11973, USA*
[3]*Department of Chemistry, Northwestern University, Evanston, Illinois 60208, USA*
[4]*Department of Applied Physics and Applied Mathematics, Columbia University, New York, New York 10027, USA*

We present a combined single-crystal x-ray diffuse scattering and *ab initio* molecular dynamics study of lead telluride, PbTe. Well-known for its thermoelectric and narrow-gap semiconducting properties, PbTe recently achieved further notoriety following the report of an unusual off-centering of the lead atoms, accompanied by a local symmetry breaking, on heating. This observation, which was named *emphanisis*, ignited considerable controversy regarding the details of the underlying local structure and the appropriate interpretation of the total scattering experiments. In this study, we identify an unusual correlated local dipole formation extending over several unit cells with an associated local reduction of the cubic symmetry in both our x-ray diffuse scattering measurements and our molecular dynamics simulations. Importantly, when averaged spatially or temporally, the most probable positions for the ions are at the centers of their coordination polyhedra. Our results therefore clarify the nature of the local symmetry breaking, and reveal the source of the earlier controversy regarding the existence or absence of off-centering. Finally, we provide an interpretation of the behavior in terms of coupled soft optical and acoustic modes which is linked also to the high thermoelectric performance of PbTe.

I. INTRODUCTION

Lead telluride (PbTe) is a narrow-gap semiconductor widely used in electronic and thermoelectric devices. Although its transverse optical (TO) phonon is soft, indicative of proximity to a ferroelectric phase transition [1], measurements of its bulk structure show that it retains its high-symmetry paraelectric $Fm\bar{3}m$ rocksalt structure at all temperatures. In contrast to its apparently simple average structural behavior, a recent analysis of the *local structure*, based on pair distribution function (PDF) analysis of neutron powder diffraction data, suggested the emergence of considerable local non-Gaussian distortions; the PDF peaks of the local structure broadened strongly with increasing temperature, accompanied by an asymmetry and the development of non-Gaussian line shapes with shoulders. The PDF could be explained with a model that included off-centering of lead atoms with respect to their high-symmetry positions, in the manner of fluctuating local dipoles, caused by Pb-Te dimerization, on heating to temperatures higher than 100 K. The phenomenon was called emphanisis [2,3].

The striking observation of an apparent local symmetry lowering *on warming*, in contrast to a conventional global symmetry-lowering phase transition that occurs *on cooling*, led to intense interest and many subsequent theoretical and experimental studies seeking to explain the behavior. A detailed understanding of the effect is still lacking, however, and indeed the existence of off-centering has even been questioned in some works. Significant anharmonicity was found in inelastic neutron scattering measurements [3,4], consistent with the non-Gaussian PDF peaks, and the appearance of an additional phonon branch above 100 K in Ref. [3] was interpreted in terms of a dynamic local symmetry breaking

on warming. However, while all experiments indicate large amplitude dynamic and anharmonic excursions of the Pb ions away from their central positions, there remains controversy regarding whether the probability distribution of the Pb ions is peaked at the high-symmetry positions or displaced away from it on average. An analysis of synchrotron powder x-ray diffraction data using the maximum entropy method [5] was consistent with large Pb atomic probability density away from the average position in all the lead chalcogenides, with refined magnitudes of the Pb displacement in PbTe (0.3 Å at 300 K) comparable to but exceeding that found in the original report [2]. Subsequent extended x-ray absorption fine structure (EXAFS) measurements [6] reported that the Pb atomic probability distribution was peaked on average at the high-symmetry position, albeit with large amplitude atomic displacement parameters (ADPs), and stated explicitly that the large displacements seen in diffraction measurements are inconsistent with the EXAFS data. A high-resolution neutron powder diffraction study found large increases in Pb ADPs on warming but did not reproduce the anomalies in their temperature dependence, attributing the earlier reports to errors in temperature calibration [7]. Finally, a recent powder x-ray diffraction study that included the effects of Pb vacancies and microstrain in the Rietveld and maximum entropy method modeling [8] was consistent with a local symmetry breaking from cubic static off-centering of 0.2 Å or less at 100 K. In addition, high concentrations of lead vacancies were found, pointing to sample dependence as a possible source of the inconsistencies between different measurements.

On the theory side, DFT calculations in the original report [2] (using the local density approximation (LDA) and the

self consistent *ab initio* lattice dynamical (SCAILD) method [9]) indicated a softer potential for local Pb displacements with increasing temperatures, counter to the usual hardening with increasing temperature of the free energy for a *long-range* ferroelectric transition. The first *ab initio* molecular dynamics (MD) study [10] (using the generalized gradient PW91 functional in a 216-atom supercell within the VASP code) confirmed the soft and strongly anharmonic TO phonon but did not identify local dipole formation and concluded that the experimental results of Božin *et al.* [2] could be attributed to abnormally large-amplitude thermal vibrations. The calculated PDFs missed key physics, however, since while they showed broad peaks and some asymmetric character in the nearest neighbor Pb-Te peak, they did not reproduce the highly non-Gaussian lineshapes and anomalous shifts in peak centroid with temperature seen in the data [2]. A subsequent *ab initio* MD study [11] (again using the VASP package but this time with 64-atom supercells) claimed to successfully reproduce the measured lattice dynamics peak broadening with rising temperature and non-Gaussian asymmetry and reported a larger lead off-centering than in the original experimental study. However, a comparison with the experimental data was not shown and the choice of exchange-correlation functional was not stated, making it difficult to compare with the study of Ref. [10]. More recently, a novel slave-mode expansion method was used to calculate the finite-temperature dynamics of an 8000-atom supercell [12]. This study reproduced the observed splitting of the phonon peak on warming [3], and used the language of competing third- and fourth-order anharmonicities—which tend to result in off-centerings—rather than a local symmetry lowering to interpret the result. Classical MD simulations of 512-atom supercells based on *ab initio* interatomic force constants (IFCs) [13] also reproduced the phonon splitting and identified unusually large cubic IFCs along the ⟨100⟩ direction as the source. In contrast, later studies [14,15] combining *ab initio* MD simulations (using 512 atom supercells and the PBE functional in the VASP code) with single-crystal and powder neutron diffraction and inelastic neutron scattering suggested that a sharp resonance in the phonon self-energy caused by nesting of phonon dispersions could combine with the anharmonicity to produce the large phonon splitting. Once again, however, while the simulated nearest-neighbor Pb-Te PDF peak showed increasing asymmetric character with temperature, the highly non-Gaussian line shapes and anomalous shifts in peak centroid were not captured.

Finally, we note that similar behaviors and the associated controversies have also been reported in other materials. In related group-IV chalcogenides, Ref. [2] (supporting online material) already reported emergent local dipoles on warming in PbS, with the formation of shoulders on both sides of the PDF nearest-neighbor peak, an interpretation supported in Ref. [5]. More intriguingly, similar behavior has been reported in SnTe above its ferroelectric phase transition at low temperature [16], although again the temperature dependence has been disputed [7]. The emergence of local displacements on warming is not exclusive to the group-IV chalcogenides. In KNi_2Si_2, the average crystallographic structure is the same at all temperatures, but analysis of the local structure has been interpreted as an emergence on warming of local Ni displacements accompanied by differences in the electron density at the Ni sites, suggesting a fluctuating charge density wave [17]. In $CsSnBr_3$, a dynamic off-centering of Sn^{2+} on warming has been reported, while again the average perovskite structure is not affected [18]. Interestingly, in the latter case, the PDF peaks showed similar asymmetries as in the earlier PbTe studies, but no clear shoulders. Finally, in $La_{1-x}Ca_xMnO_3$, local Jahn-Teller distortions have been reported in the high-temperature insulating phase that are not present in the low-temperature metallic phase, even though the average crystal structure is the same [19,20].

In summary, some aspects of the originally reported emphanitic behavior of PbTe [2,3] are reproduced by all studies, notably the asymmetry of the PDF peaks and the splitting of the TO phonon. Other features, particularly the shoulders in the PDF peaks, remain elusive in the theoretical studies, thwarting a consistent interpretation of the behavior. In particular, two seemingly contradictory interpretations need to be reconciled in order to fully understand the underlying physics: the picture of local off-centering, which is based largely on diffraction data, compared with the picture of strong anharmonicity, which is based primarily on measurements of the dynamics.

Here, we present the first single-crystal x-ray diffuse scattering study of the temperature dependence of the local structure of PbTe, which we interpret with the aid of new *ab initio* molecular dynamics simulations. We start by discussing the average structure and find, as expected, that the rock-salt structure is retained at all studied temperatures, with displacive disorder associated with positional fluctuations. Next, we study the local structure with an analysis of the diffuse scattering. We obtain a peculiar decay of the atomic pair correlations: we identify spontaneous displacements of Pb ions relative to their Te neighbors, resulting in correlated local dipoles that propagate for several unit cells. This is consistent with the earlier description of emphanitic behavior. We find, however, that in spite of these correlated displacements, the most probable position for each individual Pb ion is on average at the center of its coordinating Te polyhedron. However, our new finding that the local dipoles are correlated between unit cells resolves the apparent controversy by providing a picture that is consistent with both previously conflicting pictures: if at one instant in time, a Pb ion is displaced from the center of its coordination octahedron, say along [100], the Pb ion in the neighboring unit cell in that direction is also displaced along [100], and so on, over a correlation length of a few unit cells. The emergence of such fluctuating but correlated local dipoles on warming may then be considered as the definition of emphanisis. The correlations between the dipoles fall off in distance and in time and are evident in diffraction experiments only in the diffuse scattering signal, and propagate to the PDF in a total scattering experiment, and the 3D-ΔPDF measurements described here. From our calculations, we identify a possible origin for the asymmetry of the PDF peaks as an alternation of short and long bonds, and establish a link between the correlated dipoles and the high thermoelectric performance of PbTe.

II. AVERAGE STRUCTURE AND LATTICE DYNAMICS

We begin with an experimental and theoretical determination of the average atomic displacements as a function of

temperature, focusing in particular on whether the atomic displacements are best approximated as single minimum harmonic or anharmonic oscillators or if the atoms occupy multiminimum split positions. The experimental and computational details can be found in the Appendix. The refinement of the average crystal structure was done with the program SHELXL [21] based on single-crystal Bragg scattering. Atomic displacements were modeled in two approaches. First, Pb and Te were located at the highest-symmetry Wyckoff positions 4a (0,0,0) and 4b (0.5, 0.5, 0.5), and any static or dynamic displacements away from the high-symmetry positions had to be captured by the harmonic atomic displacement parameters (ADPs) U_{iso}^{Pb} and U_{iso}^{Te}. Second, the atomic displacements were described as a convolution of discrete split vectors, which shift the atoms away from the high-symmetry to lower-symmetry Wyckoff positions, and harmonic displacement functions. We tested such a split-position model only for Pb because its average displacements are larger than those of Te and refined models with split vectors $\langle x00 \rangle$, $\langle xx0 \rangle$, and $\langle xxx \rangle$. Vectors enclosed by angle brackets $\langle \ldots \rangle$ include all symmetry equivalent directions, i.e., the $\langle x00 \rangle$ split model includes six Gaussians, which are shifted by the same amount along positive and negative lattice vectors, while the $\langle xx0 \rangle$ and $\langle xxx \rangle$ models cover twelve and eight Gaussians shifted along the face and space diagonals, respectively. To avoid numerical correlations, U_{iso}^{Pb} and U_{iso}^{Te} were constrained to the same values in each of the split model refinements. Consequently, each of our displacement models comprised two free structural parameters: U_{iso}^{Pb} and U_{iso}^{Te} in the harmonic model and a common $U_{iso}^{Pb/Te}$ plus a Pb split vector variable x in the split models. The results of the refinements are summarized in Table I.

The refinements did not provide a unique answer for the best average displacement model, however, surprisingly, the $\langle x00 \rangle$ split model, as was proposed by Božin *et al.* [2] and Kastbjerg *et al.* [5], gave the highest R values in all cases. All other models have very similar reliability factors, but at high temperatures, the $\langle xx0 \rangle$ and $\langle xxx \rangle$ split models seem to be slightly better than the harmonic model.

Figure 1 shows the probability density functions obtained within the various displacement models. The $\langle x00 \rangle$ split model represents the most anisotropic distribution function because it has the smallest number of split positions and needs to refine the largest Pb displacement per position to explain the displacements not described by $U_{iso}^{Pb/Te}$, while the $\langle xx0 \rangle$ and $\langle xxx \rangle$ split models appear more isotropic. It is important to note that even in the cases of the split models the convolution of the ADPs with the split vectors results in a probability distribution function that is similar to a Gaussian. The major difference is that the tip of the distribution is slightly flattened and it is anisotropic, which suggests that Pb is located in a pseudoharmonic, but slightly flattened potential where the highest probability of finding a Pb atom is still at the high-symmetry Wyckoff position. In particular, we cannot identify any distinct side maxima in the probability density function that would indicate existence of a split position of Pb. We rather understand the refined split vectors as a tool to parametrize anharmonicity when being restricted to a harmonic fit model. Our *ab-initio* molecular dynamics simulations (for details see Appendix) support this interpretation, though the resulting probability distribution [Fig. 1(g)] is more isotropic than

TABLE I. Overview of the results of the average structure refinements and of the MD simulations. Displacement parameters U are given in Å^2 units and the split parameter x is given in fractional coordinates. The identical values of $U^{Pb/Te}$ for the split models $\langle xx0 \rangle$ and $\langle xxx \rangle$ are not a misprint but found as such in the refinements. The lattice constants reported are from the in-house measurements. The lattice constants observed in the synchrotron measurements are comparable. The displacement parameters from the MD simulations are comparable. The displacement parameters of the atoms from the high-symmetric Wyckoff positions.

T (K)	a (Å)	Harmonic displacements				Pb $\langle x00 \rangle$ split model				Pb $\langle xx0 \rangle$ split model				Pb $\langle xxx \rangle$ split model				MD		
		U_{iso}^{Pb}	U_{iso}^{Te}	R1	wR2	$U_{iso}^{Pb/Te}$	x(Pb)	R1	wR2	$U_{iso}^{Pb/Te}$	x(Pb)	R1	wR2	$U_{iso}^{Pb/Te}$	x(Pb)	R1	wR2	a [Å]	U_{iso}^{Pb}	U_{iso}^{Te}
293	6.4626(1)	0.0260(2)	0.0157(1)	1.56	3.50	0.0153(2)	0.0257(3)	1.99	4.62	0.0150(1)	0.0185(1)	1.59	3.31	0.0150(2)	0.0151(1)	1.63	3.25	6.538	0.0182	0.0144
250	6.4546(1)	0.0220(2)	0.0130(1)	1.53	3.49	0.0127(2)	0.0244(3)	1.75	4.13	0.0124(1)	0.0175(1)	1.46	3.06	0.0124(1)	0.0143(1)	1.51	3.00	6.532	0.0152	0.0120
200	6.4494(1)	0.0182(2)	0.0106(1)	1.62	3.91	0.0104(2)	0.0226(2)	1.73	4.18	0.0102(1)	0.0162(2)	1.49	3.46	0.0102(1)	0.0132(1)	1.48	3.54	6.527	0.0123	0.0097
150	6.4420(1)	0.0135(2)	0.0077(1)	1.64	3.93	0.0076(2)	0.0199(2)	1.72	4.28	0.0075(1)	0.0141(1)	1.65	3.96	0.0075(1)	0.0115(1)	1.68	4.05	6.521	0.0089	0.0070
125	6.4397(1)	0.0115(2)	0.0065(1)	1.62	3.75	0.0064(2)	0.0185(2)	1.75	4.19	0.0063(1)	0.0131(1)	1.63	3.80	0.0063(1)	0.0107(1)	1.61	3.79	-	-	-
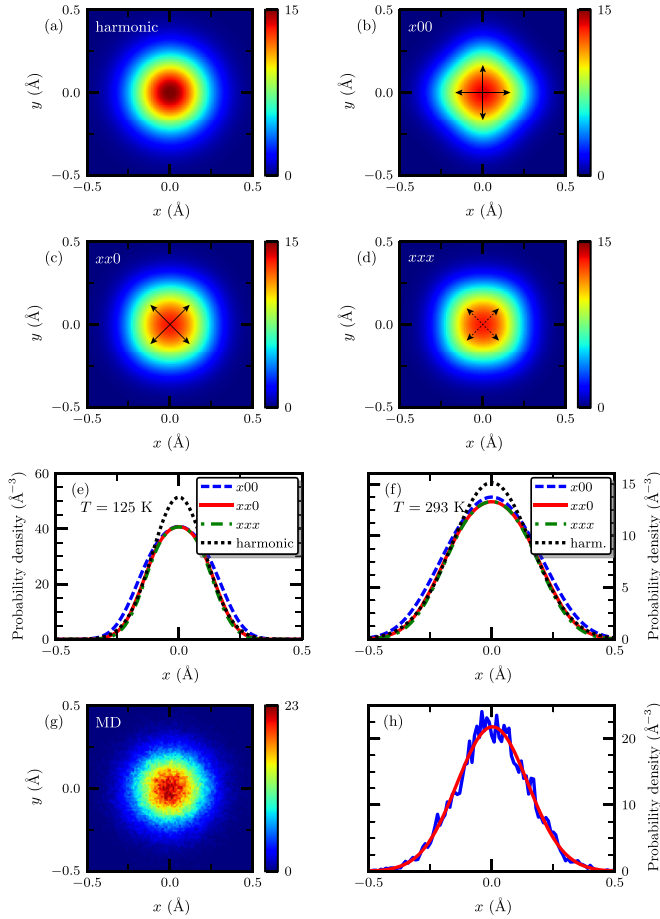
FIG. 1. Probability density functions of Pb. (a)–(d) show two-dimensional sections through the probability density functions at room temperature for the different split models indicated with the color scale representing the probability density in Å^{-3}. The arrows shown in (b) and (c) indicate the refined split vectors in the $xy0$ layer, while the dotted arrows in (d) show the projection of the out-of-plane $\langle xxx \rangle$ split vectors. The probability density functions were calculated as the summation of Gaussians located at the end points of all symmetry equivalent split vectors, i.e., six Gaussians for the $\langle x00 \rangle$ model, twelve for $\langle xx0 \rangle$, and eight for $\langle xxx \rangle$. The variances of the Gaussians were taken from the corresponding ADPs reported in Table I. (e) and (f) show scans through the center along the a axis at 125 K and at room temperature; (g) and (h) show the $2d$ section and scan through the center along the a axis for our MD simulations both at 300 K, where the red line in (h) represents a Gaussian fit.

that of any of the displaced models. Our calculated average displacements (Fig. 23 in the Appendix) are negligibly small for both Pb and Te atoms (consistent with the earlier molecular dynamics simulations discussed above) and the probability density for the lead atoms [panel (g)] indicates that they are centered on the rock-salt high-symmetry positions. However, we do not have enough statistics to definitely assess whether the tip of the distribution is flattened [panel (h)].

Figure 2 shows the temperature evolution of the ADPs compared with the temperature-corrected data by Knight [7] of the original data of Ref. [2]. Our refined ADPs show a linear dependence on temperature over the full examined
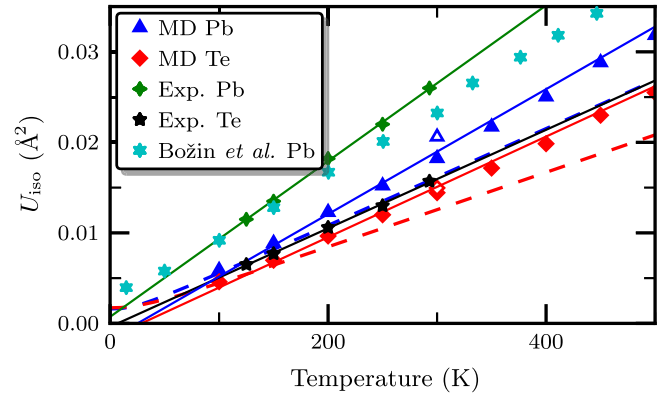
FIG. 2. Atomic displacement parameters U_{iso} obtained from our single-crystal x-ray diffraction experiments (green crosses for Pb and black stars for Te) with the harmonic model and MD calculations (blue triangles for Pb and red diamonds for Te). Turquoise stars are the temperature-corrected ADPs by Knight [7] of the original neutron diffraction based data by Božin *et al.* [2]. Green and black (blue and red) continuous lines are a linear fit to the experimental (MD) data and show the extrapolation to 0 K. Blue and red dashed lines are ADPs computed in the harmonic approximation using the $T = 0$ K phonons computed with DFT.

temperature range, however, with a larger slope than the data of Ref. [2], which were collected with powder samples. Moreover, they nicely linearly extrapolate to close to zero at 0 K indicating a dynamic origin of the atomic displacements. We also extracted the ADPs from the MD simulations as the mean squared displacements from the average positions. They exhibit the same linear dependency and are consistently larger than those expected from a harmonic model using the $T = 0$ K DFT phonons (computed using the PHONOPY package [22]) pointing to anharmonic effects. While our calculated Te ADPs compare well with experiments, the Pb ADPs are severely underestimated in our MD simulations, due to their extreme sensitivity to the soft mode phonon frequencies and correspondingly to our supercell size (the open triangle at 300 K shows the result for a larger supercell) and neglect of spin-orbit coupling.

In summary, we find good agreement in the temperature evolution of the average structure between our single-crystal Bragg measurements and *ab initio* MD simulations, as well as with the earlier literature reports; as expected, the average structure is rocksalt. In particular, our calculated and measured ADPs are consistently larger than those calculated within a harmonic model. Our fits are unable to uniquely distinguish between harmonic and anharmonic models, giving similar quality refinements in both cases. Therefore, while our average structure analysis certainly points to anharmonic behavior, it does not shed light on the details of atomic displacements in the local scale, which will be discussed in the following.

III. LOCAL STRUCTURE

We now analyze our diffuse scattering measurements and *ab initio* MD simulations to determine the local structure.
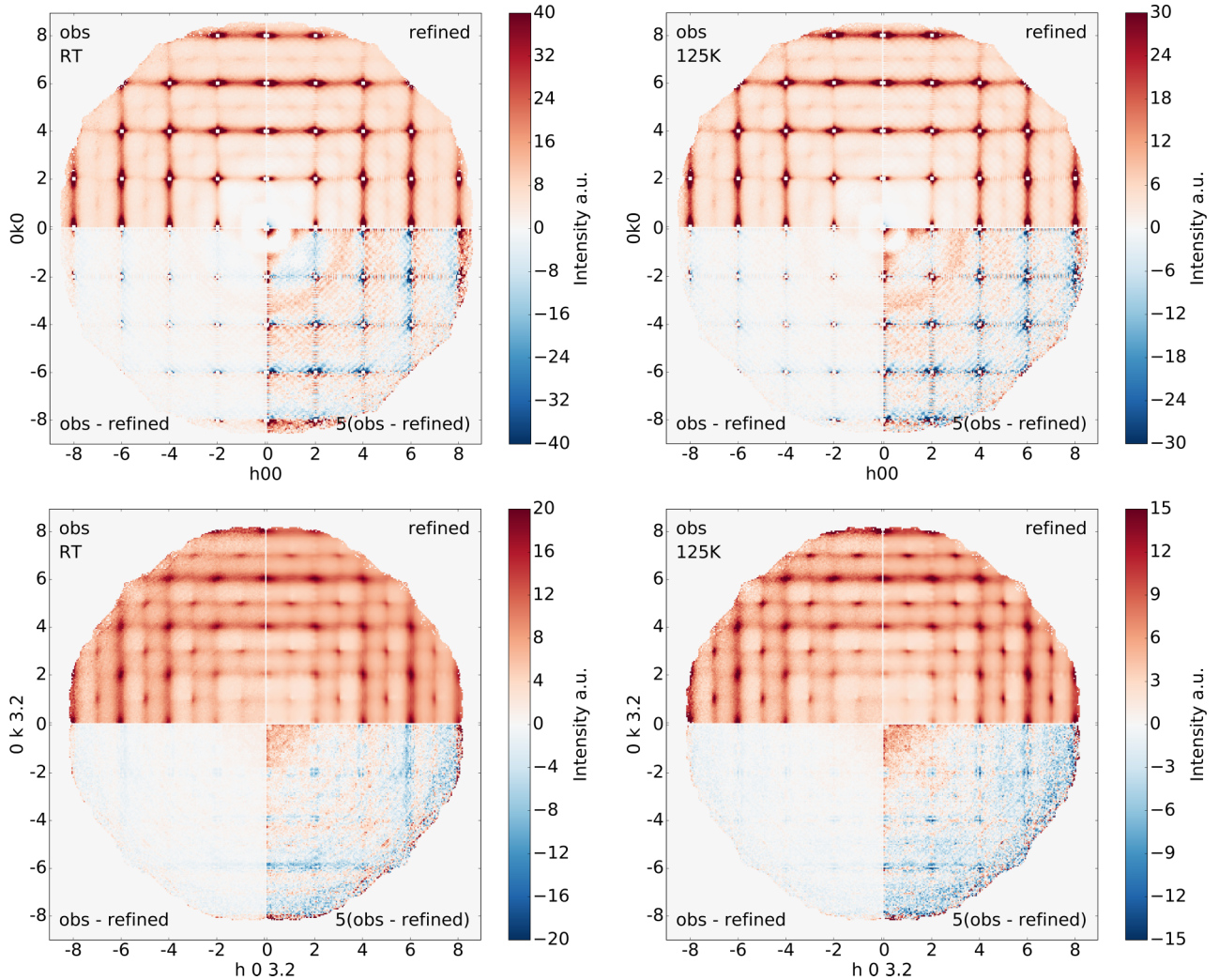
FIG. 3. Reciprocal space reconstructions of the diffuse scattering at room temperature (left) and 125 K (right). For an economic representation only the sections $hk0$ (top) and $hk3.2$ (bottom) are selected from the full data set having $360 \times 360 \times 360$ voxels. Observed intensities (obs, upper left of each panel), results from the YELL refinement (*refined*, upper right) and difference (lower) intensities of the diffuse scattering are compared. The patterns at 150, 200, and 250 K, which are not shown here, are similar (see Fig. 22) for further temperatures). The truncation ripples in the refined $hk0$ sections are due to incomplete coverage of the 3D-ΔPDF maxima. The color wedges were linearly scaled by trial and error to allow a better qualitative comparison of the diffuse scattering patterns at different temperatures; the absolute diffuse intensities decrease with decreasing temperature as expected from the evolution of the ADPs. The white squares in the $hk0$ layers at $h, k = even$ are the cutout Bragg reflection regions. Note that all quadrants include $h00$ and $0k0$ pixels or $h03.2$ and $0k3.2$ pixels, respectively, such that the pixels oriented up/down or left/right to the white lines separating the four sections in each panel have the same coordinates.

A. Observations and qualitative interpretation of diffuse scattering and 3D-ΔPDF patterns

The diffuse scattering pattern is dominated by a system of alternating weak and strong diffuse planes perpendicular to the cubic main axes. The planes are narrow but not sharp (Fig. 3). The diffuse intensities are strongest beneath the Bragg reflections that are not extinct by the Bravais lattice. The overall intensities of the planes tend to increase with increasing diffraction vector, which is a characteristic pattern of thermal diffuse scattering. The weak diffuse intensities seen in the upper row in Fig. 3 can be understood as diffuse scattering from optical phonons, which scatter close to the Brillouin zone boundary. This is an interesting observation, because the typically small optical phonon amplitudes rarely allow measurements of corresponding diffuse scattering. In addition, some

structured band and squarelike diffuse scattering is visible in higher layers (for an example see the lower row in Fig. 3). It is interesting that the diffuse diffraction patterns show almost no variation within the investigated temperature range, apart from a decrease in the total diffuse intensity with decreasing temperatures (see also Fig. 22). Therefore it can be assumed that the qualitative local-order model is valid over the complete examined temperature range, $125 \leqslant T \leqslant 298$ K, with the amplitude of the displacements decreasing with decreasing temperature in this temperature range. (We note that while studies at higher temperature, which were not possible using our experimental setup, would be desirable, the relevant emphanitic effects should already be observable in PbTe at room temperature.)

Next, we focus on the interpretation of the 3D-ΔPDF maps, obtained as the Fourier transform of the diffuse diffraction

pattern, with the Bragg reflections cut out from the diffraction pattern (see Appendix for details). The 3D-ΔPDF indicates where and how pair correlations of the real structure *differ* from the average structure model as obtained from the Bragg reflections alone. Positive values mean that finding an atom at the end of the corresponding interatomic vector is more likely than in the space and time averaged structure, while the probability is lower if the 3D-ΔPDF density is negative. For example, in the case that two atoms tend to move in-phase (*positive correlation*), the corresponding 3D-PDF peak is narrower than in the Bragg scattering based 3D-PDF map. Thus the 3D-ΔPDF peak shows positive values in the center and negative in the next neighborhood (looking like a Mexican hat pattern in the cross-section). If atoms move in antiphase (*negative correlation*) the behavior is inverse (upside-down Mexican hat). At large distances 3D-ΔPDF densities approach zero, because pair correlations of the real and the average structure become very similar due to the spatial loss of displacement correlations [23]. Figure 4 shows the $xy0$ section of the 3D-ΔPDF map at different temperatures. The 3D-ΔPDF signals are found close to integer and half-integer lattice coordinates, corresponding to the average interatomic vectors of the rocksalt structure. Signals at $x + y + z = integer$ correspond to Pb/Pb and Te/Te interatomic vectors, which overlap perfectly, while those found at $x + y + z = half-integer$ represent Pb/Te vectors. The PDF signals at overlapping homoatomic pairs are strongly dominated by local order properties of Pb/Pb pairs, because Pb has both a stronger scattering power and larger ADPs, and therefore contributes more to the diffuse scattering and 3D-ΔPDF maps. The homo- and hetero- interatomic vectors contribute similarly to the 3D-ΔPDF, with the correlations strongest along ⟨100⟩ directions and (see next section) weakest along ⟨111⟩, although some minor differences can be observed after careful inspection. In general, the 3D-ΔPDF shows positive signals at average interatomic distances and negative signals along its radial neighborhood, which, as discussed above, is a typical signature for positive displacement correlations, i.e., it is consistent with a 3D-ΔPDF pattern dominated by acoustic phonons.

B. Pair correlations

In this section, we compare and analyze the pair correlations between atomic displacements as obtained from the 3D-ΔPDF refinements and from the *ab initio* MD simulations. The experimental displacive pair correlations were described in the harmonic approximation and refined with the program YELL [24]. For each symmetry independent average interatomic vector up to about 60 Å, we have refined the corresponding 3D covariance coefficients to minimize the difference between the experimental diffuse scattering and the one calculated from the covariances. In the following, we report ADP normalized correlation coefficients instead of covariances in order to make joint displacements more readily comparable. A detailed description of the correlation coefficients, the 3D-ΔPDF model, and the refinement strategy are found in the Appendix. The PDF and reciprocal space results of the YELL refinements are shown in Figs. 3 and 4. The most significant pair correlations resulting from the YELL refinement are depicted in Fig. 5, and compared to the results extracted from our MD simulations. In
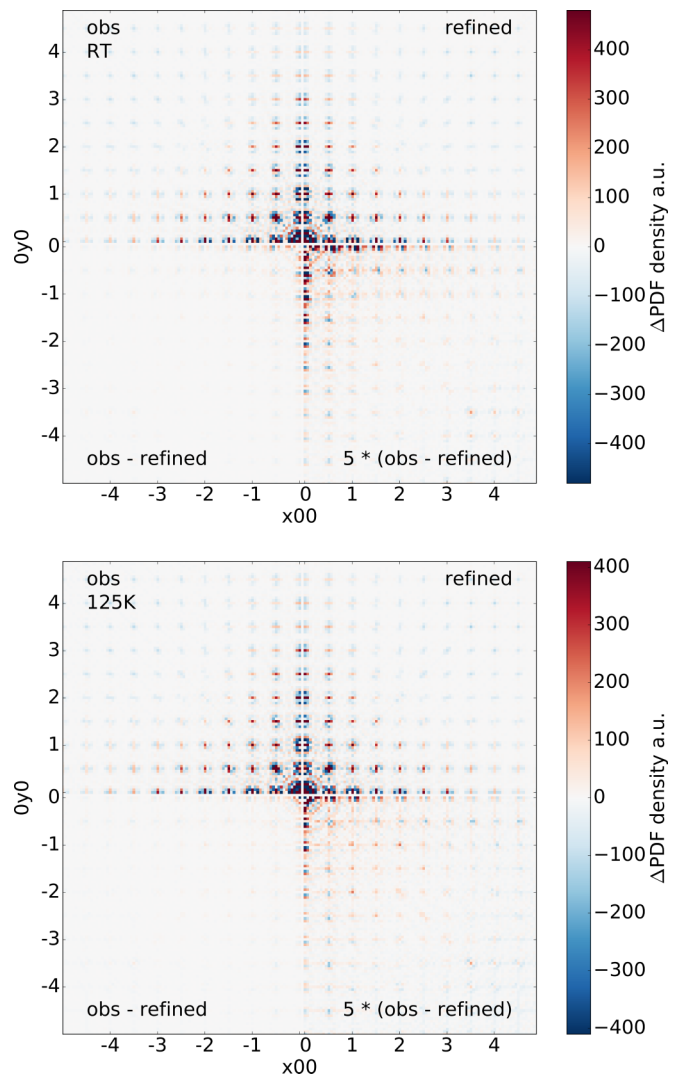
FIG. 4. 3D-ΔPDF $xy0$ layer at room temperature (top) and 125 K (bottom). Observed densities (obs), results from the YELL refinement (refined) and difference 3D-ΔPDF densities are compared. The patterns at 150, 200, and 250 K, which are not shown here, are comparable. The color wedges were linearly scaled by trial and error to allow a better qualitative comparison of the 3D-ΔPDF densities at different temperatures. Note that absolute 3D-ΔPDF densities decrease with decreasing temperature. Strongest disagreements between observed and refined densities are at ⟨x00⟩ coordinates. The origin may be anharmonic pair correlations that are not covered by our harmonic 3D-ΔPDF model, but the resolution is not good enough to allow a clear conclusion. The negative densities at large PDF distances come from artifacts due to masking diffuse scattering next to Bragg reflections. Note also that all quadrants include x00 and 0y0 pixels, such that the pixels oriented up/down or left/right to the white lines separating the four sections in each panel have the same coordinates.

agreement with the qualitative interpretation, it is seen that the correlations are very strong for pairs separated by ⟨x00⟩ vectors with strong longitudinal correlations. Most importantly, pair correlations extracted from our MD match almost perfectly (see Fig. 6).

In general, the correlations decay quickly (Fig. 6), but with the formation of "steps"—indicating that pairs of
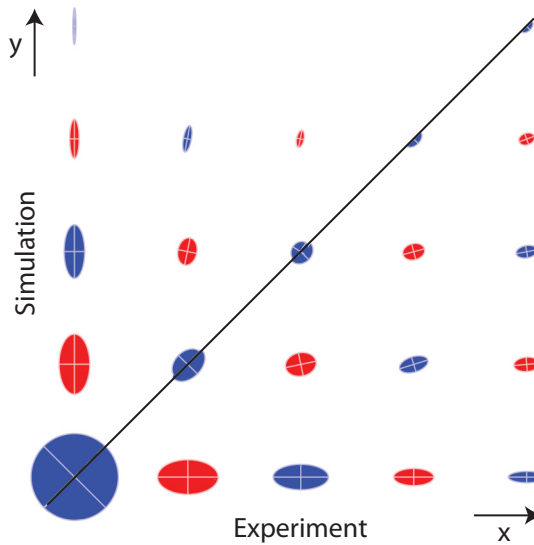
FIG. 5. Graphical representation of the displacive pair correlations as obtained from the 3D-ΔPDF refinement and from the MD simulations at RT and 300 K, respectively. The plot shows pair correlations in the $xy0$ layer. Blue ellipsoids represent correlations between homoatomic pairs, while the red ellipsoids show correlations between Pb and Te. The relative sizes and orientations of the ellipsoids indicate the strength and direction of correlations, with the large blue circle in the bottom-left corner representing the correlation of an atom to itself, which by definition is unity. The strongest correlations are found along the main crystallographic axes and along inter-atomic bonding directions. The diagonal line separates experimental and simulation results and coincides with a crystallographic mirror plane. All of the shown pairs are positively correlated along all directions. Missing ellipsoids in the simulated data have at least one, in all cases very weak, negative component indicating presence of some small negative correlations. Table II in the Appendix presents an extended overview of the numerical values of the pair correlations.

neighboring atoms have strongly correlated motions. Furthermore, correlations of the homoatomic pairs are generally

stronger than those of the heteroatomic pairs. In agreement with our qualitative interpretation, it is clear that the correlations are mostly independent of temperature over the temperature range studied. The amplitudes of the displacements change, however, in accordance with the changes in the ADPs.

We now discuss a microscopic mechanism that is consistent with these pair correlations (see Fig. 7). As presented above, the 3D-ΔPDF shows signatures of displacement correlations that are typical for acoustic phonons. These would generate positive pair correlations decaying with distance because of the short-range nature (green triangles in the figure). Optical phononlike displacements, on the other hand, have pair correlations that alternate in sign (light blue diamonds). A superposition of both kinds of displacements, taking into account that in the real system the acoustic phonons dominate, gives rise to steps, with correlations of the homoatomic pairs stronger than those of the heteroatomic pairs. This displacement pattern suggests a Pb-Te dimerization along the ⟨100⟩ direction, which results in a local polarity. This model also explains why Te has smaller ADPs than Pb: large amplitude acoustic phonon displacements are partly compensated by the optical phonon contributions (see lower inset in Fig. 7).

The presence of optical phononlike displacements, which are usually not detected in diffuse scattering, implies not only that the optical phonons are active but also that their amplitude is big enough to be seen. We propose that this is possible in PbTe, because of the soft TO mode. To test this hypothesis, we performed the same analysis using a literature Buckingham effective potential, with parameters fit to *ab initio* calculations for PbTe [25,26]. This potential was shown to reproduce reasonably the mechanical and phonon properties of bulk PbTe, except that the optical phonons calculated with the Buckingham potential are much harder than those in DFT. In particular, the TO mode at Γ is in the order of 3 THz instead of about 1 THz in DFT. Moreover, the optical and acoustic phonons are clearly separated in energy [Fig. 8(a)], so that a coupling between them is unlikely. We performed classical molecular dynamics with this potential as
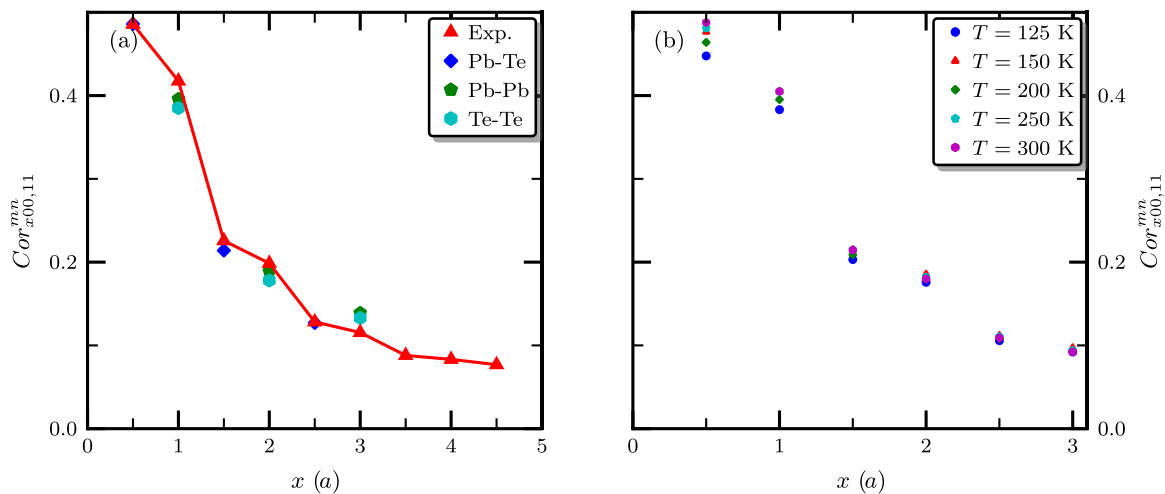
FIG. 6. Longitudinal correlation coefficients along the cubic axis: (a) comparison at 300 K between diffuse-scattering extracted quantities (red triangles), and MD values [with the $6 \times 6 \times 6$ supercell]. The plateau and even small increase in the MD correlations for distances $2.5a$ and $3a$ is a consequence of periodic boundary conditions. (b) Temperature evolution of the experimental correlation coefficients. Whether the small temperature dependent spreads at a given distance are significant or if they are artefacts from incomplete models is not fully understood.
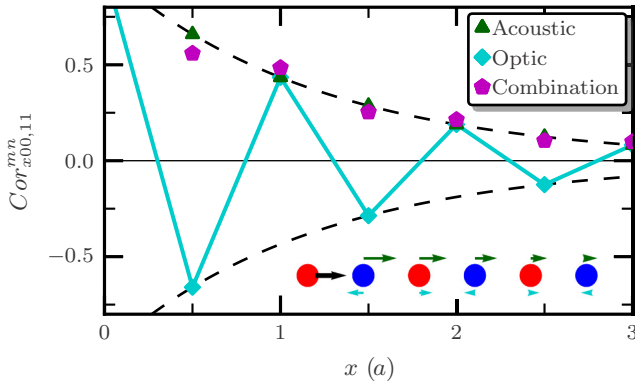
FIG. 7. Cartoon of pair correlations expected for different "phonon modes" along the $\langle 100 \rangle$ direction; in green for acousticlike displacements, in light-blue for opticlike, and in purple for a superposition of the two. The effects are exaggerated to visualize the formation of steps.

FIG. 9. Power spectrum $Z(\mathbf{q}, \nu)$ at 300 K computed from the $6 \times 6 \times 6$ supercell using *ab initio* MD. The left panel shows $Z(\mathbf{q}, \nu)$ at the Γ point (arbitrary units are used). The right panel shows the dispersion relation along the Δ line. White lines correspond to $T = 0$ K DFT calculations.

implemented in LAMMPS [27] using a $10 \times 10 \times 10$ supercell (we checked the results also with the $6 \times 6 \times 6$ supercell to make sure that the results in this supercell are not affected by finite-size effects) and, when possible, the same settings as we used in our *ab initio* MD calculations. As expected, the pair correlations are found to decay smoothly without the formation of any steps [Fig. 8(b)]. Interestingly, inelastic neutron scattering experiments by Delaire *et al.* [4] reported a strong coupling between the ferroelectric TO mode and the longitudinal acoustic (LA) modes. One of its signatures—the avoided crossing between TO and LA—is also captured by our MD simulations. Figure 9 presents the power spectrum $Z(\mathbf{q}, \nu)$ at 300 K computed as described in Ref. [12], which can be directly compared to the inelastic neutron scattering intensities. The right panel shows the dispersion relation along the Δ direction; although the $T = 0$ K DFT bands (white lines) have an LA-TO crossing, the MD results show a repulsion between LA and TO leading only to a contact between the two bands roughly midway along the Γ to X line. The left panel

presents the power spectrum at the Γ point. The peak is very broad and a splitting starts developing. Since these features are already highly enhanced with respect to a $3 \times 3 \times 3$ supercell, we expect that an even larger supercell would allow a good description of the emergence of the additional phonon mode, as in previous experiments and (classical) MD simulations [3,12–14].

Finally for this section, we show the effect of the displacement pattern linked with the pair correlations on the electronic structure, by plotting in Fig. 10 the calculated electron localization function (ELF) for a static configuration consistent with the inset at the lower right of Fig. 7. The ELF provides a measure of the valence charge density, weighted to emphasize regions of higher electron localization, and has been used effectively to analyze the electronic structure in the related ferroelectric IV-VI chalcogenides [28], where their stereochemical activity drives the dipole formation in the ferroelectric state. The central Pb atom is the most strongly displaced from its high-symmetry position (indicated by the black dashed line) with the distortion amplitudes gradually

FIG. 8. Properties derived from the Buckingham potential of Refs. [25,26]. (a) Phonon density of states (DOS) (computed using the PHONOPY package [22]); in blue with the Buckingham potential, in dashed red with CP2K. (b) Longitudinal correlation coefficients along the cubic axis at 300 K (with the $10 \times 10 \times 10$ supercell) computed using the Buckingham potential.
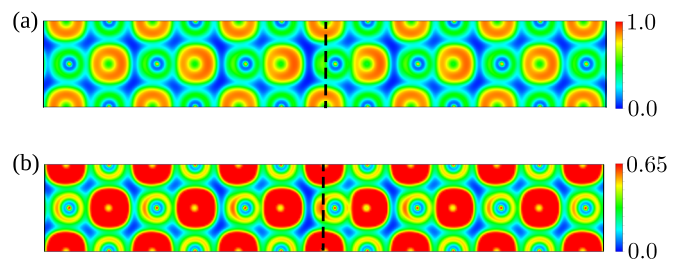
FIG. 10. Electron localization function (ELF) computed with the VASP [29] code for a structure distorted according to the pattern of pair correlations shown in Fig. 6 with the central Pb ion in the $15 \times 1 \times 1$ supercell given the largest distortion from its high-symmetry position (vertical dashed line). The displacements towards the right of the figure are exaggerated to amplify the effects. Different magnitude ranges are chosen for the upper and lower panels to illustrate the increased Pb-Te bonding as the Pb moves right towards its neighboring Te (a) and the formation of the lone pair (small red lobe) left of the Pb ions (b).

reducing with distance from the center. In the top panel (a), the scale is chosen to illustrate the enhancement of the Pb-Te chemical bond as the Pb ions displace to the right towards their Te neighbors (at the centers of the orange regions). In the lower panel (b), the scale is chosen to emphasize the red "banana-shaped" localized electrons to the left of the displacing Pb ions, which form the stereochemically active lone pair. The stereochemical activity of this lone pair of electrons drives the displacement of the Pb ions and prevents the Te ions from acquiring a similar displacement leading to dipole formation.

Note that our calculations are consistent with the reported long-ranged interactions along ⟨100⟩ through resonant bonding [30] (or equivalently lone pairs) and the recent report of anisotropic microstrain along ⟨100⟩ in all lead chalcogenide systems by Christensen *et al.* [8]. The latter paper argued that microstrain is a manifestation of the structural transition to an orthorhombic phase under pressure (in fact, the major atomic displacements in that phase transition are along ⟨100⟩ [31]), based on what they call, "anion-mediated $Pb(6s)$-$Pb(6p)$ interaction," another term for the (revised) lone pair [32] or resonant bonding [30] concept.

C. Dipole correlations

The correlations between bond lengths provide valuable information about the local dipoles present in the structure. We refer to these correlations, which involve three (if the bonds share an atom) or four (if they are separate) atoms, as *dipole correlations* in our discussion. The dipole correlations can be calculated using two approaches. First, in the harmonic approximation, they can be extracted from the experimental diffuse scattering. The second way is by directly sampling them from the MD simulation. The latter approach has the advantage that it can accurately capture all the anharmonicities present in the system. We followed both routes and found a very good agreement between them (see Appendices D and E). In this chapter, we present the results of MD simulations.

Since acoustic phonons generate in-phase displacements, they do not have a strong impact on the bond lengths. The bond length correlations shown in the following are therefore dominated by optical phonons, that is, by the effect indicated by the light-blue line in Fig. 7. In contrast, atomic displacement correlations shown in Figs. 4–6 are dominated by large amplitudes of acoustic phonons.

Figure 11 shows all computed correlations. To quantitatively assess the kind of correlation present between each pair of bonds, we compared to a reference state in which the bonds are uncorrelated (see Fig. 24 in the Appendix); the latter was computed by considering all pairs of bonds at least 15 Å apart.

We start by showing the nearest dipole correlations, i.e., the correlations between bonds that share an atom (Fig. 12; for our notation see Fig. 11). In general, the correlations should depend on the type of shared atom, so we present our results for both Pb and Te shared. Figure 12 shows probability densities for the dipole correlations. Bonds B_2^3 (lower panel) show a clear negative correlation—if one bond is longer than average, the other tends to be shorter. Note also that when the shared atom is Pb (d) the distribution is more elongated than for Te (e)—as already discussed, Pb is more polarizable, leading to
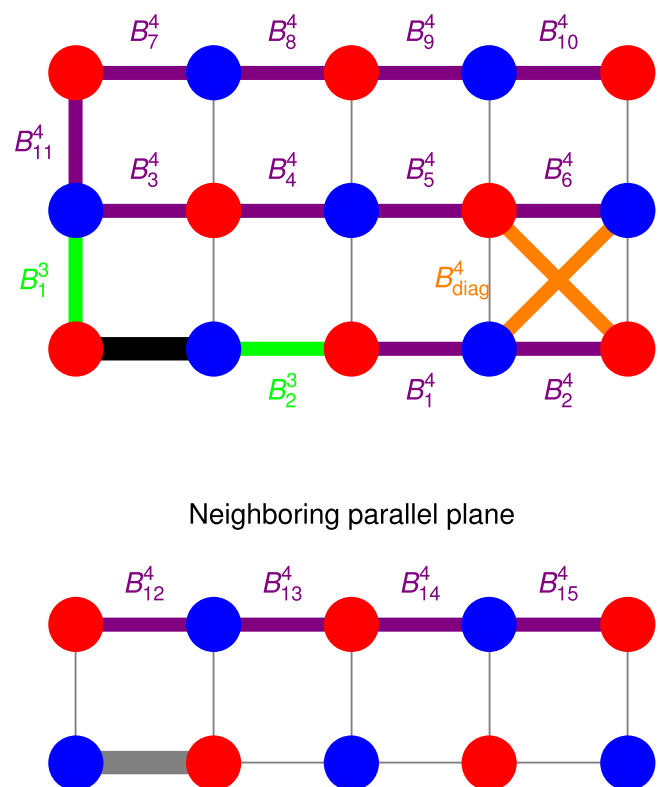
FIG. 11. Notation of our computed correlations between pairs of nearby bonds. The reference bond (bond 0 in the probability-density plots) is marked in black, with nearest-neighbor correlations in green, further neighbors in purple, and correlations between diagonal bonds in orange (in the latter case, the reference bond is one of the diagonals and not the black bond). The lower panel shows a crystal plane lying above or below the upper panel (with the gray bond lying just on top or below the reference black bond). The upper index in our notation for dipole correlations indicates the type of correlation (three- or four-body), and the lower enumerates them (the order is chosen arbitrarily).

a larger atomic displacement parameter. In the same way, B_1^3 bonds (upper panel) show a negative correlation, even though the deviations from the reference state are smaller. However, here, larger deviations are observed for bonds whose shared atom is Te.

We next analyze the further apart bonds shown in Fig. 26 in the Appendix. By close inspection of the dipole correlations' probability densities, the following local picture can be derived (Fig. 13). The horizontal [100] line containing the reference bond shows a clear alternation of short and long bonds (i.e., negative correlations), resulting in a *local* "ferroelectric-like" arrangement of electric dipoles. The neighboring, parallel [100] lines show the same pattern with a "ferroelectric" coupling to the reference [100] line. The only exception is the B_3^4 bond, which has a weak tendency to a positive correlation—strain and dipolar interaction are strong enough to counterbalance the ferroelectric coupling that would favor a negative correlation. On the other hand, the vertical [010] line also presents a ferroelectriclike arrangement of bonds, but with the formation of a "head-to-head domain wall" at the reference [100] line.
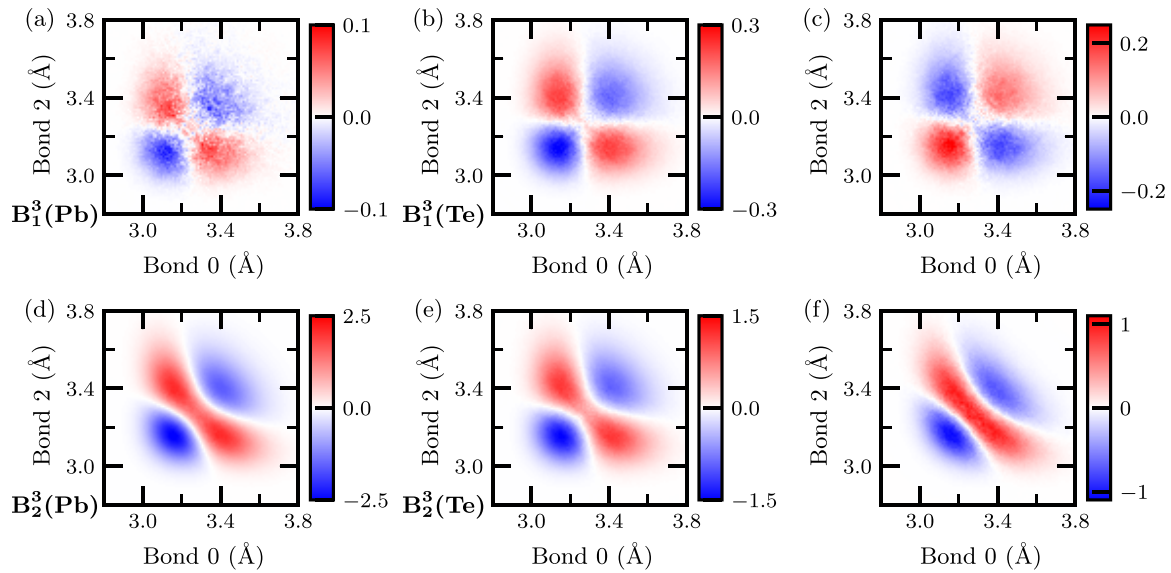
FIG. 12. Difference probability densities of nearest-neighbor dipole correlations calculated from MD. The upper panel presents bonds B_1^3; the lower panel bonds B_2^3. The first and second columns show difference densities with respect to the reference when the shared atom is Pb and Te, respectively, while the third column shows the difference between the first and second column. The color scale represents the probability density in Å^{-2}.

Note that the formation of ferroelectrically coupled ferroelectriclike [100] lines is not expected from the long-range dipole-dipole interaction, which would favor an antiferroelectric coupling of ferroelectric [100] lines. The origin of such a coupling may be found in short-range interactions depending on the chemistry of the environment, in this case the stereochemical activity of the lone pair. A similar competition was noted for the bulk ferroelectric behavior in perovskite BaTiO$_3$ by Nishimatsu *et al.* [33] with the construction of an effective Hamiltonian [34]. The authors showed that when only the dipole-dipole interaction is considered the most unstable phonon mode corresponds to the M point—the most stable

structure consists of an antiferroelectric cell-doubling state. Only when the short-range interactions are also included is the most unstable mode found at Γ producing the actual ferroelectric state.

At first sight, our findings in this section could seem in contradiction with our earlier discussion that the average structure remains high-symmetry rocksalt. However, the bond lengths averaged over all dipole correlations are unchanged from those of the reference state, with the most probable bond length still found at $a/2$ (see Figs. 24–26 in Appendix). This hints at a reconciliation between the conflicting descriptions—anomalous anharmonicity or off-centering—which we will explore further in the next section.

D. Local off-centering

Next, we discuss the implications of these correlated dipoles in the context of the proposed off-centering. In particular, we show that the existence of correlated local dipoles is consistent with an average local Pb position, which is centered in the Te coordination polyhedron. Figure 14 presents the deviations of the Pb atoms from the center of gravity of the PbTe$_6$ octahedra. Since it is also a many-body problem, this information is not directly accessible from the diffuse scattering or the 3D-ΔPDF data. Therefore we show only results from our MD simulations, which we justify by the good agreement in the local structure between MD and 3D-ΔPDF. Clearly, the distribution is centered on the origin and a Gaussian profile can not be excluded. Here, only the x-y plane is shown but the same conclusions are obtained also for all inequivalent [100], [110], and [111] directions. The same picture is obtained when considering the displacement of Te atoms with respect to the TePb$_6$ octahedra. So, we see that *on average* both Pb and Te atoms are not off-center but sit in the center of their

FIG. 13. Representative picture of the long and short bond arrangement. Red circles represent Pb atoms, blue circles Te atoms. The reference bond (black) is assumed to be longer than average. Gray standard arrows (pointing outwards) mean a positive correlation with the reference bond; if the first bond is longer, the second tends also to be longer. Gray arrows pointing inwards mean a negative correlation with the reference bond. The size and thickness of the arrows are indicative of the strength of the correlations. Green arrows indicate the size and direction of the resulting dipole moments.

FIG. 14. Probability density distribution for local lead off-centering with respect to the Te_6 coordination polyhedra from our *ab initio* MD simulations. (a) shows a cut in the x-y plane, while (b) a cut for $x = z = 0$. The red line represents the actual data, the blue line a Gaussian fit.

coordination polyhedra, consistent with our previous finding of the most probable bond being at $a/2$ (Figs. 24–26).

We next link this result with our previous discussion about correlated dipoles. In a specific unit cell, as we have just seen, the probability distribution for distortions is Gaussian without any preferential direction. As soon as one unit cell has chosen a distortion direction, however, the neighboring unit cells are no longer free to choose their distortion directions, since the pair and higher-order correlations impose a preferred orientation. The result is the development of regions of local polarity composed of correlated dipoles along the $\langle 100 \rangle$ directions. These distorted regions are randomly distributed in the crystal, however, such that averaging over them results in an (undistorted) rocksalt structure. From the decay of the correlations' strength we can roughly estimate the extent of these correlated dipoles regions to be around 30 Å. Furthermore, looking at the time evolution of the nearest-neighbor bond lengths, we can estimate the time scale associated with the correlations to be few tenths of picosecond. This is confirmed also by looking at their Fourier transform, where the dominant frequencies are in the few THz range. This is not surprising as the origin of the correlations is phononic. These correlations may resemble local distortions in relaxor ferroelectrics, as in the analysis of the diffuse scattering by Bosak *et al.* [35].

We emphasize the distinction from a static local off-centering, in which the interatomic potential would not have a single minimum, but would show other (meta-)stable states.

This could result in an alternation of long and short bonds, with the formation of one shoulder on each side of the PDF peaks, or even of multivalued peaks. Moreover, the distribution of the deviations with respect to the coordination polyhedra shown in Fig. 14 would not be Gaussian and may show multiple peaks.

We propose that our finding of correlated local dipoles combined with centered average Pb environments automatically resolves some of the controversy in the literature, which has been caused by differing interpretations of the meaning of "off-centering," 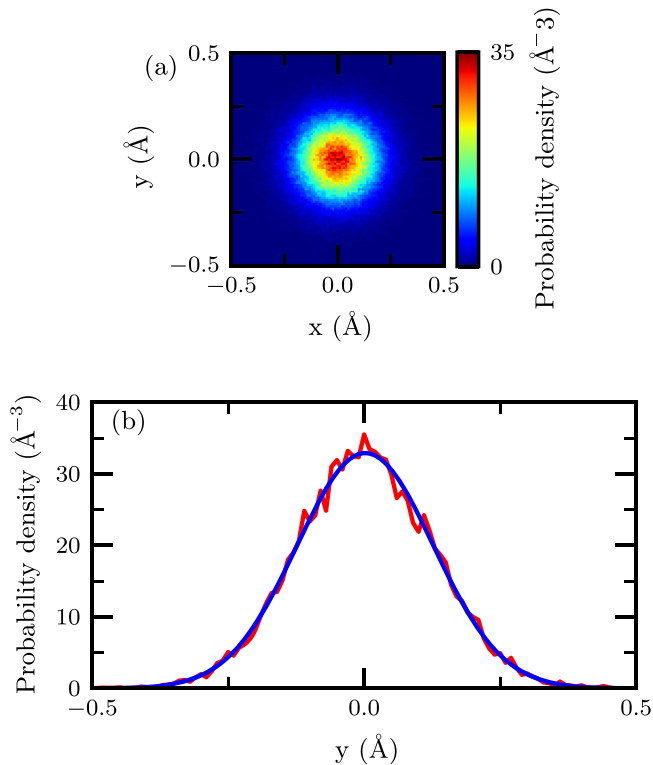such as the root mean square [11] or absolute [10,12,13,15] displacement from the rock-salt positions. Here, we show that the phenomenon called emphanisis is associated with the formation of correlated local dipoles, which can both vary in orientation throughout the structure and fluctuate in time. As a result, the positions of the ions are centered on average. The effect might be better referred to as *correlated local dipole formation* to avoid confusion in future works.

E. Radial pair distribution function analysis

Finally, we show that our finding of local correlated dipoles is largely consistent with the peculiar features of the original pair distribution function (PDF) of Božin *et al.* [2] with the exception that the shoulders in the peaks are not reproduced by our MD simulations. To do this, we first compare the radial PDF $G(r)$ extracted from our MD simulations with the original data. We computed the PDF from the MD as a histogram of the interatomic distances and by taking into account the neutron scattering lengths (9.405 fm for lead and 5.80 fm for Te [36]), with the experimental termination error from the finite Q range of the Fourier transform (Q_{max} set to 35 Å^{-1}), and scaled by a factor of 0.89 to take into account the arbitrary scaling introduced by some of the applied data corrections [37]. Figure 15 compares the MD and measured PDFs at three different temperatures, 50 (a), 450 (b), and 300 K (c). As can be seen, at the lowest temperature shown, 50 K [panel (a)], our MD calculations underestimate slightly the width of the nearest-neighbor peak—this may be ascribed to the underestimation of the ADPs originating, at this low temperature, from the lack of zero-point motion in the MD simulations. On the other hand, at the other two temperatures shown, the agreement is remarkably good. Only the shoulder on the high-r side of the peak at 450 K [panel (b)] is not captured. (The two wiggles appearing at approximately 2.8 and 3.6 Å in the experimental data are probably artifacts; their position is consistent with the periodicity of the wiggles from the finite Q range of the Fourier transform. On the other hand, we believe the shoulders at 3.0 and 3.4 Å to be real features of the experimental PDF.) In particular, Fig. 15(c) shows that our MD simulations at 300 K capture not only the correlated motion of the nearest-neighbor peak at ~3.2 Å, but also the intriguing overly sharp lattice-repeat-distance peak of the original data. In Fig. 16, we compare our 300-K MD data with a model that neglects correlated motion. We find the largest differences for the first and fourth peaks (marked by the red arrows in the figure), which are sharper (their calculated width, not shown, is smaller) than the second, third, fifth, and so on. The sharper peaks correspond to interatomic distances between atoms lying along the $\langle 100 \rangle$ directions, and their
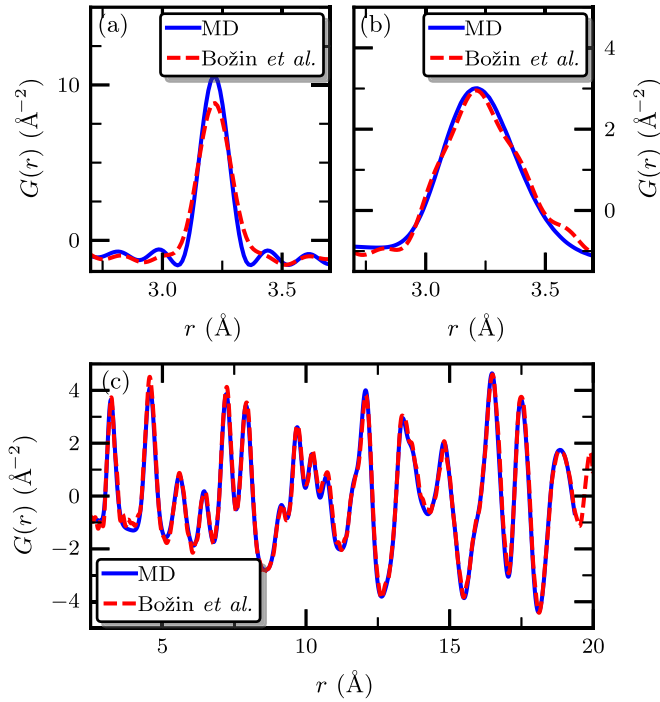
FIG. 15. Comparison between the PDFs obtained from our MD simulations (blue lines) and the original data from Božin *et al.* [2] (red dashed lines) with the temperature correction suggested in Ref. [7]; (a) $T = 50$, (b) 450, and (c) 300 K (the larger supercell was used). The MD data were multiplied by a scaling factor of 0.89.

sharpness is a result of the pair correlations being positive, and strongest along the $\langle 100 \rangle$ direction.

While visual inspection suggests that the MD peaks are less asymmetric than the data, our quantitative analysis shows that the asymmetry is actually captured quite well, in particular the trend towards more asymmetric peaks with increasing temperature. For the computation of the asymmetry, we first transform the PDF $G(r)$ to the radial distribution function (RDF) $R(r)$, such that its peak shapes describe the underlying pair-probability distribution (for a Gaussian probability distribution the peaks are symmetric) and the baseline lies at zero.
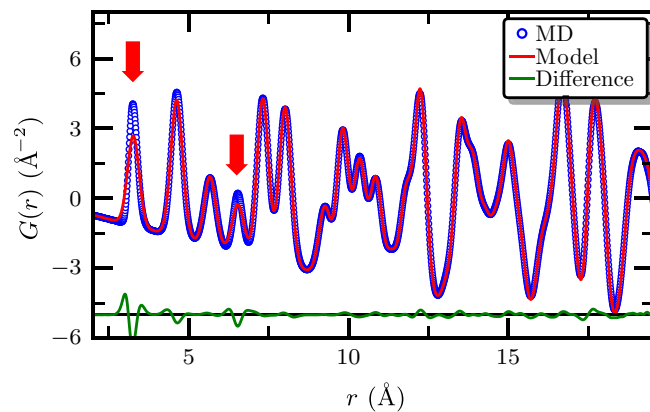
FIG. 16. Comparison of the refinement of the MD PDF at 300 K with that of a cubic $Fm\bar{3}m$ model without correlated motion taken into account.
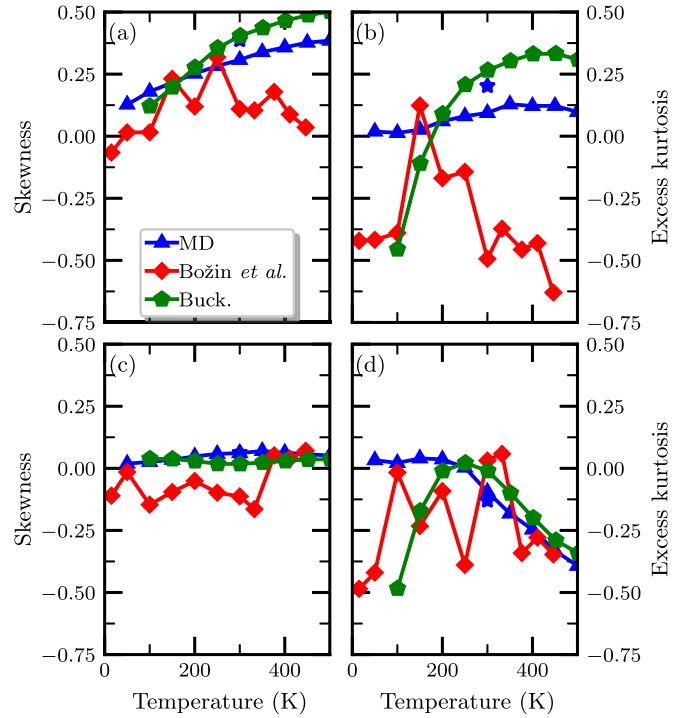
FIG. 17. Asymmetry analysis of the first two peaks of the RDF as a function of temperature. (a) and (b) show the analysis for the nearest-neighbor peak, and (c) and (d) for the next-nearest-neighbor peak. (a) and (c) present the skewness (third moment of the distribution), while (b) and (d) the excess kurtosis (fourth moment of the distribution). Blue symbols are obtained from our *ab initio* MD simulations (blue stars correspond to the larger supercell), red symbols are from the original data of Božin *et al.* [2], and green symbols are from the Buckingham potential.

To analyze the asymmetry, we use the (normalized) third and fourth moment of the distribution, the normalized skewness and excess kurtosis, defined as

$$\text{skewness} = \frac{m_3}{\sigma^3}, \quad \text{excess kurtosis} = \frac{m_4}{\sigma^4} - 3,$$

$$m_n = \frac{\int_{r_0 - \delta r}^{r_0 + \delta r} (r - \mu)^n R(r) \, dr}{\int_{r_0 - \delta r}^{r_0 + \delta r} R(r) \, dr},$$

where μ and $\sigma = \sqrt{m_2}$ are the mean and the standard deviation of the peak, respectively [6]. Figure 17 shows the temperature evolution of the two asymmetry parameters calculated from our *ab initio* MD simulations (blue), from the original data by Božin *et al.* [2] (red), and from the Buckingham potential (green). The nearest-neighbor peak shows increased asymmetry with increasing temperature for all curves with quite good agreement among them. (We note that the temperature evolution of the skewness is comparable to the T^2 evolution of C3 reported in Ref. [6], since the skewness is normalized by σ whereas the C3 value is not). The decrease of the skewness of the experimental data by Božin *et al.* [2] is caused by the shoulders on both sides of the peak [e.g., at 3.0 and 3.4 Å at 450 K in Fig. 15(c)]. On the other hand, the kurtosis captures these features and shows significant deviations from a Gaussian profile. The next-nearest-neighbor
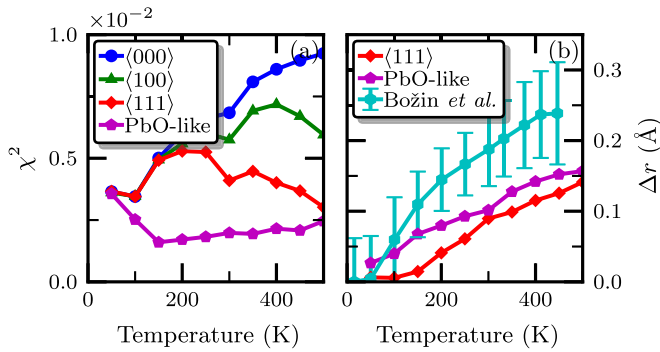
FIG. 18. Comparison of the different structural models fit to our MD simulations. (a) Quality of the fit through the χ^2 goodness parameter; (b) "off-centering" displacement, Δr, extracted for the two most probable (split) models compared to the data extracted from the study by Božin *et al.* [2] with the temperature correction proposed in Ref. [7].

FIG. 19. Representation of how anharmonicity can be introduced in real-space refinement utilities through split models.

peak is more symmetric, but the excess kurtosis indicates increasing deviations from a Gaussian profile also in this case. The large negative excess kurtosis values for the Buckingham potential at low temperatures are caused by the peaks being very narrow and the bin size too large to adequately compute the moments of the distribution.

Next, we subject the PDFs obtained from our MD simulations to the same small-box fitting protocols as in the original PDF study [2] in order to facilitate the comparison. We used the PDFGUI package [38] and set all experimental setup related parameters (scale factor, Q-space resolution, and related damping in r space) to ideal values. Various models were refined over a narrow r-range up to 6 Å, some with lead displacements allowed and some not: the cubic $Fm\bar{3}m$ rock-salt ($\langle 000 \rangle$); $\langle 100 \rangle$ and $\langle 111 \rangle$ models, where the lead sublattice is allowed to shift with respect to the Te sublattice in the specified direction; a model allowing for Pb displacements in $\langle 100 \rangle$ directions coupled with a tetragonal distortion of the unit cell, which we refer to as "PbO-like" [39].

In Fig. 18(a), we show the quality of the fits, measured by the χ^2 parameter, as a function of temperature for the various models. We see that the cubic model does progressively worse with increasing temperature, while the best fit is produced by the $\langle 100 \rangle$ PbO-like model in particular at higher temperatures, consistent with the original experimental observation [2].

Note that the $\langle 111 \rangle$ model also gives reasonably good fits. Next, we extract an "off-centering" displacement from the two best models and show our results in Fig. 18(b). The resulting values are in good agreement with the original reported values in Ref. [2] (light blue symbols).

While this finding of off-centering might seem to contradict our finding above that the Pb ions are at the center of their Te coordination polyhedra, in fact, it is a consequence of the interpretation and use of split models in current real-space refinement utilities. In fact, the small-box modeling software, PDFGUI, is not designed to handle anharmonic effects, and instead uses Gaussian distribution shapes. Instead of accounting for anharmonic effects directly, these effects are handled indirectly via discrete bond-length distributions and partial occupancies (split models). Consider the situation
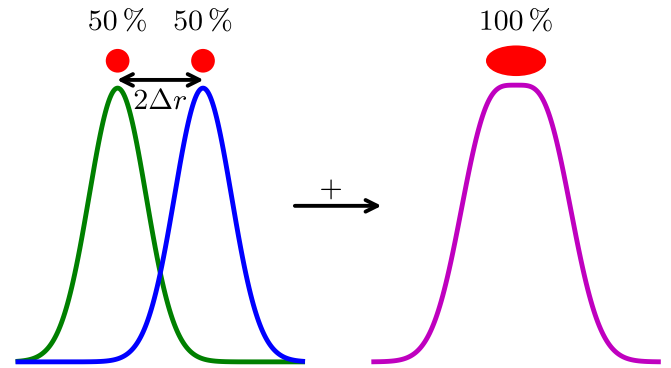
shown in Fig. 19: on the left, a split model is considered, with each split position (50 % occupancy) described by a Gaussian and separated by the "off-centering" $2\Delta r$. However, the sum of the two Gaussians (right) results in a pseudo-Gaussian distribution that mimics an anharmonic potential. This means that if the final distribution of a split model is not multivalued, anharmonicity and off-centering can not be distinguished. It would be therefore desirable to upgrade real-space refinement procedures with anharmonic features to avoid confusion in the description of strongly anharmonic systems such as the group-IV chalcogenides.

F. Origin of the peak asymmetry

Finally, we discuss the origin of the unusual behavior and conflicting literature reports in light of our new measurements and calculations. First, we address the relationship between the asymmetry of the peaks and the anharmonicity of the PbTe potential. In the previous studies that did not find any off-centering [10,12–15], the well-known anharmonicity of PbTe was considered to be the sole cause of asymmetry. Indeed, an anharmonic potential, such as the Buckingham potential used above, can explain alone (part of) the asymmetry. Figure 17 shows that also the Buckingham potential produces an increased asymmetry with good agreement with the data from Ref. [2]. On the other hand, anharmonicity alone is not enough to explain the peculiar decay of the pair correlations presented in Fig. 6, since we showed that the Buckingham potential does not lead to steps in the pair correlations (see Fig. 8).

Next, we show that the correlated dipoles can further amplify the peak asymmetry. Figure 20 shows results of calculations using VASP for a cubic supercell containing one long and one short bond. The length of these two bonds was chosen to differ by about 10 % from the equilibrium bond length, giving values of 3.5 and 2.94 Å. The large weight in the probability densities of Figs. 12(d) and 12(e) corresponding to these bond lengths shows that they are a reasonable choice. One of the bonds was changed, while the other was kept fixed, and the energy was calculated. One can see that when the short bond is varied (fixed long bond) the energy curve is steeper than when the long bond is changed (fixed short bond), because of the asymmetry of the crystal field. This produces a narrower distribution for short bonds than long ones, resulting in an
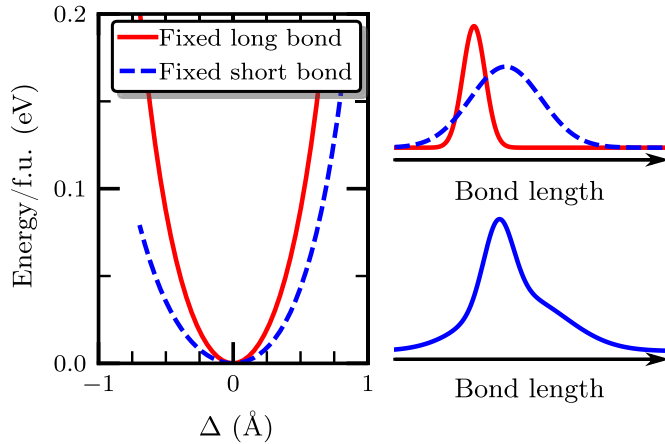
FIG. 20. (Left) Energy change when either the long (3.5 Å) or the short (2.94 Å) bond are kept fixed, and the other is varied. Δ represents the change in bond length with respect to the equilibrium bond length (the bond corresponding to the minimum energy). The calculation was done using VASP by building a $3 \times 1 \times 1$ cubic supercell and displacing two atoms to produce the sought for bond arrangement. Right panel, top, sketch of the probability distributions of the short (red) and long (dashed blue) bonds, bottom, sum of the two distributions.

overall asymmetric distribution of bonds (see right panel in Fig. 20). Thus the alternation of short and long bonds provides another microscopic contribution to peak asymmetry.

We note that the previously reported shoulder on the first PDF peak, which was interpreted as a local off-centering of the Pb-Te bonds, is not reproduced either in our molecular dynamics simulation or diffuse scattering (nor elsewhere in the literature). Therefore any additional physics associated with the existence of this peak is not captured by our analysis. Possible reasons for its absence in our molecular dynamics simulations are an insufficiently large supercell, or the absence of spin-orbit coupling in the calculations. We note, however, that the existence of such a shoulder is not essential for emphanitic behavior, which we find in our MD simulations and which has been reported for other materials such as $CsSnBr_3$ [18], where shoulders are lacking.

IV. RELEVANCE FOR THERMOELECTRICITY

In this last section, we discuss the relevance of our findings for the well-known thermoelectric performance of PbTe [40–47]. The fluctuating correlated local dipoles will likely contribute to phonon scattering; here we show that they should also influence the electronic behavior. It is well-known that lone-pair expression is beneficial for thermoelectric performance [48,49], since it tends to open electronic band gaps and suppress bipolar conduction of carriers. The electronic structure of PbTe indicates a further mechanism to increase its performance, that is, the presence of a secondary pocket along the Σ line with an energy slightly lower than those of the L pocket, where the band gap can be found [50]. By reducing the band offset between L and Σ pockets, the valley degeneracy can be increased (L pockets have a valley degeneracy of 4, while that of Σ pockets is 12), and consequently also the
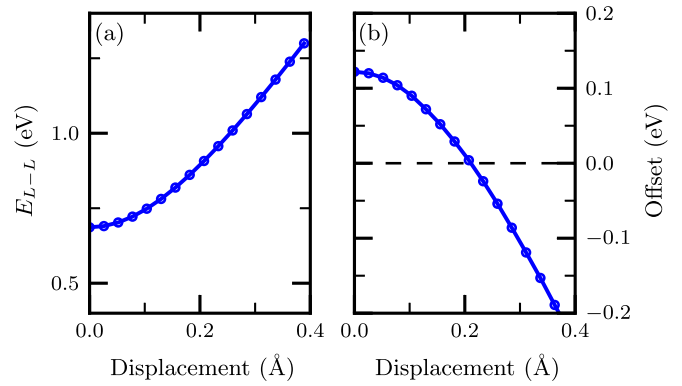
FIG. 21. Electronic properties as a function of the ferroelectric distortion along ⟨100⟩. (a) Direct band gap at L and (b) offset between L and Σ pockets.

power factor is increased [42,43,49,51–55]. Experimentally, in pristine PbTe, this decrease in the offset happens with increasing temperature, with a proposed convergence at about 700–800 K [56,57]. The band offset can also be controlled by K or Na co-doping such that the thermoelectric power factor is enhanced through the tuning of the interaction between the L and Σ bands [42].

In an attempt to link the correlated dipoles to the high thermoelectric performance of PbTe, we show in Fig. 21 the band gap and band offset between L and Σ pockets as a function of a polar distortion along ⟨100⟩. Here, we use a structure with the extreme situation of a ferroelectric distortion along ⟨100⟩, with aligned static stereochemically active lone pairs [48]. As expected, we find that the lone-pair expression is accompanied by an increase of the band gap [panel (a)]. More importantly, the band offset [panel (b)] decreases with increasing distortions, so that the band gap becomes indirect for displacements above about 0.2 Å. While the cooperative ferroelectric distortion analyzed here, of course, differs from the actual correlated local dipole behavior, we expect that the trends will be similar, with the amplitude of distortion in our calculations playing the role of temperature in the experiments. Thus the correlated dipole regions likely contribute to the high thermoelectric performance of PbTe by affecting both the electronic and phononic components.

V. SUMMARY

In summary, we have performed a combined x-ray scattering and *ab initio* molecular dynamics study of the lattice behavior of PbTe, and analyzed our results in the context of earlier PDF studies that suggested a local Pb-Te off-centering. The presented 3D-ΔPDF analysis provides a detailed quantitative picture of the atomic pair correlations up to distances of about 60 Å. This allows a comprehensive insight into the local structure of PbTe, and also demonstrates the power of the 3D-ΔPDF method for analyzing the local structure of disordered crystals.

We find a close consistency between our Bragg and diffuse x-ray scattering measurements and our molecular dynamics simulations. At the bulk level, both our Bragg scattering measurements and our calculations yield non-Gaussian peaks,

indicative of significant anharmonic behavior. At the local level, both our diffuse scattering and MD simulations find a distinctive and unusual stepwise decay with distance in the pair correlation functions. This excellent match allows us to further analyze our molecular dynamics results to extract detailed information about the atomic positions and dynamics—including higher-order correlation functions—that can not be easily obtained from experiment.

Our main finding is the unusual correlated local dipole formation, exemplified by Fig. 6, in which a displacement of an ion along a cubic axis causes correlated displacements in the atoms in neighboring cells that do not show the usual smooth decay with distance. Instead, the correlations indicate a tendency for anion-cation dimerization, and the resulting formation of local dipoles, in the direction of displacement. This behavior can be interpreted as a superposition of an acoustic phonon mode, which alone would displace all atoms in the same direction and would decay smoothly with distance, with an optical phonon mode, which causes opposite atomic displacements and therefore is responsible for the steplike behavior. Thermal activation of an optical phonon mode is clearly required for such an effect, and is possible in PbTe because of the soft transverse optical phonon mode associated with the proximity to the ferroelectric phase transition. Since the essential ingredient for the observed local structure is a coherent superposition of soft optic phonon modes with acoustic modes, similar behavior should occur, in principle, close to any ferroelectric phase transition. In this respect, it would be interesting to search for such correlated local dipole behavior above the transition temperature in ferroelectric phase transitions that have been previously regarded as displacive. The finding using EXAFS spectroscopy that the local distortions associated with the ferroelectric state in GeTe persist essentially unchanged on heating to the paraelectric phase, might indeed be an indicator of emphanisis [58].

Importantly, this correlated dipole formation does not translate into an *average* off-centering of the ions from the centers of their coordination polyhedra. Analysis of our simulations indicates that the most probable ionic position, averaged over time or space, is at the center of the polyhedron, with a smooth decrease in probability away from that point. This is consistent with different regions of the material having different orientations and amplitudes of correlated dipole formation, and with a local but not global symmetry breaking of the cubic symmetry. The question of "off-centered or not" that has recurred throughout the literature is therefore perhaps not the right question to ask in this case.

In this context, we emphasize also that there is no *a priori* geometrical dependency between correlated dipoles and atomic split positions or anharmonic probability density functions. The first requires correlated displacements of two or more atoms, while the latter are single body properties. Uncorrelated displacements of any kind would not stimulate coherent dipole formation beyond the next neighbor, regardless of whether the corresponding atomic probability density functions are harmonic, anharmonic, or split. On the other hand, even in the case of perfect harmonic atomic displacements extended dipole formations may be observed. For example, a single optical harmonic phonon mode would by definition

introduce correlated dipoles, but space and time averaging of the displacements would be perfectly harmonic.

Finally, we suggest that the correlated dipoles and the associated distortions along ⟨100⟩ are beneficial for the high thermoelectric performance of PbTe. First, the coupling between acoustic and optic phonons (as was already shown in Ref. [4]) and the regions with different orientations of the correlated dipoles in the crystal may increase the phonon scattering, consequently decreasing the thermal conductivity. Second, the distortions along ⟨100⟩ may explain two electronic features that are thought to be necessary to explain the thermoelectric performance, the increase of the band gap with temperature and, at the same time, the band convergence of the L and Σ pockets.

APPENDIX A: METHODS

1. Sample preparation

Single crystals of PbTe were prepared by mixing stoichiometric amounts of Pb (Rotometals, at 99.9 % purity) and Te (Plasmaterials, at 99.999 % purity) in an evacuated fused silica ampoule. The total amount of PbTe was 15.346 g and the length of the ampoule was approximately 18 cm. The ampoule was placed in a box furnace, heated to $1050\,^\circ$C over 16 h, and held at that temperature for 36 h. The sample was then cooled to room temperature in 24 h. Small single crystals (10–100 μm) were formed on the top part of the ampoule. Several crystals were screened on a STOE IPDS 2T diffractometer for quality evaluation.

2. X-ray diffraction

The single-crystal used for the x-ray experiments was an irregularly shaped fragment with an average diameter of about 42 μm. The experiment was done at the X06SA beamline at SLS, Villigen, Switzerland, which was equipped with a single axis goniometer and a PILATUS 6M detector. The synchrotron storage ring was operated in top-fill mode to deliver constant primary intensities. Full data sets (3600 frames, 0.1° rotation and 0.1 s exposure time per frame, wavelength 0.7085 Å, crystal-detector distance 185 mm) were recorded in the sequence room temperature, 250 K, 200 K, 150 K, and 125 K. The experimental setup did not allow access to temperatures above room temperature. The primary beam was normal to the rotation axis and to the detector plane. The detector energy threshold for accepting x-ray photons was set to 16 keV (energy of primary beam 17.5 keV) to suppress fluorescence
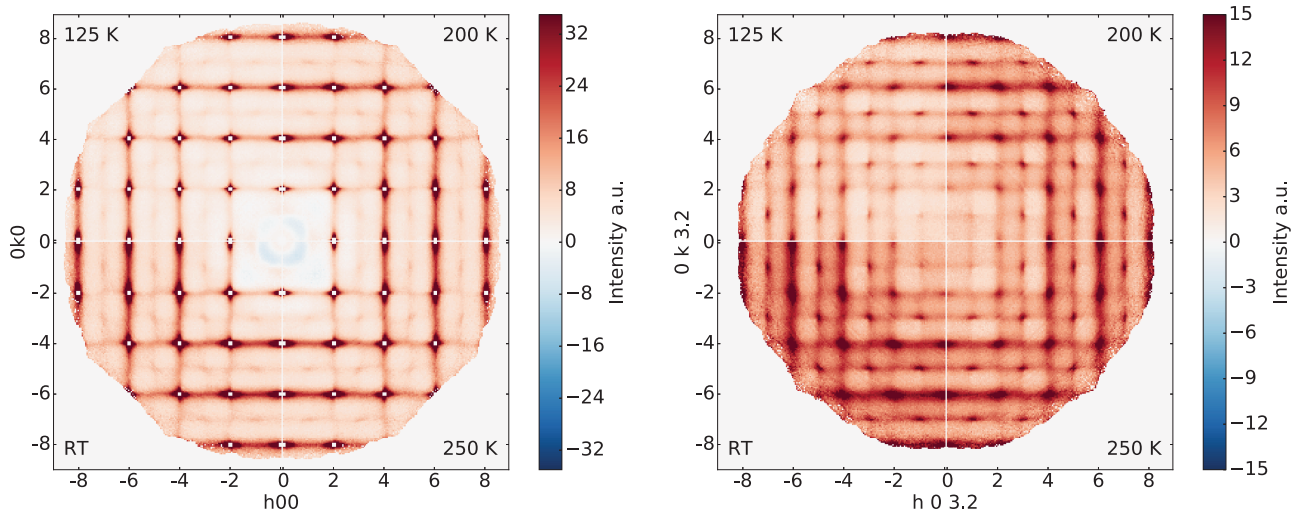
FIG. 22. Comparison of the diffuse intensities at selected temperatures.

scattering as much as possible. In addition, 100 frames were collected under the same conditions as in the diffuse scattering measurements, but without sample and sample holder. These frames were averaged and taken as a model for background scattering.

A Bragg data set collected with a strongly attenuated beam did not deliver satisfactory results, as the internal R value was well above 0.2 (the internal R value is defined as $R_{int} = \frac{\sum |I_{obs} - \langle I_{obs}\rangle|}{\sum |I_{obs}|}$, where the summations run over all reflections for which more than one symmetry equivalent reflection is averaged, I_{obs} is the corrected intensity of a reflection and $\langle I_{obs}\rangle$ is the corresponding symmetry-averaged intensity) even for the triclinic Laue group. Reasons may be strong multiple scattering effects and/or unresolved saturation problems of the detector. We therefore repeated the Bragg data collation using our in-house Xcalibur Oxford Diffraction diffractometer (Mo K_α radiation, graphite monochromator, sealed tube, Onyx CCD detector, $\theta_{max} = 45.3°$, $-12 \leqslant h, k, l \leqslant 12$ same crystal and temperatures as used in the synchrotron experiments).

3. Diffuse scattering data reduction

Reciprocal space reconstructions were done with the program XCAVATE [59]. Reconstructions were mapped onto a $360 \times 360 \times 360$ voxel volume covering the reciprocal space within the limits $-9 \leqslant h, k, l \leqslant 9$. Since the half-widths of the Bragg reflections were significantly smaller than the pixel size of the reconstructions, it was assumed that the experimental reciprocal space resolution function can be ignored to a good approximation. In contrast to the Bragg data, the diffuse scattering was corrected using a spherical absorption model for sake of simplicity. It is not expected, however, that this simplification will introduce significant systematic errors. For comparison, Bragg data corrected by spherical absorption correction resulted in slightly higher R_{int} values (0.11 versus 0.078 using the analytical approach, see below), but the refined structure parameter values from those data changed only by a few percent compared to the results obtained with analytical absorption correction. It is not expected that the choice of the absorption correction method would have a large impact on

the results extracted from the diffuse data. Finally, the data were averaged following the Laue symmetry $m\bar{3}m$. Individual voxels were rejected as outliers according to the procedure described in Blessing [60]. A voxel was rejected if its difference to median value of symmetry equivalent voxels was more than about six times the median difference (for details see Ref. [60], Eqs. (16) and (17) with $c_1, c_2, c_4 = 0, c_3 = 6$). This procedure turned out to be very helpful in eliminating most of the parasitic scattering that is not compatible with the Laue symmetry of the single-crystal diffraction pattern, such as scattering from small grains attached to the surface or secondary air scattering from strong reflections. Finally, the background was subtracted from the diffuse data. It was expected that the empirical experimental background obtained as described above would show slightly smaller background intensities compared to the background seen with the crystal, because scattering from the sample holder and from glue were not included in the background measurements. To our surprise we found, however, that the empirical background determination showed slightly larger intensities compared to those observed in the diffuse scattering measurements. This observation may be explained by the fact that the primary beam gets attenuated by the crystal and therefore the air scattering coming from the pathway between crystal and beam stop is reduced. To partly compensate this effect, we multiplied the empirical background by a factor of 0.9 to avoid larger regions of negative intensity after correction. Figure 22 shows two sections of the final diffuse scattering reconstructions at different temperatures.

4. Bragg data absorption correction

The high absorption coefficient of $\mu = 75.5$ mm^{-1} required careful absorption correction. Various strategies provided by the program CRYSALISPRO [61] were tried, namely analytical absorption correction based on a graphical estimate of the crystal's morphology and its orientation relative to the diffractometer coordinate system, spherical absorption correction, empirical absorption correction, and combinations of analytical/empirical, spherical/empirical, and analytical/optimized crystal shape approaches. The best internal R value (R_{int}

= 0.064) was obtained from the analytical/optimized crystal shape method, however, the optimized crystal shape did not well match the morphology of the sample and the results were therefore rejected to avoid overcorrection. The second best results were obtained from the analytical approach and from the combination analytical/empirical absorption correction ($R_{int} = 0.078$ in both cases). Since the latter did not deliver better data, the results obtained from the analytical correction method were used in our refinements.

5. Computational details

Our *ab initio* molecular dynamics simulations were performed using the CP2K code [62] with the hybrid Gaussian and plane-wave (GPW) scheme [63,64]. Gamma-point only calculations were performed with a plane-wave cutoff of 500 Ry. We performed GGA calculations with the PBEsol [65] exchange-correlation functional (shown to provide the best overall agreement with experimental structural and electronic properties [50,66]) and Gödecker-Teter-Hutter (GTH) pseudopotentials [67,68]. We used valence electron configurations $6s^2 6p^2$ for lead, and $5s^2 5p^4$ for tellurium. Spin-orbit coupling was not included. Calculations were performed with a $3 \times 3 \times 3$ supercell of the conventional (cubic) cell (216 atoms) at temperatures between 50 and 500 K in steps of 50 K. Long simulations (150 ps) in the isothermal-isobaric (NpT) ensemble using the thermostat developed by Bussi *et al.* [69] were performed, followed by 150 ps production runs in the microcanonical (NVE) ensemble. The time step used was 2 fs. To check for finite-size effects, one run with a $6 \times 6 \times 6$ supercell (1728 atoms) was performed at 300 K with a reduced simulation time of $60 + 60$ ps; this run was also used to analyze in detail the local structure.

VASP [29] calculations were performed using the PAW [70,71] implementation of density functional theory (DFT). We used the PBEsol [65] exchange-correlation functional and a plane-wave energy cutoff of 600 eV. For the $15 \times 1 \times 1$ supercell, we used a $1 \times 15 \times 15$ Γ-centered k-point mesh, while for the $3 \times 1 \times 1$ supercell we used a $5 \times 15 \times 15$ Γ-centered k-point mesh. Spin-orbit coupling was not included. We used valence electron configurations $5d^{10} 6s^2 6p^2$ for lead and $5s^2 5p^4$ for tellurium. The unit cell volume was fixed to the equilibrium volume (lattice constant of 6.44 Å to be compared with the experimental lattice constant of 6.43 Å [2]) obtained with a full structural relaxation.

LAMMPS [27] MD simulations were performed with a $6 \times 6 \times 6$ and a $10 \times 10 \times 10$ supercell of the conventional (cubic) cell (1728 and 8000 atoms) at temperatures between 100 K and 500 K in steps of 50 K. 150-ps simulations in the isothermal-isobaric (NpT) ensemble using the thermostat developed by Bussi *et al.* [69] and the Berendsen barostat [72] were performed, followed by 150-ps production runs in the microcanonical (NVE) ensemble. The time step used was 2 fs.

6. Design and refinement of the 3D-ΔPDF model

The 3D-ΔPDF maps were obtained as the Fourier transform of the diffuse diffraction pattern, with the Bragg reflections cut out from the diffraction pattern as follows: to be sure that the tails from very strong Bragg peaks were eliminated, volumes

of $3 \times 3 \times 3$ voxels centered at the Bragg positions were set to zero. As the strong diffuse scattering maxima coincide with the Bragg peaks, it is not possible to cleanly separate Bragg from diffuse scattering without having additional information available. The impact of cutting the Bragg peaks and diffuse scattering at the same time was shown to only significantly impact the long 3D-ΔPDF vectors, while densities at short vectors are almost unaffected by this procedure [73,74]. In contrast to Refs. [73,74], we did not fill the punched Bragg regions with the average of the surrounding, but with zero values. As a consequence, some artifacts are present at larger PDF vectors, where the 3D-ΔPDF densities are expected to become very weak. In the least squares 3D-ΔPDF refinements, the cutout volumes were ignored by giving them zero weights.

Theory. The local structure properties of PbTe were refined with the 3D-ΔPDF [23] modeling program YELL [24]. In the following, we summarize the fundamentals of the 3D-ΔPDF theory of displacive disorder.

In the harmonic approximation, the diffuse scattering of a compound showing displacive disorder may be calculated as

$$
I_{dif}(\mathbf{h}) = \sum_{\mathbf{R}_{uvw}}^{\mathrm{cryst}} \sum_{mn}^{\mathrm{cell}} \left[\exp\left(-\mathbf{h}^T \beta_{uvw}^{mn} \mathbf{h}\right) \right. \\
\left. - \exp\left(-\mathbf{h}^T \left(\beta_{\mathrm{aver}}^m + \beta_{\mathrm{aver}}^n\right)\mathbf{h}\right)\right] \\
\times f_m(\mathbf{h}) f_n^*(\mathbf{h}) \cos[2\pi \mathbf{h}(\mathbf{R}_{uvw} + \mathbf{r}_{mn})]. \quad \text{(A1)}
$$

The summations run over all atomic pairs with significantly correlated displacements. $\mathbf{R}_{uvw}$ is the lattice vector between the unit cells hosting the correlated atoms m and n and $\mathbf{r}_{mn}$ is the average distance between the sites n and m within a unit cell, i.e., $\mathbf{R}_{uvw} + \mathbf{r}_{mn}$ is the average vector between atoms m and n. The average ADPs β_{aver}^m and β_{aver}^n as well as $\mathbf{r}_{mn}$ are taken from the average structure and f_m and f_n are the conventional atomic form factors. The structural information about displacive correlations is stored in the 3×3 matrix β_{uvw}^{mn}, whose elements are defined as

$$
\beta_{uvw,ij}^{mn} = \left\langle \left(u_i^n - u_i^m\right)\left(u_j^n - u_j^m\right)\right\rangle_{uvw} \\
= \beta_{\mathrm{aver},ij}^m + \beta_{\mathrm{aver},ij}^n - 2\left\langle u_i^n u_j^m \right\rangle_{uvw}, \quad \text{(A2)}
$$

where u_i^n is the ith vector component of the displacement of atom n from its average position in fractional units and $\langle \ldots \rangle_{uvw}$ indicates space and time averaging of joint displacements of all atoms m and n that are uvw unit cells apart. The displacement covariances,

$$
\mathrm{Cov}_{uvw,ij}^{mn} = \left\langle u_i^m u_j^n \right\rangle_{uvw}, \quad \text{(A3)}
$$

are the structural variables that are optimized in YELL. For a more convenient comparison of the joint displacements of atoms, we define the correlation matrix Cor_{uvw}^{mn} with the matrix elements

$$
\mathrm{Cor}_{uvw,ij}^{mn} = \frac{\left\langle u_i^m u_j^n \right\rangle_{uvw}}{\sqrt{\beta_{\mathrm{aver},ii}^n \beta_{\mathrm{aver},jj}^m}}, \quad \text{(A4)}
$$

whose numerical values may range between -1 and 1. The extreme values represent perfect anti- and in-phase correlations, respectively.

Defining the model. For modeling the real structure, we refer to the harmonic average structure displacement model, because it implies no arbitrary constraint such as $U_{\mathrm{iso}}^{\mathrm{Pb}} = U_{\mathrm{iso}}^{\mathrm{Te}}$. Furthermore, the probability density functions of the harmonic and split models are very similar and the choice of the average structure model is not expected to have a major impact on the extracted information.

Most of the interatomic vectors in PbTe are nicely resolved in the 3D-ΔPDF maps, with the only exception being that for each Pb/Pb pair there is one Te/Te pair having exactly the same average interatomic vector. Such pair correlation parameters were constrained to the same values. The 3D-ΔPDF maps show significant correlations up to about 100 Å. Refinement of all symmetry-independent coefficients would require a least-squares optimization of about 3500 independent parameters—a task that would be beyond our computational capabilities. To overcome this problem, we identified dependencies among the pair correlation parameters, finding by trial-and-error that homo- and heteroatomic pair correlations decay exponentially along $\langle 100 \rangle$ directions for all except some very short interatomic vectors. The final model was as follows: the covariance matrices Cov_{uvw}^{mn} of the pairs corresponding to interatomic vectors $\langle 0.500 \rangle$, $\langle 100 \rangle$, $\langle 1.500 \rangle$, $\langle 200 \rangle$, $\langle 2.500 \rangle$, and $\langle 300 \rangle$ were refined independently. For any other pairs in the asymmetric unit of the point group $m\bar{3}m$ (i.e., $x \geqslant y \geqslant z \geqslant 0$), the covariance parameters were constrained to an exponential decay according to the relation $\mathrm{Cov}_{uvw,ij}^{mn}(xyz) = a_{uvw,ij}^{mn} \exp(-b_{uvw,ij}^{mn}x)$, where $a_{uvw,ij}^{mn}$ and $b_{uvw,ij}^{mn}$ were refined separately for sequences of homo- and heteroatomic pairs.

The exponential decay was assumed to be along the main crystallographic axes, because the 3D-ΔPDF maps clearly indicate that the correlations are strongest along such directions. In the case of very weak signals, it was not possible to refine $a_{uvw,ij}^{mn}$ and $b_{uvw,ij}^{mn}$ independently without obtaining strong numerical correlations. Reasonable fits were then obtained with the constraint $b_{uvw,ij}^{mn} = 1$, which was found by trial-and-error, and only $a_{uvw,ij}^{mn}$ was refined. The Laue symmetry $m\bar{3}m$ was applied to all pair correlations. The final model comprised 363 independent parameters to be optimized against the diffuse diffraction data at each temperature. Even with this reduced number of parameters, computer memory limitations did not allow refinement of all parameters at the same time, given the large number of voxels in the refinement. The models were therefore refined in blocks of about 30 parameters and the process was repeated until no further improvements could be observed. A single least-squares run took about one to two hours on a modern desktop computer. In total, a full refinement took about two working days per temperature point. The results of the refinements are shown in Figs. 3 and 4. In general, the agreement between the observed and refined intensities or PDF densities is very good and the R values are very low given the weak diffuse intensities [$R(125\,\mathrm{K}) = 0.20$, $R(150\,\mathrm{K}) = 0.19$, $R(200\,\mathrm{K}) = 0.17$, $R(250\,\mathrm{K}) = 0.15$, $R(293\,\mathrm{K}) = 0.14$; here R values are defined as $R = \frac{\sum_i (I_{\mathrm{obs},i} - I_{\mathrm{ref},i})^2}{\sum_i I_{\mathrm{obs},i}^2}$, where the summations run over all i voxels that were observed and not cut out]. The increase of R values at lower temperatures might be explained by the decreasing integral diffuse scattering intensities, which lead to lower signal-to-noise levels in the experimental diffuse data. Major disagreements between observed and refined ΔPDF

densities are found along the $\langle 100 \rangle$ directions, probably due to anharmonic contributions in the pair correlation functions that are not covered by our harmonic 3D-ΔPDF model. The anharmonicities are extended over long distances and increase as a function of temperature, consistent with the observations of Ref. [2]. As a consequence of computational and experimental limitations, the achievable PDF space resolution is much lower in the single-crystal cases as compared to powder PDF studies. Thus a more detailed analysis of the anharmonic effects is not possible in the present case. The observation of long correlation lengths of anharmonic displacements clearly supports the interpretation of Ref. [2] that this anharmonicity is not just a consequence of asymmetric pair potentials, but reflects some collective structural distortion over long distances. The anharmonic pair correlations are also seen in the $I_{\mathrm{obs}} - I_{\mathrm{ref}}$ maps, where significant asymmetries along $h00$ directions with respect to integer h positions are observable. A size-effect-like distortion, which is frequently made responsible for such asymmetries, can be excluded because of the absence of substitutional disorder.

APPENDIX B: COMPARISON OF THE OBTAINED PAIR CORRELATIONS

Table II presents an overview of our refined and calculated pair correlations for distances up to two unit cells along each direction. Note the good agreement between the 3D-ΔPDF and the MD values.

APPENDIX C: AVERAGE ATOMIC DISPLACEMENTS FROM THE MD SIMULATIONS

Figure 23 shows the average displacement of the atoms from the rock-salt positions during the simulation at 300 K. Consistent with previous MD simulations they are negligibly small.

APPENDIX D: DIPOLE CORRELATIONS

In this section, we present probability densities for the dipole correlations in the MD simulations that were not shown in the main text. We start by showing in Fig. 24 the reference state, which represents the uncorrelated bonds; for its computation all pairs of bonds at least 15 Å apart were considered. One can see that the most probable bond length can be found at $a/2$. Note also the asymmetry in the distribution with a longer tail in the direction of longer bonds, consistent with the asymmetry of the nearest-neighbor PDF peak. In fact, by integrating out one of the bonds, we directly obtain the radial distribution function (RDF) $R(r)$.

Next, in Fig. 25, we show the probability densities for the nearest dipole correlations. The dependence on the type of shared atom can be clearly recognized. Note that the negative correlation of B_2^3 bonds can be observed already by visual inspection. This is not the case for more distant dipole correlations.

Finally, Fig. 26 presents the rest of computed dipole correlations. Note the different color scale in the different panels showing the decay in correlation strength.

TABLE II. Pair correlation coefficients, $Cor_{uvw,ij}$, within the asymmetric unit of the 3D-PDF space up to a maximum distance of two unit cells along each direction; $\Delta\mathbf{x} = (u, v, w)$ is the interatomic vector in fractional units. The 3D-ΔPDF values (labeled as Exp.) were obtained at room temperature, while the MD values at 300 K. In the experimental results, Pb/Pb and Te/Te correlations cannot be distinguished but are subject of a combined refinement as described in Appendix A 6. The definition of the correlation coefficients is also described there.

Δx	Pairs	Source	Cor_{11}	Cor_{22}	Cor_{33}	Cor_{12}	Cor_{13}	Cor_{23}
	Homo	Exp.	1.0000	1.0000	1.0000	0.0000	0.0000	0.0000
0.0 0.0 0.0	PbPb	MD	1.0000	1.0000	1.0000	0.0000	0.0000	0.0000
	TeTe	MD	1.0000	1.0000	1.0000	0.0000	0.0000	0.0000
		Exp.	0.4879	0.1602	0.1602	0.0000	0.0000	0.0000
0.5 0.0 0.0	PbTe							
		MD	0.4820	0.1252	0.1289	0.0001	0.0001	0.0068
	Homo	Exp.	0.1552	0.1552	0.0812	0.0581	0.0000	0.0000
0.5 0.5 0.0	PbPb	MD	0.1101	0.1080	0.0462	0.0605	0.0012	0.0022
	TeTe	MD	0.1409	0.1388	0.0643	0.0206	0.0009	0.0004
		Exp.	0.0853	0.0853	0.0853	0.0024	0.0024	0.0024
0.5 0.5 0.5	PbTe							
		MD	0.0420	0.0728	0.0458	−0.0001	0.0002	0.0006
	Homo	Exp.	0.4051	0.0865	0.0865	0.0000	0.0000	0.0000
1.0 0.0 0.0	PbPb	MD	0.3872	0.0560	0.0556	−0.0013	−0.0004	0.0021
	TeTe	MD	0.3780	0.0561	0.0554	0.0002	0.0010	0.0069
		Exp.	0.1255	0.0755	0.0539	0.0111	0.0000	0.0000
1.0 0.5 0.0	PbTe							
		MD	0.0996	0.0504	0.0234	0.0104	−0.0000	0.0001
	Homo	Exp.	0.0778	0.0499	0.0499	0.0060	0.0060	0.0074
1.0 0.5 0.5	PbPb	MD	0.0441	0.0217	0.0161	0.0031	0.0046	0.0064
	TeTe	MD	0.0625	0.0300	0.0263	0.0020	0.0013	0.0013
	Homo	Exp.	0.0791	0.0791	0.0348	0.0116	0.0000	0.0000
1.0 1.0 0.0	PbPb	MD	0.0553	0.0488	0.0054	0.0084	−0.0011	0.0016
	TeTe	MD	0.0513	0.0442	0.0104	0.0061	−0.0004	0.0021
		Exp.	0.0526	0.0526	0.0384	0.0041	0.0024	0.0024
1.0 1.0 0.5	PbTe							
		MD	0.0238	0.0204	0.0093	0.0017	0.0006	0.0007
	Homo	Exp.	0.0378	0.0378	0.0378	0.0038	0.0038	0.0038
1.0 1.0 1.0	PbPb	MD	0.0063	0.0207	−0.0013	0.0021	−0.0014	0.0014
	TeTe	MD	0.0090	0.0248	0.0015	0.0011	−0.0011	0.0011
		Exp.	0.2145	0.0392	0.0392	0.0000	0.0000	0.0000
1.5 0.0 0.0	PbTe							
		MD	0.2068	0.0118	0.0098	0.0000	−0.0002	−0.0018
	Homo	Exp.	0.1079	0.0390	0.0299	0.0241	0.0000	0.0000
1.5 0.5 0.0	PbPb	MD	0.0807	0.0094	−0.0013	0.0217	0.0004	0.0005
	TeTe	MD	0.1053	0.0133	0.0054	0.0096	0.0006	0.0008
		Exp.	0.0664	0.0331	0.0331	0.0018	0.0018	−0.0002
1.5 0.5 0.5	PbTe							
		MD	0.0472	0.0027	0.0027	0.0005	0.0012	−0.0008
		Exp.	0.0640	0.0369	0.0255	0.0078	0.0000	0.0000
1.5 1.0 0.0	PbTe							
		MD	0.0391	0.0086	−0.0026	0.0066	0.0002	−0.0000
	Homo	Exp.	0.0478	0.0297	0.0230	0.0052	0.0053	0.0017
1.5 1.0 0.5	PbPb	MD	0.0192	0.0010	−0.0032	0.0023	0.0028	0.0004
	TeTe	MD	0.0263	0.0045	−0.0000	0.0014	0.0006	−0.0003
		Exp.	0.0366	0.0248	0.0248	0.0026	0.0026	0.0010
1.5 1.0 1.0	PbTe							
		MD	0.0076	0.0001	−0.0089	0.0009	−0.0002	0.0001
	Homo	Exp.	0.0358	0.0358	0.0151	0.0150	0.0000	0.0000
1.5 1.5 0.0	PbPb	MD	0.0096	0.0048	−0.0053	0.0133	0.0011	0.0024
	TeTe	MD	0.0113	0.0070	−0.0054	0.0064	0.0010	0.0013
		Exp.	0.0299	0.0299	0.0172	0.0038	0.0007	0.0007
1.5 1.5 0.5	PbTe							
		MD	0.0031	0.0001	−0.0069	0.0013	0.0001	0.0003

TABLE II. *(Continued.)*

Δx	Pairs	Source	Cor_{11}	Cor_{22}	Cor_{33}	Cor_{12}	Cor_{13}	Cor_{23}
	Homo	Exp.	0.0228	0.0228	0.0159	0.0052	0.0021	0.0021
1.5 1.5 1.0	PbPb	MD	−0.0033	−0.0087	−0.0081	0.0006	0.0017	−0.0005
	TeTe	MD	−0.0008	−0.0045	−0.0086	−0.0000	−0.0001	0.0010
		Exp.	0.0172	0.0172	0.0172	0.0016	0.0016	0.0016
1.5 1.5 1.5	PbTe							
		MD	−0.0102	−0.0075	−0.0132	0.0007	−0.0005	0.0005
	Homo	Exp.	0.1798	0.0170	0.0170	0.0000	0.0000	0.0000
2.0 0.0 0.0	PbPb	MD	0.1829	−0.0041	−0.0179	0.0018	−0.0003	−0.0013
	TeTe	MD	0.1710	0.0065	−0.0101	−0.0001	−0.0000	−0.0022
		Exp.	0.0873	0.0278	0.0198	0.0052	0.0000	0.0000
2.0 0.5 0.0	PbTe							
		MD	0.0706	−0.0056	−0.0052	0.0038	−0.0000	−0.0001
	Homo	Exp.	0.0591	0.0184	0.0184	0.0040	0.0040	0.0027
2.0 0.5 0.5	PbPb	MD	0.0376	−0.0008	−0.0125	0.0021	0.0021	0.0006
	TeTe	MD	0.0568	0.0033	−0.0092	0.0015	0.0020	0.0012
	Homo	Exp.	0.0585	0.0215	0.0128	0.0073	0.0000	0.0000
2.0 1.0 0.0	PbPb	MD	0.0365	−0.0041	−0.0072	0.0062	0.0004	0.0002
	TeTe	MD	0.0379	−0.0030	−0.0061	0.0036	0.0000	0.0006
		Exp.	0.0420	0.0212	0.0141	0.0028	0.0015	0.0006
2.0 1.0 0.5	PbTe							
		MD	0.0193	−0.0057	−0.0073	0.0013	0.0003	−0.0001
	Homo	Exp.	0.0308	0.0156	0.0156	0.0027	0.0027	0.0011
2.0 1.0 1.0	PbPb	MD	0.0070	−0.0021	−0.0132	0.0017	0.0010	0.0002
	TeTe	MD	0.0100	−0.0029	−0.0133	0.0001	−0.0011	0.0013
		Exp.	0.0329	0.0202	0.0114	0.0054	0.0000	0.0000
2.0 1.5 0.0	PbTe							
		MD	0.0040	−0.0046	−0.0109	0.0045	0.0001	−0.0002
	Homo	Exp.	0.0274	0.0168	0.0099	0.0050	0.0016	0.0016
2.0 1.5 0.5	PbPb	MD	−0.0010	−0.0053	−0.0103	0.0023	0.0018	0.0019
	TeTe	MD	0.0020	−0.0047	−0.0125	0.0013	0.0004	0.0004
		Exp.	0.0230	0.0152	0.0113	0.0025	0.0015	0.0008
2.0 1.5 1.0	PbTe							
		MD	−0.0066	−0.0102	−0.0124	0.0003	0.0005	0.0008
	Homo	Exp.	0.0163	0.0104	0.0104	0.0023	0.0023	0.0020
2.0 1.5 1.5	PbPb	MD	−0.0117	−0.0107	−0.0131	0.0006	0.0012	0.0020
	TeTe	MD	−0.0121	−0.0121	−0.0160	0.0006	−0.0002	0.0002
	Homo	Exp.	0.0211	0.0211	0.0062	0.0081	0.0000	0.0000
2.0 2.0 0.0	PbPb	MD	−0.0043	−0.0032	−0.0226	0.0073	−0.0039	−0.0033
	TeTe	MD	−0.0068	−0.0050	−0.0217	0.0022	0.0004	0.0004
		Exp.	0.0187	0.0187	0.0076	0.0042	0.0005	0.0005
2.0 2.0 0.5	PbTe							
		MD	−0.0078	−0.0074	−0.0208	0.0015	0.0007	0.0004
	Homo	Exp.	0.0150	0.0150	0.0069	0.0034	0.0012	0.0012
2.0 2.0 1.0	PbPb	MD	−0.0111	−0.0109	−0.0202	0.0004	0.0014	0.0007
	TeTe	MD	−0.0110	−0.0110	−0.0203	0.0001	0.0009	0.0009
		Exp.	0.0121	0.0121	0.0079	0.0017	0.0011	0.0011
2.0 2.0 1.5	PbTe							
		MD	−0.0134	−0.0145	−0.0206	0.0003	0.0006	0.0004
	Homo	Exp.	0.0079	0.0079	0.0079	0.0012	0.0012	0.0012
2.0 2.0 2.0	PbPb	MD	−0.0234	−0.0187	−0.0163	0.0010	−0.0005	−0.0010
	TeTe	MD	−0.0219	−0.0231	−0.0179	0.0008	0.0002	0.0001

APPENDIX E: EXPERIMENTAL DIPOLE CORRELATIONS IN HARMONIC APPROXIMATION

The experimental diffuse scattering only provides access to the pair distribution function. Strictly speaking, the interaction between two dipoles represents a three- or four-body problem,

and cannot be accessed experimentally. However, the strongest component of this higher-order correlations will be defined by the pairwise interaction, which we show here.

We use the harmonic approximation in this chapter, i.e., we assume that displacements of all atoms have Gaussian
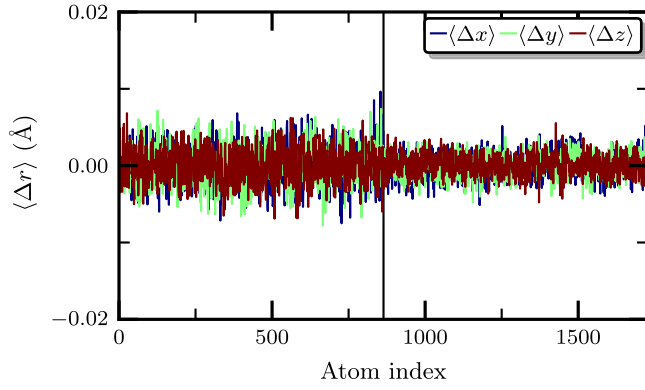
FIG. 23. Average displacements of all atoms from the rock-salt high-symmetry positions during the MD simulation at 300 K. The left side is for Pb atoms, the right for Te atoms.

distributions

$$p(r_{\text{Te}}) \propto \exp\left(-\tfrac{1}{2}r^T U^{-1} r\right).$$ (E1)

In the same manner, we approximate the distance between two atoms in a linear fashion:

$$d_i = x_{\text{Te}} - x_{\text{Pb}}.$$ (E2)

In this approximation, the interatomic distances have a Gaussian distribution. Then, the probability distribution of distances between pairs of atoms would be distributed in a jointly Gaussian manner:

$$p(d_i, d_j) \propto \exp\left[-\frac{\Delta d_i^2 + \Delta d_j^2 + 2c_{ij}\Delta d_i \Delta d_j}{2(1 - c_{ij}^2)}\right],$$ (E3)

where c_{ij} is the correlation coefficient, and $\Delta d_i = d_i - \langle d_i \rangle$. This means that the shape of the dipole distribution for B_i^j plots can be produced by subtracting two Gaussians from each
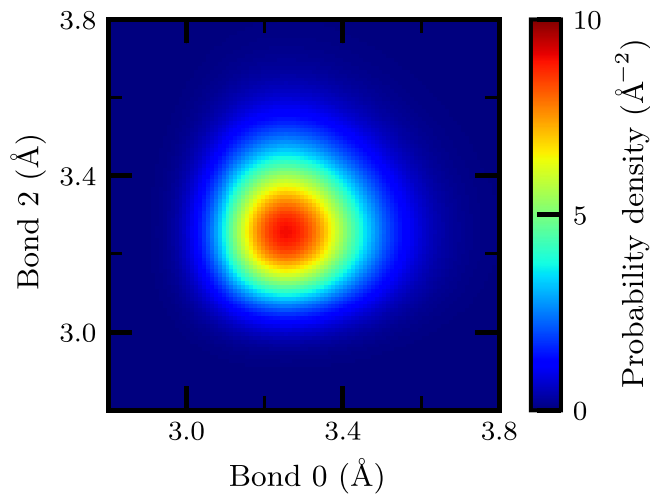

FIG. 24. Probability density for the reference state describing uncorrelated bonds; all pairs of bonds at least 15 Å apart were considered.
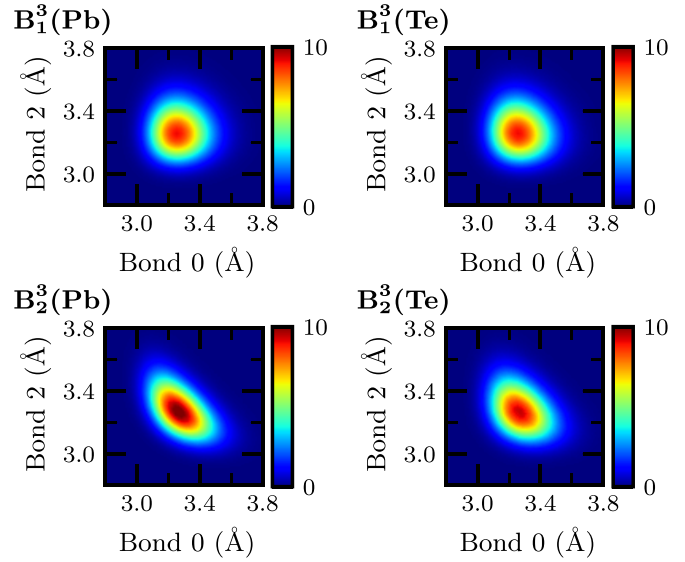

FIG. 25. Probability densities of nearest dipole correlations. The color scale represents the probability density in Å^{-2}.

other:

$$\Delta p(d_i, d_j) = p(d_i, d_j) - p(d_i)p(d_j),$$ (E4)

and thus will be defined only by the correlation coefficient between two displacements.

The correlation coefficients can be calculated from the experimental covariance matrices. By definition,

$$c_{ij} = \frac{\langle \Delta d_i \Delta d_j \rangle}{\sqrt{\langle \Delta d_i^2 \rangle \langle \Delta d_j^2 \rangle}}.$$ (E5)

In the above equation, the pair correlations and displacement parameters, and the nominator can be calculated from the atomic covariances:

$$\langle \Delta d_i \Delta d_j \rangle = \langle (u_{\text{Te}}^i - u_{\text{Pb}}^i)(u_{\text{Te}}^j - u_{\text{Pb}}^j) \rangle$$
$$= \langle u_{\text{Te}}^i u_{\text{Te}}^j \rangle - \langle u_{\text{Pb}}^i u_{\text{Te}}^j \rangle - \langle u_{\text{Te}}^i u_{\text{Pb}}^j \rangle + \langle u_{\text{Pb}}^i u_{\text{Pb}}^j \rangle.$$ (E6)

By combining Eqs. (E4)–(E6), the plots of dipole correlations can be calculated. The only input parameters required for these calculations are the atomic displacement parameters and the pairwise covariances of atomic displacements, all of which are available experimentally in Tables I and II.

Figure 27 represents the plots of $\Delta p(d_i, d_j)$ for the nearest-neighbor dipoles B_1^3 and B_2^3, and should be directly compared to Fig. 12. We see that the values calculated in the harmonic approximation compare nicely with the correlations obtained from the MD sampling. The major difference comes from the fact that MD correlations also capture the effects of anharmonicities, in particular the asymmetric distribution of the interatomic distances of individual pairs and the slight curvature, which is visible in the B_2^3(Pb).
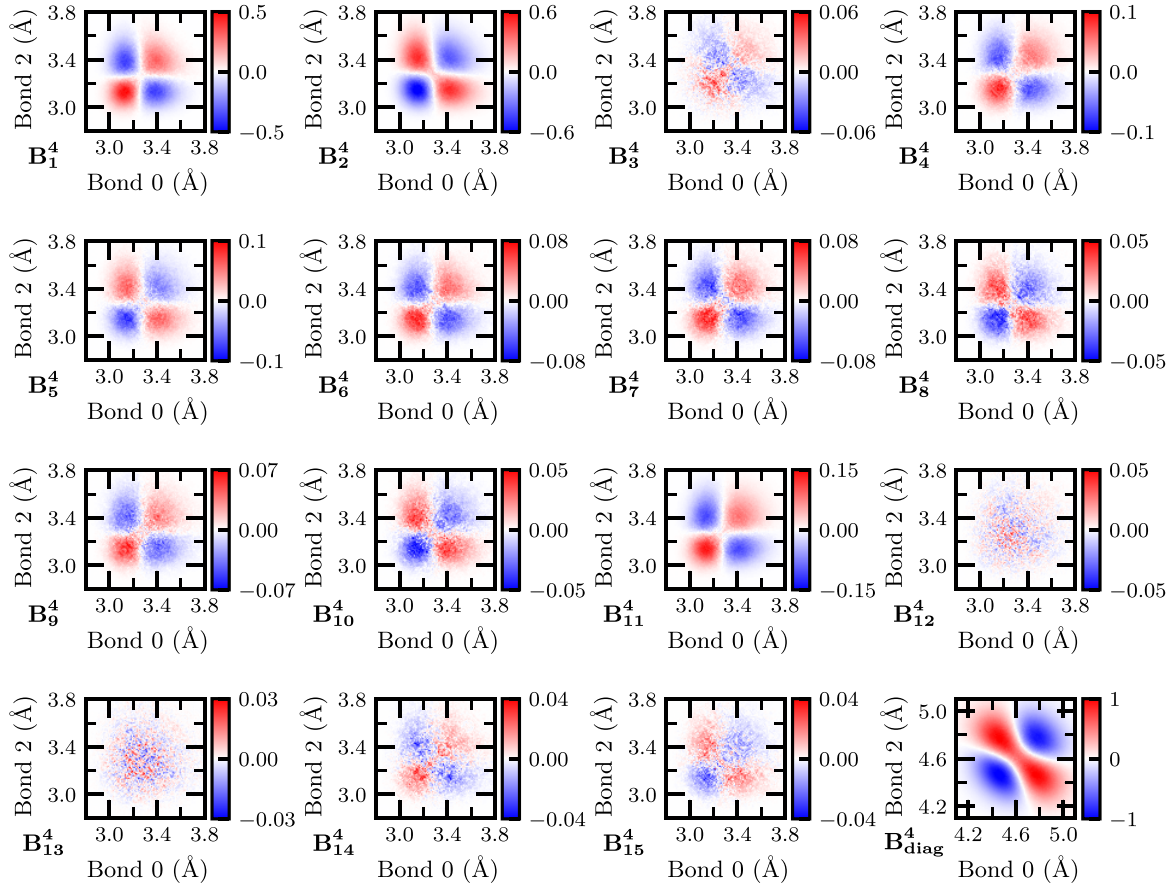
FIG. 26. Difference probability densities with respect to the neutral uncorrelated dipole distribution extracted from the MD simulations. The color scale represents the probability density in Å^{-2}. Note the different color scale in the panels showing the decay in correlation strength.
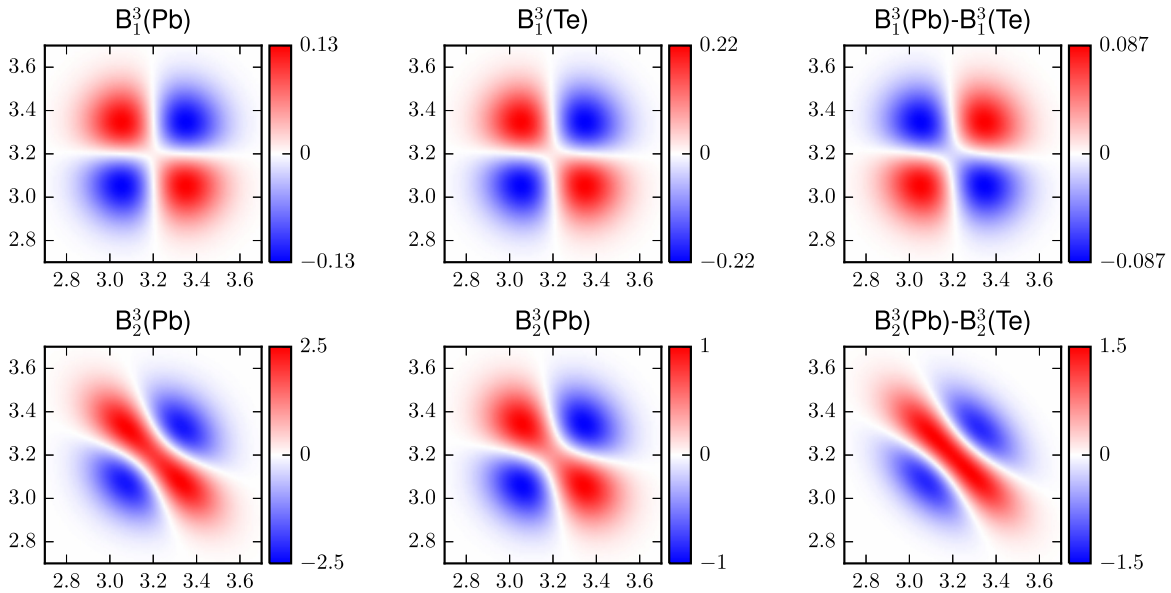
FIG. 27. Difference probability densities of dipole correlations calculated from experimental covariances. The layout is the same as in Fig. 12: the upper panel presents bonds B_1^3; the lower panel bonds B_2^3. The first and second columns show difference densities with respect to the reference when the shared atom is Pb and Te, respectively, while the third column shows the difference between the first and second column. The color scale represents the probability density in Å^{-2}.

[1] R. Bate, D. Carter, and J. Wrobel, Phys. Rev. Lett. **25**, 159 (1970).

[2] E. S. Božin, C. D. Malliakas, P. Souvatzis, T. Proffen, N. A. Spaldin, M. G. Kanatzidis, and S. J. L. Billinge, Science **330**, 1660 (2010).

[3] K. M. O. Jensen, E. S. Božin, C. D. Malliakas, M. B. Stone, M. D. Lumsden, M. G. Kanatzidis, S. M. Shapiro, and S. J. L. Billinge, Phys. Rev. B **86**, 085313 (2012).

[4] O. Delaire, J. Ma, K. Marty, A. F. May, M. A. McGuire, M.-H. Du, D. J. Singh, A. Podlesnyak, G. Ehlers, M. D. Lumsden, and B. C. Sales, Nat. Mater. **10**, 614 (2011).

[5] S. Kastbjerg, N. Bindzus, M. Søndergaard, S. Johnsen, N. Lock, M. Christensen, M. Takata, M. A. Spackman, and B. B. Iversen, Adv. Funct. Mater. **23**, 5477 (2013).

[6] T. Keiber, F. Bridges, and B. C. Sales, Phys. Rev. Lett. **111**, 095504 (2013).

[7] K. S. Knight, J. Phys.: Condens. Matter **26**, 385403 (2014).

[8] S. Christensen, N. Bindzus, M. Sist, M. Takata, and B. B. Iversen, Phys. Chem. Chem. Phys. **18**, 15874 (2016).

[9] P. Souvatzis, O. Eriksson, M. I. Katsnelson, and S. P. Rudin, Comput. Mater. Sci. **44**, 888 (2009).

[10] Y. Zhang, X. Ke, P. R. C. Kent, J. Yang, and C. Chen, Phys. Rev. Lett. **107**, 175503 (2011).

[11] H. Kim and M. Kaviany, Phys. Rev. B **86**, 045213 (2012).

[12] Y. Chen, X. Ai, and C. A. Marianetti, Phys. Rev. Lett. **113**, 105501 (2014).

[13] T. Shiga, T. Murakami, T. Hori, O. Delaire, and J. Shiomi, Appl. Phys. Express **7**, 041801 (2014).

[14] C. W. Li, O. Hellman, J. Ma, A. F. May, H. B. Cao, X. Chen, A. D. Christianson, G. Ehlers, D. J. Singh, B. C. Sales, and O. Delaire, Phys. Rev. Lett. **112**, 175501 (2014).

[15] C. W. Li, J. Ma, H. B. Cao, A. F. May, D. L. Abernathy, G. Ehlers, C. Hoffmann, X. Wang, T. Hong, A. Huq, O. Gourdon, and O. Delaire, Phys. Rev. B **90**, 214303 (2014).

[16] K. R. Knox, E. S. Bozin, C. D. Malliakas, M. G. Kanatzidis, and S. J. L. Billinge, Phys. Rev. B **89**, 014102 (2014).

[17] J. R. Neilson, T. M. McQueen, A. Llobet, J. Wen, and M. R. Suchomel, Phys. Rev. B **87**, 045124 (2013).

[18] D. H. Fabini, G. Laurita, J. S. Bechtel, C. C. Stoumpos, H. A. Evans, A. G. Kontos, Y. S. Raptis, P. Falaras, A. Van der Ven, M. G. Kanatzidis, and R. Seshadri, J. Am. Chem. Soc. **138**, 11820 (2016).

[19] S. J. L. Billinge, R. G. DiFrancesco, G. H. Kwei, J. J. Neumeier, and J. D. Thompson, Phys. Rev. Lett. **77**, 715 (1996).

[20] E. S. Božin, M. Schmidt, A. J. DeConinck, G. Paglia, J. F. Mitchell, T. Chatterji, P. G. Radaelli, T. Proffen, and S. J. L. Billinge, Phys. Rev. Lett. **98**, 137203 (2007).

[21] G. Sheldrick, Acta Crystallogr. A **64**, 112 (2007).

[22] A. Togo and I. Tanaka, Scr. Mater. **108**, 1 (2015).

[23] T. Weber and A. Simonov, Z. Kristallogr. **227**, 238 (2012).

[24] A. Simonov, T. Weber, and W. Steurer, J. Appl. Crystallogr. **47**, 1146 (2014).

[25] B. Qiu, H. Bao, and X. Ruan, in *ASME 2008 3rd Energy Nanotechnology International Conference*, Paper No. ENIC2008-53040 (ASME, 2008), pp. 45–60.

[26] B. Qiu, H. Bao, G. Zhang, Y. Wu, and X. Ruan, Comput. Mater. Sci. **53**, 278 (2012).

[27] S. Plimpton, J. Comput. Phys. **117**, 1 (1995); http://lammps.sandia.gov.

[28] U. V. Waghmare, N. A. Spaldin, H. C. Kandpal, and R. Seshadri, Phys. Rev. B **67**, 125111 (2003).

[29] G. Kresse and J. Furthmüller, Phys. Rev. B **54**, 11169 (1996).

[30] S. Lee, K. Esfarjani, T. Luo, J. Zhou, Z. Tian, and G. Chen, Nat. Commun. **5**, 3525 (2014).

[31] G. Rousse, S. Klotz, A. M. Saitta, J. Rodriguez-Carvajal, M. I. McMahon, B. Couzinet, and M. Mezouar, Phys. Rev. B **71**, 224116 (2005).

[32] A. Walsh, D. J. Payne, R. G. Egdell, and G. W. Watson, Chem. Soc. Rev. **40**, 4455 (2011).

[33] T. Nishimatsu, M. Iwamoto, Y. Kawazoe, and U. V. Waghmare, Phys. Rev. B **82**, 134106 (2010).

[34] W. Zhong, D. Vanderbilt, and K. M. Rabe, Phys. Rev. B **52**, 6301 (1995).

[35] A. Bosak, D. Chernyshov, S. Vakhrushev, and M. Krisch, Acta Crystallogr. A **68**, 117 (2012).

[36] V. F. Sears, Neutron News **3**, 26 (1992).

[37] P. Juhás, T. Davis, C. L. Farrow, and S. J. L. Billinge, J. Appl. Crystallogr. **46**, 560 (2013).

[38] C. L. Farrow, P. Juhas, J. W. Liu, D. Bryndin, E. S. Božin, J. Bloch, T. Proffen, and S. J. L. Billinge, J. Phys.: Condens. Matter **19**, 335219 (2007).

[39] P. Boher, P. Garnier, J. R. Gavarri, and A. W. Hewat, J. Solid State Chem. **57**, 343 (1985).

[40] C. Wood, Rep. Prog. Phys. **51**, 459 (1988).

[41] J. P. Heremans, V. Jovovic, E. S. Toberer, A. Saramat, K. Kurosaki, A. Charoenphakdee, S. Yamanaka, and G. J. Snyder, Science **321**, 554 (2008).

[42] J. Androulakis, I. Todorov, D.-Y. Chung, S. Ballikaya, G. Wang, C. Uher, and M. Kanatzidis, Phys. Rev. B **82**, 115209 (2010).

[43] L. D. Zhao, H. J. Wu, S. Q. Hao, C. I. Wu, X. Y. Zhou, K. Biswas, J. Q. He, T. P. Hogan, C. Uher, C. Wolverton, V. P. Dravid, and M. G. Kanatzidis, Energy Environ. Sci. **6**, 3346 (2013).

[44] A. P. Gonçalves and C. Godart, Eur. Phys. J. B **87**, 42 (2014).

[45] L.-D. Zhao, V. P. Dravid, and M. G. Kanatzidis, Energy Environ. Sci. **7**, 251 (2014).

[46] C. Han, Q. Sun, Z. Li, and S. X. Dou, Adv. Energy Mater. **6**, 1600498 (2016).

[47] G. Tan, F. Shi, S. Hao, L.-D. Zhao, H. Chi, X. Zhang, C. Uher, C. Wolverton, V. P. Dravid, and M. G. Kanatzidis, Nat. Commun. **7**, 12167 (2016).

[48] M. D. Nielsen, V. Ozolins, and J. P. Heremans, Energy Environ. Sci. **6**, 570 (2013).

[49] W. G. Zeier, A. Zevalkink, Z. M. Gibbs, G. Hautier, M. G. Kanatzidis, and G. J. Snyder, Angew. Chem. Int. Ed. **55**, 6826 (2016).

[50] P. Giraldo-Gallo, B. Sangiorgio, P. Walmsley, H. J. Silverstein, M. Fechner, S. C. Riggs, T. H. Geballe, N. A. Spaldin, and I. R. Fisher, Phys. Rev. B **94**, 195141 (2016).

[51] Y. Pei, X. Shi, A. LaLonde, H. Wang, L. Chen, and G. J. Snyder, Nature (London) **473**, 66 (2011).

[52] Y. Pei, H. Wang, and G. J. Snyder, Adv. Mater. **24**, 6125 (2012).

[53] J. He, M. G. Kanatzidis, and V. P. Dravid, Mater. Today **16**, 166 (2013).

[54] G. J. Tan, L.-D. Zhao, and M. G. Kanatzidis, Chem. Rev. **116**, 12123 (2016).

[55] H. Zhu, W. Sun, R. Armiento, P. Lazic, and G. Ceder, Appl. Phys. Lett. **104**, 082107 (2014).

[56] Z. M. Gibbs, H. Kim, H. Wang, R. L. White, F. Drymiotis, M. Kaviany, and G. Jeffrey Snyder, Appl. Phys. Lett. **103**, 262109 (2013).

[57] J. Zhao, C. D. Malliakas, K. Wijayaratne, V. Karlapati, N. Appathurai, D. Y. Chung, S. Rosenkranz, M. G. Kanatzidis, and U. Chatterjee, Europhys. Lett. **117**, 27006 (2017).

[58] P. Fons, A. V. Kolobov, M. Krbal, J. Tominaga, K. S. Andrikopoulos, S. N. Yannopoulos, G. A. Voyiatzis, and T. Uruga, Phys. Rev. B **82**, 155209 (2010).

[59] M. A. Estermann and W. Steurer, Phase Transit. **67**, 165 (1998).

[60] R. Blessing, J. Appl. Crystallogr. **30**, 421 (1997).

[61] Agilent Technologies, CRYSALISPRO 1.171.36.20.

[62] CP2K developers group, CP2K: Open Source Molecular Dynamics, http://www.cp2k.org/about.

[63] G. Lippert, J. Hutter, and M. Parrinello, Mol. Phys. **92**, 477 (1997).

[64] J. VandeVondele, M. Krack, F. Mohamed, M. Parrinello, T. Chassaing, and J. Hutter, Comput. Phys. Commun. **167**, 103 (2005).

[65] J. P. Perdew, A. Ruzsinszky, G. I. Csonka, O. A. Vydrov, G. E. Scuseria, L. A. Constantin, X. Zhou, and K. Burke, Phys. Rev. Lett. **100**, 136406 (2008).

[66] J. M. Skelton, D. Tiana, S. C. Parker, A. Togo, I. Tanaka, and A. Walsh, J. Chem. Phys. **143**, 064710 (2015).

[67] C. Hartwigsen, S. Goedecker, and J. Hutter, Phys. Rev. B **58**, 3641 (1998).

[68] M. Krack, Theor. Chem. Acc. **114**, 145 (2005).

[69] G. Bussi, D. Donadio, and M. Parrinello, J. Chem. Phys. **126**, 014101 (2007).

[70] P. E. Blöchl, Phys. Rev. B **50**, 17953 (1994).

[71] G. Kresse and D. Joubert, Phys. Rev. B **59**, 1758 (1999).

[72] H. J. C. Berendsen, J. P. M. Postma, W. F. van Gunsteren, A. DiNola, and J. R. Haak, J. Chem. Phys. **81**, 3684 (1984).

[73] M. Kobas, T. Weber, and W. Steurer, Phys. Rev. B **71**, 224205 (2005).

[74] M. Kobas, T. Weber, and W. Steurer, Phys. Rev. B **71**, 224206 (2005).

Local orbital degeneracy lifting as a precursor to an orbital-selective Peierls transition

E.S. Bozin [1], W.G. Yin [1], R.J. Koch[1], M. Abeykoon[2], Y.S. Hor[3,5], H. Zheng[3], H.C. Lei[1,6], C. Petrovic[1], J.F. Mitchell[3] & S.J.L. Billinge [1,4]

Fundamental electronic principles underlying all transition metal compounds are the symmetry and filling of the d-electron orbitals and the influence of this filling on structural configurations and responses. Here we use a sensitive local structural technique, x-ray atomic pair distribution function analysis, to reveal the presence of fluctuating local-structural distortions at high temperature in one such compound, $CuIr_2S_4$. We show that this hitherto overlooked fluctuating symmetry-lowering is electronic in origin and will modify the energy-level spectrum and electronic and magnetic properties. The explanation is a local, fluctuating, orbital-degeneracy-lifted state. The natural extension of our result would be that this phenomenon is likely to be widespread amongst diverse classes of partially filled nominally degenerate d-electron systems, with potentially broad implications for our understanding of their properties.

[1] Condensed Matter Physics and Materials Science Department, Brookhaven National Laboratory, Upton, NY 11973, USA. [2] Photon Sciences Division, Brookhaven National Laboratory, Upton, NY 11973, USA. [3] Materials Science Division, Argonne National Laboratory, Argonne, IL 60439, USA. [4] Department of Applied Physics and Applied Mathematics, Columbia University, New York, NY 10027, USA. [5] Present address: Department of Physics, Missouri University of Science and Technology, Rolla, MO 65409, USA. [6] Present address: Department of Physics and Beijing Key Laboratory of Opto-electronic Functional Materials and Micro-nano Devices, Renmin University of China, 100872 Beijing, China. Correspondence and requests for materials should be addressed to E.S.B. (email: bozin@bnl.gov) or to S.J.L.B. (email: sb2896@columbia.edu)

Broken symmetry ground states are often found in transition metal systems exhibiting emergent properties such as metal-insulator transitions[1–3], charge-ordered and charge-density wave states[4], colossal magnetoresistive effects[5], frustrated magnetism[6,7], pseudogap[8] and high-temperature super-conductivity[9,10]. These are generally driven by electronic inter-actions understood as Fermi-surface nesting[11–13], Peierls distortions[14,15], and cooperative Jahn-Teller effects[16]. These phenomena have energy scales of hundreds to thousands of meV[17], corresponding to thousands of Kelvin, yet the broken symmetries tend to appear at much lower temperatures, typically 10^1–10^2 K. The symmetry-broken states at low temperature, have been extensively studied. Fewer details are known about what happens when these materials transition to crystallographically higher symmetry structures upon warming.

Here we present a study that reveals critical insights into the unaccounted for separation in energy scales by applying a quantitative local structure probe, atomic pair distribution function analysis (PDF), to a model material system that exemplifies this behavior. The material system, $CuIr_2S_4$, has rich broken symmetries in its ground state[18], including the formation of magnetic singlet Ir–Ir pairs, which disappear on warming through a structural transition that is also, concurrently, a metal-insulator transition (MIT). The PDF analysis reveals difficult to detect but important local-structural distortions that exist at high temperatures, something that has been seen before in other systems (see for example Billinge et al.[19]). However, the special scattering characteristics of this system, together with our detailed temperature and doping dependent study with multiple dopant species, exposes fine details of the phenomenon establishing it as a robust but fluctuating d-orbital-degeneracy-lifted (ODL) state that is observed to the highest temperatures measured. Much lower elastic energies govern the long-range ordering of the pre-formed local symmetry-broken ODL objects in these structurally compliant materials[20] which therefore occurs at temperatures much lower than the electronic energies of ODL formation. Interestingly, in $CuIr_2S_4$ it is not the formation of the ODL objects, but their ordering that precipitates the MIT and magnetic dimer formation of the ground state. The fluctuating ODL state is stabilized electronically by breaking d-electron orbital degen-eracies and as such is likely to be a phenomenon that is wide-spread, though not widely appreciated, among the many materials with incompletely filled d-electron manifolds[21,22], many of which have important emergent low-temperature electronic and mag-netic behaviors, from classics such as manganites[11,23,24], cup-rates[4,9,25], and iron chalcogenides/pnictides[7,10,26–29], to materials featuring exotic low-temperature orbital molecules[30,31]. It may also explain the unexpected observation of phonon-glass-like thermal conductivity in various transition metal oxides[32].

Results

Long-range orbital and charge order and spin dimerization.

The low-temperature insulating state in $CuIr_2S_4$[33–35] consists of ordered Ir^{3+} ($5d^6$) and Ir^{4+} ($5d^5$) ions[36], with a four-fold peri-odicity, an example of tetrameric charge ordering[37]. Con-currently, spin dimerization of Ir^{4+} pairs occurs within the tetramer, with large associated structural distortions as they move towards each other, making this charge order particularly amenable to detection using structural probes[18]. Notwithstanding the complexities of the insulating state, including formation of remarkable three-dimensional $Ir_8^{3+}S_{24}$ and $Ir_8^{4+}S_{24}$ molecule-like assemblies embedded in the lattice, its quasi-one-dimensional character was unmasked and MIT attributed to an orbital-selective Peierls mechanism, postulated from topological con-siderations[38]. The global symmetry lowering at the MIT was

declared to lift the existing t_{2g} d-orbital degeneracies[38]. Although the high-temperature crystallographically cubic metallic state[18,33] appears to be undistorted, with nominally $Ir^{3.5+}$ ($5d^{5.5}$) partially filled delocalized bands[39], $CuIr_2S_4$ does not behave like a band-metal, as evidenced by anomalous transport and spectroscopic signatures[40,41]. Despite early speculations to the contrary[40–42], it was established that the structural dimers disappear on warming through the transition on all length scales, leaving the mystery of poor metallicity unresolved[39]. Curiously, the isostructural and isoelectronic sister compound, $CuIr_2Se_4$, has an order of magni-tude higher conductivity and no MIT down to 0.5 K[40], which is also difficult to rationalize within the current understanding of these systems.

In our high-sensitivity x-ray pair distribution function (xPDF) analysis of the high-temperature metallic state of $CuIr_2S_4$ we uncover a previously unobserved local symmetry lowering of the Ir pyrochlore sublattice, associated with an orbital liquid-like state that is present to the highest measured temperature. Through judicious chemical substitutions, we demonstrate that the effect is electronic and that it involves a symmetry lowering of the molecular orbitals, or Ir metal-metal bonds, on the pyrochlore sublattice. This is related to, but qualitatively different from, the dimer state observed in the insulating phase. It is Jahn-Teller like, in that the symmetry lowering breaks the degeneracy of partially filled Ir d states, which results in orbital selectivity, with charges preferrentially selecting a subset of Ir–Ir metal–metal orbitals. At high temperature the selected orbitals do not order and are presumably fluctuating. This orbital liquid-like precursor state crystallizes upon approaching the Peierls-like MIT, testifying to the crucial role of orbital physics[38].

Structural fingerprint of the ODL state.

The PDF consists of peaks whose position is at interatomic distances in a material. It is therefore sensitive to any structural perturbation, because sharp single-valued PDF peaks in a high symmetry structure become broadened or multicomponent when the symmetry is lowered. In the low-temperature state of $CuIr_2S_4$, long-range orbital and charge order results in Ir^{4+}–Ir^{4+} pairs forming structural and magnetic dimers, which have been established crystal-lographically[18]. The Ir–Ir dimer pair distance is ~0.5 Å shorter than that of the Ir–Ir non-dimer pairs, creating two well-resolved peaks in the low-temperature PDF. In fact, the PDF dimer-peaks can be clearly seen by eye in the stack of PDFs shown as a function of temperature in Fig. 1a as a vertical ridge in the waterfall plot at ≈3 Å, labeled with the red arrow.

The dimers disappear in the average structure at T_{MI}[18], but they also disappear in the local structure, as first reported in ref. 39, and which can be seen directly in the data in Fig. 1a. There is no dimer-liquid state at high temperature in $CuIr_2S_4$, and the dimers themselves disappear at T_{MI}, which rules out fluctuating dimers as the culprit behind the poor metallicity at high temperature.

We have approached the question of the anomalous metallic state by measuring a new, more complete and higher precision set of xPDF data from $CuIr_2S_4$ (Fig. 1a), where we now focus on the high-temperature metallic state above T_{MI}. The average crystal structure in this regime is cubic spinel, space-group $Fd\bar{3}m$, in which the iridium ions make a pyrochlore sublattice that consists of a network of regular corner-shared tetrahedra illustrated in Fig. 1d. The high symmetry of this cubic structure results in an apparent sharpening of peaks in the PDF, as is evident in the waterfall plot in Fig. 1a, where PDF peak sharpening is observed on warming through T_{MI} (normally PDF peaks broaden on warming due to increased atomic thermal motion). This occurs because the higher symmetry (cubic) phase has fewer PDF peaks
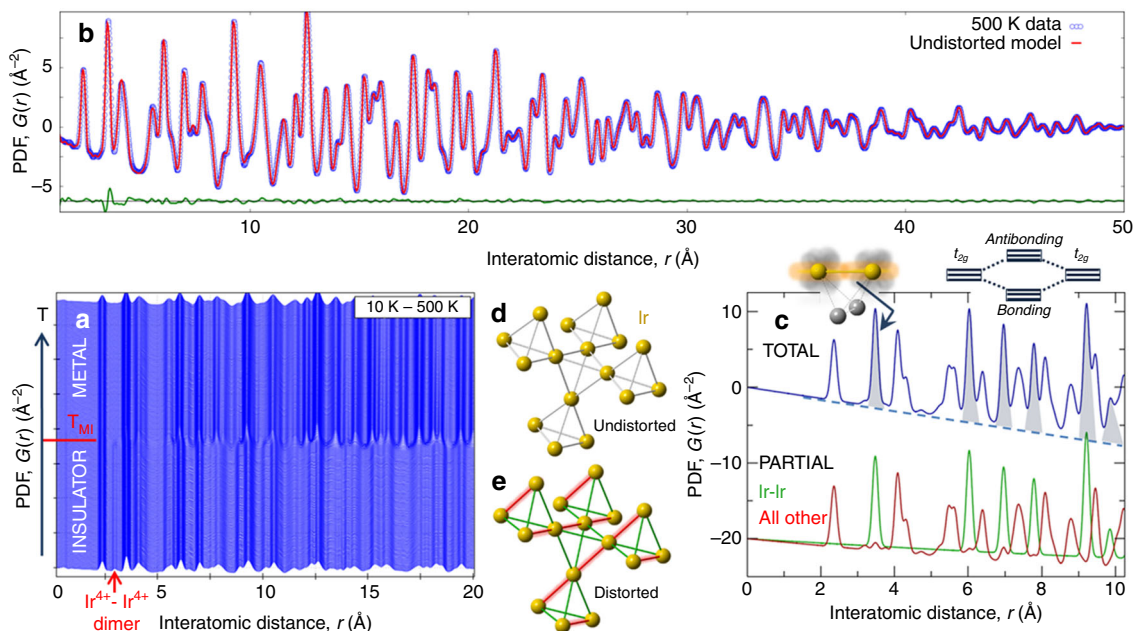
Fig. 1 Observation of high-temperature fluctuating ODL state in $CuIr_2S_4$. **a** Temperature waterfall stack of xPDFs measured on warming from 10 K (bottom) to 500 K (top) in 2 K increments. T_{MI} is the MIT transition temperature (226 K). The dimer peak at ~3 Å (marked by arrow) is only seen in the insulating phase, and disappears above T_{MI}. **b** Fit of the undistorted cubic $Fd\overline{3}m$ model (red line) to the 500 K data (blue open circles) and their difference (green line, offset for clarity) unmask the footprint of the localized ODL state at ~3.5 Å. **c** Simulated $Fd\overline{3}m$ total xPDF of $CuIr_2S_4$ (blue line), decomposed into Ir-Ir partial xPDF (green line) and its complement (red line). Shaded peaks in total xPDF are sensitive to t_{2g} orbital overlaps (sketched) and their spatial correlations. Inset: t_{2g}-derived molecular orbitals discussed in the main text. **d, e** Section of Ir pyrochlore sublattice of corner-shared Ir_4 tetrahedra for undistorted (cubic) and distorted (tetragonal) spinel structure, respectively. The strongest t_{2g} orbital overlaps (e.g. xy with xy, etc.) are along the chains formed by the tetrahedral edges of the Ir sublattice[38]

than the lower symmetry (triclinic) phase. Indeed, fits of the cubic structure model to the high-T data result in excellent agreement (e.g., for $T = 500$ K, $r_w = 5.1\%$, Fig. 1b) Under normal circumstances this would be considered a highly satisfactory PDF fit. However, careful inspection of the residual curve in green in Fig. 1b reveals a feature at around 3.5 Å, indicating a shift in intensity to higher-r in the data compared to the model.

The PDF peak centered at 3.5 Å originates almost exclusively from the Ir–Ir nearest neighbor atomic pair on the pyrochlore sublattice, as shown in Fig. 1c. The total PDF consists of the weighted sum of partial PDFs between pairs of each type of atom, and Fig. 1c shows that the Ir–Ir partial-PDF contributes more than 95% of the signal to the 3.5 Å peak in the total PDF. The residual signal therefore clearly originates from deviation of the structural geometry from the regular pyrochlore lattice implied by the cubic model. Importantly, maximal t_{2g} overlaps of the orbitals of the same type (xy with xy, yz with yz, and zx with zx) are precisely along the directions defined by the edges of the pyrochlore lattice[38], as sketched in the inset to Fig. 1c, implying that the orbital sector is involved.

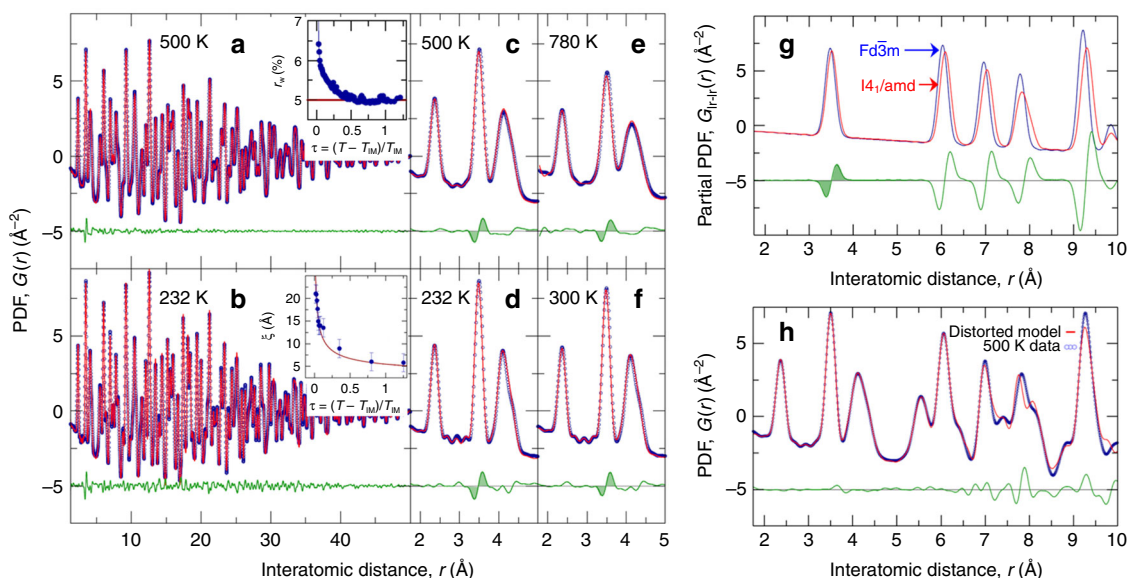**Temperature evolution and characterization of the ODL state**. To explore the temperature dependence, the same analysis is carried out on PDFs measured at temperatures up to 780 K and representative fits are shown in Fig. 2a–f. The result of the fitting for the 500 K dataset is reproduced in Fig. 2a over the entire r-range, and then on a narrower r-scale in Fig. 2c, with the residual signal highlighted. The same signal in the residual is also evident at 232 K, 300 K and in the 780 K data (Fig. 2d–f, respectively). The 232 K dataset is from immediately above the MI transition temperature (226 K on warming).

To explore the structural origin of this residual signal we utilized structural models that allowed for distortions to the

pyrochlore sublattice, and focused on a model in the $I4_1/amd$ space group that was implicated in the early studies of the low-temperature phase[33]. In particular, the tetragonal distortion lowers the symmetry of the regular Ir_4 pyrochlore tetrahedra, yielding 2 short and 4 long Ir-pair distances (Fig. 1e). Comparison of PDFs computed from the distorted and undistorted models, as seen in Fig. 2g, results in a difference curve that qualitatively reproduces the residual signal observed at 3.5 Å, Fig. 1b, when fitting with an undistorted cubic model. However, the tetragonal distortion leads to additional features in the PDF which are not seen in the measured data, suggesting that the tetragonal distortion is not appropriate at all length scales. Here we take advantage of the real-space nature of the PDF, and fit a tetragonal model over the narrow range $1.5 < r < 6$ Å. This removes the residual signal at 3.5 Å (Fig. 2h) and introduces only a single additional refinement parameter (tetragonal axis). The resulting fit produced a tetragonal distortion of 0.08(1) Å, which corresponds to long Ir–Ir bonds of 3.52 Å and short Ir–Ir bonds of 3.44 Å.

This disparity in symmetry paints a clear picture where Ir_4 tetrahedra, each with a local tetragonal distortion, are oriented in a disordered manner, such that individual distortions do not accumulate over long length scales, but rather average to a cubic symmetry. This is consistent with the observation that the low-r portion of the PDF can be reproduced well only when using a tetragonally distorted model, but that this model fails to reproduce higher-r features. Notably, the magnitude of the structural distortion at high temperature is 7× smaller than the distortion corresponding to the dimer state.

The correlation length of the ordering of such distorted tetrahedra can in principle be extracted from the PDF. Inspection of the residual curve in the 232 K data (Fig. 2b) suggests that at lower temperatures, though still above T_{MI}, the fit of the cubic

Fig. 2 Temperature evolution and character of the ODL state associated distortion. **a–f** Fit of the cubic Fd$\bar{3}$m model (red line) to the CuIr$_2$S$_4$ data at various temperatures as indicated (blue open circles). Difference curve between the data and the model (green line) is offset for clarity in all cases. **g** Simulated Ir–Ir partial xPDFs for undistorted cubic Fd$\bar{3}$m (red line) and distorted tetragonal I4$_1$/amd (blue line) structures, with the associated difference between the tetragonal and cubic models (green line) underneath, offset for clarity. **h** Short range $1.5 < r < 6$ Å fit of the distorted tetragonal model (red line) to the 500 K data (blue open circles), with associated difference curve underneath. The model and residual curves for $r > 6$ Å represent a result of extending the calculation range without altering the fitted parameters. Insets to **a**, **b** show evolution with reduced temperature of the cubic model fit residual, and the estimated local ODL distortion correlation length, respectively. Solid lines are guides to the eye

model is worse than at higher temperature and that the residual signal extends over a wider-range of r, up to 40 Å. This would be the case if the short bonds were beginning to short-range order with some correlation length. The temperature dependence of the correlation length, ξ, can be estimated using previously reported protocols[43] and further described in Methods Section. The result is shown in the inset to Fig. 2b. The correlation length is 6 Å at high temperature, but smoothly increases to 20 Å as the MI transition is approached. This divergent behavior is mimicked if we consider the cubic model fit residual, r_w, as a function of temperature (inset to Fig. 2a).

The symmetry breaking implies a breaking of the degeneracy of orbitals[42], which we refer to as an orbital-degeneracy-lifted state, dubbed ODL, on at least some of the Ir tetrahedra. The charge selects and preferrentially enters the lower energy orbitals, which may fluctuate among all the possible edges of the pyrochlore tetrahedra at high temperature (Fig. 3h). Such a phenomenon could be caused by various driving forces, including Jahn-Teller effects, covalency, or spin-orbit coupling[44,45], and we do not speculate on the origin yet. However, we note that orbital selectivity impacts phenomena in diverse systems from VO$_2$[1], K$_2$Cr$_8$O$_{16}$[15], and Sr$_{2-x}$Ca$_x$RuO$_4$[46], to FeSe[21,22,47], but the persistence of orbital selectivity to such high temperatures in a disordered orbital liquid state has not been widely observed. Our data show that the structural and metal-insulator transition on cooling corresponds not to the formation of an orbitally ordered state, but to the phase coherence and resulting long-range ordering of the pre-formed ODL objects.

Electronic manipulation of the ODL state. We now establish an electronic driving force for this ODL effect. Iridium takes on a nominal 5$d^{5.5}$ average electron configuration. In the cubic pyro-chlore lattice the t_{2g} orbitals are well separated in energy from the e_g orbitals due to crystal field effects, and the t_{2g} orbital of one Ir points directly towards the neighboring Ir ion[38,45]. The large

spatial extent of the 5d-states suggests a significant overlap of these orbitals and considerable covalency[45], though this is not required for the discussion. We could then consider the orbital selectivity[17], to happen on a basis of molecular orbitals[48] (inset to Fig. 1c). In this case there would be a symmetry breaking into short and long edges on the pyrochlore tetrahedra depending on the electron filling of the molecular orbital but the incomplete filling of the t_{2g} manifold provides a Jahn-Teller-like driving force for the distortion that lifts the orbital degeneracy. Each Ir has six neighbors to choose from and randomize orbital selectivity. These concepts are illustrated in Fig. 3g, h top.

Altering the charge state of the Ir ions offers a method by which we can test this hypothesis. We have done this by doping Zn^{2+} on the Cu^{1+} site. The zinc doping increases the electron count in the Ir sublattice, without significantly disrupting the lattice[49]. The details are provided in Supplementary Note 1 and Supplementary Fig. 1, and the results are summarized in Fig. 3. Zn doping increases the electron count in an anti-bonding ODL state, marked with an asterisk in Fig. 3g. If the observed structural distortion is driven by a local Jahn-Teller effect, the feature in the residual should diminish with increasing Zn content as doping electrons in an anti-bonding band destabilizes the ODL state. This is exactly what is observed (Fig. 3c, d), establishing the electronic driving force for the effect.

We also consider the substitution of chromium on the iridium sublattice. Chromium is a small ion and introduces a compressive chemical pressure. It also introduces quenched defects into the Ir sublattice, disrupting the ability of Ir orbitals to order over long range at low temperature and suppressing the low-temperature orbital order state[43]. Fits of the cubic model to two of the Cr doped data-sets are shown in Fig. 3e, f. They clearly show that the signal in the residual at 3.5 Å remains robustly up to $x = 8\%$, and indeed is stronger than in the CuIr$_2$S$_4$ endmember, despite the absense of a symmetry-broken ground state. The compressive chemical pressure has the effect of stabilizing the ODL state, possibly due to an increasing Ir–Ir t_{2g} orbital overlap, suggesting
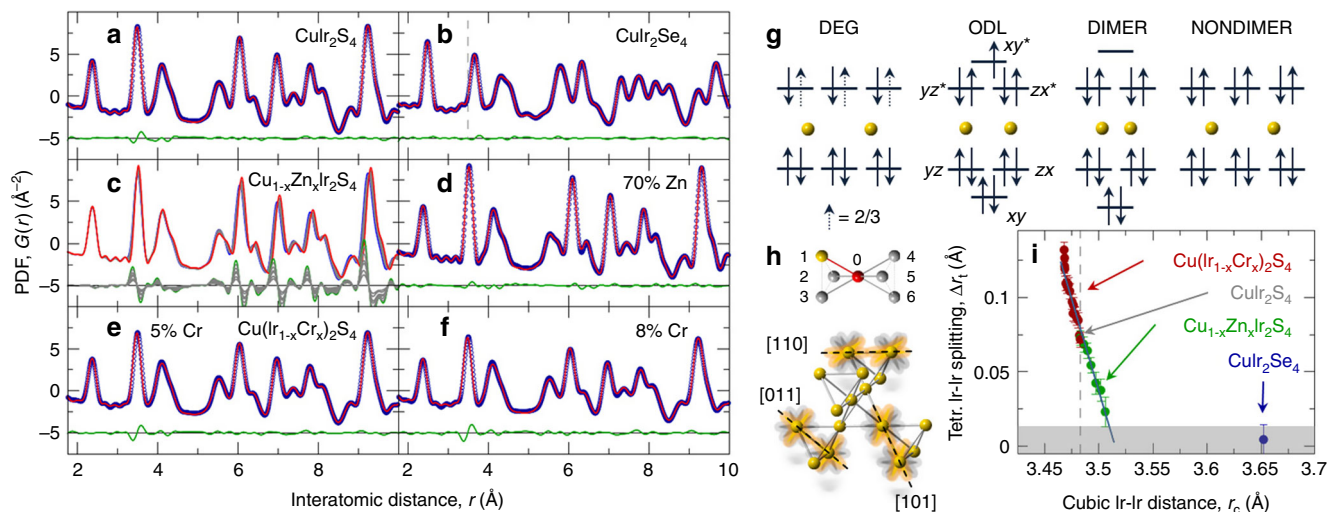
Fig. 3 Manipulation of the ODL state. **a** Fit of the cubic model (red line) to the 300 K $CuIr_2S_4$ data (blue open circles). **b** Fit of the cubic model (red line) to the 300 K $CuIr_2Se_4$ data (blue open circles). **c** Compositional stack of 300 K data for Zn-substituted $CuIr_2S_4$ with Zn content ranging from 0% (blue line) to 70% (red line) in 10% increments (gray lines). The differences between the $CuIr_2S_4$ parent and all other datasets are stacked underneath, offset for clarity. The largest difference between the 0% Zn and 70% Zn datasets is shown in green, other differences in gray, evolving uniformly with Zn content. **d** Fit of the cubic model (red line) to the 300 K 70% Zn-substituted $CuIr_2S_4$ data (blue open circles). **e, f** Fit of the undistorted cubic model (red lines) to the 300 K 5% and 8% Cr-substituted $CuIr_2S_4$ data (blue open circles), respectively. **g** Molecular-orbital (MO) view, from left to right, of degenerate MO, degeneracy-lifted MO, dimerized, and non-dimerized Ir–Ir contacts. In the legend, DEG ($Ir^{3.5+}$), ODL ($Ir^{3.5+}$), DIMER (Ir^{4+}), and NONDIMER (Ir^{3+}). **h** Sketch of [1, 1, 0]-type Ir t_{2g} overlaps (bottom) and six choices for each Ir to form an ODL state (top). **i** Evolution of the ODL distortion, defined as the difference of the Ir–Ir nearest neighbor distance on a pyrochlore lattice extracted from local tetragonal model, with the average Ir–Ir separation in the cubic structure. These are extracted from fits to 300 K data of Cr-substituted (red circles, $0 < x < 0.6$) and Zn-substituted (green circles, $0 < x < 0.7$) samples, as well as pure $CuIr_2S_4$ (gray circle) and $CuIr_2Se_4$ (blue circle). Error bars represent estimated standard uncertainties on the refined parameters. Gray shaded region marks 2σ uncertainty for detecting small tetragonal distortions by the approach utilized here. In $CuIr_2S_4$ there are 0.5 t_{2g} holes per Ir (one hole per pair)[38]. Vertical gray dashed lines in **b**, **i** refer to $CuIr_2S_4$

that the symmetry lowering is among molecular orbitals rather than atomic d-states.

Finally, we consider the sister compound $CuIr_2Se_4$. In this case the ODL signature in the fit residual is absent, Fig. 3b. In $CuIr_2Se_4$ the electron counting arguments are the same as in $CuIr_2S_4$, with the Ir t_{2g} states being at the Fermi-level, implying similar physics. However, the Se ion is considerably larger than the S ion, which would result in a larger inter-Ir distance and reduced Ir–Ir t_{2g} orbital overlap in the case of $CuIr_2Se_4$. In a traditional site-centered Jahn-Teller picture this would not affect the driving force, indeed it may even make the Jahn-Teller distortion larger by lowering the elastic stiffness of the material. However, if covalency between neighboring Ir ions is important, as the data suggest is the case here, we speculate that the reduced orbital overlap of the Ir t_{2g} orbitals would reduce the splitting of the bonding and anti-bonding orbitals, which would reduce the driving force for the distortion. Indeed, we see an anticorrelation between the size of the tetragonal distortion and the magnitude of the average Ir–Ir distance as we vary the composition by Zn doping and Cr doping (Fig. 3i), consistent with a stronger t_{2g} orbital overlap strengthening the ODL effect. The Ir–Ir distance in $CuIr_2Se_4$ is also shown in Fig. 3i, and it is much higher. Notably, we do not observe any tetragonal distortion even in the local structure in $CuIr_2Se_4$, again supporting the importance of the Ir–Ir covalency in the ODL mechanism in this case. The importance of covalency would also suggest that the orbital-degeneracy lifting may be stabilized by pressure, since pressure would increase the overlap of neighboring t_{2g} orbitals. Indeed, under pressure $CuIr_2Se_4$ does undergo a metal-insulator transition as reflected in transport measurements[50]. This observation also provides an explanation of why the MIT temperature increases with pressure in $CuIr_2S_4$[51], a trend opposite to that seen

in conventional Fermi-surface nesting driven charge-density-wave systems.

We have shown that in $CuIr_2S_4$ the origin of the orbital-degeneracy lifting is a local symmetry lowering of Ir–Ir t_{2g} molecular orbitals. We briefly note here that $5d$ ions such as Ir are also susceptible to an orbital-degeneracy lifting due to spin-orbit coupling. ODL due to spin-orbit effects are prevalent in predominately Ir^{4+} oxides such as Sr_2IrO_4[52,53] resulting in an isospin-1/2 relativistic Mott insulating ground-state. We can speculate that in the current $Ir^{3.5+}$ case, and with sufficient orbital overlap, valence electron itinerancy may dominate over the atomic picture that is the basis for the SOC[38]. Learning what factors determine whether SOC or Jahn-Teller effects govern the orbital-degeneracy lifting will be an interesting line of inquiry.

Implications. The characterization of the high-temperature state of $CuIr_2S_4$ as being an ODL state, made up of local symmetry-broken objects stabilized by orbital-degeneracy lifting, presents a potential unifying framework and a new lens through which to view multiple material systems. Calculations that derive from the crystal structure, such as density functional theory calculations, should therefore be modified to account for the very different (tenths of an angstrom) bond-lengths that may be present in the material[54]. This would not be necessary if the ground state consisted simply of ODL objects whose orbitals become ordered over long-range at low temperature. However, often the ground state is quite different from this, as in $CuIr_2S_4$ where it consists of charge order, with structural and magnetic dimers, none of which persist above the MIT and into the ODL state[39]. Likewise, if we view the insulating polaronic state in the colossal magnetoresistant 30% doped $La_{1-x}Ca_xMnO_3$ manganites[55] as an ODL state, the low-temperature ground state has been shown to be absent

structural distortions[19] and is a non-ODL state. In the $CuIr_2S_4$ case long-range ordering may be suppressed due to the geometric frustration of disordering a short Ir–Ir bond over the six edges of the tetrahedron in the pyrochlore lattice, a problem that maps onto the Pauling ice rules[56,57]. The high-temperature ODL state is in general not just a disordered form of the ground state and needs to be studied independently and in its own right. This is not straightforward, requiring probes of local structure and the local electronic system. Because the objects are local and fluctuating, they are not observable in the crystal structure. The ODL objects are also, in general, fluctuating in the disordered ODL state thus requiring probes that are also faster than any fluctuation dynamics. However, because the nature of the ODL formation is electronic, we expect that optically pumped ultrafast time-resolved measurements of local structure should be a powerful approach to investigate ODL[58,59].

Methods

Sample preparation and characterization. Polycrystalline samples of $CuIr_2S_4$, $CuIr_2Se_4$, $(Cu_{1-x}Zn_x)Ir_2S_4$, and $Cu(Ir_{1-x}Cr_x)_2S_4$ were prepared following standard solid state routes in sealed, evacuated quartz ampoules. Stoichiometric quantities of the metals and elemental sulfur or selenium were thoroughly mixed, pelletized, and sealed under vacuum. The ampoules were slowly heated to various temperatures in 650–1100 °C range, as appropriate to targeted compositions, and held at these temperatures for several weeks with intermediate grinding and pressing. All products were found to be single phase based on laboratory x-ray powder diffraction. Standard characterization of DC susceptibility and four-terminal resistivity of the samples were carried out in *Quantum Design* PPMS-9 and MPMS-XL5, and found to be in excellent agreement with other studies[18,33,35,40,49,60].

PDF data collection and analysis. PDF data for $10\,K \leq T \leq 780\,K$ were obtained using standard protocols[61] from synchrotron x-ray total scattering experiments carried out at the 28-ID-2 x-ray powder diffraction (XPD) beamline of the National Synchrotron Light Source II at Brookhaven National Laboratory. The setup utilized a 67.7 keV x-ray beam ($\lambda = 0.183\,Å$), a *Perkin Elmer* amorphous silicon detector, a closed cycle *Cryoindustries of America* helium refrigerator, and a gas flow reactor with flexible coil heater. Two dimensional (2D) diffraction data were collected in rapid acquisition mode[62], with 60 s exposure time for each data set. The raw 2D data (collected on warming) were integrated and converted to intensity versus Q using the software Fit2D[63], where Q is the magnitude of the scattering vector. Data reduction and Sine Fourier transform of measured total scattering structure functions up to a momentum transfer of $Q_{max} = 25\,Å^{-1}$ was carried out using the PDFgetX3[64] program. PDF structure refinements and simulations were carried out using the PDFgui program suite[65].

Correlation length estimate was based on a protocol utilizing a 4-Å wide box car window integration of the residual difference between the data and the cubic $Fd\bar{3}m$ model. ξ is then defined as the r value at which the integral drops by a factor of 2 from its low-r limit, with uncertainty of the estimate conservatively set to half of the window size, similar to correlation length estimates carried out in past PDF studies[43,66].

Data availability

The data supporting the findings of this study are within the Article and its Supplementary Information files and are available from the corresponding author upon request.

References

1. Aetukuri, N. B. et al. Control of the metal-insulator transition in vanadium dioxide by modifying orbital occupancy. *Nat. Phys.* **9**, 661–666 (2013).
2. Tian, Z. et al. Field-induced quantum metal-insulator transition in the pyrochlore iridate $Nd_2Ir_2O_7$. *Nat. Phys.* **12**, 134–138 (2016).
3. Liang, T. et al. Orthogonal magnetization and symmetry breaking in pyrochlore iridate $Eu_2Ir_2O_7$. *Nat. Phys.* **13**, 599–603 (2017).
4. Achkar, A. J. et al. Orbital symmetry of charge-density-wave order in $La_{1.875}Ba_{0.125}CuO_4$ and $YBa_2Cu_3O_{6.67}$. *Nat. Mater.* **15**, 616–620 (2016).
5. Savitzky, B. H. et al. Bending and breaking of stripes in a charge ordered manganite. *Nat. Commun.* **8**, 1883 (2017).
6. Zorko, A., Adamopoulos, O., Komelj, M., Arčon, D. & Lappas, A. Frustration-induced nanometre-scale inhomogeneity in a triangular antiferromagnet. *Nat. Commun.* **5**, 3222 (2014).
7. Glasbrenner, J. K. et al. Effect of magnetic frustration on nematicity and superconductivity in iron chalcogenides. *Nat. Phys.* **11**, 953–958 (2015).
8. Borisenko, S. V. et al. Pseudogap and charge density waves in two dimensions. *Phys. Rev. Lett.* **100**, 196402 (2008).
9. Keimer, B., Kivelson, S. A., Norman, M. R., Uchida, S. & Zaanen, J. From quantum matter to high-temperature superconductivity in copper oxides. *Nature* **518**, 179–186 (2015).
10. Wang, F., Kivelson, S. A. & Lee, D.-H. Nematicity and quantum paramagnetism in FeSe. *Nat. Phys.* **11**, 959–963 (2015).
11. Chuang, Y., Gromko, A., Dessau, D., Kimura, T. & Tokura, Y. Fermi surface nesting and nanoscale fluctuating charge/orbital ordering in colossal magnetoresistive oxides. *Science* **292**, 1509–1513 (2001).
12. Johannes, M. D. & Mazin, I. I. Fermi surface nesting and the origin of charge density waves in metals. *Phys. Rev. B* **77**, 165135 (2008).
13. Terashima, K. et al. Fermi surface nesting induced strong pairing in iron-based superconductors. *Proc. Natl Acad. Sci. USA* **106**, 7330–7333 (2009).
14. Lee, P. A., Rice, T. M. & Anderson, P. W. Fluctuation effects at a peierls transition. *Phys. Rev. Lett.* **31**, 462–465 (1973).
15. Bhobe, P. A. et al. Electronic structure evolution across the Peierls metal-insulator transition in a correlated ferromagnet. *Phys. Rev. X* **5**, 041004 (2015).
16. Huang, H. Y. et al. Jahn-Teller distortion driven magnetic polarons in magnetite. *Nat. Commun.* **8**, 15929 (2017).
17. Khomskii, D. I. *Transition Metal Compounds* (Cambridge University Press, Cambridge, UK, 2014). .
18. Radaelli, P. G. et al. Formation of isomorphic Ir^{3+} and Ir^{4+} octamers and spin dimerization in the spinel $CuIr_2S_4$. *Nature* **416**, 155–158 (2002).
19. Billinge, S. J. L., DiFrancesco, R. G., Kwei, G. H., Neumeier, J. J. & Thompson, J. D. Direct observation of lattice polaron formation in the local structure of $La_{1-x}Ca_xMnO_3$. *Phys. Rev. Lett.* **77**, 715–718 (1996).
20. Billinge, S. J. L. & Duxbury, P. M. Structural compliance, misfit strain and stripe nanostructures in cuprate superconductors. *Phys. Rev. B* **66**, 064529 (2002).
21. Sprau, P. O. et al. Discovery of orbital-selective Cooper pairing in FeSe. *Science* **357**, 75–80 (2017).
22. Kostin, A. et al. Imaging orbital-selective quasiparticles in the Hund's metal state of FeSe. *Nat. Mater.* **17**, 869–874 (2018).
23. Massee, F. et al. Bilayer manganites reveal polarons in the midst of a metallic breakdown. *Nat. Phys.* **7**, 978–982 (2011).
24. Panopoulos, N. et al. Polaron freezing and the quantum liquid-crystal phase in the ferromagnetic metallic $La_{0.67}Ca_{0.33}MnO_3$. *npj Quantum Mater.* **3**, 20 (2018).
25. Scagnoli, V. et al. Observation of orbital currents in CuO. *Science* **332**, 696–698 (2011).
26. Wen, Y.-C. et al. Gap opening and orbital modification of superconducting FeSe above the structural distortion. *Phys. Rev. Lett.* **108**, 267002 (2012).
27. Kasahara, S. et al. Electronic nematicity above the structural and superconducting transition in $BaFe_2(As_{1-x}P_x)_2$. *Nature* **486**, 382–385 (2012).
28. Baek, S.-H. et al. Orbital-driven nematicity in FeSe. *Nat. Mater.* **14**, 210–214 (2015).
29. Frandsen, B. A. et al. Widespread orthorhombic fluctuations in the (Sr, Na) Fe_2As_2 family of superconductors. *Phys. Rev. B* **98**, 180505 (2018).
30. Radaelli, P. G. Orbital ordering in transition-metal spinels. *New J. Phys.* **7**, 53 (2005).
31. Attfield, J. P. Orbital molecules in electronic materials. *APL Mater.* **3**, 041510 (2015).
32. Rivas-Murias, B., Zhou, H. D., Rivas, J. & Rivadulla, F. Rapidly fluctuating orbital occupancy above the orbital ordering transition in spin-gap compounds. *Phys. Rev. B* **83**, 165131 (2011).
33. Furubayashi, T., Matsumoto, T., Hagino, T. & Nagata, S. Structural and magnetic studies of metal-insulator transition in thiospinel $CuIr_2S_4$. *J. Phys. Soc. Jpn* **63**, 3333–3339 (1994).
34. Matsuno, J. et al. Photoemission study of the metal-insulator transition in cuir2s4. *Phys. Rev. B* **55**, R15979 (1997).
35. Nagata, S. et al. Metal-insulator transition in the spinel-type $CuIr_2(S_{1-x}Se_x)_4$ system. *Phys. Rev. B* **58**, 6844–6854 (1998).
36. Takubo, K. et al. X-ray photoemission study of $CuIr_2S_4$: Ir^{3+}-Ir^{4+} charge ordering and the effect of light illumination. *Phys. Rev. Lett.* **95**, 246401 (2005).
37. Croft, M. et al. Metal-insulator transition in $CuIr_2S_4$: XAS results on the electronic structure. *Phys. Rev. B* **67**, 201102 (2003).
38. Khomskii, D. I. & Mizokawa, T. Orbitally induced Peierls state in spinels. *Phys. Rev. Lett.* **94**, 156402 (2005).
39. Božin, E. S., Masadeh, A. S., Hor, Y. S., Mitchell, J. F. & Billinge, S. J. L. Detailed mapping of the local Ir^{4+} dimers through the metal-insulator transitions of $CuIr_2S_4$ thiospinel by x-ray atomic pair distribution function measurements. *Phys. Rev. Lett.* **106**, 045501 (2011).

40. Burkov, A. T. et al. Anomalous resistivity and thermopower of the spinel-type compounds $CuIr_2S_4$ and $CuIr_2Se_4$. *Phys. Rev. B* **61**, 10049–10056 (2000).

41. Takubo, K., Mizokawa, T., Matsumoto, N. & Nagata, S. In-gap state and effect of light illumination in $CuIr_2S_4$ probed by photoemission spectroscopy. *Phys. Rev. B* **78**, 245117 (2008).

42. Yagasaki, K. et al. Hopping conductivity in $CuIr_2S_4$ spinel compound: I. empirical model for electronic configuration and mechanism of metal-insulator transition. *J. Phys. Soc. Jpn* **75**, 074706 (2006).

43. Božin, E. S. et al. $Cu(Ir_{1-x}Cr_x)_2S_4$: a model system for studying nanoscale phase coexistence at the metal-insulator transition. *Sci. Rep.* **4**, 4081 (2014).

44. Streltsov, S. V. & Khomskii, D. I. Covalent bonds against magnetism in transition metal compounds. *Proc. Natl Acad. Sci. USA* **113**, 10491–10496 (2016).

45. Streltsov, S. V. & Khomskii, D. I. Orbital physics in transition metal compounds: new trends. *Phys. Uspekhi* **60**, 1121–1146 (2017).

46. de' Medici, L., Giovannetti, G. & Capone, M. Selective Mott physics as a key to iron superconductors. *Phys. Rev. Lett.* **112**, 177001 (2014).

47. Yu, R., Zhu, J.-X. & Si, Q. Orbital selectivity enhanced by nematic order in FeSe. *Phys. Rev. Lett.* **121**, 227003 (2018).

48. Lei, H., Yin, W.-G., Zhong, Z. & Hosono, H. Structural, magnetic, and electrical properties of $Li_2Ir_{1-x}Ru_xO_3$. *Phys. Rev. B* **89**, 020409 (2014).

49. Cao, G. et al. Suppression of metal-to-insulator transition and appearance of superconductivity in $Cu_{1-x}Zn_xIr_2S_4$. *Phys. Rev. B* **64**, 214514 (2001).

50. Furubayashi, T. et al. Pressure induced metal-insulator transition of selenospinel $CuIr_2Se_4$. *J. Phys. Soc. Jpn* **66**, 1563–1564 (1997).

51. Ma, L. et al. Opposite pressure effects in the orbitally-induced Peierls phase transition systems $CuIr_2S_4$ and $MgTi_2O_4$. *Dalton Trans.* **46**, 6708–6714 (2017).

52. Martins, C., Aichhorn, M., Vaugier, L. & Biermann, S. Reduced effective spin-orbital degeneracy and spin-orbital ordering in paramagnetic transition-metal oxides: Sr_2IrO_4 versus Sr_2RhO_4. *Phys. Rev. Lett.* **107**, 266404 (2011).

53. Kim, B. J. et al. Phase-sensitive observation of a spin-orbital Mott state in Sr_2IrO_4. *Science* **323**, 1329–1332 (2009).

54. Varignon, J., Bibes, M. & Zunger, A. Origin of band gaps in 3d perovskite oxides. *Nat. Commun.* **10**, 1658 (2019).

55. Millis, A. J. Lattice effects in magnetoresistive manganese perovskites. *Nature* **392**, 147–150 (1998).

56. Thygesen, P. M. et al. Orbital dimer model for the spin-glass state in $Y_2Mo_2O_7$. *Phys. Rev. Lett.* **118**, 067201 (2017).

57. Bramwell, S. T. & Gingras, M. J. P. Spin ice state in frustrated magnetic pyrochlore materials. *Science* **294**, 1495–1501 (2001).

58. Koch, R. et al. Room temperature local nematicity in FeSe superconductor. Preprint at https://arxiv.org/abs/1902.08732 (2019).

59. Konstantinova, T. et al. Photoinduced dynamics of nematic order parameter in FeSe. *Phys. Rev. B* **99**, 180102 (2019).

60. Endoh, R., Awaka, J. & Nagata, S. Ferromagnetism and the metal-insulator transition in the thiospinel $Cu(Ir_{1-x}Cr_x)_2S_4$. *Phys. Rev. B* **68**, 115106 (2003).

61. Egami, T. & Billinge, S. J. L. *Underneath The Bragg Peaks: Structural Analysis Of Complex Materials*. 2nd edn (Elsevier, Amsterdam, 2012).

62. Chupas, P. J. et al. Rapid acquisition pair distribution function analysis (RA-PDF). *J. Appl. Crystallogr.* **36**, 1342–1347 (2003).

63. Hammersley, A. P., Svenson, S. O., Hanfland, M. & Hauserman, D. Two-dimensional detector software: from real detector to idealised image or two-theta scan. *High Press. Res.* **14**, 235–248 (1996).

64. Juhás, P., Davis, T., Farrow, C. L. & Billinge, S. J. L. PDFgetX3: a rapid and highly automatable program for processing powder diffraction data into total scattering pair distribution functions. *J. Appl. Crystallogr.* **46**, 560–566 (2013).

65. Farrow, C. L. et al. PDFfit2 and PDFgui: computer programs for studying nanostructure in crystals. *J. Phys. Condens. Mater.* **19**, 335219 (2007).

66. Qiu, X., Proffen, T., Mitchell, J. F. & Billinge, S. J. L. Orbital correlations in the pseudocubic *O* and rhombohedral *R*-phases of $LaMnO_3$. *Phys. Rev. Lett.* **94**, 177203 (2005).

Author contributions

E.S.B., J.F.M. and S.J.L.B. conceived and designed the research. C.P., H.C.L., J.F.M., Y.S.H., and H.Z. developed and carried out the synthesis and did material characterizations. E.S.B., R.J.K. and M.A. carried out PDF measurements and analysis. W.G.Y. provided theoretical inputs. E.S.B., S.J.L.B. and J.F.M. wrote the manuscript with contributions from all the authors.

Additional information

Supplementary Information accompanies this paper at https://doi.org/10.1038/s41467-019-11372-w.

Competing interests: The authors declare no competing interests.

Reprints and permission information is available online at http://npg.nature.com/reprintsandpermissions/

Peer review information: *Nature Communications* thanks the anonymous reviewers for their contribution to the peer review of this work.

Publisher's note: Springer Nature remains neutral with regard to jurisdictional claims in published maps and institutional affiliations.

Rapid Communications   Editors' Suggestion

Room temperature local nematicity in FeSe superconductor

R. J. Koch,[1,*] T. Konstantinova,[1,2] M. Abeykoon,[3] A. Wang,[1,†] C. Petrovic,[1] Y. Zhu,[1,2] E. S. Bozin,[1] and S. J. L. Billinge[1,4]

[1]*Condensed Matter Physics and Materials Science Department, Brookhaven National Laboratory, Upton, New York 11973, USA*
[2]*Department of Physics and Astronomy, Stony Brook University, Stony Brook, New York 11794, USA*
[3]*Photon Science Division, Brookhaven National Laboratory, Upton, New York 11973, USA*
[4]*Department of Applied Physics and Applied Mathematics, Columbia University, New York, New York 10027, USA*

We report pair distribution function measurements of the iron-based superconductor FeSe above and below the structural transition temperature. Structural analysis reveals a local orthorhombic distortion with a correlation length of about 4 nm at temperatures where an average tetragonal symmetry is observed. The analysis further demonstrates that the local distortion is larger than the global distortion at temperatures where the average observed symmetry is orthorhombic. Our results suggest that the low-temperature macroscopic nematic state in FeSe forms from an imperfect ordering of orbital-degeneracy-lifted nematic fluctuations which persist up to at least 300 K.

In high-temperature iron-based superconductors, nematicity, or C_4 to C_2 rotational symmetry breaking, is believed to be closely related to superconductivity as both are correlation-driven electronic instabilities which often coincide in the doping phase diagram [1]. The relationship is tantalizing but its nature remains unclear, as the two are frequently entwined with spin and orbital order [2,3].

The emergence of nematicity is marked by a tetragonal to orthorhombic global symmetry-breaking structural transition at T_s [4,5] as well as a lifting of the degeneracy of electronic orbitals in the material. For example, in FeSe, angle-resolved photoemission spectroscopy (ARPES) studies have demonstrated that the $3d_{yz}$ and $3d_{xz}$ Fe-Fe molecular orbitals take on a 50-meV energy difference below $T_o = 90$ K. The observation of orbital degeneracy lifting (ODL) coincides with orbital ordering (OO) which in turn accompanies or indeed even drives [6] the global structural transition such that $T_o = T_s$ [7,8].

Although the OO and structural transition occur concurrently, a notable discrepancy exists between their energy scales. The 50-meV orbital splitting corresponds to a temperature scale of about 580 K rather than the 90 K of the transition. An alternative possibility is that the orbital degeneracy lifting happens at higher temperature, but the orbitals only order at T_s. This is similar to the case of CuIr$_2$S$_4$ [9], where a short-range-ordered (SRO) ODL state was discovered to exist well above the OO temperature.

The well-established lattice symmetry of FeSe above 90 K is tetragonal, with C_4 rotational symmetry about the c axis. The low-temperature orthorhombic lattice in this system has C_2 symmetry along the same axis [10]. A structural signature for the existence of a SRO C_2 nematic phase above 90 K should manifest as a local, SRO orthorhombic (or similar) distortion, which does not order over long length scales. The x-ray atomic pair distribution function (xPDF) measurement provides a histogram of interatomic distances in a material, and as such is well suited for probing such local distortions [9,11,12]. Here we use xPDF to study an FeSe superconducting sample at temperatures both below and well above T_o and T_s.

In analogy with observations of ODL imposed structural distortions in CuIr$_2$S$_4$ [9], our xPDF study indicates a large orthorhombic distortion in FeSe up to 300 K, well above T_s where the average structure is tetragonal. Surprisingly, even at 84 K, just below the 90 K transition temperature, the local orthorhombic distortion is significantly larger in magnitude than the average crystallographic orthorhombicity that is recovered over large length scales, suggesting an imperfect long-range ordering of the local ODL state below T_s.

The nature of the local symmetry breaking is consistent with local degeneracy lifting of $3d_{yz}$ and $3d_{xz}$ orbitals associated with Fe-Fe bond formation. Our observation of a preformed local ODL broken symmetry state at high temperature suggests a picture where crystallization of the liquidlike orbital state occurs at the global symmetry-breaking structural transition at T_s. This provides a rationale for the seemingly disparate energy scales involved. It can also explain the orbital degeneracy breaking above T_s implied by ARPES [13] and suggests that the ODL has a Jahn-Teller origin.

The FeSe sample was synthesized through a chemical vapor transport method using a eutectic mix of KCl and AlCl$_3$ as the transport agent [14,15]. Sample quality was validated by a temperature-dependent resistivity characterization (Fig. S1 in Ref. [16]), which shows evidence for the structural phase transformation at $T_s = 90$ K and a robust superconducting transition below $T_c = 10$ K. Synchrotron x-ray total scattering experiments were conducted at the 28-ID-1 (PDF) beamline at the National Synchrotron Light Source-II at Brookhaven National Laboratory. The sample was loaded into a 1-mm

---

*rkoch@bnl.gov
†Present address: School of Physics, Chongqing University, Chongqing 400044, China.
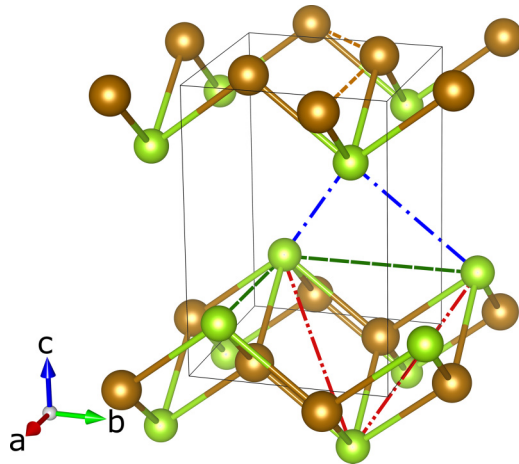
FIG. 1. Perspective view of the FeSe structure with tetragonal symmetry. Iron is shown in brown, and selenium in green. Pair distances constrained by tetragonal symmetry to be identical are highlighted by dashed lines of the same color. Tetragonal symmetry allows only a single Fe-Fe pair distance (brown dashed lines), and the orthorhomic distortion allows these distances to differentiate. The three unique Se-Se pair distances shown by red, green, and blue dashed lines become five distinct Se-Se pairs within the orthorhombic symmetry.

inner-diameter kapton capillary and data collected at 300 and 84 K using a liquid N_2 cryostream. Measurements were carried out in the rapid acquisition pair distribution function mode [17], with an x-ray energy of 74.69 keV ($\lambda = 0.1660$ Å). A two-dimensional (2D) PerkinElmer area detector was used, with a sample-to-detector distance of 204 mm determined by calibrating to a sample of known lattice parameter (Ni).

The 2D data were integrated and converted to intensity as a function of momentum transfer Q using the software FIT2D [18]. The program PDFGETX3 v2.0 [19] was used to correct, normalize, and Fourier transform the diffraction data to obtain the experimental xPDF, $G(r)$ up to a momentum transfer of $Q_{max} = 29$ Å^{-1} which was chosen as the best tradeoff between real-space resolution and noise in the data.

The average structure for FeSe is described by a tetragonal model at higher temperatures and an orthorhombic model at lower temperatures. The tetragonal model ($P4/nmm$ space group, shown in Fig. 1) consists of FeSe slabs featuring a Fe square planar sublattice. Each Fe is coordinated by four Se creating layers of edge-shared $FeSe_4$ tetrahedra, regularly stacked along the **c** lattice direction [4,5]. In this model, the asymmetric unit contains one FeSe formula unit, with Fe at (0.25, 0.75, 0.0) and Se at (0.25, 0.25, z). The lower-temperature orthorhombic model ($Cmma$ space group) is related to the tetragonal model through a rotation in the **a**-**b** plane and a rectangular distortion of the Fe sublattice [1]. Here, Fe sits at (0.25, 0.0, 0.5) and Se at (0.0, 0.25, z).

The xPDF data were fit with the PDFGUI [20] program using these two models (see Ref. [16] for details).

In Fig. 2 we show the PDF analysis results using the tetragonal model over the range $1.5 < r < 50$ Å. An abridged r range is shown for clarity and the resulting structural parameters are summarized in Table I. The fit is acceptable,
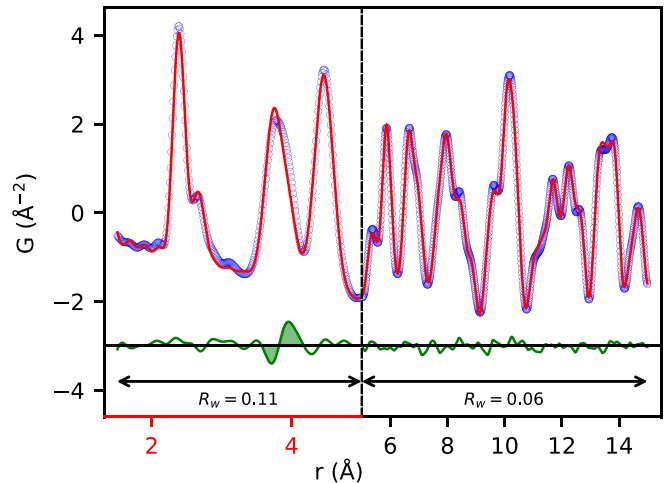

FIG. 2. The signature of local nematicity. PDF of best-fit model (red solid line) to observed data (open circles) from FeSe at 300 K, fitted up to $r = 50$ Å using the tetragonal model (overall $R_w = 0.08$). The fit is presented over the abbreviated range $1.5 < r < 15$ Å for clarity. The difference curve is shown displaced below (green solid line), and shaded to highlight the signature of local nematicity. R_w values over selected abbreviated r ranges are presented to highlight low-r misfit. Different coloring of the x axes of two panels signals that the scales are distinct to highlight the signal at low r. The y-axis scales are preserved between the two panels. Importantly, there is also a subtle misfit of the Fe-Fe peak at 2.7 Å (see text for details).

with an overall $R_w = 0.08$, suggesting that the tetragonal model adequately describes the average structure of FeSe at 300 K. However, a feature at ~3.9 Å in the local structure portion of the PDF is not well reproduced by the tetragonal model. The misfit on this peak is associated with a larger R_w of 0.11 over the range $1.5 < r < 5$ Å, compared to $R_w = 0.06$ over the range $5 < r < 15$ Å, as highlighted in Fig. 2.

The PDF misfit in a single low-r peak (Fig. 2) is reminiscent of the fingerprint of a SRO ODL state in $CuIr_2S_4$ [9]. In that system, a large misfit was observed in the first Ir-Ir PDF

TABLE I. Structural parameters and fit details for the FeSe sample at 300 K, obtained from PDF analysis using either the tetragonal or orthorhombic model. Colors in pair distances are consistent with dashed lines in Fig. 1.

Parameter	Tetragonal	Orthorhombic
r range (Å)	1.5–50	1.5–5.0
R_w	0.08	0.04
a (Å)	3.771	5.32
b (Å)		5.41
c (Å)	5.520	5.50
z	0.266	0.235
r(Fe-Se) (Å)	2.391	2.391
r(Fe-Fe) (Å)	2.667	2.661
		2.710
r(Se-Se) (Å)	3.710	3.709
		3.742
	3.771	3.795
	3.970	3.944
		3.974

peak at $r = 3.5$ Å when the PDF was fit with the reported cubic average structure, with an absence of significant misfit at other places in the PDF. This discrepancy was explained by the presence of fluctuating local symmetry-broken tetragonal domains present in the average cubic phase, that act as a precursor for the long-range-ordered symmetry-broken ground state seen at low temperature in the $CuIr_2S_4$ system.

In our FeSe system the corresponding reminiscent misfit feature occurs at $r = 3.9$ Å corresponding to a composite peak originating primarily from Se-Se nearest-neighbor (NN) correlations. The FeSe tetragonal model allows for three distinct Se-Se NN distances. The first set of NN Se-Se interatomic vectors spans the sheet created by the $FeSe_4$ tetrahedra between Se pairs with distinct z coordinates (red dashed lines in Fig. 1). The second spans the space between different sheets, again involving Se pairs with distinct z coordinates (blue dashed lines in Fig. 1). The third connects Se pairs with identical z coordinates, either fully above or below the Fe species in the same layer (green dashed lines in Fig. 1).

These symmetry constraints are lifted for some but not all of these interatomic vectors when the orthorhombic distortion occurs. The NN Se-Se interatomic vectors that connect Se ions with distinct z coordinates, represented by red and blue dashed lines in Fig. 1, all lie along the orthorhombic unit cell axes (i.e., the basal-plane projections of the interatomic vectors are parallel to a and b, respectively). The orthorhombic distortion allows these pair distances to become distinct, with the magnitude of their difference dictated by the magnitude of the orthorhombic distortion. On the other hand, the NN Se-Se interatomic vectors with zero z component, represented by green dashed lines in Fig. 1, are parallel to the diagonals of the orthorhombic a-b plane and they remain identical following the orthorhombic distortion. The reduction of symmetry associated with the orthorhombic distortion therefore results in an increase from three to five distinct Se-Se NN distances. The feature at $r = 3.9$ Å also contains a Fe-Fe nex-nearest-neighbor (NNN) contribution, but this peak is smaller than the Se-Se contributions by a factor of about 5, and the orthorhombic distortion does not split the two Fe-Fe NNN distances, as they span the unit-cell diagonals.

The feature at ~3.9 Å in the difference curve in Fig. 2 suggests intensity is shifted to the right in the measured PDF compared to the model. This indicates that the tetragonal model PDF under-represents higher-r Se-Se NN pair correlations, while lower-r Se pair correlations are over-represented.

Drawing from the previously mentioned $CuIr_2S_4$ case [9], we seek an explanation in terms of a SRO locally orbital degeneracy lifted (SRO-ODL) state which persists to temperatures well above the observed long-range OO temperature T_o. In $CuIr_2S_4$, the local structure of the material in the SRO-ODL state was well explained by the symmetry-broken model, while the high-r region was consistent with the high-temperature non-symmetry-broken structural model. We therefore followed a similar analysis strategy as adopted in the $CuIr_2S_4$ case.

As mentioned, long-range OO in FeSe manifests structurally as a tetragonal to orthorhombic transformation, which involves an increase in the number of distinct Se-Se NN distances. Our analysis applying the low-temperature orthorhombic model to the low-r ($1.5 < r < 5$ Å) region of
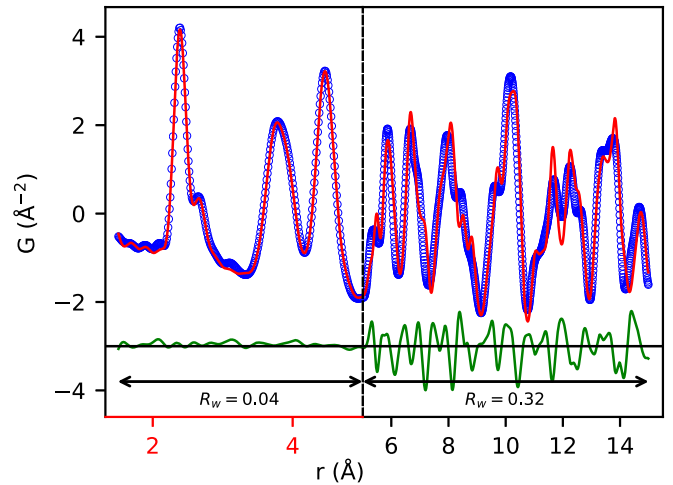

FIG. 3. PDF of best-fit model (red solid line) and observed data (open circles) from FeSe at 300 K, fitted up to $r = 5$ Å using orthorhombic (nematic) symmetry constraints ($R_w = 0.04$). The difference curve is shown displaced below (green solid line). R_w values over selected r ranges are presented to highlight the discrepancy between the optimal local structure and the observed average structure. Different coloring of the x axes of two panels signals that the scales are distinct to highlight the signal at low r. The y-axis scales are preserved between the two panels. The orthorhombic model provides an observably better account of the Fe-Fe NN PDF peak as compared to the tetragonal model (Fig. 2).

the 300 K PDF is shown in Fig. 3, with resulting structural parameters presented in Table I. This model successfully removes the reminiscent misfit feature that is observed in this r region with the tetragonal model, yielding an R_w nearly three times lower than the tetragonal model, ($R_w = 0.04$ vs 0.11) over the range $1.5 < r < 5$ Å. This strongly suggests that at 300 K the local structure is orthorhombic and is a SRO-ODL state.

Compared to the average structure, the orthorhombic distortion does not alter the Fe-Se distance, but does split the NN Se-Se and NN Fe-Fe pair distances significantly, while also shifting them to higher r. The misfit in Fig. 2 is more apparent in the NN Se-Se PDF peak at ~3.9 Å, rather than the NN Fe-Fe PDF peak at ~2.7 Å due to the stronger scattering power of Se and a larger Se-Se multiplicity, resulting in a peak that is roughly four times stronger than the NN Fe-Fe peak.

A similar sized distortion in the Fe and Se sublattices thus results in a much larger signature in the difference curve associated with Se-Se features. However, and importantly, careful inspection of the Fe-Fe peak at 2.7 Å, evident as a well resolved shoulder to the Fe-Se peak in Fig. 2, indicates that this peak is observably broader in the data than the model. This misfit, although subtle, is consistent with the presence of an ODL state in the Fe-Fe sublattice. While such a misfit alone could easily escape attention, the broader context of the large residual at ~3.9 Å highlights this region.

As in the $CuIr_2S_4$ case, if we calculate the PDF of the orthorhombic model, which reproduces the low-r region well, over a much wider r range (up to 15 Å), it results in a poor agreement to the measured PDF compared to the non-symmetry-broken tetragonal model (Fig. 3, $R_w = 0.32$ for
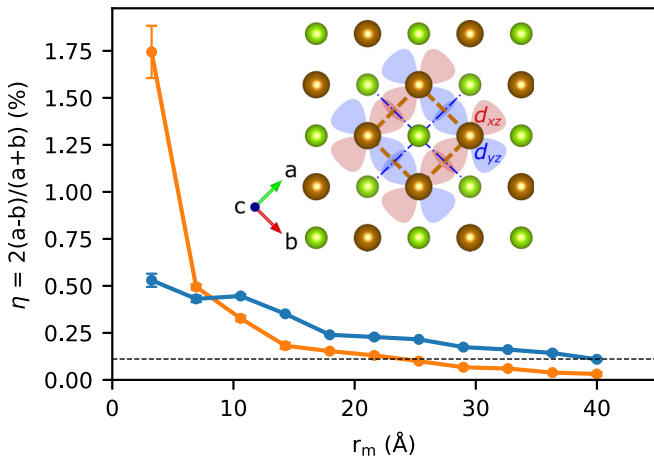
FIG. 4. The measured orthorhombic distortion obtained by using an orthorhombic model over a narrow r range, η, is plotted vs the PDF fit window center, r_m, for data measured at 300 (orange line) and 84 K (blue line). The value of η at 84 K as extracted from the average structure is represented by the dashed horizontal line. Inset is a top view of the FeSe crystal structure, schematically showing the projected orientations of the Fe $3d_{yz}$ and $3d_{xz}$ orbitals implicated in this work and elsewhere. Atom and dashed line colors are consistent with Fig. 1 and the axes labels are consistent with the orthorhombic setting. Full PDF fits associated with the distortion magnitudes in this plot are shown in Fig. S2 in Ref. [16].

$5 < r < 15$ Å compared to $R_w = 0.06$ for the tetragonal model over this range). This implies that the distortion has orthorhombic short-range character.

Given that we have found local orthorhombic domains in a globally tetragonal crystal, we would like to extract the size, or structural coherence, of the domains. To do this we use box-car style PDF fits [21,22] where the fits are carried out over a number of variable r-range regions individually. The protocol represents an extension of the fitting shown in Fig. 3, wherein the "box-car" consisted of the r range of 1.5–5 Å, and a centroid $r_m = 3.25$ Å. Each distinct r-range fit then provides structural information relevant to a distinct distance window, allowing for a quantification of the variation of local structure as a function of r (the correlation length of local features). The orthorhombic distortion η as a function of the box-car centroid, r_m, is shown in Fig. 4, demonstrating the robustness of the approach (see Fig. S2 in Ref. [16]).

Surprisingly, our analysis reveals that the local distortion above T_s is about 1.75%, more than three times larger than any observed distortion in the average structure below T_s. The magnitude of the measured distortion drops rapidly with increasing r (Fig. 4) until, at length scales greater than 40 Å, it is effectively zero and the average tetragonal structure is recovered.

Interestingly, even below T_s (at $T = 84$ K) the local orthorhombicity is larger than that observed in the average structure at this temperature, represented by the dashed horizontal line in Fig. 4. At this temperature, the local distortion also decreases with increasing r, converging to the measured average orthorhombic structure at length scales greater than 40 Å. Based on the proposed SRO-ODL explanation, the persistence of a larger-than-average local orthorhombicity below T_s suggests that the long-range ordering of the ODL state is not perfect.

The xPDF results presented here build on and extend previous studies [23,24] showing similarly local C_4 symmetry breaking in the 122 family of iron pnictide superconductors, suggesting that such fluctuations may be widespread.

Further, our findings provide a direct structural rationale for anomalous linewidth and splitting observed in NMR spectra [25] as well as unexpected energy gaps observed in the electronic spectra [13,26,27] pointing toward electronic nondegeneracy in FeSe well above T_s. The $3d_{yz}$ and $3d_{xz}$ Fe orbitals implicated in this local degeneracy lifting are oriented along the distorted orthorhombic direction (see, e.g., Fig. 4 inset) and participate in orbital-selective Cooper pairing [28,29] enhanced by nematic order [30]. Thus the xPDF discovery of a local ODL state deep in the high-temperature tetragonal regime not only defines a local structural fingerprint of the fluctuating nematic state, but also serves to reinforce the role of the orbital sector and its coupling to structure within the physics of iron-based superconductors. Local orbital overlaps governed by nematic fluctuations appear to be essential for slow dynamic correlations in FeSe and related materials [31,32]. Our observation of a broken-symmetry state at high temperature suggests that the global symmetry-breaking structural transition at T_s occurs through crystallization of the preformed liquidlike orbital state, a description which challenges present understanding of this system and invites further theoretical considerations.

To that effect, it will be of particular interest to explore the evolution of this local ODL state away from the FeSe parent, across the phase diagrams of, e.g., $FeSe_{1-x}S_x$ and $FeSe_{1-x}Te_x$ and in the regime where long-range symmetry-breaking transition is not observed at any temperature. Such studies would further inform the debate of the importance of nematic fluctuations for the superconductivity itself.

[1] A. E. Böhmer and A. Kreisel, J. Phys.: Condens. Matter **30**, 023001 (2018).

[2] R. M. Fernandes, A. V. Chubukov, and J. Schmalian, Nat. Phys. **10**, 97 (2014).

[3] Q. Si, R. Yu, and E. Abrahams, Nat. Rev. Mater. **1**, 16017 (2016).

[4] F. C. Hsu, J. Y. Luo, K. W. Yeh, T. K. Chen, T. W. Huang, P. M. Wu, Y. C. Lee, Y. L. Huang, Y. Y. Chu,

D. C. Yan *et al.*, Proc. Natl. Acad. Sci., USA **105**, 14262 (2008).

[5] S. Hosoi, K. Matsuura, K. Ishida, H. Wang, Y. Mizukami, T. Watashige, S. Kasahara, Y. Matsuda, and T. Shibauchi, Proc. Natl. Acad. Sci. USA **113**, 8139 (2016).

[6] S.-H. Baek, D. V. Efremov, J. M. Ok, J. S. Kim, J. van den Brink, and B. Büchner, Nat. Mater. **14**, 210 (2015).

[7] T. Shimojima, Y. Suzuki, T. Sonobe, A. Nakamura, M. Sakano, J. Omachi, K. Yoshioka, M. Kuwata-Gonokami, K. Ono, H. Kumigashira *et al.*, Phys. Rev. B **90**, 121111(R) (2014).

[8] T. M. McQueen, A. J. Williams, P. W. Stephens, J. Tao, Y. Zhu, V. Ksenofontov, F. Casper, C. Felser, and R. J. Cava, Phys. Rev. Lett. **103**, 057002 (2009).

[9] E. S. Bozin, W. G. Yin, R. J. Koch, M. Abeykoon, Y. S. Hor, H. Zheng, H. C. Lei, C. Petrovic, J. F. Mitchell, and S. J. L. Billinge, arXiv:1901.10104.

[10] K. Kothapalli, A. E. Böhmer, W. T. Jayasekara, B. G. Ueland, P. Das, A. Sapkota, V. Taufour, Y. Xiao, E. Alp, S. L. Bud'ko *et al.*, Nat. Commun. **7**, 12728 (2016).

[11] S. J. L. Billinge and M. G. Kanatzidis, Chem. Commun. **7**, 749 (2004).

[12] T. Egami and S. J. L. Billinge, *Underneath the Bragg Peaks: Structural Analysis of Complex Materials*, 2nd ed. (Elsevier, Amsterdam, 2012).

[13] P. Zhang, T. Qian, P. Richard, X. P. Wang, H. Miao, B. Q. Lv, B. B. Fu, T. Wolf, C. Meingast, X. X. Wu *et al.*, Phys. Rev. B **91**, 214503 (2015).

[14] R. Hu, H. Lei, M. Abeykoon, E. S. Božin, S. J. L. Billinge, J. B. Warren, T. Siegrist, and C. Petrovic, Phys. Rev. B **83**, 224502 (2011).

[15] D. Chareev, E. Osadchii, T. Kuzmicheva, J.-Y. Lin, S. Kuzmichev, O. Volkova, and A. Vasiliev, CrystEngComm **15**, 1989 (2013).

[16] See Supplemental Material at http://link.aps.org/supplemental/10.1103/PhysRevB.100.020501 for electrical transport properties, details on the xPDF analysis, and Refs. [20,33,34].

[17] P. J. Chupas, K. W. Chapman, and P. L. Lee, J. Appl. Crystallogr. **40**, 463 (2007).

[18] A. P. Hammersley, S. O. Svenson, M. Hanfland, and D. Hauserman, High Pressure Res. **14**, 235 (1996).

[19] P. Juhás, T. Davis, C. L. Farrow, and S. J. L. Billinge, J. Appl. Crystallogr. **46**, 560 (2013).

[20] C. L. Farrow, P. Juhás, J. Liu, D. Bryndin, E. S. Božin, J. Bloch, T. Proffen, and S. J. L. Billinge, J. Phys.: Condens. Matter **19**, 335219 (2007).

[21] X. Qiu, T. Proffen, J. F. Mitchell, and S. J. L. Billinge, Phys. Rev. Lett. **94**, 177203 (2005).

[22] E. S. Božin, K. R. Knox, P. Juhás, Y. S. Hor, J. F. Mitchell, and S. J. L. Billinge, Sci. Rep. **4**, 4081 (2014).

[23] T. Iye, M.-H. Julien, H. Mayaffre, M. Horvatić, C. Berthier, K. Ishida, H. Ikeda, S. Kasahara, T. Shibauchi, and Y. Matsuda, J. Phys. Soc. Jpn. **84**, 043705 (2015).

[24] B. A. Frandsen, K. M. Taddei, D. E. Bugaris, R. Stadel, M. Yi, A. Acharya, R. Osborn, S. Rosenkranz, O. Chmaissem, and R. J. Birgeneau, Phys. Rev. B **98**, 180505(R) (2018).

[25] P. Wiecki, M. Nandi, A. E. Böhmer, S. L. Bud'ko, P. C. Canfield, and Y. Furukawa, Phys. Rev. B **96**, 180502(R) (2017).

[26] Y.-C. Wen, K.-J. Wang, H.-H. Chang, J.-Y. Luo, C.-C. Shen, H.-L. Liu, C.-K. Sun, M.-J. Wang, and M.-K. Wu, Phys. Rev. Lett. **108**, 267002 (2012).

[27] P. S. Wang, P. Zhou, S. S. Sun, Y. Cui, T. R. Li, H. Lei, Z. Wang, and W. Yu, Phys. Rev. B **96**, 094528 (2017).

[28] P. O. Sprau, A. Kostin, A. Kreisel, A. E. Böhmer, V. Taufour, P. C. Canfield, S. Mukherjee, P. J. Hirschfeld, B. M. Andersen, and J. C. Davis, Science **357**, 75 (2017).

[29] A. Kostin, P. O. Sprau, A. Kreisel, Y. X. Chong, A. E. Böhmer, P. C. Canfield, P. J. Hirschfeld, B. M. Andersen, and J. C. Davis, Nat. Mater. **17**, 869 (2018).

[30] R. Yu, J.-X. Zhu, and Q. Si, Phys. Rev. Lett. **121**, 227003 (2018).

[31] I. Zaliznyak, A. T. Savici, M. Lumsden, A. Tsvelik, R. Hu, and C. Petrovic, Proc. Natl. Acad. Sci., USA **112**, 10316 (2015).

[32] T. Konstantinova, L. Wu, M. Abeykoon, R. J. Koch, A. F. Wang, R. K. Li, X. Shen, J. Li, J. Tao, I. A. Zaliznyak, C. Petrovic, S. J. L. Billinge, X. J. Wang, E. S. Bozin, and Y. Zhu, Phys. Rev. B **99**, 180102(R) (2019).

[33] T. Proffen and S. J. L. Billinge, J. Appl. Crystallogr. **32**, 572 (1999).

[34] B. H. Toby and T. Egami, Acta Crystallogr., Sect. A: Found. Adv. **48**, 336 (1992).

Correlated disorder-to-order crossover in the local structure of $K_xFe_{2-y}Se_{2-z}S_z$

P. Mangelis,[1] R. J. Koch [2,*] H. Lei,[2,†] R. B. Neder,[3] M. T. McDonnell,[4,‡] M. Feygenson,[4,§] C. Petrovic,[2] A. Lappas,[1,‖] and E. S. Bozin[2]

[1]*Institute of Electronic Structure and Laser, Foundation for Research and Technology–Hellas, Vassilika Vouton, 711 10 Heraklion, Greece*
[2]*Condensed Matter Physics and Materials Science Department, Brookhaven National Laboratory, Upton, New York 11973, USA*
[3]*Institute of Condensed Matter Physics, Friedrich-Alexander-Universität Erlangen-Nürnberg, Staudtstr. 3, 91058 Erlangen, Germany*
[4]*Neutron Scattering Division, Oak Ridge National Laboratory, Oak Ridge, Tennessee 37831, USA*

A detailed account of the local atomic structure and disorder at 5 K across the phase diagram of the high-temperature superconductor $K_xFe_{2-y}Se_{2-z}S_z$ ($0 \leqslant z \leqslant 2$) is obtained from neutron total scattering and associated atomic pair distribution function (PDF) approaches. Various model-independent and model-dependent aspects of the analysis reveal a high level of structural complexity on the nanometer length scale. Evidence is found for considerable disorder in the c-axis stacking of the $FeSe_{1-x}S_x$ slabs without observable signs of turbostratic character of the disorder. In contrast to the related FeCh (Ch = S, Se)-type superconductors, substantial Fe-vacancies are present in $K_xFe_{2-y}Se_{2-z}S_z$, deemed detrimental for superconductivity when ordered. Our study suggests that the distribution of vacancies significantly modifies the iron-chalcogen bond-length distribution, in agreement with observed evolution of the PDF signal. A crossoverlike transition is observed at a composition of $z \approx 1$, from a correlated disorder state at the selenium end to a more vacancy-ordered (VO) state closer to the sulfur end of the phase diagram. The S-content-dependent measures of the local structure are found to exhibit distinct behavior on either side of this crossover, correlating well with the evolution of the superconducting state to that of a magnetic semiconductor toward the $z \approx 2$ end. The behavior reinforces the idea of the intimate relationship of correlated Fe-vacancy order in the local structure and the emergent electronic properties.

I. INTRODUCTION

Recently discovered 122-type iron-based superconductors, with the formula $A_xFe_2Se_2$ (A = alkali metals or Tl) [1,2], and relatively high transition temperatures ($T_c \approx 30$ K) as compared to the simpler FeSe-11-type counterparts ($T_c \approx 8$ K) [3], have garnered significant interest in correlated electron systems research. This class of unconventional superconductors combines unique properties such as the coexistence of superconductivity and long-range antiferromagnetic (AF) order with large magnetic moments and Néel temperatures that far exceed room temperature [4–7], while spectroscopic studies suggest the presence of a superconducting gap below 8 meV [8]. Their behavior sets the stage for a tantalizing correlated electron materials conceptual problem, somewhat contrasting the cuprates, where superconductivity emerges from the antiferromagnetic Mott insulating state. The puzzle becomes even more complex as a wide range of ensemble

average [9–12] and local structure [13–16] methods have shown strong evidence for nanoscale phase separation, particularly, perpendicular to the iron-selenide planes [17].

In an effort to describe the coexistence of superconducting and AF states, a common approach portrays a majority insulating AF Fe-vacancy-ordered (VO) $A_2Fe_4Se_5$ phase (space group $I4/m$), which is separated from the minority superconducting $A_xFe_2Se_2$ phase (space group $I4/mmm$) [18–20]. While the latter is characterized by fully occupied Fe atomic sites [Fig. 1(a)], the presence of Fe vacancies in the former [Fig. 1(d)] was believed to be detrimental to superconductivity [21,22]. An understanding then emerged, inferring that what makes the materials nonsuperconducting is the magnetism bearing $\sqrt{5} \times \sqrt{5}$ long-range ordering of Fe vacancies. This is described in the $I4/m$ tetragonal symmetry, with two crystallographically distinct Fe-atomic sites, where one (16i) is fully occupied, while the other (4d) remains empty. Earlier neutron total scattering studies [23] of $K_xFe_{2-y}Se_2$ and the sulfide analog $K_xFe_{2-y}S_2$ revealed that the two-phase description reflects a subnanometer length scale, rendering such a model equivalent to an Fe-vacancy-disordered (VD) $I4/m$ $K_{2-x}Fe_{4+y}Ch_5$ (Ch = Se, S) single-phase case. The inhomogeneity and structural complexity of $A_xFe_{2-y}Se_2$ makes it difficult to derive concrete conclusions about the nature of the relationship between the atomic structure and the observed physical properties. Since magnetic and insulating $I4/m$ and superconducting $I4/mmm$ patches are mixed on the scale of about 100 nm [21,24], proximity effects of magnetic patches

*rkoch@bnl.gov
†Present address: Department of Physics and Beijing Key Laboratory of Opto-electronic Functional Materials & Micro-nano Devices, Renmin University of China, Beijing, China.
‡Present address: Computer Science and Mathematics Division, Oak Ridge National Laboratory, Oak Ridge, Tennessee 37831, USA.
§Present address: Forschungszentrum Jülich, JCNS, D-52425 Jülich, Germany.
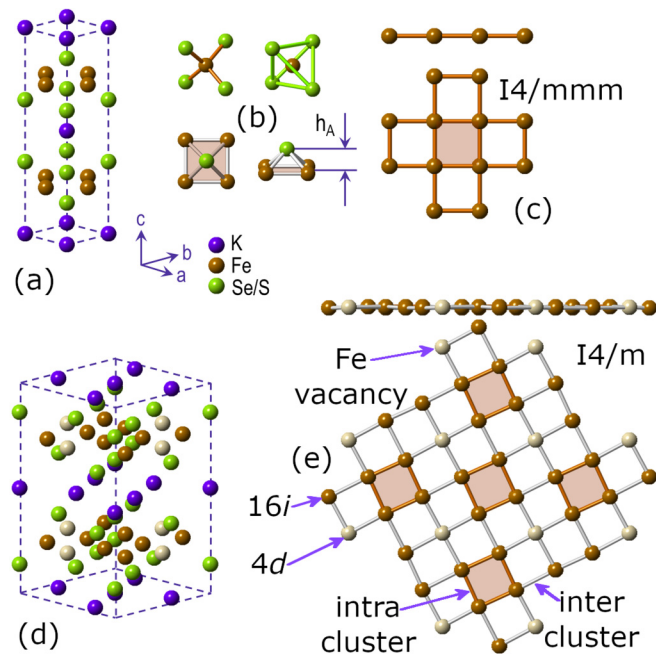‖lappas@iesl.forth.gr

FIG. 1. Two possible crystallographic models of the atomic structure of $K_xFe_{2-y}Se_{2-z}S_z$. (a) A perspective view of a single unit cell in the $I4/mmm$ Fe-vacancy-free mode. (b) A single $FeCh_4$ tetrahedron and other structural elements discussed in the text. h_A denotes the anion height. (c) The Fe sublattice viewed both along the $a - b$ plane (top) and down the c axis (bottom) in the $I4/mmm$ model. (d) A perspective view of a single unit cell in the $I4/m$ VO model. (e) The Fe sub-lattice in the $I4/m$ VO model as viewed both along the $a - b$ plane (top) and down the c axis (bottom). Symmetry-distinct Fe-sites ($4d$ and $16i$), Fe vacancies, as well as various Fe-Fe interatomic distances discussed in text are indicated by arrows.

on superconducting islands are important [25]. Indeed, spectroscopy measurements have suggested the existence of a Josephson-coupled phase in the Se end-member [26].

In an effort to resolve the delicate interplay of structural defects and properties, *in situ* scanning electron microscopy studies revealed that during the cooling of a specimen to room temperature, the formation mechanism of the superconducting phase in $K_xFe_{2-y}Se_2$ passes through an "imperfect" Fe-vacancy disorder-to-order transition, which is deemed responsible for the phase separation [27]. Crucial to mediating the physical response and the distribution of the vacancies appears to be the thermal treatment, including the quenching conditions [14,28,29]. Indeed, the Fe-vacancy order-to-disorder transition can be achieved by a simple high-temperature annealing process [30,31], an approach which has also been pinpointed by recent high energy, single-crystal x-ray diffraction experiments and Monte Carlo simulations, where superconductivity in quenched $K_xFe_{2-y}Se_2$ crystals appears at the Fe-vacancy order-to-disorder boundary [32]. Notably, rapid quenching in $K_xFe_{2-y}Se_2$ leads to a giant increase in the critical current density and yields specimens of higher T_c [33].

In view of these intricate relationships, Wu *et al.* have suggested that the nonsuperconducting, alkali-modified FeSe-based magnetic insulators, which possess such Fe VO

structures, should be considered the parent compounds of the superconducting phases [34]. Disordering the Fe-vacancy order of the parent magnetic insulating phase, $K_2Fe_4Se_5$, has been proposed as crucial for the emergence of superconductivity in $K_xFe_{2-y}Se_2$ [28]. Following this conceptual approach, x-ray absorption fine-structure studies [35,36] have provided evidence for local disorder in the structure of superconducting $K_xFe_{2-y}Se_2$, suggesting that a nonzero population of Fe atoms at the $4d$ site [Fig. 1(e)] is the key structural parameter for bulk superconductivity. As the debate still goes on as to what the role of Fe vacancies might be in the emergence of superconductivity and collapse of magnetism (or vice versa), seeking good model systems where similar features can be studied ultimately helps to broaden our knowledge base.

In this endeavor, the isostructural $K_xFe_{2-y}Se_{2-z}S_z$ ($0 \leqslant z \leqslant 2$) solid solutions offer such a possibility as the substitution of Se by the isovalent S suppresses the superconducting state and give rise to a magnetic semiconductor at $z \geqslant 1.6$ [18]. Since the interplay of superconductivity and magnetism across the $K_xFe_{2-y}Se_{2-z}S_z$ series seems to rely on intriguing structural details, we have employed neutron total scattering combined with atomic pair distribution function (PDF) analysis to probe the local atomic structure that may correlate with such notable changes in the behavior. The study was carried over a dense grid of compositions at 5 K, the temperature at which superconductivity is observed in the selenium-rich part of the phase diagram, but gets suppressed toward the sulfur-rich end of the series. Our study corroborates previous reports of disorder in the stacking of the $FeSe_{1-x}S_x$ slabs, which reflects yet another ingredient in an already structurally complex material, and has been previously linked to local potassium ordering and segregation, as well as superconductivity. Moreover, by complementing neutron PDF analysis with simulations based on large atomistic models, we explored the subtle nanoscale changes in the interatomic distances and the evolution of vacancy distribution in the Fe-chalcogen layers in the $K_xFe_{2-y}Se_{2-z}S_z$ system. We demonstrate that numerous local structural quantities correlate well with T_c, being marked by an Fe-vacancy correlated disorder to order crossover around the $z = 1$ composition. From this we can infer that the Fe-vacancy distribution likely plays a critical role in the electronic properties.

II. METHODS

Single crystals of $K_xFe_{2-y}Se_{2-z}S_z$ ($0 \leqslant z \leqslant 2$) were grown by self-flux method, and energy-dispersive x-ray spectroscopy (EDX) found no appreciable impurity elements, as described in detail elsewhere [18]. Crystals were pulverized into fine powders and seived to a maximum size of 40 μm. Samples were thoroughly characterized by x-ray powder diffraction, magnetic susceptibility, and electrical resistivity measurements, as previously reported [18].

Experiments were performed at NOMAD instrument [37] at the Spallation Neutron Source at Oak Ridge National Laboratory. Powdered samples were loaded in extruded vanadium containers and sealed under inert atmosphere, where helium was used as the exchange gas. Data were collected at 5 K, then corrected and reduced using standard protocols [38]. Neutron PDFs were obtained using the PDFGETN program [39] over

a range from $Q_{min} = 0.5$ Å^{-1} to $Q_{max} = 26$ Å^{-1}. Diffraction analysis did not find any evidence of crystal size broadening, suggesting crystal sizes were greater than 100 nm. Further details on these measurements are provided in the Appendix.

Measured and reduced data, including $I(Q)$, $F(Q)$, and $G(r)$, were analyzed using various structure-model independent approaches, outlined in the Appendix. When performing structure-model-dependent analysis of the same data, two structural models are relevant, with a space group of $I4/mmm$ or $I4/m$. The details of these are summarized in Fig. 1, with finer details presented in Appendix. Small-box PDF refinements were carried out using one or both of these models with the PDFGUI software [40] as described in the Appendix. Large-box simulated PDFs were computed with the DISCUS software package [41], using a model with space group $I4/m$ as described in the Appendix.

III. RESULTS AND DISCUSSION

A. Neutron diffraction

We start the $K_xFe_{2-y}Se_{2-z}S_z$ system assessment by looking at the neutron powder diffraction data as seen by the low scattering angle detector bank of the NOMAD instrument, Fig. 2. The data across the entire composition series display a broad, diffuse feature at the expected location (red dashed line in Fig. 2) of the (110) peak associated with the $\sqrt{5} \times \sqrt{5}$ long-range ordering of Fe vacancies. Macroscopic separation of a VO phase with a vacancy-free phase would not produce such a broad feature, but would instead produce a relatively sharp, albeit weak, (110) peak. The diffuse nature of the observed (110) peak suggests that idealized vacancy-order is not achieved, but rather that a type of imperfect order or "correlated disorder" [42,43] exists across the series. This is commonly observed in other order-disorder type systems such as, for example, in copper-gold intermetallic alloys [44–47].

Additionally, diffraction data across the entire composition series show a broad and bimodal distribution of intensity at the expected location of the (002) peak, as marked by a green dashed line in Fig. 2. Focusing on the specific example of $K_xFe_{2-y}S_2$ in Fig. 3(b), we note that the primary peak at ~0.95 Å^{-1} can be indexed in either the $I4/mmm$ or $I4/m$ space group as (002), but the additional low-Q shoulderlike feature at ~0.8 Å^{-1} cannot be indexed in either space group. Such additional diffuse intensity in the vicinity of interlayer diffraction peaks is common in clay systems with more than one interlayer distance [48–50].

DISCUS simulations considering large supercells in the $K_xFe_{2-y}S_2$ system with two distinct interlayer distances, 6.55 Å (66 % prevalence) and 8.0 Å (34 % prevalence) [see Fig. 3(a)] reproduce this experimentally observed bi-modal intensity distribution well, as seen in Fig. 3(b). Importantly, these two distinct interlayer distances exist in the *same* crystal, not segregated to distinct phases. A phase segregated physical mixture would produce two distinct diffraction features, rather than the continuous intensity distribution seen in Figs. 2 and 3(b). The relative intensity of the additional low-Q shoulder-like feature increases with increasing sulfur content (Fig. 2 inset), suggesting that the prevalence of a second longer
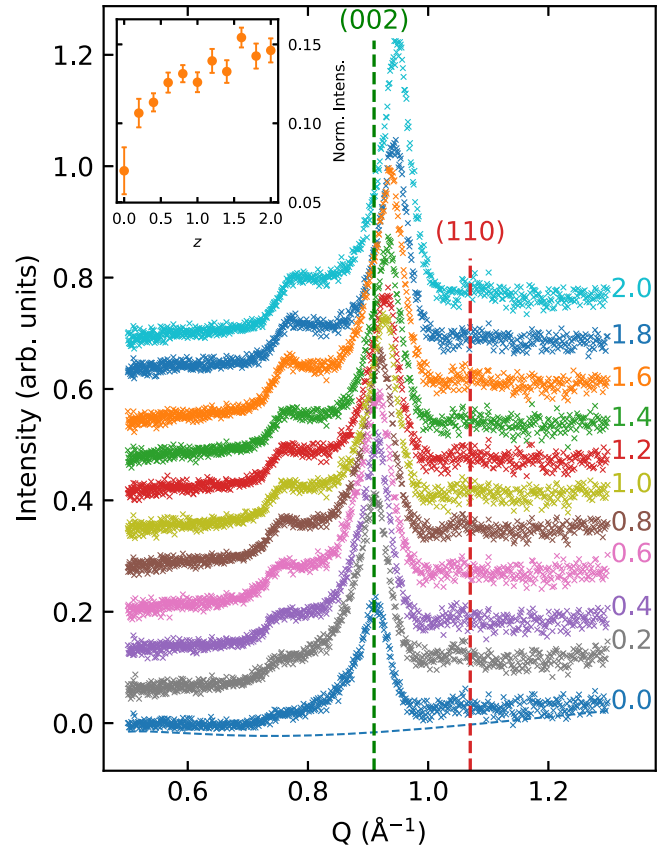

FIG. 2. Vacancy ordering in $K_xFe_{2-y}Se_{2-z}S_z$. Neutron powder diffraction data (sulphur content, z, as indicated) in the vicinity of the (110) and (002) reflections, positions of which for $z = 0$ sample are represented by vertical red and green dashed lines, respectively. Patterns are offset vertically by 0.07 y-axis units for clarity, and a background curve is plotted for the $z = 0$ data set to highlight the diffuse (110) feature. The presence of a sharp (110) reflection would indicate perfect vacancy ordering (the $I4/m$ model). Observation of broad and diffuse intensity of this reflection would imply correlated vacancy disorder. A broad shoulder at the low-Q side of the (002) reflection is noticeable for each composition. The evolution with z of its normalized integrated intensity is shown in the inset. The origin of this feature is subsequently addressed in Fig. 3 and in the text.

interlayer distance increases with increasing sulfur content. Comparison of the data for two $K_xFe_{2-y}Se_2$ samples obtained by different thermal treatment reveals that this type of disorder can be suppressed by quenching [see inset to Fig. 3(b)].

Similar DISCUS simulations with a single interlayer distance but random shifts along the a and b lattice directions [known as turbostratic disorder, see Fig. 4(a)] produce a diffraction pattern characteristic for such disorder, where hkl peaks are broadened into indistinct hk-bands [50,51]. As can be seen in Fig. 4(b), this significantly reduces the number of distinct Bragg peaks, and creates a characteristic saw-tooth pattern. In Fig. 4(b), we again present an example diffraction pattern for $K_xFe_{2-y}S_2$, where no such saw-tooth like features are observed.

These simulations effectively demonstrate that the $K_xFe_{2-y}Se_{2-z}S_z$ specimens exhibit at least two distinct interlayer distances, without observable turbostratic
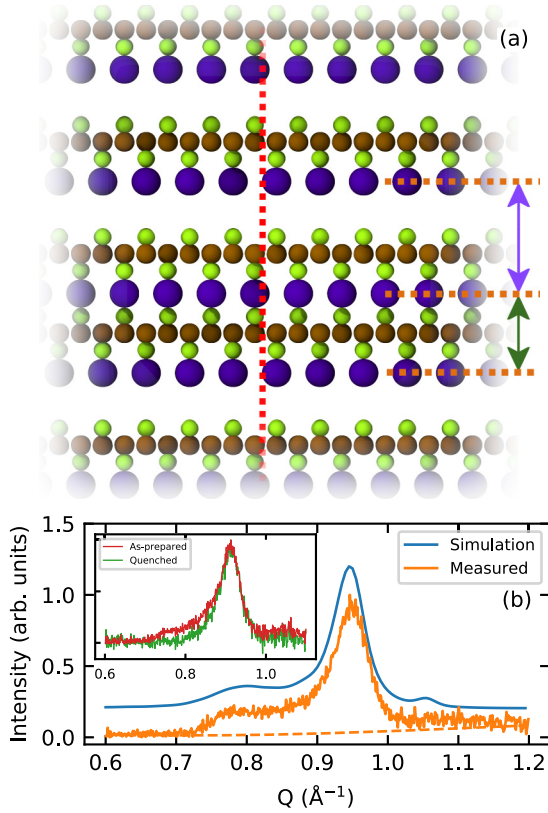
FIG. 3. Observation of stacking disorder in $K_xFe_{2-y}Se_{2-z}S_z$ system. (a) A side view of an atomistic model depicting two distinct interlayer distances along the c axis, represented by either a purple or a green double-sided arrow. Green spheres represent chalcogen, brown spheres iron, and purple spheres potassium atoms. The red vertical dashed line highlights the lack of turbostratic disorder, as discussed in the text. (b) The simulated neutron diffraction pattern (blue profile) of $K_xFe_{2-y}S_2$ for the case depicted in (a), where two distinct interlayer distances are present. Also shown is the experimental diffraction pattern for $K_xFe_{2-y}S_2$ sample at 5 K with the associated background (orange profile and dashed line, respectively) featuring (002) basal reflection at around 0.95 $\mathring{A}^{-1}$. The feature at $Q \approx 0.8$ $\mathring{A}^{-1}$ is an irrational basal reflection implying the presence of a second, longer interlayer spacing. This feature is observed for all as-prepared samples studied here (Fig. 2). Inset in (b) features data for the $K_xFe_{2-y}Se_2$ sample at 5 K, for both as-prepared (red line) and thermally quenched (green line) variants.
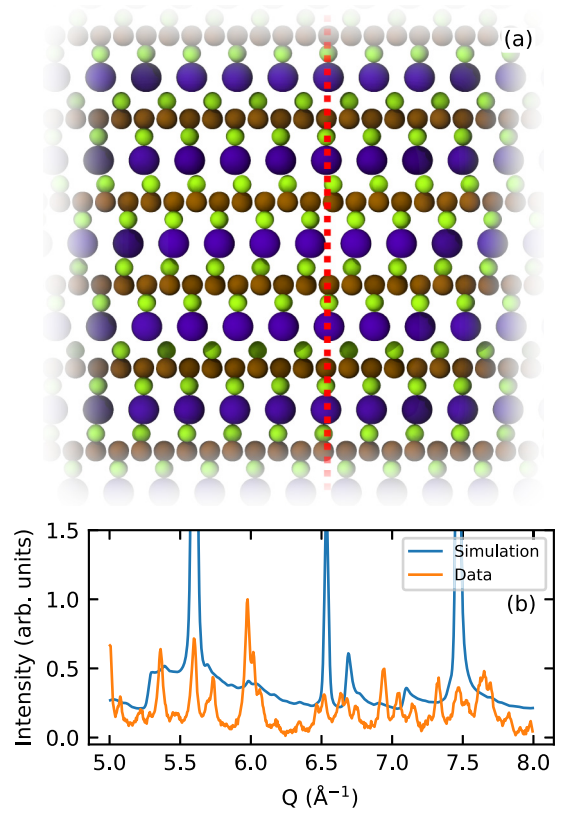

FIG. 4. Observation of stacking disorder in $K_xFe_{2-y}Se_{2-z}S_z$ system. (a) A side view of an atomistic model depicting turbostratic disorder or uniform random layer displacements along the $a - b$ lattice directions, highlighted by the vertical red dashed line. Atoms are represented as in Fig. 3, with the c axis running vertically. (b) The neutron diffraction pattern simulated for $K_xFe_{2-y}S_2$ (blue profile) in the case of turbostratic disorder depicted in (a). This type of disorder reduces the number of observed Bragg reflections, and produces characteristic sawtoothlike features, as discussed in the text. The experimental data for $K_xFe_{2-y}S_2$ (orange profile) collected at 5 K do not display the features that would imply turbostratic character of the disorder.

disorder. This anisotropic crystallinity naturally suppresses interlayer correlations, while intralayer correlations persist. Additionally, the broad nature of the (110) $\sqrt{5} \times \sqrt{5}$ ordering peak indicated that an imperfect or correlated local vacancy order is likely present, a feature which will necessarily only manifest in the local atomic structure. For these reasons, our small-box PDF modeling has focused explicitly only on the very local structure ($r < 10$ Å).

Such dual-interlayer distance has been reported previously, and was linked to potassium segregation and local ordering [29]. This additional diffraction feature is the only evidence of such local segregation and potassium ordering found here. No evidence of this behavior was found in the PDF studies

discussed below, although the PDF in this case is not particularly sensitive to potassium.

Reduced total scattering structure functions, $F(Q)$, for the $K_xFe_{2-y}Se_2$ and $K_xFe_{2-y}S_2$ end-members are shown in Figs. 5(a) and 5(c), respectively, along with the related FeSe reference in Fig. 5(e). By inspecting these data, one readily sees that Bragg peaks at high Q get suppressed when moving from the sulfur to the selenium end-member, or even when moving from the FeSe compound to either 122-type system, and that an appreciable diffuse signal appears. Suppression of Bragg peaks and appearance of diffuse intensity are indicators for the presence of disorder, suggesting that the relative amount of disorder increases when moving from the related FeSe phase to $K_xFe_{2-y}S_2$ and then to $K_xFe_{2-y}Se_2$.

The diffuse signal in $F(Q)$ is present in the data for the entire $K_xFe_{2-y}Se_{2-z}S_z$ series, as evident in Fig. 6(a), and has a sinusoidal character at high Q. Fitting with a damped sine function in the range $12 \leqslant Q \leqslant 25$ $\mathring{A}^{-1}$ allows us to quantify the amplitude and frequency of this oscillatory behavior as a
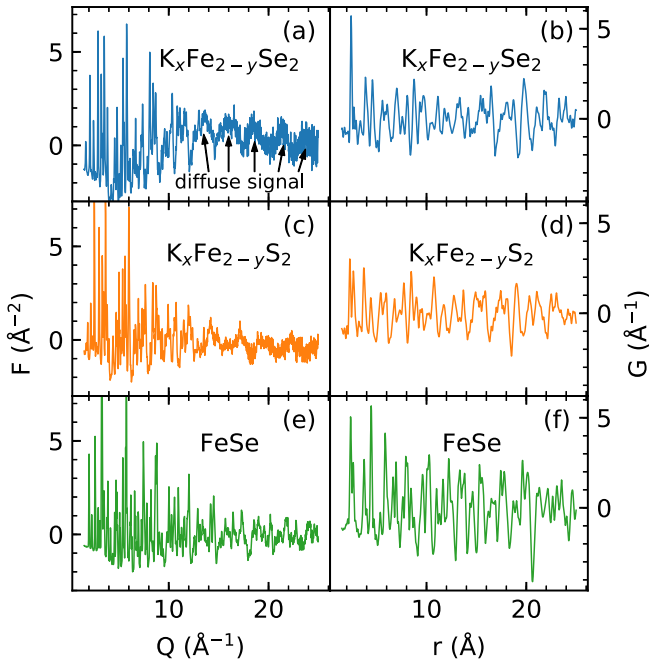
FIG. 5. Comparison of neutron total-scattering-derived data for several samples of interest. Reduced total-scattering structure functions, $F(Q)$, are shown in the left panels ($1.5 \leqslant Q \leqslant 25$ Å^{-1}), while corresponding PDFs, $G(r)$, are displayed in the right panels ($1.5 \leqslant r \leqslant 25$ Å). The panels feature (a), (b) $K_xFe_{2-y}Se_2$, (c), (d) $K_xFe_{2-y}S_2$, and (e), (f) FeSe. Data for potassium containing samples were collected at 5 K, while for FeSe at 10 K.

function of sulfur content z, shown in Figs. 6(d) and 6(e). We note that these oscillations are the strongest in the selenium end-member, and are gradually suppressed with increasing sulfur content, reaching a minimum in the range $1.2 \leqslant z \leqslant 1.6$. Above $z = 1.6$, these oscillations again increase in amplitude. This suppression and recovery is highlighted when viewing the fitted sine functions, as can be seen in Figs. 6(b) and 6(c). The frequency of the wave follows a similar two-regime behavior, delineated by the composition at $z = 1.6$.

B. PDF analysis

Interpretation of these sinelike oscillations of the diffuse signal in Q space is not straightforward. However, the presence of a sinusoidal oscillation in $F(Q)$ should map to the PDF $G(r)$, as the two are related by a Fourier transform. Specifically, a periodic signal in $F(Q)$ with frequency f and amplitude A should manifest as an enhancement (proportional to A) of the peak in $G(r)$ at $r = 2\pi f$.

Indeed, this agrees with qualitative assessments of the PDFs. The frequency and relative amplitude of the periodic signal in $F(Q)$ parallels the position and relative sharpness (compared to higher-r peaks) of the first PDF peak. The PDF of $K_xFe_{2-y}Se_2$, shown in Fig 5(b), has a sharp first peak at $r \approx 2.43$ Å, followed by relatively broad features at higher-r. Interestingly, the observed maximum of this feature is nearly twice as intense as any other feature in the PDF. Conversely, the PDF of $K_xFe_{2-y}S_2$, shown in Fig. 5(d), shows a peak at

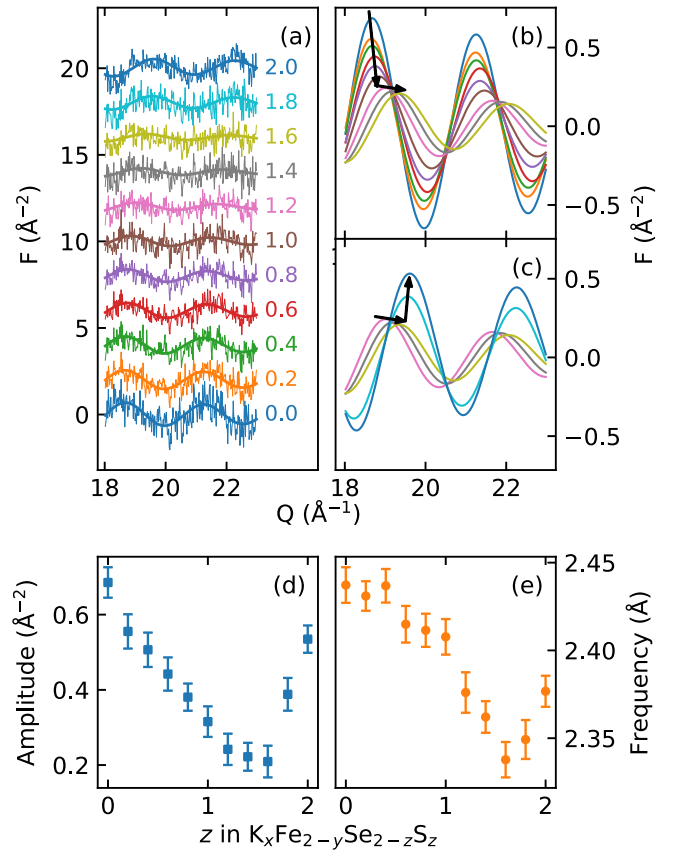FIG. 6. Analysis of the diffuse scattering signal in $F(Q)$ at high momentum transfers Q in $K_xFe_{2-y}Se_{2-z}S_z$. (a) The measured (lighter line) and fitted (heavier line) $F(Q)$ signal. The curves are sequentially offset vertically by 2 Å^{-2} for clarity. (b) The model $F(Q)$ signal over a regime of concentrations where the oscillation amplitude and frequency decrease. (c) The model $F(Q)$ signal over a regime of concentrations where oscillation amplitude and frequency increase. (d) The amplitude of $F(Q)$ diffuse oscillations as a function of sulfur content, z. (e) The frequency of diffuse oscillations as a function of z. Colors represent sulfur content, z, as indicated, and in (b) and (c) are consistent with those in (a).

$r \approx 2.38$ Å, which is of comparable sharpness to higher-r peaks.

Typically, the observation of r-dependent PDF peak widths is associated with correlated atomic motion [52]. Generally speaking, these relative widths describe the nature of the bonding in the material [53]. For example, an "infinitely" sharp first PDF peak would indicate that the nearest-neighbor pairs always move in phase, and that this bond is extremely rigid. Conversely, a first PDF peak that is of the same width as higher-r peaks would indicate that nearest-neighbor pairs do not influence each other strongly. The origin of this behavior in the system studied here will be addressed below.

The PDFs across the composition series at 5 K are shown in Fig. 7(a), and the positions of a higher-r peak as well as the first peak, representing Fe-Ch correlations, are shown in Figs. 7(b) and 7(c), respectively. Interestingly, the position of the Fe-Ch peak is nearly unchanged in the range $0.0 \leqslant z \leqslant 1.0$, signifying that the Fe-Ch pair distance is unaffected
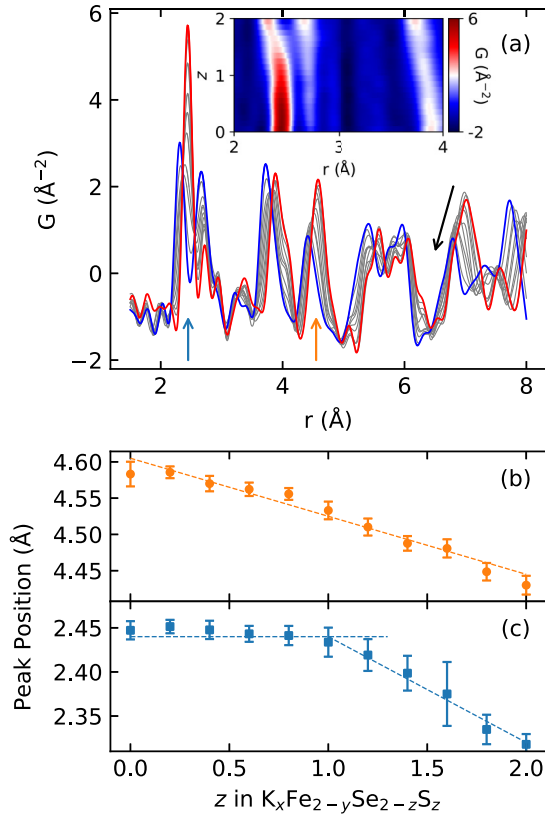
FIG. 7. 5 K PDF data of the $K_xFe_{2-y}Se_{2-z}S_z$ series. (a) The experimental PDFs in the local structure range $1.5 \leqslant r \leqslant 8$ Å. The sulfur and selenium end-members are shown with a blue and red line, respectively, while intermediate compositions are shown in gray. A black arrow is included to emphasize the continuous evolution of features at high r. Inset is a false color map representation of the same PDF data plotted vs r and z, highlighting the lack of apparent change in the position of the first PDF peak at $\sim$2.48 Å as a function of sulfur content until approximately $z = 1$. The peak starts evolving for higher z values. (b) A plot of the peak position of the feature marked by an orange arrow in (a) as a function of sulfur content z. A dashed line is a guide to the eye, included to highlight the nearly linear behavior of this peak position with z. (c) A plot of the Fe-*Ch* peak position, marked by a blue arrow in (a), as a function of z. Two dashed lines are guides to the eye, highlighting the two-regime behavior.

by the substitution of sulfur for selenium. This is in stark contrast to the typical Vegard's law-type behavior, predicting a linear change in lattice parameter as a function of chemical substitution due to steric effects [54]. This counterintuitive behavior is, however, a strictly local effect, as the expected linear pair-distance behavior is recovered if we consider the position of most higher-r peaks [Figs. 7(a) and 7(b)]. This is further evidence that the very local structure has a distinct two-regime-type behavior.

Fitting the local structure region of the observed PDFs ($1.75 \leqslant r \leqslant 10$ Å) with a two-phase model incorporating both the VO $I4/m$ and the vacancy-free $I4/mmm$ phases yielded fits which were equivalent in quality to those done with a single-phase VD $I4/m$ model, where the occupancy of Fe on the two distinct crystallographic sites is allowed to
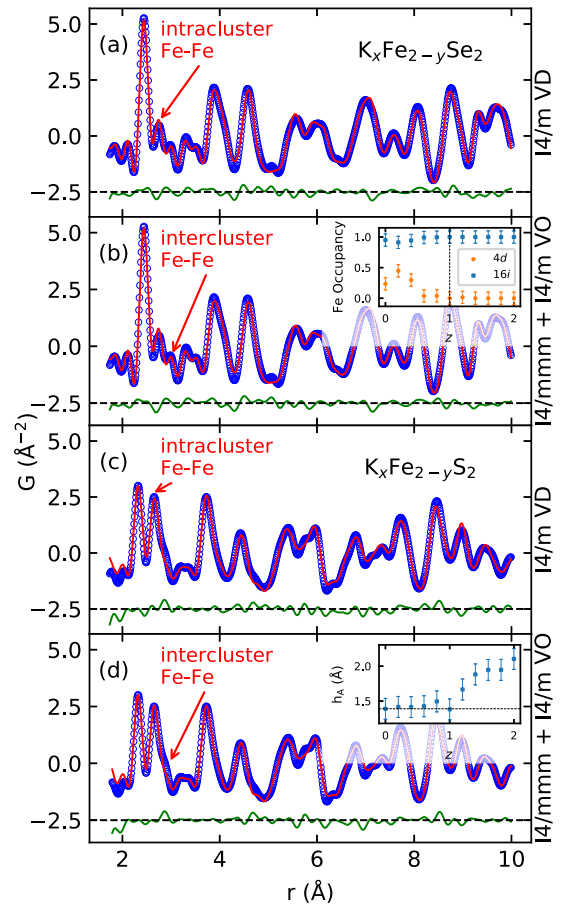

FIG. 8. Fits of the structural models to the PDF data. The fit to the observed $K_xFe_{2-y}Se_2$ PDF data using either (a) a single-phase $I4/m$ vacancy-disordered (VD) model or (b) a two-phase model with $I4/m$ VO and $I4/mmm$ vacancy-free components. Similar one- and two-phase fits for $K_xFe_{2-y}S_2$ are shown in (c) and (d), respectively, for the $K_xFe_{2-y}S_2$ PDF data. In both compositions, single- and two-phase models yielded fits of similar quality: $R_w = 0.12$ and $R_w = 0.15$ for $K_xFe_{2-y}Se_2$ and $K_xFe_{2-y}S_2$, respectively. In various panels, arrows point to intracluster and intercluster Fe-Fe PDF peaks, as indicated. See text and Fig. 1(e) for details. In all cases, fits were over the displayed r-range ($1.5 \leqslant r \leqslant 10$ Å). PDF data and fits are shown with open circles and solid red lines, respectively, and the difference curves (solid green lines) are shown offset vertically for clarity. The inset in (b) summarizes the single-phase PDF refinement-derived evolution with sulfur content of Fe occupancy of the two distinct Fe sites ($4d$ and $16i$) in the $I4/m$ VD model. Inset in (d) shows evolution of chalcogen anion height h_A with sulfur content as obtained from the $I4/mmm$ vacancy-free component of the two-phase PDF model. A horizontal dashed line represents the reported optimal anion height for superconductivity [55].

vary. Examples of these fits for the S- and Se-end-members are shown in Fig. 8. In these two-phase models, all samples across the series possess the minority $I4/mmm$ phase with an average refined volume percentage of *ca.* 8%.

Importantly, only the lower symmetry $I4/m$ model supports the existence of two unique Fe-Fe correlation peaks representing inter- and intracluster Fe-Fe correlations [see Figs. 1(e) and 8], and these two unique Fe-Fe correlation

peaks were observed throughout the entire composition range [see Fig. 7(a)]. Additionally, the absence of well-defined sharp (110) reflections (Fig. 2) indicates that perfect VO cannot be present, and thus the presence of a $I4/m$ model with exactly zero Fe $4d$ site-occupancy is inconsistent with the diffraction data. The single-phase VD $I4/m$ model is also a simpler model with fewer free parameters compared to the two-phase description. For these reasons, the single-phase VD $I4/m$ model was preferred and utilized here.

While single-phase fits using a VD $I4/m$ model may seem inappropriate, as other earlier studies have found evidence for phase separation, it is important to note that the PDF analysis presented here considers only very local (less than 1 nm) structural features. Our small-box modeling approach, shown in Fig. 8, suggests that over sub-nm length scales the $I4/m$-VD model and $I4/m - \text{VO} + I4/mmm$ model are equivalent descriptions in terms of explaining the observed data. It is important to highlight that this single phase description is not intended to contest the accepted phase separation picture of this system. It is possible and perhaps even likely that local correlated VO may manifest as phase separation over longer length scales, but our results show that the two (phase separation and a single phase with partial vacancy site occupancy) are both equivalent descriptions of the local structure when using small-box fitting approaches.

The inset in Fig. 8(b) shows the refined occupancy of the two symmetry-distinct Fe sites, at $4d$ and $16i$ extracted from the single-phase $I4/m$ VD PDF fits. This Fe site occupancy allows for the presence of both vacancy-free domains, attributed to the superconducting behavior, as well as VO AF domains. Any refinement to a nonzero Fe $4d$ site occupancy suggests that both domains are present. The refined $4d$ site occupancy then acts as an estimate of the fraction of the vacancy-free phase.

As sulfur is substituted for selenium, the $4d$ site moves from partially occupied to completely empty, whereas the $16i$ site moves from partially vacant to completely occupied. The situation where the $4d$ Fe is completely vacant and the $16i$ is completely occupied represents the VO phase, associated with suppression of superconductivity [34], whereas a partial occupancy suggests imperfect vacancy ordering, or the presence of both vacancy-free and VO domains in a single coherent lattice. Thus, we note a crossover behavior in the vacancy distribution or phase separation of the local structure, from partial to nearly ideal ordering. According to our PDF fits, this transformation occurs locally in this system at $z = 1.0$, or about 50% sulfur substitution at 5 K.

The inset in Fig. 8(d) shows the refined anion height h_A in the presumed superconducting $I4/mmm$ phase from the two phase fits. The horizontal dashed line represents the reported optimal anion height for superconductivity [55]. For $z \leqslant 1.0$, h_A is constant and adopts the ideal value, whereas for $z > 1.0$, h_A increases beyond the ideal value. The evolution of anion height across the series corroborates the Mizuguchi rule [55] and parallels the observed suppression of superconductivity for $z > 1.0$.

The results presented so far all demonstrate a two-regime behavior, and this is consistent with the electronic phase diagram. Electrical transport measurements suggest that T_c is appreciably suppressed, beginning at $z = 1.0$, with no

evidence of superconductivity above $z \approx 1.5$ [18]. The structure function $F(Q)$ shows high-Q oscillations which decrease in magnitude and frequency up to $z = 1.6$ and then recover for $z > 1.6$ (Figs. 5 and 6). The frequency and magnitude of these $F(Q)$ oscillations correlate with the position and relative sharpness, respectively, of the Fe-Ch nearest neighbor (NN) peak as observed in the PDFs of the $K_x Fe_{2-y} Se_{2-z} S_z$ series at 5 K. Furthermore, this Fe-Ch NN peak disobeys Vegard's law up to about $z = 1.0$ [Fig. 7(c)], as shown by both the $F(Q)$ and $G(r)$ analysis.

While each aspect of our analysis highlights that the $K_x Fe_{2-y} Se_{2-z} S_z$ series exhibits a two-regime behavior at 5 K, it is not immediately apparent how each individual element of this analysis is related to the others. The exaggerated sharpness of the Fe-Ch NN peak (relative to higher-r PDF peaks) in the selenium-rich regime signifies that the Fe-Ch bond length distribution (BLD) is significantly narrower compared to Fe-Ch BLD in the sulfur rich regime [23]. This Fe-Ch BLD in $K_x Fe_{2-y} Se_2$ [Fig. 5(b)] is also much sharper than that seen in FeSe, observed under similar conditions [Fig. 5(f)]. This is intriguing, as the Fe-Ch NN correlations in both $K_x Fe_{2-y} Se_2$ and FeSe are due to the same structural motif of $FeSe_4$ edge-shared tetrahedra. Thus, the observed differences in the Fe-Se BLDs between $K_x Fe_{2-y} Se_2$ and FeSe cannot be due to chalcogen size mismatch. It is then also possible that something other than simple steric differences between sulfur and selenium contribute to the differences in relative Fe-Ch BLDs (peak sharpness) across the $K_x Fe_{2-y} Se_{2-z} S_z$ series.

Notably, the results presented so far further suggest that the two-regime behavior is marked by a crossover from a correlated disorder state to more complete vacancy-order within the local structure. While it is expected that vacancy ordering impacts the overall disorder of the structure, it is also possible that it directly impacts the Fe-Ch BLD as observed through the first PDF peak.

To explore this aspect further, we considered three large atomistic models with different local vacancy distributions but similar average structure. The first was built with a uniformly disordered arrangement of vacancies [Fig. 9(a)], the second with correlated vacancy disorder [Fig. 9(c)], and the third with a completely ordered arrangement of vacancies [Fig. 9(e)]. Importantly, these three configurations were created with identical overall vacancy concentrations (20%, as suggested by previous EDX studies on these samples [18]) using the same space-group ($I4/m$) and unit cell parameters.

If each of these large configurations are folded into a single unit cell, they would appear nearly identical, with the primary difference being the occupancy of the distinct Fe sites in the $I4/m$ space group. It is clear, however, that the local structure of each is quite distinct. This local vs average discrepancy highlights the shortcomings of traditional crystallography in describing such materials [42,43,56], and reiterates our earlier observations of pervasive anisotropic broadening of the (110) diffraction peak as demonstrated in Fig. 2.

In these atomic configurations, each chalcogen species can be coordinated by either four Fe's, four vacancies, or permutations of both Fe and vacancies. For each atomistic model, we quantified the total number of each of the five possible configurations. These results are presented in Figs. 9(b), 9(d), and 9(f) in the form of normalized histograms showing the
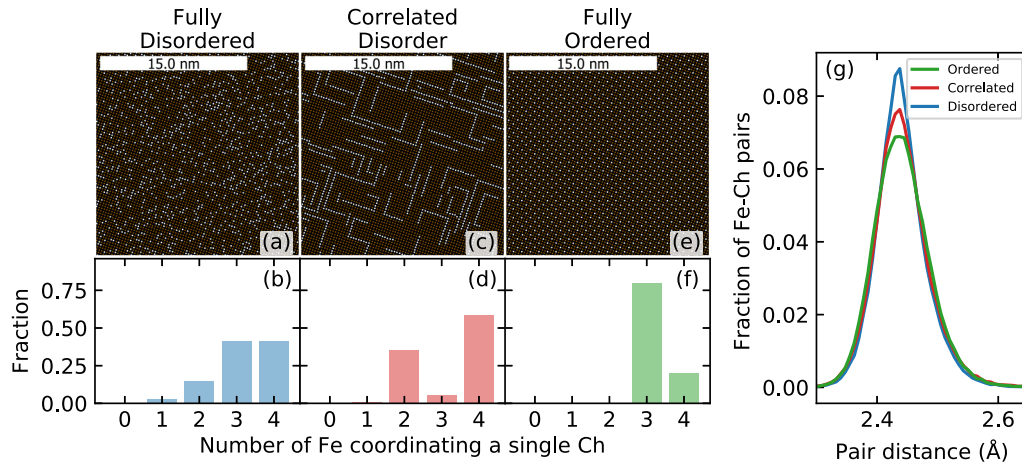
FIG. 9. The effect of vacancy ordering on the local FeCh$_4$ structural unit. (a) An atomistic model (viewed down the c axis) featuring uniform vacancy (white dots) disorder in the iron (brown dots) sublattice. (b) A histogram enumerating the total number of chalcogen species (expressed as a fraction) coordinated by either 0, 1, 2, 3, or 4 Fe in the atomic configuration represented in (a). (c) Similar to (a), except the vacancies show correlated disorder, with an increased likelihood of like neighbors in the first coordination shell and unlike neighbors in the second coordination shell. (d) Similar to (b) except pertaining to the atomic configuration in (c). (e) Similar to (a), except the vacancies are fully ordered over the Fe sublattice. (f) Similar to (b) except pertaining to the atomic configuration in (e). (g) The distribution of Fe-*Ch* pair distances following energy minimization in the presence of a Lennard-Jones (LJ) potential between Fe-*Ch* nearest neighbors, shown for the vacancy distributions represented by the atomistic model in (a), (c), and (e). LJ potential parameters were identical between the each atomic configuration, the differences in the pair distances distributions are a result of the vacancy configuration, only.

distribution of *Ch* with a specific number of Fe neighbors for the VD, correlated-disorder, and VO atomistic models, respectively.

For the VO case, the results are as expected, 20% of chalcogens are fully coordinated by four Fe's, whereas 80% of chalcogens are coordinated by three Fe's and a single vacancy, and no chalcogens are coordinated by two or more vacancies.

The VD case is more interesting: a significant fraction of chalcogens (∼20%) are severely undercoordinated, with two or more missing Fe NNs. Moreover, and importantly, the percentage of fully coordinated chalcogens nearly doubles compared to the VO case. These vacancy-free configurations can be associated with the presumed superconducting $I4/mmm$ phase [18]. Surprisingly, and somewhat counterintuitively, the increase in fully coordinated chalcogens is a result of disordering the vacancies in this system. The atomic configuration exhibiting correlated disorder, however, shows the greatest prevalence of fully coordinated chalcogens, notably the vacancy-free domains represent more than 50%, greater than the percolation threshold in a square lattice.

It is interesting to note that the atomic arrangement depicted in Fig. 9(c) shows a distinct pattern, where linear stripes of vacancies meet at right angles and are arranged around vacancy-free domains. This mirrors the striking microstructures observed in many cases in the Se-end-member (K$_x$Fe$_{2-y}$Se$_2$) system [14,27,29].

If the three configurations exemplified by Figs. 9(a), 9(c) and 9(e) are energy minimized in the presence of an *identical* Lennard-Jones potential between Fe and *Ch* NNs, as outlined fully in the Appendix, the resulting Fe-*Ch* BLDs, shown in Fig. 9(g), are *different*. Specifically, the Fe-*Ch* BLD of the energy-minimized VD configuration is noticeably sharper than the VO configuration, whereas the configuration showing correlated disorder represents an intermediate case. It is

important to note that the energy minimization did not involve site swapping or vacancy rearrangement, and as such the resulting atomistic models are indistinguishable from those shown in Figs. 9(a), 9(c), and 9(e). Our finding is quite surprising, given that the sharpest distribution originates from a system with the most overall disorder.

Our simulations demonstrate that the relative arrangement of vacancies has an intrinsic impact on the Fe-*Ch* BLD, even in the presence of identical pairwise interactions. This idea makes intuitive sense, as the VD state shows a greater prevalence of severely undercoordinated chalcogen species. Using the language of "correlated motion" of nearest neighbors, this could imply that these severely undercoordinated chalcogens will form a more rigid bond with the fewer Fe species they are coordinated by, leading to a relatively narrower Fe-*Ch* BLD.

The result also offers an explanation of the two-regime behavior. Specifically, for the selenium-rich cases, the local structure may show correlated or imperfect VO, characterized by domains with no vacancies coexisting in the same lattice with domains showing ordered vacancies. Conversely, in the sulfur-rich cases, a vacancy redistribution may create more idealized ordering. This is further supported by the increased prevalence of the longer interlayer spacing toward the sulfur end of the phase diagram, as shown in Fig. 2 and discussed in Fig. 3(b). This longer interlayer spacing has been linked in previous work on the Se-end-member to localized domains with larger-than-average potassium concentrations [29]. This same study has further shown that Fe-vacancy ordering is linked closely to superconductivity and the distribution of potassium [29].

This effect manifests in $F(Q)$ through suppression of Bragg peaks at high Q (Fig. 6), leading to the observation of a strong sinusoidal intensity oscillation. In $G(r)$, this oscillation manifests as a relatively sharp first peak followed
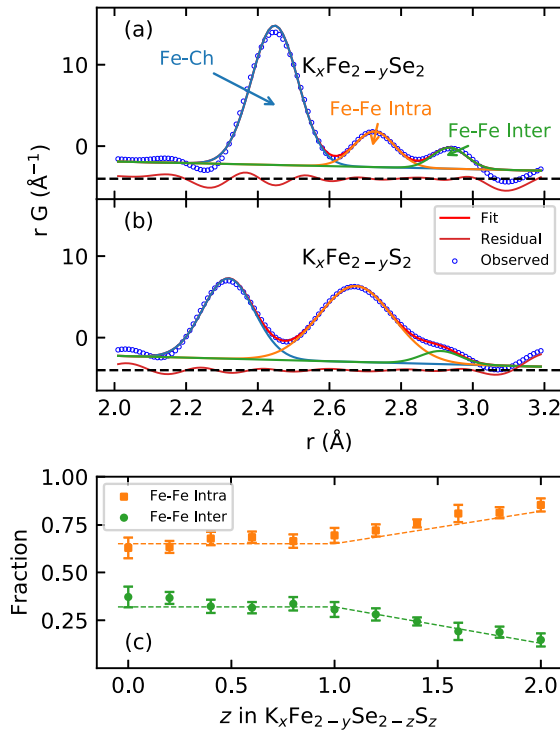
FIG. 10. Evolution of the local structure with sulfur content. (a) $K_xFe_{2-y}Se_2$ radial distribution function showing Fe-Ch and distinct Fe-Fe pair distances (see text). (b) Similar to (a) except with $K_xFe_{2-y}S_2$, highlighting the relative increase in prevalence of intracluster Fe-Fe pairs. (c) Quantification of the prevalence of different inter- and intracluster Fe-Fe pairs as a function of sulfur content z. (d) Quantification of the inter- and intracluster Fe-Fe pair distances as a function of sulfur content z.

FIG. 11. Qualitative comparison of PDF derived local structural parameters and electronic properties of $K_xFe_{2-y}Se_{2-z}S_z$. (a) Reduced observables, representing electronic and structural quantities rescaled to a fraction of their values at the end-members. By definition (see text) these reduced observables are one at $z = 0$ and zero at $z = 2$. (b) The previously reported [18] electronic phase diagram of $K_xFe_{2-y}Se_{2-z}S_z$ ($0 \leqslant z \leqslant 2$) as a function of temperature T and composition z, obtained by resisitivity and DC magnetic susceptibility measurements using a Quantum design PPMS-9 and MPMS-XL5 on single-crystal samples prior to grinding.

by broader high-r peaks (Fig. 7), corresponding to a sharper Fe-Ch BLD.

It is likely that the local structure of each sample sits somewhere between the fully VD and fully ordered case, represented by Figs. 9(a) and 9(e), respectively. To further quantify the degree of correlated disorder, we have conducted structure-model independent analysis of the first three measured PDF peaks across the series. These peaks correspond to Fe-Ch, Fe-Fe intra- and intercluster correlations, in order of increasing r.

Figures 10(a) and 10(b) show example fits of Gaussian profiles to the radial PDF $rG(r)$ for the selenium and sulfur end-members, respectively. As the Fe-Fe intra- and intercluster peaks are a result only of Fe-Fe correlations, their mutual *relative* contributions to the PDF are not impacted by the overall system chemistry, and their area normalized to the area of the pair gives an indication of the prevalence of the distinct Fe-Fe environments. In Fig. 10(c), we show the relative fraction of Fe-Fe intra- and intercluster pairs as obtained from this analysis. We see that for the selenium-rich phases up to $z = 1.0$, the relative abundance of each type of Fe-Fe pair is largely unchanged. In the sulfur-rich portion when $z > 1.0$, there is a monotonic increase in the fraction of intracluster pairs at the expense of intercluster pairs. This is consistent with vacancy redistribution and an increase in
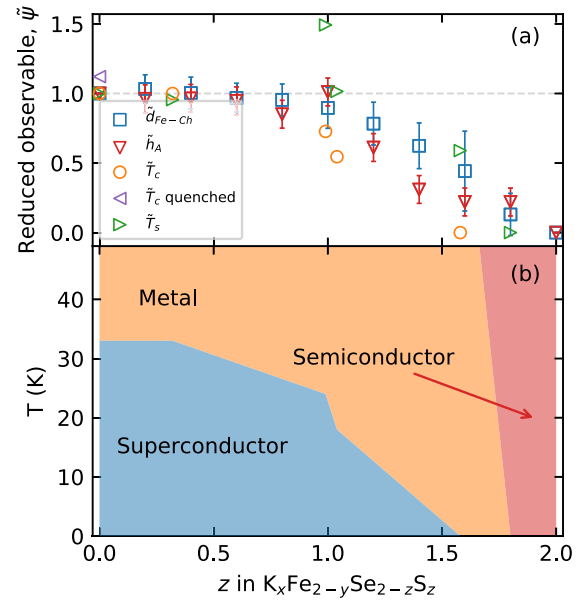
vacancy ordering when moving from Se-rich toward the S-rich end of the phase diagram, as the fully ordered configuration should maximize the fraction of intracluster Fe-Fe pairs. This analysis further supports the two-regime behavior of this system in phase space.

Finally, we explore the correlation between the measures of local structure outlined here to the electronic properties in this system in the context of "reduced observables" computed as a function of sulfur content, $\tilde{\psi}_{red}(z)$. We define a reduced observable as the observed quantity at a given composition z normalized by the same observed quantities at the composition end-members ($z = 0$ and $z = 2$) such that $\tilde{\psi}_{red}(z) = \frac{\psi(z) - \psi(z=2)}{\psi(z=0) - \psi(z=2)}$. By design, $\tilde{\psi}_{red}(0) = 1$ and $\tilde{\psi}_{red}(2) = 0$.

Results for the superconducting temperature $\tilde{T}_c$ and metal-insulator transition temperature $\tilde{T}_s$, reported previously [18], and the Fe-Ch distance $\tilde{d}_{Fe-Ch}$, as well as the anion height $\tilde{h}_A$ derived from the present PDF analysis, are plotted in Fig. 11(a). Also included for reference is the T_c of a quenched $K_xFe_{2-y}Se_2$ sample. Importantly, T_c for a quenched sample is higher than for as-prepared, in line with the idea that stacking disorder and potassium distribution play an important role for superconducting properties of this system [33].

The results are striking, as each of these reduced quantities largely follow the same trend, remaining essentially constant up to $z = 1$, then decreasing steadily in the range $1 < z < 2$. This serves to emphasize the apparent connection between the subnanometer atomic structure at 5 K, as studied here, and the electronic properties (see, e.g., Fig. 11(b) and Ref. [18]),

which invites further complementary experimental and theoretical considerations.

IV. CONCLUSIONS

In summary, the local atomic structure and structural disorder have been characterized across the phase diagram of $K_x Fe_{2-y} Se_{2-z} S_z$ ($0 \leqslant z \leqslant 2$) system, displaying both superconductivity and magnetism by means of neutron total scattering and associated atomic PDF analysis of 5 K data. Using various structure-model-independent and -model-dependent approaches, we find a high level of structural complexity on the nanometer length scale. The analysis highlights the presence of considerable disorder in the c-axis stacking of the $Fe_2 Se_{2-z} S_z$ slabs, which has a nonturbostratic character, and can be suppressed by thermal quenching. PDF fitting suggests that over subnanometer length scales, a simple two-phase physical mixture description (VO and vacancy-free) is equivalent to a single phase description, allowing for partial Fe occupancy of the vacancy site. Within this description, a nonzero Fe occupancy of the $4d$ site indicates the presence of vacancy-free superconducting domains. Complementary aspects of the analysis reveal a crossoverlike behavior, with an onset at $z \approx 1$, from predominantly correlated disorder state toward the selenium end of the phase diagram, to a more ordered vacancy distribution closer to the sulfur end of the phase diagram. Through simulations based on large scale atomistic models, we demonstrate that the distribution of vacancies can significantly modify the NN BLD, observably affecting the NN environment, as corroborated by the features in the data. The correlation of electronic properties with the Fe vacancy distribution may imply that the disorder of Fe vacancies in the local structure creates "domains" resembling Fe-vacancy-free superconducting $I4/mmm$ phase, which may be suppressed with the correlated disorder to order crossover across the series. This could imply that the SC-bearing vacancy-free phase is suppressed with S substitution, although our analysis does not directly probe this aspect. The local structure observations and their correlation with electronic properties presented here add to the nuanced picture of the role of atomic structure in this system, and should help to inform future experimental and theoretical work seeking to understand the mechanisms behind these correlations.

APPENDIX

1. Neutron total scattering

Experiments were performed using powder samples, 0.5 g of each, equally spaced across the Se/S compositional space ($\Delta z = 0.2$), loaded into 6-mm-diameter extruded vanadium containers under inert atmosphere and sealed. Each sample was mounted in the diffractometer equipped with orange cryostat. The instrument was calibrated using diamond powder standard. Powder diffraction data were collected after thorough equilibration at 5 K for 2 h of total counting time for each sample. Neutron PDFs were obtained via sine Fourier transforms over a range from $Q_{min} = 0.5$ Å^{-1} to $Q_{max} = 26$ Å^{-1}.

2. Structure-model independent analysis

Fitting of PDF data for decomposition into constituent peaks was done with the FITYK v. 1.3.1 software package [58], using Gaussian functions and a linear baseline function where the intercept term was fixed at zero. The $F(Q)$ data for each sample were fitted with a damped sine function after subtracting a fitted linear background.

3. Structural models

Within the system, two possible structural models have been put forward. The simplest model, with space group $I4/mmm$, consists of FeCh ($Ch =$ Se/S) slabs featuring a Fe square planar sublattice [Figs. 1(a)–1(c)]. Each Fe is coordinated by four Ch creating layers of edge-shared FeCh_4-tetrahedra, stacked along the c lattice direction and interleaved with K species equidistant from each layer. In this model, the asymmetric unit contains a single Fe at $4d$ (0.0, 0.5, 0.25), Ch at $4e$ (0.0, 0.0, z), and K at $2a$ (0.0, 0.0, 0.0). The relatively simple structure, with only one unique Fe site, gives little flexibility for handling vacancies on the Fe sublattice, which are common in this system [10,14,34].

A more complicated model, with space group $I4/m$, is related to the higher symmetry $I4/mmm$ model through a rotation in the $a - b$ plane and a $\sqrt{2}$ increase in the $a = b$ lattice parameters [Figs. 1(d) and 1(e)]. The increase in unit cell size doubles the number of atoms in the asymmetric unit, with two symmetry-distinct Fe's at $4d$ (0.0, 0.5, 0.25) and $16i$ (x, y, z), Ch at $4e$ (0.0, 0.0, z) and $16i$ (x, y, z), and K at $2b$ (0.0, 0.0, 0.5) and $8h$ ($x, y, 0.5$). Importantly, within both these symmetries, the FeCh_4 tetrahedra of adjacent layers are translated in the x and y direction by half-unit cell lengths. This can be contrasted with the related FeCh-11 group of superconductors, where adjacent layers of FeCh_4-tetrahedra contain no such relative x and y translations.

4. Small-box refinements

The experimental PDF data were fit with the structural models described over a 10 Å range using the PDF$_{\mathrm{GUI}}$ software [40]. Over wider r-ranges, the experimental PDF is dominated by the interlayer correlations and our analysis reveals that these are affected by appreciable stacking disorder, which is highly nontrivial to handle using conventional PDF approaches and is beyond the scope of this study. Two alternative modeling approaches were attempted in subnanometer regime. The first approach used a mixture of vacancy-free $I4/mmm$ and fully Fe VO $I4/m$ phase components. The second approach utilized only a VD version of $I4/m$. The two approaches were found to yield effectively identical fit qualities and comparable descriptions of the underlying structure [23]. The VD model with $I4/m$ symmetry, systematically applied to all data, used a total of 19 fitting parameters. These included the unit cell parameters ($a = b \neq c$), a scale factor, and a correlated motion parameter δ_1 [52]. Further, the fractional coordinates were refined according to the space group constraints (nine parameters), and the atomic displacement parameters (ADPs) were set to be isotropic ($u_{11} = u_{22} = u_{33}$) and identical for all atomic species of the same type (three parameters). The occupancies of the two symmetry-distinct Fe crystallographic sites ($4d$ and $16i$) were allowed to vary separately, while the occupancies of potassium atoms in $2b$ and $8h$ sites were constrained to be equal because of relative insensitivity of the neutron PDF to potassium (three occupancy parameters). The occupancies of Ch species were fixed at their nominal values as refinements did not suggest chalcogen sublattice ordering. Refinements were done sequentially, such that for any given composition the PDF refinement was initialized using the converged model of the previous composition. Additionally, appropriately constrained two-phase fits were used to track the evolution of the anion height estimated from the $I4/mmm$ vacancy-free component.

5. Large-box simulations

Simulated PDFs were computed with the aid of the DISCUS v 5.30.0 software package [41] using a model with space group $I4/m$. The global concentration of Fe was fixed at the nominal concentration, with full occupancy of the $16i$ site and full vacancy occupancy of the $4d$ site. The global concentration of K was fixed at the nominal concentration, spread uniformly across the $2b$ and $8h$ sites. For stacking fault simulations, the stack module of the DISCUS software package was used, with a layer supercell of 2×2 unit cells and total thickness of 1500 layers. The powder pattern was computed using the fast Fourier method in DISCUS, with a 0.001 reciprocal length unit mesh for powder integration. For simulations on the impact of vacancy disorder, a supercell of $50 \times 50 \times 1$ unit cells was used. Atoms were initialized with a random thermal displacement such that their mean squared displacement across the whole supercell was consistent with the ADP parameters refined from the $K_x Fe_{2-y} Se_{2-z} S_z$ PDF data. Following this, atomic displacement vectors were swapped between atoms of like identity to minimize the total energy E_{LJ} composed of a pairwise Lennard Jones (LJ) potential between NN Fe-Ch pairs, specifically,

$$E_{LJ} = \sum_i \sum_{n \neq i} \left[\frac{A}{d_{in}^{12}} - \frac{B}{d_{in}^{6}} \right] \qquad (A1)$$

over all atoms i, n, with

$$A = D \frac{1}{2} \tau_{in}^{12} \text{ and } B = 2D \tau_{in}^{6}. \qquad (A2)$$

The LJ potential was constructed such that the equilibrium NN Fe-Ch bond distance was that refined from the $K_x Fe_{2-y} Se_{2-z} S_z$ PDF data ($\tau_{in} = 2.44$ Å) with potential depth $D = 100$. Swaps were always accepted if they decreased the total energy, and conditionally accepted if they increased the total energy, with probability $p = \exp(-\Delta E / kT)$, where ΔE is the change in energy associated with the swap, k is the Boltzmann constant, and T is the temperature, in this case 5 K. The total number of swaps was fixed at 100 times the number of atoms in the supercell.

[1] J. Guo, S. Jin, G. Wang, S. Wang, K. Zhu, T. Zhou, M. He, and X. Chen, Phys. Rev. B **82**, 180520(R) (2010).

[2] F. Ye, S. Chi, W. Bao, X. F. Wang, J. J. Ying, X. H. Chen, H. D. Wang, C. H. Dong, and M. Fang, Phys. Rev. Lett. **107**, 137003 (2011).

[3] F.-C. Hsu, J.-Y. Luo, K.-W. Yeh, T.-K. Chen, T.-W. Huang, P. M. Wu, Y.-C. Lee, Y.-L. Huang, Y.-Y. Chu, D.-C. Yan *et al.*, Proc. Natl. Acad. Sci. **105**, 14262 (2008).

[4] W. Bao, Q.-Z. Huang, G.-F. Chen, D.-M. Wang, J.-B. He, and Y.-M. Qiu, Chin. Phys. Lett. **28**, 086104 (2011).

[5] M. Wang, M. Wang, G. N. Li, Q. Huang, C. H. Li, G. T. Tan, C. L. Zhang, H. Cao, W. Tian, Y. Zhao *et al.*, Phys. Rev. B **84**, 094504 (2011).

[6] Y. J. Yan, M. Zhang, A. F. Wang, J. J. Ying, Z. Y. Li, W. Qin, X. G. Luo, J. Q. Li, J. Hu, and X. H. Chen, Sci. Rep. **2**, 212 (2012).

[7] A. Krzton-Maziopa, V. Svitlyk, E. Pomjakushina, R. Puzniak, and K. Conder, J. Phys.: Condens. Matter **28**, 293002 (2016).

[8] A. Charnukha, J. Deisenhofer, D. Pröpper, M. Schmidt, Z. Wang, Y. Goncharov, A. N. Yaresko, V. Tsurkan, B. Keimer, A. Loidl *et al.*, Phys. Rev. B **85**, 100504(R) (2012).

[9] D. Louca, K. Park, B. Li, J. Neuefeind, and J. Yan, Sci. Rep. **3**, 2047 (2013).

[10] S. V. Carr, D. Louca, J. Siewenie, Q. Huang, A. Wang, X. Chen, and P. Dai, Phys. Rev. B **89**, 134509 (2014).

[11] D. P. Shoemaker, D. Y. Chung, H. Claus, M. C. Francisco, S. Avci, A. Llobet, and M. G. Kanatzidis, Phys. Rev. B **86**, 184511 (2012).

[12] N. Lazarević, M. Abeykoon, P. W. Stephens, H. Lei, E. S. Bozin, C. Petrovic, and Z. V. Popović, Phys. Rev. B **86**, 054503 (2012).

[13] V. Ksenofontov, G. Wortmann, S. A. Medvedev, V. Tsurkan, J. Deisenhofer, A. Loidl, and C. Felser, Phys. Rev. B **84**, 180508(R) (2011).

[14] X. Ding, D. Fang, Z. Wang, H. Yang, J. Liu, Q. Deng, G. Ma, C. Meng, Y. Hu, and H.-H. Wen, Nat. Commun. **4**, 1897 (2013).

[15] A. Ricci, N. Poccia, G. Campi, B. Joseph, G. Arrighetti, L. Barba, M. Reynolds, M. Burghammer, H. Takeya, Y. Mizuguchi *et al.*, Phys. Rev. B **84**, 060511(R) (2011).

[16] Z.-W. Wang, Z. Wang, Y.-J. Song, C. Ma, Y. Cai, Z. Chen, H.-F. Tian, H.-X. Yang, G.-F. Chen, and J.-Q. Li, J. Phys. Chem. C **116**, 17847 (2012).

[17] A. Charnukha, A. Cvitkovic, T. Prokscha, D. Pröpper, N. Ocelic, A. Suter, Z. Salman, E. Morenzoni, J. Deisenhofer, V. Tsurkan, A. Loidl *et al.*, Phys. Rev. Lett. **109**, 017003 (2012).

[18] H. Lei, M. Abeykoon, E. S. Bozin, K. Wang, J. B. Warren, and C. Petrovic, Phys. Rev. Lett. **107**, 137002 (2011).

[19] Y. Texier, J. Deisenhofer, V. Tsurkan, A. Loidl, D. S. Inosov, G. Friemel, and J. Bobroff, Phys. Rev. Lett. **108**, 237002 (2012).

[20] G. Friemel, J. T. Park, T. A. Maier, V. Tsurkan, Y. Li, J. Deisenhofer, H.-A. Krug von Nidda, A. Loidl, A. Ivanov, B. Keimer *et al.*, Phys. Rev. B **85**, 140511(R) (2012).

[21] W. Li, H. Ding, P. Deng, K. Chang, C. Song, K. He, L. Wang, X. Ma, J.-P. Hu, X. Chen *et al.*, Nat. Phys. **8**, 126 (2012).

[22] G. Friemel, W. P. Liu, E. A. Goremychkin, Y. Liu, J. T. Park, O. Sobolev, C. T. Lin, B. Keimer, and D. S. Inosov, Europhys. Lett. **99**, 67004 (2012).

[23] P. Mangelis, H. Lei, M. McDonnell, M. Feygenson, C. Petrovic, E. Bozin, and A. Lappas, Condens. Matter **3**, 20 (2018).

[24] Z. Wang, Y. J. Song, H. L. Shi, Z. W. Wang, Z. Chen, H. F. Tian, G. F. Chen, J. G. Guo, H. X. Yang, and J. Q. Li, Phys. Rev. B **83**, 140505(R) (2011).

[25] M. Yi, D. H. Lu, J. G. Analytis, J.-H. Chu, S.-K. Mo, R.-H. He, M. Hashimoto, R. G. Moore, I. I. Mazin, D. J. Singh *et al.*, Phys. Rev. B **80**, 174510 (2009).

[26] C. C. Homes, Z. J. Xu, J. S. Wen, and G. D. Gu, Phys. Rev. B **85**, 180510(R) (2012).

[27] Y. Liu, Q. Xing, W. E. Straszheim, J. Marshman, P. Pedersen, R. McLaughlin, and T. A. Lograsso, Phys. Rev. B **93**, 064509 (2016).

[28] C.-H. Wang, T.-K. Chen, C.-C. Chang, C.-H. Hsu, Y.-C. Lee, M.-J. Wang, P. M. Wu, and M.-K. Wu, Europhys. Lett. **111**, 27004 (2015).

[29] Z. Wang, Y. Cai, Z. W. Wang, C. Ma, Z. Chen, H. X. Yang, H. F. Tian, and J. Q. Li, Phys. Rev. B **91**, 064513 (2015).

[30] Y. J. Song, Z. Wang, Z. W. Wang, H. L. Shi, Z. Chen, H. F. Tian, G. F. Chen, H. X. Yang, and J. Q. Li, EPL (Europhysics Letters) **95**, 37007 (2011).

[31] C. Wang, T. Chen, C. Chang, Y. Lee, M. Wang, K. Huang, P. Wu, and M. Wu, Physica C: Supercond. Appl. **549**, 61 (2018).

[32] C. Duan, J. Yang, Y. Ren, S. M. Thomas, and D. Louca, Phys. Rev. B **97**, 184502 (2018).

[33] H. Lei and C. Petrovic, Phys. Rev. B **84**, 212502 (2011).

[34] M. K. Wu, P. M. Wu, Y. C. Wen, M. J. Wang, P. H. Lin, W. C. Lee, T. K. Chen, and C. C. Chang, J. Phys. D: Appl. Phys. **48**, 323001 (2015).

[35] A. Iadecola, B. Joseph, L. Simonelli, A. Puri, Y. Mizuguchi, H. Takeya, Y. Takano, and N. L. Saini, J. Phys.: Condens. Matter **24**, 115701 (2012).

[36] H. Ryu, H. Lei, A. I. Frenkel, and C. Petrovic, Phys. Rev. B **85**, 224515 (2012).

[37] J. Neuefeind, M. Feygenson, J. Carruth, R. Hoffmann, and K. K. Chipley, Nucl. Instrum. Methods Phys. Res. B **287**, 68 (2012).

[38] T. Egami and S. J. L. Billinge, *Underneath the Bragg Peaks: Structural Analysis of Complex Materials*, 2nd ed. (Elsevier, Amsterdam, 2012).

[39] P. F. Peterson, M. Gutmann, T. Proffen, and S. J. L. Billinge, J. Appl. Crystallogr. **33**, 1192 (2000).

[40] C. L. Farrow, P. Juhás, J. Liu, D. Bryndin, E. S. Božin, J. Bloch, T. Proffen, and S. J. L. Billinge, J. Phys: Condens. Matter **19**, 335219 (2007).

[41] T. Proffen and R. B. Neder, J. Appl. Crystallogr. **32**, 838 (1999).

[42] T. R. Welberry, Rep. Prog. Phys. **48**, 1543 (1985).

[43] D. A. Keen and A. L. Goodwin, Nature **521**, 303 (2015).

[44] J. M. Cowley, Phys. Rev. **138**, A1384 (1965).

[45] S. C. Moss and P. C. Clapp, Phys. Rev. **171**, 764 (1968).

[46] S. C. Moss, J. Appl. Phys. **35**, 3547 (2005).

[47] L. R. Owen, H. Y. Playford, H. J. Stone, and M. G. Tucker, Acta Mater. **125**, 15 (2017).

[48] A. Plançon, Clays and Clay Minerals **52**, 47 (2004).

[49] A. Guinier, *X-Ray Diffraction in Crystals, Imperfect Crystals, and Amorphous Bodies*, Dover Books on Physics Series (Dover Publications Inc., Mineola, NY, 1994).

[50] V. A. Drits and C. Tchoubar, *X-Ray Diffraction by Disordered Lamellar Structures. Theory and Applications to Microdivided Silicates and Carbons* (Springer-Verlag, Berlin, 1990).

[51] K. Ufer, G. Roth, R. Kleeberg, H. Stanjek, R. Dohrmann, and J. Bergmann, Z. Kristallogr. **219**, 519 (2004).

[52] I. Jeong, T. Proffen, F. Mohiuddin-Jacobs, and S. J. L. Billinge, J. Phys. Chem. A **103**, 921 (1999).

[53] I. K. Jeong, R. H. Heffner, M. J. Graf, and S. J. L. Billinge, Phys. Rev. B **67**, 104301 (2003).

[54] L. Vegard, Z. Phys. **5**, 17 (1921).

[55] Y. Mizuguchi, Y. Hara, K. Deguchi, S. Tsuda, T. Yamaguchi, K. Takeda, H. Kotegawa, H. Tou, and Y. Takano, Supercond. Sci. Technol. **23**, 054013 (2010).

[56] T. Proffen, Z. Kristallogr. **215**, 661 (2000).

[57] https://www.energy.gov/downloads/doe-public-access-plan.

[58] M. Wojdyr, J. Appl. Crystallogr. **43**, 1126 (2010).

Rapid Communications   Editors' Suggestion

Photoinduced dynamics of nematic order parameter in FeSe

T. Konstantinova,[1,2] L. Wu,[1] M. Abeykoon,[1] R. J. Koch,[1] A. F. Wang,[1,*] R. K. Li,[3] X. Shen,[3] J. Li,[1] J. Tao,[1] I. A. Zaliznyak,[1]
C. Petrovic,[1] S. J. L. Billinge,[1,4] X. J. Wang,[3] E. S. Bozin,[1] and Y. Zhu[1,2,†]

[1]*Brookhaven National Laboratory, Upton, New York 11973, USA*
[2]*Stony Brook University, Stony Brook, New York 11794, USA*
[3]*SLAC National Accelerator Laboratory, Menlo Park, California 94025, USA*
[4]*Columbia University, New York, New York 10027, USA*

Formation of electronic nematicity is a common thread of unconventional superconductors. We use ultrafast electron diffraction to probe the lattice interactions with electronic degrees of freedom in superconducting FeSe and find a significant lattice response to local nematicity. We observe that a perturbation by a laser pulse leads to a surprising enhancement of the high-symmetry crystalline order as a result of suppression of low-symmetry local lattice distortions, which are signatures of nematic fluctuations. The distortions are present at temperatures both below and above the nematic phase transition, as corroborated by our x-ray pair distribution function analysis and transmission electron microscopy measurements. Nonequilibrium lattice behavior of FeSe reveals two distinct time scales of nematic response to photoexcitation, 130(20) and 40(10) ps, corresponding to diffusive and percolative dynamics of nematic fluctuations respectively.

FeSe is the simplest iron-chalcogenide superconducting compound. In a common trend with other Fe-based superconductors (FBSCs), at low temperature FeSe undergoes a transition to the nematic electronic state, deemed a precursor of superconductivity, which is accompanied by a weak change in the average crystal symmetry from tetragonal $P4/nmm$ to orthorhombic $Cmma$ group. The origin of nematicity is still under debate [1], with spin [2], orbit [3], and charge fluctuations [4] considered as main mediators. Antiferromagnetic order, which usually closely follows the transition to the nematic state in iron pnictides, supports the spin scenario as a leading contender for the nematic order. FeSe, however, lacks a long-range magnetic order whereas localized spin fluctuations with subpicosecond time scales are observed [5,6], suggesting a quantum nematic paramagnet as its ground state [6] and attracting attention to local nematicity. Hence, FeSe presents a unique opportunity for the investigation of the formation of nematic order, dynamics of nematic fluctuations, and their relation to dynamical magnetism and nonconventional superconductivity.

The connection between the crystal lattice and electronic nematicity in FBSC is often neglected because of the apparently insignificant change of the unit-cell parameters in the nematic phase. In FeSe, a tetragonal-to-orthorhombic transition leads to only 0.5% distortion in the ab plane [7]. Nevertheless, there is growing evidence of coupling between the lattice and electronic degrees of freedom in this material. It includes sensitivity of superconducting temperature T_c and structural transition temperature T_S to pressure [8] and lattice

strain [9], isotope effect [10], optical-phonon anomaly [11], phonon softening [12], and enhancement of T_c in a single layer FeSe on $SrTiO_3$ substrate [13,14] and in FeSe crystals with spacer layers [15].

In this work, we use ultrafast electron diffraction (UED) to investigate the dynamics of structural changes following the photoinduced melting of the nematic order in FeSe. We also present a detailed study of the local crystal structure of FeSe using pair distribution function (PDF) analysis of x-ray powder diffraction (XPD) and transmission electron microscopy (TEM). Our experiments reveal a surprising increase of crystallinity upon melting of low-symmetry nematic order and local lattice distortions, which we associate with local nematicity [16–19]. The distortions are present in both long-range nematic (orthorhombic) and normal (tetragonal) states, however, their correlation length increases below T_S. Upon photoexcitation, the distortions are released at two distinct rates, governed by percolative and diffusive dynamics of nematic fluctuations.

Single FeSe crystals were grown by the chemical vapor transport method using a eutectic mix of the KCl and $AlCl_3$ as the transport agent [20,21]. UED measurements were performed at MeV-UED setup at SLAC National Accelerator Laboratory. The details of the UED setup are described elsewhere [22]. XPD measurements for PDF analysis were performed at the PDF (28-ID-1) beamline of National Synchrotron Light Source–II at Brookhaven National Laboratory. High-resolution XPD data were obtained at the 11-BM beamline at the Advanced Photon Source at Argonne National Laboratory. TEM measurements including diffraction and imaging were performed at BNL using a 200-keV JEOL ARM 200 CF Microscope with a probe and an imaging aberration corrector.

UED provides information about the lattice dynamics in the system driven out-of-equilibrium with a pump laser pulse

---

*Present address: School of Physics, Chongqing University, Chongqing 400044, China.
†zhu@bnl.gov

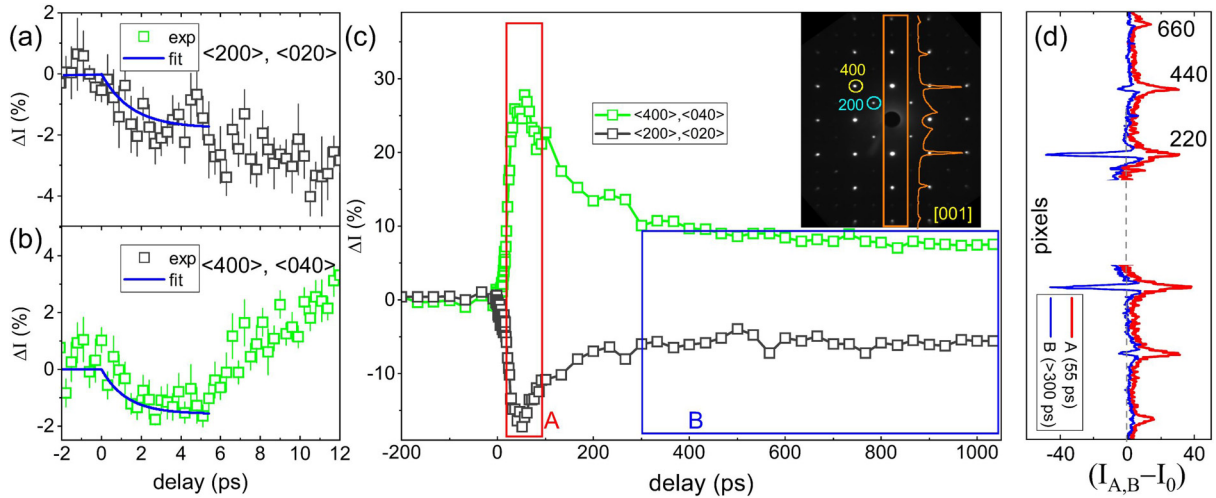FIG. 1. Decay of the Bragg intensity during the first 5 ps for $\langle 200 \rangle$, $\langle 020 \rangle$ (a) and $\langle 400 \rangle$, $\langle 040 \rangle$ (b) reflections measured with UED at 27 K at fluence 1.24 mJ/cm². Solid blue curves are exponential decay fits for the experimental data. (c) The peaks' dynamics during 1000 ps. Inset shows the FeSe diffraction pattern. The orange line in the inset shows the diffraction intensity profile integrated within the indicated frame. Frames A (red) and B (blue) show the time regions where averaged intensity differences (d) were calculated. (d) Changes of the intensity profile, shown in the inset (c), after the pump pulse with respect to the profile of the unpumped sample. Red (blue) line corresponds to changes averaged over the time frame A (B) highlighted in (c).

and probed by an electron beam. We use 1.55-eV 60-fs photon pulses to excite electronic transitions in FeSe samples at temperatures from 27 to 300 K. To get information about the lattice response we focus first on the intensity changes of the Bragg reflections that can be related to the lattice symmetry changes. Typical intensity dynamics of $\langle 200 \rangle$, $\langle 020 \rangle$ and $\langle 400 \rangle$, $\langle 040 \rangle$ at 27 K are shown in Fig. 1 (we use *Cmma* symmetry for indexing peaks, unless stated otherwise). During the first 5 ps the intensities of all observable peaks go down by a few percent of the initial equilibrium values [Figs. 1(a) and 1(b)]. At this time scale, the intensity dynamics can be fitted with a single exponential decay with a time constant of 1.5–2 ps. Such behavior is consistent with the energy transfer from the excited electrons to the lattice through electron-phonon coupling, leading to the increase of atomic Debye-Waller factors. Similar time constants were observed for the initial recovery of electronic states in the time-resolved reflectivity experiments [19] for the same material and were also attributed to the electron-phonon coupling.

Beyond the first 5 ps the dynamics of the Bragg reflections are rather unusual. The intensities of the $\langle hk0 \rangle$ Bragg peaks with $h + k = 4n + 2$ continue to drop for about 50 ps and then slowly recover. On the other hand, the intensities of the rest of the peaks ($h + k = 4n$) increase well above the initial values within the same 50 ps, before recovery. The rise of the intensity in this interval can be approximated [23] with a stretched exponential function (exponent $\beta = 2.6$) with time constant 40 ± 10 ps. The rate is similar to the rate of the photoinduced orthogonal-to-tetragonal phase transition in BaFe₂As₂ observed [24] with time-resolved x-ray diffraction. However, structural changes associated with such transition cannot lead to the observed intensity variations in the present experiment.

Consider the tetragonal 220 peak that splits into the orthorhombic 400 and 040 peaks. Such splitting is too small to be observed by UED since the experimental widths of

the Bragg peaks are several times larger than the expected splitting. Assuming the high-symmetry positions of Fe and Se atoms obtained from the Rietveld refinements, the structure factors of these peaks, which determine their intensities in a thin sample, have an identical form,

$$SF_{220}^{\text{tetr}} = SF_{040}^{\text{orth}} = 4f_{\text{Se}} \exp(-B_{\text{Se}}) + 4f_{\text{Fe}} \exp(-B_{\text{Fe}}), \quad (1)$$

where $f_{\text{Se}}(f_{\text{Fe}})$ and $B_{\text{Se}}(B_{\text{Fe}})$ are the atomic form factor and the Debye-Waller factor for Se (Fe) atoms respectively. From Eq. (1) one can see that not only the transition between the two phases does not lead to an intensity change, but that no modification of atomic positions could increase the intensity of $\langle 040 \rangle$ (and other $h + k = 4n$) peaks because for those reflections the electrons already scatter in-phase from all atoms in the unit cell. An apparent intensity increase suggests that some lattice distortions *pre-exist* at equilibrium, yielding a reduced Bragg intensity compared to the ideal structure factor of Eq. (1). In such case, a photodriven release of these distortions results in the intensity rise.

A closer look at the shape of the diffraction peaks provides additional information about the lattice dynamics. The inset in Fig. 1(c) shows the intensity profile integrated along the [110] direction. Changes in the profile [Fig. 1(d)] at time delays around +55 ps and beyond +300 ps show that the integrated intensity of $h + k = 4n$ peaks increases. However, changes at peaks' centers are different from changes at peaks' tails. A separation of an individual peak's profile into a narrow Gaussian part, corresponding to the long-range crystal order, and a wider Lorentzian part, corresponding to a short-range order [23] shows that the lattice dynamics involve three major steps. First, the photoinduced atomic vibrations lead to the decrease of the Bragg peaks' intensity, which is transferred to the thermal diffuse background. Second, the release of the pre-existing distortions, which in the absence of photoexcitation give rise to a broad diffuse scattering near $q = 0$, induces the recrystallization of the high-symmetry phase, i.e., causes
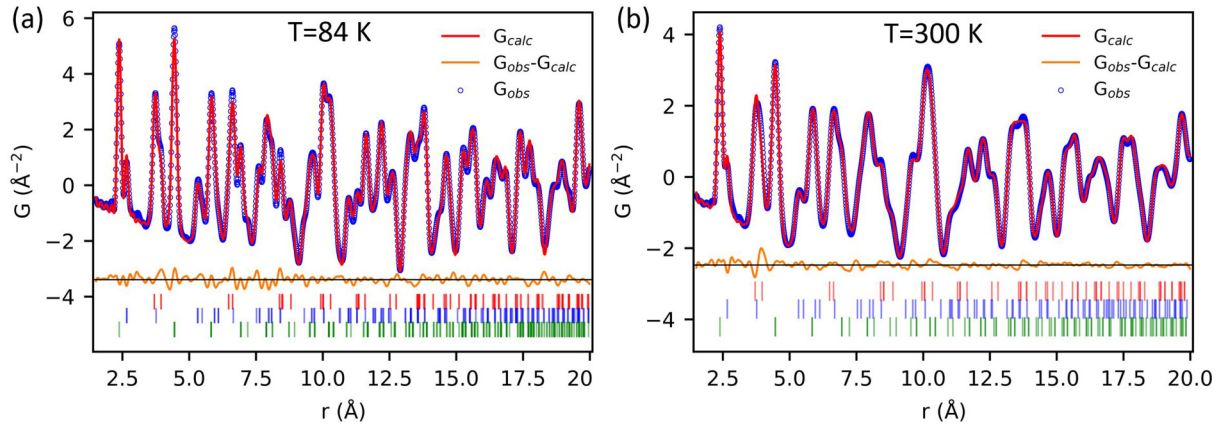
FIG. 2. (a) PDF at 84 K with the fit assuming an orthorhombic structural model. (b) PDF at 300 K with the fit assuming a tetragonal structural model. Blue circles show the experimental data, red line is the fit to the respective model, orange line shows the misfit. The plots contain green (Fe-Se), blue (Fe-Fe), and red (Se-Se) tick marks below the residual, which indicate the different unique pair distances from refining the respective models.

changes in the average crystal structure (long-range order) by moving atoms to more symmetric positions. This displacive process leads to an increase (decrease) of structure factors for $h + k = 4n$ ($h + k = 4n + 2$) peaks. The behavior of the Gaussian component is determined by the combination of vibrational and displacive effects. Third, the melting of the local distortions also creates tiny domains of high-symmetry phase, increasing the intensity of the Lorentzian component. The size of the domains determines the width of the Lorentzian component and can be estimated around 15–20 Å.

The crystal lattice in S-doped samples photoexcited under comparable conditions demonstrates a similar response [23], pointing out that the distortions are common for at least a part of the $FeSe_{1-x}S_x$ phase diagram. To understand the nature of these pre-existing local distortions, breaking the lattice symmetry at equilibrium, we turn to static techniques such as XPD and TEM.

Atomic displacements corresponding to the bond disparity of 0.1 Å have been observed in $Fe_{1+y}Te$, where they were attributed to a long-range ferro-orbital ordering [25]. To search for similar atomic displacements in FeSe, we performed pair distribution function analysis of the XPD data. PDF contains information about both long-range order and local imperfections, which is inferred from the powder-diffraction pattern. Figure 2(a) shows PDF data at $T = 84$ K together with the fit to an orthorhombic model, obtained from the Rietveld refinement. Whereas the model describes the data well at large interatomic distances r, for $r < 10$ Å there is a notable misfit. The misfit indicates that there is a disparity between the local and average atomic structure and corroborates the assumption that lattice distortions are present at equilibrium.

Remarkably, a pronounced misfit to the tetragonal model at small interatomic distances is also present at 300 K [Fig. 2(c)]. Thus, the local lattice distortions also exist in the tetragonal phase. The deviation from the tetragonal model is most pronounced for the lattice repeat peak at $r = 3.8$ Å and rapidly fades at larger r, indicating a short correlation length. The information about the distortions in PDF comes not from the Bragg peaks, but from diffuse scattering. It agrees with the UED observations, where melting of the distortions involves intensity transfer from the diffuse background centered at

$q = 0$ to locations at or near Bragg peaks. The exact structure of the distortions and the growth of the distortion's correlation length at low temperature are described elsewhere [26,27]. Neutron powder-diffraction experiments in other FBSCs have also observed [28,29] local structures that are different from the average ones. In $BaFe_2As_2$ such distortions were suggested [29] to reduce the amplitude of the long-range magnetic moment.

Whereas XPD provides structural information averaged over multiple lattice domains, TEM is a local probe and presents an opportunity to look at individual domains and to reconstruct the details that could be missed upon averaging under a large probe. The results of our TEM measurements of FeSe samples are shown in Fig. 3. The Bragg peaks in the diffraction obtained from the sample are sharp and without streaks, indicating a good sample quality. In agreement with the previous studies on FeSe [7] and LaOFeAs [30], $\langle 110 \rangle$ peaks forbidden by $Cmma$ symmetry appear in the diffraction pattern below T_S (at $T = 88$ K) [Figs. 3(a) and 3(b)] whereas they are not seen at the same sample area at $T = 300$ K. The peaks indicate that the crystal symmetry below T_S is lower than $Cmma$. Such peaks were not detected in the XPD measurements [23].

Figure 3(c) shows a high-resolution TEM (HRTEM) image obtained at 300 K with a smaller field of view than used for the diffraction measurements. Fourier analysis of such images [Fig. 3(d)] reveals nonuniformly distributed regions whose diffractograms have a pair of forbidden peaks (either $\bar{1}10$ and $1\bar{1}0$ or 110 and $\bar{1}\bar{1}0$), or a full set of four $\langle 110 \rangle$ peaks in addition to the peaks allowed by $Cmma$ or $P4/nmm$ symmetry [23]. Yet other regions have only allowed peaks. Appearance of the peaks in either of the two diagonal directions in diffractograms can be explained by presence of domains with C_2 symmetry in the ab plane, which are rotated by 90° with respect to each other. The difference in the forbidden peaks' intensities along the perpendicular directions of the diffraction pattern at 88 K [23] also supports the idea of rotated domains with C_2 symmetry below T_S, which are nonequally present in the probed volume. The inverse Fourier transform mapping [23] reveals that at 300 K the domains with the low symmetry have a typical size of 1–5 nm. This is to be contrasted with
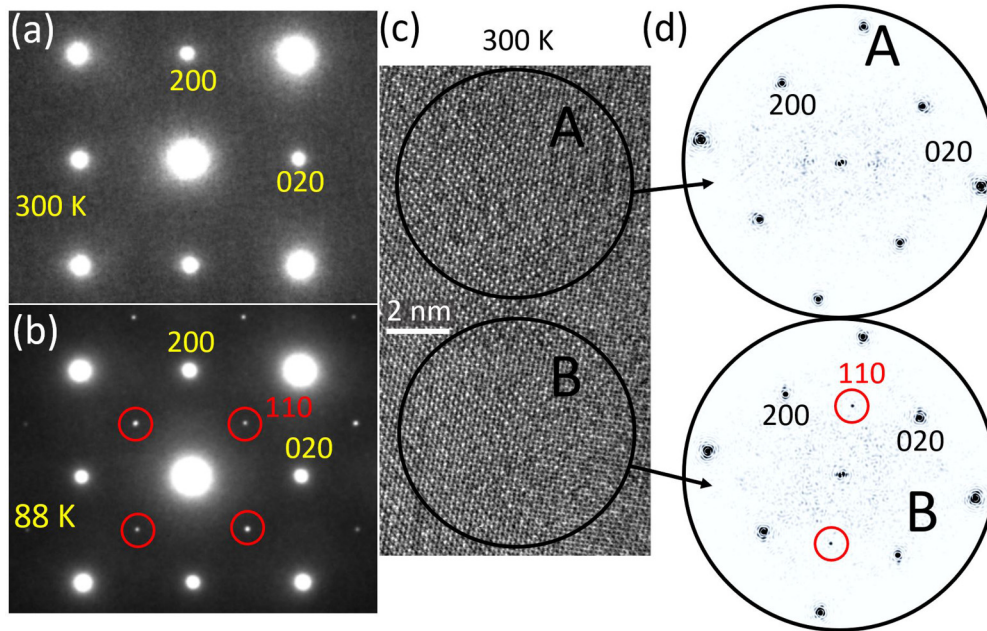
FIG. 3. (a) Electron-diffraction pattern at 300 K (b) Electron diffraction from the same area as (a) at 88 K. (c) Typical HRTEM image. (d) FFTs taken from the respective areas as shown in (c). The peaks forbidden by the orthorhombic and tetragonal symmetries are highlighted by red circles.

the crystalline domain size observed by XPD, which is about 200 nm, highlighting the distinction between the reduced symmetry domains and crystallites. Appearance of the sharp $\langle 110 \rangle$ peaks in the electron diffraction below T_S indicates that the low-symmetry domain size grows upon lowering the temperature, consistent with the behavior of the correlation length of the local distortions revealed with the PDF analysis. These observations corroborate that even at 300 K the sample has regions with the broken tetragonal symmetry, where either or both atoms in the unit cell are displaced from the high-symmetry positions, leading to the atomic bond disparity. The disparity agrees with the misfit of the PDF model described above.

The photoinduced FeSe lattice dynamics at different temperatures provide important information about changes in the system across the nematic phase transition. As shown in

Fig. 4(a), the relatively fast (within 50 ps) increase of $\langle 080 \rangle$, $\langle 800 \rangle$ peaks intensity, corresponding to the release of the distortions, is only observed at temperatures below T_S. Above T_S the intensity rises as well, however at a much slower rate, and can be described with exponential growth function with the time constant of 130 ± 20 ps. The photoinduced increase of intensity above T_S agrees with the presence of local nematic distortions observed with x ray and TEM. Remarkably, the relative intensity at 1-ns delay seems to be independent of temperature. For dynamics of other peaks refer to the Supplemental Material [23].

Fluence dependence [Fig. 4(b)] of the lattice dynamics at 27 K also reveals switching between the fast and the slow regimes. The fast component is observed only at fluences below 2.2 mJ/cm^2. The value of the maximum intensity first grows with fluence and then drops above 1.9 mJ/cm^2. Above
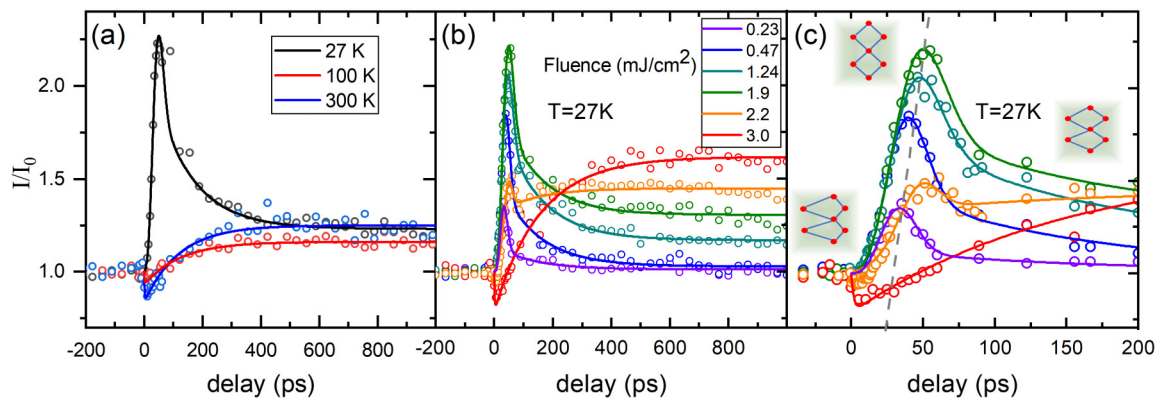

FIG. 4. (a) Dynamics of $\langle 080 \rangle$, $\langle 800 \rangle$ peaks obtained with UED at different temperatures for the incident fluence of 1.65 mJ/cm^2. Dynamics of the same peaks at different excitation fluences for the full measurement time range (b) and during the first 200 ps (c) at 27 K. The gray dashed line in (c) is a guide to eye. Insets show schematics of unequal atomic bonds at the corresponding time intervals. Open circles are the experimental data and solid lines are the fits [23].

$2.2 \, \mathrm{mJ/cm^2}$ the lattice response is the same as at high sample temperature, i.e., the slow component is observed. This can be explained by the sample heating. Based on the sample characteristics [31,32], if all absorbed energy is converted to heat the threshold fluence corresponds to a temperature increase of 75 K, which is close to a 64-K difference between the sample temperature and T_S. Thus, the process leading to the fast increase of the peaks' intensity proceeds only in the presence of a (partial) long-range nematic order. When the order is destroyed, either by temperature or through above-threshold photoexcitation, the slow process governs the lattice dynamics. The slow process is also present at the low-temperature–low fluence excitation regime. Figure 4(c) shows that the point of the maximum intensity shifts to the longer time with increased fluence, reflecting the increased impact of the slow process. Thus, the slow and the fast responses "compete" with each other: as the laser fluence (or sample temperature) increases the slower process becomes more pronounced and finally dominant.

It is often believed that weak orthorhombicity of the unit cell is the only result of coupling between the electronic nematic order and the lattice in the FeSe superconducting family. Our observations reveal an additional connection, established via atomic bonds' distortions that lower the local lattice symmetry. Such distortions are present in nanodomains at temperatures both below and above T_S and correspond to local nematic fluctuations, consistent with previous observations [16,17,19]. Their correlation length increases as domain size grows on cooling, leading to the percolative three-dimensional ordering, i.e., lowering the average lattice symmetry, below T_S. This transition and the presence of the uncorrelated low-symmetry domains both below and above the ordering temperature agrees with the theoretical predictions of the anisotropic random field Ising model (ARFIM), which was argued to describe phase transitions with the discrete two-fold symmetry breaking in layered systems [33,34]. The ordering transition in this model occurs within the extended critical state where the domains of the two phases coexist, via formation of the percolating long-range order (LRO) domains.

A notable feature of the nonequilibrium lattice dynamics is the threshold excitation fluence at low temperatures, which corresponds to the energy needed to completely melt the long-range nematic order. Below the threshold fluence, i.e., when a partial nematic order parameter is still present after the excitation, the rate of the distortion release is relatively fast. The process reflects nucleation, growth, and merging of high-symmetry domains, i.e., percolative dynamics of the nematic order parameter. Similar rates of photoinduced LRO domain growth have been observed in other systems [35,36]. Newly formed large high-symmetry domains are unstable, and the distortions are formed again within few hundred picoseconds reflecting the recovery of the nematic phase [19,37]. Excitation above the threshold fluence results in a complete melting of the nematic order parameter via "overheating" the sample and leads to a slow relaxation of the lattice distortions, the same as observed at temperatures above T_S. Change of the distortion amplitude in the slow process depends only on the excitation fluence and not on the sample initial temperature. The process corresponds to establishing balance between do-

mains of high and low symmetry through diffusive dynamics of the local nematic fluctuations. The recovery of the diffraction intensity following the rapid increase in the low fluence excitation regime proceeds on a time scale of about 80 ps, resulting from the combination of both the fast (percolative) and the slow (diffusive) dynamics of nematic fluctuations [23].

The structure of the dynamical magnetic correlations in FeSe and related Fe(Te,Se) materials is uniquely determined by local orbital overlaps, which are governed by nematic fluctuations [38]. However, the nematic time scales observed in our experiments are orders of magnitude longer than those for spin fluctuations in FeSe [5,6], clearly indicating that nematic order is the parent phase, rather than the consequence of dynamical magnetism in this material.

In summary, our study reveals dynamical dichotomy of nematic fluctuations in FeSe. In the ordered phase and at low photon fluencies, UED observes a fast ($\tau_{\mathrm{fast}} = 40 \pm 10$ ps) structural response with stretched-exponential ($\beta = 2.6 \pm 0.1$) relaxation. This is not unexpected for the percolation-type dynamics in an effective Ising model predicted by the ARFIM [33,34], which governs melting of the low-symmetry phase with nematic LRO and leads to the increase of Bragg peaks characteristic of the high-symmetry phase. We also find a slow ($\tau_{\mathrm{slow}} = 130 \pm 20$ ps) exponential relaxation process, which corresponds to the diffusive intrinsic dynamics of short-range nematic fluctuations in FeSe. These are revealed as nanodomains with local low-symmetry lattice distortions that couple to the electronic degrees of freedom. Using UED, we observe melting of these nematic nanodomains following a femtosecond laser pulse and the concomitant lattice ordering of the high-symmetry parent phase resulting in a surprising increase of coherent Bragg scattering. The pre-existing local distortions are present at equilibrium both in the absence of nematic LRO and in the ordered phase and their existence can be understood from the ARFIM. The ARFIM phase diagram predicts the domains of both low- and high-symmetry phases below and above the percolative phase transition [39,40]. The observed structural response, which is naturally explained by redistribution of the relative population of the two phases, sheds light on the formation of the nematic phase from imperfect ordering of its fluctuations in FeSe and other layered systems and stimulates further theoretical development towards full understanding of nematicity.

[1] R. M. Fernandes, A. V. Chubukov, and J. Schmalian, Nat. Phys. **10**, 97 (2014).

[2] C. Fang, H. Yao, W. F. Tsai, J. P. Hu, and S. A. Kivelson, Phys. Rev. B **77**, 224509 (2008).

[3] S. H. Baek, D. V. Efremov, J. M. Ok, J. S. Kim, J. van den Brink, and B. Buchner, Nat. Mater. **14**, 210 (2015).

[4] P. Massat, D. Farina, I. Paul, S. Karlsson, P. Strobel, P. Toulemonde, M. A. Measson, M. Cazayous, A. Sacuto, S. Kasahara, T. Shibauchi, Y. Matsuda, and Y. Gallais, Proc. Natl. Acad. Sci. USA **113**, 9177 (2016).

[5] T. Imai, K. Ahilan, F. L. Ning, T. M. McQueen, and R. J. Cava, Phys. Rev. Lett. **102**, 177005 (2009).

[6] Q. S. Wang, Y. Shen, B. Y. Pan, X. W. Zhang, K. Ikeuchi, K. Iida, A. D. Christianson, H. C. Walker, D. T. Adroja, M. Abdel-Hafiez, X. J. Chen, D. A. Chareev, A. N. Vasiliev, and J. Zhao, Nat. Commun. **7**, 12182 (2016).

[7] T. M. McQueen, A. J. Williams, P. W. Stephens, J. Tao, Y. Zhu, V. Ksenofontov, F. Casper, C. Felser, and R. J. Cava, Phys. Rev. Lett. **103**, 057002 (2009).

[8] S. Medvedev, T. M. McQueen, I. A. Troyan, T. Palasyuk, M. I. Eremets, R. J. Cava, S. Naghavi, F. Casper, V. Ksenofontov, G. Wortmann, and C. Felser, Nat. Mater. **8**, 630 (2009).

[9] S. H. Baek, D. V. Efremov, J. M. Ok, J. S. Kim, J. van den Brink, and B. Buchner, Phys. Rev. B **93**, 180502(R) (2016).

[10] R. Khasanov, M. Bendele, K. Conder, H. Keller, E. Pomjakushina, and V. Pomjakushin, New J. Phys. **12**, 073024 (2010).

[11] M. Nakajima, K. Yanase, F. Nabeshima, Y. Imai, A. Maeda, and S. Tajima, Phys. Rev. B **95**, 184502 (2017).

[12] K. Zakeri, T. Engelhardt, T. Wolf, and M. Le Tacon, Phys. Rev. B **96**, 094531 (2017).

[13] J. F. Ge, Z. L. Liu, C. H. Liu, C. L. Gao, D. Qian, Q. K. Xue, Y. Liu, and J. F. Jia, Nat. Mater. **14**, 285 (2015).

[14] W. W. Zhao, M. D. Li, C. Z. Chang, J. Jiang, L. J. Wu, C. X. Liu, J. S. Moodera, Y. M. Zhu, and M. H. W. Chan, Sci. Adv. **4**, eaao2682 (2018).

[15] M. Burrard-Lucas, D. G. Free, S. J. Sedlmaier, J. D. Wright, S. J. Cassidy, Y. Hara, A. J. Corkett, T. Lancaster, P. J. Baker, S. J. Blundell, and S. J. Clarke, Nat. Mater. **12**, 15 (2013).

[16] P. S. Wang, P. Zhou, S. S. Sun, Y. Cui, T. R. Li, H. C. Lei, Z. Q. Wang, and W. Q. Yu, Phys. Rev. B **96**, 094528 (2017).

[17] Y. C. Wen, K. J. Wang, H. H. Chang, J. Y. Luo, C. C. Shen, H. L. Liu, C. K. Sun, M. J. Wang, and M. K. Wu, Phys. Rev. Lett. **109**, 089902(E) (2012).

[18] K. Nakayama, Y. Miyata, G. N. Phan, T. Sato, Y. Tanabe, T. Urata, K. Tanigaki, and T. Takahashi, Phys. Rev. Lett. **113**, 237001 (2014).

[19] C.-W. Luo, P. Chung Cheng, S.-H. Wang, J.-C. Chiang, J.-Y. Lin, K.-H. Wu, J.-Y. Juang, D. A. Chareev, O. S. Volkova, and A. N. Vasiliev, npj Quantum Mater. **2**, 32 (2017).

[20] R. W. Hu, H. C. Lei, M. Abeykoon, E. S. Bozin, S. J. L. Billinge, J. B. Warren, T. Siegrist, and C. Petrovic, Phys. Rev. B **83**, 224502 (2011).

[21] D. Chareev, E. Osadchii, T. Kuzmicheva, J. Y. Lin, S. Kuzmichev, O. Volkova, and A. Vasiliev, CrystEngComm **15**, 1989 (2013).

[22] S. P. Weathersby, G. Brown, M. Centurion, T. F. Chase, R. Coffee, J. Corbett, J. P. Eichner, J. C. Frisch, A. R. Fry, M. Guhr, N. Hartmann, C. Hast, R. Hettel, R. K. Jobe, E. N. Jongewaard,

J. R. Lewandowski, R. K. Li, A. M. Lindenberg, I. Makasyuk, J. E. May *et al.*, Rev. Sci. Instrum. **86**, 073702 (2015).

[23] See Supplemental Material at http://link.aps.org/supplemental/10.1103/PhysRevB.99.180102 for a detailed analysis which also includes Refs. [19,20,24,37,41,42].

[24] L. Rettig, S. O. Mariager, A. Ferrer, S. Grubel, J. A. Johnson, J. Rittmann, T. Wolf, S. L. Johnson, G. Ingold, P. Beaud, and U. Staub, Struct. Dyn. **3**, 023611 (2016).

[25] D. Fobes, I. A. Zaliznyak, Z. J. Xu, R. D. Zhong, G. D. Gu, J. M. Tranquada, L. Harriger, D. Singh, V. O. Garlea, M. Lumsden, and B. Winn, Phys. Rev. Lett. **112**, 187202 (2014).

[26] R. J. Koch, T. Konstantinova, M. Abeykoon, A. F. Wang, C. Petrovic, Y. Zhu, E. S. Bozin, and S. J. L. Billinge, arXiv:1902.08732.

[27] B. A. Frandsen, Q. Wang, S. Wu, J. Zhao, and R. J. Birgeneau, arXiv:1904.06440.

[28] B. A. Frandsen, K. M. Taddei, M. Yi, A. Frano, Z. Guguchia, R. Yu, Q. M. Si, D. E. Bugaris, R. Stadel, R. Osborn, S. Rosenkranz, O. Chmaissem, and R. J. Birgeneau, Phys. Rev. Lett. **119**, 187001 (2017).

[29] J. L. Niedziela, M. A. McGuire, and T. Egami, Phys. Rev. B **86**, 174113 (2012).

[30] C. Ma, L. J. Zeng, H. X. Yang, H. L. Shi, R. C. Che, C. Y. Liang, Y. B. Qin, G. F. Chen, Z. A. Ren, and J. Q. Li, Europhys. Lett. **84**, 47002 (2008).

[31] X. J. Wu, D. Z. Shen, Z. Z. Zhang, J. Y. Zhang, K. W. Liu, B. H. Li, Y. M. Lu, B. Yao, D. X. Zhao, B. S. Li, C. X. Shan, X. W. Fan, H. J. Liu, and C. L. Yang, Appl. Phys. Lett. **90**, 112105 (2007).

[32] A. V. Muratov, A. V. Sadakov, S. Y. Gavrilkin, A. R. Prishchepa, G. S. Epifanova, D. A. Chareev, and V. M. Pudalov, Physica B: Condens. Matter **536**, 785 (2018).

[33] O. Zachar and I. Zaliznyak, Phys. Rev. Lett. **91**, 036401 (2003).

[34] I. A. Zaliznyak, Z. J. Xu, J. S. Wen, J. M. Tranquada, G. D. Gu, V. Solovyov, V. N. Glazkov, A. I. Zheludev, V. O. Garlea, and M. B. Stone, Phys. Rev. B **85**, 085105 (2012).

[35] M. Zhang, G. L. Cao, H. F. Tian, S. S. Sun, Z. W. Li, X. Y. Li, C. Guo, Z. Li, H. X. Yang, and J. Q. Li, Phys. Rev. B **96**, 174203 (2017).

[36] K. Haupt, M. Eichberger, N. Erasmus, A. Rohwer, J. Demsar, K. Rossnagel, and H. Schwoerer, Phys. Rev. Lett. **116**, 016402 (2016).

[37] A. Patz, T. Li, S. Ran, R. M. Fernandes, J. Schmalian, S. L. Bud'ko, P. C. Canfield, I. E. Perakis, and J. Wang, Nat. Commun. **5**, 3229 (2014).

[38] I. Zaliznyak, A. T. Savici, M. Lumsden, A. Tsvelik, R. W. Hu, and C. Petrovic, Proc. Natl. Acad. Sci. USA **112**, 10316 (2015).

[39] E. W. Carlson and K. A. Dahmen, Nat. Commun. **2**, 379 (2011).

[40] L. M. Nie, G. Tarjus, and S. A. Kivelson, Proc. Natl. Acad. Sci. USA **111**, 7980 (2014).

[41] T. M. McQueen, Q. Huang, V. Ksenofontov, C. Felser, Q. Xu, H. Zandbergen, Y. S. Hor, J. Allred, A. J. Williams, D. Qu, J. Checkelsky, N. P. Ong, and R. J. Cava, Phys. Rev. B **79**, 014522 (2009).

[42] E. J. Kirkland, *Advanced Computing in Electron Microscopy* (Springer, Boston, MA, 1998).

Quantum Liquid with Strong Orbital Fluctuations: The Case of a Pyroxene Family

A. E. Feiguin,[1] A. M. Tsvelik,[2] Weiguo Yin,[2] and E. S. Bozin[2]

[1]*Department of Physics, Northeastern University, Boston, Massachusetts 02115, USA*
[2]*Condensed Matter Physics and Materials Science Division, Brookhaven National Laboratory, Upton, New York 11973, USA*

We discuss quasi-one-dimensional magnetic Mott insulators from the pyroxene family where spin and orbital degrees of freedom remain tightly bound. We analyze their excitation spectrum and outline the conditions under which the orbital degrees of freedom become liberated so that the corresponding excitations become dispersive and the spectral weight shifts to energies much smaller than the exchange integral.

Introduction.—During the last 30 years a great theoretical effort has been directed at the research on quantum liquids where spin ordering either does not occur or the transition temperature is strongly reduced by fluctuations. Quantum liquids play an important role in all kinds of theoretical scenarios for exotic matter states. Quantum fluctuations increase when the symmetry manifold is extended from the ubiquitous SU(2) to a higher symmetry, for instance, SU(N). In practice such extension can occur only when orbital degrees of freedom (d.o.f.) are included which is difficult since the orbital degeneracy is usually lifted by the lattice. In this Letter we suggest that magnetic insulators from the so-called pyroxene family may provide a possible path to overcome these difficulties.
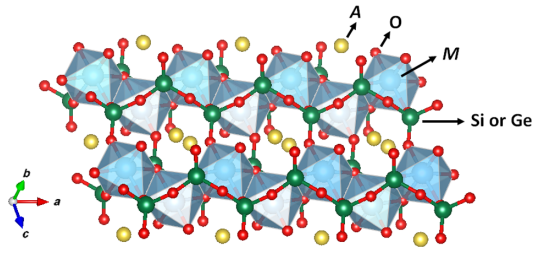
Pyroxenes are quasi-one-dimensional Mott insulators where spin and orbital d.o.f. remain tightly bound even at low energies. They compose a rich class of minerals with chemical formula $AM(\text{Si}, \text{Ge})_2\text{O}_6$ where A is mostly an alkali metal element and M a trivalent metal element. For example, greenish $\text{NaAlSi}_2\text{O}_6$ is a famous Chinese jade called Fei Tsui. The systems with partially filled d shells of the M ions commonly possess nontrivial magnetic properties ranging from antiferromagnetic (AF), ferromagnetic (FM), and spin glassy and likely to be multiferroics, as seen in $\text{NaFeSi}_2\text{O}_6$, $\text{LiFeSi}_2\text{O}_6$, and $\text{LiCrSi}_2\text{O}_6$ [1]. Their crystal structures contain characteristic *zigzag* chains of edge-sharing $M\text{O}_6$ octahedra (Fig. 1). The chains are bridged by the O-Si-O or O-Ge-O bonds, or, in other words, are separated by SiO_4 or GeO_4 tetrahedra, thus confining the motion of valence electrons to the chains.

In this Letter we discuss pyroxenes with $M = \text{Ti}$ and Ru, where the lowest t_{2g} orbitals well separated from the e_{2g} ones are occupied either by a single electron (Ti) or a single hole (Ru). At present only $\text{NaTiSi}_2\text{O}_6$ has been experimentally studied. Like the V^{4+} ions in the straight-chain system VO_2, the Ti^{3+} ions in $\text{NaTiSi}_2\text{O}_6$ have the $3d^1$ valence electron configuration and undergo the Ti-Ti dimerization upon cooling. The zigzag chain pattern makes

it more apparent that all spin, orbital, and lattice d.o.f. are active, leading to two-orbitally assisted Peierls transition [2–4] that generates spin-singlet dimers on the short Ti-Ti bonds [5] with the spin gap of ∼53 meV [6], rather than a gapless long-range antiferromagnetic (AF) state in VO_2. Note that the ordinary spin-Peierls transition seems not to work here because the doubled periodicity is not consistent with the quarter filling of the electronic bands. An early density-functional theory (DFT) study focused on the high-temperature nondimerized structure of $\text{NaTiSi}_2\text{O}_6$ attributed the spin gap to the spin-one ($S = 1$) Haldane type due to the ferromagnetic Ti-Ti interaction [7]. A subsequent DFT calculation with a U correction showed that the dominant magnetic interaction was the AF one along the Ti-Ti short bonds, supporting the picture of $S = 0$ spin dimers [8]. However, an outstanding puzzle is that the heat capacity data show the gap ∼10 meV [5] suggesting the existence of softer excitations and stronger quantum fluctuations.

We approach the problem using a combination DFT, analytic, and time-dependent density-matrix renormalization group (DMRG) methods to study their orbital and spin dynamics. The stronger quantum fluctuations originate from the involvement of the third t_{2g} orbital, which becomes active when the oxygen-atom-mediated electron hopping integral is comparable to the direct hopping integral between neighboring M atoms [1,9,10].

Hubbard model and the Sutherland Hamiltonian.—We start with a microscopic derivation of the three-orbital model Hamiltonian [11] assuming a single electron or hole occupation of the t_{2g} orbital. The strong on site Coulomb interaction $U(N-1)^2$ opens a charge gap ∼U preventing direct transitions to states with different occupation number. To describe the low energy dynamics we have to integrate out the high-energy d.o.f. as it is done in the conventional SU(2) invariant Hubbard model [17]. Here, each M cation is coordinated with six O^{2-} anions and the $M\text{O}_6$ octahedra are edge sharing to form the zigzag chain in
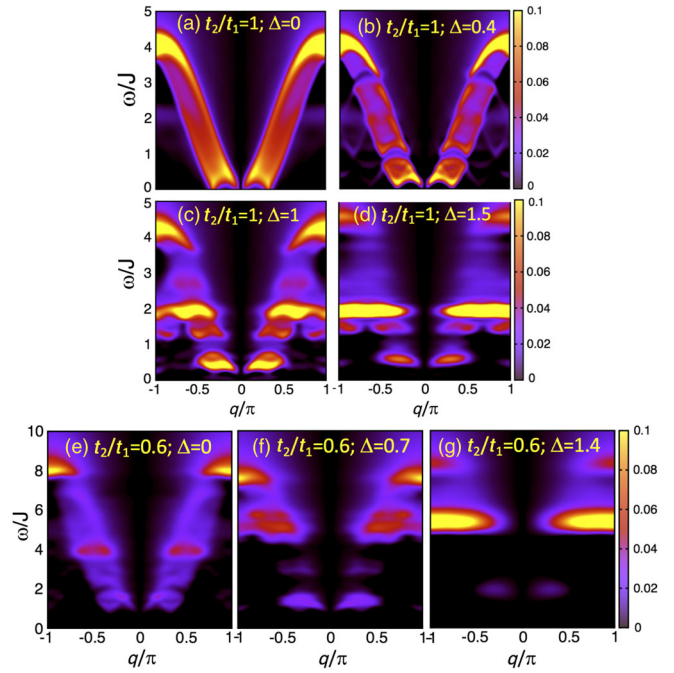
FIG. 1. Crystal structure of Na MSi$_2$O$_6$.

FIG. 2. Spin spectral function in the folded Brillouin Zone for various values of t_2/t_1 and the crystal field. With increase of Δ/J or the anisotropy the spectral weight shifts toward the dimerized configuration where the singlet-triplet gap is equal to $2J = 4t_2^2/(U - \Delta)$ corresponding to the breaking of a dimer.
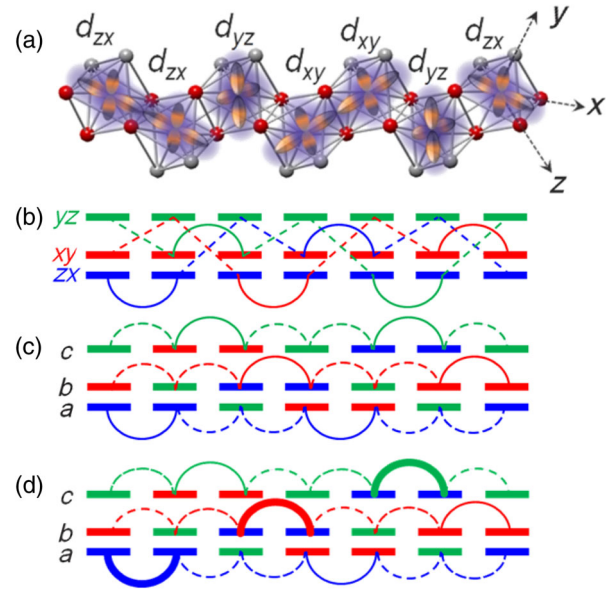
the crystallographical a axis (Fig. 1). The five d-shell orbitals of the M ion are well separated by the ligand field into the high-energy e_g ($3z^2 - r^2$ and $x^2 - y^2$) and low-lying t_{2g} (xy, yz, zx) orbitals. The latter orbitals are relevant to the low-energy physics. If one neglects all factors leading to violation of the SU(6) symmetry, such as the splitting of the t_{2g} orbitals and the Hund's interaction and adopts a diagonal tunneling matrix with identical matrix elements t for all orbitals, the result for $U \gg t$ is the SU(6)-symmetric Sutherland Hamiltonian:

$$H = J\sum_k P_{k,k+1}^{o,s}, \qquad J = \frac{2t^2}{U}, \qquad (1)$$

where $P^{o,s} = P^o \otimes P^s$ is the permutation operator acting in 6×6-dimensional space of spin and orbital quantum numbers and $P_{k,k+1}^s = 2\boldsymbol{S}_k \cdot \boldsymbol{S}_{k+1} + 1/2$ and $P_{k,k+1}^o = 2\boldsymbol{T}_k \boldsymbol{T}_{k+1} + 1/2$, where S^a, T^a are spin and isospin $S = 1/2$ operators acting on the spin and orbital subspaces, respectively. Model (1) is integrable, the spectrum consisting of collective orbital and spin excitations is gapless [18]. The excitations (spinons) are fractionalized, they carry spin and orbital quantum numbers of electrons (except the charge one which is gapped). The spin spectral function is presented on Fig. 2(a).

In reality the SU(6) symmetry is broken due to the crystal field and anisotropy of the exchange integrals originating from (i) the difference between tunneling matrix elements of different orbital states and (ii) the Hund's coupling. Since the lowest d orbital is occupied by one electron (hole), the Hund's coupling affects only the excited states. As shown in Fig. 3(a), the strong electron hopping integrals are the head-on $d_{zx} - d_{zx}$ (between the first and second M atoms) and the head-on $d_{xy} - d_{xy}$ (between the forth and fifth M atoms), whose strength is referred to as t_1 [depicted as solid arcs in Fig. 3(b)]. Yet, for the edge-sharing t_{2g} connections, it is known that the oxygen p-orbital-mediated shoulder-to-shoulder hopping paths, e.g., the $d_{zx} - p_z - d_{yz}$ between the second and third M atoms in Fig. 3(a), may be as strong [1,9,10]. These indirect paths are referred to as t_2 [the dashed lines in Fig. 3(b)]. Note that the M yz orbitals are involved in the t_2 paths only [Fig. 3(b)]; therefore, in the limit of small t_2 or large t_{2g} splitting Δ (i.e., the yz orbital is higher in energy by Δ than the xy and zx orbitals), d_{yz}

FIG. 3. (a) A graphic description of a dimerized state for an isolated NaMSi$_2$O$_6$ chain. Only t_{2g} orbital of M ions are depicted. (b) The original tunneling scheme. (c) The tunneling scheme with relabeled orbitals. We relabel the orbitals on different sites to make the tunneling diagonal. The solid lines correspond to matrix element t_1, the dashed lines corresponds to matrix element t_2. (d) The dimerization pattern in the presence of crystal field. The orbitals on which spin singlets form are shown by thick lines.

becomes irrelevant, yielding the minimal two-orbital model [2–4]. On the other hand, for a considerable t_2 and small Δ, the t_1 and t_2 paths seem to be highly entangled as shown in Fig. 3(b); however, following the red, blue, and green lines, we found that they can be completely decoupled to form three degenerate hopping paths as shown in Fig. 3(c). In this sense, the most remarkable property of NaMSi$_2$O$_6$ is that its electronic band is exactly three times as degenerate. In real space the degeneracy is reflected as the following property of the single electron wave functions: $\psi_b(k+1) = \psi_b(k) = \psi_c(k-1)$.

The corresponding band Hamiltonian in notations depicted on Fig. 3(c) has three M sites in the unit cell and is expressed as follows:

$$H = -\sum_{k,\alpha=a,b,c} \psi^+_{\alpha,\sigma}(k) \begin{pmatrix} 0 & t_1 & t_2 e^{-3ik} \\ t_1 & 0 & t_2 \\ t_2 e^{3ik} & t_2 & \Delta \end{pmatrix} \psi_{\alpha,\sigma}(k).$$

The spectrum is determined by the cubic equation

$$\epsilon^3 - \epsilon^2 \Delta - \epsilon(2t_2^2 + t_1^2) + \Delta t_1^2 - 2t_1 t_2^2 \cos 3k = 0. \quad (2)$$

At $t_1 = t_2$, $\Delta = 0$ the solution is $\epsilon = 2t \cos k$. The band is 1/6th filled with $k_F = \pi/6$. At $t_2 \neq t_1$ and $\Delta \neq 0$, spectral gaps appear at $k = \pm \pi/3$, $\pm 2\pi/3$ corresponding to the perturbations with wave vectors $q = \pm 2\pi/3$, $\pm 4\pi/3$. Since they do not coincide with $2k_F$, the weakly interacting electron system would remain gapless [19]. However, for the Mott insulator this is no longer the case. Besides the charge (Mott) gap the anisotropy generates spectral gaps in all other sectors. This is obviously related to the fact that the perturbations around the SU(6) symmetric point generate relevant operators with the wave vector $4k_F$.

Integrating over the high energy states we obtain the following Hamiltonian:

$$H = \frac{2t_2^2}{U - \Delta} \sum_k P^{o,s}_{k,k+1} + \Delta \sum_k [X_{aa}(3k+2) + X_{bb}(3k) + X_{cc}(3k+1)]\hat{I} + \sum_k \delta V_k, \quad (3)$$

$$\begin{aligned}
\delta V_k = &2\left(\frac{t_1^2}{U} - \frac{t_2^2}{U-\Delta}\right) \\
&\times [\hat{P}^s_{3k,3k+1} X_{aa}(3k) X_{aa}(3k+1) + \hat{P}^s_{3k+1,3k+2} X_{bb}(3k+1) X_{bb}(3k+2) + \hat{P}^s_{3k+2,3k+3} X_{cc}(3k+2) X_{cc}(3k+3)] \\
&+ 2t_2\left(\frac{t_1}{U} - \frac{t_2}{U-\Delta}\right)\{[\hat{P}^s_{3k,3k+1} X_{ab}(3k) X_{ba}(3k+1) \\
&+ \hat{P}^s_{3k+1,3k+2} X_{ab}(3k+1) X_{ba}(3k+2) + \hat{P}^s_{3k+2,3k+3} X_{ac}(3k+2) X_{ca}(3k+3)] + \text{H.c.}\} + \frac{2t_2(t_1-t_2)}{U-\Delta} \\
&\times \{[\hat{P}^s_{3k,3k+1} X_{ac}(3k) X_{ca}(3k+1) + \hat{P}^s_{3k+1,3k+2} X_{bc}(3k+1) X_{cb}(3k+2) + \hat{P}^s_{3k+2,3k+3} X_{bc}(3k+2) X_{cb}(3k+3)] + \text{H.c.}\},
\end{aligned}$$

$$(4)$$

where $P^s_{k,k+1}$ is the spin permutation operator and X_{ab} are Hubbard operators acting on orbital indices, defined as $(X_{pq})^{\alpha\beta} = \delta^\alpha_p \delta^\beta_q$. In [11] where the derivation is given, this Hamiltonian is written in terms of the isospin operators T^a. Since the Hund's coupling is just affects the anisotropy of the exchange integrals, we set it to zero to simplify the calculations restricting the consideration to various values of t_2/t_1 and Δ.

To get the overall picture of the correlations, we used the DMRG method [20,21] to calculate the imaginary part of the correlation function:

$$S(\omega, q) = \sum_k \int_0^\infty dt \langle S_k^z(t) S_m^z(0) \rangle e^{i\omega t + iq(k-m)}, \quad (5)$$

where S_k^z is the spin projection operator acting on site k. The spectral weight contains rich information about the excitation spectrum of the model. We carry out calculations

with a Suzuki-Trotter decomposition of the evolution operator [22,23] and a time step $\delta t = 0.1$ in units of $1/J$. We have been able to study chains with up to 48 unit cells ($L = 144$ sites) using up to 1600 DMRG states for the time evolution, and 5000 for ground state calculations, that translates into a truncation error of 10^{-5} and 10^{-8}, respectively, for the gapless case (similar accuracy is obtained in the gapped case with a smaller basis size). Most time-dependent simulations were conducted on chains with 24 unit cells ($L = 72$ sites). The local space of configurations has dimension of 6, but we use $U(1)$ symmetry corresponding to S^z and density conservation for each orbital channel (four quantum numbers in total). The density for each orbital sector is fixed at $n = 1/3$, while the spin is set to $S^z = 0$. This is equivalent to density $n = 1/6$ in the $SU(6)$ chain [24]. We calculate the spectral function in real time and space with open boundary conditions, and Fourier transform it to obtain resolution

in momentum and frequency following the prescription outlined in [22,23,25].

Limit of small Δ/J, $t_2/t_1 = 1$.—Having a broader aim than a particular case of NaTiSi$_2$O$_6$, we deem it instructive to start with the SU(6)-invariant model. The limit $\Delta = 0$, $t_2 = t_1$ allows an analytical treatment. The thermodynamics and the excitation spectrum are extracted from Bethe ansatz. At low energies the spectral function can be analyzed by means of conformal field theory. At higher energies one can also use the $1/N$ expansion.

The spectrum of the SU(6) symmetric model is gapless and the spectral weight is centered at $q = \pm\pi/3$ which corresponds to $\pm 2k_F$. The spectral function also looks squeezed into the region

$$4J\sin(q/2)\sin|k_F - q/2| < \omega < 4J\sin(q/2) \quad (6)$$

corresponding to two-spinon emission. This agrees well with $1/N$ picture where the spin operators are represented as bilinears of weakly interacting fermions. In the presence of anisotropy spectral gaps open at $q = \pm 2k_F = \pm\pi/3$ shown in Fig. 2 meaning that the anisotropy generates a relevant operator which carries momentum $4k_F$. Such an operator exists at the SU(6) quantum critical point; it transforms according to the representation of the SU(6) group with the Young tableau consisting of a vertical column with two boxes. The scaling dimension is $d = 2(1 - 1/N) = 5/3$. The presence of such perturbation also leads to spontaneous dimerization [see Figs. 3(a), 3(d), and 5]. This order breaks a discrete (translational) symmetry, all other fluctuations are gapped and short range. Obviously, small perturbations preserve the SU(6) structure of the particle multiplets such that spin and orbital excitations are degenerate. The spectral gaps grow slowly with Δ/J as shown on Fig. 4 due the high value of the scaling dimension of the perturbing operator. The SU(6) symmetry is preserved at low energies: Fig. 4 shows that at $\Delta/J < 0.4$ a difference between the gaps for excitations with different quantum numbers is practically undetectable. At larger anisotropies the multiplets will be split.

Limit of large Δ/J.—The easiest way to understand the dimerization phenomenon is to consider the limit of large crystal field. For $J = 0$ each site has two degenerate orbitals in the ground state. For sites $3n$ it may be (a, b), for sites $3n + 1 - (a, c)$, for $3n + 2 - (b, c)$ [see Fig. 3(d)], etc. At $J \neq 0$ the degeneracy is lifted and the ground state becomes dimerized. One possible sequence of occupied orbitals is $(a, a, b, b, c, c, \ldots)$ which corresponds to a nonvanishing exchange between sites $(3n, 3n + 1)$, $(3n + 2, 3n + 3)$, etc. [see Fig. 3(d)]. The other sequence is $(b, c, c, a, a, \ldots)$ with a nonvanishing exchange between $(3n + 1, 3n + 2)$, $(3n + 3, 3n + 4)$, etc. So, in the limit of infinite Δ the ground state consists of isolated periodically arranged spin dimers. Our numerical calculations demonstrate that the dimerization persists down to smallest values
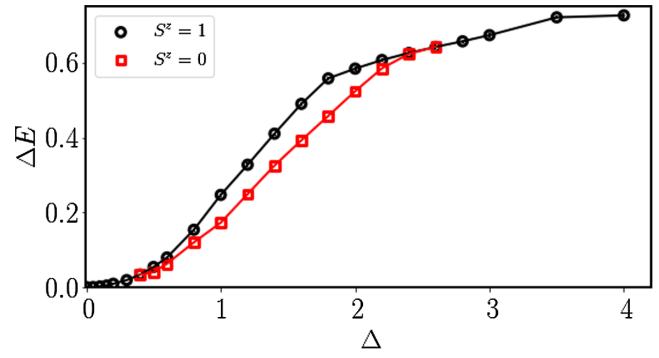

FIG. 4. Numerical results for the lowest spectral gaps for various values of the crystal field Δ and $t_2 = t_1$.

of Δ/J (see Fig. 5). It leads to two major effects for the spectrum opening gaps for all excitations and leading to a progressive shift of the spectral weight towards frequency $\omega = 2J$ corresponding to the breaking of an isolated dimer [see Figs. 2(c) and 2(d)]. Nevertheless, there is some weight at about $J/2$–13 meV, given $2J \simeq 53$ meV [6], in agreement with the gap seen in the heat capacity data [5].

According to the first-principles calculations and Wannier function analysis [11,17], NaTiSi$_2$O$_6$ has the following parameters: $U = 3.8$ eV, $J_H = 0.8$ eV, $t_1 = 0.203$ eV, $t_2/t_1 = 0.21$, $t_1^2/U \approx 0.01$ eV. Hence in NaTiSi$_2$O$_6$ the deviation from $t_2/t_1 = 1$ is quite significant. However,
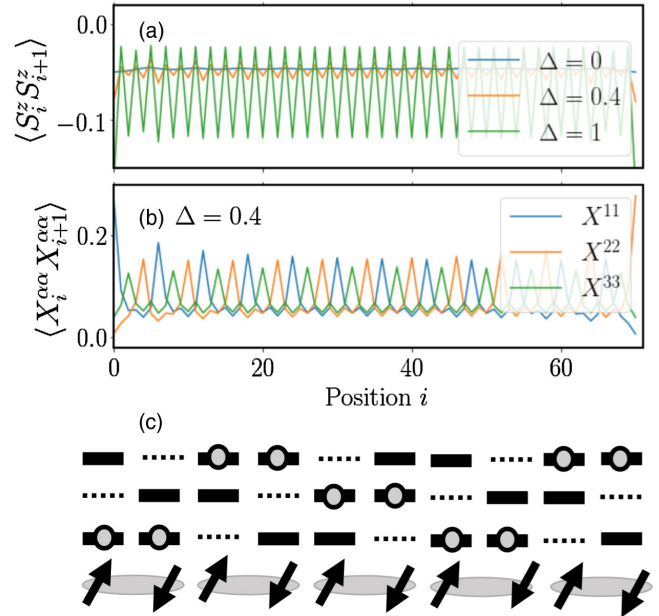

FIG. 5. Dimerization for various values of the crystal field Δ and $t_2 = t_1$. (a) Nearest neighbor spin-spin correlation; (b) density-density correlation in the orbital channel; (c) schematic illustration of the spin-orbital order in the limit of large Δ: dashed lines represent orbitals that are projected out. Charge fluctuations are suppressed and charge is frozen in the depicted pattern. Spin is only allowed to interact in pairs forming independent singlets.

due to the well-known double counting issue on the LDA $+$ U approach to correlated materials, the value of Δ is uncertain and is taken as a free parameter. As we have seen at such values of anisotropy and crystal field the excitations are gapped and practically dispersionless [Figs. 2(d), 2(f), and 2(g)] corresponding to the local dimers discussed above. This is the situation in $NaTiSi_2O_6$ which thus fails our expectations for an orbital spin liquid. However, as follows from Figs. 2(b) and 2(c), at moderate values of the anisotropy and crystal field there is a significant spectral weight at small energies. The spectral function bears some resemblance to the SU(6)-symmetric one, which is a sign that the orbital d.o.f. are not quenched. Such situation may exist in the ruthenium- or osmium-based pyroxenes where Ru^{3+} or Os^{3+} ions contain one t_{2g} hole. These are candidates for liquids with tightly bound spin and orbital excitations. In the early $3d$ transition-metal oxides such as the titanium oxide, the $3d$ energy is considerably different from the oxygen p orbitals, which creates the barrier that hinders the indirect hopping t_2. However, t_2 may become dominant as in, for example, Na_2IrO_3 and $RuCl_3$ to induce the Kitaev-type spin frustration [10]. Specifically, considering Ru^{3+} has almost the same Shannon ionic radii as Ti^{3+}, we did similar first-principles calculations for $NaRuSi_2O_6$ [11]. We found that $t_2/t_1 = 0.64$ $(t_1 = 0.132$ eV), which is much more favorable than the $NaTiSi_2O_6$ case. In addition, the yz orbital moves higher in energy, which is closer to and mixed with the hole bands of the xy and zx characters. Moreover, the experimentally observed large bond dimerization is favored in the first-principles calculation for $NaTiSi_2O_6$, but not for $NaRuSi_2O_6$. Thus, it would be interesting to synthesize $NaRuSi_2O_6$ and compare its low-energy physical properties with the present theory.

[1] S. V. Streltsov and D. I. Khomskii, Phys. Rev. B **77,** 064405 (2008).

[2] M. J. Konstantinović, J. van den Brink, Z. V. Popović, V. V. Moshchalkov, M. Isobe, and Y. Ueda, Phys. Rev. B **69,** 020409(R) (2004).

[3] J. van Wezel and J. van den Brink, Europhys. Lett. **75,** 957 (2006).

[4] T. Hikihara and Y. Motome, J. Phys. Soc. Jpn. **74** Suppl., 212 (2005).

[5] M. Isobe, E. Ninomiya, A. N. Vasili'ev, and Y. Ueda, J. Phys. Soc. Jpn. **71,** 1423 (2002).

[6] H. J. Silverstein, A. E. Smith, C. Mauws, D. L. Abernathy, H. Zhou, Z. Dun, J. vanLierop, and C. R. Wiebe, Phys. Rev. B **90,** 140402(R) (2014).

[7] Z. S. Popović, Ž. V. Šljivančanin, and F. R. Vukajlović, Phys. Rev. Lett. **93,** 036401 (2004).

[8] S. V. Streltsov, O. A. Popova, and D. I. Khomskii, Phys. Rev. Lett. **96,** 249701 (2006).

[9] F. Mila and F.-C. Zhang, Eur. Phys. J. B **16,** 7 (2000).

[10] G. Jackeli and G. Khaliullin, Phys. Rev. Lett. **102,** 017205 (2009).

[11] See Supplemental Material at http://link.aps.org/supplemental/10.1103/PhysRevLett.123.237204, which includes Refs. [12–17], for first principles calculations and a derivation of the effective Hamiltonian.

[12] K. Schwarz, P. Blaha, and G. K. H. Madsen, Comput. Phys. Commun. **147,** 71 (2002).

[13] J. P. Perdew, K. Burke, and M. Ernzerhof, Phys. Rev. Lett. **77,** 3865 (1996).

[14] W. Ku, H. Rosner, W. E. Pickett, and R. T. Scalettar, Phys. Rev. Lett. **89,** 167204 (2002).

[15] W.-G. Yin, D. Volja, and W. Ku, Phys. Rev. Lett. **96,** 116405 (2006).

[16] R. L. Barnett, A. Polkovnikov, E. Demler, W.-G. Yin, and W. Ku, Phys. Rev. Lett. **96,** 026406 (2006).

[17] W.-G. Yin and W. Ku, Phys. Rev. B **79,** 214512 (2009).

[18] B. Sutherland, Phys. Rev. A **5,** 1372 (1972).

[19] It can be gapped by electron-phonon interaction that utilizes the $2k_F$ instability to drive the Peierls transition, in which the unit cell is doubled to have six Ti atoms, compatible with Fig. 3(d).

[20] S. R. White and A. E. Feiguin, Phys. Rev. Lett. **93,** 076401 (2004).

[21] A. Daley, C. Kollath, U. Schollwöck, and G. Vidal, J. Stat. Mech. (2004) P04005.

[22] A. E. Feiguin, in *XV Training Course in the Physics of Strongly Correlated Systems, AIP Proceedings* (American Institute of Physics, Melville, 2011), Vol. 1419, p. 5.

[23] S. Paeckel, T. Kahler, A. Swoboda, S. R. Manmana, U. Schollwöck, and C. Hubig, arXiv:1901.05824.

[24] S. R. Manmana, K. R. A. Hazzard, G. Chen, A. E. Feiguin, and A. M. Rey, Phys. Rev. A **84,** 043601 (2011).

[25] S. R. White and I. Affleck, Phys. Rev. B **77,** 134437 (2008).

Unconventional Continuous Structural Disorder at the Order-Disorder Phase Transition in the Hexagonal Manganites

Sandra H. Skjærvø,[1,*] Quintin N. Meier,[2,*] Mikhail Feygenson,[3,4] Nicola A. Spaldin,[2]
Simon J. L. Billinge,[5,6] Emil S. Bozin,[5,‡] and Sverre M. Selbach[1,†]

[1]*NTNU Norwegian University of Science and Technology, Department of Materials Science and
Engineering, NO-7491 Trondheim, Norway*
[2]*ETH Zürich, Materials Theory, Wolfgang Pauli Strasse 27, CH-8093 Zürich, Switzerland*
[3]*Forschungszentrum Jülich, JCNS, D-52425 Jülich, Germany*
[4]*Chemical and Engineering Materials Division, Oak Ridge National Laboratory,
Oak Ridge, Tennessee 37831, USA*
[5]*Brookhaven National Laboratory, Condensed Matter Physics and Materials Science Department,
Upton, New York 11973, USA*
[6]*Columbia University, Department of Applied Physics and Applied Mathematics,
New York, New York 10027, USA*

The improper ferroelectricity in $YMnO_3$ and other related multiferroic hexagonal manganites is known to cause topologically protected ferroelectric domains that give rise to rich and diverse physical phenomena. The local structure and structural coherence across the ferroelectric transition, however, were previously not well understood. Here, we reveal the evolution of the local structure with temperature in $YMnO_3$ using neutron total scattering techniques, and we interpret them with the help of first-principles calculations and with a first-principles-based effective Hamiltonian. The results show that, at room temperature, the local and average structures are consistent with the established ferroelectric $P6_3cm$ symmetry. On heating, both local and average structural analyses show striking anomalies from about 800 K up to the Curie temperature and signatures of a locally more preserved structure than on average, consistent with increasing fluctuations of the order-parameter angle. These fluctuations result in an unusual local symmetry lowering into a continuum of structures on heating. This local symmetry breaking persists into the high-symmetry nonpolar phase, constituting an unconventional type of order-disorder transition, and we pinpoint it as the reason for the anomalous behavior near the phase transition. The hidden disorder revealed in $YMnO_3$ by total scattering is expected to find analogies in other materials with structural frustration or characteristic energy barriers of different magnitudes.

Subject Areas: Condensed Matter Physics,
Materials Science

I. INTRODUCTION

The multiferroic hexagonal manganites, h-RMnO$_3$ (R = Dy-Lu, In, Y, or Sc), are improper ferroelectrics where the polarization emerges as a secondary effect due to an improper coupling to the primary distortion mode. This results in unusual ferroelectric domain

---

[*]These co-authors contributed equally to this work.
[†]Corresponding author.
 selbach@ntnu.no
[‡]Corresponding author.
 bozin@bnl.gov

structures in which topological protection of the domain-wall intersections causes fundamentally and technologically interesting physical properties ranging from early universe analogues [1–3] to nanoscale conducting channels [4–11]. In spite of multiple studies, the evolution of the polarization with temperature has not been explained on a microscopic level. In particular, studies based on powder neutron [12,13] and x-ray [13–18] diffraction show good agreement with a polar model describing the average structure at low and intermediate temperatures, while structural anomalies have been reported between 800 K and the Curie temperature T_C. These findings led to a range of reported values for T_C and proposals of two distinct structural phase transitions [12–16,19], although it is now understood that there is in fact only one phase transition at T_C, with the polarization slowly emerging as a secondary effect [20–24].
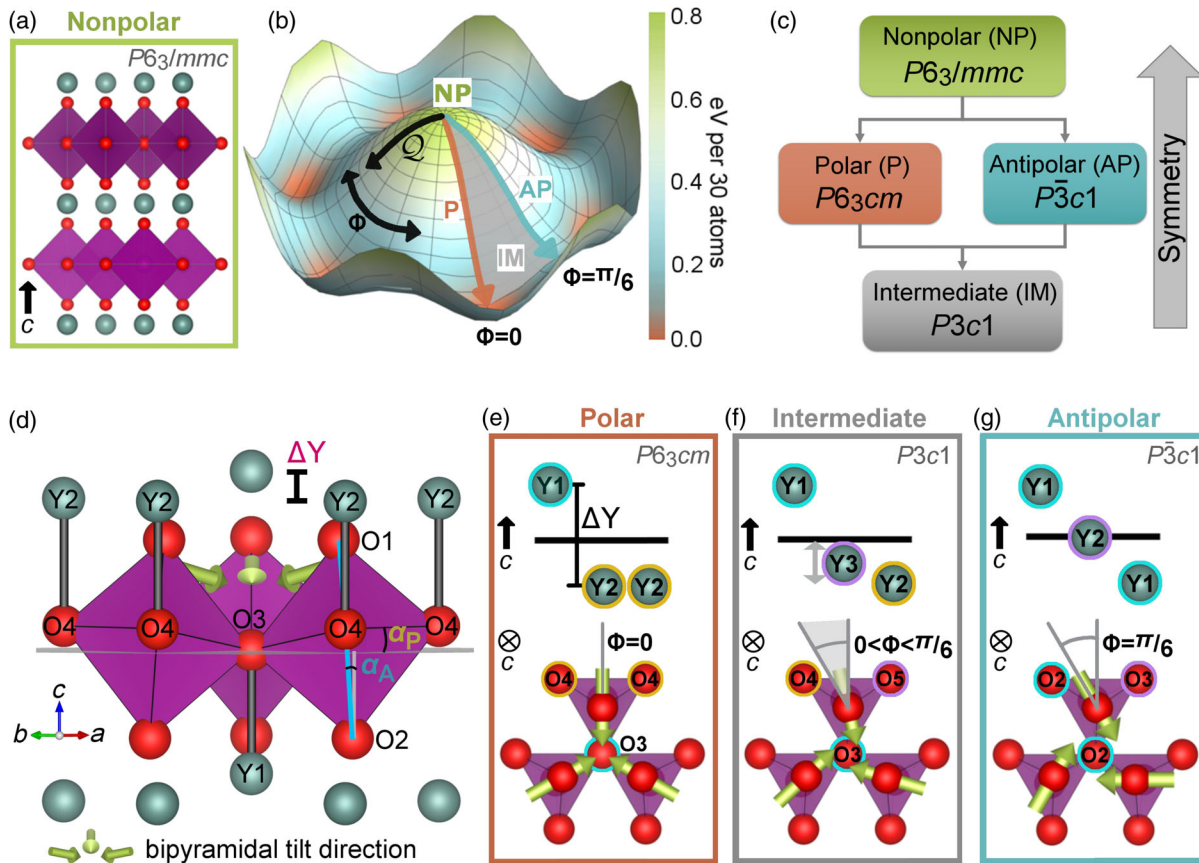
FIG. 1. Structures of YMnO$_3$ phases. (a) The high-symmetry nonpolar (NP) structure with purple MnO$_5$ bipyramids and turquoise Y cations. Oxygens are shown in red. (b) The Landau free energy of the hexagonal manganites as a function of the two-component order parameter ($\mathcal{Q}$, Φ) resembling a Mexican hat, with the NP structure at the top. In the brim of the hat, the polar (P), antipolar (AP), and intermediate (IM) subgroup structures occur at the minima, maxima, and intermediate regions, respectively. (c) Group-subgroup relationship between the high-symmetry nonpolar structure and the subgroup structures found in the brim of the Mexican-hat energy landscape. (d) The order-parameter observables for the polar subgroup are the bipyramidal tilt amplitude (angles α_A and α_P) and corrugation of Y cations (ΔY). Note that ΔY denotes the distance in the c direction between Y1 and Y2. Green arrows indicate the directions of the bipyramidal tilts. The angle between the O1-O2 line and the c axis defines the apical tilt α_A and is a robust measure of the order-parameter amplitude $\mathcal{Q}$ irrespective of the value of Φ. The plane through the three in-plane oxygens (one O3 and two O4) relative to the ab plane defines the planar tilt angle α_P and is related to both the order-parameter amplitude $\mathcal{Q}$ and angle Φ. (e)–(g), Structures of the subgroups at different order-parameter angles Φ: Y off-centering pattern (top) and bipyramidal tilting directions, indicated by green arrows (bottom). Atomic sites for the three subgroups are labeled and coded with colored circles to emphasize which positions are symmetry related in each phase. Atom positions with the same color markings are aligned along the c axis and have the same multiplicity. A detailed overview of the atomic positions for the space groups is given in Fig. S1 of the Supplemental Material [26].

The high-symmetry nonpolar average structure of the prototypical hexagonal manganite h-YMnO$_3$ above T_C displays $P6_3/mmc$ symmetry. This structure features corner-sharing MnO$_5$ trigonal bipyramids separated by layers of Y^{3+} ions, each coordinated by eight oxygens [Fig. 1(a)]. The unit cell triples across T_C at around 1250 K, as a noncentrosymmetric, but zero-polarization, zone-boundary K_3 mode condenses [25]. This K_3 distortion consists of z-axis displacements of the Y atoms and a corresponding tilt of the trigonal bipyramids. It is described by a two-component order parameter ($\mathcal{Q}$, Φ) with amplitude $\mathcal{Q}$ and angle Φ [21]. Here, $\mathcal{Q}$ is related to

the magnitude of bipyramidal tilting and Y displacements, and Φ is related to the direction of the bipyramidal tilting and the displacement pattern of the Y, e.g., up-down-down.

The resulting energy landscape resembles a Mexican hat [Fig. 1(b)] with three lower-symmetry space groups in the brim. The group-subgroup relationships are illustrated in Fig. 1(c). The subgroups are characterized by the angle of the order parameter Φ. A general angle leads to $P3c1$ symmetry [IM, Fig. 1(e)], but special values of Φ lead to higher symmetries. For $\Phi = n(\pi/3)$, with $n = 0, 1, ..., 5$, the system is polar with space group symmetry $P6_3cm$ [P, Figs. 1(d) and 1(e)]. For $\Phi = (\pi/6)(2n+1)$, the

system becomes antipolar with space group symmetry $P\bar{3}c1$ [AP, Fig. 1(g)].

Landau theory analysis of the K_3 mode following Artyukhin *et al.* [21], in combination with first-principles calculations of hexagonal $YMnO_3$, suggests an insignificantly small energy difference between the polar and antipolar symmetry when only the K_3 mode is included. Stabilization of the polar state occurs only when the K_3 mode couples to a polar Γ_2^- mode that causes a shift of the Y atoms towards the Mn-O layer. Because of this improper coupling, nearly all Φ angles result in a net polarization that reaches its maximum in the P structure (around 6 $\mu C\,cm^{-2}$ at room temperature) but vanishes for the AP structure. The P structure becomes favored by about 100 meV per unit cell in comparison with the AP structure and by more than 600 meV per unit cell in comparison with the NP structure at 0 K [21]. The exact values of the relative energies are highly temperature dependent. The resulting Z_6 symmetry of the configuration space causes the unusual sixfold ferroelectric domain patterns characteristic of h-$YMnO_3$ [27].

This established model [21] of the Mexican-hat Landau free energy [Fig. 1(b)] describes the average symmetry evolution of the system reduced to the degrees of freedom given by the order parameter, but it does not address the underlying microscopics. In particular, whether the transition mechanism is closer to the displacive limit [the order parameter $(\mathcal{Q}, \Phi)$ goes to zero both locally and on average at T_C] or the order-disorder limit (local order parameter is conserved) is not known.

Here, we provide such a local-structure description of the atomic structure of h-$YMnO_3$ from ambient temperature to 1273 K, across the ferroelectric transition T_C. We combine pair distribution function (PDF) analysis of neutron total scattering data with conventional Rietveld refinement to probe structural coherence and to distinguish short-range from average long-range order. This analysis reveals a surprising and unconventional behavior of the local structure as a function of temperature that cannot be explained either by a conventional order-disorder or by a displacive transition picture. In a conventional order-disorder transition, the low-temperature distortions persist above the transition in the local structure but are not evident in the long-range ordered structure due to averaging over variants of the distorted structure [28–30]. Our PDF results show that below about 800 K, the average and local structures evolve consistently, with smoothly decreasing distortions related to a decreased order-parameter amplitude. However, between about 800 K and T_C, the average and local structures progressively diverge from each other. Upon crossing T_C, the local structure below 16–20 Å changes significantly less than the average structure, suggesting an order-disorder transition. The fit of the polar model to the local structure gradually deteriorates, while fits with the antipolar structure gradually improve, consistent with

increasing fluctuations of the order-parameter angle Φ on heating. At T_C, where long-range cell tripling disappears in the average structure, the fits of the polar and antipolar models become equivalent, though neither model fits ideally. The transition at T_C is therefore an order-disorder transition in the sense that the average structure transitions to the undistorted high-symmetry nonpolar structure, while the structural distortions persist in the local structure. In other words, the amplitude $\mathcal{Q}$ of the order parameter never goes to zero in the local structure. However, it is unconventional in the sense that the disordering does not occur only between the local polar variants but between all possible angles of the order parameter. These total scattering results are corroborated by a first-principles-based effective Hamiltonian predicting the same behavior.

These two key discoveries—the unconventional nature of the order-disorder transition and the extensive temperature region of symmetry-lowering fluctuations below T_C where the material accesses a wide range of structures, intermediate between the polar and antipolar subgroups, at the local scale—reconcile previous inconsistencies in the literature. Such hidden disorder, revealed by total scattering, is also anticipated in other materials where competing interactions give rise to structural frustration, or where energy barriers of different magnitudes give rise to different thermal evolution of order-parameter components.

II. STRUCTURAL DESCRIPTION OF THE ORDER PARAMETER

The order parameter $(\mathcal{Q}, \Phi)$ is related to three observable atomic displacements [Fig. 1(d)]: The first, α_A, is the bipyramidal tilt angle calculated from the line connecting the apical oxygens (O1, O2) relative to the c axis; the second, α_P, is the bipyramidal tilt of the plane through the three planar oxygens (O3, O4) relative to the ab plane; and the third is the out-of-plane off-centering (corrugation) of the yttrium ions, $\Delta Y = c(z_{Y1} - z_{Y2})$. The latter two are strictly defined only for the polar ground-state symmetry [Fig. 1(d)]. Shifting the order-parameter angle Φ away from the polar symmetry and towards the antipolar or intermediate space groups breaks the symmetry of the Y2 and O4 sites such that the corresponding order-parameter observables α_P and ΔY have to be calculated by including the additional Wyckoff sites (see Fig. S1 in the Supplemental Material [26]).

III. RESULTS

A. Average structure

We first consider the average structure behavior based on qualitative and quantitative assessment of our neutron powder diffraction data. On the qualitative side, our reciprocal space data show that the (102) and (202) super-reflections of the polar structure disappear above 1223 K, corresponding to the ferroelectric Curie temperature T_C (see Fig. S2 in the Supplemental Material [26]), in line with previous reports [12,15,18,24].
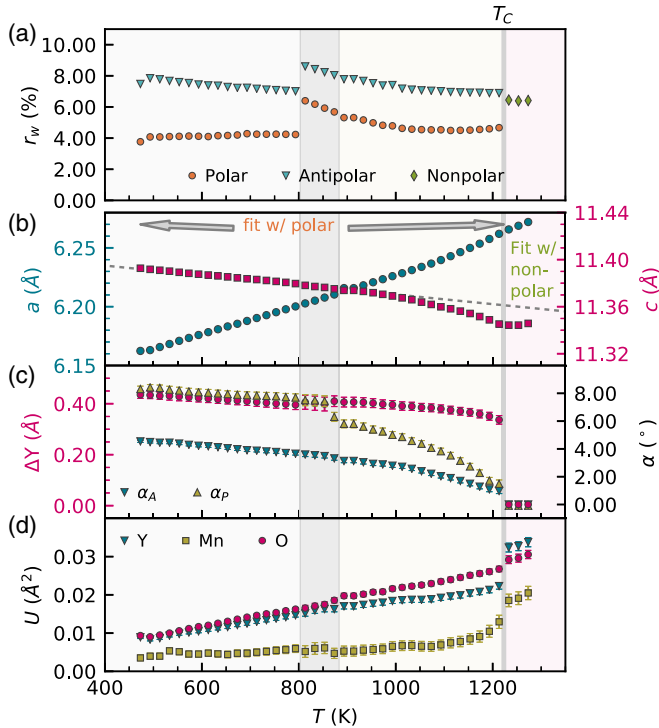
FIG. 2. Average structure refinements of YMnO₃. (a) Fitting residuals r_w of the high-symmetry NP and low-symmetry P and AP models to $I(Q)$, where Q is the reciprocal space vector. The gray vertical line at 1223 K indicates the Curie temperature T_C above which the high-symmetry nonpolar structure can be inferred from the Bragg reflections. The gray shaded area between 800 K and 880 K separates low- and intermediate-temperature regions. (b) Lattice parameters a and c; (c) Y corrugation ΔY, apical tilt angle α_A, and planar tilt angle α_P; and (d) isotropic atomic displacement parameters U—all obtained from fitting the P ground-state model below T_C and the high-symmetry NP structure above T_C to the reciprocal space neutron time-of-flight data. (Representative Rietveld fits with the polar, antipolar, and nonpolar models are shown in Figs. S3–S5 of the Supplemental Material [26]).

Quantitative analysis of the average structure of h-YMnO₃ was carried out by Rietveld refinements of the measured diffraction patterns with the three special space group models NP, P, and AP, for which representative fits are given in Figs. S3–S5 of the Supplemental Material [26]. In Fig. 2(a), we have presented the fit residuals r_w for the P and AP models, found in the brim of the Mexican-hat energy landscape, below T_C, and for the NP model, found at the top of the Mexican hat, above T_C. Refinement parameters from fitting with the P model are presented in Figs. 2(b)–2(d). The models are described and visualized in Figs. 1(e) and 1(g).

The models give adequate fits to the data with weighted profile agreement factors (r_w) below 10%. The polar model gives better agreement than the antipolar model for all temperatures below T_C [Fig. 2(a)]. Despite having fewer variables, the NP model gives a comparable r_w to that of the

P model above T_C. The most surprising observation is a discontinuous jump in r_w extracted from the P and AP models at 800 K. The lattice parameters [Fig. 2(b)] vary smoothly with temperature, also through T_C. Above T_C, the lattice parameter a of the nonpolar model is multiplied by $\sqrt{3}$ for direct comparison with the tripled unit cell of the polar model.

There is no discontinuity of the lattice parameters at 800 K that might explain the change in r_w there. However, there is a smooth drop-off from linear temperature dependence of the c-axis parameter with an onset at around 800 K. This result is highlighted in the figure by the gray dashed line extrapolated from the low-temperature linear behavior. Such a drop-off has been noted previously [12], as has the extended region of zero thermal expansion of the c axis above T_C.

We now turn to the three order-parameter observables α_A, α_P, and ΔY, whose temperature dependencies are shown in Fig. 2(c). All of these parameters have, by definition, a value of 0 in the high-symmetry nonpolar structure and are thus expected to decrease smoothly to zero on heating to T_C, as they are all direct observables of the order-parameter amplitude $\mathcal{Q}$ (Fig. 1). The refinements of the α parameters to the polar model smoothly decrease with increasing temperature, becoming close to zero at T_C, consistent with a continuous transformation. On the other hand, the corrugation parameter ΔY keeps a large value right up to T_C, which would be expected for a discontinuous transition. From about 800–880 K, the fits become unstable and the α parameters start to decrease faster than linearly, in agreement with previous studies [12], possibly explaining the jump in r_w in panel (a).

The vanishing polyhedral tilting and persistent ΔY could indicate a scenario in which the structure has off-centered Y ions combined with untilted Mn-O₅ polyhedra, which would give very long out-of-plane Y-O distances. We thus performed density functional calculations to check if this scenario is plausible and found that it is highly unfavorable (see Fig. S6 in the Supplemental Material [26]). We note that the Y and O isotropic atomic displacement parameters (ADPs) U shown in Fig. 2(d) are anomalously large compared to the Mn U, which is nonlinear upon approaching T_C. There is also a discontinuous jump in the ADPs on moving into the high-symmetry nonpolar structure, suggesting that broken local symmetry persists above T_C [31–34]. Hence, we conclude that the structural behavior obtained from the reciprocal space refinements is physically unfeasible at the local scale, motivating the use of a local structure-sensitive method.

B. Local structure

In order to investigate the local structure, we perform a PDF analysis on the same neutron scattering data as analyzed in the previous section. Representative PDFs at different temperatures are shown in Fig. 3(a), plotted over a
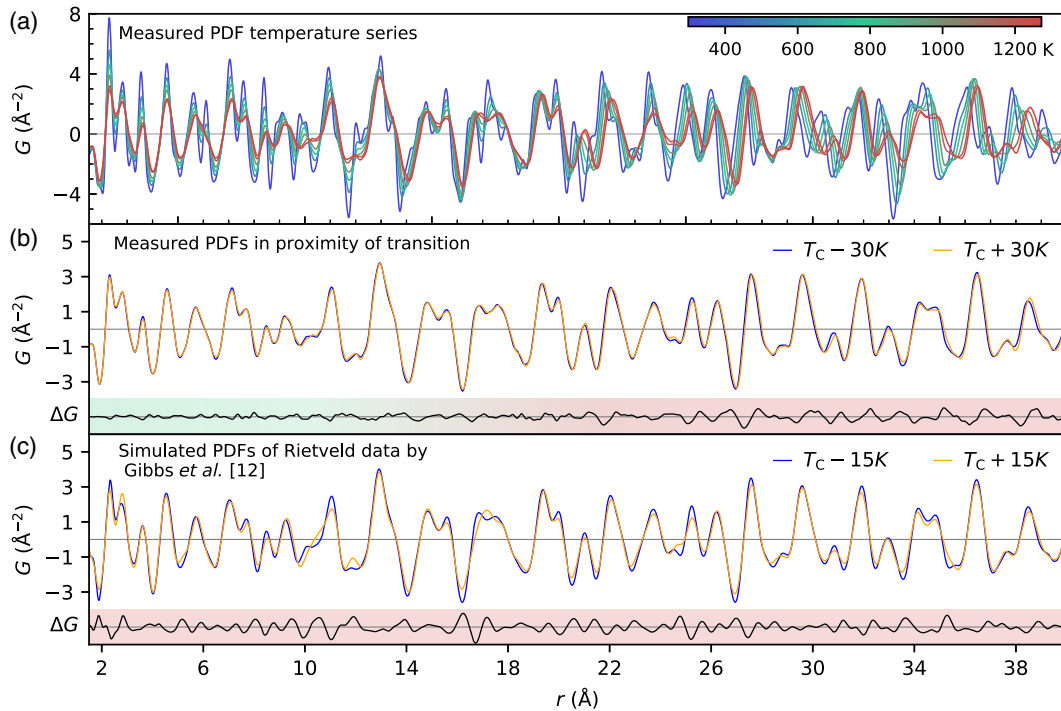
FIG. 3. (a) Experimental PDFs for 473–1273 K temperature interval in 100 K increments. The full set of PDF data on a denser ($\Delta T = 20$ K) grid and further details are provided in Figs. S7 and S8 of the Supplemental Material [26]. The data temperature is color coded, as indicated by the horizontal color bar. Comparison of PDFs for temperatures bracing the structural transition temperature T_C are shown in panels (b) and (c) as follows. Experimental PDFs from our measurements are displayed in panel (b). Simulated PDFs, calculated using the average structure information from Rietveld refined structures reported by Gibbs *et al.* [12] across the transition, are shown in panel (c). Corresponding difference curves are shown underneath. The shaded green and red areas behind the difference curve indicate, respectively, regions of low and high difference. The presence of length scales exhibiting different behavior can be readily evidenced by comparing the difference curves in panels (b) and (c). At low r, the measured PDFs change appreciably less than what would be expected if the average crystallographic picture were applicable to the local structure, as portrayed by the simulated PDFs. In contrast, the changes across the transition at high r are of similar amplitude in both panels. Note that the structural phase transition temperature in Ref. [12] is 1258 K, 35 K higher than in our measurements. Comparison of simulated PDFs based on structural parameters from the Rietveld refinements of Gibbs *et al.* to that of this work is provided in Fig. S9 of the Supplemental Material [26].

wide range of r (see detailed plots in Figs. S7 and S8 in the Supplemental Material [26].

PDF analysis utilizes both Bragg and diffuse scattering information, revealing time-averaged snapshots of the atomic structure on multiple length scales. In contrast to a conventional crystallographic approach that seeks the highest possible symmetry model consistent with the Bragg data component only, the PDF analysis explores whether such symmetry is broken on a nanometer length scale and, if so, how. The peak positions correspond to interatomic distances, while the widths of the peaks indicate distributions of interatomic distances due to thermal motion and also lower symmetry.

A characteristic of neutron PDFs of materials containing manganese (and other negative neutron scattering length materials) is that peaks corresponding to Mn–non-Mn pairs are negative. This characteristic is most clearly seen for the Mn-O nearest-neighbor bond length at around 2 Å. This peak is a doublet, as is clearly seen in the 298 K data

in Figs. 3(a) and 4(a). On heating, this doublet broadens into an unstructured peak by 1273 K [Figs. 3(a) and 4(c)]. The increased broadening of the PDF with increasing temperature is clearly evident in Figs. 3 and 4.

Apart from thermal broadening effects, several other qualitative changes can be observed in the experimental PDFs with increasing temperature, as shown in Fig. 3(a). While we observe qualitative changes in PDF features at all length scales, these seem to become much more pronounced in the high-r region (above 20 Å), suggesting length-scale-dependent structural changes on heating. The apparent order-disorder behavior of the system across T_C, inferred from unphysical behavior of structural parameters derived from the Rietveld analysis, can also be further explored by comparing measured and simulated PDFs corresponding to temperatures straddling T_C. If the transition were displacive, the PDFs would show clear changes of similar magnitude over the entire r range. We illustrate this in Fig. 3(c) by comparing simulated PDFs using the
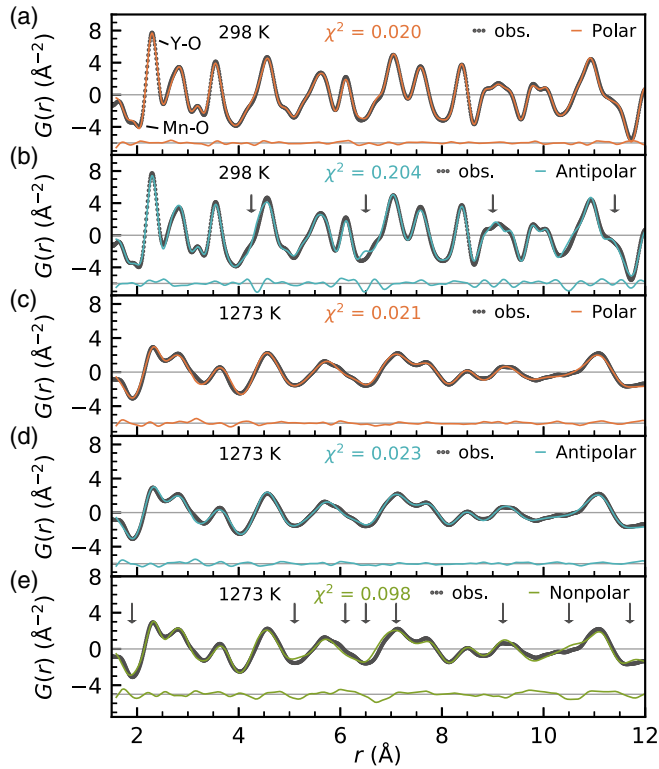
FIG. 4.   Fits of the crystallographic models to the PDF data. The $G(r)$ at 298 K fitted over the range $r = 1.6$–12 Å by the (a) low-symmetry P and (b) AP models. Corresponding difference curves are shown beneath the PDFs, and the overall fit residuals χ^2 are as indicated. Fits to the 1273 K $G(r)$ data by the low-symmetry P and AP models over the same r range are shown in panels (c) and (d), respectively. (e) Fit of the high-symmetry NP model to the 1273 K PDF data: Arrows mark regions of particularly bad fits. High fit residual and eventful difference curves demonstrate that the nonpolar model does not provide an adequate description of the local structure of the high-temperature phase. Fits of the PDF data for additional temperatures are shown in Figs. S10 and S11 of the Supplemental Material [26].

Rietveld refined structures reported by Gibbs *et al.* [12] that portray such a displacive picture. In this case, substantial structural changes are evident in the difference curve over the entire r range considered [see Fig. 3(c)]. However, this is not what is observed when experimental PDFs measured at temperatures just below and just above T_C are compared, as can be seen in Fig. 3(b). It is evident that the observed structural changes are much smaller in the low-r region up to about 15 Å, as compared to those in the r range between 20 and 40 Å. This behavior is characteristic for an order-disorder mechanism, where the local structure changes insignificantly across the transition, while the global symmetry change is evident in the measures of the average structure. The r values of 16–20 Å separating the local regime from the average regime correspond to approximately three unit cells in plane and 1.5–2 out of plane.

Quantitative information about the local structure can be further extracted by fitting the structural models to the PDF

data. When symmetry breaking occurs only in the local structure but not in the average structure, it is customary to fit the PDF data with lower-than-crystallographic symmetry models over the relevant r range [28]. We fitted the PDF data with models corresponding to the four space groups found in the Mexican-hat energy landscape: the P, AP, IM, and high-symmetry NP models over an r range of 12 Å. This length scale corresponds to 1–2 unit cells and is well within the r range implicated by the direct data comparisons, as discussed in relation to Fig. 3(b). Note that the IM model does not represent a single configuration of atoms, but it can describe any angle Φ of the order parameter in the brim of the Mexican hat, including the P and AP models.

In Fig. 4, we show representative PDFs at 298 K, fitted with the polar and antipolar space groups, and at 1273 K, fitted with the polar, antipolar, and nonpolar space groups. Importantly, and in agreement with other evidence of an order-disorder transition presented so far, the low-symmetry polar model gives much better agreement with the 1273 K data set than the high-symmetry nonpolar model, as is apparent from the appreciably lower χ^2 and clear appearance of misfit regions in the difference curve plotted below. While the antipolar structure fits the measured PDF significantly worse at room temperature [Fig. 4(b)], it provides a comparable fit to that of the polar model at 1273 K. We will return to this observation later.

Next, we consider the PDF-derived lattice parameters and order parameter observables α_A, α_P, and ΔY, shown in Fig. 5. The refined lattice parameters are in very good agreement with those obtained from Rietveld refinement, and they show the same behavior. The order-parameter observables are all expected to retain finite values above T_C for the now-established order-disorder transition. Indeed, we observe finite values of all three order-parameter observables. Surprisingly, however, they do not decrease by the same amount: α_A decreases to about half its low-T value, while α_P retains about 80% of its low-T value. Note that ΔY decreases to about 60% of its low-T value. While these observations support the suggested order-disorder behavior, they also indicate that the P model used to fit the PDF data is not able to fully represent the structural changes upon heating.

This case is further substantiated by the uncertainties of ΔY, which become significantly larger than those of α_A and α_P above 1000 K, suggesting that Y displacements become progressively more difficult to determine within the polar model with increasing temperature. We note that, as with the average structure refinements, the atomic displacement parameters and/or their uncertainties experience an anomalous increase above about 800 K, indicative of the increasing inadequacy of this model for describing the local structure as temperature increases.

Finally, we compare the quality of the fits with the P model to fits with the AP, IM, and high-symmetry NP models. The comparison of the fit residuals r_w for the four
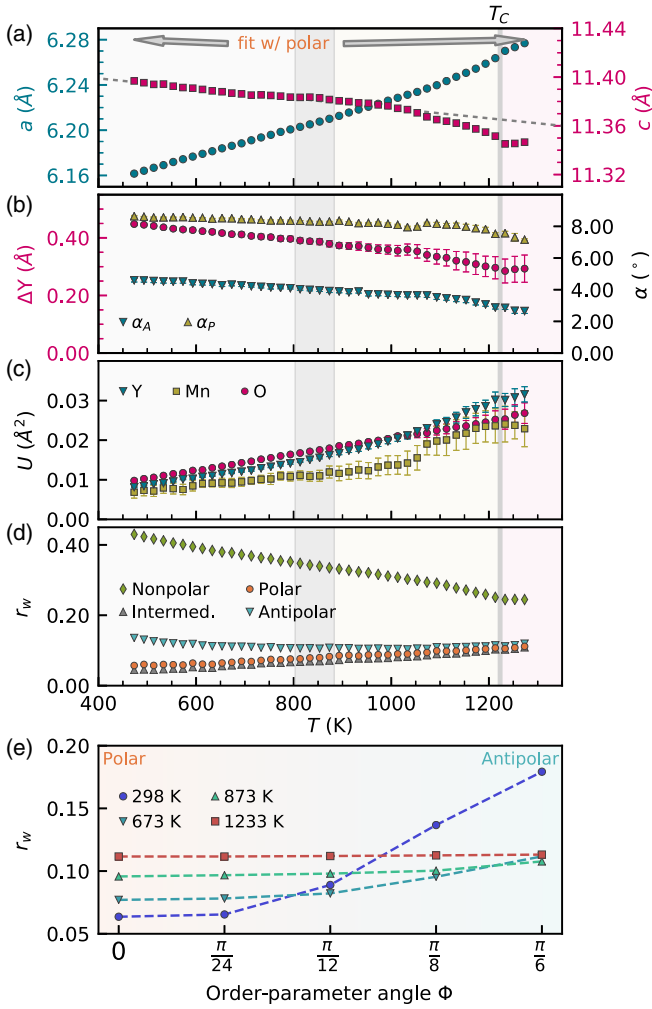
FIG. 5. Local structure refinements. (a) Refined lattice parameters from fitting $G(r)$ for $r = 1.6–22$ Å with the polar space group model. (b) Y corrugation ΔY, planar α_P, and apical α_A bipyramidal tilt angles, and (c) atomic displacement parameters U from fitting the polar model to the data in the range $r = 1.6–12$ Å with fixed lattice parameters shown in panel (a) (see Supplemental Material [26] for details on the calculation of error bars). (d) Fit residual r_w for fitting $G(r)$ between 1.6 and 12 Å for the P model found at the minima and the AP model found at the local maxima in the brim of the Mexican-hat potential using fixed lattice parameters found from refinements between 1.6 and 22 Å. The grey vertical line at 1223 K shows the Curie temperature T_C, and the grey shaded area between 800 K and 880 K shows the temperature interval where refinements become incoherent. (e) Fitting error r_w as a function of the order-parameter angle for a rotation of the angle between the P and the AP structures at constant amplitude. The amplitude for each temperature is shown in panel (b). Comparisons of the refined order-parameter observables and ADPs of the polar model with those of the antipolar and intermediate space group models are shown in Figs. S12 and S13, respectively, of the Supplemental Material [26].

models [Fig. 5(d)] clearly shows that the AP model gives distinctly worse agreement than the P model at room temperature. As temperature increases, the AP model fits progressively improve, while the polar model fits

deteriorate. This observation of stagnating or even increasing fitting error is anomalous, as for systems that do not exhibit structural changes the fit residuals are expected to decrease with heating as thermal fluctuations broaden the data (see, for example, the behavior of bulk FCC Ni in Fig. S14 of the Supplemental Material [26]). At around 1100 K, the two models provide a similar, but not ideal, fit quality, suggesting that neither one of the two provides a complete description of the underlying local structure. Notably, anomalous jumps in U are not fully reconciled by either the P, AP, or IM model of the local structure despite reasonably low fit residuals, indicating that the underlying local structure is of greater complexity than that described by these low-symmetry models (see Supplemental Material, Fig. S13). We observe that the IM model is comparable to the P model over the entire temperature range, with a slightly lower r_w, which we attribute to more degrees of freedom (16 for IM, 11 for P). This observation suggests that there is no other minimum at a different order-parameter angle Φ since the degrees of freedom in the intermediate model cover all angles in the brim of the Mexican hat.

We further examine the observation that the antipolar and polar models seem to fit equally well at higher temperatures by fitting the data to constructed models in which we manually rotate the order-parameter angle Φ. The models are constructed starting from the refined structure for the P model and rotating Φ while keeping the order-parameter amplitude Q constant. This method is justified as the Q for refinements with all three subgroup models obtains comparable values (see Fig. S11 of the Supplemental Material [26]). We then fit the models at different temperatures, allowing the polar degrees of freedom as well as the ADPs to refined as presented in Fig. 5(e). As is evident from the figure, the room-temperature data are much better fitted by the polar than the antipolar model, while as the temperature rises, the fit quality becomes independent of the order-parameter angle and the absolute fitting error increases overall. We note here that the invariance of the fitting error with respect to the order-parameter angle cannot be explained by the order-parameter amplitude Q going to zero, as the constructed models used here have the same amplitude of structural distortions as shown in panel (b), with amplitude never falling below 50%.

Thus, from our inspection of the fitting errors, we make four key observations on heating: (1) for the P model, r_w increases; (2) for the P and AP models, r_w becomes similar; (3) for the NP model, r_w, while decreasing, remains much larger; and (4) the fitting error becomes independent of the order-parameter angle when approaching T_C.

These observations can be explained by a scenario in which the local structure in the high-symmetry phase is neither described by the NP model nor does it take any well-defined average low-symmetry structure. Instead,

multiple different local configurations in the brim of the hat become represented simultaneously upon heating. Such a scenario is achieved by increasingly large fluctuations of Φ, which increase the sampled phase space and thereby reduce the local symmetry. This kind of *continuous* disorder is the most likely explanation for the observed anomalies in the fits.

C. Effective Hamiltonian analysis

To better understand the unusual behavior indicated by our local structural analysis, we next analyze an effective Hamiltonian that describes the local structure and energetics of YMnO$_3$. We focus specifically on whether our PDF analysis can be rationalized in the context of a competition between displacive *and* order-disorder behaviors. In the case of a conventional single-component order-parameter system described by a double-well potential, the two energy scales that determine whether displacive or order-disorder behavior dominates are (i) the energy cost per site, V, of removing the distortion that deforms the structure from the maximum to the minimum of the double well (this is the energy difference per unit cell between the high- and low-symmetry structures) and (ii) the intersite energy cost W associated with changes in the distortion from one unit cell to the next (this is the

additional energy of forming one locally undistorted unit cell in a background that is homogeneously distorted to the double-well minimum [35]). The displacive limit is reached when $V \ll W$ since the energy cost for removing the distortion of the units is less than the cost of introducing disorder between locally distorted units. In contrast, the order-disorder limit occurs when $W \ll V$, where locally ordered units are strongly favored and the cost of orienting them in different directions relative to each other is small [35–38]. The situation is more complex for YMnO$_3$ with its two-component order parameter, and we consider the following effective Hamiltonian, which is a lattice version of the well-established Landau free energy of Refs. [20,21] (details in Appendix C). The resulting effective Hamiltonian is analogous to an XY model with variable spin sizes. We separate the Hamiltonian into the on-site Mexican-hat-potential contribution $\mathcal{H}_V$ and the intersite interaction energy contribution $\mathcal{H}_W$, which describes the energy cost of distorting the tilt pattern:

$$\mathcal{H} = \mathcal{H}_V + \mathcal{H}_W, \tag{1}$$

where

$$\mathcal{H}_V = \sum_i \frac{a}{2} Q^2(x_i) + \frac{b}{4} Q^4(x_i) + \frac{Q^6(x_i)}{6}(c + c' \cos[6\Phi(x_i)]) - gP(x_i)Q(x_i)^3 \cos 3\Phi(x_i) + \frac{g'}{2}Q(x_i)^2 P(x_i)^2 + \frac{a_p}{2}P(x_i)^2,$$

$$\mathcal{H}_W = \frac{J}{4}\sum_{i \neq j}[Q(x_i) - Q(x_j)]^2 + 2Q(x_i)^2(1 - \cos[\Phi(x_i) - \Phi(x_j)]).$$

Here, x_i is the coordinate of the ith lattice site, where each lattice site corresponds to a 30-atom unit cell, which is the smallest unit necessary to contain the trimerization distortions. The two-component order parameter (Q, Φ) is a generalized coordinate representing the local trimerization amplitude $Q(x_i)$ and angle $\Phi(x_i)$. The polarization $P(x_i)$ is improperly coupled to $Q(x_i)$ and is the main cause of the energy barriers in the brim of the Mexican-hat potential. The parameters in $\mathcal{H}_V$ are taken directly from Ref. [21], and J is extracted from the parametrized gradient terms in the same work (see Appendix C for details and a table of values). Our goal is to determine whether this Hamiltonian, with the parameters appropriate for YMnO$_3$, describes a system in an order-disorder or displacive limit.

We begin by analyzing whether the local distortion amplitudes $Q(x_i)$ remain finite or tend to zero at T_C. We derive the following expressions for the cost of undistorting a site, V_Q, as well as the interaction energy

associated with undistorting a site within a homogeneously trimerized background, W_Q,

$$V_Q = \min_{Q,\Phi,P}[\mathcal{H}_V/N] \approx 0.61 \text{ eV}$$

$$W_Q = \frac{J}{2}nQ_0^2 \approx 0.36 \text{ eV},$$

using the parameters from Appendix C. Here, n is the number of nearest neighbors, N is the number of lattice sites, and $Q_0 = 0.96$ Å is the Q value that minimizes the local energy (it finds the bottom of the Mexican hat). We find that $V_Q/W_Q \approx 1.7$. As explained above, the limit of a fully displacive system is given by $V_Q/W_Q \ll 1$, with the small V_Q energy cost favoring the local units undistorting when approaching T_C, whereas in the opposite order-disorder limit, $V_Q/W_Q \gg 1$, the local amplitude of the order parameter is preserved on approaching T_C. Our value of $V_Q/W_Q \approx 1.7$ therefore points towards an order-disorder-like behavior of the order-parameter amplitude.

Given this finding that the local order-parameter amplitude remains finite at T_C, we next explore the displacive versus order-disorder behavior of the order-parameter angle, corresponding to changes of the angle around the brim of the Mexican hat. In this case, we compare the on-site energy barrier between two local minima within the brim of the hat, V_Φ, and the intersite energy cost W_Φ arising from a change of the trimerization angle by $2\pi/6$ (between two local minima). We obtain the values

$$V_\Phi = \min_{Q,\Phi=0,P} [\mathcal{H}_V/N] - \min_{Q,\Phi=\frac{\pi}{6},P} [\mathcal{H}_V/N] \approx 0.15 \text{ eV},$$

$$W_\Phi = JnQ_0^2 \left(1 - \cos\frac{2\pi}{6}\right) \approx 0.36 \text{ eV},$$

giving $V_\Phi/W_\Phi \approx 0.4$. The small energy barriers between neighboring states in the brim of the hat allow the system to readily access a continuum of angles, leading to a predominantly displacive-like behavior of the order-parameter angle.

In summary, our analysis of the effective lattice Hamiltonian suggests a mixed scenario in which the order-parameter amplitude shows order-disorder behavior, and the order-parameter angle shows displacive behavior at T_C. This case is consistent with the model that we proposed above to explain our PDF analysis, in that it predicts that the local order-parameter amplitude should not vanish [Figs. 5(b) and 5(d)] and that the P and AP models, which differ in their local order-parameter angle, should fit equally well at T_C [Fig. 5(d)] but still not fully represent the mix of IM phases present.

Finally, we performed a series of Monte Carlo (MC) simulations on the effective lattice Hamiltonian including only nearest-neighbor interactions. These simulations were performed using the Metropolis algorithm [39] on a $10 \times 10 \times 10$ unit cell with periodic boundary conditions, averaging six different runs over $\mathcal{O}(10^6)$ sweeps. To improve the convergence, we discretized the phase space in 36 equally spaced states in $[0, 2\pi]$ for Φ and 11 different states in the range $[0, 1.25Q_0]$ for the amplitude $Q(x_i)$. We then analyzed the behavior of the expectation value of the order parameter $\langle Q \rangle$ and the local amplitude of the order parameter $\sqrt{\langle Q^2 \rangle}$ (see Appendix C for details). We found a T_C of about 2200 K, which overestimates the experimental T_C by about 60%. This finding is not unreasonable considering our use of the long-wavelength limit for calculating J and our neglect of beyond-nearest-neighbor and nonlocal phononic effects. The latter, in particular, will cause the depth of the local Mexican-hat potential to decrease with increasing temperature and will therefore decrease the transition temperature.

The observed behavior, presented in Fig. 6, is consistent with our analysis of the effective Hamiltonian above, as well as with our interpretation of the PDF measurements. When the system crosses T_C, the local order-parameter
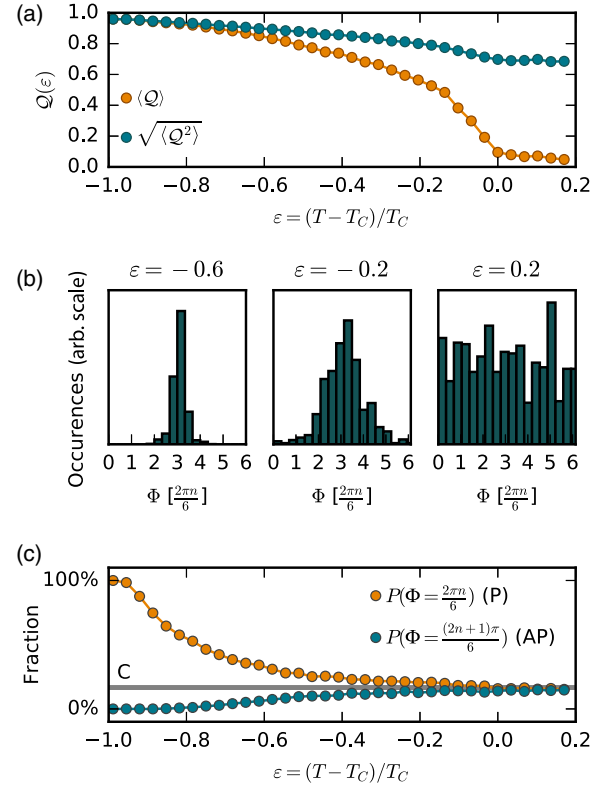

FIG. 6. Monte Carlo simulations of the effective Hamiltonian using the DFT parameters as described in the text. (a) Local order-parameter amplitude $\sqrt{\langle Q^2 \rangle}$ and its macroscopic expectation value $\langle Q \rangle$, as a function of reduced temperature. Note that the local order parameter does not go to zero above T_C, whereas its macroscopic expectation value vanishes above T_C due to the disordering of the order-parameter angle. (b) Histograms of the order parameter angle at a temperature well below T_C (left), just below T_C (center), and above T_C (right). We see that the angle is well defined at low temperatures, broadens upon heating, and can have any value above T_C. (c) Probability P that the states in the minima ($\Phi = [(2\pi n)/6]$) (brown circles) and the maxima ($\Phi = \{[(2n+1)\pi]/6\}$) (green circles) within the brim of the hat are occupied. At low T, only the minima are occupied [$P\{\Phi = [(2\pi n)/6]\} = 100\%$], but at higher temperatures, the fractions converge towards the continuous limit marked by the line denoted "C," which corresponds to an equal distribution between all angles. The probabilities were extracted by creating 36 bins in $[0, 2\pi]$, and as a result, C has a 16.7% fraction.

amplitude $\sqrt{\langle Q^2 \rangle}$ is reduced by only around 20%, while its macroscopic expectation value $\langle Q \rangle$ goes to zero [Fig. 6(a)]. Considering the distribution of angles, at low temperatures the system is localized at one angle, while the distribution becomes broader around the expectation value upon heating, and disorders between all angles at $T > T_C$ [Fig. 6(b)] [40]. We present a statistical analysis in Fig. 6(c), which shows that far away from T_C only the minimum energy states are occupied. The number of occupations of sites with intermediate order-parameter angles increases progressively with increasing temperature. The system ends up having an almost continuous

distribution of order parameter angles over a substantial region below T_C. Again, this result is consistent with the fits of the PDF data, with the AP and P phases having similar errors in a large region below T_C [Fig. 5(c)].

IV. DISCUSSION

We have studied the structural evolution with temperature of hexagonal YMnO$_3$ at both local and average length scales. The average structure from reciprocal-space Rietveld refinements is captured by the conventional P model below T_C and changes to the NP structure across the phase transition, in agreement with previous studies. However, on the local scale, both the symmetry and the structural evolution are very different from their average behavior, with the two components of the order parameter (Q, Φ) even showing distinct behavior. Combining our experimental (total scattering + PDF) and theoretical (DFT + MC) results detailed above, we present the following conceptual order-disorder model for the structural phase transition (Fig. 7).

At low temperatures, the local structure corresponds to the P model of one of the six minima, consistent with the average structure [Fig. 7(a)] [41]. Upon heating above 800 K, fluctuations of the angle Φ allow the local structure to access configurations of lower symmetry corresponding to the IM model, as illustrated Fig. 7(b). This region of the

crossover corresponds to the reduced temperature starting at around $\epsilon = 0.5$ in the MC simulations (Fig. 6), where $\langle Q^2 \rangle$ and $\langle Q \rangle^2$ start to deviate from each other and where $P\{\Phi = (2n+1)\pi/6\}$ approaches $P\{\Phi = (2n\pi)/6\}$. This case explains the anomalous increase in fit residuals r_w for the P model above 800 K and the increasingly similar r_w for the different order-parameter angles [Fig. 5(e)]. This inadequacy of a single structural model is the reason for the artifacts observed in the Rietveld fits that we described in Sec. III A.

On approaching T_C, these local fluctuations of Φ from its mean value become more pronounced. Close to, but below, T_C, the measured local structure is a dynamic superposition of structural configurations that fluctuate within a continuum of values of Φ [Fig. 7(c)] while the average order parameter retains nonzero value. This scenario explains our r_w fits (Fig. 5), where we saw a similar error of P and AP already in a region rather far below T_C. It is consistent with our results from the effective Hamiltonian, where the distribution of order-parameter angles reveals an effectively flat free-energy landscape at high temperatures [Fig. 6(c)].

Above T_C [Fig. 7(d)], long-range order is lost and the system disorders between a continuum of angles Φ, corresponding to all possible local IM structures with $P3c1$ symmetry. Since the IM structures are polar, the structure remains polar above T_C on the local scale.
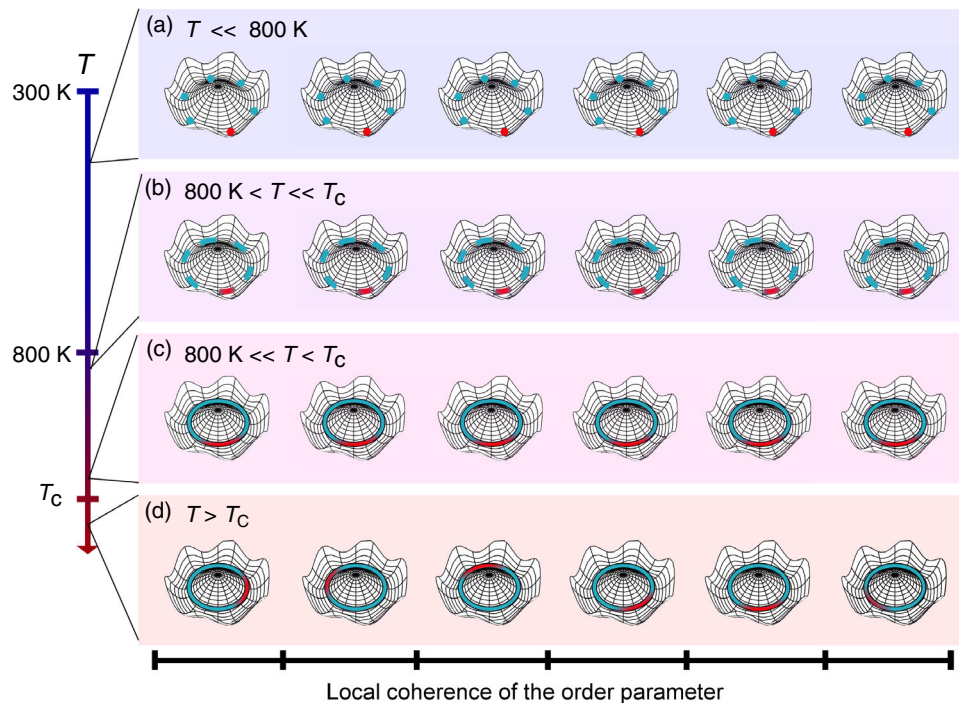

FIG. 7. Unconventional order-disorder transition of YMnO$_3$. Local value of the order parameter in different temperature regions [panels (a)–(d)] within one domain. The blue lines indicate states accessible to the order parameter, and the red colored markings show the distribution of the order parameter. (a) In the low-temperature region, the order parameter is firmly fixed within one of the six ground states. (b) Between 800 K and T_C, fluctuations smear out the local distribution of the order-parameter angle (red), but the average angle within each domain remains constant. (c) Close to T_C, the energy landscape flattens. (d) At and above T_C, coherence of the order parameter is lost and the system disorders between all possible states in the Mexican hat.

This special order-disorder transition is unconventional in the sense that it does not disorder between the six degenerate ground states of the low-temperature ferroelectric P model but between a continuum of structures with all possible angles Φ of the order parameter.

This continuous disorder above T_C distinguishes the ferroelectric transition in $YMnO_3$ from conventional order-disorder transitions, e.g., $BaTiO_3$ exhibiting disorder between different, but *discrete*, [111]-oriented ground states [28,30]. The continuous positional degree of freedom in $YMnO_3$ is, in some ways, reminiscent of α-AlF_3 [33] and cristobalite [31], in which the structures are disordered with arbitrarily bent bonds between rigid polyhedral units. Here, however, because of the complexity of the structure, the disorder involves many atoms and bonds on a much larger length scale.

The high T_C of $YMnO_3$ could also be important for the observed disorder. Notably, the corresponding $P6_3/mmc$-$P6_3cm$ improper ferroelectric transition in 2H-$BaMnO_3$ [42] at 130 K is reported to be predominantly displacive [43]. However, the crystal structure of 2H-$BaMnO_3$ is fundamentally different in terms of polyhedral units and connectivity from that of $YMnO_3$, making a direct comparison difficult. We hope that our work will motivate a detailed PDF study of the phase transition in 2H-$BaMnO_3$.

It is well established that there is only one phase transition in the hexagonal manganites at T_C with the polarization slowly emerging as a secondary effect [20–24], despite the many reported anomalies observed between 800 K and T_C. Until now, these anomalies have not been fully explained. The model we have presented here, describing how the structural order parameter behaves in the local structure, provides an explanation for these anomalies. Entering the regime where fluctuations of the order parameter become increasingly important around 800 K, the temperature dependence of the macroscopic order parameter is renormalized when approaching T_C [35,44]. This result will affect related macroscopic properties such as thermal expansion and specific heat [15], and can explain the thermal evolution of the lattice parameters: The reported change of slope 300–400 K below T_C and the flattening of the c parameter just above T_C [12,15–17,45] can be expected from the coupling of the order parameter to strain. The temperature range of these anomalies also coincides with the reported Ginzburg temperature for $YMnO_3$ [13], which is a measure of how far below T_C one must be to describe the system by mean-field theory. The accessible phase space for local order-parameter fluctuations far below T_C becomes limited to a small region around the local minimum. This freeze-in of fluctuations is in compliance with the reported glassy behavior of the system [46].

The gradual loss of long-range structural coherence upon approaching T_C, as illustrated in Fig. 7, is not easily detectable by conventional diffraction probing the average structure. Observations of α_P and α_A decreasing continuously to zero at T_C while ΔY goes abruptly to zero are demonstrated both by our own Rietveld refinements and others [12,47]. While discontinuity in one order-parameter observable across T_C has been suggested as a signature of a weakly first-order transition [47], the continuous molar volume (lattice parameters) and very subtle changes in the PDFs across T_C do not support this interpretation.

Finally, we note that order-disorder and displacive transitions show different features in their dynamical properties. For a purely displacive transition, the frequency of the soft phonon mode goes to zero at T_C. On the other hand, the soft-mode frequency always remains nonzero for a purely order-disorder transition. Instead, one observes the emergence of an additional anharmonic relaxational mode at $\omega = 0$, called the central mode [48–51]. While Gupta *et al.* [52] did not observe softening of any phonon branches below T_C, Bouyanfif *et al.* [19] and Bansal *et al.* [53] observed a partial softening upon heating towards T_C. However, it is not possible to identify a central mode from their data. These results suggest a mixed displacive and order-disorder character of the phase transition, and our model presented in Fig. 7 reconciles and explains these unusual spectroscopic observations.

We anticipate that the Mexican energy landscape will lead to unusual dynamics for the central mode. The influence of the central mode on properties like dielectric susceptibility have been studied for proper order-disorder ferroelectrics [54,55] but may be very different in the case of this improper ferroelectric with unconventional disorder. We hope our work motivates future studies in this direction.

V. CONCLUSIONS

We discovered unconventional behavior across the improper ferroelectric transition in the hexagonal manganites where the amplitude of the two-dimensional order parameter is order-disorder-like, but the order-parameter angle behaves displacively. This unusual behavior is indicated by our finding that the local structure across T_C differs strongly from the established average structure symmetry and that the local low-symmetry distortions are conserved in the high-symmetry phase, both evidence of an order-disorder mechanism. Second, we observe that the low-symmetry distortions at high temperature are not restricted to specific minima but span a continuum of structures found in the brim of the Mexican-hat-shaped energy landscape, effectively lowering the *local* symmetry from $P6_3cm$ to $P3c1$. Our findings reconcile decades of ambiguous reports on hexagonal manganites by showing that the reported anomalies in macroscopic data are caused by the onset of a continuum of local structures.

The only requirement for the presented behavior is the condensation of a disordered multicomponent order parameter with a small barrier between the different order-parameter directions. While such a continuous nature of

the order parameter on the local scale is commonly found in magnetic structures, it is highly unusual in crystalline solids where the directionality of bonds and coupling to lattice strain normally favor discrete minima in the potential energy landscape. To the best of our knowledge, this work is the first report of such fundamentally different behavior of two components of a multicomponent order parameter— one component showing order-disorder behavior and the other displacive.

Although reports of continuous structural disorder in crystalline solids are rare, the underlying structural and energetic requirements are not. Competing interactions and two characteristic energy barriers of different magnitude could lead to a frustrated structure where all bonds cannot be optimized simultaneously and where fluctuations of one order-parameter component can easily be masked by thermal vibrations. In addition to the improper ferroelectric hexagonal manganite $YMnO_3$ studied here, similar structural and energetic features can also be found in magneto-electric multiferroics [56], piezoelectrics at morphotropic phase boundaries [57], and relaxor ferroelectrics [58].

Hidden disorder is thus anticipated in a wide range of material systems with multicomponent order parameters and characteristic energy barriers of different magnitudes. Specific examples of systems where the continuous structural disorder introduced here could be relevant are the low-temperature tetragonal phase of superconducting cuprates [59], which have been shown to exhibit order-disorder characteristics [60], the pyrochlore $Cd_2Re_2O_7$ where Goldstone-like modes and order-disorder features have been reported [61–63], the shallow energy landscape of the layered ferroelectric perovskite $PbSr_2Ti_2O_7$ [64], and (111)-strained perovskite oxides like $LaAlO_3$ and $SrMnO_3$, where the curvature of the Mexican-hat-shaped potential energy surface can be tuned by strain through the choice of substrate [65,66].

This work illustrates that the atomic-scale mechanisms and underlying physics of phase transitions in complex crystalline solids with multicomponent order parameters and competing interactions can easily be overlooked if the local structure is not adequately probed, e.g., by total scattering methods.

ACKNOWLEDGMENTS

APPENDIX A: EXPERIMENTAL DETAILS, DATA REFINEMENT, AND SIMULATION OF PDFS

Bulk powder of $YMnO_3$ was prepared by firing uniaxially pressed pellets of dried and mixed Y_2O_3 (>99.99%, Aldrich) and Mn_2O_3 (>99%, Aldrich) twice for 24 h at 1573 K in air with intermediate grinding.

Neutron total scattering was performed at the Nanoscale-Ordered Materials Diffractometer (NOMAD) [67] at the Spallation Neutron Source at Oak Ridge National Laboratory. A powder sample with mass of about 1.5 g was sealed in a 6-mm-diameter vanadium container and measured in an ILL-type vacuum furnace. The NOMAD detectors were calibrated using scattering from diamond standard powder, and Si standard powder was used to obtain the instrument parameter file for Rietveld refine-ments. The data were collected at room temperature and between 473 and 1273 K in steps of 20 K for 60 min at each temperature. Measurements of two subsequent temperature cycles between 1113 K and 1373 K on the same sample were performed to investigate chemical expansion as a function of oxygen loss and were found to be insignificant (see Fig. S15 of the Supplemental Material [26]). The structure factor $S(Q)$ was obtained by normalizing the scattering intensity to the scattering from a solid vanadium rod, and the background was subtracted using an identical, empty vanadium can. Pair distribution functions (PDF) were obtained by Fourier transform of $S(Q)$ with $Q_{min} = 0.5$ Å^{-1} and $Q_{max} = 22$ Å^{-1}.

The average crystal structure over the whole temperature range was determined by Rietveld refinements with the space groups $P6_3/mmc$ and $P6_3cm$ [68], using TOPAS Academic v.5 [69]. PDFs were fitted to the same space groups at different ranges of r using PDFgui [70]. Isotropic atomic displacement factors (U) were used [26], and more details on calculation of error bars for ΔY, α_P, and α_A can be found in the Supplemental Methods [26]. We note that error bars for the real space and reciprocal space refine-ments cannot be quantitatively compared. Details of the PDF method can be found elsewhere [32]. Simulated PDFs were calculated using the PDFgui software with lattice

parameters, atomic coordinates, and atomic displacement parameters from the Rietveld refinements, both with our data and with the data from Gibbs et al. [12]; they were scaled such that direct visual comparison could be made. The parameter δ_1 was set to the value obtained for the relevant space group in the PDF refinements. For the assessment of fitting errors, we used the following quantities as implemented in PDFgui [70]:

$$\chi^2 = \frac{1}{N-p}\sum_{i=1}^{N}[G_{\text{obs}}(r_i) - G_{\text{calc}}(r_i)]^2, \qquad (A1)$$

where N is the number of data points, p is the degrees of freedom in the fit, G_{calc} and G_{obs} are the calculated and measured PDFs, and

$$r_w = \sqrt{\frac{\sum_{i=1}^{N}[G_{\text{obs}}(r_i) - G_{\text{calc}}(r_i)]^2}{\sum_{i=1}^{N}G_{\text{obs}}^2(r_i)}}. \qquad (A2)$$

APPENDIX B: COMPUTATIONAL DETAILS

For our density functional calculations, we used the LDA + U approximation [71,72] as implemented in the abinit PAW plane-wave code [73–76], with a cutoff energy of 30 Hartree and a k-point mesh of $6 \times 6 \times 2$. A collinear A-type magnetic ordering with a U of 8 eV on the Mn d orbitals was applied. While this magnetic ordering under-estimates the band gap, it does not break the space group symmetry, which is important for this study. Here, 30-atom unit cells with lattice parameters from our PDF refinements were relaxed with respect to atomic positions such that the forces were converged within 1E-6 Ha/Bohr (see Supplemental Methods [26]).

APPENDIX C: EFFECTIVE HAMILTONIAN

The conventional expression for the Landau free energy is based on a continuous field model and gives the evolution of the average of the order parameter anywhere in the system. From first principles, we are only able to access properties at 0 K.

In order to access information about the finite-temperature properties and order-parameter fluctuations, we map the Landau free energy into a discretized form.

TABLE I. Landau parameters from Ref. [21] and the derived nearest-neighbor coupling terms in this work.

a [eV/Å^2]	b [eV/Å^4]	c eV/[Å^6]	c' eV/[Å^6]	g [eV/Å^4]
−2.626	3.375	0.117	0.108	1.945

g' [eV/Å^4]	a_p [eV/Å^2]	J_z [eV/Å^2]	J_{xy} [eV/Å^2]	J [eV/Å^2]
9.931	0.866	0.120	0.140	0.133

We take the 30-atom unit cell of YMnO$_3$ as the discretized unit since a local order parameter cannot be defined for a smaller unit. The terms in the Mexican-hat-potential contribution $\mathcal{H}_V$ are taken directly from the parameters calculated by Artyukhin et al. in Ref. [21] and repro-duced in Table I. To extract the interaction energy terms $\mathcal{H}_W$, we mapped the gradient terms onto the XY model Hamiltonian,

$$J\mathcal{Q}^2\cos[\Phi(x_i) - \Phi(x_j)] = J\mathcal{Q}^2\left(1 - \frac{1}{2}(\Phi(x_i) - \Phi(x_j))^2\right), \qquad (C1)$$

in order to enforce the necessary 2π periodicity. Note that this expression reproduces the Landau free energy in the continuum limit.

We extract the coupling parameter J by dividing each gradient term (s_Q in the notation of Ref. [21]) by the square of the relevant lattice constant $J_i = s_i/a_i^2$ (to approximate the energy cost of changing the trimerization between two unit cells) and then averaging the in-plane and out-of-plane values using $J = (J_{xy}J_z)^{1/3}$ [3].

We neglect any gradient contribution from the polar mode.

In our Monte Carlo simulations, we assume that the polarization is minimized on each lattice site, giving

$$\frac{\partial \mathcal{H}}{\partial P(x_i)} = 0,$$

leading to

$$P(x_i) = \frac{g\mathcal{Q}^3(x_i)\cos 3\Phi}{g'\mathcal{Q}^2(x_i) + a_p}, \qquad (C2)$$

which we insert in Eq. (1).

To calculate the expectation values of the order param-eter, we need to project it onto an arbitrary axis, for example,

$$(\mathcal{Q}_1(x_i), \mathcal{Q}_2(x_i)) = (\mathcal{Q}(x_i)\cos\Phi(x_i), \mathcal{Q}(x_i)\sin\Phi(x_i)).$$

From this calculation, the macroscopic expectation value for the order parameter can be calculated using

$$\langle \mathcal{Q} \rangle = \sqrt{\langle \mathcal{Q}_1 \rangle^2 + \langle \mathcal{Q}_2 \rangle^2}, \qquad (C3)$$

and the expectation value of the local order-parameter amplitude is given by

$$\sqrt{\langle \mathcal{Q}^2 \rangle} = \sqrt{\langle \mathcal{Q}_1^2 + \mathcal{Q}_2^2 \rangle}. \qquad (C4)$$

[1] S. M. Griffin, M. Lilienblum, K. T. Delaney, Y. Kumagai, M. Fiebig, and N. A. Spaldin, *Scaling Behavior and Beyond Equilibrium in the Hexagonal Manganites*, Phys. Rev. X **2,** 041022 (2012).

[2] S.-Z. Lin, X. Wang, Y. Kamiya, G.-W. Chern, F. Fan, D. Fan, B. Casas, Y. Liu, V. Kiryukhin, W. H. Zurek, C. D. Batista, and S.-W. Cheong, *Topological Defects as Relics of Emergent Continuous Symmetry and Higgs Condensation of Disorder in Ferroelectrics*, Nat. Phys. **10,** 970 (2014).

[3] Q. N. Meier, M. Lilienblum, S. M. Griffin, K. Conder, E. Pomjakushina, Z. Yan, E. Bourret, D. Meier, F. Lichtenberg, E. K. H. Salje, N. A. Spaldin, M. Fiebig, and A. Cano, *Global Formation of Topological Defects in the Multiferroic Hexagonal Manganites*, Phys. Rev. X **7,** 041014 (2017).

[4] N. Fujimura, T. Ishida, T. Yoshimura, and T. Ito, *Epitaxially Grown* YMnO$_3$ *Film: New Candidate for Nonvolatile Memory Devices*, Appl. Phys. Lett. **69,** 1011 (1996).

[5] Y. Kumagai, A. A. Belik, M. Lilienblum, N. Leo, M. Fiebig, and N. A. Spaldin, *Observation of Persistent Centrosymmetricity in the Hexagonal Manganite Family*, Phys. Rev. B **85,** 174422 (2012).

[6] T. Lottermoser, M. Fiebig, and D. Fröhlich, *Symmetry and Coupling of Magnetic and Electric Order Parameters in* YMnO$_3$, J. Appl. Phys. **91,** 8251 (2002).

[7] T. Choi, Y. Horibe, H. T. Yi, Y. J. Choi, W. Wu, and S.-W. Cheong, *Insulating Interlocked Ferroelectric and Structural Antiphase Domain Walls in Multiferroic* YMnO$_3$, Nat. Mater. **9,** 253 (2010).

[8] T. Jungk, Á. Hoffmann, M. Fiebig, and E. Soergel, *Electrostatic Topology of Ferroelectric Domains in* YMnO$_3$, Appl. Phys. Lett. **97,** 012904 (2010).

[9] D. Meier, J. Seidel, A. Cano, K. Delaney, Y. Kumagai, M. Mostovoy, N. A. Spaldin, R. Ramesh, and M. Fiebig, *Anisotropic Conductance at Improper Ferroelectric Domain Walls*, Nat. Mater. **11,** 284 (2012).

[10] Y. Geng, N. Lee, Y. J. Choi, S.-W. Cheong, and W. Wu, *Collective Magnetism at Multiferroic Vortex Domain Walls*, Nano Lett. **12,** 6055 (2012).

[11] J. A. Mundy, J. Schaab, Y. Kumagai, A. Cano, M. Stengel, I. P. Krug, D. M. Gottlob, H. Doganay, M. E. Holtz, R. Held, Z. Yan, E. Bourret, C. M. Schneider, D. G. Schlom, D. A. Muller, R. Ramesh, N. A. Spaldin, and D. Meier, *Functional Electronic Inversion Layers at Ferroelectric Domain Walls*, Nat. Mater. **16,** 622 (2017).

[12] A. S. Gibbs, K. S. Knight, and P. Lightfoot, *High-Temperature Phase Transitions of Hexagonal* YMnO$_3$, Phys. Rev. B **83,** 094111 (2011).

[13] T. Katsufuji, M. Masaki, A. Machida, M. Moritomo, K. Kato, E. Nishibori, M. Takata, M. Sakata, K. Ohoyama, K. Kitazawa, and H. Takagi, *Crystal Structure and Magnetic Properties of Hexagonal* R*MnO$_3$* (R = Y, Lu, and Sc) and the Effect of Doping, Phys. Rev. B **66,** 134434 (2002).

[14] J. Kim, K. C. Cho, Y. M. Koo, Kun P. Hong, and N. Shin, *Y-O Hybridization in the Ferroelectric Transition of* YMnO$_3$, Appl. Phys. Lett. **95,** 132901 (2009).

[15] G. Nénert, M. Pollet, S. Marinel, G. R. Blake, A. Meetsma, and T. T. M. Palstra, *Experimental Evidence for an Intermediate Phase in the Multiferroic* YMnO$_3$, J. Phys. Condens. Matter **19,** 466212 (2007).

[16] T. A. Tyson, T. Wu, H. Y. Chen, J. Bai, K. H. Ahn, K. I. Pandya, S. B. Kim, and S.-W. Cheong, *Measurements and Ab Initio Molecular Dynamics Simulations of the High Temperature Ferroelectric Transition in Hexagonal* RMnO$_3$, J. Appl. Phys. **110,** 084116 (2011).

[17] S. M. Selbach, A. Nordli Løvik, K. Bergum, J. R. Tolchard, M.-A. Einarsrud, and T. Grande, *Crystal Structure, Chemical Expansion and Phase Stability of* HoMnO$_3$ *at High Temperature*, J. Solid State Chem. **196,** 528 (2012).

[18] I.-K. Jeong, N. Hur, and T. Proffen, *High-Temperature Structural Evolution of Hexagonal Multiferroic* YMnO$_3$ *and* YbMnO$_3$, J. Appl. Crystallogr. **40,** 730 (2007).

[19] H. Bouyanfif, A. M. Salah, M. Zaghrioui, and M. El Marssi, *High-Temperature Lattice-Dynamics Evolution of* YMnO$_3$ *and* YbMnO$_3$, Phys. Rev. B **91,** 224104 (2015).

[20] C. J. Fennie and K. M. Rabe, *Ferroelectric Transition in* YMnO$_3$ *from First Principles*, Phys. Rev. B **72,** 100103(R) (2005).

[21] S. Artyukhin, K. T. Delaney, N. A. Spaldin, and M. Mostovoy, *Landau Theory of Topological Defects in Multiferroic Hexagonal Manganites*, Nat. Mater. **13,** 42 (2014).

[22] R. I. Thomson, T. Chatterji, C. J. Howard, T. T. M. Palstra, and M. A. Carpenter, *Elastic Anomalies Associated with Structural and Magnetic Phase Transitions in Single Crystal Hexagonal* YMnO$_3$, J. Phys. Condens. Matter **26,** 045901 (2014).

[23] A. Cano, *Hidden Order in Hexagonal R*MnO$_3$ *Multiferroics* (R = Dy-Lu, In, Y, and Sc), Phys. Rev. B **89,** 214107 (2014).

[24] M. Lilienblum, T. Lottermoser, S. Manz, S. M. Selbach, A. Cano, and M. Fiebig, *Ferroelectricity in the Multiferroic Hexagonal Manganites*, Nat. Phys. **11,** 1070 (2015).

[25] B. B. Van Aken, T. T. M. Palstra, A. Filippetti, and N. A. Spaldin, *The Origin of Ferroelectricity in Magnetoelectric* YMnO$_3$, Nat. Mater. **3,** 164 (2004).

[26] See Supplemental Material at http://link.aps.org/supplemental/10.1103/PhysRevX.9.031001 for more details on data collection and refinement, and computational results.

[27] M. Šafránková, J. Fousek, and S. A. Kižaev, *Domains in Ferroelectric* YMnO$_3$, Czech. J. Phys. B **17,** 559 (1967).

[28] G. H. Kwei, S. J. L. Billinge, S.-W. Cheong, and J. G. Saxton, *Pair-Distribution Functions of Ferroelectric Perovskites: Direct Observation of Structural Ground States*, Ferroelectrics **164,** 57 (1995).

[29] D. A. Keen and A. L. Goodwin, *The Crystallography of Correlated Disorder*, Nature (London) **521,** 303 (2015).

[30] M. S. Senn, D. A. Keen, T. C. A. Lucas, J. A. Hriljac, and A. L. Goodwin, *Emergence of Long-Range Order in* BaTiO$_3$ *from Local Symmetry-Breaking Distortions*, Phys. Rev. Lett. **116,** 207602 (2016).

[31] M. G. Tucker, M. P. Squires, M. T. Dove, and D. A. Keen, *Dynamic Structural Disorder in Cristobalite: Neutron Total Scattering Measurement and Reverse Monte Carlo Modelling*, J. Phys. Condens. Matter **13,** 403 (2001).

[32] T. Egami and S. J. L. Billinge, *Underneath the Bragg Peaks, Structural Analysis of Complex Materials* (Elsevier, Oxford, 2003).

[33] P. J. Chupas, S. Chaudhuri, J. C. Hanson, X. Qiu, P. L. Lee, S. D. Shastri, S. J. L. Billinge, and C. P. Grey, *Probing Local and Long-Range Structure Simultaneously: An In Situ Study of the High-Temperature Phase Transition of α-AlF$_3$*, J. Am. Chem. Soc. **126**, 4756 (2004).

[34] X. Qiu, T. Proffen, J. F. Mitchell, and S. J. L. Billinge, *Orbital Correlations in the Pseudocubic O and Rhombohedral R Phases of* LaMnO$_3$, Phys. Rev. Lett. **94**, 177203 (2005).

[35] A. D. Bruce, *Structural Phase Transitions. II. Static Critical Behaviour*, Adv. Phys. **29**, 111 (1980).

[36] E. K. H. Salje, *Crystallography and Structural Phase Transitions, An Introduction*, Acta Crystallogr. Sect. A **47**, 453 (1991).

[37] S. Padlewski, A. K. Evans, C. Ayling, and V. Heine, *Crossover between Displacive and Order/Disorder Behaviour in the* Phi^4 *Model*, J. Phys. Condens. Matter **4**, 4895 (1992).

[38] M. T. Dove, *Theory of Displacive Phase Transitions in Minerals*, Am. Mineral. **82**, 213 (1997).

[39] N. Metropolis, A. W. Rosenbluth, M. N. Rosenbluth, A. H. Teller, and E. Teller, *Equation of State Calculations by Fast Computing Machines*, J. Chem. Phys. **21**, 1087 (1953), https://doi.org/10.1063/1.1699114.

[40] One can tune the Hamiltonian to become displacive when lowering the on-site energy by reducing a, and one can tune towards discrete disorder by lowering the intersite inter-action J, as is expected according to our defined criteria above (we show MC on two examples in Supplemental Material, Fig. S16 [26]).

[41] We also checked for signs of higher-order terms in the free energy previously proposed [23] but found no evidence of such hidden order.

[42] J. Varignon and P. Ghosez, *Improper Ferroelectricity and Multiferroism in* 2H-BaMnO$_3$, Phys. Rev. B **87**, 140403(R) (2013).

[43] S. Kamba, D. Nuzhnyy, M. Savinov, P Tolédano, V. Laguta, P. Brázda, L. Palatinus, F. Kadlec, F. Borodavka, C. Kadlec, P. Bednyakov, V. Bovtun, M. Kempa, D. Kriegner, J. Drahokoupil, J. Kroupa, J. Prokleška, K. Chapagain, B. Dabrowski, and V. Goian, *Unusual Ferroelectric and Magnetic Phases in Multiferroic* 2H-BaMnO$_3$ *Ceramics*, Phys. Rev. B **95**, 174103 (2017).

[44] T. Schneider and E. Stoll, *Molecular-Dynamics Study of Structural-Phase Transitions. I. One-Component Displace-ment Models*, Phys. Rev. B **13**, 1216 (1976).

[45] H. D. Zhou, J. C. Denyszyn, and J. B. Goodenough, *Effect of Ga Doping on the Multiferroic Properties of* RMn$_{1-x}$Ga$_x$O$_3$ R = (Ho, Y), Phys. Rev. B **72**, 224401 (2005).

[46] A. Barbour, A. Alatas, Y. Liu, C. Zhu, B. M. Leu, X. Zhang, A. Sandy, M. S. Pierce, X. Wang, S.-W. Cheong, and H. You, *Partial Glass Isosymmetry Transition in Multiferroic Hexagonal* ErMnO$_3$, Phys. Rev. B **93**, 054113 (2016).

[47] H. Sim, J. Jeong, H. Kim, S.-W. Cheong, and J.-G. Park, *Studies on the High-Temperature Ferroelectric Transition of Multiferroic Hexagonal Manganite* RMnO$_3$, J. Phys. Condens. Matter **30**, 105601 (2018).

[48] S. M. Shapiro, J. D. Axe, G. Shirane, and T. Riste, *Critical Neutron Scattering in* SrTiO$_3$ *and* KMnF$_3$, Phys. Rev. B **6**, 4332 (1972).

[49] J. Petzelt, G. V. Kozlov, and A. A. Volkov, *Dielectric Spectroscopy of Paraelectric Soft Modes*, Ferroelectrics **73**, 101 (1987).

[50] Y. Onodera, *Dynamical Response of Ferroelectrics in Terms of a Classical Anharmonic-Oscillator Model*, J. Phys. Soc. Jpn. **73**, 1216 (2004).

[51] J. Hlinka, T. Ostapchuk, D. Nuzhnyy, J. Petzelt, P. Kuzel, C. Kadlec, P. Vanek, I. Ponomareva, and L. Bellaiche, *Coexistence of the Phonon and Relaxation Soft Modes in the Terahertz Dielectric Response of Tetragonal* BaTiO$_3$, Phys. Rev. Lett. **101**, 167402 (2008).

[52] M. K. Gupta, R. Mittal, M. Zbiri, N. Sharma, S. Rols, H. Schober, and S. L. Chaplot, *Spin-Phonon Coupling and High-Temperature Phase Transition in Multiferroic Material* YMnO$_3$, J. Mater. Chem. C **3**, 11717 (2015).

[53] D. Bansal, J. L. Niedziela, R. Sinclair, V. O. Garlea, D. L. Abernathy, S. Chi, Y. Ren, H. Zhou, and O. Delaire, *Momentum-Resolved Observations of the Phonon Instabil-ity Driving Geometric Improper Ferroelectricity in Yttrium Manganite*, Nat. Commun. **9**, 818 (2018).

[54] Y. Girshberg and Y. Yacoby, *Ferroelectric Phase Transi-tions in Perovskites with Off-Center Ion Displacements*, Solid State Commun. **103**, 425 (1997).

[55] J. Weerasinghe, L. Bellaiche, T. Ostapchuk, P. Kužel, C. Kadlec, S. Lisenkov, I. Ponomareva, and J. Hlinka, *Emergence of Central Mode in the Paraelectric Phase of Ferroelectric Perovskites*, MRS Commun. **3**, 41 (2013).

[56] M. Fiebig, M. Lottermoser, D. Meier, and M. Trassin, *The Evolution of Multiferroics*, Nat. Mater. Rev. **1**, 16046 (2016).

[57] M. Ahart, M. Somayazulu, R. Cohen, P. Ganesh, P. Dera, H.-K Mao, R. Hemley, Y. Ren, H.-P. Liermann, and Z. Wu, *Origin of Morphotropic Phase Boundaries in Ferroelec-trics*, Nature (London) **451**, 545 (2008).

[58] B. Noheda, D. E. Cox, G. Shirane, S.-E. Park, L. E. Cross, and Z. Zhong, *Polarization Rotation via a Monoclinic Phase in the Piezoelectric* 92% PbZn$_{1/3}$Nb$_{2/3}$O$_3$—8% PbTiO$_3$, Phys. Rev. Lett. **86**, 3891 (2001).

[59] W. E. Pickett, R. E. Cohen, and H. Krakauer, *Lattice Instabilities, Isotope Effect, and High-T$_c$ Superconductivity in* La$_{2-x}$Ba$_x$CuO$_4$, Phys. Rev. Lett. **67**, 228 (1991).

[60] E. S. Bozin, R. Zhong, K. R. Knox, G. Gu, J. P. Hill, J. M. Tranquada, and S. J. L. Billinge, *Reconciliation of Local and Long-Range Tilt Correlations in Underdoped* La$_{2-x}$Ba$_x$CuO$_4$ ($0 =< x =< 0.155$), Phys. Rev. B **91**, 054521 (2015).

[61] C. S. Knee, J. Holmlund, J. Andreasson, M. Käll, S. G. Eriksson, and L. Börjesson, *Order-Disorder-Order Phase Transitions in the Pyrochlore Superconductor* Cd$_2$Re$_2$O$_7$, Phys. Rev. B **71**, 214518 (2005).

[62] C. A. Kendziora, I. A. Sergienko, R. Jin, J. He, V. Keppens, B. C. Sales, and D. Mandrus, *Goldstone-Mode Phonon Dynamics in the Pyrochlore* Cd$_2$Re$_2$O$_7$, Phys. Rev. Lett. **95**, 125503 (2005).

[63] J. C. Petersen, M. D. Caswell, J. S. Dodge, I. A. Sergienko, J. He, R. Jin, and D. Mandrus, *Nonlinear Optical Signatures of the Tensor Order in* Cd$_2$Re$_2$O$_7$, Nat. Phys. **2**, 605 (2006).

[64] S. M. Nakhmanson and I. Naumov, *Goldstone-like States in a Layered Perovskite with Frustrated Polarization: A*

First-Principles Investigation of PbSr$_2$Ti$_2$O$_7$, Phys. Rev. Lett. **104,** 097601 (2010).

[65] A. Marthinsen, S. M. Griffin, M. Moreau, T. Grande, T. Tybell, and S. M. Selbach, *Goldstone-like Phonon Modes in a (111)-Strained Perovskite*, Phys. Rev. Mater. **2,** 014404 (2018).

[66] M. Moreau, A. Marthinsen, S. M. Selbach, and T. Tybell, *First-Principles Study of the Effect of (111) Strain on Octahedral Rotations and Structural Phases of* LaAlO$_3$, Phys. Rev. B **95,** 064109 (2017).

[67] J. Neuefeind, M. Feygenson, J. Carruth, R. Hoffmann, and K. K. Chipley, *The Nanoscale Ordered Materials Diffractometer NOMAD at the Spallation Neutron Source SNS*, Nucl. Instrum. Meth. Phys., Res. B **287,** 68 (2012).

[68] B. B. van Aken, A. Meetsma, and T. T. M. Palstra, *Hexagonal* YMnO$_3$, Acta Crystallogr. Sect. C **57,** 230 (2001).

[69] J. P. Perdew and Y. Wang, *Accurate and Simple Analytic Representation of the Electron-Gas Correlation Energy*, Phys. Rev. B **45,** 13244 (1992).

[70] C. L. Farrow, P. Juhas, J. W. Liu, D. Bryndin, E. S. Bozin, J. Bloch, Th. Proffen, and S. J. L. Billinge, *PDFfit2 and PDFgui: Computer Programs for Studying Nanostructure in Crystals*, J. Phys. Condens. Matter **19,** 335219 (2007).

[71] J. P. Perdew and Y. Wang, *Accurate and Simple Analytic Representation of the Electron-Gas Correlation Energy*, Phys. Rev. B **45,** 13244 (1992).

[72] A. I. Liechtenstein, V. I. Anisimov, and J. Zaanen, *Density-Functional Theory and Strong Interactions: Orbital Ordering in Mott-Hubbard Insulators*, Phys. Rev. B **52,** R5467 (1995).

[73] X. Gonze, J. M. Beuken, R. Caracas, F. Detraux, M. Fuchs, G. M. Rignanese, L. Sindic, M. Verstraete, G. Zerah, F. Jollet, M. Torrent, A. Roy, M. Mikami, Ph. Ghosez, J. Y. Raty, and D. C. Allan, *First-Principles Computation of Material Properties: The ABINIT Software Project*, Comput. Mater. Sci. **25,** 478 (2002).

[74] X. Gonze, *A Brief Introduction to the ABINIT Software Package*, Z. Kristallog. Cryst. Mater. **220,** 558 (2005).

[75] M. Torrent, F. Jollet, F. Bottin, G. Zérah, and X. Gonze, *Implementation of the Projector Augmented-Wave Method in the ABINIT Code: Application to the Study of Iron under Pressure*, Comput. Mater. Sci. **42,** 337 (2008).

[76] B. Amadon, F. Jollet, and M. Torrent, *γ and β Cerium: LDA $+$ U Calculations of Ground-State Parameters*, Phys. Rev. B **77,** 155104 (2008).

Vacancy-Driven Noncubic Local Structure and Magnetic Anisotropy Tailoring in Fe_xO-$Fe_{3−\delta}O_4$ Nanocrystals

Alexandros Lappas[1,*] George Antonaropoulos,[1,2] Konstantinos Brintakis,[1] Marianna Vasilakaki,[3]
Kalliopi N. Trohidou,[3] Vincenzo Iannotti,[4] Giovanni Ausanio,[4] Athanasia Kostopoulou,[1]
Milinda Abeykoon,[5] Ian K. Robinson,[6,7] and Emil S. Bozin[6]

[1]*Institute of Electronic Structure and Laser, Foundation for Research and Technology-Hellas,
Vassilika Vouton, 71110 Heraklion, Greece*
[2]*Department of Chemistry, University of Crete, Voutes, 71003 Heraklion, Greece*
[3]*Institute of Nanoscience and Nanotechnology, National Center for Scientific Research Demokritos,
15310 Athens, Greece*
[4]*CNR-SPIN and Department of Physics E. Pancini, University of Naples Federico II,
Piazzale V. Tecchio 80, 80125 Naples, Italy*
[5]*Photon Sciences Division, National Synchrotron Light Source II, Brookhaven National Laboratory,
Upton, New York 11973, USA*
[6]*Condensed Matter Physics and Materials Science Department, Brookhaven National Laboratory,
Upton, New York 11973, USA*
[7]*London Centre for Nanotechnology, University College, London WC1E 6BT, United Kingdom*

In contrast to bulk materials, nanoscale crystal growth is critically influenced by size- and shape-dependent properties. However, it is challenging to decipher how stoichiometry, in the realm of mixed-valence elements, can act to control physical properties, especially when complex bonding is implicated by short- and long-range ordering of structural defects. Here, solution-grown iron-oxide nanocrystals (NCs) of the pilot wüstite system are found to convert into iron-deficient rock-salt and ferro-spinel subdomains but attain a surprising tetragonally distorted local structure. Cationic vacancies within chemically uniform NCs are portrayed as the parameter to tweak the underlying properties. These lattice imperfections are shown to produce local exchange-anisotropy fields that reinforce the nanoparticles' magnetization and overcome the influence of finite-size effects. The concept of atomic-scale defect control in subcritical-size NCs aspires to become a pathway to tailor-made properties with improved performance for hyperthermia heating over defect-free NCs.

Subject Areas: Condensed Matter Physics, Magnetism, Nanophysics

I. INTRODUCTION

Iron oxides are at the research forefront as they encompass important mixed-valent states [1] that impact their physical properties and their technological potential [2], extending from energy storage devices to catalysts and electrochemical cells. Moreover, since the principal oxidation states (II-IV) of iron carry atomic magnetic moments, spontaneous cooperative magnetic order is stabilized, which offers a highly exploitable modality,

extending from spintronics and recording media [3] to the rapidly developing field of nanobiotechnology [4]. In the latter field of interest, nanoscale magnetic particles for biomedical applications draw significant benefits from the volume dependence of magnetism, especially when superparamagnetism (a state not permanently magnetized) is established below a critical particle size [5]. Consequently, there is high demand for controlling the crossover amongst different states of magnetization in order to improve the particle's magnet-facilitated performance, for making image contrast agents, heat emission "hyperthermia" systems, or even mechanical-force nanovectors [6].

More specifically, radio-frequency magnetic heating of single-crystalline nanoparticles [i.e., nanocrystals (NCs)] is emerging as a novel strategy for activating temperature-sensitive cellular processes [7], but it requires nontoxic biocompatible nanomaterials and an understanding of how structure-morphology relationships can be used as design
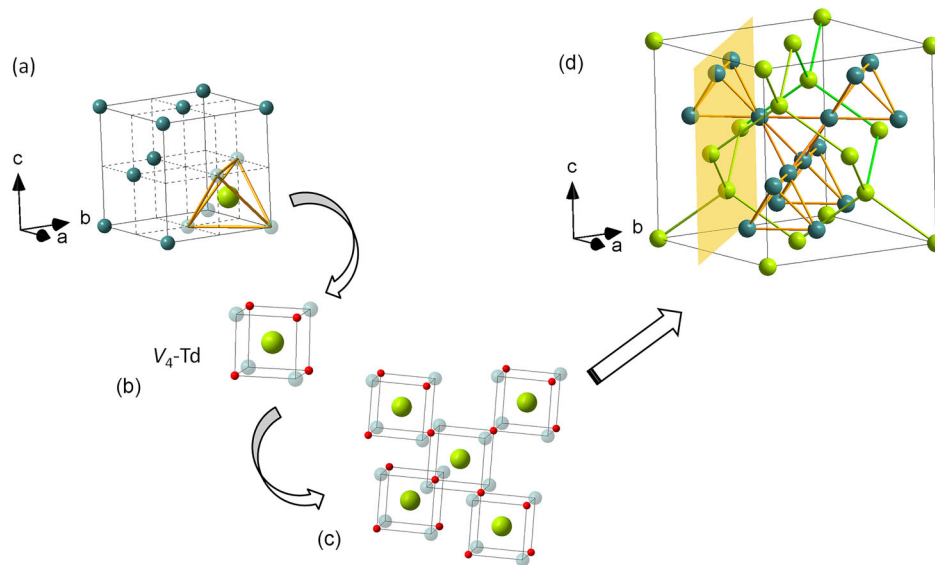
---

*Corresponding author.
lappas@iesl.forth.gr

FIG. 1. Illustrations of the Fe-site arrangement in archetype face-centered cubic crystal types of bulk iron oxides, namely, wüstite (Fe_xO) (a), a defect-mediated rock-salt structure, with octahedrally coordinated (by oxygen–not shown for clarity) ferrous (Fe^{2+}) sites (Oh; represented by dark green spheres), and interstitial ferric (Fe^{3+}) tetrahedral sites (Td; depicted by large light green spheres) in the presence of four vacant (V) iron positions (light green). Such units compose $V_4 - Td$ defect clusters (b) (oxygen shown by red spheres), whose coalescence (c) [28] offers a likely pathway towards the nucleation of $Fe_{3-\delta}O_4$ (magnetite) (d). The latter represents the ferrospinel family, with Fe atoms in both types of coordination environment, and vacancy-bearing (220) lattice planes (highlighted). Both structural types accommodate trigonal pyramids of Fe atoms as a common building block, forming a pyrochlore-type sublattice in magnetite.

parameters. Optimizing hyperthermia efficacy depends on magnetic loss mechanisms attributed to Néel-Brown relaxations, which evolve with the magnetic anisotropy constant (K) and saturation magnetization (M_S) [8]. In practice, relaxation times vary by changing intrinsic nanocrystal factors, including size [9], shape [10], and composition [11]. While single magnetic cores of pure iron-metal particles may offer superior heating efficiency, their questionable stability in biological media [12] has led researchers to develop iron-oxide particles (e.g., ferrites: $Fe_{3-\delta}O_4$, $\gamma - Fe_2O_3$, etc.) as a versatile and biocompatible class of materials [13].

The quest for NCs that surpass the performance of a single magnetic core is motivated further by the design concept of controlling the spatial distribution of chemical composition within a single motif [14] such as core@shell and thin-film heterostructures. Distinct phases grown in a core@shell topology, with contrasting magnetic-state constituents [e.g., antiferromagnetic (AFM), ferromagnetic (FM) and/or ferrimagnetic (FiM) subdomains], offer a powerful way to tune the nanoscale magnetic properties and boost the particle's hyperthermia response [10]. This case rests on the important capability to adjust the particle's anisotropy through the interfacial exchange interactions between the bimagnetic component phases [15]. The extent to which the emerging exchange bias (H_{EB}) [16] plays a key role is regulated by varying the core-shell volume ratio, the surface or interface structure, and the composition itself [17]. Thus, optimal design of hyperthermia agents requires

the right kind of defect structure to modulate favorable magnetic relaxations. As we show in this work, these mechanisms can be modeled using Monte Carlo methods.

In this endeavor, solution-chemistry methods are widely used to develop size-controlled [18] and shape-controlled [19] ferrite-based nanocrystals and to facilitate their interfacial connectivity on a nanoscale motif, e.g., $Fe@Fe_{3-\delta}O_4$ [20], $CoO@CoFe_2O_4$ [21], $FePt@MFe_2O_4$ ($M =$ Mn, Fe, Co, Zn) [22], etc. Within these systems, unforeseen magnetic properties are occasionally reported [23–26], especially when thermodynamically metastable phases such as wüstite [27] or novel interfaces are introduced during the nanoscale particle nucleation and growth. For example, during the oxidative conversion of AFM wüstite [Fe_xO, Fig. 1(a)], invoking clustering of interstitials and vacancies [Figs. 1(b) and 1(c)] [28] into a FiM spinel magnetite [$Fe_{3-\delta}O_4$, Fig. 1(d)], the internal structure of the as-made core@shell $Fe_xO@Fe_3O_4$ NCs evolves with the composition gradients influenced by stresses [29]. While a reduction in the AFM@FM interface area and core anisotropy lowers H_{EB} [30], antiphase boundaries (APBs) in the structure are found to raise the particle anisotropy. Surprisingly, this paves the way to nonzero H_{EB} even in the fully oxidized, $Fe_{3-\delta}O_4$-like derivatives of wüstite [25]. It is interesting to note that APB defects are a favored low-energy growth pathway for Fe_3O_4-films [31] that modify the exchange interactions and give rise to anomalous magnetic behavior with important applications [32,33]. These peculiar performances, for NCs in the

critical-size range of 20–30 nm, were correlated with perturbations of the periodic potential of the iron atomic coordination by lattice defects, which are hard to waive out in post synthesis treatments but are preventable by strategic redox tuning of the Fe valence during the reaction itself [34].

The preceding discussion demonstrates that the properties of otherwise single-crystalline ferrite particles are influenced by a significant fraction of atoms at the various particle "limits," the surfaces and internal interfaces [35–37]. This case necessitates characterization of the detailed atomic arrangements within the $Fe_xO − Fe_3O_4$ phase space available to the chemical synthesis methods. Effectively, research efforts focus on solving a multiple-length-scale problem [38] by combining surface (e.g., electron microscopy) and bulk (e.g., powder diffraction) sensitive probes. Total scattering experiments, though, coupled to atomic pair distribution function (PDF) analysis can reach beyond such limitations [39]. Our present work reports on the added value of the PDF method, which, in contrast to near-neighbor probes like EXAFS and NMR, is able to probe a relatively wide field of view (about 10 nm) in a single experiment by reporting how local (nanoscale) distortions are correlated throughout the structure.

While chemical phase and stoichiometry ultimately control nanoscale magnetic properties, the rational choice of the critical particle size, with optimal magnetic anisotropy [40], is about 20 nm, and it determines the applications [39,41]. In practice though, thermodynamic and kinetic parameters at nanoscale surfaces and interfaces are expected to trigger nanoscale crystal growth via energetically favorable structural-defect pathways. This process serves to render the control of defects as an extra tuning knob. Here, we investigate the nature of structural defects established during the course of the spontaneous, oxidative conversion of wüstite into $Fe_xO − Fe_3O_4$ NCs. We focus on a series of NCs with increasing particle size in the range 8–18 nm, which differ structurally and morphologically. Our results establish a quantitative relationship between favorable vacancy-induced disorder and tailored magnetic properties, a potentially important tweaking factor at subcritical particle sizes (less than 20 nm). Monte Carlo simulations demonstrate broader implications for the right kind of defect structure to mediate the magnetic loss mechanisms in favor of efficient energy transfer into heat, even for 10-nm NCs.

II. RESULTS

A. Structural insights

1. Single-particle local structure

Four nanoparticle samples were made available for this study, with specimen of spherical shape, entailing diameters of 8.1 ± 0.6 nm and 15.4 ± 1.3 nm, and of cubic shape, obtaining edge lengths of 12.3 ± 0.7 nm and 17.7 ± 1.6 nm (Fig. S1 in Supplemental Material [44]).

Henceforth, these are called S8, S15, C12, and C18, where S stands for spherical and C for cubic morphologies. Moreover, high-resolution transmission electron microscopy (HRTEM) [Figs. 2(a)—2(d)] suggests that the smaller S8 and C12 NPs entail a domain of a single-phase material, but the bimodal contrast in the larger S15 and C18 points that above a particle size of about 12 nm, two nanodomains are attained. The coexistence of dark and light contrast features in the S15 and C18 could be justified by assuming that two chemical phases, of varying electron diffracting power, share the same nanoparticle volume. Crystallographic image processing by fast Fourier transform (FFT) analysis of the relevant HRTEM images results in their corresponding (spot) electron diffraction patterns [Figs. 2(e)—2(h)]. The unequivocal indexing of reflections in the S8 and C12 specimen may suggest that these adopt the magnetite type of phase [Figs. 2(e) and 2(f)]. On the other hand, a similar conclusion cannot be made after the evaluation of the FFT patterns of the apparently bimodal contrast S15 and C18 specimen, as the cubic spinel and rock salt reflections [Figs. 2(g) and 2(h)] appear to be resolution limited. The behavior appears in line with the tendency of bulk wüstite for oxidative conversion [28,42] and infers a process analogous to its elimination from about 23-nm core@shell $Fe_xO@Fe_{3−\delta}O_4$ nanoparticles [25].

The long- and short-range modulations of the selected (hkl) atomic planes could become more easily isolated with direct space images derived from the inverse FFT synthesis of chosen families of reflections. We find that the (400) [or (200) for the core@shell S15 and C18 NPs] family generates perfect atomic planes (Figs. S2.1–S2.4 in Supplemental Material [44]), and their spacing could be attributed to the $Fe_{3−\delta}O_4$ spinel (or $Fe_{1−x}O$ rock-salt) type of structure. However, the (220) family [Figs. 2(i)—2(l)] deviates from being faultless (Fig. S3). Geometric phase analysis (GPA) [43] of the (220) reflections depicts single-colored regions [Figs. 2(m)—2(p)] that are internally homogeneous, showing no obvious inner-side distortions. The results illustrate a homogeneous structure for the S8 particle (Fig. 2m) but an increasing degree of lattice heterogeneity with size [Figs. 2(n)—2(p)]. GPA has previously pointed to a 5% crystal lattice deformation from (220) planes of about 23-nm $Fe_xO@Fe_{3−\delta}O_4$ nanocubes, while that for the (400) [or (200) for a rock-salt] family amounted to only about 1% [25].

In summary, the evaluation of the number (Nr) of defects involving the (220) planes implies that NPs of spherical morphology (S8, S15) carry a larger number of defects in their volume than the cubic ones, and those of smaller size (S8) are somewhat more susceptible to lattice faults than those of larger size (Fig. S4; Sec. S3 and Table S1 in Supplemental Material [44]). Effectively, such distorted (220) atomic planes [Fig. 1(d)] impose tensile lattice strain as the overall prevailing effect that is pronounced for the spherical morphology (from 4%–5% in the latter, which
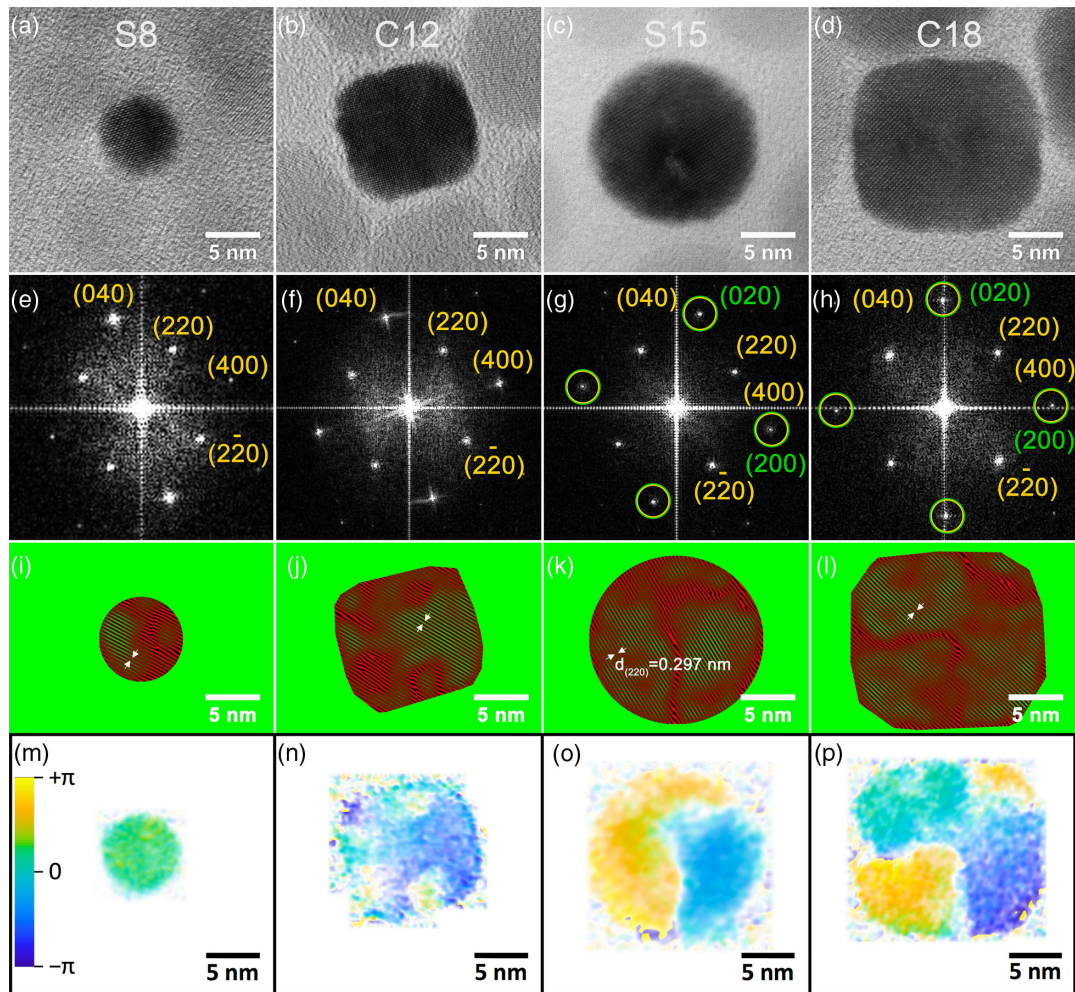
FIG. 2. High-resolution TEM images in the [001] zone axes for spherical S8 (a), S15 (c) and cubic C12 (b), C18 (d) morphology nanocrystals. The corresponding diffraction patterns (e, f and h, g) after FFT analysis of each micrograph are shown beneath. Green and yellow circles mark a set of reflections that could be indexed on the basis of either wüstite (green) or/and magnetite (yellow) rock-salt and cubic spinel crystal unit cells (see text for details). Representative real-space images of the (220) atomic lattice planes (inverse FFT synthesis; filtered from specific plane orientations) for the samples S8 (i), C12 (j), S15 (k), and C18 (l), respectively. Lattice planes have been colored with red (possible presence of atomic plane) and green (possible absence of atomic plane) pseudochrome acquired after the inverse FFT process. Lattice phase contrast images obtained by the GPA method (see text) after recentering the diffraction around one of the (220) reflections for samples S8 (m), C12 (n), S15 (o), and C18 (p).

drops down to 1%–2% in cubic shape NPs; Sec. S4 and Table S2 in Supplemental Material [44]).

2. Ensemble-average local structure

With the aim of going beyond the HRTEM findings and acquiring quantitative phase-specific structural information from a large ensemble, we measured the synchrotron x-ray PDF of selected nanoparticle specimens and compared them to the bulk magnetite (Fig. 3). As moderate Q space resolution of the experimental setup used limits the PDF field of view in the r space ($r > 5$−10 nm length scales met in bulk), our analysis focuses primarily on the low-r region in the atomic PDF ($r = 1$–10 Å). This method practically allows us to describe the local structure through

insights on bonding and lattice distortions within the $Fe_{3-\delta}O_4$ and Fe_xO unit cells.

Local structure distortions.—Bulk magnetite was taken as a reference system against which subtle distortions of the atomic lattice planes in the nanoparticles could be identified. Initial refinements were performed with the simplified, normal spinel, cubic configuration of magnetite, $(Fe^{3+})_8[Fe^{3+}, Fe^{2+}]_{16}O_{32}$ [45], where the round brackets represent tetrahedral (Td) and the square brackets octahedral (Oh) coordination by oxygen crystallographic sites (i.e., model #1; this case assumes no Fe^{2+}/Fe^{3+} inversion between Td/Oh sites–Table S3, Sec. S5 [44]). The atomic PDF in the low-r region for the bulk sample at 300 K is described well by this
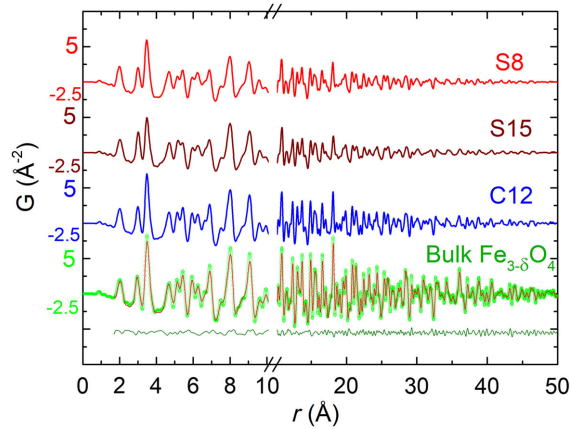
FIG. 3. Experimental atomic xPDF data at 80 K for the single-phase S8, C12 and core@shell S15 nanoparticles plotted as a function of the radial distance r up to 50 Å. The corresponding xPDF pattern for the bulk magnetite, measured under the same exact conditions, is provided as a reference material. The line over the data is the best fit based on the cubic spinel atomic configuration model (Fd-3m symmetry, model #1, and $R_w = 11.6\%$, the quality of fit factor) and below the corresponding difference between observed and calculated xPDFs for bulk magnetite.

textbook model ($R_w = 8.2\%$). A somewhat lower quality of the fit at 80 K [Fig. 4(a); $R_w = 8.9\%$] may infer some sensitivity to acentric distortions, beyond the r space resolution of our measurements, caused by the Verwey transition of bulk magnetite [46].

The same textbook model (#1) was then utilized to model the xPDF data for nanoparticles of variable size and morphology. What is particularly striking is that between 300 K and 80 K, this cubic model systematically fails to fit the peak at $r \sim 3$ Å [sample S8: Fig. 4(b), $R_w = 18.1\%$; sample C12: Fig. S6(a), $R_w = 11.9\%$]. Importantly, this result corresponds to the closest distance between the iron atoms that are octahedrally coordinated by oxygen in the structure of magnetite [forming a pyrochlore-type sublattice, Fig. 1(d)]. Moreover, the nearest distance of a pair of Fe-Fe in wüstite is also just above 3 Å. It may be expected then that if a detectably large volume fraction of wüstite phase is present in the NPs (cf. HRTEM for S15), then the intensity of the peak at $r \sim 3$ Å should be increased. In an effort to explore this case, a two-phase cubic rock-salt and spinel (FeO-Fe_3O_4) model was employed. This analysis showed that either in smaller nanocrystals (S8 and C12) or larger NPs (S15), the cubic symmetry model [Fig. 4(c); $R_w = 13.6\%$] is somewhat misplaced with respect to the 3 Å observed radial distance distribution. Per the present analysis and assessments of fits over broader r-ranges, it appears that these nanoscale samples are highly nonuniform in terms of defects (see below), and their structure is not quite cubic at high r or locally.

For these reasons, the possibility of the nanoparticle local structure deviating from the ideal cubic lattice

configuration has been factored in. However, the modest Q space resolution for resolving symmetry-lowering configurations beyond the local scale, and, in turn, the limited PDF field of view, led us to utilize approximations implemented by space groups of higher symmetry. The exemplary case of maghemite ($\gamma - Fe_2O_3$) drove this effort, as it can be considered Fe^{2+}-deficient magnetite, $(Fe)_8[Fe_{1\frac{1}{3}}\langle\rangle_{2\frac{2}{3}}, Fe_{12}]O_{32}$ (Fe_{Oh}-vacancies represented by the angular $\langle\rangle$ brackets) [47,48]. Under this defect-based scheme, randomly distributed vacancies result in a fcc lattice (model #1), but when their ordering is favored, either a primitive cubic (P4$_3$32 symmetry, model #2) [49,50] structural variant could be stabilized or a symmetry-lowering lattice distortion is triggered (P4$_3$2$_1$2 tetragonal symmetry, model #3) [51,52].

Amongst these models, only model #3 (Table S3, Sec. S5 in Ref. [44]) made a marked improvement in the description of the PDF peak positions from room temperature down to 80 K [Fig. 4d, and Figs. S6(b) and S7(c) in Ref. [44]]. The smaller NPs (≤ 12 nm) were assessed by the PDF (Fig. S5, Sec. S5 in Ref. [44]) to be 100% tetragonal at the local level, while the larger one (S15) entailed a 22.5%:77.5% [rock salt]:[tetragonal] share of volume fractions. The PDF intensities were accurately described when the Fe-site occupancies (η) were refined. The outcome indicates that nanoparticle samples of spherical morphology display the least occupied Fe sites, namely, $\eta - S8 < \eta$-S15 $< \eta$-C12 [i.e., 16.4(1) < 18.2(1) < 20.0(1), out of 24 Fe atoms/unit cell; Fig. S8, Sec. S8 in Ref. [44]]. Along this trend, we find the expansion of the in-plane (a–b) lattice dimensions and the contraction of the c axis, which suggest a more-pronounced tetragonal compression for the spherical (S8, S15 $c/a \sim 0.975$) rather than the cubic (C12, $c/a \sim 0.986$) morphology NPs. Details on the atomic PDF analysis, assessment of the outcomes, and a summary of the derived parameters (Table S4) are presented in the Supplemental Material (Sec. S5) [44].

Though the local symmetry change may be seen as a manifestation of the coupling between elastic and exchange energy terms [53], which are likely optimized by the apparently larger strain in the nanospheres, subtle crystalline electric field effects due to a local tetragonal Jahn-Teller distortion, lifting the orbital degeneracy in Fe^{2+} ($3d^6$) [54], cannot be resolved or ruled out by the structural xPDF probe on this occasion. Moreover, while we cannot completely discard the contribution of valence-swap-induced distortion [with a fraction of Fe^{2+} atoms occupying Fe^{3+} sites and vice versa, cf. $(Fe^{3+})_8[Fe^{3+}, Fe^{2+}]_{16}O_{32}$] [55], we emphasize that vacancy-driven effects are a plausibility as the relative $G(r)$ peak intensities of $Fe_{Oh} - Fe_{Oh}$ ($r \sim 3.0$ Å) and $Fe_{Oh} - Fe_{Td}$ ($r \sim 3.5$ Å) change appreciably (see below), whereas the one-electron difference between the Fe^{2+} and Fe^{3+} electronic configurations would effectively be unobservable in the xPDF peak heights. It is therefore inconceivable that
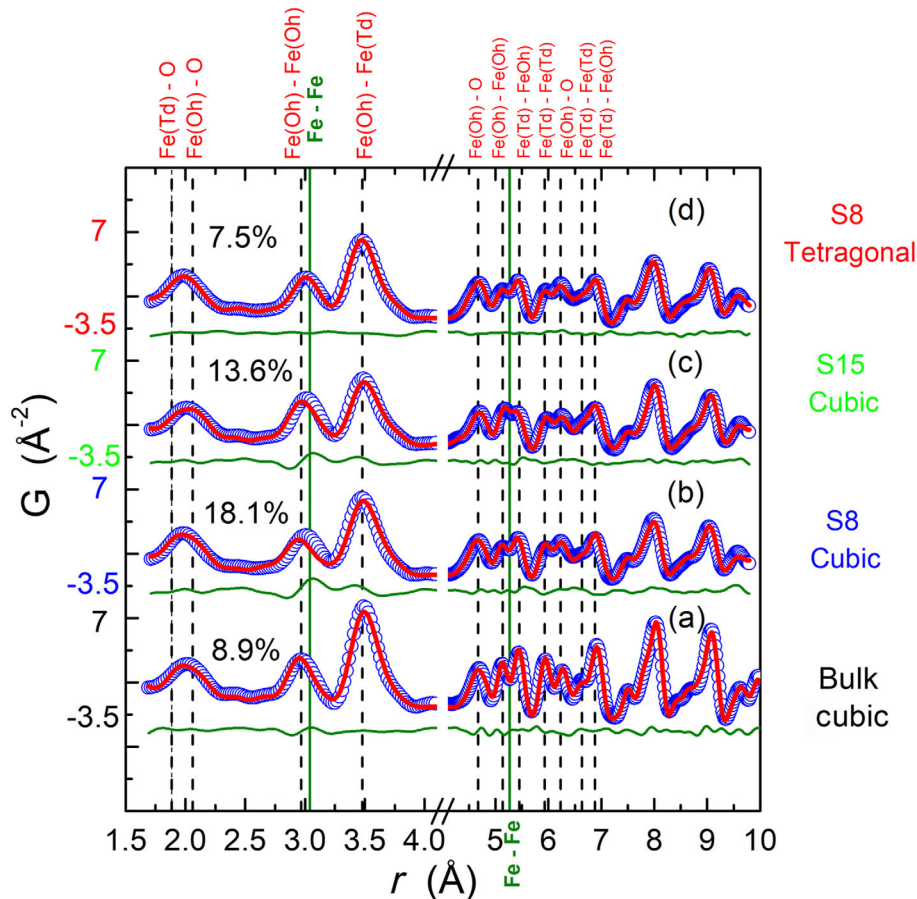
FIG. 4.   Representative xPDF fits ($T = 80$ K) of the "low-r" region for (a) the bulk magnetite assuming the cubic spinel atomic configuration [Fd-3m, model #1; $a = 8.3913(2)$ Å, $R_w = 8.9\%$], (b) the single-phase S8 nanoparticle sample with the same cubic model ($R_w = 18.1\%$), (c) the two-phase S15 nanoparticle sample with the cubic rock-salt and spinel ($R_w = 13.6\%$) crystallographic models, and (d) the single-phase S8 nanoparticle sample in the tetragonal [P4$_3$2$_1$2, model #3; $a_{Sp} = b_{Sp} = 8.4053(1)$ Å, $c_{Sp} = 8.1950(1)$ Å, $R_w = 7.5\%$] crystallographic configuration (see text for details). The blue circles and red solid lines correspond to the observed and calculated atomic PDFs, respectively. The green solid lines underneath are the difference curves between observed and calculated PDFs. The quality of fit factor, R_w (%), is given for each case. Vertical dashed lines mark the positions of typical Fe—O and Fe—Fe bond distances; Td and Oh represent tetrahedral and octahedral cation sites, respectively.

observed dramatic changes in relative PDF peak intensities originate from inverted-spinel-like electronic configurations.

Recapitulating the above PDF analysis, it is important to recognize the sensitive nature of the NPs, and especially those with spherical shape, in the local structure nonstoichiometry. Fe vacancies stabilize a tetragonally distorted local structure, inferring a relation to the large number of defects in the crystal volume, as implicated by the HRTEM-based analysis as well. Our results, albeit based on just two single-phase specimens, suggest enhanced tetragonality for spherical nanoparticle morphology.

Where the defects are located.—The question as to how structural vacancies relate to different cation lattice sites is now tackled by comparing the observed, normalized $G(r)$ patterns of the NPs against the bulk magnetite [Fig. 5(a)]. Two types of radial distance populations, represented by

the $G(r)$ peak intensity, are considered. (a) Fe$_{Oh}$ − Fe$_{Oh}$ separations ($r \sim 3.0$ Å): When the single-phase NPs peak-intensity maximum is compared to that in the bulk stoichiometric Fe$_3$O$_4$, a measure of the presence of Oh vacancies is witnessed. With ratios of about 0.8 and 0.9, for the S8 and C12 NPs, respectively, more Oh-Fe vacancies are supported in the nanospheres. For the larger NPs (S15), the enhanced $G(r)$ suggests an increased rock-salt type of phase in their volume. (b) Fe$_{Oh}$ − Fe$_{Td}$ separations ($r \sim 3.5$ Å): The progressive diminution of the $G(r)$ peak intensity also advocates that the spherical nanoscale morphology (S8, S15) adopts noticeably more empty lattice sites than the cubic one (C12), conferring that their abundance is a shape-dependent phenomenon [10].

With the purpose of further evaluating if the vacancies have a site-specific preference, xPDF patterns were simulated, while the ratio of Fe-vacancy population at the Oh
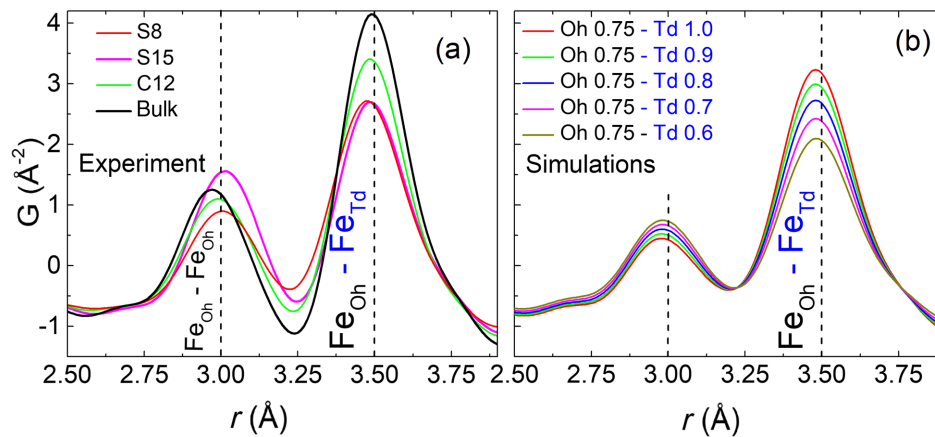
FIG. 5. (a) Adequately normalized, observed $G(r)$ patterns ($T = 80$ K) of the low-r region for all nanoparticle samples (single-phase, S8 and C12, and two-phase, S15) compared against the bulk magnetite and (b) the simulated xPDF patterns on the basis of the symmetry-lowering (tetragonal) atomic configuration. As a proof of concept, the optimally chosen set of models assumes a substoichiometric Oh Fe-site occupancy (η; kept constant at 75%, an average occupation derived from refinements of the $G(r)$ data across the samples), while the Td Fe-site occupation level is varied in a stepwise manner ($60 < \eta < 100\%$). Vertical dashed lines mark the modification of the distribution of the $Fe_{Oh} - Fe_{Oh}$ ($r \sim 3.0$ Å) and $Fe_{Oh} - Fe_{Td}$ ($r \sim 3.5$ Å) separations from bulk to nanoscale samples.

and Td sites was varied. The trend is similar assuming either the symmetry-lowering model #3 [Fig. 5(b)] or the cubic spinel model #1 [Figs. S9(b) and S9(c); Sec. S9 [44]]. The progressive intensity diminution at $r \sim 3.5$ Å, when raw and simulated patterns are compared, corroborates with a significant volume of vacancies also at the Td Fe sites (about 10%–20%; Fig. S8 [44]), inferring a limited length of structural coherence [56]. This result is in contrast to bulk spinel samples where intrinsic Oh Fe vacancies mediate the structure and properties [57]. The significant content of vacancy distribution resolved by xPDF may infer emerging strains or stresses (Fig. S10 and Sec. S10 [44]), reminiscent of those in $Fe_xO@Fe_3O_4$ nanocubes probed by single-particle local structure techniques [25,29].

Overall, the PDF indicates that during the self-passivation of wüstite, smaller NPs are single phase while larger ones attain a two-phase character. This size-mediated phase evolution is in agreement with the HRTEM findings, which also indicate that particles of spherical shape accommodate a larger number of defects in their volume [cf. xPDF refined Fe-site occupancy η−S8 $< \eta$-S15 $< \eta$-C12, i.e., 16.4(1) $<$ 18.2(1) $<$ 20.0(1), where $\eta = 24$ Fe atoms/unitcell of the bulk cubic spinel; Fig. S8 [44]]. In addition, the PDF uncovers the fact that in addition to vacancies commonly found at the Oh sites, Td-Fe is largely absent, fostering local tetragonal lattice distortions. These observations trigger questions about the impact of vacancies on the observed properties.

B. Nanometer scale effects on properties

1. Magnetic behavior

In view of the nanoparticles' deviation from perfect structural ordering, their magnetic behavior is evaluated here because of its direct relevance to hyperthermia applications. A broad maximum in the dc magnetic susceptibility, $\chi(T)$, with an irreversibility between ZFC/FC curves [Figs. 6(a)—6(c); Fig. S11(a) [44]], marks a characteristic temperature T_B that separates the superparamagnetic state from the blocked state [5]. In addition, the $\chi(T)$ for the core@shell NPs [S15 [44]; Fig. 6(c)] points to a sudden drop due to the paramagnetic-to-AFM transition (T_N) in wüstite and a subtle anomaly resembling the Verwey transition (T_V) of bulk magnetite [30,35,36]. Furthermore, the evolutions of the hysteresis loop characteristics (Sec. S11, Table S5; Figs. S11(b) and S11(c) in Supplemental Material [44]) suggest that a process beyond the coherent reversal of M is involved. In this process, $M(H)$ experiments under field cooling [$H_{cool} = 50$ kOe; Figs. 6(d)—6(f), Figs. S12 and S13 [44]] support the development of a macroscopic, exchange-bias field (H_{EB}) resulting from interfacial interactions [16]. The quick rise of H_{EB} for the S15 NPs, against the single-phase S8 and C12 (Fig. 7, and Fig. S14, Sec. S14 [44]), implies competing exchange interactions due to different kinds of interfaces.

In addition, all the NPs present a discontinuous steplike variation of the magnetization near zero field [Figs. 6(d)—6(f), Fig. S13 [44]]. The two switching field distributions, marked by maxima in dM/dH, resemble the inhomogeneous magnetic behavior arising from coexisting magnetic components of contrasting H_Cs (e.g., of mixture of particle sizes [58] or compositions [59]). Here, though, the HRTEM study of the $Fe_xO - Fe_3O_4$ NPs confers their single-crystal character and narrow particle-size distribution (Fig. S1 [44]). However, xPDF resolves Fe-site vacancies [$V = (\eta − $ S8 or η-S15 or η-C12)$:\eta$ is the
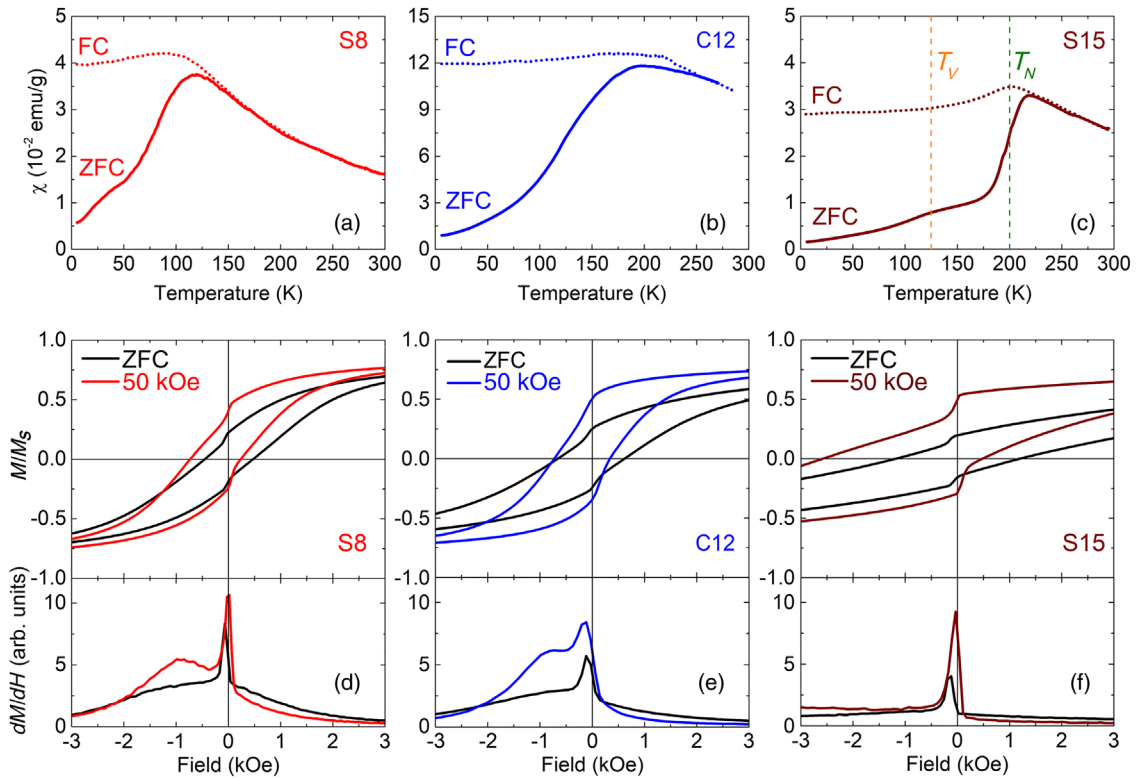
FIG. 6.   The temperature evolution of the zero-field cooled (ZFC; solid lines) and field-cooled (FC; dotted lines) susceptibility curves for the single-phase S8 (a), C12 (b), and core@shell S15 (c) nanoparticles under a magnetic field of 50 Oe. The dashed vertical lines indicate the Verwey (T_V; orange) and Néel (T_N; green) related transition temperatures met in bulk, stoichiometric Fe_3O_4 and Fe_xO, respectively. The low-field part of the normalized hysteresis loops (M/M_S) at 5 K for the single-phase S8 (d), C12 (e), and the core@shell S15 (f) nanoparticles taken under zero- and field- cooled ($H_{cool} = 50$ kOe) protocols. The panels beneath the loops present the differential change (dM/dH) of the normalized, isothermal magnetization when it is switched from positive to negative saturation.

modeling-derived content per unit cell volume, $\eta = 24$ Fe atoms/cell of bulk cubic spinel], with $V-S8(33\%) > V-S15(25\%) > V-C12(17\%)$. The existence of these defects seems to establish a spatial variation of the composition at the local level that "turns on" the observed inhomogeneous magnetism.

2. Coupling of structural defects to magnetism

To shed light on how atomic-scale defects (e.g., Td Fe-lattice site vacancies and local tetragonal distortions) couple to magnetism, we utilize Monte Carlo (MC) simulations. For this purpose, our systems are approximated by a microscopic "core-surface" model [60,61], however, with random defects introduced in the nanoparticle structure. These defects were described as weakly coupled FM pairs of spins with strong anisotropy, inferred from the symmetry-lowering local structure (Sec. II A 2) of the NPs. Their soft FiM character [62] was chosen to resemble that of $V_4 - $ Td clusters of defect units [due to coalescence of four Fe_{Oh} vacancies (V) around an Fe^{3+}_{Td} interstitial] [Figs. 1(b) and 1(c)] [28] out of which spinel magnetite has been claimed to nucleate during the oxidative conversion of Fe_xO [63]. Assuming that the

fraction of the FM pairs of spins (pinning bonds) is a tunable particle parameter, associated with the xPDF-derived Fe vacancies, the evolution of (a) the low-field jump ($\Delta M/M_S$, estimates how many magnetic moments are switched) and (b) the exchange bias (H_{EB}) have been quantified (Fig. 8).

With the purpose of assessing the former, $\Delta M/M_S$, we note that the surface is large for the smaller nanoparticles, i.e., about 50% of the S8 and about 35% of the C12 specimens, and both may assume a two-phase magnetic nature. The $\Delta M/M_S$ changes may then be a manifestation of the character stemming from the exchange-coupled hard and soft ferromagnetic and ferrimagnetic phases in the two nanodomains [64]. As the number of pinning bonds (vacancy driven) increases in the main body of these NPs, MC calculations point to the fact that the defects' strong random anisotropy leads to exchange randomness, rendering their two-phase magnetic nature more disordered. This result leads to less prominent $\Delta M/M_S$ changes in the hysteresis loops (Fig. 8). Considering the evaluation of the latter, we note that the defect-induced spin disorder within the corelike subdomains reduces the overall magnetization (Fig. S12 [44]) but supports extra pinning centers
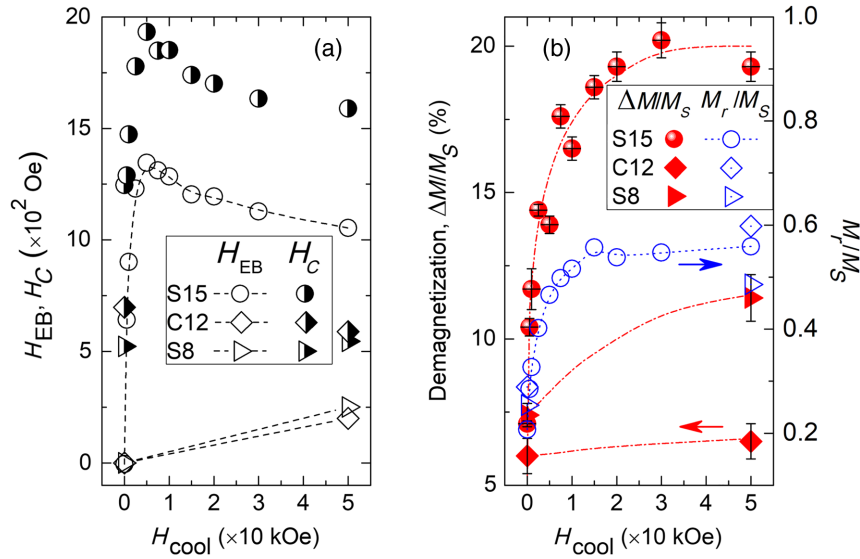
FIG. 7. The experimentally determined (a) exchange bias (H_{EB}; open symbols) and coercive field (H_C; half-filled symbols), as well as (b) low-field demagnetization ($\Delta M/M_S$; filled symbols, left y axis) and the ratio M_r/M_S (M_r, remanence: open symbols, right y axis) obtained at varying cooling-field strengths (H_{cool}). Symbol guide: circular, core-shell spherical nanoparticles (S15), triangular (S8), and diamond (C12) for single-phase spherical and cubic morphology nanoparticles. The lines are a guide to the eye.

that could foster a density of uncompensated interfacial spins, impeding easy coherent reversal [65] of the surrounding ferrimagnetic moments (Fig. S13 [44]). In line with this case are the MC simulations, which indicate that in small S8 and C12 NPs without defects, exchange bias is absent, but when the perturbation of the periodic potential of the iron coordination by lattice defects is enabled, the

FIG. 8. Monte Carlo calculations ($H_{cool} = 5\ J_{FM}/g\mu_B$) of the effect of pinning bonds (vacancy-driven) on the low-field magnetic-moment switching ($\Delta M/M_S$; filled symbols, left y axis) and the exchange bias (H_{EB}; open symbols, right y axis) of self-passivated $Fe_xO - Fe_3O_4$ nanocrystals with different morphologies. Symbol guide: circular, core-shell spherical nanoparticles (S15), triangular (S8), and diamond (C12) for single-phase spherical and cubic-shape nanoparticles.
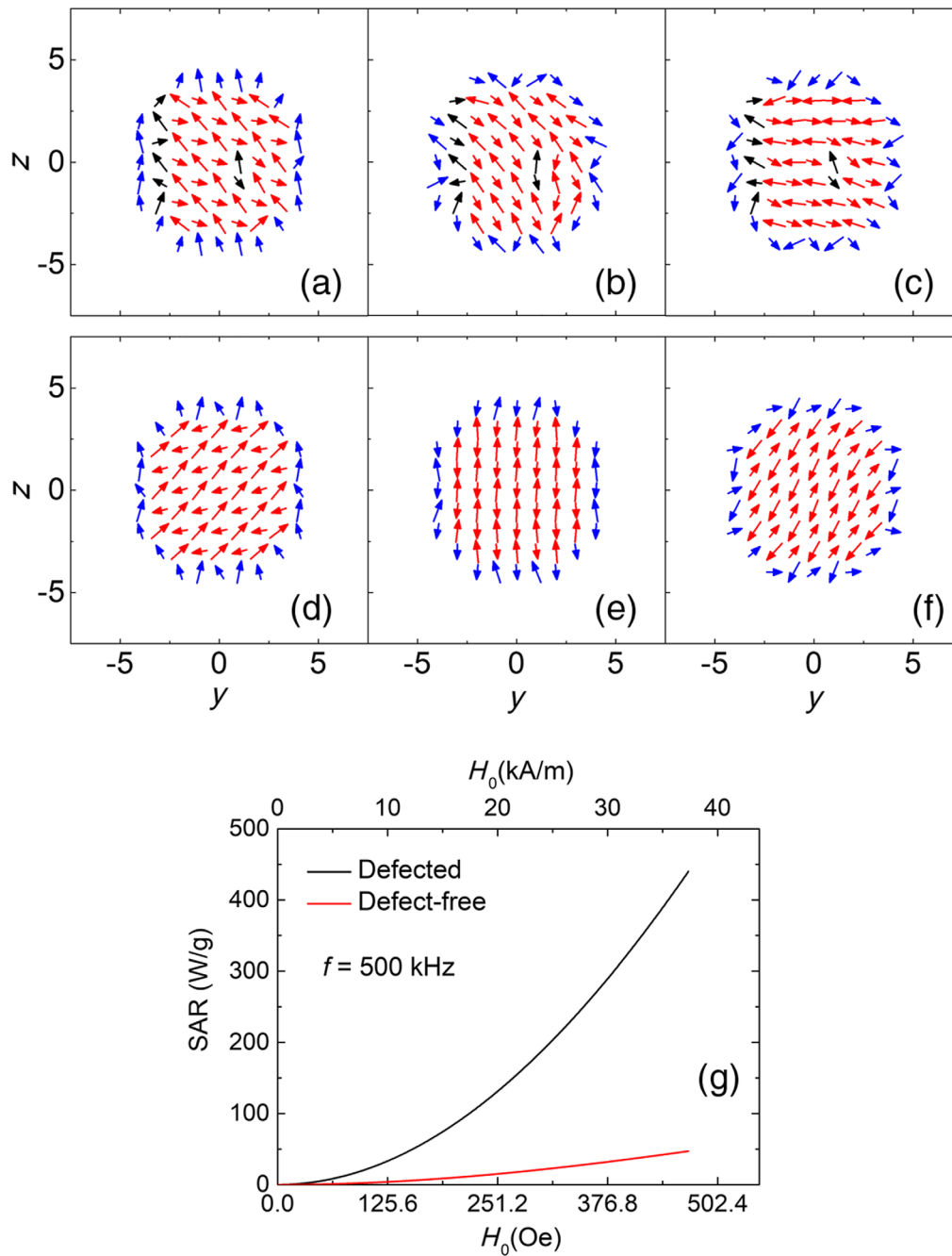
increasing number of pinning bonds in the core results in net exchange bias (Fig. 8).

The behavior is depicted in the magnetic-moment snapshots of defected [Figs. 9(a)—9(c)] versus defect-free [Figs. 9(d)—9(f)] NPs. While for nondefected NPs the soft anisotropic core follows the applied field reversal, the existence of defects generates localized antiparallel spin components, which couple to neighboring ferrimagnetic spins at the atomic-scale interface and promote the canting of the core towards the xy plane (snapshots of the spin ensemble under a full M-H loop are compiled in Fig. S15, while the mean moment orientation is shown in Fig. S16 [44]). In this way, the nanospheres' more defected internal structure generates adequate conditions that endorse exchange coupling so that $H_{EB} - S8 > H_{EB} - C12$ (while $H_C - S8 < H_C - C12$, due to differences in the NPs' magnetic volumes). As magnetization states at the different kinds of interfaces are adjusted by H_{cool}, for a matter of consistency, it is worth pointing out that MC simulations (Fig. S17 [44]) reproduce fairly well the experimental (Fig. 7) evolution of the hysteresis loop parameters (H_{EB}, H_C, $\Delta M/M_S$) even for the larger S15 NPs (Sec. S17 [44]).

The defect-rich NPs discussed here broaden the picture that growth-approach-mediated, subtle, structural microscopic factors [24,33,66] foster local-scale anisotropy that facilitates exchange bias in otherwise phase-pure, monocrystalline NCs.

3. Defect-driven magnetic heating

The observed evolutions may be related to structural and morphological variations between NPs exhibiting differences in size, surface anisotropy, and exchange

FIG. 9.   MC simulation of the $M - H$ loops made after field-cooling ($H_{cool} = 5 \, J_{FM}/g\mu_B$) and by assuming an upper maximum fraction of pinning bonds, as this was identified by the xPDF refinements. Snapshots of the spin ensemble during $M - H$ loop calculation for a small ferrimagnetic spherical nanoparticle of $R = 5$ lattice constants: (a)—(c) a fully oxidized, defected nanocrystal (S8), and (d)—(f) a defect-free case, assuming a core-surface type of MC model. Spin configurations are shown in the zy plane ($x = -1$) for positive-field ($H = +8 \, J_{FM}/g\mu_B$) magnetization saturation and after field reversal ($H = -0.2 \, J_{FM}/g\mu_B$, $H = -2.0 \, J_{FM}/g\mu_B$) towards negative saturation. The arrow color coding is as follows: core (red), surface (blue), and defects (black) magnetic moments. (g) Specific absorption rate (SAR) of small defected (S8) versus defect-free nanoparticles on the basis of susceptibility losses (ac field amplitude, H_0 and $f = 500$ kHz), calculated according to the linear response theory of a modified Néel-Brown relaxation Monte Carlo model.

anisotropy. Ferrite nanocrystals, in magnetically mediated biomedical applications, draw their versatility from the critical particle size (about 20 nm) [39], a factor that varies with the magnetic anisotropy [41]. In the present work, we have demonstrated that surface atoms can respond differently than the core ones, a prominent effect for the smaller fully oxidized derivatives (≤ 12 nm) of the $Fe_xO - Fe_{3-\delta}O_4$ NCs. Although defect elimination during synthesis can yield nanomagnetic agents (≥ 20 nm) with enhanced, concurrent diagnostic imaging and thermo-responsive performances [34], structural defects at subcritical particle sizes appear to offer a different exploitable pathway, compatible with the biological limits (e.g., set by toxicity and patient discomfort) [67]. Here, vacancies in self-passivated iron oxides of subcritical size (≤ 12 nm) act as pinning centers that favor the competition of exchange interactions, thus fostering local anisotropy enhancement. Benefits from the NPs' extended anisotropic properties may raise their application potential–for example, to afford heat generation beyond the bare susceptibility losses (Néel-Brown relaxation) mediated by finite-size effects alone (Sec. S18 [44]). [40].

The MC simulations support the fact that for small defected NPs (S8), where the effective anisotropy increases 5 times compared to the defect-free ones, the heat dissipation (specific absorption rate=SAR) is raised almost tenfold, i.e., about 450 W/g vs about 50 W/g, at 500 kHz under 37.3 kA/m [Fig. 9(g)]. For comparison, it is worth noting that, experimentally, defect-free 9-nm Fe_3O_4 NPs exhibit a SAR of 152 W/g [14]. It can be envisaged then that nanoparticle self-passivation leads to adequate perturbation of the periodic potential of the iron coordination by vacant lattice sites that, in turn, tweak the core-to-surface magnetic anisotropy ratio. Whether this might be an avenue to boost the thermal energy transfer at subcritical particle sizes (≤ 10 nm) by synergistic relaxation processes warrants further exploration. Even in the absence of extended buried AFM/FM interfaces [14], where beneficial exchange parameters attain efficient heat sources, smaller heterogeneous nanocrystals (S8, C12) may be uncovered as useful heat-therapeutic agents.

III. CONCLUSIONS

The self-passivation of nanoscale wüstite (Fe_xO) has been investigated as a testing ground to explore the consequences of thermodynamically unstable interfaces formed during the nucleation and growth of nanostructured iron oxides. As conventional oxidation evolves, grown component phases give rise to single-crystal nanoscale entities with subdomain $Fe_xO - Fe_{3-\delta}O_4$ interfacial connectivity. However, when the synthesis parameters are varied to attain smaller-size nanocrystals (≤ 12 nm), a spinel-like phase is nucleated alone. The compositional and structural complexity of these iron-oxide nanostructures is witnessed by single-particle transmission electron

microscopy and complementary, phase-specific structural information, attained from a large ensemble by high-energy synchrotron, x-ray total scattering experiments. These experiments uncover the fact that defects (with a significant volume residing at tetrahedral Fe sites) alleviate a surprising tetragonal lattice compression in the spinel-like phases. The defects entail structural vacancies with an increased number density when the nanoscale morphology changes from cubic to spherical and the particle size shrinks. Moreover, magnetometry and Monte Carlo calculations show that the nanostructures' heterogeneous character is demonstrated by a core-surface type of spin configuration that favors two switching field distributions. Larger core@shell $Fe_xO - Fe_{3-\delta}O_4$ nanocrystals support exchange bias due to the coupling across a common interface of spatially extended subdomains of AFM and FiM nature. Exchange bias is unexpectedly evident, though much reduced, in smaller-size (≤ 12 nm), fully oxidized particles, due to the existence of the defected internal structure that generates localized antiparallel spin components and uncompensated spin density at atomic-scale interfaces. The latter, in line with the noncubic local symmetry of the nucleated spinel phases, expresses the influence of local anisotropy fields, which apparently deviate from the easy-axis symmetry met in common iron oxides, favoring canting into the xy plane. The results corroborate that size-dependent evolution of the metal-cation valence state produces pinning defects that promote the competition of the exchange interactions at subcritical sizes (<20 nm). The concept raised here points to the fact that atomic-scale defect control in small particles (~ 10 nm), typically hampered by the superparamagnetic limit, may act in favor of anisotropic properties for improved magnetism-engineered functionalities (cf. heating agents and thermoresponsive cellular processes).

IV. METHODS

A. Materials

All reagents were used as received without further purification. Oleic acid (technical grade, 90%), absolute ethanol ($\geq 98\%$), octadecene (technical grade, 90%), hexane (ACS reagent, $\geq 99\%$), and sodium oleate powder (82%) were purchased from Sigma Aldrich. Iron (III) chloride ($FeCl_3 \cdot 6H_2O$, ACS Reagent) was purchased from Merck. Iron (III) acetylacetonate was purchased from Alfa Aesar, and oleylamine 80%–90% was purchased from Acros Organics.

B. Syntheses protocols

Colloidal syntheses were carried out in 100-mL round-bottom three-neck flasks connected via a reflux condenser to a standard Schlenk line setup, equipped with immersion temperature probes and digitally controlled heating mantles. The reactants were stored under anaerobic conditions

in an Ar-filled glovebox (MBRAUN, UNILab), containing less than 1 ppm O_2 and H_2O.

A gas mixture of 5% H_2/Ar has been used as a protective/reductive atmosphere. The reductive atmosphere can help us to maintain the Fe_xO (wüstite) phase instead of the oxidized Fe_3O_4 (magnetite) and/or $\gamma - Fe_2O_3$ (maghemite) forms. Previous studies have shown that Fe_xO crystallites formed under these synthetic conditions become rapidly oxidized after removing the reducing agent and exposing them to ambient air [68]. Very small particles tend to be fully oxidized to the spinel structure. A minimum diameter over about 13 nm is needed for the nanoparticle to maintain its core@shell structure.

1. Preparation of iron oleate precursor

Iron (III)-oleate was prepared before each nanoparticle synthesis and subsequently used as an iron precursor. Special care was taken to protect it from the light. The metal oleate precursor was formed by the decomposition of $FeCl_3 \cdot 6H_2O$ in the presence of sodium oleate at 60 °C, based on a slightly modified literature protocol [69]. Here, 16 mmol of $FeCl_3 \cdot 6H_2O$ salt and 48 mmol of sodium oleate were dissolved in a mixture of solvents in a round bottom flask, and 56 mL hexane, 32 mL ethanol, and 24 mL distilled water were used as solvents. The mixture was heated to 60–65 °C under Ar atmosphere for 4 hours and then left to cool down to room temperature. The organic phase containing the metal oleate complex was separated from the aqueous phase using a separatory funnel and then washed with about 30 mL distilled water and separated again. This process was repeated 4 times, and at the end, the metal-organic complex was dried under stirring and mild heating for several hours, resulting in a viscous dark-red oleate. The final product was stored in a dark place to protect it from light. Some mild heating to ensure its fluidness may be needed just before its use for each nanoparticle synthesis. The successful fabrication of the ferric oleate complex has been identified by the FTIR data (Fig. S19 [44]) [70].

2. Synthesis of iron-oxide nanoparticles

The NPs were synthesized by employing modified literature protocols [18,35,70,71] aiming to produce the wüstite type of oxide ($Fe_{1-x}O$). In a typical synthesis, 2–7 mmol of iron oleate were dissolved in octadecene in a flask under a reductive atmosphere. Oleic acid was used as a surfactant and protective ligand, in a proportion 1:2 with respect to the iron precursor. The amounts of reactants were tuned so that a final Fe-oleate molar ratio of 0.2 mol/kg solution was achieved. The synthesis protocol includes three major steps. First, a degassing step at 100 °C for 60 min under vacuum is required for the complete removal of any water and oxygen residues. Then, the mixture is heated to 220 °C, with a heating rate of about 10 °C · min^{-1}. At this temperature, which lasts for 60 min,

the so-called nucleation step allows for the crystal seeds [92] to be generated for the successive formation of the NCs. At the final stage, the mixture is heated to 320 °C, where the nanocrystals' growth takes place. At the end of the synthesis, the colloidal mixture was left to cool down at room temperature, and the NCs were precipitated upon ethanol addition. They were separated by centrifugation at 6000 rpm for 5 min, redispersed in hexane, and then centrifuged once more after adding ethanol in a 1:1 ratio with respect to the hexane. The process was repeated two more times at a centrifugation speed of 1000 rpm. The addition of sodium oleate proved to promote the formation of cubic NPs, as proposed in earlier studies [71]. We found that a metal-precursor-to-sodium-oleate ratio of 8:1 to 5:1 is adequate enough to realize such a shape transformation. Minor variations in this two-step heating protocol allow the tuning of the particles' size and the control of their size distribution [18,72]. The protocol gives rise to NPs with diameters up to 20 nm, with size control attained by modifying the growth time ($40 < t < 90$ min) at the final stage. An extended stay here produces even larger NPs, but beyond 60 min, smaller-size particles are afforded, likely due to a ripening mechanism. Four iron-oxide colloidal nanostructures, with varying size and morphological features (see above), S8, C12, S15, C18 (S: spherical, C: cubic), were finally grown and stored as colloidal dispersions in about 4 mL hexane in septa-sealed vials.

C. Characterization techniques

1. High resolution transmission electron microscopy

Low-magnification and HRTEM images were recorded, using a LaB_6 JEOL 2100 electron microscope operating at an accelerating voltage of 200 kV. All the images were recorded by the Gatan ORIUS^{TM} SC 1000 CCD camera. For the purposes of the TEM analysis, a drop of a diluted colloidal nanoparticle solution was deposited onto a carbon-coated copper TEM grid, and then the hexane was allowed to evaporate. In order to estimate the average size, statistical analysis was carried out on several low-magnification TEM images, with the help of the dedicated software ImageJ [73]. The structural features of the nanoparticles were studied by two-dimensional (2D) FFT images acquired and analyzed by ImageJ.

With the purpose to highlight the defect structure of the nanoparticles, we employed the geometric phase analysis (GPA) method of Hÿtch *et al.* [43]. The HRTEM images were Fourier transformed, and a region around one of the {220} peaks was selected with a circular window. This diffraction pattern was recentered and inverse Fourier transformed to provide a real-space image whose phase [Figs. 2(m)—2(p)] represents the projection (onto the {220} reflection chosen) of the lattice shift of that particular region of the crystal relative to the average lattice. The single-colored regions are internally

homogeneous, showing no obvious internal distortions, but have different phase shifts from their neighbors.

2. X-ray pair distribution function

X-ray synchrotron-based PDF data were acquired at the 28-ID-2 beamline of the National Synchrotron Light Source II, Brookhaven National Laboratory. Each nanoparticle powder was encapsulated in a $\oslash 1.0$ mm kapton capillary, sealed at both ends with epoxy glue. The 28-ID-2 in PDF mode used a Perkin-Elmer 2D image plate detector for fast data acquisition but of relatively modest Q space resolution, which, in turn, limits the PDF field of view in r space. Data were collected between $80 < T < 400$ K, making use of the beamline's liquid nitrogen cryostream (Oxford Cryosystems 700), with incident x-ray energy of 68 keV. Bulk magnetite powder (Fe_3O_4) was utilized as a reference.

The atomic PDF [39] gives information about the number of atoms in a spherical shell of unit thickness at a distance r from a reference atom and is defined as

$$G(r) = 4\pi r[\rho(r) - \rho_0] \qquad (1)$$

where ρ_o is the average number density, $\rho(r)$ is the atomic pair density, and r represents radial distance. The raw 2D experimental data are then converted to 1D patterns of intensity versus momentum transfer, $Q (= 4\pi \sin\theta/\lambda)$, which are further reduced and corrected using standard protocols, and then finally Fourier transformed to obtain $G(r)$:

$$G(r) = (2/\pi) \int_{Q_{min}}^{Q_{max}} Q[S(Q) - 1]\sin(Qr)dQ. \qquad (2)$$

$S(Q)$ is the properly corrected and normalized powder diffraction intensity measured from Q_{min} to Q_{max}. The experimental PDF, $G(r)$, can subsequently be modeled by calculating the following quantity directly from a presumed structural model:

$$G(r) = \left[\frac{1}{r}\sum_{ij}\frac{f_i f_j}{\langle f\rangle^2}\delta(r - r_{ij})\right] - 4\pi r \rho_0. \qquad (3)$$

Here, f stands for the x-ray atomic form factors evaluated at $Q = 0$, r_{ij} is the distance separating the ith and jth atoms, and the sums are over all the atoms in the sample. In the 28-ID-2 experiments, elemental Ni powder was measured as the standard to determine parameters, such as Q_{damp} and Q_{broad}, to account for the instrument resolution effects. Experimental PDFs, based on modest Q space resolution and $Q_{max} = 25$ Å^{-1} raw powder diffraction data, were fitted with structural models using the PDFgui [74] software suite.

3. Magnetic measurements

The magnetic characterization was conducted using a vibrating sample magnetometer (VSM, Oxford Instruments, Maglab 9T), operating at a vibration frequency of 55 Hz. The measurements of the temperature-dependent magnetization, $M(T)$, were carried out at 50 Oe at a fixed temperature rate of 1 K min^{-1} after either zero-field cooling (ZFC) or field cooling (FC) in 50 Oe from 300 K to 5 K. Selected $M(T)$ measurements were also carried out at a different applied field (100 Oe). Hysteresis loops, $M(H)$, were obtained at room temperature and at 5 K by sweeping the applied field from $+50$ kOe to -50 kOe and back to $+50$ kOe after cooling the sample from 300 K to 5 K under ZFC or an applied field $0 < H_{cool} \leq 50$ kOe (FC). In the FC procedure, once the measuring temperature was reached, the field was increased from H_{cool} to $H = 50$ kOe, and the measurement of the loop was pursued. Because of a small remnant field, common in superconducting magnets, the values of the coercive field (Table S5 in Supplemental Material [44]) have been corrected, as [magnetometer reported field] + [field error] = [real magnetic field at the sample]. The offset error in the magnetic field (max 60 Oe) was estimated through the "field error vs charge field" calibration chart of the magnetometer. Although such an amendment does not propagate to the extracted exchange-bias values, it has been taken into account in the low-field demagnetization ($\Delta M/M_S$) and the ratio of remanence against saturation (M_r/M_S) (Fig. 7). In addition, when data are recorded under a magnetic field sweep, a synchronization error of the measuring electronics can be observed if high sweeping rates, larger than 200 Oe/s, are chosen. To avoid this artifact, we evaluated $M(H)$ loops collected at step mode versus sweeping, at various rates, and found that a sweeping rate of 30 Oe/s provides adequate conditions to minimize the error propagation in the measurements.

While precautions were taken to maintain the integrity of the samples, their spontaneous chemical evolution led us to exclude one specimen (C18) from the in-depth discussion where magnetism and structural properties are correlated (Sec. II B). This is because, while TEM structural investigations were pursued soon after the sample growth, neither xPDF nor magnetic characterizations were readily available (due to remote facility timeline access restrictions) near the initial lifetime of the samples. So, while four iron-oxide colloidal nanostructures were grown initially, their self-passivation into $Fe_xO - Fe_3O_4$ nanocrystals led us to discuss magnetic data (Fig. S11 [44]) only for three samples (i.e., S8, C12, S15), which allowed a coherent picture of their structure-property relations to be attained.

D. Monte Carlo simulations

The simulations approximate the NPs by a microscopic "core-surface" model [60,61]. Three nanoparticle model

systems were considered, with somewhat different morphological features, as these were probed experimentally in the S8, C12, and S15 specimens. The spins in the NPs were assumed to interact with nearest-neighbor Heisenberg exchange interaction, and at each crystal site, they experience a uniaxial anisotropy [35,75,76]. Under an external magnetic field, the energy of the system is calculated as

$$E = -J_{\text{core}} \sum_{i,j \in \text{core}} \vec{S}_i \cdot \vec{S}_j - J_{\text{shell}} \sum_{i,j \in \text{shell}} \vec{S}_i \cdot \vec{S}_j - J_{\text{IF}} \sum_{i \in \text{core}, j \in \text{shell}} \vec{S}_i \cdot \vec{S}_j$$
$$- K_{i \in \text{core}} \sum_{i \in \text{core}} (\vec{S}_i \cdot \hat{e}_i)^2 - K_{i \in \text{shell}} \sum_{i \in \text{shell}} (\vec{S}_i \cdot \hat{e}_i)^2 - \vec{H} \sum_i \vec{S}_i. \tag{4}$$

Here, $\vec{S}_i$ is the atomic spin at site i, and $\hat{e}_i$ is the unit vector in the direction of the easy axis at site i. The first, second, and third terms give the exchange interaction between spins in the AFM core, in the FiM shell, and at the interface between the core and the shell, respectively. The interface includes the last layer of the AFM core and the first layer of the FiM shell. The fourth and fifth terms give the anisotropy energy of the AFM core, K_C, and that of the FiM shell, K_{shell}, correspondingly; the last term is the Zeeman energy.

Parameters were chosen (Sec. S20 in Supplemental Material [44]) after careful analysis of the experimental magnetic behavior, and MC simulations were implemented with the Metropolis algorithm [77]. The hysteresis loops $M(H)$ were calculated upon a field-cooling procedure, starting at a temperature $T = 3.0\ J_{\text{FM}}/k_B$ and down to $T_f = 0.01\ J_{\text{FM}}/k_B$, at a constant rate under a static magnetic field H_{cool}, directed along the z axis. The hysteresis loop shift on the field axis gave us an estimate of the exchange field, $H_{\text{EB}} = -(H_{\text{right}} + H_{\text{left}})/2$. The coercive field was defined as $H_C = (H_{\text{right}} - H_{\text{left}})/2$. Note that H_{right} and H_{left} are the points where the loop intersects the field axis. The fields H, H_C, and H_{EB} are given in dimensionless units of $J_{\text{FM}}/g\mu_B$, the temperature T in units J_{FM}/k_B, and the anisotropy coupling constants K in units of J_{FM}. In this work, 10^4 MC steps per spin (MCSS) were used at each field step for the hysteresis loops, and the results were averaged over 60 different samples (namely, random numbers).

ACKNOWLEDGMENTS

[1] C. Gleitzer and J. B. Goodenough, *Mixed-Valence Iron Oxides*, in *Cation Ordering and Electron Transfer. Structure and Bonding*, Vol. 61 (Springer, Berlin, Heidelberg, 1985), pp. 1–76.

[2] P. Tartaj, M. P. Morales, T. Gonzalez-Carreño, S. Veintemillas-Verdaguer, and C. J. Serna, *The Iron Oxides Strike Back: From Biomedical Applications to Energy Storage Devices and Photoelectrochemical Water Splitting*, Adv. Mater. **23**, 5243 (2011).

[3] E. A. Dobisz, Z. Z. Bandic, T. W. Wu, and T. Albrecht, *Patterned Media: Nanofabrication Challenges of Future Disk Drives*, Proc. IEEE **96**, 1836 (2008).

[4] Q. A. Pankhurst, J. Connolly, S. K. Jones, and J. Dobson, *Applications of Magnetic Nanoparticles in Biomedicine*, J. Phys. D **36**, R167 (2003).

[5] G. C. Papaefthymiou, *Nanoparticle Magnetism*, Nano Today **4**, 438 (2009).

[6] D. Yoo, J.-H. Lee, T.-H. Shin, and J. Cheon, *Theranostic Magnetic Nanoparticles*, Acc. Chem. Res. **44**, 863 (2011).

[7] D. Yoo, H. Jeong, S.-H. Noh, J.-H. Lee, and J. Cheon, *Magnetically Triggered Dual Functional Nanoparticles for Resistance-Free Apoptotic Hyperthermia*, Angew. Chem., Int. Ed. Engl. **52**, 13047 (2013).

[8] R. E. Rosensweig, *Heating Magnetic Fluid with Alternating Magnetic Field*, J. Magn. Magn. Mater. **252**, 370 (2002).

[9] J.-P. Fortin, C. Wilhelm, J. Servais, C. Ménager, J.-C. Bacri, and F. Gazeau, *Size-Sorted Anionic Iron Oxide Nanomagnets as Colloidal Mediators for Magnetic Hyperthermia*, J. Am. Chem. Soc. **129**, 2628 (2007).

[10] S. Noh, W. Na, J. Jang, J.-H. Lee, E. J. Lee, S. H. Moon, Y. Lim, J.-S. Shin, and J. Cheon, *Nanoscale Magnetism Control via Surface and Exchange Anisotropy for Optimized Ferrimagnetic Hysteresis*, Nano Lett. **12**, 3716 (2012).

[11] A. H. Habib, C. L. Ondeck, P. Chaudhary, M. R. Bockstaller, and M. E. McHenry, *Evaluation of Iron-Cobalt/Ferrite Core-Shell Nanoparticles for Cancer Thermotherapy*, J. Appl. Phys. **103**, 07A307 (2008).

[12] A. Meffre, B. Mehdaoui, V. Kelsen, P. F. Fazzini, J. Carrey, S. Lachaize, M. Respaud, and B. Chaudret, *A Simple Chemical Route toward Monodisperse Iron Carbide Nanoparticles Displaying Tunable Magnetic and Unprecedented Hyperthermia Properties*, Nano Lett. **12**, 4722 (2012).

[13] J. Kolosnjaj-Tabi, L. Lartigue, Y. Javed, N. Luciani, T. Pellegrino, C. Wilhelm, D. Alloyeau, and F. Gazeau, *Biotransformations of Magnetic Nanoparticles in the Body*, Nano Today **11**, 280 (2016).

[14] J.-H. Lee, J. Jang, J. Choi, S. H. Moon, S. Noh, J. Kim, J.-G. Kim, I.-S. Kim, K. I. Park, and J. Cheon, *Exchange-Coupled Magnetic Nanoparticles for Efficient Heat Induction*, Nat. Nanotechnol. **6**, 418 (2011).

[15] A. López-Ortega, M. Estrader, G. Salazar-Alvarez, A. G. Roca, and J. Nogués, *Applications of Exchange Coupled Bi-magnetic Hard/Soft and Soft/Hard Magnetic Core/Shell Nanoparticles*, Phys. Rep. **553**, 1 (2015).

[16] J. Nogués and I. K. Schuller, *Exchange Bias*, J. Magn. Magn. Mater. **192**, 203 (1999).

[17] M. Vasilakaki, C. Binns, and K. N. Trohidou, *Susceptibility Losses in Heating of Magnetic Core/Shell Nanoparticles for Hyperthermia: A Monte Carlo Study of Shape and Size Effects*, Nanoscale **7**, 7753 (2015).

[18] J. Park, K. An, Y. Hwang, J.-G. Park, H.-J. Noh, J.-Y. Kim, J.-H. Park, N.-M. Hwang, and T. Hyeon, *Ultra-Large-Scale Syntheses of Monodisperse Nanocrystals*, Nat. Mater. **3**, 891 (2004).

[19] L. Qiao, Z. Fu, J. Li, J. Ghosen, M. Zeng, J. Stebbins, P. N. Prasad, and M. T. Swihart, *Standardizing Size- and Shape-Controlled Synthesis of Monodisperse Magnetite (Fe_3O_4) Nanocrystals by Identifying and Exploiting Effects of Organic Impurities*, ACS Nano **11**, 6370 (2017).

[20] A. Kostopoulou, F. Thétiot, I. Tsiaoussis, M. Androulidaki, P. D. Cozzoli, and A. Lappas, *Colloidal Anisotropic $ZnO−Fe@Fe_xO_y$ Nanoarchitectures with Interface-Mediated Exchange-Bias and Band-Edge Ultraviolet Fluorescence*, Chem. Mater. **24**, 2722 (2012).

[21] E. Lima, E. L. Winkler, D. Tobia, H. E. Troiani, R. D. Zysler, E. Agostinelli, and D. Fiorani, *Bimagnetic CoO $Core/CoFe_2O_4$ Shell Nanoparticles: Synthesis and Magnetic Properties*, Chem. Mater. **24**, 512 (2012).

[22] H. Zeng, S. Sun, J. Li, Z. L. Wang, and J. P. Liu, *Tailoring Magnetic Properties of Core/Shell Nanoparticles*, Appl. Phys. Lett. **85**, 792 (2004).

[23] F. X. Redl, C. T. Black, G. C. Papaefthymiou, R. L. Sandstrom, M. Yin, H. Zeng, C. B. Murray, and S. P. O'Brien, *Magnetic, Electronic, and Structural Characterization of Nonstoichiometric Iron Oxides at the Nanoscale*, J. Am. Chem. Soc. **126**, 14583 (2004).

[24] M. Levy, A. Quarta, A. Espinosa, A. Figuerola, C. Wilhelm, M. García-Hernández, A. Genovese, A. Falqui, D. Alloyeau, R. Buonsanti *et al.*, *Correlating Magneto-Structural Properties to Hyperthermia Performance of Highly Monodisperse Iron Oxide Nanoparticles Prepared by a Seeded-Growth Route*, Chem. Mater. **23**, 4170 (2011).

[25] E. Wetterskog, C.-W. Tai, J. Grins, L. Bergström, and G. Salazar-Alvarez, *Anomalous Magnetic Properties of Nanoparticles Arising from Defect Structures: Topotaxial Oxidation of $Fe_{1−x}O/Fe_{3−δ}O_4$ Core/Shell Nanocubes to Single-Phase Particles*, ACS Nano **7**, 7132 (2013).

[26] A. Walter, C. Billotey, A. Garofalo, C. Ulhaq-Bouillet, C. Lefèvre, J. Taleb, S. Laurent, L. V. Elst, R. N. Muller, L. Lartigue *et al.*, *Mastering the Shape and Composition of Dendronized Iron Oxide Nanoparticles To Tailor Magnetic Resonance Imaging and Hyperthermia*, Chem. Mater. **26**, 5252 (2014).

[27] C. A. McCammon and L. Liu, *The Effects of Pressure and Temperature on Nonstoichiometric Wüstite, Fe_xO: The Iron-Rich Phase Boundary*, Phys. Chem. Miner. **10**, 106 (1984).

[28] C. R. A. Catlow and B. E. F. Fender, *Calculations of Defect Clustering in $Fe_{1−x}O$*, J. Phys. C Solid State Phys. **8**, 3267 (1975).

[29] B. P. Pichon, O. Gerber, C. Lefevre, I. Florea, S. Fleutot, W. Baaziz, M. Pauly, M. Ohlmann, C. Ulhaq, O. Ersen *et al.*, *Microstructural and Magnetic Investigations of Wüstite-Spinel Core-Shell Cubic-Shaped Nanoparticles*, Chem. Mater. **23**, 2886 (2011).

[30] X. Sun, N. F. Huls, A. Sigdel, and S. Sun, *Tuning Exchange Bias in Core/Shell FeO/Fe_3O_4 Nanoparticles*, Nano Lett. **12**, 246 (2012).

[31] D. T. Margulies, F. T. Parker, M. L. Rudee, F. E. Spada, J. N. Chapman, P. R. Aitchison, and A. E. Berkowitz, *Origin of the Anomalous Magnetic Behavior in Single Crystal Fe_3O_4 Films*, Phys. Rev. Lett. **79**, 5162 (1997).

[32] K. P. McKenna, F. Hofer, D. Gilks, V. K. Lazarov, C. Chen, Z. Wang, and Y. Ikuhara, *Atomic-Scale Structure and Properties of Highly Stable Antiphase Boundary Defects in Fe_3O_4*, Nat. Commun. **5**, 5740 (2014).

[33] Z. Nedelkoski, D. Kepaptsoglou, L. Lari, T. Wen, R. A. Booth, S. D. Oberdick, P. L. Galindo, Q. M. Ramasse, R. F. L. Evans, S. Majetich *et al.*, *Origin of Reduced Magnetization and Domain Formation in Small Magnetite Nanoparticles*, Sci. Rep. **7**, 45997 (2017).

[34] R. Chen, M. G. Christiansen, A. Sourakov, A. Mohr, Y. Matsumoto, S. Okada, A. Jasanoff, and P. Anikeeva, *High-Performance Ferrite Nanoparticles through Nonaqueous Redox Phase Tuning*, Nano Lett. **16**, 1345 (2016).

[35] H. Khurshid, W. Li, S. Chandra, M.-H. Phan, G. C. Hadjipanayis, P. Mukherjee, and H. Srikanth, *Mechanism and Controlled Growth of Shape and Size Variant Core/Shell FeO/Fe_3O_4 Nanoparticles*, Nanoscale **5**, 7942 (2013).

[36] M. Estrader, A. López-Ortega, I. V. Golosovsky, S. Estradé, A. G. Roca, G. Salazar-Alvarez, L. López-Conesa, D. Tobia, E. Winkler, J. D. Ardisson *et al.*, *Origin of the Large Dispersion of Magnetic Properties in Nanostructured Oxides: Fe_xO/Fe_3O_4 Nanoparticles as a Case Study*, Nanoscale **7**, 3002 (2015).

[37] P. Tancredi, P. C. R. Rojas, O. Moscoso-Londoño, U. Wolff, V. Neu, C. Damm, B. Rellinghaus, M. Knobel, and L. M. Socolovsky, *Synthesis Process, Size and Composition Effects of Spherical Fe_3O_4 and $FeO@Fe_3O_4$ Core/Shell Nanoparticles*, New J. Chem. **41**, 15033 (2017).

[38] S. J. L. Billinge and I. Levin, *The Problem with Determining Atomic Structure at the Nanoscale*, Science **316,** 561 (2007).

[39] T. Egami and S. J. L. Billinge, *Underneath the Bragg Peaks: Structural Analysis of Complex Materials* (Elsevier, Oxford, UK, 2003), 1 st ed., Vol. 7.

[40] G. Vallejo-Fernandez, O. Whear, A. G. Roca, S. Hussain, J. Timmis, V. Patel, and K. O'Grady, *Mechanisms of Hyperthermia in Magnetic Nanoparticles*, J. Phys. D **46,** 312001 (2013).

[41] R. Hergt, S. Dutz, and M. Zeisberger, *Validity Limits of the Néel Relaxation Model of Magnetic Nanoparticles for Hyperthermia*, Nanotechnology **21,** 015706 (2010).

[42] R. M. Hazen and R. Jeanloz, *Wüstite (*$Fe_{1-x}O$*): A Review of Its Defect Structure and Physical Properties*, Rev. Geophys. **22,** 37 (1984).

[43] M. J. Hÿtch, J.-L. Putaux, and J.-M. Pénisson, *Measurement of the Displacement Field of Dislocations to 0.03 Å by Electron Microscopy*, Nature (London) **423,** 270 (2003).

[44] See Supplemental Material at http://link.aps.org/supplemental/10.1103/PhysRevX.9.041044 for detailed comparison of different size and shape nanocrystals, including refinement of their structural parameters, together with experimental data and theoretical results quantifying their nanomagnetism.

[45] W. H. Bragg, *XXX. The Structure of the Spinel Group of Crystals*, Lond. Edinb. Dublin Philos. Mag. J. Sci. **30,** 305 (1915).

[46] M. S. Senn, J. P. Wright, and J. P. Attfield, *Charge Order and Three-Site Distortions in the Verwey Structure of Magnetite*, Nature (London) **481,** 173 (2012).

[47] G. Ferguson and M. Hass, *Magnetic Structure and Vacancy Distribution in γ-Fe_2O_3 by Neutron Diffraction*, Phys. Rev. **112,** 1130 (1958).

[48] R. J. Armstrong, A. H. Morrish, and G. A. Sawatzky, *Mössbauer Study of Ferric Ions in the Tetrahedral and Octahedral Sites of a Spinel*, Phys. Lett. **23,** 414 (1966).

[49] A. Tomas, P. Laruelle, J. L. Dormann, and M. Nogues, *Affinement de la structure des formes ordonnée et désordonnée de l'octaoxopentaferrate de lithium,* $LiFe_5O_8$, Acta Crystallogr. C **39,** 1615 (1983).

[50] S. J. Marin, M. O'Keeffe, and D. E. Partin, *Structures and Crystal Chemistry of Ordered Spinels:* $LiFe_5O_8$*,* $LiZnNbO_4$*, and* Zn_2TiO_4, J. Solid State Chem. **113,** 413 (1994).

[51] G. W. Van Oosterhout and C. J. M. Rooijmans, *A New Superstructure in Gamma-Ferric Oxide*, Nature (London) **181,** 44 (1958).

[52] C. Greaves, *A Powder Neutron Diffraction Investigation of Vacancy Ordering and Covalence in γ-Fe_2O_3*, J. Solid State Chem. **49,** 325 (1983).

[53] S. Yang and X. Ren, *Noncubic Crystallographic Symmetry of a Cubic Ferromagnet: Simultaneous Sructural Change at the Ferromagnetic Transition*, Phys. Rev. B **77,** 014407 (2008).

[54] H. Y. Huang, Z. Y. Chen, R.-P. Wang, F. M. F. de Groot, W. B. Wu, J. Okamoto, A. Chainani, A. Singh, Z.-Y. Li, J.-S. Zhou *et al.*, *Jahn-Teller Distortion Driven Magnetic Polarons in Magnetite*, Nat. Commun. **8,** 15929 (2017).

[55] B. Antic, M. Perovic, A. Kremenovic, J. Blanusa, V. Spasojevic, P. Vulic, L. Bessais, and E. S. Bozin, *An Integrated Study of Thermal Treatment Effects on the Microstructure and Magnetic Properties of Zn–Ferrite Nanoparticles*, J. Phys. Condens. Matter **25,** 086001 (2013).

[56] V. Petkov, P. D. Cozzoli, R. Buonsanti, R. Cingolani, and Y. Ren, *Size, Shape, and Internal Atomic Ordering of Nanocrystals by Atomic Pair Distribution Functions: A Comparative Study of γ-Fe_2O_3 Nanosized Spheres and Tetrapods*, J. Am. Chem. Soc. **131,** 14264 (2009).

[57] F. Walz, *The Verwey Transition—A Topical Review*, J. Phys. Condens. Matter **14,** R285 (2002).

[58] A. P. Roberts, Y. Cui, and K. L. Verosub, *Wasp-Waisted Hysteresis Loops: Mineral Magnetic Characteristics and Discrimination of Components in Mixed Magnetic Systems*, J. Geophys. Res. Solid Earth **100,** 17909 (1995).

[59] Q. Song and Z. J. Zhang, *Controlled Synthesis and Magnetic Properties of Bimagnetic Spinel Ferrite $CoFe_2O_4$ and $MnFe_2O_4$ Nanocrystals with Core–Shell Architecture*, J. Am. Chem. Soc. **134,** 10182 (2012).

[60] M. Vasilakaki and K. N. Trohidou, *Numerical Study of the Exchange-Bias Effect in Nanoparticles with Ferromagnetic Core/Ferrimagnetic Disordered Shell Morphology*, Phys. Rev. B **79,** 144402 (2009).

[61] M. Vasilakaki, K. N. Trohidou, and J. Nogués, *Enhanced Magnetic Properties in Antiferromagnetic-Core/Ferrimagnetic-Shell Nanoparticles*, Sci. Rep. **5,** 9609 (2015).

[62] P. J. Saines, M. G. Tucker, D. A. Keen, A. K. Cheetham, and A. L. Goodwin, *Coupling of the Local Defect and Magnetic Structure of Wüstite $Fe_{1-x}O$*, Phys. Rev. B **88,** 134418 (2013).

[63] T. R. Welberry, D. J. Goossens, and A. P. Heerdegen, *Local Order in Wüstite Using a Pair Distribution Function (PDF) Approach*, Mineral Mag. **78,** 373 (2014).

[64] E. E. Fullerton, J. S. Jiang, and S. D. Bader, *Hard/Soft Magnetic Heterostructures: Model Exchange-Spring Magnets*, J. Magn. Magn. Mater. **200,** 392 (1999).

[65] S. K. Arora, R. G. S. Sofin, A. Nolan, and I. V. Shvets, *Antiphase Boundaries Induced Exchange Coupling in Epitaxial Fe_3O_4 Thin Films*, J. Magn. Magn. Mater. **286,** 463 (2005).

[66] M. P. Morales, S. Veintemillas-Verdaguer, M. I. Montero, C. J. Serna, A. Roig, L. Casas, B. Martínez, and F. Sandiumenge, *Surface and Internal Spin Canting in $\gamma - Fe_2O_3$ Nanoparticles*, Chem. Mater. **11,** 3058 (1999).

[67] M. S. Carrião and A. F. Bakuzis, *Mean-Field and Linear Regime Approach to Magnetic Hyperthermia of Core–Shell Nanoparticles: Can Tiny Nanostructures Fight Cancer?*, Nanoscale **8,** 8363 (2016).

[68] C.-J. Chen, R.-K. Chiang, H.-Y. Lai, and C.-R. Lin, *Characterization of Monodisperse Wüstite Nanoparticles Following Partial Oxidation*, J. Phys. Chem. C **114,** 4258 (2010).

[69] D. W. Kavich, J. H. Dickerson, S. V. Mahajan, S. A. Hasan, and J.-H. Park, *Exchange Bias of Singly Inverted FeO/Fe_3O_4 Core-Shell Nanocrystals*, Phys. Rev. B **78,** 174414 (2008).

[70] L. M. Bronstein, X. Huang, J. Retrum, A. Schmucker, M. Pink, B. D. Stein, and B. Dragnea, *Influence of Iron Oleate*

Complex Structure on Iron Oxide Nanoparticle Formation, Chem. Mater. **19**, 3624 (2007).

[71] M. I. Bodnarchuk, M. V. Kovalenko, H. Groiss, R. Resel, M. Reissner, G. Hesser, R. T. Lechner, W. Steiner, F. Schäffler, and W. Heiss, *Exchange-Coupled Bimagnetic Wüstite/Metal Ferrite Core/Shell Nanocrystals: Size, Shape, and Compositional Control,* Small **5**, 2247 (2009).

[72] W. W. Yu, J. C. Falkner, C. T. Yavuz, and V. L. Colvin, *Synthesis of Monodisperse Iron Oxide Nanocrystals by Thermal Decomposition of Iron Carboxylate Salts,* Chem. Commun. **20**, 2306 (2004).

[73] C. A. Schneider, W. S. Rasband, and K. W. Eliceiri, *NIH Image to ImageJ: 25 Years of Image Analysis,* Nat. Methods **9**, 671 (2012).

[74] C. L. Farrow, P. Juhas, J. W. Liu, D. Bryndin, E. S. Božin, J. Bloch, T. Proffen, and S. J. L. Billinge, *PDFfit2 and PDFgui: Computer Programs for Studying Nanostructure in Crystals,* J. Phys. Condens. Matter **19**, 335219 (2007).

[75] F. Gazeau, J. C. Bacri, F. Gendron, R. Perzynski, Yu. L. Raikher, V. I. Stepanov, and E. Dubois, *Magnetic Resonance of Ferrite Nanoparticles: Evidence of Surface Effects,* J. Magn. Magn. Mater. **186**, 175 (1998).

[76] G. F. Goya, T. S. Berquó, F. C. Fonseca, and M. P. Morales, *Static and Dynamic Magnetic Properties of Spherical Magnetite Nanoparticles,* J. Appl. Phys. **94**, 3520 (2003).

[77] K. Binder and D. Heermann, *Monte Carlo Simulation in Statistical Physics: An Introduction,* 5th ed. (Springer-Verlag, Berlin, Heidelberg, 2010).

CONDENSED MATTER PHYSICS

Entropic elasticity and negative thermal expansion in a simple cubic crystal

David Wendt[1]*, Emil Bozin[1], Joerg Neuefeind[2], Katharine Page[2], Wei Ku[1†], Limin Wang[1‡], Brent Fultz[3], Alexei V. Tkachenko[4], Igor A. Zaliznyak[1§]

While most solids expand when heated, some materials show the opposite behavior: negative thermal expansion (NTE). In polymers and biomolecules, NTE originates from the entropic elasticity of an ideal, freely jointed chain. The origin of NTE in solids has been widely believed to be different. Our neutron scattering study of a simple cubic NTE material, ScF_3, overturns this consensus. We observe that the correlation in the positions of the neighboring fluorine atoms rapidly fades on warming, indicating an uncorrelated thermal motion constrained by the rigid Sc-F bonds. This leads us to a quantitative theory of NTE in terms of entropic elasticity of a floppy network crystal, which is in remarkable agreement with experimental results. We thus reveal the formidable universality of the NTE phenomenon in soft and hard matter.

INTRODUCTION

Near-zero or negative thermal expansion (NTE) is well known in metallic alloys of the invar ($Fe_{0.64}Ni_{0.36}$) family, where it is closely related to electronic magnetism (1). These alloys are widely used in applications requiring dimensional stability of metallic parts, e.g., in precision instruments, watches, and engines. Until recently, much less attention was paid to insulating NTE ceramics, which hold promise for numerous applications in electronics, optics, and medicine (2–5). Somewhat surprisingly, because of the specific crystal lattice geometry, NTE in these materials can have the same physical origin as a more common, positive thermal expansion (PTE): atomic thermal motion.

Interest in these systems was renewed with the observation of large isotropic NTE in zirconium tungstate, ZrW_2O_8, and then in the structurally related AM_2O_8, AM_2O_7, and $A_2M_3O_{12}$ phases (A = Zr, Hf, Sc, Y, ... and M = W, V, Mo, P, ...) and their solid solutions (2, 6), which opened avenues for designing ceramic materials with tailored thermal expansion (2–5). These compounds have complex crystal structures, which can be viewed as three-dimensional (3D) networks of AX_6 octahedra and MX_4 tetrahedra (X = O) that share the corner X atoms and, most importantly, contain nearly straight, twofold-coordinated M-X-M and M-X-A linkages [the so-called open framework structures (2)].

NTE in such a structure can be explained by the transverse thermal motion of anion atoms, X, in the presence of the strong M-X bond, which has small or negligible thermal expansion: the so-called guitar string effect (2, 7, 8). As the amplitude of the anion transverse vibration increases with temperature, the metal atoms in M-X-M linkages are pulled closer together, thus causing the net contraction of the structure. While this simple picture does not consider the correlated motion of nearby X anions caused by their interactions in the lattice, in what follows, we show that it provides an adequate description of NTE in ScF_3 (9).

An appealing model for including anion correlation considers vibrations that preserve the structure of the MX_n polyhedra, which thus move as rigid bodies, without deforming the anion-anion bonds (2, 10–13). The relative importance of such rigid unit modes (RUMs) has been rationalized by arguing that vibrations distorting the high symmetry of the polyhedron must have a high energy cost and therefore contribute relatively little to NTE (5). A priori, such an ad hoc assumption is not required for the NTE effect, and its relevance has been a matter of debate (2, 5, 10–20). In a structure that is underconstrained, RUMs correspond to zero-energy floppy phonon modes (5, 10). In a fully constrained structure, such as a cubic network of corner-sharing octahedra in ScF_3 (Fig. 1A), vibrations that do not distort polyhedra are only present on special low-dimensional manifolds occupying zero volume fraction of the system's phase space (5, 10). Nevertheless, it has been argued that phonons in the vicinity of these manifolds, quasi-RUM, which involve only small distortions of the polyhedra, have special importance for NTE. ScF_3 was suggested to be a perfect example of an NTE system where the tension effect is enabled by RUM (Fig. 1B) (5).
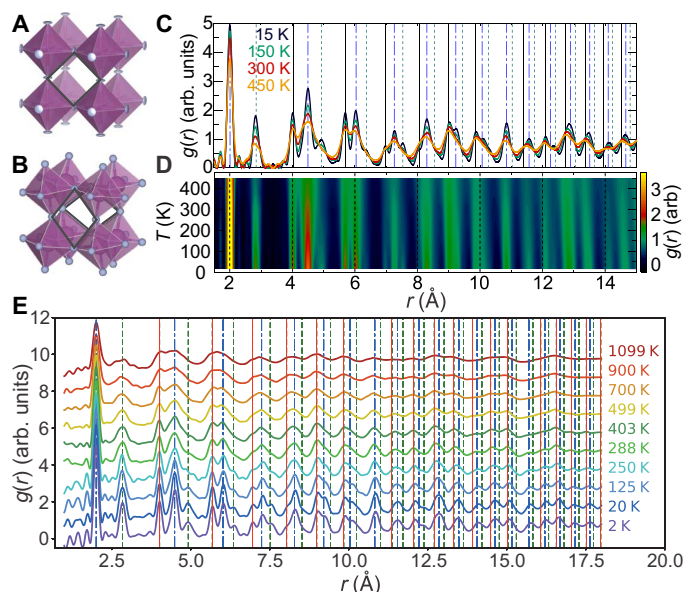
RESULTS

Pair distribution function (PDF) analysis (20, 21) of neutron total scattering is a powerful and direct experimental method for studying average local atomic structures and their relevance for NTE (5, 21). The PDF, $g(r)$, which is obtained from the measured scattering intensity, $S(Q)$, gives the probability distribution of interatomic distances weighted by the scattering lengths of the constituent atoms and thus is uniquely sensitive to local structural patterns. Figure 1 (C to E) presents the PDF of ScF_3 measured on NPDF (C and D) and NOMAD (E) neutron diffractometers at temperatures from 2 to 1099 K. These measurements are complementary and show good agreement in the temperature range where they overlap.

An inspection of $g(r)$ curves reveals several remarkable features, of which the most important is the distinct behavior of Sc-F and F-F pair distributions. NTE of the average crystal structure is manifested by the systematic negative shift to smaller r of PDF peaks from atomic pairs with large separation, r, with increasing temperature. It is most clearly seen in Fig. 1D. The nearest F-F (≈ 2.8 Å) peak shows similar NTE behavior. On the other hand, the nearest-neighbor Sc-F (≈ 2 Å) peak shifts on heating to slightly larger r, consistent with the conventional PTE (7, 22). This peak broadens only moderately with temperature, by about

[1]Condensed Matter Physics and Materials Science Division, Brookhaven National Laboratory, Upton, NY 11973, USA. [2]Neutron Scattering Division, Oak Ridge National Laboratory, Oak Ridge, TN 37831, USA. [3]Department of Applied Physics and Materials Science, California Institute of Technology, Pasadena, CA 91125, USA. [4]CFN, Brookhaven National Laboratory, Upton, NY 11973, USA.
*Present address: Stanford University, Stanford, CA 94305, USA.
†Present address: Tsung-Dao Lee Institute & School of Physics and Astronomy, Shanghai Jiao Tong University, Shanghai 200240, China.
‡Present address: GE Healthcare, Chicago, IL, USA.
§Corresponding author. Email: zaliznyak@bnl.gov

Fig. 1. Crystal structure and PDF in ScF₃. (**A**) $Pm\bar{3}m$ cubic perovskite crystal structure of ScF_3. Disc-shaped ellipsoids at the vertices of Sc-centered octahedra illustrate large and anisotropic thermal displacements (TDs) of fluorine atoms refined at 500 K. (**B**) Traditional ball-and-stick representation of the structure, which illustrates the octahedral tilts within the putative rigid unit motion (RUM) model. (**C**) PDF, $g(r)$, in the temperature range of 15 to 450 K obtained from neutron total scattering measurement of ScF_3 powder sample on NPDF using the wave vector range up to $Q_{max} = 27$ Å^{-1}. (**D**) The color map representation of the temperature evolution of $g(r)$ emphasizes the negative shift of peaks with increasing temperature, which is most evident at large r. (**E**) PDF measured on the same sample on NOMAD diffractometer for temperatures from 2 to 1100 K (bottom to top). Here, each curve is an average of $g(r)$ obtained using the wave vector ranges with Q_{max} varying from 23 to 32 Å^{-1} by increments of 1 Å^{-1}. For visibility, data at each temperature above 2 K are shifted upward by 1. The vertical lines in (C) and (E) mark nominal distances corresponding to Sc-F (dash-dotted), F-F (dashed), and Sc-Sc (overlapping with lattice repeats; solid) atom pairs in the ScF_3 structure.

20% at 450 K (this accounts for the decrease of peak maximum in Fig. 1), indicating a very stiff Sc-F bond. In contrast, the width of the nearest F-F peak increases markedly, revealing rapid loss of F-F correlation with increasing thermal motion. Even more marked is the behavior of further-neighbor F-F distributions. The corresponding peaks [marked by dashed lines in Fig. 1 (C and E)] are only present at $T \lesssim 300$ K and entirely disappear at higher temperatures, suggesting complete loss of positional correlation between further-neighbor F atoms. Such a liquid-like F-F PDF pattern indicates randomly phased transverse local motion of F atoms and is inconsistent with the RUM model where a large number of F-F distances are constrained by the rigid unit geometry (5, 18, 19). Also see the Supplementary Materials for additional discussion.

We quantify the observed behaviors by fitting the first several PDF peaks, which are well resolved and can be uniquely associated with distance distributions of particular atomic pairs, to Gaussian distributions (Fig. 2, A to C). The results of this analysis are summarized in Fig. 2 (D to F). While the Sc-F bond shows PTE of ≈5 parts per million (ppm) at 1000 K, both Sc-Sc, $r_{Sc-Sc} = a$ [lattice repeat distance (LRD)], and the nearest F-F, r_{F-F}, distances exhibit NTE about twice larger in magnitude (Fig. 2D). The large error bars on r_{F-F} reflect marked broadening of the F-F peak with temperature. While the full

width at half maximum (FWHM) of Sc-F and Sc-Sc (LRD) peaks increases by less than 50% at 1000 K, the width of the nearest F-F distribution shows nearly an order-of-magnitude larger change, increasing to nearly 1 Å (Fig. 2E). This indicates an uncertainty of the nearest F-F distance that is comparable to the r_{F-F} distance itself, invalidating the RUM model assumption of quasi-rigid ScF_6 octahedra.

The loss of F-F pair correlation is further revealed by the temperature dependence of the intensity of the LRD (≈ 4 Å) peak (Fig. 2F). It contains partial contributions from both nearest-neighbor Sc-Sc and next-nearest-neighbor F-F pairs, in proportion $\sigma_{Sc} : 3\sigma_F \approx 1.6$, where σ_{Sc} and σ_F are coherent scattering cross sections of Sc and F, respectively. A PDF peak presents the probability distribution of interatomic distance; therefore, its integral intensity must be temperature independent. This roughly holds for Sc-F peak. A small systematic drift of its intensity, which is likely caused by T-dependent background, is within the error bar of the average value. In contrast, the LRD peak rapidly loses a substantial part of its intensity above ≈300 K, where F-F correlations disappear. The decrease is consistent with the loss of the entire ≈40% partial contribution of F-F pairs, which, above ≈300 K, contribute to broad background rather than to the narrow LRD peak described by the fit.

Motivated by these observations, we use a simple model for the probability distribution of the nearest F-F distance, which is presented in Fig. 3. It assumes uncorrelated thermal motion of individual F atoms, which is subject to a single constraint of the rigid Sc-F bond. If Sc atoms were fixed at the nodes of ScF_3 lattice, then the constraint would result in F atoms following ring trajectories with the Sc-F bond sweeping a cone. The resulting r_{F-F} probability distribution would be that of a distance between two points randomly positioned on the two nearest rings. This model has no adjustable parameters because the radius of the rings, $r_\perp$ (the average transverse deviation of F), and $r_{Sc-Sc} = a$ are obtained from the Rietveld refinement of the coherent Bragg scattering contained in our data (Fig. 4, B and C).

The model can also be set up using Sc-F and Sc-Sc distances obtained from PDF peaks in Fig. 2, although the accuracy of this refinement is lower. While larger systematic error in this approach affects some of the analysis below ≈200 K where changes are weak, above this temperature, this analysis gives results in close agreement with Figs. 3A and 4A.

Unexpectedly, when broadened by convolution with the Gaussian of the same width as Sc-F peak at 2 K to account for experimental resolution (truncation), our oversimplified model provides adequate description of the measured F-F distribution for all temperatures where NTE is observed (dashed lines in Figs. 3A and 4A). In this model, the peak maximum follows lattice NTE, in agreement with Fig. 2D. The model can be further improved if, instead of rings [or conventional Gaussian thermal displacement (TD) ellipsoids; Fig. 3B], F atoms are randomly positioned on a torus-shaped Gaussian distribution peaked at the same major diameter, $2r_\perp$, and with the minor diameter representing the F part of the Sc-F peak FWHM (Fig. 3C). This improved model conjectured by Sleight (2) provides slightly better agreement with the data (Fig. 3A), as quantified by the reduced mean square deviation, χ^2, presented in Fig. 4A. The χ^2 analysis is a standard way to evaluate the goodness of fit: Where $\chi^2 \approx 1$, the data are indistinguishable from the model. With $N \approx 11$ effectively independent data points used in our comparison, $\chi^2 < 3$ places the model within 3σ interval or above 99.5% likelihood level. The model begins to fail above ≈700 K, where χ^2 increases to ~10, but NTE also fades. Below ≈200 K, the broadening of the F-F peak is small and $\chi^2 \lesssim 1$,
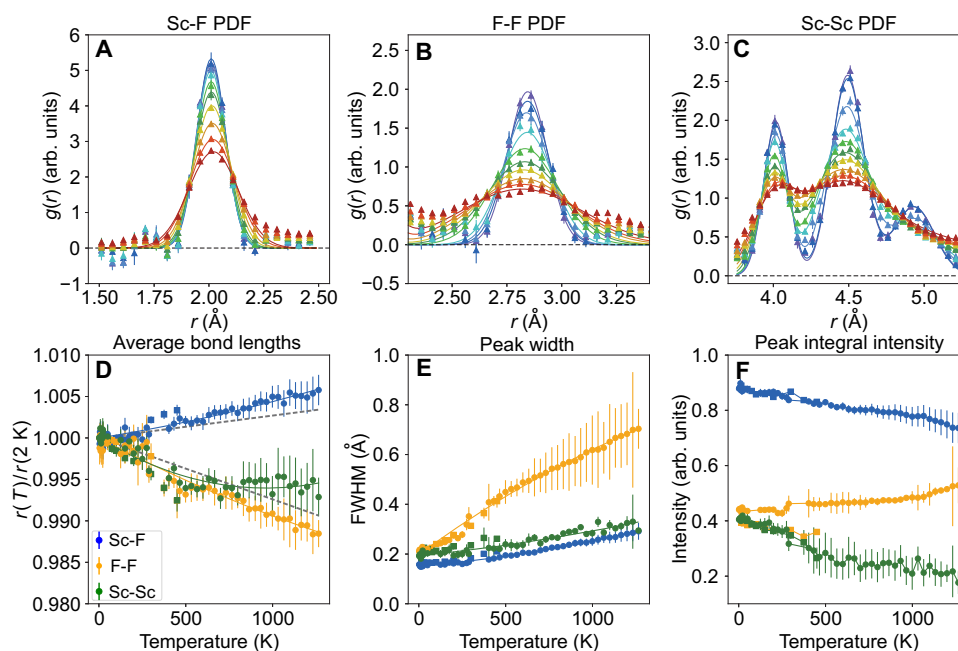
Fig. 2. Pair probability distribution for the nearest-neighbor Sc-F, F-F, and Sc-Sc (LRD) pairs. PDF data for Sc-F (**A**), F-F (**B**), and Sc-Sc [(**C**), left peak] for the same selected temperatures and with the same color coding as in Fig. 1E (symbols) with Gaussian fits (solid lines). The first two peaks, which correspond to nearest-neighbor Sc-F and F-F pairs, can be isolated and were fitted individually taking into account a small intensity overlap, which was either subtracted from the data (A) or added to the fit (B): A small overlapping intensity contribution of the F-F ($\approx$2.8Å) peak to the Sc-F ($\approx$2.Å) peak is seen in (B); this contribution has been computed from the model (see text) and subtracted from the data in (A). Because of an overlap of the LRD ($\approx$4 Å) peak with the next-nearest Sc-F and next-next-nearest F-F peaks, all three were fitted together to a sum of Gaussians, within the data range [3.75 Å, 5.25 Å]. (**D**) The temperature dependence of the bond lengths obtained from the Gaussian peak position in (A) to (C) shows normal thermal expansion of the Sc-F bond and the contraction of the lattice repeat and the F-F bond. (**E**) FWHM of the PDF peaks, reflective of the atomic thermal motion. The broadening of the F-F peak is anomalous. Solid lines in (D) and (E) show fits to quadratic polynomial serving as guides for the eye; dashed lines in (D) are our prediction from entropic elasticity theory for Sc-F and Sc-Sc distances. (**F**) The integral intensities of the PDF peaks count the participating atoms and nominally should be T independent; the anomalous loss of the lattice repeat (Sc-Sc) peak intensity indicates loss of the coherent fluorine contribution. Circles are obtained from the NOMAD data, and squares are obtained from the NPDF data. The error bars show 1 SD accounting for the systematic error; the truncation error in (A) to (C) was estimated by averaging PDFs obtained from the data truncated at different Q_{max} values, from 23 to 32 Å^{-1}.

which means that within the experimental error, our model cannot be distinguished from other models, such as RUM.

DISCUSSION

The essential implication of our analysis is that thermal motion of even the nearest F atoms is uncorrelated rather than in RUM (Fig. 3, D and E). The spread of the F-F PDF peak with temperature follows from the increase in size of the manifold (circle or torus) populated by each F atom in the course of its thermal motion. Underlying this model is the phenomenon of energy scale separation, where two very different energies govern longitudinal and transverse motion of the F ion.

Then, in some temperature range, transverse modes can be thermally excited and the corresponding degrees of freedom can be equipartitioned, while longitudinal vibrations are still frozen out. In this case, Sc-F bonds are rigid, while F transverse vibrations are uncorrelated. Inspection of the vibrational spectra measured in ScF$_3$ ([17, 18, 22]) reveals two major phonon groups, which give rise to maxima in the density of states below $\hbar\omega_t \approx 22$ meV and above $\hbar\omega_l \approx 62$ meV. These correspond to transverse and longitudinal vibrations, respectively. This separation of energy scales implies that transverse degrees of freedom are thermally excited and equipartitioned at $T > \hbar\omega_t/k_B \approx 260$ K (k_B is Boltzmann constant), while the longitudinal rigidity of the Sc-F bond persists up to at least $T \approx \hbar\omega_l/k_B \approx 710$ K. This is exactly the temperature range

where NTE is observed and where our model provides very good description of the PDF data (Fig. 4).

The exceptional longitudinal rigidity of the Sc-F bond, which underlies the NTE mechanism in ScF$_3$, is rooted in covalence, where the hybridization of Sc and F electronic orbitals that lie deep inside the valence band is responsible for the large energy cost of changing the Sc-F distance ([23–26]). Also see the Supplementary Materials for additional discussion. This Lewis-type dative bonding, where paired electrons delocalize between ions to lower their kinetic energy, has recently been described as a "charge transfer bond" ([24]). Although it has long been known that ScF$_3$ is anomalous among supposedly ionic metal trifluorides, MF$_3$ (M = Al, Sc, Fe, In, ...) ([27]), only relatively recently has the exceptional strength of the Sc-F bond been traced to the covalent nature of the valence molecular orbitals (MOs). The comparative analysis of the x-ray photoemission spectra and the density functional theory (DFT) electronic structure calculations ([25]) for the (ScF$_6$)$^{3-}$ cluster have indicated a large contribution to the Sc-F bonding energy of a specific (5a_1) $d - p$ MO at ≈ -5 eV. A modest hybridization ($|5a_1\rangle \approx 0.83 |F2p\rangle + 0.16 |Sc3d\rangle$) does not lead to sizeable charge transfer such that Sc^{3+} and F$^-$ appear to be close to their nominal ionic oxidation states. We performed DFT electronic structure calculations in ScF$_3$, which further support these findings, indicating slightly hybrid valence bands below ~ -4 eV and strong anisotropy of the effective potential of F ions ([26]). Also see the Supplementary Materials for additional discussion.
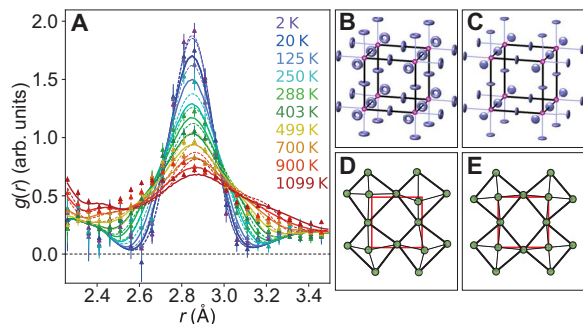
Fig. 3. Model for the fluorine motion and pair distance distribution. (**A**) PDF for the nearest-neighbor F-F bond (symbols, same as in Fig. 2B). The dashed lines show a simplified model for the F-F probability distribution, where positions of the fluorine atoms are randomly distributed on the circles whose radius is determined by the measured TD parameter obtained from Rietveld refinement. The model was broadened by convolution with the Gaussian of the same width as Sc-F peak at 2 K to account for Sc zero-point motion and truncation effects. The solid lines show an improved model, where circles are replaced by the torus-shaped Gaussian distributions peaked at the same major radius and with the width, represented by the minor radius, which is equal to $1/\sqrt{2}$ of the Sc-F peak width. The model adequately captures the evolution of the F-F peak position with temperature (Fig. 2D). (**B**) ScF_3 structure illustrating our model with the tori populated by F thermal motion under the constraint of a rigid Sc-F bond. (**C**) Traditional representation of the same structure using atomic TD ellipsoids. Both are shown for parameters refined at 500 K. (**D**) In our model, the entropic motion of F atoms distorts the fluorine octahedra, thereby erasing F-F positional correlation, in agreement with the experiment. (**E**) Opposite to what is observed, rigid octahedra in the RUM model preserve the nearest-neighbor F-F bond and also partially preserve the next-nearest-neighbor F-F correlation, which contributes to the LRD peak.

These observations immediately suggest a simple theoretical description of the NTE effect, where each Sc-F bond is treated as a rigid monomer link and the entire ScF_3 crystal structure is treated as a floppy network of such freely jointed monomers, a direct 3D analog of the celebrated model of polymer chains (Fig. 3, B and D) (28, 29). Without electrostatic interactions, the network is underconstrained (floppy): The number of constraints imposed by rigid Sc-F links is six per unit cell, while the number of degrees of freedom is 12. In particular, the motion of the Sc ion is constrained by rigid bonds in all three directions, while each of the F ions has two zero-energy displacement modes corresponding to motion orthogonal to the Sc-F bond. In the absence of external tension, the system has no rigidity and would collapse. In ScF_3, net Coulomb repulsion between charged ions provides tension (negative pressure), which stabilizes the system and balances its entropic elasticity (see the Supplementary Materials for additional discussion).

We thus separate interactions in the system into a sum of the nearest-neighbor pair potentials, which include the cumulative effect of electrostatic Coulomb attraction, core repulsion, and covalent bonding and, in the simplest approximation, are treated as rigid links and the remaining Coulomb potential of non–nearest-neighbor ions. The resulting effective Hamiltonian for the fluorine transverse motion is (see the Supplementary Materials for additional discussion)

$$H = K + \frac{3N(6-M)e^2}{4\pi\epsilon_0 r} - \sum_i \frac{\tilde{\gamma}e^2}{4\pi\epsilon_0 r^3} \frac{\mathbf{u}_{i\perp}^2}{2} \qquad (1)$$

where K is the kinetic energy, $M \approx 2.98$ is the Madelung constant for ScF_3 lattice, $r = a/2$ is half of the lattice repeat, N is the number of sites,

e is the electron charge, ϵ_0 is the vacuum permittivity, $\mathbf{u}_{i\perp}$ is the transverse displacement of the F ion at lattice site i, and $\tilde{\gamma} \approx 1.8$ was obtained by lattice summation of Coulomb interactions, similarly to the Madelung constant (See the Supplementary Materials for additional discussion). On account of the rigid link constraint, Hamiltonian (Eq. 1) describes the F floppy modes as independent Einstein-type oscillators with the frequency, $\hbar\omega_0 = \hbar e\sqrt{\frac{(6-M-\tilde{\gamma})}{4\pi\epsilon_0 r^3 m_F}} \approx 21.6$ meV. This value compares very favorably with the phonon dispersions measured in ScF_3, where low-energy peaks in the density of states are observed below $\hbar\omega_t \approx 22$ meV.

Although the Einstein approximation is expected to perform poorly at low temperatures, where the exact phonon dispersions are important for determining the bulk thermodynamic properties such as heat capacity or thermal expansion, it works well at $k_B T > \frac{1}{2}\hbar\omega_0$, where the equipartition theorem sets the thermal average of an oscillator Hamiltonian to $k_B T$ per degree of freedom. In this regime, heat capacity obeys the Dulong-Petit law, which is equally well described by both Einstein and Debye models. We thus expect our description, Eq. 1, to be applicable for $T \gtrsim 130$ K. Because each of the F floppy modes has a Hamiltonian of an oscillator with frequency ω_0, the value of $\langle u_\perp^2 \rangle = \langle u_{i\perp}^2 \rangle$ can be found with the full account for quantum effects and for an arbitrary temperature (23). We thus obtain the NTE effect, $\frac{r-r_0}{r_0} \approx -\frac{\langle u_\perp^2 \rangle}{2r_0^2} \approx \alpha T$, where r_0 is r at $T = 0$ and $\alpha = -\frac{(4\pi\epsilon_0 r_0 k_B)}{(6-M-\tilde{\gamma})e^2} \approx -10.1 \cdot 10^{-6}$K^{-1}, in an impressive agreement with the experimental value (Fig. 4C) (9).

An account for the finite rigidity of the Sc-F bond is done by replacing the rigid link constraint with an interaction potential, $V_b(r_b) \approx V_b(r_0) + f_0(r_b - r_0) + \frac{1}{2}k(r_b - r_0)^2$. Here, r_b is the bond length, f_0 is the tension force that Sc-F linkage provides to compensate the negative electrostatic pressure, and k is the effective harmonic spring constant (see the Supplementary Materials for additional discussion). From the measured frequency of the longitudinal Sc-F phonon mode, $\hbar\omega_l \approx 62$ meV, we estimate that $kr_0^2 \approx 26$ eV, which is in good agreement with our DFT results (see the Supplementary Materials for additional discussion). The minimization of the resulting free energy, which includes the entropic term, electrostatics, and bond potential, $V(r_b)$

$$F =$$
$$3N\left[-k_B T\ln\left(r_b^2 - r^2\right) + \frac{(6-M)e^2}{4\pi\epsilon_0 r} - \frac{\tilde{\gamma}e^2}{4\pi\epsilon_0 r^3}\frac{(r_b^2 - r^2)}{2} + 2V_b(r) \right]$$
$$(2)$$

with respect to both r and r_b, yields the equilibrium values $r = r(T)$ and $r_b = r_b(T)$. We thus obtain the relation $\frac{r-r_0}{r_0} - \frac{r_b-r_0}{r_0} \approx \alpha T$, which means that the net entropic tension effect is split between PTE of the Sc-F bond and NTE of the lattice. It further yields the relation $\frac{r_b-r_0}{r_0} = -\beta\frac{r-r_0}{r_0}$, where $\beta \approx 0.36$, which determines the relative split between the two effects, $\frac{r_b-r_0}{r_0} = \frac{\alpha\beta}{1+\beta}T \approx 2.7 \cdot 10^{-6}T$ and $\frac{r-r_0}{r_0} = \frac{\alpha}{1+\beta}T \approx -7.4 \cdot 10^{-6}T$ (see the Supplementary Materials for additional discussion). These predictions are shown by dashed lines in Figs. 2D and 4C, which demonstrate remarkable agreement of our simple theory with experiment. We note that in our estimates, we neglected the covalent reduction of the ionic charge on F and Sc ions, which would increase the predicted NTE effect by $\approx 20\%$. This provides a ballpark estimate for the accuracy of our predictions. The leading effect of the presence of defects, such as F vacancies, or dipolar defects, which consists of a proportional change of the negative electrostatic pressure and, correspondingly,
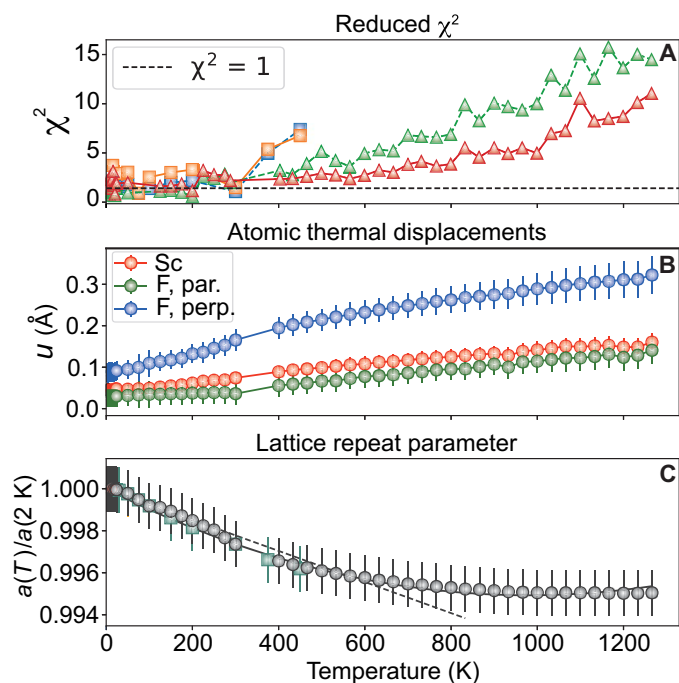
Fig. 4. The rigid-bond entropic elasticity model and NTE in ScF₃. (**A**) Reduced χ^2 quantifying the accuracy of the entropic model presented in Fig. 3 in describing our NOMAD (triangles) and NPDF (squares) data. Symbols connected by the dashed line show χ^2 for the simplified model with circles in place of tori, which is consistently slightly higher. (**B**) Atomic TD parameters and (**C**) lattice repeat, $a(T)/a$ (2 K), obtained from the Rietveld refinement of our neutron powder diffraction data, which are used to model the F-F probability distribution. Note that our model has no adjustable parameters: All numbers needed for the simulated F-F probability distribution (the lattice repeat and the F and Sc TD) are obtained from an independent analysis. Where $\chi^2 \sim 1$, the model is indistinguishable from the data. Above ≈600 K, the model begins to fail, with χ^2 reaching ~10 above 800 K. This is consistent with the failure of its basic assumption of the longitudinally rigid Sc-F bond, which is not unexpected at these high temperatures where the population of the Sc-F longitudinal (≈62 meV) phonon vibrations becomes significant (17). At the same time, the NTE effect fades away (C), indicating that its entropic origin is adequately captured by our model. Note that, at these high temperatures, the fluorine transverse TD approaches 10% of the nearest-neighbor distance [(B) and Fig. 2E], which is close to the Lindemann melting criterion (1).

the bond tension, can also be included in the effective charge. The corresponding correction to the NTE behavior is well within our estimated accuracy.

We conclude that floppy vibration modes associated with the transverse fluorine displacement in an underconstrained network crystal structure of ScF₃ give rise to both NTE of the lattice and positive expansion of the Sc-F bond. The latter effect is distinct from the conventional PTE based on cubic anharmonism of Sc-F bond potential, $V_b(r_b)$ (30). Instead, it originates from entropic elasticity via floppy modes and is already present for the harmonic Sc-F bond. RUM-like correlated vibration modes, which are important for understanding the stability of the cubic crystal structure, appear not to be essential for NTE.

CONCLUSION

In ZrW₂O₈, the RUM model was challenged by x-ray absorption fine structure studies (14) but later was argued to be consistent with

neutron PDF measurements (5, 12, 13). However, for a complex material with more than three different atom types, PDF analysis has a degree of uncertainty because the measured PDF is a sum of PDFs from all atomic pairs where some features may overlap, meaning that it is difficult to identify individual peaks with specific atomic pairs (5). This problem is absent in ScF₃, which has a simple cubic structure with only two atom types. In agreement with the earlier molecular dynamics simulations (17), our present results do not support the presence of RUM, indicating that the only rigid unit is the Sc-F bond. This makes the ScF₃ structure an underconstrained 3D analog of a freely jointed polymer chain.

Our results are directly applicable to other materials with the ScF₃ structure, such as ReO₃, where NTE is observed at ≲200 K (31), or AlF₃, where NTE is not observed because it only adopts the cubic structure above 739 K, where conventional, positive expansion dominates (32).

The general design rule for inorganic NTE materials is thus the presence of a floppy network formed by nearly straight C-A-C linkages, where an underconstrained light anion, A, such as oxygen or fluorine, in a sterically open position, is strongly bound to nearby cations, C (2). This floppy network architecture does not imply any specific geometry of the crystal structure, such as corner-sharing octahedra network in ScF₃. This is exemplified by ZrW₂O₈ and related materials, where, when looking at a crystal structure unobscured by the coordination polyhedra, one can easily identify a network of nearly straight W-O-Zr and W-O-W linkages with an underconstrained and sterically open oxygen position. While the geometry of the resulting network and ionic positions is complex (although not as complex as in polymers), NTE in this structure can still be described using our approach, albeit requiring more cumbersome calculations of electrostatics.

On the basis of our experimental observations, we developed a simple theoretical description of the NTE effect in ScF₃, which is rooted in entropic elasticity of an underconstrained floppy network, similar in spirit to the celebrated Flory–de Gennes theory of polymer elasticity (28, 29). Our approach presents a paradigm shift, where instead of focusing on peculiar energetics of low-energy lattice vibrations, such as RUM (2–5, 7, 9–11, 30, 33–35), these vibrations are approximated by Einstein local phonon modes, and the focus is on their entropic contribution to free energy. Our results provide not only a clear understanding of the entropic elasticity origin of the NTE effect in the practically important class of materials and temperature range, including at and above room temperature, but also an accurate, quantitative, textbook description of NTE, thus opening new avenues for predictive modeling of this effect in solids.

MATERIALS AND METHODS

Neutron scattering measurements for temperatures from 2 to 1266 K were carried out with NOMAD, a time-of-flight total scattering diffractometer at the Spallation Neutron Source, Oak Ridge National Laboratory, using the polychromatic neutron beam. Additional measurements for temperatures from 15 to 450 K were performed using a similar setup with an NPDF total scattering diffractometer at the Manuel Lujan Neutron Scattering Center, Los Alamos National Laboratory. For these measurements, finely pulverized polycrystalline sample (grain size, <50 μm) of cubic ScF₃ crystals (99.99% purity) was loaded into extruded vanadium containers with outer diameter of 1 cm and height of 4 cm. The same sample was used in (17).

For NOMAD measurements, the setup used an Orange cryostat for measurements between 2 and 300 K and an ILL furnace for measurements between 300 and 1266 K. For the NPDF experiment, the

sample was placed in a closed-cycle cryofurnace. The data at each temperature were collected for 15 to 30 min (NOMAD) and 120 min (NPDF) after the temperature equilibration. The Rietveld analysis of Bragg scattering in the obtained neutron powder diffraction data provided accurate information about the average atomic positions and the thermal mean square displacements of atoms in the crystal lattice (Fig. 4).

The atomic PDF analysis based on total scattering approach yields local structural information on different length scales (21), allowing refinement of the mutual positions of nuclei in different atomic pairs. The reduced PDF, $G(r)$, is obtained from the measured total scattering structure factor, $S(Q)$, via a Fourier sine transform, $G(r) = 4\pi r(\rho(r) - \rho_0) = \frac{2}{\pi} \int_0^\infty Q(S(Q) - 1)\sin(Qr)dQ$. Here, ρ_0 is the scattering cross-section weighted atomic number density of the material and $\rho(r)$ is the atomic PDF, which we analyze. It is related to the radial distribution function (RDF), $R(r) = 4\pi r^2 \rho(r) = rG(r) + 4\pi r^2 \rho_0$, which has the useful property that the quantity $R(r)dr$ gives the effective number of atoms in an annulus of thickness dr at a distance r from the given atom, and its integral counts the number of atoms. Both RDF and PDF were considered in this study. In our modeling, we analyzed the atomic PDF, $\rho(r) = R(r)/(4\pi r^2)$, which determines the probability for a pair of atoms to be at a distance r (Figs. 1 to 3).

In practice, the $S(Q)$ total scattering data are measured only within a limited range of wave vectors, Q. The upper limit of integration in the Fourier transform determining the experimental $\rho(r)$ has to be chosen at some finite value, Q_{max}, which includes the data where the measurement accuracy is acceptable. Different Q_{max} values lead to different weighting of the noisier data at large Q. The truncation of the Fourier transform also introduces systematic error in $\rho(r)$ in the form of the finite width of the PDF peaks and an oscillating "background" baseline ("truncation wiggles") (20, 21), which depend on Q_{max}. To evaluate these systematic errors, we analyzed data computed using different Q_{max} values. The nominal Q range covered in our study is [0.5, 35] Å^{-1}. The data were extrapolated to $Q = 0$ and Fourier-transformed using the wave vector ranges, [0, Q_{max}], for Q_{max} varied from 23 to 32 Å^{-1} by increments of 1 Å^{-1}. The $g(r)$ data shown in the figures here, with the exception of Fig. 1 (C and D), were obtained by averaging the data from each Q_{max} range. The error bars account both for the average statistical uncertainty and for the systematic truncation error. The latter is evaluated as the SD of the data obtained using different Q_{max} values. The obtained $g(r)$ data were modeled using custom-made Python scripts.

The model for F-F pair probability distribution was constructed as follows. Considering the Sc-F longitudinal rigidity, the average transverse deviation, $r_\perp$, of the F atoms from the Sc-Sc bond axis and the lattice repeat parameter, a, were retrieved from Rietveld refinement of the Bragg diffraction contained in the corresponding dataset. These parameters can also be obtained from the analysis of PDF peaks; using the Pythagorean theorem, $r_\perp^2 = r_{\text{Sc-F}}^2 - (a/2)^2$, where $r_{\text{Sc-F}}$ is the average Sc-F bond length and a is the lattice repeat parameter measured as the fitted position of the Sc-F and Sc-Sc PDF peaks, respectively. This approach provides generally similar, albeit less accurate, model description because it is less accurate in determining both the lattice repeat and the transverse F displacement. We therefore opted for using the Rietveld refined parameters for our model. The data for 47 temperatures were used. The nearest-neighbor F-F distance distribution was modeled by placing evenly spaced points on perpendicular rings of radius $r_\perp$ and center separation $\frac{a\sqrt{2}}{2}$. The distances between each pair of points (not on the same ring) were calculated, and a histogram was created from the

compiled set of distances. This histogram was then convoluted with a Gaussian distribution of SD equal to that of the Sc-F peak to account for truncation error and uncertainty in Sc atomic position. A second model was then created with rings replaced by Gaussian distributions peaked at these rings, which can be represented by tori of equal major diameter and separation as the rings and with the minor diameter, equal to the Gaussian FWHM, being equal to $\text{FWHM}/\sqrt{2}$ of the Sc-F peak, thus accounting for F atomic position uncertainty instead of convolution. The remaining procedure is identical to that of the first model.

SUPPLEMENTARY MATERIALS

Supplementary Text
Table S1. Scandium ionization energies, $E_i(\text{Sc})$ (45), and fluorine electron affinity, $E_a(\text{F})$ (49), used in eq. S28.
Table S2. Frozen phonon calculation of the energy change as a function of the longitudinal ($\Delta E_\parallel$) and transverse ($\Delta E_\perp$) fluorine displacement in ScF_3.
Table S3. Parameters of an effective potential, $U(x) = \frac{1}{2}kx^2 + \frac{1}{4}k_4x^4$, for the longitudinal, $U_\parallel\left(\frac{r-r_0}{r_0}\right)$, and transverse, $U_\perp\left(\frac{u_\perp}{r_0}\right)$, $r_0 = 2.0\text{Å}$ fluorine displacement in ScF_3.
Table S4. The structural parameters of ScF_3 obtained from Rietveld refinements of NOMAD data showing the standard uncertainty for the lattice spacing, a (measured in Å), and the atomic mean square displacement parameters (measured in 0.01*Å^2), isotropic for Sc ($U_{\text{iso-Sc}}$) and anisotropic for F ($U_{\text{par-F}}$ and $U_{\text{perp-F}}$, both measured in 0.01*Å^2).
Table S5. The structural parameters of ScF_3 obtained from Rietveld refinements of NPDF data including parameters R_{wp} and R_p quantifying the goodness of the fit.
Fig. S1. Electronic band structure in ScF_3.
Fig. S2. Effective potential of the fluorine ion in ScF_3.
Fig. S3. Selected plots of Rietveld refinement of structural parameters in ScF_3.
References (37–55)

REFERENCES AND NOTES

1. C. E. Guillaume, Recherches sur les aciers au nickel. Dilatations aux temperatures elevees; resistance electrique. *C. R. Acad. Sci.* **125**, 235–238 (1897).
2. A. W. Sleight, Isotropic negative thermal expansion. *Annu. Rev. Mater. Sci.* **28**, 29–43 (1998).
3. G. D. Barrera, J. A. O. Bruno, T. H. K. Barron, N. L. Allan, Negative thermal expansion. *J. Phys. Condens. Matter* **17**, R217–R252 (2005).
4. C. Lind, Two decades of negative thermal expansion research: Where do we stand? *Materials* **5**, 1125–1154 (2012).
5. M. T. Dove, H. Fang, Negative thermal expansion and associated anomalous physical properties: Review of the lattice dynamics theoretical foundation. *Rep. Prog. Phys.* **79**, 066503 (2016).
6. T. A. Mary, J. S. O. Evans, T. Vogt, A. W. Sleight, Negative thermal expansion from 0.3 to 1050 Kelvin in ZrW_2O_8. *Science* **272**, 90–92 (1996).
7. L. Hu, J. Chen, A. Sanson, H. Wu, C. Guglieri Rodriguez, L. Olivi, Y. Ren, L. Fan, J. Deng, X. Xing, New insights into the negative thermal expansion: Direct experimental evidence for the "guitar-string" effect in cubic ScF_3. *J. Am. Chem. Soc.* **138**, 8320–8323 (2016).
8. G. Ernst, C. Broholm, G. R. Kowach, A. P. Ramirez, Phonon density of states and negative thermal expansion in ZrW_2O_8. *Nature* **396**, 147–149 (1998).
9. B. K. Greve, K. L. Martin, P. L. Lee, P. J. Chupas, K. W. Chapman, A. P. Wilkinson, Pronounced negative thermal expansion from a simple structure: Cubic ScF_3. *J. Am. Chem. Soc.* **132**, 15496–15498 (2010).
10. A. K. A. Pryde, K. D. Hammonds, M. T. Dove, V. Heine, J. D. Gale, M. C. Warren, Origin of the negative thermal expansion in ZrW_2O_8 and ZrV_2O_7. *J. Phys. Condens. Matter* **8**, 10973–10982 (1996).
11. J. Z. Tao, A. W. Sleight, The role of rigid unit modes in negative thermal expansion. *J. Solid State Chem.* **173**, 442–448 (2003).
12. M. G. Tucker, A. L. Goodwin, M. T. Dove, D. A. Keen, S. A. Wells, J. S. O. Evans, Negative thermal expansion in ZrW_2O_8: Mechanisms, rigid unit modes, and neutron total scattering. *Phys. Rev. Lett.* **95**, 255501 (2005).
13. M. G. Tucker, D. A. Keen, J. S. O. Evans, M. T. Dove, Local structure in ZrW_2O_8 from neutron total scattering. *J. Phys. Condens. Matter* **19**, 335215 (2007).
14. D. Cao, F. Bridges, G. R. Kowach, A. P. Ramirez, Frustrated soft modes and negative thermal expansion in ZrW_2O_8. *Phys. Rev. Lett.* **89**, 215902 (2002).
15. J. N. Hancock, C. Turpen, Z. Schlesinger, G. R. Kowach, A. P. Ramirez, Unusual low-energy phonon dynamics in the negative thermal expansion compound ZrW_2O_8. *Phys. Rev. Lett.* **93**, 225501 (2004).

16. Z. Schlesinger, J. A. Rosen, J. N. Hancock, A. P. Ramirez, Soft manifold dynamics behind negative thermal expansion. *Phys. Rev. Lett.* **101**, 015501 (2008).

17. C. W. Li, X. Tang, J. A. Muñoz, J. B. Keith, S. J. Tracy, D. L. Abernathy, B. Fultz, Structural relationship between negative thermal expansion and quartic anharmonicity of cubic ScF_3. *Phys. Rev. Lett.* **107**, 195504 (2011).

18. S. U. Handunkanda, E. B. Curry, V. Voronov, A. H. Said, G. G. Guzmán-Verri, R. T. Brierley, P. B. Littlewood, J. N. Hancock, Large isotropic negative thermal expansion above a structural quantum phase transition. *Phys. Rev. B* **92**, 134101 (2015).

19. S. U. Handunkanda, C. A. Occhialini, A. H. Said, J. N. Hancock, Two-dimensional nanoscale correlations in the strong negative thermal expansion material ScF_3. *Phys. Rev. B* **94**, 214102 (2016).

20. C. A. Young, A. L. Goodwin, Applications of pair distribution function methods to contemporary problems in materials chemistry. *J. Mater. Chem.* **21**, 6464–6476 (2011).

21. T. Egami, S. Billinge, *Underneath the Bragg Peaks: Structural Analysis of Complex Materials* (Pergamon Press, Elsevier, ed. 2, 2012), vol. 37.

22. S. Piskunov, P. A. Žguns, D. Bocharov, A. Kuzmin, J. Purans, A. Kalinko, R. A. Evarestov, S. E. Ali, F. Rocca, Interpretation of unexpected behavior of infrared absorption spectra of ScF_3 beyond the quasiharmonic approximation. *Phys. Rev. B* **93**, 214101 (2016).

23. L. Pauling, *The Nature of the Chemical Bond* (Cornell Univ. Press, ed. 3, 1960).

24. S. Shaik, D. Danovich, B. Braida, W. Wu, P. C. Hiberty, *New Landscape of Electron-Pair Bonding: Covalent, Ionic, and Charge-Shift Bonds* (Springer International Publishing, 2016), pp. 169–211.

25. Y. A. Teterin, A. Y. Teterin, Structure of x-ray photoelectron spectra of lanthanide compounds. *Russ. Chem. Rev.* **71**, 347–381 (2002).

26. D. Bocharov, P. Aguns, S. Piskunov, A. Kuzmin, J. Purans, Electronic structure of cubic ScF_3 from first-principles calculations. *Low Temp. Phys.* **42**, 556–560 (2016).

27. J. W. Kury, A. D. Paul, L. G. Hepler, R. E. Connick, The fluoride complexing of scandium(III) in aqueous solution: Free energies, heats and entropies. *J. Am. Chem. Soc.* **81**, 4185–4189 (1959).

28. P. J. Flory, *Statistical Mechanics of Chain Molecules* (Interscience Publishers, ed. 1, 1969).

29. P. de Gennes, *Scaling Concepts in Polymer Physics* (Cornell Univ. Press, 1979).

30. T. Barron, G. White, Heat capacity and thermal expansion at low temperatures, in *International Cryogenics Monograph Series* (Springer US, 1999).

31. E. E. Rodriguez, A. Llobet, T. Proffen, B. C. Melot, R. Seshadri, P. B. Littlewood, A. K. Cheetham, The role of static disorder in negative thermal expansion in ReO_3. *J. Appl. Phys.* **105**, 114901 (2009).

32. S. Chaudhuri, P. J. Chupas, M. Wilson, P. Madden, C. P. Grey, Study of the nature and mechanism of the rhombohedral-to-cubic phase transition in $\alpha - AlF_3$ with molecular dynamics simulations. *J. Phys. Chem. B* **108**, 3437–3445 (2004).

33. M. E. Simon, C. M. Varma, Dynamics of some constrained lattices. *Phys. Rev. Lett.* **86**, 1781–1784 (2001).

34. Y. He, V. Cvetkovic, C. M. Varma, Elastic properties of a class of solids with negative thermal expansion. *Phys. Rev. B* **82**, 014111 (2010).

35. C. A. Occhialini, S. U. Handunkanda, E. B. Curry, J. N. Hancock, Classical, quantum, and thermodynamics of a lattice model exhibiting structural negative thermal expansion. *Phys. Rev. B* **95**, 094106 (2017).

36. U. D. Wdowik, K. Parlinski, T. Chatterji, S. Rols, H. Schober, Lattice dynamics of rhenium trioxide from the quasiharmonic approximation. *Phys. Rev. B* **82**, 104301 (2010).

37. Y.-R. Chen, V. Perebeinos, P. B. Allen, Density-functional study of the cubic-to-rhombohedral transition in $\alpha-AlF_3$. *Phys. Rev. B* **69**, 054109 (2004).

38. C. P. Romao, C. R. Morelock, M. B. Johnson, J. W. Zwanziger, A. P. Wilkinson, M. A. White, The heat capacities of thermomiotic ScF_3 and ScF_3–YF_3 solid solutions. *J. Mater. Sci.* **50**, 3409–3415 (2015).

39. K. A. Dill, S. Bromberg, *Molecular Driving Forces: Statistical Thermodynamics in Chemistry and Biology* (Garland Science, ed. 2, 2003).

40. I. J. Zucker, Madelung constants and lattice sums for invariant cubic lattice complexes and certain tetragonal structures. *J. Phys. A Math. Gen.* **8**, 1734–1745 (1975).

41. Y. Sakamoto, Madelung constants of simple crystals expressed in terms of Born's basic potentials of 15 figures. *J. Chem. Phys.* **28**, 164–165 (1958).

42. H. M. Evjen, On the stability of certain heteropolar crystals. *Phys. Rev.* **39**, 675–687 (1932).

43. R. D. Shannon, R. X. Fischer, Empirical electronic polarizabilities in oxides, hydroxides, oxyfluorides, and oxychlorides. *Phys. Rev. B* **73**, 235111 (2006).

44. J. D. Jorgensen, Z. Hu, S. Teslic, D. N. Argyriou, S. Short, J. S. O. Evans, A. W. Sleight, Pressure-induced cubic-to-orthorhombic phase transition in ZrW_2O_8. *Phys. Rev. B* **59**, 215–225 (1999).

45. D. R. Lide, *CRC Handbook of Chemistry and Physics* (Taylor & Francis, ed. 84, 2003).

46. D. M. P. Mingos, *The Chemical Bond II: 100 Years Old and Getting Stronger* (Springer International Publishing, 2016).

47. A. Haaland, T. Helgaker, K. Ruud, D. J. Shorokhov, Should gaseous BF_3 and SiF_4 be described as ionic compounds? *J. Chem. Educ.* **77**, 1076 (2000).

48. J. Dean, *Lange's Handbook of Chemistry* (McGraw-Hill, 1999), vol. 15.

49. C. Blondel, P. Cacciani, C. Delsart, R. Trainham, High-resolution determination of the electron affinity of fluorine and bromine using crossed ion and laser beams. *Phys. Rev. A* **40**, 3698–3701 (1989).

50. T. Kiang, R. N. Zare, Stepwise bond dissociation energies in sulfur hexafluoride. *J. Am. Chem. Soc.* **102**, 4024–4029 (1980).

51. N. Marzari, D. Vanderbilt, Maximally localized generalized wannier functions for composite energy bands. *Phys. Rev. B* **56**, 12847–12865 (1997).

52. I. Souza, N. Marzari, D. Vanderbilt, Maximally localized wannier functions for entangled energy bands. *Phys. Rev. B* **65**, 035109 (2001).

53. A. A. Mostofi, J. R. Yates, Y.-S. Lee, I. Souza, D. Vanderbilt, N. Marzari, wannier90: A tool for obtaining maximally-localised wannier functions. *Comput. Phys. Commun.* **178**, 685–699 (2008).

54. J. Kunes, R. Arita, P. Wissgott, A. Toschi, H. Ikeda, K. Held, Wien2wannier: From linearized augmented plane waves to maximally localized wannier functions. *Comput. Phys. Commun.* **181**, 1888–1895 (2010).

55. H. B. Hamed, A. Qteish, N. Meskini, M. Alouani, Calculated hybrid and semilocal functionals and *gw* electronic structure of the metal trifluorides MF_3 (M = Sc, y, al). *Phys. Rev. B* **92**, 165202 (2015).

Science Advances

Entropic elasticity and negative thermal expansion in a simple cubic crystal

David Wendt, Emil Bozin, Joerg Neuefeind, Katharine Page, Wei Ku, Limin Wang, Brent Fultz, Alexei V. Tkachenko, and Igor A. Zaliznyak

View the article online
https://www.science.org/doi/10.1126/sciadv.aay2748
Permissions
https://www.science.org/help/reprints-and-permissions

Use of this article is subject to the Terms of service

Pressure Induced Topological Quantum Phase Transition in Weyl Semimetal T_d-MoTe$_2$

Zurab Guguchia[1]*, Antonio M. dos Santos[2], Fabian O. von Rohr[3,4], Jamie J. Molaison[2],
Soham Banerjee[5], Daniel Rhodes[6], Jiaxin Yin[7], Rustem Khasanov[1], James Hone[8],
Yasutomo J. Uemura[9], M. Zahid Hasan[7], Hubertus Luetkens[1], Emil S. Bozin[5], and Alex Amato[1]

[1]*Laboratory for Muon Spin Spectroscopy, Paul Scherrer Institute, CH-5232 Villigen PSI, Switzerland*
[2]*Neutron Scatering Division, Oak Ridge National Laboratory, Oak Ridge, TN 37831, U.S.A.*
[3]*Department of Chemistry, University of Zurich, CH-8057 Zurich, Switzerland*
[4]*Department of Physics, University of Zurich, CH-8057 Zurich, Switzerland*
[5]*Condensed Matter Physics and Materials Science Division, Brookhaven National Laboratory, Upton, NY 11973, U.S.A.*
[6]*Department of Materials Science and Engineering, University of Wisconsin-Madison,
1509 University Ave, Madison, WI 53706, U.S.A.*
[7]*Laboratory for Topological Quantum Matter and Spectroscopy, Department of Physics, Princeton University,
Princeton, NJ 08544, U.S.A.*
[8]*Department of Mechanical Engineering, Columbia University, New York, NY 10027, U.S.A.*
[9]*Department of Physics, Columbia University, New York, NY 10027, U.S.A.*

We report the temperature and pressure ($p_{max} \simeq 1.5$ GPa) evolution of the crystal structure of the Weyl semimetal T_d-MoTe$_2$ by combination of neutron diffraction and the X-ray total scattering experiments. We find that the fundamental non-centrosymmetric structure T_d is fully suppressed and transforms into a centrosymmetric 1T′ structure at a critical pressure of $p_{cr} \sim 1.2$–1.4 GPa. This is strong evidence for a pressure induced quantum phase transition (QPT) between topological to a trivial electronic state. Although the topological QPT has strong effect on magnetoresistance, it is interesting that the superconducting (SC) critical temperature T_c, the superfluid density, and the SC gap all change smoothly and continuously across p_{cr} and no sudden effects are seen concomitantly with the suppression of the T_d structure. This implies that the T_c, and thus the SC pairing strength, is unaffected by the topological QPT. However, the QPT requires the change in the SC gap symmetry from non-trivial s^{+-} to a trivial s^{++} state, which we discuss in this work. Our systematic characterizations of the structure and SC properties associated with the topological QPT provide deep insight into the pressure induced phase diagram in this topological quantum material.

1. Introduction

Transition metal dichalcogenides (TMDs) have attracted a lot of attention due to their fascinating physics and promising functional applications.[1–18] TMDs share the same formula, MX$_2$, where M is a transition metal (for example, Mo or W) and X is a chalcogenide atom (S, Se, and Te). These compounds typically crystallize in a group of related structure types, including 1T′- and T_d-type lattices[19–22] as shown in Fig. 1. The 1T′ phase is monoclinic lattice and comprises a distorted octahedral coordination of the metal ions, exhibiting pseudo-hexagonal layers with zig-zag edge sharing metal chains. The T_d phase is orthorhombic and both 1T′ and T_d structures are related by a slight change in the stacking pattern of the layers. Both 1T′- and T_d are semimetals. The central difference between these two structures is that the 1T′ structure exhibits the inversion symmetric space group $P2_1/m$, while the T_d phase belongs to the non-centrosymmetric space group $Pmn2_1$.

MoTe$_2$ exhibits a 1T′–T_d structural phase transition, on warming, at $T_{str} \sim 280$ K.[17] MoTe$_2$, with the non-inversion symmetric orthorhombic T_d phase, is a type-II Weyl semimetal,[1,2,4–10] where the Weyl Fermions emerge at the boundary between electron and hole pockets. High field quantum oscillation study of the magnetoresistance (MR) for T_d-MoTe$_2$, revealed a nontrivial π Berry's phase, which is a distinguished feature of surface states.[23] Non-saturating magnetoresistance,[11–14] and superconductivity[15–17] were also observed in T_d-MoTe$_2$. Hence, T_d-MoTe$_2$ represents a rare example of a material with both a topologically non-
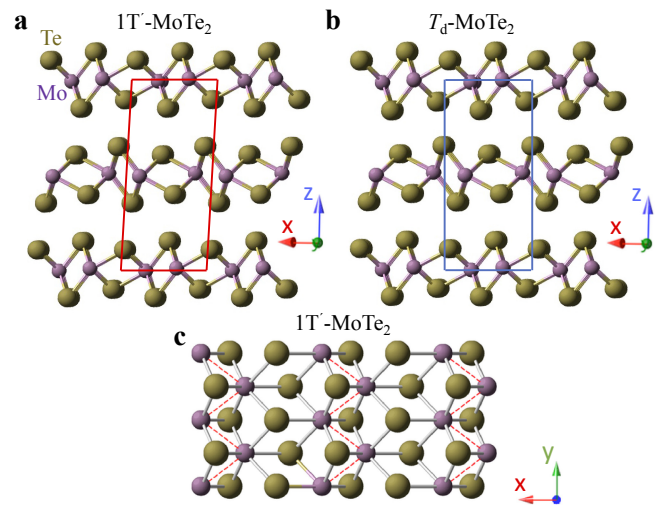
Fig. 1. (Color online) Structural representations (side view) of the centrosymmetric 1T′ (a) and non-centrosymmetric T_d (b) structures for MoTe$_2$. (c) Top view of monolayer constructed from distorted octahedral coordination.

trivial band structure and superconductivity.[24] The superconducting (SC) critical temperature of T_d-MoTe$_2$ is $T_c \simeq 0.1$ K[17] at ambient conditions. The application of hydrostatic pressure,[17,25] the substitution of Te ion by S/Se[26,27] or the creation of Te-vacancies can dramatically enhance T_c and lead to a dome-shaped superconductivity in T_d-MoTe$_2$. Experimental signatures of topological superconducting

order parameter s^{+-} within T_d structure were reported by recent muon-spin rotation μSR experiments and T_d-MoTe$_2$ is claimed to be a candidate material for a time reversal invariant topological (Weyl) superconductor (TSC).[25,28–30] These are special families of materials with unique electronic states, a full pairing gap in the bulk and gapless surface states consisting of Majorana fermions (MFs).[28–30] Therefore, the combination of Weyl physics and superconductivity may support Majorana or other exotic surface states in view of their topological nature. These states are of fundamental interest and may eventually be utilised for Quantum computing. For this reason, there is an ongoing effort aimed at achieving superconductivity in such materials and investigating their properties, either with the use of the proximity effect or by other means.

Besides the enhancement of T_c, pressure causes the suppression of the non-centrosymmetric orthorhombic T_d structure, as it was reported by resistivity experiments.[17] However, resistivity is rather indirect probe for the structural transition and relies only on a weak anomaly, appearing around the structural phase transition T_{str}. In order to understand the role of the crystal structure for the occurrence of superconductivity in MoTe$_2$, it is essential to directly investigate the structure as a function of pressure using a conventional structural probe such as neutron diffraction. Since pressure has strong effect on superconductivity in MoTe$_2$, by investigating structural properties under pressure we aim to find the correlation between pressure induced structural and electronic quantum phase transitions in this important TMD system MoTe$_2$.

2. Experimental Details

High quality single crystals and polycrystalline samples were obtained by mixing of molybdenum foil (99.95%) and tellurium lumps (99.999+%) in a ratio of 1 : 20 in a quartz tube and sealed under vacuum. The reagents were heated to 1000 °C within 10 h. They dwelled at this temperature for 24 h, before they were cooled to 900 °C within 30 h (polycrystalline sample) or 100 h (single crystals). At 900 °C the tellurium flux was spinned-off and the samples were quenched in air. The obtained MoTe$_2$ samples were annealed at 400 °C for 12 h to remove any residual tellurium.

High pressure neutron diffraction experiments on T_d-MoTe$_2$ were carried out at SNAP beamline of Spallation Neutron Source at Oak Ridge National Laboratory. SNS operates at 60 Hz, and SNAP instrument utilizes time of flight diffraction mode. The center wavelength was set to 2.1 Å, corresponding to an incident wavelength spectrum from 0.5 to 3.5 Å. Two banks of detectors cover $+/-22.5$ deg in angular range in and out of plane. Their center was placed at 50 deg scattering angle. This configuration limits the accessible Q-range, but provides increased counting statistics in the region of interest that is most relevant for discriminating between T_d and 1T' phases. Pressures up to 1.6 GPa were generated in a single wall piston-cylinder type of cell made of CuBe material, especially designed to perform neutron diffraction experiments under pressure. Daphne oil was used as a pressure transmitting medium. The pressure was always applied at room temperature, followed by cooling the sample to the base temperature (15 K) and carrying out temperature dependent measurements on warming. The pressure was
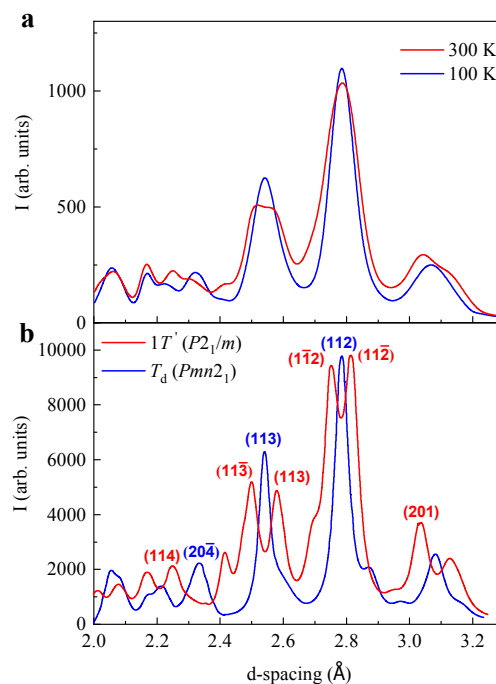

Fig. 2. (Color online) (a) Raw diffraction patterns for 300 and 100 K measurements using an incident wavelength of $\lambda = 0.18470$ Å. (b) Bragg profile calculated from unmodified candidate structures. Solid curves in red and blue are the Bragg peaks calculated from the reflections (sharp lines), broadened uniformly with an FWHM = 0.1 in 2θ (= 0.059 Å^{-1} in Q). The orthorhombic (113) reflection measured at 100 K, splits into the (11$\bar{3}$) and (113) at 300 K.

measured by tracking the Raman spectrum of lead powder as a function of pressure. The diffraction experiments were done on the samples from the same batch as the ones, which we previously studied by μSR experiments.[25]

Total scattering measurements were carried out on the XPD (28-ID-2) beamline at the National Synchrotron Light Source II (NSLS-II), Brookhaven National Laboratory. A finely ground powder of MoTe$_2$ was prepared in an inert Argon chamber, and sealed in 1.02 mm (OD) polyimide capillary. Diffraction patterns were collected in a Debye–Scherrer geometry with an X-ray energy of 67.13 keV ($\lambda = 0.1847$ Å) using a large-area 2D PerkinElmer detector (2048^2 pixels with 200 μm^2 pixel size). The detector was mounted with a sample-to-detector distance of 345 mm, to achieve a balance between q-resolution and q-range. The sample was measured at 100 and 300 K using an Oxford CS-700 cryostream for temperature control, allowing ample time for the material to thermalize. The experimental geometry, 2θ range, and detector orientation were calibrated by measuring a polycrystalline nickel standard directly prior to data collection, with the experimental geometry parameters refined using the PyFAI program.[31]

3. Results

The orthorhombic (T_d) to monoclinic (1T') structural phase transition in the MoTe$_2$ sample at ambient pressure was confirmed by the X-ray total scattering measurements, shown in Fig. 2. In Figs. 2(a) and 2(b), we index the Bragg profile and compare the raw diffraction patterns measured at 100 and 300 K to powder diffraction patterns calculated from the candidate models using the program VESTA.[32] We plot the
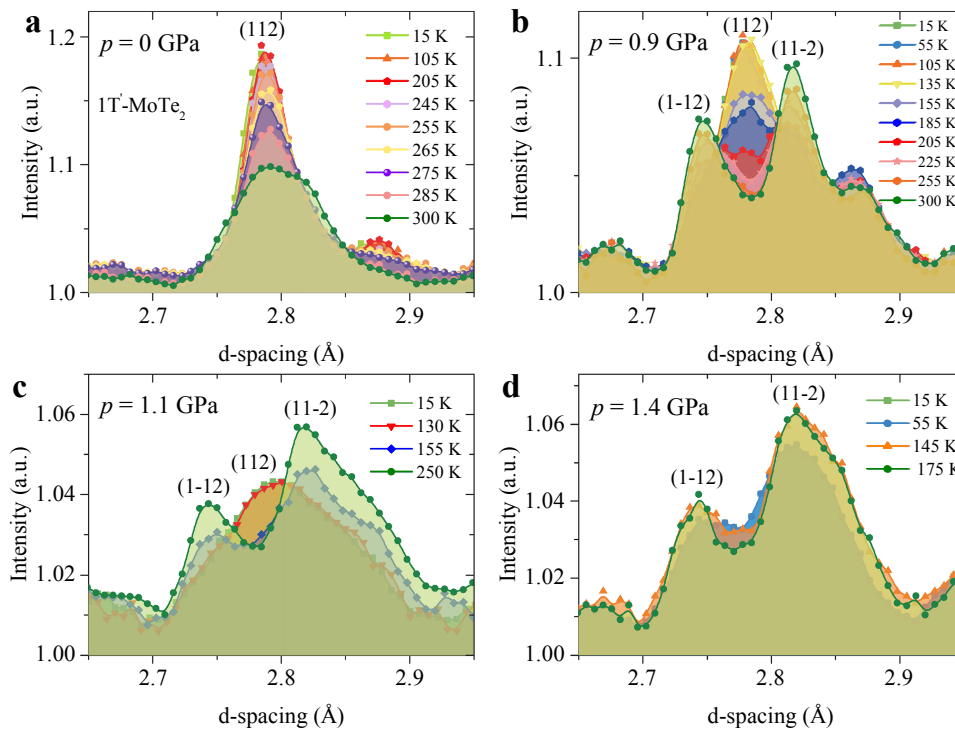
Fig. 3. (Color online) The temperature dependence of (112) Bragg peak of MoTe2, recorded at various pressures: (a) $p = 0$ GPa, (b) $p = 0.9$ GPa, (c) $p = 1.1$ GPa, and (d) $p = 1.4$ GPa.

data over a d-range where the 1T′ and T_d models have Bragg peaks that are well resolved from one another to highlight distinguishable features that differ between the phases in the measured XRD pattern. The strongest structural signatures of the transition are seen as splitting of the orthorhombic (113) and (112) reflections in monoclinic phase, as it was also reported for WTe2.[33,34]

Confirming the low temperature T_d structure as well as the signature of the structural phase transition in MoTe2, we proceed with observations made by neutron scattering measurements under hydrostatic pressure. The most intense peak is (112) at d-spacing of 2.8 Å, which was monitored at various temperatures and pressures. The results are shown in Figs. 3(a)–3(d). Figure 3(a) shows the temperature evolution of the (112) peak at ambient pressure. The (112)-peak splits into (1$\bar{1}$2) and (11$\bar{2}$) peak above 285 K, consistent with the T_d to 1T′ structural phase transition and experimental observations of XRD experiment. Upon increasing pressure, the temperature, above which the peak splits, decreases, pointing to the suppression of T_{str} with pressure. At 1.4 GPa, no single orthorhombic (112) peak is observed within the resolution of our measurement, and monoclinic peaks are observed down to the lowest temperature $T = 15$ K measured. Figure 4 shows the temperature dependence of the position of the (112)-peak, from which we can extract the structural phase transition temperature T_{str} and follow its suppression as a function of pressure. Although the measurements were performed only down to 15 K, the extrapolation of the data for $p = 1.4$ GPa to $T = 0$ K (dashed lines in Fig. 4) suggests that the splitting (e.g., monoclinic peaks) occurs down to very low temperatures, indicating the full suppression of the orthorhombic T_d structure at this pressure. Figure 5 shows the pressure dependence of the structural phase transition temperature T_{str}, superimposed with the
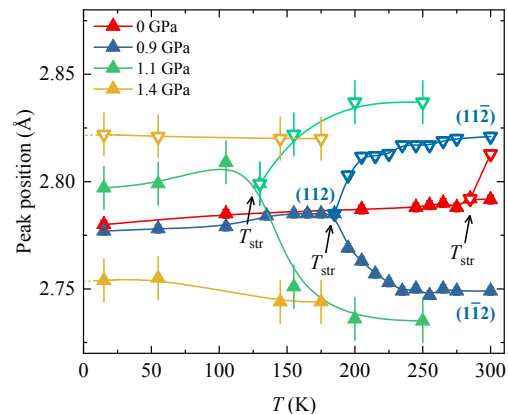
Fig. 4. (Color online) The temperature dependence of the position of the (112)-peak, which splits into (1$\bar{1}$2) and (11$\bar{2}$) above T_{str}, recorded at various pressures. The arrows mark the monoclinic to orthorhombic structural phase transition temperatures T_{str}.

dependence of SC critical temperature (taken from Ref. 25), measured on the sample from the same batch. This phase diagram shows that the orthorhombic to monoclinic quantum phase transition ($T = 0$) takes place at the critical pressure of $p_{cr} \simeq 1.2$–1.4 GPa, but T_c continues to increase smoothly and persists well beyond the p_{cr}. The absence of the measurements between 1.2 and 1.4 GPa does not allow to precisely determine the value of critical pressure, but we can safely say that it is located between 1.2 and 1.4 GPa. The suppression of the orthorhombic phase as well as the value of the critical pressure is in a very good agreement with the one $p_{cr} \simeq$ 1.2 GPa, obtained from very recent single crystal neutron diffraction[35] and the one $p_{cr} \simeq 1.1$–1.4 GPa, from the magnetoresistance measurements.[36] Strain was also recently found to suppress the orthorhombic structure.[37]
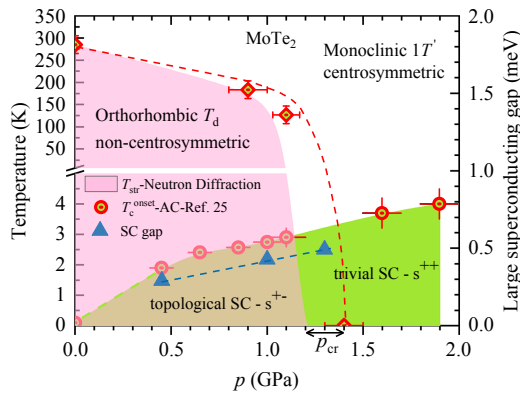
Fig. 5. (Color online) The pressure dependence of the superconducting critical temperature T_c (the red circles), the large SC gap Δ_2 (the blue triangles) and the monoclinic to orthorhombic structural phase transition temperature T_{str} (the red diamonds). The T_c and the Δ_2 values are taken from Ref. 25.

3.1 Discussion

What is the significance of such a strong negative pressure effect on T_d structure and the structural QPT in Weyl semimetal MoTe$_2$? Let us start with the fact that T_d structure breaks inversion symmetry, while 1T′ is inversion symmetric. As low pressure as 1.2 GPa is sufficient to wipe out non-inversion symmetric T_d phase. One common point of view in MoTe$_2$, mostly supported by calculations, is that Weyl Fermions and their underlying non-trivial band topology, exist only in T_d phase. Hence, the structural QPT between T_d and 1T′ corresponds to the quantum phase transition between topologically non-trivial and a trivial band structure. One of the consequences of such a topological quantum phase transition is the strong suppression of the magnetoresistance with increasing pressure. For the pressure values $p > p_{cr}$, MR is fully suppressed.[36] This was explained by the fact that MR is very sensitive to a hole-to-electron concentration ratio N_h/N_e and by driving the system into 1T′ phase, the strong deviation from the optimal ratio takes place, leading to the suppression of MR. In fact, MR is strongly suppressed already well below p_{cr}, which is ascribed to the presence of a significant band tilting around the Weyl nodes under pressure within the T_d phase, as shown by calculations.[35] When the Weyl nodes fully disappear at p_{cr}, than this leads to the full suppression of MR.[36]

Although the topological QPT has a strong effect on MR,[36] it is interesting that the superconducting critical temperature T_c as well as the SC gap Δ (Fig. 4, only the large SC gap[25] is shown) changes smoothly across p_{cr} and no sudden effects are seen due to the suppression of T_d structure. This implies that the T_c and thus the SC pairing strength is unaffected by the topological QPT. This can be understood in light of Hall conductivity measurements,[36,38] showing that a pair of electron and hole bands are dominant in the T_d structure and the carrier densities on these bands increase smoothly with pressure and no sudden changes are observed across p_{cr}. Having this in mind as well as our previous work,[25] according to which T_c scales with the superconducting carrier density, one can understand the insensitivity of T_c to topological QPT.

Since there is only a subtle change in the Fermi surface (FS) topology[36] at p_{cr}, bulk SC quantities such as T_c, Δ and

the superfluid density, are not affected by QPT. However, one more physical parameter that we should consider is the symmetry of the SC order parameter. Previously, we showed that the superconductor T_d-MoTe$_2$ represents a time-reversal-invariant Weyl semimetal, which has broken inversion symmetry below p_{cr}. Moreover, it is a two-gap superconductor both below and above p_{cr} (we have one point just above p_{cr}) and the gaps are momentum independent on each Fermi surface. Following the theoretical studies of time-reversal-invariant topological superconductivity in Weyl semimetals, the nontrivial Berry curvature at the FSs of WSMs allows the TSC to be realized for a pairing function with no special momentum dependence. A simple formula[28–30] relates the FS Chern number to the topological invariant ν for a time-invariant TSC, considering a set of FSs with Chern numbers C_j:

$$\nu = \frac{1}{2} \sum_{j \in FS} C_j \, sgn(\Delta_j), \qquad (1)$$

where Δ_j is the pairing gap function on the j-th FS. A TSC is implied by $\nu \neq 0$. Therefore, as previously discussed,[28] a necessary condition for TSC is that Δ_1 and Δ_2 have opposite signs. Thus, T_d-MoTe$_2$ is a natural candidate for topological s^{+-} SC order parameter within non-centrosymmetric T_d structure since the nontrivial Chern number is already provided by the band structure. The s^{+-} order parameter in T_d-MoTe$_2$ is also supported by strong disorder dependence of T_c.[13] It was shown that the violation of inversion symmetry stabilises the state where the ferromagnetic exchange coupling is greater than or comparable to the repulsive density–density interactions, which then results in topological superconducting state.[28] Once the inversion symmetry is recovered then the TSC is quenched. This means that at pressure above p_{cr}, where crystal structure has inversion symmetry, the trivial s^{++} state (where Δ_1 and Δ_2 have the same sign) should be favoured over the topological s^{+-} state. While a direct proof for such a pressure induced QPT between s^{+-} and s^{++} states in MoTe$_2$ is clearly lacking, we conjecture this based on solid experimental evidence gleaned from the quantum phase transition between non-centrosymmetric to a centrosymmertic structure and our previous observation of two-gap superconductivity. This paves the way for rigorous experimental as well as theoretical explorations of this idea. One immediately useful study would be that of the effects of impurities on superconductivity above p_{cr}. This should discriminate/differentiate between topological s^{+-} and ordinary s^{++} state, since according to the theoretical proposal[28] TSC in time-reversal-invariant Weyl semimetals is much more sensitive to disorder than the ordinary s^{++} superconductivity. Along this line, it is interesting to compare pressure and Se-doping[27] effects on T_c in MoTe$_2$. We note that while pressure causes the strong enhancement of T_c (from 0.3 to 3 K) within the orthorhombic T_d phase, Se-doping in MoTe$_{2-x}$Se$_x$ enhances T_c from 0.3 K to only 0.6 K.[27] T_c of MoTe$_{2-x}$Se$_x$ shows much stronger increase above the critical doping x_{cr} at which orthorhombic T_d structure is suppressed.[27] These experimental facts support the idea of topological s^{+-} superconducting state below p_{cr}, in which inversion symmetry is violated. Namely, Se-doping introduces disorder in the system and disorder was suggested to have strong negative

J. Phys. Soc. Jpn.
Downloaded from journals.jps.jp by Brookhaven Natl Lab Res Lib on 01/23/23

J. Phys. Soc. Jpn. **89**, 094707 (2020)   Z. Guguchia et al.

effect on T_c for topological s^{+-} superconductor. Indeed, by Se-doping T_c shows much weaker increase than expected within non-inversion symmetric phase. T_c shows larger increase only after we cross x_{cr}, above which the inversion symmetry is recovered, and the trivial s^{++} state is favoured with less disorder effect. Systematic disorder effect studies are required in order to shed more light on QPT between s^{+-} and s^{++} states.

4. Conclusions

In conclusion, we studied the hydrostatic pressure evolution of a monoclinic 1T′ to orthorhombic T_d structural phase transition temperature T_{str} in the polycrystalline sample of MoTe₂ using neutron diffraction. The quantum phase transition from non-centrosymmetric T_d to a centrosymmetric 1T′ structure is observed under pressure with the critical pressure of $p_{cr} \simeq 1.2$–1.4 GPa. We observed no obvious impact of such a QPT on SC critical temperature, the SC gap(s) and the superfluid density, suggesting that only subtle changes take place in the Fermi surface across p_{cr} despite the transition from a topological to a topological-trivial band structure. However, due to the recovery of inversion symmetry above p_{cr}, the trivial s^{++} superconducting state should be favoured over the topological s^{+-} state. Hence, this system may likely be the first known example of a pressure induced change between topological ($p < p_{cr}$) and trivial ($p > p_{cr}$) SC states.

*zurab.guguchia@psi.ch

1) A. A. Soluyanov, D. Gresch, Z. Wang, Q. Wu, M. Troyer, X. Dai, and B. Andrei Bernevig, Nature **527**, 495 (2015).
2) Y. Sun, S. C. Wu, M. N. Ali, C. Felser, and B. Yan, Phys. Rev. B **92**, 161107 (2015).
3) H. Zheng, G. Bian, G. Chang, H. Lu, S.-Y. Xu, G. Wang, T.-R. Chang, S. Zhang, I. Belopolski, N. Alidoust, D. S. Sanchez, F. Song, H.-T. Jeng, N. Yao, A. Bansil, S. Jia, H. Lin, and M. Zahid Hasan, Phys. Rev. Lett. **117**, 266804 (2016).
4) Z. Wang, D. Gresch, A. A. Soluyanov, W. Xie, S. Kushwaha, X. Dai, M. Troyer, R. J. Cava, and B. Andrei Bernevig, Phys. Rev. Lett. **117**, 056805 (2016).
5) A. P. Weber, P. Rußmann, N. Xu, S. Muff, M. Fanciulli, A. Magrez, P. Bugnon, H. Berger, N. C. Plumb, M. Shi, S. Blugel, P. Mavropoulos, and J. Hugo Dil, Phys. Rev. Lett. **121**, 156401 (2018).
6) S. Kourtis, J. Li, Z. Wang, A. Yazdani, and B. A. Bernevig, Phys. Rev. B **93**, 041109 (2016).
7) K. Deng, G. Wan, P. Deng, K. Zhang, S. Ding, E. Wang, M. Yan, H. Huang, H. Zhang, Z. Xu, J. Denlinger, A. Fedorov, H. Yang, W. Duan, H. Yao, Y. Wu, S. Fan, H. Zhang, X. Chen, and S. Zhou, Nat. Phys. **12**, 1105 (2016).
8) N. Xu, Z. J. Wang, A. P. Weber, A. Magrez, P. Bugnon, H. Berger, C. E. Matt, J. Z. Ma, B. B. Fu, B. Q. Lv, N. C. Plumb, M. Radovic, E. Pomjakushina, K. Conder, T. Qian, J. H. Dil, J. Mesot, H. Ding, and M. Shi, arXiv:1604.02116.
9) L. Huang, T. M. McCormick, M. Ochi, Z. Zhao, M.-T. Suzuki, R. Arita, Y. Wu, D. Mou, H. Cao, J. Yan, N. Trivedi, and A. Kaminski, Nat. Mater. **15**, 1155 (2016).
10) A. Tamai, Q. S. Wu, I. Cucchi, F. Y. Bruno, S. Riccò, T. K. Kim, M. Hoesch, C. Barreteau, E. Giannini, C. Besnard, A. A. Soluyanov, and F. Baumberger, Phys. Rev. X **6**, 031021 (2016).
11) X. Xu, W. Yao, D. Xiao, and T. F. Heinz, Nat. Phys. **10**, 343 (2014).
12) M. N. Ali, J. Xiong, S. Flynn, J. Tao, Q. D. Gibson, L. M. Schoop, T. Liang, N. Haldolaarachchige, M. Hirschberger, N. P. Ong, and R. J. Cava, Nature **514**, 205 (2014).
13) D. Rhodes, R. Schonemann, N. Aryal, Q. Zhou, Q. R. Zhang, E. Kampert, Y.-C. Chiu, Y. Lai, Y. Shimura, G. T. McCandless, J. Y. Chan, D. W. Paley, J. Lee, A. D. Finke, J. P. C. Ruff, S. Das, E. Manousakis, and L. Balicas, Phys. Rev. B **96**, 165134 (2017).
14) Z. Zhu, X. Lin, J. Liu, B. Fauqué, Q. Tao, C. Yang, Y. Shi, and K. Behnia, Phys. Rev. Lett. **114**, 176601 (2015).
15) X.-C. Pan, X. Chen, H. Liu, Y. Feng, Z. Wei, Y. Zhou, Z. Chi, L. Pi, F. Yen, F. Song, X. Wan, Z. Yang, B. Wang, G. Wang, and Y. Zhang, Nat. Commun. **6**, 7805 (2015).
16) D. Kang, Y. Zhou, W. Yi, C. Yang, J. Guo, Y. Shi, S. Zhang, Z. Wang, C. Zhang, S. Jiang, A. Li, K. Yang, Q. Wu, G. Zhang, L. Sun, and Z. Zhao, Nat. Commun. **6**, 7804 (2015).
17) Y. Qi, P. G. Naumov, M. N. Ali, C. R. Rajamathi, W. Schnelle, O. Barkalov, M. Hanfland, S.-C. Wu, C. Shekhar, Y. Sun, V. Suß, M. Schmidt, U. Schwarz, E. Pippel, P. Werner, R. Hillebrand, T. Förster, E. Kampert, S. Parkin, R. J. Cava, C. Felser, B. Yan, and S. A. Medvedev, Nat. Commun. **7**, 11038 (2016).
18) R. Yu, S. Banerjee, H. C. Lei, R. Sinclair, M. Abeykoon, H. D. Zhou, C. Petrovic, Z. Guguchia, and E. S. Bozin, Phys. Rev. B **97**, 174515 (2018).
19) R. Clarke, E. Marseglia, and H. P. Hughes, Philos. Mag. B **38**, 121 (1978).
20) D. Puotinen and R. E. Newnhan, Acta Crystallogr. **14**, 691 (1961).
21) T. Zandt, H. Dwelk, C. Janowitz, and R. Manzke, J. Alloys Compd. **442**, 216 (2007).
22) B. E. Brown, Acta Crystallogr. **20**, 268 (1966).
23) X. Luo, F. C. Chen, J. L. Zhang, Q. L. Pei, G. T. Lin, W. J. Lu, Y. Y. Han, C. Y. Xi, W. H. Song, and Y. P. Sun, Appl. Phys. Lett. **109**, 102601 (2016).
24) L. Muechler, Z. Guguchia, J.-C. Orain, J. Nuss, L. M. Schoop, R. Thomale, and F. O. von Rohr, APL Mater. **7**, 121103 (2019).
25) Z. Guguchia, F. von Rohr, Z. Shermadini, A. T. Lee, S. Banerjee, A. R. Wieteska, C. A. Marianetti, B. A. Frandsen, H. Luetkens, Z. Gong, S. C. Cheung, C. Baines, A. Shengelaya, G. Taniashvili, A. N. Pasupathy, E. Morenzoni, S. J. L. Billinge, A. Amato, R. J. Cava, R. Khasanov, and Y. J. Uemura, Nat. Commun. **8**, 1082 (2017).
26) F. C. Chen, X. Luo, R. C. Xiao, W. J. Lu, B. Zhang, H. X. Yang, J. Q. Li, Q. L. Pei, D. F. Shao, R. R. Zhang, L. S. Ling, C. Y. Xi, W. H. Song, and Y. P. Sun, Appl. Phys. Lett. **108**, 162601 (2016).
27) H. Takahashi, T. Akiba, K. Imura, T. Shiino, K. Deguchi, N. K. Sato, H. Sakai, M. S. Bahramy, and S. Ishiwata, Phys. Rev. B **95**, 100501(R) (2017).
28) P. Hosur, X. Dai, Z. Fang, and X.-L. Qi, Phys. Rev. B **90**, 045130 (2014).
29) Y. Ando and L. Fu, Ann. Rev. Condens. Matter Phys. **6**, 361 (2015).
30) A. G. Grushin, Phys. Rev. D **86**, 045001 (2012).
31) J. Kieffer and D. Karkoulis, J. Phys.: Conf. Ser. **425**, 202012 (2013).
32) K. Momma and F. Izumi, J. Appl. Crystallogr. **41**, 653 (2008).
33) P. Lu, J.-S. Kim, J. Yang, H. Gao, J. Wu, D. Shao, B. Li, D. Zhou, J. Sun, D. Akinwande, D. Xing, and J.-F. Lin, Phys. Rev. B **94**, 224512 (2016).
34) Y. Tao, J. A. Schneeloch, A. A. Aczel, and D. Louca, arXiv:2003.09489v1.
35) S. Dissanayake, C. Duan, J. Yang, J. Liu, M. Matsuda, C. Yue, J. A. Schneeloch, J. C. Y. Teo, and D. Louca, npj Quantum Mater. **4**, 45 (2019).
36) S. Lee, J. Jang, S.-I. Kim, S.-G. Jung, J. Kim, S. Cho, S. W. Kim, J. Y. Rhee, K.-S. Park, and T. Park, Sci. Rep. **8**, 13937 (2018).
37) C. Heikes, I.-L. Liu, T. Metz, C. Eckberg, P. Neves, Y. Wu, L. Hung, P. Piccoli, H. Cao, J. Leao, J. Paglione, T. Yildirim, N. P. Butch, and W. Ratcliff, II, Phys. Rev. Mater. **2**, 074202 (2018).
38) H. Takahashi, K. Hasegawa, T. Akiba, H. Sakai, M. S. Bahramy, and S. Ishiwata, Phys. Rev. B **100**, 195130 (2019).

Nanoscale degeneracy lifting in a geometrically frustrated antiferromagnet

Benjamin A. Frandsen [1,*] Emil S. Bozin [2,†] Eleni Aza,[3,4] Antonio Fernández Martínez,[3]
Mikhail Feygenson,[5,6] Katharine Page,[5,7] and Alexandros Lappas [3,‡]

[1]*Department of Physics and Astronomy, Brigham Young University, Provo, Utah 84602, USA*
[2]*Condensed Matter Physics and Materials Science Division, Brookhaven National Laboratory, Upton, New York 11973, USA*
[3]*Institute of Electronic Structure and Laser, Foundation for Research and Technology–Hellas, Vassilika Vouton, 71110 Heraklion, Greece*
[4]*Department of Materials Science and Engineering, University of Ioannina, 451 10 Ioannina, Greece*
[5]*Neutron Scattering Division, Oak Ridge National Laboratory, Oak Ridge, Tennessee 37831, USA*
[6]*Jülich Centre of Neutron Science, Forschungszentrum Jülich, 52428 Jülich Germany*
[7]*Materials Science and Engineering Department, University of Tennessee, Knoxville, Tennessee 37996, USA*

The local atomic and magnetic structures of the compounds AMnO$_2$ (A = Na, Cu), which realize a geometrically frustrated, spatially anisotropic triangular lattice of Mn spins, have been investigated by atomic and magnetic pair distribution function analysis of neutron total scattering data. Relief of frustration in CuMnO$_2$ is accompanied by a conventional cooperative symmetry-lowering lattice distortion driven by Néel order. In NaMnO$_2$, however, the distortion has a short-range nature. A cooperative interaction between the locally broken symmetry and short-range magnetic correlations lifts the magnetic degeneracy on a nanometer length scale, enabling long-range magnetic order in the Na derivative. The degree of frustration, mediated by residual disorder, contributes to the rather differing pathways to a single, stable magnetic ground state in these two related compounds. This study demonstrates how nanoscale structural distortions that cause local-scale perturbations can lift the ground-state degeneracy and trigger macroscopic magnetic order.

I. INTRODUCTION

In geometrically frustrated materials, the spatial arrangement of magnetic moments prevents the simultaneous satisfaction of competing magnetic interactions [1]. This hinders the formation of magnetic order and may occasionally lead to exotic, macroscopically degenerate spin-liquid ground states for which magnetic order is absent even at zero temperature [2,3]. In the more common case where order develops at finite temperature, the transition mechanism itself can be quite unusual, often originating from extreme sensitivity to small perturbations resulting from thermal fluctuations, single-ion anisotropy, Dzyaloshinskii-Moriya and dipolar interactions, disorder, magnetoelastic coupling, and more [4]. Coupling between magnetic and other degrees of freedom can lift the intrinsic degeneracies and even support novel phenomena beyond magnetism, such as magnetoelectric states established by uniform lattice distortions [5] and domain-wall-driven competing metastable microphases [6].

An added layer of complexity may arise when frustrated geometries occur in strongly correlated transition metal oxide (TMO) systems. The possibility of stabilizing unusual, spatially inhomogeneous ground states through competition among simultaneously active electronic degrees of freedom (i.e., spin, charge, and orbital) has been well documented in

TMOs [7,8]. Combining this affinity for spatial inhomogeneity with geometrical frustration may produce novel behavior.

The insulating sister compounds α-NaMnO$_2$ (NMO) [9] and CuMnO$_2$ (CMO) [10] provide a valuable test bed for exploring geometrically frustrated magnetism in strongly correlated TMOs. The AMnO$_2$ crystal structures [Figs. 1(a) and 1(b)] entail spacer layers of primarily monovalent A = Na or Cu cations that separate layers of edge-sharing MnO$_6$ octahedra. The Jahn-Teller active, antiferromagnetically (AF) coupled Mn^{3+} ions ($S = 2$) form an anisotropic triangular network, embodying a simple example of a frustrated topology imposed on the two-dimensional Heisenberg model. At ambient conditions, the triangles are isosceles with $r_1 < r_2 = r_3$, as shown in Fig. 1(c). Consequently, the exchange interactions J (along r_1) and J' (along r_2 and r_3) become nondegenerate, with $J'/J < 1$. The frustration of the triangular lattice is therefore partially relieved. Nevertheless, the magnetic interactions along the two isosceles legs remain degenerate, and the resulting partial frustration of the AF interactions remains important even though these systems would not be considered "highly frustrated" magnets. Indeed, the magnetic frustration has been implicated in numerous unusual properties displayed by these systems, such as quasi-one-dimensional magnetic interactions [13] and rare Higgs-type excitations [14] in NMO. In general, systems with imperfect frustration, e.g., the anisotropic triangular lattice considered here, may still exhibit rich behavior such as ordering by disorder and Peierls-type transitions [15].

In CMO, magnetic long-range order (LRO) [16] develops below $T_N = 65$ K. This is accomplished through a concomitant monoclinic-to-triclinic structural phase transition that further
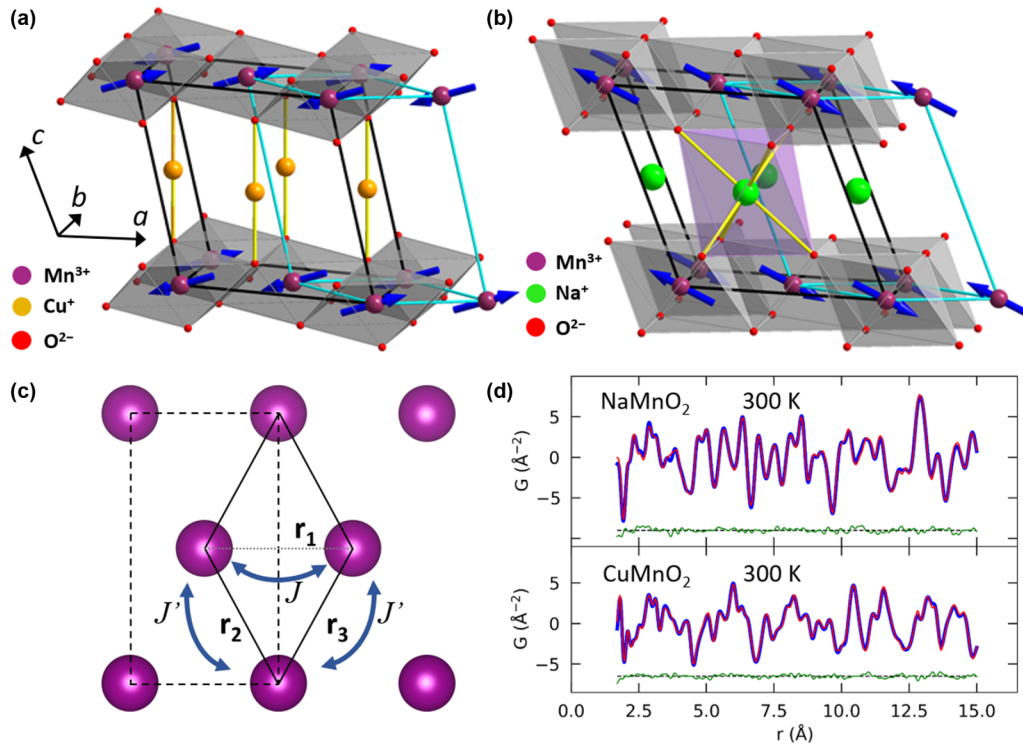
*benfrandsen@byu.edu
†bozin@bnl.gov
‡lappas@iesl.forth.gr

FIG. 1. Structure of $CuMnO_2$ and α-$NaMnO_2$. Atomic and magnetic structures of (a) $CuMnO_2$ and (b) α-$NaMnO_2$. The distortion of the monoclinic unit cell (black) to triclinic cell (blue) is depicted. The arrows depict the three-dimensional antiferromagnetic spin configurations, corresponding to propagation vectors (in the triclinic setting) of $\mathbf{k} = (0, 1/2, /1/2)$ for CMO [11] and $\mathbf{k} = (0, 1/2, 0)$ for NMO [12]. (c) Projection onto the basal plane of the triangular Mn^{3+} sublattice. Dashed and solid lines show the monoclinic and triclinic unit cells, respectively. (d) PDF patterns of $NaMnO_2$ (top) and $CuMnO_2$ (bottom) collected at room temperature. The blue curves represent the data, the red curves represent the atomic PDF fits using the monoclinic structural model, and the lower green curves represent the fit residuals, offset for clarity.

distorts the triangles such that $r_2 \neq r_3$, fully lifting the degeneracy of the triangular lattice and selecting a unique magnetic ground state [11]. The ordered state exhibits AF alignment along the shorter formerly isosceles leg and ferromagnetic alignment along the other formerly isosceles leg [Fig. 1(a)], with antiferromagnetic coupling between layers [16]. The energy gain from relieving the magnetic frustration outweighs the elastic energy cost of the triclinic distortion [17]; hence, this effect is magnetically driven. Figure 1(c) displays the projection of the monoclinic and triclinic unit cells on the Mn layer.

Although NMO is more frustrated than CMO ($J'/J = 0.44$ [18] compared to 0.27 for CMO [17], resulting in a greater degree of frustration [19]), it also exhibits AF LRO below $T_N = 45$ K [see Fig. 1(b)]. It differs from the magnetic structure in CMO only in that the coupling of adjacent manganese layers stacked along the c axis in NMO is ferromagnetic, in contrast to the antiferromagnetic coupling between layers in CMO [12]. Moreover, significant short-range magnetic correlations survive well into the paramagnetic state in NMO [12]. Surprisingly, no long-range structural phase transition accompanies the magnetic transition, implying that some other, unknown means must relieve the magnetic degeneracy. Recent work further suggested that the magnetic ground state is intrinsically inhomogeneous [20], adding to the unusual nature of the magnetism in this compound. Finally, this system exhibits polymorphism [21] and significant structural disor-

der [22] that may influence the magnetostructural properties, although how this may happen remains an open question. Clarifying these issues in NMO continues to be an important objective in the study of $AMnO_2$ systems while also presenting a valuable opportunity for a more general study of magnetic frustration, disorder, and their interplay in TMOs. This complements earlier work focused on magnetic pyrochlores and related materials [23].

Here, we discover that the magnetic phase transition in NMO occurs via an unconventional mechanism in which a nanoscale structural distortion supports macroscale magnetic order. Using atomic pair distribution function (PDF) analysis of neutron total scattering data [24], we observe a short-range triclinic distortion in NMO correlated over a 2-nm length scale that exists well above T_N and grows significantly as the temperature decreases. Complementary magnetic PDF analysis [25–27] reveals magnetic short-range order (SRO) persisting well above T_N, which likewise grows in magnitude and correlation length upon cooling until finally achieving the LRO state below T_N. Crucially, quantitative refinements confirm that the short-range triclinic distortion lifts the degeneracy of the isosceles triangular network on the nanoscale, thereby enabling the LRO state and enhancing the magnetic correlations above the transition.

While this short-range triclinic distortion is the primary actor, we find that other types of quenched structural disorder also play a role in determining the eventual ground
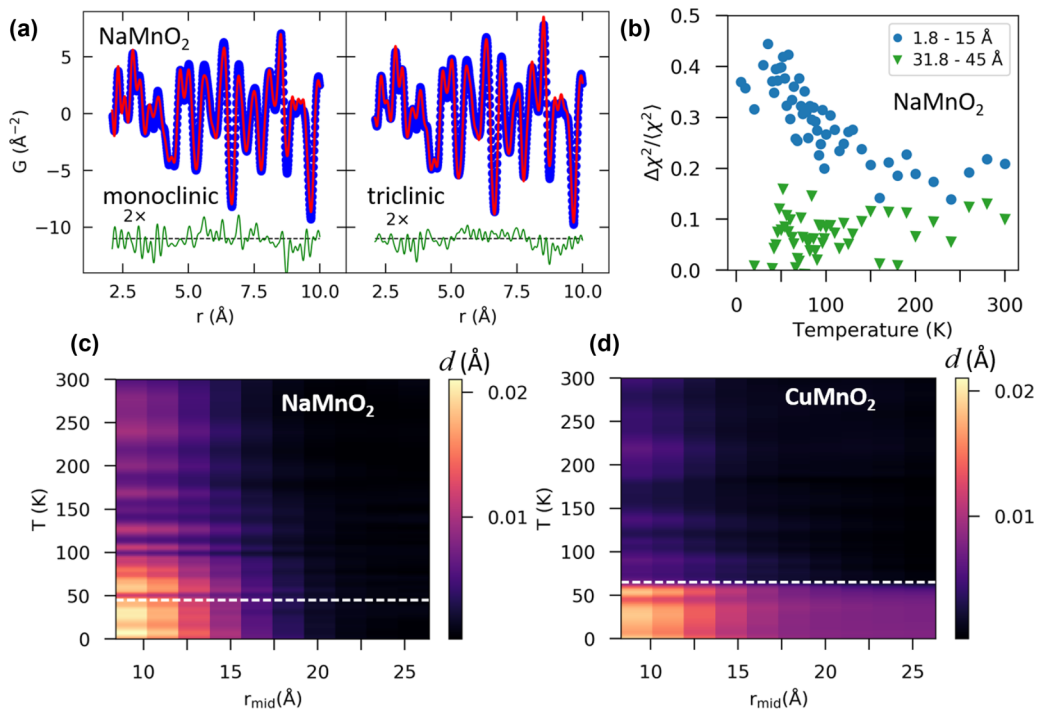
FIG. 2. Results of atomic PDF fits for $CuMnO_2$ and $NaMnO_2$. (a) PDF refinements of the $NaMnO_2$ structure at 5 K using the monoclinic (left) and triclinic (right) models. The lower green curves are the fit residuals, multiplied by 2 for clarity. (b) Normalized difference in χ^2 between the monoclinic and triclinic models of $NaMnO_2$ as a function of temperature for short (blue circles) and long (green triangles) fitting ranges. (c) Color map of the triclinic splitting in $NaMnO_2$ as a function of temperature and fitting range. The horizontal dashed line marks T_N. (d) Same as (c), but for $CuMnO_2$.

state—specifically, Na vacancies in NMO and antisite defects involving Cu atoms on the Mn site in CMO. Beyond a certain threshold, this type of disorder suppresses the long-range triclinic structural phase transition, resulting in the preservation of monoclinic symmetry in the average structure of NMO. Taken together, these results describe an unusual mechanism for establishing magnetic LRO in the presence of frustration and a spatially inhomogeneous lattice, through which short-range correlations in the lattice sector promote long-range correlations in the magnetic sector.

II. MATERIALS AND METHODS

Powder samples of $NaMnO_2$ and $CuMnO_2$ were prepared as described in Refs. [11,21]. Temperature-dependent time-of-flight neutron total scattering measurements were conducted using the Nanoscale-Ordered Materials Diffractometer (NOMAD) instrument [28] at the Spallation Neutron Source (SNS) of Oak Ridge National Laboratory (ORNL) and the General Materials Diffractometer (GEM) [29] at the ISIS neutron source of Rutherford Appleton Laboratory (RAL). A maximum momentum transfer of 35 Å^{-1} was used when generating the real-space PDF patterns. Analysis and modeling of the atomic PDF were performed with the PDFGUI program [30] and the DIFFPY suite of programs for diffraction analysis [31]. The DIFFPY.MPDF package was used for the magnetic PDF analysis. Further details about the atomic and magnetic PDF refinements are provided in the Supplemental Material [32]. Rietveld refinements were performed within the General Structure Analysis System (GSAS) software [33] using data

collected from the high-resolution backscattering banks of the GEM diffractometer.

III. RESULTS

Atomic PDF analysis. We first present the atomic PDF analysis of NMO and CMO. The PDF, obtained from the sine Fourier transform of the reduced total scattering structure function $F(Q) = Q[S(Q) - 1]$, provides a detailed account of the local atomic structure in real space, irrespective of the character of the long-range structure. Representative PDF patterns for both compounds at room temperature are shown in Fig. 1(d). The expected monoclinic structural models explain the data well, vouching for the quality of the samples. Rietveld refinements of the Bragg intensities verified these results and allowed us to refine the average site occupancies. From this analysis, the actual compositions of our samples are $Na_{0.92}MnO_2$ and $Cu(Mn_{0.98}Cu_{0.02})O_2$, in line with compositions reported in the literature [14,34]. For simplicity, we continue to label these samples as $NaMnO_2$ and $CuMnO_2$.

Intriguingly, the low-temperature PDF fits to the NMO data using the monoclinic model are worse at low r (< 20 Å) than at high r, despite the fact that the average structure is known to be monoclinic at all temperatures. This implies that the local structure on such a short length scale deviates from the average monoclinic structure. Indeed, a triclinic structural model equivalent to that of CMO provides a significantly improved fit to the low-r region at low temperature, as seen in Fig. 2(a). Inspections of the low-r fit residuals (lower green curves) for the monoclinic and triclinic models of NMO

at 5 K reveal that high-frequency features are consistently smaller for the triclinic model, resulting in a relative improvement in χ^2 of 40% over the monoclinic model. We therefore conclude that the ground state of NMO consists of regions of locally triclinic symmetry existing within the average monoclinic structure; hence, the structure is spatially inhomogeneous. We note that the PDF measurements cannot distinguish between static and dynamic distortions, so the temporal nature of this inhomogeneity is unclear. Importantly, this short-range triclinic distortion lifts the degeneracy of the triangular lattice locally, irrespective of the fact that the average crystal structure retains its monoclinic symmetry to the lowest temperature. The broad, lower-frequency signal seen in the fit residuals in Fig. 2(a) arises from the magnetic contribution to the PDF, which we will discuss later.

Establishing the temperature dependence of this local triclinic distortion is crucial for understanding its connection to the magnetism in NMO. To this end, we refined both the monoclinic and triclinic structural models against the PDF data, which were collected on a dense temperature grid between 5 and 300 K. For each temperature T, fits were performed on a sliding data window ranging from [1.8–15 Å] to [31.8–45 Å] in 2-Å steps. We then computed the normalized difference in χ^2 between the monoclinic and triclinic models as $\Delta\chi^2/\langle\chi^2\rangle = (\chi^2_{mono} - \chi^2_{tri})/(0.5[\chi^2_{mono} + \chi^2_{tri}])$ for every refinement, quantifying the improvement offered by the triclinic model: the larger this normalized difference in χ^2 is, the better the triclinic model relative to the monoclinic model is.

In Fig. 2(b), we plot $\Delta\chi^2/\langle\chi^2\rangle$ as a function of T for the shortest and longest fitting ranges. The triclinic model performs significantly better than the monoclinic model for the short fitting range at low T. As T increases, $\Delta\chi^2/\langle\chi^2\rangle$ steadily decreases until it plateaus at a nonzero value for temperatures above $\sim 150 - 200$ K. For the longer fitting ranges, the triclinic model provides a markedly smaller relative improvement, with no pronounced changes as T varies. These results confirm that the triclinic distortion in NMO has a short-range nature and is strongest at low temperature but may persist up to room temperature.

A more comprehensive view of the T and r dependence of this local distortion is given by the color map in Fig. 2(c). The intensity scales with the triclinic splitting $d = r_2 - r_3$, which is responsible for lifting the local degeneracy of the isosceles triangles. Temperature appears on the vertical axis, and the horizontal axis displays the midpoint of the fitting range. To remove any spurious results arising from possible overfitting with the triclinic model, we scaled the d values by the difference in χ^2 between the monoclinic and triclinic models (see the Supplemental Material for further details). Figure 2(c) indicates that the greatest distortion ($d \sim 0.024$ Å) occurs below ~ 7 K and at low r. This distortion is roughly three times larger than that observed in the average structure of CMO ($d \sim 0.008$ Å). Averaging over longer distances reduces the distortion, evidenced by the weaker intensity on the right side of the color map. At low temperature, we estimate the correlation length of the local triclinic distortion to be about 20 Å. With increasing temperature, the magnitude of the distortion decreases, although it remains nonzero even at room temperature.

We display the equivalent results for CMO in Fig. 2(d). Because of the long-range structural phase transition at 65 K, the triclinic splitting remains nonzero over the entire real-space range below this temperature, albeit with somewhat enhanced splitting for short distances, suggesting incomplete ordering. Above 65 K, short-range triclinicity remains, but with a smaller magnitude and shorter real-space extent than in NMO. Overall, we observe that NMO displays significantly more spatial inhomogeneity in the form of local triclinic distortions than CMO does.

Analysis of the local octahedral environment reveals that no dramatic changes in the MnO_6 octahedra occur in either compound as the temperature is varied. The splitting of the equatorial Mn-O bonds is commensurate with the overall triclinic splitting of the a and b lattice parameters (r_2 and r_3 in Fig. 1). The PDF data at room temperature reveal that the magnitude of the Jahn-Teller (JT) distortion, defined as the ratio of the apical to equatorial Mn-O bonds (r_{ap}/r_{eq}) in the MnO_6 octahedra, is smaller in $CuMnO_2$ [1.173; $r_{ap} = 2.258(1)$Å, $r_{eq} = 1.925(1)$Å] than in $NaMnO_2$ [1.240; $r_{ap} = 2.390(1)$Å, $r_{eq} = 1.928(1)$Å]. The JT distortion in $CuMnO_2$ shows a very slight decrease of 0.1% as the temperature is lowered from room temperature to 5 K. In $NaMnO_2$, the JT distortion decreases by 0.6% over that temperature range. In the triclinic state, the equatorial bonds become slightly unequal, so we take their average when computing the distortion magnitude.

Magnetic PDF analysis. Having investigated the local atomic structures of NMO and CMO, we now turn to their magnetic structures. Figure 3(a) displays a color map of the total scattering structure function $S(Q)$ for NMO, with temperature on the vertical axis and Q on the horizontal axis. The nuclear Bragg peaks are clearly visible as intense, temperature-independent features. Below 45 K, several well-defined magnetic Bragg peaks exist between the nuclear peaks, consistent with the expected long-range AF order. Some diffuse scattering remains visible below 45 K, likely due to the presence of mixed paramagnetic and AF phases in the vicinity of the transition. As the temperature increases, the magnetic LRO melts, causing the sharp magnetic Bragg peaks to dissipate into diffuse scattering that persists up to the highest temperatures measured and extends over a broad Q range. Importantly, careful inspection of this diffuse scattering reveals that its Q dependence remains nonuniform well above the transition temperature, indicative of persistent short-range magnetic correlations. To illustrate this further, we display in Fig. 3(b) cuts of $S(Q)$ at 5, 50, and 260 K. The strong and sharp magnetic Bragg peaks at 5 K give way to a weaker and more diffuse signal at 50 K, yet distinct features are still observable in the scattering pattern. At 260 K, any structure in the diffuse scattering is much less well defined.

Additional insight can be gained by analyzing the magnetic correlations directly in real space using the magnetic PDF (mPDF) method, which is sensitive to local magnetic structure even in the absence of long-range magnetic order [27,35]. Experimentally, the mPDF signal is contained in the fit residual produced by subtracting the best-fit atomic PDF from the total PDF signal; additional details appear in the Supplemental Material. Representative mPDF patterns for NMO at 5 and 50 K are displayed in Fig. 3(c). These patterns correspond
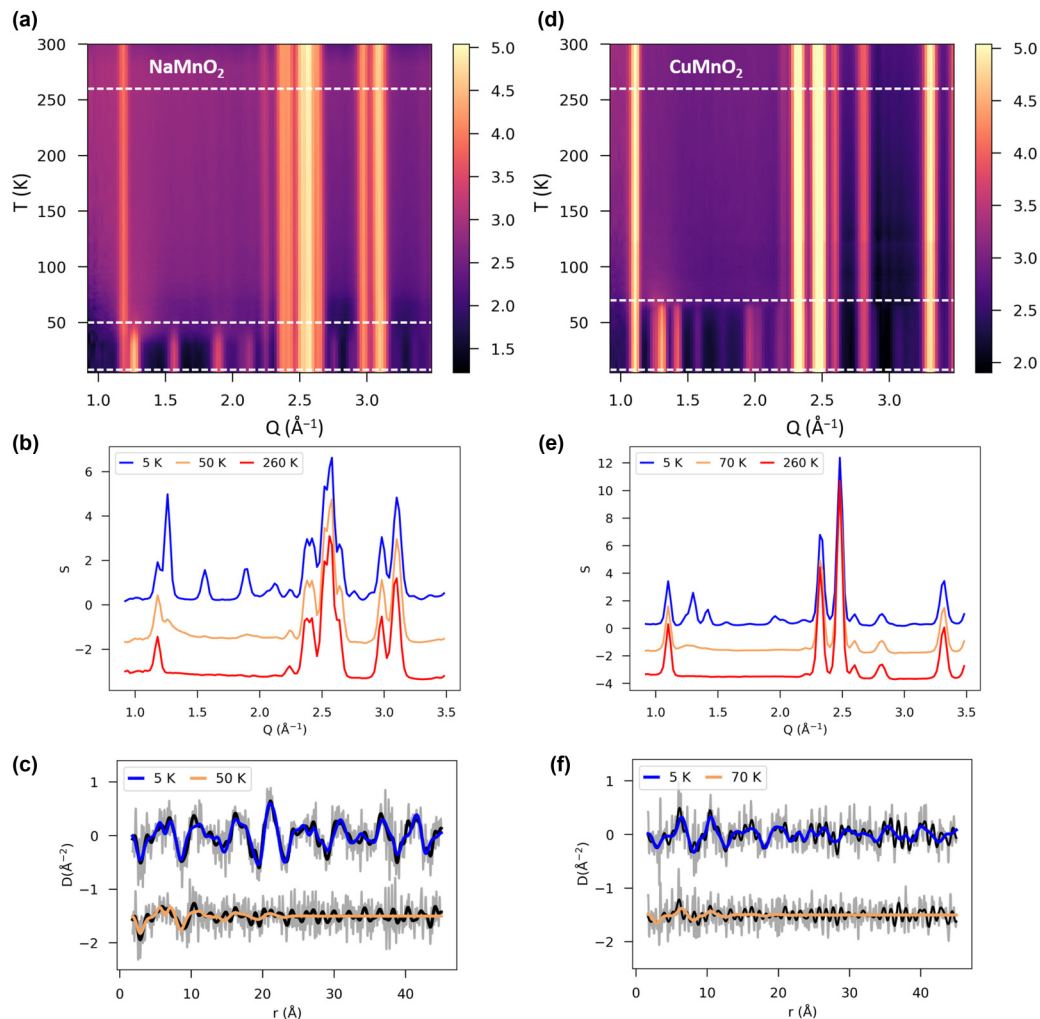
FIG. 3. Magnetic scattering and magnetic PDF analysis of CuMnO$_2$ and NaMnO$_2$. (a) Color map of the scattered intensity $S(Q)$ of NaMnO$_2$ with temperature on the vertical axis and Q on the horizontal axis. (b) $S(Q)$ for NaMnO$_2$ at 5 K (blue curve), 50 K (orange curve), and 260 K (red curve), indicated by horizontal dashed lines in (a). (c) Corresponding mPDF data for NaMnO$_2$ at 5 and 50 K. The 50 K data are offset along the y axis by -1.5 Å^{-2} for clarity. The black curves and thick gray curves represent the Fourier filtered and unfiltered data, respectively. The blue and orange curves represent the mPDF fits for 5 and 50 K, respectively. (d)–(f) Equivalent results for CuMnO$_2$. The intensity scale for (d) was chosen such that the strongest magnetic Bragg peaks for CMO and NMO have equal contrast. The magnetic model in Ref. [11] was used for the fits in (f).

to the long-wavelength oscillatory signal in the atomic PDF fit residuals shown in Fig. 2(a). The thick gray curves show the unfiltered mPDF signal mixed in with high-frequency noise, which is propagated through the Fourier transform due to the large value of Q_{max} (chosen to optimize the atomic PDF data). Applying a Fourier filter to remove all frequencies above 6.9 Å^{-1}, where the squared magnetic form factor drops below 1% its maximal value, results in the thick black curves in Fig. 3(c). This provides a cleaner signal while preserving the contribution from the magnetic scattering. The overlaid colored curves are fits that will be described subsequently. Simple inspection of the mPDF data at 5 K reveals a well-defined signal over the full r range displayed, indicative of magnetic LRO. The alternating negative and positive peaks reflect the AF spin configuration [25]. At 50 K, however, the signal is reduced in amplitude and fully suppressed in real space beyond about 20 Å, pointing to short-range magnetic correlations with a length scale of ∼2 nm.

To investigate the magnetic correlations more quantitatively, we modeled the mPDF using the known LRO AF structure published in Ref. [12]. Our model included as free parameters a scale factor (proportional to the square of the locally ordered moment), a real-space correlation length ξ, and two polar angles defining the spin direction. The mPDF fits shown in Fig. 3(c) for 5 and 50 K agree well with the data. At 5 K, the correlation length is limited by the instrumental resolution, and the refined spin direction matches previously published results [12]. Earlier work reported intrinsic inhomogeneities in the magnetic ground state in the form of nanometer-sized bubbles possessing reversed sublattice magnetization relative to the surrounding matrix of Mn spins [20]. The presence of these bubbles would cause an additional damping in the mPDF signal, which we do not observe. Therefore, any such low-temperature magnetic inhomogeneity, if present, must exist on a length scale of ∼5 nm or greater, beyond the sensitivity of the mPDF data.
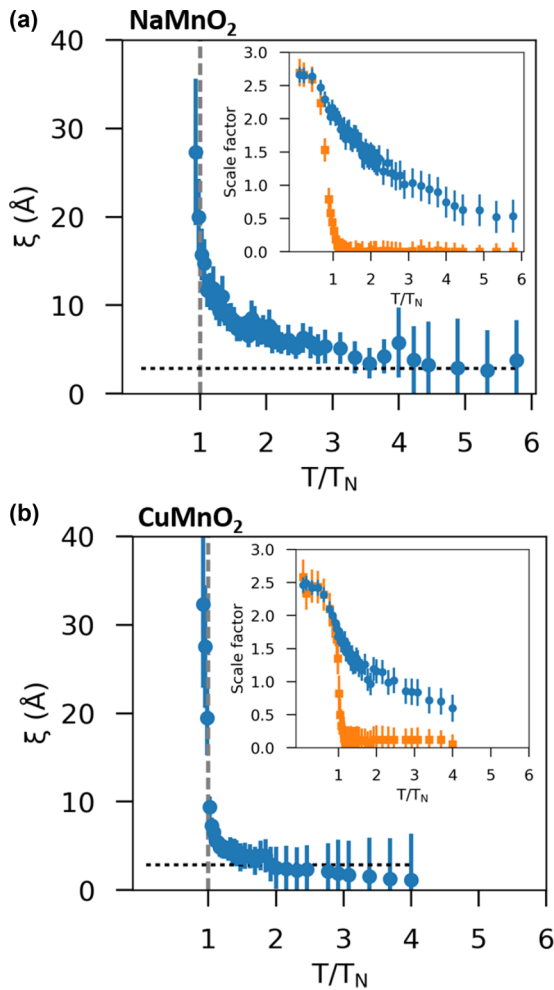
FIG. 4. Temperature evolution of magnetic correlations in $CuMnO_2$ and $NaMnO_2$. (a) Correlation length of the short-range antiferromagnetic order in $NaMnO_2$ determined from mPDF refinements using a three-dimensional model, displayed as a function of dimensionless temperature T/T_N. Below the transition (indicated by the vertical dashed line), the correlation length is limited by the instrumental resolution. The horizontal dashed line indicates the nearest-neighbor Mn-Mn distance. Inset: Refined mPDF scale factor as a function of dimensionless temperature for a fitting range of 1.8 to 15 Å (blue circles) and 30 to 45 Å (orange squares). (b) Equivalent results for $CuMnO_2$.

We note that the incommensurability of the magnetic order reported in Ref. [34] would result in a real-space modulation outside the accessible data window of these measurements. At 50 K, the fit yields a correlation length of ∼15 Å with a nearly unchanged spin direction. Interestingly, the fit can be improved by about 5% if only a single two-dimensional layer is considered and by 8% if just a one-dimensional chain of nearest-neighbor spins is used, suggesting that the short-range magnetic correlations develop a lower-dimensional character above T_N. This agrees with earlier inelastic neutron scattering analysis [13,14,34].

In Fig. 4(a), we display the refined magnetic correlation length ξ plotted against the dimensionless temperature T/T_N. Beginning slightly above $3T_N$, ξ is approximately equal to the Mn-Mn nearest-neighbor (NN) distance (illustrated by the

horizontal dashed line). Large error bars above $4T_N$ limit our ability to specify ξ at these temperatures. Below $3T_N$, the correlation length steadily increases as the temperature decreases, until it reaches its resolution-limited value below the ordering temperature of ∼45 K, marked by the vertical dashed line. The inset of Fig. 4(a) illustrates the temperature dependence of the mPDF scale factor for refinements over 1.8–15 and 31.8–45 Å. For the longer fitting range, the scale factor is zero at high temperature and shows a sharp increase for $T < T_N$, indicating a rapid onset of long-range magnetic order. In contrast, the short-range scale factor shows a much more gradual decrease as the temperature increases, remaining nonzero to 300 K, the highest measured temperature. This quantifies the persistence of significant short-range magnetic correlations at temperatures far above the long-range transition, as expected from our previous qualitative analysis of the scattering data (Fig. 3). We note that the correlation length and short-range scale factor track proportionally with the amplitude of the local lattice distortion, as seen by comparing the evolution of the local atomic structure in Figs. 2(b) and 2(c) with that of the magnetic correlations in Fig. 4(a), suggesting that they are closely connected.

The corresponding results for CMO are presented in Figs. 3(d)–3(f) and 4(b). Qualitatively, CMO shows magnetic behavior similar to that of NMO, with short-range correlations surviving into the paramagnetic phase above $T_N = 65$ K. Quantitatively, however, we find that these short-range correlations in CMO are weaker and more limited in spatial extent than for NMO. As seen in Fig. 4, the correlation length and short-fitting-range scale factor decrease above T_N significantly more rapidly in CMO than in NMO.

IV. DISCUSSION

The key experimental findings obtained from the PDF and mPDF analyses are as follows: (1) NMO exhibits a short-range triclinic distortion correlated over ∼2 nm, lifting the magnetic degeneracy locally. (2) This distortion grows in amplitude upon cooling. (3) Short-range AF correlations are present in NMO at least up to 300 K and grow in strength and correlation length upon cooling, tracking with the structural distortion, and (4) CMO exhibits a smaller local triclinic distortion and weaker AF correlations than NMO does.

Several insights can be gleaned from these results. First, they clarify the structural ground state of NMO, demonstrating that the average structure remains monoclinic, while the instantaneous local structure is triclinically distorted. Second, the observation that the triclinic distortion and magnetic SRO both grow upon cooling with a very similar temperature dependence indicates that these two effects are closely related. The relatively weaker local structural distortion and AF correlations in the paramagnetic phase of CMO compared to NMO further support this. Third, the fact that the short-range structural distortion relieves the local magnetic degeneracies naturally suggests that it promotes the growth of the AF magnetic correlations. Intriguingly, the AF correlation length increases upon cooling until matching the ∼2 nm length scale of the local triclinic distortion around T_N, at which point magnetic LRO occurs. This may indicate that magnetic coherence across neighboring triclinic regions triggers the

transition. Together, these findings provide a cohesive picture to understand the magnetic transition in NMO, in which short-range structural distortions lift the magnetic degeneracy on the nanoscale and eventually enable long-range magnetic order. In a more general context, NMO appears to be a rare example of a geometrically frustrated magnet exhibiting long-range magnetic order coupled to a short-range lattice distortion. Separately, the local triclinic distortion observed in NMO by PDF may explain various unusual experimental results in the literature, including the subtle anisotropic broadening of the low-temperature Bragg peaks seen in previous diffraction work [12], the nanoscale inhomogeneities of the ground state suggested by muon spin relaxation and nuclear magnetic resonance experiments [17,20], and the emergent magnetoelectric response [22].

Given the fundamentally similar structural and magnetic ingredients of NMO and CMO, a natural question to ask is why NMO accomplishes magnetic LRO via a short-range structural distortion, while CMO does the same with a more conventional long-range phase transition. One possibility arises from earlier *ab initio* calculations, which predicted a larger energy gain resulting from the triclinic structure in the AF state for CMO than NMO [17]. However, somewhat surprisingly, the PDF analysis demonstrates that NMO is actually more triclinic on a nanometer length scale than the average CMO triclinic distortion, counter to the predictions. Another possibility would be the presence of stronger magnetoelastic coupling in CMO than in NMO, yet this is also unlikely to be the explanation, as calculations have shown that the magnetoelastic energy scale in both materials is 2–3 orders of magnitude weaker than the magnetic exchange interactions [17].

Instead, we suggest that structural disorder plays a decisive role. In these complex systems, multiple types of disorder are present. First, the local triclinic distortion discussed previously is present in both systems and plays an active role in promoting AF correlations by lifting the magnetic degeneracy locally. Second, A-site occupancy disorder in the form of Na vacancies and excess Cu on the Mn site exist in NMO and CMO, respectively. Third, planar defects due to oxygen-layer gliding exist in both materials. The experimental evidence here and elsewhere indicates that NMO exhibits significantly more structural disorder than CMO. This is evidenced by the more pronounced distortion of the local structure in NMO than CMO, the greater percentage of site occupancy disorder (8% Na vacancies versus 2% excess Cu from antisite defects), and a higher density of planar defects (see Supplemental Material) [21,22,36]. Note that the Na vacancies and Cu impurities allow for conversion of Mn^{3+} ($S = 2$) to Mn^{4+} ($S = 3/2$) [37], which could also create magnetic disorder. It is tempting to relate such mixed-valence mediated disorder to Zener-type carriers [38,39], which may cause local inhomogeneities in the spin structure when entering bound states [40]. Verifying this scenario is beyond the resolving capabilities of our experimental probes.

These aforementioned factors of quenched disorder [41] contribute to significant exchange disorder, i.e., randomness in the magnetic exchange interactions between nearby spins. Theoretically, the NN Heisenberg model in the presence of arbitrarily weak magnetoelastic coupling predicts a critical level of exchange disorder. Below this level, a frustrated system enters the LRO Néel state through a concomitant lowering of its average lattice symmetry; above the critical level, the Néel state arises without any long-range structural distortion [42,43]. Our results suggest that CMO rests below the critical level of disorder and NMO rests above it, although differing degrees of sensitivity to perturbations between the two systems may also contribute [44]. Considering also that NMO is more frustrated than CMO and likely exhibits stronger electron-lattice coupling via an enhanced JT distortion [11,12], the larger exchange disorder may lock the spin order within the local triclinicity and thus may help NMO exit degeneracy without a long-range, symmetry-lowering phase transition as in the less frustrated and weaker JT-distorted CMO.

These arguments are in line with the observation that $CuMn_{1-x}Cu_xO_2$ displays a long-range triclinic distortion for $x < 7\%$ (which includes the current CMO sample with $x = 2\%$) but retains the high-symmetry monoclinic average structure for more disordered compounds with $x \geqslant 7\%$ [45,46]. In this picture, compounds with larger values of x possess a level of exchange disorder that exceeds the critical level, preventing the long-range structural transition to the triclinic phase, as in the case of $NaMnO_2$. Additionally, the magnetic structure in $CuMn_{1-x}Cu_xO_2$ exhibits antiferromagnetic coupling between layers for low values of x in which the triclinic phase is observed but changes to ferromagnetic coupling between layers for higher x where the long-range triclinic transition is suppressed [45,47]. $NaMnO_2$ also shows ferromagnetic coupling between the layers, further supporting the analogy between $NaMnO_2$ and heavily Cu doped $CuMnO_2$. Investigating whether the $CuMn_{1-x}Cu_xO_2$ system with $x \geqslant 7\%$ also shows a local triclinic distortion and significant short-range magnetic correlations at high temperature like NMO would be an informative follow-up study. More generally speaking, we note that the importance of local structural disorder revealed here supports similar recent findings in the canonical pyrochlore $Yb_2Ti_2O_7$ [48].

In summary, the combined atomic and magnetic PDF analysis of NMO reveals an unusual mechanism of relieving geometrical frustration in which a short-range lattice distortion results in long-range magnetic order. Comparison with CMO in the paramagnetic phase further establishes the close relationship between the short-range structural and antiferromagnetic correlations while also highlighting the role that structural disorder such as Na vacancies and Cu antisite defects plays in ground-state selection for frustrated systems. More generally, this work illuminates the cooperative intertwining of the local atomic and magnetic structures that can occur when spatial inhomogeneity meets geometrical frustration. We suggest that similar physics may be at play in numerous other TMO systems hosting geometrically frustrated magnetism. Finally, the nanoscale magnetic degeneracy lifting that occurs above T_N shares similarities with the nanoscale *orbital* degeneracy lifting observed in other systems, such as the manganites [49], iron chalcogenides [50,51], and iridates [52,53]. Together, these findings contribute to an emerging understanding of the importance of spontaneous local degeneracy lifting that appears above long-range, symmetry-broken ground states in complex materials.

The Department of Energy (DOE) will provide public access to these results of federally sponsored research in accordance with the DOE Public Access Plan [54].

[1] J. E. Greedan, Geometrically frustrated magnetic materials, J. Mater. Chem. **11**, 37 (2001).

[2] L. Balents, Spin liquids in frustrated magnets, Nature (London) **464**, 199 (2010).

[3] S.-H. Lee, H. Takagi, D. Louca, M. Matsuda, S. Ji, H. Ueda, Y. Ueda, T. Katsufuji, J.-H. Chung, S. Park, S.-W. Cheong, and C. Broholm, Frustrated magnetism and cooperative phase transitions in spinels, J. Phys. Soc. Jpn. **79**, 011004 (2010).

[4] R. Moessner and A. P. Ramirez, Geometrical frustration, Phys. Today **59**(2), 24 (2006).

[5] S. Lee, A. Pirogov, M. Kang, K.-H. Jang, M. Yonemura, T. Kamiyama, S.-W. Cheong, F. Gozzo, N. Shin, H. Kimura, Y. Noda, and J.-G. Park, Giant magneto-elastic coupling in multiferroic hexagonal manganites, Nature (London) **451**, 805 (2008).

[6] Y. Kamiya and C. D. Batista, Formation of Magnetic Microphases in $Ca_3Co_2O_6$, Phys. Rev. Lett. **109**, 067204 (2012).

[7] E. Dagotto, Complexity in strongly correlated electronic systems, Science **309**, 257 (2005).

[8] V. B. Shenoy, D. D. Sarma, and C. N. R. Rao, Electronic phase separation in correlated oxides: The phenomenon, its present status and future prospects, Chem. Phys. Chem. **7**, 2053 (2006).

[9] J.-P. Parant, R. Olazcuaga, M. Devalette, C. Fouassier, and P. Hagenmuller, Sur quelques nouvelles phases de formule Na_xMnO_2 (x ⩽ 1), J. Solid State Chem. **3**, 1 (1971).

[10] J. Töpfer, M. Trari, P. Gravereau, J. P. Chaminade, and J. P. Doumerc, Crystal growth and reinvestigation of the crystal structure of crednerite, $CuMnO_2$, Z. Kristallogr. **210**, 184 (1995).

[11] C. Vecchini, M. Poienar, F. Damay, O. Adamopoulos, A. Daoud-Aladine, A. Lappas, J. M. Perez-Mato, L. C. Chapon, and C. Martin, Magnetoelastic coupling in the frustrated antiferromagnetic triangular lattice $CuMnO_2$, Phys. Rev. B **82**, 094404 (2010).

[12] M. Giot, L. C. Chapon, J. Androulakis, M. A. Green, P. G. Radaelli, and A. Lappas, Magnetoelastic Coupling and Symmetry Breaking in the Frustrated Antiferromagnet $NaMnO_2$, Phys. Rev. Lett. **99**, 247211 (2007).

[13] C. Stock, L. C. Chapon, O. Adamopoulos, A. Lappas, M. Giot, J. W. Taylor, M. A. Green, C. M. Brown, and P. G. Radaelli, One-Dimensional Magnetic Fluctuations in the Spin-2 Triangular Lattice α-$NaMnO_2$, Phys. Rev. Lett. **103**, 077202 (2009).

[14] R. L. Dally, Y. Zhao, Z. Xu, R. Chisnell, M. B. Stone, J. W. Lynn, L. Balents, and S. D. Wilson, Amplitude mode in the planar triangular antiferromagnet $Na_{0.9}MnO_2$, Nat. Commun. **9**, 2188 (2018).

[15] F. Becca and F. Mila, Peierls-Like Transition Induced by Frustration in a Two-Dimensional Antiferromagnet, Phys. Rev. Lett. **89**, 037204 (2002).

[16] F. Damay, M. Poienar, C. Martin, A. Maignan, J. Rodriguez-Carvajal, G. André, and J. P. Doumerc, Spin-lattice coupling induced phase transition in the $s = 2$ frustrated antiferromagnet $CuMnO_2$, Phys. Rev. B **80**, 094410 (2009).

[17] A. Zorko, J. Kokalj, M. Komelj, O. Adamopoulos, H. Luetkens, D. Arcon, and A. Lappas, Magnetic inhomogeneity on a triangular lattice: The magnetic-exchange versus the elastic energy and the role of disorder, Sci. Rep. **5**, 9272 (2015).

[18] A. Zorko, S. El Shawish, D. Arčon, Z. Jagličić, A. Lappas, H. van Tol, and L. C. Brunel, Magnetic interactions in α-$NaMnO_2$: Quantum spin-2 system on a spatially anisotropic two-dimensional triangular lattice, Phys. Rev. B **77**, 024412 (2008).

[19] W. Zheng, R. R. P. Singh, R. H. McKenzie, and R. Coldea, Temperature dependence of the magnetic susceptibility for triangular-lattice antiferromagnets with spatially anisotropic exchange constants, Phys. Rev. B **71**, 134422 (2005).

[20] A. Zorko, O. Adamopoulos, M. Komelj, D. Arčon, and A. Lappas, Frustration-induced nanometre-scale inhomogeneity in a triangular antiferromagnet, Nat. Commun. **5**, 3222 (2014).

[21] A. M. Abakumov, A. A. Tsirlin, I. Bakaimi, G. Van Tendeloo, and A. Lappas, Multiple twinning as a structure directing mechanism in layered rock-salt-type oxides: $NaMnO_2$ polymorphism, redox potentials, and magnetism, Chem. Mater. **26**, 3306 (2014).

[22] F. Orlandi, E. Aza, I. Bakaimi, K. Kiefer, B. Klemke, A. Zorko, D. Arčon, C. Stock, G. D. Tsibidis, M. A. Green, P. Manuel, and A. Lappas, Incommensurate atomic and magnetic modulations in the spin-frustrated β-$NaMnO_2$ triangular lattice, Phys. Rev. Mater. **2**, 074407 (2018).

[23] J. S. Gardner, M. J. P. Gingras, and J. E. Greedan, Magnetic pyrochlore oxides, Rev. Mod. Phys. **82**, 53 (2010).

[24] T. Egami and S. J. L. Billinge, *Underneath the Bragg Peaks: Structural Analysis of Complex Materials*, 2nd ed. (Elsevier, Amsterdam, 2012).

[25] B. A. Frandsen, X. Yang, and S. J. L. Billinge, Magnetic pair distribution function analysis of local magnetic correlations, Acta Crystallogr., Sect. A **70**, 3 (2014).

[26] B. A. Frandsen and S. J. L. Billinge, Magnetic structure determination from the magnetic pair distribution function (mPDF): Ground state of MnO, Acta Crystallogr., Sect. A **71**, 325 (2015).

[27] B. A. Frandsen, M. Brunelli, K. Page, Y. J. Uemura, J. B. Staunton, and S. J. L. Billinge, Verification of Anderson Superexchange in MnO via Magnetic Pair Distribution Function Analysis and *ab initio* Theory, Phys. Rev. Lett. **116**, 197204 (2016).

[28] J. Neuefeind, M. Feygenson, J. Carruth, R. Hoffmann, and K. K. Chipley, The nanoscale ordered materials diffractometer NOMAD at the spallation neutron source SNS, Nucl. Instrum. Methods Phys. Res., Sect. B **287**, 68 (2012).

[29] W. G. Williams, R. M. Ibberson, P. Day, and J. E. Enderby, Gem–general materials diffractometer at ISIS, Phys. B (Amsterdam, Neth.) **241–243**, 234 (1997).

[30] C. L. Farrow, P. Juhás, J. Liu, D. Bryndin, E. S. Božin, J. Bloch, Th. Proffen, and S. J. L. Billinge, PDFfit2 and PDFgui: Computer programs for studying nanostructure in crystals, J. Phys.: Condens. Matter **19**, 335219 (2007).

[31] P. Juhás, C. L. Farrow, X. Yang, K. R. Knox, and S. J. L. Billinge, Complex modeling: A strategy and software program for combining multiple information sources to solve ill-posed structure and nanostructure inverse problems, Acta Crystallogr., Sect. A **71**, 562 (2015).

[32] See Supplemental Material at http://link.aps.org/supplemental/10.1103/PhysRevB.101.024423 for additional details about the atomic and magnetic pair distribution function analysis and the transmission electron microscopy characterization of $NaMnO_2$ and $CuMnO_2$.

[33] B. H. Toby, EXPGUI, a graphical user interface for GSAS, J. Appl. Crystallogr. **34**, 210 (2001).

[34] R. L. Dally, R. Chisnell, L. Harriger, Y. Liu, J. W. Lynn, and S. D. Wilson, Thermal evolution of quasi-one-dimensional spin correlations within the anisotropic triangular lattice of α-$NaMnO_2$, Phys. Rev. B **98**, 144444 (2018).

[35] B. A. Frandsen, K. A. Ross, J. W. Krizan, G. J. Nilsen, A. R. Wildes, R. J. Cava, R. J. Birgeneau, and S. J. L. Billinge, Real-space investigation of short-range magnetic correlations in fluoride pyrochlores $NaCaCo_2F_7$ and $NaSrCo_2F_7$ with magnetic pair distribution function analysis, Phys. Rev. Mater. **1**, 074412 (2017).

[36] R. J. Clément, P. G. Bruce, and C. P. Gray, Review—Manganese-based P2-type transition metal oxides as sodium-ion battery cathode materials, J. Electrochem. Soc. **162**, A2589 (2015).

[37] X. Lin, X. Ma, D. Su, L. Liu, R. Chisnell, S. P. Ong, H. Chen, A. Toumar, J.-C. Idrobo, Y. Lei, J. Bai, F. Wang, J. W. Lynn, Y. S. Lee, and G. Ceder, Direct visualization of the Jahn-Teller effect coupled to Na ordering in $Na_{5/8}MnO_2$, Nat. Mater. **13**, 586 (2014).

[38] C. Zener, Interaction between the *d* shells in the transition metals, Phys. Rev. **81**, 440 (1951).

[39] C. Zener, Interaction between the *d*-shells in the transition metals. II. Ferromagnetic compounds of manganese with perovskite structure, Phys. Rev. **82**, 403 (1951).

[40] P. G. de Gennes, Angle dependent double exchange theory, Phys. Rev. **118**, 141 (1960).

[41] J. Burgy, M. Mayr, V. Martin-Mayor, A. Moreo, and E. Dagotto, Colossal Effects in Transition Metal Oxides Caused by Intrinsic Inhomogeneities, Phys. Rev. Lett. **87**, 277202 (2001).

[42] T. E. Saunders and J. T. Chalker, Spin Freezing in Geometrically Frustrated Antiferromagnets with Weak Disorder, Phys. Rev. Lett. **98**, 157201 (2007).

[43] T. E. Saunders and J. T. Chalker, Structural phase transitions in geometrically frustrated antiferromagnets, Phys. Rev. B **77**, 214438 (2008).

[44] R. Moessner, Magnets with strong geometric frustration, Can. J. Phys. **79**, 1283 (2001).

[45] V. O. Garlea, A. T. Savici, and R. Jin, Tuning the magnetic ground state of a triangular lattice system $Cu(Mn_{1-x}Cu_x)O_2$, Phys. Rev. B **83**, 172407 (2011).

[46] M. Poienar, C. Vecchini, G. André, A. Daoud-Aladine, I. Margiolaki, A. Maignan, A. Lappas, L. Chapon, M. Hervieu, F. Damay, and C. Martin, Substitution effect on the interplane coupling in crednerite: The $Cu_{1.04}Mn_{0.96}O_2$ case, Chem. Mater. **23**, 85 (2011).

[47] N. Terada, Y. Tsuchiya, H. Kitazawa, T. Osakabe, N. Metoki, N. Igawa, and K. Ohoyama, Magnetic correlations and the influence of atomic disorder in frustrated isosceles triangular lattice antiferromagnet $CuMnO_2$, Phys. Rev. B **84**, 064432 (2011).

[48] D. F. Bowman, E. Cemal, T. Lehner, A. R. Wildes, L. Mangin-Thro, G. J. Nilsen, M. J. Gutmann, D. J. Voneshen, D. Prabhakaran, A. T. Boothroyd, D. G. Porter, C. Castelnovo, K. Refson, and J. P. Goff, Role of defects in determining the magnetic ground state of ytterbium titanate, Nat. Commun. **10**, 637 (2019).

[49] X. Qiu, Th. Proffen, J. F. Mitchell, and S. J. L. Billinge, Orbital Correlations in the Pseudocubic *O* and Rhombohedral *R* Phases of $LaMnO_3$, Phys. Rev. Lett. **94**, 177203 (2005).

[50] B. A. Frandsen, Q. Wang, S. Wu, J. Zhao, and R. J. Birgeneau, Quantitative characterization of short-range orthorhombic fluctuations in FeSe through pair distribution function analysis, Phys. Rev. B **100**, 020504(R) (2019).

[51] R. J. Koch, T. Konstantinova, M. Abeykoon, A. Wang, C. Petrovic, Y. Zhu, E. S. Bozin, and S. J. L. Billinge, Room temperature local nematicity in FeSe superconductor, Phys. Rev. B **100**, 020501(R) (2019).

[52] E. S. Božin, K. R. Knox, P. Juhás, Y. S. Hor, J. F. Mitchell, and S. J. L. Billinge, $Cu(Ir_{1-x}Cr_x)_2S_4$: A model system for studying nanoscale phase coexistence at the metal-insulator transition, Sci. Rep. **4**, 4081 (2015).

[53] E. S. Bozin, W. G. Yin, R. J. Koch, M. Abeykoon, Y. S. Hor, H. Zheng, H. C. Lei, C. Petrovic, J. F. Mitchell, and S. J. L. Billinge, Local orbital degeneracy lifting as a precursor to an orbital-selective Peirls transition, Nat. Commun. **10**, 3638 (2019).

[54] http://energy.gov/downloads/doe-public-access-plan.

Correction: Additional information for the Fulbright Foundation-Greece support statement has been inserted.

Three-dimensional Ising ferrimagnetism of Cr-Fe-Cr trimers in FeCr$_2$Te$_4$

Yu Liu (刘育) ,[1] R. J. Koch ,[1] Zhixiang Hu (胡之翔),[1,2] Niraj Aryal,[1] Eli Stavitski,[3] Xiao Tong (佟晓) ,[4]
Klaus Attenkofer,[3] E. S. Bozin ,[1] Weiguo Yin (尹卫国) ,[1] and C. Petrovic[1,2]

[1]*Condensed Matter Physics and Materials Science Department, Brookhaven National Laboratory, Upton, New York 11973, USA*
[2]*Department of Materials Science and Chemical Engineering, Stony Brook University, Stony Brook, New York 11790, USA*
[3]*National Synchrotron Light Source II, Brookhaven National Laboratory, Upton, New York 11973, USA*
[4]*Center for Functional Nanomaterials, Brookhaven National Laboratory, Upton, New York 11973, USA*

We carried out a comprehensive study of magnetic critical behavior in single crystals of ternary chalcogenide FeCr$_2$Te$_4$ that undergoes a ferrimagnetic transition below $T_c \sim 123$ K. Detailed critical behavior analysis and scaled magnetic entropy change indicate a second-order ferrimagnetic transition. Critical exponents $\beta = 0.30(1)$ with $T_c = 122.4(5)$ K, $\gamma = 1.22(1)$ with $T_c = 122.8(1)$ K, and $\delta = 4.24(2)$ at $T_c \sim 123$ K suggest that the spins approach the three-dimensional Ising ($\beta = 0.325$, $\gamma = 1.24$, and $\delta = 4.82$) model coupled with attractive long-range interactions between spins that decay as $J(r) \approx r^{-4.88}$. Our results suggest that the ferrimagnetism in FeCr$_2$Te$_4$ is due to itinerant ferromagnetism among the antiferromagnetically coupled Cr-Fe-Cr trimers.

DOI: [10.1103/PhysRevB.102.085158](https://doi.org/10.1103/PhysRevB.102.085158)

I. INTRODUCTION

Ternary ACr$_2X_4$ (A = transition metal, X = S, Se, and Te) exhibits a variety of magnetic and electronic properties. The family includes metallic CuCr$_2X_4$ and semiconducting Hg(Cd)Cr$_2$Se$_4$ ferromagnets [1–3], semiconducting Fe(Mn)Cr$_2$S$_4$ ferrimagnets [4–6], and the insulating ZnCr$_2$S$_4$ antiferromagnet [7]. The FeCr$_2X_4$ compounds show competing spin-orbit and exchange interactions [8]. FeCr$_2$S$_4$ is a ferrimagnetic (FIM) insulator below $T_c = 165$ K and shows a crossover transition from insulator to metal near T_c and colossal magnetoresistance behavior [9–11]. FeCr$_2$Se$_4$ is an insulating antiferromagnet (AFM) with $T_N = 218$ K and ferrimagnetic with a small magnetic moment of $0.007\mu_B$ below 75 K [12–14]. It should be noted that FeCr$_2$Se$_4$ crystallizes in the Cr$_3$S$_4$-type monoclinic structure described within the $C2/m$ space group, in contrast to the cubic spinel type of FeCr$_2$S$_4$. However, FeCr$_2$S$_4$ and FeCr$_2$Se$_4$ have a similar electronic structure with nearly trivalent Cr^{3+} and divalent Fe^{2+} states [15]. The magnetic moments of Cr ions are antiparallel to those of Fe ions in FeCr$_2X_4$, and there is strong hybridization between Fe 3d states and X p states [15].

FeCr$_2$Te$_4$ has not been studied much, presumably due to the difficulty in sample preparation [16–18]. Demeaux *et al.* first grew the single crystals of FeCr$_2$Te$_4$ [16]. The crystal structure was reported as a defective NiAs type within the $P6_3/mmc$ space group, where Fe and Cr occupy the same site with an alloying ratio of 1:2 and a net occupancy of 0.75 [16]. In contrast, Valiev *et al.* reported that FeCr$_2$Te$_4$ crystalizes in a CoMo$_2$S$_4$-type structure within the $I2/m$ space group, in which Fe and Cr are octahedrally coordinated by six Te [17]. Recently, a series of polycrystals FeCr$_2$Se$_{4-x}$Te$_x$ were synthesized [18]. Substitution with Te gradually suppresses the AFM order of FeCr$_2$Se$_4$ and leads to a short-range ferromagnetic (FM) cluster metallic state in polycrystal FeCr$_2$Te$_4$ [18]. In

order to study the intrinsic physical property, high-quality single crystal is required.

In this work, we successfully fabricated single crystals of FeCr$_2$Te$_4$ and performed a comprehensive study of the structural and magnetic properties. Our analysis of criticality around T_c indicates that FeCr$_2$Te$_4$ displays the three-dimensional (3D) Ising behavior, with the magnetic exchange distance decaying as $J(r) \approx r^{-4.88}$. Our first-principles calculations suggest that the ferrimagnetism in FeCr$_2$Te$_4$ stems from the itinerant ferromagnetism among the antiferromagnetically coupled Cr-Fe-Cr trimers. Since transition-metal chalcogenides represent model systems for exploring the local structure-related relationship between the broken symmetry and d-orbital magnetism [19], detailed local structure investigation of this system would be highly desirable and would bring important new insights.

II. EXPERIMENTAL DETAILS

Single crystals of FeCr$_2$Te$_4$ were fabricated by melting a stoichiometric mixture of Fe (99.99%, Alfa Aesar) powder, Cr (99.95%, Alfa Aesar) powder, and Te (99.9999%, Alfa Aesar) pieces. The starting materials were vacuum sealed in a quartz tube, heated to 1200 °C over 12 h, slowly cooled to 900 °C at a slow rate of 1 °C/h, and then quenched in ice water. The single crystal x-ray diffraction (XRD) data were taken with Cu $K\alpha$ ($\lambda = 0.15418$ nm) radiation of a Rigaku Miniflex powder diffractometer. In order to obtain more comprehensive crystallographic information, the powder XRD measurements were performed at the PDF beamline (28-ID-1) at National Synchrotron Light Source II (NSLS II) at Brookhaven National Laboratory (BNL) using a Perkin Elmer image plate detector. The setup utilized an x-ray beam with a wavelength of 0.1666 Å and a sample to detector distance of 1.25 m, as calibrated using a Ni standard. The sample was cooled

with an Oxford Cryosystems 700 cryostream using liquid nitrogen. Raw data were integrated and converted to intensity vs scattering angle using the software PYFAI [20]. The average structure was assessed from raw powder diffraction data using the General Structure Analysis System II (GSAS-II) software package [21]. The elemental analysis was performed using energy-dispersive x-ray spectroscopy (EDS) in a JEOL LSM-6500 scanning electron microscope. The x-ray absorption spectroscopy (XAS) measurements were performed at the 8-ID beamline of NSLS II (BNL) in a fluorescence mode. The x-ray absorption near-edge structure (XANES) and extended x-ray absorption fine structure (EXAFS) spectra were processed using the ATHENA software package. The AUTOBK code was used to normalize the absorption coefficient and separate the EXAFS signal $\chi(k)$ from the atom-absorption background. The extracted EXAFS signal $\chi(k)$ was weighed by k^2 to emphasize the high-energy oscillation and then Fourier transformed in a k range from 2 to 10 Å^{-1} to analyze the data in R space. The x-ray photoelectron spectroscopy (XPS) experiment was carried out in an ultrahigh-vacuum system with base pressures $<5 \times 10^{-9}$ Torr, equipped with a hemispherical electron energy analyzer (SPECS, PHOIBOS 100) and a twin-anode x-ray source (SPECS, XR50). Al $K\alpha$ (1486 eV) radiation was used at 13 kV and 30 mA. The angle between the analyzer and the x-ray source was 45°, and photoelectrons were collected along the sample surface normal. The XPS spectra were analyzed and deconvoluted using the CASAXPS software. The dc and ac magnetic susceptibilities were measured in a Quantum Design MPMS-XL5 system. The applied field H_a was corrected as $H = H_a - NM$, where M is the measured magnetization and N is the demagnetization factor. The corrected H was used for the analysis of magnetic entropy change and critical behavior.

III. RESULTS AND DISCUSSION

In the single-crystal XRD pattern (inset in Fig. 1), only $(00l)$ peaks were observed. The synchrotron powder XRD pattern of pulverized crystal of FeCr$_2$Te$_4$ can be well fitted by using a monoclinic structure with the $I2/m$ space group (Fig. 1), confirming the main phase of FeCr$_2$Te$_4$ with less than 4% FeTe impurity. The determined lattice parameters at 300 K are $a = 6.822(2)$ Å, $b = 3.938(1)$ Å, $c = 11.983(5)$ Å, and $\beta = 90.00(5)°$, close to the reported values [17,18]. No structural transition was observed on cooling, showing a compression along the c axis with $c = 11.867(5)$ Å and a slight expansion in the ab plane with $a = 6.825(1)$ Å and $b = 3.943(1)$ Å down to 105 K (Table I).

The ratio of elements in the single crystal as determined by EDS is Fe:Cr:Te = 0.99(2):1.90(2):4.0(1) [Fig. 2(a)], and it is referred to as FeCr$_2$Te$_4$ throughout this paper. The information on the valence states of Fe, Cr, and Te atoms can be obtained from the element core-level XPS spectra [Fig. 2(b)]: Fe^{2+} ($2p_{3/2} \sim 710$ eV, $2p_{1/2} \sim 723$ eV), Cr^{3+} ($2p_{3/2} \sim 575$ eV, $2p_{1/2} \sim 586$ eV), Te^{2-} ($3d_{5/2} \sim 572$ eV, $3d_{3/2} \sim 583$ eV)]. Figure 1(c) shows the normalized Cr and Fe K-edge XANES spectra, in which a similar prepeak feature is observed, indicating a similar local atomic environment for Fe and Cr atoms. The prepeak feature for the Fe K edge is somewhat weaker than that of the Cr K edge, suggesting a
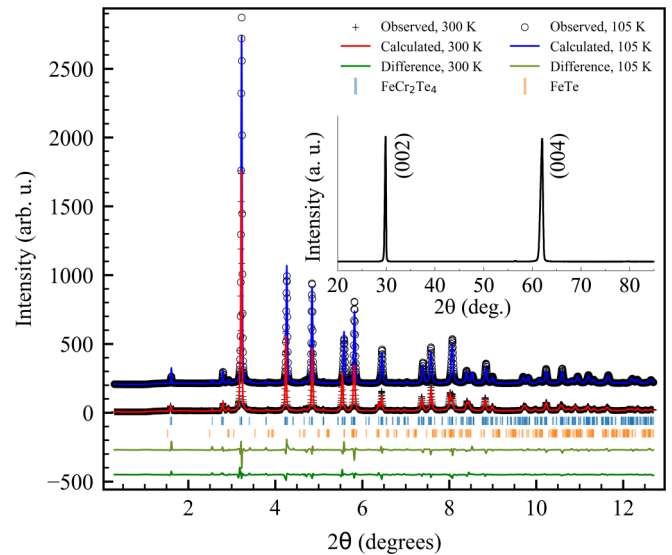

FIG. 1. Synchrotron powder x-ray diffraction (XRD) data and structural model refinements. The data are shown by + and ○; structural model fits at 300 and 105 K are shown by red and blue solid lines, respectively. The difference curves are given by green solid lines, offset for clarity. The vertical tick marks represent Bragg reflections of the $I2/m$ space group and up to 4% of FeTe impurity. The inset shows the single-crystal XRD pattern of FeCr$_2$Te$_4$ at room temperature.

weaker lattice distortion in FeTe$_6$ when compared with CrTe$_6$. The edge features are close to the standard compounds with Cr^{3+} and Fe^{2+} oxidation states [22,23], in line with the XPS result.

The local environment of Fe and Cr atoms is revealed in the EXAFS spectra of FeCr$_2$Te$_4$ measured at room temperature

TABLE I. Average and local structural parameters extracted from the powder XRD and the EXAFS spectra of FeCr$_2$Te$_4$. CN is the coordination number based on the crystallographic value, R is the interatomic distance, and σ^2 is the Debye-Waller factor.

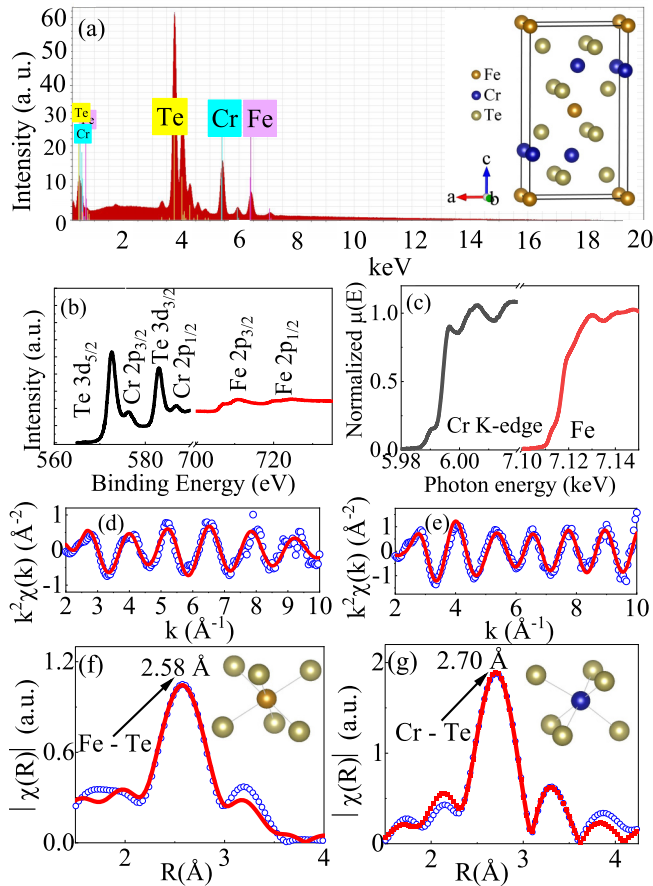|	300 K		105 K	
a (Å)	6.822(2)		6.825(1)	
b (Å)	3.938(1)		3.943(1)	
c (Å)	11.983(5)		11.867(5)	
β (°)	90.00(5)		90.01(15)	
Atom	Site	x	y	z
Fe	$2a$	0	0	0
Cr	$4i$	0.001(3)	0	0.2541(8)
Te1	$4i$	0.328(4)	0	0.3726(4)
Te2	$4i$	0.339(4)	0	0.8785(4)
Bond	CN	R (Å)	ΔR (Å)	σ^2 (Å^2)
Cr-Te1	2	2.58	0.01	0.001
Cr-Te2	1	2.67	0.01	0.001
Cr-Te3	1	2.80	0.11	0.003
Cr-Te4	2	2.86	0.11	0.003
Fe-Te1	4	2.69	0.36	0.02
Fe-Te2	2	2.75	0.24	0.02

FIG. 2. (a) Crystal structure and results of EDS analysis on $FeCr_2Te_4$. (b) Room-temperature Fe $2p$, Cr $2p$, and Te $3d$ core-level XPS and (c) normalized Cr and Fe K-edge XANES spectra. (d) and (e) Fe and Cr K-edge EXAFS oscillations and (f) and (g) Fourier transform magnitudes of EXAFS data measured at room temperature. The experimental data are shown as blue symbols alongside the model fit plotted as a red line. The corresponding first coordination shells of Fe and Cr are shown in the insets.

FIG. 3. (a) Temperature-dependent dc magnetic susceptibility $\chi(T)$ in zero-field cooling (ZFC) and field-cooling (FC) modes taken at $\mu_0 H = 0.1$ T for $\mu_0 \mathbf{H} \parallel \mathbf{c}$ and $\mu_0 \mathbf{H} \parallel \mathbf{ab}$ (inset), respectively. (b) $1/\chi(T)$ taken at $\mu_0 H = 0.1$ T along with the Curie-Weiss fit from 150 to 300 K. (c) Field dependence of magnetization for $FeCr_2Te_4$ measured at $T = 2$ K. (d) The ac susceptibility real part $m'(T)$ measured with an oscillating ac field of 3.8 Oe and frequency of 499 Hz. The chosen experimental parameters (field and frequency) allow for a well-defined moment and adequate frequency resolution.

[Figs. 1(d) and 2(e)]. In a single-scattering approximation, the EXAFS can be described by [24]

$$\chi(k) = \sum_i \frac{N_i S_0^2}{k R_i^2} f_i(k, R_i) e^{-\frac{2R_i}{\lambda}} e^{-2k^2 \sigma_i^2} \sin[2kR_i + \delta_i(k)],$$

where N_i is the number of neighboring atoms at a distance R_i from the photoabsorbing atom. S_0^2 is the passive electron reduction factor, $f_i(k, R_i)$ is the backscattering amplitude, λ is the photoelectron mean free path, δ_i is the phase shift, and σ_i^2 is the correlated Debye-Waller factor measuring the mean-square relative displacement of the photoabsorber-backscatter pairs. The corrected main peak in the Fourier transform magnitudes of Fe K-edge EXAFS around $R \sim 2.58$ Å is clearly smaller than that of Cr K-edge EXAFS at $R \sim 2.70$ Å [Figs. 1(f) and 2(g)]. The different local Fe-Te and Cr-Te bond lengths suggest that the Fe and Cr atoms might occupy different crystallographic sites, ruling out the possibility of a NiAs-type structure with the same Fe/Cr sites. Then we focus on the first-nearest neighbors of Fe and Cr atoms ranging from 1.5 to 3.5 Å. The main peak corresponds to two Fe-Te bond

lengths of 2.69 and 2.75 Å and four different Cr-Te bond lengths with 2.58, 2.67, and 2.80, and 2.86 Å, extracted from the model fits with a fixed coordination number. The peaks above 3.25 Å are due to longer Fe-Cr, Fe-Te, and Cr-Te bond distances, and the multiple scattering involving different near neighbors of the Fe/Cr atoms.

Figure 3(a) shows the temperature dependence of magnetization measured in out-of-plane field $\mu_0 H = 0.1$ T, in which χ increases with decreasing temperature and increases abruptly near T_c due to the paramagnetic (PM)-FIM transition. The in-plane $\chi(T)$ [inset in Fig. 3(a)] is much smaller than that in the out-of-plane field, indicating the presence of large magnetic anisotropy with an easy c axis. The average susceptibility $\chi_{ave} = (2/3)\chi_{ab} + (1/3)\chi_c$ from 150 to 300 K can be fitted by the Curie-Weiss law $\chi_{ave} = \chi_0 + C/(T - \theta)$ [Fig. 3(c)], which yields $\chi_0 = 0.87(1)$ emu/mol Oe, $C = 7.91(6)$ emu K/mol Oe [$\mu_{eff} = 7.95(9)\mu_B$ per formula unit], and $\theta = 126.6(2)$ K. The positive value of θ indicates the dominance of ferromagnetic or ferrimagnetic exchange interactions in $FeCr_2Te_4$. For monoclinic $FeCr_2Se_4$ with a similar layered structure, the individual spins of Fe and Cr ions have AFM coupling along the c axis with a distance of 2.956 Å, while FM coupling is along the b axis with a distance of 3.617 Å [25]. At low temperature, the FM interaction dominating over the AFM interaction results in a

FIM ground state. For $FeCr_2Te_4$, the enhanced hybridization between the d orbital of Fe and Cr with the p orbital of Te plays an important role in magnetic coupling. Based on our first-principles calculation (see below), the FIM structure where Fe and Cr atoms have opposite spin orientations is the most stable state in $FeCr_2Te_4$ when compared with the FM and AFM structures, which needs further verification by neutron scattering experiment. The bifurcation between zero-field-cooling and field-cooling curves [Fig. 3(a)] might be due to strong magnetic anisotropy and/or multidomain structure, which has also been observed in other long-range FM single crystals, such as U_2RhSi_3 [26]. The magnetization loops of $FeCr_2Te_4$ for both field directions at $T = 2$ K confirm a large magnetic anisotropy and easy c axis [Fig. 3(c)]. The sudden jumps around $\mu_0H \approx \pm 1$ T along the c axis can be ascribed to the magnetic domain creeping behavior; that is, the magnetic domain walls jump from one pinning site to another. Then we estimated the Rhodes-Wohlfarth ratio (RWR) for $FeCr_2Te_4$, which is defined as P_c/P_s, with P_c obtained from the effective moment $P_c(P_c + 2) = P_{eff}^2$ and P_s being the saturation moment obtained in the ordered state [27–29]. RWR is 1 for a localized system and is larger in an itinerant system. Here we obtain RWR ≈ 1.69 for $FeCr_2Te_4$, indicating a weak itinerant character. To obtain an accurate Curie temperature T_c, out-of-plane ac susceptibility was measured at an oscillating ac field of 3.8 Oe and a frequency of 499 Hz. The single sharp peak in the real part $m'(T)$ [Fig. 3(d)] gives $T_c = 124$ K.

In the following we discuss the nature of the PM-FIM transition for $FeCr_2Te_4$. The magnetization isotherms along the easy c axis were measured at various temperatures in the vicinity of T_c [Fig. 4(a)]. We first considered the well-known Arrott plot [30]. From the Landau theory, the Arrott plot of M^2 vs H/M should appear as parallel straight lines above and below T_c, and the line passes through the origin at T_c. It is clear that the mean-field critical exponent does not work for $FeCr_2Te_4$, as illustrated by the set of curved lines shown in Fig. 4(b).

For a second-order phase transition, the spontaneous magnetization M_s below T_c, the inverse initial susceptibility χ_0^{-1} above T_c, and the field-dependent magnetization $M(H)$ at T_c are [31–33]

$$M_s(T) = M_0(-\varepsilon)^\beta, \quad \varepsilon < 0, T < T_c, \quad (1)$$

$$\chi_0^{-1}(T) = (h_0/m_0)\varepsilon^\gamma, \quad \varepsilon > 0, T > T_c, \quad (2)$$

$$M = DH^{1/\delta}, \quad T = T_c, \quad (3)$$

where $\varepsilon = (T - T_c)/T_c$ is the reduced temperature and M_0, h_0/m_0, and D are the critical amplitudes. In a more general case, the modified Arrott plot $(H/M)^{1/\gamma} = a\varepsilon + bM^{1/\beta}$ with the self-consistent method was considered [34,35]. Figure 4(c) presents the final modified Arrott plot of $M^{1/\beta}$ vs $(H/M)^{1/\gamma}$ with $\beta = 0.32$ and $\gamma = 1.21$, showing a set of quasiparallel lines in the high-field region. Then we extracted $\chi_0^{-1}(T)$ and $M_s(T)$ as the intercepts on the H/M axis and the positive M^2 axis, respectively. The magnetic entropy change can be
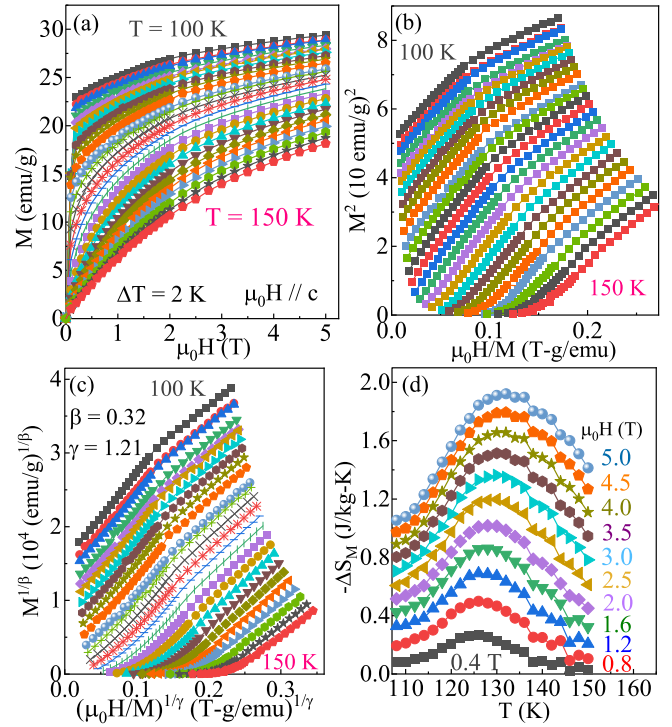

FIG. 4. (a) Typical initial isothermal magnetization curves from 100 to 150 K with a temperature step of 2 K for the $FeCr_2Te_4$ single crystal. (b) Arrott plot ($\beta = 0.5$, $\gamma = 1$) and (c) the modified Arrott plot with the optimum exponents $\beta = 0.32$ and $\gamma = 1.21$. (d) Temperature-dependent magnetic entropy change $-\Delta S_M(T)$ at various fields.

estimated using Maxwell's relation [36]:

$$\Delta S_M(T, H) = \int_0^H \left[\frac{\partial M(T, H)}{\partial T} \right]_H dH. \quad (4)$$

Figure 4(d) presents the calculated $-\Delta S_M$ as a function of temperature. $-\Delta S_M$ shows a broad peak centered near T_c, and the peak value monotonically increases with increasing field. The maximum value of $-\Delta S_M$ reaches 1.92 J kg^{-1} K^{-1} with a field change of 5 T. There is a slight shift of the $-\Delta S_M$ peak towards higher temperature with increasing field, which also excludes the mean-field model [37].

Figure 5(a) presents the extracted $M_s(T)$ and $\chi_0^{-1}(T)$ as a function of temperature. According to Eqs. (1) and (2), the critical exponents $\beta = 0.33(2)$ with $T_c = 122.9(3)$ K and $\gamma = 1.20(1)$ with $T_c = 122.7(1)$ K are obtained. The exponent β describes the rapid increase of the order parameter below T_c. The exponent γ describes how magnetic susceptibility diverges at T_c. Here the obtained result describes the critical behavior of the net spontaneous magnetization that arises in the ferrimagnet. In the Kouvel-Fisher relation [38]

$$M_s(T)[dM_s(T)/dT]^{-1} = (T - T_c)/\beta, \quad (5)$$

$$\chi_0^{-1}(T)[d\chi_0^{-1}(T)/dT]^{-1} = (T - T_c)/\gamma. \quad (6)$$

Linear fittings to the plots of $M_s(T)[dM_s(T)/dT]^{-1}$ and $\chi_0^{-1}(T)[d\chi_0^{-1}(T)/dT]^{-1}$ in Fig. 5(b) yield $\beta = 0.30(1)$ with $T_c = 122.4(5)$ K and $\gamma = 1.22(1)$ with $T_c = 122.8(1)$ K. The
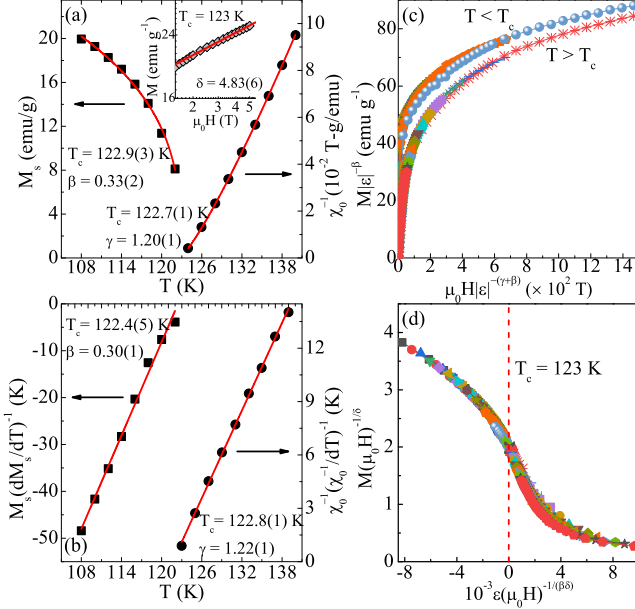
FIG. 5. (a) Temperature dependence of the spontaneous magnetization M_s (left) and the inverse initial susceptibility χ_0^{-1} (right) with solid fitting curves. The inset shows $\log_{10}M$ vs $\log_{10}(\mu_0H)$ collected at $T_c = 123$ K with a linear fitting curve. (b) Kouvel-Fisher plots of $M_s(dM_s/dT)^{-1}$ (left axis) and $\chi_0^{-1}(d\chi_0^{-1}/dT)^{-1}$ (right axis) with solid fitting curves. (c) Scaled magnetization m vs scaled field h below and above T_c for FeCr$_2$Te$_4$. (d) The rescaling of the $M(\mu_0H)$ curves by $M(\mu_0H)^{-1/\delta}$ vs $\varepsilon(\mu_0H)^{-1/(\beta\delta)}$.

third exponent δ can be calculated from the Widom scaling relation $\delta = 1 + \gamma/\beta$ [39]. From β and γ obtained with the modified Arrott plot and the Kouvel-Fisher plot, $\delta = 4.6(2)$ and $5.1(1)$ are obtained, respectively, which are close to the direct fit of $\delta = 4.83(6)$, taking into account that $M = DH^{1/\delta}$ at $T_c = 123$ K [inset in Fig.5(a)]. The obtained critical exponents of FeCr$_2$Te$_4$ are very close to the theoretically predicted values of the 3D Ising model ($\beta = 0.325$, $\gamma = 1.24$, and $\delta = 4.82$; Table II).

A scaling analysis can be used to estimate the reliability of the obtained critical exponents and T_c. The magnetic equation of state in the critical region is expressed as

$$M(H, \varepsilon) = \varepsilon^\beta f_\pm(H/\varepsilon^{\beta+\gamma}), \qquad (7)$$

where f_+ for $T > T_c$ and f_- for $T < T_c$, respectively, are the regular functions. Equation (7) can be further written in

terms of scaled magnetization $m \equiv \varepsilon^{-\beta}M(H, \varepsilon)$ and scaled field $h \equiv \varepsilon^{-(\beta+\gamma)}H$ as $m = f_\pm(h)$. This suggests that for true scaling relations and the right choice of β, γ, and δ, scaled m and h will fall on universal curves above T_c and below T_c, respectively. As shown in Fig. 5(c), all the data collapse on two separate branches below and above T_c, respectively. The scaling equation of state takes another form,

$$\frac{H}{M^\delta} = k\left(\frac{\varepsilon}{H^{1/\beta}}\right), \qquad (8)$$

where $k(x)$ is the scaling function. From the above equation, all the data should also fall onto a single curve. This is, indeed, seen [Fig. 5(d)]; the $M(\mu_0H)^{-1/\delta}$ vs $\varepsilon(\mu_0H)^{-1/(\beta\delta)}$ experimental data collapse into a single curve, and T_c locates at the zero point of the horizontal axis. The well-rescaled curves confirm the reliability of the obtained critical exponents and T_c.

Furthermore, it is important to discuss the nature as well as the range of magnetic interaction in FeCr$_2$Te$_4$. In a homogeneous magnet the universality class of the magnetic phase transition depends on the exchange distance $J(r)$. In renormalization group theory analysis the interaction decays with distance r as $J(r) \approx r^{-(3+\sigma)}$, where σ is a positive constant [40,41]. The susceptibility exponent γ is

$$\gamma = 1 + \frac{4}{d}\left(\frac{n+2}{n+8}\right)\Delta\sigma + \frac{8(n+2)(n-4)}{d^2(n+8)^2}$$
$$\times \left[1 + \frac{2G(\frac{d}{2})(7n+20)}{(n-4)(n+8)}\right]\Delta\sigma^2, \qquad (9)$$

where $\Delta\sigma = (\sigma - \frac{d}{2})$, $G(\frac{d}{2}) = 3 - \frac{1}{4}(\frac{d}{2})^2$, and n is the spin dimensionality [42]. When $\sigma > 2$, the Heisenberg model is valid for the 3D isotropic magnet, where $J(r)$ decreases faster than r^{-5}. When $\sigma \leqslant 3/2$, the mean-field model is satisfied, assuming that $J(r)$ decreases slower than $r^{-4.5}$. For the 3D Ising model with $d = 3$ and $n = 1$, $\sigma = 1.88$ is obtained, leading to spin interactions $J(r)$ decaying as $J(r) \approx r^{-4.88}$. This calculation suggests that the spin interaction in FeCr$_2$Te$_4$ is close to the 3D Ising localized-type coupled with a long-range ($\sigma = 1.88$) interaction, in line with its weak itinerant character. Meanwhile, the correlation length ξ correlates with the critical exponent ν ($\nu = \gamma/\sigma$), where $\xi = \xi_0[(T - T_c)/T_c]^{-\nu}$. It gives $\nu = 0.64(1)$ and $\alpha = 0.08$ ($\alpha = 2 - \nu d$).

To get further insight into the magnetism, we performed first-principles calculations using density function theory. We applied the WIEN2K implementation [43] of the full-potential

TABLE II. Comparison of critical exponents of FeCr$_2$Te$_4$ with different theoretical models.

	Reference	Technique	T_{c-}	T_{c+}	β	γ	δ
FeCr$_2$Te$_4$	This work	Modified Arrott plot	122.9(3)	122.7(1)	0.33(2)	1.20(1)	4.6(2)
	This work	Kouvel-Fisher plot	122.4(5)	122.8(1)	0.30(1)	1.22(1)	5.1(1)
	This work	Critical isotherm					4.83(6)
3D Heisenberg	28	Theory			0.365	1.386	4.8
3D XY	28	Theory			0.345	1.316	4.81
3D Ising	28	Theory			0.325	1.24	4.82
Tricritical mean field	36	Theory			0.25	1.0	5.0

TABLE III. The first-principles total energy (in meV) per formula unit of different magnetic patterns as shown in Fig. 6(a) using the 300 and 105 K experimental structures. In the E-AF-2 pattern, a Cr atom is antiferromagnetically and ferromagnetically aligned with the closest and farthest of its six nearest Cr neighbors, respectively; the opposite holds in the E-AF-1 pattern. FM means the ferromagnetic configuration.

Structure	Ferri	FM	C-AF	E-AF-1	E-AF-2
300 K	8	90	197	31	82
105 K	0	56	171	72	32

linearized augmented plane-wave method in the generalized gradient approximation using the PBEsol functional [44]. The basis size was determined by $R_{mt}K_{max} = 7$, and the Brillouin zone was sampled with 115 irreducible k points to achieve energy convergence of 1 meV. As shown in Table III, we found that for the experimental structure refined at 105 K, the ferrimagnetic state where the Cr and Fe atoms have opposite spin orientations is 56 meV per formula unit lower in total energy than the ferromagnetic phase and 32 meV lower than the most stable antiferromagnetic structure (i.e., E-AF-2) as observed in $FeCr_2Se_4$ [45]. A similar trend of the results holds for the experimental structure refined at 300 K (Table III). A weak easy c-axis anisotropy was obtained by inclusion of spin-orbit coupling in the calculations; namely, the total energy per formula unit is lower by less than 1 meV for the magnetization along the c axis than along the a or b axis. Thus, other sources of magnetic anisotropy such as dipole-dipole interaction are important. The calculated atom-resolved density of states (DOS) is shown in Figs. 6(b) and 6(c). For the nonmagnetic case, the Cr-derived DOS has a sharp peak at the Fermi level [Figs. 6(b)], suggesting a strong Stoner instability that yields an itinerant ferromagnetism in the Cr layers. This yields the splitting of about 2.8 eV between the spin-majority and spin-minority bands of Cr character with the dramatic reduction of the Cr-derived DOS at the Fermi level [Fig. 6(c)], indicative of the localized spin picture for the Cr atoms. However, the nonmagnetic Fe-derived DOS peaks at about 0.6 eV below the Fermi level [Fig. 6(b)] and experiences little reduction at the Fermi level upon entering the magnetic phase [Fig. 6(c)]. We infer that the magnetism of the Fe ions is established via antiferromagnetic superexchange with the neighboring two Cr ions. The Cr magnetic moment within the atomic muffin tins is about $2.88\mu_B$, which is close to the nominal Cr^{3+} $S = 3/2$ state. With the octahedral coordination, the splitting of the five $3d$ orbitals between the high-lying e_g and low-lying t_{2g} orbitals is substantial. The $S = 3/2$ state of the Cr^{3+} ion (i.e., the $3d^3$ or $t_{2g}^3 e_g^0$ electron configuration) means that the Cr t_{2g} orbitals are half filled, rendering a vanishing orbital angular moment and a negligible spin-orbit coupling effect. The Fe magnetic moment is about $2.80\mu_B$, significantly deviating from the nominal high-spin Fe^{2+} $S = 2$ state, which indicates its dual character with both localized spins and itinerant electrons. This reveals an interesting interplay of Cr and Fe electronic states, which allows the spin-majority bands of the system at the Fermi level to be of Fe character rather than Cr character [Fig. 6(c)]. We thus picture the FIM in $FeCr_2Te_4$
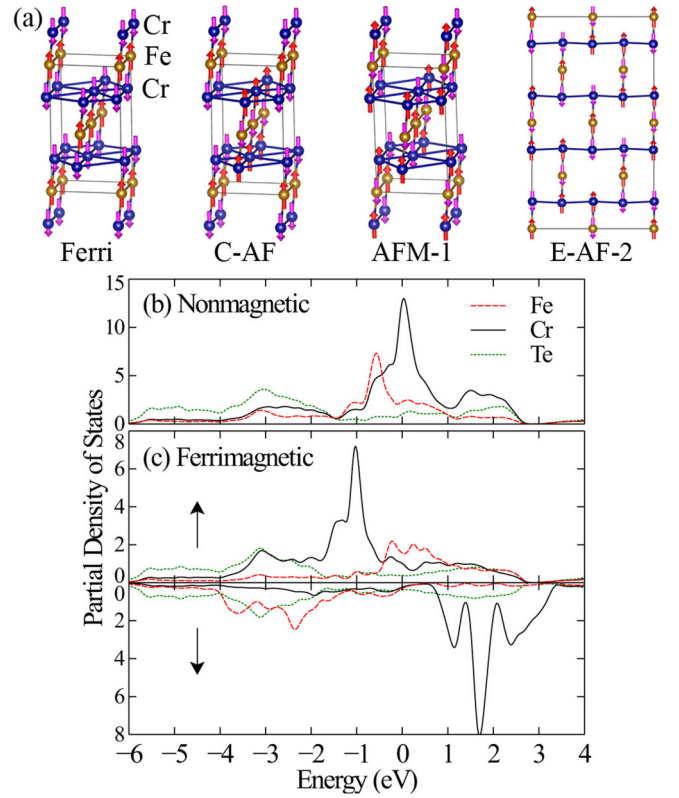

FIG. 6. (a) The antiferromagnetic structures used in the first-principles total energy calculations. Atom-resolved density of states (b) in the nonmagnetic state and (c) in the ferrimagnetic state where the Cr and Fe atoms have opposite spin orientations, which are shown in the ratio of two Cr ions to one Fe ion.

as itinerant ferromagnetism among the antiferromagnetically coupled Cr-Fe-Cr trimers. The trimers centered at the Fe sites form a body-centered orthorhombic lattice of magnetic dipoles with an effective moment of $2\mu_B S = 4\mu_B$ [Fig. 3(c)]. In addition to the effective Heisenberg exchange interaction, the ith trimer is coupled with its ten neighboring trimers [Fig. 6(a)] via dipole-dipole interaction $\propto -(\mathbf{S}_i \cdot \mathbf{r}_{ij})(\mathbf{S}_j \cdot \mathbf{r}_{ij})/|\mathbf{r}_{ij}|^5$, which tends to align the magnetic moments along the bond direction $\mathbf{r}_{ij} = \mathbf{r}_i - \mathbf{r}_j$, where j denotes one of the neighboring trimers and $\mathbf{r}_i$ is the spatial vector of the ith trimer. Since the body-centered orthorhombic structure of the trimers is substantially elongated along the c axis, easy c-axis magnetic anisotropy has the overall minimum deviation from the neighboring bond directions. We thus predict that the 3D Ising-like ferrimagnetism is sensitive to changes in the lattice structure, especially the tilting of the Cr-Fe-Cr trimers, which will be verified by future pressure experiments and computer simulations.

IV. CONCLUSIONS

In summary, we systematically investigated structural and magnetic properties of stoichiometric $FeCr_2Te_4$ that crystallizes in the $I2/m$ space group. The second-order PM-FIM transition was observed at $T_c \sim 123$ K. The critical exponents β, γ, and δ estimated from various techniques match

reasonably well and follow the scaling equation. The analysis of critical behavior suggests that $FeCr_2Te_4$ is a 3D Ising system displaying a long-range exchange interaction with the exchange distance decaying as $J(r) \approx r^{-4.88}$. Combined experimental and theoretical analysis attributes the ferrimagnetism in $FeCr_2Te_4$ to itinerant ferromagnetism among the antiferromagnetically coupled Cr-Fe-Cr trimers. Follow-up studies of local atomic structure and magnetism using x-ray and neutron scattering as well as high-pressure methods will be of particular interest for more comprehensive understanding of this system.

[1] T. Kanomata, H. Ido, and T. Kaneko, J. Phys. Soc. Jpn. **29**, 332 (1970).

[2] H. W. Lehmann and F. P. Emmenegger, Solid State Commun. **7**, 965 (1969).

[3] N. Menyuk, K. Dwight, and R. J. Arnott, J. Appl. Phys. **37**, 1387 (1966).

[4] Z. R. Yang, S. Tan, Z. W. Chen, and Y. H. Zhang, Phys. Rev. B **62**, 13872 (2000).

[5] V. Tsurkan, M. Mücksch, V. Fritsch, J. Hemberger, M. Klemm, S. Klimm, S. Körner, H. A. Krug von Nidda, D. Samusi, E. W. Scheidt, A. Loidl, S. Horn, and R. Tidecks, Phys. Rev. B **68**, 134434 (2003).

[6] K. Ohgushi, Y. Okimoto, T. Ogasawara, S. Miyasaka, and Y. Tokura, J. Phys. Soc. Jpn. **77**, 034713 (2019).

[7] J. Hemberger, T. Rudolf, H. A. Krug von Nidda, F. Mayr, A. Pimenov, V. Tsurkan, and A. Loidl, Phys. Rev. Lett. **97**, 087204 (2006).

[8] J. Bertinshaw, C. Ulrich, A. Gunter, F. Schrettle, M. Wohlauer, S. Krohns, M. Reehuis, A. J. Studer, M. Avdeev, D. V. Quach, J. R. Groza, V. Tsurkan, A. Loidl, and J. Deisenhofer, Sci. Rep. **4**, 6079 (2014).

[9] V. Tsurkan, O. Zaharko, F. Schrettle, C. Kant, J. Deisenhofer, H. A. Krug von Nidda, V. Felea, P. Lemmens, J. R. Groza, D. V. Quach, F. Gozzo, and A. Loidl, Phys. Rev. B **81**, 184426 (2010).

[10] V. Tsurkan, I. Fita, M. Baran, R. Puzniak, D. Samusi, R. Szymczak, H. Szymczak, S. Lkimm, M. Kliemm, S. Honn, and R. Tidecks, J. Appl. Phys. **90**, 875 (2001).

[11] A. P. Ramirez, R. J. Cava, and J. Krajewski, Nature (London) **386**, 156 (1997).

[12] B. I. Min, S. S. Baik, H. C. Choi, S. K. Kwon, and J. S. Kang, New J. Phys. **10**, 055014 (2008).

[13] G. J. Snyder, T. Caillat, and J. P. Fleurial, Phys. Rev. B **62**, 10185 (2000).

[14] H. N. Ok and C. S. Lee, Phys. Rev. B **33**, 581 (1986).

[15] J. S. Kang, G. Kim, H. J. Lee, H. S. Kim, D. H. Kim, S. W. Han, S. J. Kim, C. S. Kim, H. Lee, J. Y. Kim, and B. I. Min, J. Appl. Phys. **103**, 07D717 (2008).

[16] A. B. Demeaux, G. Villers, and P. Gibart, J. Solid State Chem. **15**, 178 (1975).

[17] L. M. Valiev, I. G. Kerimov, S. Kh. Babayev, and Z. M. Namazov, Russ. J. Inorg. Mater. **11**, 213 (1975).

[18] C. S. Yadav, S. K. Pandey, and P. L. Paulose, arXiv:1904.06661.

[19] E. S. Bozin, W. G. Yin, R. J. Koch, M. Abeykoon, Y. S. Hor, H. Zheng, H. C. Lei, C. Petrovic, J. F. Mitchell, and S. J. L. Billinge, Nat. Commun. **10**, 3638 (2019).

[20] J. Kieffer and J. P. Wright, Powder Diffr. **28**, 339 (2013).

[21] B. H. Toby and R. B. Von Dreele, J. Appl. Crystallogr. **46**, 544 (2013).

[22] A. Ignatov, C. L. Zhang, M. Vannucci, M. Croft, T. A. Tyson, D. Kwok, Z. Qin, and S.-W. Cheong, arXiv:0808.2134.

[23] H. Ofuchi, N. Ozaki, N. Nishizawa, H. Kinjyo, S. Kuroda, and K. Takita, AIP Conf. Proc. **882**, 517 (2007).

[24] *X-ray Absorption: Principles, Applications, Techniques of EXAFS, SEXAFS, XANES*, edited by R. Prins and D. C. Koningsberger (Wiley, New York, 1988).

[25] K. Adachi, K. Sato, and K. Kojima, Mem. Fac. Eng. Nagoya Univ. Jpn. **22**, 253 (1970).

[26] M. Szlawska, M. Majewicz, and D. Kaczorowski, J. Alloys Compd. **662**, 208 (2016).

[27] E. P. Wohlfarth, J. Magn. Magn. Mater. **7**, 113 (1978).

[28] T. Moriya, J. Magn. Magn. Mater. **14**, 1 (1979).

[29] Y. Takahashi, *Spin Fluctuation Theory of Itinerant Electron Magnetism*, Springer Tracts in Modern Physics Vol. 253 (Springer, Berlin, 2013).

[30] A. Arrott, Phys. Rev. **108**, 1394 (1957).

[31] H. E. Stanley, *Introduction to Phase Transitions and Critical Phenomena* (Oxford University Press, London, 1971).

[32] M. E. Fisher, Rep. Prog. Phys. **30**, 615 (1967).

[33] J. Lin, P. Tong, D. Cui, C. Yang, J. Yang, S. Lin, B. Wang, W. Tong, L. Zhang, Y. Zou, and Y. Sun, Sci. Rep. **5**, 7933 (2015).

[34] W. Kellner, M. Fähnle, H. Kronmüller, and S. N. Kaul, Phys. Status Solidi B **144**, 387 (1987).

[35] A. K. Pramanik and A. Banerjee, Phys. Rev. B **79**, 214426 (2009).

[36] J. Amaral, M. Reis, V. Amaral, T. Mendonc, J. Araujo, M. Sa, P. Tavares, and J. Vieira, J. Magn. Magn. Mater. **290**, 686 (2005).

[37] V. Franco, A. Conde, M. D. Kuzmin, and J. M. Romero-Enrique, J. Appl. Phys. **105**, 07A917 (2009).

[38] J. S. Kouvel and M. E. Fisher, Phys. Rev. **136**, A1626 (1964).

[39] B. Widom, J. Chem. Phys. **41**, 1633 (1964).

[40] S. Kaul, J. Magn. Magn. Mater. **53**, 5 (1985).

[41] M. E. Fisher, S. K. Ma, and B. G. Nickel, Phys. Rev. Lett. **29**, 917 (1972).

[42] S. F. Fischer, S. N. Kaul, and H. Kronmuller, Phys. Rev. B **65**, 064443 (2002).

[43] K. Schwarz, P. Blaha, and G. K. H. Madsen, Comput. Phys. Commun. **147**, 71 (2002).

[44] J. P. Perdew, A. Ruzsinszky, G. I. Csonka, O. A. Vydrov, G. E. Scuseria, L. A. Constantin, X. Zhou, and K. Burke, Phys. Rev. Lett. **100**, 136406 (2008).

[45] S. R. Hong and H. N. Ok, Phys. Rev. B **11**, 4176 (1975).

Two-orbital degeneracy lifted local precursor to a metal-insulator transition in MgTi$_2$O$_4$

Long Yang [1], Robert J. Koch [2], Hong Zheng [3], J. F. Mitchell [3], Weiguo Yin [2], Matthew G. Tucker [4],
Simon J. L. Billinge [1,2] and Emil S. Bozin [2,*]

[1] *Department of Applied Physics and Applied Mathematics, Columbia University, New York, New York 10027, USA*
[2] *Condensed Matter Physics and Materials Science Division, Brookhaven National Laboratory, Upton, New York 11973, USA*
[3] *Materials Science Division, Argonne National Laboratory, Argonne, Illinois 60439, USA*
[4] *Neutron Scattering Division, Oak Ridge National Laboratory, Oak Ridge, Tennessee 37830, USA*

The MgTi$_2$O$_4$ spinel exhibits a metal-insulator transition on cooling below $T_s \approx 250$ K, accompanied by Ti t_{2g}^1 orbital ordering and spin-singlet dimerization with associated average symmetry reduction to tetragonal. By combining x-ray and neutron pair distribution function analyses to track the evolution of the local atomic structure across the transition we find that *local* tetragonality already exists in the metallic *globally* cubic phase at high temperature. Local distortions are observed up to at least 500 K, the highest temperature assessed in this study. Significantly, the high-temperature local state is not continuously connected to the orbitally ordered band insulator ground state and so the transition cannot be characterized as a trivial order-disorder type. The shortest Ti-Ti spin-singlet dimer bond lengths expand abruptly on warming across the transition, but remain shorter than those seen in the cubic average structure. These seemingly contradictory observations can be understood within the model of a local fluctuating two-orbital t_{2g} orbital degeneracy lifted (ODL) precursor state derived from electron filling, Ti substructure topology, and point symmetry considerations. The ODL state in MgTi$_2$O$_4$ has a correlation length of about 1 nm at high temperature. We discuss that this extended character of the local distortions is consistent with the two-orbital nature of this state imposed by the charge filling and the bond charge repulsion. The MgTi$_2$O$_4$ spinel exemplifies multiorbital ODL state and presents the possibility of a widespread presence of such precursor states in scarcely studied high-temperature regimes of transition-metal-based quantum materials.

I. INTRODUCTION

The AB_2X_4 transition-metal spinels, with B cations forming a geometrically frustrated pyrochlore lattice [1], exhibit a wealth of interesting electronic and magnetic properties, such as spin dimerization [2,3], spin-lattice instability [4], orbital ordering [5], charge ordering [6], and metal-insulator transitions [7–9]. For instance, the CuIr$_2$S$_4$ thiospinel system exhibits a transition from paramagnetic metal to diamagnetic insulator on cooling [10–12], the formation of structural isomorphic octamers [2,13], and anomalous electrical properties [14,15]. In particular, CuIr$_2$S$_4$ has broken symmetries in its ground state accompanied by the formation of charge order and orbital order and the creation of magnetic spin singlets on dimerized Ir^{4+}-Ir^{4+} pairs [2]. These dimers were shown to disappear on warming through the transition, but preformed local symmetry broken states were seen at temperatures well above the global long-range-ordering structure transition [16]. Thus, on cooling, a precursor state exists that has broken local symmetry but is high symmetry over the long range. This behavior was shown to be driven by breaking of d-electron orbital degeneracies, resulting in a local fluctuating orbital degeneracy lifted (ODL) state distinct

from the spin-singlet dimer. This local state results from direct t_{2g} Ir orbital overlap promoted by the topology of the crystal structure. In the regime of partial filling and high crystal symmetry that imposes the degeneracy of the orbital manifold, a molecular-orbital-like state is formed, accompanied by local structure distortion. Many of the interesting physical properties of CuIr$_2$S$_4$ could be explained by the short-range-ordered ODL mechanism, such as the nonconventional conduction in the high-temperature metallic phase [14] and the apparently contradictory observation of the destruction of the dimers at the phase transition but the persistence of poor metallic response above the transition [17].

Similar local symmetry-broken ODL states preformed at high temperature have been observed in other nonspinel d-electron systems such as the FeSe superconductor [18,19]. Even the well-studied physics of the perovskite lanthanum manganites (LaMnO$_3$) could be interpreted in the same way [20], arguing that the ODL phenomenon may be widespread among the myriad of materials with partially filled d-electron manifolds. To explore this hypothesis it is important to seek it out systematically and characterize other materials that have the potential of revealing both commonalities and novel aspects that give more insights into the general ODL phenomenon. For instance, there is no fundamental reason for the ODL states to be exclusively comprised of one orbital per transition metal, yet multiorbital ODL states have so far not

*bozin@bnl.gov

been identified. Here we show that such a multiorbital ODL state exists in a related spinel, $MgTi_2O_4$, and that this is a consequence of the d^1-electron configuration decorating the pyrochlore lattice.

$MgTi_2O_4$ shares many features with $CuIr_2S_4$ [21]. They are both cubic spinels at high temperature with a transition-metal ion pyrochlore sublattice of corner-shared tetrahedra. In both materials the crystal field splits the d orbitals into a t_{2g} triplet and an e_g doublet with the t_{2g} orbitals partially occupied and the e_g orbitals empty. They both exhibit a temperature-dependent metal-insulator transition (MIT) [8,22], the origin of which has been attributed to an orbital-selective Peierls mechanism [21]. They both exhibit a global symmetry lowering, from cubic to tetragonal, at the MIT on cooling. They both have anomalous electrical resistivity behavior in the high-temperature metallic phase [14,23]. The symmetry lowering at the MIT is accompanied by a dimerization of transition-metal ions that results in alternating short and long metal-metal bonds and a resulting tetramerization [24], along linear chains of ions on the pyrochlore sublattice [21]. The short bonds are associated with spin-singlet dimer formation [2,3]. The charge filling is also electron-hole symmetric between the systems with Ti^{3+} having one electron in the t_{2g} manifold, while Ir^{4+} has one hole, although the nominal charge of Ir in $CuIr_2S_4$ is 3.5+, which would place half a hole per Ir in the t_{2g} antibonding band on average in this compound.

Despite the similarities, there are also notable differences. The Ti valence electrons reside in $3d$ orbitals whereas for Ir they are $5d$, which are more extended and should result in larger bandwidth. Indeed, the average separation between the transition metals on the undistorted tetrahedral pyrochlore sublattices of their cubic structures follows this expectation: Ti-Ti separation is shorter (order of 3.0 Å) than Ir-Ir separation (order of 3.5 Å). Also, experimentally, in $MgTi_2O_4$ the tetragonal distortion is shown to be compressive ($c < a$) below the MIT [3] while it is tensile ($c > a$) [10] in $CuIr_2S_4$. Dimers form helical superstructures in $MgTi_2O_4$, whereas they form octameric "molecules" in $CuIr_2S_4$, thereby lowering the symmetry further to triclinic. Both materials tetramerize below the MIT; however, $CuIr_2S_4$ has a 3+-3+-4+-4+ charge ordering (CO) that accompanies an orbital ordering [16], whereas a uniform 3+ charge on Ti rules out CO in $MgTi_2O_4$. With both similarities (t_{2g} orbitals on pyrochlore lattice and formation of dimerized singlets) to and differences from $CuIr_2S_4$ (lack of charge order and electron states rather than hole states), $MgTi_2O_4$ provides a natural next step in a deeper, broader mapping of ODL phenomena. As we show below, this includes the emergence of a multiorbital ODL state.

Neutron pair distribution function (PDF) analysis on $MgTi_2O_4$ has been performed previously [25] to study the spin-singlet dimers, suggesting that they do persist to high temperature. However, due to the weak and negative neutron scattering length of Ti and appreciable overlap with substantially stronger oxygen signal, neutron PDF analysis itself cannot fully reveal how the local structure behaves with temperature. Here we have applied a combined x-ray and neutron analysis to understand the full picture. We find unambiguously that the Ti-Ti dimers do disassemble on warming through the MIT. However, the local structure does not agree with the average structure even at high temperature. In analogy

with $CuIr_2S_4$, partially filled t_{2g} transition-metal orbital manifolds of $MgTi_2O_4$, which are triply degenerate in the average cubic symmetry, utilize their favorable overlaps fostered by the pyrochlore sublattice topology to form an ODL state. Its structural signatures are observed up to at least 500 K (order of $2T_s$), the highest temperature measured. The spatial extent of the local structural response is found to be greater than that observed in $CuIr_2S_4$, consistent with the proposed two-orbital character of the ODL state in $MgTi_2O_4$.

II. METHODS

A. Sample preparation and characterization

TiO_2, Ti metal, and an excess of MgO were mixed and reacted using a spark plasma sintering technique in a graphite crucible. Synthesis at $1100\,°C$ was complete in approximately 15 min. The sample was reground and fired a second time under similar conditions. Powder x-ray diffraction analysis of the product showed well-crystallized $MgTi_2O_4$ spinel accompanied by an extremely small concentration of Ti_2O_3 as a second phase. Magnetization measurements were conducted using a superconducting quantum interference device magnetometer on a specimen with mass of 6.2 mg. The data show a pronounced low-temperature Curie tail which was subtracted. The Curie-Weiss fit to the low-temperature data yielded a Weiss temperature of -0.45 K, consistent with isolated spins, and a Curie constant of 0.023 emu K/mol, which corresponds to approximately 3 mol % of putative Ti^{3+} spin-1/2 impurities.

B. The PDF method

The local structure was studied using the atomic PDF technique [26,27]. The PDF analysis of x-ray and neutron powder diffraction data sets has been demonstrated to be an excellent tool for revealing local structural distortions in many systems [16,18,20,28–31]. The PDF gives the scaled probability of finding two atoms in a material a distance r apart and is related to the density of atom pairs in the material. It does not presume periodicity and so goes well beyond just well-ordered crystals [26,27]. The experimental PDF, denoted by $G(r)$, is the truncated Fourier transform of the reduced total scattering structure function [32] $F(Q) = Q[S(Q) - 1]$,

$$G(r) = \frac{2}{\pi} \int_{Q_{min}}^{Q_{max}} F(Q) \sin(Qr) dQ, \tag{1}$$

where Q is the magnitude of the scattering momentum transfer. The total scattering structure function $S(Q)$ is extracted from the Bragg and diffuse components of x-ray, neutron, or electron powder diffraction intensity. For elastic scattering, $Q = 4\pi \sin(\theta)/\lambda$, where λ is the wavelength of the probe and 2θ is the scattering angle. In practice, values of Q_{min} and Q_{max} are determined by the experimental setup and Q_{max} is often reduced below the experimental maximum to eliminate noisy data from the PDF since the signal-to-noise ratio becomes unfavorable in the high-Q region [26].

C. X-ray PDF experiment

The synchrotron x-ray total scattering measurements were carried out at the PDF beamline (28-ID-1) at the National Synchrotron Light Source II (NSLS-II) at Brookhaven

National Laboratory (BNL) using the rapid acquisition PDF method (RAPDF) [33]. The $MgTi_2O_4$ powder sample was loaded in a 1-mm-diam polymide capillary and measured from 90 to 500 K on warming using a flowing nitrogen cryostream provided by Oxford Cryosystems 700 Series Cryocooler. The experimental setup was calibrated by measuring the crystalline Ni as a standard material. A two-dimensional PerkinElmer area detector was mounted behind the samples perpendicular to the primary beam path with a sample-to-detector distance of 227.7466 mm. The incident x-ray wavelength was 0.1668 Å. The PDF instrument resolution effects are accounted for by two parameters in modeling, Q_{damp} and Q_{broad} [34,35]. For x-ray PDF measurement, these were determined as $Q_{damp} = 0.039$ Å^{-1} and $Q_{broad} = 0.010$ Å^{-1} by fitting the x-ray PDF from a well-crystallized sample of Ni collected under the same experimental conditions.

In order to verify the data reproducibility, an additional set of x-ray data (in the 90–300 K temperature range on warming) was collected at the XPD beamline (28-ID-2) at the NSLS-II at BNL using a similar RAPDF setup but with x-ray wavelength of 0.1901 Å and sample-to-detector distance of 251.1493 mm. The corresponding instrument resolution parameters were determined to be $Q_{damp} = 0.032$ Å^{-1} and $Q_{broad} = 0.010$ Å^{-1}, implying similar instrument resolution effects across the two sets of measurements.

The collected x-ray data frames were summed, corrected for detector and polarization effects, and masked to remove outlier pixels before being integrated along arcs of constant momentum transfer Q, to produce one-dimensional powder diffraction patterns using the PYFAI program [36]. Standardized corrections and normalizations were applied to the data to obtain the reduced total scattering structure function $F(Q)$, which was Fourier transformed to obtain the PDF, using PDFGETX3 [37] within XPDFSUITE [38]. The maximum range of data used in the Fourier transform was chosen to be $Q_{max} = 25.0$ Å^{-1} so as to give the best trade-off between statistical noise and real-space resolution.

D. Neutron PDF experiment

The time-of-flight (TOF) neutron total scattering measurements were conducted at the NOMAD beamline (BL-1B) [39] at the Spallation Neutron Source at Oak Ridge National Laboratory. The $MgTi_2O_4$ powder sample was loaded into a 3-mm-diam silica capillary mounted on a sample shifter and data were collected from 100 to 500 K on warming using an Ar flow cryostream. The neutron PDF instrument resolution parameters were determined as $Q_{damp} = 0.0232$ Å^{-1} and $Q_{broad} = 0.0175$ Å^{-1} by fitting the neutron PDF of a NIST standard 640d crystalline silicon sample. The neutron data were reduced and transformed to the PDF with $Q_{max} = 25.0$ Å^{-1} using the automated data reduction scripts available at the NOMAD beamline.

E. Structural modeling

The PDF modeling programs PDFGUI and DIFFPY-CMI were used for PDF structure refinements [35,40]. In these refinements U_{iso} (Å^2) is the isotropic atomic displacement

parameter (ADP) and the ADPs of the same type of atoms are constrained to be the same; δ_2 (Å^2) is a parameter that describes correlated atomic motions [41]. The PDF instrument parameters Q_{damp} and Q_{broad} determined by fitting the PDF from the well-crystallized standard sample under the same experimental conditions are fixed in the structural refinements on the $MgTi_2O_4$ data set.

To estimate the length scale of local structural correlations, an r_{min}-dependent fit is performed on select high-temperature x-ray data (300, 400, and 500 K). During the fit, the average high-temperature cubic $MgTi_2O_4$ model is used, fixing the upper limit of fit range as $r_{max} = 50$ Å, but changing the lower limit r_{min} from $1 \leqslant r_{min} \leqslant 36$ Å in 0.2-Å r steps. Each fit range uses the same initial parameter values and the δ_2 term is not applied since the data fitting range does not consistently include the low-r region in all these refinements.

The Rietveld refinement on the neutron TOF Bragg data was implemented in the GSAS-II software [42]. The instrument parameters were refined to the standard silicon data collected under the same experimental conditions and then fixed in the $MgTi_2O_4$ Rietveld refinements. The sequential refinement option was used to refine the temperature series data set collected at the $2\theta = 120°$ detector bank from 100 to 500 K in a systematic manner.

F. Structural models

Two candidate $MgTi_2O_4$ models were fit against the experimental data. In the cubic $MgTi_2O_4$ model (space group $Fd\bar{3}m$), the atoms sit at the following Wyckoff positions: Mg at 8a (0.125,0.125,0.125), Ti at 16d (0.5, 0.5, 0.5), and O at 32e (x, x, x). The initial lattice parameters and atomic positions are $a = 8.509\,027$ Å and O at (0.25920, 0.25920, 0.25920) [3]. The Ti pyrochlore sublattice is shown in Fig. 1(a), indicating that all the Ti-Ti bonds are of equal length, reflecting regular Ti_4 tetrahedra. In the tetragonal $MgTi_2O_4$ model (space group $P4_12_12$), the atoms sit at the following Wyckoff positions: Mg at 4a $(x, x, 0)$, Ti at 8b (x, y, z), O1 at 8b (x, y, z), and O2 at 8b (x, y, z). The initial lattice parameters and atomic positions are $a = 6.022\,01$ Å, $c = 8.484\,82$ Å, Mg at (0.7448, 0.7448, 0), Ti at $(-0.0089, 0.2499, -0.1332)$, O1 at (0.4824, 0.2468, 0.1212), and O2 at (0.2405, 0.0257, 0.8824) [3]. The corresponding distorted Ti sublattice is presented in Fig. 1(b), showing that one Ti-Ti bond gets shorter (indicated in red) and one gets longer (in yellow) out of the six Ti-Ti bonds of each Ti_4 tetrahedron. The lattice parameters of these two models have the relationship $c_c \sim c_t \sim \sqrt{2}a_t$, where the subscripts c and t refer to the cubic and tetragonal models, respectively.

III. VANISHING SPIN-SINGLET DIMERS

A. Canonical behavior

The magnetization $M(T)$ of the sample up to 300 K is shown in Fig. 1(c). A low-temperature Curie-Weiss-like component has been subtracted to account for the effect of magnetic impurities contributing to the signal at low temperature. The onset of a broad dimerization transition is observed at around 250 K, which is close to the literature-reported
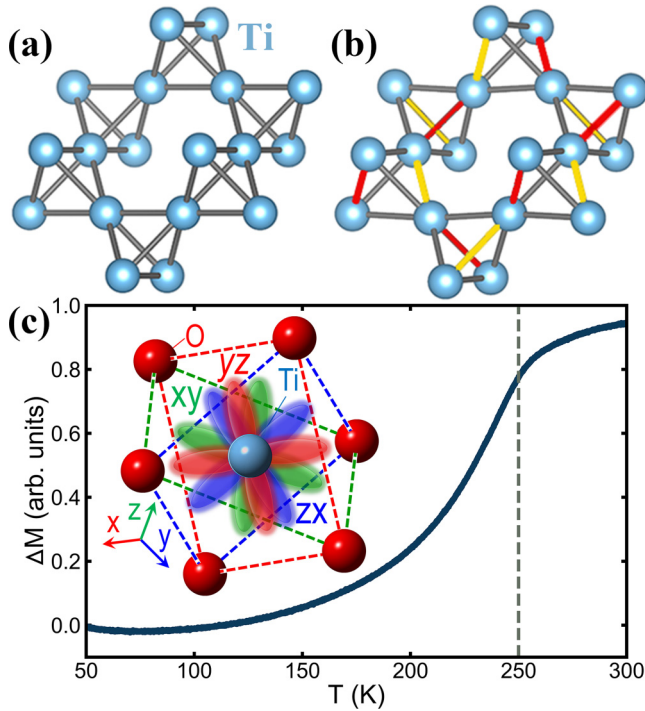
FIG. 1. The Ti pyrochlore sublattice of corner-shared Ti₄ tetrahedra for (a) undistorted (cubic) and (b) distorted (tetragonal) $MgTi_2O_4$ structures, highlighting both short (red) and long (yellow) Ti-Ti bonds in the distorted structure. (c) Temperature dependence of magnetization with the Curie-Weiss behavior contribution subtracted. The inset shows a TiO_6 octahedron and the t_{2g} orbitals that point towards O-O edges. The Ti atom is in blue and the O atom is in red. The vertical gray dashed line at 250 K marks the MIT temperature.
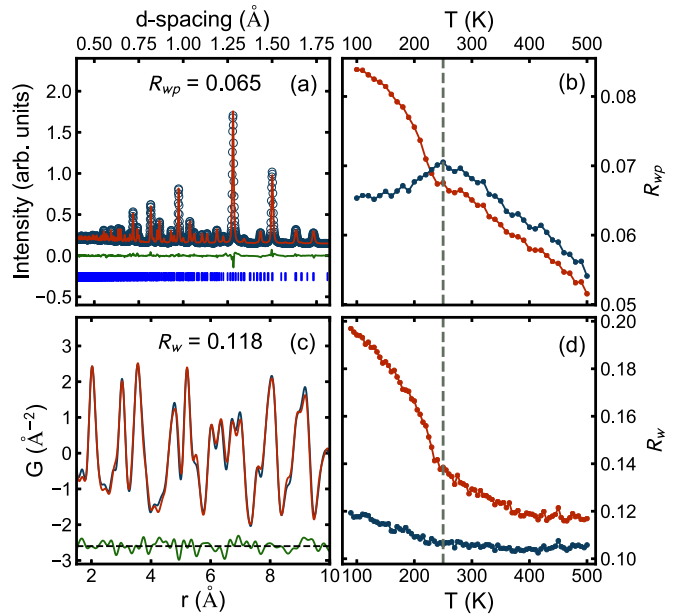

FIG. 2. (a) The 100 K neutron powder diffraction pattern (blue) collected using the $2\theta = 120°$ detector bank fit by the tetragonal $MgTi_2O_4$ model (red) with the difference curve (green) offset below. (b) Resulting neutron Rietveld refinement weighted profile agreement factor R_{wp} values versus temperature on neutron TOF Bragg data using tetragonal (blue) and cubic (red) $MgTi_2O_4$ models from 100 to 500 K (120° detector bank data). (c) The x-ray PDF of 100 K data (blue) fit by the tetragonal model (red) over the range $1.5 < r < 10$ Å. The difference curve (green) is shown offset below. (d) Resulting x-ray PDF refinement goodness-of-fit parameter R_w values versus the temperature on x-ray data using tetragonal (blue) and cubic (red) $MgTi_2O_4$ models from 90 to 500 K over the range of $1.5 < r < 10$ Å. The vertical gray dashed line at 250 K indicates the MIT temperature.

MIT temperature of 260 K [8,43] and implies the canonical behavior of our sample.

We next establish that the average structural behavior of our sample agrees with other observations in the literature [3,8,44] by carrying out Rietveld refinements fitting tetragonal and cubic $MgTi_2O_4$ models to the neutron TOF Bragg data measured from 100 to 500 K. The refinement results from select fits are reproduced in Table I presented in the Appendix, and a representative fit, of the tetragonal model to the 100 K data set, is shown in Fig. 2(a). The tetragonal distortion, given by $c/\sqrt{2}a$, is small at all temperatures and the data are not of high enough resolution to directly observe distinct peaks that would indicate any tetragonal distortion. However, the temperature dependence of the weighted profile agreement factor R_{wp} of the two models is shown in Fig. 2(b), which clearly implicates the tetragonal model as preferred at low temperature, but not at high temperature, above around 230–250 K, which is close to the literature-reported MIT temperature 260 K [8].

B. Local structure behavior

We investigate the behavior of the local structure by performing a PDF structural refinement of the x-ray total scattering PDF data from 90 to 500 K. Fits were carried out over the data ranges of $1.5 < r < 4$ Å and $1.5 < r < 10$ Å and the results are qualitatively the same. A representative fit of the

tetragonal model to the 100 K data set is shown in Fig. 2(c). This time, the temperature dependence of the goodness-of-fit parameter R_w of the tetragonal and cubic models [Fig. 2(d)] indicates that the tetragonal model fits the local structure better than the cubic model at all temperatures. In the local structure the tetragonal distortion is always evident.

To see visually in the PDF how the cubic model fails, we consider the low- and high-temperature PDFs and fits with the cubic and tetragonal models, shown in Fig. 3. The low-temperature PDFs (below the MIT) are shown in Figs. 3(a) and 3(b) and the high-temperature PDFs (above the MIT) in Figs. 3(c) and 3(d). The tetragonal model fit is shown in Figs. 3(a) and 3(c) and the cubic fit is shown in Figs. 3(b) and 3(d). At low temperature, as expected, the tetragonal model [Fig. 3(a)] fits much better than the cubic model [Fig. 3(b)]. At 300 K we have already established that the global structure is cubic; however, again we see that in these local structural fits the tetragonal model [Fig. 3(c)] is superior to that of the cubic model [Fig. 3(d)], with smaller oscillations in the difference curve. To emphasize our argument, we note that the difference curves are similar when data collected at distinct temperatures are fit using identical symmetry constraints. Specifically, careful inspection of the difference curves in Figs. 3(b) and 3(d) reveals that the positions of residual maxima and minima
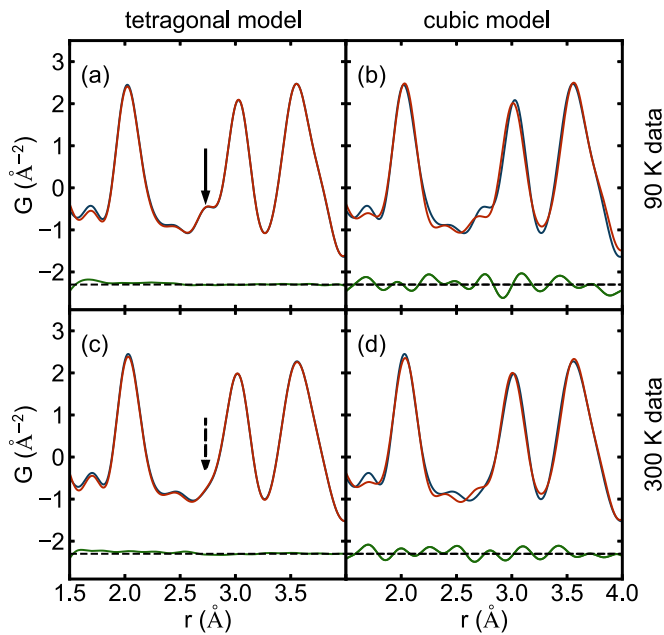
FIG. 3. The x-ray PDF data (blue) collected at the PDF beamline at (a) and (b) 90 K and (c) and (d) 300 K fit by (a) and (c) tetragonal and (b) and (d) cubic models (red) over the range of $1.5 < r < 4$ Å. The difference curves (green) are shown offset below.

FIG. 4. Simulated (a) x-ray and (b) neutron PDFs of tetragonal (blue) and cubic (red) $MgTi_2O_4$ models in the low-r region. All atoms use the same isotropic atomic displacement parameter $U_{iso} = 0.005$ Å^2. Here Q_{max}, Q_{damp}, and Q_{broad} are set as the same values as the experimental PDFs. The difference curves (tetragonal model simulation minus cubic model simulation) are shown offset below in green. The nearest Ti-Ti bonds are highlighted in the blue vertical span region. Also shown are the experimental (c) x-ray and (d) neutron PDFs from $MgTi_2O_4$ collected at 100 K (blue) and 300 K (red). The difference curves (100 K data minus 300 K data) are shown offset below in green. The vertical dashed lines at $r = 3.01$ Å represent the length of the undistorted Ti-Ti bond length in the average cubic model.

are nearly identical, although their amplitudes are smaller in Fig. 3(d). Since this difference signal represents the inability of the cubic model to fit the data, it is further support to the idea that a similar tetragonally distorted structure is present in the low-r region at 90 K and at 300 K, but smaller in amplitude at 300 K. To validate that the results are reproducible, Fig. 3 represents x-ray PDF data collected at the PDF beamline, and data collected from the XPD beamline is shown in Fig. 8 presented in the Appendix, which reproduces the same result as discussed above.

In the cubic $MgTi_2O_4$ structure unit cell, all six Ti-Ti bonds have the same length, 3.008 Å, whereas in the tetragonal $MgTi_2O_4$ model, one of the six Ti-Ti distances is shortened (2.853 Å), forming dimers, and one Ti-Ti bond is longer (3.157 Å) [44]. The dimer contact is considerably shorter than the 2.917 Å found in titanium metal [45], indicating a strong covalent interaction in $MgTi_2O_4$. From the analysis of the average structure, it was understood that the MIT was accompanied by the formation of Ti-Ti structural dimers. Above we showed the observation from the PDF of local tetragonality at high temperature, which may indicate that local dimers survive above the MIT. This would seem to be in qualitative agreement with a prior observation from a neutron PDF study that reported the persistence of Ti-Ti dimers up to high temperature [25]. In this picture the dimers survive locally but become disordered at the transition where the structure becomes globally cubic on warming. However, our PDF analysis clearly shows that the large-amplitude structural dimers actually do disappear at the MIT, as described below, and that the local tetragonality that we observe at high temperature in the PDF has a more subtle origin as we develop in greater detail below.
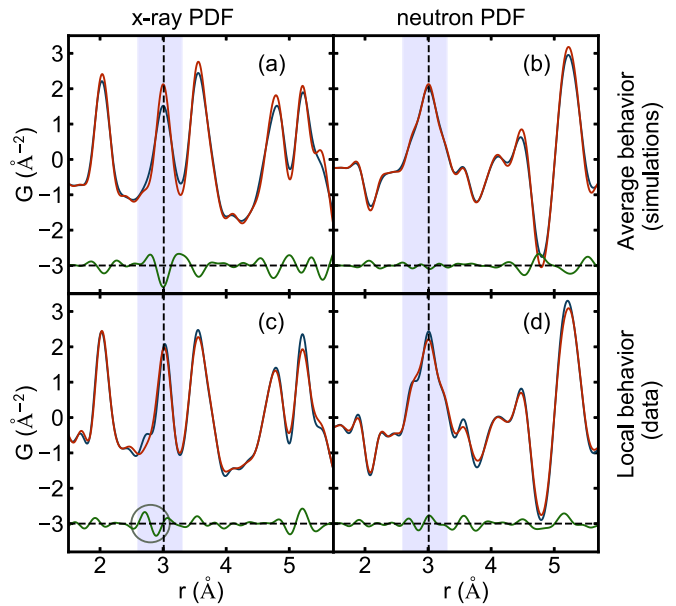
C. Orbital degeneracy lifting or spin dimerization?

To establish the disappearance of the structural dimers at the phase transition, we simulated x-ray PDFs of the cubic (no dimers) and tetragonal (dimers) models. These are plotted as the red and blue curves, respectively, in Fig. 4(a). A number of the PDF peaks are affected on the transition through the MIT, with the largest change observed on the peak at around 3.0 Å, which contains the shortest Ti-Ti distances. Based on the change in crystal structure, the expected change in the PDF results in the characteristic M-shaped signature in the difference curve seen in Fig. 4(a) which comes from the disappearance of the long and short Ti-Ti bonds associated with the dimer, leaving all the Ti-Ti distances the same. This can be compared to the difference in the measured PDF data as $MgTi_2O_4$ crosses the MIT, shown in Fig. 4(c) at 300 K (red) and 100 K (blue). First, we see a significant change in the relevant 3.0-Å peak when moving through the MIT. This change is inconsistent with the conclusion from the previous neutron PDF study that the dimers are retained, unaltered, to high temperature in the local structure [25], necessitating an order-disorder scenario in which the local structure across the transition is unchanged, with small or no change in the PDF. Instead we see a significant change in the x-ray PDF at the phase transition, with PDF intensity moving from the

short r position towards that of the average Ti-Ti distance, as indicated by the gray circle in Fig. 4(c).

It is clear from careful inspection that the observed and simulated difference curves across the transition [Figs. 4(c) and 4(a), respectively] are significantly different. The PDF peak intensity redistribution associated with the dimer removal is seen in the differential curve as a transfer of intensity from 2.71 to 2.89 Å, i.e., on the low-r side of the average Ti-Ti distance at 3.01 Å marked by the vertical dashed line in the figure. This implies that the very short Ti-Ti ion dimers disappear at the phase transition, but the associated PDF intensity is shifted to a position that is still shorter than that of the average Ti-Ti distance: Shortened Ti-Ti contacts in fact do exist at high temperature above the MIT but they are not the original spin-singlet dimers. Our results are consistent with the disappearance of dimers at the phase transition on warming, but a persistence of a local tetragonality, smaller in magnitude than that associated with the the dimer phase. This behavior is shown on an expanded scale in Fig. 5(b), where PDFs measured at multiple temperatures are compared, focusing on the peak at around 3.0 Å. The feature in the difference curve that shows the shift of the intensity associated with the Ti-Ti short bonds from 2.71 Å to the longer position (2.89 Å) is shown below, shaded green (for the loss of short bonds) and purple (for the gain in longer bonds). This result is qualitatively supported by the PDF structural modeling over the range of $1.5 < r < 10$ Å, shown in Figs. 5(e) and 5(f), where the short Ti-Ti bond shifts from 2.83 to 2.88 Å over the same temperature range, but never converges to the average cubic value of 3.01 Å at 300 K.

The full temperature dependence of the dimer disappearance may then be extracted by integrating the shaded regions in the difference curve and is shown in Fig. 5(c), where we plot the integrated area shown shaded in green in the difference curve vs temperature. In this case the difference is always taken with respect to the 500 K data set. The intensity decreases gradually until around 200 K, where it rapidly falls off. The rate of falloff in this intensity then slows again above 250 K. There are two principal contributions to the differential signal below the transition: the changes in the local structure and the thermal broadening effects. Thermal broadening effects in the differential are gradual and typically small, particularly from one data point to the next, corresponding to the trends observed below approximately 200 K and above approximately 250 K. On the other hand, the signal in the differential coming from the dimers is considerably larger, roughly proportional to the big step seen at the transition, and dissipates rapidly as the temperature passes through the MIT range. This is a model-independent way of observing how the local dimer disappears on warming.

D. X-ray PDF versus neutron PDF

We may seek an explanation for why we see the dimers disappear at the transition from our x-ray PDF measurements, whereas this was not evident in the earlier neutron PDF study [25]. Observing the local Ti dimer is complicated in the neutron case by the relatively weak and negative neutron scattering length of titanium and an appreciable overlap of titanium contributions with strong oxygen contributions. To
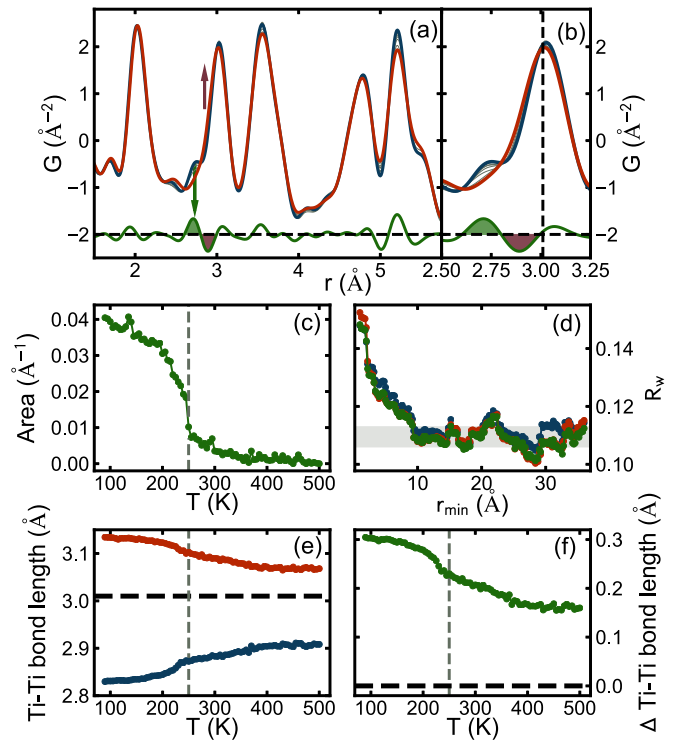

FIG. 5. (a) PDFs measured as a function of temperature from 90 K (blue) to 300 K (red) in the low-r region. The intermediate data sets are plotted in gray. The vertical green arrow at $r = 2.71$ Å and the purple arrow at 2.89 Å represent how the position of the Ti-Ti short bond changes on warming. The difference curve shown offset below is that between the 90 K data set subtracting the 300 K data set. The positive/negative feature between $2.6 < r < 3.0$ Å indicates that intensity in the PDF at 2.71 Å at low temperature is shifting to the position 2.89 Å at high temperature. (b) Re-plot of (a) over an expanded r range. The vertical dashed line at $r = 3.01$ Å represents the length of the undistorted Ti-Ti bond length in the cubic average structure. (c) Temperature dependence of the integrated area in the difference curve shown shaded green. The vertical gray dashed line at 250 K indicates the MIT temperature. (d) The x-ray PDF refinement goodness-of-fit R_w values versus a variable r_{min} (for an r_{max} set equal to 50 Å) when fitting a cubic $MgTi_2O_4$ model to 300 K (blue), 400 K (green), and 500 K (red) data. In each refinement r_{min} was allowed to vary from $1 \leqslant r_{min} \leqslant 36$ Å in 0.2-Å r steps. The fits with high r_{min} yield the behavior of the average structure. The fits with low r_{min} are weighted by the local structural signal. Also shown are (e) the temperature dependence of the short (blue) and long (red) Ti-Ti bond lengths and (f) their differences (green) from PDF structural modeling using the tetragonal structure over the range of $1.5 < r < 10$ Å. The horizontal dashed line represents the length of the undistorted Ti-Ti bond length in the cubic average structure. The vertical gray dashed line at 250 K indicates the MIT temperature.

show this, we perform the same comparison that we just made for the x-ray PDFs, but on neutron data. The neutron simulations are shown in Fig. 4(b) and the neutron experimental PDFs in Fig. 4(d). It is clear that the signals in the difference curve, both for the simulations based on the average structure and the data PDFs themselves, are much smaller than for the x-ray case. This is because the most important signal in $MgTi_2O_4$ is coming from the Ti ions that are relatively strong

scatterers in the x-ray case but not in the neutron measurement. Specifically, in the x-ray case, Ti scatters 2.75 times stronger than O and 1.8 times stronger than Mg, whereas for neutrons the scattering of Ti is 1.7 times weaker than that of O and 1.6 times weaker than that of Mg. In addition, the neutron PDF intensity in the range of interest is dominated by the contributions from O-O pairs constituting TiO_6 octahedra, evidenced in the data as the additional shoulder intensity features around the 3-Å peak [Fig. 4(d)], as compared to the x-ray case where such features are largely absent [Fig. 4(c)]. This may explain the different interpretation in the earlier neutron PDF study [25]. However, the x-ray data unambiguously show the disappearance of the full-amplitude spin-singlet Ti-Ti dimers.

E. Detection of the ODL state

This behavior, where sizable distortions associated with ordered spin-singlet dimers evolve into smaller local distortions with spin singlets disassembled, is reminiscent of that observed in the $CuIr_2S_4$ system. In that case a local symmetry-broken ODL state was observed up to the highest temperatures studied [16]. On cooling these local distortions of broken symmetry ordered into a long-range orbitally ordered state. Only below the ordering transition did charges disproportionate, forming a charge density wave accompanied by a Peierls distortion and the formation of Ir-Ir dimers with very short Ir-Ir bonds. We believe our observations in $MgTi_2O_4$ suggest a similar kind of ODL behavior, which we explore to a greater extent below, though different in detail because of the different charge filling.

As discussed above, we can rule out that the local structure is changing in the same way as the average structure. The *expected* changes in the PDF at low r due to average structure changes at the MIT make all the low-r peaks sharper for $T > T_{MIT}$, as shown in Fig. 4(a). However, the data do not show this [Fig. 4(c)]. There is a small change in the local structure, evidenced by the feature in the difference curve around 2.9 Å, indicated by the gray circle in Fig. 4(c), but it is smaller than the average structure change at the MIT. As discussed above, the short Ti-Ti dimers ($r = 2.71$ Å shoulder) go away on warming by a shift to a longer bond (around $r = 2.89$ Å), but this "longer" bond is still shorter than the average 3.01-Å Ti-Ti bond distance expected from the cubic average model. These two behaviors exactly mimic the ODL state found in $CuIr_2S_4$ [16].

As is evident in Fig. 2(d), the tetragonal model fits the local structure better than the cubic model at all temperatures to 500 K, the highest measurement temperature. As in $CuIr_2S_4$ [16] the dimers disappear at the MIT transition on warming, but the local symmetry-broken state with, presumably, fluctuating short Ti-Ti bonds is present to high temperature.

F. Spatial extent of the ODL state

It is of interest to explore whether the fluctuating short Ti-Ti bonds at temperature above the MIT correlate with each other and how this varies with temperature. To extract the correlation length of the local fluctuating symmetry-broken states, r_{min}-dependent PDF fits (see Sec. II) were performed on selected high-temperature data sets (300, 400, and 500 K).

When r_{min} is large the fit is over just the high-r region of the PDF and will retrieve the average structure and the cubic fit will be good. As r_{min} extends to lower values, progressively more of the local structure that has a tetragonal distortion is included in the fit and the agreement of the cubic model becomes degraded. The resulting $R_w(r_{min})$ is shown in Fig. 5(d). The cubic fits are good over the entire region $r_{min} > 10$ Å, with very little variation in R_w indicated by the horizontal gray band in the figure, but rapidly degrade below this length scale. This suggests that the symmetry-broken local distortions have a correlation length of around 1 nm but that this correlation length does not vary significantly in the temperature range above 300 K. This agrees well with the previously reported length scale of local tetragonality based on neutron PDF analysis [25].

IV. TWO-ORBITAL ODL STATE

A. The ODL regime

The driving force behind the high-temperature local symmetry breaking in $CuIr_2S_4$ was shown to be of electronic origin involving orbital degeneracy lifting [16]. Significantly, the isostructural and isoelectronic sister compound $CuIr_2Se_4$ remains metallic down to the lowest temperature and does not show local symmetry-breaking ODL effects. This intriguingly suggests that the ODL state could be *a prerequisite* for the MIT [16] in these spinels. Here we argue that also in $MgTi_2O_4$ local ODL effects are present and produce the local symmetry breaking in the high-temperature region that we report here. By analogy with $CuIr_2S_4$, the ODL states are precursor states to the spin-singlet dimerization and MIT.

The long-range pattern of ordered spin-singlet dimers differs in detail in the two systems, being octamers in $CuIr_2S_4$ [2] and helices in $MgTi_2O_4$ [3], and is presumably dictated by delicate energetics [46,47]. Although intriguing, these intricate aspects of long-range order are not of concern here. Our interest lies with internal dimer structure, the relationship between the dimer state and the ODL state, and the electron-hole symmetry that links the two systems [21].

Prior to pursuing the analogy between $CuIr_2S_4$ and $MgTi_2O_4$, we appraise the two systems from the perspective of a regime under which the ODL state can form in a transition-metal system [16]. Three criteria need to be fulfilled: (i) filling, where the transition metal in the system possesses partially filled d orbitals; (ii) symmetry, where the high crystallographic point symmetry of the system imposes the orbital degeneracy; and (iii) topology, where the structural topology promotes adequate highly directional orbital overlaps. In practice, materialization of the ODL state could further be impacted by the existence of other competing degeneracy lifting channels that may be available to the system, such as the relativistic spin orbit coupling, the effects of crystal field, etc. Eventually, formation of the ODL local broken-symmetry state is accompanied by associated local structure distortion. Both $CuIr_2S_4$ and $MgTi_2O_4$ systems meet the criteria: partial filling (Ir is $5d^{5.5}$ and Ti is $3d^1$), degeneracy-promoting high-symmetry structure (cubic spinel structure imposes threefold degeneracy of the t_{2g} manifolds in both materials), and favorable structural topology (edge
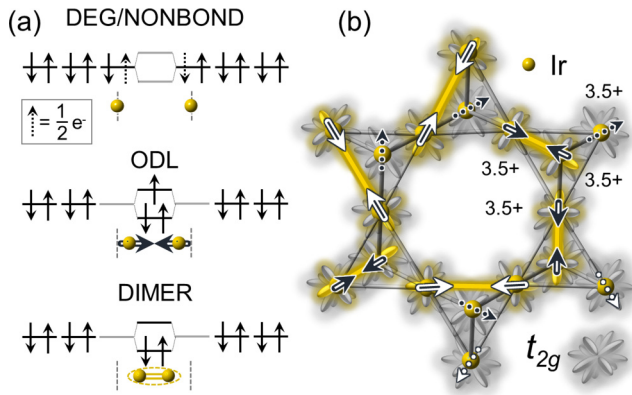
FIG. 6. Recapitulation of the ODL mechanism in the $CuIr_2S_4$ thiospinel. (a) Energy diagram of atomic and molecular orbitals for nearest Ir atom pairs in various situations: degenerate/nonbonding (DEG/NONBOND, top), orbital degeneracy lifted (ODL, middle), and spin-singlet dimer (DIMER, bottom). Horizontal arrows indicate the ODL displacements. (b) The ODL state in $CuIr_2S_4$ in the t_{2g} orbital manifold representation on a segment of pyrochlore sublattice. The ODL active t_{2g} orbitals are shown in yellow and passive orbitals are shown in gray. Each Ir atom participates in exactly one ODL state. The ODL states are randomly placed following principles discussed in the text. The arrows denote the displacements of Ir associated with the ODL states and provide mapping onto the two-in–two-out ice rules. The white arrows represent in-plane displacements, whereas the blue arrows represent displacements with an out-of-plane component. The dotted arrows mark the displacements associated with the ODL states occurring in neighboring tetrahedra that are not represented in the displayed structural segment.

shared IrS_6 and TiO_6 octahedra fostering direct t_{2g} overlap). In both systems short nearest-neighbor transition-metal contacts are observed in the high-temperature metallic regime that are distinct from the very short spin-singlet dimer bonds observed in the insulating state at low temperature.

In what follows we first review the ODL state and the dimerization mechanism within the local picture of $CuIr_2S_4$, summarized in Fig. 6. We then utilize the analogies between the two systems to put forward a scenario portraying the high-temperature state and the dimerization mechanism in $MgTi_2O_4$, illustrated in Fig. 7.

B. Single-orbital ODL state

In $CuIr_2S_4$ the dimers involve two Ir^{4+} ions in $5d^5$ configuration with hole character [16]. In the localized electron picture, the ODL state is based on molecular orbital (MO) concepts. In this, two neighboring transition-metal ions with partially filled degenerate orbitals form a MO state with shared electrons (holes) that lifts the degeneracy and lowers the system energy. In the high-temperature regime of $CuIr_2S_4$ iridium nominally has a half-integer valence (3.5+) [11,48]. This means that each $Ir^{3.5+}$ on the pyrochlore sublattice is in a nominal $5d^{5.5}$ state corresponding to half a hole per three degenerate t_{2g} orbitals [Fig. 6(a), top]. The sublattice geometry fosters direct overlaps of orbitals from the t_{2g} manifolds [Fig. 6(b)], which in turn allows neighboring Ir pairs to form a bound state sharing a single hole in the antibonding MO [16] [middle panel of Fig. 6(a)].

Importantly, for any choice of two neighboring Ir on a pyrochlore lattice only one member of the three t_{2g} orbitals
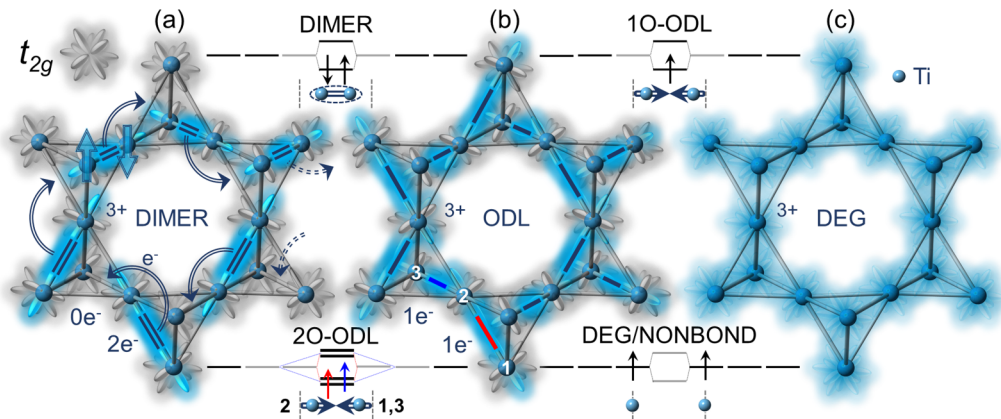

FIG. 7. The Ti t_{2g} orbital manifold on a pyrochlore sublattice of the $MgTi_2O_4$ spinel: (a) spin-singlet dimerized lattice within the tetragonal model, (b) ODL lattice within the tetragonal model, and (c) lattice of degenerate t_{2g} orbitals as portrayed by the cubic model. The charge state of all Ti in all models is +3. The electron density in t_{2g} orbitals is indicated by color (gray is empty) and its distribution is proportional to the blue color intensity. The Ti dimers in (a) are indicated by the double blue lines, while a pair of antiferromagnetically coupled block arrows on an exemplar dimer denotes its spin-singlet character. Note that all Ti atoms are involved in dimerization but only dimers contained in a section of one structural slab are indicated in (a). Out of all Ti-Ti contacts, dimerized contacts have a nominal bond charge of $2e^-$, whereas the other contacts carry no net charge in this picture. The ODL states in (b) are indicated by the single blue lines. Arc arrows in (a) denote bond charge transfer as the spin-singlet dimers convert to the ODL states, according to the model discussed in the text. The insets between the panels provide the energy diagram of atomic and molecular orbitals for nearest Ti atom pairs in various situations: degenerate/nonbonding (DEG/NONBOND, bottom right), spin-singlet dimer (DIMER, top left), one-orbital ODL (1O-ODL, top right), and two-orbital ODL (2O-ODL, bottom left). Note that the 2O-ODL state refers to two orbitals of the same Ti (e.g., one labeled 2) that are engaged in two 1O-ODL states with two *different* Ti neighbors (e.g., those labeled 1 and 3). Differently colored spins and lines denoting ODL contacts indicate this two-component aspect in the schematics for 2O-ODL. The local spin arrangement shown is for illustration purposes only and does not represent an experimentally established alignment.

overlap (e.g., xy with xy, etc.) along the Ir_4 tetrahedral edges. Due to the specifics of filling (0.5 hole/Ir) each Ir participates in exactly one such paired state at a time. We call this a one-orbital ODL (1O-ODL) state. The ODL state is hence comprised of two atomic orbitals, one from each Ir in the pair, with on average 1.5 electrons (0.5 hole) per Ir, resulting in MO with three electrons and one hole, as shown in Fig. 6(a), with a net spin of 1/2. This configuration results in the observed contraction of the Ir-Ir separation in the local structure vis-à-vis that expected if orbital degeneracy is retained. Since each iridium has six Ir neighbors to pair with, the ODL state fluctuates spatially and, presumably, temporally among (xy, xy), (yz, yz), and (zx, zx) variants, which results in an undistorted cubic structure on average [16]. One such configuration is illustrated in Fig. 6(b), with strong short-range correlations governed by the one ODL state per Ir and the Coulomb bond charge repulsion principles, resulting in a single ODL state per Ir_4 tetrahedron. Pursuant to this, the ODL state in $CuIr_2S_4$ follows the two-in–two-out ice rules [49], which will be addressed later.

In this localized picture, the ODL state is also a precursor for the spin-singlet dimer. The dimer state is attained by removing an excess electron from the antibonding MO of the ODL state, thus stabilizing the bond, as shown in the bottom panel of Fig. 6(a). The process involves charge transfer between two ODL $Ir^{3.5+}$-$Ir^{3.5+}$ pairs, one of which becomes dimerized Ir^{4+}-Ir^{4+} by losing an electron (or gaining a hole, hence hole dimer) and the other becomes non-ODL (and nondimer) Ir^{3+}-Ir^{3+} by gaining an electron (d^6-d^6 configuration).

C. Two-orbital ODL state

We now turn to $MgTi_2O_4$ starting from the local view of spin-singlet dimers. Dimerization in $MgTi_2O_4$, depicted using the Ti t_{2g} manifold representation, is shown in Fig. 7(a), overlaying a fragment of pyrochlore sublattice as seen in the $P4_12_12$ model. In $MgTi_2O_4$ the dimers involve two Ti^{3+} in the $3d^1$ configuration with a single electron in the t_{2g} manifold; hence Ti^{3+}-Ti^{3+} dimers inevitably have electron character by construction. These result in short Ti-Ti dimerized contacts observed in the tetragonal structure at low temperature. Each dimer carries $2e^-$ of net charge. Since each Ti participates in a dimer and since there is exactly one dimer per Ti_4 tetrahedron [25,46], nominal charge count results in $1e^-$/Ti site. This is consistent with no CO being observed experimentally in $MgTi_2O_4$, in contrast to $CuIr_2S_4$, implying that all Ti sites are equivalent in this regard [3]. From the average structure perspective and in the localized picture, supported by the experimentally observed paramagnetism and poor metallic conduction, above the MIT the dimers could be seen to disassemble in such a way as to statistically distribute $1e^-$ of charge evenly across the three degenerate t_{2g} orbitals, resulting in a cubic structure with all Ti-Ti nearest-neighbor contacts equivalent, as schematically presented in Fig. 7(c). This implies that, despite nominal charge equivalence of all Ti sites and no site CO observed, some charge transfer, presumably involving bond charge, still has to take place at the transition. This then inevitably implies that the ground state has to involve the bond charge order which coincides with, and is

hence indistinguishable from, the observed dimer order in the diffraction measurements.

The implication of charge being equally distributed across the triply degenerate t_{2g} manifold of Ti in a manner depicted in Fig. 7(c), presented also in an associated energy diagram (bottom right inset of the figure), would be that the pyrochlore sublattice is comprised of regular Ti_4 tetrahedra with equidistant Ti-Ti contacts corresponding to equal bond charge, as described within the cubic spinel model. However, this is not what is observed experimentally. The observations based on the PDF analyses clearly demonstrate that the pyrochlore sublattice is comprised of locally distorted Ti_4 tetrahedra with a distribution of distances, suggesting that the bond charge remains inequivalent above the MIT. One possibility is that the dimers indeed persist in the metallic regime, as hinted at in the earlier neutron study [25]. However, such an interpretation would be inconsistent with magnetization measurements of $MgTi_2O_4$ that establish the disappearance of spin singlets above the MIT. It would further be inconsistent with the elongation of the short Ti-Ti dimer contacts evidenced in our x-ray PDF analysis, which implies the disappearance of spin-singlet dimers at MIT even locally. In analogy with $CuIr_2S_4$, it is plausible that the dimer state gets replaced locally by an ODL-type state in the high-temperature metallic phase. Observation of heterogeneous local Ti-Ti contacts corresponding to inequivalent bond charge is consistent with an ODL-like state in $MgTi_2O_4$. Since the local structures at high temperature and in the ground state are distinct, the MIT in $MgTi_2O_4$ cannot be assigned to a trivial order-disorder type.

Importantly, as careful assessment shows, the ODL state in $MgTi_2O_4$ cannot be exactly mapped onto the ODL state seen in $CuIr_2S_4$, since the charge filling is different in the two systems ($1e^-$/Ti in $MgTi_2O_4$ and 0.5 hole/Ir in $CuIr_2S_4$). In the latter case two Ir neighbors can reduce the energy of the system by forming a 1O-ODL state accommodating a common hole, as described in the preceding section. This results in a three-electron state shown in the middle panel of Fig. 6(a). Given that the destruction of the spin-singlet dimer in $MgTi_2O_4$ involves removal of one of the electrons from the dimer state sketched in the energy diagram in the top left inset of Fig. 7, consistent with destabilization and elongation of the short Ti-Ti bond, in the ODL picture the one electron left behind would indeed result in an electron-hole antipode of the 1O-ODL state seen in $CuIr_2S_4$, as shown in the top right inset of Fig. 7. The issue arises with the placement of the extra electron from the dimer. In the case of $CuIr_2S_4$, due to filling, the removal of one of the two holes constituting a dimer results in generation of two 1O-ODL states on two different pairs of Ir. There, since only 50% of Ir participates in dimerization, in terms of filling one should think of this process as a replacement of the 4+–4+–3+–3+ charge tetramer with a pair of 3.5+–3.5+ ODL states achieved by hole redistribution. Since there is no site charge disproportionation in $MgTi_2O_4$ and since each Ti is involved in dimerization, the dimer density per formula unit is twice as large in $MgTi_2O_4$ as in $CuIr_2S_4$ and each Ti has to participate in two independent 1O-ODL states simultaneously. Notably, the geometry of t_{2g} orbital overlaps imposes a constraint that the two 1O-ODL states for each Ti have to be assembled with two *different* Ti neighbors, as illustrated in Figs. 7(a) and 7(b).

There, for example, the dimer in Fig. 7(a) involving Ti labeled 2 in Fig. 7(b) disassembles at the MIT to make two 1O-ODL states, one with the Ti neighbor labeled 1 and another with the neighbor labeled 3. This results in two short Ti-Ti contacts that are both longer than the dimer distance but shorter than the average Ti-Ti separation in the cubic structure. We call this a two-orbital ODL (2O-ODL) state, given that two atomic orbitals of a single Ti ion are utilized. Such a 2O-ODL state is hence comprised of a superposition of two 1O-ODL states of different variety [e.g., (xy, xy) and (yz, yz), (yz, yz) and (zx, zx), etc.] that point in different directions and lie along different edges of the pyrochlore sublattice. These ODL distances are marked as thick lines color coded as red and blue in Fig. 7(b), and the corresponding state is schematically shown on the energy diagram in the bottom left inset of the figure, where the matching color coding of the electron spins signifies that they belong to different 1O-ODL component states.

The existence of the 2O-ODL state in $MgTi_2O_4$ is corroborated by another experimentally observed difference between the two systems: The spatial extent of the local order associated with the metallic regime of $MgTi_2O_4$ is observably larger than that seen in $CuIr_2S_4$ [16]. The extended character of the local structural distortions associated with the 2O-ODL state in $MgTi_2O_4$ is expected for the following reasons. First, due to filling, the two ingredient 1O-ODL prong states in the 2O-ODL superstate cannot both be of the same type [e.g., if one is (xy, xy), the other can only be (yz, yz) or (zx, zx)], which would tend to increase local structural correlations. Second, the bond charge on different 1O-ODL bonds is of the same sign, resulting in the Coulomb repulsion, which would also maximize the span of the 2O-ODL state itself. The observed local distortions over the length scale of about 1 nm, spanning approximately three Ti_4 tetrahedra [25], are therefore consistent with the presence of the 2O-ODL state in $MgTi_2O_4$.

The energetic benefit of the 2O-ODL state over the local spin-singlet dimer state is not apparent and remains elusive. The local 2O-ODL and disordered dimer states would both increase the system entropy and in turn the entropic contribution to energy would stabilize corresponding short-range-order state at elevated temperature. On the other hand, some vestigial magnetic correlations could be expected in the high-temperature ODL regime. Another possibility then is that the principal stabilization of the 2O-ODL state stems from its presumed magnetism. The character of local spin correlations within the 2O-ODL state cannot be established by the analysis carried out in this work. In the 2O-ODL diagram shown in Fig. 7 the two spins are arbitrarily drawn as parallel to avoid any confusion with the dimer state, but their relationship has actually not been established experimentally. In fact, the magnetic response of $MgTi_2O_4$ above the MIT [Fig. 1(c)] is neither Pauli-like nor Curie-Weiss-like. Rather it resembles that of charge density wave systems at high temperature [50], the regime associated with a pseudogap in the electronic density of states [51]. In these systems magnetic susceptibility behavior at $T > T_s$ was attributed to fluctuations of the charge density wave amplitude [52,53]. It is thus tempting to speculate that in $MgTi_2O_4$ the observed magnetic response may similarly be due to ODL fluctuations. It would therefore be of appreciable interest to explore this

aspect of the 2O-ODL state by techniques sensitive to local magnetism, such as muon spin rotation [54] and magnetic PDF [55], which would be particularly informative in that regard.

While the PDF probe used here provides the information on instantaneous atomic structure and as such does not differentiate between static and dynamic disorder, the ODL state in these systems is expected to be dynamic. Spatiotemporal fluctuations then average out to the perceived undistorted cubic average structure as observed crystallographically. Notably, the resistivity just above the MIT in $CuIr_2S_4$ is about 2 mΩ cm and linearly increasing with temperature [14], ascribed to a bipolaronic hopping mechanism [15,48], whereas in the metallic regime of $MgTi_2O_4$ not only is electric resistivity substantially higher, but it decreases with increasing temperature in an insulatorlike manner [8]. This stark difference in the observed electronic transport could be considered as an important indicator, albeit indirect, of the underlying difference reflecting the 1O-ODL and 2O-ODL characters of the high-temperature states in these two systems, respectively.

Although the Ir dimers in $CuIr_2S_4$ are strictly speaking equivalent to the Ti dimers in $MgTi_2O_4$, the mechanism of their local formation from the ODL state is electron-hole symmetric and in that sense the dimers in these two systems could be considered as having a different flavor derived from their origin. Formation of dimers in $CuIr_2S_4$ requires transfer of holes from one half of the available population of ODL states to the other, and the ODLs receptors of a hole become dimers, accounting for only 50% of Ir being dimerized. In contrast, the dimers in $MgTi_2O_4$ assemble from the ODL states by a virtue of electron transfer, where 1O-ODL states that receive electrons become dimers with all Ti participating in dimerization. While in both systems the process involves bond charge disproportionation, in $CuIr_2S_4$ this consequentially results in the observed site charge disproportionation and subsequent charge order, which is presumably imposed by the specifics of the filling and reflected in the dimer density per formula unit.

D. Consequences for ice-type nanoscale fluctuations

The presence of the 2O-ODL state has another important consequence for $MgTi_2O_4$. Each Ti_4 tetrahedron inevitably hosts two 1O-ODL states. Due to the Coulomb repulsion of the bond charge, we would expect the two states to be placed on the opposite skew edges of each tetrahedron, although other constellations cannot be excluded. On the other hand, irrespective of the details of their distribution, multiple 1O-ODLs on one Ti_4 tetrahedron would cause distortions that are incompatible with the ice-type structural fluctuations in the $MgTi_2O_4$ system such as those suggested in the previous study of the local structure of $MgTi_2O_4$ [25]. Given that the spin-singlet dimer distortion in the ground state of $MgTi_2O_4$ [3] follows the two-in–two-out ice rules [49] on each individual Ti_4 tetrahedron in the structure, the proposition that the local Ti atomic displacements have the same configuration in the cubic phase [25] presumably originates in part from the order-disorder-type view of the MIT in $MgTi_2O_4$ that would be implicated by the survival of dimerlike distortions in the high-temperature phase. Our analysis does not support this picture. However, based on the considerations

described above, $CuIr_2S_4$ may possibly be a better candidate for exhibiting the distortions of the two-in–two-out type in the disordered ODL regime, as illustrated by the mapping shown in Fig. 6(b). Exploring this matter further both experimentally and theoretically should provide a more detailed understanding of these systems. Single-crystal diffuse-scattering-based methods [56–60] and dynamical mean-field and advanced first-principles approaches [61–63] would be particularly useful in that regard.

V. CONCLUSION

Here we applied joint x-ray and neutron pair distribution function analysis on the dimerized $MgTi_2O_4$ spinel, a candidate system for hosting the multiorbital ODL state, to track the evolution of its local atomic structure across its localized-to-itinerant electronic transition. Consistent with recent reports, the local structure does not agree with the average structure above the MIT temperature of 250 K and deep in the metallic cubic regime. However, in stark contrast to previous findings [25], we provide unambiguous evidence that spin-singlet dimers are vanishing at the MIT. The shortest Ti-Ti distance corresponding to spin-singlet dimers experiences a discontinuous elongation locally on warming through the MIT but remains shorter than that prescribed by the cubic average structure. The local distortion in the metallic regime is quantitatively and qualitatively different from that observed in association with the spin-singlet state, implying that the MIT is not a trivial order-disorder-type transition. The distortion characterizes the entire metallic regime and persists up to at least 500 K (about $2T_s$). The observed behavior is an identifying characteristic of the local symmetry-broken ODL state observed in the related $CuIr_2S_4$ system. The correlation length of local distortions associated with the ODL state in $MgTi_2O_4$ is about 1 nm, which is double that seen in $CuIr_2S_4$, implying two-orbital character of the ODL state. The observations exemplify that high-temperature electronic precursor states that govern emergent complex low-temperature behaviors in quantum materials can indeed have a multiorbital ODL character.

The Department of Energy will provide public access to these results of federally sponsored research in accordance with the DOE Public Access Plan [64].

TABLE I. Rietveld refinement results of tetragonal and cubic $MgTi_2O_4$ models fit to the neutron TOF powder diffraction patterns at 100 and 500 K, respectively. The models are introduced in detail in Sec. II. Here R_{wp} is the weighted profile agreement factor; x, y, and z are the refinable atomic positions in fractional coordinates; U_{iso}, in units of $Å^2$, is the isotropic atomic displacement parameter.

	Model (Temperature)	
Parameter	Tetragonal (100 K)	Cubic (500 K)
R_{wp}	0.06534	0.05154
a (Å)	6.01197	8.50833
c (Å)	8.46956	-
$c/\sqrt{2}a$	0.99616	1.0
Mg x	0.7449	-
Ti (x, y, z)	$(-0.0112, 0.2451, -0.1414)$	-
O1 (x, y, z)	$(0.4795, 0.2480, 0.1182)$	$(0.2595, 0.2595, 0.2595)$
O2 (x, y, z)	$(0.2410, 0.0219, 0.8805)$	-
Mg U_{iso} ($Å^2$)	0.0063	0.0110
Ti U_{iso} ($Å^2$)	0.0093	0.0191
O U_{iso} ($Å^2$)	0.0042	0.0071

APPENDIX: SUPPLEMENTAL RESULTS

Structural parameters obtained from Rietveld refinements of the tetragonal and cubic models fit to 100 and 500 K
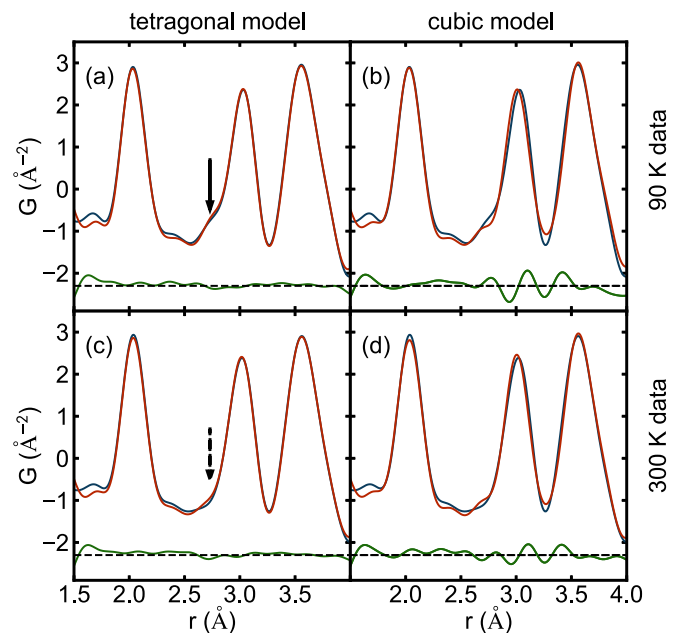

FIG. 8. The x-ray PDF data (blue) collected at the XPD beamline at (a) and (b) 90 K and (c) and (d) 300 K fit by (a) and (c) tetragonal and (b) and (d) cubic models (red) over the range of $1.5 < r < 4$ Å. The difference curves (green) are shown offset below.

neutron time-of-flight powder diffraction data, respectively, are summarized in Table I. These confirm the expected average structure behavior of our sample and are in good quantitative agreement with the values reported previously [3].

The data collected in a separate x-ray PDF experiment carried out at a different beamline under experimental conditions similar to those of the main x-ray PDF experiment are shown in Fig. 8. The PDF analysis of these data reproduces the observations from the main experiment presented in Fig. 3.

[1] K. E. Sickafus, J. M. Wills, and N. W. Grimes, J. Am. Ceram. Soc. **82**, 3279 (1999).

[2] P. G. Radaelli, Y. Horibe, M. J. Gutmann, H. Ishibashi, C. H. Chen, R. M. Ibberson, Y. Koyama, Y.-S. Hor, V. Kiryukhin, and S.-W. Cheong, Nature (London) **416**, 155 (2002).

[3] M. Schmidt, W. Ratcliff, P. G. Radaelli, K. Refson, N. M. Harrison, and S. W. Cheong, Phys. Rev. Lett. **92**, 056402 (2004).

[4] M. Matsuda, H. Ueda, A. Kikkawa, Y. Tanaka, K. Katsumata, Y. Narumi, T. Inami, Y. Ueda, and S.-H. Lee, Nat. Phys. **3**, 397 (2007).

[5] P. G. Radaelli, New J. Phys. **7**, 53 (2005).

[6] J. P. Wright, J. P. Attfield, and P. G. Radaelli, Phys. Rev. Lett. **87**, 266401 (2001).

[7] S. Nagata, N. Matsumoto, Y. Kato, T. Furubayashi, T. Matsumoto, J. P. Sanchez, and P. Vulliet, Phys. Rev. B **58**, 6844 (1998).

[8] M. Isobe and Y. Ueda, J. Phys. Soc. Jpn. **71**, 1848 (2002).

[9] M. Ito, J. Hori, H. Kurisaki, H. Okada, A. J. Perez Kuroki, N. Ogita, M. Udagawa, H. Fujii, F. Nakamura, T. Fujita, and T. Suzuki, Phys. Rev. Lett. **91**, 077001 (2003).

[10] T. Furubayashi, T. Matsumoto, T. Hagino, and S. Nagata, J. Phys. Soc. Jpn. **63**, 3333 (1994).

[11] J. Matsuno, T. Mizokawa, A. Fujimori, D. A. Zatsepin, V. R. Galakhov, E. Z. Kurmaev, Y. Kato, and S. Nagata, Phys. Rev. B **55**, R15979(R) (1997).

[12] N. Matsumoto, R. Endoh, S. Nagata, T. Furubayashi, and T. Matsumoto, Phys. Rev. B **60**, 5258 (1999).

[13] H. Ishibashi, T. Sakai, and K. Nakahigashi, J. Magn. Magn. Mater. **226–230**, 233 (2001).

[14] A. T. Burkov, T. Nakama, M. Hedo, K. Shintani, K. Yagasaki, N. Matsumoto, and S. Nagata, Phys. Rev. B **61**, 10049 (2000).

[15] K. Takubo, T. Mizokawa, N. Matsumoto, and S. Nagata, Phys. Rev. B **78**, 245117 (2008).

[16] E. S. Bozin, W. G. Yin, R. J. Koch, M. Abeykoon, Y. S. Hor, H. Zheng, H. C. Lei, C. Petrovic, J. F. Mitchell, and S. J. L. Billinge, Nat. Commun. **10**, 3638 (2019).

[17] E. S. Bozin, A. S. Masadeh, Y. S. Hor, J. F. Mitchell, and S. J. L. Billinge, Phys. Rev. Lett. **106**, 045501 (2011).

[18] R. J. Koch, T. Konstantinova, M. Abeykoon, A. Wang, C. Petrovic, Y. Zhu, E. S. Bozin, and S. J. L. Billinge, Phys. Rev. B **100**, 020501(R) (2019).

[19] B. A. Frandsen, Q. Wang, S. Wu, J. Zhao, and R. J. Birgeneau, Phys. Rev. B **100**, 020504(R) (2019).

[20] X. Qiu, T. Proffen, J. F. Mitchell, and S. J. L. Billinge, Phys. Rev. Lett. **94**, 177203 (2005).

[21] D. I. Khomskii and T. Mizokawa, Phys. Rev. Lett. **94**, 156402 (2005).

[22] S. Nagata, T. Hagino, Y. Seki, and T. Bitoh, Physica B **194–196**, 1077 (1994).

[23] J. Zhou, G. Li, J. L. Luo, Y. C. Ma, D. Wu, B. P. Zhu, Z. Tang, J. Shi, and N. L. Wang, Phys. Rev. B **74**, 245102 (2006).

[24] M. Croft, W. Caliebe, H. Woo, T. A. Tyson, D. Sills, Y. S. Hor, S.-W. Cheong, V. Kiryukhin, and S.-J. Oh, Phys. Rev. B **67**, 201102(R) (2003).

[25] S. Torigoe, T. Hattori, K. Kodama, T. Honda, H. Sagayama, K. Ikeda, T. Otomo, H. Nitani, H. Abe, H. Murakawa, H. Sakai, and N. Hanasaki, Phys. Rev. B **98**, 134443 (2018).

[26] T. Egami and S. J. L. Billinge, *Underneath the Bragg Peaks: Structural Analysis of Complex Materials*, 2nd ed. (Elsevier, Amsterdam, 2012).

[27] S. J. L. Billinge, in *International Tables for Crystallography*, edited by C. J. Gilmore, J. A. Kaduk, and H. Schenk (International Union of Crystallography, Chester, 2019), Vol. H, pp. 649–672.

[28] S. J. L. Billinge, R. G. DiFrancesco, G. H. Kwei, J. J. Neumeier, and J. D. Thompson, Phys. Rev. Lett. **77**, 715 (1996).

[29] C. A. Young and A. L. Goodwin, J. Mater. Chem. **21**, 6464 (2011).

[30] D. A. Keen and A. L. Goodwin, Nature (London) **521**, 303 (2015).

[31] J. V. Laveda, B. Johnston, G. W. Paterson, P. J. Baker, M. G. Tucker, H. Y. Playford, K. M. Ø. Jensen, S. J. L. Billinge, and S. A. Corr, J. Mater. Chem. A **6**, 127 (2018).

[32] C. L. Farrow and S. J. L. Billinge, Acta Crystallogr. A **65**, 232 (2009).

[33] P. J. Chupas, X. Qiu, J. C. Hanson, P. L. Lee, C. P. Grey, and S. J. L. Billinge, J. Appl. Crystallogr. **36**, 1342 (2003).

[34] T. Proffen and S. J. L. Billinge, J. Appl. Crystallogr. **32**, 572 (1999).

[35] C. L. Farrow, P. Juhás, J. Liu, D. Bryndin, E. S. Božin, J. Bloch, T. Proffen, and S. J. L. Billinge, J. Phys.: Condens. Matter **19**, 335219 (2007).

[36] G. Ashiotis, A. Deschildre, Z. Nawaz, J. P. Wright, D. Karkoulis, F. E. Picca, and J. Kieffer, J. Appl. Crystallogr. **48**, 510 (2015).

[37] P. Juhás, T. Davis, C. L. Farrow, and S. J. L. Billinge, J. Appl. Crystallogr. **46**, 560 (2013).

[38] X. Yang, P. Juhás, C. L. Farrow, and S. J. L. Billinge, arXiv:1402.3163.

[39] J. Neuefeind, M. Feygenson, J. Carruth, R. Hoffmann, and K. K. Chipley, Nucl. Instrum. Methods Phys. Res. Sect. B **287**, 68 (2012).

[40] P. Juhás, C. L. Farrow, X. Yang, K. R. Knox, and S. J. L. Billinge, Acta Crystallogr. A **71**, 562 (2015).

[41] I. Jeong, T. Proffen, F. Mohiuddin-Jacobs, and S. J. L. Billinge, J. Phys. Chem. A **103**, 921 (1999).

[42] B. H. Toby and R. B. Von Dreele, J. Appl. Crystallogr. **46**, 544 (2013).

[43] A. N. Vasiliev, M. M. Markina, M. Isobe, and Y. Ueda, J. Magn. Magn. Mater. **300**, e375 (2006).

[44] V. M. Talanov, V. B. Shirokov, V. V. Ivanov, and M. V. Talanov, Crystallogr. Rep. **60**, 101 (2015).

[45] A. W. Hull, J. Franklin Inst. **193**, 189 (1922).

[46] S. Di Matteo, G. Jackeli, and N. B. Perkins, Phys. Rev. B **72**, 024431 (2005).

[47] A. Rahaman, M. Chakraborty, T. Paramanik, R. K. Maurya, S. Mahana, R. Bindu, D. Topwal, P. Mahadevan, and D. Choudhury, Phys. Rev. B **100**, 115162 (2019).

[48] K. Yagasaki, T. Nakama, M. Hedo, Y. Uwatoko, Y. Shimoji, S. Notsu, K. Uchima, N. Matsumoto, S. Nagata, H. Okada, H. Fujii, H. Yoshida, H. M. Kimura, Y. Yamaguchi, and A. T. Burkov, J. Phys. Soc. Jpn. **75**, 074706 (2006).

[49] P. W. Anderson, Phys. Rev. **102**, 1008 (1956).

[50] J. L. Benchimol, F. T. Hedgcock, and F. J. Di Salvo, Solid State Commun. **25**, 677 (1978).

[51] S. V. Borisenko, A. A. Kordyuk, A. N. Yaresko, V. B. Zabolotnyy, D. S. Inosov, R. Schuster, B. Büchner, R. Weber, R. Follath, L. Patthey, and H. Berger, Phys. Rev. Lett. **100**, 196402 (2008).

[52] D. C. Johnston, Phys. Rev. Lett. **52**, 2049 (1984).

[53] J. Zhang, D. Phelan, A. S. Botana, Y.-S. Chen, H. Zheng, M. Krogstad, S. G. Wang, Y. Qiu, J. A. Rodriguez-Rivera, R. Osborn, S. Rosenkranz, M. R. Norman, and J. F. Mitchell, Nat. Commun. **11**, 6003 (2020).

[54] I. McKenzie, Annu. Rep. Prog. Chem. C **109**, 65 (2013).

[55] B. Frandsen, X. Yang, and S. J. L. Billinge, Acta Crystallogr. A **70**, 3 (2014).

[56] T. Weber and A. Simonov, Z. Kristallogr. Cryst. Mater. **227**, 238 (2012).

[57] M. J. Krogstad, S. Rosenkranz, J. M. Wozniak, G. Jennings, J. P. C. Ruff, J. T. Vaughey, and R. Osborn, Nat. Mater. **19**, 63 (2020).

[58] M. A. Davenport, M. J. Krogstad, L. M. Whitt, C. Hu, T. C. Douglas, N. Ni, S. Rosenkranz, R. Osborn, and J. M. Allred, arXiv:1909.12704.

[59] N. Roth, A. F. May, F. Ye, B. C. Chakoumakos, and B. B. Iversen, IUCrJ **5**, 410 (2018).

[60] N. Roth and B. B. Iversen, Acta Crystallogr. A **75**, 465 (2019).

[61] Y. Pramudya, H. Terletska, S. Pankov, E. Manousakis, and V. Dobrosavljević, Phys. Rev. B **84**, 125120 (2011).

[62] S. Mahmoudian, L. Rademaker, A. Ralko, S. Fratini, and V. Dobrosavljević, Phys. Rev. Lett. **115**, 025701 (2015).

[63] Z. Wang, X.-G. Zhao, R. Koch, S. J. L. Billinge, and A. Zunger, Phys. Rev. B **102**, 235121 (2020).

[64] http://energy.gov/downloads/doe-public-access-plan.

Ultrafast x-ray diffraction study of melt-front dynamics in polycrystalline thin films

Tadesse A. Assefa[1]*, Yue Cao[1]†, Soham Banerjee[1,2], Sungwon Kim[3], Dongjin Kim[3], Heemin Lee[4], Sunam Kim[5], Jae Hyuk Lee[5], Sang-Youn Park[5], Intae Eom[5], Jaeku Park[5], Daewoong Nam[5], Sangsoo Kim[5], Sae Hwan Chun[5], Hyojung Hyun[5], Kyung sook Kim[5], Pavol Juhas[6], Emil S. Bozin[1], Ming Lu[7], Changyong Song[4], Hyunjung Kim[3], Simon J. L. Billinge[1,2], Ian K. Robinson[1,8]*

Melting is a fundamental process of matter that is still not fully understood at the microscopic level. Here, we use time-resolved x-ray diffraction to examine the ultrafast melting of polycrystalline gold thin films using an optical laser pump followed by a delayed hard x-ray probe pulse. We observe the formation of an intermediate new diffraction peak, which we attribute to material trapped between the solid and melted states, that forms 50 ps after laser excitation and persists beyond 500 ps. The peak width grows rapidly for 50 ps and then narrows distinctly at longer time scales. We attribute this to a melting band originating from the grain boundaries and propagating into the grains. Our observation of this intermediate state has implications for the use of ultrafast lasers for ablation during pulsed laser deposition.

INTRODUCTION

Understanding the role and behavior of transient states during phase transitions, such as melting, is becoming increasingly important in condensed matter physics (1–4). Time-resolved (TR) pump-probe techniques are well suited to capture these transient states. An optical laser pump pulse induces the phase transition, and an ultrashort x-ray/electron pulse analyzes the properties of the transient state, which follows after a specified time delay. Pump-probe methods have been used to study time evolution (5, 6) of thermal and nonthermal melting processes in metals (7–9) and semiconductors (10, 11). These and other experiments have been widely interpreted with the help of the two-temperature model (TTM) (12), in which the pump pulse is considered to create hot electrons that subsequently transfer their heat to the crystal lattice through electron-phonon coupling within a few picoseconds (13). This model is generally accepted as describing the laser excitation process in a wide range of materials and has been incorporated into a TTM molecular dynamics simulation method, which has led to simulations that are found to be in good agreement with experimental results (14–16).

Macroscopic materials are often polycrystalline, containing a large density of differently oriented grains separated by grain boundaries (GBs). Melting has been widely studied over many decades and is believed to be initiated preferentially at defects, such as surfaces, dislocations, GBs, stacking faults, and point defects that contain atoms with lower coordination number, thus more dangling bonds than in the bulk (17, 18). According to the Lindemann criterion, which is when the amplitude of atomic vibration reaches 10% of the nearest neighbor atomic distance, melting happens at lower temperatures near these defects. Experiments, for example, by ion channeling, have shown an increase in disorder at these locations slightly below the bulk melting temperature (19). Theoretical studies have confirmed this concept that melting in granular materials starts to nucleate at dislocations and GBs (20, 21). While the location of the initiation of melting at these weak points of polycrystalline material is widely accepted, the time dependence of the progression of melting is an open question, which has been much less studied. Ultrafast electron diffraction experiments have explored the time scales of melting in free-standing single-crystal films and found different melting regimes (7).

Furthermore, it is well known that the presence of GBs affects electron transport in metals, most easily seen in their electrical conductivity (22). In metal thin films, the electron-phonon coupling constant is related to the inelastic mean free path (λ) of electrons, which varies with energy according to the "universal curve" (23). In addition, it depends on the electron reflection coefficient from defects such as GBs, film thickness, and grain size (24, 25). Depending on the electron energy, the inelastic mean free path is in the range of a hundred nanometers. This implies that most of the electrons generated from the front side of a 300-nm sample do not make it to the other side, which agrees with experiments (13). In a polycrystalline thin film, however, the separation between GBs, often assumed to scale with the film thickness, can dominate once again and provides a characteristic thickness dependence of resistivity (22). Within the framework of the TTM, it is expected that the hot electrons will couple to the lattice preferentially at GBs due to this additional electron scattering (26, 27). Electrical transport measurements indicate slower effective electron velocities in polycrystalline than in single-crystal gold thin films, due to the additional scattering at GBs (28). This results in a characteristic penetration depth of ultrafast hot electrons, which is considerably longer than the 12-nm electromagnetic skin depth at 400-nm laser wavelength in polycrystalline gold films (13). For both these reasons, we would expect to see heterogeneous melting in a granular metal when it is excited by a laser, with preferential melting at the GBs.

Our experiment was therefore designed to explore the time dependence of laser-induced structural changes in polycrystalline gold (Au) thin films of 50-, 100-, and 300-nm thicknesses prepared with the electron beam evaporation technique. A femtosecond laser pulse was used

[1]Condensed Matter Physics and Materials Science Department, Brookhaven National Laboratory, Upton, NY 11793, USA. [2]Department of Applied Physics and Applied Mathematics, Columbia University, New York, NY 10027, USA. [3]Department of Physics, Sogang University, Seoul 04107, Korea. [4]Department of Physics and POSTECH Photon Science Center, Pohang University of Science and Technology, Pohang 37673, Korea. [5]Pohang Accelerator Laboratory, Pohang, Gyeongbuk 37673, Korea. [6]Computational Science Initiative, Brookhaven National Laboratory, Upton, NY 11793, USA. [7]Center for Functional Nanomaterials, Brookhaven National Laboratory, Upton, NY 11793, USA. [8]London Centre for Nanotechnology, University College London, London WC1E 6BT, UK.
†Present address: Materials Science Division, Argonne National Laboratory, Argonne, IL 60439, USA.
*Corresponding author. Email: tassefa@bnl.gov (T.A.A.); irobinson@bnl.gov (I.K.R.)

to excite electrons at the front surface of the Au thin film with a range of fluences spanning the level needed to fully melt the film in a single shot. By measuring the x-ray diffraction (XRD) patterns of the film with a single x-ray pulse produced by the Pohang Accelerator Laboratory X-ray Free Electron Laser Facility (PAL-XFEL), we monitored the structural changes following a 400-nm optical laser excitation.

RESULTS

Single-shot TR XRD results

The XRD data were collected in a transmission Debye-Scherrer geometry to minimize background shown in Fig. 1A. A new broader "intermediate" peak is seen to appear on the lower Q side of the (111) powder ring shown in Fig. 1B. The new powder ring observed here has less azimuthal intensity variations than the (111) powder ring, indicating that the contributing material is more homogeneous. To show the full Q dependence, we azimuthally integrated each measured two-dimensional (2D) image to give the XRD profile curves shown in Fig. 2 (A to C). The powder (111), (200), and (311) Bragg peaks all show two clear peaks, a sharp powder peak, and a broader intermediate diffraction peak at lower Q, which becomes visible about 50 ps after laser excitation.

To understand the temporal evolution of the laser-induced changes in the sample, we fitted the XRD profiles measured at different times with two components, as shown in Fig. 3A, with full details in Materials and Methods. Both the crystal peak position and intensity, shown in Fig. 3 (B and C), are seen to decay and oscillate; the oscillation strength depends weakly on the incident laser fluence. The oscillatory behavior has been explained before to originate from longitudinal acoustic vibra-

Origin of the intermediate peak

The intermediate peak position, width, and integrated intensity are well described by the Gaussian function used in the fitting procedure (details below), as seen in Fig. 3A. While the intermediate peak position, around 2.655 Å^{-1}, is close to the first peak of liquid gold at 2.64 Å^{-1} (31), the peak is 10 times sharper than any known liquid gold peak, so it cannot be attributed to a conventional equilibrium liquid state. Analogous intermediate peaks are also observed near the (200) and (311) powder peaks (in Fig. 2, B and C), which do not exist at all in the liquid structure factor (32). The peak also cannot be due to the effect of thermal expansion with a continuous distribution of crystal temperatures within the sample because that would give only a monotonic tail on the crystal diffraction peak. Instead, the formation of a distinct peak due to thermal expansion implies that there has to be part of the material with a well-defined larger lattice parameter, hence preferred temperature. The only singular temperature of gold is the melting point itself, $T = T_m$ (1338 K): The crystal temperature could be trapped there during heating, while it takes up the latent heat of melting. The crystal, undergoing melting, apparently retains a single, well-defined larger lattice constant while it becomes progressively disordered. The splitting of the peak into two distinct components, identified with two different temperatures, is a direct signature of inhomogeneous melting.

The intermediate peak position, shown as a function of time in Fig. 4C, does not reach the position expected for the lattice parameter of gold at the melting point, shown as a horizontal blue dashed line in Fig. 4C. We consider that the peak position is offset by the effects of pressure in the melting layer, estimated to be around 5 GPa from the bulk modulus and thermal expansion coefficient. The pressure (P) was estimated using $P = K_0 \Delta V / V$, where K_0 is the isothermal bulk modulus for gold (167 GPa) and $\Delta V / V = 3(\Delta Q / Q)$ is the relative volume change determined by the peak shift, ΔQ. Such an induced pressure would be expected to dissipate acoustically, and we note the presence of acoustic oscillations in the peak position, which are particularly strong at a fluence of 254 mJ/cm^2, which also gives the strongest intermediate peak.

Dynamics of the crystal diffraction peak

For the 300-nm thin film, upon laser excitation, the (111) crystal peak shows an abrupt reduction of intensity for all laser fluences used in our measurements. In addition, the (111) crystal peak position shows a negative position shift due to thermal expansion of the gold. For the data measured at an incident laser fluence of 254 mJ/cm^2, the maximum excursion of the peak is $\Delta Q = -0.0047$ Å^{-1} at 60 ps after laser excitation, corresponding to a crystal temperature change of 400 K, estimated from the thermal expansion coefficient of gold, 14×10^{-6} at 300 K (33), and assuming no pressure contribution.

In all the 300-, 100-, and 50-nm thin films, shown in Fig. 5 (B, D, and E), the sharp decrease in the (111) integrated peak intensity was fitted with an exponential decay function. The dynamics of the crystal peak integrated intensity is different for the different film thickness. For all the different film thicknesses reported here, the decay time was found to depend strongly on the incident laser fluence. The integrated intensities of the 300-nm film, measured at fluences of 63, 636, and 2500 mJ/cm^2, were fitted with exponential decay times of 100 ± 33 ps, 85 ± 15 ps, and 25 ± 5 ps, respectively. These values are close to
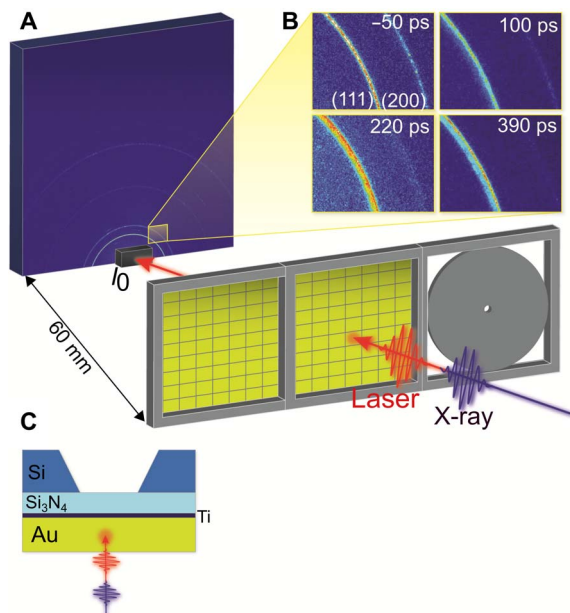

Fig. 1. Experimental configuration for TR XRD from polycrystalline gold thin films. (**A**) Experimental setup showing the sample, the Rayonix detector MX225-HS, and the photodiode (I_0) to measure the transmitted beam for normalization. The sample was mounted perpendicular to the 9.7-keV x-ray beam, and a 400-nm, 100-fs optical laser was used to excite the sample in almost colinear geometry. (**B**) 2D diffraction patterns of the 300-nm thin film collected 50 ps before and 100, 220, and 390 ps after laser excitation at an incident laser fluence of 254 mJ/cm^2. (**C**) Cross-sectional view of the gold thin film and substrate window array arrangement.
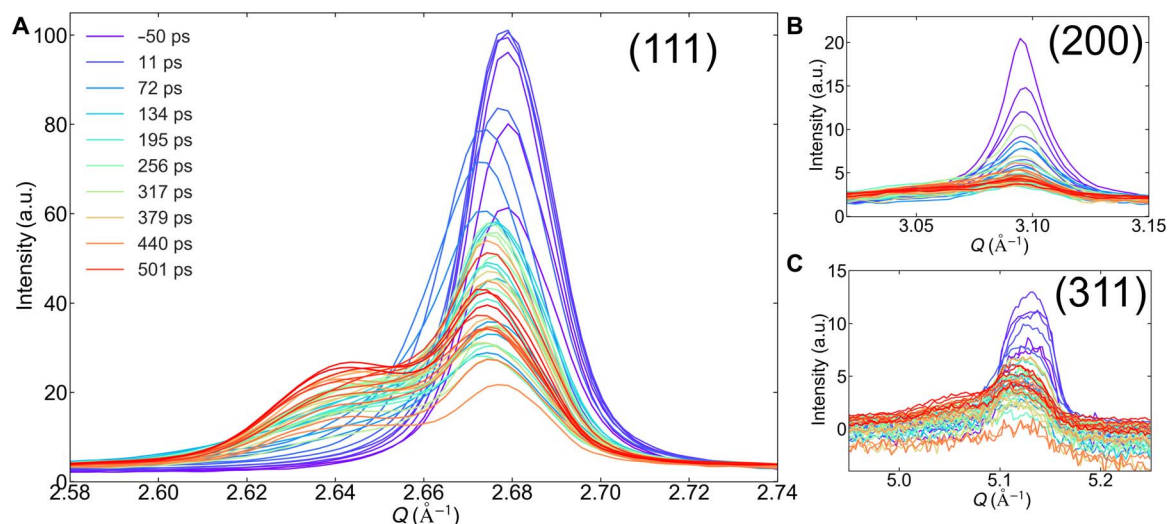
Fig. 2. Dynamics of azimuthally integrated XRD profiles of different peaks. (**A**) (111) (**B**) (200), and (**C**) (311) diffraction peaks for the 300-nm-thick thin film measured at various delay times after an incident laser fluence excitation of 254 mJ/cm². All the diffraction positions have both the crystal powder and intermediate peaks. a.u., arbitrary units.
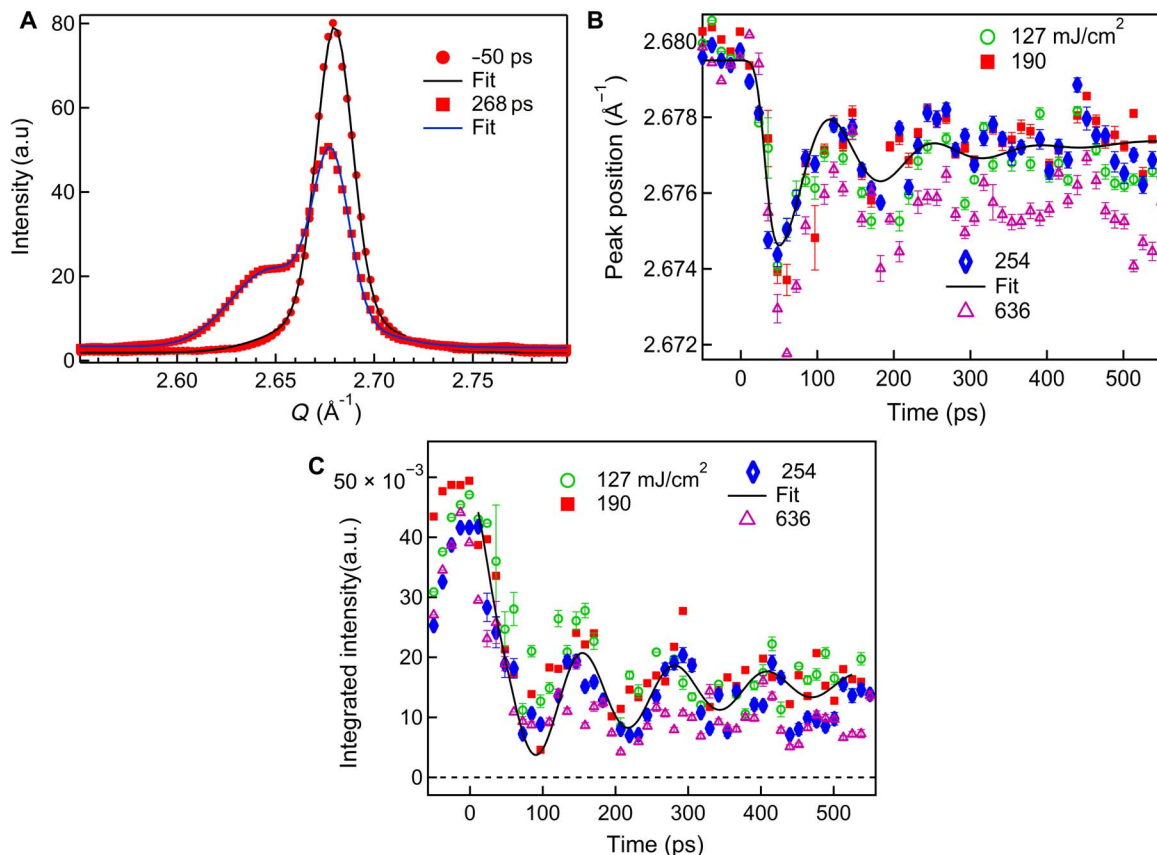
Fig. 3. Dynamics of the (111) crystal diffraction peak measured from 300-nm gold thin films. (**A**) Fits to the diffraction intensity profiles versus momentum transfer, Q, measured 50 ps before and 268 ps after excitation at an incident laser fluence of 254 mJ/cm². (**B**) Peak position and (**C**) integrated intensity as a function of time delay. For the 254 mJ/cm² data, the peak position was fitted with a sum of exponential decay (time constant, $\tau_1 = 2800 \pm 50$ ps) and an exponentially damped cosine function (with damping time constant, $\tau_2 = 90 \pm 10$ ps, and period, $T = 130 \pm 10$ ps). Similarly, an integrated intensity of 254 mJ/cm² was fitted with $\tau_1 = 2800 \pm 100$ ps, $\tau_2 = 250 \pm 45$ ps, and $T = 130 \pm 10$ ps.
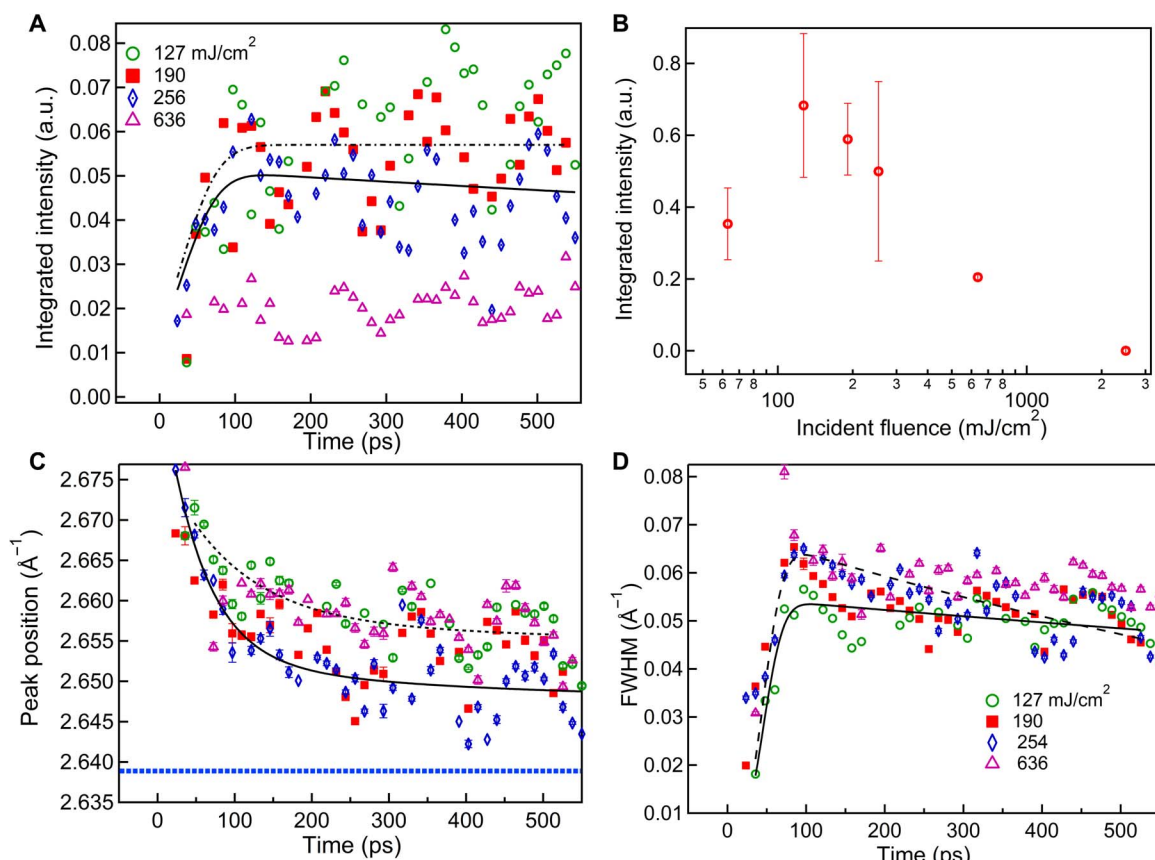
Fig. 4. Dynamics of the intermediate diffraction peak of the (111) profile. (**A**) Integrated intensity, (**B**) integrated intensity of the intermediate peak at different incident fluences, (**C**) position, and (**D**) width as a function of pump-probe delay time for 300-nm films. The data measured at different incident laser fluences are indicated with different colors. The peak width was fitted with an exponential decay convoluted with a Gaussian function. For the data measured at 254 and 127 mJ/cm^2, the time constants were 1320 ± 50 ps and 3900 ± 600 ps, respectively. The peak position measured at 254 mJ/cm^2 was fitted to a sum of two exponential functions with time constants of 50 ± 10 ps and 330 ± 20 ps convoluted with a Gaussian function. The dashed blue line shown in (C) is the expected position of the gold (111) peak at the melting point due to thermal expansion, assuming ambient pressure.

the observed rise times of the intermediate peak, consistent with a conversion of crystal into the material that gives rise to the new intermediate diffraction peak.

Analysis of crystal peak oscillations

Both the integrated peak intensity and peak positions for the 300-nm films show both a decay and damped oscillations. This behavior is interpreted as due to loss of material to melting and acoustic wave oscillations. It is fitted with a function

$$ A(t) = A_0(1 + A_1 e^{-t/\tau_1}) + A_2 (e^{-t/\tau_2}) \cos\left(\frac{2\pi t}{T} + \phi\right) $$

where A_0, A_1, and A_2 are amplitudes; τ_1 and τ_2 are decay times; T is the period of oscillation; and ϕ is a phase offset. Both τ_1 and τ_2 become shorter for higher fluence data; moreover, the time observed here is shorter than the decay time observed in gold nanocrystals (1), which were measured at fluences below the damage threshold. The damping time constant is close to the observed rise time of the intermediate peak, consistent with a conversion of crystal into the material giving the new intermediate diffraction peak. For the data measured at an incident laser fluence of 254 mJ/cm^2, the fit to the peak position gives an oscillation period (T) of 136 ± 10 ps, corresponding to acoustic waves in a 270 ±

30–nm sample thickness propagating at a longitudinal speed of sound of 3690 m/s in gold films (30). A similar oscillation period was found to fit the integrated peak intensity.

Temperature rise due to laser heating

The pulse energy (E_{pulse}) was calculated by dividing the laser power by the 10-Hz repetition rate of the laser. The laser beam size, d, at full width at half maximum (FWHM) was estimated to be 100 μm at the sample position (full description is given in Materials and Methods). The incident laser fluence (F_{in}) was then taken to be E_{pulse}/A, where $A = \pi(d^2/4)$, A is the laser beam area. Assuming that the x-rays are probing the central part of the excited region of the sample, we estimate that a maximum temperature rise, ΔT, of the thin film of thickness h can be estimated as $\Delta T = (\epsilon F_{in})/(h\rho C_P)$, where $\epsilon = 0.6$ is the absorption coefficient of gold thin at 400 nm (7), ρ is the density of gold (19.3 g/cm^3), and C_P is the specific heat capacity of gold (0.128 J/g K). The absorbed fluence F_{ab} will be smaller than this reported value due to significant reflection from the surface of the sample. For experiments performed on the 300-nm film at incident laser fluences of 127, 190, 254, and 636 mJ/cm^2, we estimated the temperature rises of 1030, 1538, 2060, and 5150 K, respectively, ignoring the latent heat contribution. These estimated temperature values are subject to uncertainties of the probe region. Whenever the laser
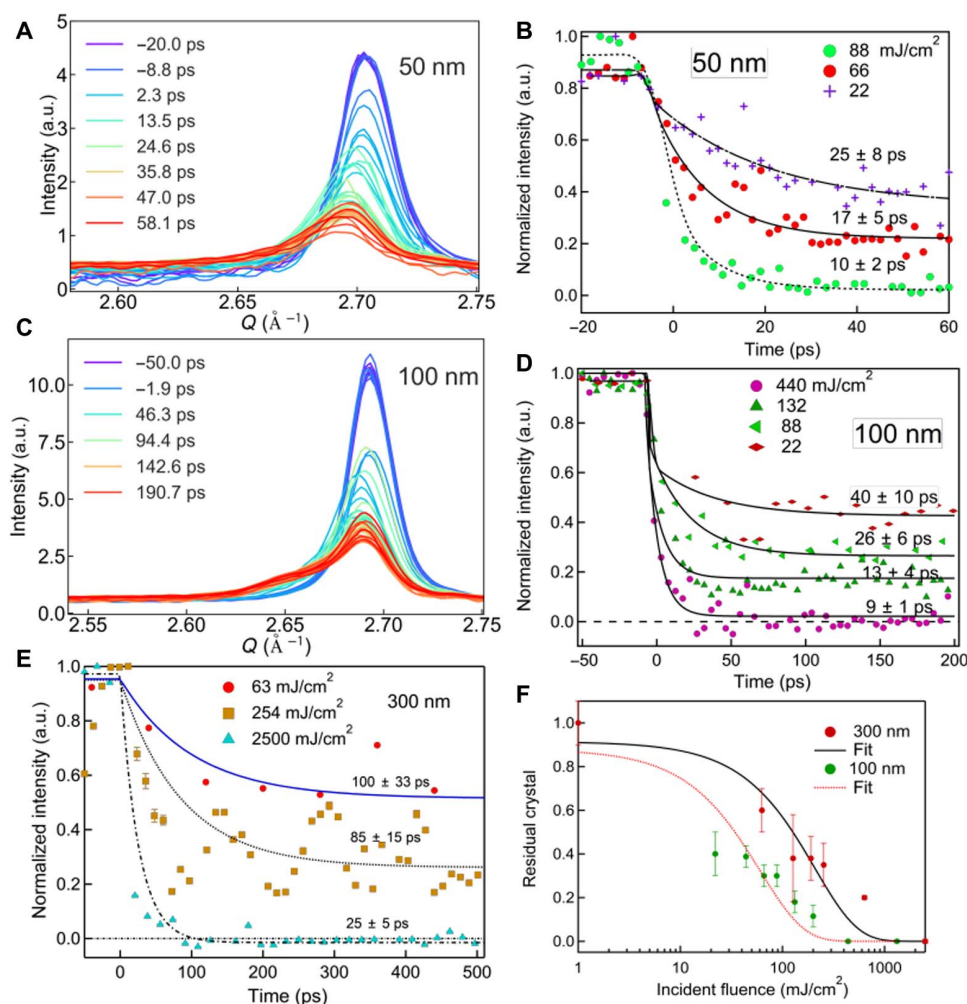
Fig. 5. Thickness dependence of the melting time of gold thin films. (**A**) Diffraction intensity profiles measured from a 50-nm-thick gold film at an incident laser fluence of 50 mJ/cm^2 at different delay times after laser excitation. (**B**) Time dependence of the integrated diffraction intensity of 50-nm thin films at different incident laser fluences. (**C**) Diffraction profiles of a 100-nm-thick gold film measured at an incident laser fluence of 66 mJ/cm^2. (**D**) Integrated intensity of the (111) peak as a function of pump-probe delay time for different fluences. (**E**) Time dependence of the crystal peak component for the 300-nm gold thin films for different incident laser fluences. (**F**) Residual crystal fraction versus fluence for 100- and 300-nm-thick films. The fraction of the crystal peak intensity remaining 500 ps after laser excitation is plotted versus incident laser fluence and fitted with a sigmoid function.

heating goes into latent heat, $L = 66$ J/g, at the melting point $T_m = 1338$ K, there will be a smaller temperature rise of 516 K. According to these estimates, an incident fluence of 254 mJ/cm^2 should be just sufficient to melt the 300-nm film sample.

Melting time and partial melting

From the estimates given above, we estimate that the absorbed fluence for complete melting should be 98, 33, and 16 mJ/cm^2 for the 300-, 100-, and 50-nm thin films, respectively. A recent result (7) showed that the threshold for complete melting of 30-nm polycrystalline gold thin films was about 15 mJ/cm^2, consistent with these numbers. In our data in Fig. 3C, for the 300-nm films, even an incident laser fluence of 636 mJ/cm^2 is still not enough to completely melt the film because there is still some intensity left in the crystal powder peak. Both the crystal peak position in Fig. 3B and intensity in Fig. 3C show an exponential decay and oscillation in the remainder of the partially melted film. At higher fluences, both the peak position and intensity oscillations become weaker. The peak was found to disappear completely within 25 ps at an incident laser

fluence of 2500 mJ/cm^2, suggesting complete melting of the film at the level of sensitivity of our measurement.

We suppose that this incomplete melting, especially of thicker films, is explained by the limited transmission of the hot electrons through the sample, due to thermal scattering and scattering from the GBs. It was seen in the previous work (13) that only a small fraction of the hot electrons are able to traverse a 300-nm gold thin film. When the samples are driven with fluences well above the estimates above for complete melting, there must be a significant temperature gradient established by the limited electron transmission: While the far side of the sample is not yet reaching the melting point, the laser-illuminated side goes well above and may reach the boiling point and/or start ablating. This conclusion was tested by examination of the fluence dependence of the decay of the crystal peak intensity of 50- and 100-nm thin films in Fig. 5 (B and D). For the 100-nm thin film, we observe complete melting within 25 ps at an incident laser fluence of 440 mJ/cm^2. Similarly, 20 ps is the melting time needed for the 50-nm film at an incident laser fluence of 88 mJ/cm^2. Melting

becomes faster as the incident laser fluence increases, in good agreement with the recently reported data on 35-nm polycrystalline thin films (7), which were interpreted as the sample crossing from heterogeneous to homogeneous melting. In Fig. 5F, we plot the residual fraction of crystal left after 500 ps of melting against the incident laser fluence, which shows a roughly sigmoid function with a threshold of 153 mJ/cm^2 for the 300-nm film. The 100-nm thin film shows similar behavior with a threshold of 60 mJ/cm^2.

DISCUSSION

Having identified that the intermediate peak arises from the material undergoing melting, we can then follow its behavior to report on the structure and properties of the melting region as a function of time and fluence. Since the peak is the structure factor of the melting material, we follow its trends, through line shape fitting, to understand the overall melting behavior. For the reasons given in Introduction, we assume that the melting initiates at the GBs of the polycrystalline film where the electrons couple preferentially to the lattice. Heat flow starting from the GBs causes a melting wave, which propagates toward the core of each grain as illustrated schematically in Fig. 6A.

Melt-front velocity

Classical thermal diffusion calculations can be used to understand the propagation of melting, once the few-picosecond electron-lattice equilibration time of the TTM has elapsed. This is shown as a temperature-position profile in Fig. 6B, illustrating how the thermal

Fig. 6. GB melting mechanism in a polycrystalline gold thin film. (A) Sketch of GB locations in a polycrystalline gold thin film and a zoomed view of how the melt front would propagate away from the GB following optical laser excitation. **(B)** Simulation of the spatial temperature distribution using the heat diffusion equation from a spike of melt created at the GB, at $x = 0$. The heat moves rapidly into the grain with a melt-front velocity determined by the heat flux. The shaded offset region is due to the uptake of latent heat, resulting in a block of melting material sandwiched between two melt fronts moving at different velocities.

spike assumed to start at the GBs diffuses rapidly into the neighboring grains and gives rise to a melt front where the temperature crosses the melting temperature, T_m. The solution of the 1D heat diffusion equation starting from a point source at the GB where a pulse of heat is injected at time $t = 0$ is a spatial Gaussian distribution, $T(x, t)$, of width $\sqrt{2kt/C_p\rho}$, where k is the thermal conductivity, C_p is the specific heat, and ρ is the density. According to Fourier's law, the heat flow, $\dot{Q}$ or (dQ/dt), is proportional to the spatial derivative of $T(x, t)$, which is $(C_p\rho A/2)T(x, t) (x/t)$, where A is the area of the GB considered. When $T = T_m$, the melting temperature, (x/t) can be considered as a melt-front velocity, v, determined by the rate of heat flow $v = 2\dot{Q}/\rho A C_p T_m$. The heat flow, $\dot{Q}$, is given by the initial conditions and is expected to be proportional to the absorbed laser fluence, which explains why melting times become shorter with fluence, as we and others observe (7).
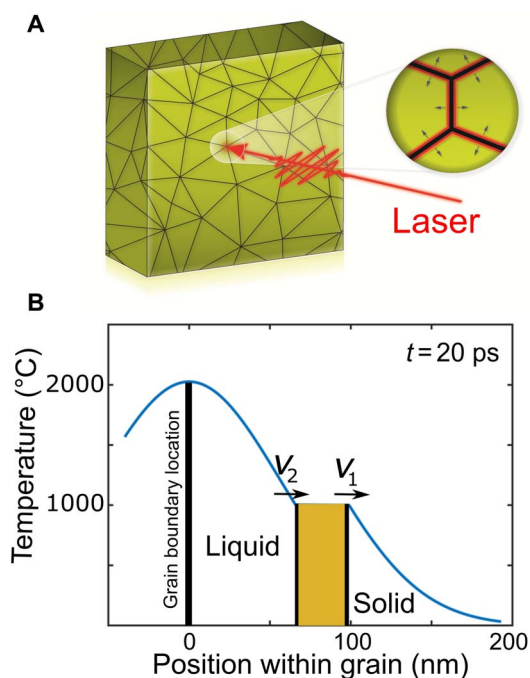
Effect of latent heat

Because of the uptake of latent heat, there can be two melt fronts with different velocities v_1 for the solid-melt boundary and v_2 for the melt-liquid boundary, indicated in Fig. 6B. These are given by $\dot{Q} = (1/2)\rho A v_1 (T_m C_p) = (1/2)\rho A v_2 (L + T_m C_p)$, where L is the latent heat. This defines a band of melting material sandwiched between the two melt fronts with $T = T_m$, which is responsible for the intermediate diffraction peak. Assuming a constant heat flow and that both fronts start together, they grow apart with a ratio, $v_2/v_1 = (L + T_m C_p)/(T_m C_p) = 1.39$, resulting in enlargement of the melt region.

Explanation of narrowing of the intermediate peak

As the melting region propagates through the grain, the gold region undergoing melting between the two melt fronts becomes larger in time, according to this model. While the associated diffraction peak in Fig. 4 shows a rise in both its integrated intensity and width within the first 50 ps, the most significant trend is a distinct narrowing of the peak width over the 100- to 500-ps delay range in Fig. 4D. We interpret this to be due to the widening band between the two melt fronts. The physical size of the band, given by $2\pi/_W$, where W, the FWHM of the intermediate peak, is 10 nm at 100 ps growing to 14 nm at 550 ps for 254 mJ/cm^2. These values, together with the model above, provide an estimate of the melt-front velocity, $v = 30$ m/s. Only the integrated intensity shows significant fluence dependence, shown in Fig. 4A, with a drop of intensity for the higher fluence, attributed to faster melting. We interpret the initial 50-ps rise time as the time needed to establish the melt front, while the quasi-stable behavior following this transition corresponds to a steady progression of the melt front while energy is being transferred from the latent heat to the melt.

Summary and implications

Our comprehensive picture of the ultrafast melting of polycrystalline gold films starts when the laser pulse is absorbed within the electromagnetic skin depth of the sample (12 nm at 400 nm wavelength), creating a population of hot electrons, which then travel through the sample at Fermi velocity (12, 34). During this process, hot electrons transfer their energy to the lattice preferentially at the GBs (27), leading to inhomogeneous melting with a pair of melt fronts being emitted from each GB, as illustrated in Fig. 6. This melting material gives rise to a well-defined new diffraction peak with quasi-static width, position, and intensity living beyond 500 ps, suggesting that the thermally expanded crystal lattice is partially preserved at $T = T_m$ during the transfer of its latent heat at the melting point. Polycrystalline thin films

are prone to have inhomogeneities associated with their GBs, surfaces, dislocations, stacking faults, and point defects. All these inhomogeneities will have atoms with lower coordination number than in the bulk, leading to spatial inhomogeneities in the electron-phonon coupling rate. For metals, the electron-phonon coupling rate increases with the density of GBs (22, 23). According to (24), increases in the number of GBs lead to a decrease in the mean free path of electrons due to an increase in electron scattering locations. When a femtosecond laser excites a polycrystalline metal thin film, the hot electrons generated will efficiently transfer energy to the lattice at these electron scattering locations. This allows more precise machining of materials with ultrafast lasers (35). It is found that granularity appears when nanosecond lasers are used, so femtosecond lasers are advantageous for precise micromachining, which significantly reduces the formation of a "heat-affected zone" in a material (36). Moreover, this will also have a consequence for laser ablation, perhaps contributing to the formation of particulates found in the ablated plume (37). In both applications, our model may explain why grain averaging when using nanosecond lasers might be needed.

MATERIALS AND METHODS
Thin film sample preparation
Gold films with a nominal thickness of 50, 100, and 300 nm were fabricated by electron beam evaporation onto standard silicon nitride (Si_3N_4) membrane windows at the Center for Functional Nanomaterials, Brookhaven National Laboratory (BNL). The silicon nitride membrane arrays were provided commercially by Silson. The windows are 500 μm × 500 μm and 200 nm thick in 24 × 24 or 9 × 7 arrays on silicon wafers. Before gold deposition on the membrane, a 2-nm titanium adhesion layer was deposited. To minimize impurities during deposition, the preparation was performed at a pressure of around 10^{-6} mbar. The sample thicknesses reported here are nominal values, estimated from the deposition rate measured on a quartz crystal balance. We observed no diffraction signal contributions from the titanium. For the 300-nm thin film, the grain sizes were estimated to be 163 ± 40 nm using the Scherrer formula, determined in a separate measurement of the (111) crystal peak width at the Advanced Photon Source, sector 34-ID-C.

Time-resolved x-ray diffraction
We performed TR XRD on the polycrystalline gold films at the PAL-XFEL. The sample was mounted perpendicular to the XFEL beam. The optical pump beam was a few degrees away from normal incidence in an almost colinear geometry. The pump pulse of 400 nm and 100 fs was generated from an 800-nm Ti:sapphire regenerative amplifier laser system (Coherent, Legend), frequency-doubled with a barium borate (BBO) crystal. The choice of 400 nm gives better optical coupling with the polycrystalline gold film than 800 nm since less light is reflected. The laser beam size was estimated by monitoring the laser power transmitted power through an aperture at the sample position. With a 200-μm aperture, 90% of the laser power was transmitted. This means that the $1/e^2$ beam size, which is often called the laser beam diameter, is less than 200 μm. From this, we estimate that the FWHM laser beam size, d, is around 100 μm, which is the distance between the 50% intensity points. The incident laser fluence (F_{in}) was then calculated conventionally as pulse energy (E_{pulse}) divided by the area, E_{pulse}/A, where $A = \pi(d^2/4)$. For our experiment, we used a range of incident pulse energies from 5 to 300 μJ, resulting in an incident

laser fluence of 63 mJ/cm^2 to 3.8 J/cm^2 at the sample position. To probe the uniformly excited part of the sample, the monochromatic XFEL beam was focused to 25 μm (FWHM) spot size at the sample position with compound refractive lenses. Temporal overlap of both beams was achieved using a GaAs metal-semiconductor-metal detector (Hamamatsu) at the sample position, while the spatial overlap was achieved by centering both beams on a 100-μm-diameter pinhole moved onto the sample position, as seen in Fig. 1A. The sample was mounted on a motorized scanner that allows single-shot measurement. The scanner was synchronized to the XFEL beam for "mesh" scans, visiting each window of the array once for each pump-probe delay time. A diffraction image from each shot was collected with a Rayonix MX225-HS area detector, 2 × 2 binned, at 10 Hz. The direct beam intensity was recorded with a quadrant beam position monitor before the sample and on a photodiode after the sample. To disregard sample damage, only the first shot on each window was considered in the data analysis. The optical taper geometry of the area detector was precalibrated as a fixed correction in the hardware. The data were background-subtracted, using both white-field and dark-field corrections, with the latter remeasured once per day. CeO_2 powder was used as a calibrant to correct for possible drifts of photon energy and small variations in the sample-to-detector distance between sample changes.

Data analysis and line shape fitting
As a first step, the calibration diffraction image was fitted using Fit2D to refine the sample-to-detector distance, detector orientation angles, and center pixel position (38). Then, all the refined values were transferred to PyFAI for azimuthal integration of the measured diffraction images (39). The direct beam was measured with a photodiode after the sample, and the data were normalized to the incident photon flux recorded at each shot. XRD images were collected at different pump-probe delay times. After calibration, normalization, and integration, each crystalline diffraction peak of the pristine sample was fitted with a sum of two Gaussian functions with constrained intensity ratio and constrained to the same peak position. The peak shape is determined by different factors such as the grain size distribution, the detector resolution, and the beam divergence and is often reported to be Voigt-shaped. However, our analysis showed that the two-Gaussian peak gave a better fit to the data. The XRD curves for (111) at positive pump-probe delay time showed two distinct peaks: the (111) crystal peak and the neighboring intermediate peak. In the peak fitting here, the (111) crystal peak shape was taken to be the same fixed-ratio sum of two Gaussian peaks, while the new intermediate peak was modeled with a third single-Gaussian peak. The fitting was performed in Python using the lmfit package, which uses nonlinear least-squares fitting. To limit the fit parameters, the following constraints were introduced:

1) The peak positions of the two Gaussians used for the crystal peak were the same. The widths of the two Gaussian components were fixed at 0.0212 and 0.063 $Å^{-1}$ (FWHM), optimized by fitting the negative pump-probe delay time data where this is the only peak.

2) Similarly, the peak intensity ratio between peaks 1 and 2 was fixed to a value of 2.47 optimized by fitting the negative pump-probe delay time data.

3) The intermediate peak was turned on only at the positive pump-probe delay time. The peak position, width, and amplitude were all allowed to be free during the fit.

This line shape fitting procedure was used to obtain the parameters plotted in Figs. 3 to 5. In addition, we extracted the powder and intermediate peak positions for the different film thicknesses. The

intermediate peak position is reported at the time delay, where we observe the maximum change. For the 300-nm film, the powder peaks were at 2.6797, 3.096, and 5.125 Å^{-1} for the (111), (200), and (311), respectively, and the corresponding intermediate peaks were at 2.655, 3.07, and 5.048 Å^{-1}. Similarly, for the 100-nm film, (111), (200), and (311) powder peaks were at 2.693, 3.11, and 5.14 Å^{-1}, respectively, and we were able to resolve only the intermediate peak close to (111) at 2.648 Å^{-1}. However, for the 50-nm thin film, we could only determine the position of (111) and (200) peaks at 2.703 and 3.117 Å^{-1}, respectively, and the intermediate peak positions were not resolved. The powder peak positions increase slightly with decreasing thickness, perhaps due to lattice contractions, as reported before (40).

REFERENCES AND NOTES

1. J. N. Clark, L. Beitra, G. Xiong, D. M. Fritz, H. T. Lemke, D. Zhu, M. Chollet, G. J. Williams, M. M. Messerschmidt, B. Abbey, R. J. Harder, A. M. Korsunsky, J. S. Wark, D. A. Reis, I. K. Robinson, Imaging transient melting of a nanocrystal using an x-ray laser. *Proc. Natl. Acad. Sci. U.S.A.* **112**, 7444–7448 (2015).

2. C. E. Wehrenberg, D. McGonegle, C. Bolme, A. Higginbotham, A. Lazicki, H. J. Lee, B. Nagler, H.-S. Park, B. A. Remington, R. E. Rudd, M. Sliwa, M. Suggit, D. Swift, F. Tavella, L. Zepeda-Ruiz, J. S. Wark, In situ x-ray diffraction measurement of shock-wave-driven twinning and lattice dynamics. *Nature* **550**, 496–499 (2017).

3. A. Rousse, C. Rischel, S. Fourmaux, I. Uschmann, S. Sebban, G. Grillon, P. Balcou, E. Fo, È. Rster, J. P. Geindre, P. Audebert, J. C. Gauthier, D. Hulin, Non-thermal melting in semiconductors measured at femtosecond resolution. *Nature* **410**, 65–68 (2001).

4. C. Rose-Petruck, R. Jimenez, T. Guo, A. Cavalleri, C. W. Siders, F. Rksi, J. A. Squier, B. C. Walker, K. R. Wilson, C. P. J. Barty, Picosecond–milliångström lattice dynamics measured by ultrafast x-ray diffraction. *Nature* **398**, 310–312 (1999).

5. N. J. Hartley, N. Ozaki, T. Matsuoka, B. Albertazzi, A. Faenov, Y. Fujimoto, H. Habara, M. Harmand, Y. Inubushi, T. Katayama, M. Koenig, A. Krygier, P. Mabey, Y. Matsumura, S. Matsuyama, E. E. McBride, K. Miyanishi, G. Morard, T. Okuchi, T. Pikuz, O. Sakata, Y. Sano, T. Sato, T. Sekine, Y. Seto, K. Takahashi, K. A. Tanaka, Y. Tange, Y. Togashi, Y. Umeda, T. Vinci, M. Yabashi, T. Yabuuchi, K. Yamauchi, R. Kodama, Ultrafast observation of lattice dynamics in laser-irradiated gold foils. *Appl. Phys. Lett.* **110**, 071905 (2017).

6. D. Milathianaki, S. Boutet, G. J. Williams, A. Higginbotham, D. Ratner, A. E. Gleason, M. Messerschmidt, M. M. Seibert, D. C. Swift, P. Hering, J. Robinson, W. E. White, J. S. Wark, Femtosecond visualization of lattice dynamics in shock-compressed matter. *Science* **342**, 220–223 (2013).

7. M. Z. Mo, Z. Chen, R. K. Li, M. Dunning, B. B. L. Witte, J. K. Baldwin, L. B. Fletcher, J. B. Kim, A. Ng, R. Redmer, A. H. Reid, P. Shekhar, X. Z. Shen, M. Shen, K. Sokolowski-Tinten, Y. Y. Tsui, Y. Q. Wang, Q. Zheng, X. J. Wang, S. H. Glenzer, Heterogeneous to homogeneous melting transition visualized with ultrafast electron diffraction. *Science* **360**, 1451–1455 (2018).

8. B. J. Siwick, J. R. Dwyer, R. E. Jordan, R. J. D. Miller, An atomic-level view of melting using femtosecond electron diffraction. *Science* **302**, 1382–1385 (2003).

9. A. M. Lindenberg, J. Larsson, K. Sokolowski-Tinten, K. J. Gaffney, C. Blome, O. Synnergren, J. Sheppard, C. Caleman, A. G. MacPhee, D. Weinstein, D. P. Lowney, T. K. Allison, T. Matthews, R. W. Falcone, A. L. Cavalieri, D. M. Fritz, S. H. Lee, P. H. Bucksbaum, D. A. Reis, J. Rudati, P. H. Fuoss, C. C. Kao, D. P. Siddons, R. Pahl, J. Als-Nielsen, S. Duesterer, R. Ischebeck, H. Schlarb, H. Schulte-Schrepping, T. Tschentscher, J. Schneider, D. von der Linde, O. Hignette, F. Sette, H. N. Chapman, R. W. Lee, T. N. Hansen, S. Techert, J. S. Wark, M. Bergh, G. Huldt, D. van der Spoel, N. Timneanu, J. Hajdu, R. A. Akre, E. Bong, P. Krejcik, J. Arthur, S. Brennan, K. Luening, J. B. Hastings, Atomic-scale visualization of inertial dynamics. *Science* **298**, 1356–1358 (2002).

10. P. Silvestrelli, A. Alavi, M. Parrinello, D. Frenkel, Structural, dynamical, electronic, and bonding properties of laser-heated silicon: An ab initio molecular-dynamics study. *Phys. Rev. B* **56**, 3806–3812 (1997).

11. C. W. Siders, A. Cavalleri, K. Sokolowski-Tinten, C. Tóth, T. Guo, M. Kammler, M. H. von Hoegen, K. R. Wilson, D. von der Linde, C. P. J. Barty, Detection of nonthermal melting by ultrafast x-ray diffraction. *Science* **286**, 1340–1342 (1999).

12. S. I. Anisimov, B. L. Kapeliovich, T. L. Perel'man, Electron emission from metal surfaces exposed to ultrashort laser pulses. *JETP* **39**, 375 (1974).

13. S. D. Brorson, J. G. Fujimoto, E. P. Ippen, Dynamics in thin gold films. *Phys. Rev. Lett.* **59**, 1962–1965 (1987).

14. Y. Giret, N. Naruse, S. L. Daraszewicz, Y. Murooka, J. Yang, D. M. Duffy, A. L. Shluger, K. Tanimura, Determination of transient atomic structure of laser-excited materials from time-resolved diffraction data. *Appl. Phys. Lett.* **103**, 253107 (2013).

15. D. S. Ivanov, L. V. Zhigilei, Effect of pressure relaxation on the mechanisms of short-pulse laser melting. *Phys. Rev. Lett.* **91**, 105701 (2003).

16. Z. Lin, E. Leveugle, E. M. Bringa, L. V. Zhigilei, Molecular dynamics simulation of laser melting of nanocrystalline Au. *J. Phys. Chem. C* **114**, 5686–5699 (2010).

17. J. W. M. Frenken, J. F. Van Der Veen, Observation of surface melting. *Phys. Rev. Lett.* **54**, 134–137 (1985).

18. T. Wejrzanowski, M. Lewandowska, K. Sikorski, K. J. Kurzydlowski, Effect of grain size on the melting point of confined thin aluminum films. *J. Appl. Phys.* **116**, 164302 (2014).

19. A. M. Alsayed, M. F. Islam, J. Zhang, P. J. Collings, A. G. Yodh, Premelting at defects within bulk colloidal crystals. *Science* **309**, 1207–1210 (2005).

20. S. R. Phillpot, S. Yip, D. Wolf, How do crystals melt? *Comput. Phys.* **3**, 20–31 (1989).

21. J. Berry, K. R. Elder, M. Grant, Melting at dislocations and grain boundaries: A phase field crystal study. *Phys. Rev. B* **77**, 224114 (2008).

22. A. F. Mayadas, M. Shatzkes, Electrical-resistivity model for polycrystalline films: The case of arbitrary reflection at external surfaces. *Phys. Rev. B* **1**, 1382–1389 (1970).

23. T. Q. Qiu, C. L. Tien, Femtosecond laser heating of multi-layer metals—I. Analysis. *Int. J. Heat Mass Transf.* **37**, 2789–2797 (1994).

24. J. W. C. De Vries, Temperature and thickness dependence of the resistivity of thin polycrystalline aluminium, cobalt, nickel, palladium, silver and gold films. *Thin Solid Films* **167**, 25–32 (1988).

25. J. K. Chen, D. Y. Tzou, J. E. Beraun, A semiclassical two-temperature model for ultrafast laser heating. *Int. J. Heat Mass Transf.* **49**, 307–316 (2006).

26. J. S. Chawla, F. Gstrein, K. P. O'Brien, J. S. Clarke, D. Gall, Electron scattering at surfaces and grain boundaries in Cu thin films and wires. *Phys. Rev. B* **84**, 235423 (2011).

27. H. E. Elsayed-Ali, T. B. Norris, M. A. Pessot, G. A. Mourou, Time-resolved observation of electron-phonon relaxation in copper. *Phys. Rev. Lett.* **58**, 1212–1215 (1987).

28. R. Henriquez, M. Flores, L. Moraga, G. Kremer, C. González-Fuentes, R. C. Munoz, Electron scattering at surfaces and grain boundaries in thin Au films. *Appl. Surf. Sci.* **273**, 315–323 (2013).

29. J. Chen, W.-K. Chen, P. M. Rentzepis, Blast wave and contraction in Au(111) thin film induced by femtosecond laser pulses. A time resolved x-ray diffraction study. *J. Appl. Phys.* **109**, 113522 (2011).

30. M. Nicoul, U. Shymanovich, A. Tarasevitch, D. von der Linde, K. Sokolowski-Tinten, Picosecond acoustic response of a laser-heated gold-film studied with time-resolved x-ray diffraction. *Appl. Phys. Lett.* **98**, 191902 (2011).

31. P. Musumeci, J. T. Moody, C. M. Scoby, M. S. Gutierrez, M. Westfall, Laser-induced melting of a single crystal gold sample by time-resolved ultrafast relativistic electron diffraction. *Appl. Phys. Lett.* **97**, 063502 (2010).

32. W. Hoyer, J. Jödicke, Short-range and medium-range order in liquid Au-Ge alloys. *J. Non-Cryst. Solids* **192–193**, 102–105 (1995).

33. F. C. Nix, D. MacNair, The thermal expansion of pure metals: Copper, gold, aluminum, nickel, and iron. *Phys. Rev.* **60**, 597–605 (1941).

34. J. Hohlfeld, J. G. Müller, S.-S. Wellershoff, E. Matthias, Time-resolved thermoreflectivity of thin gold films and its dependence on film thickness. *Appl. Phys. B* **64**, 387–390 (1997).

35. K. Sugioka, Y. Cheng, Ultrafast lasers—Reliable tools for advanced materials processing. *Light Sci. Appl.* **3**, e149 (2014).

36. X. He, A. Datta, W. Nam, L. M. Traverso, X. Xu, Sub-diffraction limited writing based on laser induced periodic surface structures (LIPSS). *Sci. Rep.* **6**, 35035 (2016).

37. B. H. Christensen, K. Vestentoft, P. Balling, Short-pulse ablation rates and the two-temperature model. *Appl. Surf. Sci.* **253**, 6347–6352 (2007).

38. A. P. Hammersley, S. O. Svensson, A. Thompson, H. Graafsma, Å. Kvick, J. P. Moy, Calibration and correction of distortions in two-dimensional detector systems[a]. *Rev. Sci. Instrum.* **66**, 2729 (1995).

39. J. Kieffer, D. Karkoulis, PyFAI, a versatile library for azimuthal regrouping. *J. Phys. Conf. Ser.* **425**, 202012 (2013).

40. J. Sheng, U. Welzel, E. J. Mittemeijer, Nonmonotonic crystallite-size dependence of the lattice parameter of nanocrystalline nickel. *Appl. Phys. Lett.* **97**, 153109 (2010).

Citation: T. A. Assefa, Y. Cao, S. Banerjee, S. Kim, D. Kim, H. Lee, S. Kim, J. H. Lee, S.-Y. Park, I. Eom, J. Park, D. Nam, S. Kim, S. H. Chun, H. Hyun, K. . Kim, P. Juhas, E. S. Bozin, M. Lu, C. Song, H. Kim, S. J. L. Billinge, I. K. Robinson, Ultrafast x-ray diffraction study of melt-front dynamics in polycrystalline thin films. *Sci. Adv.* **6**, eaax2445 (2020).

Science Advances

Ultrafast x-ray diffraction study of melt-front dynamics in polycrystalline thin films

Tadesse A. Assefa, Yue Cao, Soham Banerjee, Sungwon Kim, Dongjin Kim, Heemin Lee, Sunam Kim, Jae Hyuk Lee, Sang-Youn Park, Intae Eom, Jaeku Park, Daewoong Nam, Sangsoo Kim, Sae Hwan Chun, Hyojung Hyun, Kyung sook Kim, Pavol Juhas, Emil S. Bozin, Ming Lu, Changyong Song, Hyunjung Kim, Simon J. L. Billinge, and Ian K. Robinson

View the article online
https://www.science.org/doi/10.1126/sciadv.aax2445
Permissions
https://www.science.org/help/reprints-and-permissions

Use of this article is subject to the Terms of service

Article

Imaging the Phase Transformation in Single Particles of the Lithium Titanate Anode for Lithium-Ion Batteries

Tadesse A. Assefa,* Ana F. Suzana, Longlong Wu, Robert J. Koch, Luxi Li, Wonsuk Cha, Ross J. Harder, Emil S. Bozin, Feng Wang, and Ian K. Robinson*

Read Online

ACCESS | Metrics & More | Article Recommendations | SI Supporting Information

ABSTRACT: Lithium uptake and release in lithium titanate (LTO) anode materials during a discharge and charge cycle is one of the fundamental processes of a lithium-ion battery (LIB), still not fully understood at the microscopic level. During the discharge cycle, LTO undergoes a phase transformation between $Li_4Ti_5O_{12}$ and $Li_7Ti_5O_{12}$ states within a cubic crystal lattice. To reveal the details of the microscopic mechanism, it is necessary to track the sequence of phase transformations at different discharge/charge states under operating conditions. Here, we use *in situ* Bragg coherent diffraction imaging (BCDI) and *in situ* X-ray diffraction (XRD) experiments to examine the lithium insertion-induced materials phase transformation within a single LTO particle and a bulk battery analogue, respectively. BCDI analysis from (111) Bragg peak shows the two-phase transformation manifesting as a distinct image phase modulation within a single LTO nanoparticle occurring in the middle of the discharge region then subsiding toward the end of the discharge cycle. We observe the biggest phase variation at the two-phase stage, indicating the formation of phase domains of 200 nm in size during the discharge process. We also observe a lattice contraction of >0.2% in a single LTO nanoparticle at the (400) Bragg peak measurement, larger than that in the corresponding bulk material. Our observation of this phase transformation at a single-particle level has implications for the understanding of the microscopic/mesoscale picture of the phase transformation in anode and cathode LIBs materials.
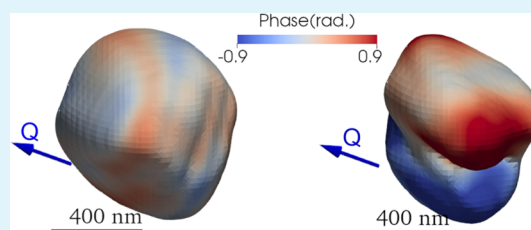
KEYWORDS: *coherent diffraction imaging, image phase variation, displacement field, battery material, lithium titanate anode*

INTRODUCTION

As the world population grows, its demand for energy grows, leading to the depletion of nonrenewable energy sources. The use of these energy sources leads to a detrimental impact on the environment, and this leads to the search for clean, renewable energy sources. Solar energy is the most abundant source of energy, but much of it is not used due to the lack of efficient energy-storage devices. Tremendous progress has been made in search and developing electrochemical storage devices; one example is rechargeable lithium-ion batteries (LIBs), which show excellent cycling stability and high-rate capability.[1−3] The performance of LIBs depends on the cathode, anode, and electrolyte/binder choices,[4] which can be optimized for different applications. In LIBs, the cathode electrode is the source of Li^+ ions, while the electrolyte serves as a conductive medium that helps Li^+ ion and electron transport, the separator prevents direct contact between anode and cathode electrodes, and the anode electrode stores and releases Li^+ ions from the cathode.[4] Since the introduction of the first commercialized rechargeable Li-ion battery in 1991 by Sony, different anode and cathode materials have been explored to improve the power density, cyclability, and safety of the battery.[5] Cathodes such as $LiFePO_4$ and $LiCoO_2$ and anodes such as Li, graphite (by forming intercalation compound LiC_6), Si, and $Li_4Ti_5O_{12}$ have been used in different combinations.[6] Li metal has been used as the anode material that could provide high specific capacity (3860 mAh/g) and lowest overall anode potential. However, cycling of the Li anode leads to the formation of dendrites, which could eventually penetrate the separator and cause a shortage and fire in the battery.[7−9] Also, graphite has high energy density and long cycle life, which makes it the most popular anode in commercial LIBs, but the low lithiation voltage (∼0.1 V vs Li/Li$^+$) can result in a short circuit and possibly fire. Although a Si anode has the highest known theoretical capacity (4200 mAh/g), its huge volume expansion, over 300%, occurring during the lithiation/delithiation cycles leads to electrical shorting/disconnection between the active materials and the current collector.[5,10−12] Li, graphite, and Si anodes have failed so far to satisfy the fast-charging capabilities in LIBs. In contrast, $Li_4Ti_5O_{12}$ (lithium titanate or LTO) has long-cycling stability

and high-rate capability because it has insignificant volume change (<0.2%) between fully lithiated and delithiated end-members;[13−15] this makes LTO a promising anode material for use in commercial fast-charging batteries, such as Toshiba's SCiB rechargeable batteries.[16]

$Li_4Ti_5O_{12}$ and $Li_7Ti_5O_{12}$ are two end-members with a defective spinel (space group $Fd\overline{3}m$) and rock-salt (space group $Fm\overline{3}m$) structure, respectively.[17−19] The crystal structure of LTO has cubic symmetry with lattice constants of $a = b = c = 8.3595$ Å and $\alpha = \beta = \gamma = 90°$. When LTO is fully discharged, three Li ions are inserted per unit cell, forming $Li_7Ti_5O_{12}$ with lattice constants of $a = b = c = 8.3538$ Å and $\alpha = \beta = \gamma = 90°$[17] showing a 0.07% lattice contraction. Compared to $Li_4Ti_5O_{12}$, the octahedral (16c) positions in $Li_7Ti_5O_{12}$ are occupied by Li, and the octahedral (16d) sites maintain the same configuration (occupation by Li and Ti). The electrochemical reaction in LTO proceeds via two-phase transformation between $Li_4Ti_5O_{12}$ (with the octahedral (16d) sites randomly occupied by Li or Ti atoms and the tetrahedral (8a) positions occupied by Li atoms) and $Li_7Ti_5O_{12}$ (the octahedral (16c) positions occupied by Li atoms and the occupancy of the octahedral (16d) identical to that in $Li_4Ti_5O_{12}$) end-member LTO phases.[17] During Li^+ uptake, the Li-ions at the 8a sites move to the empty 16c sites, and the new Li ions from the electrolyte also occupy the 16c sites. In the fully lithiated state, three additional Li^+ ions are added per unit cell. However, visualization of structural phase transformation and tracking the associated lithium migration directly with X-ray-based techniques is experimentally challenging since the lattice constant change between the two end-members is very small (<0.1%), in addition to the low atomic scattering factor of Li compared to that of O and Ti atoms. Different experimental techniques such as X-ray absorption spectroscopy,[20] electron energy-loss spectroscopy (EELS),[21] neutron powder diffraction,[22] and nuclear magnetic resonance (NMR)[23−25] have been implemented to identify the structural phase transformation in LTO anode materials. A Ti K edge X-ray absorption spectroscopy study supported by ab initio calculations by Zhang et al. proposed a new quasi solid-solution phase, which plays an instrumental role in facilitating Li^+ transport. Using STEM−EELS spectrum imaging of the lithiated $Li_7Ti_5O_{12}$, Kitta et al. showed that the two separate phases coexist inside the specimen with defined phase boundaries, and no apparent misfit strains or misorientations are detected.[26] Monte-Carlo simulation combined with density functional theory (DFT) on a large LTO system showed that the three energetic parameters, namely, the potential energy of the 8a site, the difference in the site energy between the 8a and 16c sites, and the repulsion between two Li atoms situated at the adjacent 8a and 16c sites and the topology of the Li sites, determine the system.[27] For the electrochemical potential profile, the differences in the site energy between the 8a and 16c sites play a crucial role and in the plateau region in the potential profile two structural phases coexist.[27] Recently, operando EELS on Li K edge combined with first-principle calculations identified a metastable state, which consists of distorted Li polyhedra, and is proposed to play an essential role to mediate Li^+-ion migration.[21]

The success of the LTO material for repeated cycles of charge and discharge arises from the small lattice constant change between the two LTO phases. This is its biggest advantage over alternative intercalating anode systems because it allows rapid charging and many cycles. As we will show, the small change in the lattice parameter is significant enough to cause apparent patterns of strain in micron-sized grains of LTO with a sufficiently sensitive measurement, such as our *in situ* Bragg coherent diffraction imaging (BCDI) probe a single LTO particle presented here. We observe the development of the local displacement field in 3D by BCDI under *in situ* conditions while discharging the LTO anode material. BCDI is a lensless imaging technique and, with a suitable choice of iterative algorithms, allows one to get three-dimensional shapes of the nanocrystals as complex 3D density maps.[28] In the images, the amplitude represents the ordered electron density of the particle, and the 3D phase distribution, $\varphi(r)$, is due to local displacements in strained nanocrystals. The mapping is fully quantitative and given by the relationship $\varphi(r) = \mathbf{Q} \cdot \mathbf{u}(\mathbf{r})$, where $\mathbf{Q}$ is the momentum transfer vector of the reciprocal lattice point measured and $\mathbf{u}(\mathbf{r})$ is the vector displacement field representing the distortions from the ideal crystal lattice.[29] The spatial derivative of the displacement field is a component of the formal strain tensor. Since only one component of the displacement field is measured at each Bragg reflection, phase images from three or more independent $\mathbf{Q}$-vectors must be combined to obtain 3D spatial reconstruction of the vector field $\mathbf{u}(\mathbf{r})$. As we report here, the small difference in the lattice parameter between the two structures is sufficient to produce an observable local displacement field: if side-by-side regions of $Li_4Ti_5O_{12}$ to $Li_7Ti_5O_{12}$ were to be present within the 800 nm LTO nanoparticle, there would be a phase difference of 0.89 rad, using the lattice parameters reported in ref 17 (details of derivation is given in the SI). This provides the BCDI method with plenty of sensitivity to observe nanoscale displacement fields in these materials.

In this manuscript, we present 3D renderings of phase transformation of the lithium titanate (LTO) anode material during discharging, obtained using the BCDI technique. Inverted images show the formation of nanodomains with a size of about 200 nm as positively and negatively shifted image phases in the reconstructed image in the two-phase region of the discharging cycle. This result is an experimental confirmation of the domain model proposed on the same material.[30] A slice through the rendered inverted images shows displacement field inhomogeneities in the sample but does not show dislocations. In addition, the total d-spacing change estimated in a fully discharged single LTO particle is much larger than the bulk.

■ MATERIALS AND METHODS

Sample Preparation. The samples for the *in situ* BCDI experiment were prepared using the conventional 2032-type coin cells. The $Li_4Ti_5O_{12}$ (LTO) active material from Primet Precision Materials, Inc. was mixed with a conductive agent (Super P conductive carbon black) and poly(vinylidene fluoride) (PVDF) binder in N-methyl-2-pyrrolidone (NMP) solvent with a 2:1:1 ratio, which was further coated on the carbon paper current collector and dried in a vacuum oven. The thin LTO electrode was then punched into a 10 mm disk and assembled in an Ar-filled glove box with the Li metal as the counter electrode and a Clegrad polypropylene (PP) separator. The electrolyte was prepared by mixing a 1.0 M lithium hexafluorophosphate ($LiPF_6$) solution in ethylene carbonate (($CH_2O)_2CO$):dimethyl carbonate ($C_3H_6O_3$), with a 1:1 volume ratio. For the *in situ* characterization, an X-ray-transparent Kapton window was fabricated in the stainless-steel case by sealing it with epoxy. Before the coin cell was assembled, we characterized the density and morphology of the electrodes with a scanning electron microscope (SEM) (Figure 1C). The SEM result shows faceted 400−800 nm sized LTO particles with a characteristic elongated ellipsoidal
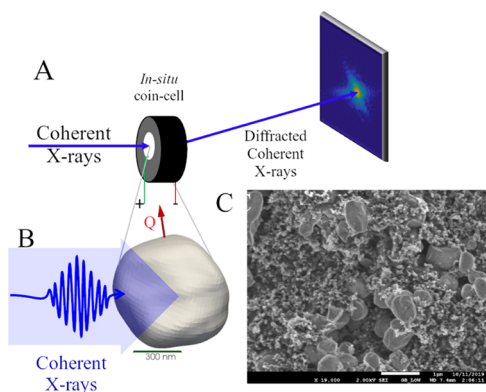
Figure 1. Experimental setup of the *in situ* Bragg coherent diffraction imaging (BCDI). (A) *In situ* BCDI setup at 34-ID-C beamline, APS. (B) Three-dimensional reconstructed image of a single LTO crystal, shown using isosurface rendering representation. For the reconstruction, two-dimensional coherent diffraction patterns were collected by rocking the sample in and out off the Bragg condition. The arrow labeled as Q is the scattering vector. (C) SEM images of newly prepared LTO crystals reveal a clear facetted morphology of the specimen. The white scale bar is 1 mm.

shape, which are ideal for BCDI experiments. We assembled several coin cells in the Argon glove box.

***In Situ* Powder X-ray Diffraction (XRD).** *In situ* X-ray diffraction data were collected at the 28-ID-2 XPD beamline of the National Synchrotron Light Source (NSLS-II). The *in situ* X-ray diffraction (XRD) testing electrodes were prepared by coating the electrode slurry, a mixture of LTO, conductive carbon black, and poly-(vinylidene fluoride) with a 8:1:1 volume ratio, on a current aluminum collector. The experiment under *in situ* conditions was conducted using the 67 keV (λ = 0.185 Å) X-ray beam 0.5 × 0.5 mm^2 in size. X-ray diffraction patterns were acquired using a 2D PerkinElmer detector (2048 × 2048 pixels with 200 mm^2 pixel size) located 1.49 m from the sample, calibrated using CeO$_2$ standard powder. The 2D diffraction images were integrated azimuthally using pyFAI and GSAS-II was used for Rietveld refinement.[31,32]

***In Situ* Bragg Coherent Diffraction Imaging.** Bragg coherent diffraction data were collected at the 34-ID-C beamline of the Advanced Photon Source (APS) (see Figure 1). For the coherent diffraction analysis shown in this manuscript, we used 11.2 and 9 keV monochromatic beams in two independent experiments. The coherent X-ray beam was focused using a pair of Kirkpatrick−Baez (KB) mirrors to ~1 × 1 μm^2 illuminating the LTO nanocrystals. As shown in Figure 1A, the measurement was done on a 10 μm thick LTO electrode in transmission geometry. We used the same *in situ* coin-cell setup, which was implemented in the previous experiments[33] with a window opening of 1 mm. The coin cell was mounted on a coin cell holder vertically with the LTO electrode located downstream to minimize the absorption of the diffracted X-rays. Prior to the experiment, the electrodes were tested via galvanostatic cycling and show a flat plateau region at about 1.5 V with a sharp voltage reduction in the early discharge. In addition, the coin cells were tested by a multimeter to ensure the open circuit voltage is 1.5 V (i.e., a fully functional coin cell). The particle density and morphology of the LTO particles were further examined with SEM, shown in Figure 1C, finding 400−800 nm sized LTO particles. From the fringe spacing in the diffraction patterns, we estimated that the measured LTO nanoparticle size is approximately 800 nm. Coherent X-ray diffraction (CXD) patterns were acquired using a Timepix photon-counting detector mounted D = 1.95 m away from the sample. We obtained full rocking curves around the (400) and (111) Bragg reflections, each in a separate measurement, and collected 2D CXD patterns using a 2D detector at two-theta angles of 38.5 and 16.4° ($\Delta\theta$ = ±0.15°), respectively. Although the full sensor of the detector has 512 × 512 pixels with 55 mm^2 pixel size, the coherent diffraction patterns were

collected utilizing just the first quadrant sensor, which has fewer bad pixels. Automatic background subtraction is implemented within the detector. For the (400) set of data, we collected 120 CXD patterns by rocking the sample in 0.0025° steps around the Bragg peak while we were cycling the coin cell at the C/2 discharge rate (the C/2 rate is the current value discharge a battery in 2 h). For the second set of data, we collected 60 CXD patterns while rocking the sample in increments of 0.005° around the (111) Bragg peak while we were cycling the coin cell at the C/2 discharge rate. For both sets of measurements, the full discharge took roughly 4 h. A full 3D diffraction pattern took about 2 min to measure. Between consecutive scans, we optimized the sample position on a piezo scanning stage, to maintain the Bragg condition and avoid sample misalignment. The coin cell was discharged using an 8-channel MACCOR battery cycler while the series of measurements progressed.

Phase Retrieval. Before feeding the 3D diffraction data to an iterative phasing algorithm, implemented in Matlab,[29,34−37] both a white-field correction and a hot pixel removal were applied for each frame of the 3D data stack. For the phase retrieval, we used a total of 620 iterations with 20 iterations of error-reduction (ER), and 180 iterations of a Hybrid-Input-Output (HIO) algorithms,[38,39] used alternately, with the iteration starting and ending with ER. We used the partial-coherence correction since this was found in the past to improve the reconstructed image quality.[34] The reconstructed 3D phase images shown throughout this manuscript were shifted with respect to the center phase value for display purposes.

Pearson Cross-Correlation Calculation. The Pearson cross-correlation coefficient (r_{AB}) between diffraction patterns A and image B was calculated the following formula

$$ r_{AB} = \frac{\sum_{i=1}^{n} (A_i - \overline{A})(B_i - \overline{B})}{\sqrt{\sum_{i=1}^{n} (A_i - \overline{A})^2} \sqrt{\sum_{i=1}^{n} (B_i - \overline{B})^2}} $$

Where the sum in i is over the 2D region of n pixels containing signal, A_i and B_i are the pixel intensity values, and $\overline{A} = 1/n \sum_{i=1}^{n} A_i$, $\overline{B} = 1/n \sum_{i=1}^{n} B_i$ are the mean intensity values of the 2D diffraction patterns A and B, taken from the slice at the center of the rocking curve, respectively. The correlation coefficient r_{AB} by definition ranges from 0 to 1, where r_{AB} = 1 implies a perfect correlation between A and B diffraction patterns and r_{AB} = 0 means no correlation between them.

Extracting *In Situ* Single-Particle Lattice Constant Changes. As a first step, we looked at the position of the (400) Bragg peak as a function of discharge voltage. We correlated the voltage cycler timestamp with each rocking scan timestamp. Since the cycler timestamp is relative to the start time, it must be corrected with the known precise starting time. Using these, we obtained the cell voltage readout of each rocking scan. The diffractometer motor positions δ, γ, χ, ϕ, and θ are all recorded in a scan file. The detector angles γ and δ are related to the total diffraction 2θ angle to a very good approximation as

$$ \cos(2\theta) = \cos(\delta)\cos(\gamma) \tag{1} $$

We calculated the γ_i and δ_i angles from the pristine state diffraction peak positions p_{x0}, p_{y0} and detector angles γ_0, δ_0 and the diffraction peak positions on the detector p_{xi}, p_{yi}

$$ \gamma_i = \frac{(p_{xi} - p_{x0})P}{D}\left(\frac{180}{\pi}\right) + \gamma_0 \tag{2} $$

$$ \delta_i = \frac{(p_{yi} - p_{y0})P}{D}\left(\frac{180}{\pi}\right) + \delta_0 \tag{3} $$

where P = 55 μm is the detector pixel size and D = 1.95 m is the sample-to-detector distance. Next, we can calculate $2\theta_i$ for each scan using eq 1 and d-spacing, d_i for each peak using Bragg's law. Finally, we calculate the relative d-spacing change, which is $\Delta d/d = (d_i - d_o)/d_o$, where d_o is the d-spacing for the pristine state. The quantities calculated using this procedure are shown in Figure 2.
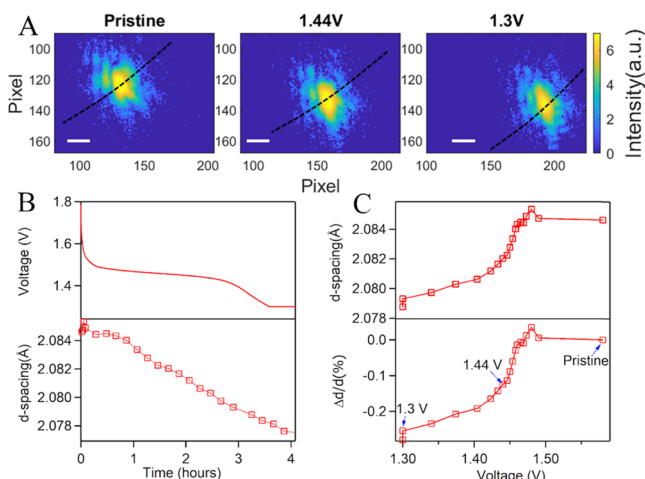
Figure 2. *In situ* Bragg coherent diffraction results during a discharge cycle on the (400) Bragg peak. (A) Logarithm of the diffraction intensity at three different discharge states measured from a single LTO particle. (B) C/2 discharging cycle of the coin cell for the experiment (upper) and *d*-spacing changes as a function of time extracted from the shift of the (400) diffraction peak on the detector (lower). (C) Extracted lattice *d*-spacing (upper) and relative changes (lower) of the same LTO particle during the discharge cycle as a function of the voltage of the coin cell. The white scale bar is 20 pixels, which corresponds to $\sim 3 \times 10^{-3}$ Å^{-1}.

■ RESULTS AND DISCUSSION

(400) Bragg Peak Results. During the *in situ* BCDI experiments, we cycled the electrode at the C/2 discharging and charging rate while tracking a single LTO particle. In the past, similar experiments were carried out on battery cathode materials.[40,41] Figure 2A shows an intensity map on the logarithmic scale of the area surrounding one of the (400) coherent diffraction peaks measured from a single LTO particle in its pristine state and at 1.44 and 1.3 V discharge states. During the discharging process (from left to right shown in Figure 2A), a two-step evolution of the diffraction peak signal was observed: (i) initially, the peak moves inward to a lower 2θ angle indicating a slight lattice expansion and it moves around the powder ring, which is due to the rotation of the LTO particle, and (ii) in later discharging states, it moves radially outward to a higher 2θ angle indicating a lattice contraction. In addition, our *in situ* XRD analysis showed an initial small lattice expansion during the early discharge cycle, followed by a $\sim 0.066\%$ of lattice contraction shown in Figure S5 of the SI.

In the later stage, Li$^+$ migration from the 8a sites to the 16c sites leads to lattice contraction. The lattice contraction observed in our bulk XRD measurement is consistent with earlier reports.[17] The voltage profile of the discharging cycle of the electrode during *in situ* BCDI measurements and the calculated *d*-spacing changes as a function of time are shown in upper and lower panels of Figure 2B, respectively; the *d*-spacing decreases continuously, with the discharge cycle consistent with lattice contraction. However, the lattice contraction measured in our BCDI experiment is larger than in earlier reports for bulk LTO samples,[17] where a difference of $\Delta a/a = 0.07\%$[18,42] was reported. In top and bottom panels of Figure 2C, we plot the *d*-spacing and *d*-spacing changes with the discharging voltage, respectively. During the early stage of discharge, both the *d*-spacing and *d*-spacing stay constant, but

below 1.48 V, we see more lattice contraction. However, the *d*-spacing observed for our 400 nm particles, $\Delta d/d \cong 0.2\%$, while larger than the bulk, is smaller than the $\Delta a/a = 0.81\%$ lattice contraction reported in even smaller size nanosized materials.[43] The lattice parameter changed from 8.3526(1) to 8.4203(1) Å and from 8.3585(1) to 8.3852(4) Å for the 44 and 120 nm nanosized samples for Li$_4$Ti$_5$O$_{12}$ and Li$_7$Ti$_5$O$_{12}$ structural phases, respectively. This implies that during a discharge the 44 nm nanosized samples showed $\Delta a/a = 0.81\%$ change, whereas the 120 nm showed $\Delta a/a = 0.32\%$. A systematic decrease of the lattice contraction effects with increasing particle size is to be expected due to the decrease in the surface area to volume ratio, which is the influence of the interface energy, which would be enhanced in smaller sized LTO samples. We note that density functional theory-based first-principles calculations predicted lattice parameter contraction between Li$_4$Ti$_5$O$_{12}$ and Li$_7$Ti$_5$O$_{12}$ structural phases,[44] which is much larger than the experimental results.[17]

The measured diffraction pattern intensity is related to the squared amplitude of the Fourier transform of the electron density of the nanocrystal. It is expected that, during the discharging process, Li ions insert into the LTO particle, which can result in the local displacement field in the particle. To explore this phenomenon, we calculate the Pearson cross-correlation coefficient between all of the different coherent diffraction patterns done at different discharge voltages with the pristine coherent diffraction pattern. As shown in Figure 3A, the result highlights the differences between two diffraction
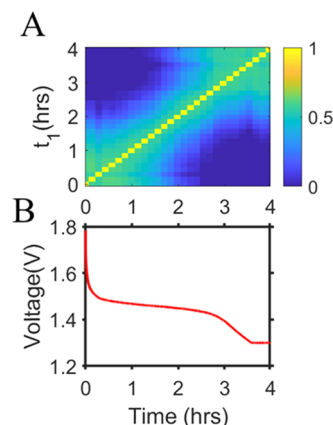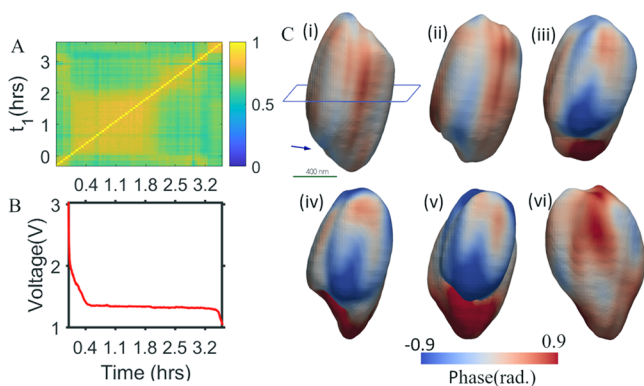

Figure 3. Monitoring structural phase transformation in LTO using the (400) Bragg peak during the C/2 discharge cycle. (A) Pearson cross-correlation of the (400) diffraction peak between different times during discharge. The correlation is calculated on the central diffraction pattern of the rocking data. (B) Voltage across the coin cell as a function of time.

patterns as changes in the correlation coefficient. Interestingly, the correlation plot shows two distinct regions, the first 2 h of the discharging process we observe a strong correlation >0.6 and the correlation drops appreciably below 0.5 in the last 2 h. Since, the change of the diffraction pattern is the reflection of phase transformation within the scattering volume of the LTO particle. Therefore, the regime between 2.5 to 4 h of the correlation plot shown in Figure 3A is due to the structural transformation of the particle, called the two-phase regime.[30] This implies that partial uptake of 1 Li ion per unit cell does change the structure locally; however, the diffraction pattern does not change significantly, which is why we get a strong

correlation for the first 2 h. An uptake of more than one Li ion per unit cell leads to decorrelation in the diffraction pattern due to a change in the structure as we can see in the correlation plot. Since radiation damage can also change the diffraction pattern, to explore this possibility we measured a single pristine LTO nanocrystal for 2 h without any voltage cycling.[45] As shown in Figure S1, this shows strong correlation at all times, which indicated no evident aging or apparent beam damage in the single LTO particle. This implies that the effect observed in Figure 3A can only be due to discharge-related changes in the LTO nanocrystal.

(111) Bragg Peak Results. On a different sample, we measured the (111) Bragg peak and calculated the Pearson correlation coefficient. The results in Figure 4A show a clear

Figure 4. Evidence of the structural phase transformation in LTO during the discharging cycle. (A) Pearson cross-correlation plot of the central (111) diffraction peak of the different discharge states. (B) C/2 discharging cycle of the coin cell for the experiment as a function of time. The (i)−(vi) indicated in the curve are points for which the images of the LTO single particles were reconstructed. (C) (i)−(vi) *In situ* BCDI images of the 3D LTO particle using the isosurface representation, colored by the phase value, measured at 3 V (pristine), 1.69 V (20 min), 1.36 V (40 min), 1.35 V (50 min), 1.35 V (1 h), and 1.3 V (3 h). The blue arrow indicated the scattering vector (Q), and the green scale bar is 400 nm. The blue plane shown in the pristine state shows the spatial location of the slices shown in Figure 5.

phase transformation of the LTO sample during the discharge, similar to what was seen for the crystal in Figure 3. Figure 4C shows reconstructed images of the LTO particle, where a clear transformation from a more uniform state to one with a stronger phase variation on its surface. The shape of the crystal was not constrained in the analysis and appears to show some small variations; we interpret this as coupling of the surface displacement field with the isosurface contour level and not a physical change. We attribute this phase variation to the coexistence of Li-poor and Li-rich regions, consistent with previously reported X-ray spectroscopic results.[30,46] To visualize how the image phase transformation develops inside the LTO particle, we examine slices parallel to the Q-vector of the reconstructed images shown in Figure 5. In the early stage of the discharge state (down to 1.44 V), there are no significant changes in the image phase variation within the crystal. However, below 1.35 V (after 1 h), there is a build-up of different sets of "nanodomains" seen as positively (red) and negatively (blue) shifted regions. Since this is the discharge stage where the sample is expected to be in transition between the two LTO phases,[47] these nanodomains are attributed to Li-rich and Li-poor regions within a single nanocrystal. It appears

that an intense image phase difference develops on one side of the LTO particle and propagates into the internal part of the particle. Although the observed image phase change is a consequence of Li insertion, our observation does not provide direct evidence of Li-ion migration, for example, whether Li enters the core of the particle or remains confined to the outer edges. However, since the diffusion coefficient, D, of Li$^+$ ions in LTO is 10^{-11} cm^2/s,[48] the average distance that the Li$^+$ ions can travel in the LTO material, calculated using Fick's law $\langle x^2 \rangle$ $= 4D\tau$, where τ is the diffusion time, is 2 μm in 1 h. Because this distance is larger than the nanoparticles we are measuring, this means that the Li$^+$ ions should invade the whole LTO nanocrystal within an hour, and the changes we observe are then due to the local Li distribution.

To quantify the displacement field inside the reconstructed images, we calculated the standard deviation of the image phase over a range of different volumes selected in the center of the particle as a function of the discharge voltage, as shown in Figure 5C. Similar trends during discharge are seen for all of the choices of volume. The significant increase of standard deviation starting in the middle of the discharge plateau quantifies the appearance of inhomogeneous displacement fields within the particle, which is presumably due to the coexistence of Li$_4$Ti$_5$O$_{12}$ and Li$_7$Ti$_5$O$_{12}$ regions within the sample.

At its maximum, there is about 0.4 radians of inhomogeneity seen in the images, extending over regions of ~100 nm lateral dimension. This is consistent with the displacement field expected from side-by-side domains of the two material phases, estimated in the Introduction of this paper. A 3D image is shown in Figure 6A in the middle of the inhomogeneous discharge state. The gray-colored background uses a low contour level to highlight the particle shape. Two clear domains with a gap in between can be seen at a higher amplitude contouring level with their surface image phases coded using the color scheme shown. The apparent gap between the domains is due to the finite resolution and the chosen contour level. The phase difference of 1.12 rad between the domains corresponds to a lateral shift (along the Q-vector) of about 1/6 of a (111) d-spacing, as illustrated by the atomic models shown in Figure 6B.

■ CONCLUSIONS AND OUTLOOK

We studied the structural phase transformation of the anode material Li$_4$Ti$_5$O$_{12}$ during its lithiation process using *in situ* BCDI measurements. When observing the (400) Bragg peak of a single LTO particle, we observed more than a 0.2% change in the d-spacing when comparing the pristine and fully lithiated states, which is significantly larger than previously reported results from powder XRD experiments.[14,15,30,49] This apparent discrepancy must be considered in the context of each measurement: the powder XRD yields the ensemble average lattice constant change of an ensemble average of a large volume of the anode material, whereas the BCDI data result from a single LTO nanocrystal. Nanoparticles are well-known to respond differently from the bulk material due to their larger relative surface area. The two-time correlation plots of the recorded coherent X-ray diffraction patterns demonstrate a clear structural evolution during the lithiation process. BCDI reconstruction, around the middle of the discharge plateau, shows that the onset of Li insertion is found to lead to a heterogeneous image phase distribution extending throughout the volume of the nanocrystal, which disappears again as the
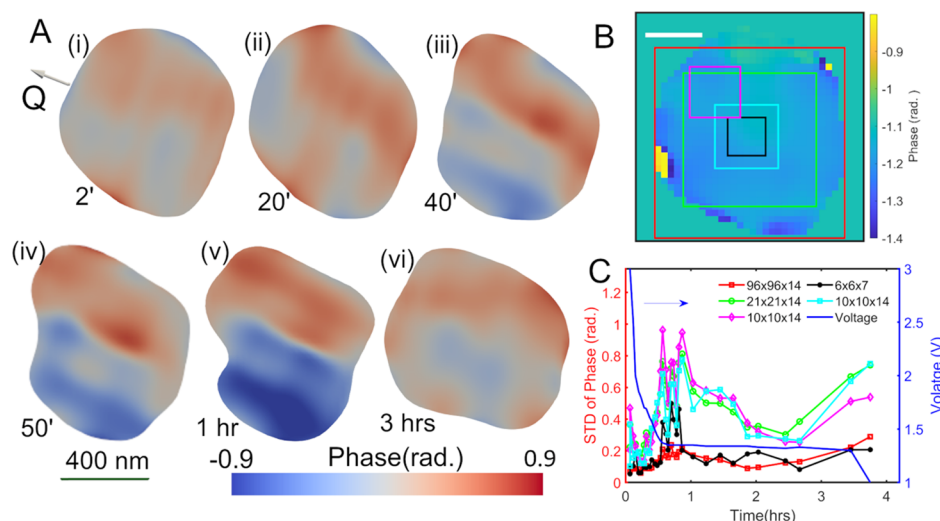
Figure 5. (A) (i)−(vi) Slices of the *in situ* BCDI reconstructed image from its (111) Bragg peak at 3, 1.69, 1.36, 1.35, 1.35, and 1.3 V, respectively, to show the internal displacement field development in the particle and approximate time of the measurement is also indicated. The biggest image phase variation and relative image phase change is clear in the plateau region of the discharging voltage. (B) Central *xy*-slice of the reconstructed image (in the detector coordinates) with the selected voxel volumes shown as rectangles $96 \times 96 \times 14$ (red), $21 \times 21 \times 14$ (green), $10 \times 10 \times 14$ (cyan), $6 \times 6 \times 7$ (magenta), and $10 \times 10 \times 14$ (black) measured at different discharge time. The white scale bar shown is 10 voxels and each voxel is about $(25 \text{ nm})^3$. (C) Calculated standard deviations (STD) and the discharge voltages for the corresponding different voxel volumes of the reconstructed image.
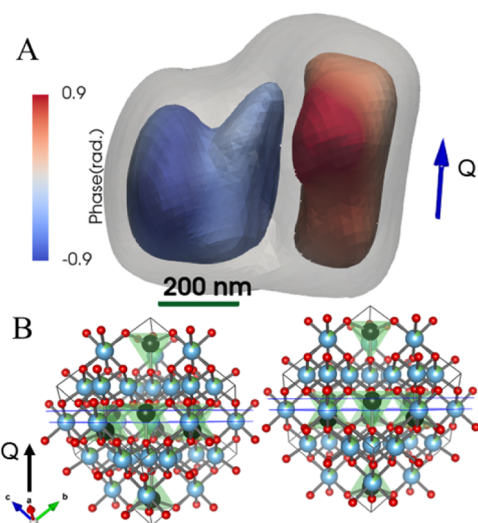
Figure 6. Material phase separation and relative image phase change in the two-phase stage. (A) Reconstructed (111) LTO single-particle image at 1.35 V, resulting in two phase-domains in the single LTO particle due to material phase separation. (B) Relative image phase change is 1.12 rad, which corresponds to the 0.8 Å translation along the *Q*-vector shown, which is equal to the Li-Ti plane separation shown.

By monitoring the standard deviation of the image phase, we observed the biggest image variation in the middle of the plateau of the discharge where the transformation from $Li_4Ti_5O_{12}$ and $Li_7Ti_5O_{12}$ would be half-completed. The heterogeneous local displacement field distribution permeating the LTO nanocrystal investigated was seen to build up during discharge and then taper off at the end of the cycle. At no point in any of our *in situ* BCDI experiments did we detect the presence of any crystal defects, such as dislocations, which are commonly observed in other battery material systems.[40,41] Dislocation-mediated transformations are not expected to reverse perfectly upon charge cycling and would be expected to lead eventually to crystal degradation processes. Both our observations of lateral strain domain formation and the absence of mobile dislocations, with Burgers vector accessible in our experimental geometry, imply that the LTO crystal lattice remains completely intact during the charge−discharge cycle. This may explain the excellent cycling stability of LTO over other battery materials, which makes it suitable for durable, long-life batteries.

■ ASSOCIATED CONTENT

ⓢ Supporting Information

The Supporting Information is available free of charge at https://pubs.acs.org/doi/10.1021/acsaem.0c02010.

Checking X-ray beam damage, two-phase transformation of the LTO particle, displacement projected along *Q*-vector, lattice constant gradient, and *in situ* X-ray diffraction results (PDF)

■ AUTHOR INFORMATION

Corresponding Authors

Tadesse A. Assefa − *Condensed Matter Physics and Materials Science Department, Brookhaven National Laboratory, Upton, New York 11793, United States;* ⓞ orcid.org/0000-0003-3904-0846; Email: tassefa@bnl.gov

discharge completes. This informs us the formation of a lateral domain structure, implying a nonuniform lithium concentration between nanodomain regions lying side-by-side within the nanocrystal, assumed to have the $Li_4Ti_5O_{12}$ and $Li_7Ti_5O_{12}$ compositions. The reconstructed image in Figure 6 in the middle of the voltage plateau region shows a $2\pi/6$ image phase change between the two spatially distinct regions of the single LTO nanocrystal. This image phase shift corresponds to $d/6$ (=0.8 Å) rigid-body shift between the two regions, corresponding to a Li-Ti layer spacing, illustrated in Figure 6B.

Ian K. Robinson − *Condensed Matter Physics and Materials Science Department, Brookhaven National Laboratory, Upton, New York 11793, United States; London Centre for Nanotechnology, University College London, London WC1E 6BT, U.K.;* Email: irobinson@bnl.gov

Authors

Ana F. Suzana − *Condensed Matter Physics and Materials Science Department, Brookhaven National Laboratory, Upton, New York 11793, United States*

Longlong Wu − *Condensed Matter Physics and Materials Science Department, Brookhaven National Laboratory, Upton, New York 11793, United States*

Robert J. Koch − *Condensed Matter Physics and Materials Science Department, Brookhaven National Laboratory, Upton, New York 11793, United States;* ● orcid.org/0000-0003-4995-2101

Luxi Li − *Advanced Photon Source, Argonne National Laboratory, Argonne, Illinois 60439, United States*

Wonsuk Cha − *Advanced Photon Source, Argonne National Laboratory, Argonne, Illinois 60439, United States*

Ross J. Harder − *Advanced Photon Source, Argonne National Laboratory, Argonne, Illinois 60439, United States*

Emil S. Bozin − *Condensed Matter Physics and Materials Science Department, Brookhaven National Laboratory, Upton, New York 11793, United States*

Feng Wang − *Condensed Matter Physics and Materials Science Department, Brookhaven National Laboratory, Upton, New York 11793, United States;* ● orcid.org/0000-0003-4068-9212

Complete contact information is available at:
https://pubs.acs.org/10.1021/acsaem.0c02010

Author Contributions

T.A.A., F.W., and I.K.R. designed the research project, T.A.A., L.W., A.S., W.C., L.X.L., R.H., F.W., and I.K.R. conducted the BCDI experiments at the 34-ID-C, APS, T.A.A. and I.K.R. analyzed the BCDI data, and R.K. analyzed the XRD data with inputs from E.S.B. The manuscript was written by T.A.A. and I.K.R., with contributions from all authors. All authors have given approval to the final version of the manuscript.

Notes

The authors declare no competing financial interest.

REFERENCES

(1) Whittingham, M. S. Electrical Energy Storage and Intercalation Chemistry. *Science* **1976**, *192*, 1126−1127.

(2) Whittingham, M. S.; Gamble, F. R. The Lithium Intercalates of the Transition Metal Dichalcogenides. *Mater. Res. Bull.* **1975**, *10*, 363−371.

(3) Whittingham, M. S. The Role of Ternary Phases in Cathode Reactions. *J. Electrochem. Soc.* **1976**, *123*, 315.

(4) Yi, T.-F.; Yang, S.-Y.; Xie, Y. Recent Advances of $Li_4Ti_5O_{12}$ as a Promising next Generation Anode Material for High Power Lithium-Ion Batteries. *J. Mater. Chem. A* **2015**, *3*, 5750−5777.

(5) Takehara, Z. I.; Kanamura, K. Historical Development of Rechargeable Lithium Batteries in Japan. *Electrochim. Acta* **1993**, *38*, 1169−1177.

(6) Whittingham, M. S. Lithium Batteries and Cathode Materials. *Chem. Rev.* **2004**, *104*, 4271−4302.

(7) Liu, K.; Pei, A.; Lee, H. R.; Kong, B.; Liu, N.; Lin, D.; Liu, Y.; Liu, C.; Hsu, P.; Bao, Z.; Cui, Y. Lithium Metal Anodes with an Adaptive "Solid-Liquid" Interfacial Protective Layer. *J. Am. Chem. Soc.* **2017**, *139*, 4815−4820.

(8) Qian, J.; Xu, W.; Bhattacharya, P.; Engelhard, M.; Henderson, W. A.; Zhang, Y.; Zhang, J. G. Dendrite-Free Li Deposition Using Trace-Amounts of Water as an Electrolyte Additive. *Nano Energy* **2015**, *15*, 135−144.

(9) Bai, P.; Guo, J.; Wang, M.; Kushima, A.; Su, L.; Li, J.; Brushett, F. R.; Bazant, M. Z. Interactions between Lithium Growths and Nanoporous Ceramic Separators. *Joule* **2018**, *2*, 2434−2449.

(10) Besenhard, J. O.; Yang, J.; Winter, M. Will Advanced Lithium-Alloy Anodes Have a Chance in Lithium-Ion Batteries? *J. Power Sources* **1997**, *68*, 87−90.

(11) Brousse, T.; et al. Thin-Film Crystalline SnO_2-Lithium Electrodes. *J. Electrochem. Soc.* **1998**, *145*, 1.

(12) Chan, C. K.; Peng, H.; Liu, G.; McIlwrath, K.; Zhang, X. F.; Huggins, R. A.; Cui, Y. High-Performance Lithium Battery Anodes Using Silicon Nanowires. *Nat. Nanotechnol.* **2008**, *3*, 31−35.

(13) Shu, J. Study of the Interface between $Li_4Ti_5O_{12}$ Electrodes and Standard Electrolyte Solutions in 0.0-0.5 V. *Electrochem. Solid-State Lett.* **2008**, *11*, A238.

(14) Shu, J. Electrochemical Behavior and Stability of $Li_4Ti_5O_{12}$ in a Broad Voltage Window. *J. Solid State Electrochem.* **2009**, *13*, 1535−1539.

(15) Ohzuku, T.; Ueda, A.; Yamamoto, N. Zero-Strain Insertion Material of $Li[Li_{1/3}Ti_{5/3}O_4]$ for Rechargeable Lithium Cells. *J. Electrochem. Soc.* **1995**, *142*, 1431.

(16) Toshiba's SCiB Rechargeable Battery.

(17) Scharner, S.; Weppner, W.; Schmid-Beurmann, P. Evidence of Two-Phase Formation upon Lithium Insertion into the Li1.33Ti1.67O4 Spinel. *J. Electrochem. Soc.* **1999**, *146*, 857.

(18) Ziebarth, B.; Klinsmann, M.; Eckl, T.; Elsässer, C. Lithium Diffusion in the Spinel Phase $Li_4Ti_5O_{12}$ and in the Rocksalt Phase $Li_7Ti_5O_{12}$ of Lithium Titanate from First Principles. *Phys. Rev. B* **2014**, *89*, No. 174301.

(19) Zhang, W.; Topsakal, M.; Cama, C.; Pelliccione, C. J.; Zhao, H.; Ehrlich, S.; Wu, L.; Zhu, Y.; Frenkel, A. I.; Takeuchi, K. J.; Takeuchi, E. S.; Marschilok, A. C.; Lu, D.; Wang, F. Multi-Stage Structural Transformations in Zero-Strain Lithium Titanate Unveiled

by in Situ X-Ray Absorption Fingerprints. *J. Am. Chem. Soc.* **2017**, *139*, 16591−16603.

(20) Wang, F.; Wu, L.; Ma, C.; Su, D.; Zhu, Y.; Graetz, J. Excess Lithium Storage and Charge Compensation in Nanoscale $Li_{4+x}Ti_5O_{12}$. *Nanotechnology* **2013**, *24* (42), 424006.

(21) Zhang, W.; Seo, D.-H. H.; Chen, T.; Wu, L.; Topsakal, M.; Zhu, Y.; Lu, D.; Ceder, G.; Wang, F. Kinetic Pathways of Ionic Transport in Fast-Charging Lithium Titanate. *Science* **2020**, *367*, 1030−1034.

(22) Pang, W. K.; Peterson, V. K.; Sharma, N.; Shiu, J.-J.; Wu, S. Lithium Migration in $Li_4Ti_5O_{12}$ Studied Using in Situ Neutron Powder Diffraction. *Chem. Mater.* **2014**, *26*, 2318−2326.

(23) Wilkening, M.; Iwaniak, W.; Heine, J.; Epp, V.; Kleinert, A.; Behrens, M.; Nuspl, G.; Bensch, W.; Heitjans, P. Microscopic Li Self-Diffusion Parameters in the Lithiated Anode Material $Li_{4+x}Ti_5O_{12}$ (0 ≤ x ≤ 3) Measured by ^7Li Solid State NMR. *Phys. Chem. Chem. Phys.* **2007**, *9*, 6199−6202.

(24) Hain, H.; Scheuermann, M.; Heinzmann, R.; Wünsche, L.; Hahn, H.; Indris, S. Study of Local Structure and Li Dynamics in $Li_{4+x}Ti_5O_{12}$ (0 ≤ x ≤ 5) Using ^6Li and ^7Li NMR Spectroscopy. *Solid State Nucl. Magn. Reson.* **2012**, *42*, 9−16.

(25) Lee, H. H.; Wang, Y. Y.; Wan, C. C.; Yang, M. H.; Wu, H. C.; Shieh, D. T. The Function of Vinylene Carbonate as a Thermal Additive to Electrolyte in Lithium Batteries. *J. Appl. Electrochem.* **2005**, *35*, 615−623.

(26) Kitta, M.; Akita, T.; Tanaka, S.; Kohyama, M. Two-Phase Separation in a Lithiated Spinel $Li_4Ti_5O_{12}$ Crystal as Confirmed by Electron Energy-Loss Spectroscopy. *J. Power Sources* **2014**, *257*, 120−125.

(27) Ozaki, H.; Tada, K.; Kiyobayashi, T. Monte-Carlo Simulation Combined with Density Functional Theory to Investigate the Equilibrium Thermodynamics of Electrode Materials: Lithium Titanates as Model Compounds. *Phys. Chem. Chem. Phys.* **2019**, *21*, 15551−15559.

(28) Miao, J.; Ishikawa, T.; Robinson, I. K.; Murnane, M. M. Beyond Crystallography: Diffractive Imaging Using Coherent x-Ray Light Sources. *Science* **2015**, *348*, 530−535.

(29) Robinson, I.; Harder, R. Coherent X-Ray Diffraction Imaging of Strain at the Nanoscale. *Nat. Mater.* **2009**, *8*, 291−298.

(30) Zhang, W.; Topsakal, M.; Cama, C.; Pelliccione, C. J.; Zhao, H.; Ehrlich, S.; Wu, L.; Zhu, Y.; Frenkel, A. I.; Takeuchi, K. J.; Takeuchi, E. S.; Marschilok, A. C.; Lu, D.; Wang, F. Multi-Stage Structural Transformations in Zero-Strain Lithium Titanate Unveiled by in Situ X-Ray Absorption Fingerprints. *J. Am. Chem. Soc.* **2017**, *139*, 16591−16603.

(31) Kieffer, J.; Karkoulis, D. PyFAI, a Versatile Library for Azimuthal Regrouping. *J. Phys. Conf. Ser.* **2013**, No. 202012.

(32) Toby, B. H.; Von Dreele, R. B. GSAS-II: The Genesis of a Modern Open-Source All Purpose Crystallography Software Package. *J. Appl. Crystallogr.* **2013**, *46*, 544−549.

(33) Li, L.; Xie, Y.; Maxey, E.; Harder, R. Methods for Operando Coherent X-Ray Diffraction of Battery Materials at the Advanced Photon Source. *J. Synchrotron Radiat.* **2019**, *26*, 220−229.

(34) Clark, J. N.; Huang, X.; Harder, R.; Robinson, I. K. High-Resolution Three-Dimensional Partially Coherent Diffraction Imaging. *Nat. Commun.* **2012**, *3*, No. 993.

(35) Yang, W.; Huang, X.; Harder, R.; Clark, J. N.; Robinson, I. K.; Mao, H. K. Coherent Diffraction Imaging of Nanoscale Strain Evolution in a Single Crystal under High Pressure. *Nat. Commun.* **2013**, *4*, No. 1680.

(36) Pfeifer, M. A.; Williams, G. J.; Vartanyants, I. A.; Harder, R.; Robinson, I. K. Three-Dimensional Mapping of a Deformation Field inside a Nanocrystal. *Nature* **2006**, *442*, 63−66.

(37) Assefa, T. A.; Cao, Y.; Diao, J.; Harder, R. J.; Cha, W.; Kisslinger, K.; Gu, G. D.; Tranquada, J. M.; Dean, M. P. M.; Robinson, I. K. Scaling Behavior of Low-Temperature Orthorhombic Domains in the Prototypical High-Temperature Superconductor $La_{1.875}Ba_{0.125}CuO_4$. *Phys. Rev. B* **2020**, *101*, No. 054104.

(38) Fienup, J. R. Phase Retrieval Algorithms: A Comparison. *Appl. Opt.* **1982**, *21*, 2758.

(39) Saxton, R. W.; Gershberg, W. O. Practical Algorithm for the Determination of Phase From Image and Diffraction Plane Pictures. *Optik* **1972**, *35*, 237−250.

(40) Ulvestad, A.; Singer, A.; Cho, H.-M.; Clark, J. N.; Harder, R.; Maser, J.; Meng, Y. S.; Shpyrko, O. G. Single Particle Nanomechanics in Operando Batteries via Lensless Strain Mapping. *Nano Lett.* **2014**, *14*, 5123−5127.

(41) Ulvestad, A.; Singer, A.; Clark, J. N.; Cho, H. M.; Kim, J. W.; Harder, R.; Maser, J.; Meng, Y. S.; Shpyrko, O. G. Topological Defect Dynamics in Operando Battery Nanoparticles. *Science* **2015**, *348*, 1344−1347.

(42) Colbow, K. M.; Dahn, J. R.; Haering, R. R. Structure and Electrochemistry of the Spinel Oxides $LiTi_2O_4$ and $Li_{4/3}Ti_{5/3}O_4$. *J. Power Sources* **1989**, *26*, 397−402.

(43) Yu, X.; Pan, H.; Wan, W.; Ma, C.; Bai, J.; Meng, Q.; Ehrlich, S. N.; Hu, Y.-S.; Yang, X.-Q. A Size-Dependent Sodium Storage Mechanism in $Li_4Ti_5O_{12}$ Investigated by a Novel Characterization Technique Combining in Situ X-Ray Diffraction and Chemical Sodiation. *Nano Lett.* **2013**, *13*, 4721−4727.

(44) Ouyang, C. Y.; Zhong, Z. Y.; Lei, M. S. Ab Initio Studies of Structural and Electronic Properties of $Li_4Ti_5O_{12}$ Spinel. *Electrochem. Commun.* **2007**, *9*, 1107−1112.

(45) Plumley, R.; Sun, Y.; Teitelbaum, S. W.; Song, S.; Sato, T.; Chollet, M.; Wang, N.; Robert, A.; Fuoss, P. H.; Sutton, M.; Zhu, D. Speckle Correlation as a Monitor of X-Ray Free Electron Laser Induced Crystal Lattice Deformation. *J. Synchrotron Radiat.* **2019**, 1470−1476.

(46) Wang, F.; Wu, L.; Ma, C.; Su, D.; Zhu, Y.; Graetz, J. Excess Lithium Storage and Charge Compensation in Nanoscale $Li_{4+x}Ti_5O_{12}$. *Nanotechnology* **2013**, *24*, No. 424006.

(47) Orikasa, Y.; Maeda, T.; Koyama, Y.; Murayama, H.; Fukuda, K.; Tanida, H.; Arai, H.; Matsubara, E.; Uchimoto, Y.; Ogumi, Z. Transient Phase Change in Two Phase Reaction between $LiFePO_4$ and $FePO_4$ under Battery Operation. *Chem. Mater.* **2013**, *25*, 1032−1039.

(48) Colbow, K. M.; Dahn, J. R.; Haering, R. R. Structure and Electrochemistry of the Spinel Oxides $LiTi_2O_4$ and $Li[Li_{4/3}Ti_{5/3}O_4]$. *J. Power Sources* **1989**, *26*, 397−402.

(49) Yi, T. F.; Shu, J.; Zhu, Y. R.; Zhu, X. D.; Yue, C. B.; Zhou, A. N.; Zhu, R. S. High-Performance $Li_4Ti_{5-x}VxO_{12}$ (0 ≤ x ≤ 0.3) as an Anode Material for Secondary Lithium-Ion Battery. *Electrochim. Acta* **2009**, *54*, 7464−7470.

On single-crystal total scattering data reduction and correction protocols for analysis in direct space

Robert J. Koch,[a]* Nikolaj Roth,[b] Yiu Liu,[a] Oleh Ivashko,[c] Ann-Christin Dippel,[c] Cedomir Petrovic,[a] Bo B. Iversen,[b] Martin v. Zimmermann[c] and Emil S. Bozin[a]*

[a]Condensed Matter Physics and Materials Science Division, Brookhaven National Laboratory, Upton, NY 11973, USA, [b]Center for Materials Crystallography, Department of Chemistry and iNANO, Aarhus University, DK-8000, Aarhus, Denmark, and [c]Deutsches Elektronen-Synchrotron DESY, 22607 Hamburg, Germany. *Correspondence e-mail: rkoch177@gmail.com, bozin@bnl.gov

Data reduction and correction steps and processed data reproducibility in the emerging single-crystal total-scattering-based technique of three-dimensional differential atomic pair distribution function (3D-ΔPDF) analysis are explored. All steps from sample measurement to data processing are outlined using a crystal of $CuIr_2S_4$ as an example, studied in a setup equipped with a high-energy X-ray beam and a flat-panel area detector. Computational overhead as pertains to data sampling and the associated data-processing steps is also discussed. Various aspects of the final 3D-ΔPDF reproducibility are explicitly tested by varying the data-processing order and included steps, and by carrying out a crystal-to-crystal data comparison. Situations in which the 3D-ΔPDF is robust are identified, and caution against a few particular cases which can lead to inconsistent 3D-ΔPDFs is noted. Although not all the approaches applied herein will be valid across all systems, and a more in-depth analysis of some of the effects of the data-processing steps may still needed, the methods collected herein represent the start of a more systematic discussion about data processing and corrections in this field.

1. Introduction

1.1. Background

Over the past several decades, total-scattering-based structural studies revealing deviations between the true local atomic structure and that obtained by averaging over relatively long length scales have become more common (Egami & Billinge, 2003). This increased interest has been spurred on by a convergence of many factors, including the availability of high-throughput synchrotron-based user facilities (Schlachter, 1994; Bilderback *et al.*, 2005) with improved detectors (Chupas *et al.*, 2003; Broennimann *et al.*, 2006; Kraft, 2010), software development (Proffen & Neder, 1997; Qiu *et al.*, 2004; Soper, 2005; Farrow *et al.*, 2007; Neder & Proffen, 2008; Tucker *et al.*, 2007; Juhás *et al.*, 2013; Yang *et al.*, 2014; Coelho *et al.*, 2015; Ashiotis *et al.*, 2015; Juhás *et al.*, 2015; Hammersley, 2016; Aoun, 2016) and, most significantly, an increased awareness by the materials research community that local deviations often represent an important ingredient in the observed material properties in diverse classes of functional materials (Egami *et al.*, 1991; Billinge *et al.*, 1994; Frandsen *et al.*, 2018; Davenport *et al.*, 2019; Wang *et al.*, 2020).

The analysis technique based on the atomic pair distribution function, resulting from a powder system [one-dimensional (1D)-PDF] has often been the tool of choice for

$Q_z = 0.00$ Å^{-1}
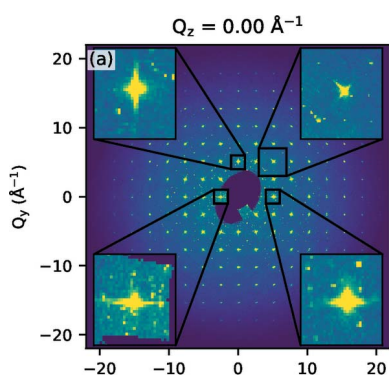
such local structure studies (Bozin *et al.*, 2019; Koch *et al.*, 2019; Yang *et al.*, 2020). The 1D-PDF measurement is effectively a modified powder diffraction experiment, where the total-scattering signal I_{tot} is collected to large momentum transfer values, Q, after which $F_{tot}(Q)$, defined as the properly corrected and background subtracted $I_{tot}(Q)$ signal, is sine Fourier transformed to obtain the 1D-PDF, $G(r)$, which is proportional to the probability of finding a pair of atoms in a material separated by a *scalar* distance r. The nature of the orientational averaging dictates that neither $I_{tot}(Q)$ nor $G(r)$ contain any directional information on atom-pair correlations (Egami & Billinge, 2003). This directional information is often retrieved by means of structural modeling (Farrow *et al.*, 2007; Juhás *et al.*, 2015).

Recently the concepts behind the 1D-PDF have been extended to single-crystal systems (Schaub *et al.*, 2007). By collecting the full momentum transfer vector **Q**-dependent intensity distribution, $I_{tot}(\mathbf{Q})$, from a single crystal and applying a Fourier transform (FT), a quantity akin to $G(r)$ is obtained, namely the three-dimensional (3D)-PDF, $P_{tot}(\mathbf{r})$, which is proportional to the probability of finding two atom pairs separated by a *vector* distance **r**. This retention of directional information in $P_{tot}(\mathbf{r})$ can be advantageous if there is ambiguous overlap of features in the scalar function $G(r)$, but it is important to keep in mind that $P_{tot}(\mathbf{r})$ and $G(r)$ are not perfect analogs. Specifically, $P_{tot}(\mathbf{r})$ is most often defined in the literature as the FT of the diffracted intensity distribution $I_{tot}(\mathbf{Q})$ (Kobas *et al.*, 2005; Schaub *et al.*, 2007; Weber & Simonov, 2012), whereas $G(r)$ is typically the FT of the reduced structure function $F(Q)$. Unfortunately this distinction can be overlooked, and although the 3D-PDF community could benefit from an extensive discussion of terminology along the lines of what has been done within the 1D-PDF community (Keen, 2001), this lengthy task will not be tackled here.

The more practical extension to the full 3D-PDF is the 3D-ΔPDF technique (Schaub *et al.*, 2007), which relies on the ability to separate the $I_{tot}(\mathbf{Q})$ function into a sum of the Bragg component, $I_{Bragg}(\mathbf{Q})$, arising due to the long-range average structure and leading to the well known Patterson function in direct space, and the diffuse component, $I_{diff}(\mathbf{Q})$, arising due to local deviations from the long-range average structure, such that $I_{tot}(\mathbf{Q}) = I_{Bragg}(\mathbf{Q}) + I_{diff}(\mathbf{Q})$. The 3D-ΔPDF, P_{diff}, is then defined as

$$P_{diff}(\mathbf{r}) = \int I_{diff}(\mathbf{Q}) \sin(2\pi\mathbf{Q} \cdot \mathbf{r}) \, d\mathbf{Q}$$
$$= \int \left[I_{tot}(\mathbf{Q}) - I_{Bragg}(\mathbf{Q}) \right] \sin(2\pi\mathbf{Q} \cdot \mathbf{r}) \, d\mathbf{Q}, \quad (1)$$

or the FT of the full 3D intensity distribution $I_{tot}(\mathbf{Q})$ after subtracting out the Bragg component $I_{Bragg}(\mathbf{Q})$. A full account of the theory behind these expressions can be found in earlier work (Schaub *et al.*, 2011; Weber & Simonov, 2012). The progression to 3D-ΔPDF analysis was preceded in large part by earlier work studying the full 3D intensity distribution $I_{tot}(\mathbf{Q})$, without the application of an FT. Many of the techniques of 3D-ΔPDF analysis then arise as an extension of this previous work (Epstein & Welberry, 1983; Weber *et al.*, 2001;

Welberry *et al.*, 2005; Welberry, 2010) to the measurement over broad **Q** ranges.

3D-ΔPDF analysis has proven effective in a number of cases, with the earliest studies largely qualitative in nature. The first application of the technique identified the presence and approximate length scales of inter- and intra-atomic cluster correlations in an Al–Co–Ni quasicrystal (Kobas *et al.*, 2005). Later qualitative works have revealed local ordering in tricarboxamides (Schaub *et al.*, 2007) and superstructure columnar units in the quasicrystal $Al_{65}Cu_{20}Co_{15}$ (Schaub *et al.*, 2011).

In a progression to a more quantitative analysis, short-range ordering parameters were successfully refined from the 3D-ΔPDFs (Simonov *et al.*, 2014b; Urban *et al.*, 2015). Later studies have revealed short-range ionic correlations in the intercalation compounds β'-$Na_{0.45}V_2O_5$ (Krogstad *et al.*, 2020) and local structure effects in the thermoelectric β-$Cu_{2-x}Se$ (Roth & Iversen, 2019).

While the usefulness of this relatively new technique may be clear, much of the methodology, particularly related to data reduction, remains murky and spread across various disparate works (Kabsch, 1988; Welberry *et al.*, 2005; Kobas *et al.*, 2005; Schaub *et al.*, 2007; Weber & Simonov, 2012; Kabsch, 2014). Here we outline the process of 3D-ΔPDF data collection and data processing, with the aim of making this new and powerful technique more accessible and transparent. We adopt the $CuIr_2S_4$ cubic spinel material (space group $Fd\bar{3}m$) as a convenient test system, as its local structure has been previously studied using standard powder PDF, where a fluctuating orbital-degeneracy-lifted state was discovered, manifesting as a subtle local-symmetry-breaking distortion on the Ir pyrochlore substructure (Bozin *et al.*, 2019) and dictating that the 3D-ΔPDF signal will be non-zero. (We emphasize that the investigation of these distortions themselves is not the focus of this study and will be addressed in a following article.) The $CuIr_2S_4$ spinel is an exemplar ternary spinel with appreciable scattering contrast between the constituent elements: Cu ($Z = 29$), Ir ($Z = 77$) and S ($Z = 16$). As will be seen from our data, pairwise correlations associated with the distortions can be observed in 3D-ΔPDF even for pair vectors corresponding to the weakest scatterers in the system.

Using this test system, we investigate the impact on the final 3D-ΔPDF of data-processing parameters, including X-ray count time, detector artifact removal, background subtraction, interframe scale correction, reciprocal-space sampling, data merging, outlier removal, data symmetrization, Bragg intensity removal and Fourier transformation. We identify a number of situations where the 3D-ΔPDF is extremely robust. In many cases, the 3D-ΔPDF is reproducible even with problematic data and incomplete data processing. We also identify and discuss a few areas where caution must be exercised.

1.2. Organization

For practical purposes this article is organized to follow the generic workflow progression involved in a 3D-PDF/3D-
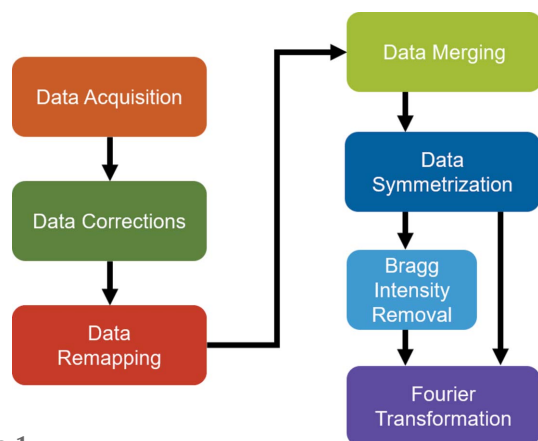
Figure 1
General data workflow: A flow chart depicting the main steps in producing a 3D-PDF and a 3D-ΔPDF. Data corrections and remapping to reciprocal space must occur prior to subsequent steps. Following this, data can be merged, symmetrized and Fourier transformed to obtain the 3D-PDF in any order. For 3D-ΔPDF, Bragg intensity removal must take place prior to the Fourier transformation step. Outlier removal can be incorporated at the data remapping, merging and symmetrization steps.

ΔPDF experiment, detailed in Fig. 1. In Section 2 we outline details of the physical diffraction experiment and crystal samples, and give a brief overview of software platforms used in the process.

We then discuss in Section 3 pathological issues with the raw diffraction data brought about by detector artifacts and sample imperfections, as well as their correction. In Section 4 we discuss the transformation of raw detector images from the detector frame of reference to crystal reciprocal space. The steps described in the subsequent Sections 5–9, respectively on merging data from a single sample, applying symmetry operations to the observed signal, outlier removal, removing Bragg intensity and applying a Fourier transform, can, with some restriction that we address later, be implemented in an

arbitrary order. The robustness of this process with regard to ordering and other factors is discussed in Section 10. Wherever possible this presentation ordering is maintained, with a few exceptions. The procedure and effects surrounding outlier removal are discussed in Section 7, but outlier removal is included in all data reconstruction, merging and symmetry averaging prior to this section. Occasionally the final Fourier transformed 3D-ΔPDF is shown prior to Section 9 to discuss the effect of various reduction steps on the direct-space data. In addition, data remapped from detector space to reciprocal space are shown prior to Section 4.3 to highlight the reciprocal-space extent of Bragg peaks.

2. Methods and approaches

2.1. Experimental details

Single-crystal diffraction measurements were carried out at the P21.1 beamline at the Positron-Elektron-Tandem-Ring-Anlage (PETRA III) facility at Deutsches Elektronen-Synchrotron (DESY), using an X-ray beam of 106 keV energy ($\lambda = 0.1170$ Å) sized to 0.5×0.5 mm.

Two octahedrally shaped single crystals of $CuIr_2S_4$ were measured. The first, herein referred to as 'sample 1', showed maximum dimensions of $\sim720 \times 630 \times 520$ µm, while the second, sample 2, showed maximum dimensions of $\sim810 \times 750 \times 650$ µm, where the dimensions listed third are those parallel to the mounting and rotation axis. When utilizing a flat-panel area detector, the instrumental resolution function is heavily impacted by the projection of the beam or crystal footprint (whichever is larger) on the detector, so achieving high spatial resolution requires that the beam or sample be as small as possible. In this study, since only relatively large crystals were available, the preference was to reduce the beam size. This resulted in primarily isotropic Bragg peaks (Fig. 2a). Instrumental resolution width in **Q**
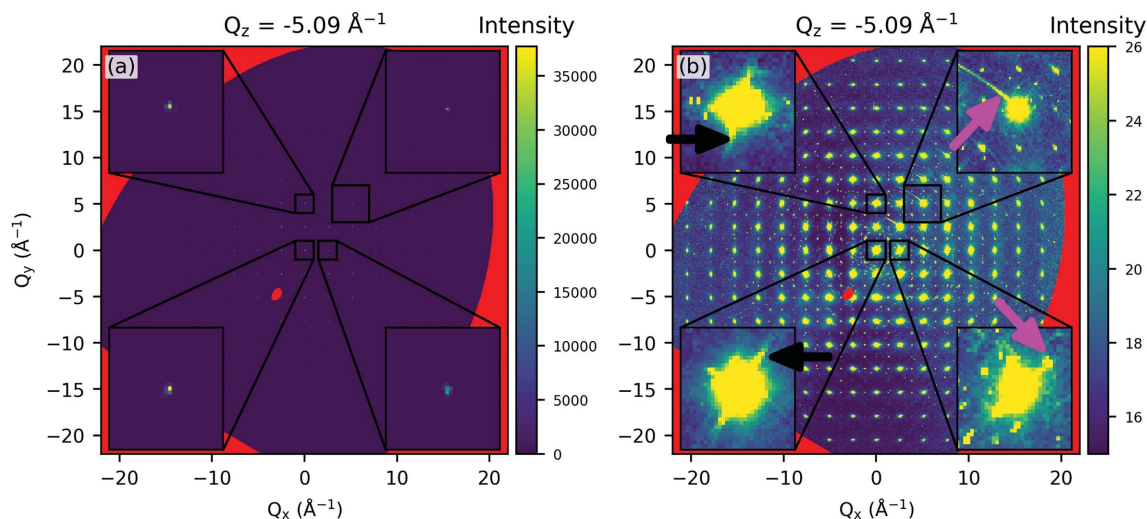

Figure 2
Examples of Bragg reflections, blooming and afterglow effects in data remapped from detector to crystal reciprocal space. (a) An intensity map of a representative slice of reciprocal space with intensity scale chosen so as to highlight the Bragg reflections, shown in corner insets on an expanded scale. Notably, Bragg reflections span 1–3 reciprocal-space voxels. (b) Identical to (a) but with a distinct intensity scale chosen to highlight the diffuse features, as well as the pathological issues caused by unmitigated detector blooming and afterglow effects (marked by black and magenta arrows, respectively) described in the text. It is common for the Bragg features to be orders of magnitude stronger than both the detector artifacts and the diffuse signal, although this can vary from system to system.

space impacts the intensity decay of the (full) 3D-PDF as a function of **r** in direct space (Weber & Simonov, 2012); specifically, a lower instrumental resolution leads to a more rapid decay of the 3D-PDF signal. It is an important aspect to consider, as one must be sure that the intensity decay of the (full) 3D-PDF extends beyond the spatial extent of any short-range distortions under investigation using the 3D-ΔPDF. **Q**-space resolution may also be relevant when considering the removal of Bragg peaks, and is discussed further in Section 8.

Each crystal was epoxy-mounted on the end of an amorphous cactus needle, which was in turn mounted on a goniometer head, with the crystal carefully aligned to achieve adequate centering. A well aligned sample implies that it resides at the center of rotation and the X-ray beam at all times. Measurements were carried out in air at ambient temperature and pressure. Each diffraction image was collected with a PerkinElmer (PE) 1621 amorphous-silicon flat-panel detector (2048×2048 pixels, 200×200 µm pixel size) located 516.6 mm away from the sample. Detector distance, tilt and rotation were calibrated using a CeO_2 standard measured in an identical geometry. With this beam energy and geometry, the detector provides a 21 Å^{-1} range coverage of reciprocal space ($Q_{max} = 21$ Å^{-1}). Notably the Q_{max} value determines the resolution in direct space, Δ_r, such that $\Delta_r = 2\pi/Q_{max}$. With the $Q_{max} = 21$ Å^{-1} achieved here, $\Delta_r = 0.3$ Å. Lower beam energies can be considered if improved **Q**-space resolution is necessary, but may lead to an unsuitably large Δ_r through a decrease Q_{max}. An example of full data processing with a lower Q_{max} is shown in the supporting information.

A single 3D measurement here consisted of an entire 360° rotation of the crystal along one axis only, with the detector counting continuously and read out at regular sub-intervals of this rotation. For each crystal, a total of 13 full 3D measurements were carried out, with exposure times per readout varying from 0.1 to 1.0 s and either 1800, 3600 or 7200 total images per full rotation (corresponding to 0.2, 0.1 or 0.05° per image, respectively). The benefit of considering such permutations of detector exposure time and angular image step size will be discussed in Section 5.

2.2. Software platforms and computation details

The vast majority of computational overhead in this work was handled with Python version 3.67 (Van Rossum & Drake, 2009) and MATLAB version 9.6.0 (MATLAB, 2019). MATLAB was used to transform raw detector images to reciprocal space and to fill reciprocal-space intensity after Bragg intensity removal. Python was used for building dynamic detector masks, to find crystal orientation (*UB*) matrices, and to normalize, merge, symmetrize, remove Bragg peaks and Fourier transform reciprocal-space intensity distributions. Specifically, we made use of the NumPy, SciPy, Dask and Matplotlib python packages (Harris *et al.*, 2020; Virtanen *et al.*, 2020; Dask Development Team, 2016; Hunter, 2007). The majority of the computations for this work were

carried out on the Maxwell computational resources operated at DESY.

2.3. Terminology

It is useful to define some terminology used throughout the work which may be unfamiliar. Diffracted intensity distributions are considered in either reconstructed crystal reciprocal space or detector space native to the measurement.

In reconstructed crystal reciprocal space the coordinate chosen is momentum transfer vector $\mathbf{Q} = Q_x\hat{\mathbf{x}}^* + Q_y\hat{\mathbf{y}}^* + Q_z\hat{\mathbf{z}}^*$ in units of Å^{-1}, where Q_x, Q_y and Q_z are continuous real numbers, and $\hat{\mathbf{x}}^*$, $\hat{\mathbf{y}}^*$ and $\hat{\mathbf{z}}^*$ are the (unitless) orthonormal reciprocal-space basis. We refer to discrete pieces of this space as 'voxels' throughout this work. In detector space the coordinate used is the position on the 2D detector. Transformation between the two spaces is discussed in Section 4.3. We refer to discrete pieces of this space as 'pixels' throughout this work. Pair distribution functions are discussed in coordinates of $\mathbf{r} = X\hat{\mathbf{x}} + Y\hat{\mathbf{y}} + Z\hat{\mathbf{z}}$ in units of Å, where X, Y and Z are continuous real numbers, and $\hat{\mathbf{x}}$, $\hat{\mathbf{y}}$ and $\hat{\mathbf{z}}$ are the (unitless) orthonormal direct-space basis. The process of removing and interpolating Bragg intensity and replacing it with diffuse intensity is colloquially called 'punch and fill', and this terminology has been adopted here. Section 3 deals primarily with the detector artifacts of blooming, where pixels adjacent to saturated pixels record erroneous intensity, and afterglow, where saturated pixels record erroneous intensity in subsequent frames. These two artifacts are a result of detector saturation, which for the purposes of this work is when the detector readout ceases to respond linearly with scattered photon fluence.

When comparing data subject to differing processing procedures (Section 10), we have quantified the difference using R_{diff}, analogous to R_{split} used in the field of serial crystallography (White *et al.*, 2013),

$$R_{diff} = \frac{1}{2^{1/2}} \frac{\sum |I_1 - I_2|}{\frac{1}{2}\sum(I_1 + I_2)} \times 100, \tag{2}$$

where I_1 and I_2 are the individual, mutually valid data points of the two data sets being compared.

3. Detector artifacts

The PE detector and other similar 2D detectors have many advantages for 3D-ΔPDF measurements. They are relatively inexpensive and as such are available at many hard-energy X-ray beamlines, and they are relatively robust against permanent beam damage that could be caused by excessively strong Bragg intensities (Perez-Mendez *et al.*, 1987). Such detectors often have high sensitivity (detective quantum efficiency greater than 65% at 80 keV), relatively fast readouts (up to 30 Hz) and small point-spread functions of less than one pixel (Chupas *et al.*, 2007; Lee *et al.*, 2008). These advantages have led to their widespread use within the powder total-scattering or one-dimensional powder PDF field (Chupas *et al.*, 2003).
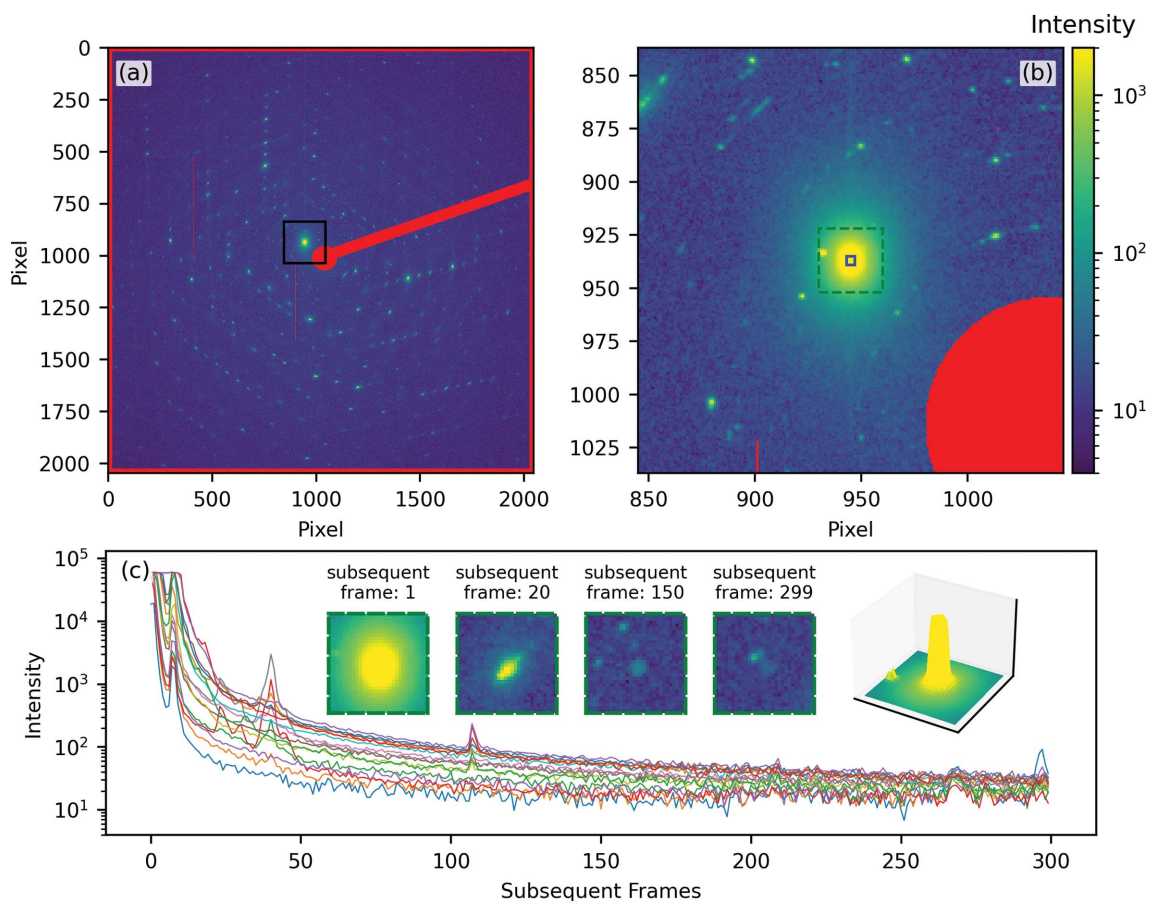
Figure 3
Examples of blooming and afterglow effects in the raw experimental data. (*a*) An intensity map of a detector image at the time point where a saturation event occurs, with a black box highlighting the location of the saturation/blooming. (*b*) An expanded view of the black box in (*a*). (*c*) A plot of pixel intensity versus the number of images subsequent to the detector saturation event shown in (*a*) and (*b*). Each plotted line in (*c*) represents one pixel from the blue box in (*b*). Inset center in (*c*) are portions of diffraction images shown on an enlarged scale after the labeled number of subsequent frames, where the initial saturation event, featured in panels (*a*) and (*b*), occurs in frame zero. Inset right in (*c*) is a 3D density plot of the portion of the detector subject to saturation, represented by the green dashed-line box in (*b*), at the time of saturation. The truncation of this peak intensity indicates that the detector has reached saturation, while the leakage of intensity into the surrounding detector area represents blooming. In (*a*) and (*b*), red portions represent masking due to the beam stop and known bad pixels. Intensity peaks observable in panel (*c*) on top of the decaying signal are subsequently detected diffraction events.

However, such detectors also suffer from a number of drawbacks. The nature of the 3D-ΔPDF measurement entails collecting the full diffraction signal from a single crystal specimen, with the intention of faithfully reproducing the diffuse intensity. This necessitates that very intense Bragg spots will be incident on the detector. With a dynamic range of the order of 10^3, these Bragg spots will frequently saturate such detectors. Under saturation such detectors will exhibit two phenomena, herein referred to as afterglow and blooming.

Afterglow can be considered a forward temporal cross-talk between detector frames collected at different times, whereby a saturated pixel or group of pixels in one readout persists to read out an erroneously elevated count rate for a finite number of detector frames following the saturation event. It is a result of the finite discharging time required of the storage capacitance in the sensor layer of the detector (Albagli *et al.*, 2005; Chupas *et al.*, 2007). Effectively, portions of the sensor layer retain charge in subsequent image readouts. Detector blooming (Welberry *et al.*, 2005) typically occurs when satu-

rated pixels overflow excess charge into neighboring pixels, causing a readout of erroneous intensity from these spatially adjacent pixels.

Examples of these two detector artifacts in detector images are shown in Fig. 3. While the given geometry should produce Bragg peaks spanning approximately 5–10 detector pixels, it is clear from Fig. 3(*b*) that the Bragg peak causing saturation of the detector leads to elevated counts in the surrounding 60 detector pixels, showed by the halo of intensity surrounding the Bragg peak. Further, plotting the intensity of the saturated pixels as a function of the subsequent frame number, shown in Fig. 3(*c*), reveals that the saturated pixels continue to readout elevated counts for at least 150 subsequent frames.

Importantly, both artifacts introduce undesirable erroneous intensity into the measurement, causing issues in the intensity distribution when this is transformed into crystal reciprocal space, as shown in Fig. 2(*b*). Blooming creates a roughly equiaxed area of bright pixels surrounding the saturated pixel(s) within a detector image. Since each detector image intersects the reciprocal-space origin, a disc of intensity in
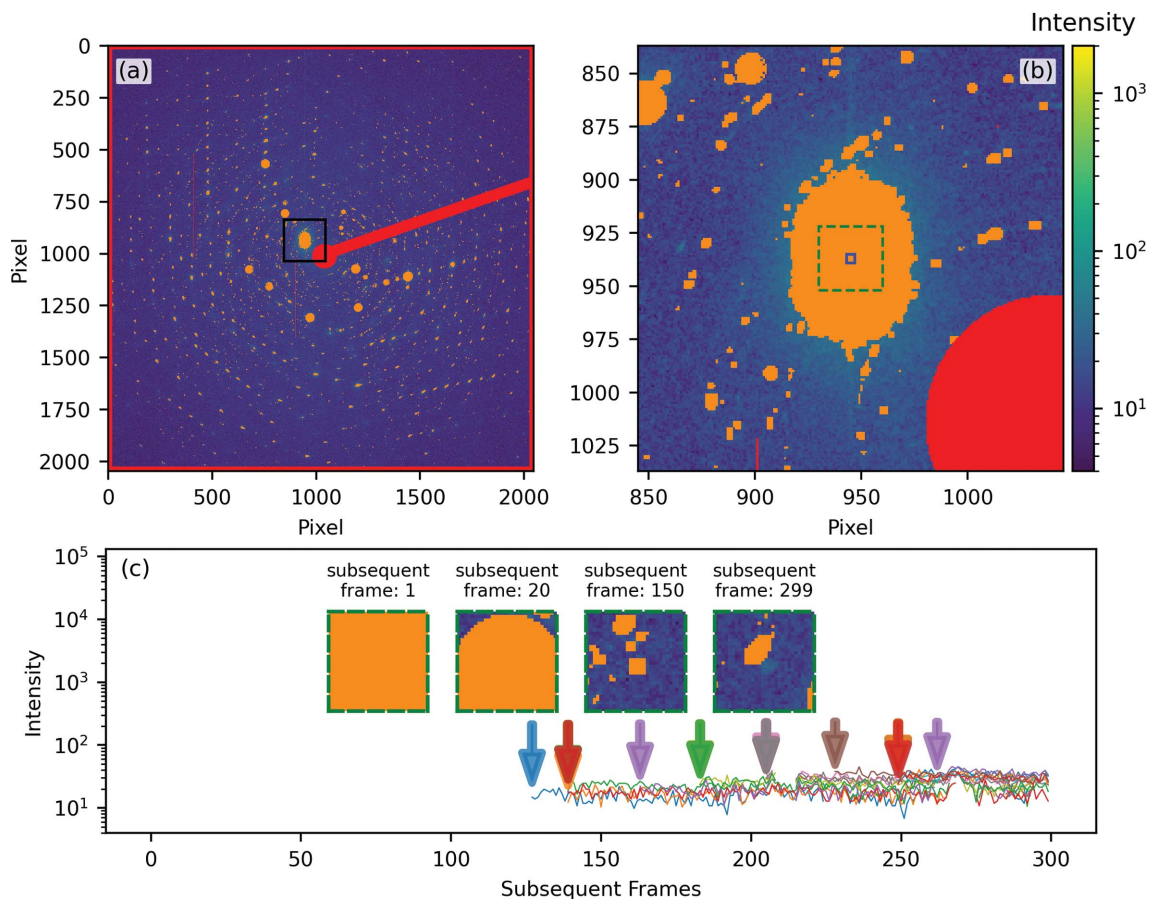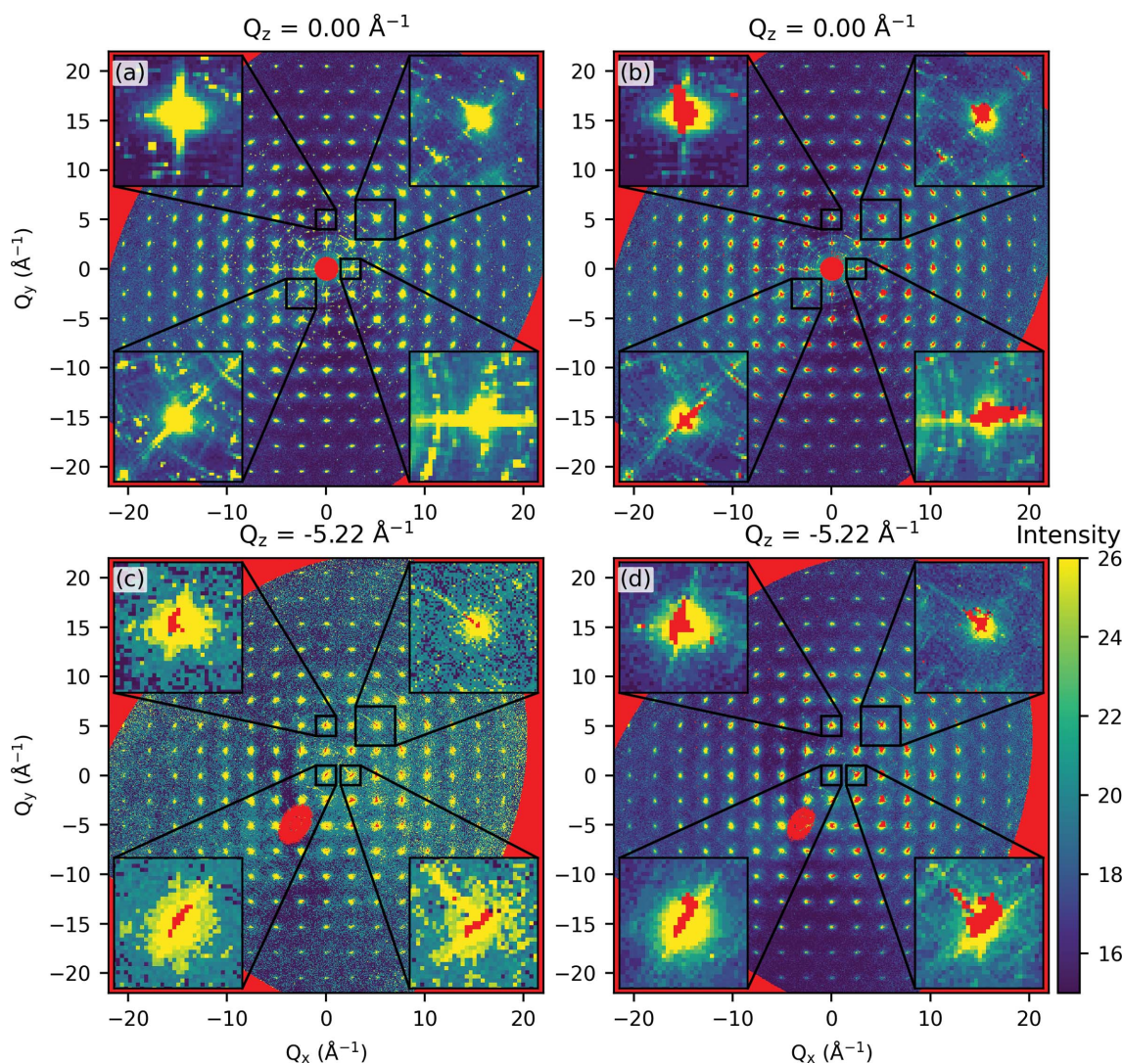
Figure 4
Examples of the application of the dynamic masking heuristic adopted in this work. Panels (*a*) and (*b*) are identical to Fig. 3(*a*) and (*b*), where raw data masked due to detector blooming and afterglow have been colored orange. (*c*) Identical to Fig. 3(*c*), where raw data masked due to detector blooming and afterglow have been omitted from the intensity plot. Colored arrows in (*c*) indicate the frame at which a given pixel becomes unmasked, and colors correspond to the line colors plotted in (*c*). Note that, in the detector region affected by the saturation event, the pixels do not fully recover until at least 150 frames after the saturation event, with all pixels recovering by 275 frames after the saturation event.

detector space corresponds to a disc in reciprocal space sitting on a surface which intersects the reciprocal-space origin. In 2D slices of reciprocal space, detector blooming manifests as streaks of intensity sitting on arcs which are oriented towards the reciprocal-space origin, as indicated by black arrows in the upper- and lower-left insets of Fig. 2(*b*).

Detector afterglow is a persistence of elevated counts in the pixel(s) across multiple subsequent frames. While it can occur for any pixel after it registers intensity, the effects are most notable and problematic when measuring bright Bragg peaks. The scalar *magnitude* of the momentum transfer vector of each pixel in the detector is fixed by the detector position and orientation, and does not change as the crystal is rotated in laboratory coordinates. The *direction* of the momentum transfer vector associated with each detector pixel is, however, altered by the crystal rotation. As a result, detector pixels affected by afterglow are mapped in reciprocal space to bright arcs around the reciprocal-space origin, with constant momentum transfer magnitude. In 2D slices of reciprocal space, detector afterglow manifests as arc-like streaks of intensity centered at the reciprocal-space origin, such as those seen in the upper-right inset of Fig. 2(*b*) (features indicated by magenta arrows). The reciprocal-space orientations of both

blooming and afterglow artifacts are determined by the crystal orientation and rotation axis. In this work, we adopted a heuristic whereby we identified detector saturation along with the subsequent afterglow and blooming within the raw detector images through a simple intensity threshold approach of 40 000 counts. The pixels surpassing the intensity threshold were masked within the subsequent 200 frames to reduce afterglow. To reduce blooming, pixels within a diameter of 40 pixels encompassing any saturated pixel were masked in the initial frame, and this diameter was decreased linearly in the subsequent 100 frames. By processing an entire image sequence using this heuristic prior to remapping to reciprocal space, an evolving or dynamic mask of excluded pixels was built and subsequently applied to each measured detector image during reciprocal-space remapping. In our study, this masking heuristic was based simply on the number of subsequent frames, but in adapting this to other problems and varying count times and/or step sizes more dramatically, it may be useful to instead consider the total time passed since a saturation event. Further, one could consider measuring with brief pauses between frame readouts to reduce the temporal cross-talk between frames, although this could substantially lengthen measurement time.

Figure 5
Examples of the impact of dynamic masking in the data remapped to reciprocal space. Intensity maps of representative slices of reciprocal space (*a*) without and (*b*, *c*, *d*) with the dynamic masking heuristic described in the text to mitigate the effects of detector blooming and afterglow. Q_z slices were chosen to best demonstrate the effect, and are maintained throughout many of the figures. Images used in the reconstruction for (*c*) were counted for 0.1 s per frame, and those in (*a*, *b*, *d*) were counted for 0.8 s per frame. A few regions heavily impacted by the masking, with missing data eliminated by masking marked in red, are shown inset on an enlarged scale. Note that the counting time, contrasted in (*c*) and (*d*), heavily impacts the extent of dynamic masking and overall noise. Shorter counting time results in less masking but noisier data, while longer counting improves the statistics but requires more masking.

In Fig. 4 we demonstrate the application of such dynamic masking heuristic to the detector images. Dynamically masked pixels are shown in panels (*a*) and (*b*) in orange, and are excluded from the intensity plot in panel (*c*). The dynamic masking excludes all saturated pixels, along with a large portion of the surrounding detector area in the initial frame. In subsequent frames [shown inset in panel (*c*)] the original masked area shrinks until it is removed entirely, unless a subsequent saturation event occurs nearby. Fig. 4(*c*) demonstrates that the dynamic masking effectively excludes afterglow intensity until the detector has recovered to baseline count rates, with recovery beginning and ending approximately 150 and 275 frames after the saturation event, respectively.

The dynamic masking heuristic we outline here uses the raw detector images as an input to generate image-wise masks, which are then used in reconstruction to reciprocal space. The processes leads to the exclusion of portions of the measured data, producing empty regions of reciprocal space if these voxels are not successfully measured in other detector images. Examples of dynamically masked reciprocal-space reconstructions are presented in Fig. 5, using a significantly abbreviated color scale to highlight the weaker features of interest. Reconstructions with and without masking are shown in Fig. 5(*a*) and (*b*), respectively, and demonstrate that that dynamic masking removes a considerable amount of the strongest effects due to detector saturation, blooming and afterglow. The lower insets in these panels, focusing on areas near the reciprocal-space origin, also reveal that masking reduces the prominence of what can be considered parasitic scattering contributions. Composed of a collection of bright spots, these ring-like features are not expected in a single-crystal

measurement, and are likely to be a result of small poly-crystalline inclusions and/or smaller crystals attached to the faces of the main crystal. Originating from sample imperfections, this situation yields what could be considered sub-critical scattering data, but can be remedied to a great extent through the dynamic masking process.

Although dynamic masking does aid in removing detector artifacts, some streaking does persist in the reciprocal-space intensity maps. While it may seem that this could be remedied by a more aggressive dynamic detector masking, we found that the reported dynamic detector masking parameters and the associated results represent an optimal point, beyond which we see diminishing returns. That is, adopting a more aggressive approach results in significant masking of regions not impacted by detector blooming/afterglow, without providing a justifiable improvement in actual blooming/afterglow effects. As will be seen in subsequent sections, further processing of the reconstructed data, including merging (Section 5) and symmetrization (Section 6) significantly mitigate the effects of detector artifacts that survive dynamic masking, especially when including outlier rejection (Section 7).

The quantity and size of the masked regions in reciprocal space are dependent on the parameters of the masking heuristic and the degree of afterglow and blooming, which is related to the exposure time per frame. As can be seen in Fig. 5(c) and (d), respectively, short exposure times result in less masking and fewer/smaller completely masked regions, while longer exposure times result in more masking and more/larger completely masked regions. We found that across all data sets, each comprised of a full rotation of the crystal, dynamic masking with the parameters we utilized resulted in a mean pixel rejection rate of about 3%, with a maximum rejection rate per image of about 7%, a relatively small fraction of the information content of each image.

As will be seen in our subsequent discussions, the missing portions of reciprocal-space data (holes in the data) created by this limited dynamic masking are nearly completely filled (recovered) after merging data sets collected over distinct exposure times and angular meshes (Section 5) and by applying crystal symmetry (Section 6). Thus, any compromised/excluded signal of relevance in reciprocal space can be recovered by the over-sampling that is achieved in detector space over the course of the measurement and data processing. Further, many of these holes exist at positions of Bragg peaks, which are punched and filled later in the data-analysis pipeline (Section 8). We can conclude that with a crystal with relatively high space-group symmetry and extensive data over-sampling, such a dynamic masking heuristic and the resulting apparent gaps in individual data sets should not represent any significant issue for the analysis of the final treated data. In situations where the crystal has lower space-group symmetry, it may be necessary to recover masked intensity (achieve over-sampling) by utilizing more than a single rotation axis during measurement, as the orientation of detector artifacts is dictated by the rotation axis.

4. Transforming from detector to reciprocal space

4.1. Background subtraction

As with 1D-PDF experiments, it is important in a 3D-ΔPDF experiment to ensure that only coherent scattering from the sample under study contributes significantly to the final reduced 3D-ΔPDF. Contributions not due to coherent scattering from the sample can include air scattering, scattering from the sample mount or housing, or incoherent contributions from the crystal, such as fluorescence and Compton scattering. First priority should be given to minimizing the contribution of each extraneous scattering source. Failing this, these contributions must be removed or their effect taken into account during analysis of the final 3D-ΔPDF.

If the diffraction measurement is carried out in air, or if the crystal is mounted in such a way that additional material is present in the beam (such as epoxy or a mounting stub) and the background component does not vary as a function of crystal rotation, it is likely to be simplest to conduct a pixel-wise subtraction of a single, averaged, background image collected from an identical setup without the the crystal sample present. If the crystal absorbs a large portion of the primary beam, it is possible that the air scattering occurring between the crystal position and the beam stop shows a substantial difference between when the crystal is present or absent. This can be remedied by minimizing air scattering and using a crystal with low absorption or, failing this, a scale parameter can be fitted to minimize the background signal (Holm *et al.*, 2020). If the background has many components (both air and epoxy, for example), it may be necessary to independently subtract a scaled diffraction pattern of each isolated component. It is best practice to minimize this component of the background signal as much as possible, *e.g.* by carrying out the experiment in a low-scattering chamber, minimizing the beam path in air (collimator and beam stop close to crystal), or ensuring that no components of the mounting fixture are in the X-ray beam.

Incoherent contributions to the background, such as fluorescence and Compton scattering from the crystal, cannot be remedied by subtracting the measurement of an empty sample environment. The relative fraction of these two contributions compared with the coherent signal should be optimized by utilizing suitably chosen high-energy X-rays (Ramsteiner *et al.*, 2009) and/or energy-discriminating detectors, if available (Broennimann *et al.*, 2006; Henrich, 2008).

There are a number of approaches within 3D-ΔPDF studies to handling background. Examples are fitting the background, including the incoherent contributions, with smooth functions for subtraction (Holm *et al.*, 2020), assuming that certain portions of reciprocal space contain no diffuse signal and interpolating between these regions (Schaub *et al.*, 2007; Weber & Simonov, 2012; Simonov *et al.*, 2014a), or taking the floor (minimum) counts of averaged detector frames to build a reciprocal-space map of the background for subsequent subtraction (Krogstad *et al.*, 2020). A number of works avoid mentioning incoherent contributions explicitly, presumably implicitly grouping fluorescence and Compton scattering into
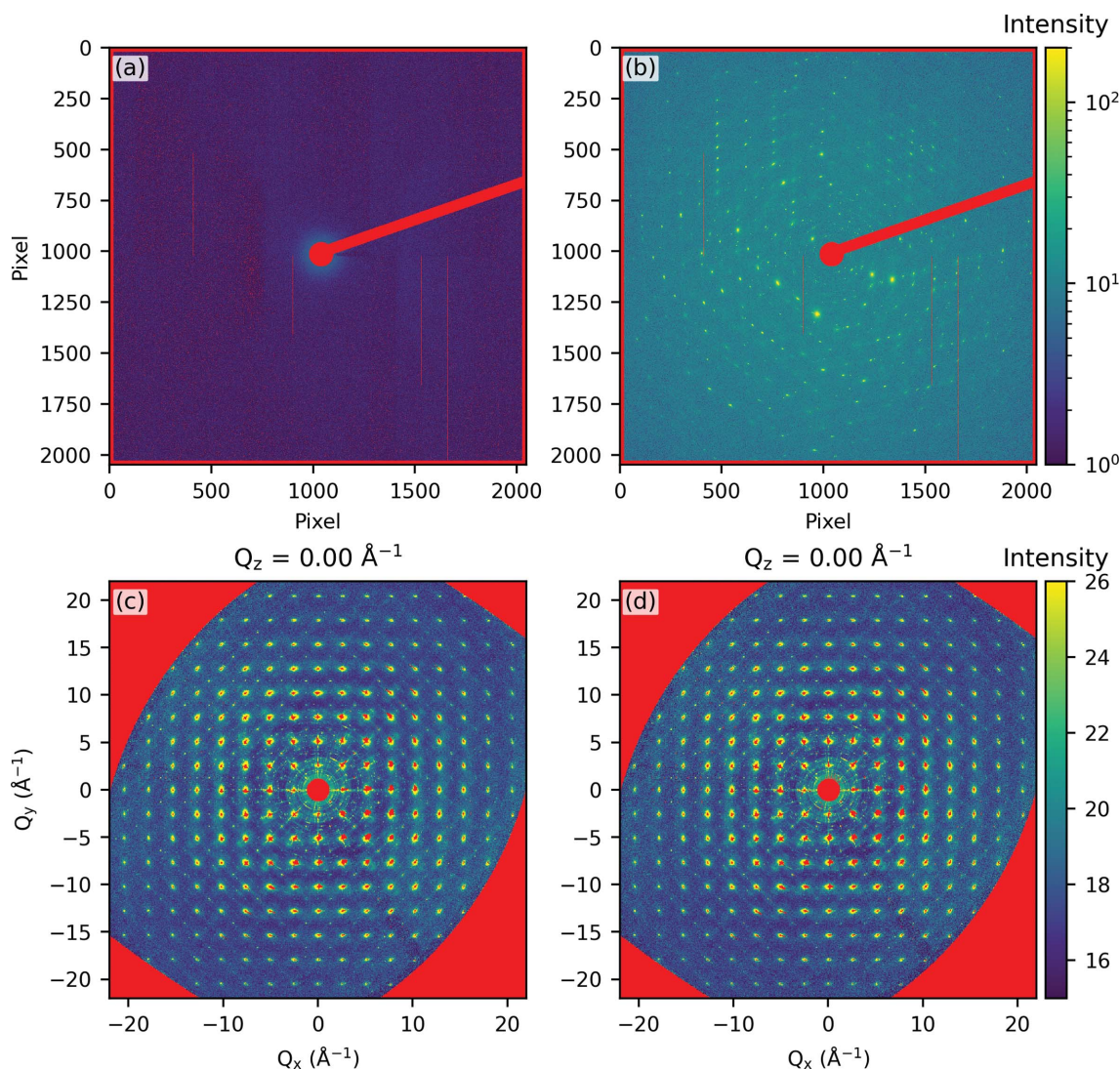
Figure 6
The impact of experimental background on data remapped to reciprocal space. (*a*) The background diffraction signal measured for this experiment. The data are relatively featureless aside from a small region surrounding the direct beam. (*b*) A raw detector image after background subtraction. (*c*) An intensity map of a representative slice of reciprocal space with background subtraction. (*d*) The same slice of reciprocal space without background subtraction. In our example, the relatively strong signal from the crystal dominates, with very little contribution from the background.

a general background (Schaub *et al.*, 2007, 2011; Krogstad *et al.*, 2020; Roth & Iversen, 2019). As fluorescence and Compton scattering from the sample are both smooth and vary slowly in reciprocal space as a function of scalar Q rather than vector $\mathbf{Q}$, their contributions should bias scale factors during quantitative modeling/fitting of the 3D-ΔPDF. In such situations, imposing additional physically reasonable constraints for pair correlations can help to resolve this bias (Weber & Simonov, 2012; Simonov *et al.*, 2014*a*). Neglecting fluorescence and Compton scattering entirely can provide adequate data for identifying gross features and trends in the 3D-ΔPDF (Roth & Iversen, 2019), and has also yielded meaningful quantitative results (Krogstad *et al.*, 2020).

In the current work, a diffraction pattern of an unloaded sample environment was used as background, and subtraction was done pixel-wise for each detector image. In our particular experiment, the background signal from an unloaded sample environment was several orders of magnitude smaller than that of the sample, and primarily concentrated at the reciprocal-space origin [Fig. 6(*a*)]. In this case, background subtraction does not result in a significant difference in the raw detector image [Fig. 6(*b*)] or the reciprocal-space intensity distributions [Fig. 6(*c*) and (*d*)]. This may not hold true in situations where the magnitude of the background scattering is comparable to that of the sample, for example for less crystalline samples, physically smaller crystals, or if an *in situ* diffraction cell contributes significant background.

Line cuts of the reciprocal-space intensity distributions shown in Fig. 6(*c*) and (*d*) (see the supporting information) demonstrate that the air-scattering signal is flat beyond $|Q| \geq 5 \text{ Å}^{-1}$. The background-subtracted intensity distribution also does not show a strong increasing or decreasing trend with Q, suggesting a minimal contribution of incoherent scattering.
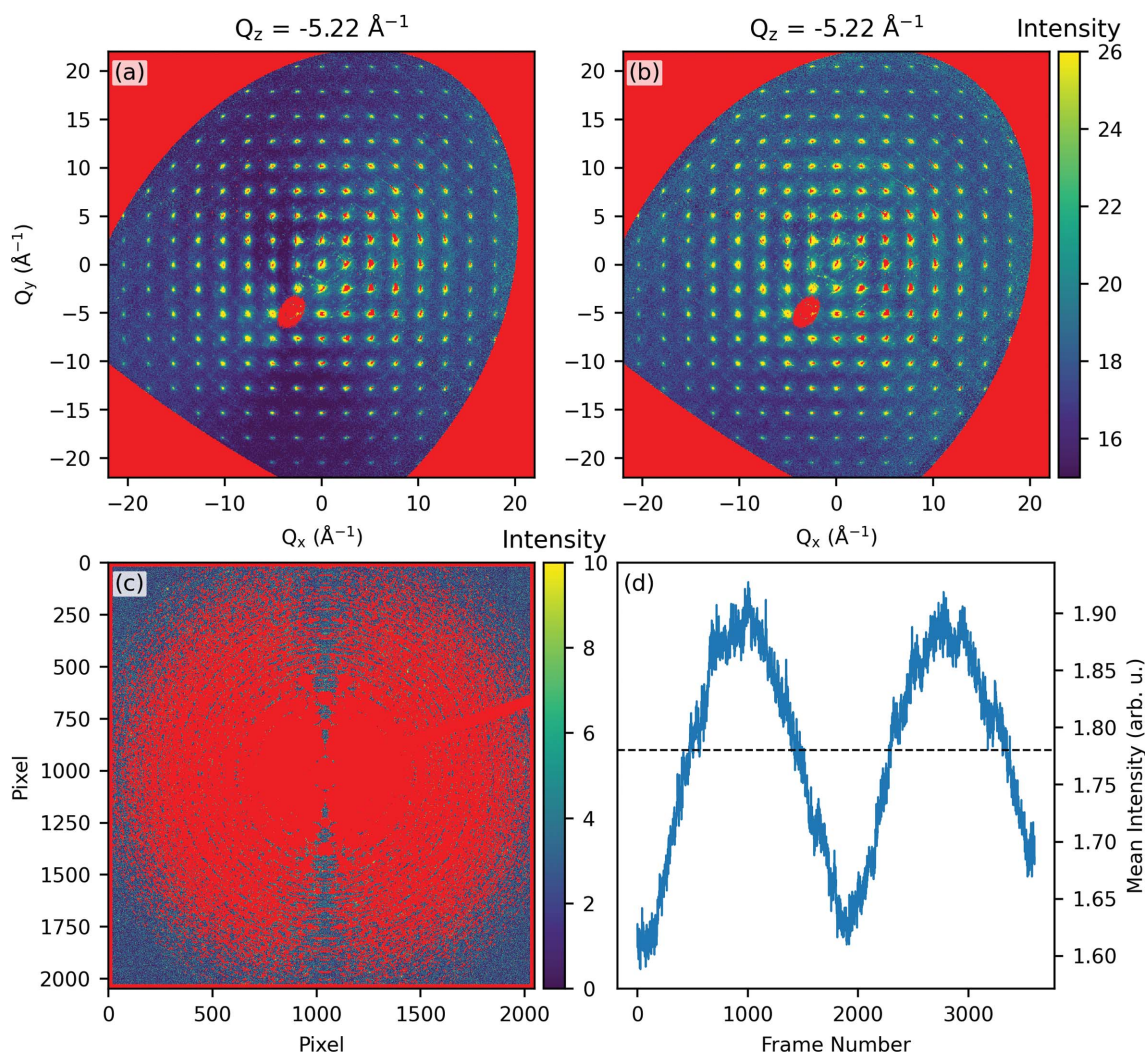
Figure 7
The impact of sample interframe scale fluctuation on reciprocal-space data. (*a*) An intensity map of a representative slice of reciprocal space prior to applying an interframe scale correction. Note the dark cones in the intensity distribution. (*b*) The same data as in (*a*), after applying the interframe scale correction described in the text. (*c*) An example portion of the detector used in correcting for interframe scale fluctuations, with excluded pixels masked in red. (*d*) The mean intensity considering all non-masked pixels in (*c*) for each frame in a data set, as well as the mean across the entire data set, represented by a horizontal dashed line. The dark cones seen in (*a*) have been replaced by a more uniform intensity distribution in (*b*) as a result of scaling each image such that the frame-to-frame variation seen in (*d*) is eliminated.

4.2. Interframe scale correction

If the crystal is relatively large and the morphology is not perfectly equiaxed, a variation in diffracted intensity will be observed across the series of images measured while rotating the crystal. This occurs because the volume of the crystal in the beam changes during rotation, impacting the absorption and amount of scattering. Within the data remapped to crystal reciprocal space, this is manifested as dark cones observable in the background intensity distribution, which can be seen in Fig. 5 and Fig. 7(*a*). The extent of this variation can generally be minimized by selecting an adequate beam energy and utilizing a suitably small crystal with an isotropic morphology, if such an ideal crystal is available.

To mitigate the impact of these frame-to-frame fluctuations in the current study we have adopted an empirical approach used in previous work (Welberry *et al.*, 2005). We identified the portion of the detector that does not show any diffraction peaks when considering a full crystal rotation data set, utilizing the dynamic masks generated in Section 3. That is, all pixels of the detector that are never subjected to a dynamic mask were used. A representative example of this portion of the detector is shown in Fig. 7(*c*). The mean pixel intensity across this portion of the detector was then computed individually for each detector image in a full data set.

In Fig. 7(*d*) we show an example of the frame-wise mean intensity for the detector region shown in Fig. 7(*c*), along with the overall mean for the entire data set (all frames), represented by a horizontal dashed line. To remove the interframe intensity fluctuations, each image is scaled prior to reconstruction to reciprocal space by the ratio of the frame mean to the overall mean for a given data set such that the variation in this mean intensity from frame to frame is eliminated.

An example of a reciprocal-space intensity distribution before and after such correction can be seen in Fig. 7(*a*) and Fig. 7(*b*), respectively. The application of this crystal-
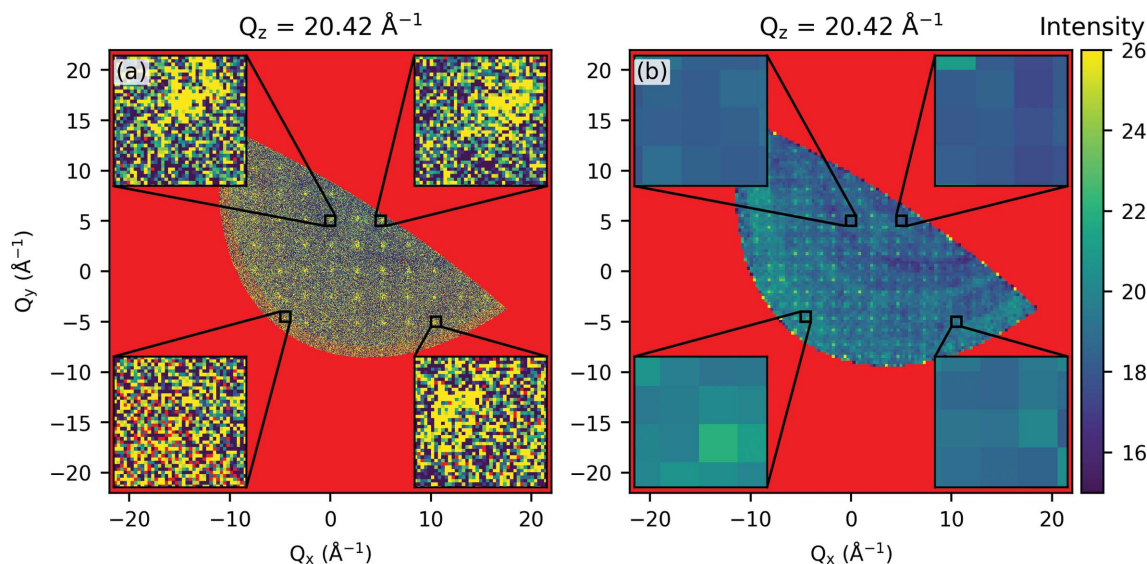
Figure 8
Choice of reciprocal-space sampling grid. (*a*) An intensity map of a representative slice of reciprocal space with a step size of 0.026 Å^{-1} (1701 × 1701 × 1701 voxels). Note that, within the inset regions on an enlarged scale, portions of reciprocal space inside the maximum momentum transfer vector of the experiment contain no data (represented by red pixels among other colored pixels). (*b*) Similar to (*a*), with a step size of 0.29 Å^{-1} (151 × 151 × 151 voxels). The insets demonstrate that diffuse features and Bragg peaks now span the same 1–3 voxels, and would be difficult to disentangle during the punch and fill process.

orientation-dependent, frame-wise interframe scale correction successfully removes the dark cones in the intensity distribution, leading to a more uniform intensity distribution.

4.3. Geometric data remapping protocol

Following data collection and correction for pathological detector-related issues, each data set is transformed from detector to crystal reciprocal space. This is carried out using information such as the calibrated beam energy, detector position and orientation, unit-cell dimensions of the sample, and known crystal rotation step size between detector images used in the experiment for a given data set.

Effectively, the reciprocal-space momentum transfer vector for each pixel in an image is computed, and if this pixel is not subject to masking, the measured intensity, corrected for polarization effects (Milch & Minor, 1974; Kabsch, 1988; Zachariasen, 1994; Kabsch, 2014), is binned into the appropriate voxel in reciprocal space and the reciprocal-space voxel bin count, representing the total number of pixels contributing to a given voxel, is incremented. Once each image for a given measurement (data set) is processed, the voxel bin is normalized (divided) by its bin count and written to a file.

The voxel bin counts can also be written out, as they can subsequently be used as bin weights in further transformations.

4.4. Reciprocal-space sampling

During the remapping from detector to reciprocal space, which transforms the units from physical pixels used in the detector space to reciprocal-space units, one must choose a voxel grid in reciprocal space on which to map the detector-space pixels. The choice of this grid is important, as it can impact both the quality of the result and the computational overhead associated with the data processing. A grid that is too coarse will impart a graininess to the reciprocal-space intensity distribution, impede the punching and filling of Bragg peaks, and will limit the field of view of the 3D-ΔPDF, possibly producing issues with aliasing. An example of under-sampling in reciprocal space is shown in Fig. 8(*b*). Here, a reciprocal-space grid step size of 0.29 Å^{-1} was chosen, equating to a 151 × 151 × 151 voxel grid. It is clear that, with such a coarse voxel grid, Bragg peaks spanning 0.19 Å^{-1} are spread across a larger portion of reciprocal space, overlapping significantly with diffuse peaks. This could potentially lead to issues during removal of Bragg features in subsequent steps.

A grid that is too fine leads to other but equally problematic situations. Fine voxel grids can produce arrays that are too large to handle easily. If we assume a single voxel bin requires 16 bytes of memory, a grid such as the one used throughout the majority of this work (701 × 701 × 701 voxels, step size of 0.063 Å^{-1}) requires about 5.5 gigabytes (GB) of memory and/or disk space. Decreasing the step size to 0.026 Å^{-1} (1701 × 1701 × 1701 voxels) increases the array size by a factor of more than 10, to almost 80 GB, which can become problematic if multiple arrays are to be handled simultaneously (as in merging and applying symmetry operations). A too-fine grid can also result in regions of reciprocal space inside the measured Q range that have not been sampled by the detector, leaving holes in the transformed reciprocal-space intensity distribution. This can be seen in Fig. 8(*a*), where a reciprocal-space grid of 1701 × 1701 × 1701 voxels corresponding to a grid step size of 0.026 Å^{-1} voxels was used. The figure insets show unsampled points, represented by red pixels, dispersed within regions of the intensity map that are within the measured Q range. To avoid such under-sampling, the
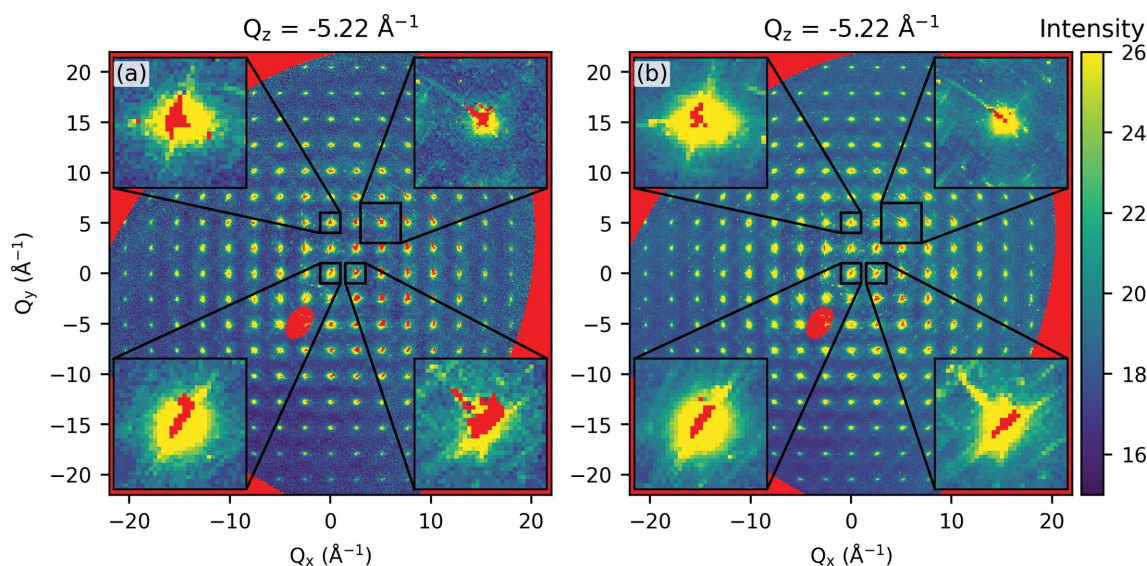
Figure 9
Merging data collected at different exposures. Intensity maps of a representative slice of reciprocal space of (*a*) a single data set (1 s exposure per frame) and (*b*) data after merging 13 full data sets collected from the same sample with differing exposure times. A few regions heavily impacted by the merging process are shown inset on an enlarged scale, with missing data in red. Merging multiple data sets reduces anomalies due to detector blooming and afterglow, impacting the streaks highlighted in Fig. 2(*b*). Also, note that the merging process has partially filled in the missing intensity introduced by the dynamic masking process (see *e.g.* Fig. 5).

voxel size should approximately match the portion of reciprocal space spanned by pixels on the outer edges of the detector.

4.5. Crystal orientation

Our experiments were carried out on a single crystal of unknown orientation, with known unit-cell dimensions. Knowledge of the crystal orientation (*UB* matrix) is not required to move from the detector reference frame to an arbitrary reciprocal-space reference frame, as the latter is determined only by the detector position and orientation and the beam energy. It is however useful and common to transform to a *specific* reciprocal-space reference frame whereby the reciprocal lattice of the crystal has a known relationship to the principal Cartesian axes. To achieve this, knowledge of the unit-cell dimensions and Laue class is required, and the crystal orientation (*UB*) matrix must be determined (in this case after the measurement is completed).

There are numerous strategies for determining a crystal orientation (*UB*) matrix (Kabsch, 1976, 1988, 2014). Here, we applied the Kabsch algorithm (Kabsch, 1976), choosing to find the crystal orientation using difference vectors with coordinates corresponding to the {440} family of Bragg peaks in the $Fd\bar{3}m$ space group describing this system at ambient conditions.

This process was carried out independently for each set of the full crystal rotation measurements done in this study, where we varied the exposure time and the crystal rotation step size. The crystal orientation matrices were then used for each transformation from detector space to reciprocal space, such that the reciprocal-lattice vectors of the crystal are parallel to the principal Cartesian axes. The condition that reciprocal-lattice vectors are parallel to the principal Cartesian axes is only possible with orthogonal crystal systems, as is

the case here. One could transform into the crystal coordinates of non-Cartesian systems. This would then dictate that the intensity space array indices no longer correspond to Cartesian axes, and additional care is required when plotting, for example. This scenario can however be advantageous for certain data-processing steps, such as symmetrization.

5. Merging data

Complete data sets collected from the same crystal can be merged into a single data set at any point in the data pipeline *after* the transformation from detector to reciprocal space has been completed. In practice this requires computing a weighted arithmetic mean of the intensity of each voxel bin across all relevant full data sets, where the weights are given by the total number of detector pixels contributing to each voxel, as discussed earlier.

Merging data sets collected with different exposure times and angular grid meshes defined by the crystal rotation step size improves statistics, reducing the scatter of the overall data set, which can arise from electronic glitches or shot noise. Merging also facilitates filling in of the portions of reciprocal space that were excluded because of detector saturation and the associated blooming and/or afterglow. Shorter exposure times [see *e.g.* Fig. 5(*c*)] produce less afterglow and blooming, and thus more faithfully reproduce the intensity distribution closer to Bragg peaks, at the expense of undercounting weak features far from Bragg peaks. Conversely, longer exposure times [see *e.g.* Fig. 5(*d*)] produce more afterglow and blooming, and lead to more and larger holes in the reciprocal-space intensity distribution, but also more faithfully reproduce weak features far from Bragg peaks.

In Fig. 9 we show an example reciprocal-space slice (*a*) before and (*b*) after merging 13 full data sets collected from a
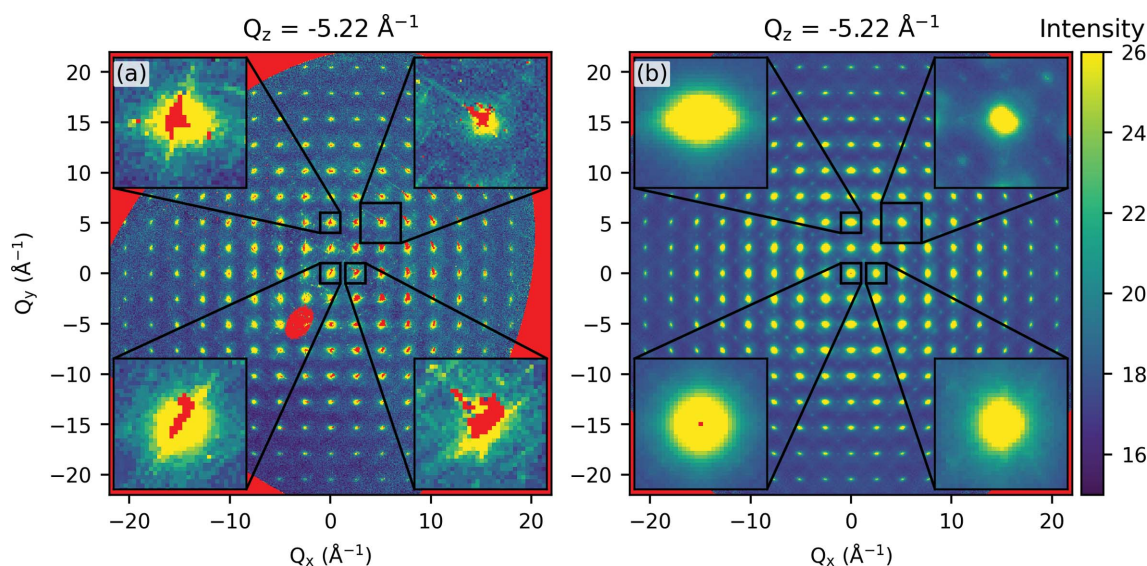
Figure 10
Applying symmetry operations. Intensity maps of a representative slice of reciprocal space of a single data set (1 s exposure per frame) (*a*) before and (*b*) after averaging over all relevant symmetry operations. A few regions heavily impacted by the symmetry-averaging process are shown inset on an enlarged scale, with missing data in red. The process of applying symmetry operations has filled in the majority of the missing intensity introduced by the dynamic masking process (see *e.g.* Figs. 5 and 9). A small hole does remain in the lower-right inset of panel (*b*), but this occurs at a Bragg position and is filled in subsequent steps. The symmetry averaging has also removed all residual streaking associated with detector afterglow/blooming.

single crystal with various exposure times and crystal rotation steps. The holes introduced by our dynamic detector masking heuristic (see *e.g.* Fig. 5) have been filled in to a large extent, and the regions between Bragg peaks show less scatter after merging. Note that some very weak features are observable within reciprocal-space slices that are inconsistent with the structure of $CuIr_2S_4$. These are likely to be due to small quantities of impurity polycrystalline inclusions and/or smaller crystals attached to the faces of the main crystal of the primary $CuIr_2S_4$ phase. Many of these reside at fixed Q values and thus constitute powder-ring-like features. The presence of such parasitic scattering contributions is best avoided by a careful selection of the crystal, as they can propagate to the 3D-ΔPDF and cause spurious features. As will be seen, these are remedied to a large degree by the data processing in later steps.

6. Symmetrization

With some exceptions, the full intensity distribution (Bragg + diffuse) measured from the crystal should obey the same Laue point-group symmetry governing the long-range average structure of the crystal (Weber *et al.*, 2001; Welberry, 2010). This may not be the case if, for example, the crystal shows structural heterogeneity over length scales of the same order of magnitude as the beam footprint (Weber *et al.*, 2001). For the $CuIr_2S_4$ crystal used here, this was not the case, as the beam footprint was relatively large, and the results are robust between individual single crystals. We can apply the symmetry operators associated with this Laue point group to the data under consideration. This symmetrization improves statistics, reduces the scatter of the data set, fills in portions of reciprocal space that were excluded because of detector saturation and

the associated blooming and/or afterglow, and also fills in portions of the space that were not measured because of limited crystal rotation.

In the $CuIr_2S_4$ case, the Laue symmetry is $m\bar{3}m$, which contains 48 symmetry operations. The application of each symmetry operation requires computing a weighted arithmetic mean of the intensity of each voxel bin across all relevant symmetry operators, where the weights are the total number of detector pixels contributing to each voxel. The set of all symmetry-equivalent voxels and their weights are obtained by applying the Laue symmetry to the (*HKL*) coordinate of each voxel and voxel weight. Examples of these 48 symmetry images and a few select intensity distribution histograms are shown in the supporting information.

Fig. 10 shows a representative slice of a reciprocal-space intensity distribution (*a*) before and (*b*) after applying all relevant symmetry operators to a data set which had been previously merged as described in the previous section. The process of applying symmetry operators with outlier removal has nearly completely filled in the vast majority of holes associated with the dynamic masking heuristic, and has resulted in a substantially cleaner and more uniform intensity distribution. The small quantity of remaining holes [see *e.g.* Fig. 10(*b*), lower-left inset] are a result of dynamic masking, and located at Bragg positions filled during the punch and fill process. In addition, portions of reciprocal space that were not measured due to crystal orientation and detector geometry (outside a given **Q** range) have been filled in by the symmetrization process. In situations where fewer symmetry operators are applicable, it may be necessary to achieve the required level of over-sampling through repeated measurement of the crystal utilizing distinct rotation axes.

7. Outlier removal protocol

In situations where data are prone to systematic errors it is often useful to implement some method of outlier removal, where individual observations that are distant from the mean are excluded. In 3D-ΔPDF experiments, systematic errors can arise due to detector blooming/afterglow, small crystal impurities and/or shot noise in the detector. Outlier removal has been successfully applied in 3D-ΔPDF data-reduction protocols previously, specifically at the symmetry-averaging step (Sangiorgio *et al.*, 2018; Holm *et al.*, 2020). Here, we have utilized outlier removal at three distinct steps of data processing: when transforming from detector to reciprocal space, during merging of distinct data sets and during symmetry averaging. Outlier removal effectively entails first computing the mean intensities and their standard deviation for each voxel bin in reciprocal space, and then subsequently recomputing the means after the outlier values are removed using an outlier exclusion criterion. During each of the above-mentioned steps of data processing we have chosen to exclude, as an outlier, any observation that falls outside a two standard deviations window around the mean. We have elected to use the mean rather than the median (Blessing, 1997) such that the required system memory and computation times are reduced by an order of magnitude to tractable ranges. Whenever possible the median is preferred, as the mean can be strongly biased if there are strong outliers. The impact of outlier removal is distinct at each of the three averaging steps where it was applied.

Example slices of reciprocal space where the data transformation from detector to reciprocal space was done with either just standard averaging or with outlier removal are shown in Fig. 11(*a*) and (*b*), respectively. The panel insets show some moderate improvements. The Q_z of each slice was chosen to demonstrate the maximum difference between outlier removal/inclusion. The primary effect is to decrease the intensity of some features that may be considered spurious. At the data-reconstruction step, data points subject to outlier removal are individual detector pixel intensities. Thus outlier removal serves to screen out pixels that are inconsistent with the mean of associated voxel to which the pixel is mapped. For this reason, outlier removal at the data-reconstruction step does not create large regions of differences when comparing Fig. 11(*a*) and (*b*), but rather isolated individual voxel changes.

Shown in Fig. 11(*c*) and (*d*) are the effects of merging data with either standard averaging or with outlier removal averaging, respectively. In this case, the insets show a significant difference, with the intensity of many streak-like features diminished after outlier removal. These features are associated with detector blooming/afterglow, and their diminished prevalence in Fig. 11(*d*) suggests that outlier removal during data merging offers a considerable benefit.

Lastly, Fig. 11(*e*) and (*f*) show the effect of symmetrization with either standard averaging or with outlier removal, respectively. The panel insets show moderate improvement; those on the left show a remedy of dark regions arising from data-set edge effects (regions around the beam-stop support that create holes in reciprocal space). The upper-right panel shows a subtle reshaping of diffuse peaks, while the lower-right panel shows the removal of a spurious peak-like feature in the vicinity of a diffuse peak.

8. Removing Bragg intensity

At this point in the reduction process (see Fig. 1) there are two possible directions leading to direct-space data (Weber & Simonov, 2012). The first is to compute the total 3D-PDF by performing a Fourier transform of the full reciprocal-space data, and the second is to separate the components of scattering corresponding to the ordered average structure (Bragg scattering) and to the deviations from it (diffuse scattering), leading to the 3D-ΔPDF.

Computing the 3D-ΔPDF from the reciprocal-space intensity distribution requires removal of any Bragg peak contribution while retaining all diffuse signal contributions. This is typically called 'punch and fill' and a number of procedures have been outlined for the process, including filling with average intensity values (Kobas *et al.*, 2005), convolution-based filling adopted from the astrophysics community (Krogstad *et al.*, 2020), and even a structure-model independent approach based on statistical outlier detection (Weng *et al.*, 2020).

Practically speaking, 'punch and fill' involves locating Bragg peaks, removing them from the data, and filling in any and all diffuse intensity removed by punching, which can include both broad and sharp features. The filling process effectively represents an attempt to best compensate for the removed part of the diffuse signal at the locations of punched Bragg peaks. It can be carried out in the raw detector images, or within the reciprocal-space intensity distribution, but most techniques require knowledge of the crystal orientation, unit-cell dimensions and space group, as this information is necessary and sufficient to locate and remove all (and only) Bragg peaks. Within this work, we have elected to operate on the reciprocal-space intensity distribution, although this choice does not change the generality. Generally, any three-dimensional shape can be used to remove Bragg intensity from the data. In situations where the instrument resolution leads to Bragg peaks that are significantly anisotropic in crystal reciprocal space (or detector space) (Weber & Simonov, 2012), it may be useful to adopt an anisotropic punch shape. In this study, we found that Bragg peaks, which were on average about three orders of magnitude more intense than the observed diffuse features, were largely isotropic with a full width at half maximum (FWHM) spanning at most 1.5 voxels (0.09 Å^{-1}) (see *e.g.* Fig. 2 and the supporting information). For this reason we adopted here an isotropic spherical voxel punch.

The size of the voxel punch is relevant, as a punch that is too large can remove important features in close proximity to Bragg peaks, often corresponding to long-range features in direct space, while a punch that is too small can leave behind Bragg intensity tails. In our work, we have tested three
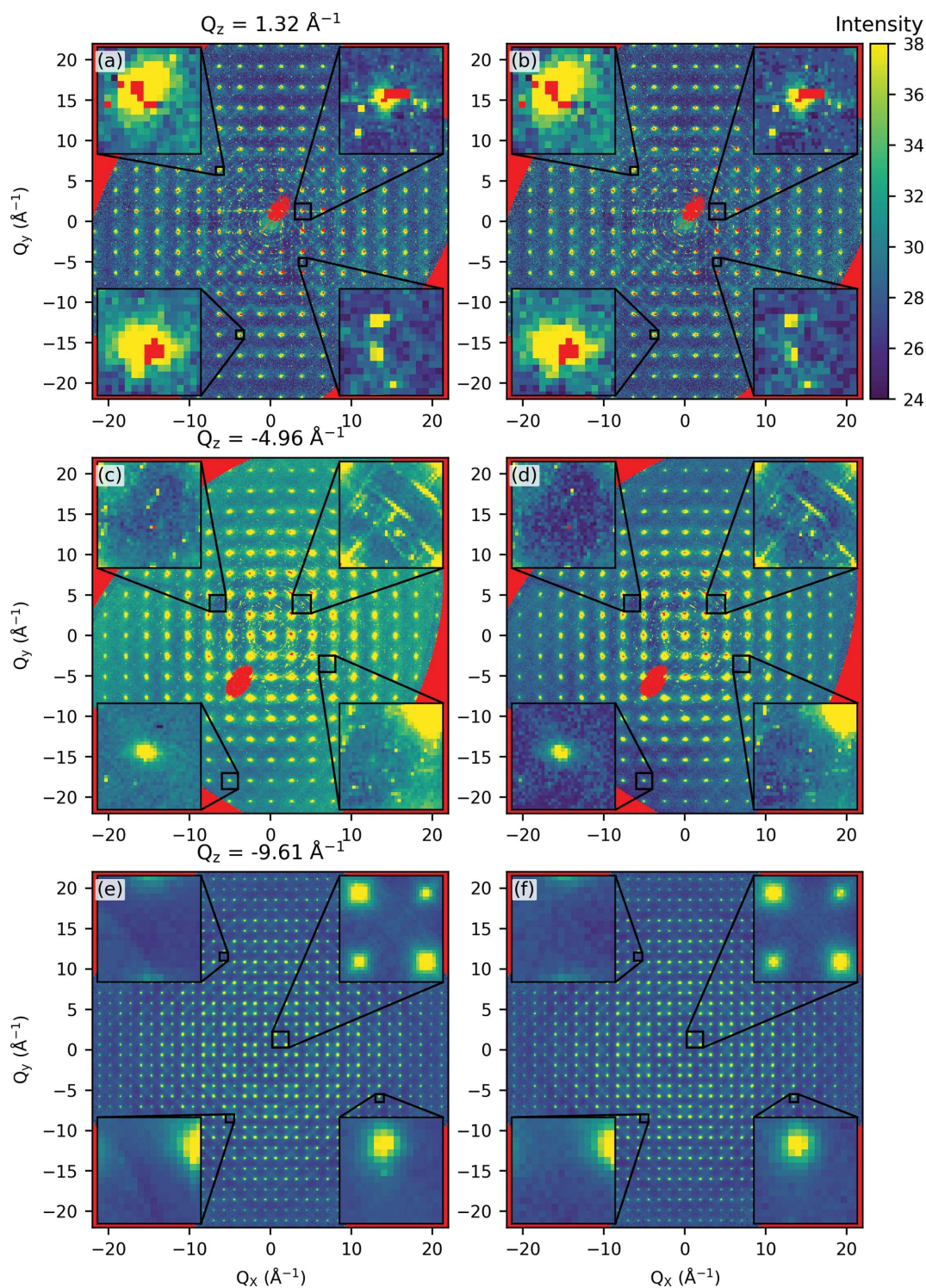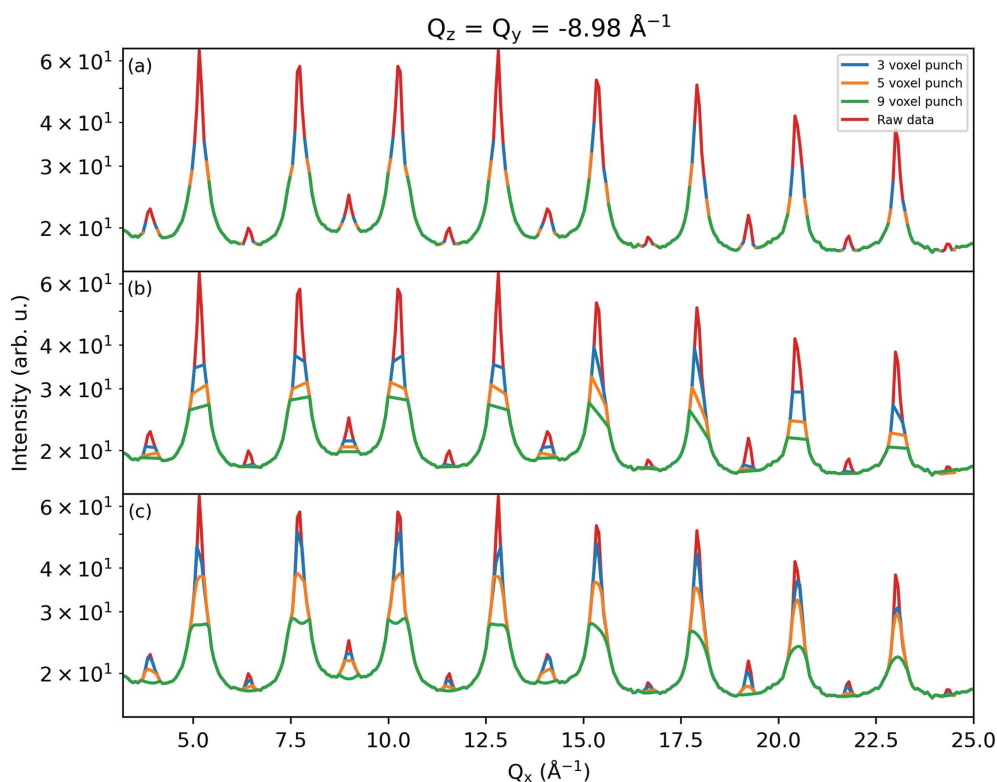
Figure 11
Outlier removal. Intensity maps of a representative slice of reciprocal space at different stages of data processing without (*a*, *c*, *e*) and with (*b*, *d*, *f*) outlier removal for (*a*, *b*) the process of reconstructing from detector to reciprocal space, (*c*, *d*) merging data with different exposure times and crystal rotation step sizes, and (*e*, *f*) applying symmetry averaging. Each plot contains insets showing enlarged scales for features of interest.

different punch sizes, with a diameter of either 3, 5 or 9 voxels, spanning 0.189, 0.315 or 0.567 Å^{-1}, respectively. For Gaussian peaks, 3, 5 or 9 voxels correspond to a removal of 98.7, 99.996 and essentially 100% of the total peak area, respectively. For each reciprocal-space data set, we have computed the location within the associated data array of all Bragg peaks based on both the known crystal unit-cell size/shape and the associated data array Q step. We have applied a punch at this location, which is computationally handled by setting array values inside the punch to 'not a number' (NaN) to mark the locations for subsequent filling. Examples of the punch effect in a line scan of intensity in reciprocal space are shown in Fig.

Figure 12
Bragg punch size as seen from a line-scan perspective. (a) A line scan through a slice of reciprocal-space intensity, demonstrating the effect of punch sizes of 3, 5 or 9 voxels spanning 0.189, 0.315 or 0.567 Å^{-1}, respectively. The associated linear interpolation (b) or DCT (c) filling. Note that all data are plotted on a log scale to highlight both Bragg and diffuse features. The plotted raw data represent reciprocal space intensity, without punching.

12(a), while similar examples for a slice of reciprocal space intensity are shown in the lower-right quadrants of Fig. 13(a, c, e).

Once all Bragg peaks have been punched from the data, a suitable filling or interpolation algorithm must be chosen so as to replace any diffuse intensity co-located with the punched Bragg peaks. In the case considered here, where we have elected to operate on the reciprocal-space intensity distribution, our filling algorithm must be capable of interpolating a three-dimensional function. In situations where the diffuse intensity surrounding and underneath the Bragg peaks is relatively flat or broad, simple linear or quadratic interpolation may be sufficient. It is clear however that the diffuse intensity distribution within the data shown in Fig. 12(a) contains peak-like features centered at the location of Bragg peaks, although the diffuse peaks are significantly broader and an order of magnitude less intense (see e.g. Fig. 10). In this situation, linear interpolation may be insufficient.

Here, we have tested two simple filling techniques and a third more complex technique. For the simpler approaches, punched portions of reciprocal space were filled either with zero intensity or by using linear interpolation. As a more complex approach, we have adopted an algorithm typically used when handling large three-dimensional geophysical data sets (Wang et al., 2012). This approach fills gaps by iteratively updating a reconstructed, gapless data set with weighted residuals propagated through inverse and forward discrete cosine transforms (DCTs). It has been found to produce a

global normalized error of less than 5×10^{-5} in test data sets (Garcia, 2010).

To investigate the result of our punch and fill tests, we again look at line scans of the reciprocal-space intensity distribution under a number of situations, shown in Fig. 12. The result of filling these punched data with linear interpolation are shown in Fig. 12(b), while the use of an iterative DCT interpolation algorithm is shown in Fig. 12(c). The trivial case of zero filling is not shown.

As expected, linear interpolation creates clear discontinuities in the slope of the filled intensity distribution, apparent in intensity line scans [Fig. 12(b)]. These discontinuities are less apparent in the maps of reciprocal-space intensity shown in the upper-right quadrants of Fig. 13(a, c, e), probably because they are obscured by the narrow color scale, which was chosen to highlight weak features.

Conversely, the DCT filling routine largely preserves the peak-like feature underneath the Bragg peak upon filling, as can be seen in Fig. 12(c). The relative intensities of these diffuse peaks are also preserved, with the largest difference being within the absolute intensities of this peak. We do note that filling of the largest 9-voxel punch does lead to some anomalous 'crater'-like features, suggesting that this punch is perhaps too large, or that the iterative DCT filling routine has failed to converge in some situations.

Ultimately, the most important aspect of the punch and fill process is the impact on the full 3D-ΔPDF itself, and as such we will visit this topic here even if the Fourier transform processing step will not be introduced until the next section.
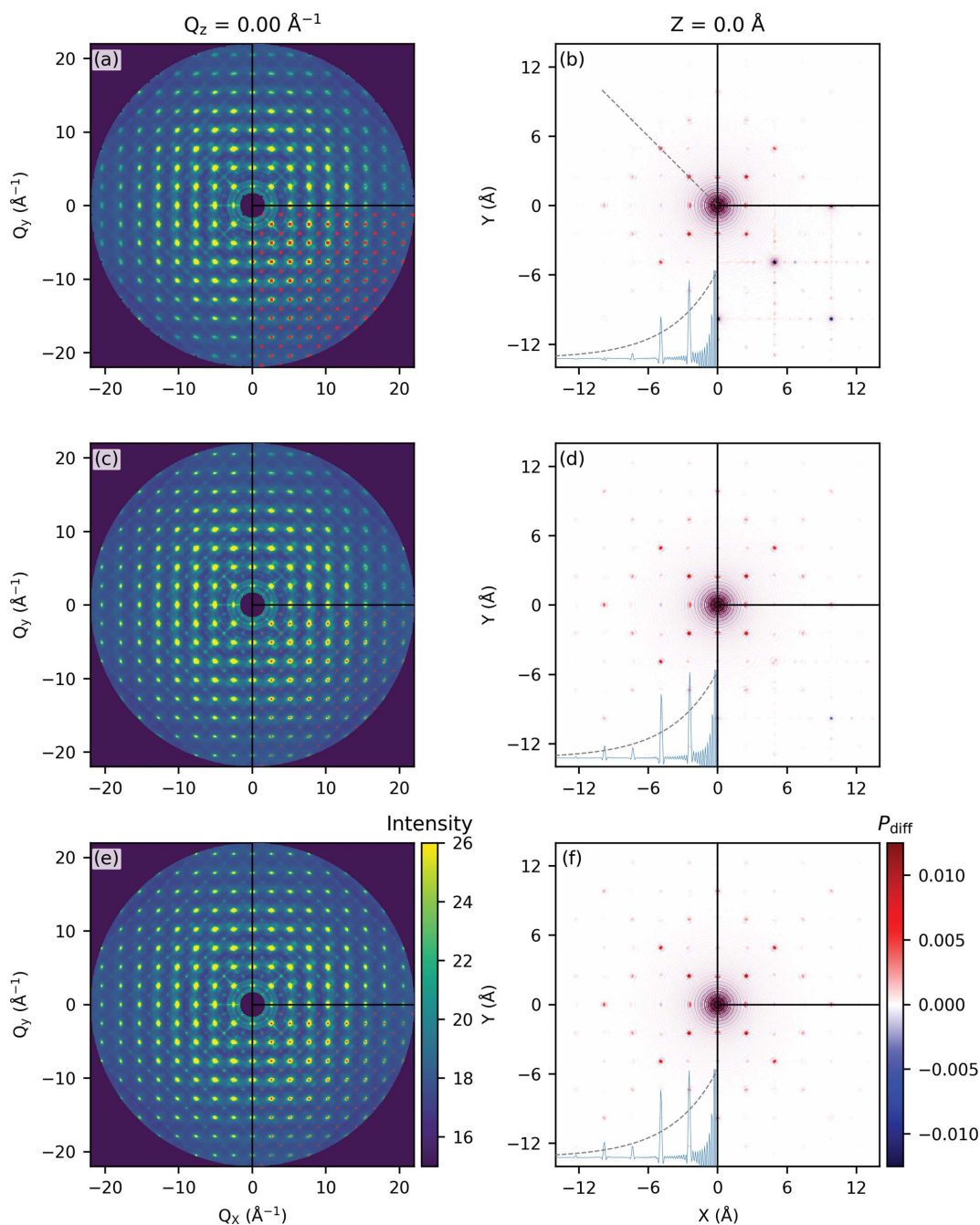
Figure 13
The choice of Bragg peak punch size. Representative slices of reciprocal space and associated slices of the 3D-ΔPDF after punching and filling with a punch size of (a, b) 9 voxels, (c, d) 5 voxels and (e, f) 3 voxels. The lower-right quadrants of (a, c, e) show the punch used in red, while the upper-right quadrants show the result of a linear interpolation filling and the left halves show the result of a DCT interpolation filling. The lower-right quadrants of (b, d, f) show the 3D-ΔPDF result of filling punched areas uniformly with zero, while the upper-right quadrants show the result of a linear interpolation filling and the left halves show the result of a DCT interpolation filling. Inset in the lower-left corners of (b, d, f) are 3D-ΔPDF profiles along the ⟨110⟩ direction depicted by the dashed straight line in (b). Each inset is plotted on an identical scale, and contains an identical but arbitrary exponential decay curve for comparison. Differences observed across punch sizes and/or filling technique are discussed in the text.

The result of varying the punch size and filling approach is shown in representative reciprocal-space intensity maps and the associated 3D-ΔPDFs in Fig. 13. Also shown in Fig. 13(b, d, f) for quantitative comparison are line scans along the ⟨110⟩ direction depicted by the dashed straight line in panel (b). Each line scan is superimposed with an identical exponential decay curve (dashed line) so that the relative heights of the 3D-ΔPDF features can be compared.

Clearly in our example, the choice of punch size has little qualitative impact on the final 3D-ΔPDFs when combined with an iterative DCT filling routine, as each contains the same key features. The line scans shown inset in Fig. 13(b, d, f) reveal that there are subtle quantitative differences in the relative intensities of the 3D-ΔPDF features when moving from the largest (9-voxel) punch to the intermediate (5-voxel) punch. Specifically, features decay more quickly as a function

of pair distance in the 3D-ΔPDF associated with the 9-voxel punch. Coversely, the feature decay rate is preserved when comparing the intermediate (5-voxel) and smallest (3-voxel) punch. With the exception of the small feature at 10 Å along the ⟨110⟩ direction, the relative intensities of these features are otherwise largely unchanged.

Given the subtle quantitative differences that can arise due to variations in punch size, one should note the aim of the 3D-ΔPDF study prior to setting out on measurement and data reduction. If a qualitative appraisal, based on *e.g.* the presence/absence of certain features, or the relative signs of two or more related features (Schaub *et al.*, 2007), is the goal, analysis may not be particularly sensitive to punch size and filling algorithm.

If detailed quantitative analysis is required, where the relative intensity and/or decay rate of features as a function of pair distance is critically important (Holm *et al.*, 2020), the choice of punch size may critically alter interpretation, especially in cases where diffuse features are peak-like and co-located with Bragg peaks in reciprocal space. A strategy for choosing a punch size could be to begin with a punch significantly larger than the instrumental resolution, such that some diffuse features are also removed. If the punch is gradually decreased in size, these diffuse features will be restored and the associated 3D-ΔPDF will change. In a continuum of gradually decreasing the punch size, one could seek an ideal point where further marginal decreases in punch size do not produce substantial changes in the observed 3D-ΔPDF. Naturally, further large decreases in the punch size beyond this ideal point would begin to admit Bragg intensity, showed by large changes in the 3D-ΔPDF. Additionally, one can investigate the obtained 3D-ΔPDF to be sure that the features obtained when using a punch of a given size are physically consistent with the average atomic structure (Schaub *et al.*, 2007; Holm *et al.*, 2020).

9. Fourier transform

Once a satisfactory reciprocal-space intensity distribution has been obtained and the Bragg intensity removed, obtaining the full 3D-ΔPDF requires applying a discrete Fourier transform. As the intensity distribution is a real-valued even function (it obeys inversion symmetry), its Fourier transform is also a real-valued even function, and as such only the real part of the Fourier transform is non-zero.

9.1. Window function

Following detector-to-reciprocal-space remapping, data merging and the application of all symmetry operations, the filled portion of reciprocal space is often irregular. In order to avoid the appearance of problematic Fourier effects, it is helpful to apply a window function to the reciprocal-space intensity distribution prior to applying the discrete Fourier transform. Many options for this exist, including filling the area outside a given radius with a constant intensity value (Roth & Iversen, 2019; Krogstad *et al.*, 2020). Choosing this

intensity value can be problematic however, and can cause discontinuities in the reciprocal-space intensity which will manifest as artifacts in the 3D-ΔPDF. An extreme case of this is shown in Fig. 14(*a*), where data beyond a scattering vector magnitude of 21 Å^{-1} have been set to zero, effectively representing a hard-sphere window function. In Fig. 14(*b*) we show the resulting 3D-ΔPDF from this hard-sphere window function, which is heavily impacted by the window-function ripples, observable as concentric circles in the figure, superimposed over the origin. These ripples propagate far into the 3D-ΔPDF, effectively corrupting the features nearest and second nearest to the origin. Similar plots resulting from filling beyond 21 Å^{-1} with non-zero values, selected as the median intensity between 20.5 and 21 Å^{-1}, are also shown in Fig. 14(*c*, *d*). This can remedy the Fourier ripples somewhat, but selecting this non-zero constant filling is rather arbitrary.

The alternative adopted here is the application of, through point-wise multiplication, a modified Lorch function L_1 with the formula (Soper & Barney, 2012)

$$L_1(Q, \Delta_1) = [3/(Q\Delta_1)^3](\sin Q\Delta_1 - Q\Delta_1 \cos Q\Delta_1), \quad (3)$$

where Q is the magnitude of the momentum transfer scalar and Δ_1 is the smearing radius in reciprocal space, here taken as 21 Å^{-1}. A similar approach is sometimes used in the powder total-scattering community when computing the full 1D-PDF (Lorch, 1969; Soper & Barney, 2011). An example of the application of this damping window function to our reciprocal-space intensity distribution is shown in Fig. 14(*e*). Here, it can be seen that the intensity decreases uniformly towards zero at the boundary of reciprocal space. The 3D-ΔPDF resulting from the application of this damping window function is shown in Fig. 14(*f*). Notably, the ripples present in Fig. 14(*b*) have been effectively mitigated, yielding a clearer picture of the features nearest and second nearest to the origin. Although it is known that the application of such a damping window function does reduce the effective resolution of the data, we can see from Fig. 14(*f*) that even after its application, we can still resolve each individual 3D-ΔPDF feature. If fine resolution may be required, one should naturally carefully compare the filtered and unfiltered 3D-ΔPDF.

10. Robustness

Given that this work has taken great length to expand upon many of the steps in obtaining the 3D-ΔPDF, it is worth questioning the robustness of this approach, not only against errors or omissions in data collection and processing, but also against a variation in observations between physically unique samples of a given material.

10.1. Data-processing sequence

In general, raw detector images that have been dynamically masked to mitigate the effects of detector afterglow and blooming, background subtracted, corrected for interframe scale fluctuation effects, and transformed to crystal reciprocal space can subsequently be processed in any number of ways.
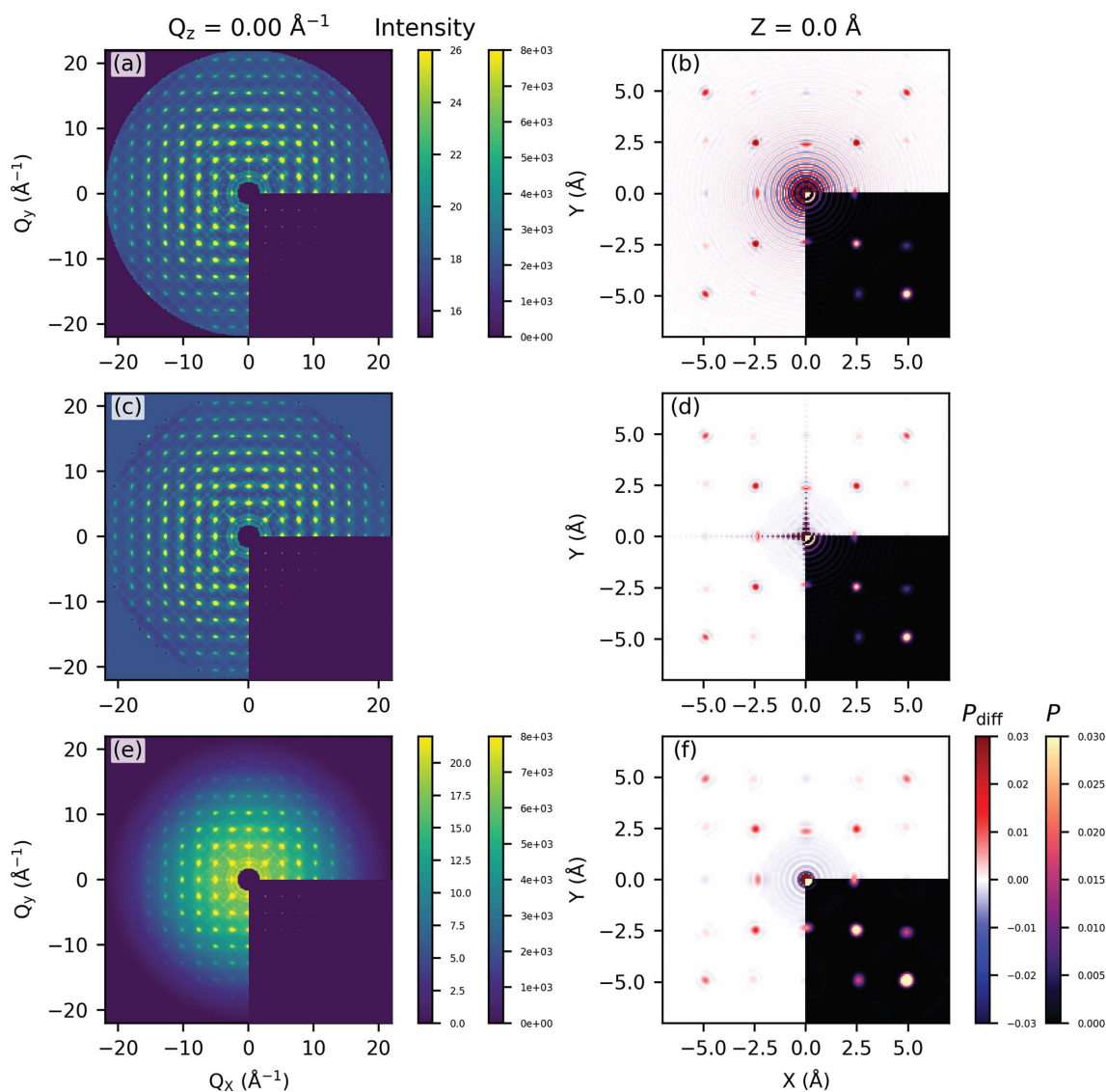
Figure 14
Application of a damping window function. Representative slices of reciprocal space and an associated slice of the 3D-ΔPDF (*a*, *b*) as processed, (*c*, *d*) after filling beyond Q_{max} with a constant value as described in the text and (*e*, *f*) after the application of the damping window function as described in the text. The lower-right quadrants of (*a*, *c*, *e*) and (*b*, *d*, *e*) show the result of retaining all Bragg peaks in reciprocal space and the associated full 3D-PDF, respectively. The primary impact is the reduction of Fourier transform termination ripples, as can be seen in panel (*f*).

With the only requirement that punching and filling of Bragg peaks occurs prior to discrete Fourier transform, merging multiple data sets, applying symmetry operations and removing Bragg intensity can be done in any order. The merging and the application of weighted symmetry averaging can also be applied to the 3D-ΔPDF itself, as it should adhere to the same point symmetry as the reciprocal-space intensity distribution.

Given that the choice of workflow ordering is largely arbitrary, it is interesting to explore the extent to which the 3D-ΔPDF is reproducible across different orderings of the data-processing steps. To investigate this, we have tested all possible permutations of data-processing steps, each with the three distinct Bragg peak punch sizes outlined in Section 8. The reciprocal-space intensity distributions and 3D-ΔPDFs resulting from a subset of these permutations are shown in Fig. 15. Remarkably, both the reciprocal-space intensity distribu-

tions and 3D-ΔPDFs are quite robust against variations in workflow ordering, being qualitatively identical. Quantitatively, these reciprocal-space intensity distributions show an average and maximum R_{diff} of 0.2% and 1.0%, respectively. While this may not be surprising, it is encouraging to note that the final 3D-ΔPDF is largely invariant under these conditions.

10.2. Crystal variation and mounting

3D-ΔPDF analysis relies on detection of quite subtle features within the reciprocal-space intensity distribution. Given this, it is interesting to explore the extent to which these subtle features are reproducible between repeated measurements of distinct crystals of the same material. To address this matter, we have measured the full reciprocal-space intensity distribution from two distinct $CuIr_2S_4$ crystals. These samples are of comparable quality and show identical physical prop-
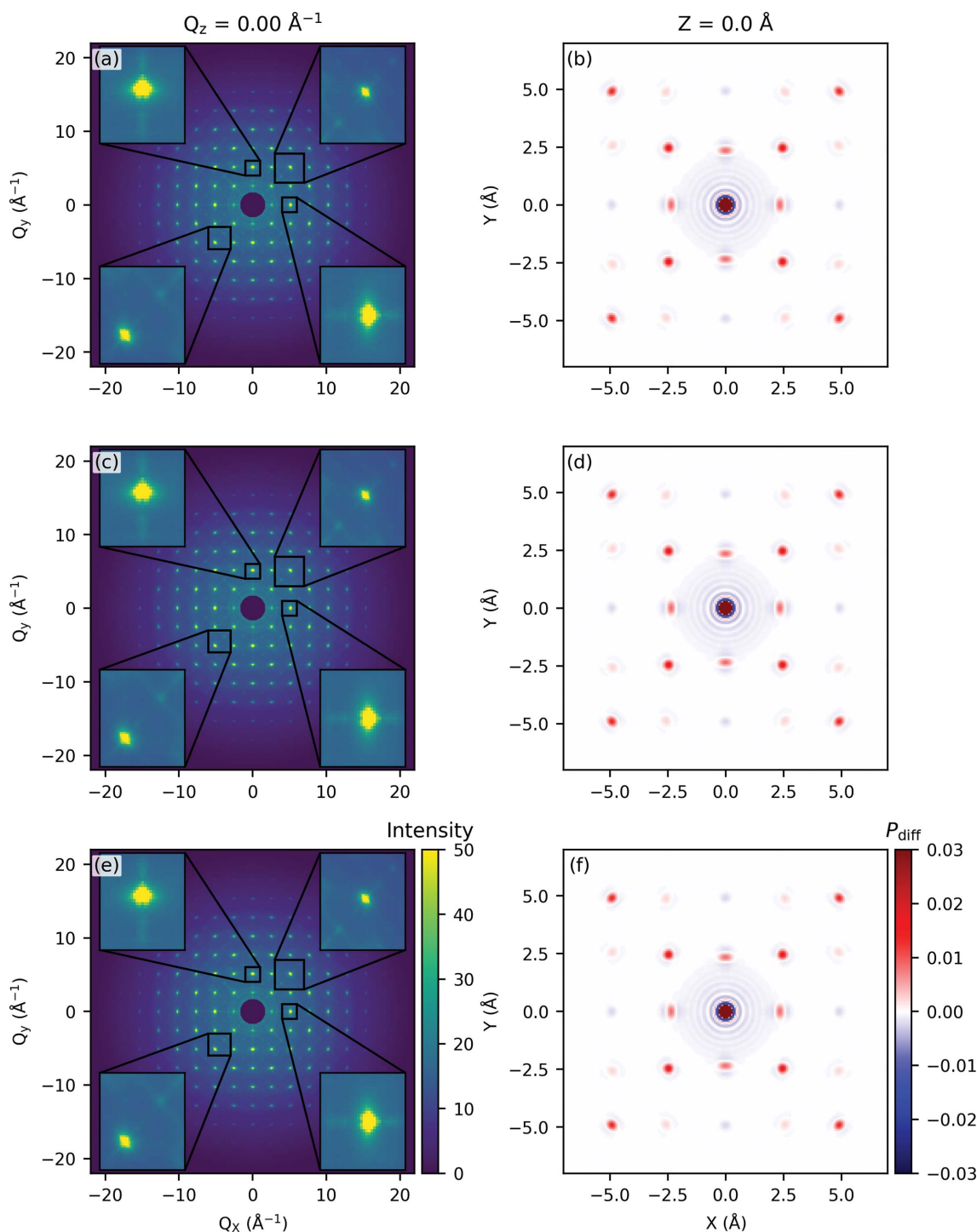
Figure 15
The role of workflow ordering on the final intensity distribution and 3D-ΔPDF. Representative slices of reciprocal space and an associated slice of the 3D-ΔPDF when varying the ordering of the data-processing steps. A few regions of interest in reciprocal space are shown inset on an enlarged scale. (*a*, *b*) Data were symmetrized, different exposure times were merged, punched, filled and then Fourier transformed. (*c*, *d*) Data were symmetrized, punched, filled, Fourier transformed and then different exposure times were merged. (*e*, *f*) Data were punched, filled, symmetrized, different exposure times were merged, and then Fourier transformed. Visually, the difference is nearly impossible to detect within the reciprocal-space maps.

erties. Their primary difference from the experimental standpoint are slightly different physical dimensions and a distinct crystal orientation dictated by the random mounting process. A representative reciprocal-space map and the 3D-ΔPDF from each sample are shown in Fig. 16. When comparing the two samples, we note only slight variations in

the persistence of streaking in the reciprocal-space intensity distributions, visible within the insets of Fig. 16(*a*, *c*). This is likely to be due to variations in the effectiveness of our dynamic masking heuristic between the two physically distinct crystals. Quantitatively, the two intensity distributions show $R_{diff} = 0.1\%$, comparable to the mean value obtained by
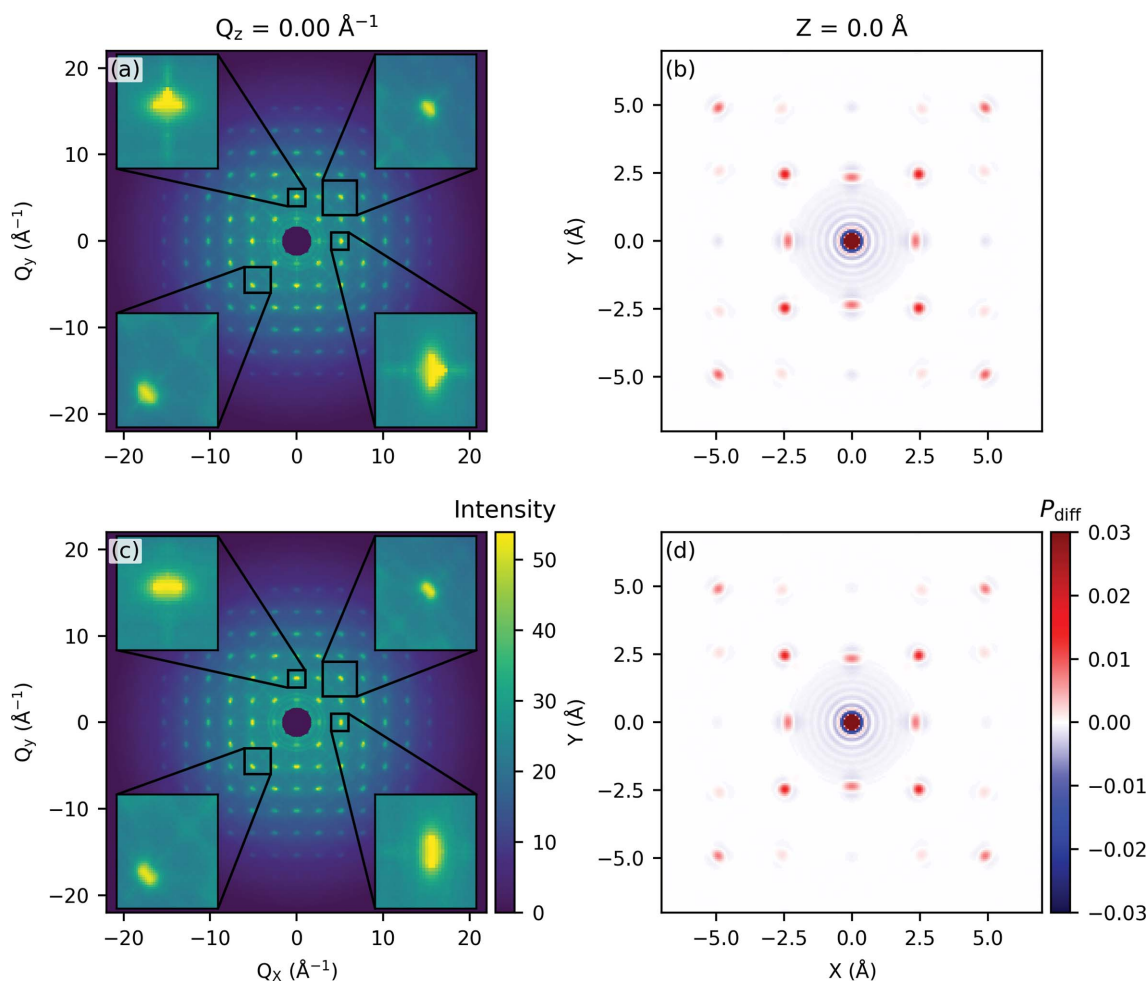
Figure 16
Sample-to-sample reproducibility in the final intensity distribution and 3D-ΔPDF. Representative slices of reciprocal space and an associated slice of the 3D-ΔPDF measured and processed from distinct $CuIr_2S_4$ crystals. A few regions of interest in reciprocal space are shown inset on an enlarged scale. (*a*, *b*) Data collected and processed from the single crystal of $CuIr_2S_4$, sample 1, featured throughout the manuscript. (*c*, *d*) Data collected and processed from sample 2, a different single crystal of $CuIr_2S_4$. Both the reciprocal-space maps and the 3D-ΔPDFs are nearly identical, demonstrating the reproducibility of the technique.

varying the order of data-reduction steps. Despite these small variations in reciprocal space, we observe nearly no differences in direct space. This demonstrates that the technique is quite robust against sample-to-sample variation imposed by crystal size or mounting. It is worth noting that crystal orientation as it pertains to mounting may become relevant when dealing with low-symmetry systems and/or a limited rotation angle during measurement. In these cases, care must be taken to orient and rotate the crystal so as to cover all of reciprocal space within the desired Q range, and measurement along multiple rotation axes may be necessary.

10.3. Variably processed data

Our results thus far suggest that both the reciprocal-space intensity distribution and the 3D-ΔPDF measured from a given material are robustly reproducible in a number of situations. As a final test, we envision several hypothetical scenarios for both measurement and data processing for a single data set with minimal counting of 0.1 s per frame, with

no interframe scale correction or background subtraction, where outliers have been included in all steps, and a small (3-voxel) Bragg punch has been applied. We have tested three permutations of this processing. First, we have used only linear filling at the location of punched Bragg intensity, and omitted both the relevant symmetry operations and any dynamic masking. This represents the most pessimistic case. Second, we have used DCT filling of punched Bragg intensity, and included the relevant symmetry operations, but omitted any dynamic masking. Third, we have used DCT filling, have included dynamic masking, and applied the relevant symmetry operations so as to ensure that the reciprocal-space intensity distribution fully fills our voxel map.

Representative slices of the reciprocal-space intensity distributions and the associated 3D-ΔPDFs are shown in Fig. 17. In the worst case, shown in panels (*a*, *b*) with linear filling and without symmetrization or dynamic masking, both the reciprocal-space intensity distributions and 3D-ΔPDFs show spurious features. The lack of symmetry averaging has produced a reciprocal-space intensity distribution that does
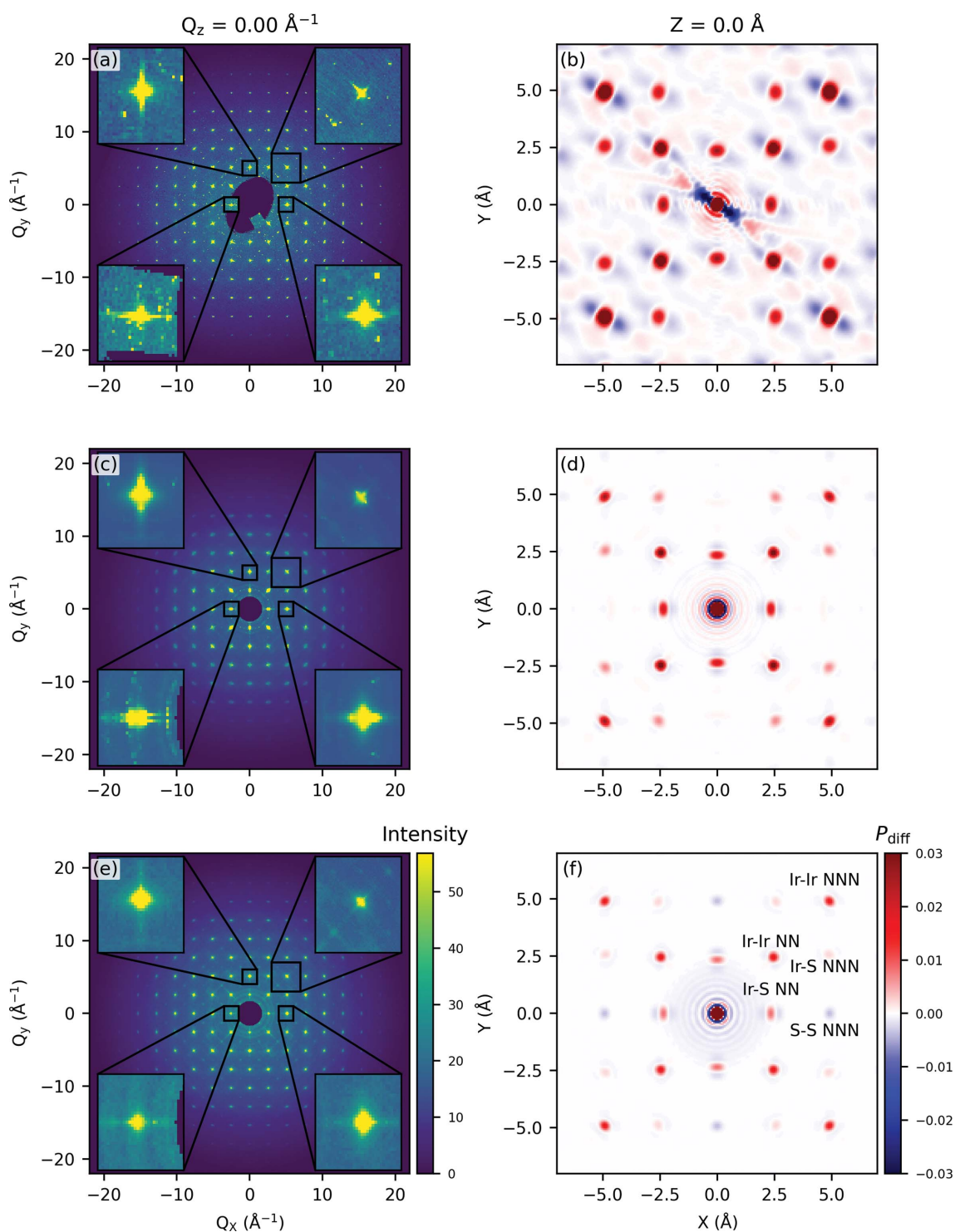
Figure 17
Variably processed data sets. (*a*, *c*, *e*) Representative slices of reciprocal space and (*b*, *d*, *f*) the associated slices of the 3D-ΔPDF which have been taken through fewer data-processing steps. A few regions of interest in reciprocal space are shown inset on an enlarged scale to emphasize the differences associated with each level of processing. Data in (*a*, *b*) represent one single full crystal rotation, with an exposure time of just 0.1 s per frame, where both dynamic masking and symmetry averaging have been omitted. Data in (*c*, *d*) have undergone the full extent of data processing (merging exposure times, symmetry averaging), but have not undergone dynamic masking. A 3-voxel punch and DCT fill process was used, with a Lorch window function prior to Fourier transformation. Data in (*e*, *f*) represent one single full crystal rotation, with an exposure time of 0.1 s per frame. In this case, data have been remapped to reciprocal space after dynamically masking, have undergone symmetry averaging and a 3-voxel punch and linear fill process, with a Lorch window function prior to Fourier transformation. In all cases, no background subtraction or interframe scale corrections have been applied. Observations regarding these different processing pathways are discussed in the text.

not uniformly fill **Q** space. It is clear from the insets in Fig. 17(a) that, without dynamic masking, there is substantial streaking still present in the diffracted intensity distribution. Additionally, ring-like collections of parasitic Bragg peaks, previously removed by our dynamic masking, are again now visible near the origin in Fig. 17(a). Compared with a fully processed data set, the intensity distribution in Fig. 17(a) gives an excessively large $R_{diff} = 143\%$.

The 3D-ΔPDF associated with this intensity distribution, shown in Fig. 17(b), is characterized by strong unphysical artifacts with the same intensity scale as the relevant atom-pair features. This is likely to be due to both the incomplete nature of the reciprocal-space data set and also the spurious features not removed by dynamic masking. This scenario is only marginally similar to those shown in e.g. Fig. 16, suggesting that this would not be useful even for a cursory screening of the presence of local distortions.

The reciprocal-space intensity distribution and associated 3D-ΔPDF shown in Fig. 17(c, d) represent a significant improvement over those shown in Fig. 17(a, b). These data were processed similarly, with symmetry averaging included, and with DCT rather than linear filling. In both cases, dynamic masking was excluded. Notably, the inclusion of symmetry averaging has produced a reciprocal-space intensity distribution that does uniformly fill **Q** space. It has also mitigated some spurious features, which can be seen when comparing the upper-left insets of Fig. 17(a) and (c). Unfortunately, as dynamic masking was not included, streaking is still present, and symmetry averaging has actually compounded the issue. This is apparent when comparing the upper-right or lower-left insets of Fig. 17(a) and (c), where streaks have been clearly propagated by symmetry averaging. Additionally, ring-like features are actually exacerbated by symmetry averaging. Compared with a fully processed data set, the intensity distribution in Fig. 17(c) gives $R_{diff} = 89\%$, a significant improvement over that shown in Fig. 17(a), but still rather large.

The 3D-ΔPDF associated with this intensity distribution is shown in Fig. 17(d). The inclusion of symmetry averaging has substantially improved the appearance of the 3D-ΔPDF when compared with that in panel (b). Indeed, when compared with the 3D-ΔPDFs shown in e.g. Fig. 16, both contain the same features, and the general properties of each features are retained. Some spurious features however do remain, with significant quantitative differences, and there appear to be ring-like features superimposed, likely to be due to the ring-like features in the reciprocal-space intensity distributions.

Fig. 17(e, f) shows the results when dynamic masking is added to the processing steps that produced the data shown in Fig. 17(c, d). The insets in panel (e) suggest that the inclusion of dynamic masking when transforming from detector to reciprocal space (prior to merging or symmetry averaging) significantly reduces the streaking and parasitic ring-like scattering seen in Fig. 17(a, c). Remarkably, in this case, the 3D-ΔPDF shows intense, well resolved features. Indeed, the reciprocal-space intensity distributions and 3D-ΔPDFs for the case including dynamic masking in Fig. 17(e, f) are both

qualitatively identical to those shown in e.g. Fig. 16(a, b), where quite extensive data processing has been conducted. Although qualitatively identical, the intensity distribution in Fig. 17(e) gives $R_{diff} = 54\%$ when compared with a fully processed data set. This represents a significant improvement over that shown in either Fig. 17(a) or (c), but may be too large for useful quantitative analysis.

Nonetheless, with an exposure time of just 0.1 s per frame and a rotation step size of 0.1°, the data shown in Fig. 17 were collected in about 6 minutes. This result implies that the qualitative features present in the 3D-ΔPDF can be reproducible even under the non-ideal conditions and with marginal data processing, and that, while all the data-processing steps discussed herein contribute to a clean 3D-ΔPDF, some steps, such as dynamic detector masking, are more essential than others. Of course, it is always the aim to collect data of as high quality as possible, but this can unfortunately come at the expense of efficient utilization of resources, which could be more effectively spent probing additional states of the system (e.g. temperature dependence) or even other systems. It is thus advantageous to know the point at which diminishing returns are achieved when collecting and/or processing 3D-ΔPDF data.

It is important to point out here that these pessimistic scenarios were partially successful in the $CuIr_2S_4$ case, but that more complex systems may present additional challenges, requiring full data processing to garner usable data. Related to this, the use of different 2D detectors may yield different results, especially if the detector benefits from additional dynamic range. That being said, even large improvements in dynamic range are unlikely to eliminate all detector artifacts, and some improved detectors create new issues. For example, spatial module gaps in the PILATUS series of detectors (Broennimann et al., 2006; Kraft, 2010) create further holes in reciprocal space, where symmetrization, merging of distinct data sets with slightly different detector positions (Roth & Iversen, 2019; Davenport et al., 2019; Holm et al., 2020; Krogstad et al., 2020) and/or crystal rotation around multiple axes are of increased importance. A blooming-like effect has also been reported in these more modern detectors (Krogstad et al., 2020), underscoring the need for a continuing discussion on measurement artifacts.

10.4. Material-specific observations

Finally, we explore some qualitative observations regarding the 3D-ΔPDF that are specific to the $CuIr_2S_4$ system. We note that a full quantitative analysis will be the subject of subsequent work, and requires a full description of any and all disorder present in the long-range average structure to which the 3D-ΔPDF is referenced, including e.g. anisotropic atomic displacement parameters and atomic coordinates/occupancies. Care must be taken to check that any interpretation is consistent with this full description of the long-range average structure, as the 3D-ΔPDF can be misinterpreted in some cases. The following is based on an assumed, minimally disordered, description of the long-range average structure
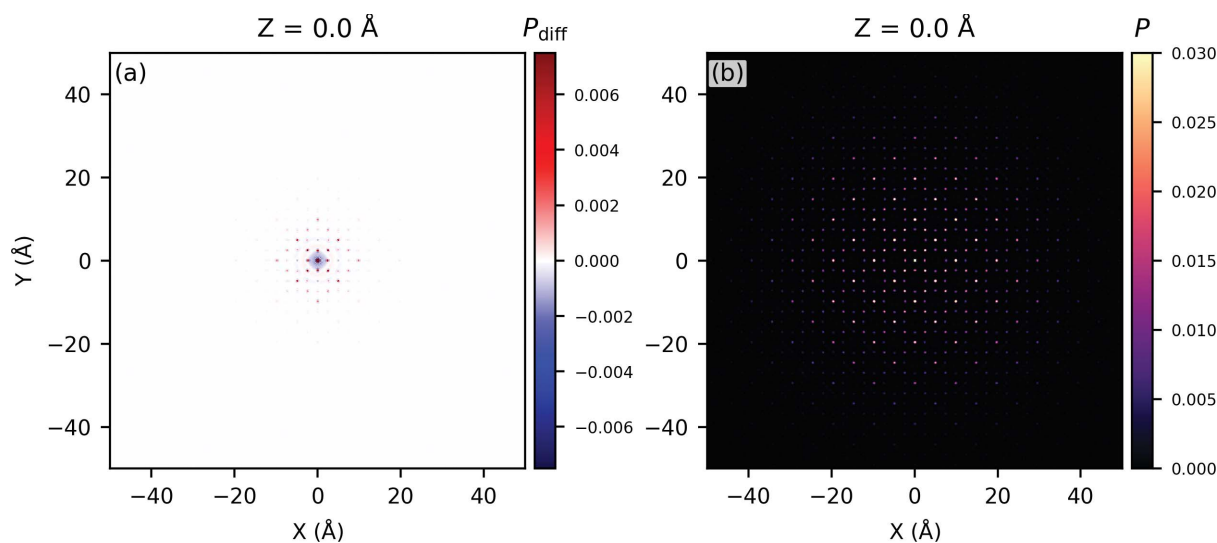
Figure 18

3D-PDF and 3D-ΔPDF data. (*a*) A representative fully processed slice of the 3D-ΔPDF, where DCT filling and a 5-voxel punch was used. Note that the majority of the signal decays to zero by $r = 10$ Å, suggesting that any deviation between the local and long-range structure has a finite correlation length in direct space. In the $CuIr_2S_4$ system, 10 Å corresponds to about one unit cell. (*b*) A representative fully processed slice of the full 3D-PDF, obtained by retaining the full reciprocal-space intensity distribution (not removing Bragg peaks). Note that the majority of the signal decays to zero by $r = 35$ Å, highlighting the effect of finite **Q**-space resolution. To emphasize weak features, color scales in both panels are adjusted such that the strong features at shorter interatomic vectors are saturated.

published in the literature (Bozin *et al.*, 2019). In Fig. 17(*f*) we label a few selected interatomic vector contributions for the $Z = 0$ cut of the 3D-ΔPDF. This labeling is not exhaustive, and pairs that do not demonstrate obvious connectivity [*i.e.* Cu–Cu nearest neighbor (NN) pairs that exist in separate CuS_4 tetrahedra] are not labeled. The strongest observed contributions to the differential are due to Ir–Ir NN and next-nearest neighbor (NNN) pairs along the ⟨110⟩ family of directions. This is not surprising, as Ir is the strongest scatterer in the system and the nature of the local distortion involves predominantly the Ir substructure (Bozin *et al.*, 2019), where strong bonding is present. Importantly, the same cut also shows observable, albeit weaker, Ir–S NNN and S–S NNN contributions, as labeled. The S–S NNN contributions are themselves unusual, as they appear as faint peaks of apparent negative intensity. This is strictly a function of the color scale, which was chosen to emphasize stronger features. The fully three-dimensional S–S NNN feature consists of a negative central lobe surrounded by a weaker diffuse positive outer lobe, suggesting it is associated with some sort of negatively correlated displacive disorder (Weber & Simonov, 2012). The integral of this feature over a cube (1.5 Å on a side) is zero within a small tolerance.

The significance of a non-zero differential intensity corresponding to the NNN S–S pair is as follows. In the presence of a similar pair-correlation strength for the underlying local structural distortion, the S–S intensity is expected to be ∼20 times weaker than the Ir–Ir contribution, since the two pairs have identical multiplicity, and for a given pair of atoms the PDF intensity scales with the product of their scattering form factors. In a 1D-PDF of $CuIr_2S_4$, where the three-dimensional information is lost due to powder averaging, any S–S NNN information associated with a local structural distortion is effectively suppressed, not only because S scatters

X-rays much more weakly than Ir does, but also due to significant overlap of S–S NNN with Ir–Ir NN PDF peaks (Bozin *et al.*, 2019). Within the 3D case, Ir–Ir NN and S–S NNN contributions do not overlap, as the corresponding interatomic vectors are in different directions, as can be seen in Fig. 17(*f*).

It is also important to note that within 1D-PDF analysis, Bragg information becomes mixed with any local structural signal, and disentangling the two is non-trivial during structural fitting, where phenomenological modeling of correlated atomic motion can mask the effects of what is in actuality a local structural distortion (Jeong *et al.*, 1999, 2003). The ability to directly observe a differential S–S NNN signal in the 3D-ΔPDF of $CuIr_2S_4$ therefore implies that the sensitivity of the 3D-ΔPDF approach to local deviations in systems comprised of light and heavy elements is not limited to heavier atoms, but is also suitable, at least in principle, for exploring local correlations among weaker scatterers.

The spatial extent of local distortions is considered in Fig. 18(*a*), where we plot the $Z = 0$ slice of the $CuIr_2S_4$ 3D-ΔPDF, containing Ir–Ir contributions, over an extended spatial range. From this one sees that the extent of local structural correlations is limited to sub-nanometre length scale, in agreement with powder measurements (Bozin *et al.*, 2019). The ability to assess the extent of local structural correlations directly using a 3D-ΔPDF approach relies on this length scale being smaller than the PDF field of view. The latter is defined as the length scale over which the intensity of the experimental PDF signal decays to zero as a result of finite instrumental resolution width in **Q** space. This can be established by examining the full 3D-PDF over a wide r range. For the $CuIr_2S_4$ data discussed here such a view of the full 3D-PDF is shown in Fig. 18(*b*). The intensity scale is selected to bring the strongest features intentionally to saturation in order to expose weak inten-

sities at large interatomic distance. Fig. 18(*b*) reveals that the intensity decays to zero by ∼35 Å. In contrast, the intensity of the 3D-ΔPDF [Fig. 18(*a*)] decays to zero by ∼10 Å, which is well within the field of view of the measurement.

The observations of this experiment confirm that local distortions first observed in the 1D-PDF (Bozin *et al.*, 2019) are also present in the single-crystal CuIr$_2$S$_4$ system. Thorough characterization of these observations and their implications for CuIr$_2$S$_4$ are beyond the scope of this report.

11. Conclusions

We have extensively outlined the data-processing steps necessary for obtaining a reproducible 3D-ΔPDF from a single-crystal sample, including measurement, crystal orientation, transforming from detector to reciprocal space, handling detector artifacts, merging different data sets, applying symmetry operations, removing Bragg intensity and applying a discrete Fourier transform. These steps have thus far been spread across various different sources, or maintained only as an in-house procedure.

Further, we have investigated aspects of 3D-ΔPDF reproducibility under a number of conditions, including a variation of workflow ordering, sample-to-sample variation, and worst-case measurement and data-processing conditions. We have found that across the majority of tested situations, the 3D-ΔPDF is remarkably robust, with few qualitative differences. Failure to obtain a complete and regularly shaped data set in reciprocal space, due to a limited measurement range or a crystal with low space-group symmetry (or both), can result in spurious features in the 3D-ΔPDF. The 3D-ΔPDF also showed nearly no quantitative differences across the majority of tested situations. An important exception is the impact of the Bragg punch size. If the punch is too large, it can affect the decay rate of features in the 3D-ΔPDF. This is particularly important if the diffuse features of interest are relatively sharp and co-located with Bragg peaks. The 3D-ΔPDF then appears largely robust even given a relatively large crystal size, the presence of small polycrystalline inclusions and the use of a detector with limited dynamic range. This observation reinforces the power of this emerging technique, and should underscore observations arising from past and future 3D-ΔPDF studies.

References

Albagli, D., Han, S., Couture, A., Hudspeth, H., Collazo, C. & Granfors, P. (2005). *Proc. SPIE*, **5745**, 1078.

Aoun, B. (2016). *J. Comput. Chem.* **37**, 1102–1111.

Ashiotis, G., Deschildre, A., Nawaz, Z., Wright, J. P., Karkoulis, D., Picca, F. E. & Kieffer, J. (2015). *J. Appl. Cryst.* **48**, 510–519.

Bilderback, D. H., Elleaume, P. & Weckert, E. (2005). *J. Phys. B At. Mol. Opt. Phys.* **38**, S773–S797.

Billinge, S. J. L., Kwei, G. H. & Takagi, H. (1994). *Physica B*, **199–200**, 244–245.

Blessing, R. H. (1997). *J. Appl. Cryst.* **30**, 421–426.

Bozin, E. S., Yin, W. G., Koch, R. J., Abeykoon, M., Hor, Y. S., Zheng, H., Lei, H. C., Petrovic, C., Mitchell, J. F. & Billinge, S. J. L. (2019). *Nat. Commun.* **10**, 3638.

Broennimann, Ch., Eikenberry, E. F., Henrich, B., Horisberger, R., Huelsen, G., Pohl, E., Schmitt, B., Schulze-Briese, C., Suzuki, M., Tomizaki, T., Toyokawa, H. & Wagner, A. (2006). *J. Synchrotron Rad.* **13**, 120–130.

Chupas, P. J., Chapman, K. W. & Lee, P. L. (2007). *J. Appl. Cryst.* **40**, 463–470.

Chupas, P. J., Qiu, X., Hanson, J. C., Lee, P. L., Grey, C. P. & Billinge, S. J. L. (2003). *J. Appl. Cryst.* **36**, 1342–1347.

Coelho, A. A., Chater, P. A. & Kern, A. (2015). *J. Appl. Cryst.* **48**, 869–875.

Dask Development Team (2016). *Dask: Library for dynamic task scheduling.* https://dask.org.

Davenport, M. A., Krogstad, M. J., Whitt, L. M., Hu, C., Douglas, T. C., Ni, N., Rosenkranz, S., Osborn, R. & Allred, J. M. (2019). arXiv:1909.12704 [cond-mat.str-el].

Egami, T. & Billinge, S. J. L. (2003). *Underneath the Bragg Peaks: Structural Analysis of Complex Materials.* Oxford: Pergamon Press/ Elsevier.

Egami, T., Toby, B. H., Billinge, S. J. L., Rosenfeld, H. D., Jorgensen, J. D., Hinks, D. G., Dabrowski, B., Subramanian, M. A., Crawford, M. K., Farneth, W. E. & McCarron, E. M. (1991). *Physica C*, **185–189**, 867–868.

Epstein, J. & Welberry, T. R. (1983). *Acta Cryst.* A**39**, 882–892.

Farrow, C. L., Juhas, P., Liu, J. W., Bryndin, D., Božin, E. S., Bloch, J., Proffen, T. & Billinge, S. J. L. (2007). *J. Phys. Condens. Matter*, **19**, 335219.

Frandsen, B. A., Taddei, K. M., Bugaris, D. E., Stadel, R., Yi, M., Acharya, A., Osborn, R., Rosenkranz, S., Chmaissem, O. & Birgeneau, R. J. (2018). *Phys. Rev. B*, **98**, 180505.

Garcia, D. (2010). *Comput. Stat. Data Anal.* **54**, 1167–1178.

Hammersley, A. P. (2016). *J. Appl. Cryst.* **49**, 646–652.

Harris, C. R., Millman, K. J., van der Walt, S. J., Gommers, R., Virtanen, P., Cournapeau, D., Wieser, E., Taylor, J., Berg, S., Smith, N. J., Kern, R., Picus, M., Hoyer, S., van Kerkwijk, M. H., Brett, M., Haldane, A., del Río, J. F., Wiebe, M., Peterson, P., Gérard-Marchant, P., Sheppard, K., Reddy, T., Weckesser, W., Abbasi, H., Gohlke, C. & Oliphant, T. E. (2020). *Nature*, **585**, 357–362.

Henrich, B. (2008). *Proceedings of The 16th International Workshop on Vertex detectors – PoS(Vertex 2007)*, **057**, 049. Lake Placid, NY, USA: Sissa Medialab. https://dx.doi.org/10.22323/1.057.0049.

Holm, K. A. U., Roth, N., Zeuthen, C. M., Tolborg, K., Feidenhans'l, A. A. & Iversen, B. B. (2020). *Phys. Rev. B*, **102**, 024112.

Hunter, J. D. (2007). *Comput. Sci. Eng.* **9**, 90–95.

Jeong, I. K., Heffner, R. H., Graf, M. J. & Billinge, S. J. L. (2003). *Phys. Rev. B*, **67**, 104301.

Jeong, I.-K., Proffen, T., Mohiuddin-Jacobs, F. & Billinge, S. J. L. (1999). *J. Phys. Chem. A*, **103**, 921–924.

Juhás, P., Davis, T., Farrow, C. L. & Billinge, S. J. L. (2013). *J. Appl. Cryst.* **46**, 560–566.

Juhás, P., Farrow, C., Yang, X., Knox, K. & Billinge, S. (2015). *Acta Cryst.* A**71**, 562–568.

Kabsch, W. (1976). *Acta Cryst.* A**32**, 922–923.

Kabsch, W. (1988). *J. Appl. Cryst.* **21**, 916–924.

Kabsch, W. (2014). *Acta Cryst.* D**70**, 2204–2216.

Keen, D. A. (2001). *J. Appl. Cryst.* **34**, 172–177.

Kobas, M., Weber, T. & Steurer, W. (2005). *Phys. Rev. B*, **71**, 224205.

Koch, R. J., Konstantinova, T., Abeykoon, M., Wang, A., Petrovic, C., Zhu, Y., Bozin, E. S. & Billinge, S. J. L. (2019). *Phys. Rev. B*, **100**, 020501.

Kraft, P. (2010). *PILATUS 2M: a Detector for Small Angle X-ray Scattering.* PhD thesis, ETH Zurich, Switzerland.

Krogstad, M. J., Rosenkranz, S., Wozniak, J. M., Jennings, G., Ruff, J. P. C., Vaughey, J. T. & Osborn, R. (2020). *Nat. Mater.* **19**, 63–68.

Lee, J. H., Aydıner, C. C., Almer, J., Bernier, J., Chapman, K. W., Chupas, P. J., Haeffner, D., Kump, K., Lee, P. L., Lienert, U., Miceli, A. & Vera, G. (2008). *J. Synchrotron Rad.* **15**, 477–488.

Lorch, E. (1969). *J. Phys. C.: Solid State Phys.* **2**, 229–237.

MATLAB (2019). Version 9.6.0.1072779 (R2019a). Natick, Massachusetts: The MathWorks Inc.

Milch, J. R. & Minor, T. C. (1974). *J. Appl. Cryst.* **7**, 502–505.

Neder, R. B. & Proffen, T. (2008). *Diffuse Scattering and Defect Structure Simulations.* Oxford University Press.

Perez-Mendez, V., Kaplan, S., Ward, W., Qureshi, S. & Street, R. (1987). *Nucl. Instrum. Methods Phys. Res. A*, **260**, 195–200.

Proffen, Th. & Neder, R. B. (1997). *J. Appl. Cryst.* **30**, 171–175.

Qiu, X., Thompson, J. W. & Billinge, S. J. L. (2004). *J. Appl. Cryst.* **37**, 678–678.

Ramsteiner, I. B., Schöps, A., Reichert, H., Dosch, H., Honkimäki, V., Zhong, Z. & Hastings, J. B. (2009). *J. Appl. Cryst.* **42**, 392–400.

Roth, N. & Iversen, B. B. (2019). *Acta Cryst.* A**75**, 465–473.

Sangiorgio, B., Bozin, E. S., Malliakas, C. D., Fechner, M., Simonov, A., Kanatzidis, M. G., Billinge, S. J. L., Spaldin, N. A. & Weber, T. (2018). *Phys. Rev. Mater.* **2**, 085402.

Schaub, P., Weber, T. & Steurer, W. (2007). *Philos. Mag.* **87**, 2781–2787.

Schaub, P., Weber, T. & Steurer, W. (2011). *J. Appl. Cryst.* **44**, 134–149.

Schlachter, A. S. (1994). *New Directions in Research with Third-Generation Soft X-ray Synchrotron Radiation Sources*, edited by A. S. Schlachter & F. J. Wuilleumier, pp. 1–22. Dordrecht: Springer Netherlands.

Simonov, A., Weber, T. & Steurer, W. (2014*a*). *J. Appl. Cryst.* **47**, 2011–2018.

Simonov, A., Weber, T. & Steurer, W. (2014*b*). *J. Appl. Cryst.* **47**, 1146–1152.

Soper, A. K. (2005). *Phys. Rev. B*, **72**, 104204.

Soper, A. K. & Barney, E. R. (2011). *J. Appl. Cryst.* **44**, 714–726.

Soper, A. K. & Barney, E. R. (2012). *J. Appl. Cryst.* **45**, 1314–1317.

Tucker, M. G., Keen, D. A., Dove, M. T., Goodwin, A. L. & Hui, Q. (2007). *J. Phys. Condens. Matter*, **19**, 335218.

Urban, P., Simonov, A., Weber, T. & Oeckler, O. (2015). *J. Appl. Cryst.* **48**, 200–211.

Van Rossum, G. & Drake, F. L. (2009). *Python 3 Reference Manual.* Scotts Valley, CA: CreateSpace.

Virtanen, P., Gommers, R., Oliphant, T. E., Haberland, M., Reddy, T., Cournapeau, D., Burovski, E., Peterson, P., Weckesser, W., Bright, J., van der Walt, S. J., Brett, M., Wilson, J., Millman, K. J., Mayorov, N., Nelson, A. R. J., Jones, E., Kern, R., Larson, E., Carey, C. J., Polat, İ., Feng, Y., Moore, E. W., VanderPlas, J., Laxalde, D., Perktold, J., Cimrman, R., Henriksen, I., Quintero, E. A., Harris, C. R., Archibald, A. M., Ribeiro, A. H., Pedregosa, F., van Mulbregt, P., Vijaykumar, A., Bardelli, A. P., Rothberg, A., Hilboll, A., Kloeckner, A., Scopatz, A., Lee, A., Rokem, A., Woods, C. N., Fulton, C., Masson, C., Häggström, C., Fitzgerald, C., Nicholson, D. A., Hagen, D. R., Pasechnik, D. V., Olivetti, E., Martin, E., Wieser, E., Silva, F., Lenders, F., Wilhelm, F., Young, G., Price, G. A., Ingold, G., Allen, G. E., Lee, G. R., Audren, H., Probst, I., Dietrich, J. P., Silterra, J., Webber, J. T., Slavič, J., Nothman, J., Buchner, J., Kulick, J., Schönberger, J. L., de Miranda Cardoso, J. V., Reimer, J., Harrington, J., Rodríguez, J. L. C., Nunez-Iglesias, J., Kuczynski, J., Tritz, K., Thoma, M., Newville, M., Kümmerer, M., Bolingbroke, M., Tartre, M., Pak, M., Smith, N. J., Nowaczyk, N., Shebanov, N., Pavlyk, O., Brodtkorb, P. A., Lee, P., McGibbon, R. T., Feldbauer, R., Lewis, S., Tygier, S., Sievert, S., Vigna, S., Peterson, S., More, S., Pudlik, T., Oshima, T., Pingel, T. J., Robitaille, T. P., Spura, T., Jones, T. R., Cera, T., Leslie, T., Zito, T., Krauss, T., Upadhyay, U., Halchenko, Y. O. & Vázquez-Baeza, Y. (2020). *Nat. Methods*, **17**, 261–272.

Wang, G., Garcia, D., Liu, Y., de Jeu, R. & Johannes Dolman, A. (2012). *Environ. Model. Softw.* **30**, 139–142.

Wang, Z., Zhao, X., Koch, R., Billinge, S. J. L. & Zunger, A. (2020). arXiv:1911.02670 [cond-mat.mtrl-sci].

Weber, T., Estermann, M. A. & Bürgi, H.-B. (2001). *Acta Cryst.* B**57**, 579–590.

Weber, T. & Simonov, A. (2012). *Z. Kristallogr.* **227**, 238–247.

Welberry, T. R. (2010). *Diffuse X-ray Scattering and Models of Disorder.* International Union of Crystallography Monographs on Crystallography, No. 16. Oxford: IUCr/Oxford University Press.

Welberry, T. R., Goossens, D. J., Heerdegen, A. P. & Lee, P. L. (2005). *Z. Kristallogr.* **220**, 1052–1058.

Weng, J., Dill, E. D., Martin, J. D., Whitfield, R., Hoffmann, C. & Ye, F. (2020). *J. Appl. Cryst.* **53**, 159–169.

White, T. A., Barty, A., Stellato, F., Holton, J. M., Kirian, R. A., Zatsepin, N. A. & Chapman, H. N. (2013). *Acta Cryst.* D**69**, 1231–1240.

Yang, L., Koch, R. J., Zheng, H., Mitchell, J. F., Yin, W., Tucker, M. G., Billinge, S. J. L. & Bozin, E. S. (2020). *Phys. Rev. B*, **102**, 235128.

Yang, X., Juhas, P., Farrow, C. L. & Billinge, S. J. L. (2014). arXiv:1402.3163 [cond-mater.mtrl-sci].

Zachariasen, W. H. (1994). *Theory of X-ray Diffraction in Crystals.* New York: Dover Publications.

Comment on "Colossal Pressure-Induced Softening in Scandium Fluoride"

In a recent Letter [1], Wei *et al.* report neutron powder diffraction measurements at variable temperature and pressure of negative thermal expansion material, scandium fluoride ScF_3 [2]. The diffraction patterns were fitted using the Rietveld method to refine the lattice and the atomic displacement parameters, with other aspects of the crystal structure fixed by $Pm\bar{3}m$ cubic symmetry. From the structural refinement of the measured diffraction patterns, authors obtain the isothermal compressibility curves. These results thoroughly characterize the equation of state of this material in the low-pressure cubic phase (with increasing pressure, ScF_3 undergoes a structural transition to the rhombohedral structure).

The results reported by Wei *et al.* [1] are indeed very interesting and important because these results can be confronted with predictive, quantitative theories of negative thermal expansion (NTE) and pressure-induced softening and allow one to corroborate or invalidate certain approaches. Wei *et al.* discuss their observations in the context of model molecular dynamics simulations and simple one-dimensional models, which capture qualitative features of the observed phenomena, but do not provide a quantitative theory. On the other hand, a microscopic theory of vibrational and thermomechanical properties of empty perovskite crystals with ReO_3 structure (also rooted in neutron diffraction results [3]) has recently been proposed. This theory describes empty perovskite structures with strong nearest-neighbor bonds as Coulomb floppy networks (CFNs, floppy networks of rigid links stabilized by Coulomb interaction) and provides a very accurate quantitative description of NTE in ScF_3 [3,4].

Motivated to further corroborate the CFN theory, we compared its prediction for the mean-squared transverse displacement of the F atoms, $U_{\rm perp} \equiv \langle u_{\rm perp}^2 \rangle$, with that obtained by Wei *et al.* and observed a marked discrepancy. The experimental values are much smaller than those expected from theory (Fig. 1). In fact, the $U_{\rm perp}$ values of Wei *et al.* appear unphysically small, falling for $T \lesssim$ 150 K well below the quantum limit for the Fluorine mean-squared transverse displacement due to zero-point motion at $T = 0$, $\langle u_0^2 \rangle = \hbar/m_F \omega_+ \approx 0.006$ Å^2 (dashed line in Fig. 1; $\hbar$ is Planck constant, m_F is mass of the F ion, and $\hbar\omega_+ \approx 37$ meV is the transverse F phonon bandwidth). We then compared these results with the previously published x-ray diffraction data of Greve *et al.* [2] and
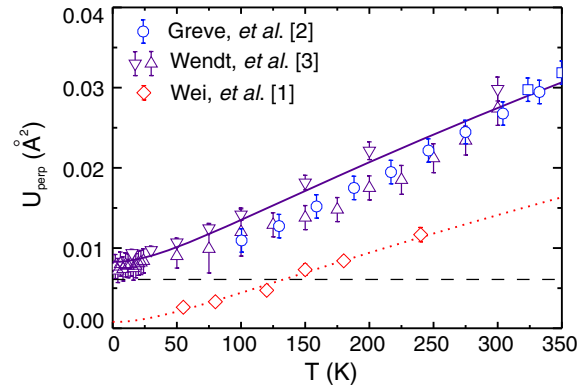
FIG. 1. Mean-squared transverse displacement of the F atoms obtained from refinement of the crystal structure at $P \approx 0$. The triangles show the results of Rietveld refinement of neutron diffraction data measured on NPDF diffractometer at Los Alamos Neutron Science Center (down triangles) and NOMAD diffractometer at Spallation Neutron Source (up triangles) from Fig. 4(b) of Wendt *et al.* [3]. The circles and squares correspond to the x-ray data from Supplementary Material Fig. 1 of Greve *et al.* [2]. The (red) diamonds are the data of Wei *et al.* [1]. The solid line is theoretical prediction of Ref. [4]; the horizontal broken line shows the quantum limit for the Fluorine mean-squared transverse displacement due to zero-point motion at $T = 0$.

the neutron diffraction data of Wendt *et al.* [3]. We found the latter two datasets to be in good agreement with each other, as well as with the prediction of CFN theory (Fig. 1).

We thus observe that $U_{\rm perp}$ values reported in Fig. 5 of Ref. [1] are substantially incorrect. In our experience, such an underestimate of atomic displacement parameters can be caused by an incorrect accounting for the effects of beam absorption in the sample and sample environment (such as pressure cell in measurements of Wei *et al.*) in the Rietveld treatment of the diffraction data. This also explains unphysical negative atomic displacement parameters reported in Supplementary Material Figs. S7 and S8 of Ref. [1], where authors indeed write "the negative values are consistent with not including the effects of beam attenuation in the refinement process, which at this point could be taken into account by a positive constant shift of all values." Whether the systematic error of $U_{\rm perp}$ in Fig. 5 of Ref. [1] can be accounted for by a simple shift is unclear.

An evaluation of large systematic errors present in Fig. 5 of Wei *et al.*, which is vitally important for comparison of those data with quantitative theories, is markedly missing in their Letter. Our Comment addresses this unfortunate omission and presents such an evaluation (Fig. 1), providing a reference for future such comparisons.

The purpose of this Comment is twofold: (i) to caution the researchers against using the $U_{\rm perp}$ data of Wei *et al.* [1] for direct quantitative comparisons with theory and (ii) to encourage the authors of Ref. [1] to reconsider their analysis and try to obtain reliable $U_{\rm perp}$ data by better accounting for the beam transmission and attenuation

effects. We believe that the data are of sufficient interest and importance to attempt an analysis [5], which would eliminate, or markedly reduce, the systematic error that is currently present in Fig. 5 of Ref. [1].

I. A. Zaliznyak[1,*] E. Bozin[1] and A. V. Tkachenko[2]
[1]Condensed Matter Physics and Materials Science Division
Brookhaven National Laboratory
Upton, New York 11973, USA
[2]CFN, Brookhaven National Laboratory
Upton, New York 11973, USA

*zaliznyak@bnl.gov

[1] Z. Wei, L. Tan, G. Cai, A. E. Phillips, I. da Silva, M. G. Kibble, and M. T. Dove, Phys. Rev. Lett. **124**, 255502 (2020).

[2] B. K. Greve, K. L. Martin, P. L. Lee, P. J. Chupas, K. W. Chapman, and A. P. Wilkinson, J. Am. Chem. Soc. **132**, 15496 (2010).

[3] D. Wendt, E. Bozin, J. Neuefeind, K. Page, W. Ku, L. Wang, B. Fultz, A. V. Tkachenko, and I. A. Zaliznyak, Sci. Adv. **5**, eaay2748 (2019).

[4] A. Tkachenko and I. Zaliznyak, Phys. Rev. B **103**, 134106 (2021).

[5] MANTID User Documentation, www.mantidproject.org; https://docs.mantidproject.org/nightly/concepts/AbsorptionAndMultipleScattering.html.

Dual Orbital Degeneracy Lifting in a Strongly Correlated Electron System

R. J. Koch[1,*] R. Sinclair,[2] M. T. McDonnell[3,†] R. Yu[1,‡] M. Abeykoon,[4] M. G. Tucker[3]
A. M. Tsvelik[1] S. J. L. Billinge[1,5] H. D. Zhou,[2] W.-G. Yin[1,§] and E. S. Bozin[1,∥]

[1]*Condensed Matter Physics and Materials Science Division, Brookhaven National Laboratory, Upton, New York 11973, USA*
[2]*Department of Physics and Astronomy, University of Tennessee, Knoxville, Tennessee 37996, USA*
[3]*Neutron Scattering Division, Oak Ridge National Laboratory, Oak Ridge, Tennessee 37831, USA*
[4]*Photon Sciences Division, Brookhaven National Laboratory, Upton, New York 11973, USA*
[5]*Department of Applied Physics and Applied Mathematics, Columbia University, New York, New York 10027, USA*

The local structure of $NaTiSi_2O_6$ is examined across its Ti-dimerization orbital-assisted Peierls transition at 210 K. An atomic pair distribution function approach evidences local symmetry breaking preexisting far above the transition. The analysis unravels that, on warming, the dimers evolve into a short range orbital degeneracy lifted (ODL) state of dual orbital character, persisting up to at least 490 K. The ODL state is correlated over the length scale spanning ~ 6 sites of the Ti zigzag chains. Results imply that the ODL phenomenology extends to strongly correlated electron systems.

Introduction.—The emergence of technologically relevant quantum orders in materials [1] stems from complex interaction of electronic charge, spin, and orbitals and their coupling to the host lattice [2,3]. Orbital sector is often engaged in transition metal systems, owing to partially filled d manifolds [4]. Because of the coupling to both spin and lattice, of particular interest is when the lattice topology imposes orbital degeneracy [5] and/or electronic frustration [6]. The removal of orbital degeneracy and the relief of frustration impact symmetry lowering and electronic properties [7]. Complexities of the low temperature symmetry breaking have been thoroughly studied in relation to diverse emergent behaviors such as frustrated magnetism [8,9], colossal magnetoresistivity [10], charge and orbital order [11,12], metal-insulator transition [13–15], pseudogap [16,17], and high temperature superconductivity [18,19]. Their understanding employs Fermi surface nesting [20,21], Peierls [22,23], and band Jahn-Teller mechanisms [24,25].

When orbital degeneracies are anticipated, it is often assumed that crystallographic symmetry lowering at the temperature driven phase transitions implies simultaneous orbital degeneracy lifting (ODL) via some cooperative mechanism [5,6,26]. Consequently, the high temperature regimes possessing high crystallographic symmetry remain less explored. In contrast, probes of local symmetry qualify the ODL as a local electronic effect existing at temperatures well above [27,28] the global symmetry breaking transitions. In spinels $CuIr_2S_4$ [27] and $MgTi_2O_4$ [28] with weak electron correlations, a highly localized ODL state involving two transition metal ions is discovered as a high-temperature precursor to an orbitally driven metal-insulator transition [29]. Albeit discontinuously connected

to the ground state, the ODL in these spinels is a prerequisite for charge and orbital order and spin dimerization [11,30,31], thus, enabling the transition.

The ubiquity and role of the ODL in the emergent phenomena are yet to be established [28,32]. It is important to understand whether the ODL state is a peculiarity of weakly coupled electronic systems in proximity to a localized-to-itinerant crossover, or if it could also be realized deep in the Mott insulating regime with strong on-site Coulomb interactions, where the charge fluctuations are suppressed. An opportunity to explore this is offered by the quasi-one-dimensional $NaTiSi_2O_6$ clinopyroxene [33], one of the rock-forming silicate minerals constituting the upper Earth's mantle [34]. It is a paramagnetic strongly correlated Mott insulator with a ~ 2 eV gap [35], featuring zigzag chains of skew edge-shared TiO_6 [Figs. 1(a) and 1(b)], with Ti^{3+} in d^1 ($S = 1/2$) nominally triply degenerate t_{2g} orbital configuration. The ground state of $NaTiSi_2O_6$ with a 53 meV spin gap [36] establishes on cooling through a 210 K [37] structural transition where ferro-orbital ordering stabilizes intrachain Ti spin singlet dimerization [38]. Once thought to host Haldane $S = 1$ chains [35,39,40], $NaTiSi_2O_6$ is considered a candidate for quantum liquid with strong orbital fluctuations [41].

By combining neutron and x-ray total scattering based atomic pair distribution function (NPDF and XPDF) approaches [42], we find compelling local structural evidence for a fluctuating ODL state of dual orbital character in $NaTiSi_2O_6$ at high temperature. The spatial extent of associated short range structural correlations consistent with Peierls-like instability at 1/6 filling suggests relevance of all three Ti t_{2g} orbitals in this regime. The pair distribution function (PDF) observations establish that
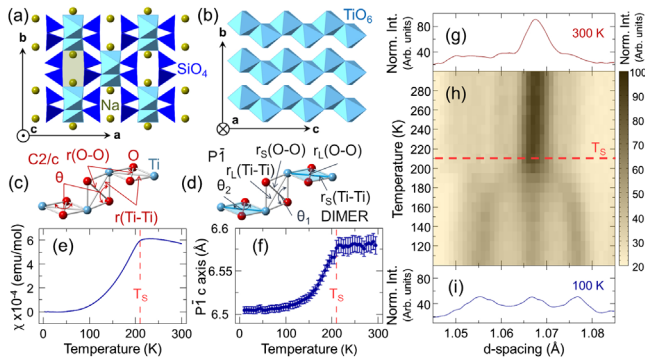
FIG. 1. Properties of NaTiSi$_2$O$_6$. (a) $C2/c$ structure; (b) quasi-1D zigzag TiO$_6$ chains; (c) undistorted TiO$_2$ plaquettes of the $C2/c$ phase featuring uniform Ti-Ti and O-O distances; (d) distorted TiO$_2$ plaquettes of the dimerized $P\bar{1}$ phase with Ti-Ti and O-O distances bifurcated (S = short, L = long); (e) the Curie law subtracted dc magnetic susceptibility; (f) the c axis parameter from $P\bar{1}$ model fits to the XPDF data; (g)–(i) temperature evolution of a selected segment of neutron total scattering data. Note: zigzag chains run along c axis in $C2/c$, and along a axis in $P\bar{1}$.

the ODL phenomenology does extend to materials with strong electron correlations, reinforcing the notion of its ubiquity. This intricate short range orbital precursor to spin dimerization provides a rationale for a number of puzzling high temperature anomalies reported for this system [36,43,44].

Polycrystalline NaTiSi$_2$O$_6$ used in powder diffraction measurements was obtained via a solid state route [36,37,45] and displays a transition to a spin-singlet dimer state at T_s = 210 K, Fig. 1(e). Total scattering data for PDF analysis were collected over 100 K ≤ T ≤ 300 K (neutrons), and over 10 K ≤ T ≤ 300 K range and at 490 K (x rays). The approach utilizes both Bragg and diffuse scattering, and provides information on the average structure and on the local deviations from it [42]. Robust crystallographic symmetry change at T_s is evident in the x ray [Fig. 1(f)], and neutron data [Figs. 1(g)–1(i)]. Experimental and analysis details are provided in the Supplemental Material [45].

Crystallographic perspective.—NaTiSi$_2$O$_6$ crystallizes in a monoclinic $C2/c$ structure, Fig. 1(a), featuring characteristic zigzag chains of edge-sharing TiO$_6$ octahedra, Fig. 1(b), giving the system a quasi-one-dimensional character [38]. The chains are embedded in a somewhat disordered SiO$_4$ network encompassing Na [45,54,55]. Within the chains, the shared-edge O pairs and Ti centers constitute TiO$_2$ plaquettes, identical in $C2/c$, which alternate in orientation, as shown in Fig. 1(c). Magnetically active Ti have +3 valence in 3d^1 configuration [56], confirmed by neutron Rietveld refinement based bond valence sum calculations [45,57]. The dominant octahedral crystal field splits the Ti 3d orbitals into a partially filled t_{2g} triplet and an empty e_g doublet [37]. Nominally triply degenerate

t_{2g} orbitals [5] are oriented toward the TiO$_6$ edges: xy and zx point toward the common edges of the zigzag chains, while yz is perpendicular to the general chain direction (for illustration see the top right corner inset in Fig. 5). Partial degeneracy alleviation is expected from slight trigonal distortion of TiO$_6$ [43], placing the single electron into a two fold degenerate low lying t_{2g}-derived (zx, xy) doublet [41] and rendering the third (yz) orbital inert [36,43,58]. The edge-sharing topology fosters direct (xy, xy) and (zx, zx) overlaps of t_{2g} orbitals belonging to neighboring Ti along the chains. This promotes Ti-Ti dimerization [43] in the ferro-orbitally ordered regime [38] upon cooling below T_s, lifting the t_{2g} degeneracy and lowering the average symmetry to triclinic ($P\bar{1}$) [56].

The average structure change observed in diffraction across the transition is associated with the splitting of Ti-Ti distances in the zigzag chains. The dimerization takes place within the TiO$_2$ plaquettes of just one of the two available orientations [zig or zag, Fig. 5(b)]. Consequentially, the Ti-Ti and O-O interatomic distances on the plaquettes bifurcate, Fig. 1(d): Ti-Ti (3.18 Å) and O-O (2.74 Å) contacts on the plaquettes in $C2/c$ become (3.11 Å, 3.22 Å) and (2.69 Å, 2.81 Å) in $P\bar{1}$, respectively. The dimerized plaquette has nominally two electrons (2e) [56] [see Fig. 5(a)]. Neighboring TiO$_2$ plaquettes become inequivalent as the Ti dimers and the associated $\cdots - 2e - 0e - 2e - 0e - \cdots$ bond-charge order form, thus, removing the zx-xy degeneracy. The $C2/c$ and $P\bar{1}$ models explain our neutron Bragg data in the high and low temperature regimes, respectively [45]. All Ti sites participate in dimerization in $P\bar{1}$ but remain equivalent (+3 valence) [45,56]. The fingerprint of the average structural change across T_s, simulated using crystallographic models [56] for NPDF [Figs. 2(a) and 2(b)] and XPDF [Figs. 2(c) and 2(d)], illustrates the expected PDF response should the local structure follow the average behavior. In Figs. 2(c) and 2(f), the crystallographically observed Ti-Ti splitting [56] is shown by scattering-weighted partial PDFs, revealing a
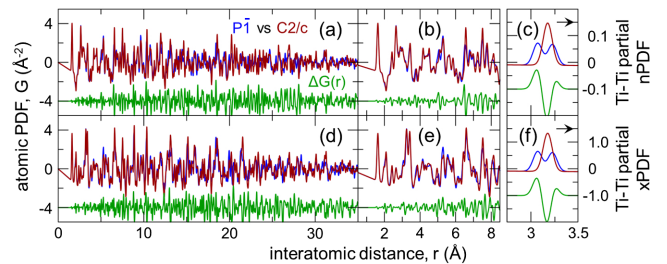

FIG. 2. Comparison of simulated PDFs. Crystallographic $P\bar{1}$ (blue) and $C2/c$ (red) models with their differential (green) offset for clarity for neutron probe over a wide (a) and a narrow (b) r range. (c) Neutron Ti-Ti partial PDF for the two models. Corresponding PDFs for x-ray probe are shown in (d)–(f). Simulations use uniform 0.001 Å^2 atomic displacement parameters for all atoms, and are scaled to match the data shown in Fig. 3.

considerably weaker signal in NPDF than in XPDF case. The pair contributions to PDF of Ti-Ti when compared to O-O are an order of magnitude stronger in XPDF, whereas in NPDF, they are three times weaker.

Local perspective.—While crystallography implies that the lifting of Ti orbital degeneracy and associated dimer formation occur at T_s, the complexity increases when the local structure information from PDF data is considered. If we compare the PDF signal from $T = 150$ K (well below T_s) to that from $T = 230$ K (just above T_s), the difference signal ΔG for interatomic distances $r > 15$ Å is large, as expected when passing through a structural transition [Figs. 3(a) and 3(c)]. However, and in contrast to the expectations shown in Fig. 2, ΔG is substantially smaller over the shorter distances ($r < 15$ Å) reflecting local structure, as highlighted in Figs. 3(e) and 3(g), especially in the NPDF case, which is less sensitive to Ti.

Actually, the local ΔG observed across the transition is comparable in magnitude to that observed in a 70 K difference ΔG which is fully above the transition [Figs. 3(e)–3(h)], where only changes due to thermal motion variations are expected. While the structural transition associated with the dimer formation is clearly apparent in the average structure, the same cannot be said regarding the local structure, revealing a curious local vs average disparity in $NaTiSi_2O_6$. This may suggest that spin singlet dimers do not disassemble locally on warming

across T_s, in contrast to magnetic susceptibility measurements according to which the spin singlet dimers cannot be retained above the transition. We argue that the transition is not of a trivial order-disorder type, as one may deduce from the NPDF analysis alone [45], Figs. 3(a) and 3(b), but that it has an ODL-type character [27] evident from the XPDF analysis. In contrast to the differential NPDF signal implying minute change across the transition over the length scale corresponding to ~6 Ti sites, the ΔG signal in XPDF, Figs. 3(c) and 3(d), suggests that some local structural modification does occur at T_s.

Vanishing spin singlets.—This motivates a closer look at the temperature resolved XPDF data. Temperature evolution of the PDF differential, $\Delta G(T)$, underneath the Ti-Ti PDF peak at ~3.2 Å, where the dimer signal should be present, is particularly informative. Comparing the data at $T = 90$ K ($T < T_s$) and at T_s reveals a subtle but clear shift in pair probability from shorter to longer distances, Fig. 4(a), with an "M" shaped feature in $\Delta G(T)$, consistent with removal of the dimer distortion. When data at T_s and at $T = 300$ K ($T > T_s$) are compared, Fig. 4(b), the differential is much smaller for a comparable temperature difference. The NPDF data are not sensitive to this not only due to unfavorable scattering contrast, but also because the dimer-related distortions involve Ti and O displacements of opposite sign on the TiO_2 plaquettes, Fig. 5(a). For systematic assessment, we use a high temperature reference for calculating $\Delta G(T)$ [45]. The evolution of the $\Delta G(T)$

FIG. 3. Comparison of experimental PDFs. Data at temperature below (150 K) and above (230 K) the transition temperature, T_s, for neutrons (NPDF) over broad (a) and narrow (e) r ranges. Matching x-ray data (XPDF) scaled to NPDF are shown in (c) and (g). Comparison of NPDFs within the same crystallographic phase, $C2/c$, at 230 K and 300 K, is shown in (b) and (f). The same for XPDF is shown in (d) and (h). Differential PDFs, $\Delta G(r)$ are shown underneath each data, offset for clarity. The vertical dotted lines in panels (a)–(d) and (e)–(h) correspond to the fifth and the first Ti-Ti nearest neighbor distances along the zigzag chains, respectively, marked, also, by horizontal double arrows as 6 Ti (2 Ti) intrachain interatomic separations.
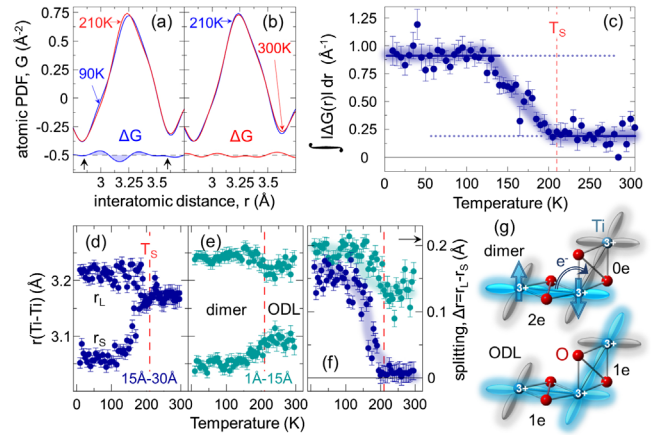

FIG. 4. The spin-singlet dimer disappearance. Comparison of XPDF data at $T_s = 210$ K with (a) 90 K and (b) 300 K data. Differentials $\Delta G = G(T) - G(T_s)$ are offset for clarity, revealing the spin-singlet signature (shaded signal) for 90 K set. (c) $\Delta G(T)$ signature (for 285 K reference) integrated over the range marked by arrows in (a) [45]. Horizontal lines are guides to the eye. The nearest neighbor Ti-Ti distances from $P\bar{1}$-based fits over (d) 15 Å $\leq r \leq$ 30 Å and (e) 1 Å $\leq r \leq$ 15 Å ranges. Corresponding r(Ti-Ti) splittings are shown in (f). (g) The spin-singlet dimer and ODL states sketched as t_{2g} orbital manifold overlaps. The color transparency indicates the bond charge filling, as noted.
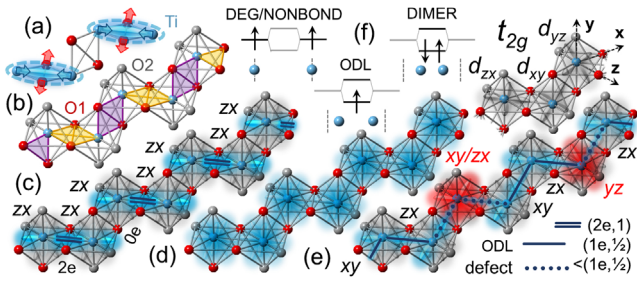
FIG. 5. $NaTiSi_2O_6$ orbital considerations. (a) TiO_2 dimerization plaquettes. (b) The two choices; the zig and the zag. (c) Dimerization of the zx variety within the $P\bar{1}$ structure. (d) Uniform chain with degenerate t_{2g} manifolds as portrayed by the $C2/c$ structure model. (e) Local model of the chain for $T \geq T_s$ featuring ODL and orbital defect states. (f) Molecular-orbital (MO) view, counterclockwise, of Ti-Ti contacts with degenerate or nonbonding Ti-Ti contacts, degeneracy-lifted MO, and dimerized Ti-Ti contacts. In the legend, DEG/NONBOND (Ti^{3+}), ODL ($1e^-$ per Ti-Ti bond), and DIMER ($2e^-$ per Ti-Ti bond). Corner insets: orbital geometry of the t_{2g} manifold (upper right), and bond chart with bond charge and bond order as noted (lower right).

integral, Fig. 4(c), is consistent with the dimers disassembling at T_s. The dimer contribution to the differential corresponds to the signal jump seen in Fig. 4(c).

To quantify this, we fit the temperature-resolved XPDF data using the low temperature $P\bar{1}$ structure over different r ranges. When the fit range excludes the local structure portion, the optimized model structure refined over $15\ \text{Å} < r < 30\ \text{Å}$ range adopts two unique Ti-Ti distances below T_s, which become degenerate above T_s, Fig. 4(d), consistent with dimers vanishing. When the average structure portion of the PDF is excluded and $1\ \text{Å} < r < 15\ \text{Å}$ range is used, instead, the model structure again adopts two unique Ti-Ti distances below T_s, but these two distances remain distinct above T_s, albeit with significantly reduced splitting, Fig. 4(e). Thus, at $T > T_s$ $NaTiSi_2O_6$ shows a regularization of the Ti chains over long structural length scales, but this regularization is not present locally. Residual degeneracy lifting is apparent above T_s up to 300 K [Fig. 4(f)], with splitting of 0.12(4) Å still present in our 490 K XPDF data.

Dual ODL precursor.—The behavior where short spin-singlet dimer bonds give way to longer local-symmetry-breaking transition metal contacts upon heating above the crystallographic transition is a hallmark of the ODL phenomenology seen in spinel dimer systems proximal to a localized-to-itinerant crossover. Initially observed in $CuIr_2S_4$ [27], and recently, also in $MgTi_2O_4$ [28], the ODL state is evidenced in their high temperature metallic regimes. There, at the metal-insulator transition, the spin singlet dimers comprised of pairs of strongly bonded holes ($CuIr_2S_4$) or electrons ($MgTi_2O_4$) dismount via bond charge transfer upon warming and are succeeded in the metallic phase by twice as many spatiotemporally

fluctuating single charge Hund-Mulliken molecular-orbital-like states [5] that lift the t_{2g} degeneracy [27,28]. The dimer and ODL states are shown in Fig. 5(f) using energy diagram representation. The observed high crystallographic symmetry ensues from three-dimensional spatiotemporal averaging.

In addition to thermal evolution of the transition metal sublattices, the similarity of Ti pyroxenes and the spinels extends to observed pressure effects. In the spinels, pressure increases t_{2g} orbital overlaps and stabilizes the transition [59,60] and the ODL state [27]. In $LiTiSi_2O_6$, which is isostructural and isoelectronic to $NaTiSi_2O_6$, ~3.1% volume reduction also pushes T_s to higher temperature [37,45], further corroborating the equivalence of the underlying orbital behaviors. Following the spinel ODL phenomenology, in $NaTiSi_2O_6$ the Ti dimers exhibit a "$2e - 0e$"-type bond charge (ferro-orbital) order along the zigzag chains for $T < T_s$ [Fig. 5(c)], which for $T > T_s$ converts into the ODL state of antiferro-orbital character [61] with the zx-xy degeneracy lifted locally, Fig. 4(g).

However, pursuing full analogy with the spinels, particularly with $MgTi_2O_4$ which has the same Ti t_{2g} filling as in $NaTiSi_2O_6$ and whose ODL states have a two-orbital (2O-ODL) character [28] sketched in Fig. 4(g), encounters two challenges. First, in $NaTiSi_2O_6$, 2O-ODL would imply a single valued Ti-Ti distance distribution akin to the degenerate orbital case portrayed crystallographically, Fig. 5(d). This is not what is seen experimentally. Second, quasi-one-dimensional topology of Ti zigzag chains in $NaTiSi_2O_6$ necessitates a modified scenario for reconciling the different length scales.

The local bimodal distribution observed above T_s implies variation of the bond charge along the zigzag chain. We propose a model featuring short ODL bonds (bond order $1/2$) and destabilized ODL bonds (of order $< 1/2$) triggered by fluctuating orbital defects. Two such defects which interrupt the underlying antiferro-orbital order are illustrated on different chain segments in Fig. 5(e). Model considerations based on antiferro-orbital order [61] and orbital disorder [41] uncover different spin configurations very close in energy (see Fig. S8 [45]), where strong competition between the spin superexchange interaction and the Hund's-rule coupling, manifested as deviation of magnetic susceptibility from the Curie-Weiss behavior, leads to orbital frustration at high temperature [61]. Such an energy landscape may yield a mixed-orbital zx-xy defect naturally emerging as the domain wall between two antiferro-orbital ordered segments, resulting in longer Ti-Ti distances [45]. Alternatively, t_{2g} electrons on some Ti sites may populate the inert nonbonding yz orbitals, introducing the $0e$ long bonds [45]. In principle, there can be long bonds of several lengths; however, as the short ODL bonds contract, all the longer bonds mainly make rotational moves—instead of stretching—and, thus, have similar lengths, unresolvable by our analysis. The NPDF data comparison in Fig. 3(a) and

model assessment of the 290 K XPDF data [45] demonstrate that local structural correlations extend to ~13.3 Å (~6 Ti sites), implying that defect randomization beyond this length scale provides the averaging mechanism. This would lead not only to lower-energy excited states than the triplet excitations of the dimerized bonds [45], but also an increased contribution of the entropy term in the free energy at higher temperature, thus, stabilizing the ODL state in $NaTiSi_2O_6$ which can be considered to have dual (xy, xy)-(zx, zx) character indicated in Fig. 5(e) by solid blue lines connecting affected Ti sites. In this regard, the present dual ODL phenomenon can be considered as an orbital analog to the spin-crossover transition in materials with magnetic atoms changing between high- and low-spin configurations [62–64].

Concluding remarks.—Notably, a number of anomalies were observed in the $T > T_s$ regime of $NaTiSi_2O_6$ and attributed to various electronic instabilities. Anomalies include unusual temperature dependence of magnetic susceptibility [37], the lack of recovery in the muon asymmetry at longer times, and lack of sharp change in electronic relaxation rate λ at T_s in μSR measurements [65], anomalous and unusually broad phonon modes in Raman [43,58] and neutron scattering [36] and infrared reflectivity [66], glass-like temperature evolution of thermal conductivity [44], as well as anomalous peak broadening in x-ray diffraction [36]. They were assigned to short-range correlations enhancing spin-singlet dimer fluctuations [65], orbital disorder [43,58,66], rapidly fluctuating orbital occupancy [44], and presence of bond disorder due to orbital fluctuations [36], respectively. Observation of the ODL state, which is presumably dynamic, provides a concrete rationale for their understanding and invites reexamination of the transition mechanism [36,61,67]. Such high temperature anomalies could, in fact, be indicators of the ODL state in a diverse class of transition metal systems with an active orbital sector [44,68–70], reinforcing the idea of ubiquitous ODL precursors, extending the phenomenology to strongly correlated electron systems.

[*]rkoch@bnl.gov
[†]Present address: Computer Science and Mathematics Division, Oak Ridge National Laboratory, Oak Ridge, Tennessee 37831, USA.
[‡]Present address: Institute of Physics, Chinese Academy of Science, Beijing 100190, Peoples Republic of China.
[§]wyin@bnl.gov
[∥]bozin@bnl.gov

[1] Y. Tokura, M. Kawasaki, and N. Nagaosa, Nat. Phys. **13,** 1056 (2017).

[2] Editorial, Nat. Phys. **12,** 105 (2016).

[3] B. Keimer, S. A. Kivelson, M. R. Norman, S. Uchida, and J. Zaanen, Nature (London) **518,** 179 (2015).

[4] Y. Tokura and N. Nagaosa, Science **288,** 462 (2000).

[5] S. V. Streltsov and D. I. Khomskii, Phys. Usp. **60,** 1121 (2017).

[6] M. Vojta, Rep. Prog. Phys. **81,** 064501 (2018).

[7] D. I. Khomskii, *Transition Metal Compounds* (Cambridge University Press, Cambridge, England, 2014).

[8] A. Zorko, O. Adamopoulos, M. Komelj, D. Arčon, and A. Lappas, Nat. Commun. **5,** 3222 (2014).

[9] J. K. Glasbrenner, I. I. Mazin, H. O. Jeschke, P. J. Hirschfeld, R. M. Fernandes, and R. Valenti, Nat. Phys. **11,** 953 (2015).

[10] B. H. Savitzky, I. El Baggari, A. S. Admasu, J. Kim, S.-W. Cheong, R. Hovden, and L. F. Kourkoutis, Nat. Commun. **8,** 1883 (2017).

[11] P. G. Radaelli, Y. Horibe, M. J. Gutmann, H. Ishibashi, C. H. Chen, R. M. Ibberson, Y. Koyama, Y.-S. Hor, V. Kiryukhin, and S.-W. Cheong, Nature (London) **416,** 155 (2002).

[12] A. J. Achkar, F. He, R. Sutarto, C. McMahon, M. Zwiebler, M. Hücker, G. D. Gu, R. Liang, D. A. Bonn, W. N. Hardy *et al.*, Nat. Mater. **15,** 616 (2016).

[13] N. B. Aetukuri, A. X. Gray, M. Drouard, M. Cossale, L. Gao, A. H. Reid, R. Kukreja, H. Ohldag, C. A. Jenkins, E. Arenholz *et al.*, Nat. Phys. **9,** 661 (2013).

[14] Z. Tian, Y. Kohama, T. Tomita, H. Ishizuka, T. H. Hsieh, J. J. Ishikawa, K. Kindo, L. Balents, and S. Nakatsuji, Nat. Phys. **12,** 134 (2016).

[15] T. Liang, T. H. Hsieh, J. J. Ishikawa, S. Nakatsuji, L. Fu, and N. P. Ong, Nat. Phys. **13,** 599 (2017).

[16] S. V. Borisenko, A. A. Kordyuk, A. N. Yaresko, V. B. Zabolotnyy, D. S. Inosov, R. Schuster, B. Büchner, R. Weber, R. Follath, L. Patthey *et al.*, Phys. Rev. Lett. **100,** 196402 (2008).

[17] M.-Q. Ren, S. Han, S.-Z. Wang, J.-Q. Fan, C.-L. Song, X.-C. Ma, and Q.-K. Xue, Phys. Rev. Lett. **124,** 187001 (2020).

[18] F. Wang, S. A. Kivelson, and D.-H. Lee, Nat. Phys. **11,** 959 (2015).

[19] P. O. Sprau, A. Kostin, A. Kreisel, A. E. Böhmer, V. Taufour, P. C. Canfield, S. Mukherjee, P. J. Hirschfeld, B. M. Andersen, and J. C. S. Davis, Science **357,** 75 (2017).

[20] M. D. Johannes and I. I. Mazin, Phys. Rev. B **77,** 165135 (2008).

[21] K. Terashima, Y. Sekiba, J. H. Bowen, K. Nakayama, T. Kawahara, T. Sato, P. Richard, Y.-M. Xu, L. J. Li, G. H. Cao *et al.*, Proc. Natl. Acad. Sci. U.S.A. **106,** 7330 (2009).

[22] P. A. Lee, T. M. Rice, and P. W. Anderson, Phys. Rev. Lett. **31**, 462 (1973).

[23] P. A. Bhobe, A. Kumar, M. Taguchi, R. Eguchi, M. Matsunami, Y. Takata, A. K. Nandy, P. Mahadevan, D. D. Sarma, A. Neroni *et al.*, Phys. Rev. X **5**, 041004 (2015).

[24] J. Kanamori, J. Appl. Phys. **31**, S14 (1960).

[25] H. Y. Huang, Z. Y. Chen, R.-P. Wang, F. M. F. de Groot, W. B. Wu, J. Okamoto, A. Chainani, A. Singh, Z.-Y. Li, J.-S. Zhou *et al.*, Nat. Commun. **8**, 15929 (2017).

[26] A. M. Oleś, P. Horsch, L. F. Feiner, and G. Khaliullin, Phys. Rev. Lett. **96**, 147205 (2006).

[27] E. S. Bozin, W.-G. Yin, R. J. Koch, M. Abeykoon, Y. S. Hor, H. Zheng, H. C. Lei, C. Petrovic, J. F. Mitchell, and S. J. L. Billinge, Nat. Commun. **10**, 3638 (2019).

[28] L. Yang, R. J. Koch, H. Zheng, J. F. Mitchell, W.-G. Yin, M. G. Tucker, S. J. L. Billinge, and E. S. Bozin, Phys. Rev. B **102**, 235128 (2020).

[29] D. I. Khomskii and T. Mizokawa, Phys. Rev. Lett. **94**, 156402 (2005).

[30] M. Schmidt, W. Ratcliff, P. G. Radaelli, K. Refson, N. M. Harrison, and S. W. Cheong, Phys. Rev. Lett. **92**, 056402 (2004).

[31] E. S. Božin, A. S. Masadeh, Y. S. Hor, J. F. Mitchell, and S. J. L. Billinge, Phys. Rev. Lett. **106**, 045501 (2011).

[32] R. J. Koch, T. Konstantinova, M. Abeykoon, A. Wang, C. Petrovic, Y. Zhu, E. S. Bozin, and S. J. L. Billinge, Phys. Rev. B **100**, 020501(R) (2019).

[33] H. Ohashi, T. Fujita, and T. Osawa, J. Jpn. Assoc. Mineral., Petrol. Econ. Geol. **77**, 305 (1982).

[34] D. L. Anderson, *New Theory of the Earth* (Cambridge University Press, Cambridge, England, 2012).

[35] S. V. Streltsov, O. A. Popova, and D. I. Khomskii, Phys. Rev. Lett. **96**, 249701 (2006).

[36] H. J. Silverstein, A. E. Smith, C. Mauws, D. L. Abernathy, H. Zhou, Z. Dun, J. van Lierop, and C. R. Wiebe, Phys. Rev. B **90**, 140402(R) (2014).

[37] M. Isobe, E. Ninomiya, A. N. Vasil'ev, and Y. Ueda, J. Phys. Soc. Jpn. **71**, 1423 (2002).

[38] S. V. Streltsov and D. I. Khomskii, Phys. Rev. B **77**, 064405 (2008).

[39] Z. S. Popović, Ž. V. Šljivančanin, and F. R. Vukajlović, Phys. Rev. Lett. **93**, 036401 (2004).

[40] Z. S. Popović, Ž. V. Šljivančanin, and F. R. Vukajlović, Phys. Rev. Lett. **96**, 249702 (2006).

[41] A. E. Feiguin, A. M. Tsvelik, W.-G. Yin, and E. S. Bozin, Phys. Rev. Lett. **123**, 237204 (2019).

[42] T. Egami and S. J. L. Billinge, *Underneath the Bragg Peaks: Structural Analysis of Complex Materials*, 2nd ed. (Elsevier, Amsterdam, 2012).

[43] M. J. Konstantinović, J. van den Brink, Z. V. Popović, V. V. Moshchalkov, M. Isobe, and Y. Ueda, Phys. Rev. B **69**, 020409(R) (2004).

[44] B. Rivas-Murias, H. D. Zhou, J. Rivas, and F. Rivadulla, Phys. Rev. B **83**, 165131 (2011).

[45] See Supplemental Materials at http://link.aps.org/supplemental/10.1103/PhysRevLett.126.186402 for experimental and analysis details, lengthscale estimate, pressure effect and competing states considerations, which includes Refs. [46–53].

[46] P. J. Chupas, K. W. Chapman, and P. L. Lee, J. Appl. Crystallogr. **40**, 463 (2007).

[47] A. P. Hammersley, S. O. Svenson, M. Hanfland, and D. Hauserman, High Press. Res. **14**, 235 (1996).

[48] P. Juhás, T. Davis, C. L. Farrow, and S. J. L. Billinge, J. Appl. Crystallogr. **46**, 560 (2013).

[49] J. Neuefeind, M. Feygenson, J. Carruth, R. Hoffmann, and K. K. Chipley, Nucl. Instrum. Methods Phys. Res., Sect. B **287**, 68 (2012).

[50] A. C. Larson and R. B. Von Dreele, Los Alamos National Laboratory Report No. LAUR-86-748, 2004.

[51] B. H. Toby, J. Appl. Crystallogr. **34**, 210 (2001).

[52] C. L. Farrow, P. Juhás, J. Liu, D. Bryndin, E. S. Božin, J. Bloch, T. Proffen, and S. J. L. Billinge, J. Phys. Condens. Matter **19**, 335219 (2007).

[53] P. Juhás, C. L. Farrow, X. Yang, K. R. Knox, and S. J. L. Billinge, Acta Crystallogr. Sect. A **71**, 562 (2015).

[54] M. G. Tucker, M. P. Squires, M. T. Dove, and D. A. Keen, J. Phys. Condens. Matter **13**, 403 (2001).

[55] X. Qiu, T. Proffen, J. F. Mitchell, and S. J. L. Billinge, Phys. Rev. Lett. **94**, 177203 (2005).

[56] G. J. Redhammer, H. Ohashi, and G. Roth, Acta Crystallogr. Sect. B **59**, 730 (2003).

[57] R. D. Shannon, Acta Crystallogr. A **32**, 751 (1976).

[58] M. J. Konstantinović, J. van den Brink, Z. V. Popović, V. V. Moshchalkov, M. Isobe, and Y. Ueda, J. Magn. Magn. Mater. **272**–**276**, E657 (2004).

[59] T. Furubayashi, T. Kosaka, J. Tang, T. Matsumoto, Y. Kato, and S. Nagata, J. Phys. Soc. Jpn. **66**, 1563 (1997).

[60] L. Ma, H. Han, W. Liu, K. Yang, Y. Zhu, C. Zhang, L. Pi, D. Liu, L. Zhang, and Y. Zhang, Dalton Trans. **46**, 6708 (2017).

[61] T. Hikihara and Y. Motome, Phys. Rev. B **70**, 214404 (2004).

[62] *Spin Crossover in Transition Metal Compounds I, II, and III. Topics in Current Chemistry*, edited by G. Gütlich and H. A. Goodwin (Springer-Verlag, Berlin, 2004), Vols. 233, 234, 235.

[63] W. Yin, arXiv:2006.08921.

[64] W. Yin, arXiv:2006.15087.

[65] P. J. Baker, S. J. Blundell, F. L. Pratt, T. Lancaster, M. L. Brooks, W. Hayes, M. Isobe, Y. Ueda, M. Hoinkis, M. Sing *et al.*, Phys. Rev. B **75**, 094404 (2007).

[66] Z. V. Popović, M. J. Konstantinović, Z. Dohčević-Mitrović, M. Isobe, and Y. Ueda, Physica (Amsterdam) **378**–**380B**, 1072 (2006).

[67] J. van Wezel and J. van den Brink, Europhys. Lett. **75**, 957 (2006).

[68] Z. Hiroi, Prog. Solid State Chem. **43**, 47 (2015).

[69] J. P. Attfield, APL Mater. **3**, 041510 (2015).

[70] T. Katsufuji, T. Okuda, R. Murata, T. Kanzaki, K. Takayama, and T. Kajita, J. Phys. Soc. Jpn. **85**, 013703 (2016).

ARTICLE   OPEN

Check for updates

Charge density waves in cuprate superconductors beyond the critical doping

H. Miao [1] ✉, G. Fabbris [2], R. J. Koch[1], D. G. Mazzone [1,7], C. S. Nelson[3], R. Acevedo-Esteves[3], G. D. Gu[1], Y. Li[1], T. Yilimaz[3], K. Kaznatcheev[3], E. Vescovo[3], M. Oda[4], T. Kurosawa [4], N. Momono[5], T. Assefa[1,8], I. K. Robinson [1,6], E. S. Bozin[1], J. M. Tranquada [1], P. D. Johnson[1] and M. P. M. Dean [1] ✉

The unconventional normal-state properties of the cuprates are often discussed in terms of emergent electronic order that onsets below a putative critical doping of $x_c \approx 0.19$. Charge density wave (CDW) correlations represent one such order; however, experimental evidence for such order generally spans a limited range of doping that falls short of the critical value x_c, leading to questions regarding its essential relevance. Here, we use X-ray diffraction to demonstrate that CDW correlations in $La_{2-x}Sr_xCuO_4$ persist up to a doping of at least $x = 0.21$. The correlations show strong changes through the superconducting transition, but no obvious discontinuity through $x_c \approx 0.19$, despite changes in Fermi surface topology and electronic transport at this doping. These results demonstrate the interaction between CDWs and superconductivity even in overdoped cuprates and prompt a reconsideration of the role of CDW correlations in the high-temperature cuprate phase diagram.

INTRODUCTION

The cuprate high-T_c superconductors are often conceptualized as doped Mott insulators, in which the electronic ground state spontaneously breaks rotational and/or translational symmetry[1–4]. While cuprate CDW correlations were discovered over two decades ago[5], their possible contribution to the material's anomalous electronic properties remains a matter of vigorous debate[1,6–10]. This issue has gained increasing attention in light of the ubiquity of CDW order in different cuprate families[5,11–19]. The cuprate phase diagram, shown in Fig. 1a, shows that pseudogap, strange metal, and superconducting phases exist over an extensive doping range below a critical doping level of $x_c \approx 0.19$, above which the cuprate electronic properties become gradually more Fermi-liquid-like[20–27]. If CDW correlations are confined to underdoped cuprates, as previously suggested[11–21], that would preclude the possibility of CDW correlations having an important role in the anomalous electronic properties. For instance, it has been argued that since CDW correlations disappear at $x \ll x_c$, the quantum critical point (QCP) at $x = x_c$ must be magnetic in nature[8]. Tunneling spectroscopy studies have suggested a vestigial nematic QCP on a similar basis[28,29]. Very recent nuclear magnetic resonance results have reported the disappearance of spin glass behavior near x_c[30]. Whether this disappearance is associated with the loss of stripe correlations (i.e., coupled spin and charge density waves) remains unresolved. Moreover, the existence of CDW correlations is also crucial for the relevance of intertwined order. Many theoretical models for pair density wave superconducting states, for example, require the presence of CDW correlations[1,31].

Studies of underdoped and optimally doped cuprates have shown that CDW correlations exist up to temperatures well above the nominal C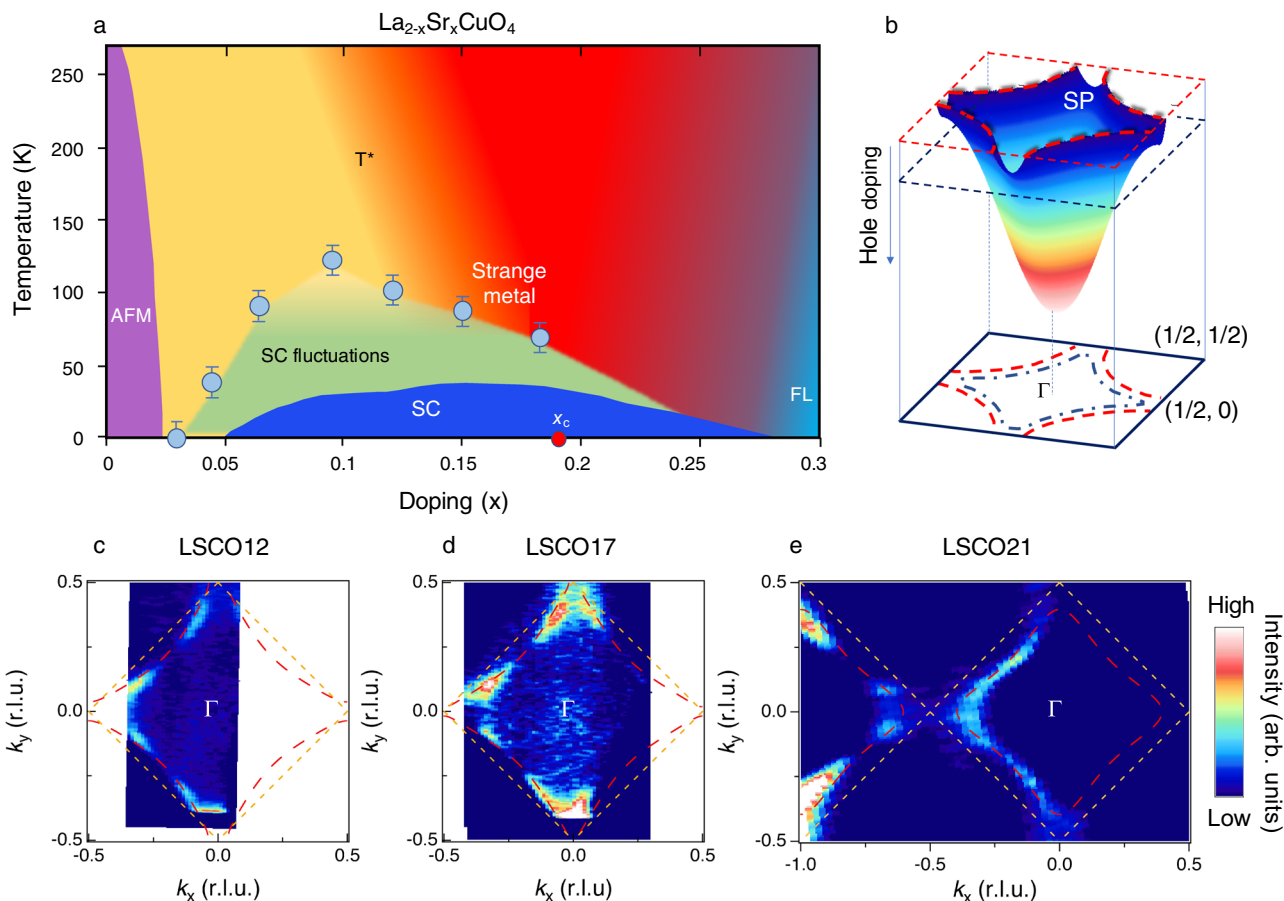DW transition temperature[32,33]. More recently, re-entrant charge order, disconnected from the CDW at lower doping, was observed in overdoped $(Bi, Pb)_{2.12}Sr_{1.88}CuO_{6+\delta}$[19]. These results motivate a reconsideration of the cuprate phase diagram, in which CDW correlations may extend up to higher dopings than previously thought[33]. Herein, we address this issue by focusing on $La_{2-x}Sr_xCuO_4$ (LSCOx) ($x = 0.12, 0.17, 0.21$, and 0.25) single crystals in view of its particularly well-characterized transport properties and the feasibility of synthesizing high-quality samples across the entire phase diagram[21,24–27] (see Methods section).

RESULTS

Electronic structure

Previous measurements of LSCO established the presence of a critical doping $x_c \sim 0.19$, which was defined as the doping above which the electronic transport acquires partial Fermi-liquid-like properties[21,24]. This point coincides with, and is perhaps related to, the doping where the Fermi surface (FS) topology undergoes a Lifshitz transition[34,35]. To prove the Sr doping, x, is consistent with previous studies, and that we indeed access the $x > x_c$ region of the overdoped phase diagram, we show the electronic structure evolution with doping in Fig. 1b–e. The angle-resolved photo-emission spectroscopy (ARPES) methods used are described in the Methods section. Figure 1b illustrating the two-dimensional electronic structure. At low doping, to the extent that a FS exists, it is hole-like and centered at the Brillouin zone corner. With increasing hole concentration, the chemical potential drops and eventually passes through the saddle point. This results in a Lifshitz transition to an electron-like FS at the Brillouin zone center. In LSCO, the saddle point is three-dimensional with small k_z dispersion. Near x_c, the saddle point coincidentally crosses the

Fig. 1 Doping-dependent electronic structure of LSCO. **a** Phase diagram of the hole-doped cuprates, constructed from magnetization, Nernst effect, and resistivity data for LSCO[20,52]. T^* is the extracted pseudogap onset temperature[20,52]. **b** Schematic band structure of LSCO. The Fermi energy, E_F, crosses the anti-nodal saddle point (labeled as SP) near $x_c \approx 0.19$ triggering a Lifshitz transition. **c–e** Fermi surface topology of LSCO12, LSCO17, and LSCO21. The intensity plots are obtained by integrating the spectra within ± 10 meV of E_F. Orange dashes outline the antiferromagnetic Brillouin zone. Red dashed contours represent a tight-binding fit of the Fermi surface (see Supplementary note 1). The data shown in **c–e** were collected at 11 K.

Fermi level. It should be noted that the carrier concentration determined by the FS area is significantly larger than the nominal Sr doping. The origin of this effect remains unresolved[34,35]. Nevertheless, the well-established FS evolution in LSCO can be used to confirm the Sr doping in this study. Figure 1c–e shows ARPES measurements for LSCO12, LSCO17, and LSCO21. An electron-like FS is observed in LSCO21, consistent with $x_c = 0.19$ and in agreement with previous ARPES studies[34,35].

CDW order

Having confirmed the electronic structure, we now present our main experimental finding of CDW correlations beyond x_c. Figure 2 plots X-ray reciprocal space scans for LSCO21 at $T = 16$ K, where reciprocal space is defined in terms of scattering vector $Q = (H, K, L)$ using effective tetragonal lattice constants $a = b \approx 3.8$ Å and $c \approx 13.2$ Å. High sensitivity is achieved by exploiting the high brightness of the National Synchrotron Light Source II (NSLS-II) and by careful configuration of the detection system to suppress background signal (see Methods section). Superlattice peaks are observed at (0.235, 0, 12.5), and equivalent locations, along both the H and K directions [Fig. 2a, b]. The observed $H = 0.235$ matches the CDW wavevector in underdoped LSCO[16–18,36] and is consistent with the charge stripe picture[5]. The peaks are symmetric with respect to $\pm H$ and K and are observed in multiple Brillouin zones including $(\pm 0.235, 0, L)$ for $L = 8.5$ and 12.5. An L-scan along $Q = (-0.235, 0, L)$ [Fig. 2d] reveals that the CDW

intensity is broadly peaked at half-integer L similar to underdoped LSCO[17,18,37]. These results demonstrate the presence of CDW correlations beyond x_c. Subsequent inelastic X-ray scattering studies show that the CDW is associated with phonon softening even in the overdoped regime[38].

CDW temperature dependence

Figure 3 summarizes the doping and temperature dependence of the CDW correlations. In Fig. 3a, Lorentzian-squared fits to the data are shown, which are parameterized in terms of amplitude, $I_{CDW}(T)$, and in-plane correlation length, $\xi_{\parallel}(T) = 1/$HWHM (where HWHM is half-width at half-maximum) (see Supplementary note 2). Since domain formation can lead to transverse peak splitting in LSCO [c.f. refs. [16,18,36] and Fig. 3a], we scanned through the peaks in all three reciprocal space directions. Two Lorentzian-squared functions displaced in the K (transverse) direction were used, where necessary, to account for the full intensity distribution. Peak widths and correlation lengths are determined using the H (longitudinal) cut. $I_{CDW}(T)$ is found to be largest near T_{SC} for all dopings [Fig. 3b]. Above T_{SC}, both I_{CDW} and $\xi_{\parallel}(T)$ decrease with increasing temperature but remain finite up to at least $T = 90$ K [Fig. 3a]. In agreement with previous X-ray diffraction studies of LSCO[16,17,36], the correlation length can be separated into a marginally-ordered regime where $\xi_{\parallel}(T)$ is ~4-unit cells (about one period of the CDW order), and a strongly T-dependent regime where $\xi_{\parallel}(T)$ continues to expand until superconductivity
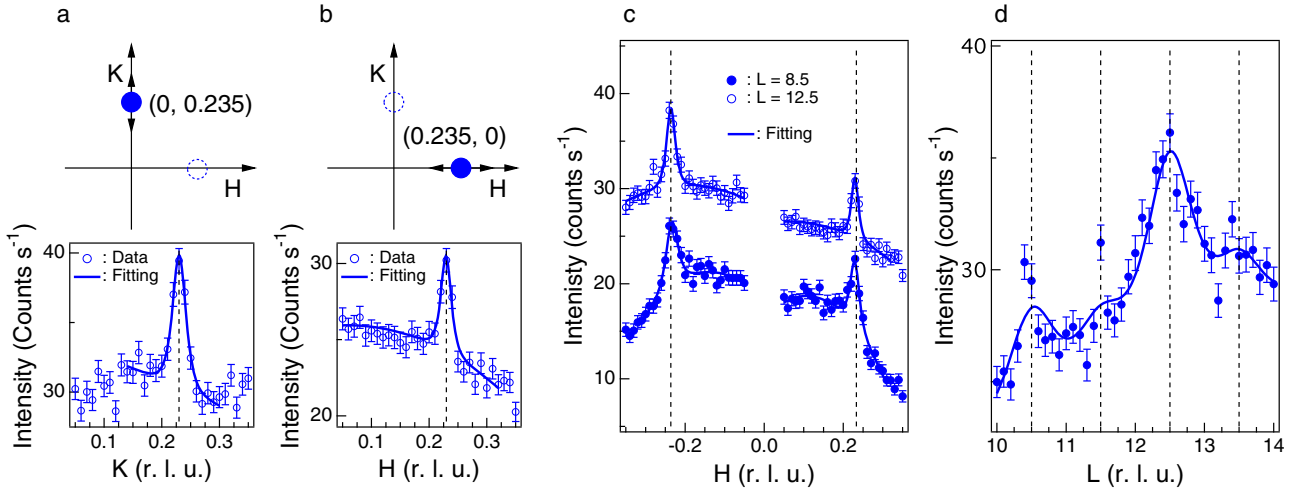
Fig. 2 Discovery of a CDW beyond x_c. a, b X-ray diffraction measurements of LSCO21 at $T = 16$ K along $(0, K, 12.5)$ and $(H, 0, 12.5)$. Supperlattice peaks are observed at $(0, 0.235, 12.5)$ and $(0.235, 0, 12.5)$. The H-scans in **c** reveal further CDW peaks at $(\pm 0.235, 0, L)$ for $L = 8.5$ and 12.5. The data at $L = 8.5$ are offset by -10 counts s^{-1} for visibility. **d** The L-dependence of the intensity along $(-0.235, 0, L)$ demonstrates poorly correlated out-of-phase CDW stacking along the c-axis. Solid lines are fits to the experimental data as described in the text and Supplementary note 2. Error bars are one standard deviation based on Poissonian statistics.
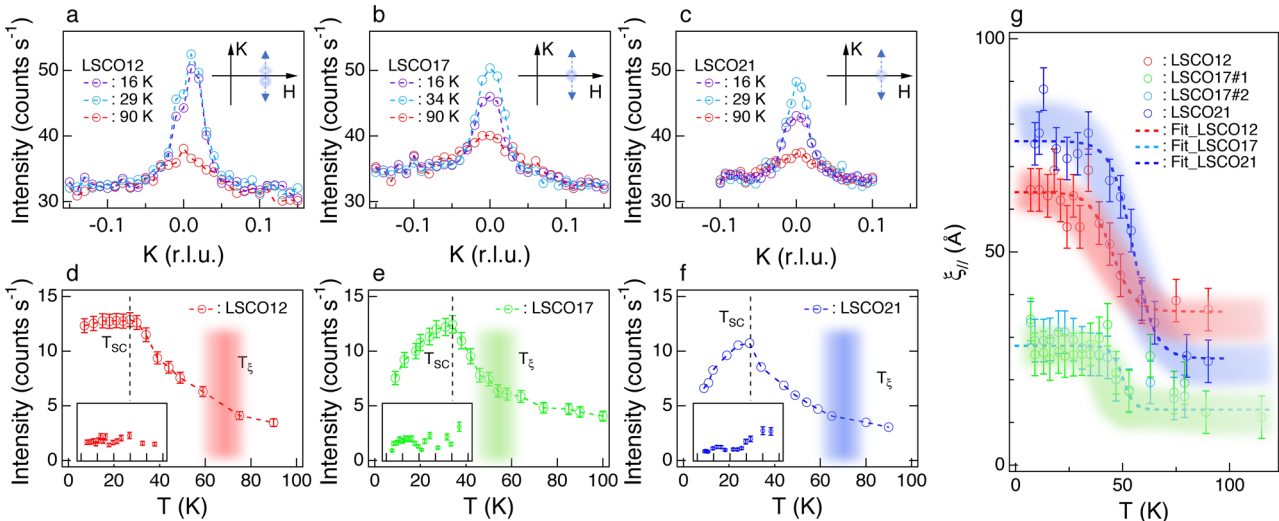
Fig. 3 CDW temperature dependence. Doping dependence of the CDW peak intensity for temperatures $T < T_{SC}$, $T \approx T_{SC}$, and $T > T_{SC}$ for **a** LSCO12, **b** LSCO17, and **c** LSCO21. The inset of each panel represents the respective cut in reciprocal space. All data were taken at $L = 8.5$. Temperature dependence of the CDW intensity in LSCO for **d** LSCO12, **e** LSCO17, and **f** LSCO21. The shaded area corresponds to T_ξ where the in-plane CDW correlation length, $\xi_\parallel$, starts to increase [as determined in **g**]. The main panels show peak height intensity and the insets show integrated intensity. **g** Temperature dependence of $\xi_\parallel$. The colored shaded curves are phenomenological fittings, $a + \frac{b}{1+e^{(T-T_0)/4\Delta T}}$, of the temperature-dependent $\xi_\parallel$ for different dopings. Here we define $T_\xi = T_0 + \Delta T$. $\xi_\parallel$ increases with decreasing temperature for $T_{SC} < T < T_\xi$. Two independent measurements of LSCO17 samples at different beamlines show consistent suppression of $\xi_\parallel$ and T_ξ, indicating that systematic errors are minimal. Due to the short correlation length, the uncertainty of T_ξ may be larger in LSCO17 than other dopings. Error bars are one standard deviation from either Poissonian statistics or least-squares fitting.

intervenes. We refer to the CDW in the T-independent regime as "precursor" CDW correlations in the sense that they come before the emergence of a stronger, more correlated CDW at low temperatures. Note that for these measurements we do not have the energy resolution to directly distinguish between dynamic and static correlations. The short correlation length and quasi-temperature-independent nature of the percursor CDW indicates that it might be dynamic in nature. This phenomenology is consistent with resonant inelastic X-ray scattering (RIXS) scattering studies of La$_{2-x}$Ba$_x$CuO4 (LBCOx) and YBa$_2$Cu$_3$O$_{6+\delta}$ which show a similar two-stage CDW formation[32,33,39,40]. While the CDW evolves smoothly from LSCO12 to LSCO21, both $\xi_\parallel$ and the onset

temperature of the longer-range CDW, T_ξ, are suppressed in the overdoped regime around x_c [Figs. 3c and 4]. The Q-integrated scattering intensity, as estimated by $I_{CDW}\xi_\parallel^2$, shows minimal variation through T_{SC}, indicating that while superconductivity alters the CDW correlation length, it does not strongly suppress the order parameter. We do not observe any CDW correlations in our high-sensitivity X-ray measurements at $x = 0.25$ (see Supplementary note 3).

Previous measurements of the same $x = 0.12$ sample allow us to compare the CDW order parameter, taken to be captured by the total Q-integrated scattering intensity, to other cuprate systems[16]. The CDW order parameter of LSCO12 is only four times weaker than
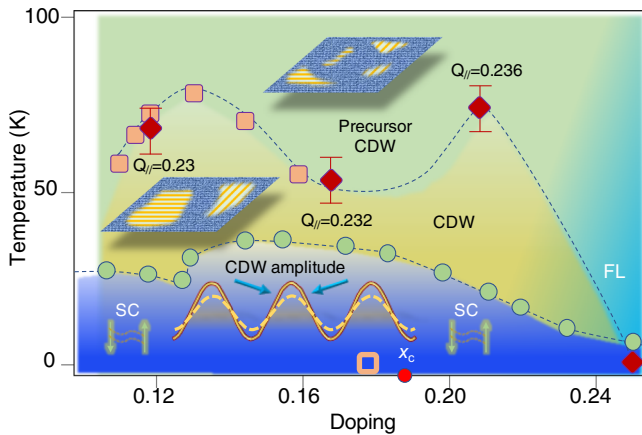
Fig. 4 Illustration of the extent of CDW correlations in the cuprate phase diagram suggested by this work. Green-yellow tones represent our main result—the presence of CDW correlations, from $0.12 < x < 0.21$. Green denotes the precursor CDW, which appear at high temperature and which have a correlation length of approximately one CDW period[32,33,39,40]. At lower temperature, the correlations start to grow into larger CDW domains, as evidenced by the increased correlation length, which we denote by the yellow tone. Red points mark where the correlation length starts to increase. This should be considered an approximate cross-over and not over-interpreted as a well-defined phase transition. At lower temperatures still, bulk d-wave superconductivity intervenes at T_{SC} whereupon both the CDW amplitude and the correlation length saturate or start to decrease. The doping dependence reveals an anticorrelation between T_ξ and T_{SC}, providing evidence for an interaction between the CDW and superconductivity. This is illustrated by the cartoon in the bottom of the diagram in which superconducting pairing (green spin pairs) suppress the CDW (yellow solid and dashed sinusoidal curves). The CDW intensity disappears in heavily overdoped LSCO25, where a Fermi-liquid-like state is recovered (Supplementary notes 3 and 5). The red diamonds reflect the present study. Pink squares and green circles are data from previous work[16,17,36,52].

$La_{1.875}Ba_{0.125}CuO_4$ (which has the strongest zero-field CDW order). With increasing doping, the LSCO CDW becomes somewhat stronger for $x = 0.17$ and drops appreciably for $x = 0.21$ (see Supplementary note 4). Consequently, CDW correlations can have an appreciable effect on the physics of LSCOx for dopings through x_c.

DISCUSSION

Figure 4 summarizes our main observations—that CDW correlations exist far into the overdoped regime of the cuprate phase diagram. This immediately yields three important consequences for LSCO. Firstly, very similar CDW properties are observed either side of the Lifshitz transition. This provides a vivid demonstration that CDW correlations cannot be explained within a weak coupling FS nesting picture nor Friedel oscillations. Instead, the nearly constant Q_{CDW} for dopings $x \geq 0.125$ support strong coupling mechanisms, which date back to seminal work in the late 1980s[2–4]. In these mechanisms, one considers the balance between Coulomb interactions and kinetic energy. When doping a Mott insulator, holes can save energy by clustering together as this breaks fewer magnetic bonds than widely dispersed holes. At the same time, this clustering is disfavored by the increased Coulomb repulsion and kinetic energy reduction. Since these different interactions act on different lengthscales, the overall minimum energy solution is expected to involve a spatially modulated state. Modern numerical solutions of the Hubbard model further support this idea[41–43] and models based on filled stripes can reproduce a doping-independent CDW wavevector from $x = 1/8$ to $x = 1/4$[44]. We also note that precursor CDW

correlations are emerging as a ubiquitous feature for many cuprates, including LSCO in this study, underdoped LBCO[40], underdoped and optimally doped YBCO[33], underdoped Bi2212[45], and $HgBa_2CuO_{4+\delta}$[46]. In underdoped and optimally doped YBCO, the precursor correlations appear to exist at the same wavevector around 0.3 r.l.u. different to the doping-dependent low-temperature CDW[33]. It would consequently be interesting to consider a possible role for strong coupling mechanisms for all cuprates. An obviously desirable experiment would be to test whether other cuprates, such as YBCO, also exhibit CDW correlations up to similarly high dopings as LSCO. Such experiments are, however, currently held back by challenges in stabilizing high-quality heavily overdoped YBCO crystals. The robust presence of CDW correlations in LSCO seen here as a function of temperature and doping, as well as the fact that model Hamiltonian calculations reliably predict CDW correlations[41–43], would point towards their likely presence. The issue of differing wavevectors in different cuprates would, however, not necessarily be solved by such an experiment. In this regard, it is important to point out the low-temperature ordering wavevector can be influenced by coupling between the CDW and spin correlations or coupling between the CDW and the lattice, as has been suggested theoretically[47], so differences in CDW wavevectors could arise from secondary interactions rather than necessarily indicating a distinct origin for the correlations. Prior work has pointed towards this as a possible explanation for temperature-induced changes in CDW wavevector in LBCO[32].

A second immediate conclusion is that the continuous evolution of the CDW correlations is inconsistent with the proposed QCP that is associated with x_c arising from CDW or coupled CDW/spin density wave order[6,10]. Such theories can still be excluded even if one postulates a very narrow range of criticality around x_c, since they require either a disappearance or a symmetry change of the CDW through x_c.

Last but not least, the disappearance of CDW in LSCO25 suggests that the CDW dome in LSCO terminates between $x = 0.21$ and 0.25, where the Fermi-liquid behavior starts to recover[21,24,25]. This is, again, consistent with a strong coupling CDW mechanism as Coulomb repulsion is largely screened in the Fermi-liquid state. We note that in LSCO, the structural high-temperature tetragonal to low-temperature orthorhombic (LTO) phase transition also terminates near $x = 0.21$[48]. It has been argued that the local LTO distortion may help to stabilize the CDW[49]. The persistence of CDW correlations up to $x = 0.21$ observed in this study is consistent with this scenario and indicates that electron-phonon coupling might be an important ingredient for the CDW formation[38,39].

The observations herein also urge a re-examination of the potential role of CDWs in the anomalous electronic properties of the cuprates. CDW correlations are a prerequisite (but not a proof) of several prominent theories of cuprate properties, which would be expected to apply across the phase diagram and not just in the underdoped region where CDW correlations have been studied extensively in the past. This include the possibility that CDW correlations play a key role in the electronic transport properties[6,10]. Theories of pair density wave order[1,31,50,51], which predict competition between the CDW and uniform d-wave superconductivity, also fall into this category. As shown in Fig. 3, neither the CDW peak intensity nor the CDW correlation length shows the type of divergent-behavior associated with a typical phase transition. This behavior is consistent with a possible fluctuating CDW component, potentially influencing cuprate transport properties[24–27,33].

Finally, we note that a charge Bragg peak has recently been observed in overdoped $(Bi, Pb)_{2.12}Sr_{1.88}CuO_{6+\delta}$ (Bi2201), with a maximum doping comparable to that observed here[19]. This state, termed re-entrant charge order, has several properties that are different to CDW states in LSCO and other cuprates. Re-entrant

charge order appears to exist only in an isolated region of the overdoped phase diagram, disconnected from the underdoped CDW order. The correlation length and temperature scale of this state are also far higher than other cuprates. Intriguingly, no interaction between re-entrant charge order and superconductivity is observed in Bi2201. In contrast, similarly well-correlated CDW states are associated with a strong suppression of superconductivity. All these behaviors are in strong contrast with the CDW in overdoped LSCO, where the CDW wavevectors, correlation length, and temperature dependence evolve smoothly from the properties of underdoped LSCO and strongly intertwine with superconductivity and low-temperature transport. Based on the electronic structure of Bi2201 and the wavevector of re-entrant charge order around 0.1 r.l.u., which extrapolates roughly linearly from the underdoped CDW wavevector, re-entrant charge order was proposed to arise from a van Hove singularity[19]. The overdoped CDW in LSCO appears to have no connection to this mechanism, since the CDW remains unchanged regardless of the proximity to the van Hove singularity at $x = x_c$. Instead, our observations support strong coupling mechanisms.

In summary, high-sensitivity X-ray measurements have revealed that cuprate CDW correlations persist across almost the whole cuprate doping phase diagram, despite dramatic changes in the transport properties and FS topology, before disappearing when Fermi-liquid-like properties are restored. We have shown that these correlations impact superconductivity even in overdoped cuprates, suggesting that CDW correlations can have a far more extensive role in the cuprate phase diagram than previously envisaged, prompting investigations of CDW correlations in other overdoped cuprates. The discovery of CDWs beyond x_c is confirmed by subsequent RIXS studies, which uncovered an unusual coupling between the CDW and lattice vibrations[38].

METHODS
Samples
Single crystals of $La_{2-x}Sr_xCuO_4$ ($x = 0.12$, 0.17, 0.21, and 0.25) were grown by the traveling-solvent floating-zone method. For each composition, a single feed rod of 20 – 25 cm long was used, the first few centimeters of which was removed and discarded after growth. The remaining rod was annealed in flowing O_2 at 980 °C for 1 week. The superconducting transition temperatures, 28, 37, 30, and 10 K were determined by dc magnetization measurements in an applied field of 1 mT (after cooling in zero field). Our tight-binding fits to our ARPES measurements of these samples, described in Supplementary note 1, confirm the hole concentration matches the strontium content x.

ARPES
ARPES measurements were performed at the 21-ID-1 beamline of the NSLS-II using a Scienta-DA30 analyzer. Due to the small incident beam spot-size (less than 10×10 μm²), both the sample position and the incident light angle are fixed during the measurement. The ARPES intensity maps are obtained using the mapping-mode of the DA30 analyzer, which can cover 30° of cone acceptance without sample rotation. All samples were cleaved in-situ and measured at 11 K within a vacuum better than 7×10^{-11} mbar. The photon energy was set to 60 eV for LSCO12 and LSCO17 with 18 meV energy resolution. To confirm the FS of LSCO21 is a closed loop at the Γ point, we set the photon energy to 195 eV for LSCO21 with 90 meV energy resolution. At this energy, we were able to cover the second Brillouin zone without sample rotation. The chemical potential is calibrated based on the ARPES spectra on Silver that are recorded before and after the ARPES measurement.

Non-resonant hard X-ray scattering
High-precision X-ray scattering measurements were performed at the in-situ and resonant 4-ID beamline of NSLS-II and 4-ID-D beamline of the Advanced Photon Source (APS). The incident photon energy was set to 8.98 keV; slightly below the Cu K-edge to minimize the fluorescence background. The measurements at NSLS-II were carried out with an avalanche photodiode detector. A LiF(004) crystal analyzer was used to
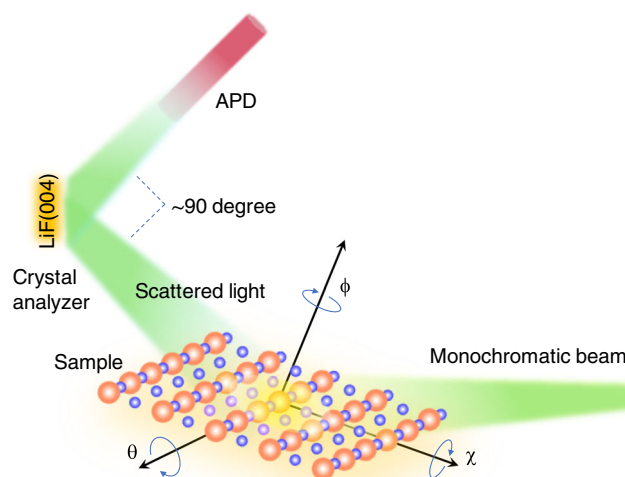
Fig. 5 Experimental setup. Illustration of the experimental geometry at the 4-ID beamline of NSLS-II.

further suppress the background signal (Fig. 5). The measurements at the APS used a Vortex Si drift detector without any crystal analyzer.

DATA AVAILABILITY
Data are available from the corresponding author upon reasonable request.

REFERENCES
1. Fradkin, E., Kivelson, S. A. & Tranquada, J. M. *Colloquium*: theory of intertwined orders in high temperature superconductors. *Rev. Mod. Phys.* **87**, 457–482 (2015).
2. Zaanen, J. & Gunnarsson, O. Charged magnetic domain lines and the magnetism of high-T_c oxides. *Phys. Rev. B* **40**, 7391–7394 (1989).
3. Machida, K. Magnetism in La_2CuO_4 based compounds. *Physica C Supercond.* **158**, 192–196 (1989).
4. Emery, V. J., Kivelson, S. A. & Lin, H. Q. Phase separation in the $t - J$ model. *Phys. Rev. Lett.* **64**, 475–478 (1990).
5. Tranquada, J., Sternlieb, B., Axe, J., Nakamura, Y. & Uchida, S. Evidence for stripe correlations of spins and holes in copper oxide superconductors. *Nature* **375**, 561–563 (1995).
6. Castellani, C., Di Castro, C. & Grilli, M. Singular quasiparticle scattering in the proximity of charge instabilities. *Phys. Rev. Lett.* **75**, 4650–4653 (1995).
7. Sachdev, S. Where is the quantum critical point in the cuprate superconductors? *Phys. status solidi B* **247**, 537–543 (2010).
8. Doiron-Leyraud, N. & Taillefer, L. Quantum critical point for stripe order: an organizing principle of cuprate superconductivity. *Physica C Supercond.* **481**, 161–167 (2012).
9. Sebastian, S. E. & Proust, C. Quantum oscillations in hole-doped cuprates. *Annu. Rev. Condens. Matter Phys.* **6**, 411–430 (2015).
10. Caprara, S., Di Castro, C., Seibold, G. & Grilli, M. Dynamical charge density waves rule the phase diagram of cuprates. *Phys. Rev. B* **95**, 224511 (2017).
11. Hoffman, J. et al. A four unit cell periodic pattern of quasi-particle states surrounding vortex cores in $Bi_2Sr_2CaCu_2O_{8+\delta}$. *Science* **295**, 466–469 (2002).
12. Howald, C., Eisaki, H., Kaneko, N. & Kapitulnik, A. Coexistence of periodic modulation of quasiparticle states and superconductivity in $Bi_2Sr_2CaCu_2O_{8+\delta}$. *Proc. Natl. Acad. Sci. USA* **100**, 9705–9709 (2003).
13. Ghiringhelli, G. et al. Long-range incommensurate charge fluctuations in (Y,Nd)$Ba_2Cu_3O_{6+x}$. *Science* **337**, 821–825 (2012).
14. Comin, R. et al. Charge order driven by Fermi-arc instability in $Bi_2Sr_{2-x}La_xCuO_{6+\delta}$. *Science* **343**, 390–392 (2014).
15. Tabis, W. et al. Charge order and its connection with Fermi-liquid charge transport in a pristine high-T_c cuprate. *Nat. Commun.* **5**, 5875 (2014).

16. Thampy, V. et al. Rotated stripe order and its competition with superconductivity in $La_{1.88}Sr_{0.12}CuO_4$. *Phys. Rev. B* **90**, 100510 (2014).
17. Croft, T. P., Lester, C., Senn, M. S., Bombardi, A. & Hayden, S. M. Charge density wave fluctuations in $La_{2-x}Sr_xCuO_4$ and their competition with superconductivity. *Phys. Rev. B* **89**, 224513 (2014).
18. Christensen, N. B. et al. Bulk charge stripe order competing with superconductivity in $La_{2-x}Sr_xCuO_4$ ($x = 0.12$) Preprint at https://arxiv.org/abs/1404.3192 (2014).
19. Peng, Y. et al. Re-entrant charge order in overdoped $(Bi, Pb)_{2.12}Sr_{1.88}CuO_{6+\delta}$ outside the pseudogap regime. *Nat. Mater.* **17**, 697–702 (2018).
20. Wang, Y., Li, L. & Ong, N. P. Nernst effect in high-T_c superconductors. *Phys. Rev. B* **73**, 024510 (2006).
21. Cooper, R. A. et al. Anomalous criticality in the electrical resistivity of $La_{2-x}Sr_xCuO_4$. *Science* **323**, 603–607 (2009).
22. Keimer, B., Kivelson, S., Norman, M., Uchida, S. & Zaanen, J. From quantum matter to high-temperature superconductivity in copper oxides. *Nature* **518**, 179–186 (2015).
23. Ramshaw, B. J. et al. Quasiparticle mass enhancement approaching optimal doping in a high-T_c superconductor. *Science* **348**, 317–320 (2015).
24. Badoux, S. et al. Critical doping for the onset of Fermi-surface reconstruction by charge-density-wave order in the cuprate superconductor $La_{2-x}Sr_xCuO_4$. *Phys. Rev. X* **6**, 021004 (2016).
25. Giraldo-Gallo, P. et al. Scale-invariant magnetoresistance in a cuprate superconductor. *Science* **361**, 479–481 (2018).
26. Boebinger, G. S. et al. Insulator-to-metal crossover in the normal state of $La_{2-x}Sr_xCuO_4$ near optimum doping. *Phys. Rev. Lett.* **77**, 5417–5420 (1996).
27. Michon, B. et al. Thermodynamic signatures of quantum criticality in cuprate superconductors. *Nature* **567**, 218–222 (2019).
28. Nie, L., Tarjus, G. & Kivelson, S. A. Quenched disorder and vestigial nematicity in the pseudogap regime of the cuprates. *Proc. Natl. Acad. Sci. USA* **111**, 7980–7985 (2014).
29. Mukhopadhyay, S. et al. Evidence for a vestigial nematic state in the cuprate pseudogap phase. *Proc. Natl. Acad. Sci. USA* **116**, 13249–13254 (2019).
30. Frachet, M. et al. Hidden magnetism at the pseudogap critical point of a cuprate superconductor. *Nat. Phys.* **16**, 1064–1068 (2020).
31. Agterberg, D. F. et al. The physics of pair-density waves: cuprate superconductors and beyond. *Annu. Rev. Condens. Matter Phys.* **11**, 231–270 (2020).
32. Miao, H. et al. High-temperature charge density wave correlations in $La_{1.875}Ba_{0.125}CuO_4$ without spin–charge locking. *Proc. Natl. Acad. Sci. USA* **114**, 12430–12435 (2017).
33. Arpaia, R. et al. Dynamical charge density fluctuations pervading the phase diagram of a Cu-based high-T_c superconductor. *Science* **365**, 906–910 (2019).
34. Yoshida, T. et al. Systematic doping evolution of the underlying Fermi surface of $La_{2-x}Sr_xCuO_4$. *Phys. Rev. B* **74**, 224510 (2006).
35. Horio, M. et al. Three-dimensional Fermi surface of overdoped La-based cuprates. *Phys. Rev. Lett.* **121**, 077004 (2018).
36. Wen, J.-J. et al. Observation of two types of charge-density-wave orders in superconducting $La_{2-x}Sr_xCuO_4$. *Nat. Commun.* **10**, 3269 (2019).
37. Thampy, V. et al. Comparison of charge modulations in $La_{1.875}Ba_{0.125}CuO_4$ and $YBa_2Cu_3O_{6.6}$. *Phys. Rev. B* **88**, 024505 (2013).
38. Lin, J. Q. et al. Strongly correlated charge density wave in $La_{2-x}Sr_xCuO_4$ evidenced by doping-dependent phonon anomaly. *Phys. Rev. Lett.* **124**, 207005 (2020).
39. Miao, H. et al. Incommensurate phonon anomaly and the nature of charge density waves in cuprates. *Phys. Rev. X* **8**, 011008 (2018).
40. Miao, H. et al. Formation of incommensurate charge density waves in cuprates. *Phys. Rev. X* **9**, 031042 (2019).
41. Corboz, P., Rice, T. M. & Troyer, M. Competing states in the t-J model: uniform d-wave state versus stripe state. *Phys. Rev. Lett.* **113**, 046402 (2014).
42. Huang, E. W. et al. Numerical evidence of fluctuating stripes in the normal state of high-T_c cuprate superconductors. *Science* **358**, 1161–1164 (2017).
43. Zheng, B.-X. et al. Stripe order in the underdoped region of the two-dimensional Hubbard model. *Science* **358**, 1155–1160 (2017).
44. Lorenzana, J. & Seibold, G. Metallic mean-field stripes, incommensurability, and chemical potential in cuprates. *Phys. Rev. Lett.* **89**, 136401 (2002).
45. Chaix, L. et al. Dispersive charge density wave excitations in $Bi_2Sr_2CaCu_2O_{8+\delta}$. *Nat. Phys.* **13**, 952 (2017).
46. Yu, B. et al. Unusual dynamic charge correlations in simple-tetragonal $HgBa_2CuO_{4+\delta}$. *Phys. Rev. X* **10**, 021059 (2020).
47. Zachar, O., Kivelson, S. A. & Emery, V. J. Landau theory of stripe phases in cuprates and nickelates. *Phys. Rev. B* **57**, 1422–1426 (1998).
48. Hücker, M. et al. Dzyaloshinsky-Moriya spin canting in the low-temperature tetragonal phase of $La_{2-x-y}Eu_ySr_xCuO_4$. *Phys. Rev. B* **70**, 214515 (2004).
49. Chen, X. et al. Charge density wave memory in a cuprate superconductor. *Nat. Commun.* **10**, 1435 (2019).
50. Lee, P. A. Amperean pairing and the pseudogap phase of cuprate superconductors. *Phys. Rev. X* **4**, 031017 (2014).
51. Berg, E. et al. Dynamical layer decoupling in a stripe-ordered high-T_c superconductor. *Phys. Rev. Lett.* **99**, 127003 (2007).
52. Yamada, K. et al. Doping dependence of the spatially modulated dynamical spin correlations and the superconducting-transition temperature in $La_{2-x}Sr_xCuO_4$. *Phys. Rev. B* **57**, 6165–6172 (1998).

AUTHOR CONTRIBUTIONS

H.M., T.Y., K.K., E.V., and P.D.J. performed the ARPES measurements. H.M., G.F., R.J.K., D.G.M., C.S.N., R. A.-E., T.A., I.K.R., E.S.B., and M.P.M.D. performed the X-ray measurements. Y.L., G.D.G., M.O., K.K., and N.M. grew the LSCO samples and characterized their transport properties. H.M., P.D.J., and M.P.M.D. analyzed the data. H.M., J.M.T., and M.P.M.D. wrote the paper.

COMPETING INTERESTS

The authors declare no competing interests.

ADDITIONAL INFORMATION

Supplementary information The online version contains supplementary material available at https://doi.org/10.1038/s41535-021-00327-4.

Correspondence and requests for materials should be addressed to H.M. or M.P.M.D.

Reprints and permission information is available at http://www.nature.com/reprints

Publisher's note Springer Nature remains neutral with regard to jurisdictional claims in published maps and institutional affiliations.